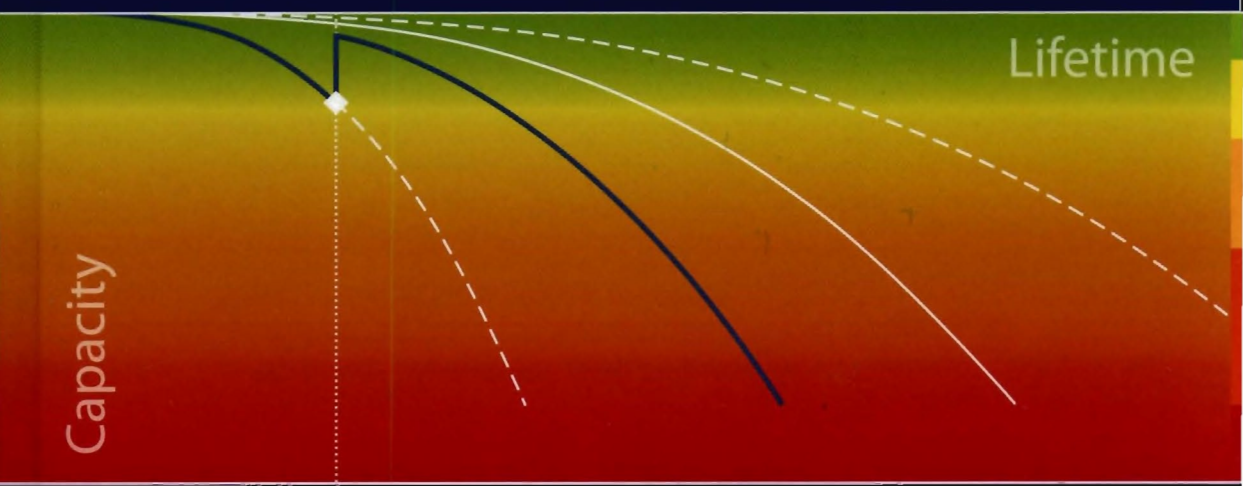
Helmut Wenzel
Coordinator



IRIS

Industrial Safety and Life Cycle Engineering

Technologies / Standards / Applications



Foreword

The activities involved in value chain based production have become more complex with an increasing amount of interdependencies, new technologies and materials that introduce new risks in an ever changing environment. At the same time our society has become more risk averse.

Until the start of the IRIS project in 2008 very little had been done to identify industrial risk factors in a systematic manner and risk assessment and management was largely characterized by its methodical diversity and fragmented approach. A shift to a new safety paradigm was therefore required in order to combine a more competitive, innovative and better risk informed industry with a safer society in mind.

This is exactly what IRIS has done in a systematic and structured way as duly illustrated through several large-scale demonstrations performed together with the industry. The demonstrations have been done to cover and visualize as many aspects of potential risks in the industry as possible, while keeping the users safety in mind, in order to better mitigate future risks.

The main concept of IRIS was to focus on diverse industrial sectors' main safety problems as well as to transform its requirements into integrated and knowledge-based safety technologies, standards and services. The IRIS Risk Paradigm is based on three steps: 1) System modelling; 2) Risk quantification; 3) Uncertainty estimation. It is a comprehensive generic framework for risk management with the use of several interconnected tools.

The demonstrations of the value of the IRIS Risk Paradigm have been very impressive indeed, some at a nearly unprecedented scale for an EU project (e.g. the destructive testing of an existing bridge on motorway A1 in Austria) and have led to new CEN standardization in the area. The data obtained through the demonstrations have led to results that can be applied globally and have yielded a technical competitive expertise in Europe that will have long lasting consequences for the industrial safety as well as public safety. This is exactly the kind of results that are targeted in the European Framework Programme for Research and provides the "reason d'etre" for its existence.

A project like IRIS is of course not possible without a team of world class experts in the field. In the case of IRIS this team consisted of 37 different partners from 14 countries in the European Union and 3 global partners as well as many more collaborators outside the project. All bound together and catalysed by the efficient and competent management from the Coordinator Johannes Kepler University Linz and VCE that enabled the team to deliver all the envisioned objectives. Every team has a champion. For the IRIS project this champion was Dr. Helmut Wenzel, without whom the project would never have even started and without whom it would not have been possible to achieve such a successful outcome. On behalf of DG RTD and the European Commission I would like to congratulate the consortium with such an excellent outcome and hope that the obtained results will have a lasting impact on our future.

On behalf of DG Research & Innovation, G2 – New Generation of Products
Jose-Lorenzo Valles, Head of Unit

Contents

1 *Helmut Wenzel*
Introduction to Industrial Safety and Life Cycle Engineering 7

2 *Demos Angelides, Yiannis Xenidis, Nick Bassiliades, Eva Loukogeorgaki, Alexandros Taflanidis, Dimitris Vrakas, Stella Arnaouti, Georgios Meditskos*
The Development of a New Framework for Managing Risks in the European Industry: The IRIS RISK PARADIGM 23

3 *Hiroshi Tanaka, Michaela Höllrigl-Binder, Helga Allmer, Helmut Wenzel*
The IRIS Damage Assessment Methodology 57

4 *Sebastian Thöns, Michael Havbro Faber, Werner Rücker*
Life Cycle Cost Optimized Monitoring Systems for Offshore Wind Turbine Structures 75

5 *Michael Döhler, Falk Hille, Laurent Mevel, Werner Rücker*
Estimation of Modal Parameters and their Uncertainty Bounds from Subspace-Based System Identification 91

6 *Gianluca Ruocci, Antonino Quattrone, Luca Zanotti Fragonara, Rosario Ceravolo, Alessandro De Stefano*
Experimental Testing of a Masonry Arch Bridge Model Subject to Increasing Level of Damage 107

7 *Andrea Enrico Del Grosso, Francesca Lanata, Paolo Basso*
SHM and Adaptivity Concepts in the Reduction of Risks Associated to Structural Failures 123

8 *Frank Barutzki, Christa Gurr-Beyer, Gereon Hinz, Klaus Kerkhof, Joachim Schwenkkros*
Identification and Reduction of Piping-Vibrations under Different Conditions 165

9 *Mengxi Wu*
Seepage and Slope Stability of Chinese Hydropower Dams 195

10 *Adrian Bekö, Peter Roško*
Testing of Stiff Shear Walls 213

11 *Barbara Theilen-Willige*
Remote Sensing and GIS Methods for the Safety of Industrial Facilities and Infrastructure in Europe 235

12 *David Schäfer*
EQvis – Advanced Seismic Loss Assessment and Risk Management Tool 257

13 *Jürgen Engelhardt, Herbert Friedmann*
IRIS Active Vibration Absorber (AVA) for Vibration Reduction at Piping Systems in Chemical Plants 279

14 *Bianca Weihnacht, Thomas Klesse, Robert Neubeck, Lars Schubert*
Monitoring of Hot Pipes at the Power Plant Neurath Using Guided Waves 293

15 *Dionysius M. Siringoringo, Tomonori Nagayama, Yozo Fujino, Di Su, Chondro Tandian, Hirotaka Miura*
Vibration Study and Application of Outlier Analysis to the S101 Bridge Full-Scale Destructive Testing 305

16 *Wolfgang Niemeier, Lars Johannes*
Worker Safety 331

17 *Josef Küng, Erik Sonnleitner, Reinhard Stumptner, Andreea Hilda Kosorus, Stefan Anderlik*
Utilizing Ontologies to Integrate Heterogeneous Decision Support Systems 353

18 *Ángel Faz, José A. Acosta, Dora M. Carmona, Sebla Kabas, Silvia Martínez-Martínez, Raúl Zornoza*
Reduction of Risk for Human and Ecosystems in Mine Tailing Properties 375

19 *Fritz Kopf, Adrian Bekö, David Schäfer, Johannes Pistrol, Michael Pietsch, Ludwig Rossbacher*
Assessment of the Soil-Structure-Interaction based on Dynamic Measurements 405

20 *Helmut Wenzel, Robert Veit-Egerer, Monika Widmann*
Case Study: S101 423

21 *Helmut Wenzel, Robert Veit-Egerer, Monika Widmann*
Life Cycle Analysis Applied to the New Jersey Case Study 443

22 *James Brownjohn*
Structural Health Monitoring of the Tamar Bridge 465

23 *Eleni Sakoumpenta, Panagiotis Panetsos, Manolis Haralabakis*
Bridge Maintenance Management System for Egnatia Motorway 491

24 *Helmut Wenzel, Robert Veit-Egerer, Tzu-Kang Lin, Zheng-Kuan Lee, Monika Widmann, Martin Stöger*
Application of IRIS Technologies on the Earthquake Damaged Chi Lu Cable-Stayed Bridge 515

25 *Jonathan Nuttall, Michael Hicks, Marti Lloret-Cabot*
Stochastic Approach to Slope Stability Analysis with In-Situ Data 527

26 *Robert Veit-Egerer, Monika Widmann, Helmut Wenzel*
Monitoring and Evaluation of an Arch Bridge Affected by the Blasting of the Adjacent Highway Bridge 539

27 *Robert Veit-Egerer, Helmut Wenzel, Rui Lima*
Ageing Behaviour of Structural Components for Integrated Lifetime Assessment & Asset Management 553

28 *Alexander Iliev, Marin Kostov, Anton Andonov*
An Approach for Reliability Based Control of Post-Tensioned Containment Structure 567

29 *Yogita Mahendra Parulekar, Rohit Rastogi, G. Rami Reddy, Vivek Bhasin, Keshav Krishna Vaze*
Assessing Safety of Shear Walls: an Experimental, Analytical and Probabilistic Study 589

30 *Barbara Theilen-Willige, Helmut Wenzel, Laszlo Weisz, Antal Papp, Gábor Sárossy, Imre Árvai*
IRIS Demonstration – Hungary 2011 611

31 Authors & Contributors 630

32 Index 649

Acknowledgements

The success of the IRIS project has many fathers. Without the vision of Dr. George Katalagarianakis who supported ETPIS and the Industrial Safety topic and carefully organized the process IRIS would not exist. Søren Bowadt of the European Commission has been very helpful and patient in overcoming administrative problems with partnership verification and the fact that an SME intended to lead such a large project. The officer Antonio Cipollaro and the reviewer Michalis Loupis accompanied the project with understanding and advice.

Without the funding by the European Commission under Agreement number CP-IP 213968-2 this development combining deep basic research with real on-site requirements would not have been possible. The IRIS Project was lucky to receive the right size of support and funding for this important subject. This framework has been rated excellent by "jealous" researchers worldwide.

Special thanks go to the Johann Kepler University Linz, which in order to overcome the administrative deadlock by taking over the administrative coordination, have saved the project from collapse before kick-off. This was realized under the burden of having to trust in private management practice. The frictionless performance of coordination under these difficult circumstances has been highly appreciated.

Finally, the consortium has to thank all the excellent individuals that contributed to the success of the project. Unprecedented engagement, in combination with the clear determination to follow the rules of the project's steering committee, allowed targeted development work and contributed the required pieces to the IRIS technology puzzle. A comprehensive list of authors is provided in chapter 31.

We hope that the trust given to the consortium is awarded by the achievements made and the numerous applications in industry, not only in Europe but worldwide.

1

Introduction to Industrial Safety and Life Cycle Engineering

Author:
Helmut Wenzel



1-1 Introduction

European industries are challenged by competition from low cost economies and ageing problems. Innovative approaches are required to harmonize competitiveness with end of design life issues as well as safety concerns. These are directly addressed by the research and development work presented here.

Coordinated industrial research enables the reduction of fatalities and injuries and increases the competitiveness keeping key industrial jobs in Europe.

The Consortium conducting the large European Collaborative Research Project IRIS (CP-IP 213968-2) was driven by the motivation that current practices in risk assessment and management for industrial systems are characterized by their methodical diversity and fragmented approaches. In retrospect these risk and safety paradigms resulted from diverse industries driven and limited by available knowledge and technologies. The need for a change based on industrial research and development work has been identified. This formed the basis for IRIS.

At present the European industry recognizes their obligation to reconsider risk and safety policies, having a more competitive industry and more risk informed and innovative accepting society in vision. The IRIS project has identified, quantified and mitigated existing and emerging risks to create societal cost benefits, to increase industrial safety and to reduce impact on human health and environment. The project was led and driven by industry consolidating and generating knowledge and technologies which enable the integration of new safety concepts related to technical, human, organizational and cultural aspects. More than 300 researchers participated in an industrial consortium that represented over one million workers.

IRIS focused on diverse industrial sectors to transform their specific requirements into integrated and knowledge based safety technologies, standards and services. This book displays a relevant portion of the results produced by IRIS between 2008 and 2012.

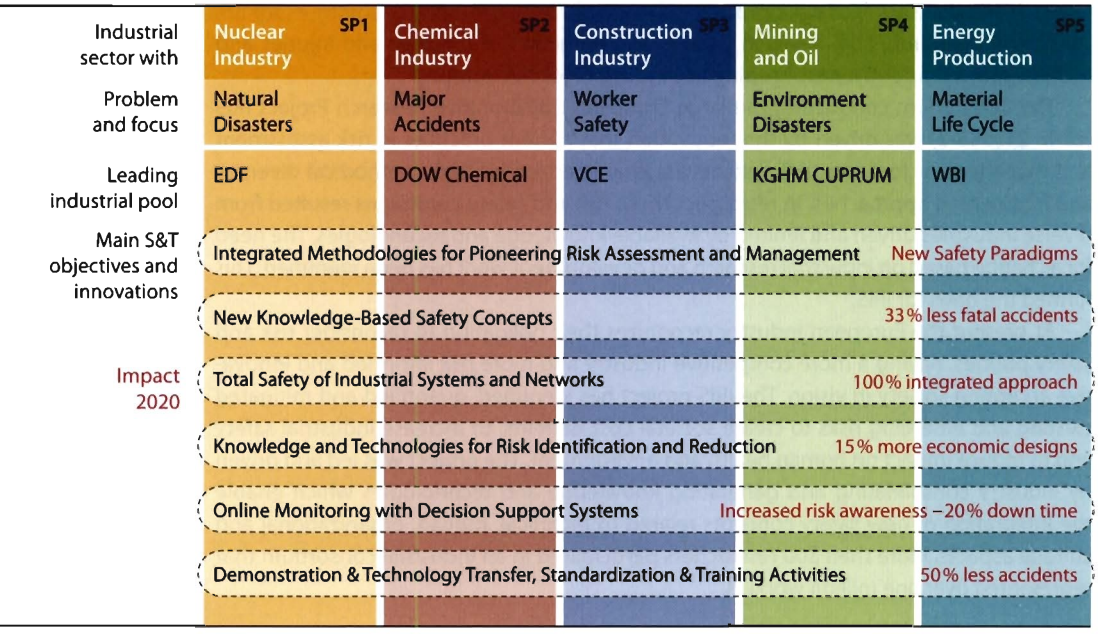
An overview of the conception for the various industries and the expected impact is given in F.1-1.

1-2 Success Factors and Historical Background

Large collaborative research projects represent an exceptional management challenge. The usual success factors teaming and participation have to be coached actively. It needs the right team as well as it needs the team right. IRIS was able to select among the top researchers and institutions in this domain and it was important to allow everyone the suitable position within the team.

The desire to get participation right and to achieve the right participation was satisfied as well. A core group of well experienced elder experts formed the executive board and a large group of selected hungry young researchers have been motivated to give their best. The fact that the coach has been an expert insider as well enabled the desired top performance. It shall be particularly acknowledged that this did not happen by accident but was enabled by trust and understanding between the main stakeholders, the European Commission (funding agency), industry (organized through a targeted net-

Integration of industries and objectives F.1-1



work) and the research community identified through well prepared work programmes in targeted research frameworks.

The transition from analogue to digital concepts opened a wide range of opportunities for innovation. The framework programmes of the European Commission appreciated these opportunities and called for proposals in this domain regularly. Partners of the IRIS consortium performed a number of successful projects in various constellations which have been ranked among the top projects in the EC's NMP programmes since 1995.

// The HARIS project (BRPR-CT95-0072) coordinated by VCE in the Brite-EuRam Programme developed innovative isolation systems for high-speed railways. It led to a multi-billion contract for the Taiwan high-speed rail project led by European industry.
// The CasCo project (GRD1-1999-11095) followed concentrating on vibration and noise emission on railway bridges and tunnels. Monitoring became part of the procedure.
// The IMAC project (G1RD-CT-2000-00460) developed an innovative methodology to assess cables which has led to a European dominance in this domain. The methodology is now applied worldwide.

As a consequence of these successful individual projects in the 5th Framework Programme the European Commission decided to fund a targeted network on monitoring assessment and control of structures.

// The SAMCO Network (FP5 G1RT-CT-2001-05040) enabled the identification and consolidation of the respective community and issued the first standards in this domain. It has been extended successfully to global scale with the SAMCO international supplement. The resulting publications "Ambient Vibration Monitoring" and "Health Monitoring of Bridges" are mainly based on SAMCO results. They comprise bestsellers in the very competitive international technical publication market.
// The project SAFEPIPES (Contract no.: 003766) in the 6th Framework Programme focused on the implementation of the technologies to industrial pipelines. A wide industrial participation has been achieved. The door to key industries was opened.

Thanks to the foresight of the European Commission with the backup of the demand of an ageing European industry, proposals for projects in the industrial safety domain have been called in the early stage of the 7th Framework Programme. The consortium of 38 partners performed the project from late 2008 till mid-2012. Details are sustainably kept under www.vce.at/iris for information and download.

IRIS consortium and core competences T.1-1

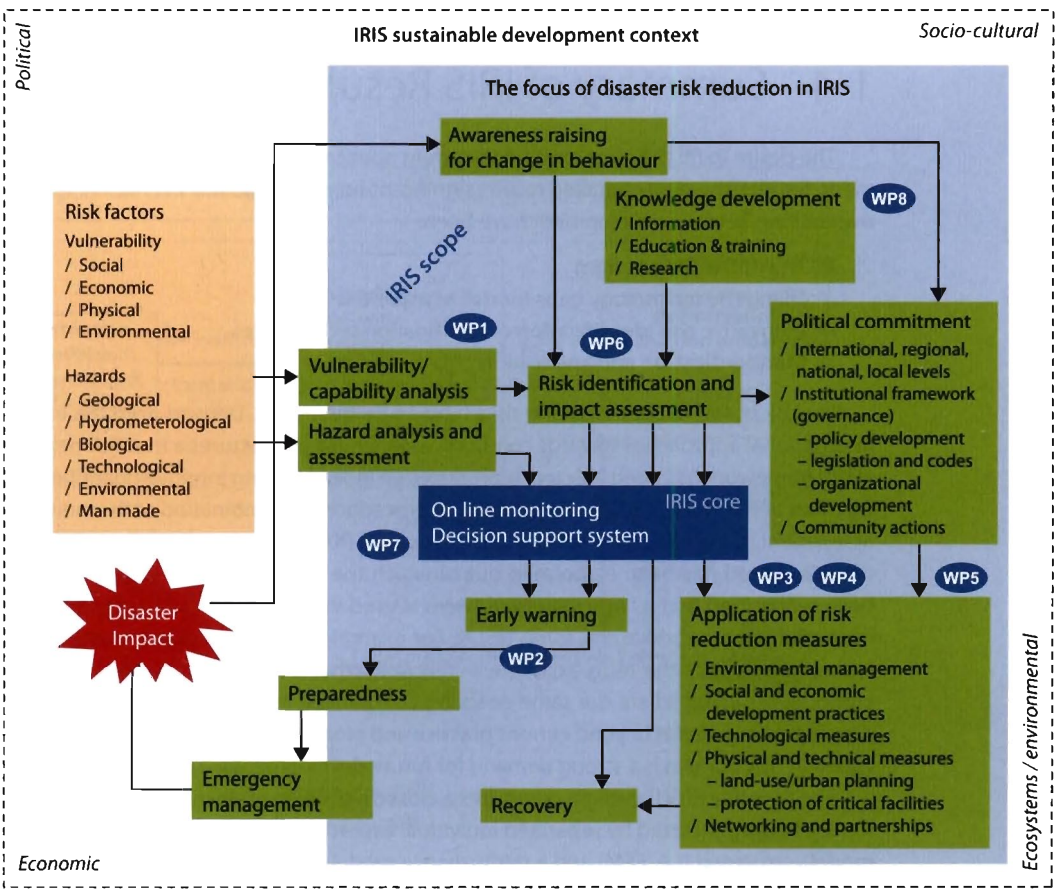
No.	Organizwation name	Org. type	Role in IRIS	Country
1 C	Johannes Kepler University Linz (JKU)	RES	Financial coordinator, decision support systems, cyber infrastructure	Austria
2	EDF	IND	World largest nuclear power operator, natural hazard assessment, safety	France
3	DOW Deutschland	IND	Safety in chemical industry	Germany
4	EGNATIA	IND	Management and supervision, construction safety	Greece
5	KGHM Cuprum	SME	Mining control, environmental monitoring	Poland
6	RWE	IND	Energy production issues, life-time estimation	Germany
7	WBI	SME	Standardization, safety conception NPPs	Germany
8	USTUTT	RES Inst.	Testing, evaluation, safety assessment	Germany
9	CEA	RES Inst.	Nuclear laboratory, proliferation issues	France
10	JRC ELSA Laboratory	RES Inst.	Structural safety and security	EU
11	INRIA	RES Inst.	Pattern recognition	France
12	POLITO	RES	Embedded sensor development, monitoring	Italy
14	TU Braunschweig (TUB)	RES	Galileo, tracking of workers	Germany
15	AUTH	RES	Risk and safety concept	Greece
16	MEGA Risk	IND	Operational risk management systems	Germany
17	BBT	IND	Tunnel construction, monitoring of workers	Italy, Austria
18	Kozloduy NPP	IND	New member state NPP	Bulgaria
19	ICEMENERG	RES Inst.	Energy research and development, environmental factors	Romania
20	RISKENG	IND	Risk engineering	Bulgaria
21	CTU	RES	Cyber infrastructure	Czech R.
22	DTCDM	Stake-holder	National civil protection	Hungary
23	ERF	SME	Online monitoring	Germany
24	BAGF	SME	Remote sensing technology	Germany
25	BAM	RES Inst.	Testing of infrastructure	Germany
27	Aplica	SME	Computational fluid dynamics, engineering	Austria
28	VR Vis	RES	Virtual reality and visualization	Austria
29	University Genoa	RES	Permanent monitoring	Italy
30	University of Manchester	RES	Geotechnical research	UK
31	University of Cartagena	RES	Monitoring of mining activities	Spain
32	TU Lulea	RES	LIDAR technology for vulnerability assessment	Sweden
33	Fraunhofer	RES	Guided waves	Germany
34	CVS	SME	Safety of industrial components	Russia
35	BARC	RES	Reactor safety – health, safety and environment	India
36	CAS	RES	Micro scale mechanics and microsystems mechanics	China
37	University of Shefflied	RES	Damage detection, assessment, localization	UK
38	VCE	SME	Technical coordinator, online monitoring, decision support system	Austria
39	TU Delft	RES	Geotechnical research	Netherlands

1-3 Main S&T Objectives of the IRIS Project

For the success of European industry and the benefit of European society the following objectives, which are to be integrated into a sustainable development context, have been identified:

// Integrated methodologies for pioneering risk assessment and management to combine practical operation with risk management.
// New knowledge based safety concepts through refinement of the risk identification, assessment and control processes to continuously improve economics obeying safety concerns.
// Total safety of industrial systems and networks to understand systemic interdependencies and identification of risks in the increasing complex value chain based production activities.

Project context with reasonable allocation of Work Packages (integration) F.1-2



// Knowledge and technologies for risk identification and reduction to consider the re-assessment of exposure and vulnerability of environment, society, industry and to mitigate the impact of natural, technical and man-made hazards.
// Online monitoring and decision support systems to enable continuous risk assessment by online monitoring of the interactions in the industrial systems during their life cycle.
// Pattern recognition in signal processing to identify system parameters and attributes characterizing evolving damages in materials and systems. This includes the transfer from parameters to key performance indicators (KPIs).
// Demonstration, technology transfer, standardization and training activities. The intention has been to apply the developments directly in industry and to standardize successful technologies.

The figure graphically represents the flow and inter-dependencies of activities and highlights the IRIS scope within this wider context. Around the IRIS core comprising the online monitoring and decision support system the eight work packages (WP1–WP8) are situated contributing to the various activities.

1-4 Summary of IRIS Results

The desire to fill the gaps existing in current applications has driven the IRIS development. Besides the many detailed results significant breakthrough has been achieved. The overarching fields of development have been:

// The **IRIS Risk Paradigm**
// Filling the technology gaps for **risk assessment**
// Innovative **risk identification** and mitigation technologies
// **Standardization** and application

For risk based decision making risks have to be quantified. Derived from the various international approaches towards condition assessment of structures a multi-dimensional risk framework has been erected. It produces an index allowing intuitive quantified recognition of risk situations. The quantification procedure is a combination of the individual assessment of identified key performance indicators (KPIs). A harmonized glossary for the terms involved has been elaborated out of which the risk formulation is derived. It has been recognized that a large variety of terms is used in this domain, which nevertheless, in combination, produce the same result. For example the hazard domain used in IRIS is described under the term exposure in relevant other elaborations. Nevertheless, the components involved are the same enabling comparable results. In this respect the IRIS development goes far beyond current practice and pioneers risk quantification. Harmonization in this domain is a strong demand for future development work.

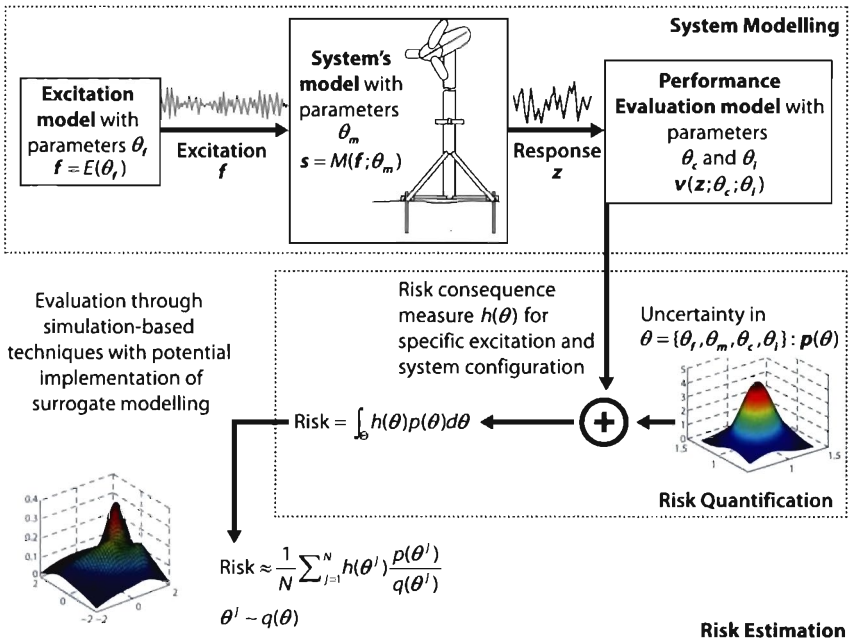
The new IRIS Risk Paradigm comprises a closed definition of the elements of risks. The input usually generated by separated individual expertise is combined to excitation (load model), structural (i. e. FEM) and a performance model introducing time as an additional

dimension. The involved parameters come along with specific uncertainties which are summarized in logic combinations. The formulation is open to any kind of input for which a model can be erected knowing the boundaries of uncertainties. In a normalization process the result can be fitted into a commonly used colour scheme. Using the degradation law standardized in the project prediction on development over time is feasible providing early warning and defining the remaining time till intervention. By the variation of individual parameters, sensitivity studies can be performed as a basis for decision making. The methodologies for comparative risk assessment (CRA) are directly supported by these results and allow the introduction of an innovative risk management that fits into the ISO 31 000 framework.

It is recognised that in practice the excessive density of regulations seems to exclude such an innovative approach even so the usefulness and charm is appreciated by all players involved. To overcome this difficulty a first step towards standardization of the degradation law has been performed within the project successfully in a CEN Workshop (CEN WS63).

The subsequent figure gives a graphic representation of the new IRIS Risk Paradigm with its models and uncertainties involved. Details are described in chapter two of this publication.

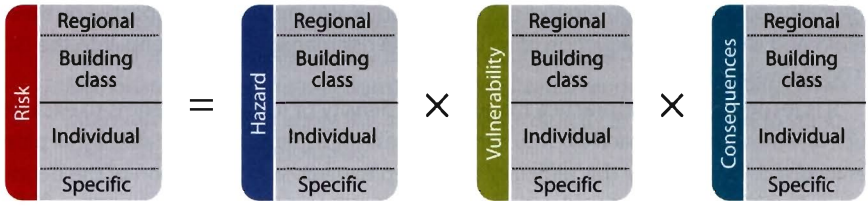
Concept of the new IRIS Risk Paradigm F.1-3



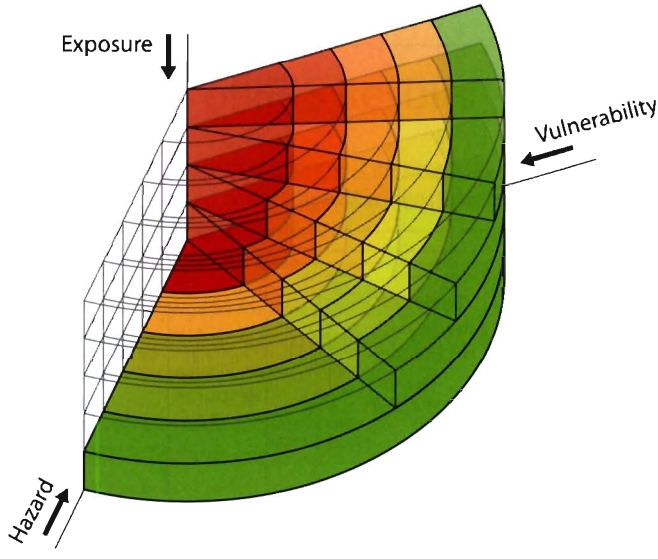
Risk is described in a simple formulation as a combination of hazard, vulnerability and consequences. The individual information used is targeted towards these elements.

The determination of the final risk index is symbolized by the following figure showing how the individual results of the risk components led to an individual risk index.

Elements of risk F.1-4



Risk quantification scheme F.1-5



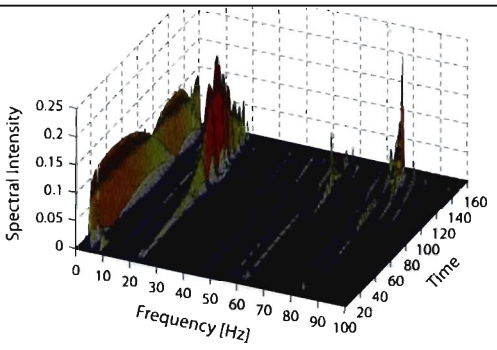
It has been found during the course of this project that the individual industries require tailored applications for their individual cases. This is reflected in the selection of parameters that are finally used as key performance indicators and in the weighting of issues in the individual complex procedure. For this reason a mathematical formulation (one size fits all) is not feasible. An individual element consisting of engineering input and sometimes subjective expertise remains necessary. Nevertheless, this fact gives the process managers and operators sufficient control over the process to satisfy the definition of their experience and steering role.

1-5 Individual Results

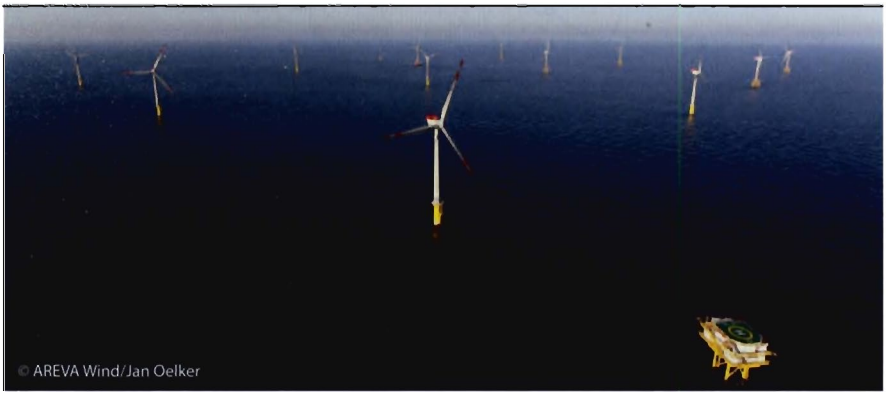
A selection of individual project results has been made enabling understanding the features and background of the technology highlighting remarkable achievements.

Chapter 2: describes the new IRIS Risk Paradigm. The previously fragmented way creating problems with interfaces and quantification has been replaced by a consistent methodology providing a conceptual framework for harmonized risk assessment and quantification.

Chapter 3: describes the IRIS damage assessment methodology, a major desire of the SHM community. The idea that the condition of a structure is represented in the character of its dynamic system response converts monitoring data into Life Cycle Information.



Chapter 4: describes the application to Life Cycle Cost optimized monitoring systems for offshore wind turbine structures. The efficient operation of offshore wind parks based on monitoring results showing Life Cycle Cost benefit analysis is addressed.

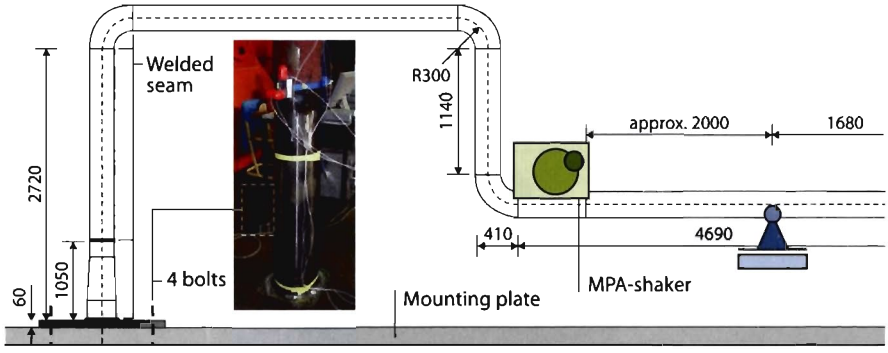


Chapter 5: addresses the complex identification of linear time invariance by output only measurement under consideration of statistical uncertainty. The application to enlarge full scale field test, S101 bridge case, is used for verification.

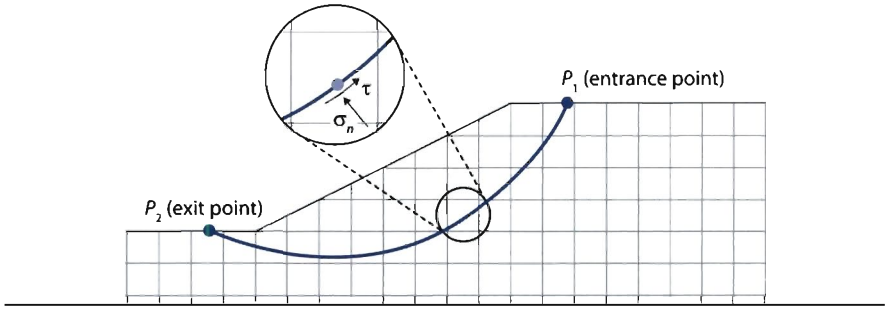
Chapter 6: describes the application of the IRIS Risk Paradigm to experimental testing of a masonry arch bridge model subject to damage. The proof of concept has successfully been given in this laboratory test.

Chapter 7: provides an overview on SHM and adaptivity concepts for risk reduction in structures. A conclusive solution for the European transportation infrastructure is presented.

Chapter 8: concentrates on integrity assessment, identification and reduction of pipe vibrations in industry. Very specific applications in the chemical, energy and nuclear industry are addressed.



Chapter 9: contributes with stability problems of large Chinese hydropower dams. It concentrates on sub-structure issues with high uncertainties involved. It represents the Chinese contribution to the IRIS project.

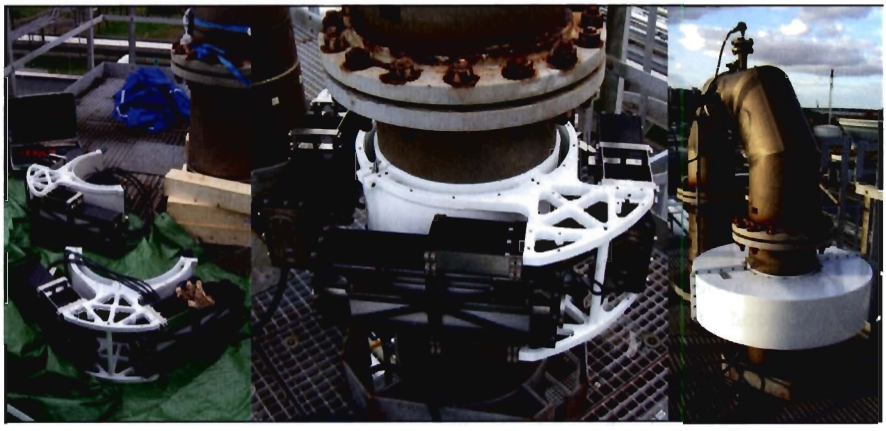


Chapter 10: Lessons learned from the earthquakes in Kashiwazaki (2007) and Fukushima (2011) revealed insufficient knowledge in actual shear behaviour of thick concrete walls. A comprehensive monitoring and testing campaign has been designed and performed at JRC in Ispra.

Chapter 11: describes a comprehensive set of tools that are used in risk management based on remote sensing technologies embedded in a tool box featuring a GIS environment interface for practical handling.

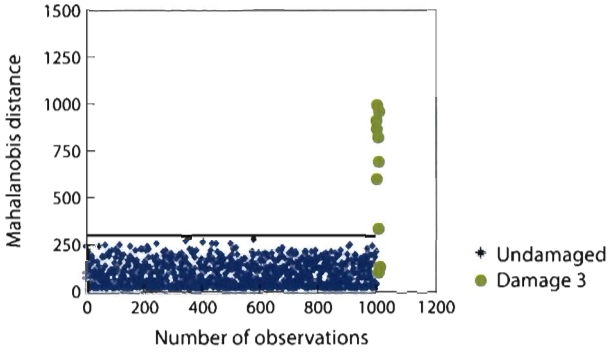
Chapter 12: describes the developed IT-platform EQvis (European Earthquake Visualization System) which has been made fit for industrial application and multi-risk assessment. The Open source software platform is freely available for download including a comprehensive tutorial.

Chapter 13: describes the IRIS active vibration absorber (AVA) and its application to a vibrating reactor system in a European chemical plant.

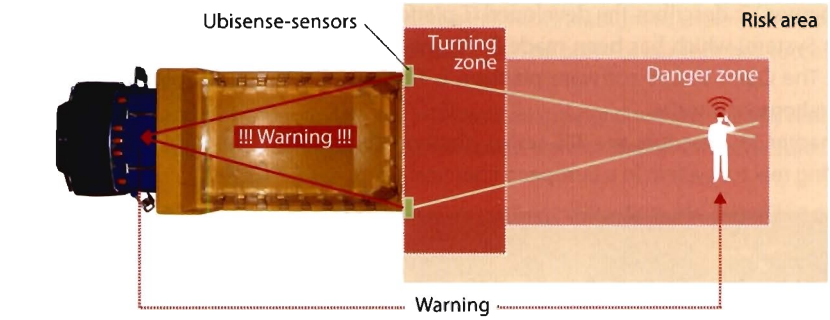


Chapter 14: informs about the unique application of monitoring of hot pipes (up to 700 °C) at a power plant in operation. Besides the evaluation technology new sensors for hot pipe application have been developed.

Chapter 15: describes the application of an outlier analysis to the S101 Bridge full scale destructive test. This contribution of the University of Tokyo provides a very welcome proof of concept.



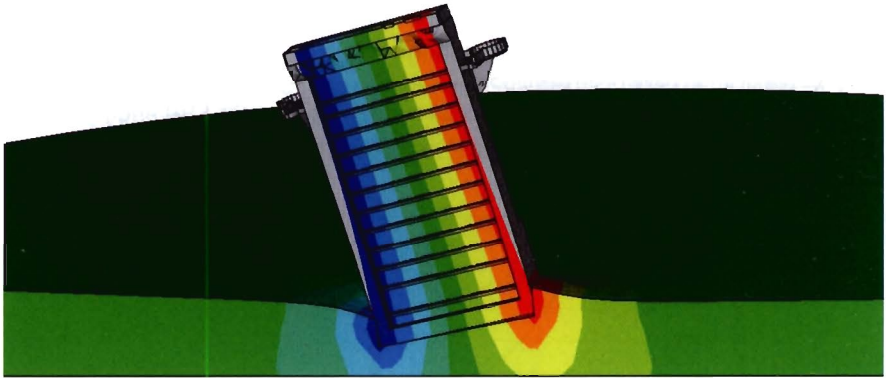
Chapter 16: addresses various aspects of worker safety in the construction industry. It comprises the management of risks at scaffolds as well as worker allocation and warning in situations with the presence of moving vehicles.



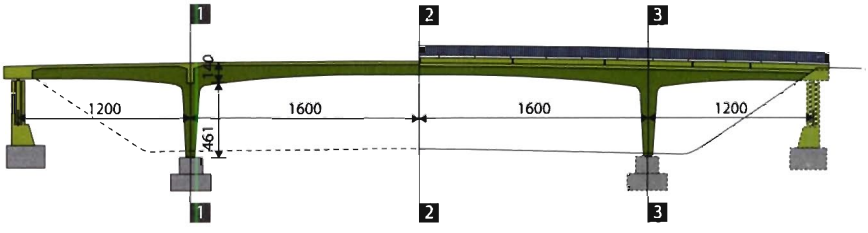
Chapter 17: describes the ontologies to integrate heterogeneous decision support systems into the process. It summarizes part of the IT-development performed within the IRIS project.

Chapter 18: describes a specific application of risk reduction in human and ecosystems in historic mine tailing ponds in Spain.

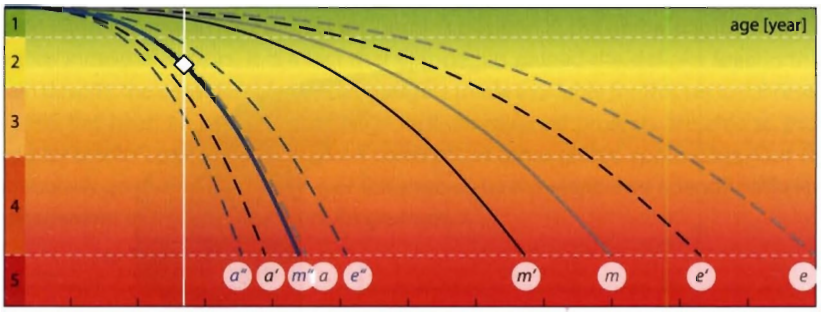
Chapter 19: comprises the assessment of the soil-structure interaction based on the dynamic monitoring methodologies applied in the project. A unique experiment has been performed.



Chapter 20: The opportunity for comprehensive, destructive testing of an existing bridge in Austria (S101) on motorway A1 has been taken to collect well proven damage data. The dataset has been extensively used by many research teams.



Chapter 21: reports about the results of a global harmonization activity at the New Jersey Bridge Study performed by 18 parties from IRIS, America, China, Japan and Korea. The new IRIS Life Cycle Approach has been demonstrated successfully.



Remaining Life
16

Costs
Retrofit
476,040 €
631,753 $

Replacement
11,901,000 €
15,794,000 $

Chapter 22: describes the application of the IRIS technologies to the Tamar Bridge in the United Kingdom where through an extensive monitoring campaign the feasibility of reducing uncertainties in key structures has been demonstrated.

Chapter 23: shows a major demonstration case at the Egnatia Motorway in Greece. The combination of a landslide with an earthquake hazard is successfully demonstrated.

Chapter 24: describes the demonstration of IRIS technologies to an earthquake damaged bridge in Taiwan in collaboration with the National Center for Research on Earthquake Engineering (NCREE) in Taipei, Taiwan, Republic of China. This has been a very successful proof of concept.

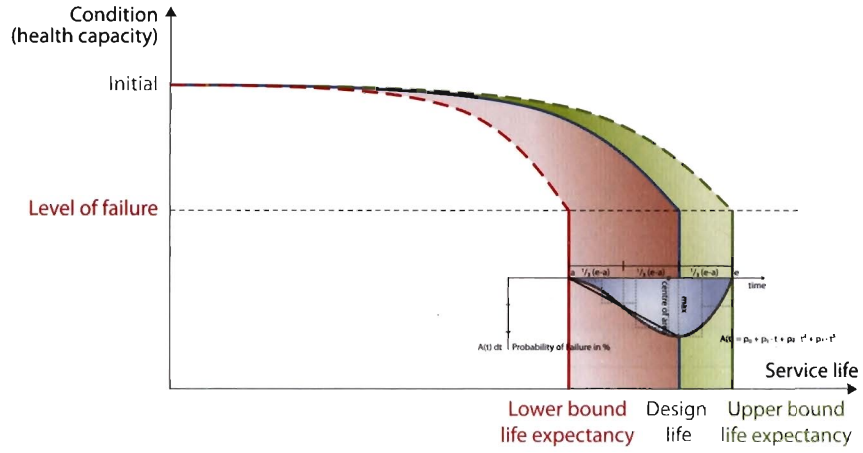


Chapter 25: concentrates on the stochastic approach to slope stability analysis with in-situ data where inherent heterogeneous geo materials are properly modelled.

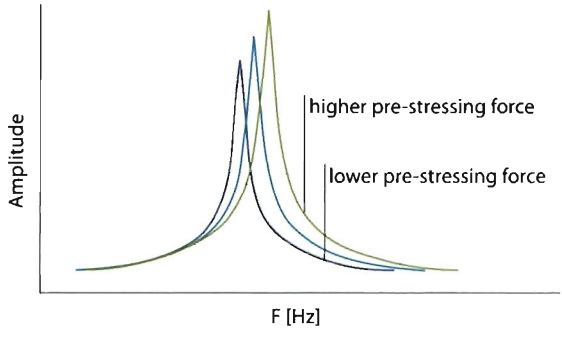
Chapter 26: reports about a unique application of the IRIS Life Cycle Technology to the blast of two arch bridges within the Austrian motorway system.

Chapter 27: represents the results of the CEN-workshop 63 "Condition, determination for integrated lifetime assessment of constructed facilities and components". The generic degradation law developed within IRIS has been standardized. It serves to determine the

design life or the residual life of existing structures and helps to assess the real degradation process enabling the development of optimized maintenance plans.



Chapter 28: describes the application of the IRIS technology for reliability bases control of post-tension containment structures exemplarily executed at the Kozloduy Nuclear Power Plant in Bulgaria. This is a worldwide unique industrial demonstration that confirmed the applicability of innovative assessment methods in strongly regulated sectors. Further applications for the benefit of the European energy policy and society are expected.



Chapter 29: The opportunity to collaborate on global scale was realized in the collaboration with the partners from India. A series of tests has been performed with vice versa participation and comparison of test results.

Chapter 30: describes the results of the large IRIS demonstration in Hungary in 2011. In an exercise comprising over 500 participants the feasibility of application of the methodology to complex disaster management scenarios including life images from targeted satellites has been demonstrated.

Last but not least short CVs of the researchers involved are presented.

It is acknowledged that without the generous support of the European Commission within the NMP programme of the 7th Framework Programme research on this level of size and complexity would not have been feasible. IRIS is an excellent example how this combined effort can make huge impact on Europe's position in the global competition within various industrial sectors. It is a fact that Europe has gained the definite lead in this domain despite the considerably smaller budgets made available for this sectorial research.

IRIS has been an example that large well-coordinated projects are able to produce superior results compared to previous concepts or other global approaches. Our thanks particularly go to the wise steering of this process by the respective scientific officers and management of the 7th Framework Programme.

1-6 Open Issues and Recommendations for Further Development

Every answer to a scientific question usually comes along with another question and ideas for further improvement. It therefore becomes essential to keep the momentum of such a successful development and invest into further improvement. What needs to be done can be highlighted in a few sentences:

// The **IT-component** has been considerably underrepresented in the IRIS Project. A joint ICT-NMP project would be necessary in order to transform the theoretical results into a generally applicable IT-solution.

// The individual methodologies developed within the IRIS project are based on very specific cases available to the consortium. Further **generalization and extension to other cases** is desirable. This includes the introduction of the results of other European projects which could usefully contribute to an improvement of the technology.

// Further effort has to be put into **standardization** particularly in the risk quantification domain. The various heterogeneous approaches have to be harmonized and standardized subsequently.

// There is a wide open field for further **damage detection technologies**, sophisticated concepts for monitoring and assessment and harmonization in data management and elaboration.

// There are still considerable gaps in **Life Cycle Engineering** which has been introduced to this process recently. Future work will have to concentrate on innovative methodologies and approaches towards an adaptive sustainable application.

Finally it has to be mentioned that the IRIS work mainly addresses the industrial concerns directly. Efforts to support the underlying political and juristic environment are important as well. The sector of consequences has to be treated with priority including a wide range of social sciences.

2

The Development of a New Framework for Managing Risks in the European Industry: The IRIS RISK PARADIGM

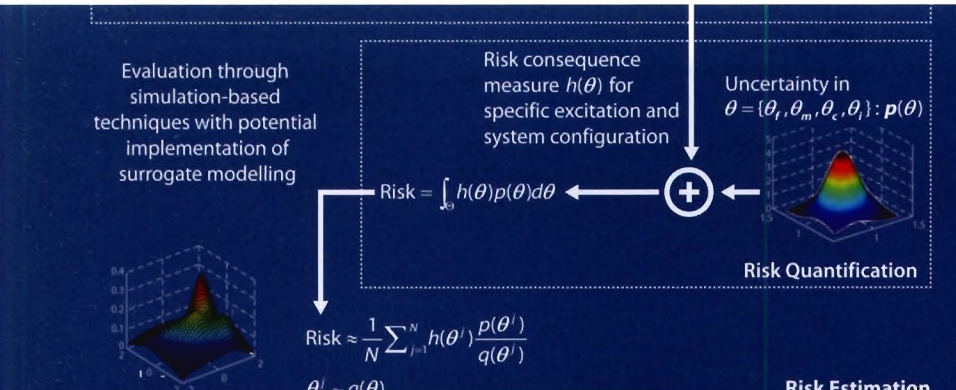
Authors:
Demos Angelides
Yiannis Xenidis
Nick Bassiliades
Eva Loukogeorgaki
Alexandros Taflanidis
Dimitris Vrakas
Stella Arnaouti
Georgios Meditskos

Motivation

Risk assessment has been performed in a fragmented way creating problems with interfaces and quantification. A consistent methodology for risk quantification is required.

Main Results

The new IRIS Risk Paradigm provides a conceptual framework for consistent harmonized risk assessment and quantification.



2-1 Introduction

Risk management approaches adopted in the European industries are fragmented, thus representing a roadblock in the establishment of an Integrated European Industrial Risk Reduction System that would allow for:

a) greater synergies between the industries,
b) reduction of the production-cost of the European industrial product, and
c) advanced safety conditions and standards for production, maintenance and use of the industrial product.

The IRIS Risk Paradigm was conceived as an idea aiming to respond to the demand of a holistic approach for managing risks in the European industry, in order to overcome the above mentioned fragmentation and its consequent constraints. By the term "holistic", a comprehensive theoretical and application tool is defined that would assist risk managers in their job at all steps of the risk management process. Given that such an approach is innovative and first-of-a-kind, it comprises a paradigm, i. e. a typical example or pattern to follow that describes distinct concepts.

The IRIS Risk Paradigm evolved from a conceptual framework to a fully-developed approach and tool for risk management in the European industry. The methodological approach that was applied was deductive; starting from a theoretical point of view and investigating notions and concepts with application to several knowledge fields, the IRIS Risk Paradigm was developed through and tested to specific case studies, which are presented in this chapter. Through a recursive process the Risk Paradigm was continuously elaborated with regard to its core components, namely the Risk Identification Method (RIM), the Risk Assessment Tool (RAT), the Risk Monitoring and Control System (RIMOCOS), and the Risk Prevention and Mitigation Strategy (RIPREMIS). All these components that constitute stand-alone tools and best practices for the respective processes in risk management (i. e. identification, assessment, monitoring and response) are unified to the IRIS Risk Portal, which is an effective web-reside, computational tool that can be accessed directly by practitioners and individuals who face real, complex and demanding risk problems across the various industry sectors.

This chapter is structured in five sections to present the IRIS Risk Paradigm, which, in order of appearance, refer to the following issues:

a) the paradigm's concept and architecture,
b) the Risk Assessment Tool,
c) the application case studies,
d) the Risk Monitoring and Control System and the Risk Prevention and Mitigation Strategy, and
e) the IRIS Risk Knowledge Portal.

2-2 The Concept and Architecture of the Risk Paradigm

The IRIS Risk Paradigm is a comprehensive framework acting as an interface that allows the processing of risk management by the use of several interconnected modules. These modules, which consist of stand-alone frameworks, methodologies or tools that are integrated in the context of the paradigm are:

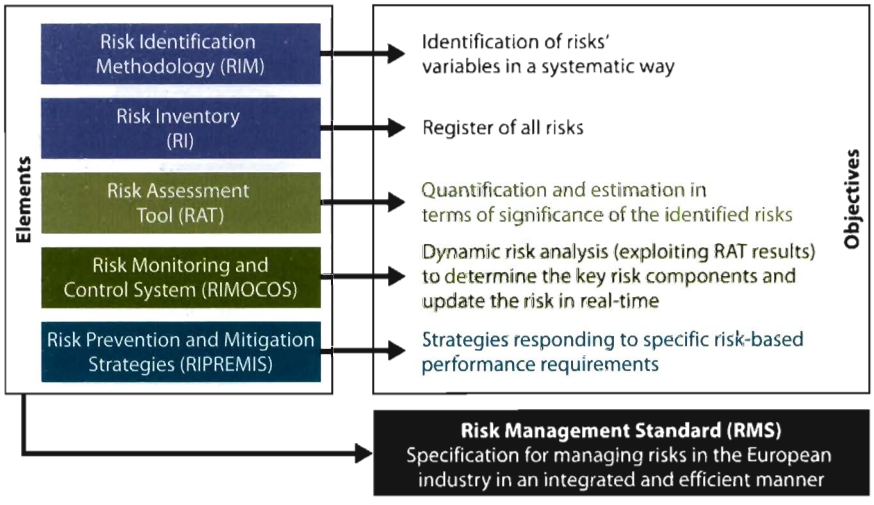
Risk Identification Methodology (RIM).

A methodology that introduces a systematic way to identify risk factors (i.e., contributors to risk), risk components and attributes (i.e., constituents and exhibitors of risks) and risk occurrence mechanisms (i.e., modes of risk occurrence). The methodology is applicable to various industries and cases. Therefore, the application of the paradigm can constitute a common approach for European industries to perceive and identify risks.

Risk Inventory (RI).

The inventory includes risks of different nature (e.g. technical, financial, legal, etc.) generally applied in all industries. The inventory facilitates the risk analysis in practice because it minimizes the extent of the risk identification process for the risk analyst. Specifically, a list of generally applied risks in all cases readily available for the risk analyst allows the analyst to focus only on the identification of the case-specific risks. The RI constitutes a generally applied list of risks for all European industries that sets a minimum level of risk management requirements in European industrial processes and products.

IRIS Risk Paradigm elements and their objectives F.2-1



Risk Assessment Tool (RAT).

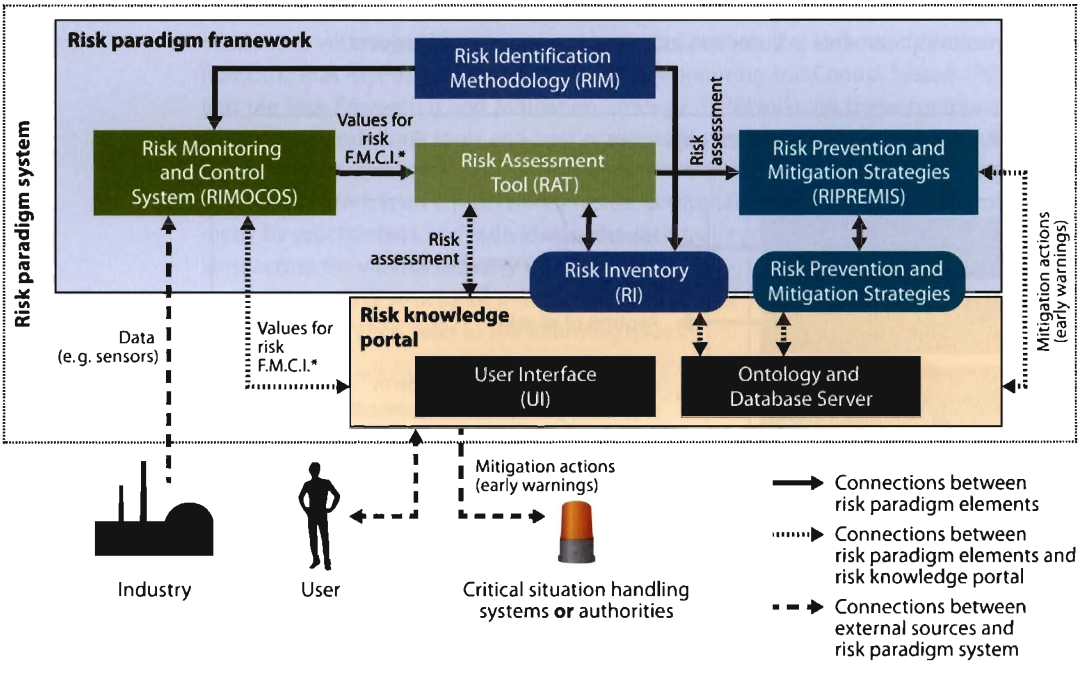
The tool quantifies and ranks the risks in terms of significance identified after analyzing the input through appropriate algorithms. These algorithms provide ready-to-use results for risk communication and decision-making (an example of a type of results is a threshold for early warning systems). The tool addresses the elaboration of data and information drawn through a real-time monitoring and control system to allow for a dynamic risk analysis, i.e. a real-time assessment and response to risks. The tool is applicable to European industries to assess risks and produce results to decide upon various performance quantifications, including expected operation conditions, reliability or Life Cycle Cost, etc.

Risk Monitoring and Control System (RIMOCOS).

In order for RAT to be able to allow a dynamic risk analysis, a prototype of a risk monitoring and control system is timely required. RIMOCOS is a system that responds to this requirement and is defined in terms of: a) elements (e.g. what is monitored), b) devices (e.g. types of sensors), c) networking (e.g. plan of sensor arrangements) and d) methodology for combined analysis of data from networking of sensors.

This integrated system: a) broadens the level and enhances the quality of conclusions of risk monitoring and control of several industries and b) allows the refinement of existing devices to extend their field of application.

IRIS Risk Paradigm System: Architecture of the IRIS Risk Paradigm F.2-2



* F: Factor, M: Mechanisms, C: Components, I: Impacts

Risk Prevention and Mitigation Strategy (RIPREMIS).

The strategy is tailored to the output of RAT and RIMOCOS to achieve compliance with real situations and best relate to performance requirements. In this way, the European industry is equipped with a risk prevention and mitigation strategy that is not static but, instead, responds to specific risk-based performance requirements.

Risk Management Standard for the European industry (RMS).

The standard describes comprehensively and explicitly the risk paradigm in a manner of best practice of application for the European industries.

The modules of the IRIS Risk Paradigm and their individual operation and contribution to the overall framework are schematically presented in F.2-1. It is, though, the architecture of the IRIS Risk Paradigm, as presented in F.2-2 that allows for the framework to fulfil the determined goals; this architecture is based on several interconnections (synergies) between the several modules and their connections with the Risk Knowledge Portal, i.e. a web based platform that constitutes the User Interface (UI) for the Risk Paradigm System. The variables Factor, Mechanism, Component and Impact included in F.2-2 are defined in T.2-1, which presents the application of the risk identification process on a specific case study.

2-3 The IRIS Risk Assessment Tool (RAT)

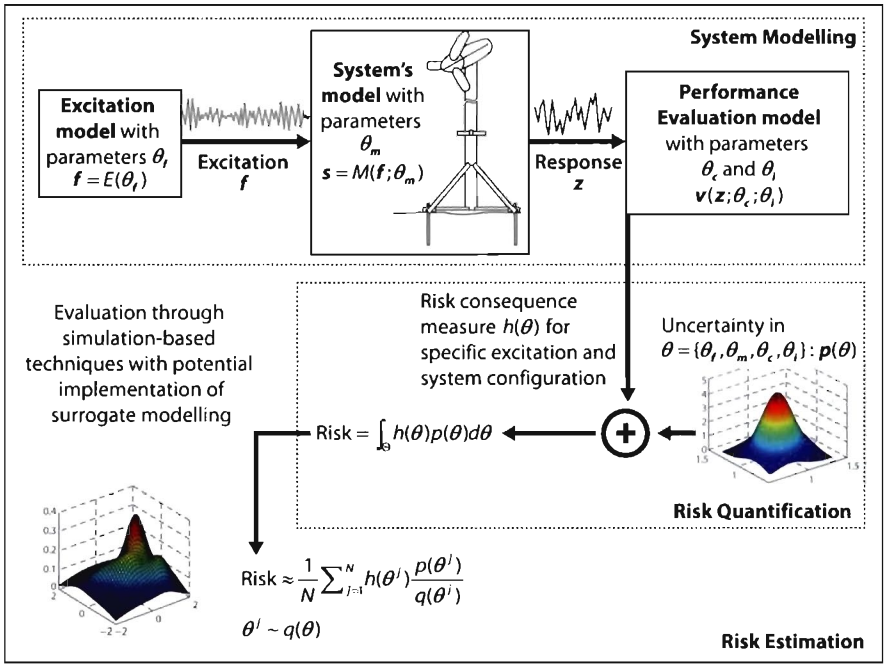
The Risk Assessment Tool (RAT) constitutes a core module of the IRIS Risk Paradigm in terms of significance and contribution to the overall risk management framework. It follows the risk identification methodology and assesses in a quantified manner the significance of the identified risks.

The implementation of RAT is established via the following three steps, which are also illustrated in F.2-3: a) System Modelling, b) Risk Quantification and c) Risk Estimation. This is similar to the approach advocated in [Taflanidis and Beck, 2009]. In the following sections the steps, the framework and the guidelines of the IRIS RAT are presented. It is emphasized that though the illustration in F.2-3 corresponds to the case study of offshore wind turbines, which was used for the development of RAT and is presented in detail in the following section, it applies to any other types of systems/applications with the appropriate modifications in terminology and case characteristics.

2-3-1 Step I of IRIS RAT: System Modelling

The first step for the IRIS RAT is the adoption of appropriate, numerical models for the various components of the overall system. These models must be able to provide a detailed, faithful representation of the behaviour of the true system under consideration. They can be based on physics or on empirical approximations. No specific requirements are imposed for them; they can be high-fidelity, computationally intensive numerical models. In most cases (though this is not an absolute necessity) the following sub-systems

Schematic for implementation of IRIS RAT (illustration example corresponds to offshore wind turbine risk assessment) F.2-3



can be distinguished: excitation, system and performance evaluation models, with model parameters θ_f (excitation model – "factor"), θ_m (system model – "mechanism") and θ_c ("component") and θ_l (performance evaluation model – "impact") (see F.2-3). The excitation model represents the "hazard" (or more generally, risk factor) and ultimately provides an "excitation" to the system, whereas the performance evaluation model assesses the impact to the system and, ultimately, transforms the system response to quantities meaningful to the stakeholders (e.g., distinction between acceptable or unacceptable performance, loss of revenue due to downtime or "performance" degradation, repair costs due to damages, and so forth). The overall system performance is assessed through the risk consequence measure $h(\theta)$ which can be calculated numerically as a function of the augmented model parameter vector $\theta = \{\theta_f, \theta_m, \theta_c, \theta_l\}$ composed of all individual subsystem parameters. Any modelling or numerical-approximation error (for example because of use of surrogate models as discussed in Step III later) should be also augmented in vector θ.

2-3-2 Step II of IRIS RAT: Risk Quantification

Foundation of the IRIS RAT is characterization of the uncertainty in the model parameter vector θ, through an appropriate probability model $p(\theta)$, once a faithful model description is developed (in step I). Selection of the specific probability model $p(\theta)$ will depend on the application considered; it can be based on regional measured data (for example for the statistical distribution of the environmental conditions), on engineering

judgement or on real-time measurements obtained during the Life Cycle of the system. For most applications, the most important source of uncertainty corresponds to the excitation model, since significant variability is anticipated for it during the Life Cycle of the system. But the uncertainty in the other subsystems needs to be also carefully considered as it can have an important impact on the overall performance. Ultimately risk is expressed as the expected value of the risk consequence measure over the established probability models

$$\text{Risk} = H \equiv \int_{\Theta} h(\theta) p(\theta) d\theta \qquad \text{E.2-1}$$

Different definitions for the risk consequence measure will lead to different characterizations for risk. For example if $h(\theta) = C_{In}(\theta) + C_{lif}(\theta)$, where $C_{In}(\theta)$ corresponds to the initial cost and $C_{lif}(\theta)$ to the additional cost over the lifetime of the system, then Risk corresponds to Life Cycle Cost. If $h(\theta) = I_F(\theta)$, where $I_F(\theta)$ is the indicator function against some event F (0 if F does not occur and 1 if it does), then risk corresponds to the failure probability against F.

2-3-3 Step III of IRIS RAT: Risk Estimation

For estimation of risk according to E.2-1 the multi-dimensional integral representing risk needs to be estimated. An efficient approach to perform this estimation is though stochastic simulation [Taflanidis and Beck, 2008]; using a finite number, N, of samples of θ simulated from some importance sampling density $q(\theta)$, an estimate for risk is given by

$$\text{Risk} \approx \hat{\text{H}} \equiv \frac{1}{N} \sum_{j=1}^{N} h(\theta^j) \frac{p(\theta^j)}{q(\theta^j)} \qquad \text{E.2-2}$$
$$\theta^j \sim q(\theta)$$

where vector θ^j denotes the sample of the uncertain parameters used in the j^{th} simulation. As $N \to \infty$, then $\hat{\text{H}} \to \text{H}$ but even for finite, large enough N, E.2-2 gives a good approximation for E.2-1. The quality of this approximation is assessed through its coefficient of variation, δ. An estimate for δ may be obtained through the information already available for the risk assessment using the following expression:

$$\delta \approx \frac{1}{\sqrt{N}} \sqrt{\frac{\frac{1}{N} \sum_{j=1}^{N} \left(h(\theta^j) \frac{p(\theta^j)}{q(\theta^j)} \right)^2}{\hat{\text{H}}^2} - 1} \qquad \text{E.2-3}$$

Thus, the simulation-based risk assessment provides not only an estimate for the risk integral, but simultaneously a measure for the accuracy of that estimate. The importance sampling density $q(\theta)$ may be used to improve this accuracy and, ultimately, the efficiency of the estimation of E.2-2. This is established by focusing the computational effort on regions of the Θ space that contribute more to the integrand of the risk integral in E.2-1. The simplest selection is to use $q(\theta) = p(\theta)$, then the evaluation in E.2-2 corresponds to direct Monte Carlo analysis.

This simulation-based approach for the risk estimation creates no constraints for the numerical or probability models adopted, thus facilitating a detailed description of system risk. It is though computationally intensive since a large number of evaluations of the model response is typically required to approximate risk according to E.2-2, while establishing good accuracy [small coefficient of variation according to E.2-3]. For problems involving high-fidelity, computationally demanding models, approaches for alleviating the associated computational burden are required. A common solution for this problem is to rely on surrogate models for the system-model evaluations needed for estimation of E.2-2 [Simpson et al., 2001; Taflanidis et al., 2011]. Such surrogate models can be developed using a relatively small number of evaluations of the real system model, and then used for all subsequent evaluations of the system response needed for estimation of the risk integral.

Finally, it is mentioned that the IRIS RAT framework for risk assessment can be also extended in order to include an efficient sensitivity analysis. Such analysis aims to identify which the critical risk parameters (i.e. uncertain model parameters) are that contribute most to the overall risk, considering their probabilistic characterization (i.e. not simply a parametric analysis). The sensitivity analysis can be efficiently performed with minimal additional computational effort over the risk assessment task. This is established through an information entropy definition of the sensitivity, and efficient calculation based on advanced stochastic sampling techniques. This innovative sensitivity analysis is based on the ideas initially proposed by [Taflanidis, 2009].

IRISOW Case Study risk identification example (technical/structural risk) T.2-1

Code	TECH.1.11
Name	Risk of failure due to extreme wind and wave conditions in parked situations
Class	Technical/Structural risk
Factors	Combination of extreme (return period of 50 years) wind and wave loads in parked situations (the wind and waves may be misaligned or not, extreme oblique wind inflow may be also present)
Components	Excessive deformations, excessive yielding or buckling, bending, excessive or premature cracking, fracture
Mechanism	Extreme waves and winds may produce extreme loads that will lead to extreme stresses on the parts of the OWT that may result to: a) loss of structural resistance (excessive yielding and buckling), b) failure of the OWT parts due to brittle fracture, c) loss of static equilibrium of the structure, or of a part of the structure, e.g. overturning or capsizing, d) failure of critical parts of the structure caused by exceeding the ultimate resistance or the ultimate deformation of these parts, e) transformation of the structure into a mechanism (collapse or excessive deformation)
Impact (description)	Repair/maintenance cost of the support structure and/or of the tower and/or of the RNA, replacement cost of the tower and the RNA and/or of the whole OWT, loss of revenue (power production loss)
Impact (value)	€ 77 000 (maintenance), € 581 000 (tower replacement), € 2 600 000 (RNA replacement), € 6 300 000 (whole OWT replacement), 92.82 €/MWh (loss of revenue)
Significance	Important
Allocation	Operator

2-4 Application to the Offshore Wind Turbines (IRISOW) Case Study

The IRIS risk paradigm methodology and more specifically, the RIM, the RI and the RAT modules have been applied to the "Offshore Wind Turbines" (IRISOW) Case Study to validate the use of the proposed framework in the energy industry. The prototype considered for the IRISOW Case Study is that of the MULTIBRID M5000 Offshore Wind Turbine (OWT), a fixed bottom OWT with a tripod support structure. The required design and monitoring data were provided by the Offshore Wind Industry (OWI) in the context of a synergy between OWI and the partners of the IRIS project, AUTH and BAM.

2-4-1 IRISOW Case Study: Risk Inventory

A specific RI for the IRISOW case study has been developed based on the RIM approach of the IRIS Risk Paradigm. This inventory refers particularly to the technical/structural risks and the environmental risks associated with the establishment and operation of an OWT. Additionally, some operational and construction risks have been identified. T.2-1 presents indicatively an excerpt referring to 1 out of the 21 identified technical/structural risks.

2-4-2 IRISOW Case Study: Risk Assessment and Sensitivity Analysis

In the case of the IRISOW Case Study the IRIS RAT has been applied considering extreme environmental conditions (risk case included in T.2-1), under which the OWT is in standstill/parked situation (non-operational). Moreover, focus is given on the tripod support structure and the tower of the investigated prototype OWT.

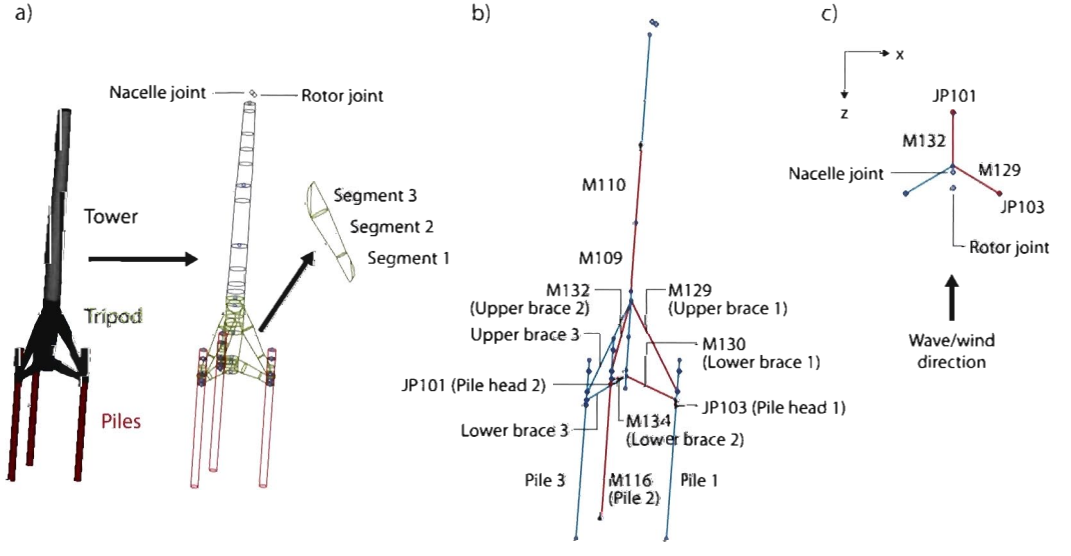
High-Fidelity OWT Model

A comprehensive structural analysis tool (MicroSAS) is used for modelling the OWT assuming standstill conditions. The tool is appropriate for the modelling, the static/dynamic analysis and the design (stress analysis) of offshore structures and has been extensively used in the offshore industry. It is based on the Finite Element Method utilizing the direct stiffness method for the structural analysis and, furthermore, has the capability of performing stress analysis according to [American Petroleum Institute, 2000]. The modelled geometry of the examined OWT is included in F.2-4.

With regard to the foundation, the non-linear soil-pile interaction is taken into account considering non-linear horizontal and vertical springs distributed along the length of each pile, with characteristics presented by P-Y and T-Z curves, respectively. The P-Y curves are taken into account for $Q=15$ different elevations below the mudline, which correspond to elevation depths in the range between 2 m and 36 m below the mudline. According to the available data, the soil of the sea bed is characterized by three different soil friction angles ($\varphi_1, \varphi_2, \varphi_3$) and two soil submerged specific weights (γ_{s1}, γ_{s2}). For each q^{th}, $q=1,\ldots,15$, elevation, the corresponding P-Y curve is calculated as function of the spe-

cific elevation depth and the corresponding soil friction angle and soil submerged specific weight based on the [American Petroleum Institute, 2000]. On the other hand, the values of the T-Z curves are obtained with digitization of existing T–Z curves. For a specific wave excitation, described by the significant wave height, H_s, and zero up-crossing period, T_z, Morison equation is applied in order to calculate the hydrodynamic forces on the support structure of the OWT, with water particle kinematics evaluated using Stokes wave theory. The drag, C_D, and inertia, C_M, coefficients present inputs to the numerical model that are calculated as functions of the Reynolds and Keulegan-Carpenter number, and of the relative surface roughness according to [Det Norske Veritas, 2007]. On the other hand, for a specific wind excitation, described by a reference wind velocity, V_{hub}, selected here at the hub height, the wind loading is obtained considering a wind velocity profile that follows a specific power low according to [Germanischer Lloyd, 2005]. The inertia loads are calculated based on an eigenvalue analysis, where the foundation piles are replaced with equivalent linear and rotational springs, after an appropriate linearization of the piles' behaviour. All the above loads are then combined using appropriately defined partial safety factors [Germanischer Lloyd, 2005] in order to form the loading combination for the structural and stress analysis. Based on the results of this analysis, the quantities that describe the performance of the OWT, i.e. joints' displacements, member forces, stresses ratios, etc., are, finally, obtained. More details about the high-fidelity OWT model can be found in [Taflanidis et al., 2011; 2013]. All the above define a computationally expensive high fidelity numerical model for the prediction of the dynamic response of the OWT. Thus, for approximating efficiently E.2-2, an approximate response-surface-based

a) Structural model of the MULTIBRID M5000 OWT (3D frame view), F.2-4
b) and c) Members and joints used for OWT's performance evaluation in XYZ and X-Z view respectively (from [Taflanidis et al., 2013] after modifications)



surrogate model has been further developed, based on information obtained by a small number of high fidelity runs [Taflanidis et al., 2011; 2013].

Uncertain Model Parameters – Probabilistic Description of these Parameters

Regarding the excitation model, the quantities H_s, T_z and V_{hub} form the vector $\boldsymbol{\theta}_f$, namely, $\boldsymbol{\theta}_f = [H_s\ T_z\ V_{hub}]^T$. As far as the $\boldsymbol{\theta}_m$ vector, considering that the soil of a sea bed where a MULTIBRID M5000 OWT is located is characterized by three different soil friction angles ($\varphi_1, \varphi_2, \varphi_3$) and two soil submerged specific weights (γ_{s1}, γ_{s2}), these parameters are used in order to form $\boldsymbol{\theta}_m$, namely, $\boldsymbol{\theta}_m = [\gamma_{s1}\ \gamma_{s2}\ \varphi_1\ \varphi_2\ \varphi_3]^T$.

Values for all the uncertain parameters above are derived from appropriate probability models for both the excitation and the OWT system. These probability models are chosen to reflect our available prior knowledge about the behaviour/properties of the true system and its environment. For the $\boldsymbol{\theta}_f$ vector parameters a joint distribution is established for the triplet H_s, T_z and V_{hub} as commonly suggested in the literature. The characteristics of this joint model are based on statistical data for the area of interest for the OWT. A truncated Weibull distribution is used for the mean wind speed V_{hub} with shape parameter 20.3 m/sec and scale parameter 1.7 m/sec. Since there is an assumption of extreme weather conditions the truncation for the Weibull distribution is selected so that the wind speed at the hub height is larger than 25 m/sec. A conditional on the mean wind velocity at 10 m above the Mean Water Level, $U(10)$, Weibull distribution is selected for H_s, with shape and scale parameters given, respectively from E.2-4:

$$a_H = 2 + 0.135 \cdot U(10), \quad b_H = 1.8 + 0.1 \cdot U(10)^{1.322} \qquad \text{E.2-4}$$

Finally, a conditional on H_s lognormal distribution is chosen for the wave period with mean value and standard deviation for $\ln(T_s)$, given respectively by E.2-5:

$$\mu_T = 0.7 + 0.898 H_s^{0.243}, \quad \sigma_T = 0.025 + 0.263 e^{-0.148 \cdot H_s} \qquad \text{E.2-5}$$

The soil friction angles ($\varphi_1, \varphi_2, \varphi_3$) are assumed to follow a Gaussian distribution with mean values (32°, 36°, 39°), respectively, standard deviation 1° and correlation coefficient 50% between successive angles (i.e. $\varphi_1 - \varphi_2$ and $\varphi_2 - \varphi_3$) and 20% between φ_1 and φ_3. The soil submerged weights (γ_{s1}, γ_{s2}) are assumed to follow a Gaussian distribution with mean values (10 gr/cm³, 11 gr/cm³), standard deviation 0.3 gr/cm³ and correlation coefficient 50%.

Performance and Risk Quantification

The performance of the OWT is described in terms of joint displacements, as well as in terms of member stress ratios. These stress ratios correspond to: a) overall strength stress ratio (SRs) in all tubular members and b) stress ratio due to local buckling in conical transition members (SRc). The SRs is defined as the maximum value among the stress ratio due to combined axial compression and bending and the stress ratio due to combined axial tension and bending. The SRc is defined as the stress ratio due to axial compression and bending in the case of conical transition members. In the case of pile members the stress ratio due to column buckling (SRp) is taken into account. Taking advantage of the sym-

metry of the OWT and its loading to reduce the required response variables needed to be monitored, 27 performance quantities related to joint displacements and stress ratios of appropriately selected members of the OWT were finally considered [Taflanidis et al., 2011; 2013].

Two different risk quantifications are considered. The first one, termed reliability-risk, is the probability that any of the twenty-seven performance quantities will exceed the threshold defining acceptable performance, which is set to one for all of them:

$$H = P\left[\bigcup_{i=1}^{27} y_i \geq 1\right] \qquad \text{E.2-6}$$

where y_i, $i=1,\ldots,27$ express the selected performance quantities.

The second one, termed Life Cycle Risk, is the repair cost due to replacement of parts of the OWT. This cost is calculated assuming that extreme weather conditions occur according to a Poisson distribution, independent of previous occurrences, as:

$$H = \int_{\Theta} \nu t_{life} L(\theta) p(\theta) d\theta \qquad \text{E.2-7}$$

where $t_{life} = 20$ years is the lifetime of the OWT, $\nu = 5$ is the annual rate of occurrence of extreme conditions with wind speed at hub height larger than 25 m/sec, and $L(\theta)$ is the replacement cost for the excitation/system configuration described by θ. The latter is calculated based on the recommendations in [Fingersh et al., 2006] by considering the five mutually top-down exclusive failure scenarios presented in [Taflanidis et al., 2013].

Moving Least Squares Response Surface Surrogate Model

For the risk assessment, a total of 400 configurations θ for the excitation and OWT were selected and the high-fidelity computational model was then used to predict the response and performance of the system model for each of them. These configurations constitute the support points (database) for building a surrogate model that allows efficient approximation for the system response for any other configuration θ (not included in the initial database). In particular, a response surface approximation was chosen for this purpose among the different candidate surrogate model approximations. More details about the surrogate model can be found in [Taflanidis et al., 2013]. The computational efficiency of the surrogate model, relying entirely on simple matrix manipulation, is high; 10000 evaluations of the model are performed in just 40 sec in a single 3.2 GHz Xeon core.

Risk Assessment and Results

For the risk assessment the finite number of samples, N, in E.2-2 is selected as 106 whereas a Gaussian importance sampling density is selected for V_{hub} with mean 50 m/sec and standard deviation 10 m/sec, truncated below 25 m/sec. For all other morel parameters the importance sampling density $q(.)$ in E.2-2 is selected equal to $p(.)$.

T.2-2 shows the results for the estimated reliability-risk along with the coefficient of variation of the estimate, which is a measure of its accuracy [Taflanidis et al., 2013]. Apart from the total risk, the reliability-risk for appropriately defined subgroups of performance

quantities is also considered. In all cases, risk is defined as the probability of occurrence of unacceptable performance for the quantities of interest. The risk for the joints is higher than any other performance variable; actually failure for all other variables is always accompanied in this investigation with unacceptable behaviour for the joints (since the overall risk is equal to the joint-displacement risk). The risk for the tripod members is also significantly high, whereas it is negligible for the piles or for tower member M109 (F.2-4b). Note that the risk reported here is conditioned on extreme weather conditions. It should be additionally noted that small coefficients of variation are established for all critical cases (except from the two corresponding to extremely rare events), which further testifies to the efficiency of the proposed computational framework.

As far as the second risk quantification (E.2-7), the Life Cycle Risk is estimated at $ 1.2458 million with again a small coefficient of variation for estimate 0.39 %.

Finally, results for the sensitivity analysis are shown in T.2-3, which includes the relative information entropy for four different cases for the risk quantification for the eight uncertain model parameters. Comparison between the different model parameters for each case reveals their relative importance. This is illustrated more clearly with respect to the normalized relative entropy shown in parenthesis, where the normalization is established with respect to the entropy for V_{hub}. The results show that wind speed V_{hub} has the highest

Reliability-risk assessment results [Taflanidis et al., 2013] T.2-2

Case description	Risk estimate (failure probability)	Coefficient of variation for estimate [%]
Overall risk	$2.281 \cdot 10^{-3}$	0.32
Risk for joint displacement	$2.281 \cdot 10^{-3}$	0.32
Risk for tower related to M110 (F.2-4b)	$0.121 \cdot 10^{-3}$	0.66
Risk for tower related to M109 (F.2-4b)	$0.142 \cdot 10^{-6}$	156
Risk for tripod	$1.279 \cdot 10^{-3}$	0.38
Risk for piles	$7.102 \cdot 10^{-6}$	31.7

Sensitivity analysis results [Taflanidis et al., 2013] T.2-3

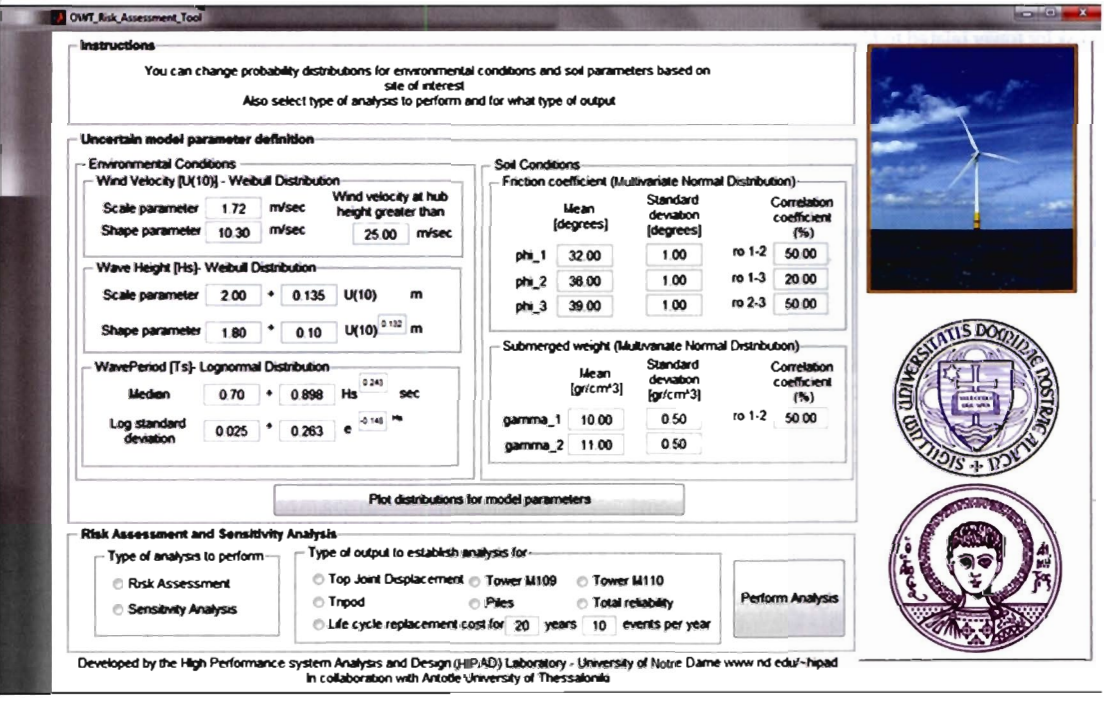
Model parameter	Relative entropy for each case (normalized with respect to the entropy for V_{hub} in parenthesis)			
	Reliability-risk			Life Cycle Risk
	Overall risk	Risk for tower M110	Risk for tripod	
V_{hub}	5.204 (1.000)	17.023 (1.000)	6.336 (1.000)	6.413 (1.000)
H_s	7.564 (1.454)	18.180 (1.067)	9.355 (1.476)	9.356 (1.459)
T_z	4.649 (0.894)	10.663 (0.627)	5.213 (0.822)	5.052 (0.787)
φ_1	0.003 (0.001)	0.009 (0.001)	0.003 (0.001)	0.028 (0.004)
φ_2	0.005 (0.001)	0.004 (0.001)	0.005 (0.001)	0.012 (0.002)
φ_3	0.006 (0.002)	0.007 (0.001)	0.004 (0.001)	0.024 (0.004)
γ_{s1}	0.011 (0.002)	0.009 (0.001)	0.004 (0.001)	0.014 (0.002)
γ_{s2}	0.007 (0.001)	0.008 (0.001)	0.004 (0.001)	0.040 (0.006)

importance out of all independent risk factors. More details about the implementation of the sensitivity analysis and the corresponding results can be found in [Taflanidis et al., 2011; 2013].

Automated Risk Assessment Tool

Exploiting the computational efficiency of the developed surrogate model, a stand-alone risk assessment tool has been developed [Taflanidis et al., 2013], with Graphical User Interface (GUI), shown in F.2-5, for automated implementation of the probabilistic evaluation. The tool accepts as input the probability models $p(\theta)$ for all model parameters. Based on this input and the pre-computed information from the high fidelity simulations, the surrogate response surface approximation is used to predict the risk as well as the sensitivity with respect to different risk parameters (uncertain model parameters). This allows the user to easily investigate the impact on the OWT risk of the regional environmental conditions as well as estimate this risk for different locations, characterized by different statistics for the wind/wave distributions [and thus different probability models $p(\theta)$]. A straightforward comparison between different candidate sites for the OWT can be established through this approach.

Graphical user interface (GUI) for OWT risk assessment tool F.2-5



2-5 The Żelazny Most Tailings Dam Case Study

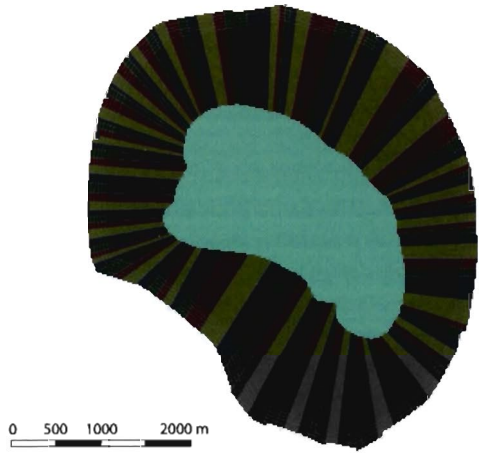
In order to present the applicability of IRIS Risk Paradigm to various cases of different nature and industry, the methodology has been, also, applied to an environmental case, namely the Żelazny Most tailings pond, a dam constructed to deposit contaminated mining wastes in Poland.

2-5-1 Description of the Żelazny Most Tailings Dam

Three copper mines owned by KGHM Polska Miedź S. A. company exist in South-West Poland to exploit the great ore body. The great majority of the extracted material – about 95 % – is waste, called tailings, which contains heavy metals and other contaminants that need to be safely deposited at the ground surface. That purpose is served by the Żelazny Most tailings dam. The tailings dam is constructed according to the upstream method; a starter dam is constructed and after that the tailings are discharged in the periphery of the structure using spigots or cyclones. As the tailings slurry is released, the coarser materials settle quickly forming the new perimeter dike and the wide beach area while the finer material moves along the beach to the pond.

The Żelazny Most tailings dam started operating in 1977. Since then, it receives approximately 80000 tonnes of tailings in liquid form per day, causing its height to increase by about 1.50 m per year [Jamiolkowski et al., 2010]. At its current state the dam has a maximum height of 60 m above natural terrain and a periphery of 14.3 km; the area oc-

Plan view of the Żelazny Most tailings dam. The pond at the centre of the structure is shown with cyan. Different colours are used to illustrate the different geological cross-sections F.2-6



cupied by the structure is about 13.94 km^2 [KGHM, 2011], forming the largest tailings dam in Europe. A plan view of the dam is shown in F.2-6. Based on site investigation, the dam's body and its foundation can be divided into 116 different geological cross-sections.

The tailings dam is a key feature of the mining process because an incapacity of the dam to receive the waste will result in an abrupt stoppage of the whole mining activity. At the same time, the release of the contaminated slurry from the pond downhill can cause huge environmental problems and jeopardise the health of the nearby town population. The present study concerns the risk assessment of the Żelazny Most tailings pond with respect to slope instability.

2-5-2 Model Parameter Vector $\boldsymbol{\theta}$

Probabilistic Description of Uncertain Parameters

There are three sources of uncertainty considered in the present study, the seismic acceleration acting on the dam, the water table elevation and the soil properties of the dam's body and its foundation.

Seismicity

Poland does not actually present natural seismicity. However, the tailings dam is subjected to vibrations caused by the nearby mining activity. The great majority of the mining induced seismic activity is located at the South-West part of the dam where the mining operations take place. Following the methodology proposed by [Pytel, 2010], the probability of distribution of the vertical and horizontal accelerations acting on each one of the 116 cross-sections of the dam has been estimated based on the vibrations recorded by four accelerometers at the dam's area within a time period of nine years (2002–2010).

Water Table Elevation

An exponential distribution with mean value obtained from site investigation and maximum value that coincides with the slope surface was adopted for the water table variation. So, a fluctuation of the water table of about 1.5 m around the mean value was considered for the majority of cases, while the analysis included the very rare cases where extreme rainfalls along with drainage malfunction (circumferential drains exist in the dam to maintain the water table at low levels) can rise the water table up to the slope's surface.

Soil Properties

There are three soil types forming the dam's body and forty different soil types encountered at the dam's foundation. A probability distribution has to be selected for the three soil properties, namely the density ρ, the effective friction angle φ' and the effective cohesion c' of those soil types. Indeed, a normal distribution with a coefficient of variation of 3%, 10% and 20% has been selected for ρ, φ' and c' respectively based on literature [Hammitt, 1966; Shannon & Wilson Inc. and Wolff, 1994; Trevor and Denys, 2008]. Especially for the three soil types forming the dam's slope, the determination of the effective friction angle point variation is based on the statistical analysis of an extensive site investigation consisting of more than 480 cone penetration tests (CPTs) performed

at the Želazny Most tailings dam from 1995 to 2008. The procedure is presented in detail in [Arnaouti et al., 2012]. Since the variability of the strength parameters is used for the determination of the slope stability, their variability along the sheared soil layer is more appropriate than the variability at a specific point. Indeed, across the failure surface extremely high and extremely low values of φ' may be encountered, but what is actually needed for the analysis is the φ' of the whole failure surface, which intuitively is expected to have the same mean but less standard deviation compared to the point φ'. To take into account this effect, the methodology proposed by [Vanmarcke, 1977] is adopted.

2-5-3 Sensitivity Analysis

To finalize the components of the model parameter vector θ, a sensitivity analysis has been performed in four cross-sections located at the four sections of the dam. The results revealed that the seismic accelerations, both horizontal and vertical, do not actually affect the stability of the structure since negligible changes of the safety factor are observed. Great changes in slope stability are observed due to changes in friction angle and the water table, while smaller yet significant changes are caused by the density and cohesion variations. Conclusively, the uncertainty vector θ consists of the water table elevation plus the soil properties, i.e. the density, the effective friction angle and the effective cohesion of all the 43 soils encountered in the cross-sections:

$$\theta = [w\ \rho_1\ \rho_2 \ldots \rho_n\ \varphi'_1\ \varphi'_2 \ldots \varphi'_n\ c'_1\ c'_2 \ldots c'_n]^T,\quad n = 43 \qquad \text{E.2-8}$$

2-5-4 Risk Assessment

Slope Stability Analysis

An effective stress non-circular slope stability analysis is performed using the Morgenstern and Price method [Morgenstern and Price, 1965] to determine each cross-section's two-dimensional safety factor SF_{2D}. The problem under study is highly non-planar, so, in order to take account of the side effects, the three-dimensional safety factor SF_{3D} is further estimated by SF_{2D} through the Skempton's formula [Skempton, 1985]. When a cross-section exhibits SF_{3D} less than unity, it fails.

Failure Definition

In the majority of the failed cross-sections, the slip surface lies near the periphery of the dam and far from the pond; this means that the failure cannot cause environmental impacts since there is no slurry release. However, the tailings dam behaviour resembles that of an egg, in the sense that the stronger materials are located along the periphery of the dam while less fortunate conditions (weaker soil layers and a higher water table elevation) are encountered towards the centre of the structure. So, when a part of the dam's periphery fails due to slope instability, it is of question whether the rest of the dam will reach a new stable state shortly or if this slope failure will initiate a slope instability that will extend to the dam's pond releasing the contaminated slurry. Furthermore, the intense monitoring system that records dam's displacements may allow immediate measures to

be taken, thus, restricting the extent of the problem at the dam's periphery. In the present study, the risk for two failure states is estimated. In the first state, the system is assumed to fail when at least one cross-section fails ($SF_{3D} < 1$). In the second case, the system fails when slurry from the pond is released due to slope instability. Given the previous statements, the latter state is more likely to happen when the width of the sliding area is large and the distance between the pond and the slip surface is small. Thus, it is assumed that a slope failure can reach the dam's pond and release the slurry when the width b of the adjacent failed cross-sections is at least half of the distance L between the pond and the slip surface.

Risk Assessment

To assess the risk, $N = 15000$ random samples of the model parameter vector θ were determined and for each one of the samples the three-dimensional safety factors of the 116 cross-sections were estimated.

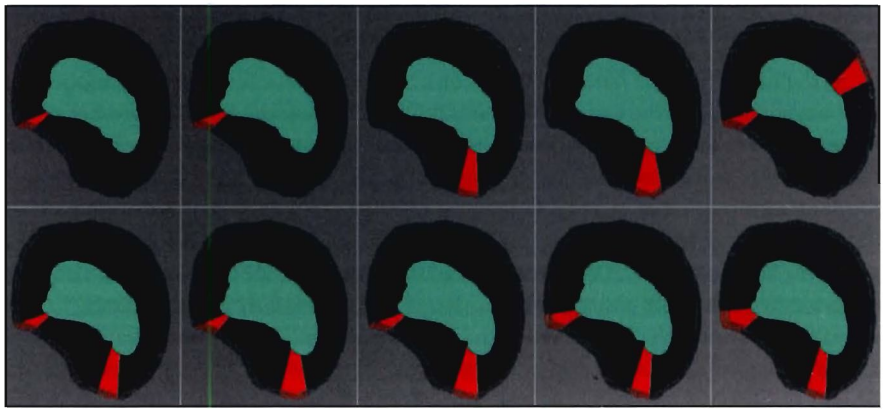
The indicator function against the first failure state, $I_{F,1}(\theta)$ equals unity when at least one cross-section of the dam fails ($SF_{3D} < 1$) and zero otherwise. The probability of failure is:

$$H_1 = \frac{1}{N}\sum_{i=1}^{N} I_{F,1}(\theta) = \frac{2507}{15000} = 16.70\% \qquad \text{E.2-9}$$

With regard to the second failure state, the system performance is considered non-acceptable (indicator function for the second failure state $I_{F,2}(\theta)$ equals unity) if there is at least one set of failed cross-sections ($SF_{3D} < 1$) with $b/L \geq 0.5$. F.2-7 shows in plan view the ten combinations of sliding cross-sections encountered at this failure state. The probability of failure of the system is:

$$H_2 = \frac{1}{N}\sum_{i=1}^{N} I_{F,2}(\theta) = \frac{27}{15000} = 0.18\% \qquad \text{E.2-10}$$

Combinations of sliding cross-sections encountered at the second failure state. The failed cross-sections are shown in red. F.2-7



2-6 The Risk Monitoring and Control System (RIMOCOS)

This system constitutes the base for dynamic risk analysis by exploiting the RAT results to determine the key risk components and update in real-time the assessment of risk. The system's definition shall be in terms of: a) elements (e.g. what is monitored), b) devices (e.g. types of sensors), c) networking (e.g. plan of sensor arrangements) and d) methodology for combined analysis of data from networking of sensors.

In order to define the requirements of such a system, a review was made concerning monitoring technologies specifically in the construction industry that allowed the selection of the appropriate monitoring network and devices among a wide range of available options. More specifically the Automated Data Collection (ADC) techniques that were reviewed were: a) Bar codes, b) RFID systems, c) Vision-based tracking methods, and d) UWB technologies. The review has shown that these techniques and technologies are currently used, mostly, for material and equipment management, scheduling and construction site management, while, this far, they have not been exploited in the field of risk management, despite their appropriateness and need for such a use. A comparative study between the most applied techniques in construction sites is presented in T.2-4. Considering the requirements for an effective risk assessment in the framework of the IRIS Risk Paradigm, a first attempt of providing an example for a monitoring network was made. For this ex-

Comparison between the characteristics of ADC technologies most applied in construction T.2-4

Characteristics	Bar codes	RFID	Vision-based tracking methods
Visual contact between the element and the device for data collection	Required	Not required	Required
Reading spectrum	≈ 1 in.	1 in. ÷ 100 ft	>> 100 ft
Input data renewal	Static. Data included in bar codes are not modifiable	Dynamic. Data can be updated in the "read-write" type of labels	Dynamic. No labels required
Input data volume	Few data can be included in bar codes	More data can be included in labels compared to bar codes	All existing data are included in images
Tracking ability	Identification of an element but not of its quantity	Identification of both an element and its quantity	Identification of an element and, conditionally, of its quantity
Concurrent data collection	No. Bar codes are read one at a time	Yes. Multiple labels are simultaneously readable	Yes. All data available in the visual spectrum are simultaneously readable
Reading rate	Slow. The scanner reads one by one the bar codes	Fast. 1000 labels per second can be read	Dependent on the analyst's requirements
Durability in the construction site	Not much	Yes, provided that the label is properly encased	Satisfactory
Cost	Very low cost	High cost	Low cost

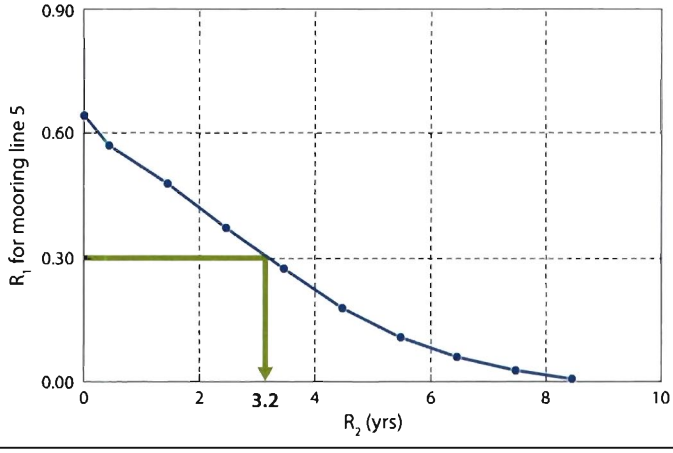
ample a vision-based tracking method was explored in terms of application (devices and networking) and fitness of use in the RIMOCOS context [Xenidis and Tamvakis, 2011]. The initial results have been satisfactory indicating further research on the application of the specific technology to the development of the RIMOCOS product.

2-7 The Risk Prevention and Mitigation Strategy Tool (RIPREMIS)

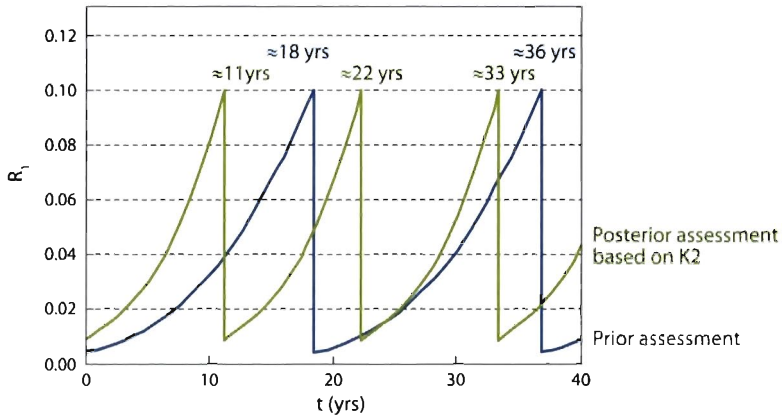
The RIPREMIS module was originally expected to constitute a strategy tailored to the output of RAT and RIMOCOS modules to provide risk response alternatives compliant with real situations and best related to performance requirements. Therefore, research on this module was, initially, focused on the compliance of the RAT outputs with appropriate decision-making approaches. For that reason an example concerning the mooring chains of a cable-moored array of floating breakwaters was developed to define the appropriate timing for taking risk-response measures and particularly maintenance of the mooring chains that, in this case, is equivalent with their replacement.

The approach that was implemented was risk-based decision making, i.e. the proposed decision was based on the assessed risk from the partial application of the RAT tool. The criteria that were applied concerned the probability of failure (R_1) and the expected remaining lifetime, i.e. the time till failure (R_2) and more specifically the evolution of R_1 with the decrease of R_2 over time. F.2-8 depicts the results for the specific example, which is presented in [Diamantoulaki and Angelides, 2011]. Extension of the above resulted to a risk-based maintenance scheduling model using monitoring data, which is presented in detail in [Diamantoulaki and Angelides, 2013]. Typical results of this model are shown in F.2-9.

Risk-based definition of the appropriate time for taking risk-response measures (maintenance) F.2-8



Risk-based maintenance scheduling using monitoring data F.2-9

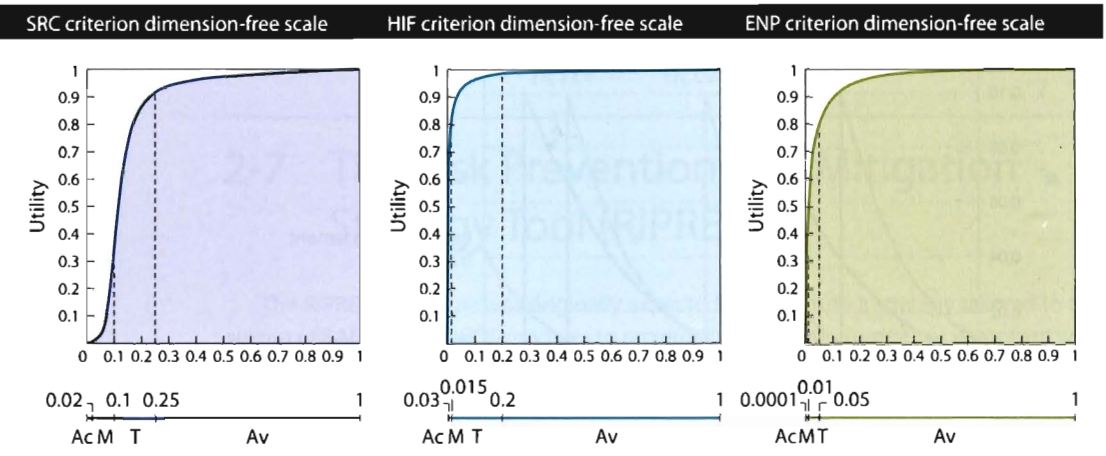


The same direction, i.e. a risk-based decision making approach with application to more complex, multi-risk problems where more than one strategy (instead of measures) for risk-response should be considered was followed to develop RIPREMIS, which, eventually, evolved from a strategy to a risk-based decision making methodology.

A review and comparative analysis between several well-established decision making methodologies revealed significant limitations with regard to complex systems; moreover, a new approach was required to comply with the overall approach of the Risk Paradigm. Therefore, RIPREMIS was developed as the tool to achieve the integration of various strategies, which are optimum for each different impact upon the occurrence of a specific risk to one single strategy that best confronts all the different impacts on the system simultaneously.

RIPREMIS identifies the four alternative decisions for risk-response proposed by the Project Management Body of Knowledge (PMBOK 4th edition), namely: a) risk acceptance, b) risk mitigation, c) risk transfer, and d) risk avoidance. These alternatives apply, in general, to all types of projects or situations and can be quantified either according to regulations, specifications, and legal frameworks or based on the strategy and policy of the organization that manages risk. RIPREMIS provides the technique for that quantification in a way that risk assessments estimated by RAT can be used as indicators for the appropriate risk-response strategy. The selection of the appropriate strategy is achieved through a utility-theory based concept that ensures a systematic way for the expression of the decision maker's preference of the alternative decisions evaluated over different decision criteria. The whole approach is applied to an example of a power plant under seismic risk where the decision upon the appropriate risk response strategy is based on the criteria of: a) the minimization of the system's recovery costs, SRC, after the occurrence of a damaging earthquake, b) the prevention of human injury or fatality, HIF, during the occurrence of the earthquake, and c) the prevention of environmental pollution, ENP, because of the damages in the plant due to the earthquake. Although developed much earlier and presenting a high level analysis of a power plant for which the source of energy

Utility curves for the preference over each decision-making criterion in the example of a risk of failure of a power plant due to earthquake F.2-10



is not defined, the example becomes very timely after the earthquake in Japan and the explosion at the Fukushima nuclear power plant. For each one of the three criteria, utility curves are derived such those presented in F.2-10; these curves can be used for evaluating the alternative decisions and eventually selecting by comparison the optimum between them. T.2-5 presents the results for the application example. Based on these results, the Risk Avoidance strategy is the optimum.

The proposed methodology is characterized by the following features:

// It considers the variability of impact upon risk occurrence by using appropriate risk values, which are estimated for each criterion under study. The traditional ap-

Utility values for the alternative decisions for each decision-making criterion in the example of risk of failure of a power plant due to earthquake T.2-5

Criterion	Alternative Decision	Utility
SRC	Risk acceptance (Ac)	0.00058
	Risk mitigation (M)	0.07361
	Risk transfer (T)	1.13112
	Risk avoidance (Av)	7.33324
HIF	Risk acceptance (Ac)	0.01106
	Risk mitigation (M)	0.08325
	Risk transfer (T)	1.76021
	Risk avoidance (Av)	7.98551
ENP	Risk acceptance (Ac)	0.00001
	Risk mitigation (M)	0.02922
	Risk transfer (T)	0.27364
	Risk avoidance (Av)	9.29736

proach integrates different risk values to a single one that, allegedly, denotes an overall risk value; on the contrary, the proposed methodology utilizes actual risk values that correspond to the different decision criteria.

// It involves the preference of the decision maker not in a way that alters the evaluation criteria of the decision as is done in Multi Attribute Utility Theory methods, but, rather, in a way that is restricted to the expression of tolerance of certain risk events in case they occur. This means that the boundaries for the alternative decisions with regard to different influences are predefined and constant, regardless of the risk event and any per case variation of the preference of the decision maker.

// It compares preference of decisions instead of preference of alternatives. This means that the risk analysis that precedes the decision making process provides results that directly indicate the appropriate decision regarding a specific criterion and, then, these decisions are compared and the most preferred one is selected.

// It involves risk-response strategies that respond to the system's requirements for increasing its resilience.

More details for the review of the existing decision-making approaches and their limitations, the insight of the RIPREMIS methodology and its application to an application example are presented in [Xenidis et al., 2011] and [Xenidis and Angelides, 2013].

2-8 The IRIS Risk Knowledge Portal

The IRIS Risk Knowledge Portal has been developed on top of the IRIS Risk Ontology (http://irisportal.csd.auth.gr/ontology/iris.owl) [Meditskos et al., 2012] and constitutes an application available over the http://irisportal.csd.auth.gr that serves three main goals:

1) To manage and disseminate the Risk Inventory's case studies, by simplifying the definition and management of risk knowledge and by offering searching capabilities based on semantics rather than just keywords.
2) To make the risk registry publicly available, so there will be a single web reference point for risk management that is continuously updated and refined, and
3) To integrate all the aspects of the new IRIS Risk Paradigm, namely monitoring, assessment, inventory and mitigation.

The portal offers various functionalities to the users including various user roles with different capabilities, risk ontology management including semantic checking, semantic searching, browsing and filtering, and, finally, user profiling via the definition of favourites.

The IRIS Portal constitutes an integrated system containing the IRIS risk paradigm tools, namely the RAT, the RIMOCOS, and the RIPREMIS. As a proof of concept, a risk assessment tool has been implemented and embedded in the portal for offshore wind turbines. The RAT was implemented in JAVA as a web service exchanging SOAP messages (SOAP is a protocol for exchanging messages over the web used by web services). The web service accepts numerical values concerning the risk variables from the portal, executes a number

of mathematical models developed on-site and the results are returned to the portal in order to be stored and properly presented to the user.

The underlying ontology infrastructure provides an upper-level schema that describes terms, relationships and restrictions of risk identification and assessment and it allows the formal representation of the risk knowledge. The semantic representation of the knowledge can be used in order to:

// integrate risk assessment practices from different domains
// perform consistency checking using state-of-the-art ontology reasoners
// build a network of semantically interconnected concepts freely accessible in the Web of Data (or Linked Data)

2-8-1 The Risk Ontology

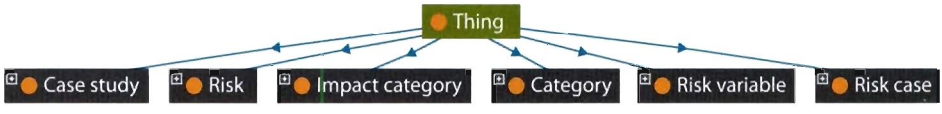
The risk case knowledge is represented in terms of an OWL-2 [Hitzler et al., 2012] ontology. The ontology was designed in such a way so that complexity should be avoided, in order to increase reasoning and querying performance. This requirement is very important, since there is a need for online (real-time) reasoning and querying tasks in order for the portal to be able to respond fast and to provide consistent results to users. The representation of the terms, relationships and restrictions of the domain e.g. case studies, risk cases, risk variables and their relationships, is based on 28 classes and 32 properties. F.2-11 shows the top-level class hierarchy. The CaseStudy class represents the case studies of the domain and it is defined as a subclass of five property restrictions:

```
Class: CaseStudy
    SubClassOf:
        hasRiskCases only RiskCase,
        versionDate exactly 1 xsd:string,
        editor min 1 xsd:string,
        version exactly 1 xsd:string,
        acronym exactly 1 xsd:string
```

The hasRiskCases property is an object property that associates a case study with its corresponding risk cases (a case study may have zero or more risk cases). The other four data type properties are used in order to define basic information about the case study, such as the acronym, the editor, the version and the date the case study was posted to the portal.

The RiskCase class represents the risk cases of the domain and serves as the top-level class of a risk case hierarchy. The ontology defines seven subclasses that correspond to the seven categories where the risk case can be classified, namely Financial, Operational,

Top-level class hierarchy F.2-11



Environmental, Technical-Structural, Design-Procedure, Construction and Legal risk. The RiskCase class is defined as subclass of ten property restrictions. It should have at least one risk (consistsOf) and it should belong to a single case study (the appearsInCaseStudy property and the hasRiskCases property of the CaseStudy class are inversed). A risk case can also belong to a category (riskCaseClass) and it can be associated with the risk variables of its risks, based on entailment rules that are described later. Finally, there are data type properties for defining basic information about risk cases, such as the code and the editor.

```
Class: RiskCase
    SubClassOf:
        code exactly 1 xsd:string,
        riskCaseEditor exactly 1 xsd:string,
        consistsOf min 1 Risk,
        hasVariables only RiskVariable,
        appearsInCaseStudy exactly 1 CaseStudy,
        hasFactors only RiskFactor,
        hasComponents only RiskComponent,
        riskCaseClass exactly 1 Category,
        hasImpacts only RiskImpact,
        hasMechanisms only RiskMechanism
```

The classification of the risk cases in the risk case hierarchy is performed by the ontology reasoner based on the riskCaseClass property. For example, the FinancialRiskCase class is defined as:

```
Class: FinancialRiskCase
    EquivalentTo:
        RiskCase and (riskCaseClass value financial)
    SubClassOf:
        RiskCase,
        consistsOf only FinancialRisk,
        consistsOf min 1 FinancialRisk
```

The class definition contains a class equivalence restriction on the riskCaseClass property that is used by the reasoner in order to classify risk cases with the financial instance value in the FinancialRiskCase class. The class expressions of the other subclasses are analogous. Similar to the RiskCase class, the Risk class serves as the upper-level class of a risk hierarchy. The Risk class is defined as:

```
Class: Risk
    SubClassOf:
        hasFactor exactly 1 RiskFactor,
        hasComponent min 1 RiskComponent,
        hasVariable min 1 RiskVariable,
        hasImpact exactly 1 RiskImpact,
        belongsTo exactly 1 RiskCase,
        riskClass max 1 Category,
        hasMechanism min 1 RiskMechanism
```

A risk should have only a single factor and impact and at least one component and mechanism. Furthermore, a risk may have a category (riskClass) and should belong to a single risk case (the belongsTo property and the consistsOf property of the RiskCase class are inversed). The classification of the risk instances to the risk hierarchy is performed based on the values of the riskClass property, in a similar way to the classification of the risk cases to the risk case hierarchy. For example, a risk is classified in the EnvironmentalRisk if it has the value environmental in the riskCase property:

```
Class: EnvironmentalRisk
    EquivalentTo:
        Risk
        and (riskClass value environmental)
    SubClassOf:
        Risk,
        belongsTo only EnvironmentalRiskCase,
        belongsTo min 1 EnvironmentalRiskCase
```

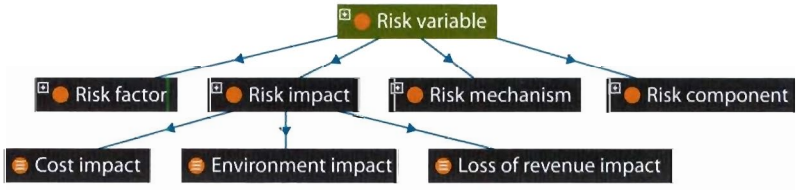
The factors, components, mechanisms and impacts of risk cases are defined as direct instances of the RiskFactor, RiskComponent, RiskMechanism and RiskImpact classes, respectively. Furthermore, an impact may also be categorized in three classes, namely CostImpact, EnvironmentImpact and LossOfRevenueImpact. The RiskVariable class hierarchy is depicted in F.2-12.

The RiskVariable class has a single property, namely isVariableOf that defines the risk where the variable belongs to (this is the inverse property of the hasVariable property in the Risk class). The ontology contains also two classes for defining category instances. The instances of the Category class are used by the reasoner to classify the risk cases in subclasses, as we explained previously. Similarly, the instances of the ImpactCategory class are used for classifying the impacts in the impact class hierarchy. For example, the CostImpact class is defined as:

```
Class: CostImpact
    EquivalentTo:
        RiskImpact and (impactCategory value cost)
    SubClassOf:
        RiskImpact
```

In that way, an instance of the RiskImpact class is classified to the CostImpact class if it has the value cost in the impactCategory property.

Risk variable hierarchy F.2-12



2-8-2 Portal Architecture

The system architecture is depicted in F.2-13 and consists of the Risk Ontology Web Service, the IRIS Risk Knowledge Portal and the RAT Web Service.

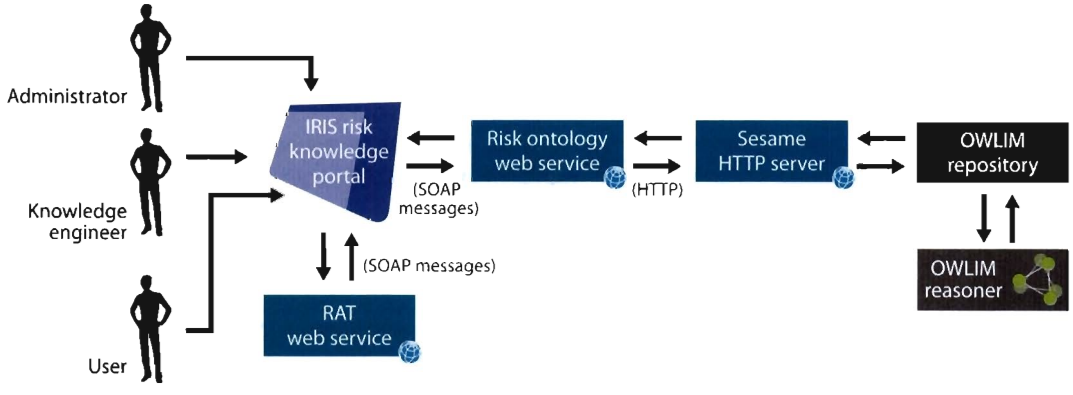
Risk Ontology Web Service

In order to enable the semantic processing of the risk ontology, an ontology repository is used with reasoning capabilities that ensures the consistency of the ontological knowledge during the various administrative tasks (additions, deletions and updates), as well as, it serves as the core component of the query and searching tasks. The reasoning infrastructure of the portal is based on OWLIM Lite (www.ontotext.com/owlim) that is a high-performance semantic repository including a native RDF rule entailment engine for handling the semantics of OWL. It is implemented in Java and packaged as a Storage and Inference Layer (SAIL) for the Sesame openRDF framework (www.openrdf.org).

The ontology repository is accessed through the Sesame API using the Sesame HTTP Server. The semantic repository follows the complete materialization reasoning approach, that is, all the inferences are pre-computed in order to increase the query performance at runtime. The reasoning is performed based on a set of entailments production rules for the OWL2 RL language that OWLIM implements using efficient indexing mechanisms.

The Sesame HTTP Server is a Web application that allows interaction with repositories using the HTTP protocol. It runs in a JEE compliant server container, e. g. Tomcat, and allows client applications to interact with repositories located on remote machines. The repository allows for the addition and deletion of statements and provides a query interface for the SPARQL query language. The communication of the portal with the repository, e. g. for query evaluation or knowledge updates (addition/deletion of case studies and risk cases etc.) is performed through the Risk Ontology Web Service. This Web service actually acts as an interface of the Sesame HTTP Server that prepares and validates the data that flows between the portal and Sesame.

System architecture F.2-13



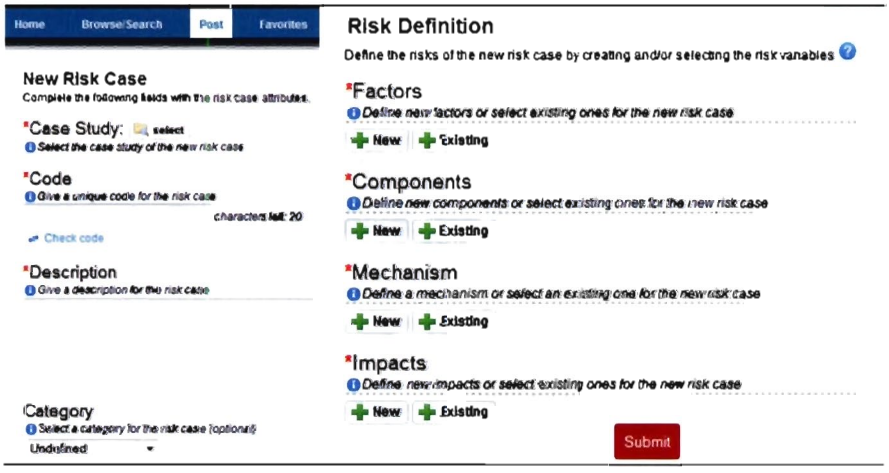
IRIS Risk Knowledge Portal

The Risk Ontology Web Service is consumed by the IRIS Risk Knowledge Portal that acts actually as a Web Service client, following a Service-Oriented architecture. The communication between the portal and the Risk Ontology Web Service is realized by SOAP messages that are exchanged based on the published WSDL Web Service interface description. This loosely coupled architecture accounts for a greater degree of flexibility during the development of the architectural components, disengaging the development of the IRIS Risk Knowledge Portal from the development of the Risk Ontology Web Service. The Risk Ontology Web service communicates with the Sesame HTTP Server in order to retrieve the results of the queries and to perform updates in the knowledge base. Both modules exist in the same server in order to reduce network connection overheads. However, this can change at any time if the deployed version of the portal should have a different architectural setting for any reason (e.g. separation of the modules for security or performance reasons). The portal has been developed in the ASP.NET 4.0 Web application framework implementing asynchronous client-server communication.

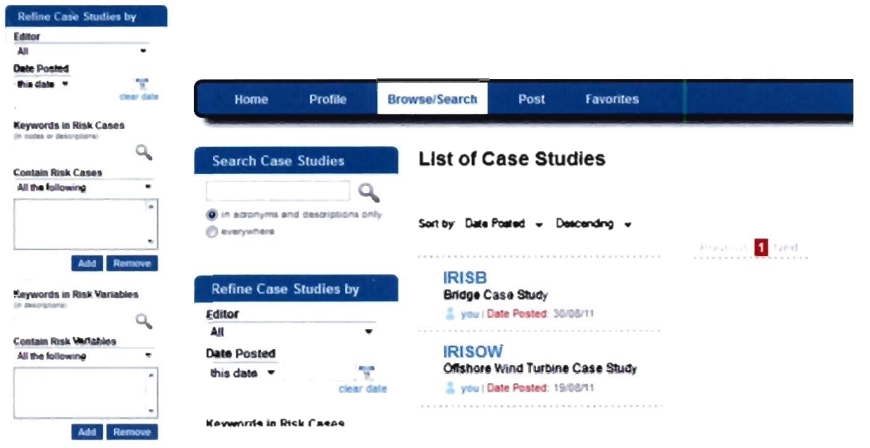
RAT Web Service

As a proof of concept, an on-line risk assessment tool has been implemented and connected to the IRIS Risk Portal as a Web service, in order to be able to provide on-line risk consultation for the Offshore Wind Turbines case study. The RAT (Risk Assessment Tool) Web service implements mathematical models providing to users on-line risk consultation services based on values that are submitted through the IRIS Portal. Similarly to the Risk Ontology Service, the communication between the portal and the Rat Web service is realized by SOAP messages, following a Service-Oriented architecture. Specifically, the mathematical models were originally developed in Matlab. In order to provide this model as a web application, we transformed the Matlab program into a Java application, and then the latter was exported as a Web Service exchanging SOAP messages, in order to accept input parameters and return results related to risk assessment. The RAT web service can be accessed through the IRIS Risk Portal.

New risk case form F.2-14



Browsing and searching case studies F.2-15



Portal Functionality

The portal supports user authentication based on roles (Administrator, Knowledge Engineer and User), in order to decide which operations the user may execute and which resources the user may access. The addition of new risk cases (F.2-14) involves the definition of the various risk attributes, such as, codes, factors, components, mechanisms and impacts, as well as, the definition of new case studies. Based on the underlying risk ontology schema, the portal provides the necessary Web forms for adding or editing the ontology knowledge. The portal notifies the user about potential errors, such as the submission of a case study with an already existing acronym or the submission of a risk case without risks. The portal allows also the modification or the deletion of existing ontological knowledge. The underlying reasoning infrastructure will ensure the consistency of the risk ontology after any modification, for example, after modifications of risk attribute values or the deletion of factors and components that are used by other risk cases.

Apart from the administrative tasks, the portal provides operations in order to allow end users to search, browse/navigate and query the risk ontology. More specifically, users are able to search the risk ontology about various aspects, such as case studies and risk cases that meet their requirements. The searching criteria are given in plain text (keywords) that are matched against the various attributes of the ontology, such as names, descriptions, factors, etc. The users are also able to define constraints on the attributes values (faceted search), as well as, there is the ability to further restrict the returned results exploiting the semantic relationships of the ontology, for example, by defining risk case category filters from a list of supported ontology risk types. F.2-15 depicts the case study browsing and searching page.

Querying Infrastructure

The querying infrastructure of the portal is based on the dynamic generation and execution of SPARQL 1.1 queries in the OWLIM repository. Based on the end-users' actions, the portal generates and sends for execution SPARQL queries (through the Risk Ontology

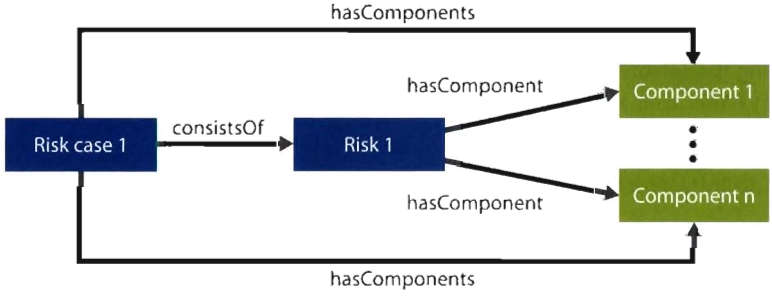
Web Service), whose results are then displayed back to the users. Some example SPARQL queries are presented in the following:

```
[query1]
SELECT DISTINCT ?ID ?Acronym ?Description ?Editor ?Version ?Ver-
sionDate
WHERE { ?ID rdf:type iris:CaseStudy;
        iris:acronym ?Acronym; iris:description ?Description;
        iris:version ?Version; iris:versionDate ?VersionDate;
iris:editor ?Editor. }
[query2]
SELECT DISTINCT ?CaseStudy ?Acronym ?Description ?Editor ?Version
?VersionDate
WHERE { ?CaseStudy rdf:type iris:CaseStudy;
     iris:acronym ?Acronym; iris:description ?Description;
iris:date ?date;
        iris:version ?Version; iris:versionDate ?VersionDate;
iris:editor ?Editor.
     ?CaseStudy iris:hasRiskCases ?RiskCase0.
     ?RiskCase0 iris:hasVariables iris:component622427b2-4e0a-83e4-
83c4b309b618. }
```

The first query retrieves all the case studies of the repository, returning the ID, acronym, description, editor, version and the date posted to the portal. The second query is more complex and retrieves all the case studies that are related to the "blade deflections" variable. The query actually joins the case studies and the risk cases on the hasRiskCases property and for each risk case, it checks the value of the hasVariables property in order to determine if it contains the ID of the "blade deflections" instance variable.

OWLIM is an entailment-based ontology reasoner, meaning that the inference is performed using rules (forward-chaining). OWLIM comes with predefined sets of inference rules and we configured the repository to use the OWL 2 RL rule set. However, there is the possibility to enhance the predefined rule sets with custom rules in order to infer more semantic relationships, based on domain knowledge. A custom rule inference case is depicted in F.2-16. A risk case is related with risks through the consistsOf property and a risk

Custom rule inference example F.2-16



is related to its components though the hasComponent property. In order to associate a risk case with the components of its risks through the hasComponents property, the following custom rule is needed. The rule is expressed in the triple-based rule syntax of the OWLIM rule engine:

```
Id: AssociateRiskCaseAndComponents
    x <rdf:type> <iris:RiskCase>
    x <iris:consistsOf> r
    r <iris:hasComponent> c
------------------------------
    x <iris:hasComponents> c
```

Risk Assessment Calculations

Finally, the implemented RAT Web Service allows users to consult the portal in order to retrieve the results of risk assessment for specific risks. Currently, this functionality is enabled for risk cases that contain wave and wind factors (risk cases TECH.1.1 and TECH.1.11 of the IRISOW case study). In order to display the form for inserting the values for a specific risk, users need to navigate to the details view of the risk (by clicking the "View Risk" link on the right) and selecting the "Risk Assessment Calculation" button. There are several available forms that contain the fields whose values are required by the RAT service. Currently, the RAT Web service can handle only wave and wind factors. Furthermore, users are able to save different configuration values for future use. After submitting the input values for the service, the user is redirected to the results page of the risk assessment service (F.2-17).

The result page of the risk assessment F.2-17

Reliability Risk Assessment Results

Case Description	Risk estimate (failure probability)	Coefficient of variation for estimate (%)	
Overall risk	0.002219	1.732834	show image
Risk for joints' displacement	0.002219	1.732834	show image
Risk for tower related to M110	0	NaN	show image
Risk for tower related to M109	0.000067	2.499695	show image
Risk for tripod	0.001274	1.81218	show image
Risk for piles	0	NaN	show image

Life-cycle Risk Assessment Results

Risk estimate (life-cycle cost) ($)	Coefficient of variation for estimate (%)
1,233,758.72	1.81218

back

2-9 Conclusions

The IRIS Risk Paradigm was an idea developed from scratch that goes beyond a re-statement of the state-of-the-art. It is a comprehensive risk management framework that is comparable to any other risk management practice standards such as: a) the ISO 31000:2009 – Risk management – Principles and guidelines, b) the Practice Standard for Project Risk Management published by PMI, c) the Risk Management Standard published by AIRMIC, ALARM, IRM: 2002, etc. In fact, it is more than a standard. It does not describe processes; it comprises sophisticated tools integrated with methodological proposals for applying risk management processes. That renders the whole approach a significant advancement from current practice in managing risk.

A second very important advancement that the IRIS Risk Paradigm offered is that the approach is fully quantified and manageable even to non-expert users through the IRIS Portal (at least in terms of operating the tool). In this way, the common phenomenon of limiting the conduct of risk analysis to qualitative approaches is successfully treated. In other words, conducting quantitative risk analysis is now more feasible for more practitioners through the IRIS Risk Paradigm.

Concerning the future and in relation to the application and further improvement of the IRIS Risk Paradigm the following research objectives should be planned to accomplish:

1) Further application of the IRIS Risk Paradigm to the case studies developed so far for other types of risks (e.g. static liquefaction and seepage for the tailing pond, etc.) and development of new case studies.
2) Enhancement of structures' risk assessment with aging:
   a) Making numerical models accurate in describing the real world.
   b) Use of model-based reasoning techniques to enhance diagnosis.
   c) Use of knowledge-based techniques to suggest model enhancements, when diagnosis feedback suggests model inadequacy.
3) Development of new algorithms that will be integrated to monitoring systems for real-time dynamic risk assessment.
4) Use of risk assessment framework to guide optimal mitigation strategies. Efficiently integrate real-time dynamic assessment for this purpose through use of monitoring data.
5) Development of resilience systems based on IRIS Risk Paradigm.
6) Application of the "Risk-based maintenance scheduling using monitoring data" developed in IRIS to complex indeterminate structural systems.
7) Development of software systems for all the above and integration into the IRIS Risk Portal as web services.
8) Seamless integration in the IRIS Portal of new web services for Risk Monitoring, Assessment, and Mitigation.

The IRIS Risk Paradigm is an innovative output both in the theoretical and the practical fields that could and should become the basis for advanced research endeavours towards the same and related new directions.

References

American Petroleum Institute, 2000. *Recommended Practice for Planning, Designing and Constructing Fixed Offshore Platforms–Working Stress Design, Offshore Standard.* API recommended practice 2A-WSD (RP 2A-WSD), 21st edition.

Arnaouti, S., Angelides, D., Chatzigogos, Th. and Pytel, W., 2012. *Variability of Soil Strength Parameters and its Effect on the Slope Stability of Želazny Most Tailing Pond.* International Conference on Computational Statistics and Data Analysis (ICCSDA), July 25–26, Amsterdam.

Det Norske Veritas, 2007. *Design of Offshore Wind Turbine Structures.* Offshore Standard, DNV-OS-J101, Oslo, Norway, 2nd Edition.

Diamantoulaki, I. and Angelides, D. C., 2011. *Time-Evolution of Risk for an Array of Moored Floating Breakwaters Using Stochastic Simulation.* In: Proceedings of the 21st International Offshore (Ocean) and Polar Engineering Conference, ISOPE, Maui, Hawaii, USA, June 19–24.

Diamantoulaki, I. and Angelides, D.C., 2013. *Risk-Based Maintenance Scheduling Using Monitoring Data for Moored Floating Breakwaters.* Journal of Structural Safety, Elsevier, 41:107–118.

Fingersh, L., Hand, M. and Laxson, A., 2006. *Wind Turbine Design Cost and Scaling Model.* Technical Report NREL/TP-500-40566. Golden, Colorado: National Renewable Energy Laboratory.

Germanischer Lloyd, 2005. *Guideline for the Certification of Offshore Wind Turbines.* 2nd Edition, Hamburg, Germany.

Hammitt, G., 1966. *Statistical Analysis of Data from a Comparative Laboratory Test Program sponsored by ACIL.* Miscellaneous Paper 4–785.

Jamiolkowski, M., Carrier, W., Chandler, R., Hoeg, K., Swierczynski, W. and Wolski, W., 2010. 1st Za Chieh-Moh Distinguished Lecture: the Geotechnical Problems of the Second World Largest Copper Tailings Pond at Zelazny Most, Poland. Geotechnical Engineering Journal of the SEAGS & AGSSEA 1–15.

KGHM, 2011. *Tailings Management Division.* Retrieved Feb. 2011, from KGHM Polska Miedz S.A.: www.kghm.pl

Meditskos, G., Bassiliades, N., Vrakas, D. and Vlahavas, I., 2012. *IRIS Portal: A Semantic Portal for Industrial Risk Cases Management.* Proc. 2nd International Conference on Web Intelligence, Mining and Semantics (WIMS'12), ACM, Craiova, Romania, June 13–15, 243–250.

Morgenstern, N.R. and Price, V.E., 1965. *The Analysis of the Stability of General Slip Surfaces.* Geotechnique 15:70–93.

Hitzler, P., Krötzsch, M., Parsia, B., Patel-Schneider, P.F. and Rudolph, S., 2012. *OWL 2 Web Ontology Language Primer (2nd Edition).* W3C Recommendation. www.w3.org/TR/owl2-primer/

Pytel, W., 2010. *Risk Assessment of Mine Tailings/Waste Surface Ponds.* Mine Waste 2010: Proceedings of the 1st International Seminar on the Reduction of Risk in the Management of Tailings and Mine Waste, Sept. 29 – Oct. 01, Perth, Australia, 229–242.

Shannon & Wilson Inc. and Wolff, T., 1994. *Probability Models for Geotechnical Aspects of Navigation Structures*. Report to the St. Louis District, U.S. Army Corps of Engineers.

Simpson, T.W., Peplinski, J.D., Koch, P.N. and Allen, J.K., 2001. *Metamodels for Computer-Based Engineering Design: Survey and Recommendations*. Engineering with Computers 17:129–150.

Skempton, A., 1985. *Residual Strength of Clays in Landslides, Folded Strata and the Laboratory*. Geotechnique 35(1):3–18.

Taflanidis, A.A., 2009. *Stochastic Subset Optimization with Response Surface Methodologies for Stochastic Design*. Proceedings 1st International Conference on Soft Computing Technology in Civil, Structural and Environmental Engineering, 1–4 September, Madeira, Portugal.

Taflanidis, A.A. and Beck, J.L., 2008. *An Efficient Framework for Optimal Robust Stochastic System Design Using Stochastic Simulation*. Computer Methods in Applied Mechanics and Engineering 198(1):88–101.

Taflanidis, A.A. and Beck, J.L., 2009. *Life Cycle Cost Optimal Design of Passive Dissipative Devices*. Structural Safety 31(6):508–522.

Taflanidis, A.A., Loukogeorgaki, E. and Angelides, D.C., 2011. *Risk Assessment and Sensitivity Analysis for Offshore Wind Turbines*. Proceedings 21st International Offshore and Polar Engineering Conference, June 19–24, Maui, Hawaii, USA, 1:479–486.

Taflanidis, A.A., Loukogeorgaki, E. and Angelides, D.C., 2013. *Offshore Wind Turbine Risk Quantification/Evaluation under Extreme Environmental Conditions*. Reliability Engineering and System Safety, 115:19–32.

Trevor, L. and Denys, B., 2008. *Eurocode 7 and Reliability-Based Design*. In K.-K. Phoon, Reliability-based design in geotechnical engineering (p. 530). U.S.A.: Taylor and Francis.

Vanmarcke, E., 1977. *Probabilistic Modeling of Soil Profiles*. Journal of the Geotechnical Engineering Division 103(GT11):1227–1246.

Xenidis, Y. and Angelides, D.C., (to be published 2013). *A Risk-Based Decision Making Methodology for Planning and Operating Safe Infrastructure Systems against Various Hazards*. (invited book-chapter), In: Computational Methods in Earthquake Engineering, Vol. 2, edited by Papadrakakis, M., Fragiadakis, M. and V. Plevris, Springer.

Xenidis, Y. and Tamvakis, P., 2011. *Automated Risk Assessment in Construction: Combining Novel Concepts with Cutting Edge Technologies*. In: Proceedings of the 6th International Conference on Construction in the 21st Century (CITC-VI) "Construction Challenges in the New Decade", Kuala Lumpur, Malaysia, July 5–7.

Xenidis, Y., Skiadopoulou, A.S. and Angelides, D.C., 2011. *Risk-Based Decision Making for Resilient Systems*. In: Proceedings of the III ECOMAS Thematic Conference in Computational Methods in Structural Dynamics and Earthquake Engineering (COMPDYN 2011), Corfu, Greece, May 26–28.

3

The IRIS Damage Assessment Methodology

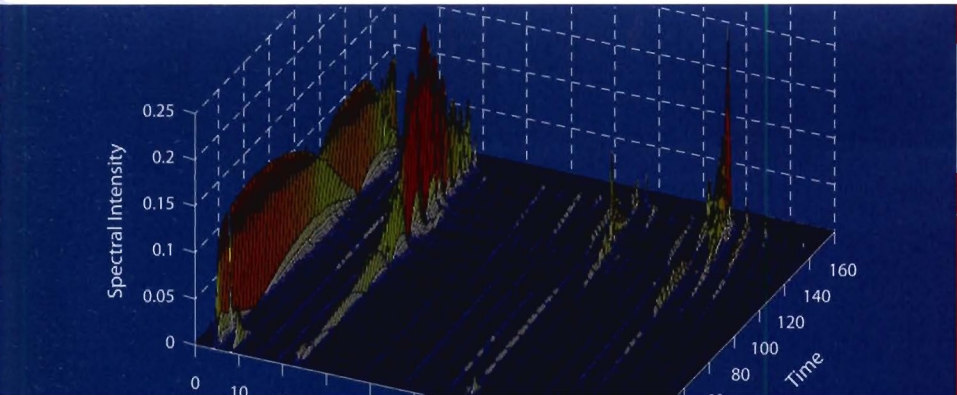
Authors:
Hiroshi Tanaka
Michaela Höllrigl-Binder
Helga Allmer
Helmut Wenzel

Motivation

Damage quantification is a major desire of the SHM community. Methodologies to introduce a quantity for actual condition of a structure into the assessment process are desired.

Main Results

The idea that the condition of a structure is represented in the character of its dynamic response is fully accepted by the SHM community. The VCLIFE methodology quantifies condition analysing input from monitoring.





3-1 Introduction

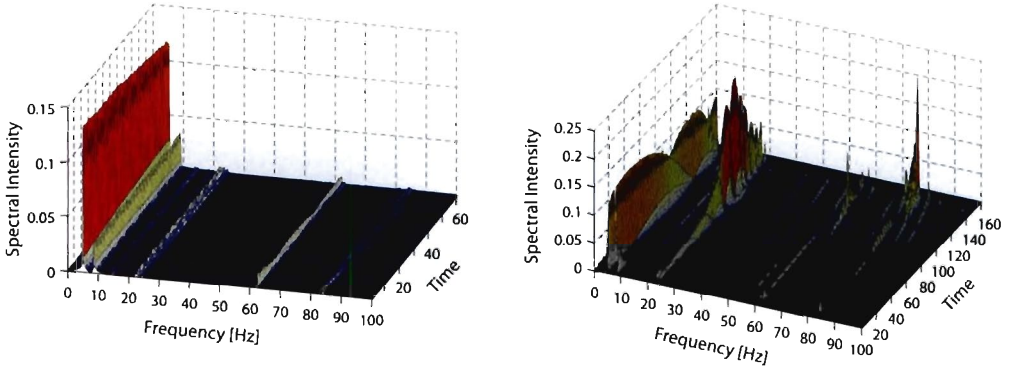
Damage detection in civil engineering has long been concentrated on the change of stiffness with increasing damage. This indicator, however, has been proven to be by far not sensitive enough to satisfy the practical requirements. Our experience is that a more sensitive indicator could be observed when the measured frequencies of higher order are carefully examined. While the lower fundamental frequencies appear not much affected by the stiffness changes, the higher frequencies can indicate much earlier signs of it. It was found that actually an energy transfer is happening from lower to higher frequency ranges with increasing damage. F.3-1 is an example showing this phenomenon. The reduction of eigenfrequencies and the transfer of energy are both observed in this graph.

This phenomenon has never been described in literature before except it was briefly mentioned in an earlier article by VCE after the first observation of this kind. Meanwhile it is also identified that the increase of damping goes along with a drop of spectral peaks caused by increasing damage. It is obvious that this is not the modal damping and it needs to be described by a system behaviour parameter. The physical concept, the mathematical modelling and a clear simulation of the phenomena are not available yet.

3-2 Structural Non-Linearity and Energy Transfer

Cascading energy transfer in a dynamical system could be caused by the development of non-linear characteristics of the structural response caused by various reasons. Suppose there is a development of non-linear mechanisms in both damping and stiffness of the structure, whose dynamic behaviour is simply expressed by an SDOF model, associ-

Spectral development over time for a sound structure (left) and during a damage test at MPA Stuttgart (right) F.3-1



ated with the progress of a structural damage. It can be typically represented in the equation of motion by modifying both damping and stiffness terms as follows:

$$m\ddot{z} + c[1+\varepsilon_2(z)]\dot{z} + k[1-\varepsilon_1(z)]z = 0 \qquad \text{E.3-1}$$

where ε_1 and ε_2 are the linear or non-linear correction terms introduced corresponding to the development of structural damage and $z(t)$ represents the dynamic response of the structure in general. Note that it is unlikely to have any change in the inertia term. E.3-1 can be rewritten as

$$m\ddot{z} + c\dot{z} + kz = k\varepsilon_1(z)z - c\varepsilon_2(z)\dot{z} = F(z,\dot{z}) \qquad \text{E.3-2}$$

where $F(z,\dot{z})$ is generally a non-linear function of z and/or $\dot{z}$, such as

$$F(z,\dot{z}) = C_1 z^2 + C_2 \dot{z}^3 \qquad \text{E.3-3}$$

for example. It implies that if z is given as a vibration with frequency ω, $F(z,\dot{z})$ is generally a function of fluctuations with the frequencies expressed by the multiples of ω. For example, substitution of $z = A\sin\omega t$ to E.3-3 results in

$$F(z,\dot{z}) = \frac{C_1 A^2}{2}(1-\cos 2\omega t) + \frac{C_2 A^3 \omega^3}{4}(3\cos\omega t + \cos 3\omega t) \qquad \text{E.3-4}$$

which in turn will result in the dynamic response including functions of twice, thrice higher frequencies of the original for this case. The same process will be repeated as time allows and, as a result, a part of the system's dynamic energy will be gradually distributed to higher and higher frequency ranges. Where would this process end? For the case of damage-caused non-linearity, the high frequency energy components dissipate as heat or noise and, if not, the destruction or rupture of the structure would play a role. Even if it does not reach the destruction point, the mechanism of structural response will change largely when damage progressed that far.

3-3 The Energy Cascade in Turbulence

Energy cascading, such as the one described above, can be associated with various types of non-linear physical phenomena. It is typically observed in the dynamics of turbulent fluid flow. In fact, the case of fully developed turbulence, the energy cascading process is one of the most central issues.

An English physicist L. F. Richardson (1881–1953) conceived turbulence as an assembly of eddies of different sizes, where eddies could be hypothetically visualized as individual vortices of some measurable diameter. He then had the idea that large eddies are

prone to break into smaller eddies, which break up into even smaller eddies and so on as spelled out by the famous parody as follows:

"Big whirls have little whirls
That feed on their velocity,
And little whirls have lesser whirls
And so on to viscosity." *by Richardson (1922)*

In each break-up process, the larger eddy transfers its dynamic energy to the smaller ones without dissipating it, meaning that the energy transfer process in turbulence is inviscid, or, in this process, the role of viscous forces is negligible in comparison to the inertia forces. However, energy has to be eventually dissipated somewhere, at much smaller length scales, or higher frequencies, which is a viscous process. Fluid viscosity has an important role only at those small scales.

This process can be mathematically considered as follows: the Navier-Stokes equation is a non-linear equation because of an inherent non-linearity of fluid inertia as seen in the equation below:

$$\rho\left(\frac{\partial u_i}{\partial t}+u_j\frac{\partial u_1}{\partial x_j}\right)+\frac{\partial p}{\partial x_j}=\frac{\partial}{\partial x_j}\left(\mu\frac{\partial u_1}{\partial x_j}\right) \qquad \text{E.3-5}$$

Out of the three terms involved in the equation, the pressure gradient can be ignored in the present discussion. In the energy dissipation process described above, the inertia term becomes less important in comparison to the viscous force in higher frequency ranges, and hence the whole equation becomes almost linear for this case, whereas at much larger length scales, or in the lower frequency ranges, the inertia term becomes predominant and hence the equation becomes highly non-linear, and this is where cascading takes place. Note therefore that the non-linear characteristics of the equation, in particular of the inertia force for this case, are deeply associated with the energy cascading phenomena explained by Richardson.

3-4 Non-Linear Damping

The relationship of energy cascading with non-linearity of dynamical systems is therefore evident in these two different phenomena. A very interesting aspect of this point is that the detection of energy cascading could be potentially utilized as a tool for the structural health monitoring. As mentioned earlier, the traditional idea of knowledge-based structural health monitoring is by identifying the reduction of stiffness, which has been proved to be far less sensitive than desired for practical purposes. In contrast to that, by finding the transfer of dynamic energy to higher frequencies through spectral analysis of the ambient vibration survey, it may be possible to detect the damage development in a structure at its earlier stage. Any extent of structural damage can of course change the

local structural damping or energy dissipation and stiffness. As a consequence, the global dynamic properties of the structure, i.e. the eigenfrequencies, mode shapes and modal damping would be all somewhat influenced.

It needs to be kept in mind that structural non-linearity is attributed, however, not only to developing damages. Field experience indicates that the magnitude of modal damping is often amplitude dependent. Increase of damping, when the vibration amplitude is significant, is due to energy consumption at increased friction at bearings, bending action of piers, behaviour of the bridge outfitting and also the structure-vehicle interaction [Wenzel, 2009].

Admittedly the present method would also detect the developing structural non-linearity due to large motion. However, if there is a development of structural damage as its consequence, the non-linear characteristics will remain with the structure after the large amplitude motion disappeared and should be thus detected.

3-5 Data Analysis

For identifying the energy cascading phenomena, the following data analysis can be applied.

3-5-1 Data Preparation

Acceleration signals $a_i(t)$ are measured for a period of $t_i \le t \le t_i + T$, where $i = 1,2,\ldots,n$, with the sampling frequency and measuring period of typically $f_s = 500\,\text{Hz}$ and $T = 5\,\text{min}$, respectively. n is the number of files.

3-5-2 Analysis

Calculation of the acceleration spectra $G_i(f)$ by a conventional FFT routine for the frequency range of $0 \le f \le f_M$ is required first. $f_M = f_S/2$ is the folding frequency. The normalized spectral density functions are then calculated as

$$F_i(f) = \frac{G_i(f)}{\sigma_i^2} \quad \text{where} \quad \sigma_i^2 = \sum_f G_i(f)\Delta f \qquad \text{E.3-6}$$

Normalization of spectral density makes sense since our interest is only in the change of energy distribution patterns and not in actual magnitudes of the spectral density, which depends on the total dynamic energy supplied by excitation and is always expected to change during the ambient vibration survey. It is also useful to calculate the fraction of dynamic energy corresponding to less than any particular frequency level (f) as follows:

$$E_i(f) = \sum_{k=0}^{f} F_i(k)\Delta k \qquad \text{E.3-7}$$

$E_i(f)$ is the spectral distribution function which is expected to more clearly reveal the fraction of energy transferred to different frequency ranges, resulting in the change of its pattern.

3-5-3 Presentation

Visual presentation of $F_i(f)$ and $E_i(f)$ against time (i) and frequency (f) would indicate the transfer of energy to higher frequencies by the change in spectral pattern, where $1 \leq i \leq n$ and $0 \leq f \leq 250$ Hz.

3-5-4 Reading of Spectral Patterns

When the distribution function $E_i(f)$ is examined, it should be noted that the energy cascading caused by structural non-linearity as discussed in this document is only a partial transfer of energy through the free vibration process of the structure, and, as it is evident from the discussion in section 3-2 above, not all the dynamic energy is transferable to high frequency ranges. Some of the energy should remain with the lower vibration modes.

Another important point is that, while the vibration survey is carried out, there may be various dynamic excitations or disturbances from the external environment acting on the structure. There will be, as a result, new dynamic energy supplied to the system and it will augment the energy fraction at corresponding frequencies. The characteristics of these excitations are often not readily identifiable. However, when there are any predominant excitation frequencies, there may be distinct spectral peaks observed at those particular frequencies. If the excitation is more broad-band noise, a part of this energy will be absorbed at eigenfrequencies and corresponding spectral peaks will show up as additional spikes in the figures.

The change of pattern in $E_i(f)$ is, therefore, not expected to be monotonous. Hence, what needs to be observed is a general tendency of the energy shift, which will be hopefully indicated by a gradual change of the coloured pattern.

The shift of pattern can be quantified by locating the centroid of the area under the spectral distribution $E_i(f)$ as follows:

$$\bar{r} = \sum_f f E_i(f) \Delta f \,/\, \sum_f E_i(f) \Delta f \qquad \text{E.3-8}$$

Again, also in terms of the centroid, its shift is unlikely to be monotonous. What should be observed is the general tendency of its change.

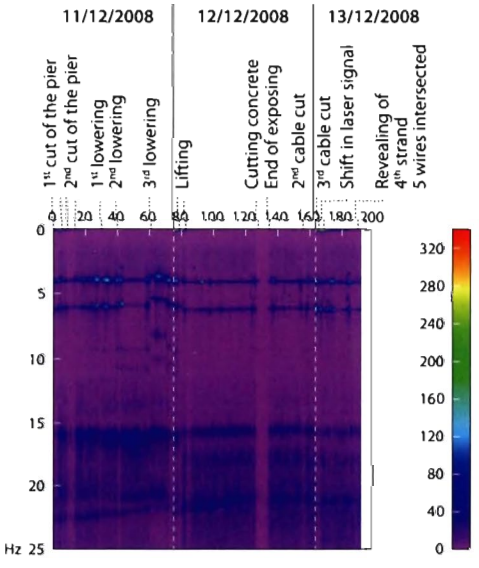
3-6 Example: Overpass S101 in Reibersdorf (2008)

An example given below is based on the measurement of the dynamic bridge response carried out in December 2008 for the highway overpass S101 in Reibersdorf, Upper Austria. Prior to the demolition, progressive damages were deliberately exerted on the structure to observe their effects on dynamic characteristics [Wenzel et al., 2009]. Sampling frequency of the acceleration record was 500 Hz.

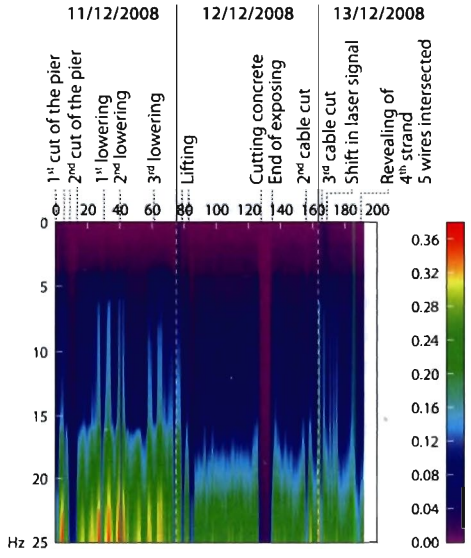
F.3-2 and F.3-3 depict the progressive change of the normalized acceleration spectrum $F_i(f)$ and the distributed spectrum $E_i(f)$ for the frequency range of $0 \leq f \leq 25$ Hz from the measured results. There were a number of physical operations applied to the bridge during a three-day measurement period and some of them are specified beside the figures. Some of these operations can be clearly identified from the pattern of $F_i(f)$ and $E_i(f)$ functions. When the concrete pier or slab is being cut, presumably the severing operation produced a large extent of high frequency noise and, consequently, a large fraction of the total dynamic energy appears in a much higher frequency range, which appears as a substantial spike in $E_i(f)$. In the afternoon of the third day, for example, there was "a vibrating roller working next to the bridge, causing clearly noticeable vibrations on the bridge", the measurement report states. This noise may be also contributing to the above mentioned spikes.

It is clear by observing $E_i(f)$ patterns that, with the progressive damage artificially exerted on the bridge, more and more fractions of dynamic energy were redistributed to the higher frequency ranges, which is indicated by the shift of dark blue and yellow band

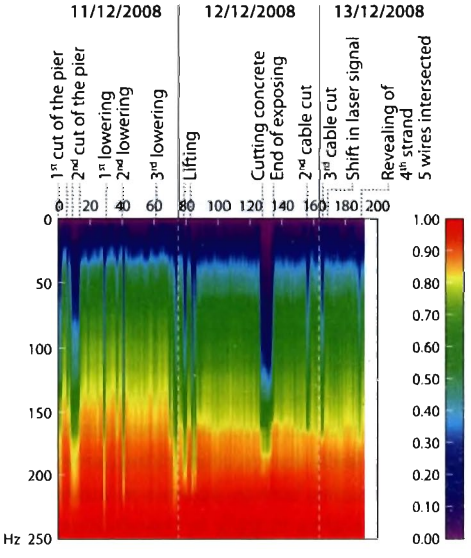
Normalized acceleration spectra $F_i(f)$ F.3-2



Spectral distribution functions $E_i(f)$ F.3-3



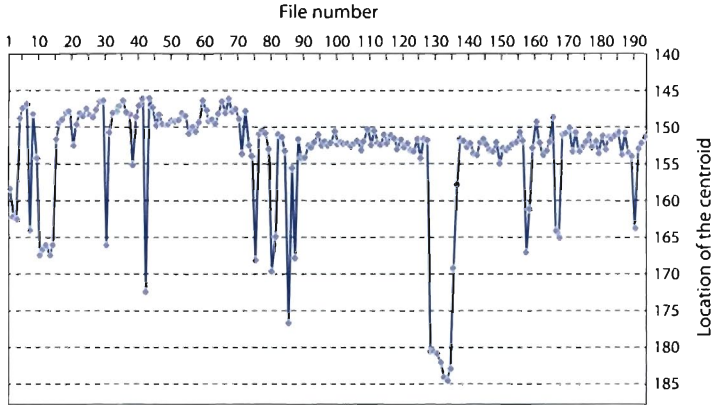
Spectral distribution functions $E_i(f)$ F.3-4



towards right, meaning the higher percentage fraction is in the high frequency side of the figure. F.3-4 is the same $E_i(f)$ function shown for a much wider frequency range up to 250 Hz. It is clear that almost stepwise energy shift took place after the lifting of the damaged pier at the beginning of the second day.

The same tendency is presented even more clearly by calculating the shift of the centroid $\bar{r}$ of the area under $E_i(f)$ as shown in F.3-5 By disregarding the spikes due to various kinds of noise, the general tendency is clear – it is shifting towards higher frequency ranges with time.

Normalized acceleration spectra $F_i(f)$ F.3-5

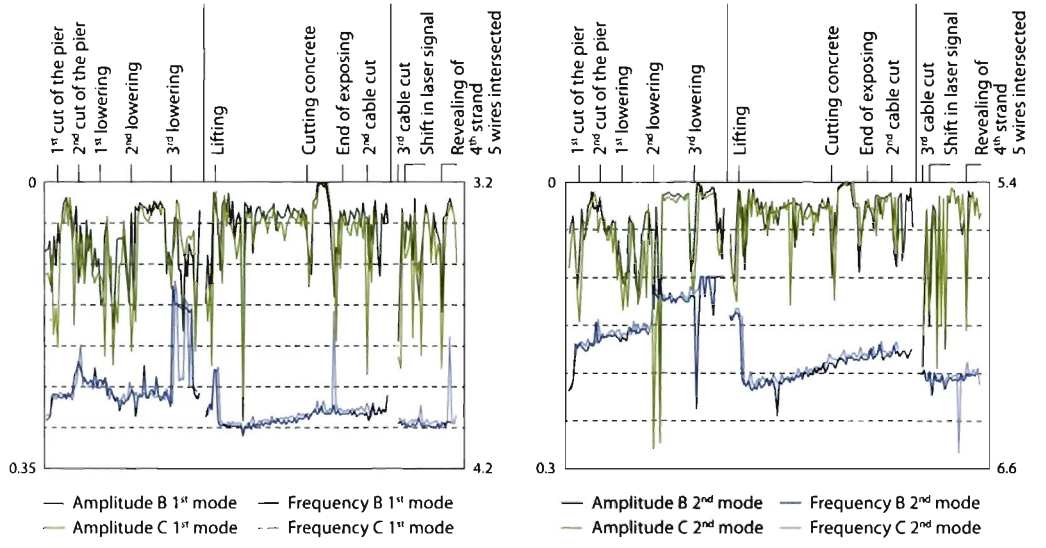


3-6-1 Further Discussion on the Test Results

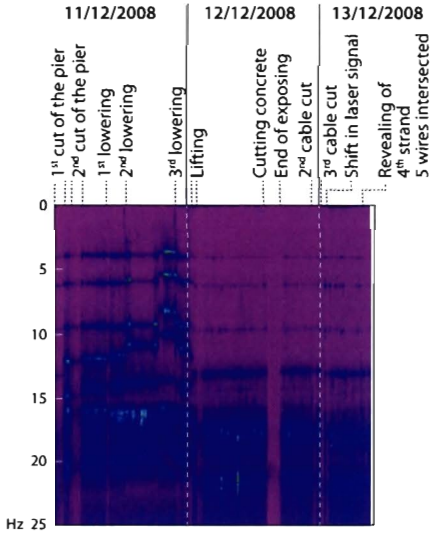
F.3-6 shows some changes in 1st and 2nd eigenfrequencies during these three days, most likely caused by the change in the bridge's physical conditions. What is shown as "amplitude" indicates the ordinate of the normalized spectra at this particular frequency, namely the modal intensity of the dynamic energy. Artificial damage of the bridge pier was applied on the north-west column of the bridge and the measurements B and C were taken at the mid-span of the bridge on the west and east side, respectively.

It is evident that there were two steps of frequency reduction, though the second one is less clear, corresponding to the cutting of the pier on the first day, the first artificial damage exerted on the bridge. Immediately following the second cut, the first mode frequency was recovered but it did not happen in the second mode. Note that the column position was still kept up at the original elevation by being jacked up. The measurement report [Wenzel et al., 2009] states that "no restoring forces were observed" for the same period. Most conspicuous loss of stiffness, both in the first and second modes, took place during the lowering of the pier. At the same period of time, it was observed that a part of the dynamic energy started being clearly transferred to the higher frequency range. This corresponds to the reported development of cracks in the structure due to its optimal settling by itself. The recovery of both frequencies on the second day corresponds to re-lifting of the column and insertion of steel plates under the column. Substantial transfer of energy is observed compared to the day before. It is also evident from the plot of the modal energy (shown as "amplitude"), both in the first and second modes, only a small fraction of energy remains associated with these modes through this period. Gradual reduction of both frequencies through the day may be caused by the change of ambient temperature or a gradual settling of the structure. The further cascading process seems

Change of the 1st (left) and 2nd (right) frequency F.3-6

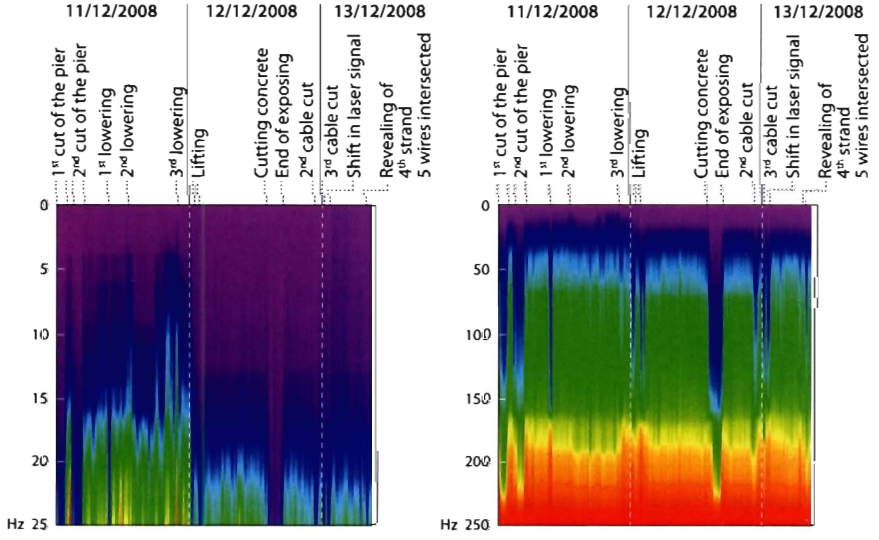


Normalized acceleration spectra $F_i(f)$ on the pier F.3-7



to be associated with the cutting of concrete slab and steel tendons. It is interesting to observe that no change of the first and second eigenfrequencies was observed during this operation. The third tendon was severed on the third day and apparent re-settling of the structure was stated in the measurement report. Further transfer of dynamic energy is obvious in F.3-3, though again this operation had no visible effects on lower eigenfre-

Spectral distribution functions $E_i(f)$ on the pier F.3-8



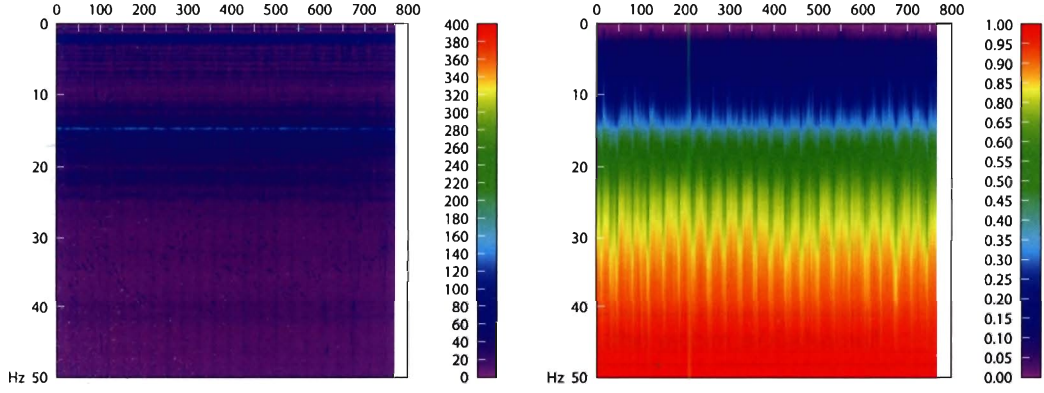
quencies. Another set of spectral presentations, F.3-7 to F.3-8, results from the acceleration record obtained right above the damaged pier.

The general tendency, namely the reduction of eigenfrequencies and energy transfer towards high frequency ranges, is the same as seen in the other results but it can be observed even more clearly with this set of data. What is clearly different from the other sets of data is that conspicuous spectral peaks are found in the frequency range of $8 \leq f \leq 13$ Hz. Explanation of these peaks is not immediately given.

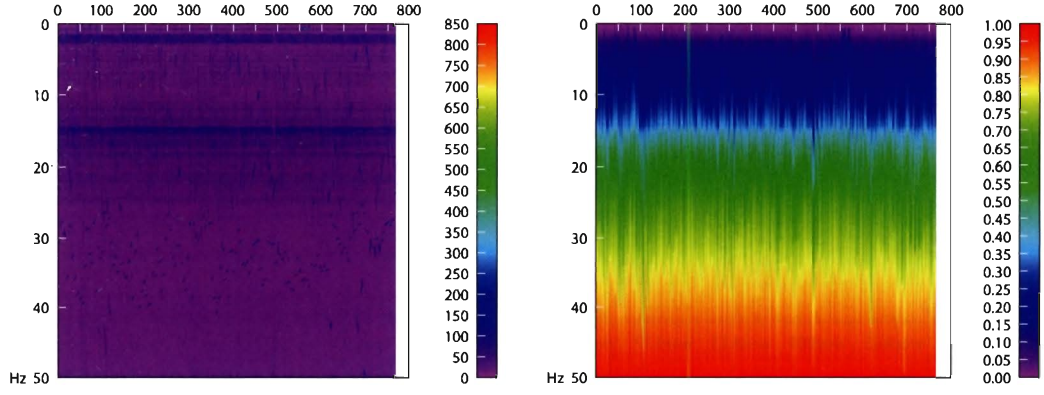
3-7 Other Sample Cases

The proposed spectral analysis method for damage identification seems to be successful at least in the case of the S101 overpass. Admittedly, however, it was rather an ideal case where the scheduled damage was successively applied to the structure and

Europabrücke: based on midday records F.3-9



Europabrücke: based on midnight records F.3-10



the measurement was carried out in a protected environment without being disturbed by on-going traffic, for example. Being encouraged by this case, nevertheless, the method has been further tried out for some other bridges. This is a brief summary of sample cases.

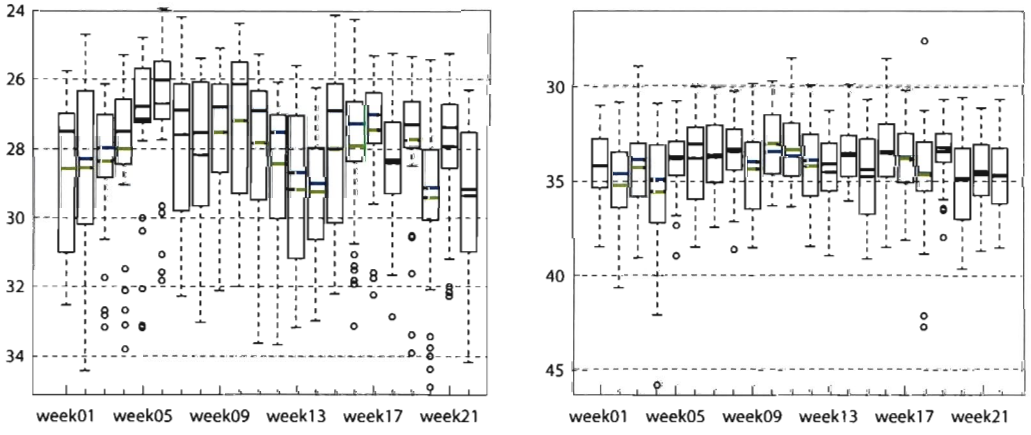
3-7-1 Europabrücke (2005)

The Europabrücke, opened in 1963, is one of the main alpine north-south routes for urban and freight traffic and currently stressed by over 30000 motor vehicles per day. Due to the requirement to assess the prevailing vibration intensities with regard to possible fatigue damage, a permanent measuring system has been installed since 2003. The superstructure is a steel box girder of variable height along the span with an orthotropic deck. The bridge is 657 m long and consists of six spans of different length, carrying six lanes, three for each direction, over a total width of 25 m. Existing records of vibration measurement are quite extensive. Attached F.3-9 and F.3-10 represent the analysed results from May to October of the records in 2005, at middays and midnights, respectively. They basically show a healthy, stable condition of the structure, no indication of serious structural non-linearity being detected.

The statistical evaluation of this structure gives a significant change of the pattern for 80 % of energy after the 4th week of observation, but the whole plot shows a fluctuation that might be due to different traffic. F.3-11 are the boxplots of midday and midnight results.

It has to be kept in mind, however, that the existence of structural non-linearity, both or either in stiffness and damping, is not necessarily 100 % equivalent to the state where the structure is damaged in any ways. There may be a case where micro-cracks are developing, for example, but the overall structural behaviour does not show any sign of non-linearity.

Europabrücke: midday (left) and midnight (right) – boxplot of 80 % of energy F.3-11

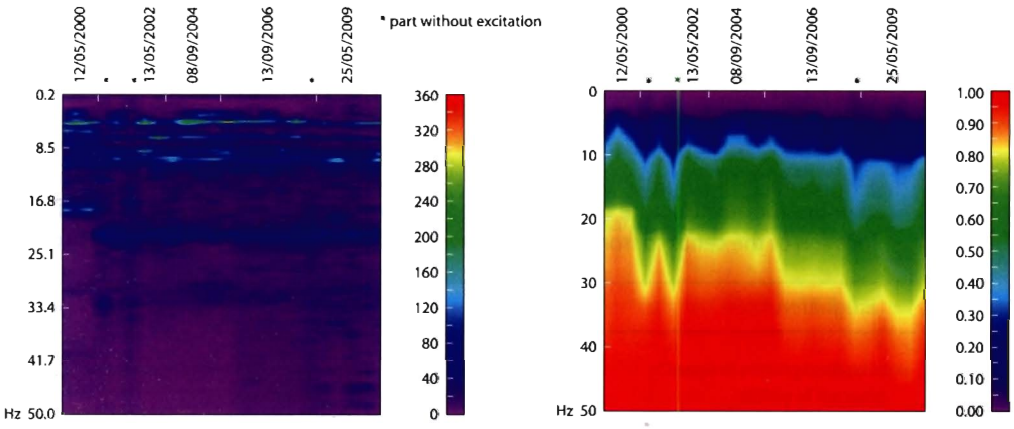


3-7-2 Melk B3A (2000–2009)

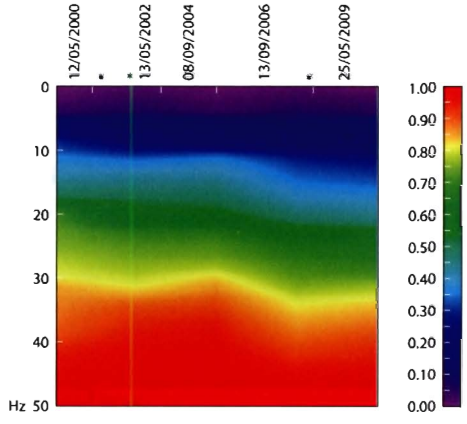
An example of a structure deteriorating over a period of nine years is demonstrated here. Disregarding some irregularities, the gradual change of the spectral pattern (F.3-12) clearly indicates that more and more dynamic energy is transferred towards higher frequency ranges.

One important matter in looking at the change in spectral patterns is that comparison must be made between the cases of the same structure under similar physical conditions. For example, all measurements of this particular bridge were carried out under its service conditions, namely open to the traffic load excitation. Since the traffic loads tend to enhance the bridge vibration in a certain limited range of frequency, the resulted spectral pattern is different from that obtained under more random ambient excitations such as micro-tremors or wind. It tends to shift the spectra towards a lower frequency range com-

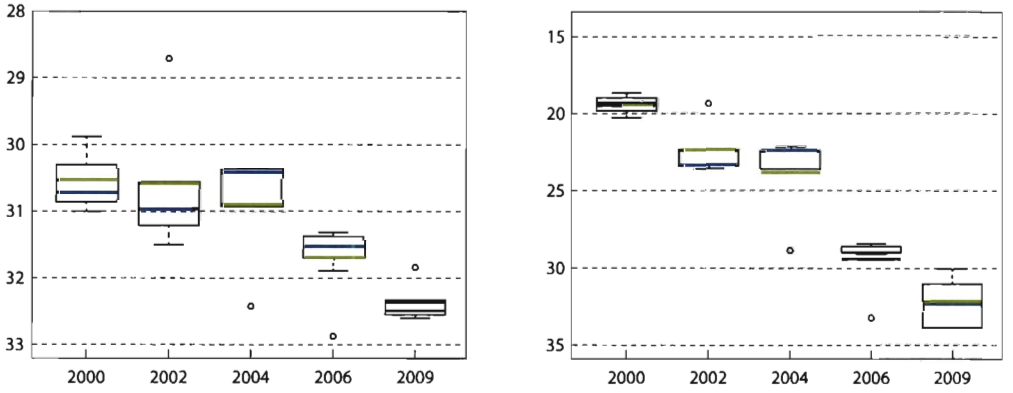
Melk B3A F.3-12



Melk B3A: without traffic F.3-13



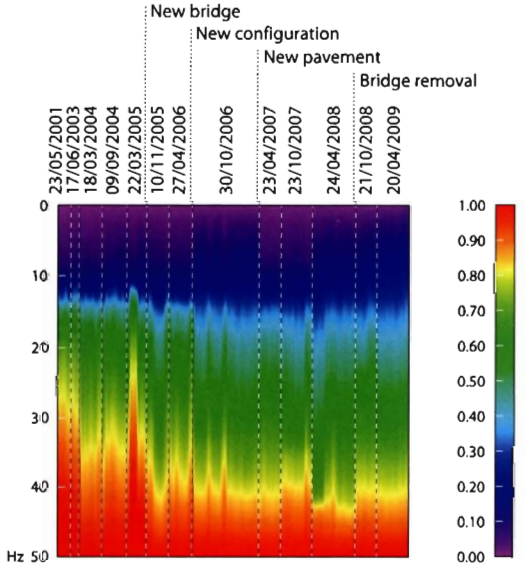
Melk B3A: boxplot of the centroid (left) and boxplot of 80 % of the energy (right) F.3-14



pared to the time without traffic. In order to avoid this effect, an effort was made to extract some data obtained when the bridge was freely vibrating without traffic loads. The resulting spectral pattern without traffic excitation is shown in F.3-13.

Concerning the statistical evaluation of this bridge, it depends on which value is used. For this bridge the results of the location of the centroid of the energy distribution and the value of 80 % of energy are presented to show that there can be a difference: significant changes for this structure can be observed with the analysis of variance (ANOVA) for the location of the centroid from the 5th observation period (that is the year 2006) and for the

Flughafen F.3-15



value for 80% of energy from the 4th observation period (that is the year 2004). F.3-14 shows the boxplots of these results.

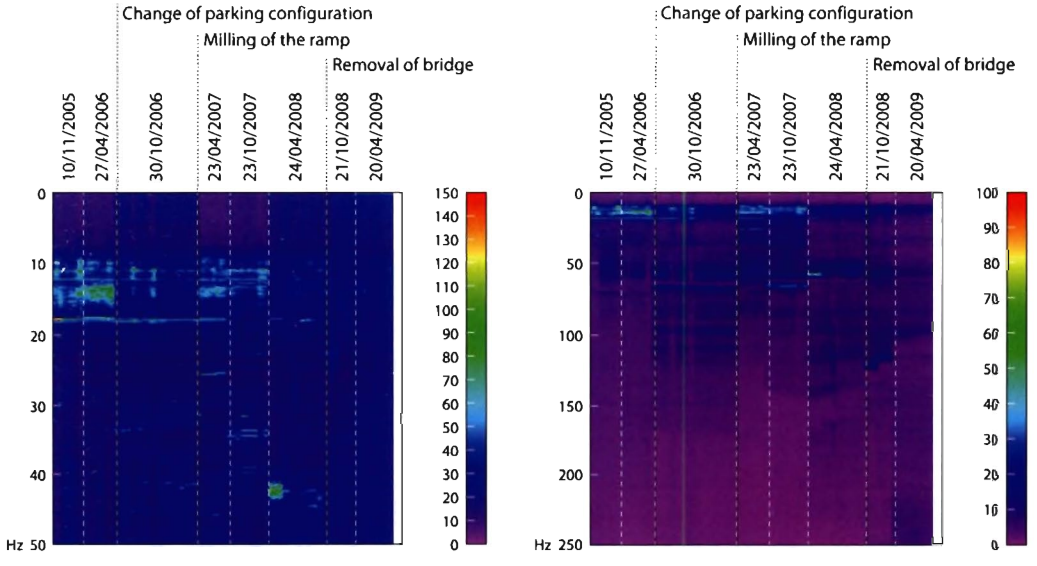
3-7-3 Flughafen Vorfahrt (2004–2009)

The access bridge in front of the terminal 2 of the Vienna International Airport was established in 1956 and widened to 10.5 m in 1968. Measurements of the dynamic characteristics took place after a concern was expressed regarding its load carrying capacity. Available data are from eleven different groups of files accumulated over a period of five years, March 2004 through April 2009, while the construction work was progressing. There were a number of changes in structural configuration, therefore, over this period [Furtner, 2009]. Regardless of the history of various events happening on the structure, there is clearly a general trend of dynamic energy shift towards higher frequency ranges throughout the period (F.3-15).

Out of existing data files, the first 33 files were measured with the sampling frequency of 100 Hz and the last 98 files were at 500 Hz. When the sampling frequency was 100 Hz, any spectral information in high frequencies beyond 50 Hz would have been lost. An important issue is, whether any meaningful engineering judgement could be made based only on the information of less than the cut-off frequency. The effects of sampling rates on the depicted spectral patterns were examined, because of this reason, based on the data of this bridge only from the last 98 files, by comparing the following two cases:

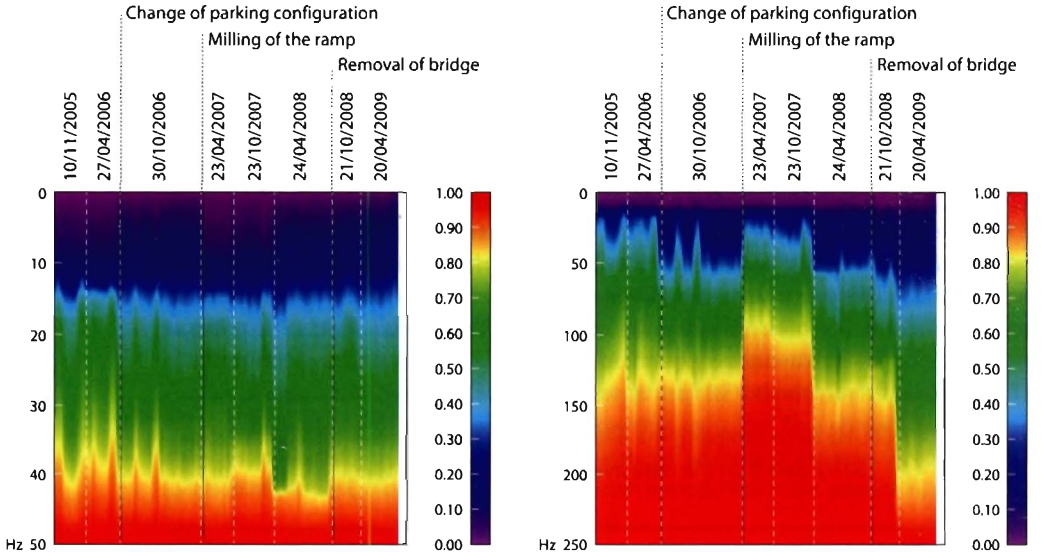
// for $0 < f \leq 50$ Hz by re-sampling the data at 100 Hz, namely every fifth points and
// for $0 < f \leq 250$ Hz based on the data available at 500 Hz sampling.

Flughafen: $F_i(f)$ the last 98 files F.3-16

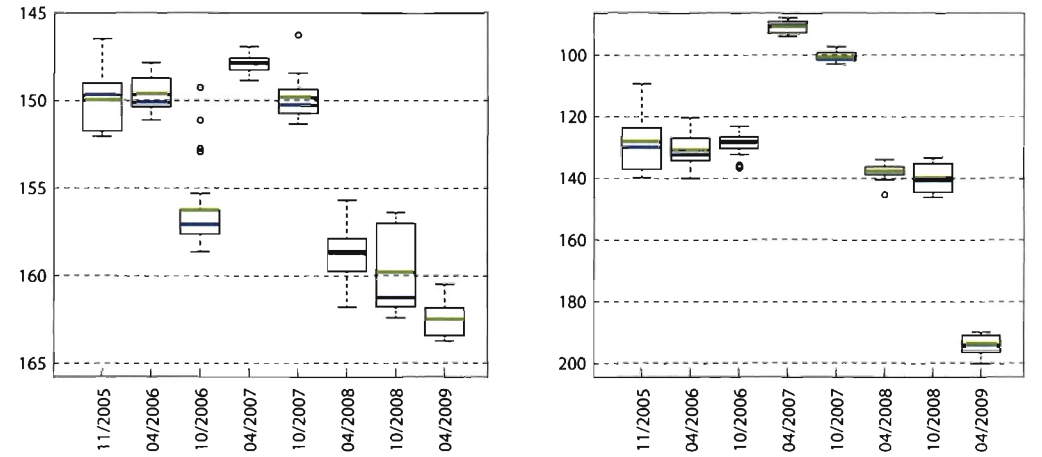


F.3-16 and F.3-17 compare the normalized spectra $F_i(f)$ and the cumulative distribution $E_i(f)$ of both cases. It is obvious that (B) has much more information than (A). Transfer of energy to a higher frequency range that took place between various events is clearly better recognized by the results of (B). The high spectral peaks started appearing in the higher frequency range after milling of the ramp started in April 2007, indicating a signifi-

Flughafen: $E_i(f)$ the last 98 files F.3-17



Flughafen: boxplot of the centroid (left) and boxplot of 80 % of the energy (right) F.3-18



cant change of spectral pattern. In terms of the cumulative spectral energy $E_i(f)$, it is more clearly recognized by case (B) rather than (A), since presumably more and more energy is transferred to the frequency range beyond 50 Hz. Note, however, that high frequency noise is also effectively cut off for the case of (A) due to low sampling frequency and it sometimes makes it easier to look at the colour pattern since the spikes caused by operational noise are reduced.

The statistical analysis gives significant changes for this structure with the analysis of variance (ANOVA) for the location of the centroid from the 3rd observation period (that is the year 2006) and for the value for 80 % of energy from the 4th observation period (that is the year 2004). F.3-18 shows the boxplots of these results.

3-8 Concluding Remarks

The proposed spectral method (VCLIFE) was applied to the results of on-site measurements at several different bridges. The presented results here further emphasize a possibility of effectively detecting the development of structural damages by looking at the change of the spectral pattern due to the shift of dynamic energy towards a higher frequency range. In relation to this observation, it should be noted that the results are more informative when the sampling frequency is high enough, generally speaking.

This energy shift seems to be quite characteristic to the structures with developing damages. It is considered now that a combination of the ambient vibration survey and the proposed spectral analysis can be an effective tool, which is applicable as a simple structural health monitoring tool. To this end, it would be ideal if a criterion for the extent of structural damage corresponding to any indicator of the energy shift can be established. Locating the centroid of the area under $E_i(f)$ curves is one possibility but its practicability would require further discussion.

For the future measurements, it is advisable to have a sampling frequency of 500 Hz. For identifying the high frequency shift of dynamic energy, it is desirable to minimize the effects of extraneous disturbances, particularly the traffic load. Ideally, if the spectrum of excitation force can be identified even approximately, its contribution towards the output spectra can be estimated but this is not the case most of the time. Minimization of noise effects could be achieved by taking a long enough record so that undesirable noise, including the traffic load, can be regarded more or less an evenly distributed excitation. Taking several consecutive files, each 330 seconds long, would suffice. Ideally, the free vibration record of the structure should be observed over a certain period of time. It should be also mentioned that, in any measurements involving multi-locations on the structure, it is desirable to keep the reference point at the same location throughout the campaign.

References

Furtner, P., 2009. *Flughafen Wien Schwechat Vorfahrt Ost Terminal 2 – Objekt 102, Dynamische Charakteristik der Bauwerke, Periodische Nachmessung und Interpretation der Ergebnisse*. Report 09/1042, April 2009.

Wenzel, H., Veit-Egerer, R., Widmann, M. and Jaornik, P., 2009. *WP3 Demonstration Report*. Deliverable D11.1, October 2009.

Wenzel, H., 2009. *Health Monitoring of Bridges*. Wiley.

4

Life Cycle Cost Optimized Monitoring Systems for Offshore Wind Turbine Structures

Authors:
Sebastian Thöns
Michael Havbro Faber
Werner Rücker

Motivation

Monitoring information should be utilized to support optimal decisions. In this sense monitoring systems should be designed such as to optimize expected Life Cycle Costs.

Main Results

The essential finding of the research is that the efficiency of operation of wind turbine structures can be substantially supported by Life Cycle optimized monitoring systems. It is found that a significant expected operational benefit over the Life Cycle of a structure can be achieved by the developed approach, namely, the conceptual integration of structural monitoring techniques, structural reliability theory and reliability based inspection and repair planning.



4-1 Introduction

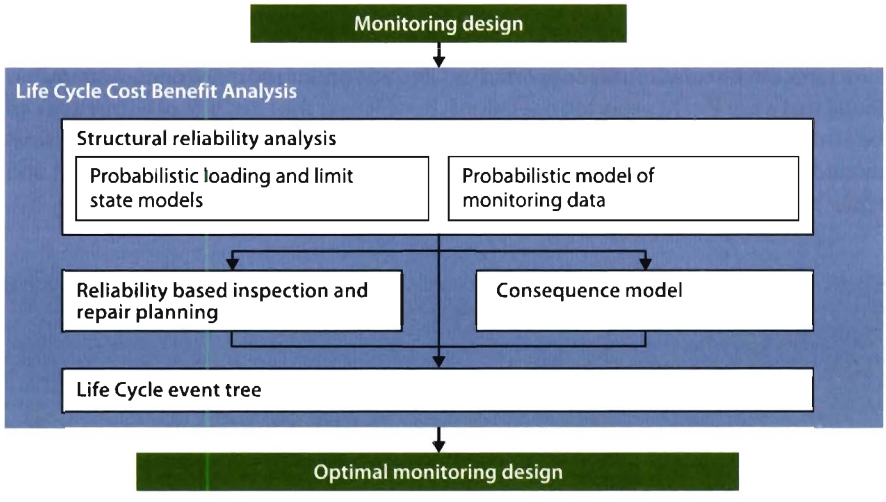
As more offshore wind parks are commissioned, the focus is shifting from a planning and construction focus to an operation, maintenance and investment return focus. In the latter case, the efficient operation of wind parks is highly important.

In this study, a framework for the quantification of the expected Life Cycle Costs for wind turbine structures is developed to facilitate and to support optimal decisions. The framework builds upon the approaches of structural reliability theory and Bayesian decision theory. The calculation of the Life Cycle Costs is performed utilizing an event tree which facilitates to assess the probabilities of events associated with consequences applying structural reliability theory. For the determination of the inspection and repair events, reliability based inspection and repair planning is utilized. Furthermore, the characteristics of monitoring data in a structural reliability analysis are outlined and approaches for modelling monitoring data are introduced.

The framework given in F.4-1 illustrates how optimal decisions may be identified for the design and utilization of a monitoring system in the perspective of the Life Cycle of the structure. The decision analysis, namely the analysis supporting the design of a monitoring system for a structure to be commissioned, constitutes a Bayesian pre-posterior decision analysis. A pre-posterior analysis facilitates a decision analysis on the basis of not yet known data, i.e. not yet known monitoring data, which are modelled based on the developed monitoring system and data models. In this way the Life Cycle Costs associated with the utilization of a monitoring system are calculated.

In order to derive a Life Cycle optimal monitoring system, the expected Life Cycle Costs for various monitoring systems are calculated and the optimal monitoring systems

Framework for the quantification of Life Cycle Costs and its utilization for monitoring system design F.4-1



are identified on this basis. A comprehensive description of the approaches and a case study is contained in the following sections.

Section 4-2 contains an approach for monitoring based condition assessment based on an uncertainty modelling of monitoring systems which is developed focusing on the measurement uncertainties. Furthermore, the characteristics of monitoring data in a structural reliability analysis are elaborated with focus on the model uncertainties.

In section 4-3 the framework for a Life Cycle Cost-Benefit Analysis including the costs for monitoring is developed. Consecutively, the benefit associated with monitoring is defined. Within the framework of the Bayesian decision theory, a pre-posterior decision analysis is formulated to derive optimal design parameters for the design of a monitoring system.

Section 4-4 contains a case study of a Multibrid M5000 wind turbine support structure. Here, the results of a structural reliability analysis are summarized and the assumptions in regard to the reliability based inspection and repair planning, the consequences and the set of decision alternatives are described. The monitoring benefit with regard to the operation costs, structural risks and total Life Cycle Costs is quantified and the optimal decisions for different decision situations are derived. The chapter closes with the summary and conclusions in section 4-5.

4-2 Monitoring Based Structural Condition Assessment

The utilization of monitoring data for the structural condition assessment (see e.g. [JCSS, 2001; Rücker et al., 2006]) facilitates reliability updating on the basis of temporal continuous information. This problem complex has recently gained significant interest in various fields of engineering (see e.g. [Enright, 2006; Straub, 2011; Thöns, 2012]). Monitoring data constitute time continuous measurement data. However, the modelling of all relevant uncertainties in a structural reliability analysis (as e.g. required by [JCSS, 2006]) for what concerns monitoring data is mostly performed generically rather than on a systematic basis.

The thesis by [Thöns, 2012] contributes to the modelling of monitoring uncertainty by suggesting an approach for the determination of the measurement uncertainty utilizing all available information which comprises information about the physical measurement process and observations of the measurement process (section 4-2-1). Furthermore, with generic fatigue reliability analyses the characteristics and the modelling of monitoring data in the context of structural reliability analyses are outlined (section 4-2-2).

4-2-1 Monitoring Uncertainty Modelling

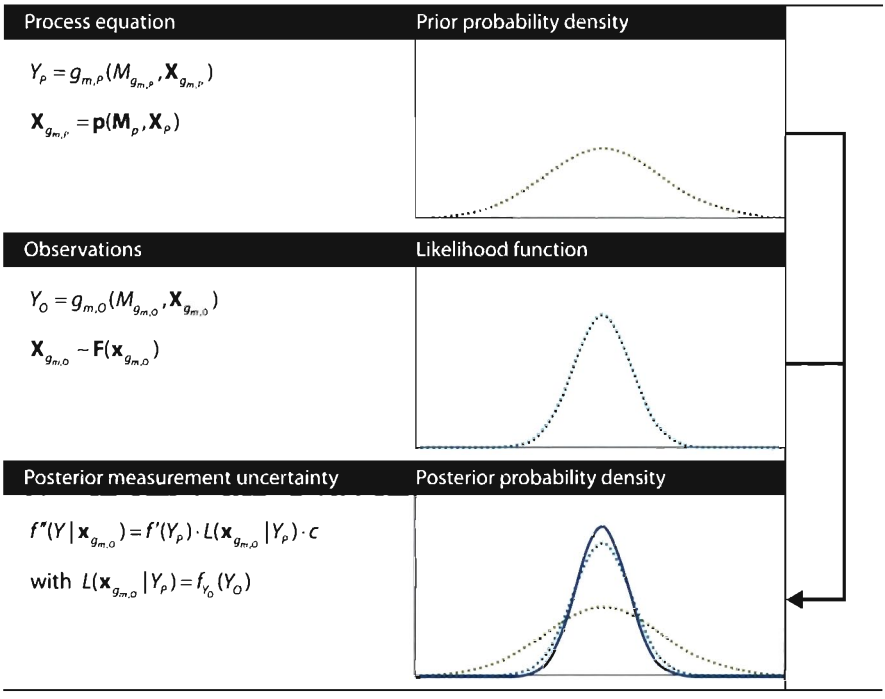
The approach for the determination of measurement uncertainties which is outlined in the following has been developed in [Thöns, 2012]. The approach is based on the Bayesian definition of probability and builds upon the structural reliability analysis framework of the Joint Committee on Structural Safety [JCSS, 2006] and the methods of the Guide to the Expression of Uncertainty in Measurement [ISO, 2008].

The measurement uncertainty is defined as the probability distribution function of a measurement quantity Y. The measurement quantity Y is per definition not directly measured and is calculated with the measurement equation g_m (E.4-1). The measurement quantity is dependent on the random variables $\mathbf{X}$ constituting the measured quantities and the random variable M_{gm} which is defined as the measurement equation model uncertainty.

$$Y = g_m(M_{gm}, \mathbf{X}) \qquad \text{E.4-1}$$

The probability distribution function of the measurement quantity Y, i.e. the measurement uncertainty, can be determined on the basis of a process equation and on the basis of observations. These two types of measurement uncertainties differ in the way how the measured quantities $\mathbf{X}$ are determined and can further differ in the formulation of the measurement equation g_m.

Approach for the determination of the measurement uncertainty E.4-2



Taking a process equation as the basis for the determination of the measurement uncertainty, i.e. the distribution of the measured quantity Y_P, the measurement equation is defined as $g_{m,P}$ in dependency on the model uncertainty of the measurement equation $M_{g_{m,P}}$ as well as on the vector of the measured quantities $\mathbf{X}_{g_{m,P}}$. The probability distribution functions of the measured quantities $\mathbf{X}_{g_{m,P}}$ are here determined with a vector of process equations $\mathbf{p}$, with the random variables $\mathbf{M}_P$, i.e. the vector of process equation model uncertainties, and the random variables $\mathbf{X}_P$ constituting the parameters of the process equations. The process equations model the physical measurement processes with probabilistic electrical, optical and/or mechanical models and thus facilitate the determination of the probabilistic model of the measured quantities $\mathbf{X}_P$.

On the basis of observations, the measurement quantity Y_O is calculated with the measurement equation $g_{m,O}$ dependent on the model uncertainty of the measurement equation $M_{g_{m,O}}$ and the vector of the measured quantities $\mathbf{X}_O$. Observations of the measured quantities $\mathbf{x}_{g_{m,O}}$ are utilized for the determination of the vector of the probability distribution functions $\mathbf{F}$ of the measured quantities. Here, the measured quantities $\mathbf{X}_O$ are probabilistically modelled given observations of the physical measurement processes under defined conditions.

The measurement uncertainty determined on the basis of the probabilistic process equation is defined as the prior measurement uncertainty. This definition takes basis in an informative approach to the prior measurement uncertainty (e.g. in contrast to [Sommer et al., 2009]) constituting the physical relations which facilitate to conduct a measurement. The likelihood function is then the probability density function of measurement quantity determined on the basis of observations, i.e. $L(\mathbf{x}_{g_{m,O}} | Y_P) \sim f_{Y_O}(Y_O)$. With these definitions the posterior measurement uncertainty, i.e. the posterior probability density function of the measurement quantity $f''(Y | \mathbf{x}_{g_{m,O}})$, is calculated by Bayesian updating (E.4-2, with the constant c).

The introduced approach in this general formulation facilitates the quantification of the measurement uncertainty for various measurement technologies. The approach is further applied for the quantification of the monitoring uncertainty as a part of the probabilistic models in a structural reliability analysis.

4-2-2 Structural Reliability Analyses and Monitoring Data

A structural reliability analysis can be based on design data, i.e. on the data available before a structure is commissioned, and on the basis of monitoring data, i.e. on measurement data from the commissioned structure. Both design and monitoring data require specific modelling principles which are elaborated here (on the basis of [Thöns, 2012]) to show the characteristics of monitoring data in a structural reliability analysis.

Considering monitoring data as strain measurements from components of a structural system, monitoring data can be assigned to either the loading model $S_{des/m}$ or the resistance model R taking basis in the generic format of a limit state equation g for a structural component (E.4-2). The assignment of monitoring data to the resistance model constitutes the approach of proof loading [Thöns et al., 2011].

$$g = R - S_{des/m} \qquad \text{E.4-2}$$

Assuming that the strain measurements are interpreted as loading model information, the probabilistic model of the loading S_m can be formulated as the multiplication of the model uncertainty B_m, the measurement uncertainty U, and the loading S (E.4-3). The measurement uncertainty U is quantified with the introduced approach in section 4-2-1.

$$S_m = B_m U S \qquad \text{E.4-3}$$

The probabilistic model for the determination of the loading model utilizing design data S_{des} may be expressed in terms of the model uncertainty B_{des} and the loading S.

$$S_{des} = B_{des} S \qquad \text{E.4-4}$$

When design data are utilized for the reliability calculation, the calculation of the strains and stresses of a structural component requires a rather complex (Finite Element) model of the structure. These complex models are associated with the model uncertainty B_{des}, which can be modelled following e. g. the Probabilistic Model Code JCSS [JCSS, 2006].

In contrast, the model uncertainty in a reliability analysis utilizing monitoring data B_m can be rather low as models with low complexities are applied. However, additional uncertainties like the measurement uncertainty U (section 4-2-1) have to be considered.

The outlined characteristics of monitoring and design data in regard to the uncertainty modelling can lead to the situation that the monitoring data are more certain than design data. The structural reliability of a component can then be higher when monitoring data are utilized based on the same distribution of the loading S. For instance, a significant higher fatigue reliability for a hot spot due to the reduction of the model uncertainties in combination with relatively low measurement uncertainties for strain gauge measurements is quantified in [Thöns, 2012].

4-3 Approach for the Optimization of the Expected Life Costs by Monitoring Systems

The structural condition assessment based on information on structural reliability and risks constitutes an essential part of the operation of structures. Monitoring can be used for the structural condition assessment and can contribute to the structural reliability by more certain information on the condition of the structure, as described in section 4-2 and [Thöns, 2012]. However, monitoring systems can be further utilized aiming at the minimization of the expected operation costs and risks. In order to proceed in this direction the generic design decision for a monitoring system is formulated within the framework of the Bayesian decision theory utilizing a Life Cycle Cost-Benefit Analysis.

4-3-1 Life Cycle Modelling and Definition of a Monitoring Benefit

A Life Cycle Cost-Benefit Analysis for the management of structural integrity of a steel structure comprises the assessment of the expected values of the costs associated with inspection, repair and failure (e.g. [Straub, 2004]). A Life Cycle Cost-Benefit Analysis necessitates the formulation of various probabilistic and deterministic models such as degradation models, inspection models, repair models and a structural event tree model.

The expected value of the total Life Cycle Costs $E[C_T]$ is the sum of the expected value of failure costs $E[C_F]$ and the expected operation costs of a structure $E[C_{OPEX}]$ which consists of the expected inspection costs $E[C_I]$ and the expected repair costs $E[C_R]$ (see E.4-5). The dependency on inspection quality, repair policy and service life is suppressed here for clarity.

$$E[C_T] = E[C_F] + E[C_{OPEX}] \quad \text{with} \quad E[C_{OPEX}] = E[C_I] + E[C_R] \qquad \text{E.4-5}$$

When a monitoring system is applied, the expected value of operation costs $E[C^M_{OPEX}]$ is calculated on the basis of modified expected inspection and repair costs ($E[C$] and $E[C^M_R]$) and additionally with the expected value of monitoring operation costs $E[C_M]$ (E.4-6). The expected value of the monitoring costs $E[C_M]$ is calculated from the number of sensors dependent (or channel (k) dependent) costs of the system $C^M_{Sys}(k)$ the costs of the installation of the system $C^M_{Inst}(k)$ as well as the costs of the operation of the system C^M_{Op} (E.4-7). The monitoring system operation costs are discounted to the present value dependent on the time of the cash flow t and are multiplied by the yearly probability of no failure $(1-\Delta p_F)$.

$$E[C^M_{OPEX}] = E[C^M_I] + E[C^M_R] + E[C_M] \qquad \text{E.4-6}$$

$$E[C_M] = C^M_{Sys}(k) + C^M_{Inst}(k) + (1-\Delta p_F) \cdot C^M_{Op} \cdot \frac{1}{(1-i_r)^t} \qquad \text{E.4-7}$$

The expected value of the benefit associated with monitoring $E[B_M]$ is defined as the expected total Life Cycle Costs $E[C_T]$ minus the expected total Life Cycle Costs associated with the application of a monitoring system $E[C^M_T]$ (E.4-8).

$$E[B_M] = E[C_T] - E[C^M_T] \qquad \text{E.4-8}$$

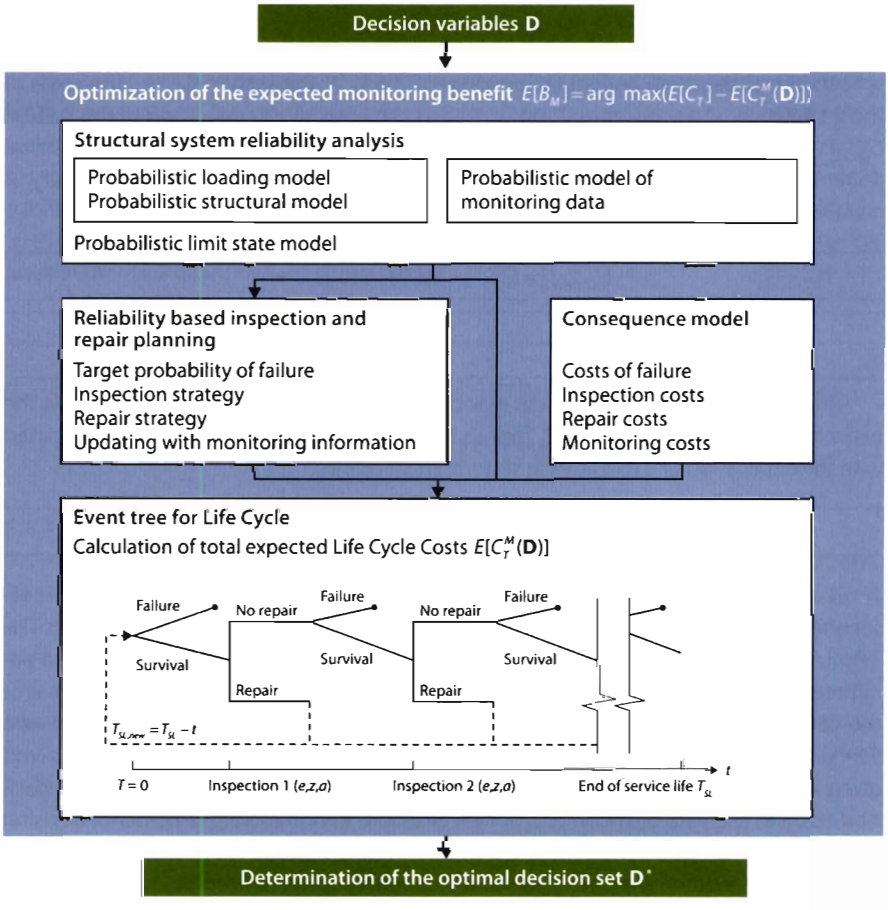
The outlined approach facilitates the calculation of the expected value of benefit associated with monitoring including the expected value of the costs for monitoring. The calculation of the expected monitoring benefit is dependent on various models and parameters. In order to quantify the effect of certain parameters on the expected value of the benefit associated with monitoring the Bayesian decision analysis (see [Raiffa and Schlaifer, 1961]) is utilized. The Bayesian decision theory defines decision situations with given information (prior decision analysis), with additional information (posterior decision analysis) and with unknown, i.e. not yet available, information (pre-posterior decision analysis). For these decision situations expected costs are calculated and optimized in dependency of decision variables, i.e. certain parameters of the utilized models.

Based on a pre-posterior Bayesian decision analysis, the expected value of the benefit of monitoring can be optimized in dependency of yet unknown monitoring information. This information can be modelled by the approaches of the structural reliability accounting for the measurement uncertainty and its effect on the structural reliability (see section 4-2). Further, decision variables **D** can be introduced which define the design of the monitoring system (E.4-9).

$$E[B_M] = \arg\ \max(E[C_T] - E[C_T^M(\mathbf{D})]) \qquad \text{E.4-9}$$

The probabilistic models which are utilized for the optimization of the expected value of the benefit of monitoring $E[B_M]$ are indicated in F.4-3. The individual structural events no failure, failure, inspection and repair are modelled through a structural event tree for each service year. The probabilities of the events of no failure and of failure are calcu-

Utilized model for the optimization of the expected monitoring benefit with an event tree from [Straub, 2004] F.4-3



lated through structural system reliability analyses which require probabilistic models for loading, resistances and limit state models (F.4-3). The inspection events are accounted for using the approaches of reliability based inspection planning which themselves build upon structural reliability analyses and necessitate that inspection and repair strategies are defined and that the annual target probability of failure is defined. The consequence model accounts for the costs of the structural events in the event tree.

The event tree as depicted in the lower part of F.4-3 is taken as the basis for the following analyses additionally considering the costs of monitoring which apply to the case of survival of the structure in each year of the service life (see E.4-6). An important characteristic of the event tree is the assumption of the simplification rule which is associated with the behaviour of a repaired element; that is that a repaired component behaves like a new component ([Straub, 2004], see F.4-3).

4-3-2 Definition of Decision Variables

Monitoring is only sensible when a decision set can be found which leads to a positive monitoring benefit $E[B_M]$. The underlying decision, denoted with D_1, is thus the decision whether to monitor or not to monitor (E.4-10).

$$D_1 = \{M, \bar{M}\} \qquad \text{E.4-10}$$

The decision to monitor depends on the decision which components to monitor and which type of monitoring system should be applied. The decision set D_2 contains the monitored hot spot set (E.4-11) consisting of n_2 monitored hot spot sets c_{HS}. The monitored hot spot set influences the monitoring system investment and installation costs (see E.4-7) because $k = 3$ channels are assumed to monitor one hot spot.

$$D_2 = \{c_{HS,1}, c_{HS,2}, \ldots, c_{HS,n_2}\} \qquad \text{E.4-11}$$

The decision set D_3 models the type of the monitoring system in terms of its precision. D_3 contains n_3 variables δ which describe the uncertainty reduction due to monitoring (E.4-12 and see section 4-2-2). However, in section 4-2-2 the underlying assumption is that the probabilistic loading model S is the same for the design data and for monitoring data which must not necessarily be given in a practical situation. Then, the uncertainty reduction factor δ describes the combination of the different probabilistic loading models in combination with the probabilistic model uncertainty and measurement uncertainty models.

$$D_3 = \{\delta_1, \delta_2, \ldots, \delta_{n_3}\} \qquad \text{E.4-12}$$

4-4 Case Study

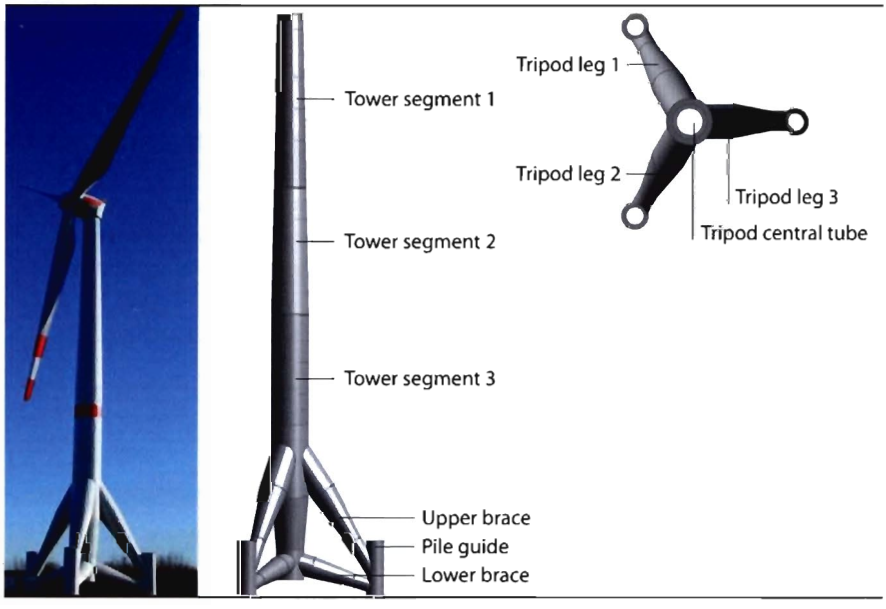
The case study contains the Life Cycle Cost-Benefit Analysis investigating various monitoring solutions for the support structure of a Multibrid M5000 offshore wind turbine prototype as depicted in F.4-4.

The support structure of the wind energy converter consists of a tower divided in segments by ring flanges, the tripod consisting of upper braces, lower braces, the pile guide as well as the foundation, which consists of circular reinforced concrete slabs attached to a pile group. The support structure involves 11 tower components assigned to three tower segments and 24 tripod components as parts of the tripod legs and central tube as well as their connections. For this case study a reliability analysis [Thöns et al., 2010] on the basis of a developed model basis was performed.

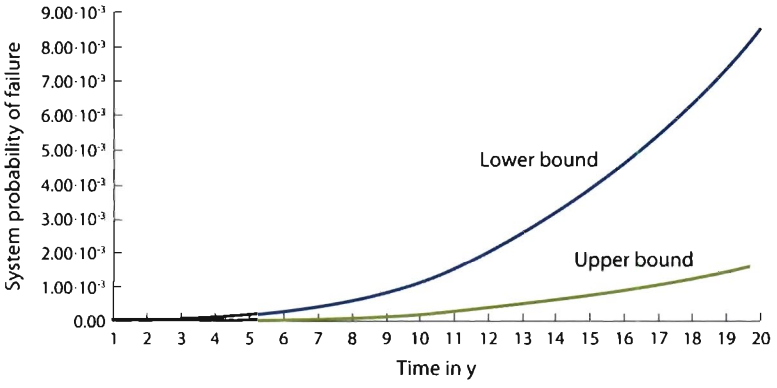
4-4-1 Results of the Structural Reliability Analysis

The structural reliability analysis builds upon probabilistic structural, loading and limit state models comprising design, production and construction data. This model basis is derived by analysing various aspects of the developed structural, loading and limit state models and on the basis of the results of a sensitivity study in conjunction with the developed probabilistic models [Thöns et al., 2012a; 2012b]. The complexity of the individual models dictates an efficient solution scheme for the reliability analysis. Such an algorithm is developed consisting of an adaptive response surface algorithm and an importance sampling Monte-Carlo algorithm in [Thöns et al., 2010].

Prototype of a Multibrid M5000 offshore wind turbine and support structure with the structural parts F.4-4



Support structure system probability of failure for a service life of 20 years F.4-5



The calculation of the probabilities of fatigue failure involves the connections of all tower and tripod components with an SN limit state model. The probability that a fatigue failure occurs can be calculated with the simple bounds of system reliability theory (see e.g. [Ditlevsen, 1979]) based on a serial system. Then the probability that fatigue failure occurs results at the end of the service life for the tower in the bounds of $1.66 \cdot 10^{-3}$ and $5.15 \cdot 10^{-3}$, for the tripod in the bounds of $9.28 \cdot 10^{-4}$ and $3.30 \cdot 10^{-3}$ and for the support structure in the bounds of $1.66 \cdot 10^{-3}$ and $8.43 \cdot 10^{-3}$ (F.4-5).

The calculated probabilities of failure should be in accordance with acceptance criteria such as target probabilities of failure given for components in the [DIN EN 1990, 2010] and for structural systems in the Probabilistic Model Code [JCSS, 2006]. A detailed analysis in [Thöns et al., 2010] has shown that these requirements are fulfilled or not contradicted.

4-4-2 Reliability Based Inspection and Repair Planning

The inspection strategy builds upon the approaches of the reliability inspection planning and is based on the models in [Straub, 2004] utilizing the documented database. A magnetic particle inspection (MPI) is assumed as the inspection technology [Straub, 2004; Visser, 2000]. A probability of failure threshold $\Delta p_{F2}^{T} = 1.00 \cdot 10^{-4}$ is assumed. The repair event is defined on the basis of a measured crack size during an inspection [Straub, 2004].

The inspection plans are modified in dependency of the variable δ in the decision set D_3 which models the uncertainty reduction due to monitoring and consequently the reduction of the probability of failure of the hot spot. The modification of the inspection plans follows the approach described in [Straub, 2004] based on the calculation of a fictive installation year at the modification time (which here equals the monitoring system installation time plus one year) for which the inspection plan is then derived. This approach accounts for the properties of the underlying fracture mechanics model. The new inspection plan for the remaining service life is derived in combination with the original inspection plan considering already performed inspections before the modification time.

4-4-3 Consequence Model

The consequence model takes a structural failure associated with the loss of the structure and with the loss of the monitoring system (when applied) into account. For survival of the structure the consequences are inspections and repair (according to the reliability based inspection and repair planning) as well as the monitoring system operation.

The cost model consists of generic and normalized values for the failure costs ($C_F = 1$), the inspection costs ($C_I = 10^{-3}$) and the repair costs ($C_R = 10^{-2}$) per component and an interest rate of $i_r = 5\,\%$ [Straub, 2004]. In relation to this cost model, a monitoring cost model for the reference case is introduced. The costs of the monitoring system are assumed to $C^M_{Sys}(k) = 1.33 \cdot 10^{-4}$ per channel, where three channels (i.e. sensors) are used with the monitoring of one hot spot. The costs of installation are assumed to $C^M_{Inst}(k) = 1.33 \cdot 10^{-4}$ per channel and the operation costs are assumed to $C^M_{Op}(k) = 6.67 \cdot 10^{-4}$ per year. As an example for the cost model the reference case is considered assuming generic costs of 1,500,000 € per megawatt (European Wind Energy Association [EWEA, 2009]). The resulting costs for the reference case are summarized in T.4-1.

Consequence for the case study T.4-1

Type of costs	Value
Failure costs C_F	7,500,000 €
Inspection costs per component C_I	7,500 €
Repair costs per component C_R	75,000 €
Costs of monitoring system per channel $C^M_{Sys}(k)$	1,000 €/k
Costs of system installation per channel $C^M_{Inst}(k)$	1,000 €/k
Costs of system operation per year C^M_{Op}	5,000 €/a

4-4-4 Decision Set Definition

The decision set D_2 contains $n_2 = 20$ hot spot sets c_{HS}. The hot spot set is determined beginning with the hot spot with the highest probability of failure. Consecutively, the hot spot with the second lowest probability of failure is added to the set. The 20 hot spot sets cover the relevant hot spots for the calculation of the system probability of failure (see section 4-4-1 and [Thöns, 2012]). The decision set D_3 consists of $n_3 = 11$ variables with δ in the range of 1.0 to 1.5 modelling the reduction of the probability of failure by a monitoring system. The factor is generically assumed based on the results of a generic fatigue reliability analysis in [Thöns, 2012].

4-4-5 Expected Total Life Cycle Costs and Calculation of the Monitoring Benefit

The total expected Life Cycle Costs for the support structure, as designed (see E.4-5), of the wind turbine structure are calculated utilizing the cost model and the results of the structural reliability analysis (section 4-4-1). The total expected Life Cycle Costs amount to $4.88 \cdot 10^{-2}$ with $3.85 \cdot 10^{-2}$ expected cost for the operation (inspection and repair) and with

$1.03 \cdot 10^{-2}$ expected failure costs (risks). The monitoring benefit is calculated separately in relation to expected failure costs, i.e. in regard to the risks ($E[B_{M,F}]$ see E.4-13), in regard to the expected operation costs ($E[B_{M,OPEX}]$ see E.4-14) and in regard to the total Life Cycle Costs $E[B_M]$ (E.4-9).

$$E[B_{M,F}] = E[C_F] - E[C_F^M(\mathbf{D})] \qquad \text{E.4-13}$$

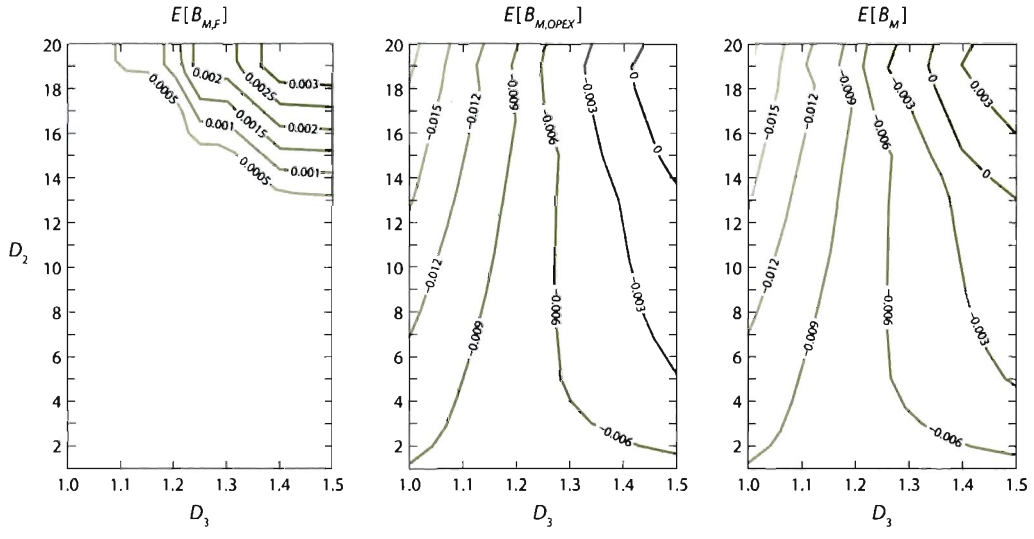
$$E[B_{M,OPEX}] = E[C_{OPEX}] - E[C_{OPEX}^M(\mathbf{D})] \qquad \text{E.4-14}$$

The monitoring benefit in regard to the risks $E[B_{M,F}]$ is positive ranging from 0.0 to $3.4 \cdot 10^{-3}$ (F.4-6 left) which corresponds to 0.0 to 33.0 % of the expected failure costs. The higher the number of monitored hot spots (decision set D_2), the higher the expected monitoring benefit $E[B_{M,F}]$. The same applies to a higher uncertainty reduction factor for monitoring (decision set D_3). The monitoring benefit in regard to the risks increases more for a higher number of monitored hot spots and for a higher uncertainty reduction factor.

The monitoring benefit in regard to the operation costs $E[B_{M,OPEX}]$ ranges from $-8.9 \cdot 10^{-3}$ to $1.5 \cdot 10^{-3}$ which is −23.1 % to 3.90 % of the expected operational costs (F.4-6 middle). The monitoring benefit is positive for high uncertainty reduction factors due to monitoring (decision set D_3) and at the same time monitoring at least the 14 hot spots with the highest probabilities of failure (decision set D_2).

The influence of the monitoring uncertainty reduction factor (decision set D_3) is more pronounced in comparison to the number of monitored hot spots (decision set D_2) for the monitoring benefit in regard to the operation costs. The reason here is that the monitoring uncertainty reduction factor does not affect the costs of monitoring.

Expected monitoring benefit with regard to the risks $E[B_{M,F}]$ (left) and with regard to the expected operation costs $E[B_{M,OPEX}]$ (middle) and with regard to the total Life Cycle Costs $E[B_M]$ (right) F.4-6



The expected monitoring benefit in regard to the total Life Cycle Costs $E[B_M]$ is the sum of the expected monitoring benefit in regard to the risks $E[B_{M,F}]$ and in regard to the operation costs $E[B_{M,OPEX}]$. The expected monitoring benefit $E[B_M]$ ranges from $-8.9 \cdot 10^{-3}$ to $5.3 \cdot 10^{-3}$ (−18.2 % to 10.9 % of the total Life Cycle Costs, see F.4-6).

The optimal decisions for the monitoring benefit in regard to the risks, the expected operational costs and the expected total Life Cycle Costs are shown in T.4-2. For the utilization of monitoring systems to reduce risks optimal decision sets D_2^* and D_3^* can be found for which the monitoring benefit $E[B_{M,F}]$ is maximized. The optimal decision sets D_2^* and D_3^* are the maximum number of monitored hot spots ($c_{HS,20} = 20$) and a monitoring system possessing the maximum (considered) uncertainty reduction factor of $\delta = 1.5$, respectively (T.4-2). Each element of D_2^* and D_3^* leads to a positive benefit here. It follows that the decision is to monitor for risk reduction, i.e. $D_1^* = \{M\}$.

The maximization of the monitoring benefit for the operational costs $E[B_{M,OPEX}]$ also leads to the decision that a monitoring system should be applied ($D_1^* = \{M\}$) because a positive benefit can be achieved. However, only certain combinations of the decision variables lead to a positive monitoring benefit. The optimal decision is to monitor ($c_{HS,19} = 19$) hot spots with a monitoring system possessing the maximum uncertainty reduction factor of $\delta = 1.5$. The same result is found for the maximization of the total Life Cycle Costs monitoring benefit $E[B]$ (T.4-2).

4-5 Summary and Conclusions

One of the major challenges in the field of renewable energies represents the development of large scale offshore wind parks as this has been the research focus in the last decade. By the time the IRIS project is completed the commissioning of the first German commercial wind parks has started in significant water depths. In preparation for the next step, namely the operation of offshore wind parks, this research work contains conceptual and applied research results on Life Cycle Cost optimized monitoring systems of offshore wind turbine structures.

The essential finding of the research is that the operation efficiency of wind turbine structures can be substantially supported by optimized Life Cycle Monitoring Systems. It is found that an expected benefit for the operation, the risks and the total Life Cycle Costs can be achieved by the conceptual integration of structural monitoring techniques, the structural reliability theory and the reliability based inspection and repair planning. The integration should be bidirectional in the sense that the generic design decisions for structural monitoring systems are based on Life Cycle Cost-Benefit Analysis and that simultaneously

Optimal decision sets for the monitoring system design T.4-2

Decision situation	Decision set D_1	Decision set D_2	Decision set D_3
Risk reduction	$D_1^* = \{M\}$	$D_2^* = \max\{c_{HS}\}$	$D_3^* = \max\{\delta\}$
Operational expenditure reduction	$D_1^* = \{M\}$	$D_2^* = \{c_{HS,19} = 19\}$	$D_3^* = \max\{\delta\}$
Total Life Cycle Cost reduction	$D_1^* = \{M\}$	$D_2^* = \{c_{HS,19} = 19\}$	$D_3^* = \max\{\delta\}$

a possible reduction of the uncertainty associated with the condition is utilized for the structural reliability assessment and thus for the inspection and maintenance planning.

With this research it is shown on the basis of a pre-posterior decision analysis how an increase of information and knowledge (here by monitoring data) for the implementation of optimal decisions (monitoring systems, inspection, repair and risks) can and should be utilized.

In a broader sense the introduced approach facilitates the quantification of the value of monitoring information based on the difference between the Life Cycle Costs applying monitoring or not. The introduced approach thus constitutes the starting point for the development of a general approach for the quantification of the value of structural health monitoring (SHM) as recently published in [Thöns and Faber, 2013; Faber and Thöns, 2013].

The research results contribute to the aims of the European Strategic Energy Technology Plan (SET-Plan: [European Union, 2010]) focusing on the improvement of the competitiveness of the wind energy production. In this way the research results also support the German and European Union energy politics aiming at the establishment of renewable energies as a major component of future energy production.

4-5-1 Conclusions with Regard to the IRIS Objectives

The achievements of the research contribute directly to the objectives of the IRIS project [VCE, 2011]:

1) Integrated Methodologies for Pioneering Risk Assessment and Management
   The developed approaches pioneer structural condition assessment on the basis of monitoring data. This facilitates the quantification of risks for the Life Cycle of a wind turbine support structure.
2) Knowledge and Technologies for Risk Identification and Reduction
   The conceptual developments of the monitoring based condition assessment constitute a knowledge progress and facilitate the utilization of monitoring technologies for risk identification and risk reduction. The risk reduction is achieved by the lower uncertainties of measurement data in comparison to design data of a structure. This fact has been quantified for the first time in the context of the structural reliability theory.
3) Online Monitoring with Decision Support Systems
   The decision support is achieved by the explicit decision theoretical formulation facilitating an optimization of the expected Life Cycle Costs of an offshore wind turbine support structure. In this way the monitoring system design decisions are based upon a Life Cycle Cost-Benefit Optimization.

References

DIN 2010. *Eurocode: Basis of Structural Design*. DIN EN 1990.

Ditlevsen, O., 1979. *Narrow Reliability Bounds for Structural Systems*. Journal of Structural Mechanics 7(4):453–472.

Enright, M. P., Hudak, S. J., McClung, R. C. and Millwater, H. R., 2006. *Application of Probabilistic Fracture Mechanics to Prognosis of Aircraft Engine Components*. AIAA JOURNAL 44:311–316.

European Union, 2010. *The European Strategic Energy Technology Plan: SET-Plan*.

EWEA, 2009. *The Economics of Wind Energy*. European Wind Energy Association.

Faber, M. H. and Thöns, S., 2013. *On the Value of Structural Health Monitoring*. ESREL 2013, Amsterdam, The Netherlands.

ISO 2008. *Part 3: Guide to the Expression of Uncertainty in Measurement (GUM:1995)*. ISO/IEC Guide 98–3.

JCSS, 2001. *Probabilistic Assessment of Existing Structures*. A publication of the Joint Committee on Structural Safety, RILEM Publications S.A.R.L.

JCSS, 2006. *Probabilistic Model Code*. JCSS Joint Committee on Structural Safety.

Raiffa, H. and Schlaifer, R., 1961. *Applied Statistical Decision Theory*. New York, Wiley (2000).

Rücker, W., Hille, F. and Rohrmann, R. G., 2006. *Guideline for the Assessment of Existing Structures*. SAMCO F08a.

Sommer, K.-D., Kühn, O., León, F. P. and Siebert, B. R. L., 2009. *A Bayesian Approach to Information Fusion for Evaluating the Measurement Uncertainty*. Robotics and Autonomous Systems 57(3):339–344.

Straub, D., 2004. *Generic Approaches to Risk Based Inspection Planning for Steel Structures*. Chair of Risk and Safety, Institute of Structural Engineering. ETH Zürich.

Straub, D., 2011. *Reliability Updating with Equality Information*. Probabilistic Engineering Mechanics 26(2):254–258.

Thöns, S., 2012. *Monitoring Based Condition Assessment of Offshore Wind Turbine Structures*. Institute of Structural Engineering, ETH Zurich, IBK Report 345, e-collection. library.ethz.ch/eserv/eth:6828/eth-6828-01.pdf, VdF Hochschulverlag AG, Zurich.

Thöns, S. and Faber, M. H., 2013. *Assessing the Value of Structural Health Monitoring*. 11th International Conference on Structural Safety & Reliability (ICOSSAR 2013). New York, USA.

Thöns, S., Faber, M. H. and Rücker, W., 2010. *Support Structure Reliability of Offshore Wind Turbines Utilizing an Adaptive Response Surface Method*. 29th International Conference on Ocean, Offshore and Arctic Engineering (OMAE 2010). Shanghai, China.

Thöns, S., Faber, M. H. and Rücker, W., 2011. *On the Utilization of Monitoring Data in an Ultimate Limit State Reliability Analysis*. 11th International Conference on Applications of Statistics and Probability in Civil Engineering (ICASP). Zurich. Switzerland.

Thöns, S., Faber, M. H. and Rücker, W., 2012a. *Fatigue and Serviceability Limit State Model Basis for Assessment of Offshore Wind Energy Converters*. Journal of Offshore Mechanics and Arctic Engineering (JOMAE) 134(3):031905.

Thöns, S., Faber, M. H. and Rücker, W., 2012b. *Ultimate Limit State Model Basis for Assessment of Offshore Wind Energy Converters*. Journal of Offshore Mechanics and Arctic Engineering (JOMAE) 134(3):031904.

VCE, 2011. *IRIS Integrated European Industrial Risk Reduction System (CP-IP 213968-2), Description of Work V21*.

Visser Consultancy Limited, 2000. *POD/POS Curves for Non-Destructive Examination*. Offshore Technology Report 2000/018.

5

Estimation of Modal Parameters and their Uncertainty Bounds from Subspace-Based System Identification

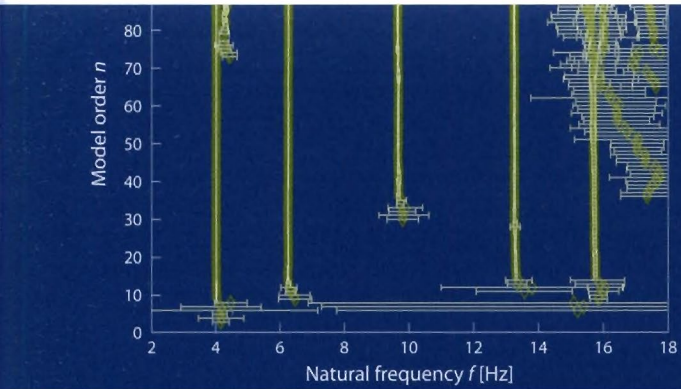
Authors:
Michael Döhler
Falk Hille
Laurent Mevel
Werner Rücker

Motivation

Operational Modal Analysis of existing structures is performed using output only vibration measurements. To evaluate the quality of the resulting modal parameters (natural frequencies, damping ratios, mode shapes) from system identification it is essential to know their statistical uncertainty content.

Main Results

An innovative and efficient algorithm to estimate the modal parameters and their uncertainties from subspace-based system identification has been developed. Applications to output only measurements have been demonstrated on the S101 Bridge case.



5-1 Introduction

Subspace-based system identification methods have proven to be efficient for the identification of linear-time-invariant systems (LTI), fitting a linear model to input/output or output only measurements taken from a system. An overview of subspace methods can be found in [Benveniste and Fuchs, 1985; Benveniste and Mevel, 2007; Döhler and Mevel, 2012; Van Overschee and De Moor, 1996].

During the last decade, subspace methods found a special interest in mechanical, civil and aeronautical engineering for modal analysis, namely the identification of vibration modes of structures from the eigenvalues (natural frequencies and damping ratios) and observed eigenvectors (mode shapes) of an LTI system. For Operational Modal Analysis, the identification of a structure under operation conditions, it is often impractical to excite the structure artificially, so that vibration measurements are taken under unmeasured ambient excitation. Therefore, identifying an LTI system from output-only measurements is a basic service in vibration analysis, see e.g. [Basseville et al., 2001; Peeters and de Roeck,1999].

For any system identification method, the estimated modal parameters are afflicted with statistical uncertainty for many reasons, e.g. finite number of data samples, undefined measurement noises, non-stationary excitations, model order reduction etc. Then the system identification algorithms do not yield the exact system matrices and identification results are subject to variance errors. For many system identification methods, the estimated parameters are asymptotically normal distributed, e.g. for estimates from prediction error methods [Ljung, 1999], maximum likelihood methods [Pintelon et al., 2007], or the here considered subspace methods [Benveniste et al., 2000; Chiuso and Picci, 2004]. A detailed formulation of the covariance computation for the modal parameters from covariance-driven stochastic subspace identification is given in [Reynders et al., 2008], where covariance estimates are based on the propagation of first-order perturbations from the data to the modal parameters. These methods are very attractive for modal analysis, as covariance estimates are obtained in one shot: From the same data set that is used to estimate the modal parameters, all the covariance information is obtained by cutting the available data into blocks, which is then propagated to the modal parameters, without the need of computing the modal parameters on the blocks.

The variance information on the modal parameters is essential for many applications. From statistical theory it is known that uncertainty bounds of estimated natural frequencies are much smaller than those of damping ratios [Gersch, 1974]. To evaluate the quality especially of the estimated damping ratios from system identification, it is essential to know their uncertainty bounds. Also, a comparison of modal parameters estimated from different data sets is not meaningful unless one knows the uncertainty bounds of the parameters to evaluate if a significant change happened or not.

In this chapter, the identification of the modal parameters from output-only measurements and the computation of their uncertainty bounds is described. They are demonstrated on the system identification of S101 Bridge.

5-2 Stochastic Subspace Identification

Stochastic Subspace Identification methods are state-of-the-art methods for modal parameter estimation. They provide unbiased and consistent estimates, even under non-stationary excitation [Benveniste and Fuchs, 1985; Benveniste and Mevel, 2007]. In this section, an overview of the identification algorithm is given.

5-2-1 Models and Parameters

The behaviour of a mechanical system is assumed to be described by a stationary linear dynamical system

$$M\ddot{z}(t)+C\dot{z}(t)+Kz(t)=v(t) \qquad \text{E.5-1}$$

where t denotes continuous time, $M,C,K\in\mathbb{R}^{d\times d}$ are the mass, damping and stiffness matrices, high-dimensional vector $z\in\mathbb{R}^d$ collects the displacements of the degrees of freedom of the structure and the external force v is unmeasured and considered as noise. The eigenstructure of [E.5-1] with the modes μ_i and mode shapes (observed eigenvectors) $\psi_i\in\mathbb{R}^r$ is a solution of

$$\det(\mu_i^2M+\mu_iC+K)=0,\quad (\mu_i^2M+\mu_iC+K)\phi_i=0,\quad \psi_i=L\phi_i,$$

where matrix $L\in\mathbb{R}^{r\times d}$ maps the r sensor locations to the d degrees of freedom of the structure. Observing model [E.5-1] at the r sensor locations (e.g. by acceleration, velocity or displacement measurements) and sampling it at some rate $1/\tau$ yields the discrete model in state-space form

$$\begin{aligned} x_{k+1}&=Fx_k+v_k\\ y_k&=Hx_k+w_k \end{aligned} \qquad \text{E.5-2}$$

where $F\in\mathbb{R}^{n\times n}$ is the state transition matrix, $H\in\mathbb{R}^{r\times n}$ is the observation matrix, $x_k\in\mathbb{R}^n$ are the states of the system and $y_k\in\mathbb{R}^r$ the output measurements at the discrete times $t=k\tau$, where n is the system order. The vectors v_k and w_k are the unmeasured input and output disturbances. The eigenstructure of system is given by

$$\det(F-\lambda_iI)=0,\quad (F-\lambda_iI)\phi_i=0,\quad \varphi_i=H\phi_i. \qquad \text{E.5-3}$$

The eigenstructure of the continuous system [E.5-1] is related to the eigenstructure of the discrete system [E.5-2] by

$$e^{\tau\mu_i}=\lambda_i,\quad \psi_i=\varphi_i. \qquad \text{E.5-4}$$

From the eigenvalues λ_i, the natural frequencies f_i and damping ratios ρ_i of the system are directly recovered from

$$f_i = \frac{\sqrt{a_i^2 + b_i^2}}{2\pi\tau}, \quad \rho_i = \frac{-b_i}{\sqrt{a_i^2 + b_i^2}} \quad \text{where} \quad a_i = \arctan\frac{\mathrm{Im}(\lambda_i)}{\mathrm{Re}(\lambda_i)}, \quad b_i = \ln|\lambda_i| . \qquad \text{E.5-5}$$

5-2-2 Covariance-Driven Stochastic Subspace Identification

To obtain the eigenstructure of system [E.5-3] and the modal parameters from vibration measurements $(y_k)_{k=1,\ldots,N+p+q}$ the stochastic subspace identification algorithm is used [Benveniste and Fuchs, 1985; Peeters and de Roeck, 1999]. In the first step, the block Hankel matrix **H** is filled with the output correlations $R_i = \mathbf{E}(y_{k+i} y_k^T)$

$$\mathbf{H} = \begin{pmatrix} R_1 & R_2 & \cdots & R_q \\ R_2 & R_3 & \cdots & R_{q+1} \\ \vdots & \vdots & \ddots & \\ R_{p+1} & R_{p+2} & & R_{p+q} \end{pmatrix} = Hank(R_i), \qquad \text{E.5-6}$$

that can be estimated from

$$\hat{R}_i = \frac{1}{N}\sum_{k=1}^{N} y_{k+i} y_k^T \in \mathbb{R}^{r\times r} . \qquad \text{E.5-7}$$

In the case of measurements at many coordinates, a subset of $r_0 \le r$ sensors can be chosen as reference sensors in the output vector $y_k \in \mathbb{R}^r$, corresponding to the reference output vectors $y_k^{(\mathrm{ref})} \in \mathbb{R}^{r_0}$. Then, the output correlations

$$\hat{R}_i = \frac{1}{N}\sum_{k=1}^{N} y_{k+i} y_k^{(\mathrm{ref})T} \in \mathbb{R}^{r\times r_0}$$

are estimated instead of E.5-7 to increase computation time and to improve the quality of the results [Peeters and de Roeck, 1999]. The parameters p and q in the block Hankel matrix E.5-6 are chosen such that $\min\{pr, qr_0\} \ge n$, with in general $p+1=q$.

Matrix **H** possesses the factorization property $\mathbf{H} = \mathbf{O}\,\mathbf{C}$ into observability matrix **O** and stochastic controllability matrix **C**, where **O** is obtained from **H** by a singular value decomposition (SVD) and truncation at the desired model order

$$\mathbf{H} = (U_1 \quad U_0)\begin{pmatrix} \Delta_1 & \\ & \Delta_0 \end{pmatrix} V^T, \quad \mathbf{O} = U_1 \Delta_1^{1/2} \overset{\mathrm{def}}{=} \begin{pmatrix} H \\ HF \\ \vdots \\ HF^p \end{pmatrix} \in \mathbb{R}^{(p+1)r\times n}. \qquad \text{E.5-8}$$

From the observability matrix **O** the matrices H in the first block row and F from a least squares solution of

$$\overline{\mathbf{O}}F = \underline{\mathbf{O}} \quad \text{with} \quad \overline{\mathbf{O}} = \begin{pmatrix} H \\ HF \\ \vdots \\ HF^{p-1} \end{pmatrix}, \quad \underline{\mathbf{O}} = \begin{pmatrix} HF \\ HF^2 \\ \vdots \\ HF^{p} \end{pmatrix} \qquad \text{E.5-9}$$

are obtained. The eigenstructure (λ_i, φ_i) of the system E.5-3 and the modal parameters are finally obtained from E.5-3 to E.5-5.

5-2-3 Stabilization Diagram

In Operational Modal Analysis, the eigenstructure of mechanical, civil and aeronautical structures is identified from output-only data under ambient excitation. The model order n of the discrete-time system E.5-2 is generally unknown (and is in fact infinity for the mechanical system in most practical cases).

On the other side, the input and output noise processes $(v_k)_k$ and $(w_k)_k$ in model E.5-2 are hardly stationary Gaussian white noise sequences in practice. It was shown that the identified system parameters converge to the true values when the number of data samples goes to infinity also under non-stationary excitation [Benveniste and Fuchs, 1985; Benveniste and Mevel, 2007]. Moreover, coloured noise can be considered. Then, the estimated eigenstructure corresponds to a combined system of a higher model order, where the modes corresponding to the noise dynamics are also contained.

Thus, the selection of the model order in E.5-8 is a major practical issue. In order to retrieve a desired number of modes, an even larger model order must be assumed while performing identification. A number of spurious modes appears in the identified model due to this over-specification, as well as due to coloured noise that appears in practice. Techniques from statistics to estimate the best model order may lead to a model with the best prediction capacity, but one is rather interested in a model containing only the physical modes of the investigated structure, while rejecting the spurious modes.

Based on the observation that physical modes remain quite constant when estimated at different over-specified model orders, while spurious modes vary, they can be distinguished using so-called stabilization diagrams. The system is identified truncating in E.5-8 at multiple model orders [Döhler and Mevel, 2012], and frequencies from this multi-order system identification are plotted against the model order. From the modes common to many models and using further stabilization criteria, such as threshold on damping values, low variation between modes and mode shapes of successive orders etc., the final estimated model is obtained. Like this, stabilization diagrams provide a GUI where the user is assisted in selecting the identified modes of an investigated structure.

5-3 Covariance Estimates of Modal Parameters

The statistical uncertainty of the estimated modal parameters is necessary to assess the quality of the estimates from the data. The uncertainty bounds of damping ratios are particularly interesting, as the estimates of damping ratios are in general afflicted with a high uncertainty according to statistical theory, and are thus difficult to obtain.

When estimated from a finite number of data samples, not the "true" parameters of the system are obtained, but estimates that are naturally subject to variance errors depending on the data and the estimation method, as the input of the system E.5-2 is unmeasured noise. A variance analysis of the system matrices obtained from Stochastic Subspace Identification is made e.g. in [Chiusi and Picci, 2004] and expressions for their computation in the context of structural vibration analysis are given in [Döhler et al., 2013; Döhler and Mevel, 2013; Reynders et al., 2008]. These computations are based on the propagation of first-order perturbations from the data to the identified parameters by a sensitivity analysis. Like this, the uncertainties of the modal parameters at a chosen system order can be computed from the uncertainty of the block Hankel matrix $\mathbf{H}$, whose covariance $\Sigma_{\mathbf{H}}$ can be estimated by cutting the sensor data into blocks on which instances of the Hankel matrix are computed. In the following, the underlying theory and the computation are explained in detail.

5-3-1 Uncertainty Propagation

First, the principle of the uncertainty propagation is stated. Let θ be some parameter vector and $\hat{\theta}_N$ its estimate based on N data samples, whose expected value $\bar{\theta}_N = \mathbf{E}\hat{\theta}_N$ tends to θ_* as N goes to infinity. Define the estimated covariance $\mathrm{cov}(\hat{\theta}_N) = \mathbf{E}\left((\hat{\theta}_N - \bar{\theta}_N)(\hat{\theta}_N - \bar{\theta}_N)^T\right)$ and let $\hat{\theta}_N$ fulfill the Central Limit Theorem

$$\sqrt{N}(\hat{\theta}_N - \theta_*) \xrightarrow{d} \mathcal{N}(0, \Sigma). \qquad \text{E.5-10}$$

for $N \to \infty$, where Σ is the asymptotic covariance and $\mathcal{N}$ designates the normal distribution. As the number of data samples N is usually large, the distribution of $\hat{\theta}_N$ is approximated to be normal with $\mathrm{cov}(\hat{\theta}_N) \approx \frac{1}{N}\Sigma$. Property E.5-10 is fulfilled directly for estimates e.g. from subspace methods, maximum likelihood or prediction error methods.

Now, let $f(\theta)$ be a vector-valued function of the parameter. Suppose that its first derivative, the sensitivity matrix $\mathcal{J}_f = \mathcal{J}_f(\theta_*)$ exists in θ_* and that it is full row rank. Using the Taylor approximation

$$f(\hat{\theta}_N) = f(\theta_*) + \mathcal{J}_f(\hat{\theta}_N - \theta_*) + O(\|\hat{\theta}_N - \theta_*\|^2),$$

it follows

$$\sqrt{N}(f(\hat{\theta}_N) - f(\theta_*)) \xrightarrow{d} \mathcal{N}(0, \mathcal{J}_f \Sigma \mathcal{J}_f^T),$$

which is known as the *delta method*, and the covariance of $f(\hat{\theta}_N)$ can be approximated by

$$\operatorname{cov}(f(\hat{\theta}_N)) \approx \mathcal{J}_f \operatorname{cov}(\hat{\theta}_N) \mathcal{J}_f^T . \qquad \text{E.5-11}$$

Note that $\mathcal{J}_f = \mathcal{J}_f(\theta_*)$ in the derivation above. A consistent estimate of the sensitivity is then obtained from $\mathcal{J}_f(\hat{\theta}_N)$. Thus, starting from the covariance $\operatorname{cov}(\hat{\theta}_N)$ of an estimate $\hat{\theta}_N$, that can for example be obtained from a sample covariance, the covariance of a function of this estimate is obtained in E.5-11.

For subspace-based system identification, this initial covariance estimate is the covariance of the vectorized Hankel matrix $\Sigma_{\mathbf{H}} = \operatorname{cov}(\operatorname{vec}(\mathbf{H}))$ that can be obtained as a sample covariance by cutting the available data into blocks and computing instances of $\mathbf{H}$ on each block, where vec is the column-stacking vectorization operator. As the system matrices and subsequently the modal parameters are functions of $\mathbf{H}$, it is the objective to compute the sensitivities of these parameters with respect to vec($\mathbf{H}$) to finally obtain their covariance from E.5-11.

In order to obtain the desired sensitivity matrices, *first-order perturbations* are used. Let the vector θ be close to the true value θ_* and let the scalar ε be the *perturbation magnitude*, writing $\theta_* = \theta(0)$ (meaning no perturbation) and $\theta_* = \theta(\varepsilon)$. Then, a first-order perturbation is defined as

$$\Delta\theta = \varepsilon \frac{\partial \theta}{\partial \varepsilon} = \theta_* - \theta + O = \theta(\varepsilon^2),$$

and a first-order perturbation of $f(\theta)$ yields

$$\Delta f(\theta) = \varepsilon \frac{\partial f(\theta)}{\partial \varepsilon} = \varepsilon \mathcal{J}_f \frac{\partial \theta}{\partial \varepsilon} = \mathcal{J}_f \Delta\theta .$$

Thus, the desired sensitivity matrices can be obtained by applying first-order perturbations. The following definitions are needed in the following sections. Let I_a the identity matrix of size $a \times a$ and $0_{a,b}$ the zero matrix of size $a \times b$. Define the selection matrices

$$S_1 = [I_{pr} \quad 0_{pr,r}], \quad S_2 = [0_{pr,r} \quad I_{pr}],$$

such that $S_1 \mathbf{O} = \overline{\mathbf{O}}$, $S_2 \mathbf{O} = \underline{\mathbf{O}}$. Also, some properties of the vectorization operator are important. For $a, b \in \mathbb{N}$ define the permutation

$$\mathcal{P}_{a,b} = \sum_{k=1}^{a} \sum_{l=1}^{b} E_{k,l}^{a,b} \otimes E_{l,k}^{b,a} ,$$

where $E_{k,l}^{a,b}$ is a matrix of size $a \times b$ that is equal to 1 at position (k,l) and zero elsewhere, and $\otimes$ denotes the Kronecker product. Then, for any matrix $X \in \mathbb{R}^{a,b}$ it holds

$$\operatorname{vec}(X^T) = \mathcal{P}_{a,b} \operatorname{vec}(X)$$

For any compatible matrices X, Y and Z the vectorization operator yields the relation

$$\operatorname{vec}(XYZ) = (Z^T \otimes X) \operatorname{vec}(Y)$$

5-3-2 Covariance of the Hankel Matrix

The covariance $\Sigma_{\mathbf{H}} = \mathrm{cov}(\mathrm{vec}(\mathbf{H}))$ of the vectorized Hankel matrix is the starting point on the right hand side in E.5-11 before propagating it to the covariance of estimates that are a function of this matrix. For its calculation, the available data is separated into n_b blocks of the same length N_b for simplicity, with $n_b \cdot N_b = N$. Each block may be long enough to assume statistical independence between the blocks. The correlations

$$\hat{R}_i^{(j)} = \frac{1}{N_b} \sum_{k=1+(j-1)N_b}^{jN_b} y_{k+i} y_k^{(\mathrm{ref})T} \qquad \text{E.5-12}$$

are computed each of the blocks and the corresponding Hankel matrix

$$\mathbf{H}_j = Hank(\hat{R}_i^{(j)}) \qquad \text{E.5-13}$$

is filled. Then, $\mathbf{H} = \frac{1}{n_b} \sum_{j=1}^{n_b} \mathbf{H}_j$ and the covariance of the Hankel matrix in follows from the covariance of the sample mean as

$$\Sigma_{\mathbf{H}} = \frac{1}{n_b(n_b-1)} \sum_{j=1}^{n_b} \left(\mathrm{vec}(\mathbf{H}_j) - \mathrm{vec}(\mathbf{H})\right)\left(\mathrm{vec}(\mathbf{H}_j) - \mathrm{vec}(\mathbf{H})\right)^T.$$

As this matrix of dimension $(p+1)qrr_0 \times (p+1)qrr_0$ can get very large and for practical applications the number of available data blocks is usually smaller, $n_b < (p+1)qrr_0$, it is proposed to store instead the matrix [Döhler and Mevel, 2013]

$$T_{\mathbf{H}} = \begin{bmatrix} t_1 & t_2 & \dots & t_{n_b} \end{bmatrix} \quad \text{where} \quad t_j = \frac{1}{\sqrt{n_b(n_b-1)}} \left(\mathrm{vec}(\mathbf{H}_j) - \mathrm{vec}(\mathbf{H})\right). \qquad \text{E.5-14}$$

Then, the relationship

$$\Sigma_{\mathbf{H}} = T_{\mathbf{H}} T_{\mathbf{H}}^T \qquad \text{E.5-15}$$

holds and will be used for the computations.

5-3-3 Sensitivities of the System Matrices

The sensitivities of the system matrices A and C are obtained in two steps: First, a perturbation $\Delta\mathbf{H}$ of the Hankel matrix is propagated to a perturbation $\Delta\mathbf{O}$ of the observability matrix, and second, a perturbation $\Delta\mathbf{O}$ is propagated to perturbations ΔA and ΔC in the system matrices.

In order to obtain $\Delta\mathbf{O}$, the sensitivities of the singular values and vectors in E.5-8 are necessary. They have been derived in [Pintelon et al., 2007].

Lemma 1 [Pintelon et al., 2007]. Let σ_i, u_i and v_i be the i-th singular value, left and right singular vector of the matrix $\mathbf{H} \in \mathbb{R}^{(p+1)r \times qr_0}$ and $\Delta\mathbf{H}$ be a first-order perturbation on $\mathbf{H}$. Then it holds

$$\Delta\sigma_i = (v_i \otimes u_i)^T \operatorname{vec}(\Delta\mathbf{H}), \quad B_i \begin{bmatrix} \Delta u_i \\ \Delta v_i \end{bmatrix} = C_i \operatorname{vec}(\Delta\mathbf{H})$$

where

$$B_i = \begin{bmatrix} I_{(p+1)r} & -\frac{1}{\sigma_i}\mathbf{H} \\ -\frac{1}{\sigma_i}\mathbf{H}^T & I_{qr_0} \end{bmatrix}, \quad C_i = \frac{1}{\sigma_i}\begin{bmatrix} v_i^T \otimes (I_{(p+1)r} - u_i u_i^T) \\ (u_i^T \otimes (I_{qr_0} - v_i v_i^T))\mathcal{P}_{(p+1)r,qr_0} \end{bmatrix}.$$

Using this result, the sensitivity of the observability matrix is derived.

Lemma 2 [Reynders et al., 2008]. Let B_i and C_i be given in *Lemma 1* for $i = 1, \ldots, n$. Then,

$$\operatorname{vec}(\Delta\mathbf{O}) = \mathcal{J}_{\mathbf{O},\mathbf{H}} \operatorname{vec}(\Delta\mathbf{H}) \qquad \text{E.5-16}$$

where $\mathcal{J}_{\mathbf{O},\mathbf{H}} \in \mathbb{R}^{(p+1)rn \times (p+1)rqr_0}$ with

$$\mathcal{J}_{\mathbf{O},\mathbf{H}} = \frac{1}{2}(I_N \otimes U_1 \Sigma_1^{-1/2}) S_3 \begin{bmatrix} (v_1 \otimes u_1)^T \\ \vdots \\ (v_n \otimes u_n)^T \end{bmatrix} + (\Sigma_1^{1/2} \otimes \begin{bmatrix} I_{(p+1)r} & 0_{(p+1)r \times qr_0} \end{bmatrix}) \begin{bmatrix} B_1^+ C_1 \\ \vdots \\ B_n^+ C_n \end{bmatrix}, \quad S_3 = \sum_{k=1}^{n} E_{(k-1)n+k,k}^{n^2,n}$$

Proof. From the definition of $\mathbf{O}$ follows

$$\Delta\mathbf{O} = U_1 \Delta\Sigma_1^{1/2} + \Delta U_1 \Delta\Sigma_1^{1/2} = U_1 \tfrac{1}{2}\Sigma_1^{-1/2}\Delta\Sigma_1 + \Delta U_1 \Sigma_1^{1/2},$$

$$\operatorname{vec}(\Delta\mathbf{O}) = \tfrac{1}{2}(I_n \otimes U_1 \Sigma_1^{-1/2}) \operatorname{vec}(\Delta\Sigma_1) + (\Sigma_1^{1/2} \otimes I_{(p+1)r}) \operatorname{vec}(\Delta U_1).$$

The sensitivities of Σ_1 and U_1 are obtained from Lemma 1 by stacking as

$$\begin{bmatrix} \Delta\sigma_1 \\ \vdots \\ \Delta\sigma_n \end{bmatrix} = \begin{bmatrix} (v_1 \otimes u_1)^T \\ \vdots \\ (v_n \otimes u_n)^T \end{bmatrix} \operatorname{vec}(\Delta\mathbf{H}), \quad \operatorname{vec}\begin{bmatrix} \Delta U_1 \\ \Delta V_1 \end{bmatrix} = \begin{bmatrix} B_1^+ C_1 \\ \vdots \\ B_n^+ C_n \end{bmatrix} \operatorname{vec}(\Delta\mathbf{H})$$

and the assertion follows.

The results of [Reynders et al., 2008] on the sensitivity of the system matrices are collected in the following lemma.

Lemma 3 [Reynders et al., 2008]. Let the system matrix A be obtained from $\mathbf{O}$ in E.5-9 and C from the first block row of $\mathbf{O}$. Then, a perturbation on $\mathbf{O}$ is propagated to A and C by

$$\mathrm{vec}(\Delta A) = \mathcal{J}_{A,\mathbf{O}}\mathrm{vec}(\Delta\mathbf{O}), \quad \mathrm{vec}(\Delta C) = \mathcal{J}_{C,\mathbf{O}}\mathrm{vec}(\Delta\mathbf{O}) \qquad \text{E.5-17}$$

where $\mathcal{J}_{A,\mathbf{O}} \in \mathbb{R}^{n^2\times(p+1)rn}$, $\mathcal{J}_{C,\mathbf{O}} \in \mathbb{R}^{rm\times(p+1)rn}$, with

$$\mathcal{J}_{A,\mathbf{O}} = (I_n \otimes \overline{\mathbf{O}}^{+}S_2) - (A^T \otimes \overline{\mathbf{O}}^{+}S_1) + ((\underline{\mathbf{O}}^T S_2 - A^T\overline{\mathbf{O}}^T S_2)\otimes(\overline{\mathbf{O}}^T\overline{\mathbf{O}})^{-1})\mathcal{P}_{(p+1)r,n},$$

$$\mathcal{J}_{C,\mathbf{O}} = I_n \otimes \begin{bmatrix} I_r & 0_{r,pr} \end{bmatrix}$$

Proof. Using the product rule for a perturbation on $A = \overline{\mathbf{O}}^{+}\underline{\mathbf{O}} = (\overline{\mathbf{O}}^T\overline{\mathbf{O}})^{-1}\overline{\mathbf{O}}^T\underline{\mathbf{O}}$ and Kronecker algebra leads to the assertion.

5-3-4 Sensitivities of the Modal Parameters

The natural frequencies and the damping ratios are functions of the eigenvalues of system matrix A and the mode shapes depend on both A and C. In [Reynders et al., 2008], the sensitivity derivations for the eigenvalues and eigenvectors of a matrix and subsequently for the modal parameters are stated, based on derivations in [Golub and van Loan, 1996; Pintelon et al., 2007]. They are summarized in the following.

Lemma 4. Let λ_i, ϕ_i and χ_i be the i-th eigenvalue, left eigenvector and right eigenvector of A with

$$A\phi_i = \lambda_i\phi_i, \quad \chi_i^{*}A = \lambda_i\chi_i^{*},$$

where * denotes the complex conjugate transpose. Then,

$$\Delta\lambda_i = \mathcal{J}_{\lambda_i,A}\mathrm{vec}(\Delta A), \quad \Delta\phi_i = \mathcal{J}_{\phi_i,A}\mathrm{vec}(\Delta A),$$

where $\mathcal{J}_{\lambda_i,A} \in \mathbb{C}^{1\times n^2}$, $\mathcal{J}_{\phi_i,A} \in \mathbb{C}^{n\times n^2}$, with

$$\mathcal{J}_{\lambda_i,A} = \frac{1}{\chi_i^{*}\phi_i}(\phi_i^T \otimes \chi_i^{*}), \quad \mathcal{J}_{\phi_i,A} = (\lambda_i I_n - A)^{+}\left(\phi_i^T \otimes \left(I_n - \frac{\phi_i\chi_i^{*}}{\chi_i^{*}\phi_i}\right)\right).$$

Lemma 5. Let λ_i and ϕ_i be the i-th eigenvalue and left eigenvector of A and $\tilde{\lambda}_i = \ln(\lambda_i)/\tau = (b_i + a_i i)/\tau$ the eigenvalue of the corresponding continuous-time state transition matrix as in E.5-5. Let furthermore the natural frequency f_i and the damping ratio ρ_i be given in E.5-5. Then,

$$\Delta f_i = \mathcal{J}_{f_i,A}\mathrm{vec}(\Delta A), \quad \Delta\rho_i = \mathcal{J}_{\rho_i,A}\mathrm{vec}(\Delta A), \quad \Delta\varphi_i = \mathcal{J}_{\varphi_i,A,C}\begin{bmatrix}\mathrm{vec}(\Delta A)\\ \mathrm{vec}(\Delta C)\end{bmatrix}, \qquad \text{E.5-18}$$

where $\mathcal{J}_{f_i,A}$, $\mathcal{J}_{\rho_i,A} \in \mathbb{R}^{1\times n^2}$, $\mathcal{J}_{\varphi_i,A,C} \in \mathbb{C}^{r\times(n^2+rn)}$, with

$$\begin{bmatrix} \mathcal{J}_{f_i,A} \\ \mathcal{J}_{\rho_i,A} \end{bmatrix} = \begin{bmatrix} \mathcal{J}_{f_i,\lambda_i} \\ \mathcal{J}_{\rho_i,\lambda_i} \end{bmatrix} \begin{bmatrix} \mathrm{Re}(\mathcal{J}_{\lambda_i,A}) \\ \mathrm{Im}(\mathcal{J}_{\lambda_i,A}) \end{bmatrix}, \quad \mathcal{J}_{\varphi_i,A,C} = \begin{bmatrix} C\mathcal{J}_{\phi_i,A} & \phi_i^T \otimes I_r \end{bmatrix}, \text{ and}$$

$$\begin{bmatrix} \mathcal{J}_{f_i,\lambda_i} \\ \mathcal{J}_{\rho_i,\lambda_i} \end{bmatrix} = \frac{1}{\tau|\lambda_i|^2|\tilde{\lambda}_i|} \begin{bmatrix} 1/(2\pi) & 0 \\ 0 & 100/|\tilde{\lambda}_i|^2 \end{bmatrix} \begin{bmatrix} \mathrm{Re}(\tilde{\lambda}_i) & \mathrm{Im}(\tilde{\lambda}_i) \\ -\mathrm{Im}(\tilde{\lambda}_i)^2 & \mathrm{Re}(\tilde{\lambda}_i)\mathrm{Im}(\tilde{\lambda}_i) \end{bmatrix} \begin{bmatrix} \mathrm{Re}(\lambda_i) & \mathrm{Im}(\lambda_i) \\ -\mathrm{Im}(\lambda_i) & \mathrm{Re}(\lambda_i) \end{bmatrix} \in \mathbb{R}^{2\times 2}.$$

5-3-5 Summary of the Computation

From Equations E.5-16, E.5-17 and E.5-18 it follows that perturbations on a frequency f_i, damping ratio ρ_i and mode shape φ_i can be written as

$$\begin{bmatrix} \Delta f_i \\ \Delta\rho_i \end{bmatrix} = \begin{bmatrix} \mathcal{J}_{\lambda_i,A} \\ \mathcal{J}_{\rho_i,A} \end{bmatrix} \mathcal{J}_{A,\mathbf{O}} \mathcal{J}_{\mathbf{O},\mathbf{H}} \mathrm{vec}(\Delta\mathbf{H}), \quad \Delta\varphi_i = \mathcal{J}_{\varphi_i,A,C} \begin{bmatrix} \mathcal{J}_{A,\mathbf{O}} \\ \mathcal{J}_{C,\mathbf{O}} \end{bmatrix} \mathcal{J}_{\mathbf{O},\mathbf{H}} \mathrm{vec}(\Delta\mathbf{H}).$$

From this expression and E.5-11, the covariance of a frequency and damping ratio of a mode *i* yields

$$\mathrm{cov}\left(\begin{bmatrix} f_i \\ \rho_i \end{bmatrix} \right) = \begin{bmatrix} \mathcal{J}_{f_i,A} \\ \mathcal{J}_{\rho_i,A} \end{bmatrix} \mathcal{J}_{A,\mathbf{O}} \mathcal{J}_{\mathbf{O},\mathbf{H}} \Sigma_{\mathbf{H}} \mathcal{J}_{\mathbf{O},\mathbf{H}}^T \mathcal{J}_{A,\mathbf{O}}^T \begin{bmatrix} \mathcal{J}_{f_i,A} \\ \mathcal{J}_{\rho_i,A} \end{bmatrix}^T, \qquad \text{E.5-19}$$

and the covariance of the real and imaginary parts of a mode shape yields

$$\mathrm{cov}\left(\begin{bmatrix} \mathrm{Re}(\varphi_i) \\ \mathrm{Im}(\varphi_i) \end{bmatrix} \right) = \begin{bmatrix} \mathrm{Re}(\mathcal{J}_{\varphi_i,A,C}) \\ \mathrm{Im}(\mathcal{J}_{\varphi_i,A,C}) \end{bmatrix} \begin{bmatrix} \mathcal{J}_{A,\mathbf{O}} \\ \mathcal{J}_{C,\mathbf{O}} \end{bmatrix} \mathcal{J}_{\mathbf{O},\mathbf{H}} \Sigma_{\mathbf{H}} \mathcal{J}_{\mathbf{O},\mathbf{H}}^T \begin{bmatrix} \mathcal{J}_{A,\mathbf{O}} \\ \mathcal{J}_{C,\mathbf{O}} \end{bmatrix}^T \begin{bmatrix} \mathrm{Re}(\mathcal{J}_{\varphi_i,A,C}) \\ \mathrm{Im}(\mathcal{J}_{\varphi_i,A,C}) \end{bmatrix}^T. \qquad \text{E.5-20}$$

From these covariances, the standard deviations of the respective modal parameters are obtained from the square roots of the diagonal entries. The following procedure summarizes an efficient computation of the covariance estimates for the modal parameters at some model order *n*, which is equivalent to computing the products E.5-19 to E.5-20. It takes into account the relation $\Sigma_{\mathbf{H}} = T_{\mathbf{H}} T_{\mathbf{H}}^T$ in E.5-15 for a covariance estimate of the vectorized Hankel matrix, reducing the size of the involved matrices significantly:

1) Compute matrix $T_{\mathbf{H}}$ from n_b blocks of the available data in equations E.5-12, E.5-13, E.5-14
2) Compute products $T_A = \mathcal{J}_{A,\mathbf{O}} \mathcal{J}_{\mathbf{O},\mathbf{H}} T_{\mathbf{H}}$ for frequency and damping covariance, and $T_C = \mathcal{J}_{C,\mathbf{O}} \mathcal{J}_{\mathbf{O},\mathbf{H}} T_{\mathbf{H}}$ for mode shape covariance
3) For each mode *i* compute the covariance of the frequency and damping estimate from

$$\operatorname{cov}\left(\begin{bmatrix} f_i \\ \rho_i \end{bmatrix}\right) = T_{f_i\rho_i} T_{f_i\rho_i}^T \quad \text{where} \quad T_{f_i\rho_i} = \begin{bmatrix} \mathcal{J}_{f_i,A} \\ \mathcal{J}_{\rho_i,A} \end{bmatrix} T_A ,$$

and the covariance of the mode shape estimate from

$$\operatorname{cov}\left(\begin{bmatrix} \operatorname{Re}(\varphi_i) \\ \operatorname{Im}(\varphi_i)_i \end{bmatrix}\right) = T_{\varphi_i} T_{\varphi_i}^T \quad \text{where} \quad T_{\varphi i} = \begin{bmatrix} \operatorname{Re}(\mathcal{J}_{\varphi i,A,C}) \\ \operatorname{Im}(\mathcal{J}_{\varphi i,A,C}) \end{bmatrix} \begin{bmatrix} T_A \\ T_C \end{bmatrix}.$$

For a detailed discussion of this computation and its numerical optimization the interested reader is referred to E.5-14.

5-4 Modal Analysis of S101 Bridge

5-4-1 S101 Bridge

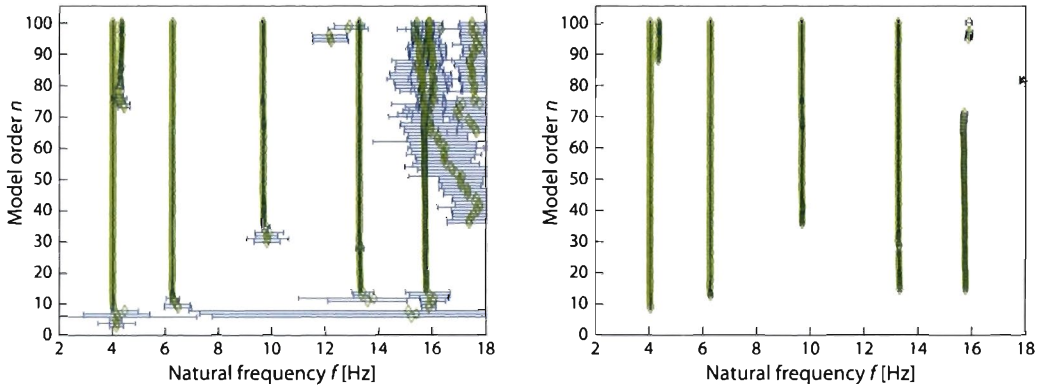
Within the IRIS project an extensive measurement campaign of the prestressed concrete road bridge S101 [Döhler et al., 2011a; 2011b; VCE, 2009] was taken, which was planned and organized by the Austrian company VCE and accomplished by VCE and the University of Tokyo [VCE, 2009].

For vibration measurements a BRIMOS® measurement system was used, consisting in 15 sensor locations on the bridge deck, where 14 sensors were placed on one side of the deck and one sensor on the other side of the deck. In each location the bridge deck's vertical, longitudinal and transversal directions were measured. Altogether, 45 acceleration sensors were applied. All values were recorded permanently with a sampling frequency of 500 Hz. During the three days measurement campaign 714 data files with 165 000 data points were produced. In this study only the first dataset is used.

Bridge S101 [VCE, 2009] F.5-1



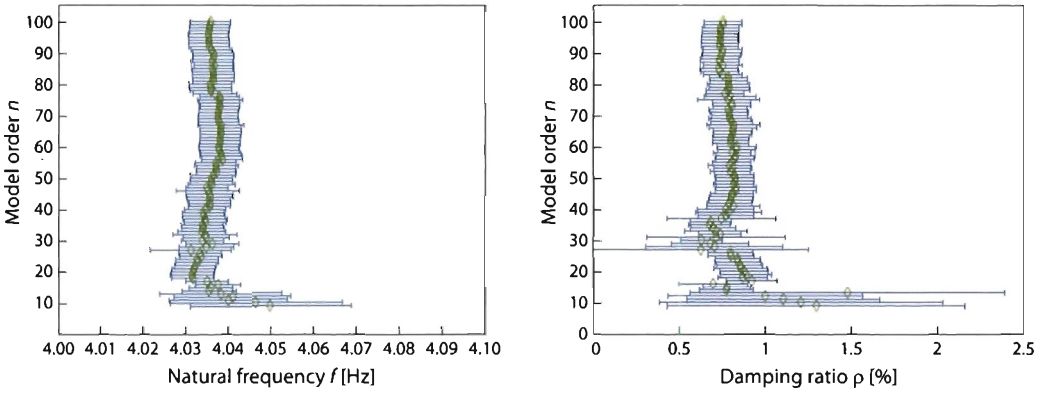
Stabilization diagrams containing the natural frequencies of the first five modes with their confidence intervals (horizontal bars) F.5-2



5-4-2 Confidence Intervals of Modal Parameters

Restricting the system identification to the first five modes in the frequency range [0–18 Hz], the data was downsampled from sampling rate 500 Hz by factor 5. System identification and the covariance computation was done with the covariance-driven subspace identification detailed in chapter 5-2 with parameters $p+1=q=35$ at model orders $n=1,\ldots,100$. All $r=45$ sensors were used and $r_0=3$ reference sensors were chosen. The covariance computation on all identified modes at the different model orders was accomplished with the strategy explained in chapter 5-3. For the covariance estimate on the Hankel matrix, the data was cut into $n_b=100$ blocks. In F.5-2 (left), the stabilization diagram of the natural frequencies vs. the model order are presented, where a confidence interval (± one standard deviation) of each frequency is plotted as a horizontal bar. In

Zoom on first mode: estimated natural frequencies (left) and corresponding damping ratios (right) at different model orders F.5-3

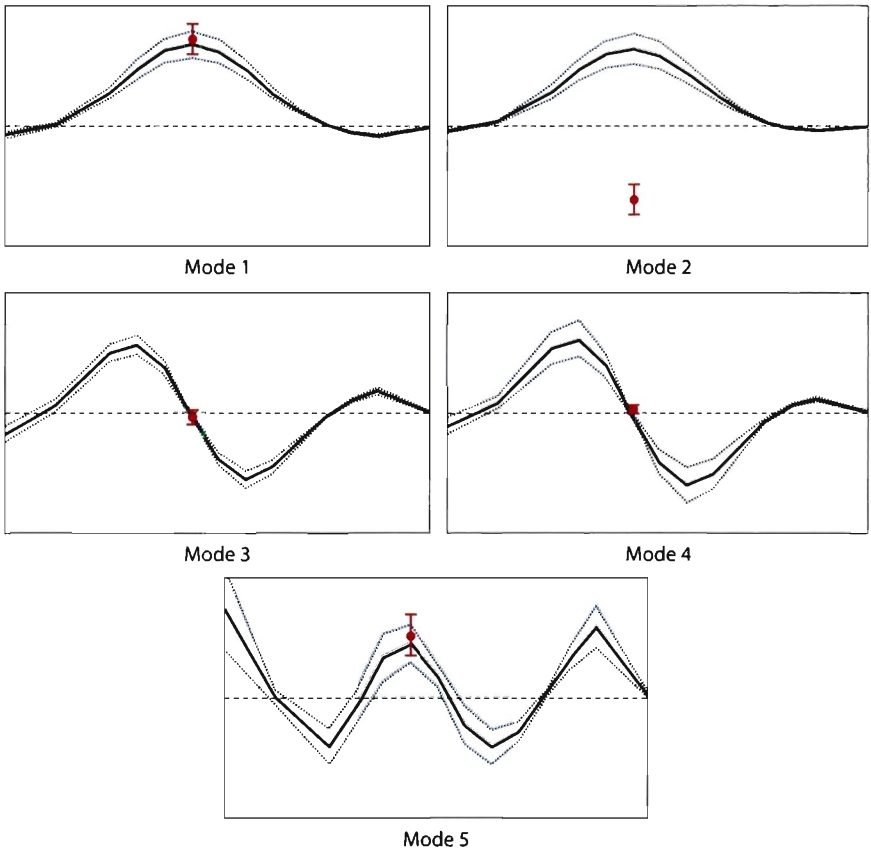


Overview of the estimated first five modes with natural frequencies f, their variation coefficient $\tilde{\sigma}_f = \sigma_f / f \cdot 100$, the damping ratios ρ and their variation coefficient $\tilde{\sigma}_\rho = \sigma_\rho / \rho \cdot 100$ T.5-1

mode	f [Hz]	$\tilde{\sigma}_f$	ρ [%]	$\tilde{\sigma}_\rho$
1	4.036	0.12	0.78	15
2	6.281	0.08	0.56	20
3	9.677	0.18	1.3	14
4	13.27	0.13	1.5	13
5	15.72	0.37	1.3	17

F.5-2 (left) it can be seen that the (true) structural modes seem to have much lower uncertainty bounds than spurious modes. With this observation, a threshold of 1 % was put on the variation coefficient of the frequencies (standard deviation divided by frequency), which leads to a much clearer diagram in F.5-2 (right). Such a cleaned diagram would also

First five mode shapes in vertical direction on one side of the deck (line) and the sensor on the other side of the deck (red point) with their $\pm 2\sigma_\nu$ uncertainty bounds F.5-4



be easier to evaluate for an automated modal parameter extraction. In F.5-3, the frequency and damping ratio of first mode identified at the different model orders is magnified for a better visibility of the confidence bounds. Using the information from these confidence bounds, values for the frequency and the damping ratio of a mode can be chosen that are optimal for different model orders, as the true model order is unknown.

From the stabilization diagrams, the modal parameters are chosen. In T.5-1, the system identification results with their variation coefficients are summarized. As expected, the variation coefficients of the frequency estimates are very low (lower than 0.5 %), while the estimates of the damping ratios show much higher variation coefficients (up to 20 % in this case). In F.5-4, the real parts of the obtained mode shapes in the vertical direction at the 14 sensors of one side of the bridge deck are displayed with their uncertainty bounds (±2 standard deviations). From the 15th sensor on the other side of the bridge deck, whose contribution is marked as the red point in F.5-4, information about the kind of the mode is obtained: modes 1, 3 and 5 are vertical bending modes and modes 2 and 4 are torsional modes.

5-5 Conclusion

In this chapter, a method was presented to identify modal parameters – frequencies, damping ratios and mode shapes – and their uncertainty bounds from output-only vibration measurements. The knowledge of the uncertainty bounds is essential to evaluate any identified parameter and as it is known that especially estimated damping values show large uncertainties in system identification.

In operational modal analysis, where the system order is unknown and the input cannot be measured, output-only subspace-based identification methods are very convenient. It was shown how the uncertainty bounds on the identified modal parameters can improve system identification in this case by giving additional information to choose modes in a stabilization diagram from identification results at different model orders. An efficient implementation of the method was suggested and successfully applied to the identification of modal parameters from output-only vibration data of S101 Bridge.

References

Basseville, M., Benveniste, A., Goursat, M., Hermans, L., Mevel, L. and van der Auweraer, H., 2001. *Output-Only Subspace-Based Structural Identification: from Theory to Industrial Testing Practice.* ASME Journal of Dynamic Systems, Measurement and Control 123(4):668–676.

Benveniste, A. and Fuchs, J.J., 1985. *Single Sample Modal Identification of a Non-Stationary Stochastic Process.* IEEE Transactions on Automatic Control, AC-30(1):66–74.

Benveniste, A., Basseville, M. and Mevel, L., 2000. *Convergence Rates for Eigenstructure Identification Using Subspace Methods*. Proc. 39th IEEE Conference on Decision and Control, 1550–1554.

Benveniste, A. and Mevel, L., 2007. *Non-Stationary Consistency of Subspace Methods*. IEEE Transactions on Automatic Control 52(6):974–984.

Chiuso, A. and Picci, G., 2004. *The Asymptotic Variance of Subspace Estimates*. Journal of Econometrics 118(1–2):257–291.

Döhler, M. and Mevel, L., 2012. *Fast Multi-Order Computation of System Matrices in Subspace-Based System Identification*. Control Engineering Practice 20(9):882–894.

Döhler, M. and Mevel, L., 2013. *Efficient Multi-Order Uncertainty Computation for Stochastic Subspace Identification*. Mechanical Systems and Signal Processing, in press. DOI: 10.1016/j.ymssp.2013.01.012

Döhler, M., Hille, F., Lam, X.B., Mevel, L. and Rücker, W., 2011a. *Confidence Intervals of Modal Parameters During Progressive Damage Test*. Proc. 29th International Modal Analysis Conference, Jacksonville, FL, USA.

Döhler, M., Hille, F., Mevel, L. and Rücker, W., 2011b. *Structural Health Monitoring during Progressive Damage Test of S101 Bridge*. Proc. 8th International Workshop on Structural Health Monitoring, Stanford, CA, USA.

Döhler, M., Lam, X.B. and Mevel, L., 2013. *Uncertainty Quantification for Modal Parameters from Stochastic Subspace Identification on Multi-Setup Measurements*. Mechanical Systems and Signal Processing 36:562–581.

Gersch, W., 1974. *On the Achievable Accuracy of Structural System Parameter Estimates*. Journal of Sound and Vibration 34(1):63–79.

Golub, G. and Van Loan, C., 1996. *Matrix Computations*. 3rd Edition, Johns Hopkins University Press.

Ljung, L., 1999. *System Identification: Theory for the User*. Prentice Hall, Englewood Cliffs, NJ, USA.

Peeters, B. and De Roeck, G., 1999. *Reference-Based Stochastic Subspace Identification for Output-Only Modal Analysis*. Mechanical Systems and Signal Processing 13(6):855–878.

Pintelon, R., Guillaume, P. and Schoukens, J., 2007. *Uncertainty Calculation in (Operational) Modal Analysis*. Mechanical Systems and Signal Processing 21(6):2359–2373.

Reynders, E., Pintelon, R. and De Roeck, G., 2008. *Uncertainty Bounds on Modal Parameters Obtained from Stochastic Subspace Identification*. Mechanical Systems and Signal Processing 22(4):948–969.

Van Overschee, P. and De Moor, B., 1996. *Subspace Identification for Linear Systems: Theory, Implementation, Applications*. Kluwer.

VCE, 2009. *Progressive Damage Test S101 Flyover Reibersdorf (draft)*. Tech. Report 08/2308.

6

Experimental Testing of a Masonry Arch Bridge Model Subject to Increasing Level of Damage

Authors:
Gianluca Ruocci
Antonino Quattrone
Luca Zanotti Fragonara
Rosario Ceravolo
Alessandro De Stefano

Motivation

Masonry arch bridges represent a large sample in the European bridge stock. Insufficient knowledge on their behaviour under scour condition, which is the collapse reason #1 in bridge failures, is a matter of concern for owners and managers. Better approaches are desired to monitor their structural integrity.

Main Results

In a comprehensive experimental campaign the feasibility to apply the IRIS Risk Paradigm with the IRIS damage detection methodologies has been demonstrated.



6-1 Introduction

This work presents a series of test campaigns performed on a masonry arch bridge model from 2006 to nowadays. The experimental model was mainly built to study the evolution of damage mechanisms related to the settlements of the central pier in twin-span bridges and to develop a suitable application of the diagnostic monitoring methodologies to the protection of historical bridges from scour.

In the last few years the model was subject to a wide gamma of characterization tests and analyses. The paper elucidates the knowledge course that has been chosen to investigate the model and how the various tests were planned and carried out.

During the realisation of the model, a set of preliminary tests was carried out, mainly on the bridge materials. In this phase also a hydraulic flume test on a further scaled model was performed to simulate the scour effect. Two finite element (FE) models were built in order to predict the behaviour of the experimental mock-up: the first model implements a linear constitutive law to compute the modal parameters and designing vibration tests, the second model uses a non-linear law for predicting crack patterns due to the settlement application. The second phase of testing concerned the dynamic characterization of the bridge model at different damage steps. Nine damage steps were planned to be applied through a settlement application device. At each step a wide set of vibration tests were carried out, using different excitation sources, such as ambient vibrations, sledge hammer impact and an electro-mechanical shaker. Through modal identification techniques, the modal parameters have been identified and monitored during the whole experimentation. The monitoring of modal parameters supported the design of a structural health monitoring system based on the outlier analysis [Ruocci, 2010; Worden et al., 2000].

Instantaneous fitting techniques [Ceravolo, 2004] allowed identifying punctual variations in the modal parameters during the application of the settlements [Quattrone et al., 2010]. Moreover, the forced vibration tests using a shaker allowed the detection of non-linear phenomena. Current works deal with the identification of non-linearity using instantaneous techniques [Ceravolo et al., 2010].

The scaled masonry bridge: notice the settlement application device under the central pier F.6-1



6-2 The Masonry Arch Bridge Model

The 1:2 scaled model of the masonry arch bridge shown in F.6-1 was built in the laboratory of the Department of Structural and Geotechnical Engineering at the Politecnico di Torino. The prototype this model comes from is not an existing bridge but was designed taking into account common features, geometric proportions and historical design codes of a series of masonry arch bridges.

The model is a twin-arch bridge with a length of 5.90 m, a width of 1.60 m and a height of 1.75 m. The two arches are segmental arches with a radius of 2.00 m and an angular opening of 30°. Each span is 2.00 m long between the supports and the thickness of the arch is equal to 0.20 m. The mock-up was built with handmade clay bricks also scaled to 130×65×30 mm to respect the adopted modelling scale law. Low compressive strength elements were chosen and a mortar with poor mechanical properties was used to bound them in order to reproduce the typical materials of historical constructions.

The mid-span masonry pier, which was cut at a hypothetical middle-height section to allow the insertion of a settlement application system, is imagined to be placed inside the streambed and subjected to the scour of its foundation.

Hydraulic flume tests were carried out on a further scaled down model of the bridge pier in order to simulate the scour effects in the lab. The foundation settlements and rotations resulting from these investigations were then replicated on the bridge model by means of the four independent screws installed at the extremities of the settlement application system. The spherical plain bearings placed at the head of the screws allow the plate that supports the central pier rotating about axes parallel to the longitudinal and transversal directions of the bridge.

In order to simulate the streambed material surrounding the foundation of the central pier, a polystyrene mould was introduced. A polystyrene layer is used as interface between the pier and the settlement application device and a polystyrene ring surrounds the pier.

6-3 Preliminary Studies

The experimental investigations carried out on the masonry arch bridge model were divided into two different sessions. The first session was conceived to reduce the high uncertainties referring to the material properties and the structural behaviour of this complex structure. Several destructive tests were performed on samples collected during the construction of the mock-up in order to estimate the mechanical properties of the masonry material. The estimated parameters were then introduced into a numerical model of the bridge to obtain a preliminary calculation of the modal parameters. The information acquired in these preliminary analyses was helpful to plan the following dynamic tests and to interpret the first results of the modal identification. At the same time the hydraulic tests conducted on a reduced model of the central pier allowed to quantify the settlement to be applied.

6-3-1 Material Characterization Tests

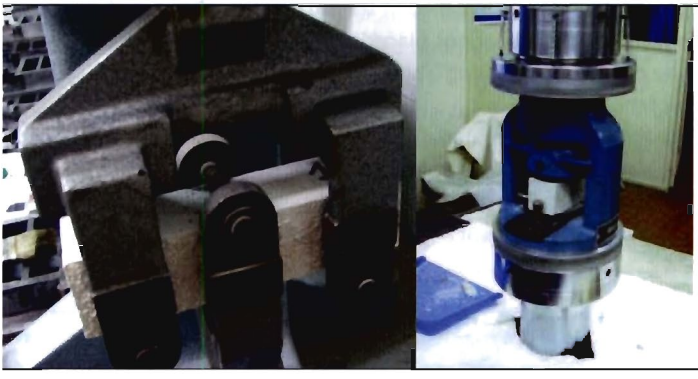
Several tests were carried out in order to characterize the mechanical properties of the mortar and of the masonry used to build the model.

The characterization tests on the mortar samples were performed following the prescriptions proposed by the European standard code EN 998-2:2003 which were adapted to take into account the scaled measure of bricks. The collected samples belong to the M2.5 class of the European standard code EN 998-2:2003 which is one of the poorest in terms of mechanical properties.

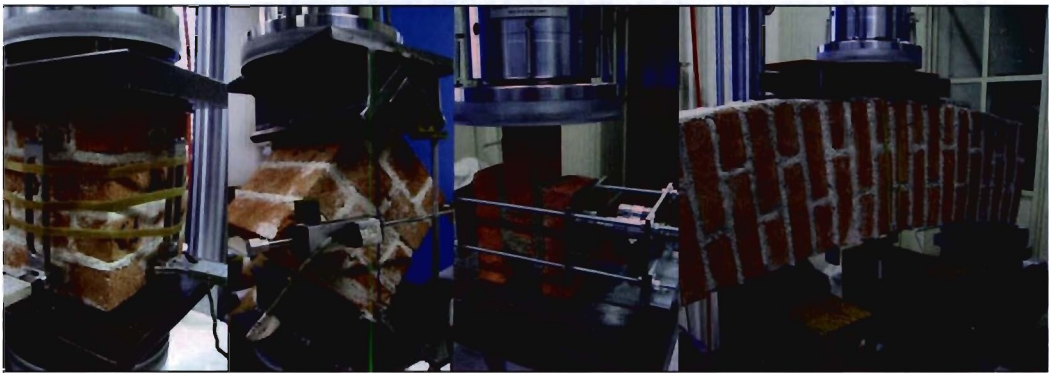
The characterization tests on the masonry samples were performed following the prescriptions proposed by the European standard code UNI EN 1052-1, EN 052-3:2002 and the American standard code ASTM E 518-02. The masonry samples were adapted in order to resemble the shape of required test specimens while the testing procedures were followed strictly. The destructive tests performed on the masonry samples were:

// Axial compression on cubic samples
// Diagonal compression on cubic samples
// Shear test on masonry triplets
// Four point bending test on a segment of arch

Tests carried out on mortar samples F.6-2



Tests conducted on the masonry samples F.6-3



Results from the compressive tests, diagonal tests, shear tests and four point bending tests: average values (μ) and standard deviations (σ) T.6-1

Test	μ [N/mm^2]	σ [N/mm^2]
Compressive tests: tensile strength	4.278	0.354
Compressive tests: Young modulus *E*	1451	472
Diagonal tests: tensile strength	0.304	0.088
Diagonal tests: shear strength	0.430	0.125
Diagonal tests: shear Young modulus *G*	940	436
Shear tests (0.1 kN pre-compression): shear strength	0.794	0.301
Shear tests (0.5 kN pre-compression): shear strength	1.013	0.188
Four point bending tests: *R* modulus of rupture	0.22	//

6-3-2 Flume Tests

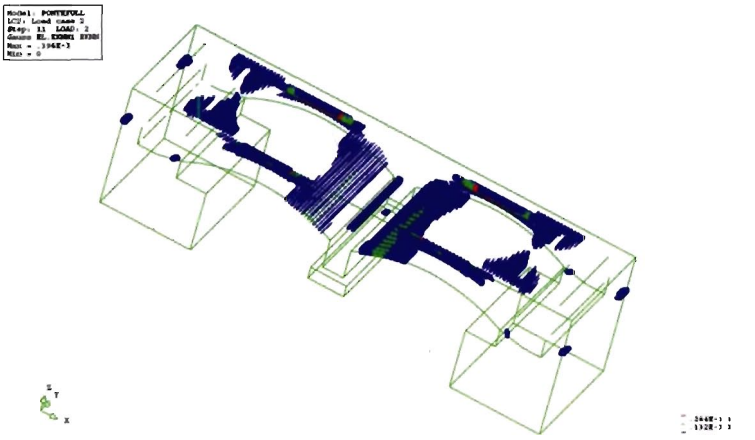
The hydraulic model was designed scaling the pier dimensions down so that the ratio between the length of the bridge and the width of the pier was maintained. The bottom section of the pier scaled model was connected with a hypothetic foundation base. The rectangular foundation was dipped into the bed material, whose uniform mean diameter was 0.80 mm. The pier was hung up and fixed to preserve any movement during the flume tests. The evolution of the soil profile produced by the induced scour was periodically monitored through a laser scanner acquired by a digital camera. The images taken during the tests were then automatically processed to define the portion of the foundation lateral face not covered by the bed material at each time step. The corresponding portion on the arch bridge model was freed from the polystyrene ring surrounding the bottom part of the pier to simulate the reduction of the lateral restrain at the foundation base.

Also the undermining effects were experienced in the flume tests, especially when the foundation base was not excessively dipped in the bed material. The erosion of the soil underneath the foundation, and consequently the loss of its bearing action, is simulated in the experimental model through the settlement application device previously described.

6-3-3 Numerical Models

A 3D numerical model of the arch bridge was realised in the ADINA Finite Element package to estimate and assimilate the modal parameters. The purpose was to better understand the dynamic behaviour of the structure and to accurately plan the following vibration analyses. In fact, the selection of the sensor location must be assessed carefully in order to allow a suitable resolution in the mode shapes for the highest number of identified modes. The model mainly consists of solid elements and spring elements able to simulate the polystyrene layer and the settlement application device. The mechanical properties have been inherited from the material characterization tests. The model is subdivided into a series of element groups, where each group includes all those finite elements which share common mechanical features or structural functions.

Non-linear model: smeared crack pattern with an applied settlement of 14 mm F.6-4



In order to predict crack locations, a numerical model of the masonry arch bridge [Invernizzi et al., 2009] was built in the DIANA FE package which was able to simulate the non-linear behaviour of masonry. The FE package implemented a smeared cracking law which incorporates a tension cut-off, tension softening and shear retention. After the results of the non-linear analysis, it was decided to add masses at the top of the central pier so as to take into account the weight of the missing part of the pier and to partially compensate the arch effect developed by massive abutments.

Damage steps, middle pier settlement, pier rotation, removed polystyrene percentage T.6-2

Experimental campaign	Damage steps	Settlement [mm]	Rotation [rad]	Polystyrene [%]
1st campaign	HS (healthy state)	0	0	0
2nd campaign	DS1	0	0	18%
	DS2	0.25	0	25%
	DS3	1	$4.21 \cdot 10^{-4}$	37.5%
	DS4	2.25	$1.01 \cdot 10^{-3}$	47%
3rd campaign	DS5	2.25	$1.23 \cdot 10^{-3}$	56%
	DS6	2.8	$1.23 \cdot 10^{-3}$	72%
	DS7	3.6	$1.27 \cdot 10^{-3}$	81%
	DS8	4.7	$1.30 \cdot 10^{-3}$	91%
	DS9	7.6	$1.28 \cdot 10^{-3}$	100%

6-4 Experimental Test

6-4-1 Experimental Test Programme

As previously stated, the main objective of the experimental test was to determine the capability of a structural health monitoring system, based mainly on dynamic measurements, to detect damage (such as scour at the bridge pier foundation). In this framework, dynamic testing ensures to identify a set of parameters to be monitored. A sensitivity analysis has been carried out on the parameters to choose the most reliable set to detect the damage. Several damage steps have been applied to the structure in accordance with hydraulic flume tests as shown in T.6-2.

T.6-3 shows the timeline of the experimental tests. Different excitation sources were applied to the bridge model: ambient vibrations (AV), impact hammer (IH) and an electro-mechanical shaker (S). Several physical quantities were monitored under the different excitations: acceleration measurements (ACC), strain deformation (SG and OPT) and temperature (T).

The experimental test involved three different experimental campaigns. The first campaign regarded the undamaged structure (October 2008 to March 2009): an extensive set of dynamic tests was carried out on the bridge model in order to characterize its "healthy" state (HS). Monitoring of dynamic properties of the bridge showed a decrease in the structure stiffness through the whole campaign. This may be due to the development of some rheologic phenomena, for instance the concrete block creep and the mortar shrinkage,

Experimental test timeline T.6-3

	Time	Step	Excitation	Measurements
1st campaign	Oct. 2008	HS	AV, IH	ACC, SG, T, OPT
	Nov. 2008	HS	AV, IH	ACC, SG, T, OPT
	Jan. 2009	HS	AV, IH	ACC, SG, T, OPT
	Feb. 2009	HS	AV, IH	ACC, SG, T, OPT
	Mar. 2009	HS	AV, IH	ACC, SG, T, OPT
2nd campaign	Apr. 2009	HS	AV, IH	ACC, SG, T, OPT
		DS1	AV, IH, S	ACC, SG, T, OPT
		DS2	AV, IH, S	ACC, SG, T, OPT
		DS3	AV, IH, S	ACC, SG, T, OPT
		DS4	AV, IH, S	ACC, SG, T, OPT
3rd campaign	Sep. 2010	DS5	AV, IH, S	ACC, SG, T, OPT
		DS6	AV, IH, S	ACC, SG, T, OPT
	Oct. 2010	DS7	AV, IH, S	ACC, SG, T, OPT
		DS8	AV, IH, S	ACC, SG, T, OPT
		DS9	AV, IH, S	ACC, SG, T, OPT

leading to strains incompatible with the stiffness of the arch barrels, which might have produced a partial detachment between the masonry abutments and the arch barrels.

The second campaign (April 2009) started after the application of additional masses on the central pier, in order to take into account the weight of the missing part of the pier. In the same campaign the first four settlement steps were applied on the upstream side of the pier. In addition, parts of the polystyrene ring were removed at each step to simulate the erosion of streambed around the foundation according to the hydraulic flume tests. Dynamic tests were conducted in correspondence with each settlement step.

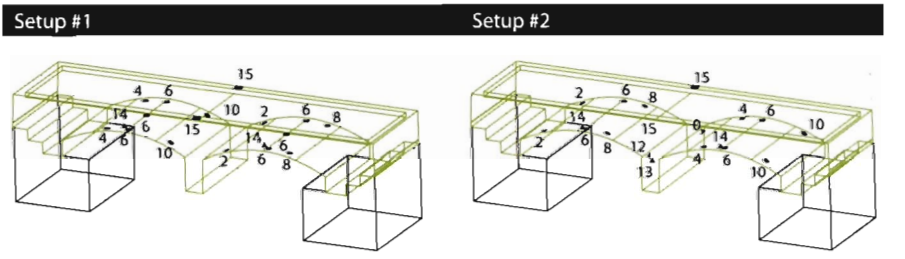
During the latter campaign (September 2010 to October 2010) five further settlement steps were applied. In this phase the removal of the polystyrene ring continued until all the polystyrene was removed.

6-4-2 Experimental Setups

Dynamic vibration tests require a careful identification of an optimal sensor location. In order to achieve a good mode shape resolution, a heuristic approach was employed. The arch barrels were subdivided into eleven segments whose ends were assumed as measuring points for both the edge and the middle lines. Other six positions at the springing sections of the pier were materialized to capture the longitudinal displacements. The four mid-span sections of the arch barrels' lateral faces and the two pier frontal faces were considered for the lateral and torsional modes. Finally, the two positions on the longitudinal spandrel walls at the middle section of the deck were added to identify the vertical modes.

The sampling frequency was fixed to a value of 400 Hz to acquire the signals produced by both ambient noise and impact hammer excitations, using an instrumented hammer. A 180 second time lap was adopted for the ambient noise acquisitions. Several impacts were acquired in a 60 second period, even if only one impact per acquisition was used in the dynamic identification. The hammer impacts were applied to the same sensor positions along the longitudinal, transversal and vertical directions of the bridge model in order to properly excite a large set of the modes estimated by the numerical modal analysis. Two setups were used for each vibration test in order to capture the higher number of natural modes. Each setup consisted of 18 channels leading to 36 instrumented positions (F.6-5).

Experimental setups for vibration tests F.6-5



Forced vibration tests were performed by using a shaker TIRA TV 51220, capable of supplying a rated peak force of 200 N. The force applied was acquired by using a mechanical impedance sensor PCB Piezotronics 288D01 (measurement range ±222.4 N pk). Five types of excitation tests were carried out:

// Random: random excitation in a 10 to 100 Hz band
// Sweep sine: linear chirp from 10 to 100 Hz
// Shock: impulsive excitation
// Resonance: sine excitation at resonance frequencies
// Sine: sine excitation from 10 to 100 Hz, with 1 Hz resolution

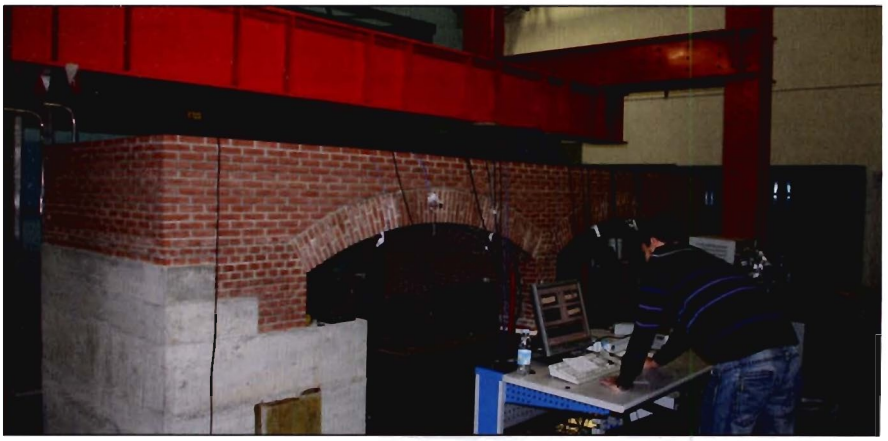
Accelerometers

The selected sensors for the dynamic tests performed on the structure were capacitive accelerometers. The employed dynamic acquisition system was composed of a set of 18 monoaxial PCB Piezotronics accelerometers with a sensitivity of 1 V/g, a measurement range of ±3 g, a broadband resolution of 30 μg and a weight of 17.5 g. The accelerometers were connected through coaxial cables to the LMS Difa-Scadas data acquisition system which also provided the signal amplification. The acquired signals were recorded on the hard drive of a laptop computer interfaced with the data acquisition system and running a specific signal acquisition software.

Strain Gauges

The responses of the arch barrels to the settlement application were measured by means of a set of 16 120 Ω resistive strain gauges 160 mm long and 10 mm wide. The length of the strain gauges allowed to cross at least five bricks and thus to obtain a representative information of the masonry behaviour. The transducers were divided into two sets and were uniformly distributed at the intrados of the arch barrels at the upstream side of the bridge model. As expected from the numerical analyses, the settlement application led to tensile strains in the central portion of the bridge and compressions in the lateral

Accelerometer setup with acquisition system F.6-6

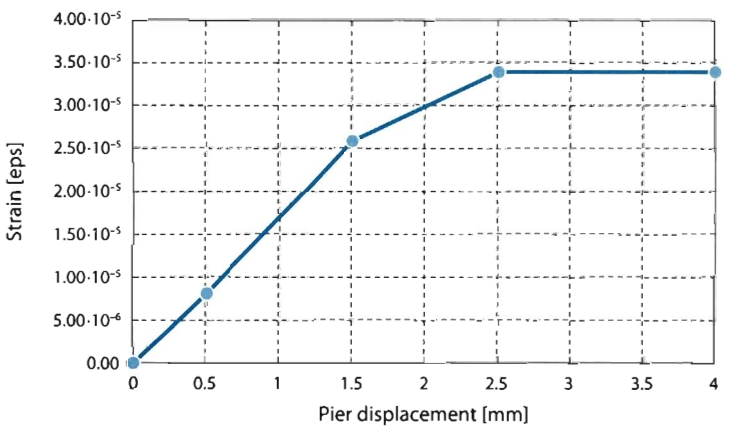


parts. The distribution of the strains throughout the first three steps resulted unchanged and a progressive increase of the deformations was recorded.

Optical Fibres

Fibre optic technology is widely used to measure different structural quantities. In particular, Fibre Bragg Gratings (FBGs) are simple sensing elements, which can be photo-inscribed into a silica fibre and exploit all the advantages normally attributed to fibre sensors. They are suited to measure strain to a 1 με resolution they are insensitive to electrical alterations. The strain sensors employed in this work are based on the so-called "patch sensor" technology [Bassam and Ansari, 2008].Twelve patch sensors were directly glued on the structure in order to measure the strain in correspondence with the masonry joints. The measured reduction in the positive strain moving from the upstream to the downstream side of the bridge agrees with the results of the numerical analyses. However, the most encouraging result for a future early warning application on real bridges was provided by the sensor glued on the bridge pier along the vertical direction. This sensor was able to detect the decompression of the pier due to the removal of the base support from the first step application. In F.6-7 the cumulative strain produced by the progressively induced settlement of the pier support is plotted.

Cumulative measured pier strain related to the first five settlement steps F.6-7



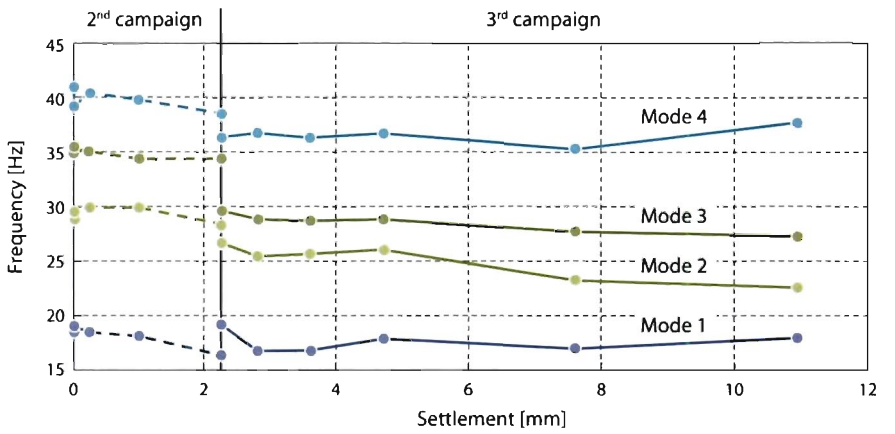
6-5 Data Analysis and Assimilation

The first step of the data analysis consisted of an experimental modal analysis. It was decided to employ two techniques working in the time domain due to the great spectral resolution they offer and their modal uncoupling capability. The Eigenvalue Realization Algorithm (ERA) was used to analyse the free decay responses, whilst ambient vibration signals called for a Stochastic Subspace Identification (SSI).

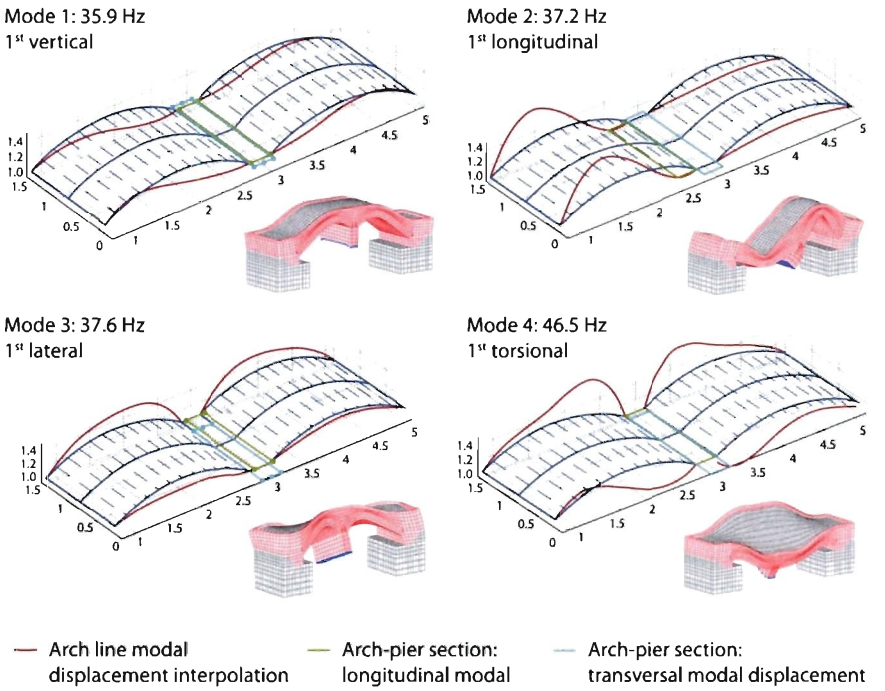
6-5-1 Modal Parameters and Symptom Evolution

The estimation of both natural frequencies and dampings did not show a monotonic trend during the different campaigns. F.6-8 shows the trend of the first four natural frequencies. It is noteworthy that, whilst in second campaign the trend of the first frequency is almost monotonic and highlights stiffness degradation (mainly related to the boundary conditions of the pier), in the third campaign the interpretation of the curve is more complex. Firstly, the first frequency increased up to 19.23 Hz, this meaning that relaxation made the pier settle, increasing the boundary condition stiffness. In fact, after DS4, the pier was almost completely suspended. Secondly, this phenomenon mainly governs the first modal shape, as it can be seen from the 2nd and 4th natural frequencies which retain their values almost equal between the 2nd and the 3rd campaign. A good agreement between the experimentally identified and numerically calculated mode shapes was observed (F.6-9). However, their changes with the applied damage states were minor compared to natural frequencies and damping rates.

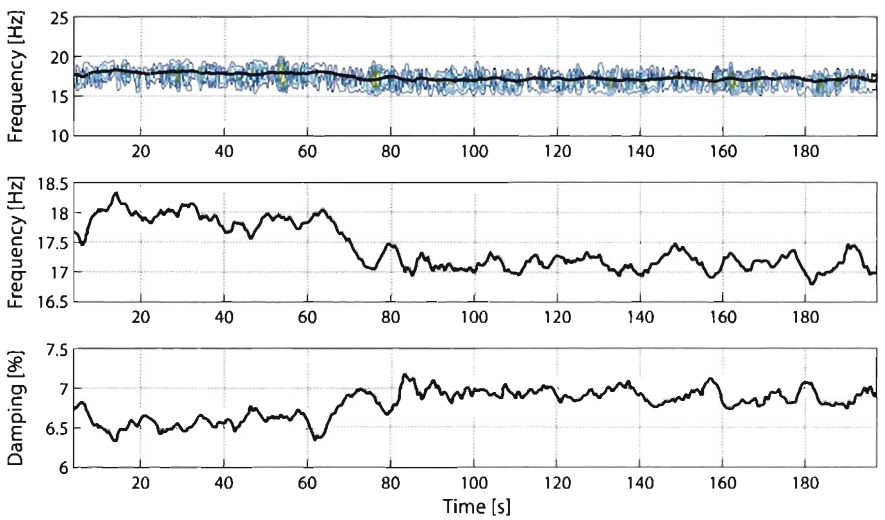
Natural frequencies of the first four modes through the various damage steps (damage step 0 corresponds to the healthy state of the bridge)
Left side: 2nd campaign, right side: 3rd campaign — F.6-8



Experimental and numerical modal shapes F.6-9



Results of the curve-fitting procedure for the first vibration mode: spectrogram of a filtered signal (top), modal frequency instantaneous estimate (middle), damping instantaneous estimate (bottom) F.6-10



6-5-2 Study of the Transient after the Application of Settlements

Diagrams such as those represented in F.6-8 pose important problems regarding the real capacity of current diagnostic tools to distinguish between changes in linear parameters induced by damage and other rheologic and indirect actions, including relaxation, ageing etc. In order to derive information about the evolution of the modal parameters throughout the settlement application, the dynamic response was represented in the time-frequency domain by the Choi-Williams transform [Choi and Williams, 1989]. A non-stationary behaviour was detected relative to highly coupled modes in the high-frequency range.

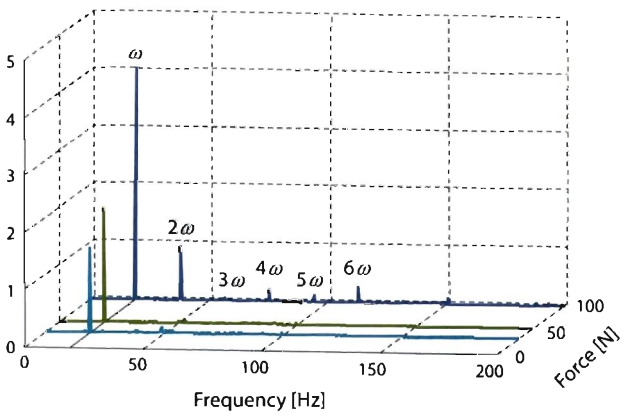
In order to further investigate the transient phenomena, an instantaneous estimation of the modal parameters associated with the Frequency Response Function (FRF), was carried out. The implemented methodology follows the optimization procedure proposed by [Ceravolo, 2004].

F.6-10 shows the results of the curve fitting procedure used to calibrate the modal parameter estimates. This allowed detecting the decreasing and increasing variation of the natural frequency and the damping ratio of the first identified mode, respectively. The increase in relative damping is fictitious here, being associated with the assumption of viscous damping.

6-5-3 Non-Linearity Tests

The tests conducted with the electro-dynamic shaker allowed investigating the presence of non-linear phenomena. Interesting results were found in the resonance tests with different excitation levels. F.6-11 clearly shows the presence of super-harmonics in the resonance test of the first natural frequency, which become particularly intense at the higher sine-excitation test (100 N).

Super-harmonics of the first natural frequencies manifest themselves at higher excitation levels F.6-11



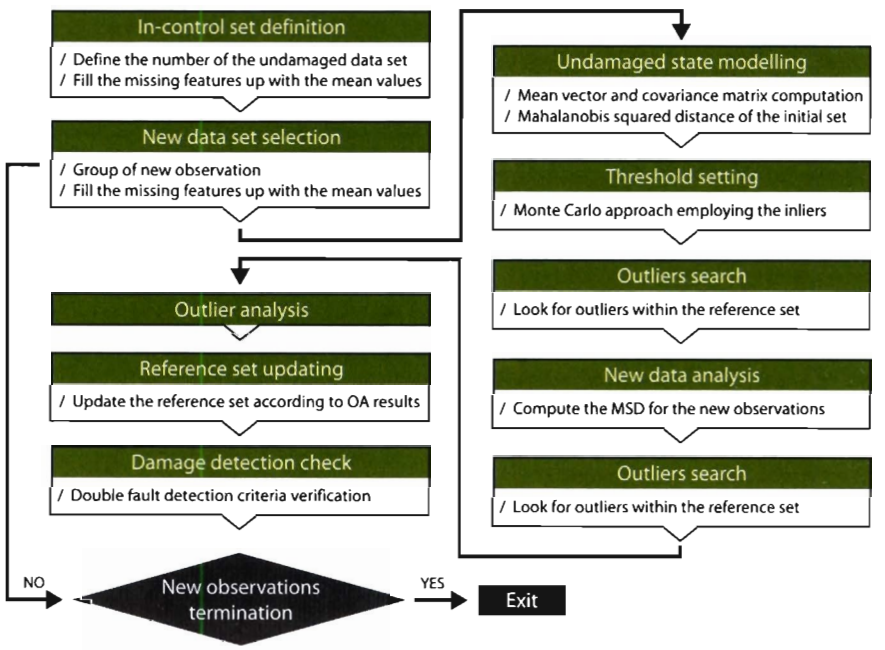
These non-linear effects will be subject of further studies, such as non-linear identification using an evolution of a recently developed technique [Ceravolo et al., 2010]. In order to characterize the non-linear behaviour of the bridge, a static test will be performed in the same locations where the shaker was used. This will allow quantifying the tangent stiffness matrix related to an associated theoretical oscillator.

6-5-4 Structural Health Monitoring

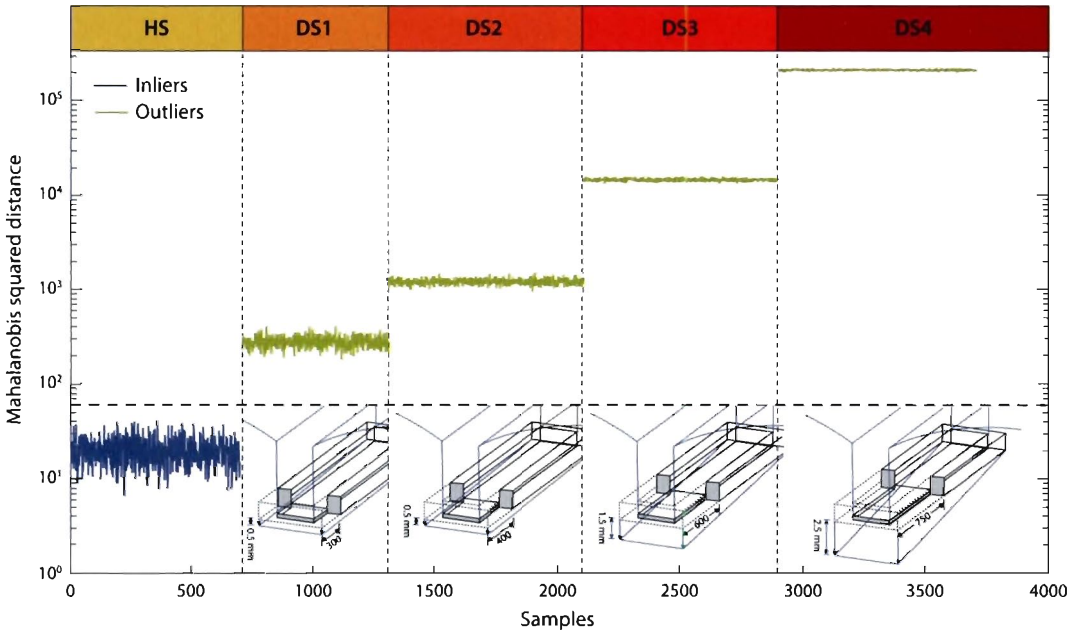
An SHM methodology was developed using outlier analysis [Worden et al., 2000] in order to exploit its limited computational effort, the damage sensitivity and the result accuracy. The choice of a data-driven approach for damage detection was forced by the complexity and uncertainties of the structure, which prevented the definition of a reliable numerical model. The difficulties to incorporate the noise effects, which are unavoidable in the vibration measurements, motivated the adoption of a stochastic approach. Several outlier analyses were carried out both in the time and in the frequency domain [Ruocci, 2010]. An on-line outlier analysis procedure was also developed and the flow-chart of its algorithm is presented in F.6-12.

By way of example, F.6-13 shows the result for the outlier analysis carried out at the measurements of the second campaign. The acquired signals were analysed in the frequency domain in terms of transmissibility functions. Small portions of the spectra were selected by means of a genetic algorithm and used as inputs to compute the statistical

On-line outlier analysis methodology pursued F.6-12



Results of outlier analysis F.6-13



distance assumed as damage index. All the sets concerning the measurements acquired after the introduction of the settlement steps are above the threshold which defines the in-control field. This result proves the accuracy of the damage detection method and the sensibility of the selected features.

6-6 Conclusions and Perspectives

This work has documented the extensive test campaigns carried out on a scaled masonry arch bridge subject to progressive damage steps. The experimental tests covered the span of three years and the data analysis is still in progress. The final prospect is the development of new vibration-based SHM approaches. This paper, in particular, describes the whole test programme in its various stages and strives for marking out a definite experimental path, as well as for outlining new plans and perspectives for SHM.

References

Bassam, A. and Ansari, F., 2008. *Post-Seismic Structural Health Monitoring of a Column Subjected to near Source Ground Motions*. Journal of Intelligent Material Systems and Structure 19(10):1163–1172.

Ceravolo, R., 2004. *Use of Instantaneous Estimators for the Evaluation of Structural Damping*. Journal of Sound and Vibration, 274(1–2):385–401.

Ceravolo, R., Demarie, G.V. and Erlicher, S., 2010. *Instantaneous Identification of Degrading Hysteretic Oscillators under Earthquake Excitation*. Structural Health Monitor 9(5): 447–464.

Choi, H.I. and Williams, W.J., 1989. *Improved Time-Frequency Representation of MultiComponent Signals using Exponential Kernels*. IEEE Trans. Acoust. Speech Signal Process 37(6):862–871.

Invernizzi, S., Lacidogna, G., Manuello, A. and Carpinteri, A., 2009. *Damage Assessment of a Two-Span Model Masonry Arch Bridge*. Proceedings of the SEM Annual Conference. Albuquerque, USA.

Quattrone, A., Ruocci, G., Ceravolo, R., Worden, K. and De Stefano, A., 2010. *Non-Linearity Detection in a Masonry Arch Bridge Subject to Artificial Settlements*. Proceedings of Fifth European Workshop Structural Health Monitoring, Sorrento, Italy.

Ruocci, G., 2010. *Application of the SHM Methodologies to the Protection of Masonry Arch Bridges from Scour*. PhD Thesis, Department of Structural and Geotechnical Engineering.

Worden, K., Manson, G. and Fieller, N.R.J., 2000. *Damage Detection Using Outlier Analysis*. Journal of Sound and Vibration 229(3):647–667.

7

SHM and Adaptivity Concepts in the Reduction of Risks Associated to Structural Failures

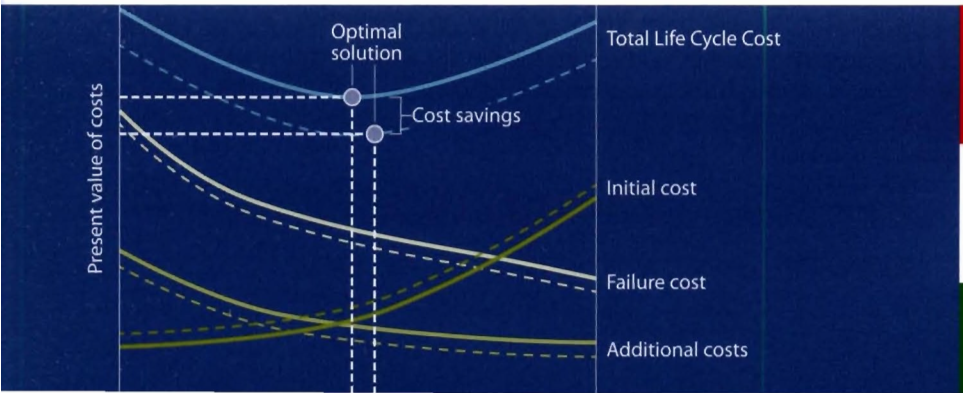
Authors:
Andrea Enrico Del Grosso
Francesca Lanata
Paolo Basso

Motivation

Risk management of the European transportation infrastructure requires an innovative push. The transition from deterministic via semi-probabilistic to pure probabilistic approaches is desired.

Main Results

With the application of the new IRIS Risk Paradigm and the monitoring and damage detection technologies developed a conclusive solution for the European transportation infrastructure has been presented.



7-1 Introduction

Construction industry is a primary activity playing a paramount role in nearly all the sectors relevant to the economy of industrialized countries and is a very important economic activity itself. Today the construction industry necessitates a profound innovation. Referring to the infrastructure management sector, the European Construction Technology Platform [ECTP, 2005] has for example identified the following research needs:

// Modelling the performance of the infrastructure,
// Monitoring the performance of the network,
// Improving the performance of the infrastructure: materials and construction techniques,
// Enhanced management.

The above needs are somehow related to the management of risks. Management of risks covers many different aspects; the aspect that has been dealt with within the activity performed by UNIGE in the IRIS framework is related to the risks associated to the failure of a structural component. The term failure in the above sentence, does not necessarily mean collapse, but it also means the acquired inability of a structural component to perform as expected, thus covering both the concepts of service and ultimate limit states. Two different aspects have in fact been thoroughly examined and developments with respect to the existing state-of-the-art have been produced. Both aspects have been contextualized in the process flow of the IRIS Risk Paradigm.

As concerning structural health monitoring, the issue of reliability determination of the damage identification process has been faced, developing an innovative approach. Experience and data collected from real or experimental monitoring cases have been used to experimentally validate the effectiveness of the proposed approach. Although the algorithms considered are conceived in the context of static monitoring, they may be used within a dynamic monitoring approach as well.

The second aspect is related to the opportunities offered in risk reduction strategies by innovative approaches to structural control. In particular, adaptivity has been considered as an innovative approach to improve structural performance in terms of safety and reliability. The research performed relates to the RIPREMIS module in the IRIS Risk Paradigm. Adaptivity indicates the ability of the structure to modify its characteristics to optimize the response to external loads with respect to some performance measure and it is somehow different from the classical active control approach, where a system of control forces is generated inside the structure to balance the effects of external loads.

The adaptivity concept has been applied to the specific case of building envelopes and an overview of the variable geometry structural systems that may be adopted to build an adaptive envelope has been performed. The interface role of the envelope between the structure and a fluid excitation (i. e. wind, water) has been analysed and a novel strategy, called Finite State Control Strategy (FSCS) has been proposed to control the adaptive envelope.

The present work summarizes the main achievements with respect to both aspects; extensive details on the studies can be found in the IRIS Final Report [IRIS, 2012].

7-2 Risk Reduction in Structural Engineering

Dealing with civil structures, risk reduction is still often limited to the design of the structure itself, leaving the installation of monitoring and control systems to the management of strategic or very special structures only. This can of course be viewed as a consequence of the normal behaviour of civil structures, which makes a control system only convenient in case of particular external excitations (i.e. typically earthquakes or winds with a great frequency of occurrence) and a monitoring system only convenient depending, for instance, on the complexity of maintenance problems.

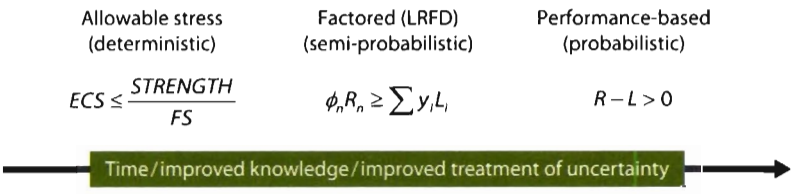
In this context design methods and codes have evolved the most in order to integrate the increasing knowledge and to reduce the risk. A brief overview of this evolution is given in F.7-1.

Despite differences in their treatment of uncertainty, each method (deterministic, semi-probabilistic, and probabilistic) seeks an optimal balance between economical design and safe performance:

- // In allowable stress design, safety has been assumed to exist if elastically computed stresses (ECS) did not exceed allowable working stresses (e.g. a preset fraction of the concrete strength, yield strength). Uncertainty is accounted for through the use of a factor of safety (FS) obtained through expert opinion.
- // In factor-based methods such as the LRFD, load and resistance factors have been developed through expert opinion and calibration efforts.
- // In performance-based approaches, the engineer is responsible for the specification of all random variables contributing to loads and resistances.

As for example discussed by [Aktan et al., 2007], the primary motivation to adopt a probabilistic-based approach is then to change the design experience from "specification-based" and "process-oriented" to "performance-based" and "product-oriented" to allow the engineer more flexibility to leverage new materials and technologies. However probabilistic methods (i.e. FORM, SORM, Monte Carlo, etc.) are to date not generally used in design practice. In fact, codes that incorporate the reliability index in assessment guidelines, such as the Canadian Highway Bridge Design Code, specifically state that the guidelines will not be utilized for design purposes [Ministry of Transporation, 2006]. Along with the treatment of uncertainty, precautions, rules of practice and construction details must be

Evolution of design methods F.7-1



considered equally relevant to the risk assessment since they often represent the only way to deal with the category of neglected, unrecognized or unforeseeable actions. Design standards usually translate all these aspects into requirements and prescriptions regarding material treatment, structural morphology, etc., exploiting fundamental concepts of robustness like redundancy (system level) and ductility (material level).

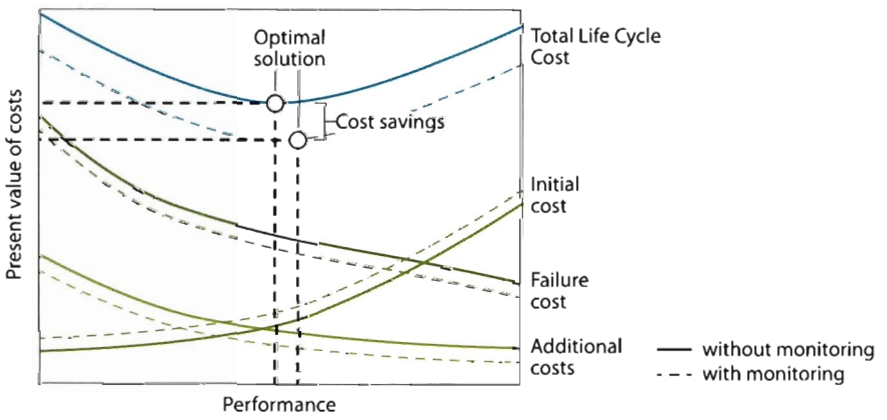
7-2-1 Monitoring Systems

Apart from the advantages provided in maintenance problems, when monitoring strategies are used to improve the safety of a civil structure, the approach can be twofold and relates to the design method that is being considered. On the one hand, monitoring can provide data that can be utilized to confirm or improve existing load factors, resistance factors, and load combinations for extreme events used in existing code provisions (semi-probabilistic). On the other hand monitoring can be utilized to improve design by providing the engineer with the statistical information necessary to employ performance-based design (fully probabilistic). As such, monitoring would serve as the catalyst to enable a change in methodology itself. In this approach the designer has much greater flexibility, but also bears the responsibility of quantifying and appropriately treating all of the uncertainties that determine member resistances, load effects, and load combinations. A brief overview of this evolution is given in F.7-2.

Likely evolution of assessment, prediction and management models (adapted from [Messervey and Frangopol, 2008]). F.7-2



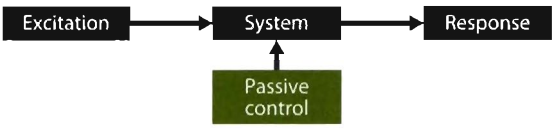
Optimum design solution based on Life Cycle Cost minimization with and without monitoring (adapted from [Frangopol and Liu, 2007]) F.7-3



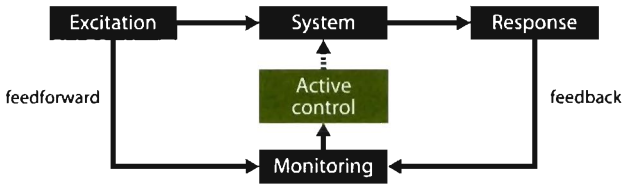
It is reasonable to expect that the use of an SHM-enabled, reliability-based approach would lead to a more optimal design solution as shown in F.7-3. Although monitoring does not change the relationship between the costs (i.e. that higher initial costs result in lower failure and additional costs) monitoring does change each cost itself. Specifically, the initial cost is increased (upfront SHM system cost), the failure cost is decreased (less risk), and the additional costs are decreased (improved optimal management decisions) across the entire profile. This reduction in total Life Cycle Cost is also expected to be paired with a higher level of performance.

Block diagrams of control F.7-4

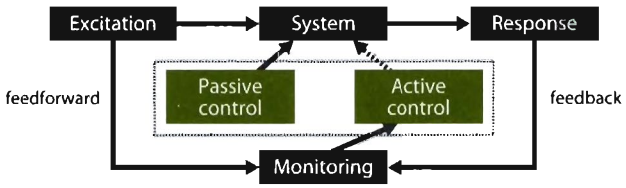
a) Block diagram of passive control



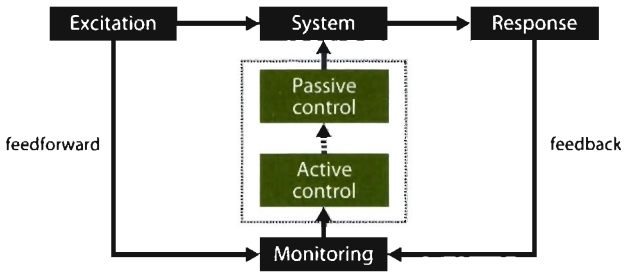
b) Block diagram of active control



c) Block diagram of hybrid control



d) Block diagram of semi-active control



7-2-2 Control Systems

Structural control for civil engineering applications has a number of distinctive features, largely due to implementation issues, that set it apart from the general field of feedback control. In particular, when addressing civil engineering structures, there is considerable uncertainty, including non-linearity, associated with both physical properties and disturbances such as earthquakes and wind, the scale of the forces involved can be quite large, there are only a limited number of sensors and actuators, the dynamics of the actuators can be quite complex, the actuators are typically very large, and the systems must be fail-safe [Dyke et al., 1995; Housner et al., 1994; 1997; Kobori, 1994; Soong, 1990]. Four main kinds of control systems are usually distinguished: passive (F.7-4a), active (F.7-4b), hybrid (F.7-4c)and semi-active (F.7-4d). For an active control system located at the interface with the excitation, it seems normal to expect a feedforward configuration while, on the contrary, a feedback configuration is typical when the active control acts on the response of the system. However, it is worth noting that even if the relationship described above generally holds, it should not be seen as a rule and it is advisable to keep aside the implications of the different characteristics of the system.

7-3 Reliability of Damage Detection Algorithms

Damage detection algorithms (DDA) form the core of a Structural Health Monitoring process. Experience has shown that SHM efficiency depends on the ability of the algorithms to detect structural changes under real environmental and operational conditions [Sohn, 2007]. Apart from the applications directly studied, a lot of damage detection methods have been tested and reported in the literature in the last few years, on static [Omenzetter et al., 2004] and dynamic data [Kim et al., 2010], and on laboratory [Park et al., 2006] and in-field experiments [Benedetti et al., 2011; Cheung et al., 2008]. Despite of the above interest that has been largely expressed by means of research papers in conferences and scientific journals, very few practical examples can be reported to date, the main reasons being the lack of extensive field evidence in the disclosure of structural defects and the inability to interpret the data obtained from hundreds of sensors in a timely manner. Robust and reliable methods capable of detecting, locating and estimating damage whilst being insensitive to changes in environmental and operating conditions have yet to be agreed upon.

The objective of the following sections is to present the expansion of the probabilistic modelling of inspection results through NDT tools originally developed by [Rouhan and Schoefs, 2003] to the probabilistic modelling of damage detection from data processing algorithms. With reference to the long-term experiment presented in the next subparagraph, this section is aimed at discussing the performance of the Proper Orthogonal Decomposition as a damage detection algorithm [Lanata and Del Grosso, 2006]. The damage indicators extracted from the proposed algorithm are used to set a reference

period and a threshold value associated to damage presence. The uncertainties affecting the damage identification process on the assessment of the structural health state will be taken into account, in particular uncertainties due to environmental changes.

Based on the characteristics of real monitoring data, the performance estimate of damage detection algorithms (DDA) for a given detection threshold is discussed through the Receiver Operating Characteristic (ROC) curve [Schoefs et al., 2009]. A Bayesian modeling of monitoring results is introduced by defining the probability of detecting damage conditional to an actual existing damage (Probability of Detection, PoD) and the probability of detecting damage conditional to non-existing actual damage (Probability of False Alarm, PFA). The process performance can be completely described by the couple (PoD, PFA). Looking for the best detection performances, the probability of detection should always take larger values than the probability of false alarm (low noise sensitivity).

Special emphasis is placed on the influence of the environmental conditions on the probability of false alarm because the latter depends on the noise level and the chosen threshold only. On the contrary, the probability of detection depends on the damage extension. The difficulties in obtaining a good performance curve in presence of strong temperature variations (noise) and small levels of damage is also discussed and the possibility of improvement of the detection process through post-processing of acquired data is illustrated. The discussion is based on the availability of a reference period in which the structure can be considered as undamaged.

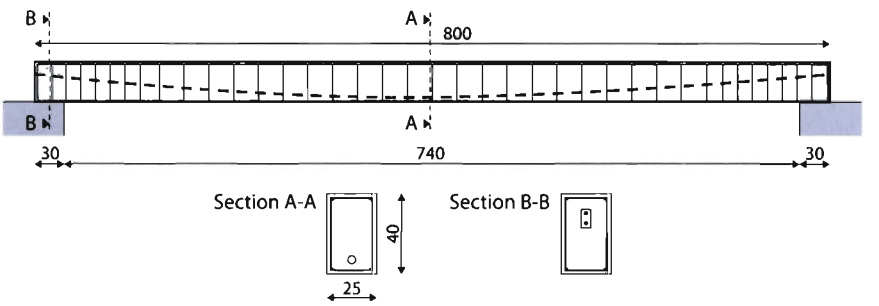
7-3-1 Long-Term Experiment on Prestressed Beam Specimens

The University of Genoa has obtained from Autostrade per l'Italia (ASPI S.p.A.) the authorization to use two prestressed concrete beams, available at their Laboratory in Romagnano Sesia, Italy for research purposes. The experimental tests have been performed with the cooperation of Ecole Politechnique Fédérale de Lausanne (EPFL) and SMARTEC, Switzerland.

Geometrical and Material Properties

The tested specimens, cast in 1992, are post-tensioned concrete beams of 8m in length with a rectangular cross section (0.25 large and 0.40 height). Each beam has a post-tensioned inclined cable formed by two standard tendons of 0.6" diameter and four addi-

Geometrical properties of the specimens F.7-5



Material properties (design values) T.7-1

Concrete: C35/40	**f_{ck} = 35 N/mm²**
Compressive strength [N/mm²]	16.8
Flexural tensile strength [N/mm²]	2.8
Prestressing steel	**f_{plk} = 1900 N/mm²**
Diameter [mm]	13.3
Tensile strength [N/mm²]	1445
Reinforcing steel: FeB44k	**f_{yk} = 430 N/mm²**
Diameter [mm]	10
Tensile strength [N/mm²]	374

tional reinforcing bars at the corner of the section (10 mm diameter). Shear reinforcement consists of 8 mm diameter stirrups spaced at 250 mm in the central section and at 150 mm near the supports. The geometric characteristics of the beams are shown in F.7-5.

Each tendon was post-tensioned, giving an initial force of 130 kN, and anchored to the end of the beam. The metallic duct was finally grouted using cement slurry having consistency of 0.3-w/c ratio. The design of the beams and the design characteristic values for the material properties are based on the Italian codes and they are reported in T.7-1.

From the available design data, a bending moment of about 50 kNm has been assessed for the cracks opening in the central section of the beam. The only weight of each beam gives a bending moment of about 15 kNm. It was decided to add a dead load on the beams in order to increase the bending moment up to 25 kNm.

Experimental Programme

The beams have been located outside and exposed to environmental conditions. The environmental conditions are related to the geographic position of the laboratory, located on the hills close to the Alps in the North of Italy. Temperature reaches +40 °C in summer and −15 °C with snow during winter. Moisture is influenced by rainy springs and autumns. The beams are exposed to wide temperature variations due to night/day cycles

View of the specimens during tests F.7-6

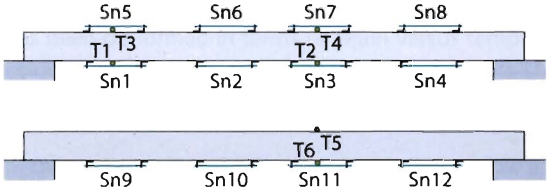


such as effect of sun exposition. The thermal gradients between the upper and the lower surfaces of the beam induce deformations to be measured. It has to be observed that beam B is more protected by sun and rain exposure because of the jutting out ledge of the nearby shed (F.7-6).

The system installation has been completed on 16 and 17 April 2008 when the beams were simply supported without any added dead loads. The sensor instrumentation was supplied by SMARTEC and the acquisition system was supplied by EPFL. The first beam (called beam A) was instrumented with four fibre optic deformation sensors (SOFO) at the lower surface and four fibre optic deformation sensors at the upper surface (F.7-7 right); the second beam (beam B) was instrumented with only four fibre optic deformation sensors at the lower surface. Each sensor has an active length of 1 metre. Six thermocouples were glued on the upper and lower beam surfaces to measure temperature changes. The sensor location for the two specimens is shown in F.7-7 (left).

Four measurements per hour were scheduled. The first set of measurements showed to be very well correlated with temperature and it was decided to continue the tests with the same frequency of acquisition. The dead load was put on the beams on 8 May 2008 and this has to be considered as the reference condition of the beams (F.7-8). The structural response of the beams in the reference condition was measured for about 40 days. After this period, the beam instrumented with eight sensors was progressively damaged. The first damage was introduced on 18 June 2008. A cut of about 1 cm in the middle section of the beam A was produced using a saw. The cut was deepened on 23 June 2008 until the reinforcing bars were reached (about 3 cm in depth). A third level of damage was

Sensor location (left) and installed SOFO sensor (right) F.7-7



Sn ... SOFO sensor
T ... Thermocouple



View of the beams after the placement of the dead load F.7-8



Events list T.7-2

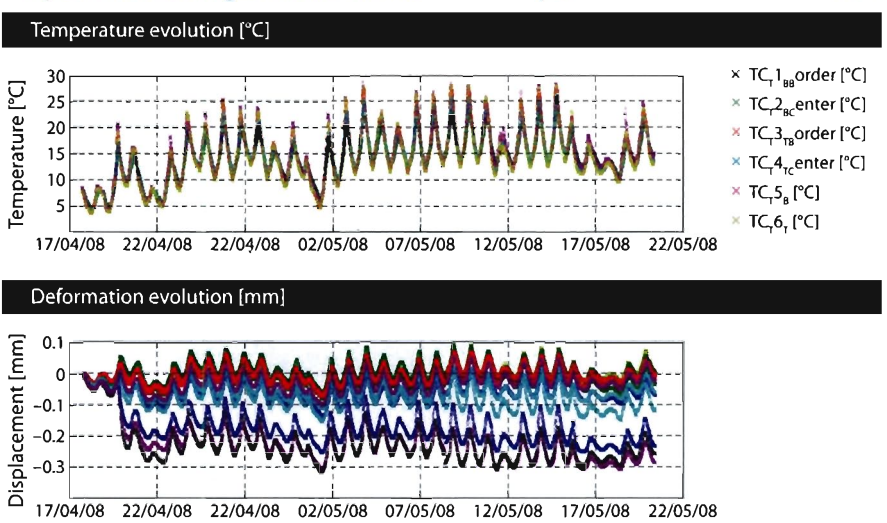
#	Date	Event
1	08/05/2008	Ballast load
2	18/06/2008	1st damage (1 cm cut, middle section)
3	23/06/2008	2nd damage (2 cm cut, middle section)
4	09/07/2008	3rd damage (cut of half of the rebar, middle section)
5	16/07/2008	4th damage (complete cut of the rebar, middle section)
6	21/01/2009	5th damage (cut of the rebar between Sn3 and Sn4)
7	17/11/2009	6th damage (partial cut of one tendon, middle section)

created on 9 July 2008. The previous cut was deepened again by cutting also the lower reinforcing bars (about 5 cm in depth). A further damage, consisting in a cut about 5 cm in depth, was introduced at a section between sensors 3 and 4 on 21 January 2009. The last damage was the partial cutting of one of the pre-stressing tendon, as reported in T.7-2. Beam B has been kept undamaged for reference.

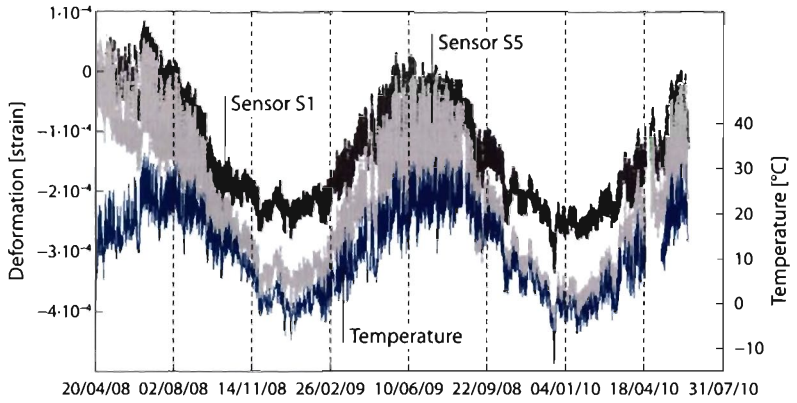
Processing of the Raw Strain Time Histories

In the first phase of monitoring, the reference state and the behaviour under changing conditions like temperature and other environmental effects have been observed. The time histories from measurements of sensor strain show a good correlation with temperature and the daily cycles are detectable and related to the elongation measurements, even if they are strongly variable also in short term period (F.7-9). After the first days of measurements (unloaded condition), a shift in the strain measurements due to the dead load positioning was observed. The data measured between the load positioning and the introduction of the first cut represents the undamaged situation to be compared with the damaged ones.

Temperature and elongation time histories (reference period) F.7-9



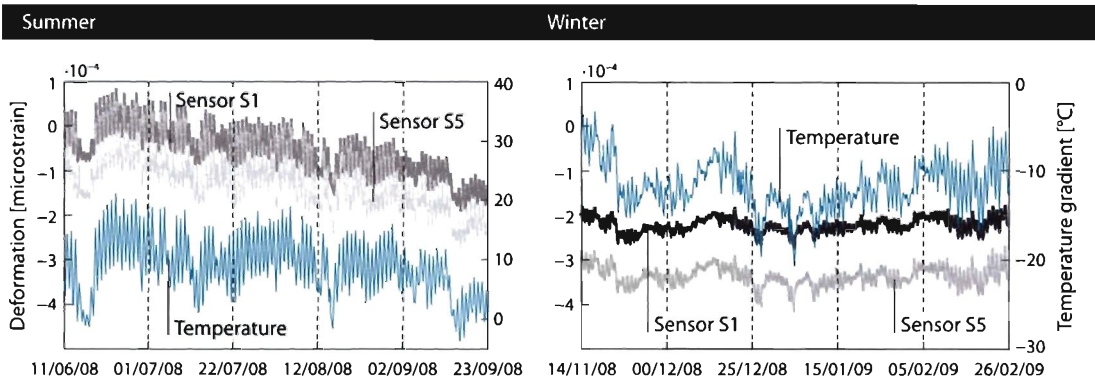
Complete time histories of temperature and strains at sensors S1 and S5 F.7-10



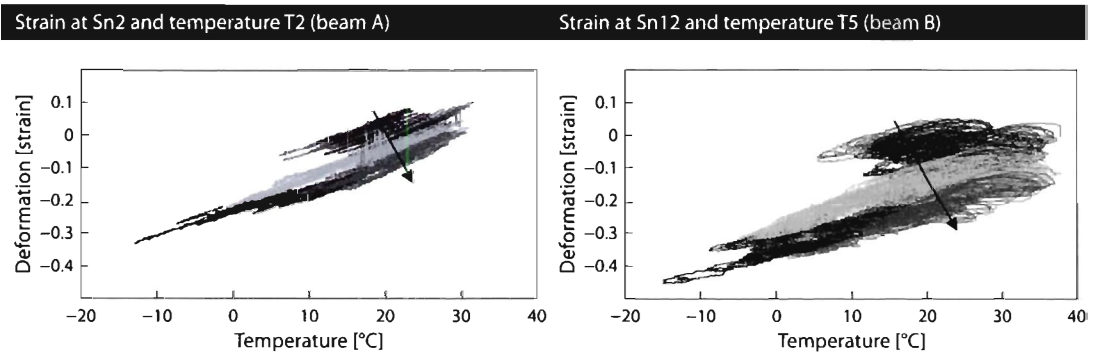
The plot in F.7-10 depicts the complete time histories of the strains at sensors S1 and S5 and of the temperature gradient in the corresponding section (difference between T1 and T3). Similar trends are experienced for the other sensors. It can be noted that the influence of temperature on the measurements is very large and that more than one year of measurements is needed to characterize seasonal cycles. Plots in F.7-11 illustrate the difference that has been observed between winter and summer cycles. The comparison shows that the strain histories are much smoother in winter time, starting from the middle of September.

A comparison between the strain time histories experienced by beam A and beam B has been performed in terms of strain versus temperature plots (F.7-12). Different grey colours represent the artificially introduced events (T.7-2). The plots put into evidence that the beams' behaviour is different although the specimens are located in the same place. In particular, beam B has a greater delay in the thermal response shown by larger hysteresis cycles. Sensors at different locations show a similar behaviour. The response of

Comparison of strain histories in summer (left) and winter (right) cycles F.7-11



Relationship between strain and temperature. Grey colours represent the events (T.7-2) and the arrow indicates time progress. F.7-12



beam B, which shows a delayed thermal behaviour, is probably more protected by the effects induced by sun, rain, ice, snow due to its position partially under the ledge of the shed. The second remark that can be made regards the shifts observed in the linear strain-temperature relationships during the monitoring period. These shifts are usually associated to changes in the mechanical system, related or not to damage [Glisic and Inaudi, 2007]. While the first observed shift corresponds to the first event on the beams (ballast load), the further detected shifts are not clearly related to introduced artificial damages, except for the last damage that is only observed for beam A. That means that something not controlled occurred in both beams during monitoring, independently on the introduction of artificial damage.

The POD has been applied to these not processed strain histories as a damage detection algorithm. The variations of the extracted eigenvectors for beam A are shown in Figures F.7-13 and F.7-14. The first eigenvector (F.7-13) shows that the load positioning and the introduced damages (sections and tendon cuts) are not clearly detected. On the contrary, the last eigenvector plotted in F.7-14 shows a shift related to the load positioning (visible for all the sensors), but the damages remain undetected.

On the contrary, some strong environmental variations, such as some consecutive days of rain, could be associated to a damage initiation. This first attempts to use real field measurements, without any data pre-processing, to identify the induced damages have apparently failed, producing false positives or unclear evidence of disturbances in the features of the signals associable to damage.This has put into evidence some failure of the applied algorithm and has shown that POD as the other tested damage detection algorithms are very sensitive to environmental changes.

From the above plots, it can be observed that the data analysis discloses significant effects of the anomalies in temperature variation and of other environmental effects like direct exposure to sunshine. It has to be noted that weather in the Italian sub-alpine regions may be unstable in spring and in summer. As concerning the effect of the above findings on damage identification procedures, the focus issue of the analysis seems to be the removal of the variability due to the environment, especially when the yearly cycle has not been completed yet.

As a consequence, in real cases, data pre-processing aimed at removing thermal effects is needed for improving the sensitivity of the damage detection algorithms and having a reliable damage identification. The removal of the environmental variations will be presented in the following, as well as the results of the POD algorithm on these filtered strain time histories.

Strain Pre-Processing for Thermal Effects Removal

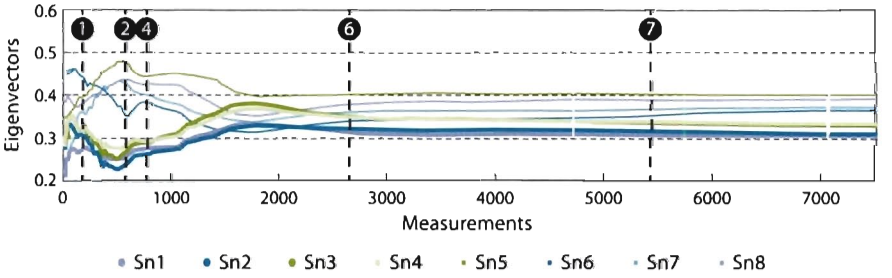
The analysis has been addressed to extract some information on the dilatation coefficient of the beams. The dilatation coefficient represents the sensitivity of measured strain variations to temperature variations and can be computed for each location containing also temperature sensors. The following relationship has been used:

$$a = \frac{\Delta\varepsilon}{\Delta T} \qquad \text{E.7-1}$$

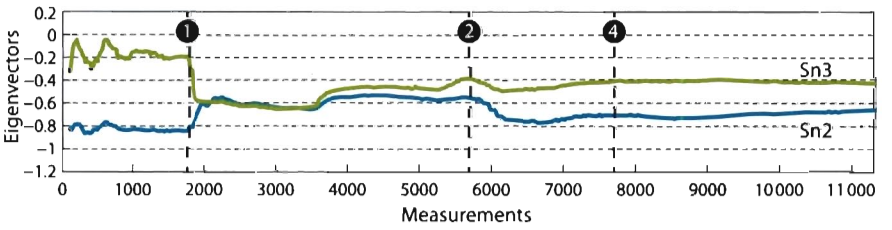
where $\Delta\varepsilon$ is the strain variation between two time instants and ΔT is the temperature variation registered at the same time instants.

As high values of the dilatation coefficient are retrieved for low ΔT, a filter has been applied to data in order to cut the temperature variations inducing a strain lower than the sensor sensitivity (2 μm/m). Consecutive measurements with the same temperature are also neglected.

First eigenvector variation for sensors on beam A during the whole monitoring period. Vertical dotted lines indicate the artificial events listed in T.7-2 F.7-13



Zoom on the first period of the monitoring of the last eigenvector variation for Sn2 and Sn3. Vertical dotted lines indicate the artificial events listed in T.7-2 F.7-14

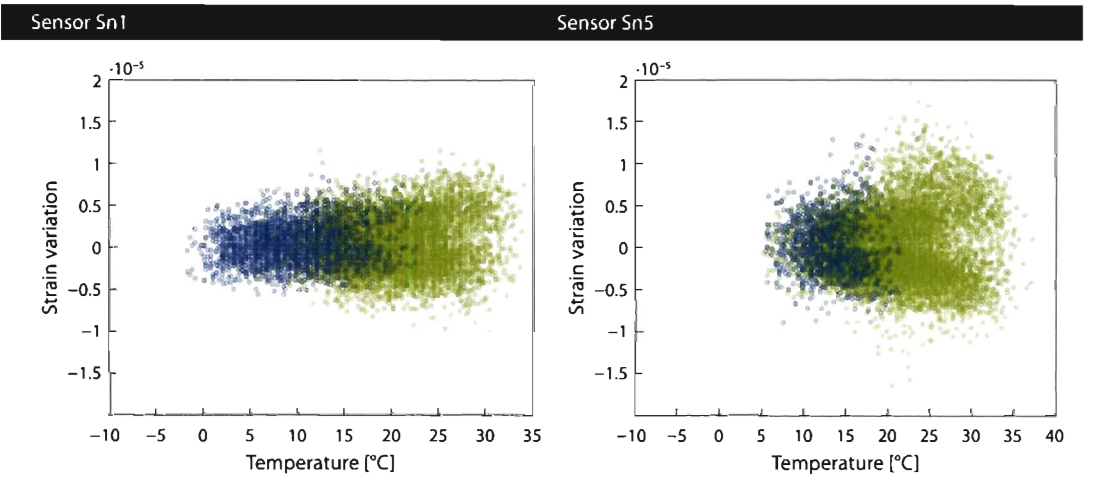


The values of the dilatation coefficient α are expected to be positive, as an increase in the temperature should result in an increase in the strains and vice versa. On the contrary, several negative values have been retrieved. This behaviour has also been observed in other monitored structures, such as presented in [Lanata and Schoefs, 2011].

Negative values of the dilatation coefficient can be considered as representative of anomalous behaviours in the sense that an increase in temperature causes a decrease in strain or vice versa. Negative values in the dilatation coefficient are supposed to be related to fast (and not persistent in time) changes in temperature that the structure is not able to follow, because they finish before having a global effect on the structure. They can be explained as dynamic variations that the static behaviour of the structure cannot catch. As the work aims to give an interpretation of the static structural response, it has been decided to neglect the negative values of the dilatation coefficient. By the way, the rate of discarded values does not affect the statistical analysis thanks to the high number of measurements. About 15 % of negative dilatation coefficient values have been discarded before further performing the analysis.

F.7-15 shows the variation of the strain measured by sensors Sn1 and Sn5 with temperature. The blue points on the left represent the measurements during the winter period, while the green points on the right represent the measurements performed in summer. Both plots show a quite constant value of the dilatation coefficient, independently from the observation period. It means that the process can be considered as stationary with time. The dilatation coefficient during winter (values associated to low temperatures) has the same behaviour as the one during summer (values on the right side of the plots). Even if the slope remains the same, the sensor on the top (Sn5) shows a higher scatter, more evident during the summer period, probably related to secondary effects e. g. direct sun or rain. All the data from time-history sets were gathered for statistical analysis to assess the value of the dilatation coefficient for each sensor location. The statistical analysis of the estimated values of the dilatation coefficient has shown that the behaviour can be properly described by the exponential distribution having mean value $\tilde{a}$ 8.53 μstrain °C^{-1}

Strain variation versus temperature measured by sensor Sn1 and Sn5 F.7-15



for Sn1 location, 9.33 μstrain °C^{-1} for Sn3, 9.36 μstrain °C^{-1} for Sn5 and 10.32 μstrain °C^{-1} for Sn7 (F.7-16). Regarding the other beam, less exposed to rain and direct sun, a mean value of 7.45 μstrain °C^{-1} has been obtained on the lower surface.

The mean assessed values of the dilatation coefficient are coherent with the known dilatation coefficient of concrete structures. In fact, the assessed value of the dilatation coefficient (between 7.3 and 10.5 μstrain °C^{-1} by considering confidence intervals of 99 %) is of the same order of the known dilatation coefficient in concrete structures (usually varying between 6 and 13 μstrain °C^{-1} depending on the relative humidity and the aggregates). After the statistical analysis on the local dilatation coefficients, it is possible to remove from the strain time histories the variations due to temperature that sometimes can induce strong variations that could be wrongly interpreted as anomalous behaviours. In fact, when a change in temperature occurs, the thermo-elastic strains can be written as:

$$\varepsilon = \varepsilon^{thermal} + \varepsilon^{second-order} \qquad \text{E.7-2}$$

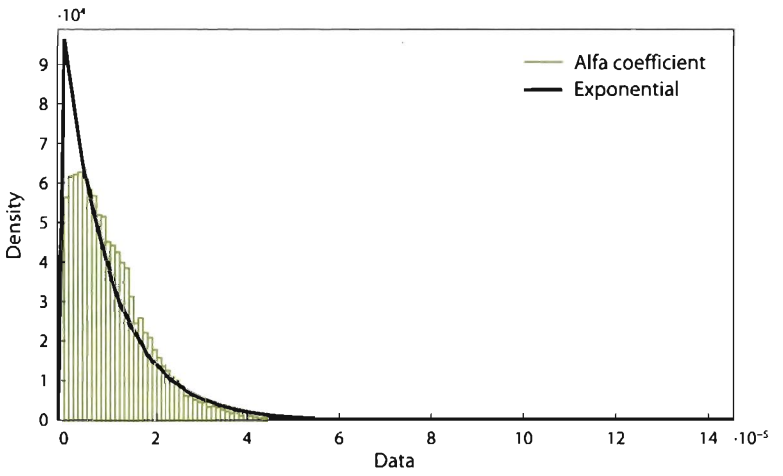
where $\varepsilon^{thermal}$ is the thermal strain in the linear theory and $\varepsilon^{second-order}$ is the residual strain due to non-linear effects with the temperature and other mechanical effects. The strain caused by a change in temperature from T_0 in the reference configuration to T in the current configuration is called thermal strain and it can be expressed by the linear relation:

$$\varepsilon^{thermal} = a(T - T_0) \qquad \text{E.7-3}$$

where a is the dilatation coefficient. In this analysis, the estimated mean value of thermal strain, obtained by using the estimated mean value of the dilatation coefficient $\tilde{a}$, has been removed to retrieve the second-order strains:

$$\varepsilon^{second-order} = \varepsilon - \tilde{\varepsilon}^{thermal} = \varepsilon - \tilde{a}(T - T_0) \qquad \text{E.7-4}$$

Probability density function of the dilatation coefficient for section Sn7 F.7-16



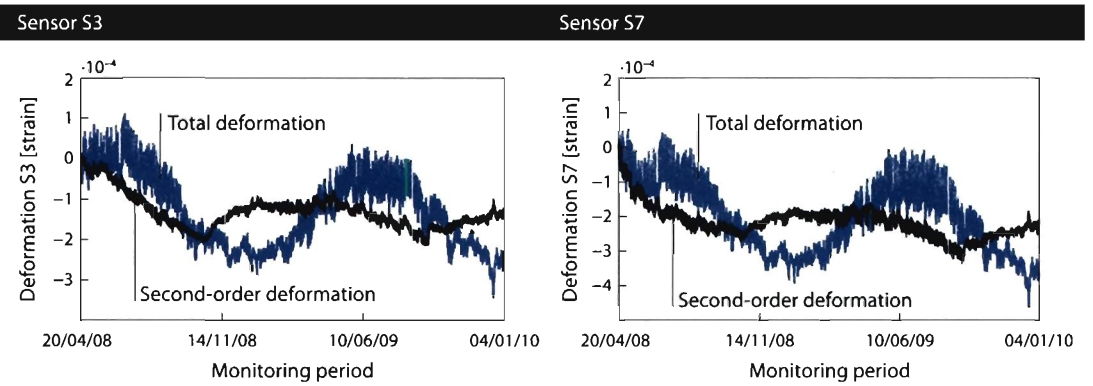
F.7-17 shows the total strain and the second-order strain after removing thermal strain respectively for sensor Sn3 on the lower surface and for sensor Sn7 on the upper surface. The plots show that the second-order strains are significantly smoother than the total ones in particular during summer, when higher temperature variations induce greater strains. By the way, a little periodicity still remains in the filtered time histories. In the first period of the monitoring both plots show a gradual decrease in strain with time, probably related to the application of the dead load and to introduced damages. In the original strain this behaviour was not so clear. Sensor Sn7 seems to show the variations better due to the application of the dead load in the first period, while Sensor Sn3 in particular, shows a discontinuity in the trend at the end of October to become very stable during the following winter period. Similar trends are experienced for the other sensors.

Damage Detection Analysis after Strain Pre-Processing

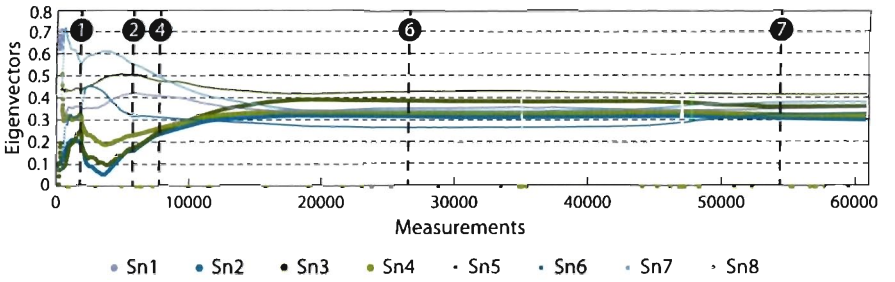
The POD method has finally been applied on the processed strain histories. The eigenvectors are more stable with time and potentially more sensitive to possible variations induced by damages. The shift related to the load positioning is already well detected by the first eigenvector for all the sensors (F.7-18), while the not-processed data needed the last eigenvector to clearly identify the shift (F.7-14). The shifts related to strong environmental variations, previously detected, do not give anymore a false indication of damage. By the way, the analysis of all the eigenvectors gives no clear detection of events 2, 4 and 6; little variations in the eigenvectors are visible around the induced events but some doubts remain because the variations interest all the sensors and not only the ones closest to damage.

The most important result of the filtering pre-processing is reported in F.7-19. The plot shows that after removing thermal strain, the event 7, i.e. the partial cut of one tendon, is successfully detected by the POD algorithm. For this damage event, the algorithm shows to be reliable in the detection and also able to distinguish the type of damage. As a matter of fact, in the case of tendon damage, the trend of all eigenvectors, starting from the second one, changes for all sensors, to indicate a global change in the structure; on the contrary, when a local degradation occurs, just the sensors closest to damage should be affected by variations in the corresponding eigenvectors.

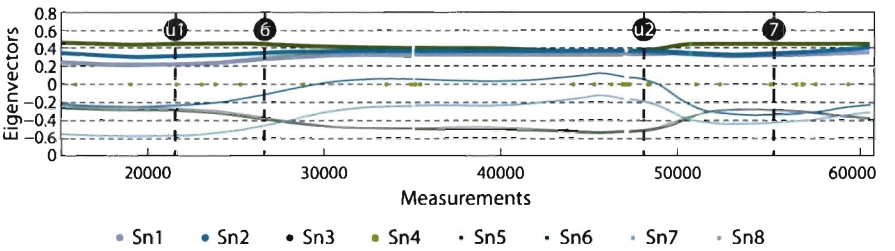
Residual second-order strain after removing thermal strain (sensors Sn3 and Sn7) F.7-17



First eigenvector variation for sensors on beam A after the pre-processing F.7-18



Zoom on the last period of the monitoring with unknown events u1 and u2 F.7-19



Furthermore, some false indications of damage still remain. The comparison with the undamaged beam B shows that the eigenvector deviation around the measurement 21 000 (u1) has been experienced by both beams, while the great shift detected on beam A around the measurement 48 000 (u2) has not concerned beam B too.

7-3-2 Probability of Detection and Probability of False Alarm

The most common concept which characterizes the performance of inspection tools is the Probability of Detection (PoD). Let a_d be the minimal defect size, called the detection threshold, under which it is assumed that no detection is possible. PoD is defined as in E.7-5:

$$\mathrm{PoD}(a) = P(\hat{D} \geq a_d) \qquad \text{E.7-5}$$

where $P()$ represents a probability measure, $\hat{D}$ is the variable that represents the measured defect size (response level of NDT tool, i.e. "signal & noise"). The real defect size (i.e. the real signal without noise) is D.

Nevertheless, the use of the PoD alone is not suitable. Another information which is called probability of false alarm (abbreviated PFA) is to be considered to take into account the role of uncertainties. False alarms correspond to the detection of non-existing damage. It is induced especially by noise with several possible sources: human, nature

of phenomenon to be measured, environmental conditions and so on. In harsh in-situ conditions, false detections increase dramatically and non-existing large damages can be detected. The probability of detection (PoD) and the probability of false alarm (PFA) are both needed to characterize, even partially, the results of a DDA. All algorithms have limitations and, in particular in complex environment and harsh conditions, their capabilities and abilities to perform well are different from those given by numerical simulations and laboratory sets. This leads to lower performances than theoretically expected.

The proposed strategy uses the whole information from the damage identification process to optimize the results. Assuming that the probability density functions of noise and signal amplitude are known, after fitting empirical distribution for instance, PoD and PFA have the following expression:

$$\mathrm{PoD} = \int_{a_d}^{+\infty} f_{\hat{D}}(\hat{d})\partial\hat{d} \qquad \text{E.7-6}$$

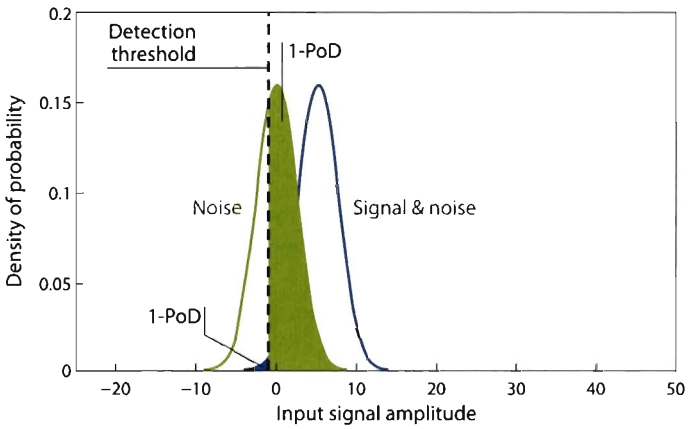
$$\mathrm{PFA} = \int_{a_d}^{+\infty} f_{\Lambda}(\eta)\partial\eta \qquad \text{E.7-7}$$

where η is the noise, $f_{\hat{D}}$ and f_{Λ} are respectively the probability density functions of the "signal & noise" $\hat{D}$ (or measured defect) and the "noise" Λ. In the following noise Λ and signal D are considered as independent random variables.

Thus, PoD is a function of the detection threshold, the measured defect size and the noise while PFA depends on the detection threshold and noise only. Noise is dependent on the decision-chain "physical measurement-decision on defect measurement transfer of information", the conditions of inspection (harsh environment, surface quality, electronic noise, ...) and the complexity of testing procedure (accessibility, mounting of the device, ...).

F.7-20 illustrates the Probability Density Function (PDF) and the area to be computed for the evaluation of PoD and PFA for a given detection threshold in the case where "signal & noise" $\hat{D}$ and "noise" Λ are normally distributed.

Illustration of PoD and PFA (signal & noise and noise normally distributed) for detection threshold a_d F.7-20



7-3-3 Receiver Operating Characteristic (ROC) Curves

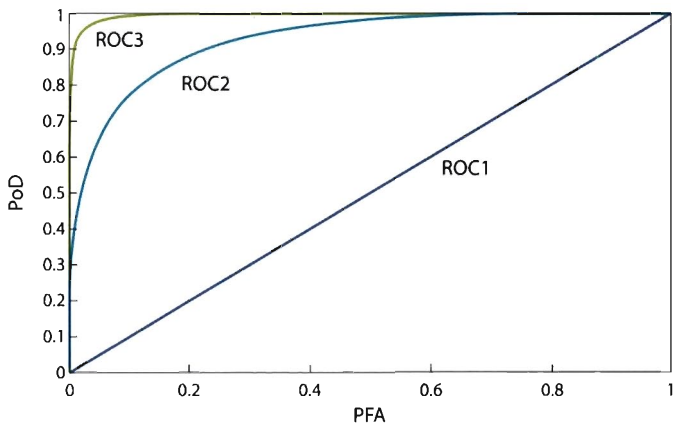
The ROC curve links the Probability of Detection and the Probability of False Alarm. For a given detection threshold, the pair (PFA, PoD) defines NDT performance. This pair can be considered as coordinates of a point in R2 (square integrable space of real numbers) with axes representing PFA and PoD. Let us consider that a_d takes values in the range $]-\infty;+\infty[$; these points belong to a curve called Receiver Operating Characteristic (ROC) which is a parametric curve with parameter a_d and defined by E.7-6 and E.7-7 [Arques, 1982].

The example of an ROC curve (ROC 3) plotted on F.7-21 is computed with the PDF presented in F.7-20 corresponding to normal distributions.

F.7-21 presents three theoretical ROC curves, each one corresponding to a different NDT tool performance. The worst curve is ROC 1 (line of no performance), meaning that noise can be easily detected as a defect even if nothing is to be detected. This finally leads to a high number of false alarms. As a result, overall performances are poor. In contrast, the best plotted ROC curve is ROC 3, which differs considerably from the previous curve. The probability of detection reaches values near one, with small probabilities of false alarms for high values of PoD. Overall performances are very good.

Looking for the best detection performances, the probability of detection should always take larger values than the probability of false alarm (low noise sensitivity), so that PoD ≥ PFA. When reading ROC curves, one must remind that the probability of false alarm depends on the noise and detection threshold only. It does not depend on damage size. The probability of detection is a function of the detection threshold, the damage size, and the noise. Thus, for a given detection threshold, the probability of false alarm is a constant, but the probability of detection is an increasing function of the damage size. The ROC curve is therefore a fundamental characteristic of the NDT tool performance for a given defect size. Perfect tool is represented by an ROC curve reduced to a single point whose coordinates are: (PFA, PoD) = [0, 1]. An ROC curve represents an NDT tool performance facing a given PDF of a defect or a defect range.

Example of ROC curves with several NDT performances F.7-21



These ROC curves can be obtained by considering two techniques and the same defect range, one technique and two defect ranges, one technique with two settings and the same defect range, or one technique applied in various conditions (even if the testing procedure is rigorously followed during inspection). In the following we will consider two settings and the same defect.

A simple geometric characterization of ROC curves is the distance between the curve and the best performance point (BPP) of coordinates (PFA = 0, PoD = 1) [Schoefs and Clément, 2004]. By definition, the bigger the distance, the worse is the performance. The point on the ROC curve corresponding to the lowest distance between BPP and the curve is called the performance point of the NDT tool (NDT-BPP). This distance (Euclidean measure) can thus be considered as a measure of performance. This section defines a curve characterization by using the polar coordinates of the NDT-BPP. The NDT-BPP polar coordinates are defined by:

// the radius α_{NDT} equals the performance index (NDT-PI) (distance between the best performance point and the ROC curve);
// δ_{NDT} is the angle between axis (PFA = 0) and the line (BPP, NDT-BPP).

It has been shown in [Barnouin et al., 1993] that a_{NDT} is essential to provide complete risk analysis, including consequence assessment after inspection. However, such a study is beyond the scope of this particular study so this parameter will not be analyzed here. Assessment of PoD and PFA from the knowledge of detection threshold can be directly deduced from inter-calibration of NDT tools from statistical analysis of inspection results [Rudlin, 1996]. Generally these projects are expensive, and consequently, it is sometimes necessary to choose another approach. Calculation of PFA and PoD thereby results from probabilistic modelling of the "noise" and "signal & noise" PDF [Schoefs et al., 2010].

More generally in this framework, variables $\hat{D}$ and a_d in E.7-5 can represent the observed current value and the threshold value of one or more features extracted from the measurements by the particular damage identification algorithm. In this case, the threshold value a_d should be defined observing the variation of the feature/s for a reference period during which the structure is supposed to be undamaged.

Here the objective is to find the best parameters for the algorithm that lead to a good assessment of defect. ROC curves are built from statistics and then the best set of parameters that lead to the detection threshold that minimizes δ_{NDT} are deduced. Thus the PoD and PFA are computed from E.7-8 and E.7-9:

$$\text{PoD} \approx \frac{Card(A)}{n_m} \quad \text{with} \quad A = \{i \in \Im; \hat{f}_{p,i} > a_d\} \tag{E.7-8}$$

$$\text{PFA} \approx \frac{Card(B)}{n_m} \quad \text{with} \quad B = \{i \in \Im; \eta_i > a_d\} \tag{E.7-9}$$

where Card(.) indicates the cardinal of a particular set and where $\Im = \{1, \ldots, n_m\}$. n_m denotes the number of measurements.

As the definition of the threshold value in the case of damage detection algorithm is not easy to achieve, a parametric study using a vector **c** of threshold values is suggested. The threshold can be for example defined using an adequate confidence interval assessed from the observations of the reference period. The best threshold value that minimizes δ_{NDT} has to be set for each tested DDA.When assessing the ROC curve using experimental data, discrete values for PFA and PoD are obtained for given conditions. Several numbers can be defined as a function of the vector **c** of the fixed threshold values:

$n_b(c)$: number of existing damages that are detected by the algorithm;
$n_f(c)$: number of non-existing damages that are detected by the algorithm;
$n_n(c)$: number of existing damages that are not detected by the algorithm;
$n_r(c)$: number of non-existing damages that are not detected by the algorithm.

As the number of the detected damages can exceed the number of existing damages, the corresponding ratio is not a probability. For this reason, two sets of probabilities are defined:

$$P_b(c) = \{p_b(c), p_r(c)\} \quad \text{where} \quad \begin{cases} p_b(c) = \dfrac{n_b(c)}{n_b(c) + n_n(c)} \\ p_r(c) = \dfrac{n_r(c)}{n_f(c) + n_r(c)} \end{cases} \qquad \text{E.7-10}$$

$$P_f(c) = \{p_f(c), p_n(c)\} \quad \text{where} \quad \begin{cases} p_f(c) = \dfrac{n_f(c)}{n_f(c) + n_r(c)} \\ p_n(c) = \dfrac{n_n(c)}{n_b(c) + n_n(c)} \end{cases} \qquad \text{E.7-11}$$

The first probability concerns the probability of good assessment (PGA) and is somehow related to PoD, while the second one deals with the probability of wrong assessment (PWA) and has to be considered as an indicator of the PFA.

With the same logic, a Bayesian approach from decision theory can be used [Rouhan and Schoefs, 2003]. After data analysis, the detection result could be: no damage, or presence of damage. Anyway, as for in-service structures the state of the structure is not known, it is necessary to consider four events:

E1: no presence of damage, conditional to no damage detection;
E2: no presence of damage, conditional to damage detection;
E3: presence of damage, conditional to no damage detection; and
E4: presence of damage, conditional to damage detection.

Considering the binary random variable "presence of damage" X, whose value is 1 if damage is present, 0 otherwise, it is possible to note as $d(X)$ the random damage decision function, whose value is 1 if damage is detected, 0 otherwise. Then four events are defined:

$E1 = [d(X) = 0 \mid X = 0]$; $\quad E3 = [d(X) = 1 \mid X = 0]$;
$E2 = [d(X) = 0 \mid X = 1]$; $\quad E4 = [d(X) = 1 \mid X = 1]$.

By definition, these events are not independent and some of them are complementary. Thus, the probability of false alarm PFA and the probability of detection PoD could be written, according to Bayes' rule:

$$\mathrm{PoD}(X) = P(\mathrm{E4}) = P(d(X) = 1 \mid X = 1) \qquad \text{E.7-12}$$

$$\mathrm{PFA}(X) = P(\mathrm{E3}) = P(d(X) = 1 \mid X = 0) \qquad \text{E.7-13}$$

This gives the right definitions of the PoD and the PFA:

// the PoD is the probability to decide damage presence (damage detection), conditional to an actual existing damage;
// the PFA is the probability to decide damage presence (damage detection), conditional to no actual existing damage.

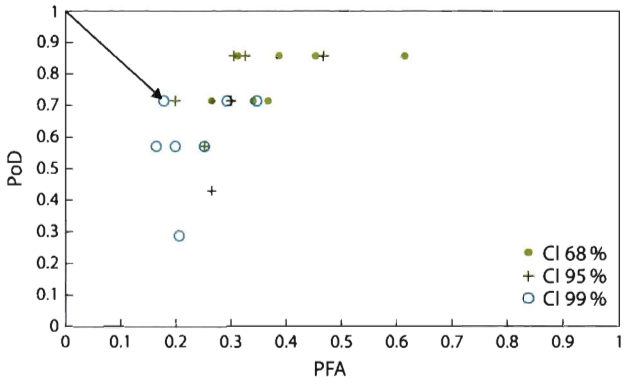
The eigenvectors extracted by the Proper Orthogonal Decomposition in the previous subparagraphs are used as damage features in the analysis of PoD and PFA. For each structural static mode, the time variation of the relative eigenvector at each sensor location is available. In this way, the method allows to follow the time variations of the eight extracted eigenvectors, but gives also a spatial information following each eigenvector at each sensor location. As a consequence, 64 time trajectories are available to assess the ROC point.

The extracted eigenvectors need a certain period of time to get a stationary behaviour to be assumed as reference state. As damages have been introduced too early during the monitoring, they are mixed to the non-stationary initial trend of the eigenvectors; for this reason, three months at the end of the monitoring have been assumed as the reference undamaged period to define the damage detectable threshold. Three thresholds have been defined using the standard deviation of measurements of the reference state: the first one corresponds to a confidence interval of 67% (mean ±standard deviation), the second one to 95% (mean ±2*standard deviation) and the third one to 99% (mean ±3*standard deviation).

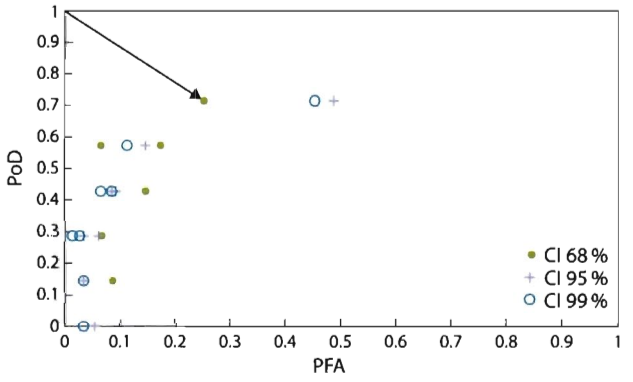
The computation is initially performed on rough data. The extracted eigenvectors contain the structural response and also all the environmental information. A vector of damage threshold is defined for each structural mode at each sensor location. A time window of 5 and 15 days respectively is used to discretize the monitoring period in N intervals, each one containing or not the artificial damage. The PGA and the PWA are evaluated as described giving a maximum value for the PGA of 0.82 and a minimum value for the PWA of 0.18 for the first mode. No significant differences are noticed in results obtained with the two time windows. The ROC points are then obtained for each eigenvector and plotted for the three investigated thresholds. Considering the distance α_{NDT} between the experimental points and the best performance point with coordinates (0, 1), it is possible to have an evaluation of the optimal efficiency of the DDA under specific conditions. F.7-22 shows that the higher damage threshold leads to a shorter distance α_{NDT}. Similar results are obtained for the other modes (F.7-23).

The same procedure is performed on pre-processed filtered data to remove the effect of temperature variations, as presented before. In this case, the PGA and the PWA give

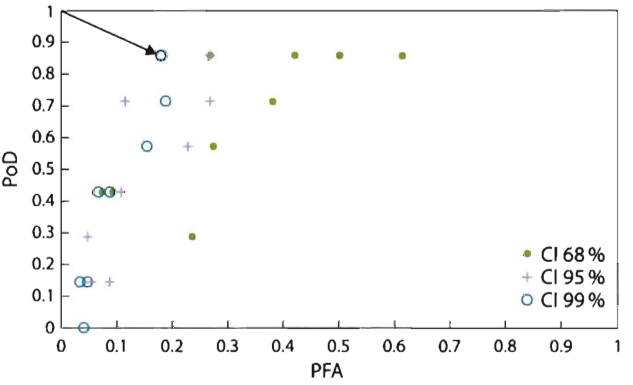
ROC points from experimental data. Mode 1 at each sensor location (from 1 to 8) corresponding to different damage thresholds F.7-22



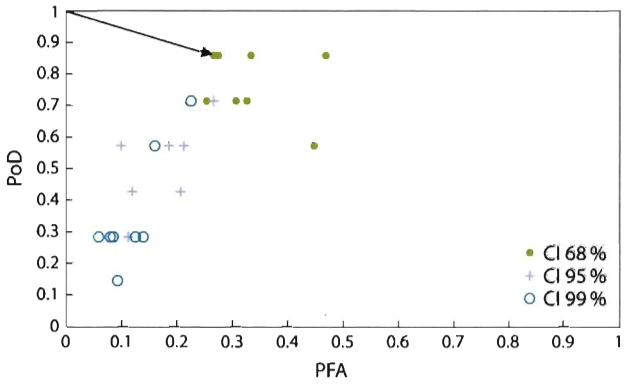
ROC points from experimental data. Mode 5 at each sensor location (from 1 to 8) corresponding to different damage thresholds F.7-23



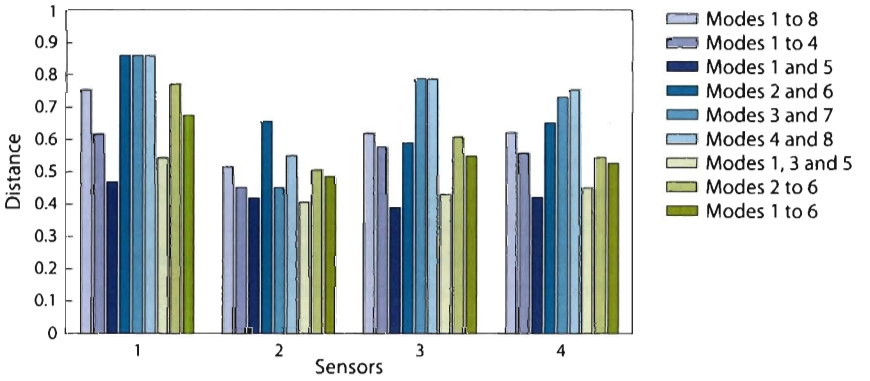
ROC points from experimental data after pre-processing. Mode 2 at each sensor location (from 1 to 8) corresponding to different damage thresholds F.7-24



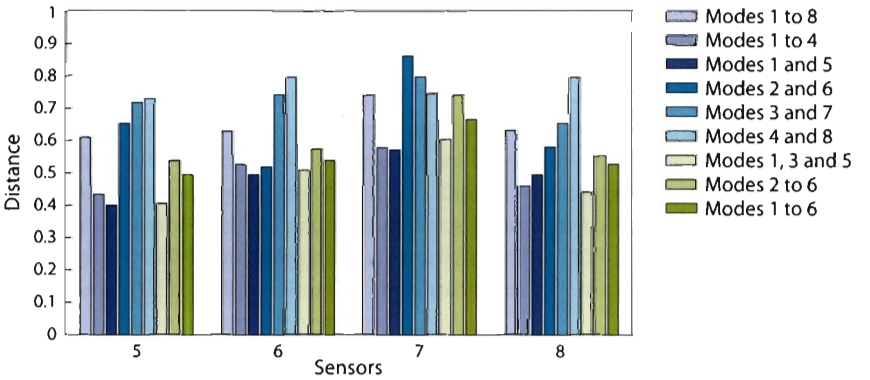
ROC points from experimental data after pre-processing. Mode 3 at each sensor location (from 1 to 8) corresponding to different damage thresholds F.7-25



Distance αNDT for different combinations of eigenvectors (modes) at each sensor location (from 1 to 4) F.7-26



Distance αNDT for different combinations of eigenvectors (modes) at each sensor location (from 5 to 8) F.7-27



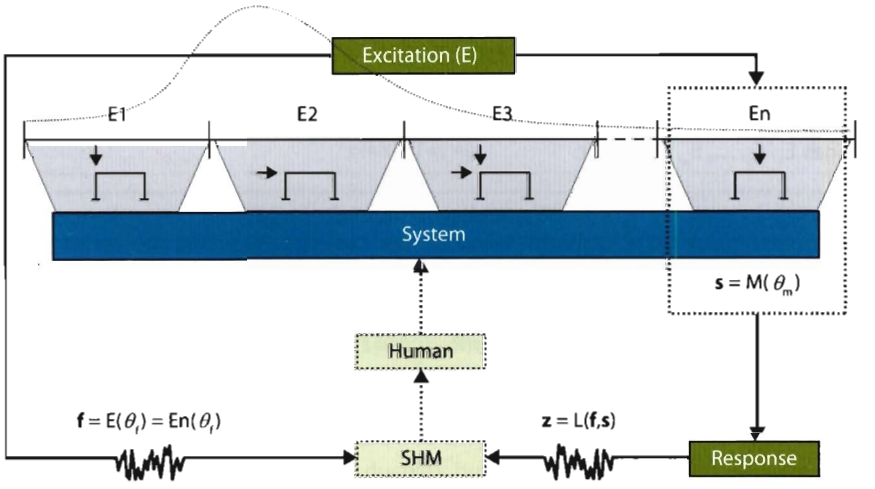
a maximum value for the PGA of 0.92 (corresponding to +12%) and a minimum value for the PWA of 0.08 (corresponding to –55%). A better performance of the DDA on pre-processed data is evident. The ROC points are finally obtained for each eigenvector and plotted for the three investigated thresholds. F.7-24 shows again that the higher damage threshold leads to a shorter distance α_{NDT} and that a better efficiency of the DDA is obtained. Similar results are obtained for the other modes (F.7-25).

As confirmed from the previous data interpretation, the performance of the Proper Orthogonal Decomposition improves after the data pre-processing to remove the noise due to temperature effect. A further improvement can be obtained computing the PGA and the PWA using a combination of different eigenvectors. Plots in F.7-26 and F.7-27 show the results using tentative combinations. It can be observed that the best results are obtained combining the first odd modes, 1 and 5 or 1, 3 and 5. It has still to be verified if these modes are the ones with the higher correlation coefficients and if also these results are associated to the higher damage threshold.

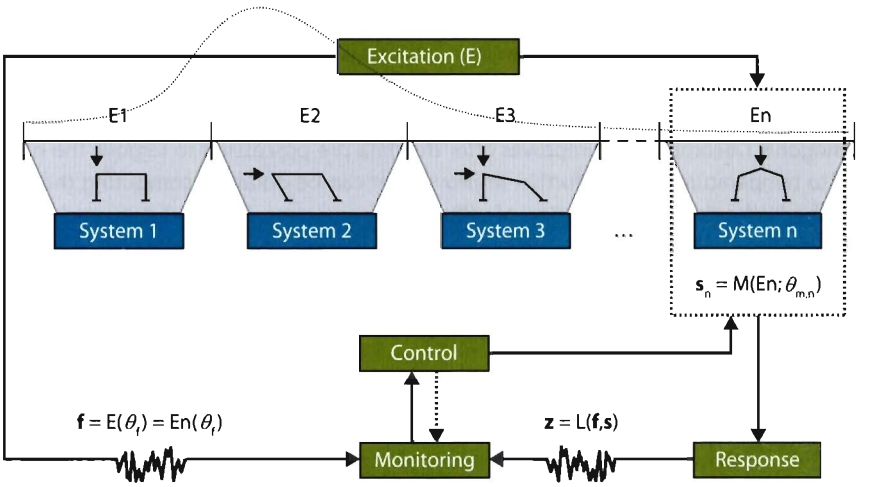
7-4 Reliability of Adaptive Structures and Adaptive Skins

Within the field of structural engineering, depending on the context and the focus, the meaning of adaptivity may therefore become inherent to the morphological change of the structure. Some clarification is however required to correctly contextualize this concept in the field of structural reliability. At first, the concept of structural adaptivity is indeed much closed to the concept of active structural control since, in both cases some

Block diagram of system without control. Dashed arrows and boxes are to be considered optional components of the flow chart F.7-28



Block diagram of system with control. Dashed arrows and boxes are to be considered optional components of the flow chart F.7-29



actuation force is expected in response to an occurring excitation in order to improve the behaviour of the structure. The term adaptivity implies here that the improvement of the structural behaviour comes specifically from a change in the morphology (shape) or in the system configuration (i. e. the actuation force is responsible for this change).

It is possible to qualitatively estimate the benefit in terms of safety coming from structural adaptivity by making a comparison between F.7-28 and F.7-29 and recalling the IRIS paradigm symbolism. F.7-28 represents the case of a system without any kind of control device on it while F.7-29 shows the case of an adaptive structure.

Assuming a basic limit state function:

$$g(R,L) = R(s) - L(f,s) = R - L \qquad \text{E.7-14}$$

where R represents the system carrying capacity and L represents the load effect on the system, if we refer to F.7-29 we can divide the excitation range into n incompatible subranges $E_1, E_2, \ldots, E_n$, such that:

$$g_i(R,L) = R(s) - L(f_i,s) = R - L_i \forall i \in [1,n] \text{in} N \qquad \text{E.7-15}$$

Then the failure probability of the system can be expressed as:

$$p_{fail,1} = \sum_{i=1}^{n} p(R - L_i \leq 0 \,|\, E_i) p(E_i) \qquad \text{E.7-16}$$

Analogously, in the case of an adaptive structure (F.7-29) the limit state functions would read:

$$g_i(R,L) = R(s_i) - L(f_i, s_i) = R_i - L_i \forall i \in [1,n] \text{in} N \qquad \text{E.7-17}$$

leading, in turn, to the following probability of failure:

$$p_{fail,2} = \sum_{i=1}^{n} p(R_i - L_i \le 0 \mid E_i) p(E_i) + \sum_{i=1}^{n} p(\bar{R}_i - L_i \le 0 \mid E_i \cap \text{MCD}) p(\text{MCD} \mid E_i) p(E_i) \qquad \text{E.7-18}$$

where MCD represents the event of malfunction of the control devices. Assuming that MCD and E are statistically independent events then E.7-18 can be rewritten as:

$$p_{fail,2} = \sum_{i=1}^{n} p(R_i - L_i \le 0 \mid E_i) p(E_i) + \sum_{i=1}^{n} p(\bar{R}_i - L_i \le 0 \mid E_i \cap \text{MCD}) p(\text{MCD}) p(E_i) \qquad \text{E.7-19}$$

When comparing E.7-16 and E.7-19 we should assume that, for the specific sub-range of events E_i, the corresponding optimal configuration of the adaptive structure performs equally or better than a static system which is designed to support the whole range of events E. In other words:

$$\sum_{i=1}^{n} p(R_i - L_i \le 0 \mid E_i) \le \sum_{i=1}^{n} p(R - L_i \le 0 \mid E_i \qquad \text{E.7.20}$$

We shall call adaptivity gain (Ag) the difference:

$$Ag = \sum_{i=1}^{n} p(R - L_i \le 0 \mid E_i) - \sum_{i=1}^{n} p(R_i - L_i \le 0 \mid E_i \qquad \text{E.7.21}$$

According to E.7-20 it is then obvious that:

$$p_{fail,2} < p_{fail,1} \Leftrightarrow Ag > p(\text{MCD}) \cdot \sum_{i=1}^{n} p(\bar{R}_1 - L_i \le 0 \mid E_i \cap \text{MCD}) p(E_i) \qquad \text{E.7.22}$$

and it is reasonably expected that:

$$Ag < \sum_{i=1}^{n} p(R - L_i \le 0 \mid E_i) - \sum_{i=1}^{n} p(R_i - L_i \le 0 \mid E_i \qquad \text{E.7.23}$$

From E.7-22 and E.7-23 the important conclusion to remark is that the reliability of the whole system is heavily determined by the control system. Consequently an important design objective to make the adaptive structure convenient should be:

$$p(\text{MCD}) \ll Ag \qquad \text{E.7.24}$$

The malfunction of the control system may happen when the actuators fail but also when the sensors are unable to detect the excitation/response of the system or because of a wrong interpretation of it. This means that the reliability level of the monitoring system is also involved in determining p(MCD).

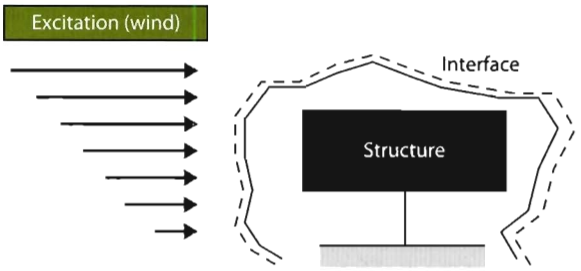
From the considerations above it seems reasonable that the main concepts of robustness have reason to migrate from the design of the structure to the design of the control system, redundancy being the most important among them. Of course, this does not mean that the design process is allowed to ignore the structure capacity in terms of energy absorption, redundancy and ductility but it becomes of primary importance to

ensure the reliability of a control system which is in charge to manage the structural form since it plays the major role in contributing to robustness [Agarwal et al., 2012]. To this aim it would be feasible, for instance, to take advantage of the installed monitoring system to check also the state of the control devices, as suggested in F.7-29 (dashed arrow). The design should also provide, if possible, a safe configuration, i. e. an intermediate state among the possible configurations, in case of malfunction of the control devices.

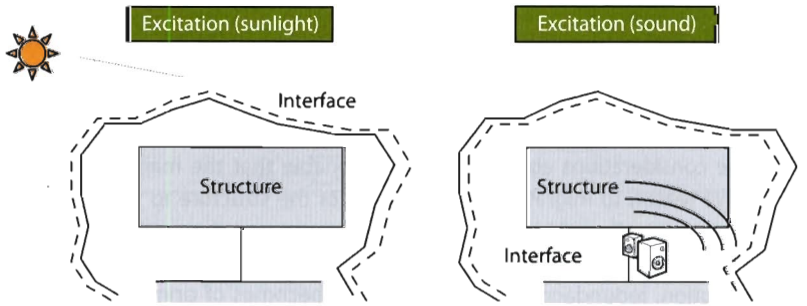
Besides the reliability of the control system, specific issues when dealing with adaptivity in the field of civil structures are the scale factor and the time. Contrary to what happens in mechanical engineering, automotive engineering or space engineering where structures are often much lighter and considered to be in motion, it is unlikely that a civil structure is able to change its configuration in a very short time.

Because of these reasons, the adaptive behaviour can neither belong to nor can come from all the elements of the structure at the same time. Specifically referring to buildings, the existing proposals involving structural adaptivity are in fact usually focussing on the internal and/or external envelope – i. e. the "building skin". Shells and grid-shells, where the distinction between walls and roof becomes weaker or even disappears, are probably the kind of structures which could be more easily tailored to fit the concept of adaptive skins and with the greater potential. Other immediate applications may relate to roof structures and façades. Restricting adaptivity to the building skin means that mechanisms

The "building skin" as the interface to the external excitation by wind F.7-30



The "building skin" as the interface to non-structural external and internal design drivers F.7-31



are developed exclusively at the boundary, thus reducing kinetic inconsistencies with the internal space and possibly allowing a main static structure to be the core of the building. This, in turn, implies that adaptivity tends to come from mechanisms distributed all over the envelope in order to provide a better change of shape. A consequent distribution of sensors and actuators is also expected, which may contribute to easily satisfy the previously mentioned redundancy requirements.

The envelope plays then an interface role towards most of the environmental actions, both externally (e.g. wind see F.7-30) and internally (e.g. people walking).

Moreover, this interface role is exploited with respect to "shape-dependent" actions other than loads, which makes adaptive skins suitable for a wide range of purposes. F.7-31 gives an example of two possible fields of application.

This aspect makes possible to take advantage of the same adaptive system to improve different performances of the building and it perhaps represents the most relevant feature when comparing structural adaptivity with more traditional control approaches.

In the present section a Finite State Control Strategy (FSCS) is proposed for the design and control of MDOFs adaptive envelopes. The main advantage of the FSCS is that a set of optimal configurations (finite states) are investigated during the design phase to partially or totally avoid the computational cost of the real-time control. It is worth noting, however, that the finite states, being a limited number of achievable configurations, influence the possibility of mutation of the structure in service. Particularly, the configurations will always or almost always be suboptimal since the structure remains in a given state for a whole range of possible excitations, but these limitations are expected to be negligible in the context of civil structures, especially when compared to the advantages in terms of easiness of design integration, energy gain to energy consumption ratio and real-time control simplification.

The strategy can handle any kind of variable geometry structure (VGS) which can be associated to the framework representation defined in the following. The framework representation is central to the strategy development, mainly because the matrix analysis of frameworks is used to control the kinematic properties of the envelope. The scheme of the proposed design and control procedure is then described, with emphasis on the key steps of the constrained optimization process. The key steps are namely the optimization of the envelope configuration (finite state selection), the post-optimization of the framework topology and the management of the actuators location.

7-4-1 Frameworks

The Framework Representation

A framework (F.7-32), from the structural engineering point of view, can be defined as a discrete set of one-dimensional elements in the three-dimensional space, connected at their ends to points called nodes. Frameworks are therefore general enough to represent a huge variety of structural systems as, for instance, trusses, cable-nets, tensegrity, membranes, reciprocal frames, etc.

The basic properties of a framework can be derived from graph theory. In this context a framework is equivalent to a weighted graph $\mathcal{G}=(\mathcal{N},\mathcal{A})$ – usually simple, i.e. a graph

with no loops and no more than one edge between any two different nodes – where the nodal coordinates are weights associated to each node. In other words:

$$\mathcal{G}=(\mathcal{N},\mathcal{A})\xrightarrow{w_{i,j}=f(l_{i,j})}\mathcal{F}(framework) \qquad \text{E.7-25}$$

where N represents the nodes (vertices) of the framework, A represents the edges (arcs) of the framework and w_{ij} and l_{ij} represent the weight and the length of the edge $(i,j)\in\mathcal{A}$ respectively.

Definition 1. A framework $F=(N,A)$ is a weighted graph where: each node $i\in\mathcal{N}$ has associated with it a weight $w_i=f(x_i,y_i,z_i)$ and each edge $(i,j)\in\mathcal{A}$ has associated with it a weight $w_{ij}=f(l_{ij})$.

Therefore a graph and a framework share two fundamental characteristics: the topology and the attributes. Theoretically, everything in a framework could be described as a function of only these two elements and this has some advantages as explained by [Basso and Del Grosso, 2011]. Among the advantages, the generality and clarity of this representation are the main reasons of its use herein.

Framework Kinematics

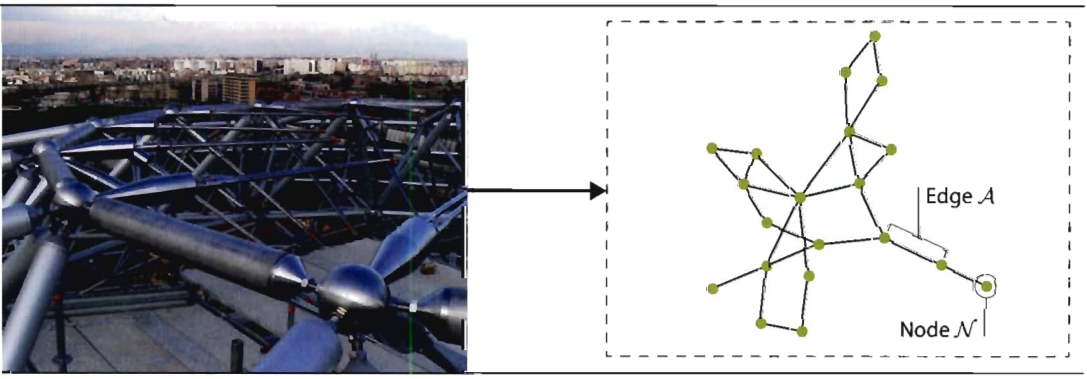
Referring to the framework definition given in the previous sub-section, here matrix analysis is introduced as a way to identify those mechanisms which are to be considered in the design of a VGS. The considerations made hereafter are then preliminary to the proposed strategy and are meant to state some required kinematic properties of the framework associated to the designed adaptive envelope.

The concept of kinematical indeterminacy is central to an understanding of the mechanisms of a framework. This information can be obtained by analysing the four fundamental subspaces of the equilibrium matrix **E** of the framework. Particularly a framework is considered to be kinematically indeterminate if:

$$m=rank(E)-3n>0 \qquad \text{E.7-26}$$

where n is the number of nodes of the framework and m (≥ 0) is the number of independent inextensional mechanisms; m is also equal to the number of vectors which span the

Framework representation F.7-32



nullspace of **E**. Besides, the analysis of each vector composing the basis of the nullspace of **E** gives further insight into the mechanism behaviour as explained by [Pellegrino and Calladine, 1986].

Once a framework is known to be kinematically indeterminate it is then important to distinguish infinitesimal mechanisms from finite mechanisms. According to Koiter's definition [Koiter, 1984] "an infinitesimal mechanism of the first order is characterized by its property that any infinitesimal displacement of the mechanism is accompanied by second-order elongations of at least some of the bars. An infinitesimal mechanism is called of second (or higher) order, if there exists an infinitesimal motion such that no bar undergoes an elongation of lower than the third (or higher) order".

A more precise definition of the order of mechanisms can take advantage of the formulation submitted by [Tarnai, 1984], formulation extended to multi-parametered case by [Vassart et al., 2000]. An internal mechanism is called mechanism of order "r" ($r \geq 1$) if there exists infinitesimal node displacement d (of the first order) such as member length variations are equal to zero until order r, but there does not exist infinitesimal node displacement d such as member length variations are equal to zero at order $r+1$.

$$\text{Mechanism of order } r \Leftrightarrow \begin{cases} \exists d = O_1 (\text{i.e. } d \neq 0) : e^{(1)} = 0, e^{(2)} = 0, \ldots, e^{(r)} = 0 \\ \forall d = O_1 : e^{(r+1)} \neq 0 \end{cases} \qquad \text{E.7-27}$$

where d is a vector of node displacements related to reference configuration and e is a vector of member length variations evaluated in respect of the reference configuration.

Finally, a mechanism is called finite mechanism if there exists a displacement which does not generate length variations of any order.

Many authors have worked on mechanism order determination for kinematically indeterminate systems. Among the more recent approaches it is worth mentioning the one of [Vassart et al., 2000] who describe an analytic method for which only geometrical properties of kinematically indeterminate systems are taken into account. With this method, the order of infinitesimal mechanisms can be evaluated without limitation for order's level. A stop criterion is also given so as to detect possible finite mechanisms of a kinematically indeterminate system.

However, dealing with the mechanism order to determine if a mechanism is finite or not, it is not proved to be a safe method. The following alternative approaches are instead more effective:

// Symmetry identification;
// Simulation;
// Self-stress states avoidance ($s = 0$).

The analysis of framework symmetries has been successfully used by several authors [Tachi, 2010a; Tarnai, 1980] in order to recognize finite mechanisms. The drawback of this method is the limited range of possible applications.

The simulation of motion proves that a mechanism is finite if at every step, provided that the step is small enough, the number of inextensional mechanisms m remains constant. In other words, the finite motion is ensured by keeping the degrees of freedom

(DOFs) of the mechanism positive throughout the transformation. The method has been discussed by [Tachi, 2009] and successfully used to deal with origami foldability. However sometimes it may be preferable to avoid the simulation process which may be computationally expensive.

The third approach takes advantage of the fact that a framework with no self-stress states ($s = 0$) and $m > 0$ has exactly m finite inextensional mechanisms. The extended Maxwell's formulation defines the relationship between the number of framework elements and the number of framework mechanisms and self-stress states as:

$$s - m = b - 3n + k \qquad \text{E.7-28}$$

where b is the number of edges of the framework, n is the number of nodes, k is the number of external constraints, s (≥ 0) is the number of independent states of self-stress and m (≥ 0) is the number of independent unextensional mechanisms. If the structure is unconstrained and in the three-dimensional space E.7-28 becomes:

$$m = m_i + 6 = 3n - b + s \qquad \text{E.7-29}$$

where m_i is the number of internal independent inextensional mechanisms. The m_i mechanisms are finite if:

$$s = b - \text{rank}(\mathbf{E}) = 0 \qquad \text{E.7-30}$$

where $\mathbf{E}$ is the equilibrium matrix of the framework. This method is the best when E.7-30 is satisfied, otherwise further investigation of the nullspace of $\mathbf{E}$ is required to determine which mechanisms are stiffened by the self-stress states – e.g. by means of a simulation.

To ensure that E.7-30 is satisfied by the frameworks generated within the optimization process is one of the requirements of the proposed strategy as explained in the next sub-section.

7-4-2 Finite State Control Strategy

The Finite State Control Strategy (FSCS) is a general procedure for the design of adaptive structural envelopes, i.e. VGSs, which can be associated to a "single-layer" framework. The procedure is basically a combination of two main parts: a meta-heuristic optimization process, which aims at discovering new optimal configurations – i.e. finite states – according to some defined purpose, and a gradient-based optimization process which acts as a constraint for the kinematic compatibility maintenance. In principle any meta-heuristic technique and gradient-based algorithm could be coupled according to the defined scheme. However, the specific choice here is to use an evolutionary algorithm to lead the search for optimal solutions and the Virtual Force Density Method (VFDM) [Basso et al., 2009] to ensure the compatibility of the resulting configurations.

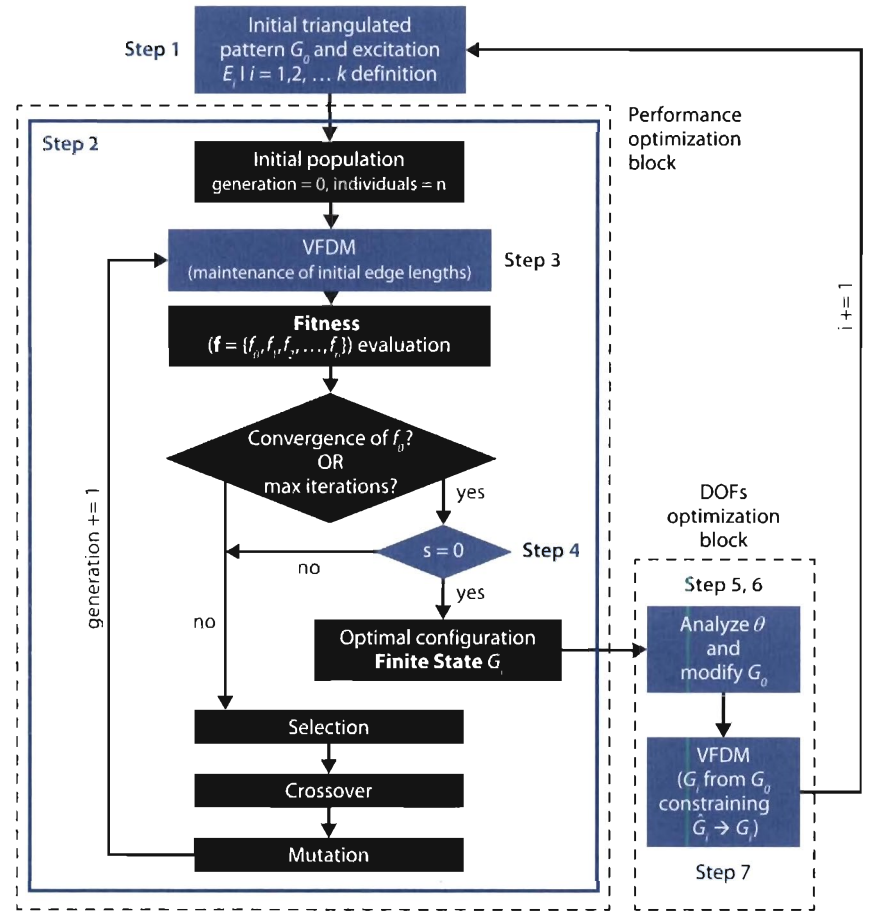
A topology optimization process, which aims at decreasing the number of DOFs of the structure while retaining its ability to achieve the optimal configurations, is proposed as an integration of the finite state selection.

F.7-33 shows the flow-chart of the FSCS. The initial framework to be optimized (G_0) must have a triangular pattern and the choice of this initial pattern parameters is determinant to achieve a good result. Specifically the result highly depends on the density of the defined pattern – i.e. how many nodes and edges are needed. A coarser pattern has fewer possible configurations compared to a denser one but more DOFs to manage. Moreover the framework should represent a real envelope made with real panels which always come with a limited range of possible measures.

The topology of the initial framework – i.e. how the edges are connected – is another important factor because it constrains the "folding" process. It is for instance important to start with a symmetric pattern if the envelope is expected to fold symmetrically.

Topology and density of the initial framework pattern may be part of the whole optimization process but, on the other hand, these two elements are also fundamental to the definition of the envelope appearance. Consequently, thinking at a building façade, roof or internal ceiling, these turn to be architectonical parameters most of the time. Topology

Flowchart of the FSCS F.7-33



and density of the initial framework pattern are therefore left outside the optimization process here since they are directly considered a designer choice.

The performance optimization block, which involves steps 2 to 4, is basically an evolutionary algorithm where complex constraints for the compatibility maintenance among the solutions are managed by the VFDM. Solutions are equivalent to optimal configurations geometrically compatible one with the other. These optimal configurations are called finite states (G) here. The number of finite states to be found is a function of the framework morphology (i. e. initial pattern density and topology), of the considered excitation range (E) and of the target performance.

The topology optimization block, which involves steps 5 to 7, is described here with the assumption that the framework nodes are equivalent to pin-joints. This assumption does not affect too much the range of real structures that can be handled by the algorithm but greatly simplify the computations and helps the clarity of the explanation.

The two blocks, together with a step-by-step description of the whole algorithm, are further explained hereafter.

The optimal state selection is led by an evolutionary technique. Specifically a Memetic Algorithm (MA) [Elbeltagi, 2005] is used to illustrate the FSCS here. However, as already mentioned, any other meta-heuristic method could be adapted to the proposed approach.

The fundamental aspect to underline here concerns instead the kinematic compatibility maintenance which is coupled to the optimal state selection. Two precautions are taken to this aim:

// The VFDM applies in order to maintain the system geometry constraints;
// An initial planar configuration is chosen as a reference.

The compatibility maintenance among different configurations can be translated in a geometrical optimization problem with a very low tolerance. This means that it cannot be tackled effectively by the evolutionary process only [Basso et al., 2009]. The VFDM is therefore integrated inside the MA loop to accomplish this task. Depending on the problem at hand, it is still within the setting of the VFDM that the type of structure is taken into account while the exploration of the design space by the MA remains unaffected.

The second precaution is not always necessary but it is needed to avoid possible snap-through behaviour between two configurations when the envelope is allowed to vary bi-directionally. Alternatives to the assumed precaution could be to verify the existence of the path "a posteriori", e. g. by interpolating between the configurations as explained by [Tang et al., 2010], or to define a crease pattern "a priori".

It is worth noting that, since the kinematic simulation is not involved, this way of looking for the optimal states potentially allows changing both topology and geometry on the fly with a very robust behaviour. Two examples of optimal state selection given two different VGSs are reported by [Del Grosso and Basso, 2010].

Assuming the framework represents a pin-joint envelope, the topology of the framework can then be managed according to the following considerations in order to achieve a convenient number of DOFs. The topology of a framework can be represented by its adjacency matrix while the kinematics can be analysed by investigating the four fundamental subspaces of the equilibrium matrix of the framework. In particular the left-nullspace

of the equilibrium matrix is the one which defines all the inextensional mechanisms of the framework. Referring to E.7-28 (extended Maxwell's rule), the number of internal independent inextensional mechanisms m for an unconstrained framework in the three-dimensional space can be derived as follows:

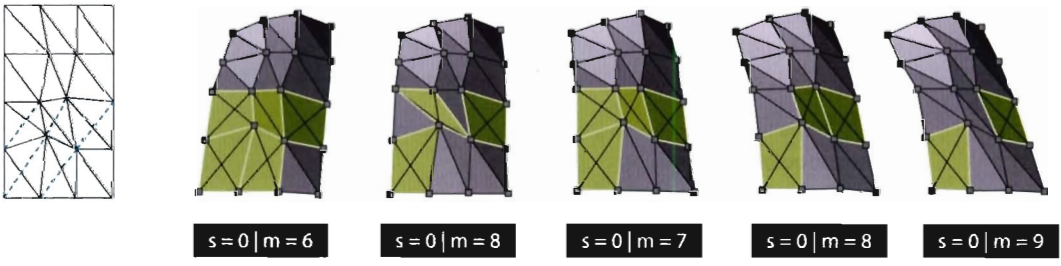
$$m = 3n - b + s - 6 \qquad \text{E.7-31}$$

where b is the number of frames, n is the number of nodes and s is the number of self-stress states of the framework. It has been shown by [Tachi, 2010b] that ensuring a positive number for m during the transformation from one configuration to another is an effective way to prove the foldability of a pattern. However, it is possible that m is a combination of both infinitesimal and finite mechanisms. This, in turn, means that the hypothetical number of actuators needed to transform the structure to all its possible configurations would be less than m. A way to ensure that all the m mechanisms are finite is to keep $s = 0$ which is practically the most common case for a randomly generated triangular pattern associated to an envelope in the three-dimensional space. In other words $s = 0$ if the triangular pattern is neither planar nor presents other singularities. Therefore two configurations of an MDOFs framework which share a triangular pattern with these characteristics (i.e. $s = 0$) can be transformed into each other by means of (maximum) m actuators. The compatibility of the two configurations – i.e. the fact that they share exactly the same triangular pattern – can be ensured by constraining the lengths of the frames to remain constant during the transformation.

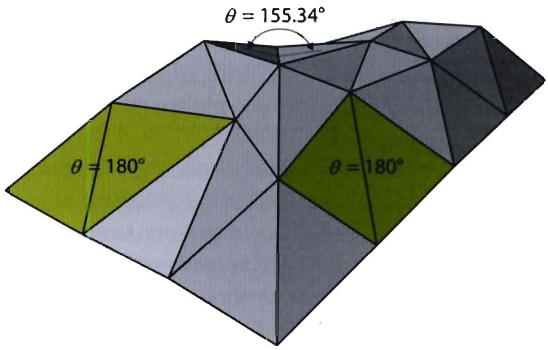
The number of finite mechanisms m can then be managed by affecting the topology of the pattern. An increment of m can be trivially achieved by a further discretization of the pattern while decreasing m it is possible by replacing two triangles with a quadrilateral face. Precisely, assuming a non-singular triangular pattern, it is known that the replacement of two adjacent triangles by a quadrilateral panel results in the loss of a DOF such that

$$\forall \text{ quadrilateral which is converted into two triangles} \Rightarrow m \rightarrow m - 1 \qquad \text{E.7-32}$$

Frameworks with different combinations of triangular and quadrilateral panels. Under each configuration both the number of self-stress states and internal (finite) mechanisms is reported F.7-34



Dihedral angles F.7-35



Such a substitution would affect globally the nodal positions of the pattern if performed on a three-dimensional configuration but is easy to be made when the pattern configuration is planar. Looking at a planar representation of the framework, a quadrilateral panel can be simply defined by adding a frame connecting the two disconnected nodes of two adjacent triangles. Every transformation of the pattern, made by constraining the lengths of the frames to remain constant, would then maintain the quadrilateral panel. F.7-34 shows several variations of a generic triangular pattern by addition of quadrilateral panels (green coloured) according to this criterion.

A proposed criterion for making this substitution is based on the analysis of the dihedral angles θ (F.7-35) of the pattern. When θ is close to 2π then the folding of the two associated triangles can be considered as marginal in the whole transformation process. The closer θ to 2π the less the replacement of triangles by quadrilateral panels will affect the resulting configuration. The choice of a limit for the θ values to be considered can be made by iteratively checking how each value affects the performance of the analysed configuration.

Design Procedure

The procedure to design adaptive envelopes which can be associated to single-layer frameworks is defined by the following steps:

1) define a planar triangulated pattern G_0;
2) transform G_0 to find k optimal finite states $G_1, G_2, \ldots, G_k$ according to the set purpose (performed via MA);
3) $\forall\, G_i \mid i = 1,2,\ldots k$, constrain G_i to be compatible with G_0 (performed via VFDM);
4) $\forall\, G_i \mid i = 1,2,\ldots k$, if $s = 0$ and $m > 0$ continue, else modify G_i (return to step 2).

If the framework is pin-jointed then the following steps can be performed to optimize the topology (i.e. reducing the DOFs):

5) $\forall\, G_i \mid i = 1,2,\ldots k$, analyze the dihedral angle $\theta_{i,j}$ between each couple j of adjacent triangles;

6) $\forall j$, if $\max \theta_{i,j} \to 2\pi \mid i = 1,2,\ldots k$, substitute the *j*-th couple of triangles in G_0 with a quadrilateral panel and check that $m > 0$;
7) $\forall \hat{G}_i \mid i = 1,2,\ldots k$, build $\hat{G}_i$ from G_0 constraining $\hat{G}_i$ to be as close as possible to G_i (performed via VFDM) and check that the performance requirements are maintained.

It is worth to be noted that the initial planar (developed) configuration has the scope to avoid possible "snap-through" mechanisms which may otherwise happen passing from one configuration to another.

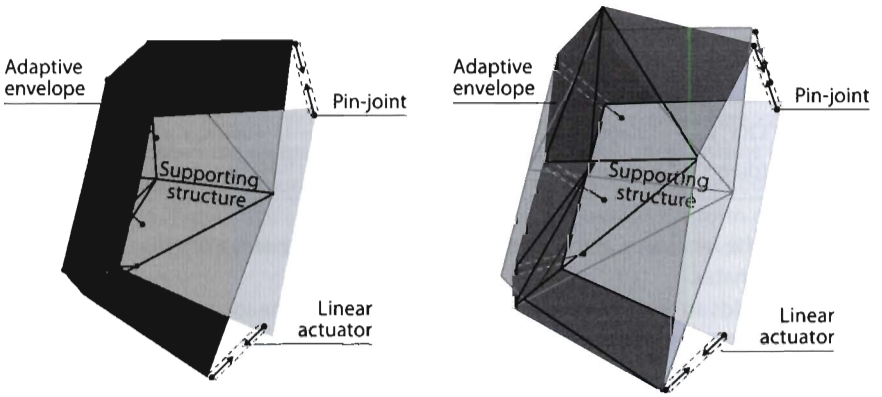
Actuation Process

Once the number of DOFs is determined, so is the number of actuators needed. Here the actuators are assumed to be linear and to be linked both to the adaptive envelope and to a supporting structure (or ground) through pin-joints as shown in F.7-36.

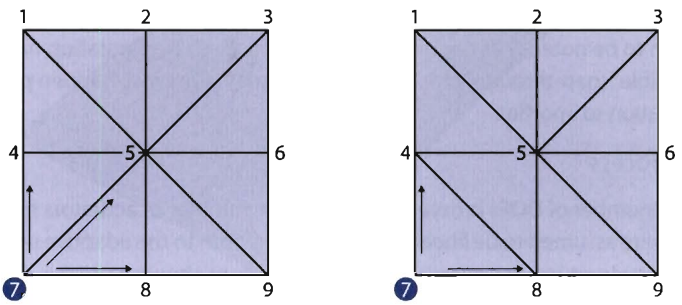
Every actuator belonging to this type and that is correctly placed on a node of the framework constrains a maximum of three mechanisms. A wrong placement may instead generate self-stress states leaving some of the mechanisms untouched. Therefore the location of the actuators cannot be chosen arbitrarily in order to control all the mechanisms.

This concept is better illustrated by comparing F.7-37 (left and right). Note that the two frameworks have the same number of nodes, the same number of edges and also the same edge lengths. Moreover the number of mechanisms ($m = 11$) is exactly the same when assuming the framework unconstrained in the 3D space. But in F.7-37 (right), if no actuators are placed at node 7 and neither node 7 is constrained, it is not possible to manage the face 4-7-8 rotation around the edge 4-8. This does not happen instead in F.7-37 (left) because of the different topology of the pattern. The above example leads to the first important conclusion that no nodes with connectivity ≤2 can be left unconstrained or not actuated.

Left: Scheme of an adaptive envelope linked to the supporting structure and Right: a different configuration of the same envelope when actuated. The envelope is represented by a triangular pattern (9 nodes and 16 edges) which is linked to the supporting structure by linear actuators. Actuators are pin-jointed both to the supporting structure and to the envelope F.7-36



Two frameworks with the same number of nodes and edges but with a different pattern topology. Right: node 7 has connectivity ≤2 and needs to be controlled directly F.7-37



The second important observation is that actuators and constraints should be placed first on nodes which are not directly connected one to the other. For instance, still looking at F.7-37, it turns out that a minimum of four actuators/restraints are needed to control the 11 mechanisms and at least one self-stress state is expected (3 DOFs × 4 actuators – 11 mechanisms = 1). The only group of four nodes which can be selected avoiding nodes inside the same group to be connected to each other is the one composed by nodes 1, 3, 7 and 9. Controlling these four vertices through pin-joint restraints or actuators results in zero mechanisms and only one self-stress state of the framework. Assuming the same kind of restraints/actuators, every other combination of four nodes would end up with more self-stress states.

Inverse kinematics can then be used both to plan and to verify the actuation process. The inverse kinematics of the framework can be controlled by the Moore-Penrose generalized inverse of the Jacobian of the non-linear vector equation representing the geometry constraints (constraint equation). The constraint equation for a pin-joint framework reads:

$$\boldsymbol{\Omega}(\mathbf{x},\mathbf{y},\mathbf{z}) = [\mathbf{l} - \mathbf{l}_0] = \mathbf{0} \qquad \text{E.7-33}$$

where $\mathbf{l}$ is the vector of the edge lengths at the current step and $\mathbf{l}_0$ is the vector of the initial edge lengths. E.7-33 can be written in terms of the Cartesian nodal coordinates:

$$\Omega(x,y,z) = (\mathrm{diag}(Cx)^2 + \mathrm{diag}(Cy)^2 + \mathrm{diag}(Cz)^2)^{1/2} - l_0 = 0 \boldsymbol{\Omega}(\mathbf{x},\mathbf{y},\mathbf{z}) = (\mathrm{diag}(\mathbf{Cx})^2 + \mathrm{diag}(\mathbf{Cy})^2 + \mathrm{diag}(\mathbf{Cz})^2)^{1/2} - \mathbf{l}_0 = \mathbf{0} \qquad \text{E.7-34}$$

where $\mathbf{C}$ is the incidence matrix of the framework and $\mathbf{x}$, $\mathbf{y}$ and $\mathbf{z}$ are the vectors of the nodal coordinates.

E.7-34 yields an underdetermined system, by exploring the solution space of which it is possible to obtain variations in the configuration. Valid shapes are found by perturbing the nodal coordinates according to the nullspace of the Jacobian $\boldsymbol{J} = [\frac{\partial \Omega}{\partial \mathbf{x}} | \frac{\partial \Omega}{\partial \mathbf{y}} | \frac{\partial \Omega}{\partial \mathbf{z}}] J = [\frac{\partial \Omega}{\partial x} | \frac{\partial \Omega}{\partial y} | \frac{\partial \Omega}{\partial z}]$.

The solution is calculated using the pseudoinverse $\boldsymbol{J}^{+}$ of the Jacobian as follows:

$$\mathbf{du} = (\mathbf{I} - \boldsymbol{J}^{+}\boldsymbol{J})\mathbf{du}_0 \qquad \text{E.7-35}$$

where $\mathbf{du}_0$ represents the initial perturbation and $\mathbf{I}$ is the identity matrix.

E.7-35 finds the valid perturbation closest to $\mathbf{du}_0$ by orthogonal projection to the solution space. An integration of this infinitesimal motion has to be executed and, for each step, the residual has to be eliminated (e. g. Newton-Raphson method).

It is worth noting that considerations are limited to geometric ones and elastic or plastic behaviour of the structure with specific materials is not analysed. With reference to E.7-35 the perturbation vector $\Delta\mathbf{u}_0 = [\Delta x_1, \Delta x_2, \ldots, \Delta x_n]^T_{1xn}$ is then built from the zero vector $[0,\ldots,0]^T_{1xn}$ by substituting the zero values corresponding to the "actuated" nodes with the distance between the node at the current position and the node at the target position.

7-5 Conclusions

The contribution resulting from the present work can be summarized as follows.

Structural Health Monitoring has been recognized as a key issue in risk management and facility management to improve efficiency, safety and security of constructed systems. The issue of formally expressing the reliability or the level of confidence that can be attributed to the recognition of a given state of the system has been taken into consideration. A general approach, based on the use of Receiver Operating Characteristics curves has been proposed for giving estimates of a kind of "confidence coefficient" or "weighting function" to be applied at the identified level of damage. This coefficient is a function of the threshold in damage intensity. The assessment of the confidence level of the structural condition identified by means of an SHM system is crucial when the identified condition is used to update the lifetime functions of the structural system and in the development of Decision Support Systems based on lifetime functions and reasoning models.

The concept of adaptive structures has also been interpreted as an evolution of the concept of actively controlled structures. Adaptivity has been considered a property of the structural system able to mitigate the risk of failures (both in service and in ultimate limit states). Based on the concept of discretizing the external conditions producing loadings (or any type of demand) onto the structure into a finite number of states, characterized by given ranges of environmental parameters, a corresponding number of structural configurations satisfying some optimality condition for the reference state can also be identified. By solving the inverse kinematic problem, actuation mechanisms have been identified allowing the structural system to switch from any given configuration to another. The result is a "finite-state control strategy", according to which the form of the structural system can be modified to optimally cope with the requirements of the different environmental states.

References

Agarwal, J., Haberland, M., Holicky, M., Sykora, M., and Thelandersson, S., 2012. *Robustness of Structures: Lessons from Failures*. Structural Engineering International 22(1):105–111.

Aktan, A.E., Ellingwood, B.R., and Kehoe, B., 2007. *Performance-Based Engineering of Constructed Systems*. Journal of Structural Engineering 133(3):311–323.

Arques, P.Y., 1982. *Decisions en Traitement du Signal*. Editions Masson, Paris.

Barnouin, B., Lemoine, L., Dover, W.D., Rudlin, J.R., Fabbri, S., Rebourget, G., Topp, D., Kare, R., and Sangouar, D., 1993. *Underwater Inspection Reliability Trials for Offshore Structures*. 12th International Conference on Offshore Mechanics and Arctic Engineering, Glasgow, Scotland, 20–24 June, 2:883–890.

Basso, P., Del Grosso, A., Pugnale, A. and Sassone, M., 2009. *Applications of a Virtual Force Density Method*. International Association for Shell and Spatial Structures (IASS) Symposium, Valencia, Spain, 28 September – 2 October.

Basso, P. and Del Grosso, A.E., 2011. *Form-Finding Methods for Structural Frameworks: a Review*. IABSE–IASS Symposium, London, UK, 20–23 September.

Basso, P., Del Grosso, A., Pugnale, A., and Sassone M., 2009. *Computational Morphogenesis in Architecture: the Cost Optimization of Free-Form Grid-Shells*. International Association for Shell and Spatial Structures (IASS) Symposium, Valencia, Spain, 28 September – 2 October, 143–150.

Benedetti, M., Fontanari, V. and Zonta, D., 2011. *Structural Health Monitoring of Wind Towers: Remote Damage Detection Using Strain Sensors*. Smart Materials and Structures 20:(13pp).

Cheung, A., Cabrera, C., Sarabandi, P., Nair, K.K., Kiremidjian, A. and Wenzel, H., 2008. *The Application of Statistical Pattern Recognition Methods for Damage Detection to Field Data*. Smart Materials and Structures, 17:12pp.

Del Grosso, A.E., and Basso, P., 2010. *Adaptive Building Skin Structures*. Smart Materials and Structures, 19(12), 124011.

Dyke, S.J., Spencer Jr., B.F., Quast, P. and Sain, M.K., 1995. *The Role of Control-Structure Interaction in Protective System Design*. Journal of Engineering Mechanics 121(2):322–338.

ECTP, 2005. *Networking Europe: Vision 2030 and Strategic Research Agenda – Focus Area: Networks*. 4 November.

Elbeltagi, E., Helgazy, T. and Grierson, D., 2005. *Comparison among Five Evolutionary-Based Optimization Algorithms*. Advanced Engineering Informatics 19:43–53.

Frangopol, D.M., and Liu, M., 2007. *Maintenance and Management of Civil Infrastructure Based on Condition, Safety, Optimization, and Life Cycle Cost*. Structure and Infrastructure Engineering 3(1):29–41.

Glisic, B. and Inaudi, D., 2007. *Fiber Optic Methods for Structural Health Monitoring*. John Wiley and Sons.

Housner, G., Soong, T.T., and Masri, S.F., 1994. *Second Generation on Active Structural Control in Civil Engineering*. 1st World Conference on Structural Control, Pasadena, CA, 3–5 August, 3–18.

Housner, G.W., Bergman, L.A., Caughey, T.K., Chassiakos, A.G., Claus, R.O., Masri, S.F., Skelton, R.E., Soong, T.T., Spencer Jr., B.F. and Yao, T.P., 1997. *Structural Control: Past, Present, and Future.* Journal of Engineering Mechanics 123(9):897–971.

IRIS, 2012. *Final Report.* CP-IP 213968-2, Project no. FP7-NMP-2007-LRGE-1.

Kim, J.T., Park, J.H., Honga, D.S. and Park, W.S., 2010. *Hybrid Health Monitoring of Prestressed Concrete Girder Bridges by Sequential Vibration-Impedance Approaches.* Engineering Structures 32(1):115–128.

Kobori, T., 1994. *Future Direction on Research and Development of Seismic-Response-Controlled Structure.* 1st World Conference on Structural Control, Pasadena, CA, 3–5 August, 19–31.

Koiter, W.T., 1984. *On Tarnai's Conjecture with Reference to Both Statically and Kinematically Indeterminate Structures.* Report No.788 of Laboratory for Engineering Mechanics, Delft.

Lanata, F., and Del Grosso, A., 2006. *Damage Detection and Localization for Continuous Static Monitoring of Structures using a Proper Orthogonal Decomposition (POD) of Signals.* Smart Materials and Structures 15(6):1811–1829.

Lanata, F. and Schoefs, F., 2011. Multi-Algorithm *Approach for Identification of Structural Behavior of Complex Structures under Cyclic Environmental Loading.* Structural Health Monitoring 11(1):51–67.

Ministry of Transportation, 2006. *Canadian Highway Bridge Design Code (CHBDC).* Ontario, Canada.

Messervey, T.B. and Frangopol, D.M., 2008. *Innovative Treatment of Monitoring Data for Reliability-Based Structural Assessment.* Fourth International IABMAS Conference, Seoul, Korea, 13–17 July.

Omenzetter, P., Brownjohn, J.M.W. and Moyo P., 2004. *Identification of Unusual Events in Multi-Channel Bridge Monitoring Data.* Mechanical Systems and Signal Processing 18:409–430.

Park, S., Ahmad, S., Yun, C.B. and Roh, Y., 2006. *Multiple Crack Detection of Concrete Structures Using Impedance-Based Structural Health Monitoring Techniques.* Experimental Mechanics 46(5):609–618.

Pellegrino, S., and Calladine, C.R., 1986. *Matrix Analysis of Statically and Kinematically Indeterminate Frameworks.* International Journal of Solids and Structures 22(4):409–428.

Rouhan, A. and Schoefs, F., 2003. *Probabilistic Modelling of Inspections Results for Offshore Structures.* Structural Safety 25:379–399.

Rudlin, J.R., 1996. *Reliability of Inspection for Fatigue Cracks in Offshore Structures.* Institution of Electrical Engineers Colloquium on Inspection Reliability, London, UK, 21 November, 6/1–6/3.

Schoefs, F. and Clément, A., 2004. *Multiple Inspection Modeling for Decision Making and Management of Jacket Off-Shore Platforms: Effect of False Alarms.* First International Forum on Engineering Decision Making, Stoos, Switzerland, 5–9 December.

Schoefs, F., Clément, A. and Nouy, A., 2009. *Assessment of ROC Curves for Inspection of Random Fields.* Structural Safety 31(5):409–419.

Schoefs, F., Clément, A., Boéro, J. and Capra, B., 2010. *The αδ-Method for Modeling Expert Judgment and Combination of NDT Tools in RBI Context: Application to Marine Structures.*

Structure and Infrastructure Engineering: Maintenance, Management, Life Cycle Design and Performance 8(6):531–543.

Sohn, H., 2007. *Effects of Environmental and Operational Variability on Structural Health Monitoring*. Philosophical Transactions of the Royal Society A 365:539–560.

Soong, T.T., 1990. *Active Structural Control: Theory and Practice*. Longman, UK and Wiley, New York.

Tachi, T., 2009. *Generalization of Rigid Foldable Quadrilateral Mesh Origami*. Journal of the International Association for Shell and Spatial Structures 50(3):173–179.

Tachi, T., 2010a. *Freeform Rigid-Foldable Structure Using Bidirectionally Flat Foldable Planar quadrilateral Mesh*. Second Advances in Architectural Geometry Conference, Vienna, Austria, 18–21 September, 87–102.

Tachi, T., 2010b. *Geometric Considerations for the Design of Rigid Origami Structures*. IASS Symposium on Temporary and Permanent Structures for Expo, Shanghai, China, 8–12 November.

Tang, X., Thomas, S., Coleman, P. and Amato, N.M., 2010. *Reachable Distance Space: Efficient Sampling-Based Planning for Spatially Constrained Systems*. The International Journal of Robotics research 29(7):916–934.

Tarnai, T., 1980. *Simultaneous Static and Kinematic Indeterminacy of Space Trusses with Cyclic Symmetry*. International Journal of Solids and Structures 16:347–359.

Tarnai, T., 1984. *Comments on Koiter's Classification of Infinitesimal Mechanisms*. Technical Report, Hungarian Institute for Building Science, Budapest.

Vassart, N., Laporte, R. and Motro, R., 2000. *Determination of Mechanism's Order for Kinematically and Statically Indeterminate Systems*. International Journal of Solids and Structures 37(28):3807–3839.

8

Identification and Reduction of Piping-Vibrations under Different Conditions

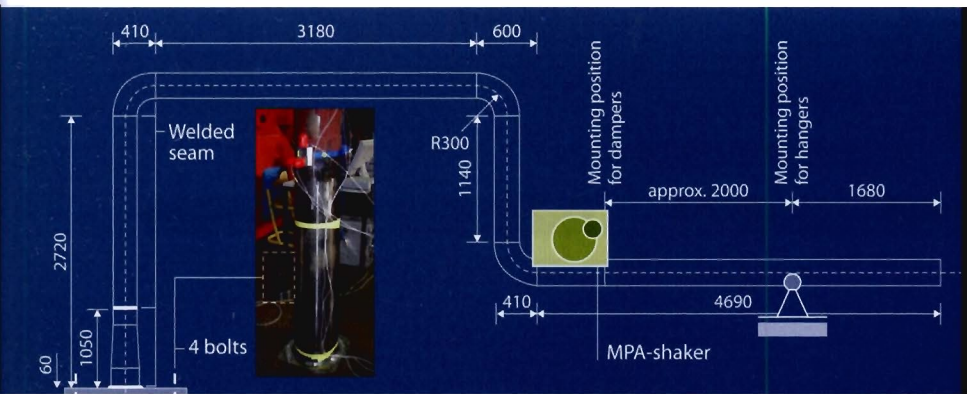
Authors:
Frank Barutzki
Christa Gurr-Beyer
Gereon Hinz
Klaus Kerkhof
Joachim Schwenkkros

Motivation

Safe operation, availability and lifetime assessment of piping systems are of utmost concern for plant operators. Optimized plants and safe operation under changing surrounding and boundary conditons are of concern. Integrity assessment in these cases is to be performed and demonstrated in corresponding experiments.

Main Results

In a number of field and laboratory tests the feasibility of system identification and integrity assessment has been demonstrated. Uncertainties are considerably reduced by monitoring results and measures like vibration reduction.



8-1 Objective

This chapter presents results of work package "WP2 – Chemical Industry".

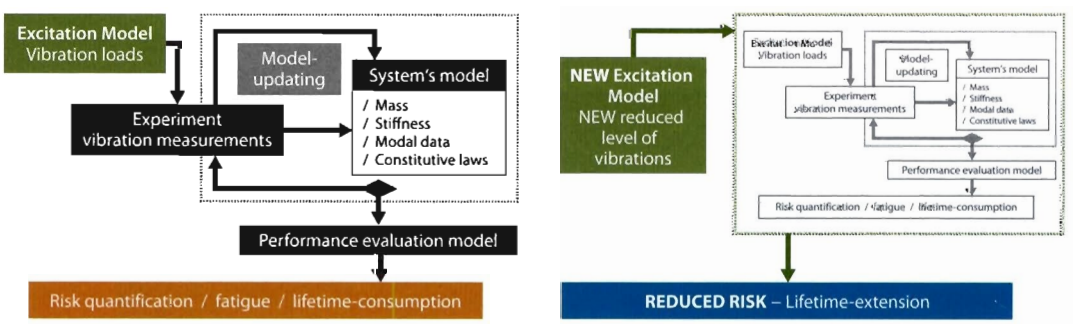
Investigations on the vibration behaviour and on understanding of possible corresponding damage mechanisms are especially important in the framework of integrity assessment (F.8-1).

The prediction of failure of safety related components is directly linked to the understanding of failure mode and damage mechanisms. One objective of WP2 was to demonstrate, by large scale testing, the overall load bearing behaviour of safety related components subjected to extreme loading (e.g. resonance excitation, earthquake loading etc.). Another objective was to investigate influences of flaws and damage mechanisms on the vibration behaviour. Such demonstrations need suitable test facilities, which are available at MPA Stuttgart. Furthermore in-situ investigations at industrial components were carried out at Dow Chemical and in a lignite power plant in Neurath.

Due to underestimated vibrations or undetected flaws, like local wall thinning, failure caused by fatigue, bursting, or collapse could occur. Also malfunctions in static boundary conditions like blocked spring-hangers could influence the load bearing behaviour of piping systems and should be detected in time. To perform reliable stress analysis, properties of piping systems have to be identified and corresponding calculation models have to be adjusted. Therefore model-updating procedures are required to understand the current load bearing behaviour of e.g. safety related industrial piping.

System identification by means of experimental modal analysis is still a challenge for piping in conventional power plants because of non-linearities and stick-slip effects due to friction. Therefore it is of interest to provide an updated calculation model which reflects the current state of the system. To investigate, whether system changes could be identified by experimental modal analysis with OOMA (Output Only Modal Analysis) during operation, malfunctions like blocked hangers were simulated experimentally and numerically. The detection of such changes of the static system, by means of OOMA, and consequences of local wall thinning for the dynamical characteristics of piping systems is reported herein.

Methodology for safety assessment F.8-1

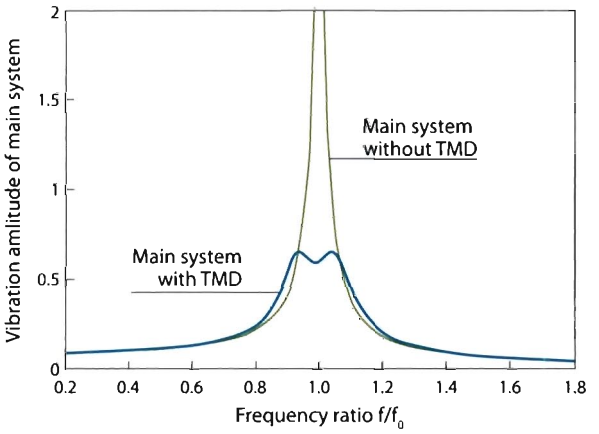


The use of tuned mass dampers is a rather new approach for reducing vibrations to avoid high cycle fatigue in piping systems. First design ideas for new passive vibration absorbers were investigated in laboratory tests with a mock-up piping system. Thereafter an industrial piping system was investigated: This piping system is supported by a tall structure fixed at the base. As a result, the steel building stiffness decreases with height. Large piping elbow forces act at the top of the building, which lead to large vibration amplitudes. Since both piping system and supporting structure exhibited these large vibration amplitudes, dampers or shock absorbers placed between them would prove less effective [Barutzki, 2009]. Therefore, special vibration absorbers, so called Tuned Mass Dampers (TMD) were developed for such piping systems. The first step to achieve the objectives mentioned above is to create an evaluation model on the basis of vibration analysis (experimental modal analysis) and model-updating, as shown in F.8-1. Then a new excitation model with a reduced level of vibration – e.g. realized by vibration absorbers – shoud be created. The final evaluation model comprises reduced risk. Parts of this investigation have been described in [Hinz and Kerkhof, 2013] and [Dwenger, 2011].

8-2 Identification and Reduction of Piping Vibrations Using Dynamic Vibration Absorbers

Dynamic vibration absorbers are often used, e.g. [Meinhardt et al., 2008], to reduce the response of a vibration system to dynamic excitations and to increase the internal damping of an otherwise low damped vibration system. By attaching an auxiliary mass to a vibrating system by spring and damping devices absorber effects can be utilized, F.8-2. By vibrating out of phase with the main system counteracting forces are developed and energy is dissipated.

General effect of a vibration absorber – tuned mass damper (TMD) F.8-2



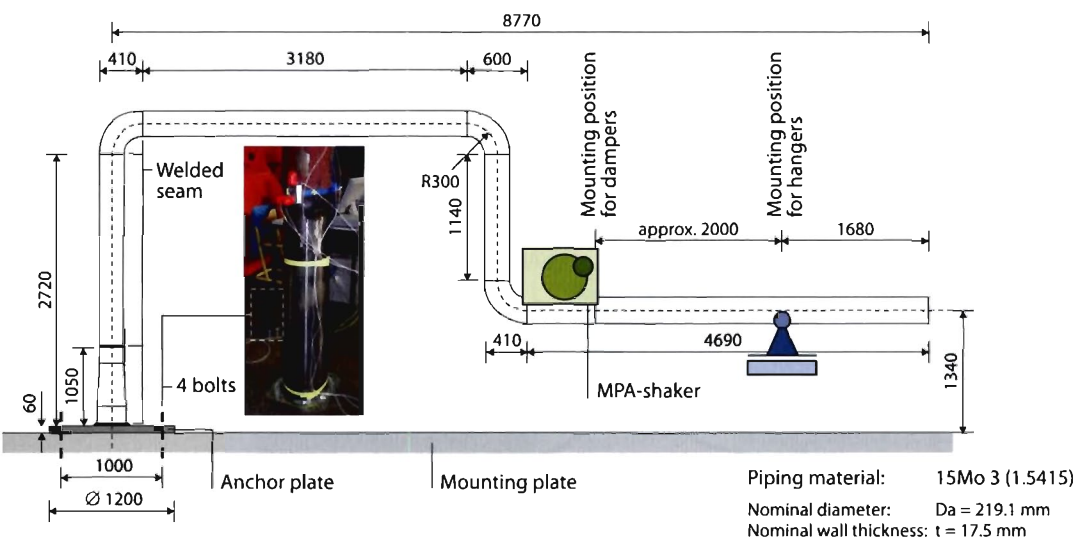
Today dynamic vibration absorbers can be found in easily excitable structures such as street and pedestrian bridges, terraces, chimneys or long-span floors. When excited with frequencies close to a natural frequency these usually slightly damped structures respond with large deflections, which are often sensed as uncomfortable, but which are sometimes also dangerous and service life reducing. Large piping systems in power or industrial plants are also slightly damped, highly flexible and complex structures. The increase of system damping is often the only efficient way to reduce system responses to all kinds of dynamic excitations. Viscous dampers are often used for this purpose but they require a stiff support point. Especially in tall piping structures these stiff supports are missing and therefore the use of passive dynamic vibration dampers with efficient damping capability is a promising approach to increase system damping and to solve the vibration problems in these systems. In general dynamic vibration absorbers consist of a mass that is elastically connected to the main structure by springs or pendulum systems. Additional dampers acting in parallel to the springs or pendulums dissipate the vibration energy and widen the working range of these elements. In case of large structures and depending on the critical mode shape to be dampened several absorbers can be installed along the structure to work in parallel.

8-2-1 Mock-up Tests with Vibration Absorbers (TMD)

Within [IRIS, 2012] and [Safepipes, 2008] different kinds of support components were mounted onto a mock-up and investigated by several project partners. Only one test series will be reported herein, namely

// Vibration analysis of the system without damping from vibration absorber and
// Vibration analysis using a newly developed passive vibration absorber.

Dimension and construction of mock-up F.8-3



Piping material: 15Mo 3 (1.5415)
Nominal diameter: Da = 219.1 mm
Nominal wall thickness: t = 17.5 mm

The system consists of one fully clamped support at the anchor plate and a sliding support constructed by means of two vertical struts. The construction is shown in F.8-3.

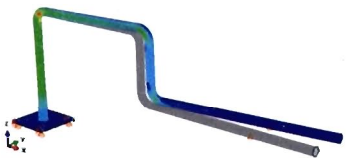
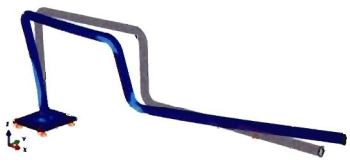
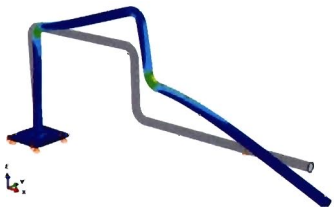
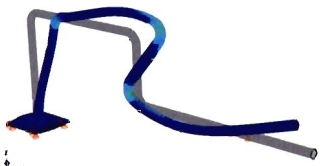
In the first coarse finite element (FE) model the whole system with its nominal piping diameter and the quadratic anchor-plate, which is mounted onto the mounting plate with four anchors, was modelled altogether with 3D-Volume tetrahedron-elements by using the Finite Element Programme ABAQUS. The first six calculated eigenfrequencies and corresponding mode-shapes are given in F.8-4. Within this calculation a concentrated mass for the MPA-shaker was taken into account.

For time history dynamic integrations an updated FE model was created with extended beam elements so called ELBOW31 elements of the ABAQUS element library which take into account cross section ovalization. The element length is about 20 mm. The whole system was modelled with these elements. Therefore also the decay of the ovalization in adjacent beams following an elbow are taken into account as well. The conical cross section, close to the mounting, was divided into five beam elements.

The torsion stiffness of the pipe connection to the ground at the anchor-plate which itself is mounted to the concrete-mounting plate of the laboratory by four anchors was idealized by two torsion springs in the direction of the in-plane and out-of-plane bending moment at the connection point of the pipe. These torsion springs and the pipe wall thicknesses – simulating the deviations to the nominal wall thicknesses – were the main parameters used for the model-updating process.

The measurement data of T.8-1 represent the free vibrations of the system without vibration absorber system without damping from the vibration absorber, but including the mounted MPA-shaker with a mass of 65 kg. The modal data was evaluated by means of Endevco accelerometers Type 7754-1000 and LMS Test.Lab 6A Operational Modal Analysis. The deviations between snap-back test results and impact hammer excitation results were less than 1 %. Therefore mean values of test series are given. All mode shapes cor-

Coarse FE model, Modes 1 to 6 F.8-4

Mode 1	Mode 2	Mode 3
1.38 Hz (out-of-plane mode)	5.44 Hz (in-plane mode)	6.92 Hz (out-of-plane mode)
		
Mode 4	**Mode 5**	**Mode 6**
8.62 Hz (in-plane mode)	10.63 Hz (out-of-plane mode)	23.61 Hz (in-plane mode)
		

Comparison Measurement – updated FE model, mock-up system without any damping components T.8-1

Mode No.	Mock-up system without damper but with MPA-shaker			Type of mode
	Measurement * [Hz]	Elbow-element model [Hz]	Volume-element model (F.8-4) [Hz]	
1	1.50	1.50	1.38	out-of-plane
2	5.54	5.55	5.44	in-plane
3	7.17	7.17	6.92	out-of-plane
4	8.66	8.74	8.62	in-plane
5	10.72	11.10	10.63	out-of-plane
6	23.64	23.60	23.61	in-plane

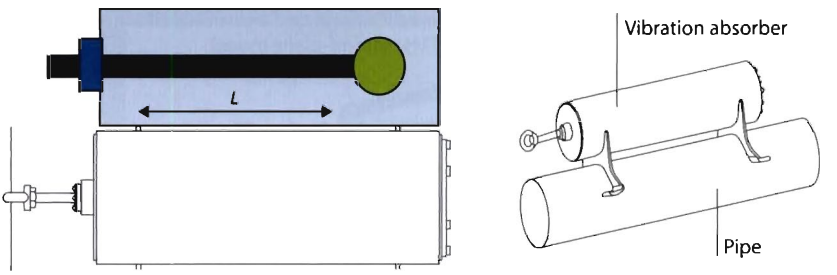
* Mean value from snap-back and impact tests

respond with the calculated modes mentioned above. A comparison of measurement data with both, the updated Elbow-Element Model and the first design calculation for the system including a shaker mass of 65 kg is given in T.8-1. Measurements and calculations correspond well.

The principal design of the newly developed passive vibration absorber (TMD, tuned mass damper) for piping consists of a cantilever beam with a concentrated mass at the end, vibrating in a cylinder. The vibration velocities are damped by a special fluid within the cylinder as sketched in F.8-5. The bending eigenfrequency depends on the stiffness of the member which in turn depends on the length L of the cantilever beam. For tuning purposes this length L is adjustable.

For energy dissipation the vibrating mass of the dynamic absorber moves in a highly viscous fluid. The absorber can be attached to the pipe in various positions and the direction of the absorber vibration adapts itself to the motion of the pipe. Two different mounting positions of the vibration absorber (horizontal and vertical) on the mock-up were investigated during the laboratory experiments. The system with the horizontally mounted vibration absorber is shown in F.8-6. The results of the two manually controlled sine-sweep excitation tests up to 8 Hz (near second vertical natural frequency) and afterwards down to zero are shown in F.8-6. The results of the horizontal (blue) position are given by the dark blue line, the results of the vertical (green) position by the green line. The orange line represents the system response without vibration absorber. The results in F.8-6 show strong amplitude reductions in the vicinity of the frequency of mode 2. Also

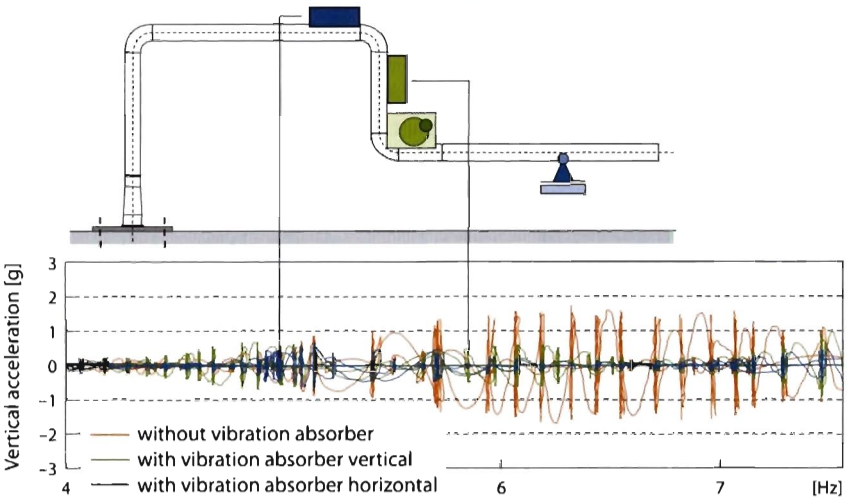
Principal design of installed TMD F.8-5



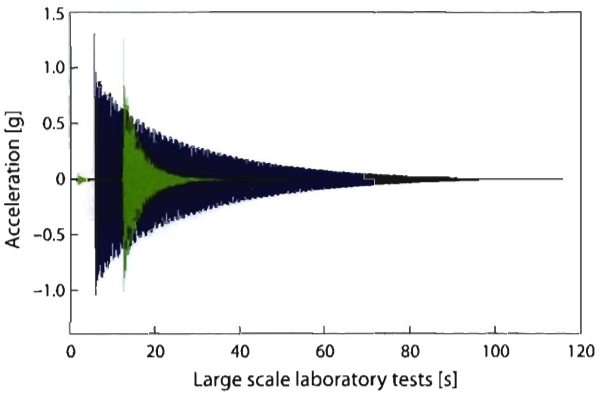
much more energy absorbing effects are observed when the absorber is mounted in the "blue" position. Mode 2 has larger vertical than horizontal displacements in this region.

The TMD only absorbs energy of mode 2. The next resonant excitation during run up, not visible in F.8-6, occurs at 7.8 Hz (10% below mode 4 due to the added mass of the TMD), therefore current investigations are focussed on TMDs for absorbing two adjacent modes. F.8-7 shows a comparison of snap-back tests with and without TMD. F.8-7 consists of two different curves: The blue line shows the vertical displacements at the centre of the piping without TMD (cut of wire at $t_1 = 7$ s) and the green line shows the response of the system with TMD in blue position (cut of wire at $t_2 = 14$ s). The effect of damping starts within the first cycle.

Results of sine-sweep tests with two different mounting positions (above) of the vibration absorber F.8-6



System response with (green) and without (blue) vibration absorber due to snap-back tests with 3 mm initial vertical deflections at the free end of the mock-up F.8-7



8-2-2 Identification of the Vibration Behaviour at the Investigated Large Scale Piping System

After laboratory studies on the behaviour of the newly developed piping vibration absorbers, the challenge arose to design them for plant installation. Since the upper part of the plant has much less rigidity, because cross sections of the steel structure are smaller and the top part even rises above the structure, see F.8-8, the idea of using vibration absorbers came up. The piping system is not covered by a building and so it is subjected to weather conditions like heavy storms near the North Sea and of course temperature changes. All these conditions lead to stochastic vibration of the plant, which cannot be controlled easily by commercially available damping elements. Therefore, strong requirements exist on the design of vibration absorbers. Also extensive investigations of the whole plant system and measurement campaigns have been carried out described in more detail in the deliverables of the IRIS project [IRIS, 2012].

To understand damage mechanisms, endurance limit tests on plane specimens of the applied piping material applied – presented in [Safepipes, 2008] – were performed.

First of all, vibration measurements were carried out [Safepipes, 2008] to investigate the overall vibration behaviour and the current state of the system. With the experience of [Bachmann und Ammann, 1987; Gurr-Beyer et al., 2003; Mattheis et al., 2000] the structural vibration behaviour was detected by seismic transducers and the piping vibration behaviour by accelerometers including operational modes. Interactions between piping and steel construction, see F.8-9, were found. A mode shape of the coupled piping-building system, which shows resonance effects, was found in the vicinity of 10 Hz, with mostly in-plane movements of both upper elbows. Before designing the vibration absorber, vibration measurements, regarding the top of the piping system, were carried out [IRIS, 2012].

Upper part of investigated piping system and steel construction F.8-8

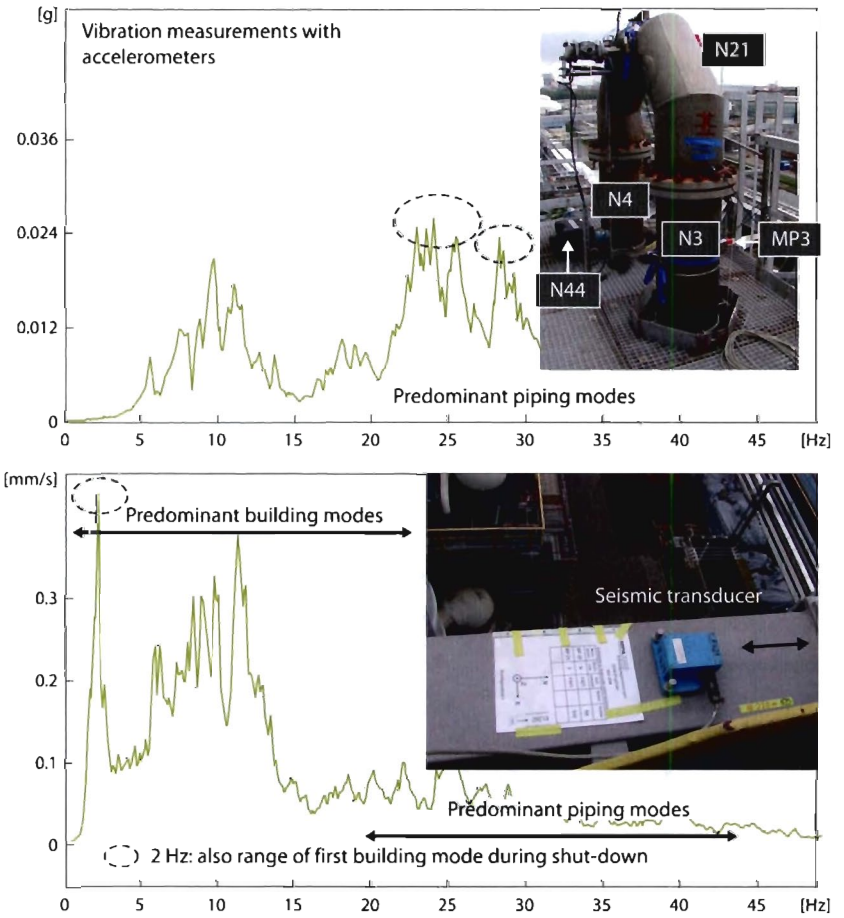


8-2-3 Root Cause Analysis and Design Calculations for Two Vibration Absorbers

In a first step model-updating was done to adjust the calculated model to the experimental modal analysis data. Taking into account construction details such as stiffness of nodes of the skeleton framing and masses of gratings, balustrades and heavy girders carrying only cables brought about a reasonable agreement between the experimentally determined and calculated mode shapes regarding the region of investigated resonance in the vicinity of 10 Hz, F.8-9.

Furthermore, understanding the resonance excitation was of interest. Load simulations were created to describe the mass flow excitation. F.8-10 also explains an approach for possible excitation-forces acting at the upper elbow: Impact deviation forces act on

Vibration measurement campaign of the whole piping system (with position of nodes 21, 3, 4, 44 of the FE model shown in F.8-10) F.8-9



the piping at the elbows because the system is a plug-flow system. If the time duration $t = t_2 - t_1$ of the mass flow between the turn-around points is given by the distance x of the centreline and the velocity V, the frequency of the acting excitation force was calculated at a frequency of 9.7 Hz.

By means of the updated model, harmonic frequency analysis was performed and on the basis of these calculations design parameters for the passive vibration absorber were determined as explained hereafter. The mathematical background for a SDOF (Single Degree Of Freedom) tuned mass damper is given in [Bachmann and Ammann, 1987; VDI, 2009]. F8-11 shows the effect of an optimized TMD nominated herein as vibration absorber. The optimum damping ratio [Bachmann and Ammann, 1987] becomes

$$\xi_{T,opt} = \sqrt{\frac{3\mu}{8(1+\mu)^3}}. \qquad \text{E.8-1}$$

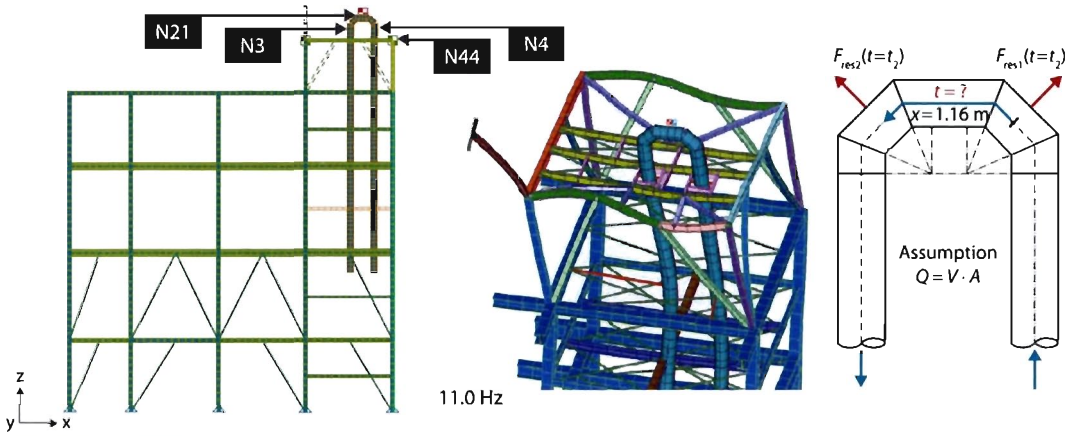
The final frequency of the system including vibration absorber yields

$$f_T = \frac{f_H}{1+\mu} \quad \text{and} \quad \mu = \frac{m_T}{m_H} \qquad \text{E.8-2}$$

where m_T denotes the absorber mass, m_H represents the concentrated mass of the upper vibrating system and f_H is the eigenfrequency of the system without vibration absorber. The added mass of the TMD slightly reduces the eigenfrequencies of the system.

With the finally chosen calculation parameters, T.8-2, the system frequency response regarding uniform force excitation of 1 N in x-direction at the top of the piping system for the case with two vibration absorbers of m_T = 175 kg tuned at 11 Hz is presented in F8-11.

FE model of the complete system with some simplifications of the lower part of the system, calculated mode shape in the vicinity of the resonant frequency of 10 Hz and approach for an explanation of the acting excitation-forces at the upper elbow F.8-10



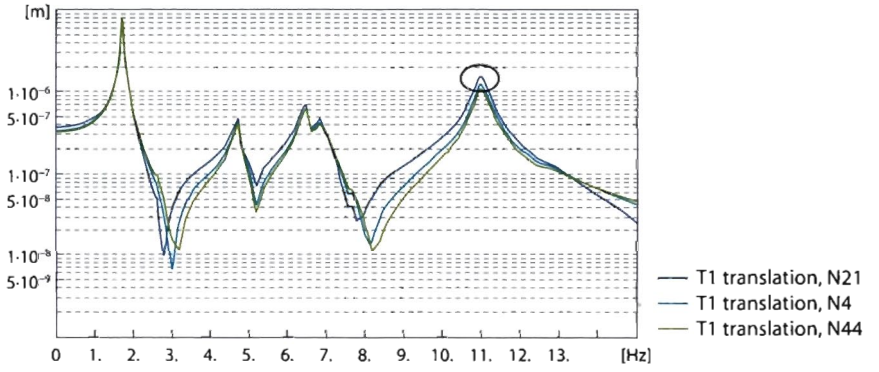
The predicted amplitude reduction has the factor of 1/6 in the range of 10–12 Hz, as we can see from the comparison of both response functions in F.8-11.

Final parameters of the TMD T.8-2

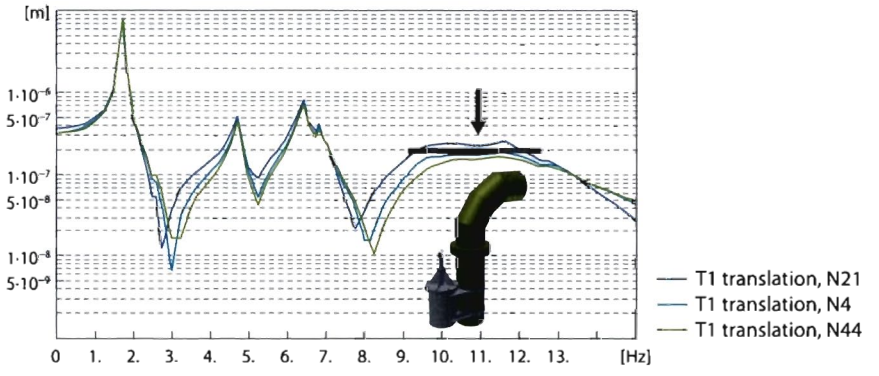
Frequency main mass f_H [Hz]	11.0
Concentrated mass m_H [kg]	7000
Mass ratio μ	0.05
Absorber mass m_T [kg]	2 × 175
Absorber stiffness k_T [N/m]	$2 \times 7.6 \cdot 10^5$
Absorber damper c_T [Ns/m]	$2 \times 2.9 \cdot 10^3$
Damping ratio D_T	12.7 %

Frequency response in [m] due to uniform force (1 N) excitation in x-direction at the top of the piping system for the case without (above) and with (below) two vibration absorbers of m_T = 175 kg tuned at 11 Hz. Design calculation: reduction of amplitudes by the factor of ~1/6 F.8-11

Frequency response without two vibration absorbers



Frequency response with two vibration absorbers



8-2-4 Final Design of Passive Vibration Absorbers for the Investigated Piping System

Piping systems are complex three-dimensional structures usually with many and complicated mode shapes. The design of a dynamic vibration absorber has to consider the specific requirements of the piping systems in question and should enable easy and safe installation. The optimal mounting location in regard to vibration reduction is not always available. Therefore the dynamic absorber should work in many positions. The selected design works analogously to the mock-up test with a defined mass that is connected to a member. The bending eigenfrequency depends on the stiffness of the member which in turn depends on the free and vibrating length. For tuning purposes this length is adjustable, see F.8-5.

For energy dissipation the vibrating mass of the dynamic absorber moves in a highly viscous fluid. The absorber can be attached to the pipe in every position and the direction of the absorber vibration adapts itself to the motion of the pipe. Vibrating mass, stiffness and damping were chosen in accordance to known optimization criteria for harmonic and random vibrations.

Based on measurements and finite element calculations the modal or resonant mass of the structure was determined. With a mass ratio of 5 % the total vibrating mass of the absorber was 350 kg. The optimal damping ratio of the absorber is about 11 %. In the discussed case two absorbers with half the required vibrating mass were designed to minimize the additional weight attached to one point of the pipe.

8-3 Investigation of Local Wall Thinning on Piping Vibrations

The system response of a piping system which is excited by vibrations depends on the magnitude of the excitation, its frequency spectrum, and the structural-dynamic characteristics of the whole piping. The structural-dynamic characteristics of such a system can change over time due to ageing and damage mechanisms. An important damage mechanism in facilities worldwide is local wall thinning (LWT) due to erosion-corrosion, which can lead to sudden failures such as bursting, break, or collapse as well as fatigue [Dooley and Chexal, 2000; Michel et al., 2001; NISA, 2005; Tinga and Ma, 1999]. Local wall thinning reduces burst pressure, failure load, deformation capacity and the lifetime of elbows [Ahn et al., 2002; Kim et al., 2003]. Knowing the deformation and damage mechanism behaviour of these components is important to predict the dynamical behaviour of the system and its ability to resist operation related vibrations and earthquakes. Although plastic limit load, burst pressure, fatigue due to bending and fracture behaviour of elbows and straight pipes with local wall thinning have been a focus of recent investigations [Hasegawa et al., 2011; Kim et al, 2008, 2009a, 2009b; Kim and Park, 2008, 2003; Oh et al., 2007; Oyamada et al., 2012; Takahashi et al., 2009, 2010], only few investigations exist on the change of the dynamical behaviour of piping under seismic loading due to

local wall thinning in elbows [Namita et al., 2003; Nakamura et al., 2010; Schmidt et al., 1991]. No structural dynamic investigations could be found of systems dealing with a small diameter branch, containing elbows with local wall thinning, which are attached to larger diameter piping. Therefore it is important to investigate the implications of local wall thinning on the integrity and the dynamical characteristics of piping and to develop procedures to predict related safety margins.

Within WP2 experiments are conducted at MPA Stuttgart to measure and predict the changes of the structural-dynamic characteristics of piping due to local wall thinning. Low cycle fatigue tests under seismic loading and numerical studies are performed to investigate influences of local wall thinning on the integrity of the system. Material investigations and system identification as well as model-updating are performed.

8-3-1 Investigated System and Design Studies

The objective of the design studies was to find a geometry, which adds a small diameter branch, containing an elbow with local wall thinning, to the mock-up, to create a piping system, which fulfills the following criteria:

// The system's first natural mode shape in vertical direction should have maximum von Mises stress concentrated in the elbow with local wall thinning. The stress in all other parts of the piping should be significantly lower.
// The natural frequency, belonging to this mode shape, should be as low as to be excited by a common earthquake-acceleration-input.
// Flanges should be added to the branch, to allow simple replacement of damaged elbows.
// Ovalization of the damaged elbow should be possible and not constrained by adjacent flanges.

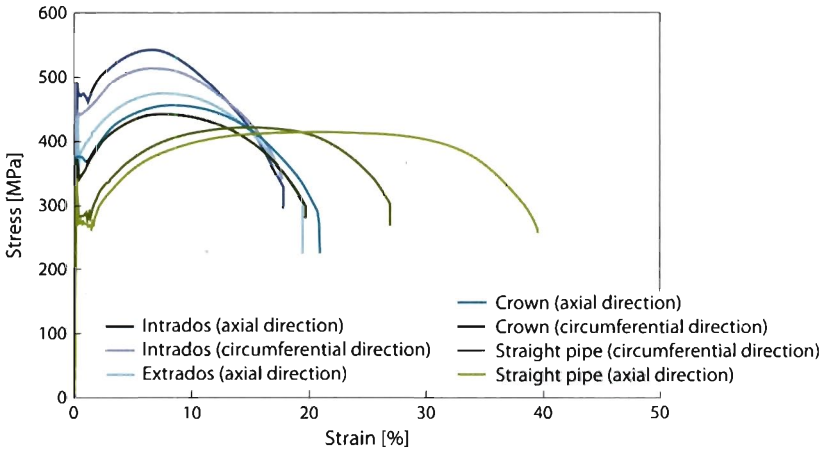
The small diameter branch is made of structural grade carbon steel (material no. 1.0308), which is a commonly used material for elbows in power plants, affected by local wall thinning.

The material characteristics of 1.0308 were determined with tensile tests at room temperature with test specimens from different positions of the elbow. As expected, the bending procedure of the elbow led to different stress-strain curves at different positions of the elbow (see F.8-12).

An exemplary comparison of two investigated design geometries is shown below and the reasons which lead to the chosen geometry are explained. To study the eigenmodes and eigenfrequencies of various investigated geometries, an FE model consisting of 30211 C3D8R elements was created. Straight pipes were added to the elbow with local-wall thinning, to allow undisturbed ovalization. Flanges were added to the straight pipes to allow simple exchange of damaged elbows. The branch is added vertically to the mock-up. Different locations for the attached branch were compared (Position 1: close to mock-up elbow, position 2: close to free end). F.8-13 shows a comparison of the first eigenfrequencies and mode shapes of two systems with different branch attachment positions. Both supports of the mock-up (at the end of the small diameter branch and at the vertical end of the mock-up) are clamped.

Material characteristics (above) and Stress-Strain curves (below) at different positions of the elbow made of material with no. 1.0308 F.8-12

Material	Young's Modulus [MPa]	Density [kg/m³]	Poisson's ratio	Yield strength [MPa]
1.5415	212600	7850	0.28	275
1.0460	210000	7850	0.28	240
1.0308	207000	7850	0.28	see stress



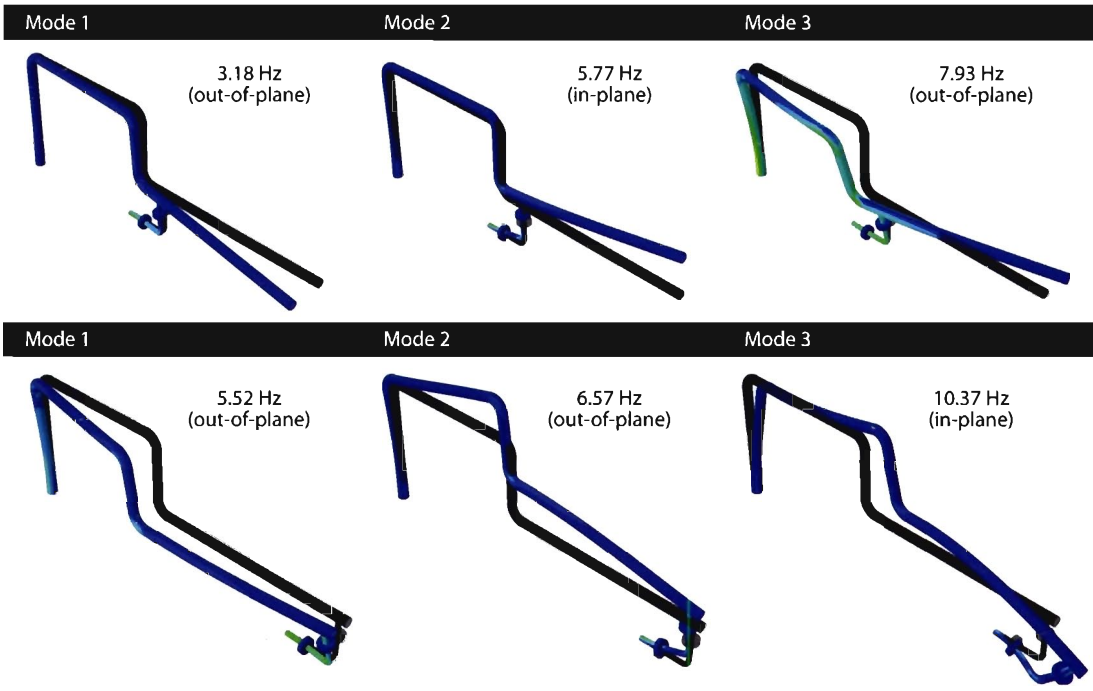
A comparison of the different geometries yielded the following results: Depending on the position of the branch, the static boundary conditions, and the length of the straight pipes in the branch, the locations of peak von Mises stress and the eigenfrequencies change. Compared with the out-of-plane mode shapes, the in-plane mode shapes yielded better concentration of stress in the elbow of the branch. F.8-14 shows the first vertical mode shape with maximum von Mises stress in the connecting weld between the branch and the large piping. An attachment of the branch in position 1 reduced the stress in the weld between the branch and the large piping.

Utilizing the results of the design studies it was possible to select a final geometry (compare F.8-17), reducing stresses in the welds and increasing stresses in the elbow. By using a hinge as support for the branch (allowing free rotation around the y- and z-axis) a system with a first vertical eigenfrequency of 4.8 Hz, with low stress in the weld between the branch and the large diameter piping and high stress in the locally wall thinned elbow was created.

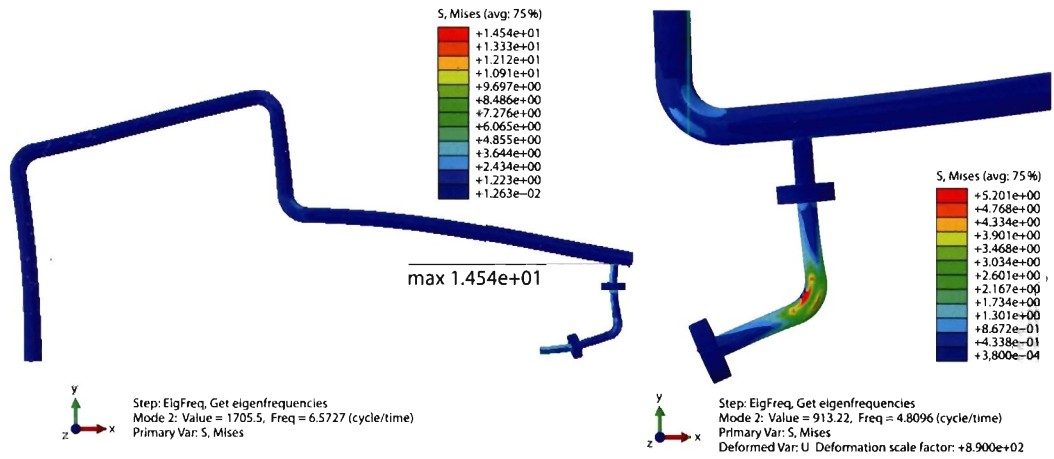
F.8-15 shows the reaction forces (RF) and the reaction moments (RM) around the x-axis, at the hinge, for the first five eigenmodes of the piping. Modes 1, 3 and 5 are horizontal. Modes 2 and 4 are vertical. Mode 2 reduces stress in the weld between the branch and the large diameter piping, while mode 4 increases the stress in the weld.

This hinge and the fixed support at the bottom of the large diameter piping are the only supports of the system. The straight pipes and the elbow in the branch have an outer diameter of $D_a = 101.6$ mm and a wall thickness of $t_b = 10$ mm. The elbow has a bending radius of $R = 175$ mm. With a diameter ratio of $u = 1.245$, the elbow is considered thick-

Eigenmodes of geometric variations of the mock-up, above: branch position 1 with a hinge support at the branch, below: branch position 2 with a fixed supported branch F.8-13



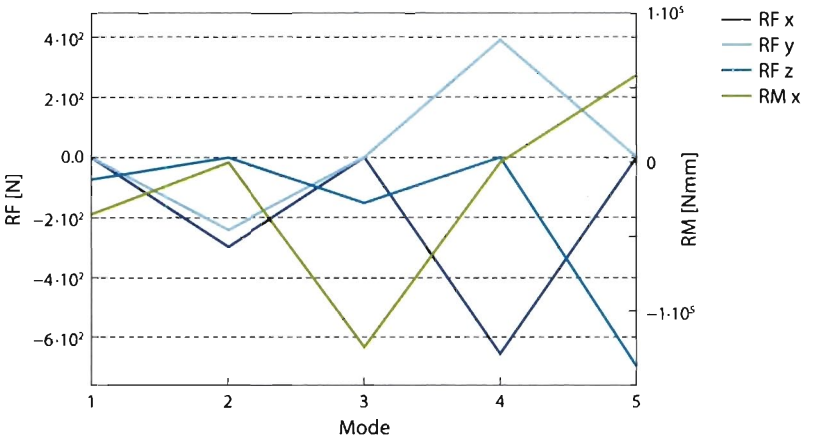
First vertical eigenmode (position 2, without hinge) with maximum stress in the connecting weld between the small and the large diameter piping (left), first vertical eigenmode (position 1, with hinge) with maximum stress in the elbow of the branch (right) F.8-14



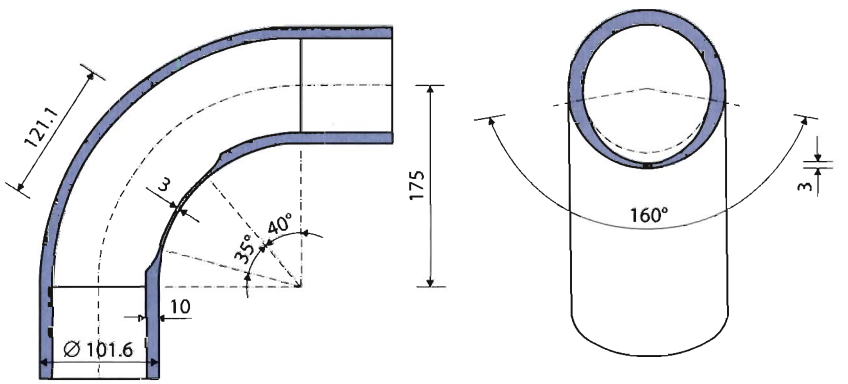
walled. The flanges are kept outside of the descending ovalization in the adjacent straight pipes caused by in-plane bending. The length of descending ovalization was calculated to 1.8 D_a = 183 mm according to [Diem, 1994].

Bending of the elbows was done by mandril-bending, which leads to a thickening of the intrados and a thinning of the extrados, while the thickness of the crowns remains more or less constant. Ovalization due to the bending process is small [Diem, 1994]. The elbow in the attached branch was wall thinned by eroding on the inside of the elbow. At the intrados the wall thickness was reduced by 70 % (see F.8-16).

Reaction forces (RF) and reaction moments (RM), at the hinge, for different mode shapes. Modes 2 and 4 are the first and second vertical mode shapes. Modes 1, 3 and 5 are the first three horizontal mode shapes F.8-15



Geometry of elbow with Local Wall Thinning, cross section views F.8-16



8-3-2 System Identification and Model-Updating

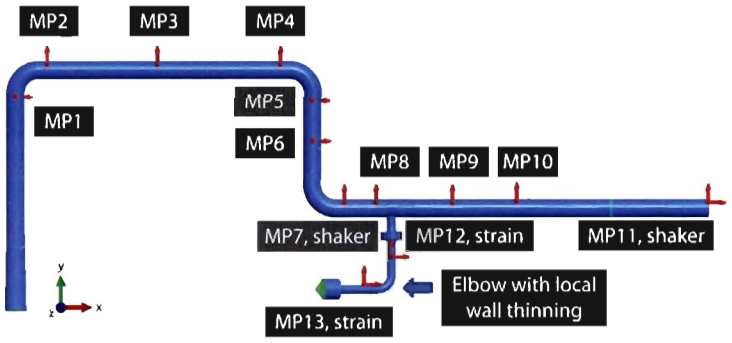
In the following discussion, first the final model of the chosen system with local wall thinning in the elbow and afterwards another model without wall thinning will be described. In order to keep time analysis studies within reasonable bounds, the number of elements was kept as low as possible, yet considered adequate. The large diameter piping is modelled with 24 S8R shell elements in circumferential direction – altogether 4892 elements, using Simpson's thickness integration rule and five thickness integration points. The small diameter branch is modeled with C3D20 solid elements, two over the thickness and 48 in circumferential direction – altogether 5160 elements. This model was chosen as final because further mesh refinement studies showed changes in eigenfrequencies smaller than 0.008 % when increasing the amount of solid elements across the wall thickness from 2 to 3.

The two different element regions are connected with a surface-to-surface tie constraint. The thickness of the shell elements is adjusted according to wall thickness measurements. For the straight pipes modelled with shell elements, a wall thickness of t_{sp} = 17.7 mm is used. For the wall thickness of the elbows near MP2, MP4 and MP7 in F.8-17, wall thicknesses of t_{eb1} = 17.3 mm, t_{eb2} = 17.4 mm and t_{eb3} = 17.5 mm are used. The shaker has a mass of m = 72.4 kg and is adjusted to be able to excite the system in the vertical direction. It was used in two positions, see F.8-17. The shaker is modelled as a mass point in the centre of the pipe taking into account the rotatory mass moment of inertia. As the two supports are not perfectively stiff, they are modelled with translational and rotational springs. For determining these parameters model-updating was carried out using Output Only Modal Analysis (OOMA).

OOMA was performed during all experimental studies. The system with local wall thinning, shown in F.8-17, was investigated with impact-tests and snap-backs. Additionally strain gauges were applied to the branch.

The identified natural frequencies and mode shapes were used for model-updating of the FE model. Modal analysis was carried out for the system with the shaker position at MP11. Using FEM tools for sensitivity studies and model-updating brought about a strong

FE model of the investigated system and the added branch and measurement positions F.8-17



influence of the rotational spring stiffness on the eigenfrequencies. The starting value for model-updating, a spring stiffness of $k_{start} = 4.5 \cdot 10^{12}$ Nmm/rad, was selected for all springs. By adjusting the spring stiffnesses in this way (see T.8-3), the average error of the first 10 eigenfrequencies could be reduced from 3.7 % to 1.1 %.

Including the influence of the load case dead load and performing non-linear geometry analysis, the eigenfrequencies of the system are reduced. The average error decreases from 1.1 % to 0.84 %. T.8-4 shows the comparison of the final, updated model with the measured natural frequencies and mode shapes.

The first six modes of the updated FE model of the system with the attached branch containing local wall thinning are shown in F.8-19 and can be compared with the modes of the former system given in F.8-4 and with the design studies, without hinge and shaker-mass, before construction of the system and model updating shown in F.8-13.

Damping ratio was determined for the different modes by means of impact tests (see F.8-18). In the case of rotation around the y-axis (see mode 1 and mode 5 in F.8-19) damping is significantly higher compared to the other modes. This may be caused by friction in the hinge.

After model-updating of the FE model with local wall thinning, described above, the second model was created by replacing the wall thinned elbow with an elbow without wall thinning. The amount of elements in the system does not change. The elements stay in the same position. Only the size of the elements changed, which had no influence on the mesh quality. For system identification, acceleration measurements were carried out at 13 different positions in three directions (MP1 to MP13).

The FE model without local wall thinning, shows the position of maximum von Mises stress at the connection between the branch and the large diameter piping for modes 1,

Rotational spring stiffness before and after updating (HX, HY, HZ, rotation around x-, y-, z-axis) T.8-3

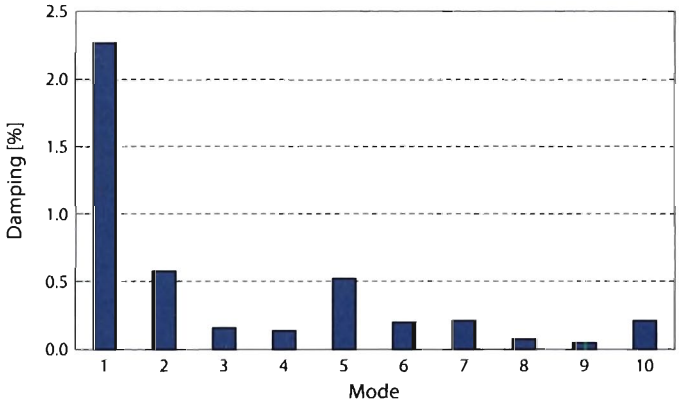
Position	DOF	Start value [Nmm/rad]	End value [Nmm/rad]
Branch	HX	$4.5 \cdot 10^{12}$	$4.11 \cdot 10^{12}$
Large diameter piping	HX	$4.5 \cdot 10^{12}$	$6.16 \cdot 10^{10}$
	HY	$4.5 \cdot 10^{12}$	$9.48 \cdot 10^{13}$
	HZ	$4.5 \cdot 10^{12}$	$5.18 \cdot 10^{10}$

Comparison: measurement – updated calculation T.8-4

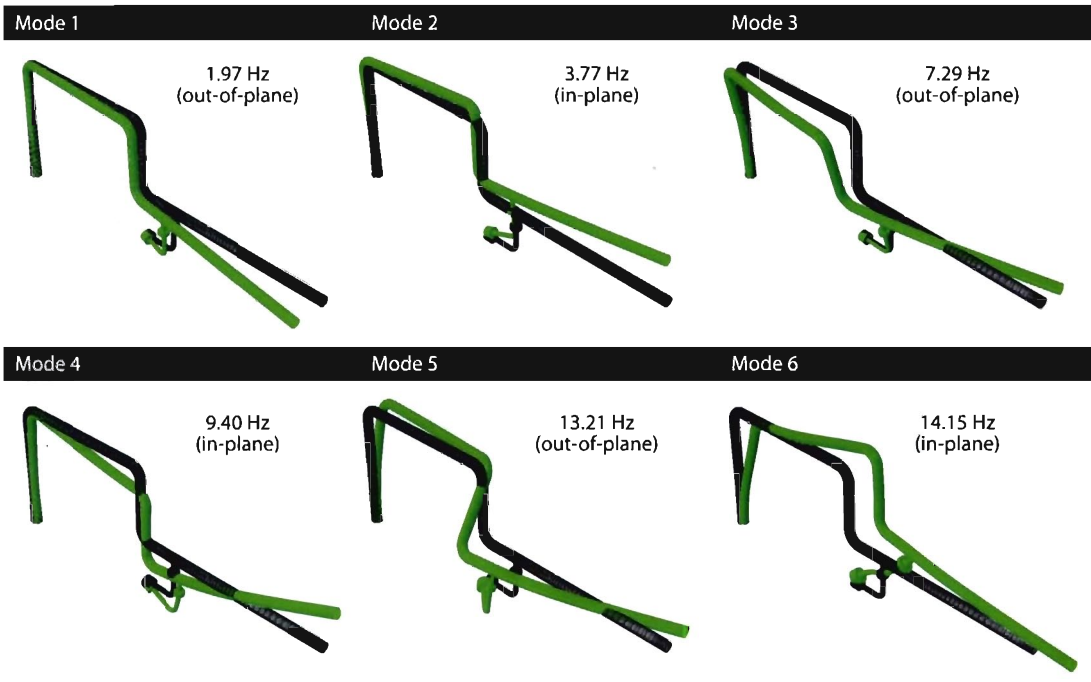
No. of mode	Experiment [Hz]	FEM [Hz]	Error [%]	MAC [%]
1	1.96	1.97	0.51	99.6
2	3.76	3.77	0.27	96.1
3	7.21	7.29	1.11	99
4	9.48	9.40	–0.84	97.3
5	13.10	13.21	0.84	99
6	14.33	14.15	–1.26	98
7	24.68	24.44	–0.97	95.4
8	26.40	26.12	–1.06	95.6
9	46.62	46.58	–0.09	92.3
10	46.88	47.55	1.43	95.2

3, 4, 5 and 6, while mode 2 has maximum von Mises stress at the crown of the elbow. In comparison to this, the system with wall thinning shows the position of maximum von Mises stress at the intrados of the wall thinned elbow for modes 1, 2 and 3. Modes 4, 5 and 6 have maximum von Mises stress at the connection weld between the branch and the large diameter piping. Because of the reduction of the wall thickness, the location of maximum bending and failure during excitation of the first vertical mode moves from the crown of the elbow to the intrados, which is in agreement with [Takahashi et al., 2009].

Damping ratio determined from acceleration measurements during impact-tests F.8-18



First 6 modes of the updated FE model of the piping with local wall thinning F.8-19

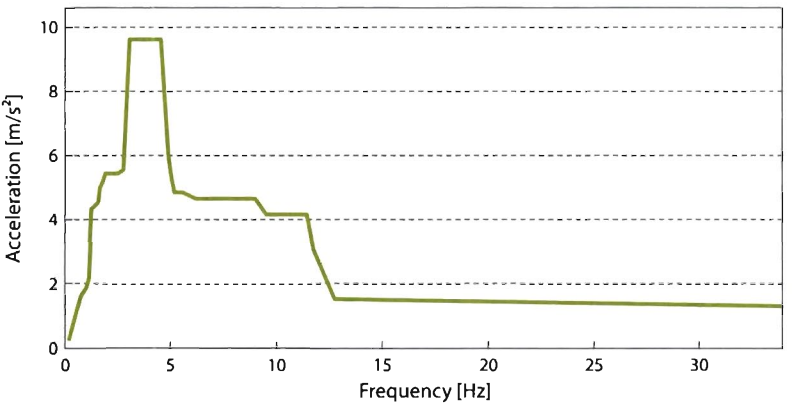


8-3-3 Earthquake Loading and System Excitation

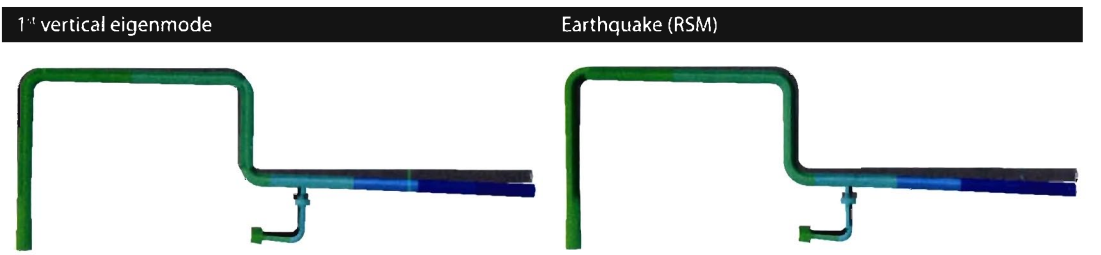
For system design, a seismic floor response spectrum of a German nuclear power plant for 2% damping was used, F.8-20. The response was calculated with the response spectrum method (RSM) using Complete Quadratic Combination (CQC).

The response spectrum shows a strong excitation in the range between 3.0 Hz and 4.6 Hz which underlines the selection of the investigated mock-up system with a first natural vertical mode of 3.77 Hz. This range includes the first vertical natural frequency of the piping. Because of this, the first vertical mode of the piping strongly resembles the calculated response to the vertical component of earthquake loading, as can be seen by comparing the deformations in F.8-21. To study the failure modes and systems response due to dynamic excitation, the first two vertical eigenfrequencies are excited with the shaker. Using vertical sinusoidal excitation at MP7 with an amplitude of F = 225 N and a frequency close to the first vertical eigenfrequency, vertical displacement amplitudes of $u_{vertical}$ = 35 mm were realized (measured at MP10) during the experiment. In comparison, the response of the piping to a design earthquake response spectrum as shown in F.8-20

Seismic floor response spectrum of a German nuclear power plant for 2% damping F.8-20



Calculated system response due to vertical earthquake loading (left) compared with 1st vertical mode (3.77 Hz, right). The grey shade shows the undeformed model. The scale of colours shows displacement in vertical direction F.8-21



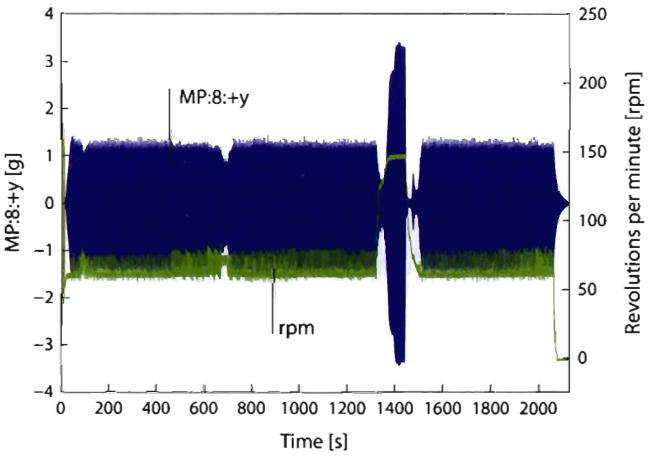
is calculated as $u_{vertical}$ = 15 mm (at MP10), which is only half as large as the displacement realized with the shaker excitation. Besides this the earthquake response to the spectrum in F.8-20 was calculated for both the FE model with and without wall thinning, as described above. The result shows that global displacements, calculated with RSM, remain equal, while stress in the wall thinned elbow increases.

8-3-4 Sinusoidal Shaker Excitation and Failure

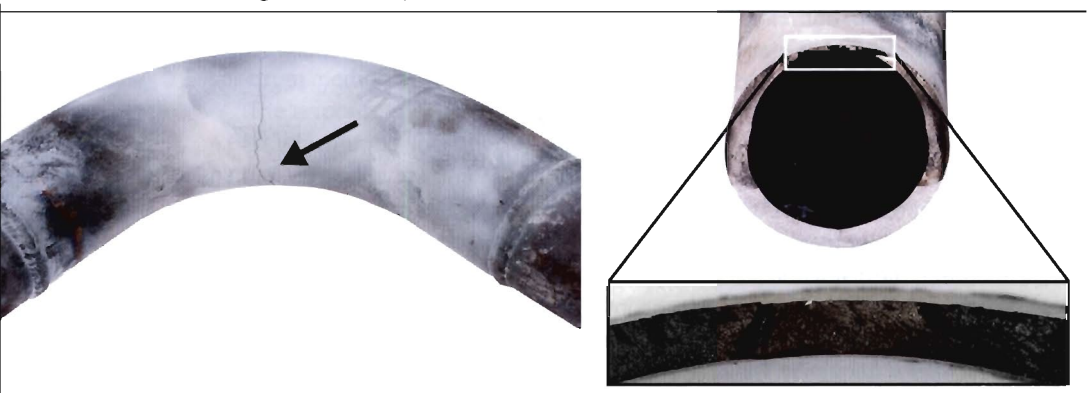
The force of the shaker used in the project rises with frequency. Because of this a 5.8 times larger force could be realized at the second vertical natural frequency compared to excitation with the first natural frequency. Excitation in the second vertical natural frequency leads to two highly loaded areas the intrados of the elbow and the tee branch. Since the tee branch is not the focus of the investigation, the piping was mainly excited with the first natural frequency. F.8-22 shows the load history and acceleration measurements of the piping with shaker-excitation at approximately 4 Hz and 10 Hz. The strong increase in amplitude for the excitation at 10 Hz is due to the increasing force of the shaker. At 10 Hz the sine-wave, generated by the shaker, is of almost constant frequency. At 4 Hz the influence of the dynamics of the piping on the dynamics of the shaker is much stronger, which leads to periodic acceleration and deceleration of the shaker, while the system's dominant answer is a sine-wave around 4 Hz.

Description of resonance loading until through-wall crack at the intrados of the elbow was detected (above) and an example of acceleration measurement in the direction of the excitation of the first (4 Hz) and second (10 Hz) vertical eigenfrequencies of the piping system (below) F.8-22

Load history, step	Excitation frequencies	Input-force [N]	Time [min]
1	1st vertical	225	56
2	2nd vertical	1300	18
3	1rd vertical	225	266



Crack at the centre of the intrados of the elbow, broken elbow under liquid nitrogen, stereoscope view of area with crack starters F.8-23



During interruption points of the test, no crack was detected at the elbow by visual inspection. No cracks at the elbow were determined by ultrasonic testing after step 1 and 2. A local increase of temperature of a few degree of Kelvin was measured at the location at which the crack was detected later, while the rest of the piping remained at room temperature. After indicators of non-linearity were seen in acceleration measurement signals the test was stopped and visual inspection brought about a crack at the centre of the intrados in the wall thinned area. F.8-23 shows the crack at the elbow. Crack starters can be seen in the photo (stereomicroscope) of the centre of the intrados after the elbow was broken up under liquid nitrogen. The crack started at the outer surface of the elbow.

8-3-5 Modal Analysis Before and After Crack

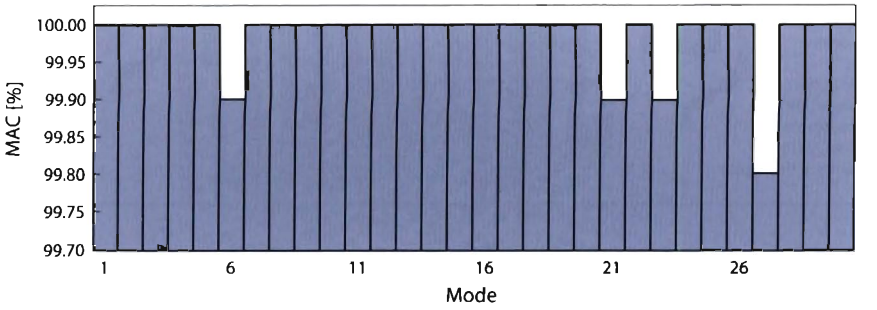
As described in [Farrar and Worden, 2013] large changes of natural frequencies occur when cracks change the load-paths through the piping. However, if a closed crack changes load paths only locally, this will have a small influence on resonant frequencies. This is in agreement with the small changes in natural frequencies and modes before and after the occurrence of the crack, which were identified with impact tests causing only small displacements. In the range up to 50 Hz only the 6th natural frequency shows a frequency shift of > 0.5 % from 14.18 Hz to 14.11 Hz. MAC values remain unchanged. The crack was included in the FE model and simulations of snap-back tests with small deflections show that, due to the dead load of the piping, the crack remains closed for small excitations.

8-3-6 Influence of Local Wall Thinning on Modal Parameters

The change in modal parameters due to local wall thinning at the intrados as described above was investigated by comparing the updated FE model with and without local wall thinning. The change in eigenfrequency due to local wall thinning in this study does not change the order of any eigenfrequencies, which is ensured by comparing MAC values. The largest changes in frequencies happen in the first 30 eigenfrequencies up to

Calculated eigenfrequencies with largest change in frequency due to local wall thinning in the elbow (above) and MAC values comparing two FE models with and without local wall thinning in the elbow (below) F.8-24

Number of mode	Frequency with LWT [Hz]	Frequency without LWT [Hz]	Difference [%]
2	3.765	3.816	−1.32
6	14.145	14.31	−1.15
21	200.8	202.12	−0.65
1	1.966	1.975	−0.46
29	334.65	335.9	−0.44



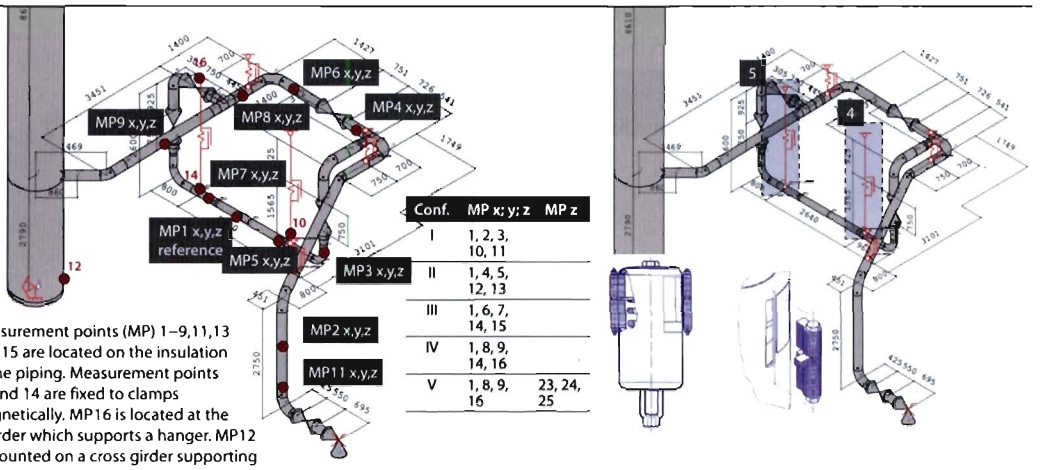
350 Hz. The greatest difference (−1.32 %, see F.8-24) occurs in the first vertical eigenfrequency with which the system was also excited during the experiment to cause damage at the wall thinning. The change in MAC values in the first 30 mode shapes is very small, which explains the lack of change in global displacement in the calculated earthquake response (see chapter 8-3-3).

8-4 System Identification of Piping System in a Lignite Power Plant

A piping system of the "hot reheat system" (HZÜ) in a lignite-fired power plant was investigated [Dwenger, 2011]. Geometry of the system and measurement plan are shown in F.8-25. The piping system consists of three pipes: One hot reheat line, the main line, and the bypass mounted for research purposes. The valves to the bypass were closed when the measurements were carried out, so that the lower loop of the pipeline (bypass) was depressurized and without any flow.

One part of the research objectives was to detect malfunctions of boundaries – like blocked hangers – and whether they could be detected by vibration measurements and its changes. This objective was investigated by means of measurement-configuration IV. The following spring hangers were blocked: No. 4, No. 5 and then both No. 4 and 5, F.8-25.

Geometry of piping system, measurement plan and blocked spring hangers F.8-25



Conf.	MP x; y; z	MP z
I	1, 2, 3, 10, 11	
II	1, 4, 5, 12, 13	
III	1, 6, 7, 14, 15	
IV	1, 8, 9, 14, 16	
V	1, 8, 9, 16	23, 24, 25

Measurement points (MP) 1–9,11,13 and 15 are located on the insulation of the piping. Measurement points 10 and 14 are fixed to clamps magnetically. MP16 is located at the T-girder which supports a hanger. MP12 is mounted on a cross girder supporting the vessel. Measurement points 23-25 are only vertical measuement points at the bypass.

The investigated piping system – with the exception of the bypass – is insulated over the entire length. The vibration measurements were carried out on the insulation, as the demounting of insulation is of great expenditure and not possible during operation. Investigations during former research projects [Kerkhof et. al., 2001] showed that up to a frequency of about 20 Hz vibration measurements on insulation can be carried out reliably. Therefore, a limited number of eigenfrequencies and corresponding mode shapes are investigated and evaluated in the following. In case of the piping system examined, there are numerous restrictions regarding the accessibility of relevant points. For accessibility of the main line section above the bypass, a scaffold was set up. The scaffold was located half-height between the bypass and the mainline. Access to the section of the main line above the bypass was only possible via scaffold. The other main line sections were accessible only to a limited extent.

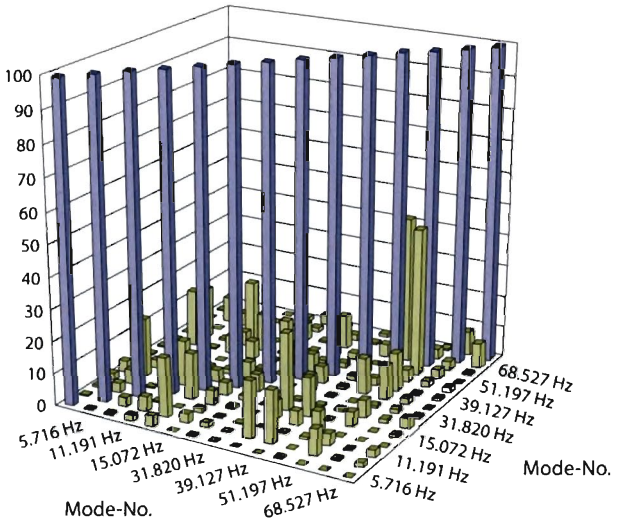
The evaluation of the acceleration measurements was carried out with LMS Test.Lab and the application OMA "Operational Modal Analysis" was used. For the calculation of the stable poles all cross power spectra of the respective measurement-configurations were selected and the LMS Test.Lab add-in "Operational Polymax" was used. Stable poles were calculated in the range from 0 to 80 Hz, see F.8-26.

During the evaluation of modal analysis results of systems with blocked hangers and systems with operating (unblocked) hangers not only the frequency shift, but also the characteristics of pole stabilization diagrams and the correlations were investigated. The differences in case of blocked hanger H5 are visible in the pole diagrams, in the correlation and in the frequency shift, see F.8-27 and T.8-5. The natural frequency of 5.9 Hz disappears, a natural frequency of 8.0 Hz appears within the low frequency domain.

At 13.2 Hz a bad correlation is given between the modes of the corresponding natural frequencies. In the case of two blocked hangers a natural frequency-shift of 1.1 Hz from

Natural frequencies of the system with damping values and MAC-matrix F.8-26

Natural frequency [Hz]	5.7	8.2	11.2	13.2	15.1	22.6	31.8	34.6	39.1	49.4	51.2	54.8	68.5	75.4
Damping [%]	1.2	1.1	0.5	0.8	0.7	0.3	0.3	0.3	0.2	0.2	0.1	0.2	0.1	0.1



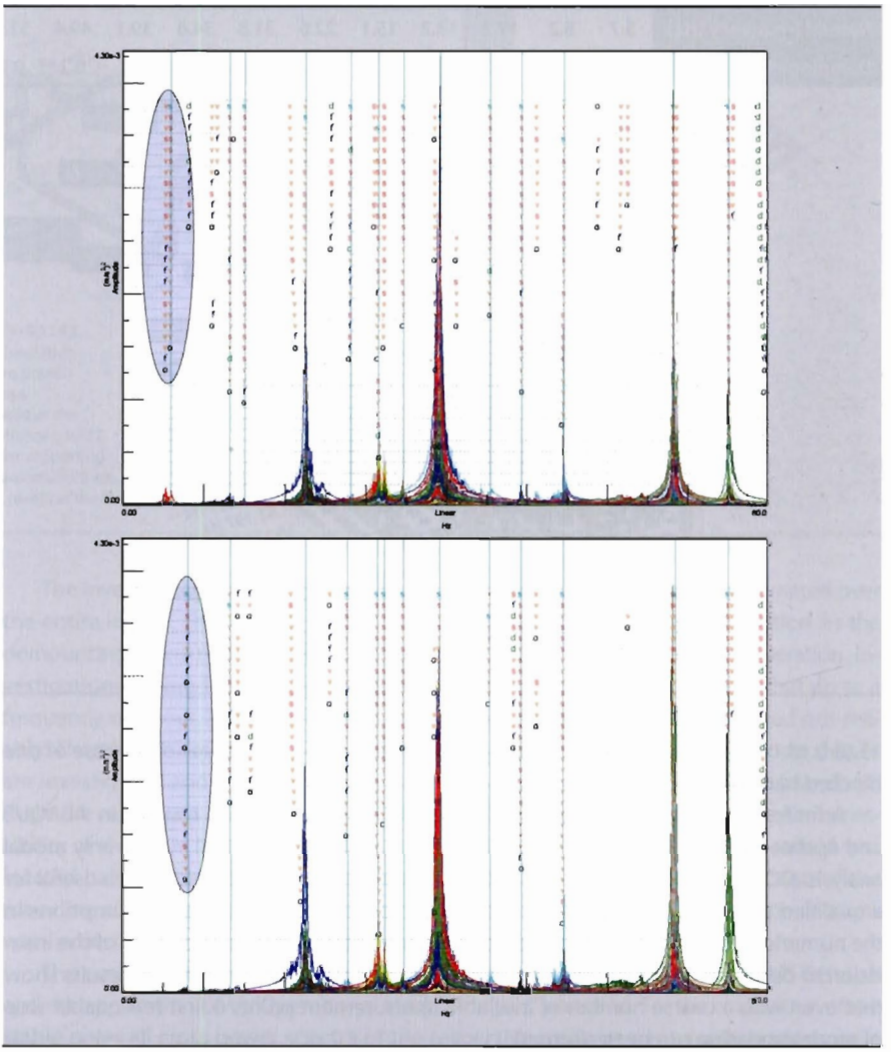
15.0 Hz to 16.1 Hz can be observed in addition to the monitored differences in case of one blocked hanger.

A finite element model, consisting of ELBOW31 elements, was created in ABAQUS and updated with FEM tools, to match the results of the experimental output only modal analysis (OOMA). A higher amount of points of measurements would have been useful for a qualified model updating procedure, because there are a lot of rough assumptions in the numerical model. The agreement, achieved by updating the mass density of the insulation to determine a reasonable mass distribution, is shown in T.8-6. These results show that even with a coarse number of available measurement points a first reasonable step of model-updating can be performed.

Difference in natural frequencies and MAC values with and without blocked spring-hanger T.8-5

No. of mode	Conf. IV [Hz]	H5 blocked Conf. IVb [Hz]	MAC [%]
1	5.9	–	no correlation
2	–	8.0	no correlation
3	13.2	13.3	51.9
4	15.0	–	no correlation
5	22.5	22.6	99.3

Pole diagrams (0–80 Hz), no hanger blocked (above), hanger H5 blocked (below) F.8-27



Comparison of updated FE model with measurement results T.8-6

Paired mode no.	Updated model		Measurement		Difference [%]	MAC [%]
	Mode	Frequency [Hz]	Mode	Frequency [Hz]		
1	6	6.4	1	5.7	12.0	88.0
2	12	11.7	3	11.2	4.2	79.9
3	14	13.7	4	13.2	4.0	71.8
4	20	18.3	5	15.1	21.6	99.2
5	25	23.0	6	22.6	1.6	98.5
Average [%]					8.7	87.5

8-5 Conclusion

Safe operation, availability and lifetime assessment of piping are of utmost concern for chemical plants. The investigated piping reactor is supported by a tall structure fixed at the base. As a result, the steel building stiffness decreases with height. Furthermore large piping-elbow forces act at the top of the building, which leads to large vibration amplitudes in the vicinity of 10 Hz where coupled piping-building resonance excitations occur due to plugs running through the line. Since both piping system and supporting structure exhibited these large vibration amplitudes, dampers or shock absorbers placed between them would prove less effective.

Therefore, a special vibration absorber was developed for such piping systems. This special vibration absorber for piping consists of a cantilever beam with a concentrated mass at the end, vibrating in a cylinder. The vibrations are damped by a special fluid within the cylinder. The bending eigenfrequency of the cantilever beam depends on the stiffness of the member which in turn depends on the free and vibrating length L of the TMD. For tuning purposes this length is adjustable. The absorber can be attached to the pipe in various positions and the direction of the absorber vibration adapts itself to the motion of the pipe. A prototype of this vibration absorber was tested at the laboratory of MPA Stuttgart with success. Root cause analysis of the large vibrations at the piping reactor such as thorough measurement campaigns and detailed FE models updated by operational modal analysis data brought about a system-identification and an understanding of the resonance effect. On this basis a reasonable design for two vibration absorbers connected to the piping in the upper part of the structure was found.

The load bearing behaviour of a laboratory piping system with a branch containing an elbow with local wall thinning (thickness reduced by 70 % at the intrados) was investigated. System identification by means of experimental modal analysis and model-updating is still a challenge, if one of the objectives is to detect local flaws. Model-updating of the FE model by adjusting support stiffness led to very good agreement between measured and calculated modal characteristics. Due to local wall thinning, the location of damage changed from crown to intrados. Numerical investigation of the influence of the local wall thinning at the intrados on the modal characteristics showed small changes in eigenfrequencies (largest change is 1.3 % at the first vertical eigenfrequency), while the change in mode shapes was very small except for a few modes of higher order. Afterwards the system was subjected to a simulation of in-plane bending caused by earthquake loading to test the safety margin of the system with the wall thinned elbow. No damage occurred in the wall thinned elbow of the branch. Subsequently sinusoidal shaker excitation was carried out in the natural frequency of the first vertical mode leading to a fatigue crack at the pre-calculated position (circumferential, in the wall thinned area of the intrados).

For piping in conventional power plants it is very difficult to achieve a good agreement between numerical and experimental modal analysis, because of the model size, difficult boundary conditions, and non-linearities like stick-slip effects due to friction. Amplitude dependent vibration behaviour might be present. Reasonable model-updating results could be achieved regarding the mass distribution in respect to the density of the insulation even with a coarse number of available measurement points. System changes

due to one blocked hanger could be reflected in different pole stabilization-diagrams of OOMA, in the correlations by means of the MAC values and in one case in a clear frequency shift (blocking of two hangers).

Acknowledgements

This work was performed with support from the EU (European Union) in the framework of the Large Collaborative Research Project IRIS (Integrated European Industrial Risk Reduction System, CP-IP 213968-2) in work package WP2.

References

Ahn, S.-H., Nam, K.-W., Yoo, Y.-S., Ando, K., Ji, S.-H., Ishiwata, M. and Hasegawa, K., 2002. *Fracture Behavior of Straight Pipe and Elbow with Local Wall Thinning*. Nuclear Engineering and Design 211.

Bachmann, H. and Ammann, W., 1987. *Schwingungsprobleme bei Bauwerken – durch Menschen und Maschinen induzierte Schwingungen*. Series Structural Engineering Documents 3d, 193 pp., International Association for Bridge and Structural Engineering (IABSE), Zurich, ISBN 3-8574-8051-3.

Barutzki, F., 2009. *Reduzierung von Rohrleitungsschwingungen mittels Schwingungsdämpfern*. 24th FDBR-Fachtagung Rohrleitungstechnik on 24 and 25 March 2009, Magdeburg.

Diem, H., 1994. *Untersuchung zum Geometrieeinfluss auf das Verformungs- und Versagensverhalten von Rohrbogen*. Techn.-Wiss. Ber. MPA Stuttgart.

Dooley, R. B. and Chexal, V. K., 2000. *Flow-Accelerated Corrosion of Pressure Vessels in Fossil Plants*. International Journal of Pressure Vessels and Piping 77.

Dwenger, F., 2011. *Systemidentifikation und Zustandsanalyse einer Rohrleitung in einem Kohlekraftwerk auf der Basis gemessener Schwingungen*. Studienarbeit, Institut für Materialprüfung, Werkstuffkunde und Festigkeitslehre, Universität Stuttgart.

Farrar, C. R. and Worden, K., 2013. *Structural Health Monitoring: A Machine Learning Perspective*. John Wiley & Sons, Ltd, Chichester.

Hasegawa, K., Meshii, T. and Scarth, D. A., 2011. *Assessment of Piping Field Failures and Burst Tests on Carbon Steel Pipes With Local Wall Thinning Using ASME Section XI Code Case N-597-2*. Journal of Pressure Vessel Technology 133(3).

Gurr-Beyer, C., Heiland, D., Jaquet, T. and Flöttmann, H., 2003. *Vibration Maps – Qualitätssicherung in schwingungsempfindlichen Produktionsstätten*. VDI-Tagung „Baudynamik" Kassel 2003, VDI-Bericht Nr. 1754.

Hinz, G. and Kerkhof, K., 2013. *System Identification and Reduction of Vibrations of Piping in Different Conditions*. ASME 2013 Pressure Vessels & Piping Division, K-PVP Conference, to be published.

IRIS, 2012. Large Collaborative Research Project IRIS (Integrated European Industrial Risk Reduction System, FP7-CP-IP 213968-2), European Union, 2008–2012.

Kerkhof, K. et al., 2001. *Integrity of Safety-relevant Piping by means of Vibration Analysis*. Phase II, German Reactor Safety Research - Project No. 150 1062.

Kim, J., Na, M. and Park, C.-Y., 2008. *Effect of Local Wall Thinning on the Collapse Behavior of Pipe Elbows Subjected to a Combined Internal Pressure and In-Plane Bending Load*. Nuclear Engineering and Design 238:1275–1285.

Kim, J., Na, Y.-S. and Lee, S.-H., 2009b. *Experimental Evaluation of the Bending Load Effect on the Failure Pressure of Wall-Thinned Elbows*. Journal of Pressure Vessel Technology 131(3).

Kim, J., Weon and Park, C.Y., 2003. *Criterion for Failure of Internally Wall Thinned Pipe under a Combined Pressure and Bending Moment*. Transactions of the 17th International Conference on Structural Mechanics in Reactor Technology (SMiRT 17) Prague, Czech Republic.

Kim, J.W., Lee, S.H. and Park, C.-Y, 2009a. *Experimental Evaluation of the Effect of Local Wall Thinning on the Failure Pressure of Elbows*. Nuclear Engineering and Design 239:2737–2746.

Kim, Y.-J., Kim, J., Ahn, J., Hong, S.-P. and Park, C.-Y., 2008. *Effects of Local Wall Thinning on Plastic Limit Loads of Elbows using Geometrically Linear FE Limit Analyses*. Engineering Fracture Mechanics 75.

Kima, J.W. and Park, C.-Y., 2003. *Effect of Length of Thinning Area on the Failure Behaviour of Carbon Steel Pipe Containing a Defect of Wall Thinning*. Nuclear Engineering and Design 220(3).

Kussmaul, K. and Kerkhof, K., 1998. *Realistic Boundary Conditions Determined by Ambient Vibration Analysis and Model-Updating*. ASME/JSME Joint Pressure Vessels and Piping Conference, San Diego, July.

Mattheis, A., Trobitz, M., Kussmaul, K., Kerkhof, K., Bonn, R. and Beyer, K.-H., 2000. *Diagnostics of Piping by Ambient Vibration Analysis*. Nuclear Engineering and Design, Elsevier, 198 (2000):131–140.

Meinhardt, D., Dressen, O. and Dalmer, F., 2008. *Increase of the Structural Damping due to the Application of Tuned Mass Dampers TMD Subject to the Footbridge Construction*. Third International Conference, Footbridge.

Michel, F., Reck, H. and Schulz, H., 2001. *Experience with Piping in German NPPs with Respect to Ageing-Related Aspects*. Nuclear Engineering and Design 207.

Nakamura, I., Otani, A. and Shiratori, M., 2010. *Comparison of Failure Modes of Piping Systems with Wall Thinning Subjected to In-Plane, Out-of-Plane, and Mixed Mode Bending Under Seismic Load: An Experimental Approach*. Journal of Pressure Vessel Technology 132(3).

Namita, Y., Suzuki, K., Abe, H. and Ichihashi, I., 2003. *Seismic Proving Test of Eroded Piping: Status of Eroded Piping Component and System Test*. ASME Pressure Vessels and Piping Conference, , paper PVP 2003–2097.

NISA, 2005. *Secondary Piping Rupture Accident at Mihama Power Station, Unit 3, of the Kansai Electric Power Co., Inc. (Final Report)*. The Nuclear and Industrial Safety Agency, March 30.

Oh, C.-S., Kim, Y.-J. and Park, C.-Y., 2007. *Plastic Loads of Elbows with Local Wall Thinning under In-Plane Bending*. International Journal of Fracture 145(1).

Oyamada, K., Konosu, S. and Ohno, T., 2012. *Development of a Plastic Collapse Assessment Procedure in the P–M Diagram Method for Pipe Bends with a Local Thin Area under Com-*

bined Internal Pressure and External In-Plane Bending Moment. Nuclear Engineering and Design 247:42–57.

Safepipes, 2008. *European Union Research Project SAFEPIPES (Safety Assessment and Lifetime Management of Industrial Piping Systems)*. FP6-STRP-013898, European Union, 2005–2008.

Schmidt, R. A., Wilkowski, G. M. and Mayfield, M. E., 1991. *The International Piping Integrity Research Group IPIRG Program: An Overview*. SMiRT 11 Transactions.

Takahashi, K., Watanabe, S., Ando, K., Urabe, Y., Hidaka, A., Hisatsune, M. and Miyazaki, K., 2009. *Low Cycle Fatigue Behaviors of Elbow Pipe with Local Wall Thinning*. Nuclear Engineering and Design 239.

Takahashi, K., Tsunoi, S., Hara, T., Ueno, T., Mikami, A., Takada, H., Ando, K. and Shiratori, M., 2010. *Experimental Study of Low-Cycle Fatigue of Pipe Elbows with Local Wall Thinning and Life Estimation Using Finite Element Analysis*. International Journal of Pressure Vessels and Piping 87:211–219.

Ting, K. and Ma, Y. P., 1999. *The Evaluation of Erosion-Corrosion Problems of Carbon Steel Piping in Taiwan PWR Nuclear Power Plant Nuclear Engineering and Design 191*.

VDI, 2009. *Guideline VDI 3833 Part 1 and 2: Dynamic Damper and Dynamic Vibration Absorber*.

9

Seepage and Slope Stability of Chinese Hydropower Dams

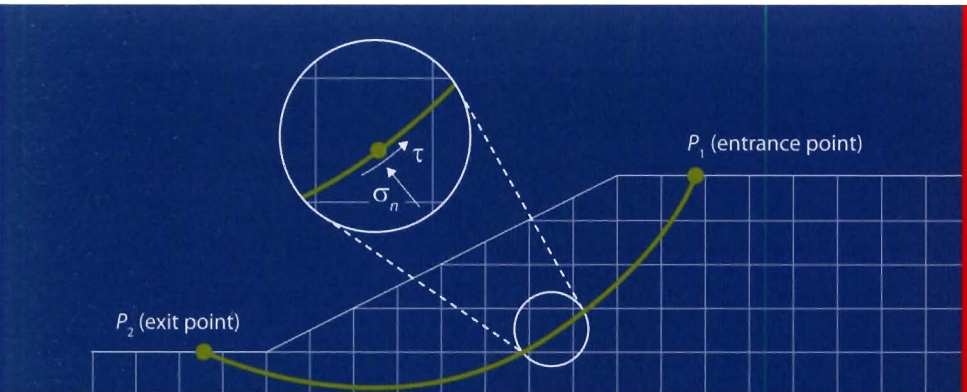
Author:
Mengxi Wu

Motivation

Hydropower dams are growing bigger and are placed in regions with high natural disaster probabilities. Knowledge on seepage and slope stability of these structures is desirable.

Main Results

A software tool to compute seepage stimulations and slope stability analysis has been created and applied to a number of examples of Chinese hydropower dams.



9-1 Problem Statement

Seepage simulation and slope stability analysis are steps necessary in the risk analysis procedures of embankment dams, nature and engineering slopes. As part of the work in WP4, our research is mainly focused on improving the numerical methodology of seepage and slope stability analysis.

Catastrophic failures of embankment dams can occur as a result of subsurface erosion. They are likely to occur without any apparent warning, at full reservoir, sometimes many years after the reservoir has been put into operation. The erosion may start at springs feed by seepage and proceed insidiously upstream toward the reservoir, following lines of least resistance along foundation slabs, conduits, or irregularities in the bedrock, or it may develop entirely in the subsoil in a pattern that depends on unknown details of the stratification. When the erosion channel reaches the reservoir it enlarges rapidly; the release of water may destroy the dam and its foundation and devastate the valley downstream. Failure of a dam by subsurface erosion thus ranks among the most serious accidents in civil engineering.

Internal erosion within the body of zoned embankment dams may also have serious consequences. The water retaining element or core of such dams, usually consisting of clay or other relatively impervious soils, may develop cracks as a result of differential settlements or other causes, may not be sealed tightly against the foundation or abutments, or under the influence of seepage pressures may tend to migrate, particle by particle, into the coarser shell materials intended to support the core. The loss of core material by migration or erosion may result in sinkholes, in weakening and dislocation of the fill material, and sometimes in a breakthrough to the reservoir. If this occurs, the results can be as catastrophic as those of subsurface erosion.

The occurrence of sliding failures in embankments and excavated slopes is common. Collapses in these cases often bring serious consequences to both life and property. The risks involved justify the need to adequately assess and assure safety. The choice of suitable methods of safety analysis is important. Limit equilibrium methods provide a powerful means of evaluating safety. The calculation of stresses of the conventional limit equilibrium methods is based on slices. The assumptions about the distribution of stresses between slices have to be made in those methods. The impact of seepage on the effective stresses of a slope with complicated underground flow situations can hardly be evaluated reliably by these methods. It is obvious that stresses from methods of slices may not agree with actual soil stresses in an unacceptably large extent in many situations, such as rock fill dams, and their foundations, river and water reservoir banks, and many nature and engineering slopes in rainy seasons. Meaningful stability analysis can be made only if the stress distribution within the structure can be predicted reliably [Clough and Woodward, 1967].

In this report, a finite element algorithm for variably saturated flow and a modified gradient procedure for slope stability based on a finite element stress analysis are presented.

9-2 Numerical Method for Seepage Simulation and Slope Stability Analysis

9-2-1 A Finite-Element Algorithm for Modelling Variably Saturated Flows

The standard approach to model variably saturated flow is through the use of numerical solution to Richards' equation (RE). This report provides a general, mass-conservative and computationally efficient multi-dimensional finite element algorithm for modeling variably saturated seepage [Wu, 2010; Wu et al., 2013]. Water flowing through porous media is described by the Darcy equation written in the form:

$$q_i = -h_{,j} k_r(s) K_{ij} = -(\psi + z)_{,j} k_r(s) K_{ij} \qquad \text{E.9-1}$$

According to the mass conservative principle and E.9-1, Richards' equation (1931) governing saturated-unsaturated flows in porous media can be deduced as:

$$[-(\psi + z)]_{,j} k_r(\psi) K_{ij}]_{,j} + \varepsilon \frac{\partial s(\psi)}{\partial t} = Q \qquad \text{E.9-2}$$

In E.9-1 and E.9-2, q is the Darcy flux vector, $k_r(s)$ or $k_r(\psi)$ is the relative conductivity, K is the tensor of permeability for saturated media, h is the hydraulic head, ψ is the pressure head, z is the elevation above a reference datum, ε is the porosity and Q is the source/sink term. The subscripts i,j = 1,...,D are spatial indices of the Cartesian coordinates, and D denotes the number of spatial dimension (2 or 3). Note that the summation convention is used for repeated indices. Van Genuchten's (VG) equation [Van Genuchten, 1980] for the soil water retention curve and Mualem's [Mualem, 1976] unsaturated relative permeability function are used to describe the soil properties. The relationship between saturation and pressure head is given by:

$$s_e(\psi) = \frac{s(\psi) - s_r}{1 - s_r} = \begin{cases} (1 + |\alpha\psi|^n)^{-m}, & \psi < 0 \\ 1, & \psi \geq 0 \end{cases} \qquad \text{E.9-3}$$

Where s_e is the effective saturation, s is the saturation, s_r is the residual saturation, α is a parameter related to the mean pore size, n a parameter related to the uniformity of the size distribution and $m = 1 - 1/n$. Based on Mualem's [Mualem, 1976] model, the relationship between effective saturation and relative permeability is given by :

$$k_r(s_e) = s_e^{1/2}[1 - (1 - s_e^{1/m})^m]^2 \qquad \text{E.9-4}$$

The finite element algorithm for E.9-2 given by [Wu, 2010] is:

$$[K_{IJ}(\psi) + O_{IJ}(\psi)] \cdot \psi_J^n = F_I(\psi) + \tilde{O}_{IJ}(\psi) \cdot \psi_J^{n-1} - K_{IJ}(\psi) \cdot z_J \qquad \text{E.9-5}$$

Where:

$$K_{ij}(\psi) = \sum_e \int_{\Omega_e} N_{I,i} k_r(\psi^{n,m-1}) K_{ij} N_{J,j} d\Omega \qquad \text{E.9-6}$$

$$O_{ij}(\psi) = \sum_e \int_{\Omega_e} \frac{1}{l} \frac{\bar{C}(\psi^{n,m-1})}{\Delta t} \beta(\psi^{n,m-1}) \delta_{ij} d\Omega \qquad \text{E.9-7}$$

$$\tilde{O}_{ij}(\psi) = \sum_e \int_{\Omega_e} \frac{1}{l} \frac{\bar{C}(\psi^{n,m-1})}{\Delta t} \beta(\psi^{n-1}) \delta_{ij} d\Omega \qquad \text{E.9-8}$$

$$F_I(\psi) = \oint_L -q_n N_I dL + \sum_e \int_{\Omega_e} Q N_I d\Omega \qquad \text{E.9-9}$$

In E.9-7 and E.9-8:

$$\beta(\psi) = \begin{cases} 1, & \psi \geq 0 \\ 0, & \psi < 0 \end{cases} \qquad \text{E.9-10}$$

$$\bar{C}(\psi^n) = \begin{cases} \dfrac{\theta(\psi^n) - \theta(\psi^{n-1})}{\beta(\psi^n) \cdot \psi^{n,m-1} - \beta(\psi^{n-1}) \cdot \psi^{n-1}}, & \left| \beta(\psi^n) \cdot \psi^n - \beta(\psi^{n-1}) \cdot \psi^{n-1} \right| \geq 0.01 \\ \dfrac{\theta(\psi^n) - \theta(\psi^n - 0.01)}{0.01}, & \left| \beta(\psi^n) \cdot \psi^n - \beta(\psi^{n-1}) \cdot \psi^{n-1} \right| < 0.01 \end{cases} \qquad \text{E.9-11}$$

In these finite element equations, I is the node number of an element, δ_{ij} is the Kronecker delta. N is the nodal basis shape function of an element and I or *J* is the serial number of a node in the element, *n* is the iterative step of the time *t*, *m* is the iterative step for solving the seepage field at the time t^n.

Dirichlet, Neumann, and seepage-face boundaries are considered. Dirichlet nodes, where the pressure heads are known, are described by:

$$\psi_I = {}^t\psi_I \qquad \text{E.9-12}$$

where ${}^t\psi_I$ are the known pressure heads at the node I. The I-th equation in E.9-5 is substituted by E.9-12 directly.

Neumann boundaries which are also named as flux boundaries, are treated in E.9-5. If the soil of the elements related to a flux boundary is unsaturated and extremely dry, and the flux is relatively larger than the moisture conductivity, convergence difficulties may arise. Under these situations, the conductivity of the elements related to the boundary nodes is small and unable to transmit the water away quickly from the boundary node, resulting in a very large hydraulic gradient and unphysical surface pressure head bounds. The way to alleviate this problem is to provide a proper feedback in the matrix to the flux to keep the result within the physical bounds [Zhang et al., 2002]. The convergence

problem is solved but error may occur when the simulated percolating flux is less than the actual flux. This error can be reduced by the thickness reduction of the boundary elements [Wu, 2010].

A seepage face is an external boundary of the saturated zone where water leaves the soil and the pressure head ψ equals the surrounding air pressure which is usually set to be zero. The mathematical expression of a seepage face is:

$$\begin{cases} \psi = 0 \\ q_n > 0 \end{cases} \quad \text{E.9-13}$$

where ψ is the pressure head, q_n is the Darcy's flux of a face.

The position of a seepage face is initially unknown and it constitutes a non-linear boundary condition. The adjustment procedures are applied during the iterative solution so that atmospheric pressure is maintained inside the seepage face, negative pressures are maintained outside the seepage face, and flux is directed outward across the seepage face [Cooley, 1983]. The nodes with a positive pressure should be changed as Dirichlet nodes with a zero pressure value, the prescribed seepage face nodes with a negative flux should be picked out and treated as nodes outside the seepage face in the next iteration [Wu and Gao, 1999]. The flux of nodes with zero values can be evaluated by:

$$Q_I = -K_{IJ} \cdot (\psi + z)_J \quad \text{E.9-14}$$

where Q_I is the flux at node I which may or may not be on the seepage face which is characterized by $\psi = 0$. If $Q_I > 0$, node I can be classified as a node on the seepage face, otherwise, it is classified as no-flow boundary node [Wu and Gao, 1999; Wu, 2010].

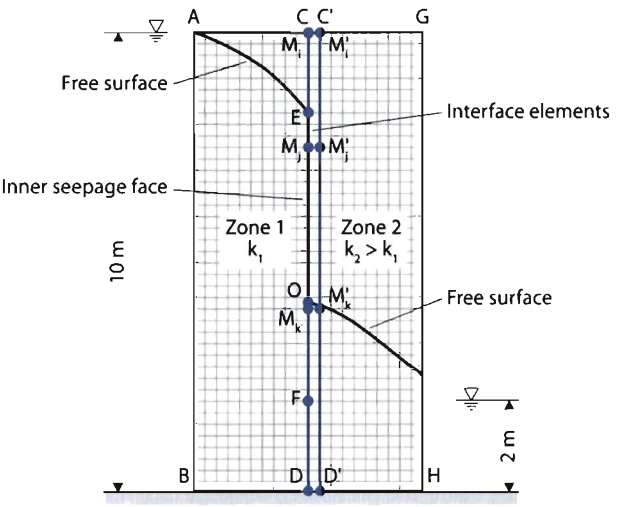
9-2-2 Simulation Procedure of an Inner Seepage Face in a Heterogeneous Field

As given by [Wu, 2013], an inner seepage face may appear at an interface of two materials inside the domain as shown in F.9-1. Because the seepage feature at the left side of Line EO in F.9-1 meets the condition of E.9-13, it can be named an inner seepage face. An inner seepage face is also a boundary between saturated and unsaturated areas like a free surface, with an essential feature difference that there is no flux flow out of a free surface in a saturated-only simulation, however, flux comes out of an inner seepage face and passes to the next zone. The mathematical expression of a free surface is given as:

$$\begin{cases} \psi = 0 \\ q_n = 0 \end{cases} \quad \text{E.9-15}$$

Experimental results show that there is no liquid flow from a porous material with a higher saturation to a coarser material with a larger saturated permeability in an unsaturated area [Wang et al., 2003]. This principle is widely accepted and has been applied

Schematic map of interface element and inner seepage face F.9-1



in the design of nuclear waste dumping engineering for decades. Thus, no water flows through line CE in F.9-1 but the unsaturated pressure from the left side to the right side alters sharply at the point on line CE.

An inner seepage face may appear while unconfined water flows from one porous media to another with a higher permeability. Both in a saturated-only analysis and in a variably saturated analysis, each node in the seepage face needs two numbers, one for the left area and another for the right area, because the pore pressure at the left side is zero and it is below zero at the right side. The elements located at the two sides of a seepage face are separated in this way and the flux flowing out of the left side is equal to the flux infiltrating into the right side. Although the inner seepage face EO in F.9-1 is located at the interface line CD, the range is unknown a priori, changing even with time in transient flow problems. It needs to be determined in the course of iteration. The elements along the material interface which may be within an inner seepage face or above it need to be separated by this way. Because of the difficulty to put two numbers to a node and separate the elements along an interface by a mesh tool, a layer of elements along the interface inside the porous media with the larger conductivity, elements in the rectangle CDD'C' as shown in F.9-1, are used as interface elements to separate the two areas. The range and flux of an inner seepage face need to be determined and the flux needs to be transmitted to the right side of the face.

Special treatment of the interface elements is needed in the numerical iteration process. All interface elements in the area CDD'C' as shown in F.9-1 are treated as ordinary elements as the others in the field in the first iteration step. In the following steps the seepage feature of an interface element can be identified by the pressure values of its nodes. An interface element in which more than a half nodes have a water pressure no less than zero is treated as an ordinary element which is below or crossing the free surface. These el-

ements need no special treatment. The other elements are on an inner seepage face or in an unsaturated area. These elements do not participate in the seepage coefficient tensor assemblage as expressed in E.9-5 at the next iteration step, thus separating the saturated and unsaturated area at the interface in the next iterative solution of the finite element equations. Nodes on the inner seepage face can be determined and their node flux can be obtained according to the procedure mentioned above. As shown in F.9-1, CE is a zero flux boundary, hence a node with a negative pressure needs no treatment for no water passes it to the downstream area. The EO is an inner seepage face boundary for zone 1 and the flux boundary for zone 2. The flux of a node on the inner seepage face needs to be added to the downstream area, e.g., the flux of node M_j adds to the opposite node M'_j therefore the mass conservation law is abided. The flux which flows through the boundary EO is so small that the flow situation from the left side to the right side of the line is similar to the infiltration of dry soil. The relative conductivity at a Gaussian integral point in the element with a small infiltration flux in the two consecutive iteration steps changes suddenly during the iteration and the ratio of the conductivity between neighbouring Gaussian points at the element may be up to several orders of magnitude. This may cause poor iterative efficiency and serious divergent problems. To avoid this situation the total flux flow out of the seepage face EO can add to a line $M_k M'_k$ which is proximal to the free surface at the downstream side.

All the undetermined boundary conditions including an inner seepage face condition are determined according to the pore water pressure obtained by the last iteration step in the course of the iteration. The procedure to deal with an inner seepage face problem is as follows:

1) An array should be set at first to store the node numbers of all nodes located at the interface and their attribute values, 1 for nodes below the seepage face which has a positive water pressure, 0 for nodes on the seepage face and –1 for nodes above the seepage face which has a negative pressure.
2) During the iteration, the fluxes of nodes on the seepage face need to be calculated according to E.9-12, the attribute values of those nodes which have a negative flux should be changed from 0 to –1 as a non-free surface node.
3) The attribute values of nodes with a positive pressure and –1 value need to be changed to 1 as a free surface node.
4) Interface elements where more than a half of the total element nodes are non-negative pore pressure nodes are marked as normal elements, non-normal elements do not participate in the seepage coefficient tensor assemblage at the next iteration step.
5) Nodes on the interface with 0 attribute value are treated as Dirichlet boundary nodes with 0 pore pressure and the flux of the nodes is added to downstream nodes as described in the previous paragraph.

9-2-3 A Modified Gradient Procedure for Locating the Critical Slip Surface Based on Finite Element Stress Analysis

The choice of suitable methods of safety analysis is important. The direct finite element method can obtain both the factor of safety and information about the collapse mechanism [Naylor, 1982]. It is, however, not easy to obtain a factor of safety accurately within the confidence limits as achieved by limit equilibrium methods. A fine mesh is required, a code capable of giving reliable results with the Mohr-Coulomb elastic-plastic model for loading states close to failure is needed, and finally it is usually necessary to carry out a set of analyses with load increased or the strength parameters c and $\tan\varphi$ reduced progressively by a factor which will become the factor of safety when failure is eventually reached. These analyses become progressively more expensive as the factor of safety is increased.

Limit equilibrium methods provide a powerful means of evaluating safety. The calculation of stresses of the conventional limit equilibrium methods is based on slices. The assumptions about the distribution of stresses between slices have to be made by those methods. The impact of seepage on the effective stresses of a slope with complicated underground flow situations is difficult to be evaluated reliably by these methods. It is obvious that stresses from methods of slices may not agree with the actual ones in an unacceptably large extent in many situations, such as rock fill dams, foundations, river and water reservoir banks, and many slopes in rainy seasons. Meaningful stability analysis can be made only if the stress distribution within the structure can be predicted reliably [Clough and Woodward, 1967].

The assumptions related to the inter slice force in limit equilibrium methods are unnecessary when a finite element stress analysis is used. Kulhawy [Kulhawy, 1969] developed a computer program to obtain an independent assessment of the normal and shear stresses along an assumed slip surface to calculate an overall factor of safety. Only one finite element analysis is required. The limit equilibrium methods based on finite element stresses analysis can be categorized as enhanced limit methods [Naylor, 1982]. They provide an alternative way for obtaining the factor of safety. A case study shows that factors of safety computed when using the enhanced limit method are generally slightly lower than those computed using conventional limit equilibrium methods of slices [Pham and Fredlund, 2003]. Assumptions regarding the uncertainty of the shape of the critical slip surface can be omitted when an appropriate optimization technique is introduced into the analysis [Pham and Fredlund, 2003].

Optimization techniques have been developed by several researchers for over three decades and have provided a variety of approaches to determine the shape and location of the critical slip surface. Generally, optimization algorithms can be divided into two basic classes: deterministic and heuristic algorithms. Deterministic methods [Baker, 1980; Baker and Garber, 1978; Bardet and Kapuskar, 1989; Celestino and Duncan, 1981; Chen and Shao, 1988; Nguyen, 1985; Menon et al., 2001] are based on the gradient information of the objective function and constraints, they may lead to a false critical slip surface due to the presence of several local minima points over the solution domain [Chen and Shao, 1988; McCombie and Wilkinson, 2002; Taha et al., 2010]. Heuristic approaches, including several algorithms such as genetic algorithms, simulated annealing, Tabu search,

ant colony optimization, and particle swarm optimization, use stochastic techniques and include randomness in moving from one solution to the next. They usually find a solution close to the best one, and they find it quickly and easily, but they do not guarantee that the best will be found; therefore, they may be considered as approximate and not accurate algorithms [Cheng and Lau, 2008]. In this report, an improved steepest descent procedure for slope stability based on a finite element stress analysis is presented.

Evaluation of the Safety Factor of a Specified Slip Surface Based on a Finite Element Stress Analysis

The factor of safety of a slip surface P_1P_2 in F.9-2, F, is defined as the ratio of the total restraining forces (shear strength) over total sliding forces (shear stress) along the slip surface:

$$F = \int_{\Gamma} \tau_f d\Gamma \Big/ \int_{\Gamma} \tau d\Gamma \qquad \text{E.9-16}$$

where Γ is the slip surface, τ_f and τ are the shear strength and the shear stress along the slip surface respectively, and $d\Gamma$ is an increment of length along the slip surface. The shear strength for a soil is given by the equation:

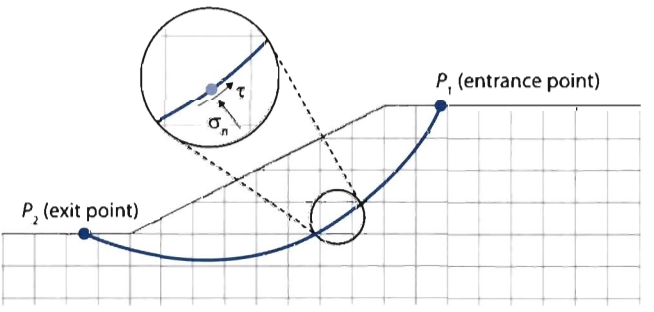
$$\tau_f = c + \sigma_n \tan\varphi \qquad \text{E.9-17}$$

Where c, φ is the cohesive and the internal friction angle of a soil, respectively, σ_n is the normal stress acting on the slip. As shown in F.9-2, the slip surface P_1P_2 is divided into many segments by the element mesh. The forces of each segment can be integrated by Gaussian numerical method through the calculation of stresses of integration points. The stress tensor of an integration point, σ_{ij}, is given by the equation:

$$\sigma_{ij} = (\sigma_{ij}^{node})_J N_J \qquad \text{E.9-18}$$

where (σ_{ij}^{node}) is the stress tensor at nodal point J in the element, which can be calculated from the stresses at Gaussian integration points of the element; the subscripts $i, j = 1,2,...,D$ are spatial indices of the Cartesian co-ordinates, and D denotes the number

Sketch of the calculation of the factor of safety of a slope F.9-2



of spatial dimension (2 or 3); N_J is the shape function of the point at nodal J of the element; summation convention is used for repeated indices. The shape function N can be calculated directly from the local coordinates which can be transformed from the global coordinates of the point according to the numerical inverse iso-parametric mapping method [Murti and Valliappan, 1986].

The stress vector of an integrated point at the slip surface, T_i, can be calculated from the stress tensor of the point as follows:

$$T_i = \sigma_{ij} n_j \qquad \text{E.9-19}$$

where n_j is the unit vector of the normal direction of the slip surface at the point. The normal and shear stresses of the point can be calculated as follows:

$$\sigma_n = T_i n_i \qquad \text{E.9-20}$$

$$\tau = T_i l_i \qquad \text{E.9-21}$$

where l_i is the unit vector of the tangent direction of the curve at the point. The total restraining or sliding force in E.9-16 is the sum of the force of all the curve segments. Thus the factor of safety of the slip surface can be obtained from E.9-16 ~ E.9-21.

Modified Gradient Method

Finding the critical slip surface related to the minimum factor of safety, F_{min}, involves a mathematical procedure for minimizing the factor of safety function $F(\boldsymbol{Z})$ of the slip surface expressed by a certain mathematical pattern and the vector $\boldsymbol{Z}(z_1, z_2, ..., z_n)$ formed by a set of geometric variables $(z_1, z_2, ..., z_n)$.

The search process starts from an initial slip surface $\boldsymbol{Z}^0(z_1^0, z_2^0, ..., z_n^0)$ and terminates at a location with the factor of safety F_{min}. Different choices of the initial slip surface will not affect the solution unless the problem exhibits multi-minima behaviour. The slip surface position with the minimum factor of safety locates at the range boundary of the vector Z or at a minimum point where the gradient vector G equals zero as stated as:

$$\boldsymbol{G}(F_{,1}, F_{,2}, ..., F_{,n}) = 0 \qquad \text{E.9-22}$$

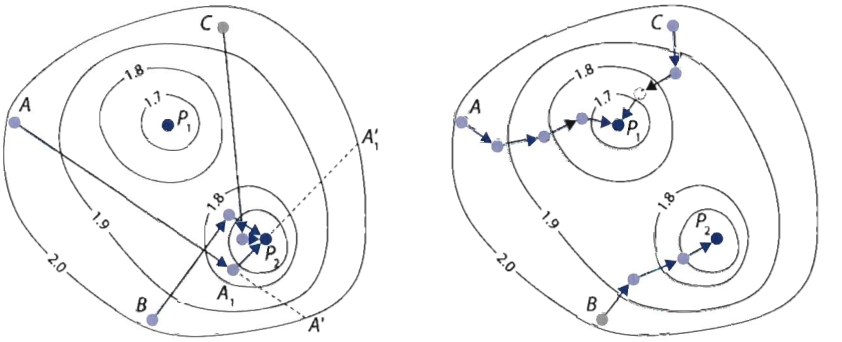
For the current step at iteration m with the slip surface $\boldsymbol{Z}^m$ moves to the next position $\boldsymbol{Z}^{m+1}$ with respect to a step coefficient α and a certain direction vector S, and it may be anticipated that the factor of safety at the new position will be smaller.

$$\boldsymbol{Z}^{m+1} = \boldsymbol{Z}^m + \alpha \boldsymbol{S}^m \qquad \text{E.9-23}$$

The steepest descent method defines the minimizing direction $\boldsymbol{S}$ as the negative of the gradient vector $\boldsymbol{G}$, that is:

$$\boldsymbol{S} = -\boldsymbol{G} = -(F_{,1}, F_{,2}, \ldots, F_{,n}) \qquad \text{E.9-24}$$

Sketch of the steepest descent search method: classic method (left) and modified method (right) F.9-3



In the classic method, the determination of the α value is through the solution of the following equation [Chen and Shao, 1988].

$$\frac{\partial F}{\partial \alpha} = \frac{\partial}{\partial \alpha}[F(\boldsymbol{Z}^m + \alpha \boldsymbol{S}^m)] = 0 \qquad \text{E.9-25}$$

A modified method is proposed in this study. A fixed small α value is used directly in E.9-23 other than to solve E.9-25 to find the minimum point along the direct vector in the whole domain. The value of the objective function will undergo a steady reduction along the negative gradient direction approximately as shown in F.9-3 (right). If the objective value of the tentative position is not decreased compared with the previous point, $F(\boldsymbol{Z}^{m+1}) \geq F(\boldsymbol{Z}^m)$, the function across the space of the search step must undergo a process of decreasing to increasing from $\boldsymbol{Z}^m$ to $\boldsymbol{Z}^{m+1}$, illustrated that there is a minimum in the range $[\boldsymbol{Z}^m, \boldsymbol{Z}^{m+1}]$ along the line. Single variable optimization can be used to determine the minimum point position and take this position as the new start in the next step. The minimum points P_1 and P_2 have been found out according to the modified method. The search point in the modified method moves forward approximately according to the steepest descent direction. Hence it is a veritable down-hill method. The contours information of the objective function can be figured out from a group of search routes, therefore the global minimum can be obtained.

Normalization of the domain of each variable to [0, 1] and normalization of the direction vector except when it is equal to zero can make the choice of the search step coefficient α easy and independent of the geometric size of the problem. Given the range of the control variable of the sliding surface z_i as $[z_i^{\min}, z_i^{\max}]$, the normalization equation of the variable is

$$\bar{z}_i = (z_i - z_i^{\min}) / (z_i^{\max} - z_i^{\min}) \qquad \text{E.9-26}$$

The tentative new slip surface position vector $\bar{\boldsymbol{Z}}^{m+1}$ based on the current step vector $\bar{\boldsymbol{Z}}^m$ is defined as

$$\bar{\boldsymbol{Z}}^{m+1} = \bar{\boldsymbol{Z}}^{m} + \alpha \bar{\boldsymbol{S}}^{m} \qquad \text{E.9-27}$$

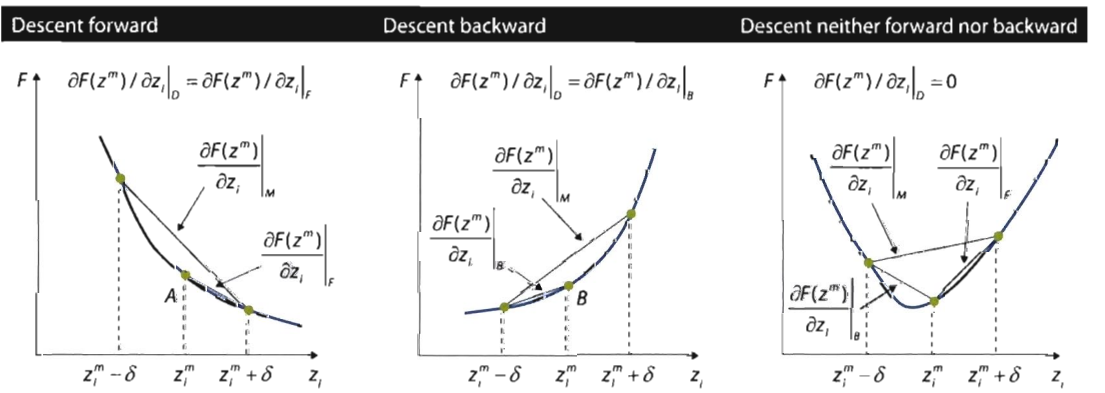
where $\bar{\boldsymbol{S}}^{m}$ is the normalized direction vector, $\bar{\boldsymbol{S}}^{m} = -\boldsymbol{G}^{m} / \left\| \boldsymbol{G}^{m} \right\|_2$.

If the direction vector is equal to zero ($\boldsymbol{S}^{m} = 0$) according to the descent difference scheme introduced in the next section, a minimum point must be located in the approximate δ neighbourhood of the point $\boldsymbol{Z}^{m}$. One dimensional optimization could be used for variable z_i, $i = 1,\ldots,n$, in interval $[\boldsymbol{Z}^{m} - \delta \boldsymbol{e}_i, \boldsymbol{Z}^{m} + \delta \boldsymbol{e}_i]$, the minimum location could be found after several times of the single variable optimization. In order to avoid that a search falls into a pit, the range of single variable optimization is recommended to broaden to $[\boldsymbol{Z}^{m} - \beta \boldsymbol{e}_i, \boldsymbol{Z}^{m} + \beta \boldsymbol{e}_i]$ (β equal to α is usually a good choice), if the minimum value is located outside the range $[\boldsymbol{Z}^{m} - \delta \boldsymbol{e}_i, \boldsymbol{Z}^{m} + \delta \boldsymbol{e}_i]$, the minimum in the δ neighbourhood of point $\boldsymbol{Z}^{m}$ is a local minimum which can be ignored and the search should continue with the new point.

Difference Scheme for the Partial Derivative of the Objective Function

It is generally recognized that either forward or backward difference is unfit for the calculation of the director vector, for the vector obtained via these methods may be the opposite direction of the actual descent direction near the extreme point [Chen, 2003; Zhu et al., 1984]. Central difference is generally used to calculate the vector. However, the direction vector calculated by the central difference scheme drifts off the true negative gradient at a point where the objective function is not linearly changed with the coordinate in the δ (δ is the difference step) neighbourhood of the point. The objective function is non-linear at areas where the contours of the function form a trench or at concave area where a minimum exists, the direction vector obtained differs from the steepest descent direction greatly. The search usually terminates at a point just close to the minimum, but not the exact position. The direction vector may even point to a rising direction and thus terminates the search process at a false minimum. A descent difference scheme is presented as shown in F.9-4. The descent difference value is equal to the forward difference at situation (left), equal to the backward difference at situation (middle), and is set to zero at situation (right). As a matter of fact, compared with the central difference, the descent

Sketch of the descent difference scheme: descent forward (left); descent backward (middle); descent neither forward nor backward (right) F.9-4



difference value is closer to the steepest descent direction of the function if the function is monotonous among the range $[\boldsymbol{Z}^m - \delta \boldsymbol{e}_i, \boldsymbol{Z}^m + \delta \boldsymbol{e}_i]$ as shown in F.9-4 (left) and (middle), where $\boldsymbol{e}_i$ is the unit vector along the coordinate axis i and δ is the difference step.

The descent difference scheme is given by the equation:

$$\partial F(z^m)/\partial z_i\Big|_D = \begin{cases} \partial F(z^m)/\partial z_i\Big|_F, F(\boldsymbol{Z}^m - \delta \boldsymbol{e}_i) > F(\boldsymbol{Z}^m) > F(\boldsymbol{Z}^m + \delta \boldsymbol{e}_i) \\ \partial F(z^m)/\partial z_i\Big|_B, F(\boldsymbol{Z}^m - \delta \boldsymbol{e}_i) < F(\boldsymbol{Z}^m) < F(\boldsymbol{Z}^m + \delta \boldsymbol{e}_i) \\ 0, F(\boldsymbol{Z}^m - \delta \boldsymbol{e}_i) \geq F(\boldsymbol{Z}^m) \leq F(\boldsymbol{Z}^m + \delta \boldsymbol{e}_i) \end{cases} \quad \text{E.9-28}$$

where, $\partial F(z^m)/\partial z_i\Big|_F$ and $\partial F(z^m)/\partial z_i\Big|_B$ are the forward and backward differences, respectively. They are calculated by the following formulae.

$$\partial F(z^m)/\partial z_i\Big|_F = [F(\boldsymbol{Z}^m + \delta \boldsymbol{e}_i) - F(\boldsymbol{Z}^m)]/\delta \quad \text{E.9-29}$$

$$\partial F(z^m)/\partial z_i\Big|_B = [F(\boldsymbol{Z}^m) - F(\boldsymbol{Z}^m - \delta \boldsymbol{e}_i)]/\delta \quad \text{E.9-30}$$

The calculation of the partial difference at point $\boldsymbol{Z}^m$ along the axis i starts with a guess of the descent direction. The descent direction of the last step is used as the guess. The value $F(\boldsymbol{Z}^m + \delta \boldsymbol{e}_i)$ at descent forward guess or $F(\boldsymbol{Z}^m - \delta \boldsymbol{e}_i)$ at descent backward guess is calculated. Then the actual descent direction can be checked via the comparison of the obtained value with $F(\boldsymbol{Z}^m)$. If the guess is right, the descent difference can be calculated like the last step, otherwise, the factor of safety of the point at the other side of $\boldsymbol{Z}^m$ along the axis should be calculated and the partial difference value can be calculated according to E.9-28. The number of times of the calculation of the factor of safety is $n+1$ in a moving step in case of right guess which is usually the situation while a small moving step coefficient is adopted, whereas the number in a central difference scheme is $2n+1$.

Error Estimation and Convergence Criterion

An error estimation is a necessary but often overlooked item in a non-linear optimization. As given by [Chen and Shao, 1988], the optimization terminates at the condition stated as:

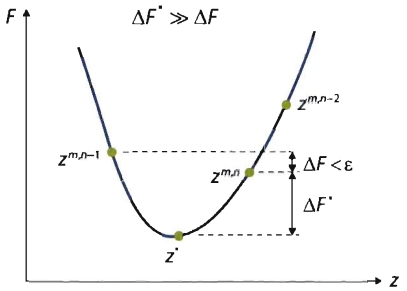
$$\left|F(\boldsymbol{Z}^m) - F(\boldsymbol{Z}^{m-1})\right| \leq \varepsilon \quad \text{E.9-31}$$

where, ε is a tiny value used to be taken as 1.0×10^{-5}. The actual deviation of the current factor of safety to the minimum values may be far greater than the given value, ε, $\Delta F^* \gg \Delta F$ as shown in F.9-5.

An error estimation formula and a new convergence criterion is given in this study. For the minimum value location problem in a given single minimum interval $[\boldsymbol{Z}^m, \boldsymbol{Z}^{m-1}]$, the gradient of the objective function is not increasing in the process of moving toward the minimum position $\boldsymbol{Z}^*$ from either side if the function is concave. That is:

$$\left|[F(\boldsymbol{Z}^{m,n}) - F(\boldsymbol{Z}^*)]/(\boldsymbol{Z}^{m,n} - \boldsymbol{Z}^*)\right| \leq \left|dF(\boldsymbol{Z}^{m,n})/d\boldsymbol{Z}\right| \quad \text{E.9-32}$$

Comparison of the true error with the difference of the two consecutive iterations F.9-5



During the searing process with the golden section method, the minimum point $\boldsymbol{Z}^*$ always lies between $[\boldsymbol{Z}^{m,n}, \boldsymbol{Z}^{m,n-1}]$, that means $\left|\boldsymbol{Z}^{m,n} - \boldsymbol{Z}^*\right| \le \left|\boldsymbol{Z}^{m,n} - \boldsymbol{Z}^{m,n-1}\right|$.

The error estimation formula is stated as:

$$\left|F(\boldsymbol{Z}^{m,n}) - F(\boldsymbol{Z}^*)\right| \le \left|\boldsymbol{Z}^{m,n} - \boldsymbol{Z}^{m,n-1}\right| \cdot \left|dF(\boldsymbol{Z}^{m,n}) / d\boldsymbol{Z}\right| \quad \text{E.9-33}$$

The sufficient condition to fulfill the error is less than ε and is given as:

$$\left|\boldsymbol{Z}^{m,n} - \boldsymbol{Z}^{m,n-1}\right| < \varepsilon / \left|dF(\boldsymbol{Z}^{m,n}) / d\boldsymbol{Z}\right| \quad \text{E.9-34}$$

E.9-34 is the new convergence criterion for one dimensional optimization or multivariable optimization along a line. The modified gradient method combined with the finite element stress analysis is effective to determine the accurate global minimum of a slope.

9-3 Application for Seepage Analysis of a Dam

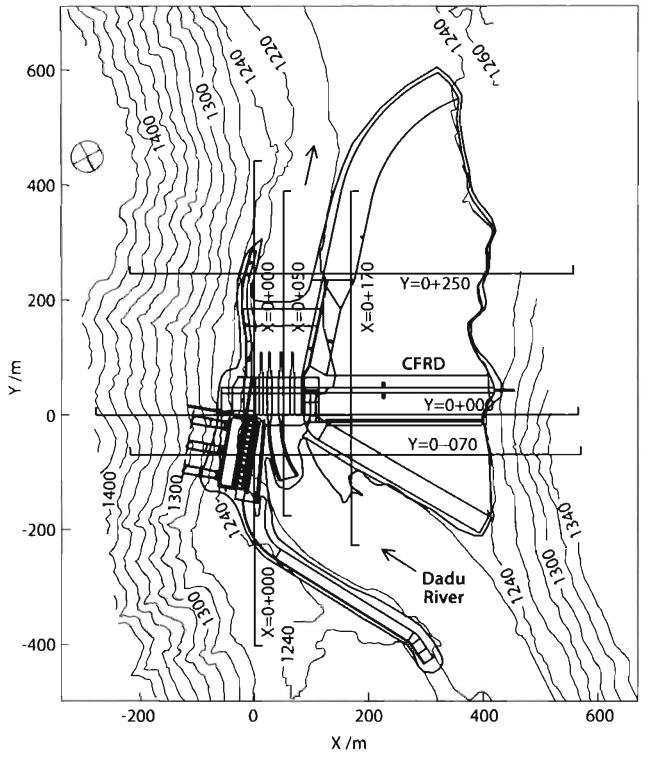
The example is the foundation of Ying-liang-bao gate dam which consists of five layers of sand or gravel soils with a total depth up to 126.5 m. The ratio of the conductivity between layers is up to 2 or 3 orders. Although the cross water head of the dam is only 30 metres, the subsoil of a scheme with a suspended cutoff wall is susceptible to internal erosion. Not only the erosion risk in the relatively impermeable layers is difficult to reduce via increasing the depth of a suspended cutoff wall, but also the risks in the soils beneath the suspended wall increase greatly and thus jeopardize the structure safety of the cutoff wall. The scheme with a closed cutoff wall is of course erosion safe, however the seepage gradient in the foundation soils is still very large. The erosion risk of the foundation is discussed. A scale reduced element is proposed to evaluate the appropriate position of the cutout boundary in the covering layers.

9-3-1 Seepage Analysis of a Gate Dam with a Layered Deep Deposit Foundation

Ying-liang-bao diversion type hydropower station in Lu-Ding county of Sichuan province, is the 13th step among the 22-step stations planned to be constructed in the Dadu River in southwest China. It is at the preliminary design stage. As shown in F.9-6, the dam mainly consists of a gate dam section and a concrete face rockfill dam (CFRD) section. The elevation of the crest and the bottom of the gate dam are 1248.5 m and 1216.0 m respectively. The normal reservoir water level is 1246.0 m and the ecological downstream water level is 1216.2 m, with a corresponding water head difference of 29.8 m.

Failure of a dam by subsurface erosion ranks among the most serious accidents in civil engineering. The main purpose of the seepage analysis of the foundation is to evaluate the feasibility of the proposed seepage control scheme to the risk of subsoil erosion, and if possible, to recommend a preferable scheme. Based on a 3D FEM model of the foundation, the steady seepage field of the dam foundation of the design scheme of an 80-metre-depth cutoff wall is evaluated and the corresponding erosion risk is analyzed. The effect of depth of the cutoff wall on the seepage field of foundation is also discussed.

The plane layout of the project F.9-6



Finite Element Model – Model Range and Permeability of Materials

The 3D FEM model of the foundation of the dam is shown in F.9-7. The top of the model is at Z = 1400 m, and the bottom is at Z = 1000 m. The left and the right side is at X = −400 m and X = 750 m respectively. The appropriate position of the upstream and downstream side of the model is difficult to define. Because the permeability of the bedrock is much less than the covering layers, the range of the model is large enough for the seepage analysis of the foundation even if the fluxes at all the rock cutoff boundaries are set to zero. However, the fluxes at the upstream and downstream side of the covering layers may have significant impact on the seepage field of the foundation. Here scale reduced elements [Wu et al., 2012] which can represent any desired width in a seepage cutoff boundary are used at both the upstream and downstream side of the model. Area of covering layers with gravel piles is equivalent to even continuum with an equivalent seepage tensor.

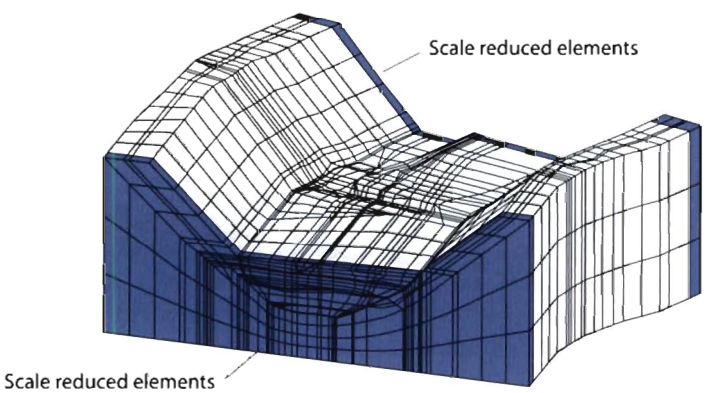
Seepage and Erosion Risk Analysis of the Foundation – Scheme with the Complete Cutoff Wall

F.9-8 is the hydraulic gradient contour at the typical cross section of the gate of the complete cutoff wall. Although the water gradient in the layer 4 and layer 2 adjacent to the upstream face of the cutoff wall is still large and exceeds the permissible value of the soils, the seepage direction points to the cutoff wall and the risk of erosion is low if the wall is not cracked here. The hydraulic gradient contour in layer 4 at the horizontal section beneath the gravel piles reduced to 17 % compared with the 80 m depth cutoff wall scheme. The gradients in the covering layers fall below the permissible value of the soils fundamentally. The complete cutoff wall scheme is recommended to be the preliminary design of the project.

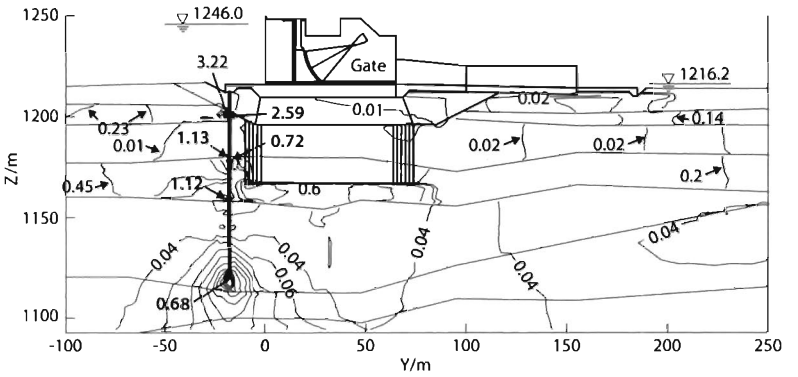
Conclusion

The appropriate position of the cutoff boundary of the covering layers is discussed and a scale reduced element is proposed to simulate different boundary positions. The appropriate position of the zero flux boundaries of the covering layers should be set far

Finite element model of the dam foundation F.9-7



Hydraulic gradient contour at the typical cross section of the gate of the complete cutoff wall F.9-8



away from the central part of the foundation in an object like the project. The risk of the internal or subsoil erosion of the foundation in the 80 m depth scheme is very high and it cannot be mitigated markedly by extending the depth of the partial cutoff wall, unless the covering layers are cut off completely by a closed cutoff wall. The scheme with a closed cutoff wall is recommended.

References

Baker, R. and Garber, M., 1978. *Theoretical Analysis of the Stability of Slopes*. Geotechnique 28:341–395.

Baker, R., 1980. *Determination of the Critical Slip Surface in Slope Stability Computations*. International Journal for Numerical and Analytical Methods in Geomechanics 4(4):333–359.

Bardet, J. and Kapuskar, M., 1989. *A Simplex Analysis of Stability*. Computers and Geotechnics 8(4):329–348.

Celestino, T. B. and Duncan, J. M., 1981. *Simplified Search for Noncircular Slip Surface*. Proceedings of the 10th International Conference on SMFE, 391–394.

Chen, Z. Y., 2003. *Soil Slope Stability Analysis – Theory Methods and Programs*. Beijing: China Water Power Press.

Chen, Z. Y. and Shao,C. M., 1988. *Evaluation of Minimum Factor of Safety in Slope Stability Analysis*. Canadian Geotechnical Journal 25(4):735–748.

Cheng, Y. M. and Lau, C. K., 2008. *Slope Stability Analysis and Stabilization [M]*. Routledge.

Clough, R. W. and Woodward, R. J. III, 1967. *Analysis of Embankment Stresses and Deformations*. Journal of the Soil Mechanics and Foundations Division, ASCE 93(SM4):529–549.

Cooley, R. L., 1983. *Some New Procedures for Numerical Solution of Variably Saturated Flow Problems*. Water Resources Research 19(5):1271–1285.

Kulhawy, F. H., 1969. *Finite Element Analysis of the Behaviour of Embankments*. PhD Thesis, University of California, Berkley, California, USA.

McCombie, P. and Wilkinson, P., 2002. *The Use of the Simple Genetic Algorithm in Finding the Critical Factor of Safety in Slope Stability Analysis*. Computers and Geotechnics 29(8):699–714.

Menon et al., 2001.

Mualem, Y., 1976. *A New Model for Predicting the Conductivity of Unsaturated Porous Media*. Water Resources Research 12:513–522.

Murti, V. and Valliappan, S., 1986. *Numerical Inverse Isoparametric Mapping in Remeshing and Nodal Quantity Contouring*. Computers & Structures 22(6):1011–1021.

Naylor, D. L., 1982. *Finite Elements and Slope Stability*. In Numerical Methods in Geomechanics, D. Reidel Publishing Company, J. B. Martins (eds), 229–244.

Nguyen, V. U, 1985. *Determination of Critical Slope Failure Surface*. J. Geotech. Eng., ASCE 111(2):238–250.

Pham, H. T. V. and Fredlund, D. G., 2003. *The Application of Dynamic Programming to Slope Stability Analysis*. Canadian Geotechnical Journal 40:830–847.

Richards, L. A., 1931. *Capillary Conduction of Liquids through Porous Mediums*. Physics 1: 318–333.

Taha., M. R., Khajehzadeh, M. and El-Shafie, A., 2010. *Slope Stability Assessment Using Optimization Techniques: an Overview*. Electronic Journal of Geotechnical Engineering 15(R):1901–1915.

Van Genuchten, M. Th., 1980. *A Closed-Form Equation for Predicting the Hydraulic Conductivity of Unsaturated Soils*. Soil Science Society of America Journal 44:892–898.

Wang, Z. M., Jiang, H., Yao, L., et al., 2003. *Qualitative Experiment of Unsaturated Water Vadose through Two-Layer Porous Media*. Radiat Prot 23(1):8–13.

Wu, M. X. and Gao, L. S., 1999. *Numerical Simulation of Saturated-Unsaturated Transient Flow in Soils*. Journal of Hydraulic Engineering (Chinese) 1999(12):38–42.

Wu, M. X., 2010. *A Finite-Element Algorithm for Modeling Variably Saturated Flows*. Journal of Hydrology, 394(3–4):315–323.

Wu, M. X., Yang, L. Z. and Hu, X. H., 2012. *Seepage Analysis of a Gate Dam with a Layered Deep Deposit Foundation*. Proceedings of the Third International Symposium on Life Cycle Civil Engineering, Hofburg Palace, Vienna, Austria, 3–6 October 2012.

Wu, M. X., Yang, L. Z. and Yu, T., 2013. *Simulation Procedure of Unconfined Seepage with an Inner Seepage Face in a Heterogeneous Field*. Science China Physics, Mechanics & Astronomy 56(6):1139–1147.

Zhang, X. X., Glyn Bengough, A., Crawford, J. W. and Young, I. M., 2002. *Efficient Methods for Solving Water Flow in Variably Saturated Soils under Prescribed Flux Infiltration*. Journal of Hydrology 260:75–87.

Zhu, B. F., Li, Z. M. and Zhang, B. C., 1984. *Principles and Applications of Optimal Structure Designing [M]*. Beijing: Water conservancy and electric power press.

10

Testing of Stiff Shear Walls

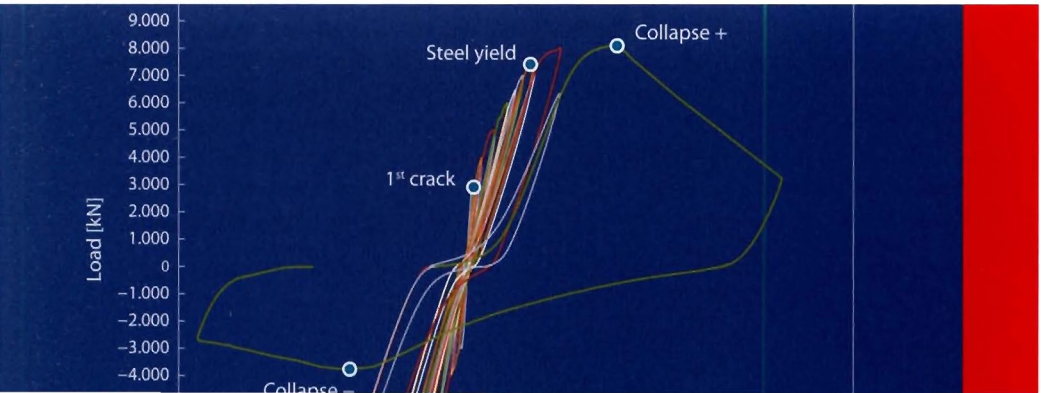
Authors:
Adrian Bekő
Peter Roško

Motivation

The scaling of specimens for laboratory testing limits the applicability of the test results. A full scale test of a reinforced concrete wall with a thickness of 40 cm was desired.

Main Results

Five specimens have been cast and tested at JRC in the ELSA laboratory in Ispra. For the first time a test on such a large specimen working in shear was realized. A prediction contest was organized and a wide participation in the tests was enabled. The data are made available for any future investigations.



10-1 Introduction

Reinforced concrete shear walls are frequently used in civil engineering as structural elements resisting horizontal forces in the plane of the wall. The stiffness of the shear wall has to keep drifts within reasonable limits. During recent earthquakes in the world many structures (among them also reinforced concrete walls) collapsed suddenly and led to catastrophic failures which occurred due to dynamic shear loading. Consequences of earthquakes have proven the need to study thoroughly the shear mechanism of reinforced concrete walls. Therefore the scientific research in this area is very intensive and has resulted in many experimental and numerical tests in the last years.

Because of the parameter variability, each experimental or numerical research is but a contribution to the knowledge base. The applicability of results is limited by the type of wall and parameter subspace. A number of failure modes can occur depending on parameters such as the type of cross-section, reinforcement detailing and quantities, properties of reinforcing steel, concrete compressive strength and boundary conditions. Complex destructive phenomena include concrete cracking, interaction effects between steel and concrete, steel yielding and concrete crushing in compression. It is not simple to generalize any given experimental or numerical test because of reasons mentioned above. When a test studies a specific type of structure and well defined loading, the outcome is of great interest.

Generally, shear walls are divided into two groups based on their geometry: high-rise or tall and low-rise or squat/short shear walls. High-rise shear walls are governed by flexural behaviour similar to a cantilever beam. The flexural behaviour of reinforced concrete walls has been examined and it is theoretically described (see historical references below or a more current one by [Orakcal et al., 2006]). The behaviour of low-rise shear walls is governed mainly by shear behaviour. Although there has been considerable activity directed towards low-rise shear walls this area of research is still in progress. One of the reasons is that low-rise shear walls are frequently used in nuclear power plants. Investigations presented here were focused on a low-rise wall specifically a more massive specimen which could be classified as a thick shear wall. Here we present the results of a joint research activity to study a full scale shear wall with a thickness of 400 mm.

Our research presented here builds on the contemporary knowledge in the field. Historical development of the research into reinforced concrete shear walls can be outlined by certain milestones.

Some of the first test results of low-rise shear walls under static loads are available in the literature of the fifties by [Galletly, 1952]. Advancing the subject were [Benjamin and Williams, 1957; 1960] with significant experimental research. During the 1960s most experimental research aimed at understanding the behaviour of reinforced concrete elements was directed towards moment resisting frames. Later in the 1970s the interest in the seismic behaviour grew and induced the experimental investigation of reinforced concrete walls. [Paulay, 1975] presented design aspects of shear walls for seismic areas. Studies of [Barda, 1972] led to the improved wall design provisions in ACI 318-71, including seismic requirements. Other wall tests of the decade were conducted by [Iliya and Bertero, 1980; Oesterle et al., 1976; 1979; Vallenas et al., 1979] and. In the coming years

shear walls were continued to be studied. [Maier and Thürlimann, 1985] analysed the behaviour of rectangular shear walls subjected to monotonic and cyclic loading. Walls with height to length ratios of 0.5 were subjected to static and cyclic tests by [Fouré, 1993]. [Rothe, 1992] tested the static monotonic, static cyclic, and dynamic behaviour of cantilever walls.

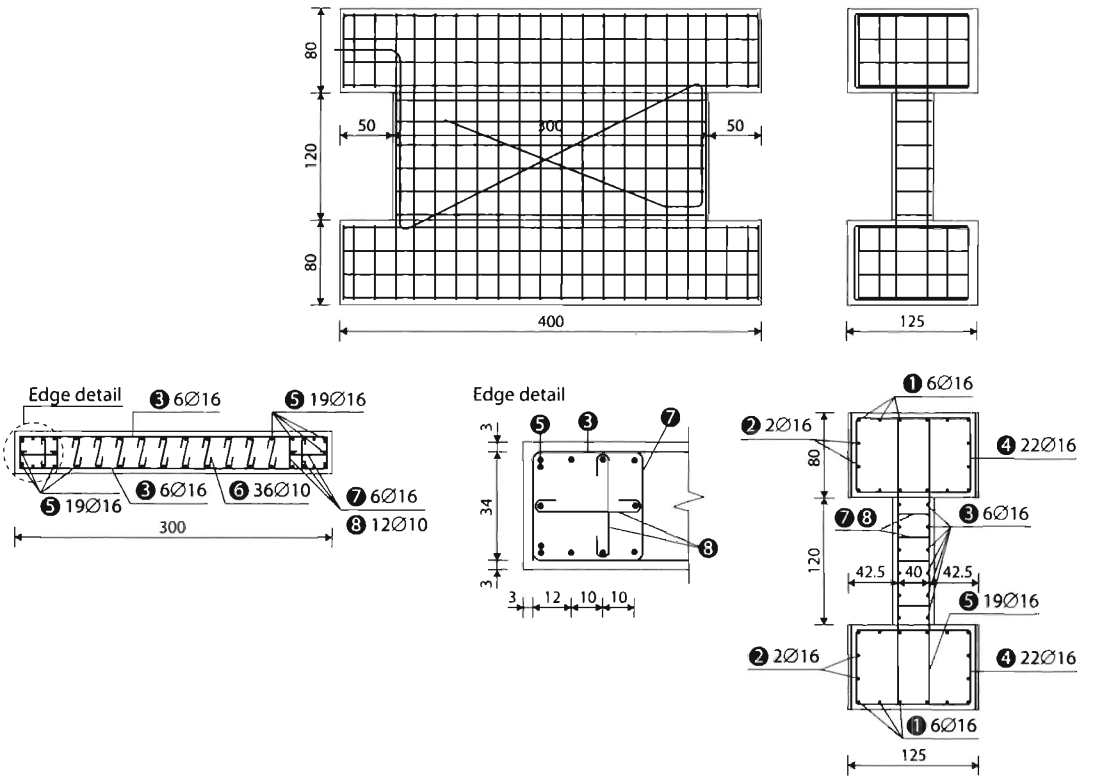
The last two decades produced some more interesting and valuable insight into the topic of shear walls. [Mo and Chan, 1996] tested the behaviour of reinforced-concrete-framed shear walls. Experimental shear-dominated response of reinforced shear walls with design implication was presented by [Lopes, 2001]. [Salonikios et al., 1999] carried out an experimental investigation of the validity of the design provisions of EC8 for walls of height to length ratios of 1.0 and 1.5. On the basis of experimental testing [Brun et al., 2003] presented a simple shear wall model with stiffness degradation. [Greifenhagen and Lestuzzi, 2005] reported static cyclic tests on lightly reinforced concrete shear walls. [Thomson et al., 2009] explained the pinching effect and damage of squat reinforced concrete shear walls. [Brun et al., 2011] carried out pseudo-dynamic tests on low-shear walls and proposed a simplified model based on the structural frequency drift.

The currently applicable codes treat the problem in a variety of ways. Some of the more modern codes like the [Eurocode 8, 2010] or the New Zealand code aim specifically at preventing shear failure by the use of capacity design. However, low-rise shear wall design with intended use in nuclear facilities where a shearing failure is the only mode is not addressed by the Eurocode. The design of RC shear walls in the US is governed by [ACI 318]. No special seismic provision for wall design was available in ACI 318 until the 1970s. Since then, significant changes have been implemented to improve the behaviour of structural walls under earthquake loading. For example, requirements for wall boundary regions were included for the first time in 1971 and seismic provisions for shear design were placed in 1983. The current ACI 318-11 provisions call for a displacement-based seismic design procedure, where the wall boundaries are designed and detailed to achieve the expected response of the structure in a ductile manner [Wallace, 1995]. The complementary code for nuclear facilities is the ACI 319 which follows the same design principles.

10-2 Experimental Testing of Shear Walls

The ability to accurately predict and model shear wall behaviour is of the utmost importance. The reason for testing the specimens to complete failure is that there is not much data on complete failure tests. As the intention was to investigate a more massive or so-called thick wall, experimental testing remains the only accurate means of assessment of shear response and capacity. The two main distinctive features of the tests were, first the thickness of the wall which was robust enough not to let the wall go into buckling and second the top of the wall was kept horizontal to load the wall predominantly in shear as much as it was possible to achieve (with corresponding axial load).

Designed reinforcement F.10-1



Concreted specimen and reinforcement with steel plates before concreting F.10-2



10-2-1 Specimen

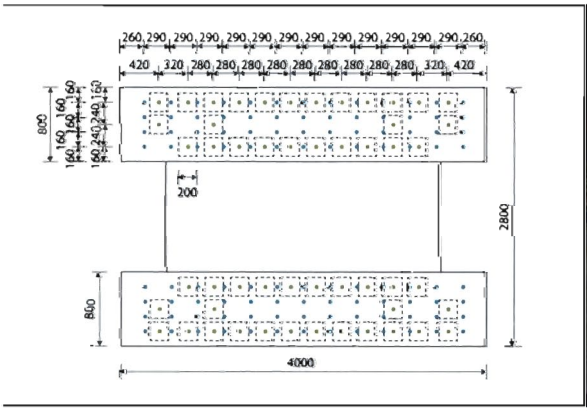
The specimens were designed and commissioned by VCE, the loading apparatus was designed by JRC in cooperation with VCE and commissioned by VCE. The lab tests were carried out by ELSA at JRC at their facilities in Ispra, Italy. The specimens were to be loaded by a cyclic quasi-static load regimen.

The reinforced concrete specimen comprises three main parts. The actual wall part which is 3 m long, 1.2 m high and 0.4 m thick is lined with two beams at the bottom and the top with a cross section of 0.8 × 0.8 m. The beams are cantilevered 0.5 m on either side of the wall which results in the 4.0 m total length of the specimen. A design of the reinforcements and principal dimensions are shown in F.10-1. The actual execution of the elements can be seen in F.10-2. The middle part of the specimen classifies as a rectangular wall without boundary elements. With an aspect ratio of 0.4 it also classifies as a short wall.

The reinforcement was designed to support the type of loading the specimen was to undergo. The edges of the wall were strengthened with concentrated reinforcement to take the bending moment occurring in the wall. The mesh of vertical and horizontal (shear) reinforcement was designed based on structural principles. As the wall is short direct load transfer is possible and engagement of shear reinforcement for force transfer was not foreseen. Vertical reinforcement runs from the bottom of the bottom beam through the wall to the top of the top beam creating a solid connection of the segments.

The specimens were concreted in their vertical positions to reduce inhomogeneities along the height of the wall. The concrete cubic strength was 54 MPa. The reinforcement yield strength was 500 MPa. The loading frequency is small and no notable increase in the strength of the materials is to be expected. An important aspect of the specimen design and manufacture was the load transfer from the apparatus to the concrete wall. The wall was not loaded directly but through the upper and lower containment beams. The solution used is a pair of 3 cm thick steel plates on both sides of the containment beams which were connected to the concrete through connecting studs and later casting. For a possible maximum load of 6000 kN per surface and considering an optional safety fac-

Force transfer mechanism layout (framed circles are high-tensile prestressing bars, unframed circles are connection studs in the concrete) (left), detail of prestressing-bar heads with a safety beam running across (right) F.10-3





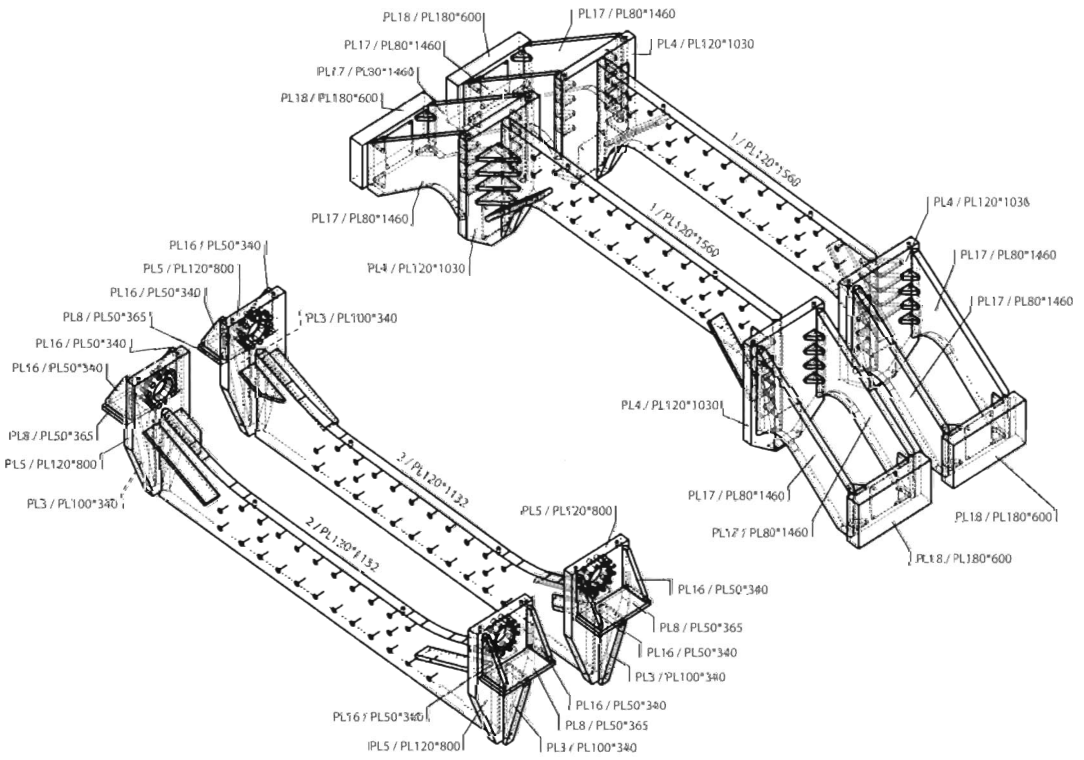
tor of 1.35 there were 52 studs designed for each steel plate. The force from the loading machine to the steel plates of the specimen was to be transferred by steel to steel friction. A large enough normal force was required to allow for the transmission of the total shear force which was originally anticipated to run possibly as high as 12000 kN. The necessary friction was obtained by using hi-tensile smooth (Glatter Stab) Dywidag bars (∅ = 36 mm) running through the containment beams of the specimen anchored on the outer surfaces of the loading apparatus. Twenty-six bars were used per beam including a 35% safety margin. The solution is shown in F.10-3.

10-2-2 Apparatus and Instrumentation

Due to the robustness of the wall to be tested the required forces to carry the specimen to failure could have damaged the reaction wall at the ELSA laboratory. For this reason the shear testing was conceived in a self-equilibrating manner. The complete loading equipment consists of three systems: the main loading system, a system controlling the rotations at the end of the actuators and a restraining system that controls the lateral motion.

The main loading system, a four part jaw-like steel frame, was designed to be placed around the specimen on the lower and upper containment beams. The frame was con-

Main loading system F.10-4

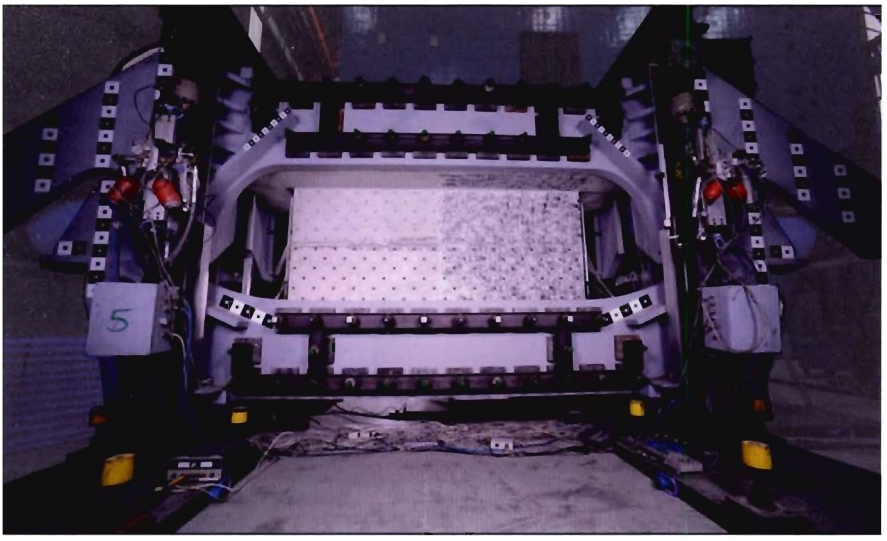


ceived so that the load is applied at the height of the wall's centreline as not to introduce additional bending of the specimen. The load is equally distributed to the lower and upper beams. This type of loading does result in moment acting on the system as a whole that would induce rotation. It has been analysed whether the self-weight of the entire system is sufficient to suppress uplift. It has been shown that uplift on one side would occur and so the lower part of the steel section was anchored. The steel frame was optimized to maximize stiffness while minimizing element thickness.

The horizontal actuators were placed between the upper and lower jaw of the steel frame. These were fixed to the lower part of the main loading frame and pushed against the plates of the upper part of the system. The four 300 ton actuators were unidirectional devices capable of pushing in positive and negative direction. All four actuators worked in a synchronized fashion to exert the required loads. When the wall was being sheared in a given direction the two actuators on one end applied forces to the external plates of the upper jaws while the two actuators at the other end applied the same load to the inner plates of the upper frame. Once maximum load has been reached the actuators are driven back until contact with the original plates is lost and next they are driven in the other direction as first contact with the reverse plates is made and finally load application in the opposite direction can advance. From the nature of the load application it follows that actuation is not continuous. The control of the horizontal loading was adopted in the form $F_i + \alpha u_{ti} = \text{ramp}$, with $i = 5, 6, 7, 8$; where F_i are the forces on the horizontal actuators, u_{ti} are the displacements on the Temposonic sensors on the actuators and α is a constant chosen in relation to the wall stiffness.

The shearing of the wall translates also to vertical displacements and rotations at the point of load application to the frame which might exceed the shear or bending capacity of the acting rod. Moreover, the specimen was anticipated to elongate due to crack opening which could introduce additional spurious vertical forces. In order to protect the actuators a sliding and a rotation protective system has been devised.

Prepared and instrumented set up (courtesy of P. Pegon, ELSA, JRC) F.10-5



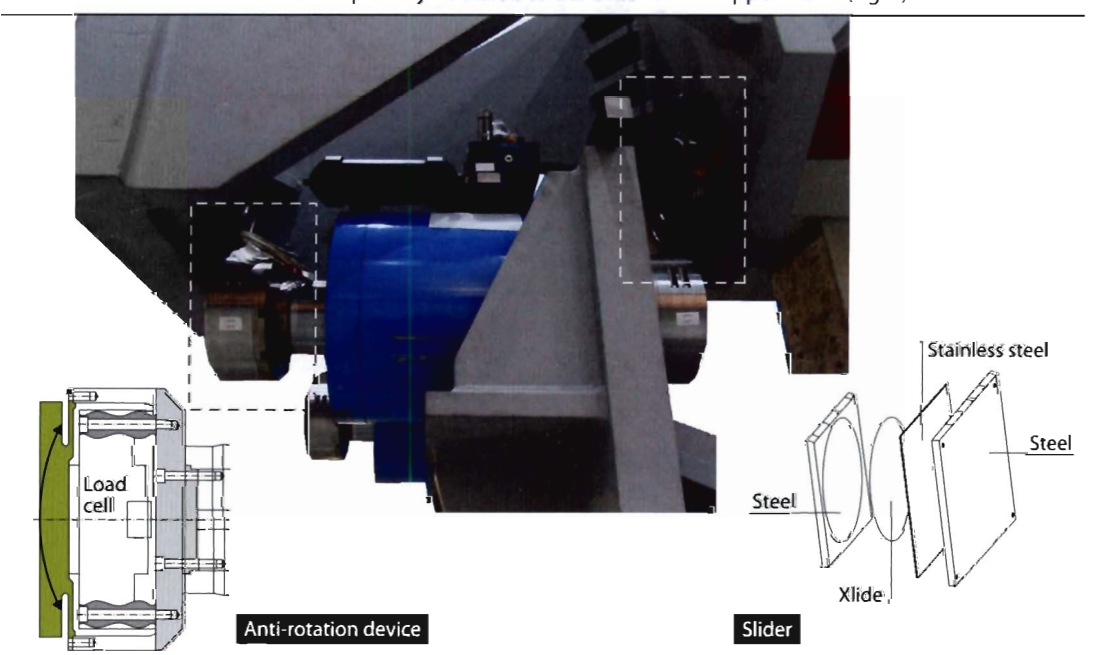
The sliding system was developed by JRC in collaboration with ALGA for a maximum normal load of 3000 kN and maximum lateral displacement of 30 mm. The system is made up of an 18 mm thick steel plate onto which the action rod presses into which a 7 mm thick Xlide antifriction disk is partially inserted; a 2 mm thick contact stainless steel plate and another base plate of steel (18 mm) mounted onto the loading plate of the upper frame. The Xlide antifriction disk was designed with a friction coefficient of 0.019 at maximum load but actual values are less than 1 % for lubricated disks with a cumulative slide path no greater than 22 m.

The rotation system is a round box around the spherical load cell. The baseplate (40 mm thick) was connected to the actuation rod. In the middle there were two half cylinders that connect the two support plates. The system is closed by a 48 mm thick steel plate which works as a membrane on one side and is up against the load cell in the middle. The other side of this plate is in contact with the sliding system. The plate is notched so, when under load, it may rotate over the head of the load cell.

Lastly, to stabilize the wall laterally and to prevent spurious distortions out of plane the top section of the main loading system was on one side braced against the reaction wall by means of two steel bars capable of resisting 550 kN buckling load.

To force the specimen in shear mode as much as possible considerable effort was devoted to keeping the top of the specimen horizontal. Four additional actuators were placed around the specimen vertically. These were fixed to the ground and connected to

Top of the loading apparatus being lowered. Two of the 300 t actuators visible with the rotation correction devices (left) attached to both ends of the actuation rod. The sliding devices with the rotation plate of the rotation eliminating device are visible temporarily attached to the slider on the upper frame (right) F.10-6



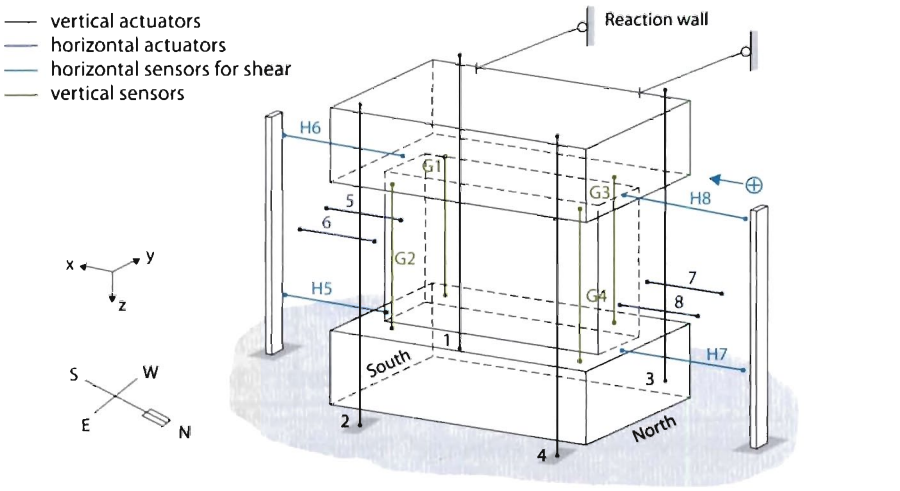
the top of the loading frame by transversal beams. These actuators operated in a push-pull mode, thus being able to exert forces in both directions. These jacks were also used to simulate the additional vertical load on the structure. The control of these actuators was implemented in such a way that equilibrium of forces was to be maintained diagonally, i.e. assuming notation according to F.10-7 $F_1+F_4=0$ and $F_2+F_3=0$ or actually for non-zero vertical forces the sum of each couple had to equal half of the required vertical load. Also, in-plane and out-of-plane rotation was controlled by the condition posed upon displacements $u_1=u_4$ and $u_2=u_3$.

The objective was to follow the behaviour of the stiff wall in cyclic shear loading up to its failure. For measuring the shear displacement four transducers were mounted at the top and bottom of the wall on each end. These Heidenhain sensors (H5–H8) were actually fixed to the containment beams close to the wall since failure of the wall could render them useless. For measuring the horizontal motion four Temposonic transducers were mounted on the horizontal actuators. These sensors recorded cumulative displacements.

The measurement of displacements in the vertical direction was serviced by four Heidenhain transducers each next to the vertical actuators. These were connected to support plates welded onto the main loading system. It was assumed the deformations of the loading system were small and there was no sliding between the loading system and the wall. These devices have a resolution of two microns and were used also for the vertical control. Additionally there were four Gefran transducers (G1–G4) mounted at the four corners of the wall between the upper and lower containment beams. These directly measured the displacements of the wall.

Load cells were installed as part of the rotation system at the end of the action rods of horizontal actuators. The eight 5 MN load cells comprised four ADOS devices (~1.7 mV/V) and four PAVONE devices (~2 mV/V). For the vertical control standard 1 MN load cells were mounted at the head of the vertical actuators. Moreover, there were extra sensors mounted to monitor the relative sliding of the main loading frame with respect to the specimen,

Main instrumentation of the specimen F.10-7



the lateral deformation and the relative motion of the sliding system with respect to the loading plate of the upper jaw.

Finally, an optical measurement system was set up to monitor the motion and degradation of the wall. Both faces of the wall were kept void of conventional testing devices not to hinder the application of high resolution cameras. Two stereo PCO.Edge cameras (with scale of 1.2 mm/pixel) were placed on both sides of wall. These cameras were to monitor displacements, crack initiation, evolution, opening and sliding. The surface of the specimen had to be treated in a special way to allow for following the crack propagation. Except for the standard Gaussian square targets the wall surface was painted with a black and white natural-artificial pattern that is not repetitive but has repeating features. Furthermore, two DTA cameras (with scale of 5.5 mm/pixel) were placed behind the PCO set on one side to monitor the motion of the loading frame.

10-2-3 Testing and Output

Four specimens were tested in a comparable fashion. Each wall was subjected to a combination of constant vertical load applied at the top of the shear wall and variably increasing horizontal load. Generally on all tested walls ten initial cycles of 500 kN were performed. For monotonic cases the load was increased in steps of 500 kN to 1000 kN and two cycles were performed at each load level until failure. A load cycle was defined as reaching the target load in one direction then retracting the actuators and subsequently pushing the wall in the opposite direction until target load has been reached then released. On the second cycle only the maximum displacement recorded corresponding to the target load

Load histories for the tested walls T.10-1

Wall 4		Wall 5		Wall 1		Wall 2	
0.5 MN/2c	11/07/2012	0.5 MN/9c	25/05/2012	0.5 MN/2c	02/10/2012	0.5 MN/2c	20/11/2012
0.5 MN/7c	12/07/2012	1.0 MN/2c		0.5 MN/7c	04/10/2012	0.5 MN/7c	22/11/2012
0.5 MN/1c		2.0 MN/2c	05/06/2012	0.5 MN/1c		0.5 MN/1c	
1.0 MN/2c		3.0 MN/2c		7.0 MN/2c	08/10/2012	7.0 MN/2c	23/11/2012
2.0 MN/2c	16/07/2012	4.0 MN/2c		4.0 MN/2c		4.0 MN/2c	
3.0 MN/2c		5.0 MN/2c	06/06/2012	3.0 MN/2c		3.0 MN/2c	26/11/2012
4.0 MN/2c		6.0 MN/2c		6.0 MN/2c	08/10/2012*	6.0 MN/2c	
5.0 MN/2c	17/07/2012	6.5 MN/1c	07/06/2012	5.0 MN/4c		5.0 MN/2c	27/11/2012
6.0 MN/2c		7.0 MN/2c	08/06/2012	5.5 MN/1/2c	09/10/2012	5.5 MN/2c	
6.5 MN/2c	18/07/2012	7.5 MN/2c		–5.5 MN/0.5c	10/10/2012	6.0 MN/2c	
7.0 MN/2c	24/07/2012	8.0 MN/1c	11/06/2012	6.0 MN/2c		6.5 MN/2c	28/11/2012
7.5 MN/2c		Final cycle	12/06/2012	6.5 MN/2c	10/10/2012*	7.0 MN/2c	
8.0 MN/2c				7.0 MN/2c		7.5 MN/2c	29/11/2012
Final cycle	26/07/2012			7.5 MN/2c	11/10/2012	1.0 MN/2c	04/12/2012
				8.0 MN/2c		8.0 MN/2c	
				8.0 MN/1/2c	12/10/2012	Final cycle	05/12/2012
				Final cycle			

on the first cycle was followed up. The detailed load histories of these tests are summed up in T.10-1. The "c" character denotes cycles.

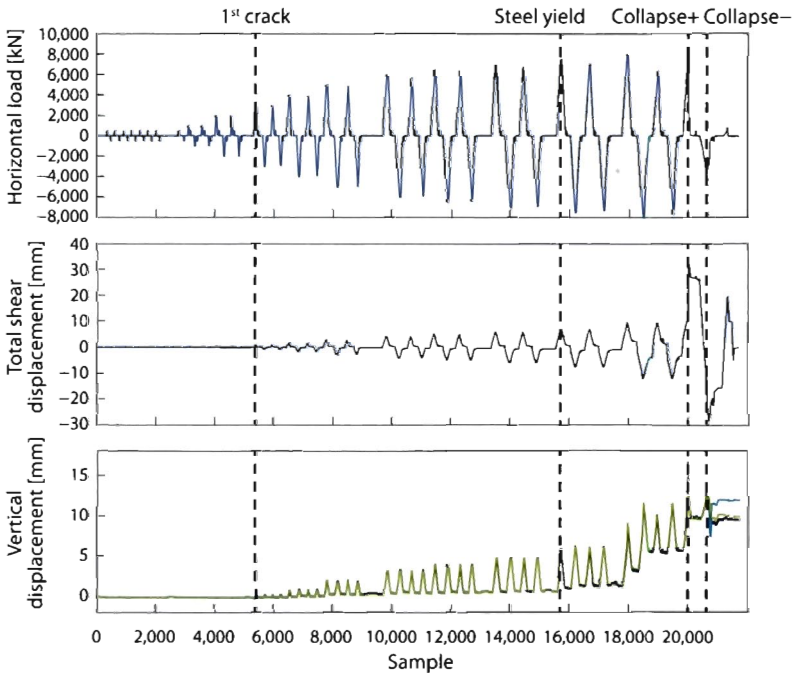
Testing at different load levels was treated as separate stages. The loading stage of a specimen followed this basic sequence: increase global vertical force from 0 to 600 kN – equilibrate forces in the vertical actuators by offsets in vertical displacement – start the motion of horizontal actuators – carry out all cycles of the stage – bring horizontal actuators back to middle position – decrease vertical force to 0 – switch off pressure system. In special cases continuous measurements were done for wall 1 from one stage to another, marked by an asterisk at the date in T.10-1. In these cases the vertical load was maintained and the pumps were not shut down. After each main half-cycle a small loading loop of 500 kN was carried out to allow for assessment of residual stiffness and damping for smaller load levels after a certain state of damage had been reached.

10-2-4 Load-Displacement Curves

As a representative specimen wall 4 which had a standard increasing loading scheme was selected. The plots show the performance of the wall in the main parameters, i.e. horizontal load, shear displacement, vertical displacement. Major points of interest have been marked in the data.

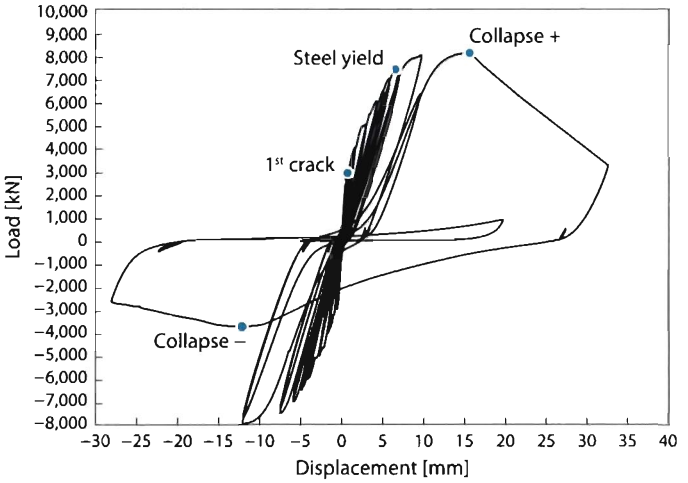
The moment of the first major crack appearing is defined as the point when the vertical displacements start to accumulate. This occurs when the two surfaces slide enough

Horizontal load, shear displacement and vertical displacements over "time" F.10-8

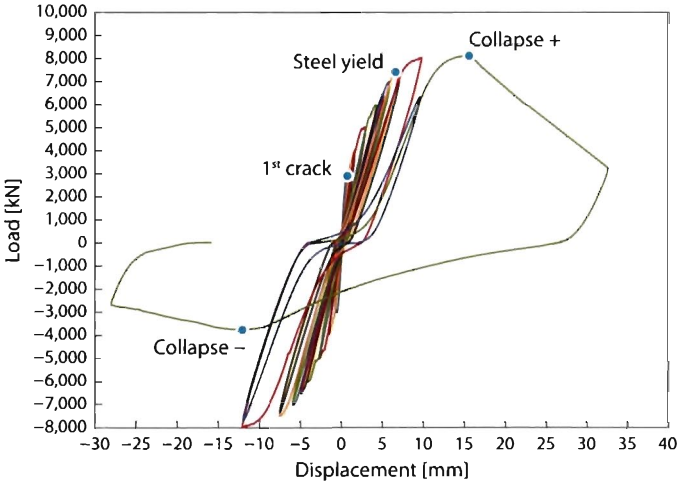


with respect to each other and aggregate interlocking prevents perfect closure in the crack. The onset of yielding in the reinforcement is difficult to accurately determine lacking direct instrumentation of the reinforcing bars. Nonetheless, the section after which the effect of steel yielding is apparent in the form of a significant step of vertical displacements can be identified (F.10-12). This corresponds to about 3.75‰ vertical elongation and 2.3‰ shear distortion. Also the pinching around the origin becomes more pronounced after this point. To clearly differentiate which bars are under yielding is unreasonable; nonetheless judging from the deformation of the wall the reinforcement in the

Load-displacement curve – full data set F.10-9



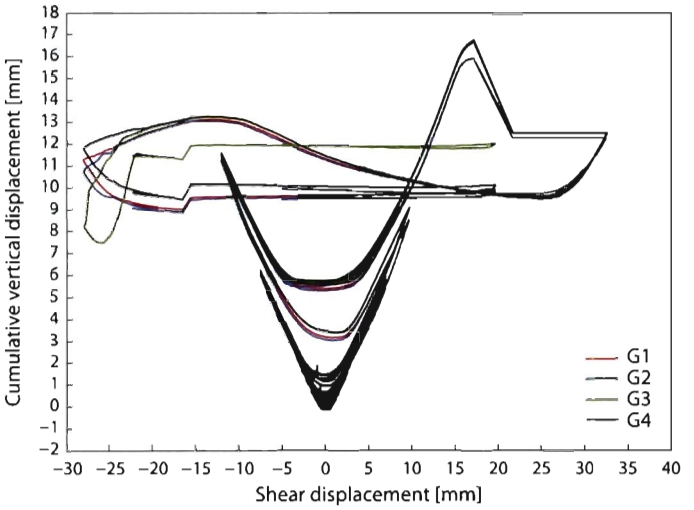
Load-displacement curve cleared, separated into cycles and absent of replica loops F.10-10



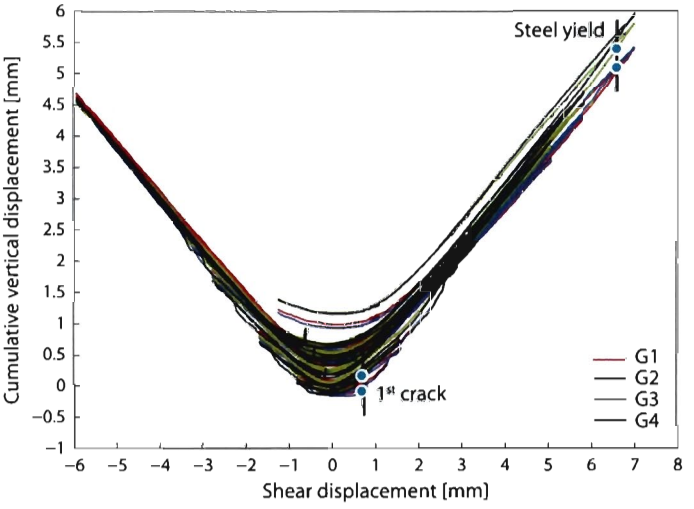
direction of shearing is not the one under excessive strain. The point of collapse is well defined by the sudden drop of the horizontal load, which in this case also indicates the failure was due to crushing of the concrete.

By the end of the test the specimen had developed a well-defined pattern of parallel diagonal cracks in both directions provoked by load reversals (F.10-13).

Shear displacement vs. cumulative vertical displacement for sensors G1–G4 F.10-11



Detail of shear displacement vs. cumulative vertical displacement for sensors G1–G4. Effect of the yielding reinforcement is visible after unloading in the last cycle plotted F.10-12

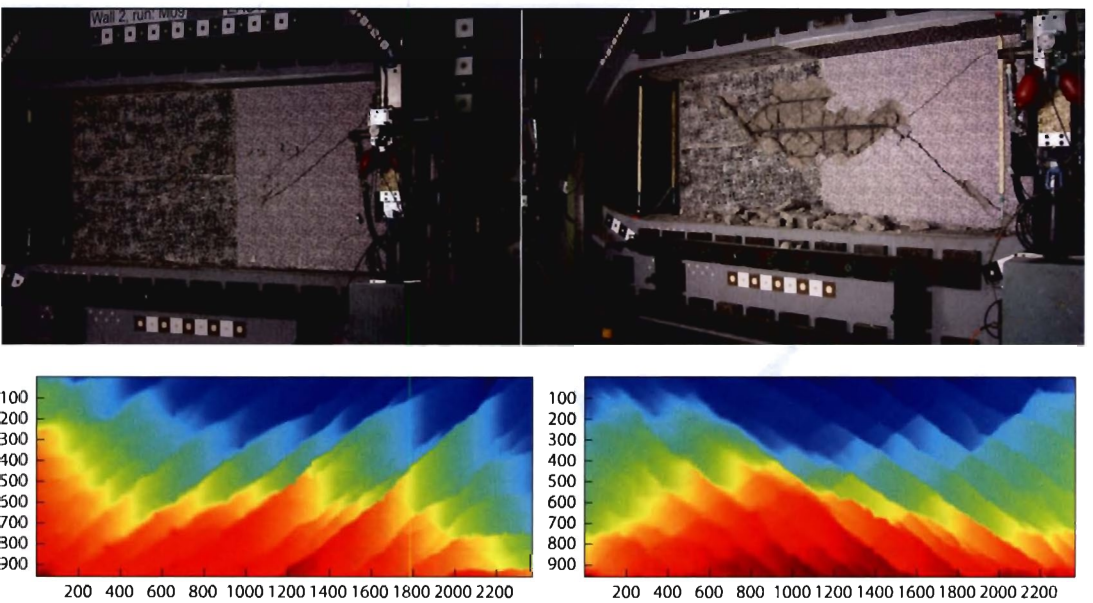


10-3 Results and Discussion

The behaviour of a reinforced concrete shear wall cannot be separated into distinct linear and non-linear regions because concrete has an inherently plastic behaviour. Although steel has a defined yield point, concrete is non-linear from initial loading and so the specimen as a whole shows a composite behaviour. The hysteresis presented in the previous section shows well the cyclic strength degradation as the second cycle on a damaged specimen does not reach the set load level at an equal horizontal displacement, which was the controlled variable. Progressive degrading phenomena occur, starting with concrete cracking, trough reinforcement yielding until the specimen fails by concrete crushing in the middle region of the wall. According to damage mechanics the behaviour of the shear wall specimen can be characterized as unilateral. During the cyclic loading of the wall to specific directions of the shearing two distinctive sets of shear cracks form in the wall (F.10-13). When the shear force changes sign one set of cracks tends to close and its presence has a reduced effect in the wall behaviour while the other set of cracks tends to open and becomes the dominant stiffness reduction phenomenon. During opening and closing of existing cracks the reinforcement in the disturbed areas is activated.

In the load-displacement curves of the test (F.10-10) a pinching around the origin can be seen. The phenomenon of pinching is due to sliding between the already cracked surfaces of concrete before they come in full contact. This can be observed in the hysteresis curves where the sign of the shear force changes upon load reversal. This action of sliding

Crack pattern at the end of the test of wall 2 (above). Vertical displacements from the optical system in the penultimate cycle in one direction and the terminal cycle in the opposite direction (below, courtesy of P. Capéran, ELSA, JRC) F.10-13



across a shear crack can be explained in terms of Coulomb friction. Under extensive shear load a crack has been formed in the wall. As the load is reduced to zero the crack remains partially open. Once the load is applied in the opposite direction friction across the crack is small initially but as the crack begins to close, friction gradually increases which translates into increased resistance of sliding. Furthermore, if reinforcement yielding has occurred upon the crack opening, it is evident that in order to close the crack completely the reinforcement must yield in compression. An interaction between two phenomena exists here: sliding across the shear cracks and yielding of the reinforcement. Both mechanisms contribute to the plastic behaviour of the wall. The features related to these phenomena are observable in the load displacement plots in F.10-10 and F.10-11. Next, some properties for the specimen "wall 4" are calculated and discussed.

10-3-1 Damping

Damping is a fundamental property of any structure and a crucial one for dynamic applications and thus it can be difficult to assess it realistically. [Raggett, 1975] proposed a practical way of predicting damping for real structures. Essentially, it is based on fundamental mechanics of energy dissipation in viscous damping of an SDOF system [Chopra, 2007]. A condensed description is given here. Considering an SDOF system in a steady-state motion with harmonic excitation the energy dissipated by viscous damping can be expressed as

$$E_D = \int_0^T (c\dot{d})\dot{d}dt = \pi c\omega D^2 = 2\pi\zeta\frac{\omega}{\omega_n}kD^2$$

where T is the period, c is the damping coefficient, $d(t)$, $\dot{d}(t)$ are displacement and velocity respectively, k is the stiffness, ζ is the damping ratio and D is the maximum displacement in the cycle. The energy dissipated is proportional to the square of the amplitude of motion. Analogously the elastic energy belonging to the spring of the system is related to the maximum amplitude of the cycle as

$$E_S = \int_0^T (kd)\dot{d}dt = \frac{1}{2}kD^2$$

The damping force is defined as

$$f_D = c\dot{d}(t) = c\omega D\cos(\omega t - \phi) = c\omega\sqrt{D^2 - d(t)^2}$$

which can be rewritten as an equation of an ellipse

$$\left(\frac{d}{D}\right)^2 + \left(\frac{f_D}{c\omega D}\right)^2 = 1$$

As the $f_D - d$ curve is a hysteresis loop the area enclosed by the ellipse, which equals $\pi c\omega D^2$, gives the dissipated energy. Now the damping force can be calculated based on the energy of a cycle as

$$f_D = \frac{E_D}{\pi D^2}\sqrt{D^2 - d^2}$$

Finally, the equivalent viscous damping is commonly defined by equating the energy dissipated in a vibration cycle of an actual structure with that of the equivalent SDOF viscous system. The energy dissipated in the actual structure in a hysteresis loop is the area enclosed by this loop and for discretized data can be computed using the trapezoidal rule

$$E_D = \sum_{1}^{N-1} f_{av,n}(d_n - d_{n+1})$$

where N is the number of data points in the record and $f_{av,n}$ is the average force at step n. Placing this equal to the energy dissipated in viscous damping yields

$$\zeta_{eq} = \frac{1}{4\pi}\frac{2}{\omega/\omega_n}\frac{E_D}{E_S} \quad \text{or} \quad \zeta_{eq} = \frac{1}{4\pi}\frac{E_D}{E_S} \quad \text{for} \quad \omega = \omega_n$$

The elastic energy of the system E_S is required next, and here we must realize that the total force measured in an experiment is the sum of the elastic and damping forces

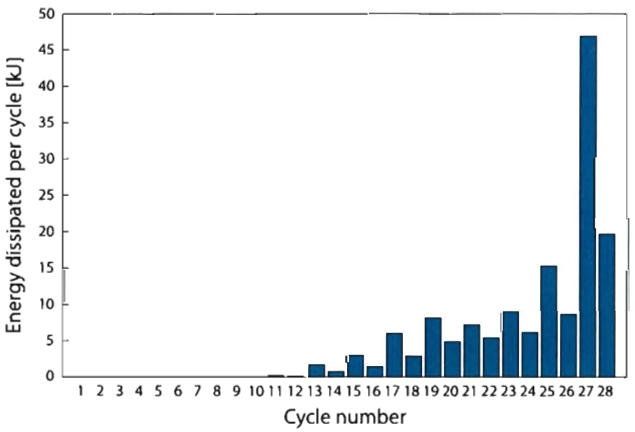
$$f^M = f_S + f_D = kd + c\omega\sqrt{D^2 - d^2}$$

which then allows for the extraction of the elastic force f_S once f_D is known. Eventually, to calculate the elastic energy of the cycle E_S we need an equivalent stiffness for the entire hysteresis loop. This can be achieved by applying a linear regression of f_S over the cycle as

$$k = \frac{N\sum(df_S) - \sum d \sum f_S}{N\sum d^2 - (\sum d)^2}$$

Based on the method described above the damping ratios for each test cycle on wall 4 was computed. The corresponding total energy of the cycles is given in F.10-14. The data is very consistent as the energy of the cycles is increasing on average with the second cycle at the same load level dissipating less energy than the first. The final "cycle" in which failure occurred is omitted. Next, F.10-15 shows the resulting damping ratios for the test

Total energy dissipated in each cycle for wall 4 (area enclosed by the hysteresis loop) F.10-14



cycles of wall 4. It can be seen that there is a general trend of decreasing damping with increased loading. However significant discrepancies are present the reason for which, though not entirely clear, is quite probably a shape of the cycle starkly different from an ellipse. The final values of damping given in the figure are the minimum values of various different estimations where the equivalent stiffness k was calculated in different ways. Besides the linear regression, a slope based on the centre of mass of the positive and negative segments of the loop to the origin was calculated and also a secant stiffness at 10% and 50% of the maximum load for the cycle. The differences between these estimates can reach up to 3% in final damping values, nonetheless these methods did not alter the general picture of the damping ratios. The overall energy dissipated by the specimen is limited as it depends on the number of cycles.

10-3-2 Shear Capacity

The final capacity of wall 4 in the negative direction, the direction the experiment started in, was 8117 kN. It is useful to compare this with normative values of the bearing capacity of the wall. The shear strength of the wall is calculated using various standards.

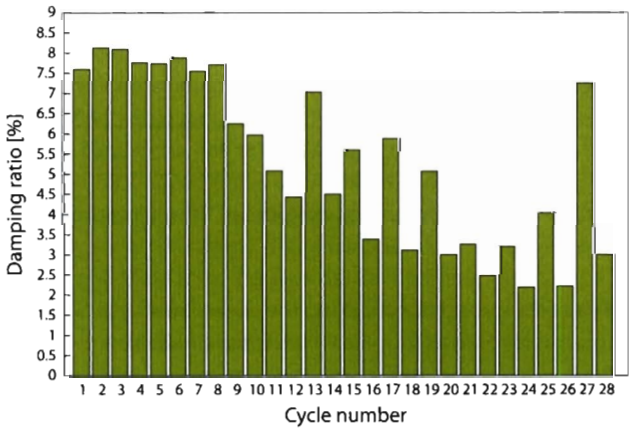
Eurocode 2, Clause 6.2.5

As the Eurocode 8 does not have specific provisions for low-rise shear walls the shear-friction concept is taken. The shear resistance of the wall connection plate at its bottom is to be calculated as

$$\upsilon_{Rdl} = cf_{ctd} + \mu\sigma_n + \rho f_{yd}(\mu \sin\alpha + \cos\alpha) \leq 0.5\nu f_{cd}$$

where c and μ are factors depending on the roughness of the interface, $f_{ctd} = \alpha_{ct} f_{ctd,0.05} / \gamma_c$, α_n is the stress per unit area caused by the normal force, $\rho = A_s / A_i$, A_s is the area of the reinforcement crossing the interface, A_i is the area of the interface, α is the angle between the shear friction reinforcement and shear plane. On the right-hand side ν is the reduc-

Damping estimate for the test cycles of wall 4 F.10-15



tion factor for concrete cracked in shear and f_{cd} is the design compressive strength of concrete. According to the code only the first term is factored with the material safety factor for concrete while the second term is taken at full value and the third term constituting the reinforcement is factored with γ_s. The shear capacity of the wall according to the EC2 equation is 5655 kN, (relegating safety factors V_r equals 5805 kN).

US code ACI 349, Clause 11.7

Design provisions are given in ACI 318 for regular structures and ACI 349 for nuclear structures. This approach may be applied when shear transfer across a given plane is warranted. The nominal shear force is taken as

$$V_n = A_{vf} f_y (\mu \sin\alpha + \cos\alpha)$$

where μ is the coefficient of friction, A_{vf} is the area of reinforcement in the shear plane, f_y is the yield strength of the reinforcement and α is the angle between reinforcement resisting shear and the shear plane. The value of V_n is limited between $0.2 f_c A_c$ and $5.5 A_c$. In this code the safety factor is not material but rather behavioural. For shear phenomena the factor is $\phi = 0.75$. Although the above equation does include a term for normal pressure the ACI 349 permits to add it to $A_{vf} f_y$ when calculating the required A_{vf}. The shear capacity of the wall including the effect of the axial force and applying the given safety factor is 4087 kN, while without the safety factor capacity equals to 5450 kN.

US code ACI 349, Clause 11.10

A special provision is given for shear transfer in case of walls. In term of shear stresses the capacity is given as follows

$$v_t = 0.75(0.216\sqrt{f_c} + 0.2\sigma_u + 0.8\rho_t f_y)$$

where f_c is the concrete strength in compression, σ_u is the normal stress pre-unit area and ρ_t is the ratio of reinforcement resisting shear. Based on this formula the wall strength is evaluated at 4340 kN.

US code ACI 349, Clause 21.7.4

A special clause is given for low-rise shear walls with aspect ratio $H/L \leq 1.5$. The factored capacity per unit area is given by

$$v_t = 0.75(0.25\sqrt{f_c} + \rho_t f_y)$$

where ρ_t is the ratio of reinforcement resisting shear. The wall capacity according to this equation is 5137 kN.

A commonly used approach for checking the shear capacity of walls applied in many cases over the years is Hirosawa's formula which is presented here

Shear capacity of wall specimen as predicted by various formulae T.10-2

	Without safety factors [kN]	Factored for safety [kN]
EN 1992	5805	5655
US 349 clause 11.7	5450	4087
US 349 clause 11.10	5787	4340
US 349 clause 21.7	6849	5137
Hirosawa's formula	5553	

$$V_{ult} = \left(\frac{0.0679 \rho_t^{0.23} (f_c + 1.76)}{\sqrt{M/VL} + 0.12} + 0.845 \sqrt{f_{wh} \rho_{wh}} + 0.1 \sigma_0 \right) tj$$

where ρ_t is the effective tensile reinforcement ratio as percentage equal to $(100 A_{st})/t(L - a_l/2)$, A_{st} is the area of the longitudinal reinforcement in the tension side boundary region, $M/(VL)$ is the shear span to depth ratio, M is the moment at the base of the wall, V is the base shear at the wall, ρ_{wh} is horizontal wall reinforcement ratio, f_{wh} is the yield stress of the horizontal reinforcement, t is the thickness of the wall section, σ_0 is the average axial stress per unit area, $j = 7/8(L - a_l/2)$, L is the length of the wall and a_l is the length of the boundary wall edge region usually taken as 10% of wall length. The shear span M/V calculated in an elastic calculation is $\lambda = 0.912$. The ultimate shear capacity of the tested wall according to Hirosawa's formula excluding all safety factors is 5553 kN.

T.10-2 sums up the capacity predictions of the multiple approaches presented. The actual bearing capacity of the wall in shear proved to be significantly higher than the values predicted by codes. The reason that can be given for this is the failure mechanism in which the wall eventually failed. Wall 4 failed in shear compression, i.e. by crushing concrete in the centre region of the wall whereas the codes treat the shear walls in nuclear facilities by way of a friction concept which is an estimate of the joint strength observed as a weak point.

10-3-3 Ductility

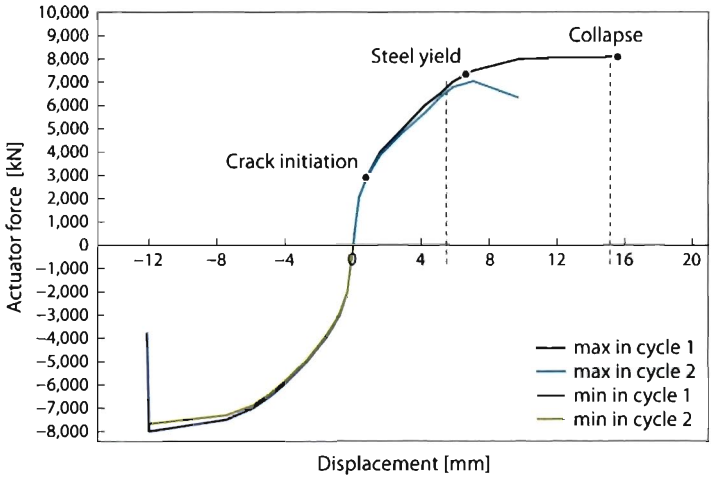
Because a reinforced concrete wall is essentially a composite element a number of failure modes can occur depending on parameters such as the geometry of cross-section, reinforcement detailing and quantities, properties of the reinforcing steel, quality of concrete and boundary conditions. The main failure modes for shear walls are flexure, shear, crushing, sliding and rocking. Of these only flexure and rocking are truly ductile where the latter is rather concerned with foundation and soil mechanics. The design of concrete structures is typically set by standards; in the European community these are the EC2 for concrete structures and EC8 for earthquake resistance. These standards apply a capacity design principle in which based on the structural ductility class a behaviour factor is chosen which then governs the design process.

Displacement ductility ratio of a reinforced concrete element is defined as the ultimate displacement to the yield displacement. Yield displacement is taken at the load level

when reinforcement at the resultant of tensile stresses yields. The ultimate displacement is assumed until the point where the load level stays above the yield load. A ductile member with such properties can dissipate energy while retaining fundamental structural integrity and it is the desired type of response of flexural members. Likewise, for shear walls a brittle failure mode is preferentially to be avoided. In spite of this non-ductile shear failures do commonly occur in seismic events. The walls for this investigation were tested in almost pure shear which is a scenario that does not fall within the domain of capacity design. Yet the test results show that in the shear failure mechanism the specimen is forced into it can be taken past the yield point of the tensile reinforcement.

A conservative position is taken in establishing the yield point of the tensile reinforcement. It is picked at a state when the effects of the yielding are apparent (F.10-12). The vertical displacements measured by the Gefran (G1–G4) sensors show a permanent change at this stage which cannot be consolidated by reverse loading. The shear displacement at this point is 6.6 mm. An envelope of the maxima of the positive cycles is shown by the black curve in F.10-16. It is evident that the specimen indicates to have reserves beyond the yield point even if this is established in a conservative manner. The final failure is brittle and comes about at a horizontal displacement of 15.6 mm. This is not to say that a ductility ratio of above 2 could be established as capacity design should generally not be considered in the case of an element failing by concrete crushing. Once concrete crushing is reached in one direction the wall does not possess any additional displacement capacity in the opposite direction over the previously reached displacements. This follows from the final part of the blue curve in F.10-16. Nonetheless, before failure by crushing sets in there are plastic reserve capacities that a low-rise shear wall can allow even in shear failure mode. This fact may contribute to the explanation of the higher than design resistance of actual low-rise shear walls in nuclear facilities. In addition ductility can be related to the dissipated energy [Chopra, 2007].

Envelopes of cycle maxima separately for the series of first and second cycles for both positive and negative loading directions F.10-16



10-3-4 Summary

Strong short shear walls have been tested in a novel way where shearing was the dominant mode of behaviour all the way to failure. The shear wall had a thickness of 40 cm to closer represent a structural part existent in nuclear facilities. A special loading device was constructed allowing a symmetrical closed system loading. An elaborate displacement and rotation control was needed at the load transfer point. Additionally, the top of the specimen was held horizontal to promote shear behaviour. The quasi-static loading was administered in cycles of preconceived load levels. The unilateral response of the wall was monitored by a group of horizontal and vertical transducers. On the resulting load displacement curves features of degradation are identifiable. Wall 4 was selected for primary data processing. The failure load in the initial loading direction was 8117 kN, which was due to concrete crushing in the middle of the wall. The experimental strength was compared to various design checks based on different codes. Reserves based on these comparisons ranged from 43% to 98%. It is well to be noted though, that the failure mechanisms in the case of the experiment versus the codes are not comparable. The data was further investigated and we looked at other characteristics like damping and ductility. A short shear wall failing in a brittle mode still shows remaining displacement capacities after the onset of yielding in the reinforcement. The damping estimates for the wall show discrepancies between cycles but are consistently higher than generally assumed for this type of structure in design.

References

ACI 318, 2011. *Building Code Requirements for Reinforced Concrete.* ACI Committee, American Concrete Institute, Michigan.

Barda, F., 1972. *Shear Strength of Low-Rise Walls with Boundary Elements.* PhD dissertation, Lehigh University.

Benjamin, J. R. and Williams, H. A., 1957. *The Behavior of One-Storey Reinforced Concrete Shear Walls.* Journal of the Structural Division, ASCE 83:1–49.

Benjamin, J. R. and Williams, H. A., 1960. *Reinforced Concrete Shear Walls Assemblies.* Journal of the Structural Division, ASCE 86(8):1–32.

Brun, M., Reynouard, J. M. and Jezequel, L., 2003. *A Simple Shear Wall Model Taking into Account Stiffness Degradation.* Engineering Structures 25:1–9.

Brun, M., Labbe, P., Betrand, D. and Courtois, A., 2011. *Pseudo-Dynamic Tests on Low-Shear Walls and Simplified Model Based on the Structural Frequency Drift.* Engineering Structures 33:769–812.

Chopra, A. K., 2007. *Dynamics of Structures.* Prentice Hall, 3rd edition.

Eurocode 8, 2010. *Design Provisions for Earthquake Resistance of Structures, Part 1–3: General Rules – Specific Rules for Various Materials and Elements.* CEN: European Committee for Standardization, Bruxelles.

Fouré, B., 1993. *Un Programme Dèssais des Murs de Contreventement.* In: Colloquium AFPS-SECED experimental methods in earthquake engineering and structural dynamics, Saint-Rémy-lés-Chevreuse, AFPS – Association Francaise du Genie Parasismique.

Galletly, G. D., 1952. *Behavior of Reinforced Concrete Shear Walls under Static Load*. Department of Civil and Sanitary Engineering, MIT Cambridge, MA.

Greifenhagen, C. and Lestuzzi, P., 2005. *Static Cyclic Test on Lightly Reinforced Concrete Shear Walls*. Engineering Structures 27(11):1703–1712.

Iliya, R. and Bertero, V., 1980. *Effects of Amount and Arrangement of Wall-Panel Reinforcement on Hysteretic Behavior of Reinforced Concrete Walls*. Report No. UCB/EERC 80/04, Berkeley, University of California.

Lopes, M. S., 2001a. *Experimental Shear-Dominated Response of RC Walls. Part I: Objectives, Methodology and Results*. Engineering Structures 23:229–239.

Lopes, M. S., 2001b. *Experimental Shear-Dominated Response of RC Walls. Part II: Discussion of Results and Design Implications*. Engineering Structures 23:564–574.

Maier, J. and Thürlimann, B., 1985. *Bruchversuche an Stahlbetonscheiben*. IBK Bericht 8003-1 Zurich ETH.

Mo, Y. L. and Chan, J., 1996. *Behavior of Reinforced-Concrete Shear Walls*. Nuclear Engineering and Design 166:55–68.

Oesterle, R., Fioratio, A., Johal, L., Carpenter, H. and Corley, W., 1976. *Earthquake Resistant Structural Walls – Tests of Isolated Walls*. PCA Construction Technology Laboratories.

Oesterle, R., Aristizabal-Ochoa, J., Fiorato, A., Russel, H. and Corley, W., 1979. *Earthquake Resistant Structural Walls – Tests of Isolated Walls – Phase II*. PCA Construction Technology Laboratories, Skokie (Illinois).

Orakcal, K., Massone, L. M. and Wallace, J. W., 2006. *Analytical Modeling of Reinforced Concrete Walls for Predicting Flexural and Coupled-Shear-Flexural Responses*. PEER Report 2006/07 Pacific Earthquake Engineering Research Center, Berkley.

Paulay, T., 1975. *Design Aspects of Shear Walls for Seismic Areas*. Canadian Journal of Civil Engineering 2(3):321–344.

Raggett, J. D., 1975. *Estimating Damping of Real Structures*. ASCE Technical Publication 1823–1835.

Rothe, D., 1992. *Untersuchungen zum nichtlinearen Verhalten von Stahlbetonwandscheiben unter Erdbebenbeanspruchung*. VDI-Forschrittsberichte, Düsseldorf, VDI-Verlag, 4(117).

Vallenas, J., Bertero, V. and Popov, E., 1979. *Hysteretic Behavior of Reinforced Concrete Structural Walls*. Report no UCB/EERC-79/20, University of California, Berkeley.

Salonikios, T., Kappos, A., Tegos, A. and Penelis, G., 1999. *Cyclic Load Behaviour of Low Slenderness Reinforced Concrete Walls: Design Basis and Test Results*. ACI Structural Journal 96(4):649–660.

Thomsona, E. D., Perdomob, M. E., Picón, R., Maranteb, M. E. and Flórez-López, J., 2009. *Simplified Model for Damage in Squat RC Shear Walls*. Engineering Structures 31:2215–2223.

Wallace, J., 1995. *Seismic Design of RC Structural Walls. Part I: New Code Format*. Journal of Structural Engineering 121(1):75–87.

11

Remote Sensing and GIS Methods for the Safety of Industrial Facilities and Infrastructure in Europe

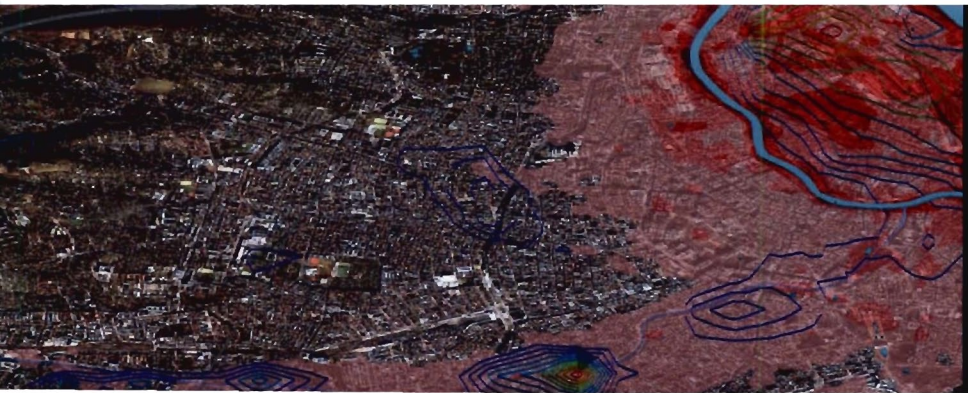
Author:
Barbara Theilen-Willige

Motivation

Remote sensing technologies provide information in large areas. Technologies to properly exploit the information given in the images are desired to be used in subsequent risk management.

Main Results

A comprehensive set of tools has been developed to quantify a major number of parameters and established information on key performance indicators. These tools are introduced in the GIS based software platform developed by the IRIS project.



11-1 Introduction

Europe is experiencing an increasing number and impact of disasters due to natural hazards and technological accidents caused by a combination of changes in its physical, technological and human/social systems. Natural risks may interact with the risks coming from the industrial plants, especially from the high risk ones, giving rise to a negative synergism. In order to get an almost complete evaluation of the interactions between industrial settlements and environment, it is necessary to consider their double connection: the effects both of a natural event on the plant and of the plant itself on the surrounding environment. Therefore, information about features, like hydrogeological and geomorphologic factors, and suitable safety measures is needed. Industrial facilities and critical infrastructures, as well as individual production or service areas, are subject to different levels of risk from natural events.

The assessment of potential natural hazards is fundamental for planning purposes and risk preparedness, especially with regard to supervision and maintenance of industrial facilities and of extended lifelines. Areas at particular risk include networks, buildings, production, extracting and processing plants and non-electronic data records [Federal Ministry of the Interior, 2009]. Technical interdependencies between infrastructures have the potential for initiating widespread cascading effects of failure or loss of service. The clash of a climate change driven increase of flooding hazards such as storm surge and flash floods with explosive, uncontrolled urban sprawl and changing urban patterns constitutes a further increasing risk.

Industrial accidents triggered by natural events, such as e.g. earthquakes, floods, lightning etc., are referred to as "Natech" accidents. Natech accidents have occurred in relation to natural hazards and disasters and have resulted in the release of hazardous substances leading to fatalities, injuries, environmental pollution and economic losses [Krausmann et al., 2011]. One of the principal problems of most Natech accidents is the simultaneous occurrence of a natural disaster and a technological accident, both of which require simultaneous response efforts in a situation in which lifelines needed for disaster mitigation are likely to be unavailable. Natech risk differs from technological or natural risk as its multi-hazard nature requires an integrated approach to risk management. The catastrophic events in March 2011 in Japan have demonstrated this.

When natural hazards happen and affect cities, settlements and infrastructure, immediate and efficient actions are required which ensure the minimization of the damage and loss of human life [Savvaidis et al., 2012]. Proper mitigation of damages following disastrous events highly depends on the available information and the quick and proper assessment of the situation. Responding local and national authorities should be provided in advance with information and maps where the highest damages due to unfavourable, local site conditions in case of stronger earthquakes and earthquake-related secondary effects such as landslides, liquefaction, soil amplifications or compaction can be assumed. The better a pre-existing reference database of an area at risk is prepared and elaborated, the better a crisis-management can react in case of hazards and related secondary effects [Theilen-Willige et al., 2012]. Hence it is imperative to identify those areas most susceptible to different types of natural hazards as earthquakes, landslides, flooding or storms.

The ability to undertake this natural hazard assessment, monitoring and modelling can be improved to a considerable extent through the current advances in remote sensing and GIS technology. Geographic Information Systems (GIS) provide the appropriate platform for the registration and management of information on natural hazards and their impact on industrial facilities. Meanwhile disaster GeoInformationSystems (GIS) have been implemented in nearly all European countries, however, still with different standards and definitions, terminology, data bases and details, in spite of the on-going European INSPIRE activities. Therefore the compatibility of data and information is one of the major problems. The consideration of property rights of data is another obstacle for the international use and data exchange.

In case of larger accidents, changes often become visible by comparing a reference data base with most actual satellite imageries, that can be evaluated and, then, be part of decision processes. For example RapidEye – or Sentinel – satellite data can form an important part of such a reference data base before and after an event providing data within several hours.

Hence, the aim of this part of the IRIS-project was to elaborate an approach, in which Geographic Information Systems (GIS) used with integrated remote sensing data, contribute to the analysis and representation of information required for the geo-hazard assessment, that could cause industrial accidents and cascading, interfering effects affecting the safety of industrial facilities. Objective was the detection of areas susceptible to natural hazards and, thus, as a consequence, the susceptibility assessments of industrial facilities to these hazards according to a standardized, systematic and clearly arranged approach that can be used in any area due to the meanwhile standardized, open-source availability of the basic data input.

Causal or critical environmental factors influencing the disposition of industrial and infrastructural facilities to be affected by natural hazards and the potential damage intensity can be analysed interactively in a GIS database. The interactions and dependencies between the different causal factors can be visualized and weighted step by step in this GIS environment. Objective was to elaborate susceptibility maps for the detection of areas that are assumed to be more affected by natural hazards due to aggregation of causal/preparatory factors and merge these maps with data of industrial facilities. A further objective was the investigation of the question how the elaboration of a database for factors of local site conditions, which influence the damage potential of hazards, for example in case of earthquakes the shock intensities, could become part of a comprehensive industrial risk management system in the future.

Maps of European countries were created providing an overview of areas that are more susceptible to earthquake shock or flooding due to regional and local site conditions following the standardized work flow developed in the scope of the IRIS project. As demonstration example for this study the Vienna area in Austria was chosen.

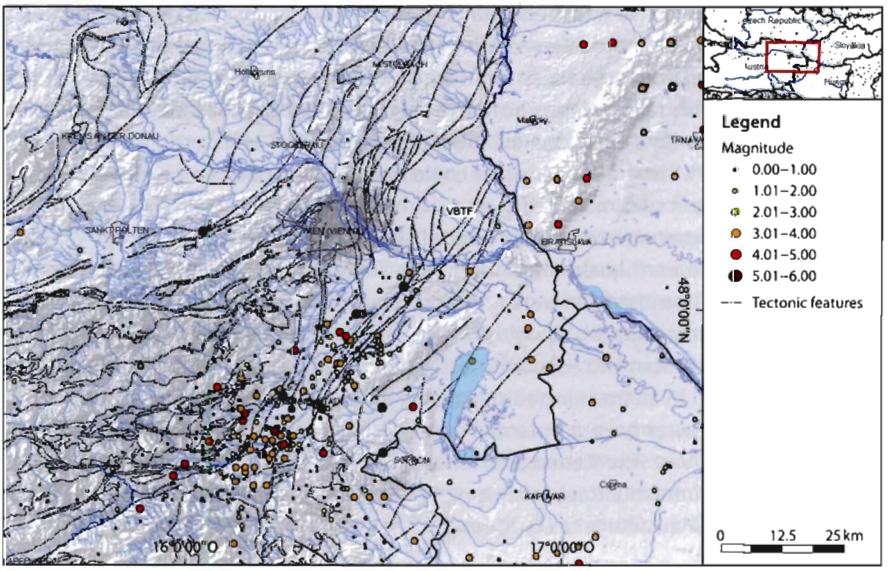
The potential of social and economic losses due to earthquake events and secondary processes triggered by them, is increasing as well in Austria. Technical interdependencies between infrastructures have a potential in triggering widespread cascading effects of failure or loss of service. The Vienna area for example has more than two million inhabitants and sensitive infrastructure. Seismic hazard assessment and mitigation is therefore an important task [Hausmann et al., 2010].

11-2 Geomorphologic and Geotectonic Setting

Information of long-term information of geodynamic processes in the Eastern Alps and its environments (uplift, subsidence, horizontal movements) are a basic need for the maintenance of the buildings, infrastructure and industrial facilities in the Vienna area. As the geodynamic processes are linked with the morphologic development in the Vienna area, its morphometric properties have to be taken into account as well.

Vienna is situated at the western margin of the Vienna Basin, a pull-apart structure formed due to lateral extrusion between the Eastern Alps and the Western Carpathians. It developed during the Miocene and was reactivated in Pleistocene times [Beidinger et al., 2011]. The Vienna basin is surrounded by the Eastern Alps, the West Carpathians, and the western part of the Pannonian Basin. It strikes roughly southwest-northeast, is 200 km long and nearly 60 km wide. It extends from Gloggnitz (Lower Austria) in the SSW to Napajedl (Czech Republic) in the NNE [Harzhauser and Piller, 2004]. Major NE-striking fault systems of the Vienna Basin are related to the seismically active Vienna Basin Transfer Fault System (VBTF). The Vienna Basin fault system is a slow moving (1–2.5 mm/y) active sinistral fault extending from the Alps through the Vienna Basin into the Carpathians [Hinsch and Decker, 2010]. This is in good agreement with GPS data showing about 2 mm slip per year and precise levelling proving surface subsidence up to 1 mm/y. Three of these branch faults, which have at least been active through the Pleistocene, pass through the urban centre of Vienna. The landscape of large parts of the city of Vienna is dominated by Quaternary terraces of the Danube river.

Earthquakes in the Vienna Basin F.11-1



11-3 Earthquakes in the Vienna Basin

The Vienna Basin is one of the main seismic active areas in Austria. During the 20th century 345 earthquakes in the Vienna Basin and adjacent areas in Styria could be felt, 17 earthquakes caused building damage [Hausmann et al., 2010; Meurers et al., 2004]. Most of the epicentres line up along the Vienna Basin Transfer Fault System (VBTF), see F.11-1. The region at the VBTF is in general characterized by moderate seismicity with almost medium sized earthquakes (Magnitude: ML 5.0–5.5). A stronger event, the Neulengbach earthquake, 1590 AD (ML about 6) was recorded in historic times [Hinsch and Decker, 2010]. The earthquake in the wider area of Neulengbach in 1590, about 30 km northwest of Vienna, had an epicentral intensity of about 9, according to the analysis of historical documents [Lenhardt et al., 2007].

The available seismic hazard estimates for Austria were established on probabilistic and statistical analyses of historical earthquake data [Grünthal et al., 1998]. Such approaches assume that the future seismicity will be the same as past observed activity, implying higher earthquake probabilities in areas, where historical earthquakes occurred and lower probabilities for areas, where only few or small earthquakes occurred [Hinsch and Decker, 2010]. However, maps of active faults and computed seismic slip deficits indicate that previous hazard analyses for the surroundings of Vienna may both underestimate the probability of severe earthquakes and the maximum credible earthquake. The subsurface geologic structure of the Vienna basin has the potential to amplify and lengthen the duration of strong shaking in some places, such as in areas with surficial and shallow deposits of artificial fill and youngest, unconsolidated alluvium (Danube river deposits).

11-3-1 Local Site Conditions

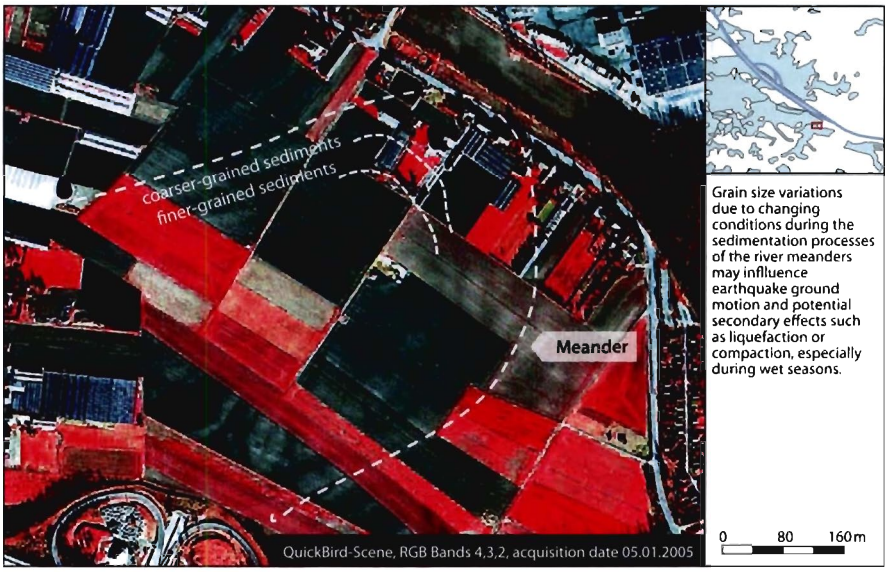
Local site conditions play an important role when considering earthquake shaking and damage intensities and their local variations. The ground-shaking during an earthquake predominantly depends on several factors such as the magnitude, properties of fault plane solutions, the distance from the fault and local geologic conditions. An estimation of expected ground motion is fundamental for earthquake hazard assessment.

Generally, ground motion and damage are influenced by the magnitude of the earthquake, the distance from the seismic source to the site, and the local ground conditions [Atkinson, 2004]. Empirical attenuation relation, a practical way to estimate ground motion parameters, gives information about how these parameters depend on the abovementioned source, path, and site effects. This, namely ground condition, must be considered, because the same earthquake recorded at the same distance may cause different damage according to ground conditions [Irikura et al., 2004]. The most intense shaking experienced during earthquakes generally occurs near the rupturing fault area, and decreases with distance away from the fault. Within a single earthquake event, however, the shaking at one site can easily be stronger than at another site, even when their distance from the ruptured fault is the same. Local geologic conditions are the cause of difference in shaking intensity, but often there is little certainty of the particular conditions in a spe-

cific area that are most responsible, and the degree to which they affect earthquake shaking. The variability in earthquake-induced damage is mainly determined by the local geologic and hydrogeologic conditions. These conditions, internally influence the amplitude, the frequency and duration of ground motion at a site. Groundwater level variations and associated saturation changes in sand layers within near-surface aquifers can influence local response spectra of the ground motion, through modification of shear-wave velocity. Changes of the groundwater level can also have a considerable influence upon the liquefaction potential of a region. Special attention is drawn to in-situ pore-water pressure responses in aquifers during earthquakes, to observe and explain the triggering mechanism of liquefaction [Hannich et al., 2006].

Previous earthquakes have indicated that the damage and loss of life are mostly concentrated in areas underlain by deposits of soft soil and high ground water tables as for example the Mexico City earthquake in 1985 [Steinwachs, 1988]. Soft soils amplify shear waves and, thus, amplify ground shaking. Wetlands have a higher damage potential during earthquakes due to longer and higher vibrations. The fundamental phenomenon responsible for the amplification of motion over soft sediments is the trapping of seismic waves due to the impedance contrast between sediments and underlying bedrock. When the structure is horizontally layered, this trapping affects body waves, which travel up and down in the surface layers. When the structure is a 2D or 3D structure, i.e., when lateral heterogeneities are present (such as thickness variations in sediment-filled valleys), this trapping also affects the surface waves, which develop on these heterogeneities. The interferences between these trapped waves lead to resonance patterns, the shape and the frequency of which are related with the geometrical and mechanical characteristics of the structure [Ehret and Hannich, 2004].

Traces of ancient river meanders with sediment depositions of different grain sizes as visible on a QuickBird satellite image scene F.11-2

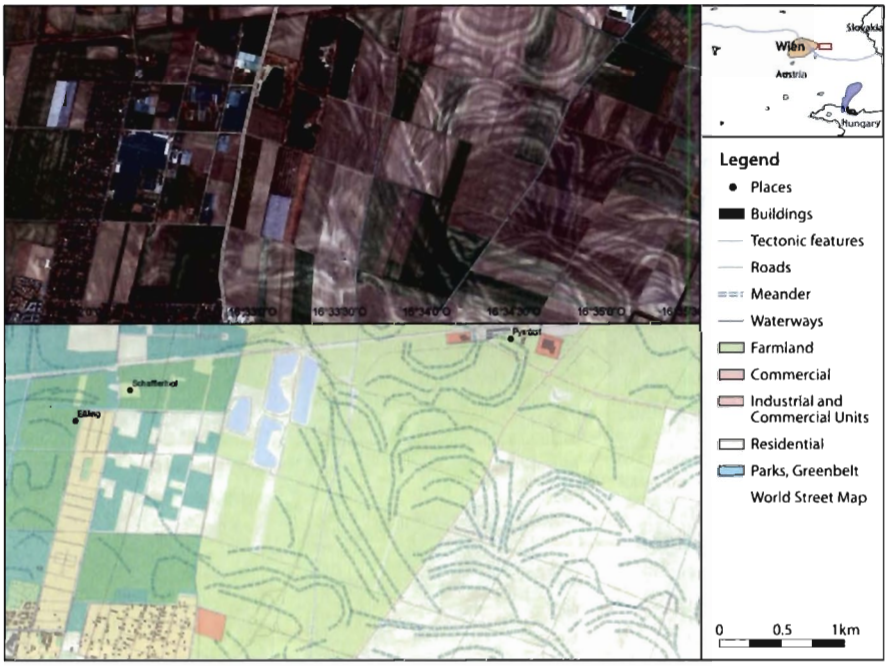


Factors as lithology (loose, unconsolidated sedimentary covers), faults, or steeper slopes (landslide susceptibility) or areas with higher groundwater tables were analysed in the Vienna area. Special attention was focussed on the detection of depressions filled with youngest sedimentary covers, wetlands, meanders, landslide areas and traces of sub-surface structures as these specific site conditions play an important role related to earthquake ground motion. F.11-2 and F.11-3 visualize the influence of varying ground conditions within ancient river meanders due to even small grain size and thickness variations of the layers, or height level differences.

Maps of seismic site conditions on regional scales require substantial investment in almost detailed geological and geotechnical data acquisition and interpretation. However, detailed macroseismic maps, that can help to detect local site conditions, are often covering only selected areas and based on different standards and scales. In many seismically active regions of the world, information about surficial geology and shear-wave velocity (VS) either, does not exist, varies dramatically in quality, varies spatially, or is not easily accessible.

There is a strong need to improve the systematic, standardized inventory of areas that are more susceptible to earthquake ground motions or to earthquake related secondary effects such as landslides, liquefaction, soil amplifications or compaction.

River meander sediments in the Marchfeld area northeast of Vienna F.11-3



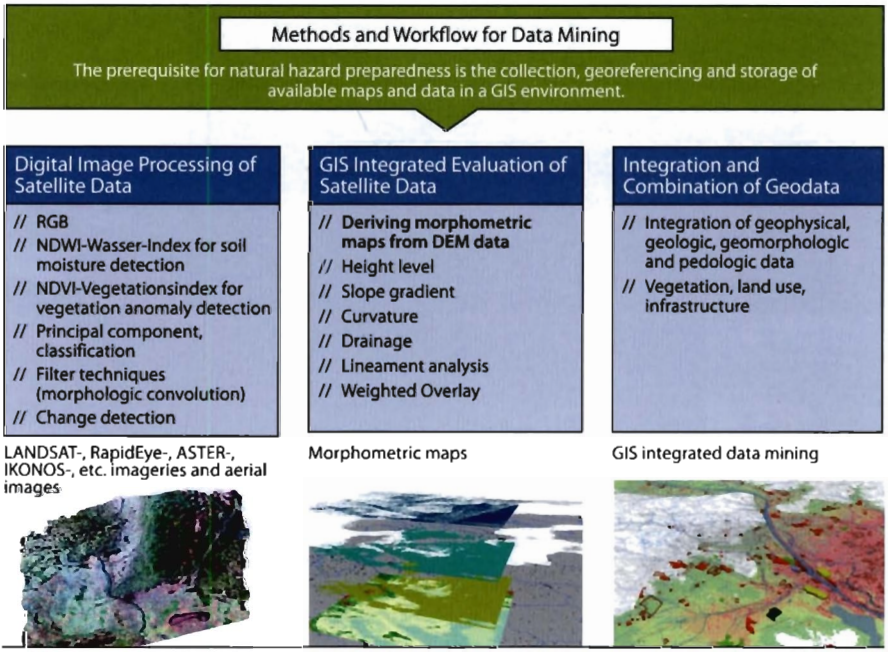
11-4 Methods

The hazard assessment derives places, which might be prone to higher earthquake damage during earthquakes. When searching for areas susceptible to soil amplification, liquefaction or compaction the so-called causative or preparatory geofactors have to be taken into account such as lithologic and hydrogeologic conditions and structural/tectonic conditions.

The existing data for this study include ASTER Global Digital Elevation Model (DEM)-data. To automatically identify the landform types that affect site conditions, the relief elements are grouped into terrain features. Terrain features can be described and categorized into simple topographic relief elements or morphometric units by parameterizing the DEM such as in height levels, slope gradients, and terrain curvature.

The prerequisite for natural hazard preparedness is the collection, georeferencing and storage of available maps and data in a GIS environment (F.11-4). GIS and related technologies can be used for monitoring and responding to disasters, as well as for planning community rebuilding or even for relocation in extreme cases. For disaster preparedness the almost detailed detection and documentation of settlements, infrastructure, industrial facilities, etc. that might be exposed to earthquake and other hazards, especially their different exposures to soil amplification, landslides or active tectonic processes is necessary. Thus, in the scope of this study spatial data layers come from various sources such as topographic maps and thematic maps (soil maps, geologic and hydrogeologic maps, land use etc.) and field survey were included and stored in a Geoinformation System (GIS) as

Elaboration of a basic GIS data base F.11-4

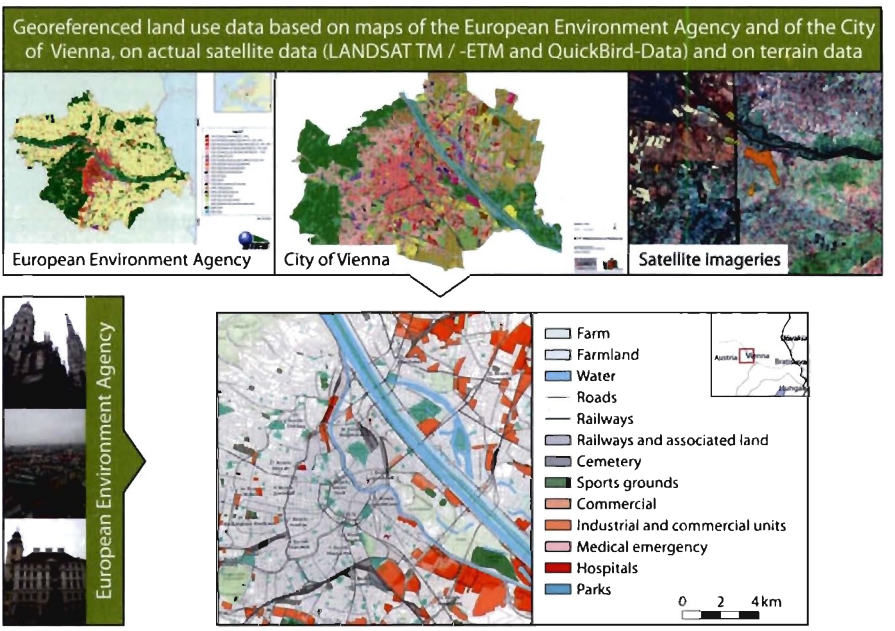


well as documents of past hazards such as landslides or flooding events. Using web-services of the actual land use information was derived from evaluations and classifications of the available LANDSAT, ASTER and Google Earth data, in addition to available open-source data such as open-street-map, Google Earth and ESRI-geodata. The workflow for the GIS data base creation is described in F.11-4. An important aspect was the availability of satellite data in order to create a most current, high spatial resolution GIS integrated reference database, aiming at visualizing critical points and areas and providing information about damage in case of emergency due to natural hazards as fast as possible, as the civil protection units need this information for their management.

11-4-1 Land Use Assessment

Some data layers, such as land use and forests, are dynamic in nature and need to be updated frequently. For risk assessment and mapping at a regional scale, information about the land use and building stock distribution in the Vienna area was derived from high resolution QuickBird satellite data, aerial images and from available information such as of the Vienna City Map (access: www.wien.gv.at/stadtplan). Data for hospitals and health centres, schools, governmental buildings, police, fire stations and industrial buildings were stored in the GIS data base (F.11-5). The tools of ArcScene/ESRI were used to exaggerate the artificial height (extrusion tools) of industrial and commercial facilities, mapped based on QuickBird-imageries, and derived from the city map of Vienna as well as from open-street-map data.

Inventory of land use types based on satellite data and land use maps of the European Environment Agency and the City of Vienna and on terrain data F.11-5



11-4-2 Evaluations of Digital Elevation Model Data (DEM) for the Extraction of Causal Factors

The GIS integrated geodata were used as well to visualize causal/preparatory factors related to the occurrence of higher earthquake shock and earthquake induced secondary effects such as lithology (loose, unconsolidated sedimentary covers), faults, or steeper slopes (landslide susceptibility) or areas with higher groundwater tables. Information of QuickBird-images were merged with actual city maps or open-source data for getting information on the functions of the different land use types and buildings. Maps of hazard-prone areas such as flood maps were superimposed on the land use maps, especially merged with available data of industrial, commercial and infrastructural facilities.

The factors influencing the occurrence, type and intensity of earthquake induced secondary effects that can be separated into causal and triggering. The causal factors determine the initial favourable conditions for the occurrence, while the triggering factors such as high precipitation rates principally determine the timing. Causal factors are, among others, the slope gradient, curvature, lithology and groundwater table level. The triggering mechanisms are quite unpredictable, as they vary in time. However, some of the causal factors can be integrated as layers into a GIS.

The influence of causal factors on earthquake ground motion is not equally important in the analysis. It varies according to the specific local settings (surface geology, structure) or according to the distance of the earthquake source. The percentage of influence of one factor also changes in consideration of seasonal and climatic factors. In very hot and dry seasons the risk of liquefaction and landslides is generally lower than in wet seasons with high precipitation.

Depressions filled with youngest sedimentary covers, wetlands and meanders, landslide areas and traces of sub-surface structures play an important role related to earthquake ground motion. Those areas are considered to be more susceptible to soil amplification wherein the following causal factors are summarizing and aggregating their effects: lowest height level of the terrain combined with relatively high groundwater tables, flat morphology with low slope gradients and no curvature, loose sedimentary covers within a basin topography or within flat areas. Deriving morphometric properties of a terrain from Digital Elevation Model (DEM) data such as the minimum curvature or lowest slope gradient and the lowest local height level helps to detect flat accumulation zones: areas with almost recent, unconsolidated sediments, generally being prone to relatively higher earthquake shock and to secondary effects as liquefaction or compaction.

Some of the causal factors were determined systematically then: From slope gradient maps those areas with the steepest slopes, and from curvature maps the areas with the highest curvature were extracted as these are more susceptible to landslides. Height level maps helped to search for topographic depressions covered by almost recently formed sediments, usually linked with higher groundwater tables. Flat areas with no curvatures of the terrain and low to no slope gradients and the lowest areas were extracted. In case of stronger earthquakes those areas often show the highest earthquake damage intensities (F.11-6).

Some of the causal factors can be determined systematically from SRTM and ASTER DEM data such as

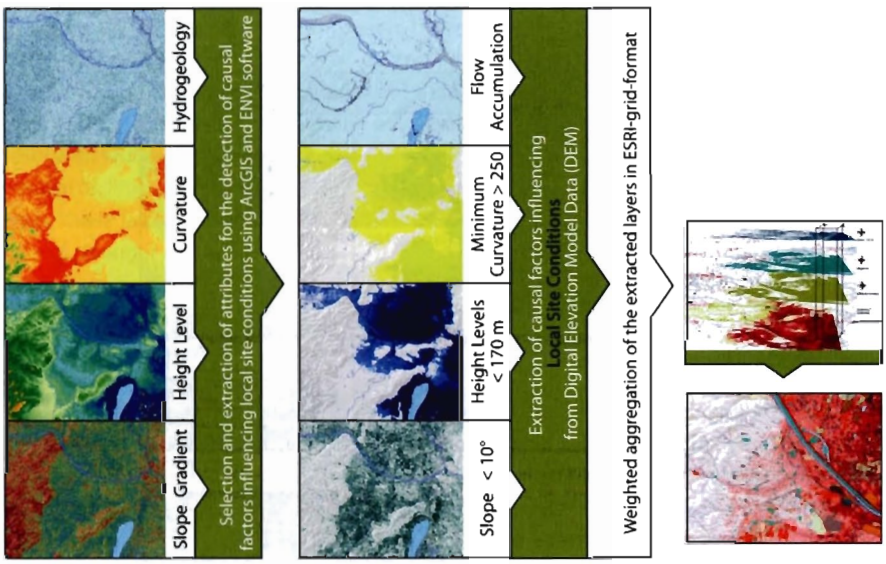
// Slope degrees <10°, indicating flat areas
// Drop raster calculation <100 000 to 200 000 (calculated in ArcMap using the raster calculator), providing information of highest surface water flow input.
// Minimum curvature >250 (calculation in ENVI-software providing information upon flat, broader valleys, basins and depressions with younger sedimentary covers and higher groundwater tables, resulting in a grey-tone image with values between 0 and 255); curvature calculation in ArcMap using the Spatial Analyst-Surface-tools by extracting then areas with curvature = 0 which correspond to flat areas.
// The lowest local height levels are indicating areas with relatively higher groundwater tables.
// Flow accumulation >1, highest flow-accumulations, providing information about areas with higher surface water-flow input.

The morphometric maps derived from DEM data were combined and merged with lithologic and seisomotectonic information as layer in the GIS data base.

// Quaternary sediment distributions and faults derived from geologic maps.
// Lineaments derived visually from LANDSAT ETM+ and RapidEye imageries.
// Earthquake data downloaded from International Earthquake Centres (International Seismological Centre – ISC, US Geological Survey – USGS, etc.).
// Vs30-IDW-interpolation (data from USGS).
// Shake maps, macroseismic observation records and further available data.

The different factors were converted into ESRI-GRID-integer format and summarized/aggregated and weighted in per cent in the weighted overlay-tool of ArcGIS according

Extraction of causal factors and their aggregation in a weighted overlay approach F.11-6

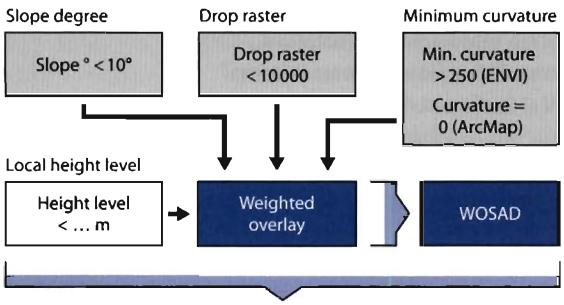


to their estimated influence on the local specific conditions. For example, as a stronger earthquake during a wet season will probably cause more secondary effects than during a dry season, the percentage of the weight of the different factors has to be adjusted to seasonal effects and to the local geomorphologic and geologic settings.

The integration of different factors in a GIS environment using weighting procedures serves as one of the key objectives in the GIS application in the frame of this study. The weighted overlay method takes into consideration the relative importance of the parameters and the classes belonging to each parameter (ESRI, online support in ArcGIS).

The application of a weight-linear-combination in susceptibility assessment has been identified as a semi-quantitative method, involving both expert evaluation and the idea of ranking and weighting factors. The basic pre-requisite for the use of weighting tools of GIS is the determination of weights and rating values representing the relative importance of factors and their categories. The efficacy of the weighted overlay-method lies

Workflow for the weighted overlay approach aggregating factors with influence on local site conditions F.11-7



Weighted overlay calculation based on causal or preparatory factors derived from morphometric maps based on SRTM DEM data:

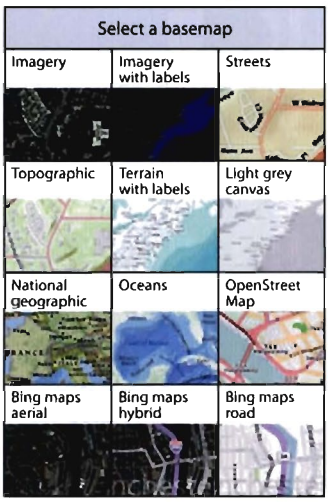
// slope < 10°
// lowest, local height level < ... m
// minimum curvature > 240–250, calculated in ENVI-software
// curvature = 0, calculated in ArcGIS (raster calculator in ArcMap)
// drop raster < 100000, calculated in ArcGIS (raster calculator in ArcMap)

WOSAD – Weighted Overlay for Soil Amplification Detection – a Standardized Approach

+

// Lithologic and seismotectonic information in a GIS data base as
// Quaternary sediment distributions and faults derived from geologic maps
// Lineaments derived from LANDSAT ETM imageries
// Earthquake data (ISC, USGS, EMSC, GFZ, etc.) downloaded from International Earthquake Centres
// Vs30-IDW-interpolation (data from USGS)
// Shake maps and
// Further available information

+



Open-source information provided by ESRI, OpenStreet-Map, etc.

in the fact that human judgements can be incorporated in the analysis. The weights and ratings are determined using the expert's subjective knowledge. The method starts by assigning an arbitrary weight to the most important criterion (highest percentage), as well as to the least important attribute according to the relative importance of parameters. The sum over all the causal factors/layers that can be included into GIS provides some information about the susceptibility to the amplification of seismic signals. This susceptibility is calculated by adding every layer, as described below, to a weighted influence and summing all layers. After weighing (in percent) the factors according to their probable influence on ground shaking, susceptibility maps can be elaborated, where those areas are considered as being more susceptible to higher earthquake shock intensities, where "negative" causal factors occur aggregated and are interfering with each other. The resulting maps are divided into susceptibility classes. The susceptibility to soil amplification is classified by values from 0 to 6, where the value 6 stands for the strongest, assumed susceptibility to soil amplification due to the aggregation of causal factors. The approach mentioned above is described as the Weighted-Overlay for Soil Amplification Detection (WOSAD) approach using ArcGIS and ENVI-software (F.11-6, F.11-7).

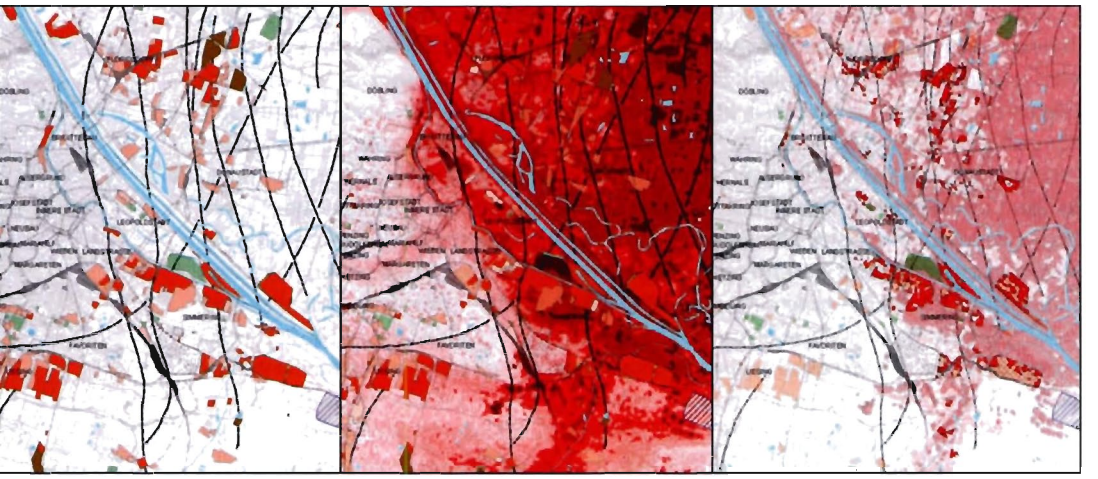
Comparing the results of the weighted overlay-calculations with geologic maps, there is a clearly visible coincidence of areas with higher susceptibility values and the outcrop of unconsolidated, quaternary sediments in broader valleys and depressions.

Whenever an earthquake happens, it can now be better derived where the "islands" of higher ground shaking are most likely to occur in the affected areas by adding the specific information of the earthquake to the susceptibility map using the WOSAD-weighted overlay-approach. The approach hereby presented is proposed to serve as a first basic data stock for getting a perception of potential sites susceptible to higher earthquake ground motion, including in the next steps the integration of further, available data such as movements along active faults, focal planes, 3D structure, lithologic properties and thickness of lithologic units or shear wave velocities. The analysis method and integration rules can be easily modified in the open GIS architecture as soon as additional information becomes available. The limitation of the approach, however, lies in the constricted accuracy of the SRTM and ASTER DEM data sets of up to several metres. At least, it is suited to obtain a first basic overview on the susceptible areas and hazard perspectives according to a standardized approach. This might be of interest especially for countries with low financial resources where such maps are still unavailable. The information of the industrial/commercial facilities were overlaid in ArcGIS with the results of the WOSAD approach (F.11-8). Thus, those facilities were visualized that are situated in potentially endangered areas in case of stronger earthquakes.

11-4-3 Digital Image Processing and Evaluations of Satellite Imageries

To deliver information about a disaster in near real time is vital to save lives of people involved and to prepare measurements. High resolution satellite data are needed for this purpose, however, most of them are available with a time delay. An important aspect is the delivery of satellite data for both, for creating a most actual, high spatial resolution, GIS integrated reference data base visualizing critical points and areas, and for providing

Overlay of industrial/commercial units with the results of the WOSAD approach indicating industrial/commercial facilities situated in areas assumed to have the highest susceptibility to soil amplification in red F.11-8



Industrial/commercial units in Vienna area

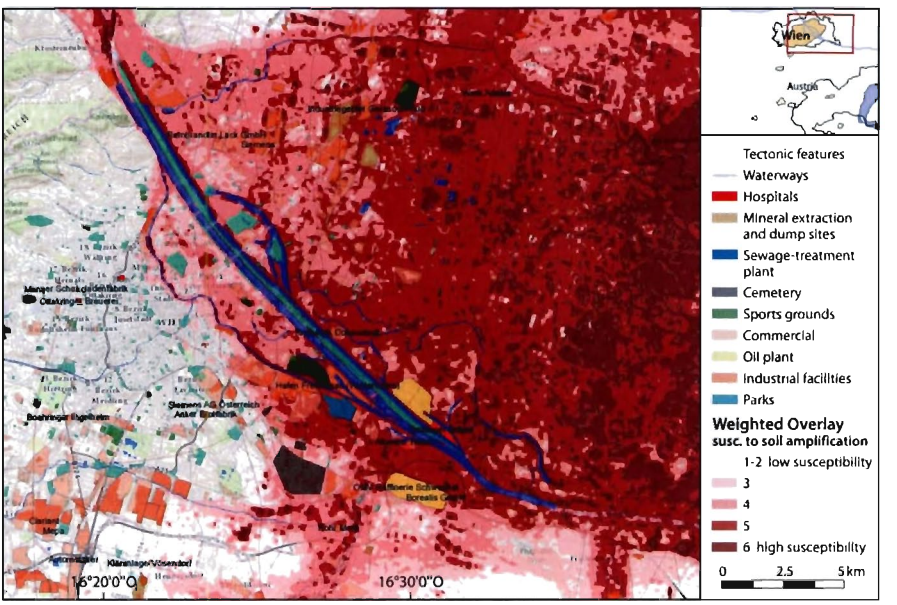
Mapping of industrial/ commercial facilities

Overlay with the WOSAD approach

Detection of those industrial/commercial units situated in areas of higher susceptibility to soil amplification according to the Weighted Overlay for Soil Amplification Detection (WOSAD) approach by intersection of the data in ArcGIS

- Railways and associated land
- Airport
- Sports grounds
- Roads
- Railways
- WO landuse industry intersect
- Oil plant intersect with WO SRTM-6
- Industrial
- Oil plant
- Cemetery
- WO as m 5
- WO SRTM 6
- Tectonic features

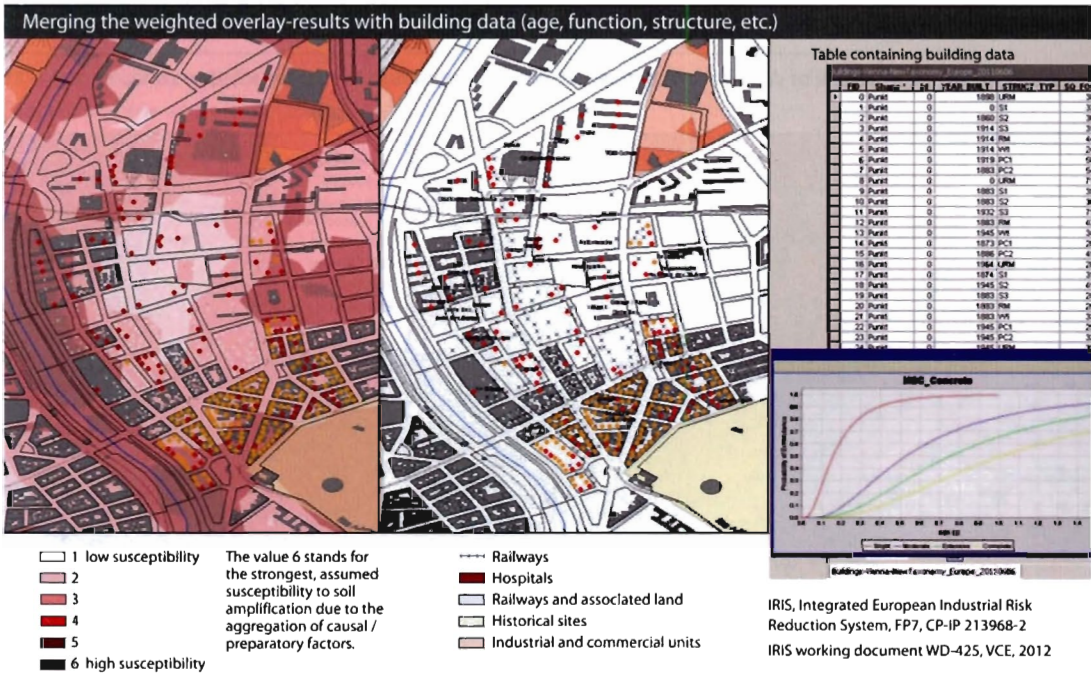
Weighted overlay of causal, morphometric factors based on ASTER DEM data F.11-9



information of damages in case of emergency due to an accident in an industrial plant or due to natural hazards as fast as possible, as the civil protection units need the information for their management.

For a better overview of seasonal influences on earthquake ground motion and on secondary effects multi-temporal analysis of different satellite data and aerial images were carried out, in combination with evaluations of geotechnical data, climatic data, long-term soil moisture and groundwater table measurements and data of vegetation status. Digital image processing tools for the different satellite data providing the best results for this purpose were investigated. Based on multispectral satellite data combinations of different RGB combinations of the spectral bands were tested. Low pass and high pass filters and directional variations were used for the detection of subtle surface structures such as meanders or landslides. The visibility of linear features in the images that might be related to sub-surface structures was enhanced. Lineament analysis based on LANDSAT imageries or DEM derived morphometric maps such as hillshade or slope maps helped to detect possible fault and fracture zones in the subsurface. Merging the "morphologic" image products derived from "Morphologic Convolution" image processing in ENVI software with the RGB-satellite imageries, the evaluation feasibilities were improved. Tectonic features (GBA, Vienna) were included to focus on the potential influence of sub-surface structures on seismic wave propagation and on their important role for horizontal and vertical movements, especially for subsidence in the Mitterndorf-Graben-area. Earthquake damage can be amplified by guided seismic waves along fault zones. Seismic waves travel-

Overlay of the WOSAD-results with detailed building information F.11-10



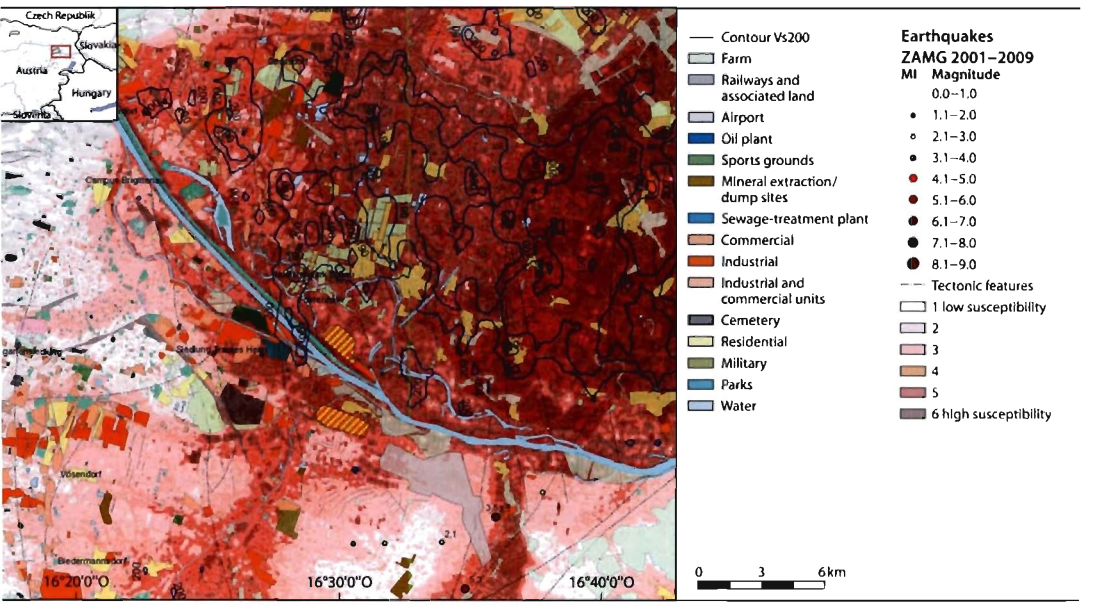
IRIS, Integrated European Industrial Risk Reduction System, FP7, CP-IP 213968-2
IRIS working document WD-425, VCE, 2012

ling in the subsurface might be refracted at sharply outlined discontinuities as faults, and, thus, arrive at a summation effect that influences the damage intensity. Fault segments, their bends and intersection are more apt to concentrate stress and amplify seismic shock and, thus, provide an assumption where summation effects can be expected.

11-4-4 Evaluations of Shear Wave Velocity Data

In order to provide a first-approximation of local site conditions, an approach was developed to characterize potential ground motions on the basis of known correlations between variations in shear-wave velocity and topographically distinctive landforms by applying geomorphometry, a quantitative description of landforms based on DEMs [Wald and Allen, 2007; Yong et al., 2008]. Hereby, Vs30-measurements (the average shear-velocity down to 30 m) are correlated against topographic slope. These authors also compared topographic slope-based Vs30 maps to existing site condition maps based on geology and observed Vs30 measurements, where they were available, and found favourable results. Thus, for getting a first impression of shear velocities in the Vienna area, the estimated Vs30-data provided by USGS were used. The Vs30-data were converted into point-shapefiles, serving as a base for interpolations. From the interpolated Vs30 contour lines the values below 300 m/sec were extracted as lower Vs30-values are correlated in their position with unconsolidated Quaternary sediments, what is assumed to contribute to higher earthquake damage. The resulting interpolation contour-lines were merged with other geodata such as geologic, geophysical and hydrogeologic maps as for example provided by GBA Online. The Vs30-interpolation results were combined as well with the weighted overlay results (F.11-9).

Merge of WOSAD calculation results with estimated Vs30 interpolation contour lines F.11-11



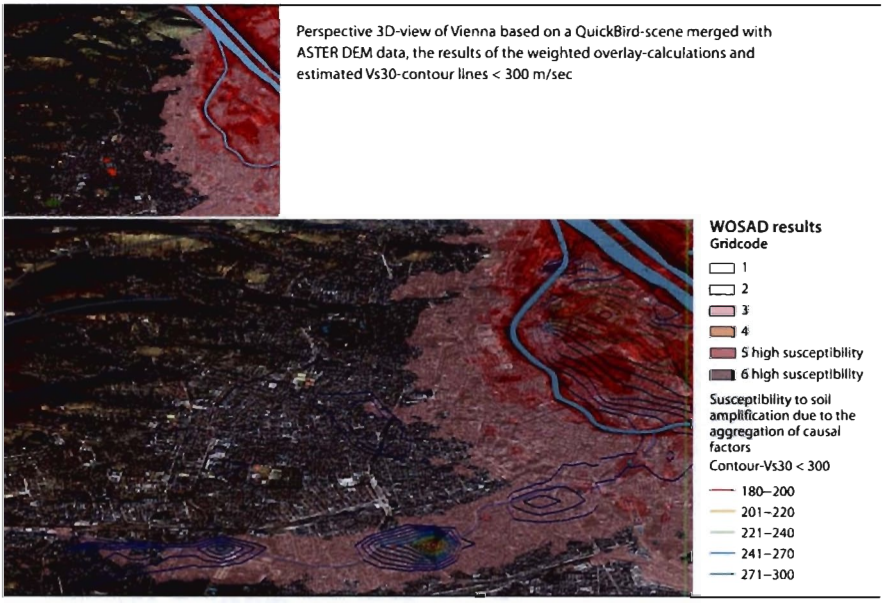
11-5 GIS Integrated Evaluations of Remote Sensing and Different Geo-Data

According to the described methods the WOSAD approach was investigated based on SRTM- and ASTER DEM data providing an overview of areas with aggregation of causal factors in the Vienna area, where the susceptibility to damages can be assumed to be higher in case of stronger earthquakes due to local site conditions

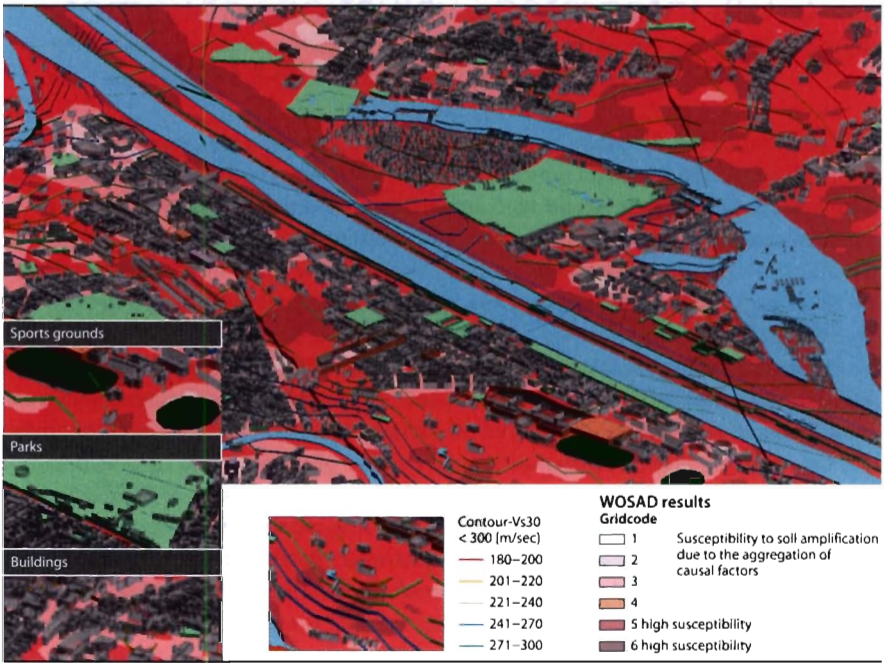
11-5-1 Results of the WOSAD Approach

The overlay of industrial/commercial facilities with the results of the WOSAD approach contributes to the detection of those facilities that might be exposed to higher soil amplification due to the aggregation of causal factors (F.11-9). However, whether these facilities are exposed in fact to higher damages in case of stronger earthquakes, depends on factors such as the building construction type, function, the age, or the used material. Therefore an almost detailed inventory of building properties is required. Based on the developments of the MaeViz-software in the United States and an innovative disaster management platform, the software EQvis was created in the scope of the EU-funded IRIS-project by VCE allowing quick reactions in case of disasters as well as simulations for the improvement of disaster preparedness. Simulation and visualization can be performed on the EQvis platform. By introducing various hazard scenarios the response of the infrastructure can be computed (F.11-10).

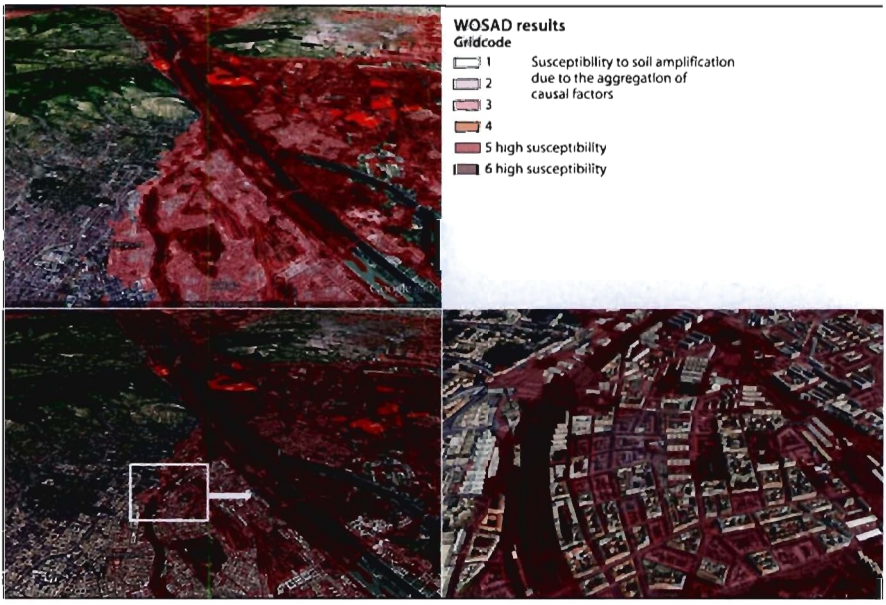
3D perspective view of the weighted overlay results combined with the QuickBird-scene and estimated Vs30-data < 300 m/sec (USGS) F.11-12



WOSAD results presented in 3D views using ArcScene-tools F.11-13



Use of Google Earth for visualization of areas with assumed higher susceptibility to soil amplification due to the aggregation of causal factors F.11-14



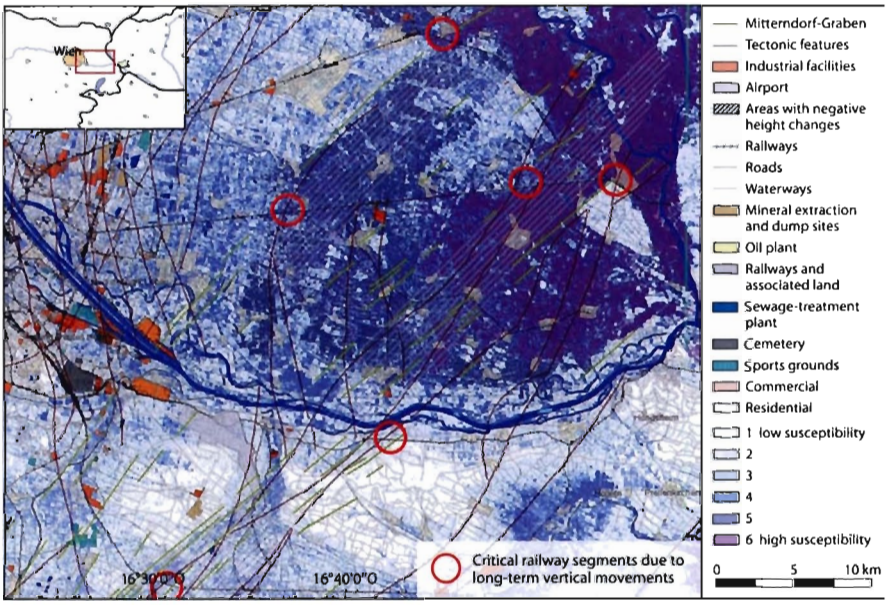
When combining the results of the weighted overlay-approach (summarizing factors with influence on earthquake shock), and the estimated shear wave velocities (Vs30), a better understanding and visualization of differences and "islands" of higher earthquake damage and potentially affected areas can be achieved. There is a clearly visible coincidence of areas with lower Vs30-values such as assumed Vs30 < 200 m/sec, and areas with higher susceptibility to soil amplification due to the aggregation of factors influencing the specific local site conditions as well as a distinct correlation with areas covered by unconsolidated, Quaternary sediments. The Vs30-values < 300 m/sec were confirmed by field measurements during the SEISMID-project (SEISMID – Seismic system identification for the Vienna Basin-Project, 2007–2011 [VCE, 2011]).

Infrastructural data and weighted overlay results were merged with QuickBird satellite data (F.11-12). The visualization of the susceptibility to soil amplification in the Vienna area was enhanced by 3D perspective views (F.11-13). The 3D-perspective views clearly show where industrial facilities are underlain by so far known sub-surface structures and where these facilities are built in areas with relatively higher susceptibility to soil amplification in case of stronger earthquakes. These data were converted into *.kmz*-format for being displayed in Google Earth. The weighted overlay results were presented in Google Earth, combined then with the detailed 3D views of the buildings (F.11-14).

11-5-2 Neotectonic Movements

The analysis of the drainage pattern can help to detect the location of active structures [Yang et al., 2007]. Meanders typically develop under conditions of limited bedloads, fine-grained sediments and low river-bed gradient [Burnett and Schumm, 1983]. Even little uplifting or subsiding can change the network of rivers. The Marchfeld-area

Weighted overlay of causal factors indicating lowest and flattest areas F.11-15



north of Vienna and the Little Hungarian Plain are characterized by meandering rivers with relatively low surface slope and river gradient, but high river sinuosity. The Danube river area has slightly tilted terraces with river meanders and many tributaries developed on its surface. QuickBird and LANDSAT ETM imageries allow the detailed mapping of these rivers and meanders. A distinct relationship between active tectonics, topographic evolution and drainage pattern development can be observed. When combining and comparing the traces of meanders with geodetic measurements, it becomes obvious that the occurrence and density of meanders coincides with areas of subsidence. Negative, vertical movements as measured by precise geodetic measurements of height differences are prevailing and concentrated in the Danube river [Szeidovitz and Gibrovski, 2004]. There is a clearly visible spatial coincidence between subsidence areas and meander development. The result of the weighted overlay of morphometric properties (height level <150 m, slope gradient $<10°$, curvature $=0$, drop raster <100000) shows as well a coincidence between these morphometric properties and subsidence areas. As vertical and horizontal movements are influencing the long-term stability of infrastructural facilities such as piping, sewage, railroads and roads, especially in the transition zones between uplift and subsidence, an inventory of infrastructural facilities situated in those "critical" areas is necessary (F.11-15).

11-6 Conclusions

RS and GIS data and results can be combined with updateable and dynamic scenarios for earthquakes in the geo-databases of a GIS, assisting the procedure of preparedness and increasing the organization and effectiveness of response activities. GIS integrated evaluations of different satellite data can contribute considerably to the detection of subsurface structures in Eastern Austria and those areas that are assumed to be prone to relatively higher earthquake ground motion due to the aggregation of preparatory factors. This supports the monitoring of infrastructural facilities. Finally, WebGIS components can be used for the collection and analysis of real damage to the built environment in case of stronger earthquakes and related secondary effects, thus, providing valuable information on the behaviour of buildings and the cost of repair and re-habilitation procedures.

References

Atkinson, G.M., 2004. *Empirical Attenuation of Ground-Motion Spectral Amplitudes in Southeastern Canada and the Northeastern United States*. Bulletin of the Seismological Society of America 94(3):1079–1095.

Beidinger, A., Decker, K. and Roch, K.H., 2011. *The Lassee Segment of the Vienna Basin Fault System as a Potential Source of the Earthquake of Carnuntum in the Fourth Century A.D.* Int. Journal of Earth Sciences (Geol. Rundschau) 100(6):1315–1329.

Burnett, A.W. and Schumm, S.A., 1983. *Alluvial River Response to Neotectonic Deformation in Louisiana and Mississippi*. Science 222:49–50.

Grünthal, G., Mayer-Rosa, D. and Lenhardt, W.A., 1998. *Abschätzung der Erdbebengefährdung für die D-A-CH-Staaten – Deutschland, Österreich, Schweiz*. Bautechnik 10:3–17. Stuttgart: Verlag Ernst & Sohn.

Hausmann, H., Hoyer, S., Schurr, B., Brückl, E., Houseman, G. and Stuart, G., 2010. *New Seismic Data Improve Earthquake Location in the Vienna Basin Area, Austria*. Austrian Journal of Earth Sciences 103(2):2–14.

Hannich, D., Hötzl, H. and Cudmani, R., 2006. *Einfluss des Grundwassers auf die Schadenswirkung von Erdbeben – ein Überblick*. Grundwasser 11(4):286–294.

Harzhauser, M. and Piller, W.E., 2004. *Integrated Stratigraphy of the Sarmatian (Upper Middle Miocene) in the Western Central Paratethys*. Stratigraphy 1(1):65–86.

Hinsch, R. and Decker, K., 2010. *Seismic Slip Rates, Potential Subsurface Rupture Areas and Seismic Potential of the Vienna Basin Transfer Fault*. Int. Journal of Earth Sciences (Geol. Rundschau) 100(8):1925–1935.

Irikura, K., Miyake, H., Iwata, T., Kamae, K., Kawabe, H. and Dalguer, L.A., 2004. *Recipe for Predicting Strong Ground Motion from Future Large Earthquake*. Proceedings of the 13th World Conference on Earthquake Engineering, Paper No. 1371.

Lenhardt, W.A., Švancara, J., Melichar, P., Pazdirkova, J., Havir, J. and Sykorova, Z., 2007. *Seismic Activity of the Alpine-Carpathian-Bohemian Massif Region with Regard to Geological and Potential Field Data*. Geologica Carpathica 58:397–412.

Meurers, R., Lenhardt, W.A., Leichter, B. and Fiegweil, E., 2004. *Macroseismic Effects of the Ebreichsdorf Earthquake of July 11, 2000 in Vienna*. Austrian Journal of Earth Sciences 95/96:20–27.

Savvaidis, P., Theilen-Willige, B., Tziavos, I.N., Grigiriadis, V.N. and Papadopoulou, I.D., 2012. *Detection of Earthquake Vulnerable Areas in the Grevena Region/Northern Greece using Remote Sensing and WebGIS Methods*. Proceedings of International Symposium "Modern Technologies, Education and Professional Practice in Geodesy and Related Fields", Sofia, 8–9 November 2012.

Steinwachs, M., 1988. *Das Erdbeben am 19. September 1985 in Mexiko – Ingenieurseismologische Aspekte eines multiplen Subduktionsbebens*. In: Steinwachs, M. (ed). Ausbreitungen von Erschütterungen im Boden und Bauwerk. 3. Jahrestagung DGEB, Trans Tech. Publications, Clausthal, Germany.

Szeidovitz, G. and Gibrovski, K., 2004. *Seismic Hazard of Dunafoldvar*. In: Mentes, G. and Eperne, I. (eds), Landslide Monitoring of Loess Structures in Dunaföldvar, Hungary. Sopron: Geodetic and Geophysical Research Institute, Hung. Acad. of Sciences: 24–35.

Theilen-Willige, B., Savvaidis, P., Tziavos, I.N. and Papadopoulou, I, 2012. *Remote Sensing and Geographic Information Systems (GIS) Contribution to the Inventory of Infrastructure Susceptible to Earthquake and Flooding Hazards in North-Eastern Greece*. Geosciences 2(4):203–220.

Yang, C.B., Chen, W-S., Wu, L.-C. and Lin, C.W., 2007. *Active Deformation Front Delineated by Drainage Pattern Analysis and Vertical Movement Rates, Southwestern Coastal Plain of Taiwan*. Journal of Asian Earth Sciences 31:251–264.

Yong, A., Hough, S.E., Abrams, M.J. and Wills, C.J., 2008. *Preliminary Results for a Semi-Automated Quantification of Site Effects Using Geomorphometry and ASTER Satellite Data for Mozambique, Pakistan and Turkey.* Journal of Earth System.

VCE, 2011. *Erdbeben im Wiener Becken – Beurteilung, Gefährdung, Standortrisiko.* GRASL Druck & Neue Medien GmbH, Vienna.

Wald, D.J. and Allen, T.I., 2007. *Topographic slope as a proxy for seismic site conditions and amplification.* Bulletin of the Seismological Society of America 97(5):1379–1395.

Earthquake Data

European Mediterranean Seismological Centre – EMSC:
www.emsc-csem.org/Earthquake/earthquake.php?id=107436
International Seismological Centre – ISC:
www.isc.ac.uk/help/search/custom/maptool.html
US Geological Survey – USGS:
http://earthquake.usgs.gov/earthquakes/eqarchives/epic/
http://earthquake.usgs.gov/hazards/apps/vs30/
Central Institute for Meteorology and Geodynamics – ZAMG:
www.zamg.ac.at/erdbeben/jahrbuch/?ts=1322646001

GIS-Data

OpenStreetMap:
http://download.geofabrik.de/osm/europe/
Land Use:
www.eea.europa.eu/data-and-maps/figures/urban-atlas
www.wien.gv.at/stadtentwicklung/grundlagen/stadtforschung/siedlungsentwicklung/realnutzungskartierung.html

Satellite Data

ASTER DGDEM:
www.gdem.aster.ersdac.or.jp/search.jsp
SRTM DEM:
http://srtm.csi.cgiar.org/SELECTION/inputCoord.asp
LANDSAT:
http://glcfapp.glcf.umd.edu:8080/esdi/index.jsp
http://earthexplorer.usgs.gov/

Geologic Data

Geologische Bundesanstalt in Vienna (GBA):
www.geologie.ac.at
http://geomap.geolba.ac.at/MASS/intro_start1.cfm

12

EQvis – Advanced Seismic Loss Assessment and Risk Management Tool

Author:
David Schäfer

Motivation

Disaster management depends on the availability of data, the technologies for assessment and the capabilities for prediction and optimization of scenarios. A risk management software based on the new IRIS risk paradigm (refer chapter 2) has been desired.

Main Results

The software platform EQvis follows the consequence based risk management methodology using a visually based menu-driven system to generate damage estimates from scientific and engineering principals and data. Multiple mitigation strategies and scenario development optimization routines are provided. It enables policy and decision makers to ultimately develop risk reduction strategies and implement mitigation plans.



12-1 Introduction

12-1-1 About EQvis

EQvis is an advanced seismic loss assessment, and risk management software which stands on the Consequence-based Risk Management (CRM) methodology. CRM provides the philosophical and practical bond between the cause and effect of the disastrous event and mitigation options.

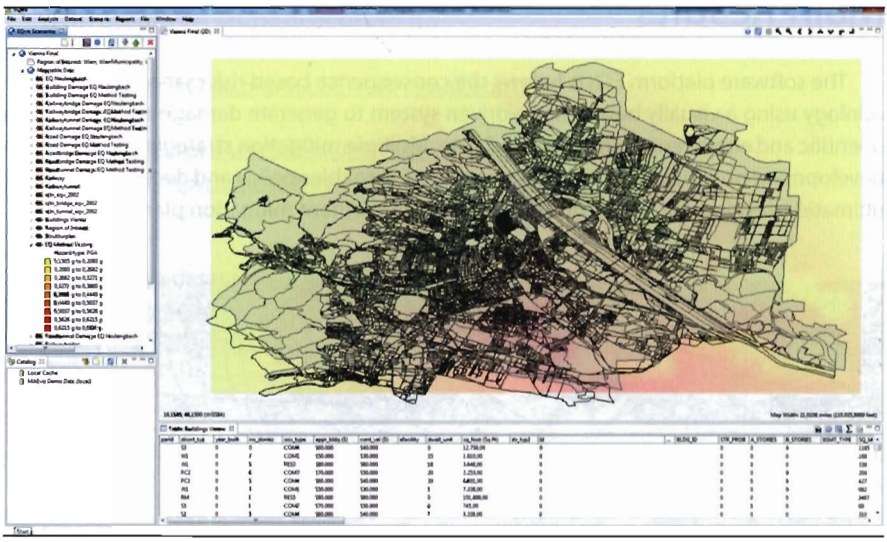
EQvis follows the CRM methodology using a visually-based, menu-driven system to generate damage estimates from scientific and engineering principles and data, test multiple mitigation strategies, and support modelling efforts to estimate higher level impacts of earthquake hazards, such as impacts on transportation networks, social or economic systems.

It enables policy-makers and decision-makers to ultimately develop risk reduction strategies and implement mitigation actions. In EQvis, a wide range of user-defined parameters are introduced. The breadth of user-defined parameters enables emergency planners to model a virtually unlimited number of scenarios.

EQvis is based on the open-source-platform MAEviz, developed by the Mid-America Earthquake (MAE) Center and the National Center for Supercomputing Applications (NCSA).

It has an open-source framework which employs the advanced workflow tools to provide a flexible and modular path. It can run over 50 analyses ranging from direct seismic impact assessment to the modelling of socioeconomic implications. It provides 2D and 3D mapped visualizations of source and result data and it provides tables, charts, graphs and printable reports for result data. It is designed to be quickly and easily extensible.

Interactive surface of EQVIS: scenario manager, data catalogue, tables, hazard map F.12-1



When new science, source data or methodologies are discovered, these can be added to the system by developers or end users via a plug-in system. Furthermore, the extensibility allows EQvis to be used for other future scenarios, such as other hazardous events like hurricanes, fires, landslides, etc.

Methodology

EQvis implements Consequence-Based Risk Management (CRM) using a visual, menu-driven system to generate damage estimates from scientific and engineering principles and data. It can also estimate impacts on transportation networks, social or economic systems.

It requires the following as inputs: hazard, inventory and fragility models. This information is useful to estimate the damage and the losses. It can consider different types of assets such as buildings, bridges and lifelines (gas, water, electric facilities, etc.).

With regard to buildings, it estimates structural and non structural damage, economic losses and liquefaction damage. With regard to bridges, it computes damage, loss of functionality and repair cost analysis. Concerning lifelines it calculates the network damage and the repair rate analysis. Finally, it computes socio-economic losses such as shelter needs, fiscal and business interruption.

IT Details

EQvis is an open source software. It is written in Java Language using Eclipse RCP. Eclipse RCP is a platform for building and deploying rich client applications. It includes Equinox, a component framework based on the OSGi standard, the ability to deploy native GUI applications to a variety of desktop operating systems, such as Windows, Linux and Mac OSX and an integrated update mechanism for deploying desktop applications from a central server. RCP made it possible to make EQvis modular and extensible. In fact, EQvis provides a framework to add new data and algorithms or update existing ones.

It also uses NCSA GIS Baseline that is a rich client application. This latter is composed of three main functions: data management (typing, ingestion, access, provenance tracking), visualization (support for 2D and 3D views, zoom, selection, highlighting), analysis execution (support for local multi-threaded execution, visual dataflow system in development).

The extensions to NCSA GIS and RCP are all provided by plug-ins. The technologies used by EQvis are all open source software like geotools, vtk (Visualization Toolkit), Jasper Reports (for generating various kinds of outputs), JfreeChart and Ktable. EQvis is also planning/developing a "cyberinfrastructure/cyberenvironment" that wants to provide universal access to the calculated results through "grid computing", both for the calculation part and the rendering part. By using as main transport SOAP/HTTP, the concept of repositories, and grid computing, the project is not only a client that makes risk analysis, but an entire platform that enables the user to use data from different places (data sources).

EQvis can easily integrate spatial information, data and visual information to perform seismic risk and analysis. It supports *.shp file that is really useful to immediately visualize input and output data. Concerning output data it provides different formats of results such as *.dbf table, *.shp file and *.pdf file. The level of resolution depends on the size of the geo-unit that can be defined by the user. The geographical unit could be a regional

unit, a provincial unit, a local unit and it could be an arbitrary polygon (regular or irregular).

Finally, EQvis has a user-friendly Graphical User Interface (GUI) that guides the user through the analyses. In the catalog box, in the lower left corner, the databases are stored and the user can utilize this box to select default data or their own data that are saved herein. In the scenario box, in the upper left corner, the analyses that have been run can be selected and can be visualized on the right box of the GUI.

12-1-2 Using the Manual

Many roads lead to Rome – this policy also applies to working with EQvis: graphics, tables and the data catalog are on an equal footing. To maintain the character of a reference book, the manual follows the order and the structure of the commands. The individual tables are described in detail column by column. Instead of presenting general Windows features, the manual rather gives practical hints and notes.

If you are new to the program, you should work through the introductory example step by step. Thereby, you will get familiar with the most important features of EQvis.

12-2 Installation

12-2-1 System Requirements

In order to use EQvis comfortably, we recommend the following system requirements:

// Operating system Windows XP Sp3/Vista/7
// CPU with 2 GHz
// 2 GB RAM
// DVD-ROM for installation, alternatively a network installation is possible
// 1 GB hard disk capacity, including approximately 500 MB for installation
// Graphic card with OpenGL acceleration and a resolution of 1024 × 768 pixels, onboard solutions and shared-memory-technologies are not recommended

No product recommendations are made, with the exception of the operating system, as EQvis and its additional modules basically run on all systems that fulfill the system requirements. If EQvis is used for intensive calculations, the guiding principle "more is better" is applicable.

When working on large systems, huge amounts of data will be produced. As soon as the main memory is not sufficient for taking the data, the hard drive will take over. This can slow down the computer significantly. Therefore, an increased memory will speed up the calculation much more than a faster processor. When selecting a motherboard, make sure that the main memory can be expanded.

12-2-2 Installation Process

Installation from DVD

Once you located the folder *setup_files*, follow the instruction reported in Network Installation.

Network Installation

EQvis

1) Create the following local folder, and place here all the setup files
   C:\EQvis\setup_files
2) Install Oracle Java JRE by launching
   C:\EQvis\setup_files\jre-6u30-windows-i586-s.exe
3) Install the software to the folder C:\EQvis by running
   C:\EQvis\setup_files\eqvis-setup-2.3.exe

Fragility Function Manager

1) Launch C:\EQvis\setup_files\Fragility Function Manager.msi
2) Copy the folder Fragility Function Files to C:\EQvis\

Database of Vienna

1) Copy the folder Data Vienna to C:\EQvis\

Installing Updates and New Modules

New versions of the suite will be delivered.

12-3 Introductory Example

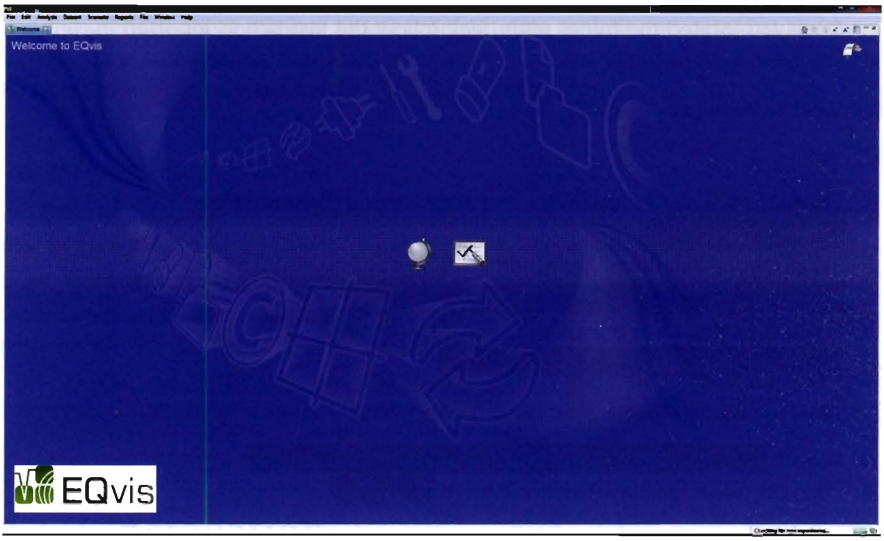
This chapter helps you to become familiar with the most important functions of EQvis by using a simple example. As there are so many different ways to achieve specific objectives it might make sense to use one or the other, always depending on the situation and the user's preferences. This example wants to inspire you to discover the possibilities and options of EQvis on your own.

In this tutorial, EQvis will be used to determine the impact of an earthquake occurring in Vienna, mainly on its buildings. The tool will be used as a specific Emergency Manager would use it. In the process it will be shown how to launch the application, load the GIS data, and generate earthquake hazard information based on the scenario of interest.

When the base information is loaded it is possible to choose and display information for specific items of interest such as buildings, and load fragility information about these particular structures.

12-3-1 Welcome Screen

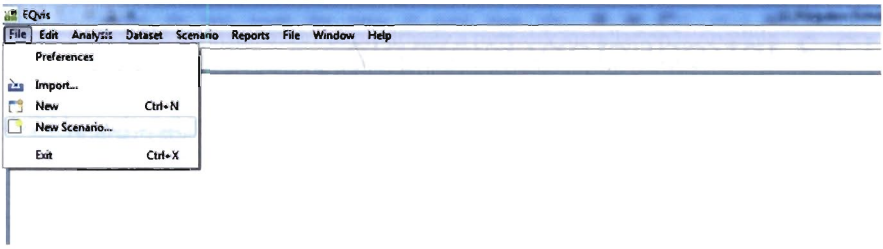
// When you start the software for the first time, you will be led to the welcome screen.



// To begin working, click the rightmost icon which will take you directly to the workbench.

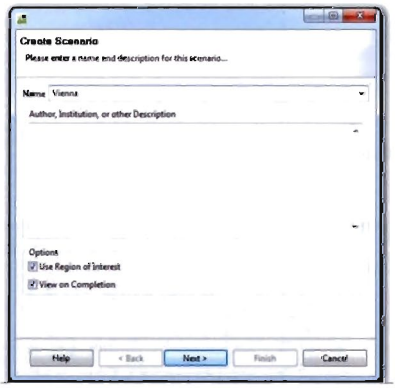
12-3-2 New Scenario

// From the application's menu bar, click File → New Scenario.

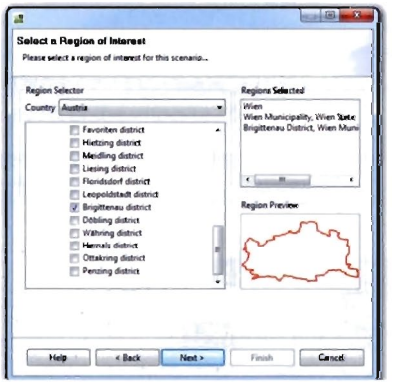


// Alternatively, you can click the New Scenario button from the Scenario View's tool bar.

// Enter a **name** for your scenario, such as "Vienna", and then optionally enter any descriptive information about the scenario in the large text box. Click **next**.

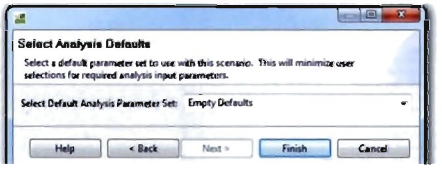


// Select **Austria** from the Country menu.
// Select **Brigittenau district** and select the box. A tick will appear next to the name. Then click **next**.



This wizard allows adding multiple regions of interest by selecting more boxes at the same time. Anyway this tutorial will only focus on Vienna.

// From the dropdown menu, select **Empty Defaults**, then click **finish**.



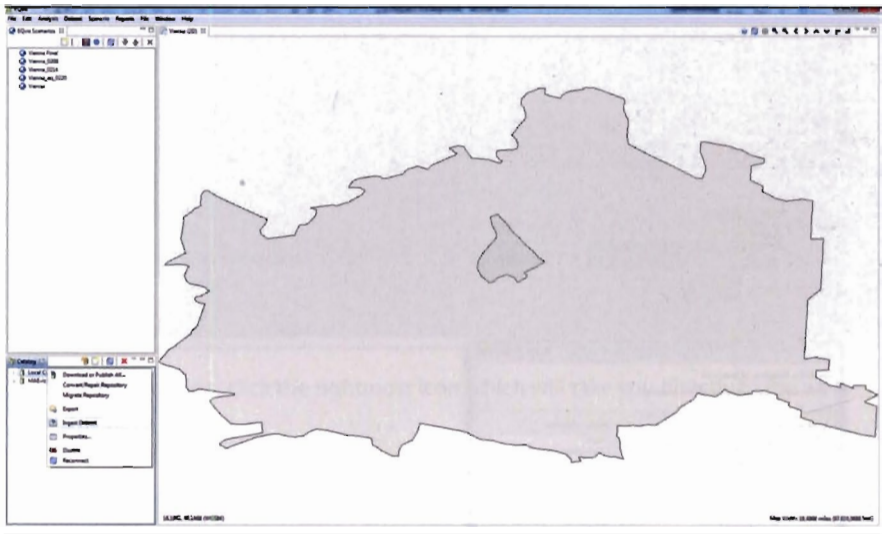
This screen allows the selection of a default set. This will populate the analysis pages with default data where applicable (e.g. fragilities, fragility mapping, etc).

// At this point, your scenario has been created. It will appear on the list of the Scenario View. A blank outline of Vienna will also appear in the Visualization View.

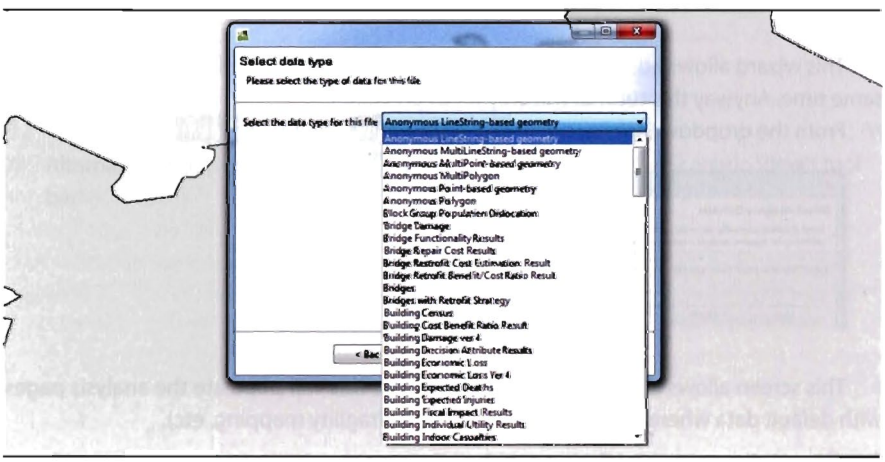
12-3-3 Adding Data to the Scenario

Adding the City Plan of Vienna

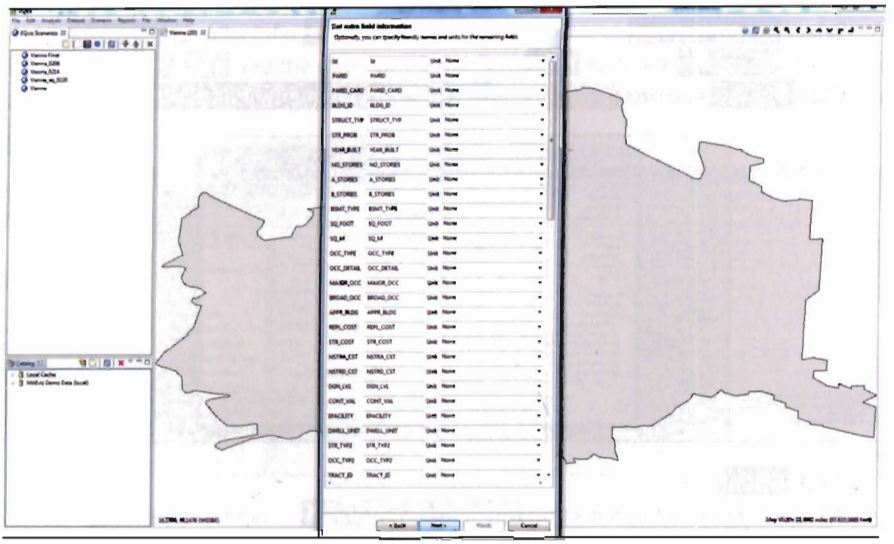
// Right click on **Local Cache** (bottom-left area).
// Select Ingest **Dataset**.



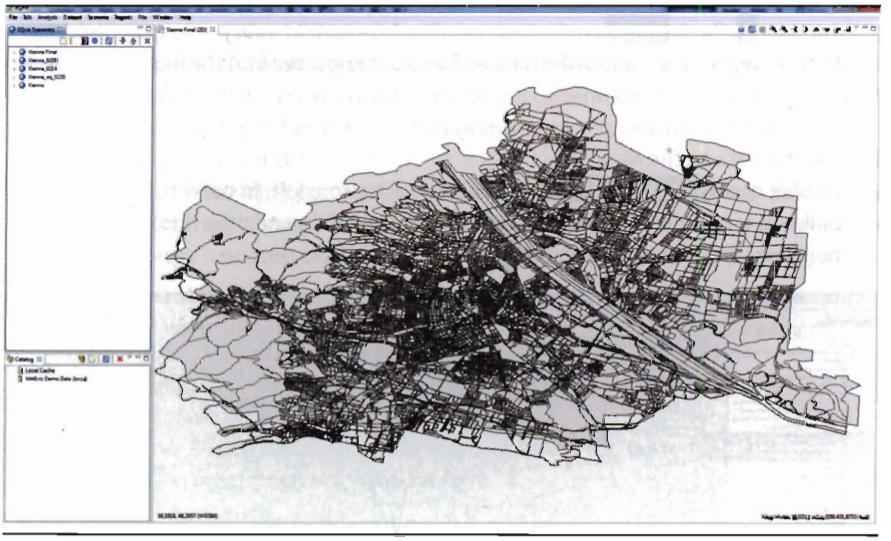
// Select **Shapefile** and click **next**.
// Click **Browse** and go to the folder **C:\EQvis\Data Vienna\City Plan**.
// Select the file **Strukturplan.shp** and click **next**.
// Select **Anonymous LineString-based geometry** and click **next**.



// Click next.
// Click next.



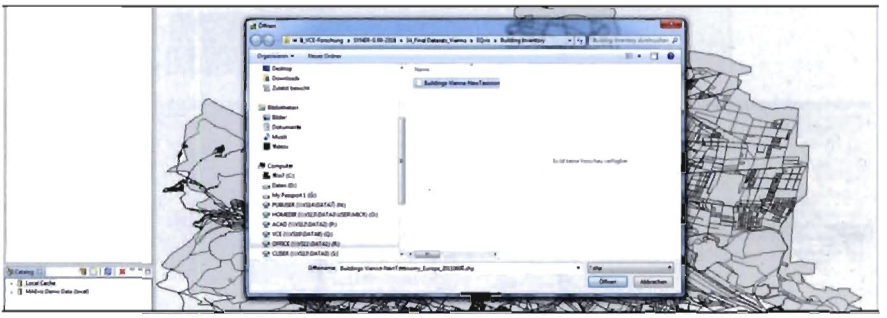
// Give "Vienna City Plan" as name, and version number 1.
// Wait while ingesting. It does not take long.
// Double click Vienna City Plan (bottom left of the main window) to visualize a 2D render of the imported City Plan.



Adding the Building Dataset

Importing

// Right click on **Local Cache** (bottom-left area).
// Select **Ingest Dataset**.
// Select **Shapefile** and click **next**.
// Click **Browse** and go to the folder **C:\EQvis\Data Vienna\Buildings Vienna**.



// Click **Open**.
// Define the data set by selecting **Building Inventory v4**.
// Press **next**.

This page allows the user to import the information present in the database. The association of the information contained in the imported database with preset labels allowing the mapping is possible here. In this case, nothing has to be changed.

// Press **next**.
// Give a descriptive name to the imported dataset, e. g. **Buildings Vienna**. Version number **1**. Press **finish**.

At this stage of the tutorial the dataset has been imported into the local cache repository.

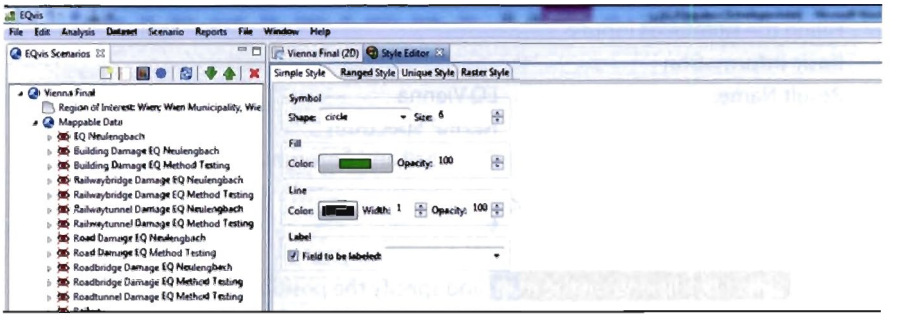
Display the Data on the Map

// Double click **Buildings Vienna** in the Catalog (bottom left) in order to display the building set on the 2D map. Alternatively, you can drag and drop it to the Visualization View.



Change Layer Style

// From Scenario View, expand Vienna, then Mappable Data.
// Right click on Change Layer Style.
// In Style Editor, select the Simple Style label.
// Adjust color, size and the other properties as required.
// Once finished, confirm by pressing the Apply style button in the Style Editor's tab bar.



// Navigate the 2D render.
To zoom/pan/etc., use the controls at the top of the Visualization View.

12-3-4 Execute Analysis

Analysis 1: Create Scenario Earthquake

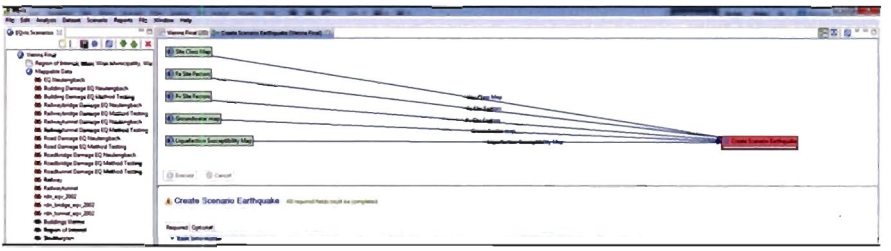
A basic map of the area of interest has been created in the previous section "Adding Data to the Scenario". The next step regards the setup and the run of an analysis. By analysis any sort of calculation is meant which leads to the generation of outcome data.

The first reported type of analysis is a deterministic earthquake map, based on a magnitude and epicentre input data.

Subsequently, a building damage analysis will be performed in order to proficiently estimate the occurring damage information on buildings. It will be based on both the created earthquake map, and on the imported building characterization (building inventory).

This section goes through all the procedures preliminary to the run.

// Launch the Run Analysis Wizard by clicking the Execute Analysis button.
// Expand Hazard and select Create Scenario Earthquake. Press finish.
// Select the scenario Vienna.
// In the Analysis Wizard (simple or complete) click on the red button Create Scenario Earthquake in order to access the input form.



// Filling the Required inputs:

Basic information

Result Name:	EQ Vienna
Periodic Spectrum Method:	NEHRP Spectrum
Attenuation:	Campbell and Bozorgnia 2006 NGA

Earthquake location

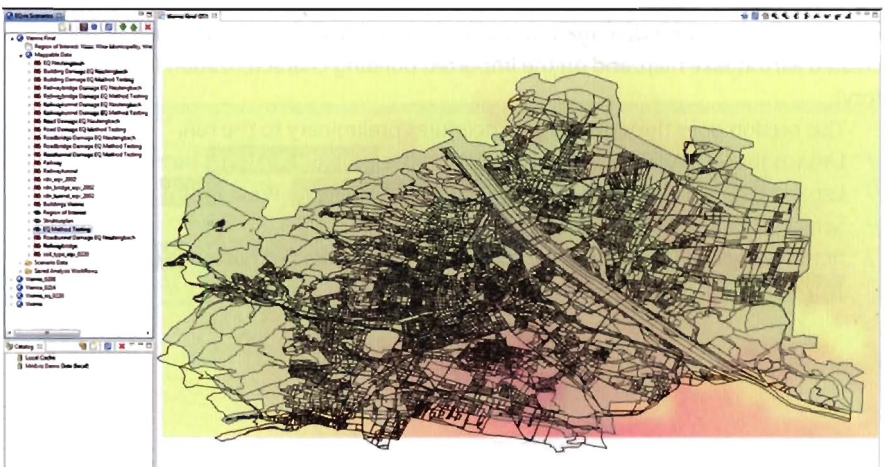
Magnitude:	6
Depth:	15 km

// Click Select by clicking on the map and specify the position of the Epicentre.
It is also possible to specify its exact location in the WGS 84 coordinate system. In this tutorial the epicentre will be located slightly south with respect to the Vienna City Centre.

// **Raster Display Information**
Set the Display raster to PGA.
The other parameters define the area which will be displayed in the Visualization View. Leave them as default.

// **Advanced Parameters**
Depending on the Attenuation Functions that you choose, different parameters can be selected. In this tutorial they will be left as default.

// The button execute should appear green, press it.
The earthquake should be very quickly generated and the name should appear in the scenario view. Close the analysis and observe the 2D map.

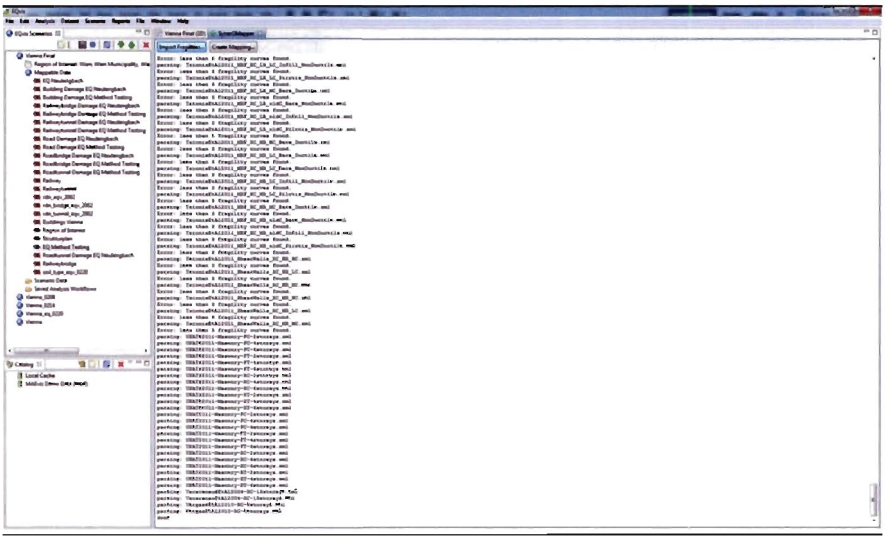


Analysis 2: Building Structural Damage

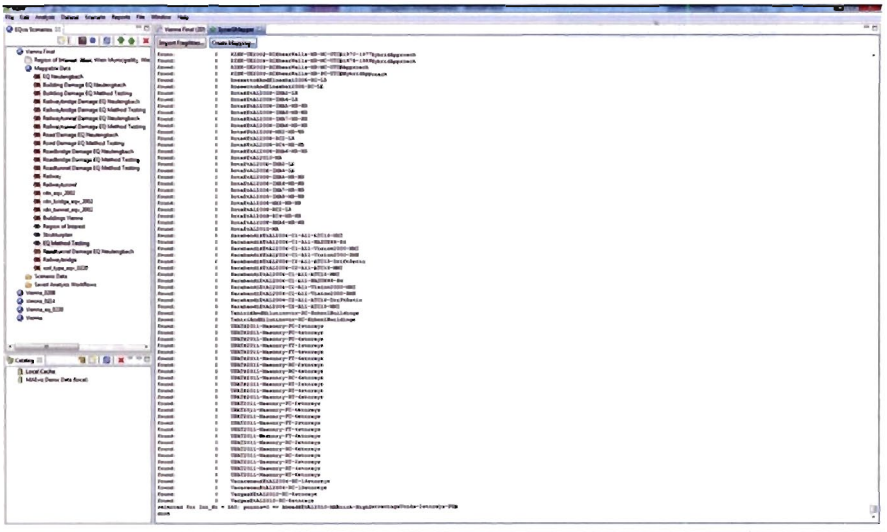
Building Characterization: Importing the Fragility Curves

For this purpose, the fragility mapping file containing the fragility functions to associate to the buildings is assigned to the taxonomy contained in the building dataset shapefile.

// Click on **Window**, then **Show View**. Expand the subfolder **other**. Double click on **SynerGMapper**.
Press **Import Fragilities**.

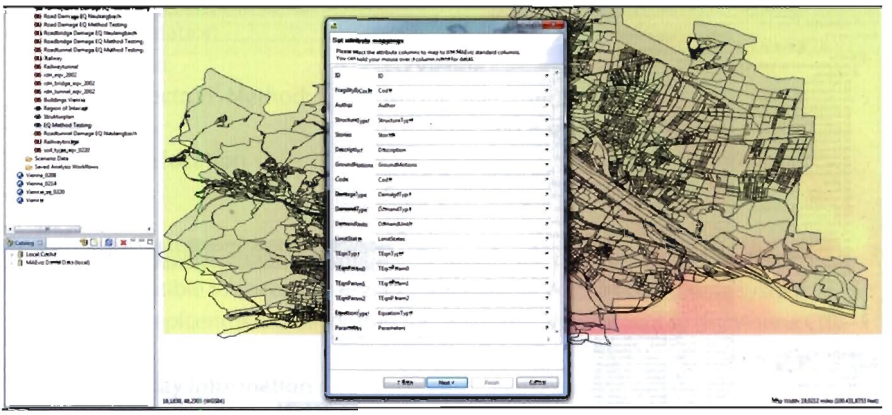


// When the fragilities are imported, click **create mapping**. It may take a while, depending on the number of the specified buildings.



Ingest the Fragilities

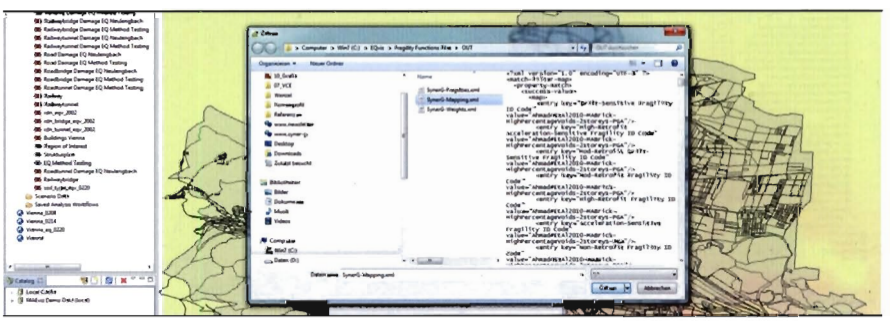
// Right click on Local Cache (bottom-left area).
// Select Ingest Dataset.
// Select Fragility from the menu.
// Browse C:\EQvis\Fragility Functions Files\OUT, show the *.xml files and choose Eqvis-Fragilities.xml.
// Click next.
// Select Building Fragilities. Click next.



// Click next.
// Specify EQvis Building Fragility, revision number 1. Click finish.

Ingest the Fragility Mapping

// Right click on Local Cache (bottom-left area).
// Select Ingest Dataset.
// Select Mapping from the menu.
// Select SynerG-Mapping.xml.

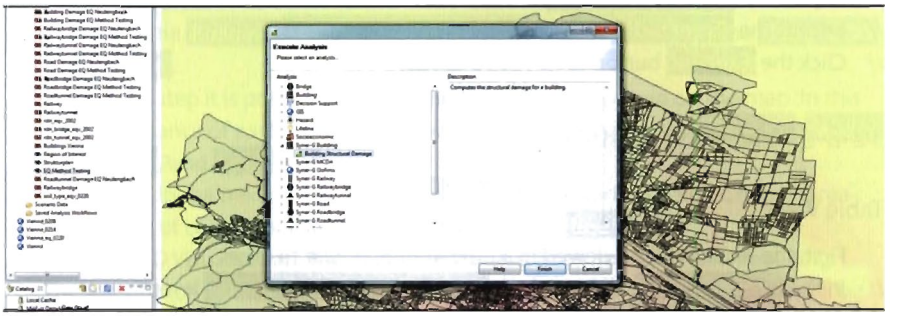


// Click next.
// Select Building Fragilitiy Mapping.
// Click next.
// Specify EQvis Building Fragility Mapping, revision number 1. Click finish.

Execute the Damage Analysis

// Go to the Analysis Wizard by clicking the **Execute Analysis** button on the toolbar.

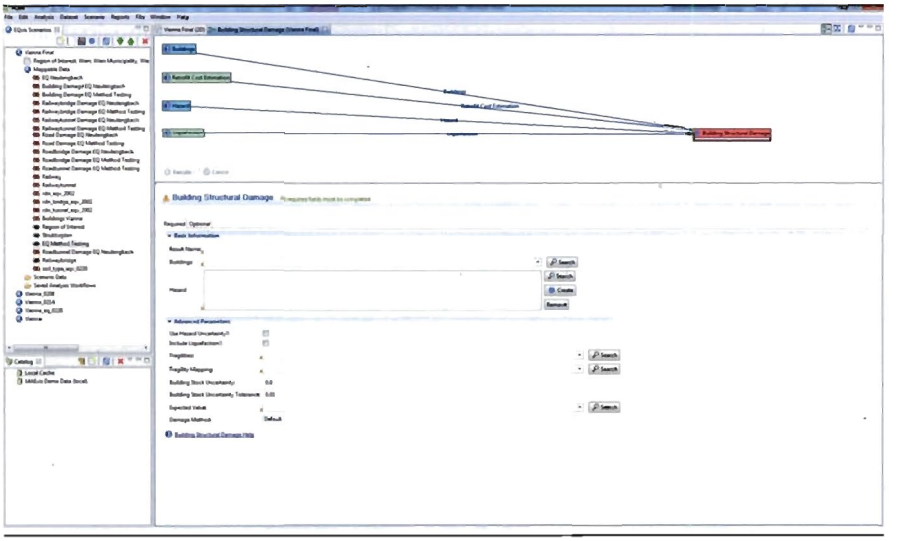
// Expand **SynerG Building** and select **Building Structural Damage** analysis.



// Specify the Scenario of interest: **Vienna**

// Click on **Building Structural Damage**.
This page represents a graphical view of the damage analysis, including the required inputs. If the background of the Building Structural Damage button is red, the input data are missing.

// Under the tab **required** of the form, you will need to provide several inputs. If the form is blank no datasets containing Fragilities, Expected Value or Fragility have been defined.
Result name: **Building Structural Damage**



// To run this analysis, load datasets that contain the data: press the **Find Dataset** button.
The window that appears contains a list box of all fragility datasets that could be found in any of the connected data repositories.

// Select Buildings Vienna (local cache) from the list, and click Finish.
// Select the Hazard EQ Vienna.
// Import the Fragilities and the Fragility Mapping.
// Import the Fragility Mapping.
// Import the Expected Values of Building Damage Ratios.
// Click the Execute button to run the analysis.

12-3-5 View the Results

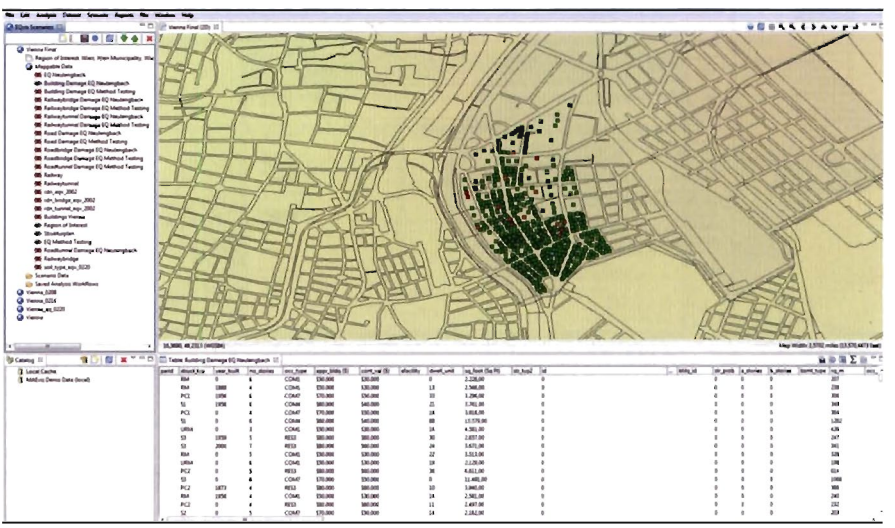
Table View

First, the results will be viewed in a tabular grid, similar to excel.

// In the Scenario View, right click on Building Structural Damage layer.
// Select Show Attribute Table. The Table View appears in the bottom right of the application window. Moving or resizing operation is possible.

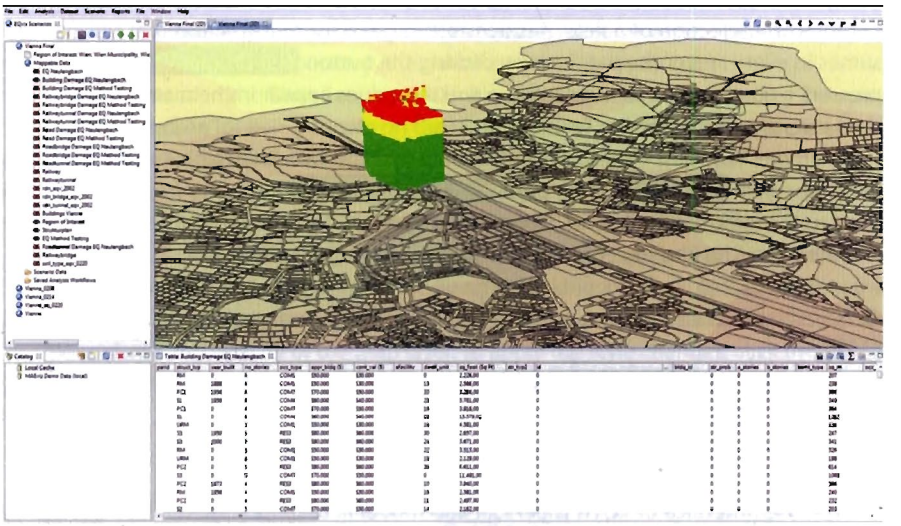
Localization of the Most Damaged Buildings

// Scroll to the right edge of the table view, and click the column header labelled MeanDamage (0–1). This is the column where the mean damage values of the buildings are shown. The table is now sorted by mean damage value.
// Visualization of the buildings on the map of the area:
// At this stage, the Building Damage layer shall be selected in the Scenario View; and the visualization should be the 2D visualization view.
// In the Table View, click on the first row with mean damage (value of highest). The dots correspondent to the selected building changes its colour in the Visualization View.
// Hold shift and click the last row with desired mean damage value (e.g. 0.04). This will select all the buildings in between the specified range. The whole set of building will change colour in the Visualization View.



12-3-6 3D Damage Bars

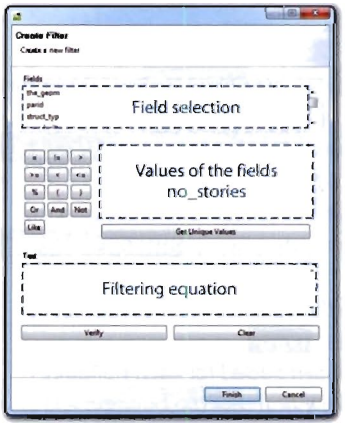
// To facilitate the visualization of the damages across the area of interest, a 3D bar view can be activated.
// Right click the Building Damage layer in the Scenario View, and choose Ranged 3D Visualization.
// During this step it is possible to select the fields to be displayed on the map. In this case, the chance of each damage state will be represented. Select Insignific, Moderate, Heavy, and Complete.
// Click next. In the next screen, associate colors to the various fields. Choose a reasonable set of colours or use the defaults, then press finish.
// Open the 3D Visualization. The damage bars have been added for each building.
// The size of each colour in the bar represents the likelihood that the building will be in a certain damage state.



12-3-7 Filtering Data

Visualize Buildings with Less than Three Stories

// Right click the Building Damage layer, and select Filter.
// This brings up the filter dialog. In the Create a Filter dialog, double click the field no_stories.
// This adds the field to the query at the bottom of the page. Next, click the <= sign button. Finally, insert the number 3.
// Press Finish.



Get Unique Values Button

After the selection of a field, it is possible to get a list of the values that this field assumes in every line of the database by clicking the button **Get Unique Values**. When it is pressed, a query is sent to the database and the values appear in the matrix. They can be then inserted in the Filtering Equation.

Example: We want to display on the map just the buildings with 1, 2 and 3 floors. Select the field **no_stories**, then press **Get Unique Values**. The query from the database gives us the information that no_stories can vary from 1 to 17. Then double click one value and complete the filtering equation.

12-4 User Interface

12-4-1 Overview

The user interface of EQvis is flexible and modular. Each module can be displayed in several positions of the main window, or can be either minimized to a Taskbar.

The EQvis workbench is built by a number of Views containing and displaying information about the specific modules. Each View is like a sub-window within main window, and can be minimized, maximized, or moved from the main window into its own window. These interactions are done by clicking the minimize/maximize icons in the view's title bar, or by clicking and dragging on the view's border or title bar.

12-4-2 Terminology

Scenario View

The Scenario View includes the list of the data for each scenario. They can be either mappable or not. Each scenario is listed as a top-level item in the view. It can be expanded by clicking the plus icon next to its name (+). All the details become then visible.

Inside each scenario, you can see a list of Mappable Data. These are the layers of data that are possible to visualize on the rendered map. The list of Scenario Data includes all non-renderable data for the scenario (e. g. tables).

The Scenario View is the platform where to perform the major operations on the scenarios such as adding an earthquake hazard or other data, running damage analyses, etc.

Visualization View

The Render Window is the area where the rendered maps appear. Each scenario can have its own rendered 2D and 3D map, where it is possible to represent the results of your analyses. The control of the camera position is possible by using the mouse, or by clicking the view control buttons in the toolbar.

Data Catalogue

The Data Catalogue is the list of all the input data of the project. It is constituted either by preloaded data (such as libraries) or by data ingested in the cache during the ongoing session. It is organized by repositories which can represent local data or data stored on a remote server. Within each repository, the data are sorted by typology.

The data sorted in the Data Catalogue can be added to a Scenario and they can subsequently be chosen for being shown on the map. The data can be added to the Scenario by drag and drop or double click.

Style Editor View

The Style Editor is used to adjust the way in which a layer of data is displayed in the Visualization View. Style Editor is reachable by right-clicking a Mappable Data layer in the Scenario View, and by selecting **Change Layer Style**. Several features are available such as colour, shape and opacity of the map layer. To apply the style changes, click the **Apply** button in the view's toolbar.

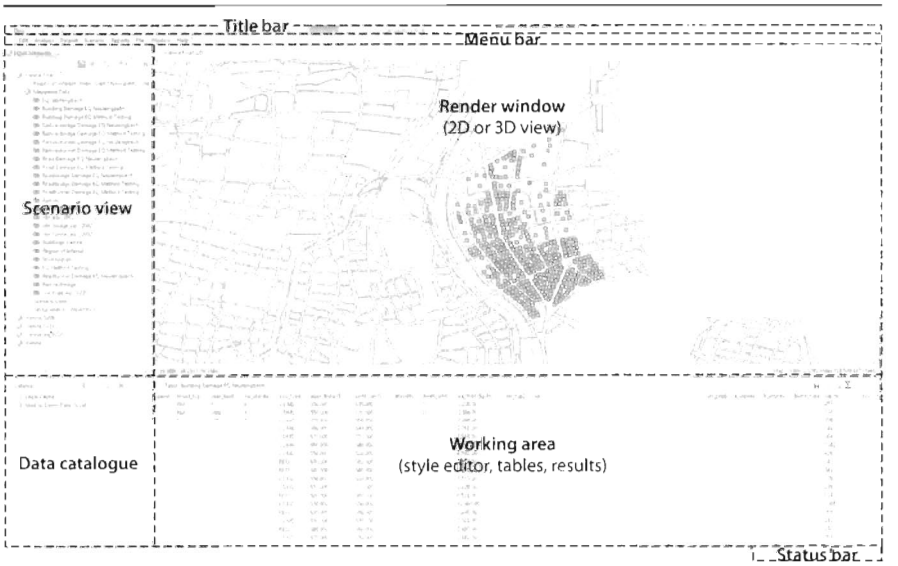


Table View

The Table View is used to display tabular data, generally the attributes of a set of inventory data or analysis results. The most common way to see this view is by right-clicking a Mappable Data layer in the Scenarios View and selecting Show Attribute Table.

Fragility View

If you right-click a fragility dataset from the Catalog View, you can select View Fragility to access the Fragility View. The Fragility View shows a list of fragility types, that you can drill down into to select and view a particular fragility curve. Choose the suitable literature model and then view it by right-click. Then select View Fragility Set to view a graph of the fragility curve.

Status Bar

The status bar is useful to recognize whether EQvis is proceeding in multitasking with background operations. A label with the current operation will be shown in this position. Such operations could be, for instance: look for new repositories, load the cartography belonging to a determined scenario, etc.

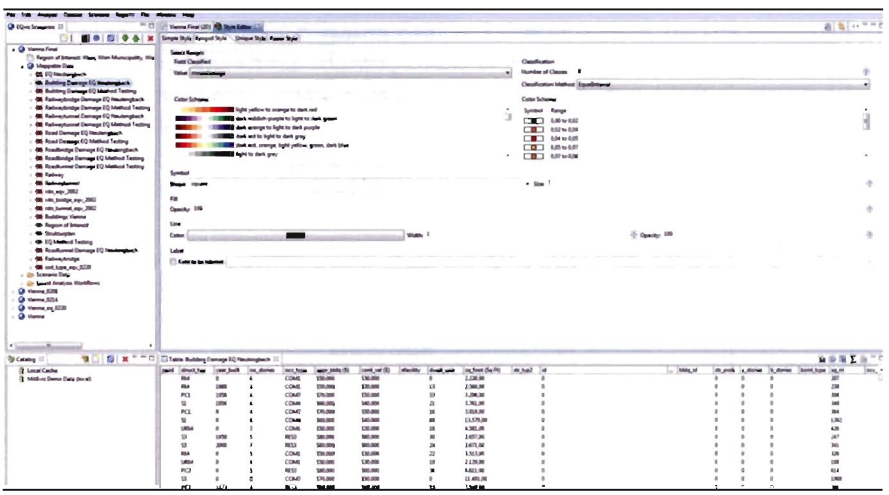
12-4-3 Special Functions

Managing the Layers of the Map

The layers can be sorted by means of these buttons. To optimize the render view, keep the layer with the contour plot of the simulated earthquake as last item of the list. In this way, it will be the background for the other layers.

Improving the Visualization

In the Style Editor of the EQ Vienna layer it is possible to select several options to improve and customize the 2D or the 3D renders. For example it is possible to vary the chromatic scale for the representation.



References

Achs, G. et al., 2010. *Erdbeben im Wiener Becken*. Wien, www.seismid.com

DeMeritt, M., 2012. *Sim Disaster – a Better Approach to Disaster Consequence Management*. ArcUser magazine.

Duenas-Osorio, L. A., 2005. *Interdependent Response of Networked Systems to Natural Hazards and Intentional Disruptions*. Ph. D. Dissertation, Georgia Institute of Technology.

EQvis – IRIS-exercise 2011. *Simulation of Catastrophic Events*. Tolna County/Hungary.

Flesch, R., 1993. *Baudynamik*. Band 1, Bauverlag.

GEM. *Technical Report 2010-5*. Crowley, H., Cerisara, A., Jaiswal, K., Keller, N., Luco, N., Pagani, M., Porter, K., Silva, V., Wald, D. and Wyss, B.

Genctürk, B., 2007. *Improved Fragility Relationships for Populations of Buildings Based on Inelastic Response*. MS Thesis, Department of Civil and Environmental Engineering, University of Illinois at Urbana-Champaign, Urbana, IL.

Genctürk, B., Elnashai, A. S. and Song, J., 2008. *Improved Fragility Relationships for Populations of Buildings Based on Inelastic Response*. The 14th World Conference on Earthquake Engineering. Beijing, China. 12–17 October.

Kim, Y. S., 2007. *Seismic Loss Estimation and Mitigation of Critical Urban Infrastructure*. Ph. D. Dissertation, University of Illinois at Urbana-Champaign.

Kim, Y. S., Spencer, B. F., Song, J., Elnashai, A. S. and Stokes, T., 2007. *Seismic Performance of Interdependent Lifeline Systems*. Mid-America Earthquake Center, University of Illinois at Urbana-Champaign, CD Release 07–16, September.

Kim, Y., Spencer, B. F. and Elnashai, A. S., 2008. *Seismic Loss Assessment and Mitigation for Critical Urban Infrastructure Systems (NSEL-007)*. Newmark Structural Engineering Lab, Urbana, IL: University of Illinois.

MAEviz 2.3. *Tutorial Charleston Bridges*.

MAEviz 2.3. *Tutorial_Shelby_County_Buildings*.

Mid-America Earthquake Center, 2009. *Impact of New Madrid Seismic Zone Earthquakes on the Central USA*. MAE Center Report 09–03.

Seismid Report 48, 2011. *Boden-Gebäude Interaktion*. Interner Bericht im Projekt Seismid, www.seismid.com

Sheffi, Y., 1985. *Urban Transportation Networks: Equilibrium Analysis with Mathematical Programming Methods*. Englewood Cliffs, NJ: Prentice-Hall.

Studer, J., Laue, J. and Koller, M., 2007. *Bodendynamik*. 3. Auflage, Springer Verlag.

SYNER-G WD-045. *Tutorial for Syner-G platform Version 1.1*

Wardrop, J. G., 1952. *Some Theoretical Aspects of Road Traffic Research*. Proceedings of Institute of Civil Engineers (part II) 1:325–378.

Wen, Y. K, Ellingwood, B. E. and Bracci, J., 2003. *Vulnerability Function Derivation for Consequence-Based Engineering*. Mid-America Earthquake Center Report.

Wen, Y. K. and Wu, C. L., 2001. *Uniform Hazard Ground Motions for Mid-America Cities*. Earthquake Spectra 17:359–384.

Youd, T. L. and D. M. Perkins, 1978. *Mapping of Liquefaction Induced Ground Failure Potential*. Journal of the Geotechnical Engineering Division, ASCE 104(4):433–446.

13

IRIS Active Vibration Absorber (AVA) for Vibration Reduction at Piping Systems in Chemical Plants

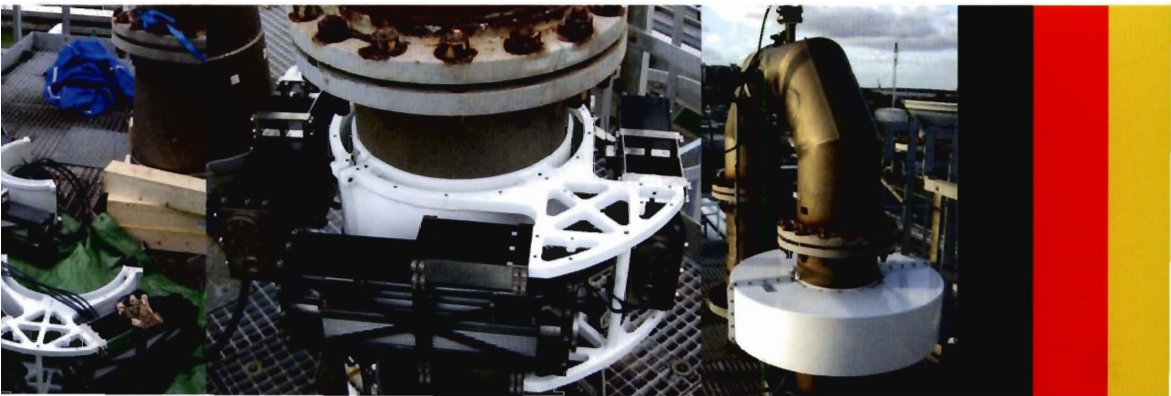
Authors:
Jürgen Engelhardt
Herbert Friedmann

Motivation

Vibration reduction in piping systems is a very common task in chemical plants. There are several different types of damping devices like visco-dampers etc. available. However all of those devices need a fixed support. Only the AVA introduced in this article needs no support to hold up. AVA is a kind of "sky hook". In the IRIS project the development of AVA was part of the Risk Mitigation and Prevention Strategy. AVA should become part of an integrated Risk Management Standard in chemical plants.

Main Results

An active vibration absorber for vibration reduction at piping systems in chemical plants has been developed, installed and tested over a period of two years.



13-1 Introduction

In the past 30 years, vibration problems at piping systems in plant engineering have become increasingly important. This trend is basically due to the growing requirements regarding the utilization of materials and the lifetime of the plants.

These circumstances are also a cause for the frequent need to take vibration reduction measures at existing piping systems subsequently. Conventional vibration reduction methods often do not lead to the desired results or require a rather intense intervention in the piping system, causing high cost in terms of construction, time and money. An efficient alternative to conventional vibration reduction methods is the application of an active vibration absorber.

An active vibration absorber consists of a reaction mass which is coupled to the structure via an actuator. Parallel to the reaction mass, a spring and a damper can be arranged. There is at least one sensor which records the structural vibrations or their effect respectively. The sensor signal is processed in a controller generating a control signal which is supplied to the actuator. The actuator moves the reaction mass and a force proportional to the acceleration of the reaction mass is exerted on the structure, which will reduce the existing vibrations. Active vibration absorbers are capable of a broadband vibration reduction. The efficiency of an active vibration absorber is independent of the chosen mass ratio between absorber mass and vibrating mass of the structure; here the representative actuator force is decisive.

The present essay serves to describe the development and initial operation of an active vibration absorber (AVA) for the pipe reactor of a chemical plant.

13-2 Description of the Pipe Reactor

The on-going chemical process in the pipe reactor causes strong vibration excitations of the piping system. There is great interest to reduce the vibration level of the reactor in order to diminish the risk of damage on the one hand and to allow for an increase of the flow rate on the other hand. Consequently, various vibration reduction measures were taken, e. g. the installation of dampers with liquid damping media, however without much success. The development of an active vibration absorber shall now contribute to a significant reduction of the vibration level.

The pipework is made of titanium sheet and is fixed to a scaffold. The connection to the scaffold is carried out with connection elements partly acting like a rigid coupling and partly showing spring or damper effects. For stiffening purposes several improvements were made at the accessible scaffold.

Two media of different phases (liquid and gaseous) are supplied to the reactor. These media react with one another during the further processing. Basically the vibration excitation is caused by rising gas bubbles that undergo a double 45° deflection. At this point the vibration level shows the highest values.

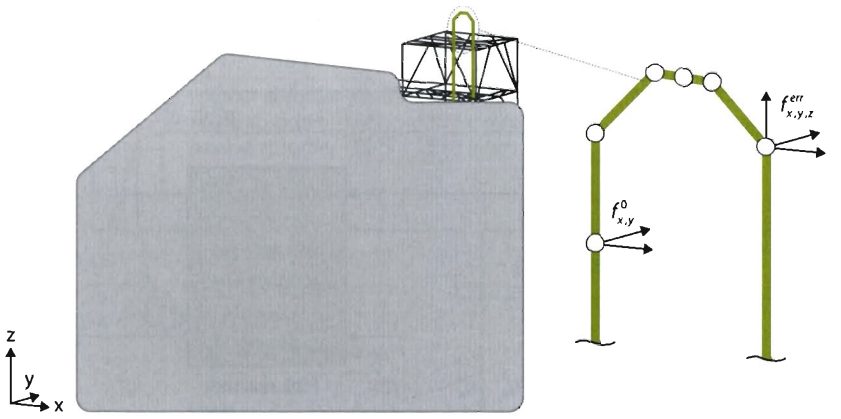
The data of an operating vibration measurement at full load from 2006 show that the highest vibration amplitudes occur horizontally in the longitudinal direction of the reactor (north-south, responding x-direction) (F.13-1). The vibration level in the vertical direction (z-direction) is comparatively low. It can be seen that a significant decrease of the vibration velocities is correlated with increasing distance to the deflection. The vibration level at the pipe exceeds that at the scaffold.

The amplitude spectra of the measured vibration velocities make obvious that the frequency content of the vibration velocities is basically limited to the range below 40 Hz. There is an accumulation of resonance points in the range around 10 Hz. Due to high vibration amplitudes of the scaffold at the point of deflection, the utilization of viscodampers at this point appears to be little promising since these are effective only with significant relative displacements between pipe and scaffold. This requirement, however, is not fulfilled here since the vibrations of pipe and scaffold are almost uniform.

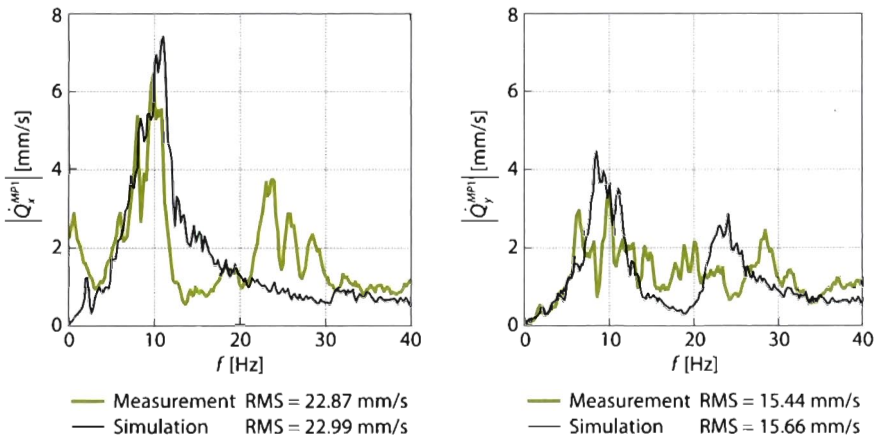
13-3 Simulation of the Pipe Reactor with Active Vibration Absorber

In order to determine the necessary actuator forces and travels for the AVA, a global simulation model is generated consisting of pipe reactor, AVA and a control system. The pipe reactor is described by a state space model based on the finite-element-model shown in F.13-1. It basically consists of beam elements. The piping system and the scaffold are connected to each other by means of spring elements at the respective cross points. The piping system is provided with an additional weight per unit area, corresponding to the media in the reactor. The excitation of the system is idealized by concentrated loads f^{err} in the three directions in space that act at the node of the first 45° deflection. The forces of the AVA f^{0} should be introduced near the highest vibration level. The location of ap-

Upper part of the finite-element-model of the pipe reactor F.13-1



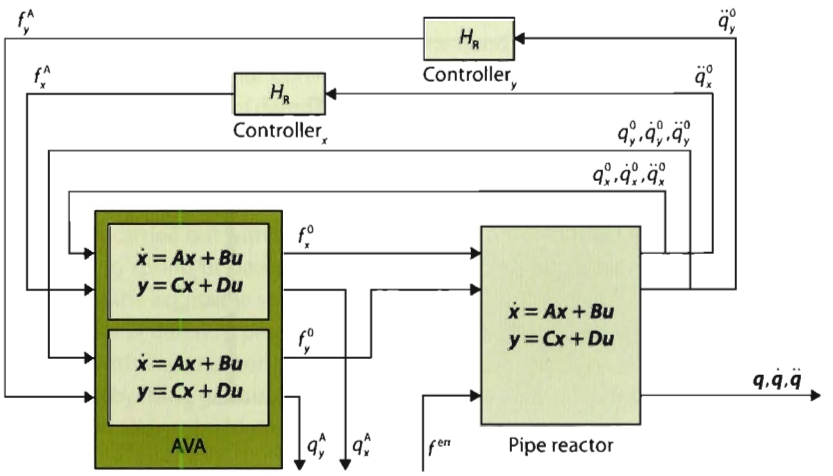
Amplitude spectra of the vibration velocities from measurement and simulation F.13-2



plication will be the point which is accessible at the real reactor and which is located near the deflection, see F.13-1.

The modal parameters in the range up to 40 Hz are analysed. The state space model of the plant is generated therefrom and is adapted in terms of quality and quantity to the existing operating vibration measurements. This is done by scaling the excitation forces and degrees of damping of the individual modes. For this purpose, time domain simulations with broadband noise excitation up to 40 Hz are considered, with the simulated rms-values of the vibration velocities at the location of excitation being opposed to the

Simulation of model pipe reactor with AVA and control mechanism F.13-3

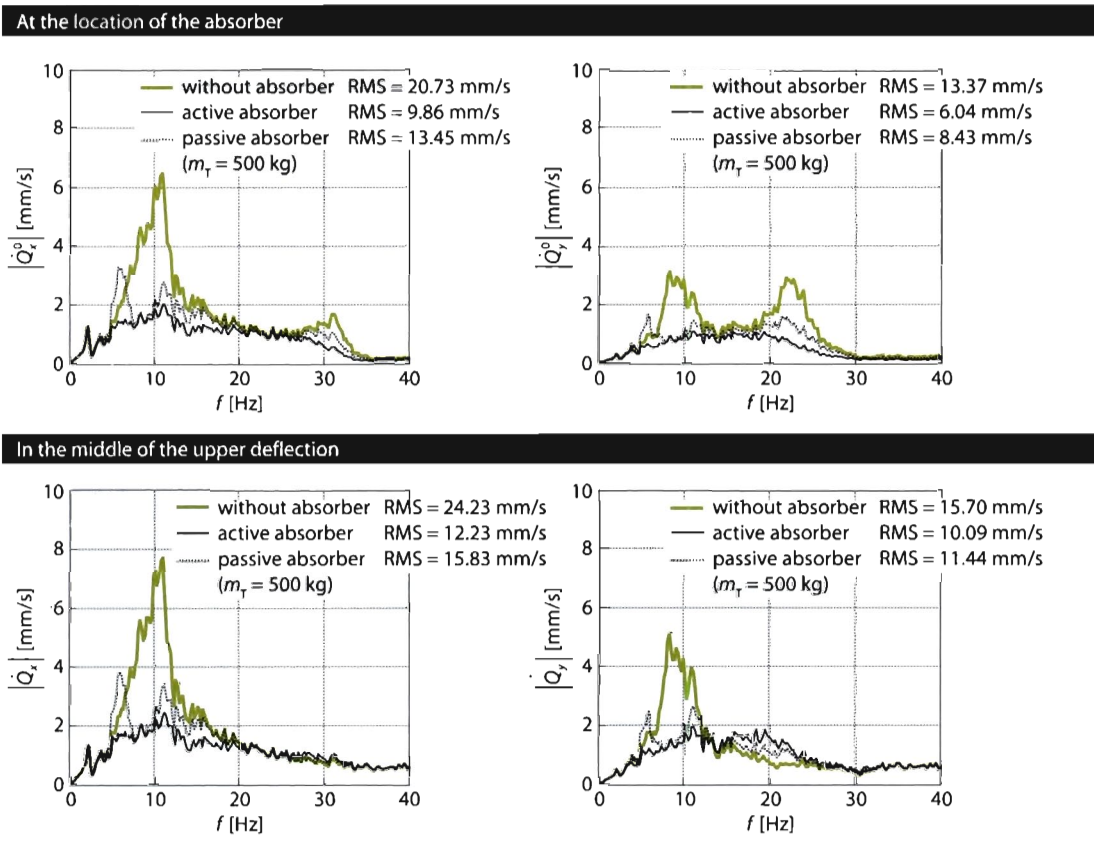


measured ones. Moreover, a qualitative agreement of the frequency spectra in the range around 10 Hz is envisaged. A comparison of the measured amplitude spectra of the vibration velocities to the simulated ones is shown in F.13-2. For the purpose intended here the agreement of the model with the real plant is sufficient.

F.13-3 shows the global simulation model which is composed of the state space model of the pipe reactor and of the AVA, in connection with the control mechanism. With this it is now possible to simulate the effect of the AVA and determine the design data for the actuator system. The numerical investigations of the global model are effected by time domain simulations. Since the frequency content of the excitation is unknown, a broadband noise excitation in the frequency range from 0.1 to 40 Hz is applied.

The amplitude spectra of the vibration velocities at the location of the AVA and at the point of the highest vibration level – which is located in the middle of the upper deflection – are considered. F.13-4 shows a comparison of the behaviour with and without AVA in x- and y-direction. For the spectral amplitude reduction a value of 69 % in x-direction or 65 % in y-direction respectively is obtained.

Comparison of the effect of active and passive absorber: at the location of the absorber (above) and in the middle of the upper deflection (below) F.13-4



The consideration of the actuating variables in the time domain provides information on the necessary actuator force and the actuator travel.

For a comparative evaluation of the effect of a passive absorber at the pipe reactor, the design is done for the range around 10 Hz. The passive absorber acts in x- and y-direction. As an example, the absorber mass is applied to be 500 kg, corresponding to seven times the reaction mass of the AVA. F.13-4 compares the amplitude reductions by the AVA and the passive absorber. A clear vibration reduction with the passive absorber can be recognized, however, it is significantly lower than that of the AVA. Due to the broadband vibration problem, the passive absorber is not capable of reducing all resonance amplitudes in the range around 10 Hz likewise. This would only be possible by further increasing the absorber mass. Here the AVA shows the advantage of its broadband effect, without requiring a higher absorber mass. Thus the static additional load acting on the piping system due to the vibration reduction measure remains low.

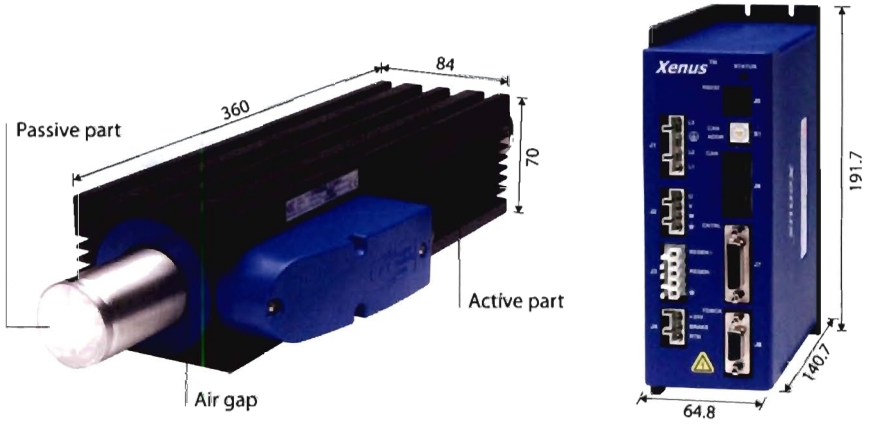
13-4 Constructive Realization of the AVA

13-4-1 Selection of Actuator

When implementing the AVA for the pipe reactor a requirement on the actuator system is that it must be possible to represent the force and travel requirements. Furthermore it must be possible to integrate the actuator system into the conceptional design of the AVA. In addition, good controllability and linear actuator behaviour in the considered frequency range are required.

A servotube motor of Copley Controls is chosen as actuator, see F.13-5 (left). The forcer of this linear motor contains coils as well as an integrated position measurement system, which is necessary for the drive control.

Servotube motor (left) and digital servo amplifier (right) F.13-5



Properties of servotube motor, Xenus servo amplifier T.13-1

Actuator XTB 3808S		Amplifier XTL-230-36-S
Continuous force: $\tilde{F}^{A}_{Dauer} = 232$ N	Peak force: $\tilde{F}^{A}_{Spitze} = 1488$ N	Operating voltage: $U^{SV} = 100–240$ VAC
Max. velocity: $\dot{\tilde{Q}}^{A}_{max} = 3.5$ m/s	Travel (peak-peak): $\tilde{Q}^{A}_{sp\text{-}sp}$: up to 1219 m	Continuous current: $i^{SV}_{Dauer} = 12$ A
Dim. active part: 360 mm · 122 mm · 70 mm	Dim. passive part: L : 0.4–1.6 m ∅ 38 mm	Peak current: $i^{SV}_{Spitze} = 36$ A
Mass active part: 4.55 kg	Mass passive part: 8.3 kg/m	Control voltage: $U = \pm 10$ V
Force constant: $\kappa^{A} = 74.4$ N/A		Amplification: $V^{SV} = 1.344$ A/V

The rod consists of a stainless steel tube which is equipped with rare earth magnets. Due to the rotating symmetric structure the system is free of shear forces. Due to the air gap with a width of 1 mm between forcer and rod high tolerance requirements on the guiding system are avoided. Active cooling is not necessary. By selecting the appropriate length of the rod the representative actuator travel is arbitrary to a large extent.

In order to meet the requirements on the actuator force, four identical servotube motors are used. Two motors at a time are arranged parallel to each other. T.13-1 shows the basic data of the actuators.

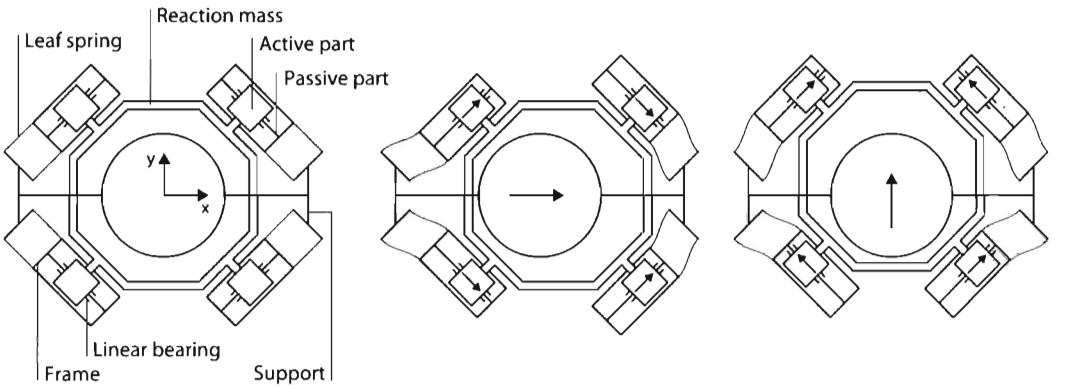
Digital servo amplifiers of the Xenus-series of Copley Controls are used for the supply of the actuators, see F.13-5 (left).

13-4-2 Conceptional Design of the AVA

The aim was to find a possibility to affect all modes of vibration that occur in a plane vertical to the pipe axis. This can be achieved by arranging two AVAs perpendicular to each other. It appears more useful, however, to develop an AVA with two degrees of freedom. For the purpose of optimization of weight it is appropriate to use one joint reaction mass for the two degrees of freedom. F.13-6 shows the functional principle of the AVA with two degrees of freedom. The actuators used have a long and slender structure in the effective direction, leading to an unhandy global structure when radially arranged to the piping system. Therefore the actuators are arranged tangentially. The active parts of the actuators are coupled to each other by a ring-shaped connection and thus form the reaction mass. The four actuators are guided in a framework structure which is connected to a support by means of leaf springs. The support is attached to the piping system. When activating the actuators accordingly, they move in x- and y-direction respectively, see F.13-6.

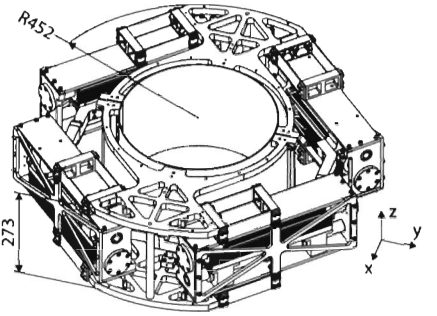
F.13-7a shows the implementation of the functional principle. F.13-7b-d show the design in different functional groups. At each active part, two bearing housings for the support of the linear ball-bearings are attached, each of them rigidly connected to the bearing housing of the adjacent active part, see F.13-7b, thus forming a closed ring-

Functional principle of AVA with two degrees of freedom: structure (left), operation in x-direction (middle) and operation in y-direction (right) F.13-6

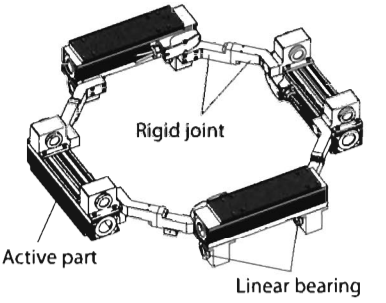


Structure of the AVA: a) overall design, b) reaction mass, c) framework structure and d) support F.13-7

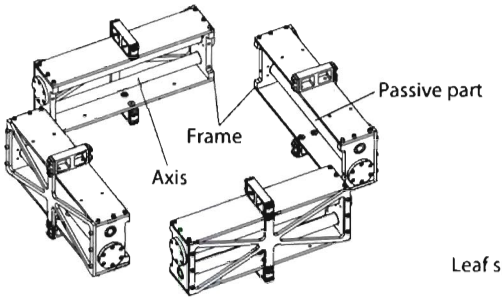
a) Overall design



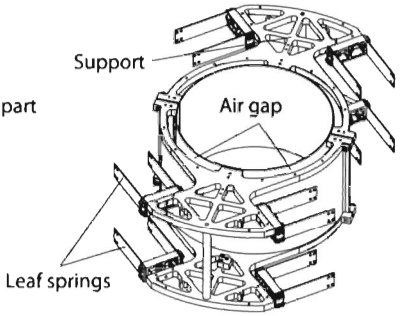
b) Reaction mass



c) Framework structure



d) Support



shaped structure representing the reaction mass. In addition, a heat sink is attached to each forcer. The reaction mass is guided relative to the four frames. Each frame consists of a rod with one hollow shaft arranged parallel thereto, representing the axis of the linear guidance, see F.13-7c. Rod and axis are each clamped into the frame at both sides. Each of the frames is connected to the support at the upper and lower side by leaf springs, see F.13-7d. By means of the leaf springs, the frames are guided in radial direction. The support is a two-part structure and is executed as welded construction, which is attached to the piping system by a bolted clamping connection. By loosening the corresponding bolted connections of the support and the reaction mass in the y-z-plane, the AVA can be divided in two parts for assembly purposes.

Since the location of assembly of the AVA is in an area subject to explosion hazards, appropriate measures must be taken to guarantee sufficient explosion protection. For this purpose an enclosure is built around the AVA which is purged with air. A constant overpressure is maintained so that no explosive atmosphere can penetrate the enclosure. At the same time, the enclosure serves as weather protection.

The continuous forces of the actuators according to T.13-1 apply to ambient temperatures of 25 °C. With increasing temperature the actuator force decreases. With an increase of the ambient temperature from 25 °C to 40 °C the possible continuous force of the actuators is reduced by 11 %. Due to the reaction process in the pipe reactor, however, this shows a constant temperature of 80 °C. In order to keep the heat transport from the pipe in the enclosure of the AVA and thus the ambient temperature of the actuators low, the support has been designed as a clam-shell construction. This leads to a radial air gap of 36 mm (cf. F.13-7d) which is divided only at the upper and lower side of the support by four cross beams at a time. The contact surface of the cross beams in relation to the entire contact surface of the support to the piping system is 2.5 %.

Concerning the fabrication of the AVA linear bearings, axes and heat sinks are provided as purchased parts. To protect them against corrosion, the support and enclosure are electro-galvanized and powder-coated. The other steel parts are chemically nickel plated, aluminium parts are anodized.

Basic data of the AVA — T.13-2

Total mass (excl. enclosure)	$m^0 + m_T = 147$ kg
Moving mass	$m_T = 72.5$ kg
Mass enclosure	$m_{Geh} = 22$ kg
Actuator travel (peak-peak)	$\tilde{Q}^A_{peak\text{-}peak} = 84$ mm
Resulting actuator travel	$\tilde{Q}^{A\,*}_{x,y} = \sqrt{2}\tilde{Q}^A = 59$ mm
Resulting continuous force	$F^{A\,*}_{Dauer,x,y} = 2\sqrt{2}\tilde{F}^A_{Dauer} = 656$ N
Resulting peak force	$F^{A\,*}_{peak,x,y} = 2\sqrt{2} \cdot \kappa^A \cdot V^{SV} \cdot U^{max} = 2828$ N

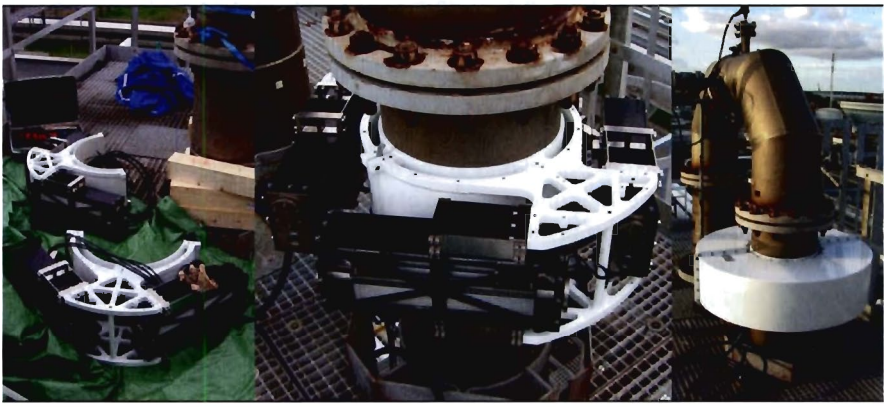
* only applies to pure operation in x-resp. y-direction

In order to avoid local stress peaks at the piping system during the installation of the AVA, a 5 mm elastomer layer is applied between support and pipe. T.13-2 shows the resulting basic data of the AVA.

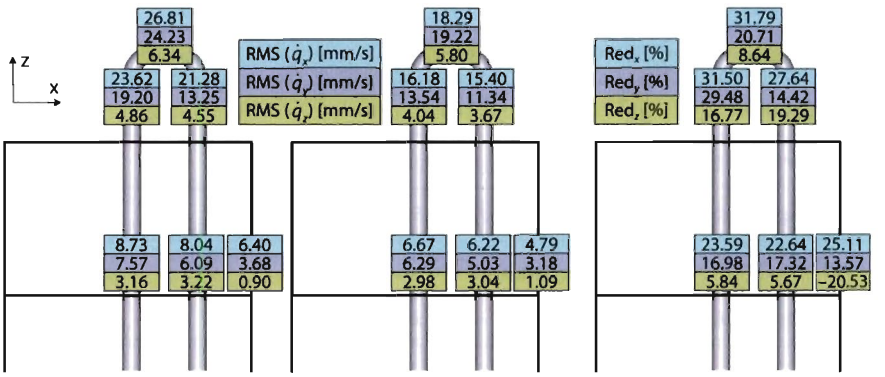
13-5 Initial Operation in the Chemical Plant

The initial operation of the AVA in the chemical plant is carried out by utilization of the reactor at a capacity of 105 % of the nominal flow rate. The operating loads of the reactor are investigated at 25 measuring points in total. For this purpose, nine tri-axial acceleration sensors in combination with a 32-channel measurement system are used. The sensor positions are relocated twice; one measuring point remains unchanged as reference point for all measurement series.

Installation of the AVA at the pipe reactor F.13-8



Rms-values of the vibration velocities: without AVA (left), with AVA (middle) and reduction of the rms-values by the AVA (right) F.13-9



In order to record the actual condition, operating vibrations without AVA are measured first. Then the AVA is installed at the pipe reactor, see F.13-8.

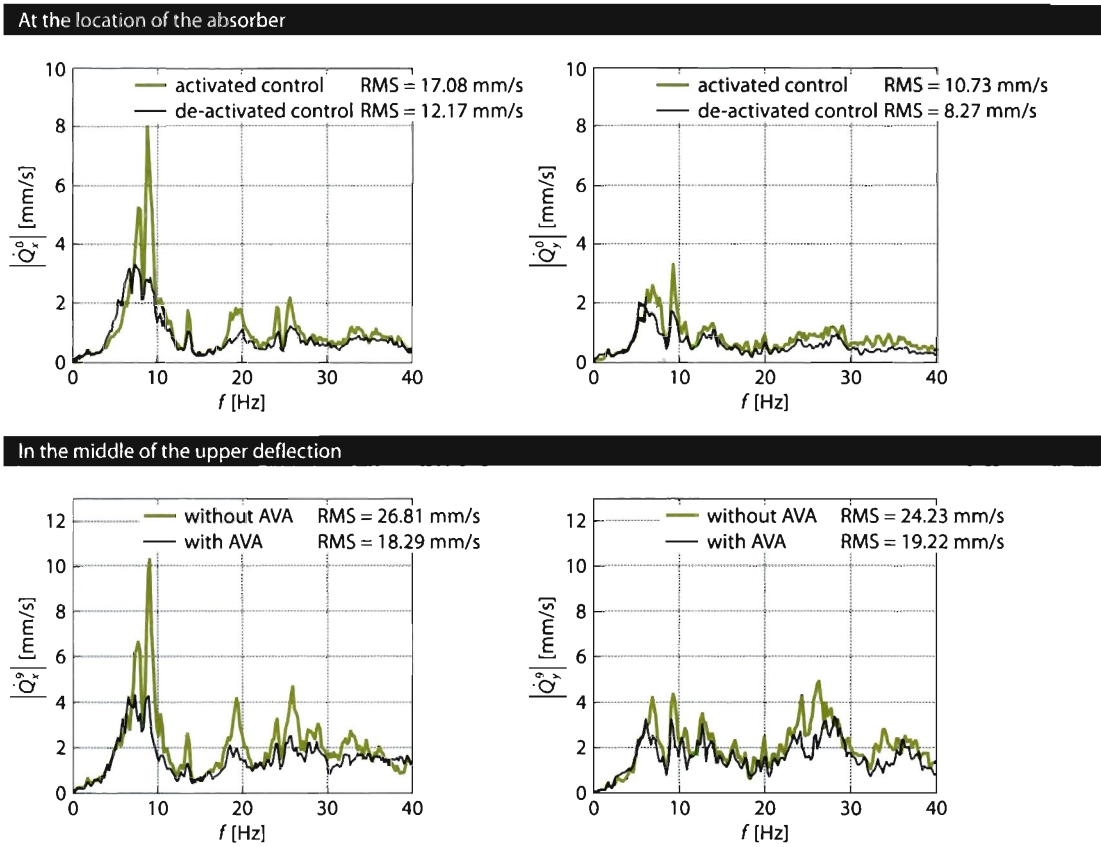
First the measurement results in the time domain are evaluated. For this purpose the rms-values of the vibration velocities for the individual measuring points are calculated. The vibration velocities are obtained by integrating the measured accelerations. F.13-9 shows the rms-values with and without AVA in the area of the upper deflection.

F.13-9 (right) shows the reduction of the rms-values by the AVA. In the area of the highest vibration level at the deflection, the rms-values are reduced by up to 32 %. With increasing distance to the deflection, both the vibration level and the reduction effect of the AVA decrease.

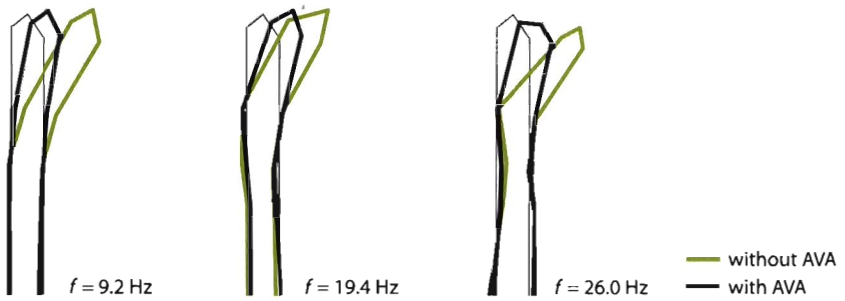
Generally, a global reduction of the vibration velocities in all directions in space can be recognized. There are only few points where a slight increase of the vibration velocities is observed, but these points generally have a low vibration level.

F.13-10 shows the evaluation of the measurement results in the frequency domain, considering the amplitude spectra of the vibration velocities in x- and y-direction at the

Amplitude spectra of the vibration velocities: at the location of the absorber (above) and in the middle of the deflection (below) F.13-10



Operation deflection shapes with and without AVA (non-proportional representation) F.13-11



location of the absorber with activated or de-activated control, as well as in the middle of the deflection with and without AVA as an example. The amplitude reduction in the range of the resonance points is clearly recognizable. The highest reduction can be observed in x-direction in the range around 9.2 Hz. Here an amplitude reduction of approx. 60 % can be observed. Vibrations are reduced in the whole frequency range considered.

Clear amplitude reduction can also be recognized in the ranges of 19.4 Hz and 26.0 Hz. The related operation deflection shapes with and without AVA are shown in F.13-11. Nevertheless, the clear resonance of the deflections in the upper area of the pipe reactor as well as the effect of the AVA can be recognized. In y-direction, less vibration reduction than in x-direction can be observed, which is due to the absence of concise resonance points.

13-6 Conclusion

The effect of the AVA with two degrees of freedom and joint reaction mass under real operating conditions at the pipe reactor of a chemical plant could be proved.

The numerical analyses show that a comparable vibration reduction by means of passive absorbers can be achieved only by applying much higher reaction masses; in addition to that the effect is principally limited to the range of the vibration-absorbing frequency.

The absorber was installed in the area of the highest vibration level. Here the advantage of the AVA compared to visco-dampers could be clearly shown, since no fixed support is required.

The results of the experimental investigations can be considered very positive, particularly in comparison with the measures taken in the past to reduce the vibrations of the pipe reactor.

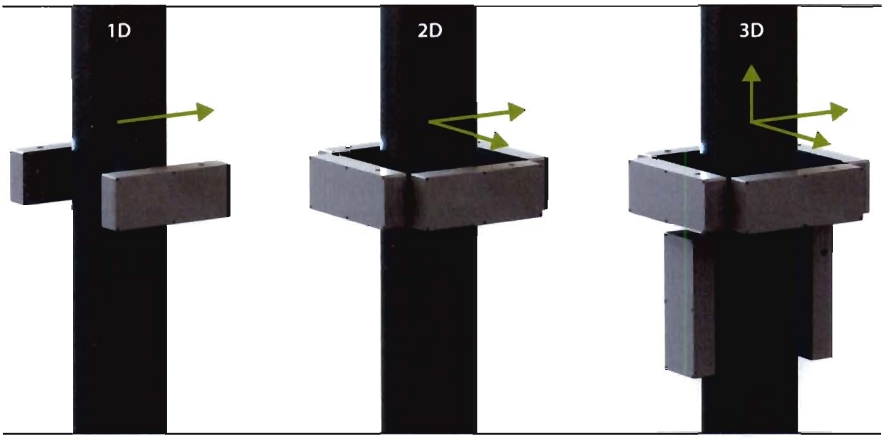
13-7 AVA becomes ADD.Pipe® – from the Research Project IRIS to a Product

In the core of the European Union's efforts expressed in the Lisbon Strategy is the so-called "knowledge triangle" with the corner points research, education and innovation. Based on those corner points the EU tries to become the "most dynamic competitive knowledge-based economy in the world". Therefore, within the Seventh Framework Programme, the goals of growth, competitiveness and employment have become a primary concern. This is even more important in the current economic situation which underlines the great importance to finally develop engineering services, new products etc. after a successfully terminated R&D project.

One important outcome of IRIS was the above described AVA, which was further developed after the IRIS project. With the further development, AVA changed its name to ADD.Pipe®, which is the acronym for "**A**ctive **D**amping **D**evice Reducing Vibrations of **Pipes**". More important than the name change was the fact that the design was changed, too. Now ADD.Pipe® is a patented and scalable product to solve 1D, 2D and 3D vibration problems. Due to the mass and size of the vibrating structure, several actuators can be combined either in one, two or three directions.

ADD.Pipe® can not only be used for piping systems, but also for other structures with problems with broadband vibrations. ADD.Pipe® can handle changing frequencies and needs no fixed support to act against. It can be adapted to the vibrating structure when the vibration problem occurs. Compared to passive absorbers, considerably less reaction mass is necessary. However, the reduction of amplitudes is much higher with ADD.Pipe® than with a passive tuned mass absorber, which can only reduce one frequency.

Acting directions of ADD.Pipe®: 1D, 2D or 3D F.13-12



ADD.Pipe® for 1D with mounting and thermal isolation. The open cover allows a glance to the reaction mass with the Wölfel-Logo F.13-13



Reference

Engelhardt, J., 2010. *Aktiver Tilger zur Schwingungsminderung von Rohrleitungssystemen im Anlagenbau*. Darmstadt, Germany.

14

Monitoring of Hot Pipes at the Power Plant Neurath Using Guided Waves

Authors:
Bianca Weihnacht
Thomas Klesse
Robert Neubeck
Lars Schubert

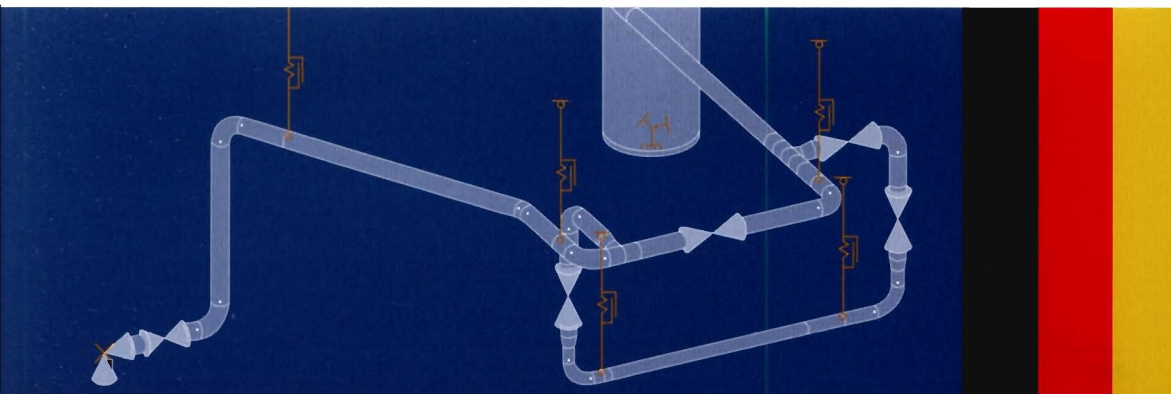
Weihnacht, B., Klesse, T., Neubeck, R. and Schubert, L., 2013. *Monitoring of Hot Pipes at the Power Plant Neurath Using Guided Waves.* Conference Proceedings SPIE Smart Structures and Materials & Nondestructive Evaluation and Health Monitoring, San Diego, March 11–14, 2013.

Motivation

The increase of operating temperatures of power plants up to 720 °C requires novel high performance steels in the piping systems. This goes along with higher risks of damage and instability. A monitoring system to measure the underlying effects is desired.

Main Results

All necessary components of a monitoring system to be operated at hot pipes have been developed and the application has been tested in the field at a bypass pipe under real operating conditions.



14-1 Introduction

In order to reduce the CO_2-emissions and to increase the energy efficiency in power plants, the steam parameters are increased. The commonly used live steam temperatures of about 600 °C are to be increased beyond 700 °C in order to increase the efficiency of the entire plant over 50 %. For such high operating temperatures novel high-performance steels like P 91 and P 92 must be applied for the piping systems. The material Life Cycle and especially the creep rupture properties of these novel high-performance steels, however, are not yet sufficiently known so that periodical inspections of such plants are not sufficient, due to reasons of safety. Particularly piping systems made of these materials which are exposed to high internal pressure must be subject to integral monitoring.

Higher temperatures lead to a higher risk of damaging and have a direct impact on the structure stability and the deposition structure which have a large influence on the long-term stability under load and the damage behaviour. Adequately trusted results for the prediction of the residual service life of those high strength steels are hard to achieve. This causes security problems that avoid the application of those steels or demand for early exchange of the pipe components. To overcome these problems the implementation of an online monitoring system is needed in addition to periodic inspection. The system should enable the characterization and evaluation of the actual state of the material. Only with an accurate prediction of the residual life time of the components, the safety and the availability and resulting from that the efficiency of power plants can be guaranteed.

The monitoring of modern combined heat and power plants is currently focused on the age consumption which is determined by the probabilistic calculation from real load data and in the advanced stage by additional material investigation during shut-off times. The live-time reserves of the materials can be used more efficiently by applying monitoring systems. This leads to a more efficient and furthermore safer operation of the power plant.

High resolution NDT-methods based on ultrasound methods or X-ray are state of the art for periodic inspections in order to detect cracks and wall thickness reductions by perpendicularly introduced ultra-sound. The clear disadvantage lies in the fact that only local condition information of the specimen (local wall thickness, local cracks) can be obtained. While using only NDT-methods – the testing of hundreds of metres of pipes would be very expensive. Additionally, the power plant has to be shut down during the measurement.

It has to be stated that the existing monitoring methods are not applicable neither for the existing martensitic steels and nickel alloys nor for the materials under development. They do not allow for a detailed description of the damage processes. Contrary to the low alloyed steels applied in a lower temperature range, the structure stability which refers to the stability of the time- and load-dependent precipitation is of great importance.

14-2 Materials and Methods

14-2-1 Measuring Technique Acousto Ultrasonics (AU)

An active SHM system uses a pulser for excitation of elastic waves and receiver transducers with resonant frequencies in the ultrasonic range and wave propagation dynamics predictions for damage detection (see F.14-1 left).

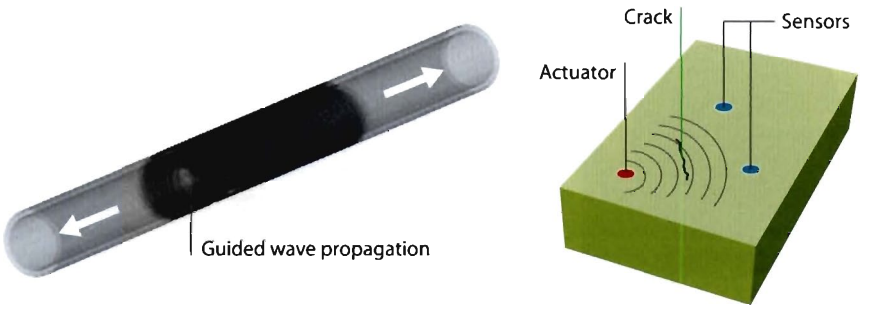
Acousto Ultrasonics (AU) uses ultrasonic methods in a frequency range between 10 and 500 kHz. Ultrasonic waves are reflected by surfaces and interfaces, attenuated by dispersion and absorption, and undergo mode changes during reflection and transmission.

These effects depend strongly on the frequency of the wave, its direction of propagation, its initial mode, and the location and orientation of surfaces and damage. When damage has occurred to a structure, changes in the signal and therefore the transfer function indicate the type of damage like cracks and wall thickness reductions due to corrosion. By pre-calculating the expected changes in the signal from given types and degrees of damage, the damage can be evaluated from AU measurements [Schubert, 2004; Schubert et al., 2008; 2009]. This kind of measurements is repeated according to the expected damage velocity. Using e.g. hourly measurement intervals, the growing of the damaged can be described with high time resolution. A high spatial resolution is achieved by using high frequencies with the disadvantage of shorter possible travel paths. An initial situation (baseline) must be measured to describe the undamaged situation at different load levels since the damage might be load dependent.

14-2-2 Site Description and Waveguide Positions

RWE operates the lignite power plant Neurath. In Block E of this power plant the bypass is installed and operated. All test and research activities have to be checked regarding their safety and to be coordinated with the business operation of the plant. In order to investigate the environmental noise level and the influences of the steam flow in the pipe,

Propagation of guided waves in pipes [Köhler et al., 2004] (left) and measurement principle of Acousto Ultrasonic (AU) measurements (right) F.14-1



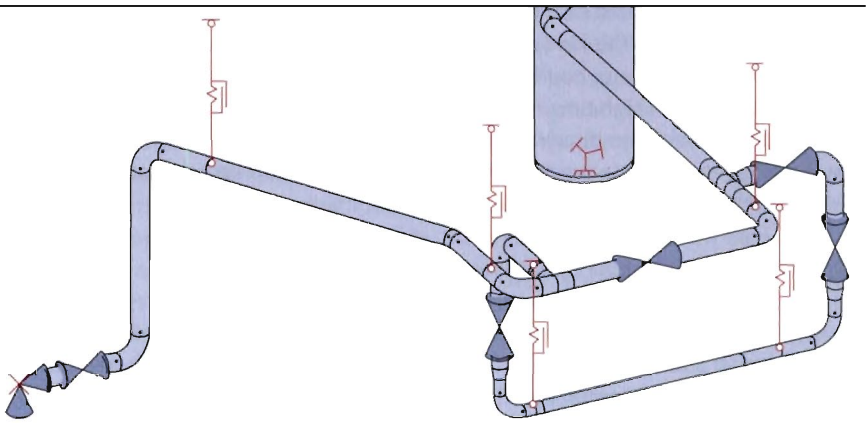
an extra bypass for research purposes was established. This made the investigations independent from the power plant operating. The bypass is made of high temperature steel with 9% chrome. It has a diameter of 190.0 mm and the wall thickness equals 25.6 mm (see F.14-2 and F.14-3 left).

The external surface temperature of the bypass reaches up to 520 °C. Therefore an insulation is applied to minimize energy losses (see F.14-3 right).

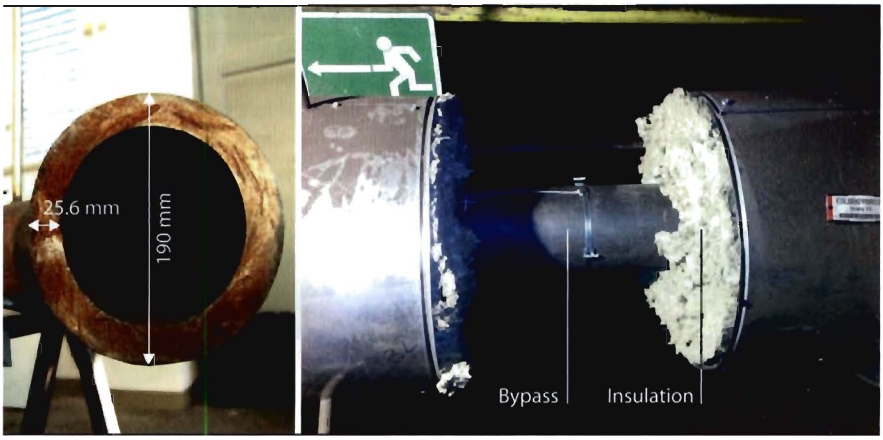
In order to protect the actuators and sensors from the heat radiated from the pipe wave guides were welded to the bypass on burlings used for the stabilization of the insulation (see F.14-4 and F.14-5). The wave guides have a length of 1 m and a diameter of 1 mm. Four measurement locations were chosen for installation at the bypass in the power plant Neurath. The wave guides are located in semicircles at two locations at a distance of 1.20 m and 90° shifted.

For these measurements, artificial drillings were performed between the wave guides with a depth of 7 mm (1/3 wall thickness).

Bypass location within the power plant (right side, lowest part) F.14-2



Pipe dimensions (left) and bypass at the power plant with insulation (right) F.14-3

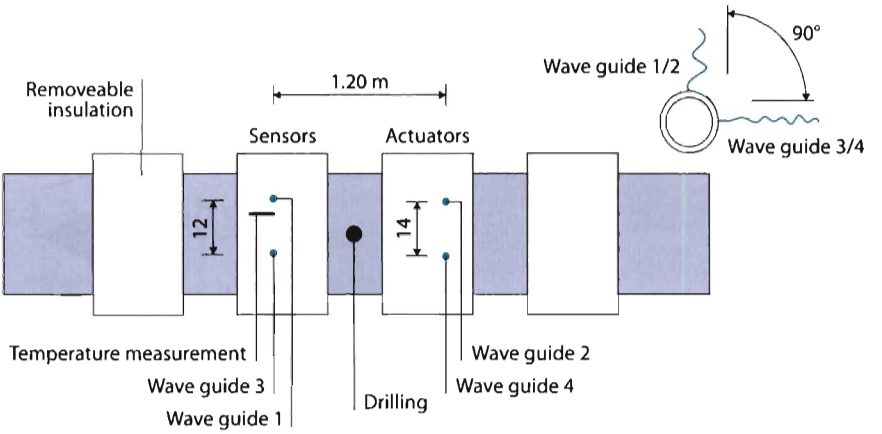


14-2-3 Measuring Setup

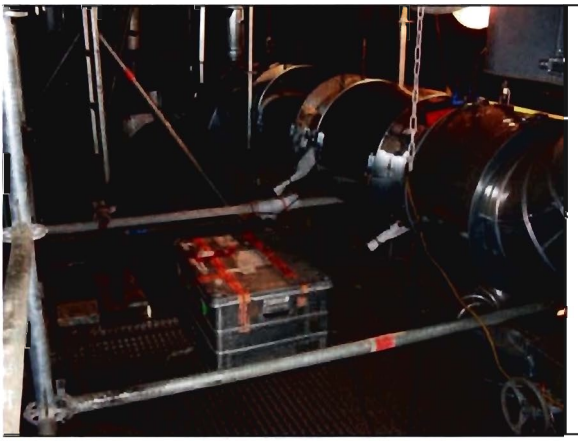
For the excitation of the acoustic waves with the piezoelectric actuators and for receiving the acoustic waves, the multi-channel acoustic measurement system (MAS) is developed for long-term monitoring of technical structures and plants (F.14-6 left and data sheet T.14-1). The system is based on a universal digital and customer adapted analogue device. The individual system adaptability is guaranteed by a digital signal processor (DSP), by standardized data transfer ports as well as by the reconfigurable logic and software. The networking possibility of the varying MAS systems ensures the design of complex sensor networks for the monitoring of different system parameters.

The internal setup of the sensor/actuator and the pre-amplifier is shown in F.14-6 (right). It can be used as well for low frequency (e.g. modal analysis) and high frequency (acoustic emission, Acousto Ultrasonics) applications. They support the sending and receiving of acoustic waves in the frequency range of 10...500 kHz.

Wave guide distribution at the bypass F.14-4



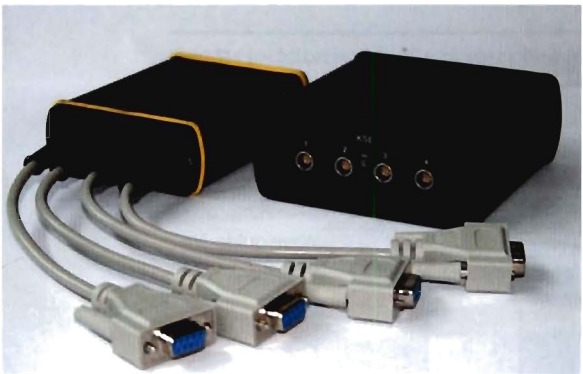
Location of the measurements in the power plant F.14-5

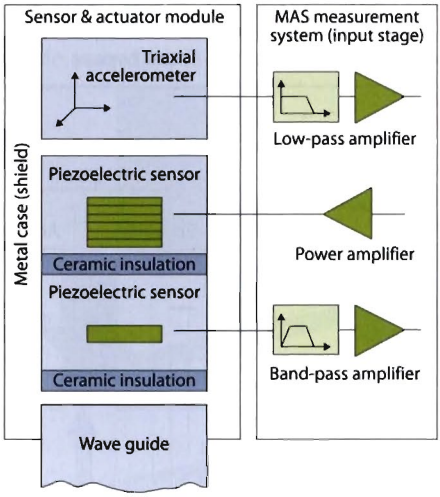


Analogue input and output for piezoelectric sensors of the measuring device MAS T.14-1

	Output	Input
Number of differential channels	4	4
Resolution	max. 160 Vpp @10 nF	12 Bit
Sample rate	Arbitrary	12.5 MHz
Input level	14 Bit	10 Vpp, 100 Ohm
Frequency domain	18.75 MHz	10…500 kHz
Post amplifier for each channel separate		–22…+20 dB

MAS-measurement system (left) and simplified schematic of the measurement system with sensor/actuator and pre-amplifier (right) F.14-6





14-2-4 Processing of the Data

In the following sections lower-cased bold letters mark vectors, lower-cased non-bold letters scalar values, capitalized bold letters matrices and the upper index the step of the processing, whereby zero stands for the initial measurement.

Mathematically a single measurement could be described as:

$$\mathbf{u}^0(\mathbf{t},T,Z)=f(\mathbf{t},T,Z)+\mathbf{e} \qquad \text{E.14-1}$$

Whereas $\mathbf{u}^0 \in \mathbb{R}^m$ is the measured signal voltage in [V], equidistantly sampled using m samples over the time $\mathbf{t} \in \mathbb{R}^m$ in [s], by a given temperature $T \in \mathbb{R}$ in [°C] and the damage indicator $Z \in \mathbb{R}$, which indicates the artificial hole diameter in [mm]. The abstract function $f : \mathbb{R}^m \times \mathbb{R} \times \mathbb{R} \rightarrow \mathbb{R}^m \times \mathbb{R} \times \mathbb{R}$ characterizes the undisturbed system, material and geometry behaviour, which is superimposed by a statistically distributed noise $\mathbf{e} \in \mathbb{R}^m$.

The damage parameter and the temperature are assumed as scalar values not varying significantly over a measurement interval of a few microseconds.

The goal is to find a set of k operators $g^i : \mathbb{R}^m \times \mathbb{R} \times \mathbb{R} \rightarrow \mathbb{R}^m \times \mathbb{R} \times \mathbb{R}$ with $i = 1,\ldots,k$:

$$\mathbf{u}^i(\mathbf{t},T,Z) = g^i(\mathbf{u}^{i-1}(\mathbf{t},T,Z)), \qquad \text{E.14-2}$$

which could transform every signal initially measured at the temperature T to a signal at a reference temperature T_R with the same damage parameter:

$$\mathbf{u}^0(\mathbf{t},T_R,Z) \approx \mathbf{u}^k(\mathbf{t},T,Z). \qquad \text{E.14-3}$$

The signal at the reference temperature was approximated stepwise, whereas $\mathbf{u}^i$ should converge with increasing index i to the signal $\mathbf{u}^0(\mathbf{t},T_R,Z)$ measured under these specific conditions:

$$\left\|\mathbf{u}^0(\mathbf{t},T_R,Z) - \mathbf{u}^0(\mathbf{t},T,Z)\right\| > \left\|\mathbf{u}^0(\mathbf{t},T_R,Z) - \mathbf{u}^1(\mathbf{t},T,Z)\right\| > \ldots > \left\|\mathbf{u}^0(\mathbf{t},T_R,Z) - \mathbf{u}^k(\mathbf{t},T,Z)\right\| \approx 0 \qquad \text{E.14-4}$$

The challenge lies in the construction of an operator set which performs the transformation over a wide range of temperatures sufficiently and also conserves the influence of the damage parameter on the signal and the associated damage class.

14-3 Results

14-3-1 Temperature Correction

In order to correct the temperature influence on the signals correctly, a data processing procedure was developed for the measured temperature range from 20 °C to 500 °C and is described in the following sections.

For the processing, only the first two wave packets of each measured signal were considered for simplicity because of their stability over a wide temperature range. The challenge of the proposed procedure lies in the definition of boundaries to be specified for the wave packet extraction which are unstable and strongly depending on the temperature.

Therefore the boundaries were redefined after each step of constructing the phase correction operator in time domain. For this specific case, the boundary is a function of the location of the right or left minima over the temperature. Those two univariate polynomial functions of the chosen degree $l-1$ are observed by using two L_p-regressions of the form:

$$\left\|\mathbf{A}\mathbf{x} - \mathbf{b}\right\|_p^p \rightarrow \min_x, \qquad \text{E.14-5}$$

where $\mathbf{A} \in \mathbb{R}^{n \times l}$ is the *Vandermonde*-matrix of our n measurements, $\mathbf{b} \in \mathbb{R}^n$ a vector of the minimum locations on the time axis and $\mathbf{x} \in \mathbb{R}^l$ are the unknown polynomial coefficients. Because of the strong temperature dependency we used the L_1-norm, which is more ro-

bust against outliners than the more commonly used L_2-norm. To guarantee uniqueness, we chose the minimum p-norm solution. The signal was tapered afterwards.

14-3-2 Phase Correction in Time Domain

The process of constructing a phase correction operator is based on the work of Schubert [Schubert, 2012] and divided into two parts. At first the signal based on the envelope $\mathbf{h}^0 \in \mathbb{R}^m$ of the initially measured wave packet was corrected and then, after redefining the boundaries, on a shifted form of the wave packet itself. The envelope $\mathbf{h}^i(\mathbf{t},T,Z)$ is calculated by the absolute of the *Hilbert*-transformation $\mathcal{H}$ of the signal:

$$\mathbf{h}^i(\mathbf{t},T,Z) = \left|\mathcal{H}(\mathbf{u}^i(\mathbf{t},T,Z))\right| . \qquad \text{E.14-6}$$

Subsequently the time shift Δt in [s] between the envelope and the envelope of the reference temperature is calculated for each of the n measurements by searching for the argument of the maximum of the cross-correlation between those envelopes (note that the results of E.14-7 have to be reduced by $m-1$ to get the real time shift) :

$$\Delta t = \arg\max_t \left|\left(\mathbf{h}^i(\mathbf{t},T,Z)\cdot\mathbf{h}^i(\mathbf{t},T_R,Z)\right)(\mathbf{t})\right| . \qquad \text{E.14-7}$$

Afterwards an L_1-regression is performed according to E.14-5 with $\mathbf{b}$: vector of the n time shifts. This procedure is also successfully applicable if the solution of E.14-7 is non-unique, because multiple values just become extra columns in $\mathbf{b}$ and $\mathbf{A}$ is also extended with the corresponding temperature entries. Based on the time shift function over the temperature obtained by the L_1-regression, a circular shift is performed on each signal.

The phase correction of the wave packet itself is the same procedure apart from an additional redefinition of the shifted time signal boundaries. After shifting the signal the boundaries have to be finally redefined. The results of the whole procedure are a pair of final boundary-location functions and two shift functions, which could be superimposed to one function and converted to a shift function regarding any arbitrary reference temperature. The last point has the advantage that we do not need a reference signal at the exact reference temperature while calculating the time shifts, for example we could use a signal measured near the reference temperature instead.

14-3-3 Phase and Amplitude Correction in Frequency Domain

After the phase correction in time domain the wave packets have the same length and nearly no time shift but in general differ in amplitude and slightly in phase due to dispersion effects. To adjust such effects, the *Fourier*-transformation $\mathcal{F}$ was performed to convert the signals into frequency domain:

$$\mathbf{z}^i(\mathbf{f},T,Z) = \mathcal{F}(\mathbf{u}^i(\mathbf{t},T,Z)) . \qquad \text{E.14-8}$$

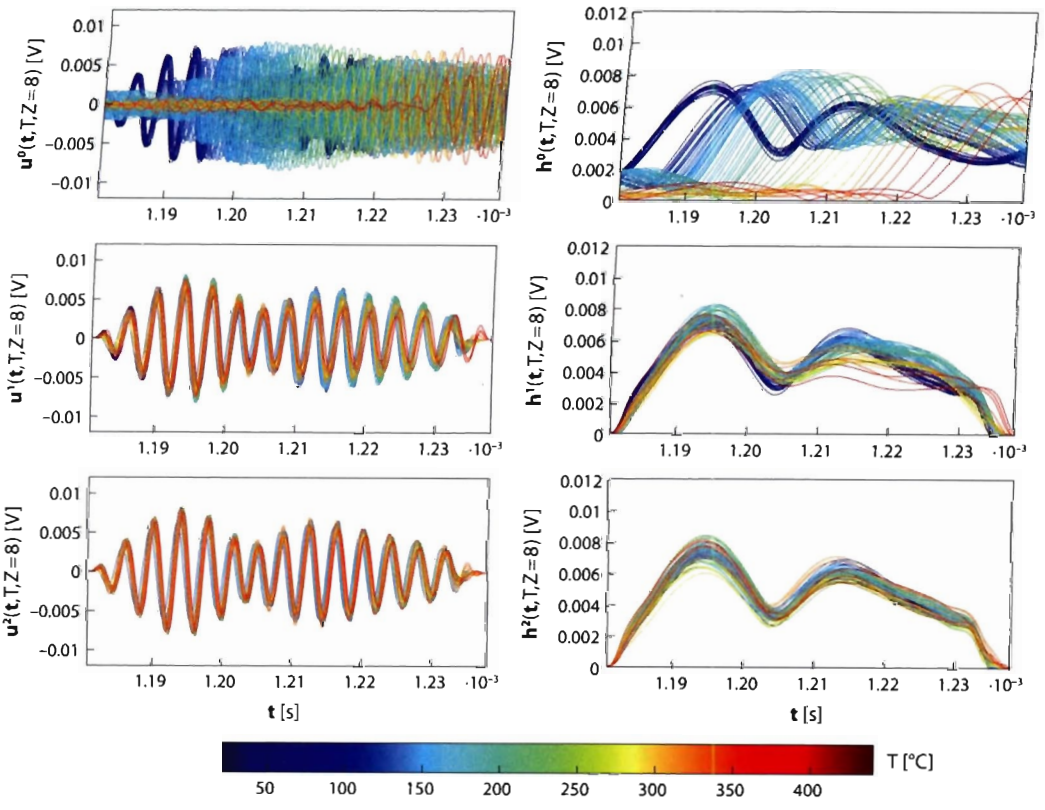
The vector $\mathbf{z}^i(\mathbf{f},T,Z) \in \mathbb{C}^m$ is the *Fourier*-transformed signal, whereby every column carries the information about amplitude and phase of one certain frequency, which are

all together superimposing to the wave packet. The E.14-5 was solved for each frequency component (m-times) separately with $\mathbf{b} \in \mathbb{C}^n$ as the vector of the certain *Fourier*-component for all n corrected signals.

The *Vandermonde*-matrix remained unchanged. The L_2-norm was applied for this step since it showed smoother results. Note that $\mathbf{b}$ is a complex vector and therefore also $\mathbf{x} \in \mathbb{C}^l$ and the resulting m polynomial correction functions have complex coefficients.

As a next step the polynomial functions were shifted so that they equal zero at T_R. The resulting functions describe the difference of each *Fourier*-component from the reference temperature and have therefore to be subtracted from each corrected signal in frequency domain. The results are shown in F.14-7. The left side shows the time domain signals and the right side the envelopes. On the top, the original signals at different temperatures are displayed. The middle column shows the results after the first time shift corrections in time domain. On the bottom, the signals are show after the last step, the correction in frequency domain.

Results of the temperature correction for 8 mm hole. Top: original signal, middle: signal after correction in time domain (time shift), bottom: signal after correction in time and frequency domain (phase and amplitude correction) F.14-7



14-3-4 Damage Detection

Holes with diameters of 8 and 10 mm and with depth of 1/3 of the wall thickness (7 mm depth) each were introduced. Data for all the different states were gathered. F.14-8 shows the correlation of the normalized amplitude and time of the second maximum in the wave packet for diameters of 0, 8 and 10 mm respectively as an example of a successful temperature compensation and damage detection. The ellipses mark 95 % of the variance.

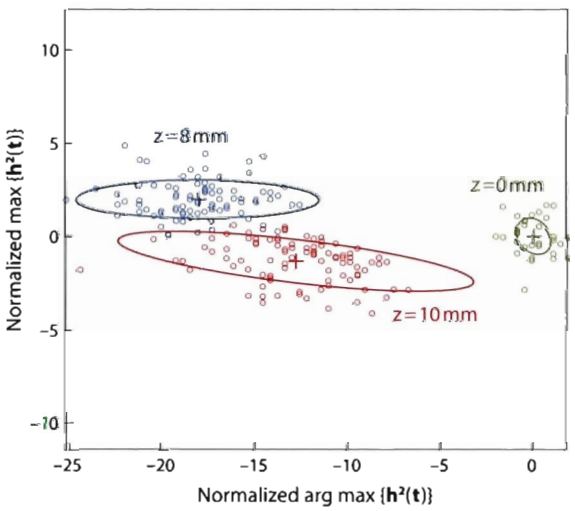
14-4 Conclusions

As demonstrated, the data recorded in the power plant could be successfully corrected regarding the temperature influence that would make any differential measurements for damage detection impossible. It can be clearly seen that the first correction step does not take any dispersion effects into account. Only the correction in frequency domain gives satisfactory results and also reconstructs the maximum of the second wave packet correctly.

Furthermore, the damages of 8 mm and 10 mm holes with 1/3 of the wall thickness (7 mm depth) could be detected and separated from the initial undamaged condition.

For future applications, this experiment will be repeated to prove the approach. It is also planned to use cluster analysis for the detection of unknown damages.

Normalized maximum amplitude and corresponding time of the second wave packet F.14-8



Acknowledgement

The present work has been supported by the Commission of the European Communities in the framework of the specific targeted research project IRIS (Integrated European Industrial Risk Reduction System) under the 7th Framework Programme (FP7-NMP-2007-LARGE-1). This support is gratefully acknowledged. We also thank all our partners in the IRIS consortium, especially RWE, for providing us with the access to the power plant and the operating and support of the bypass measurements.

References

Köhler, B., Schubert, F. and Frankenstein, B., 2004. *Numerical and Experimental Investigation of Lamb Wave Excitation, Propagation and Detection for Structural Health Monitoring*. Proceedings of the 2nd European Workshop on Structural Health Monitoring, Munich, Germany, 7–9 July, Eds: C. Boller, W. J. Staszewski, 993–1000.

Schubert, F., 2004. *Basic Principles of Acoustic Emission Tomography*. Journal of Acoustic Emission 22:147–158.

Schubert, F., Frankenstein, B., Klesse, T., Kerkhof, K., Schuler, X., Friedmann, H., Henkel, F. O. and Wenzel, H., 2009. *Structural Health Monitoring and Lifetime Management of Industrial Piping Systems*. In: Encyclopedia of Structural Health Monitoring, Eds: C. Boller, F.-K. Chang, Y. Fujino, John Wiley & Sons, Chichester, UK.

Schubert, L., Barth, M., Klesse, T., Köhler, B. and Frankenstein, B., 2008. *Guided Elastic Waves and their Impact Interaction in CFRP Structures Characterized by 3D Laser Scanning Vibrometry*. SPIE 03/2008, San Diego.

Schubert, L., 2012. *Condition Monitoring of Fiber Composite Materials by Guided Waves*. Dissertation, TU Dresden, ISBN 978-3-942710-72-5, 2012 TUDpress.

15

Vibration Study and Application of Outlier Analysis to the S101 Bridge Full-Scale Destructive Testing

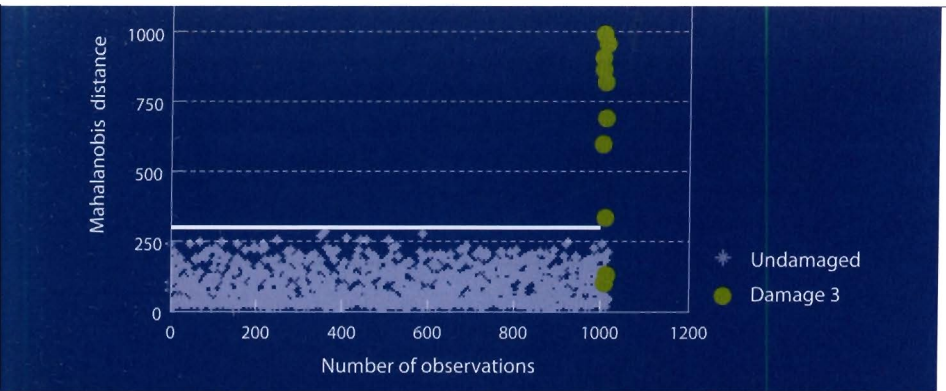
Authors:
Dionysius M. Siringoringo
Tomonori Nagayama
Yozo Fujino
Di Su
Chondro Tandian
Hirotaka Miura

Motivation

The detection of outliers in multi-variant data by online technologies, screening continuous data streams from monitoring systems, needs to be established in a quick and error free environment. Stable methods in order to avoid false alarms are desired.

Main Results

An outlier detection routine capable to be linked to permanent monitoring systems has been developed. A novel damage detection application based on outlier analysis of the spectral functions, called Mahalanobis distance, has been created.



15-1 Introduction

Structural health monitoring (SHM) of bridges is a subject that has received considerable attention in recent years. Recent incidents such as the collapse of the I-35W Bridge in the US, give a clear indication of the importance of SHM. In practice, bridge assessment includes several measures such as inspection, data interpretation, and development of engineering recommendation. Inspection as a starting point requires reliable and useful structural information on global and local performance, for which visual inspection, instrumentation, and monitoring have been recognized as indispensable tools.

For global structural assessment in particular, vibration monitoring has been widely used. Vibration characteristics, captured from vibration monitoring, provide global information on structural behaviours such as stiffness, connectivity, boundary conditions, mass distribution and energy dissipation. The underlying principle of vibration-based structural assessment is that structural changes or defects will create changes in the dynamic response that can be detected from the changes in vibration characteristics. In other words, changes in frequencies, mode shape, and modal damping can be used as indicators of the changes of physical properties of structures such as mass distribution, stiffness, connectivity, boundary conditions, and energy dissipation. Extensive works have been done on developing methods and algorithms for damage detection using vibration characteristics. [Doebling et al., 1996] present a comprehensive list of literature in damage detection and divide the detection algorithms into four levels of increasing complexity. They are: level 1 determination that damage is present in the structure, level 2 determination of the geometric location of the damage, level 3 quantification of severity of damage, and level- 4 prediction of the remaining service life of the structure.

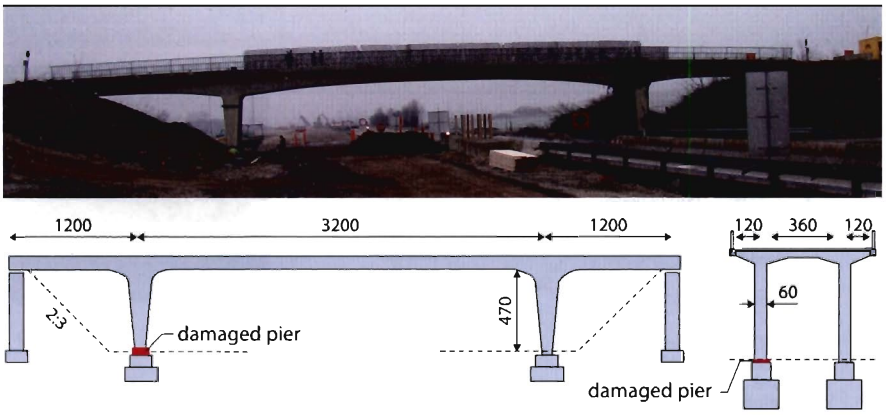
Although many algorithms have been developed, most of them have been of theoretical or computational nature and verified in finite element simulation or laboratory-scale experiments. There are only few studies that involve verification on a full or near full-scale test of an actual structure subjected to controlled damage. This is understandable since progressive damage tests are costly and sometimes impossible. Therefore, vibration measurement during a progressive damage test of full-scale structure is a very important learning opportunity. From such measurement, one can observe evolution of dynamic characteristics, validate damage detection methods, and formulate the baseline criteria for typical structural deteriorations. Notable studies on the full-scale test damage detection of the bridge are the Z24 Bridge in Switzerland [Peeters and Roeck, 2001] and the Alamosa Canyon Bridge [Farrar et al., 2000]. Both studies have provided a benchmark for damage detection methods and emphasized the importance of environmental effect on the dynamic characteristics of the bridge.

Realizing the importance of a full-scale bridge damage test, observations and lessons learned from such a test are presented in this paper. The paper summarizes the process of vibration measurement and destructive test, analyses the data and presents the results of vibration analysis. Ambient vibration measurements were conducted before, during and after introduction of damage. Sensitive features that can be utilized as indicators of damage were extracted from vibration characteristics.

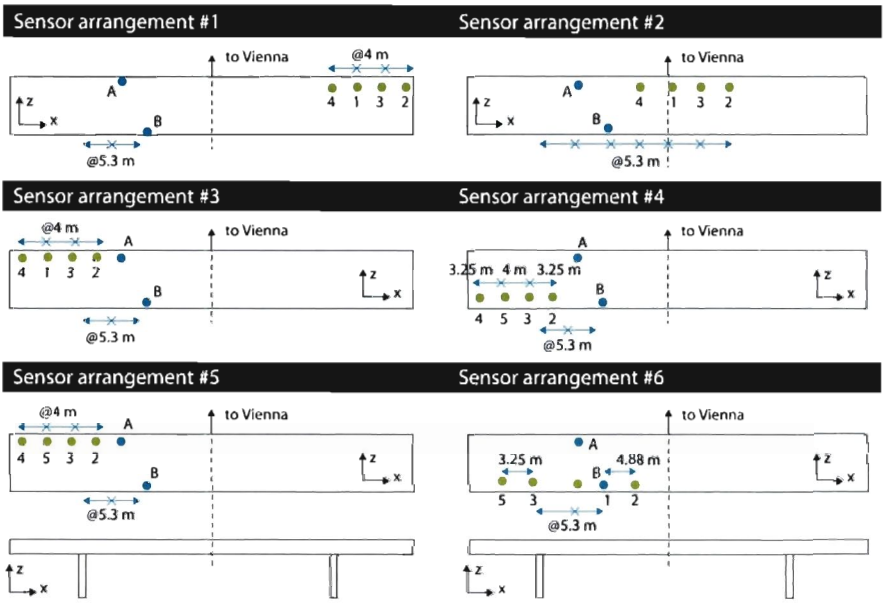
15-2 Description of S101 Overpass Bridge and Sensing System

The tested bridge is the S101 bridge overpass located in Reibersdorf, Upper Austria, which is west of Vienna, Austria. The bridge crosses over the motorway A1 Westautobahn Austria. It is a post-tensioned concrete bridge with a main span of 32 m, side spans of 12 m, and a width of 6.6 m (F.15-1). The deck is continuous over the piers and is built into the abutment. The bridge, built in 1960, was a typical overpass in the motorway. Although there were no known structural problems, the bridge had to be demolished to allow a space for an additional lane underneath. Before demolition, a series of vibration tests was carried out by VCE. The authors participated in a two-day measurement from 10 until 11 December 2008. On the first day, preliminary experimental vibration tests were conducted. The purpose of the tests was to obtain an initial estimate of the bridge modal parameters. An ambient vibration test was conducted with the main source of vibration from the motorway traffic underneath the bridge. The sensing system consists of six triaxial-accelerometers CV-373 produced by Tokyo Sokhushin. The sensors measured accelerations at six measurement nodes. Due to limited number of sensors, six sets of sensor arrangements were utilized (F.15-2). Two sensors (i.e. node A and B) were kept at the same place throughout the measurement to provide reference for time-synchronization. Four other sensors were the roving sensors that moved from one end to the other end of the bridge. To measure the bridge in undamaged condition, three sensor arrangements were utilized (i.e. sensor arrangement 1–3). On the second day, 11 December 2008, a destructive test was conducted. At this time the sensing system consisted of three sensor arrangements (i.e. sensor arrangement 4–6), where they were mainly placed on the bridge side near the location of damage. Like on the first day, two sensors were placed in the middle of the bridge span and kept at the same place throughout the damage process as a reference for previous measurement. During the two-day measurement, temperature conditions were relatively equal with an average temperature of –3°C.

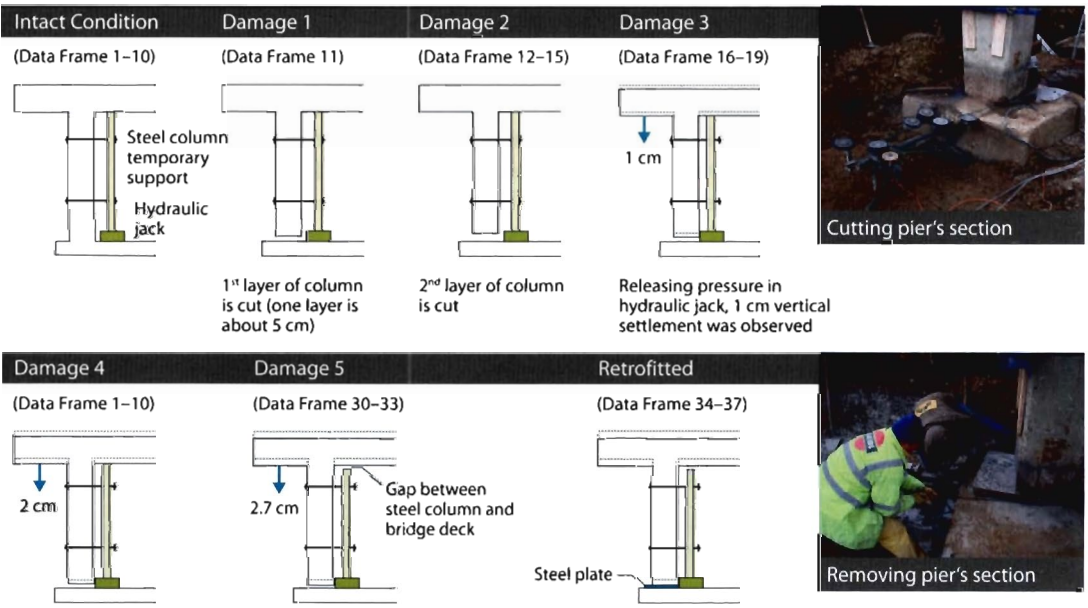
View of the S101 bridge and bridge dimension F.15-1



Sensor arrangement for vibration measurement (note: A and B are the reference sensors) F.15-2



Schematic figures of the complete damage process F.15-3



15-3 Damage Scenarios and Finite Element Model

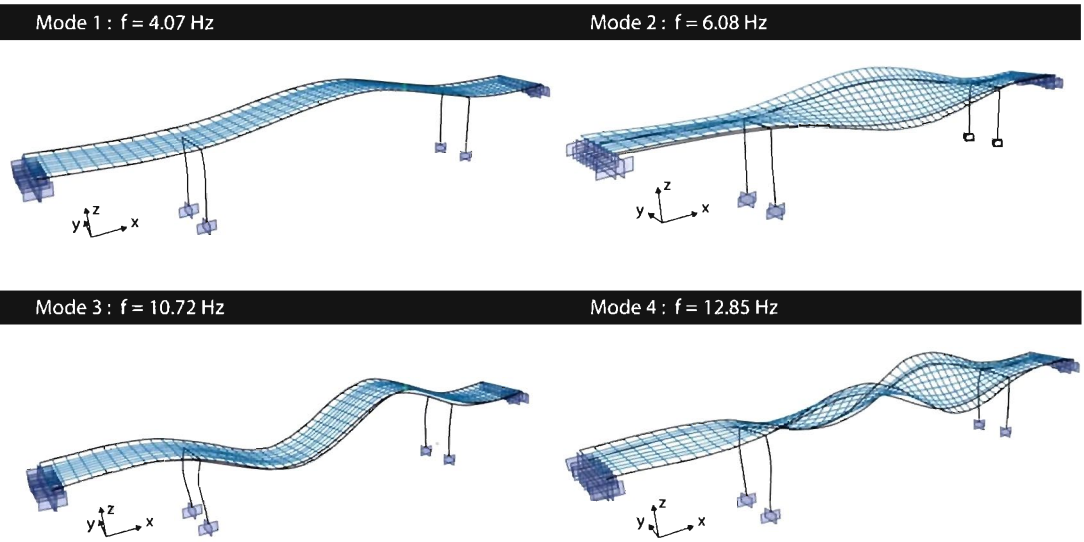
F.15-3 illustrates the scenarios of damage simulated in this test. Damage was introduced to the structure by cutting the pier just above the footing. The cutting was made twice, the first was 2 cm layer of column (named hereafter as damage 1) and the second was another 2 cm (damage 2). During the cutting process, a steel column was placed alongside the pier and tightened to the pier with steel rods to provide temporary support. When the pier had completely severed from the footing cap, the temporary support was gradually released until the pier was completely suspended. During this time vertical settlement of the bridge at the pier location was recorded continuously until the total settlement reached 2 cm (damage 3 and damage 4). Finally, the pier was completely suspended and no further settlement was observed (damage 5). At the last stage, a steel plate was inserted to close the gap between pier and the footing. In this condition the pier rested on the plate and the stage was named retrofitted stage. Throughout the damage process an ambient response of the bridge was recorded at the sampling rate of 100 Hz. The records were divided into 37 time-windows (frames) of five minutes signal each. Details of the damage stage, sensor position and data framing are listed in T.15-1.

In order to provide a reference for comparison of experimental modal analysis, a Finite Element Model (FEM) was built in [SAP 2000]. The model utilizes 360 frame elements for columns and beams, and 504 shell elements for the deck slab. It is made using as-built drawings by assuming the concrete material of 2400 kg/m^3 density and the Young's modulus of $2.48 \cdot 10^{10}$ N/m. Interaction with soil is not taken into consideration in the model and all degrees of freedom of the piers are restrained at the footings. At the abutments, the longitudinal beam and the slab are assumed to be fixed. This assumption was considered after observing the real condition of the bridge. F.15-4 shows the corresponding mode shapes of the undamaged bridge. FEM reveals that the vertical modes are predominant, and the bridge is relatively stiffer in transverse direction than in vertical direction.

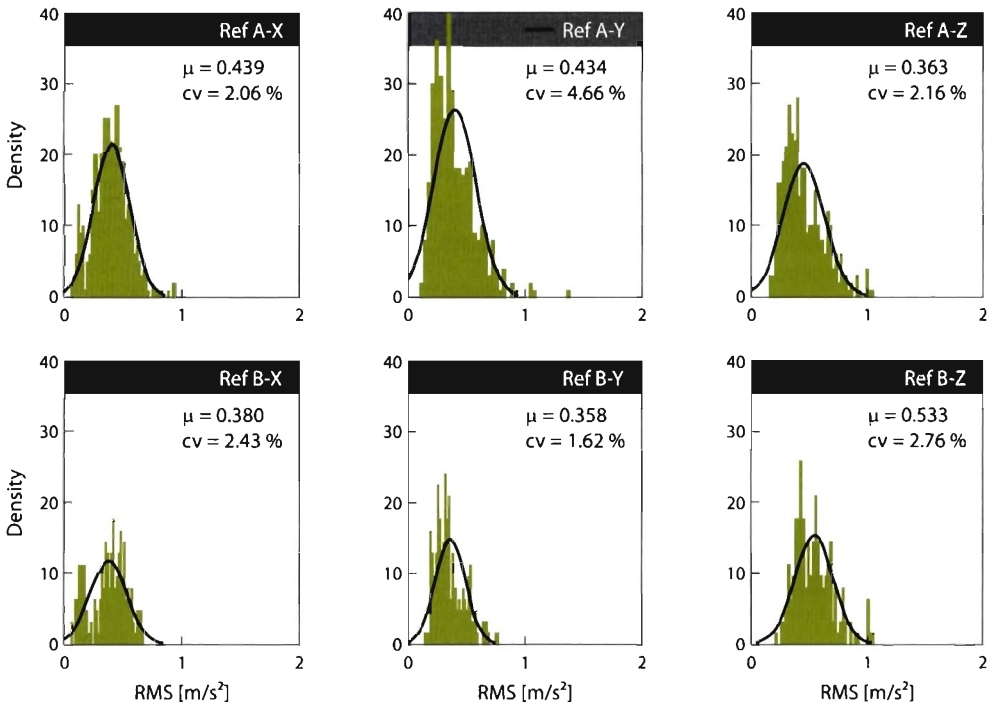
Damage stage, sensor position and data framing T.15-1

Damage code	Frame no.	Sensor arrangement	Bridge condition
Undamaged	1–4	#1	Structure intact
Undamaged	5–6	#2	Structure intact
Undamaged	7–10	#3	Structure intact
Damage 1	11	#4	1st layer of column is sliced
Damage 2	12–15	#5	2nd layer of column is sliced
Damage 3	16–19	#6	1 cm vertical settlement
Damage 4	20–29	#6	2 cm vertical settlement
Damage 5	30–33	#6	No further settlement, column is completely suspended
Retrofitted	34–36	#6	Steel plate inserted

Mode shapes of the bridge generated by FEM F.15-4



Distribution of RMS of acceleration recorded at reference channels F.15-5



Dominant modes are well separated within the range of 3–18 Hz. The 1st, 3rd and 5th mode correspond to the 1st, 2nd and 3rd bending respectively, while the 2nd and 4th mode are the torsion modes.

15-4 Methodologies for Vibration Analysis

In this section methodologies employed to analyse vibration data are explained in detail. At first, we examine the vibration level and test the stationary assumption. The ambient responses were analysed in both frequency and time domain. In frequency domain the spectrogram analysis is used. In time-domain global system identification using ERA and local (single-node) identification are employed to check the consistency of modal parameter estimates.

15-4-1 Vibration Level Analysis

Preliminary data analysis in time domain is conducted to obtain information about vibration level and to verify stationary assumption. For these purposes the root mean square (RMS) values of the acceleration are calculated. Since only two sensor nodes were placed on the same position throughout the measurement (i.e. reference A and B in F.15-2), only the RMS of these records were relevant for comparison. To observe the stationary of the response, RMS values of accelerations are calculated for three cases: every minute, every five minutes and for the whole data. F.15-5 shows distribution of acceleration RMS for references A and B in three directions calculated from one minute sampling time. The figure shows that the RMS distributions fit the normal distribution. In all three directions, deviations of RMS are very small as denoted by the largest c.o.v of 4.7 %. The same results can be seen for the five minute time sampling (T.15-2), where the largest c.o.v is 3.6 %. The small c.o.v. indicates that the responses are relatively stationary. Also note from T.15-2 that the mean values of RMS of one-minute and five minute sampling-time differ only slightly with the mean value of RMS for the whole record, suggesting ergodicity of the response. These observations indicate that the responses recorded throughout measurement are stationary and ergodic.

RMS of acceleration measured on reference sensor A and B (longitudinal, transversal and vertical direction) T.15-2

Sampling time	Mean of RMS of acceleration response at reference sensors (m/s^2)					
	A-longitudinal	A-transverse	A-vertical	B-longitudinal	B-transverse	B-vertical
1 minute	0.438 (0.021)	0.434 (0.047)	0.3623 (0.022)	0.380 (0.024)	0.357 (0.016)	0.533 (0.028)
5 minutes	0.447 (0.013)	0.446 (0.036)	0.369 (0.017)	0.387 (0.019)	0.364 (0.012)	0.545 (0.015)
all data	0.461	0.484	0.391	0.407	0.379	0.558

Note: value in the bracket denotes the coefficient of variation

15-4-2 Spectrogram Analysis

A spectrogram of the vibration response provides a close-up look on the frequency components of vibration as function of time. In this study a spectrogram plot shows power-spectra-density (PSD) of acceleration computed at each time-window and normalized to the maximum value. The ordinate of spectrogram denotes the time-window (in this case frame number) that corresponds to the time when responses were sampled and the subsequent damage stage. The abscissa represents the frequency component of the acceleration. By observing a spectrogram plot, one can follow evolution of frequency components throughout the measurement.

15-4-3 NExT – ERA Global System Identification

Global modal parameters are derived from ambient acceleration response under the assumption of stationary random excitation. To extract modal parameters, the Natural Excitation Technique (NExT) [James et al., 1993] and Eigensystem Realization Algorithm [Juang and Pappa, 1985] are employed in this study. In the NExT the cross-correlation function (CCF) between reference and roving nodes is computed and treated as the free-vibration responses. Considering sensor arrangement, the global system identification is performed in two parts, one is for undamaged stage where fourteen measurement nodes are used, and the other is for damaged stage, where only six measurement nodes are used. For the damage stage, responses of six nodes are sampled simultaneously. For the undamaged stages, however, the responses were not sampled simultaneously, so that a time-normalization technique is required before starting the system identification procedure. Assuming that the responses are stationary as indicated by the result of investigation in the previous section, the relation between reference and roving nodes can be established. As is shown in [Siringoringo and Fujino, 2009], the relation between the response of reference node R_j and roving node (X_y), both sampled at time t_j, and the response of reference node R_k and roving node (X_{ik}), both sampled at time t_k, can be defined as:

$$G_{X_{ik}R_k}(\omega) = \frac{P_{R_kR_k}(\omega)}{P_{R_jR_j}(\omega)} G_{X_{ij}R_j}(\omega) \qquad \text{E.15-1}$$

where $G_{uy}(m) = F^*[u(t)]F[y(t)]$ and $P_{uu}(m) = F^*[u(t)]F[u(t)]$, respectively as defined in [Bendat and Pierson, 1980], and F denotes the Fourier transform and (*) is the complex conjugate. E.15-1 indicates that the cross-spectrum of roving nodes and the reference nodes measured at starting time t_j are different from the cross-spectrum at starting time t_k by factor of $y(m) = P_{RR}(m)JP_{RR}(m)$. Therefore we can compute the cross-spectra of all sensors by multiplying each cross-spectrum response with its corresponding $y(m)$ factor. After computing cross-spectra, the cross-correlation function of each node is generated using inverse Fourier transform. By employing E.15-1 and selecting a sensor at location B as reference, responses from 14 nodes that were sampled in three different time bases (i.e. sensor arrangement #1, #2 and #3) can be normalized into one equal time base. Since

there are four data frames in sensor arrangement #1, two data frames in sensor arrangement #2, and four data frames in sensor arrangement #3, a total of 32 time-normalized CCF data sets are obtained. Once the CCFs are calculated, the Hankel matrix is constructed to implement the ERA method.

$$[H(k-1)] = \begin{bmatrix} CCF(k) & CCF(k+1) & \cdots & CCF(k+q-1) \\ CCF(k+1) & CCF(k+2) & \cdots & CCF(k+q) \\ \vdots & \vdots & \ddots & \vdots \\ CCF(k+p-1) & CCF(k+p) & \cdots & CCF(k+p+q-2) \end{bmatrix} \quad \text{E.15-2}$$

where p and q are the user-defined quantities that represent the number of columns and rows in the Hankel matrix, respectively. To select the system order, the singular value decomposition (SVD) of the Hankel matrix is performed (i.e. $[H(0)] = [P][D_\setminus][V]^T$), in which $[{}^\setminus D_\setminus]$ is a diagonal matrix of singular values that corresponds to the modal parameters. Large singular values indicate the strong participation of the modes in the response. To realize the system matrices, only several large singular values (N) are retained. The first N sub-vectors form the matrices D_N, P_N and V_N that are used to generate the state matrix [A] according to the following equation:

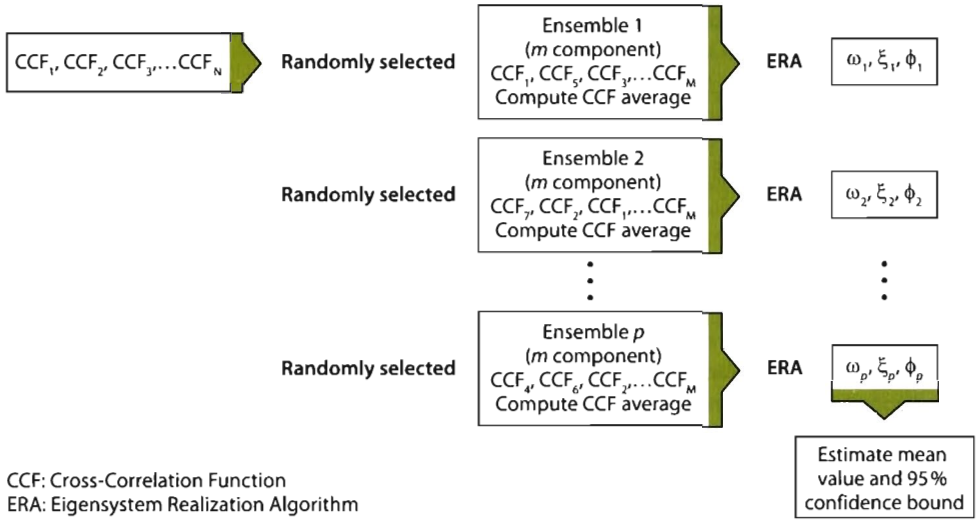
$$[A] = [D_N]^{-1/2}[P_N]^T[H(1)][V_N][D_N]^{-1/2} \quad \text{E.15-3}$$

The quantity $[H(1)]$ in E.15-3 denotes the time-shifted Hankel matrix. [A] is the system state matrix, whose eigenvalues characterize the dynamic parameters of the system, and generate the natural frequencies and modal damping ratios. The eigenvectors of the state space matrix produce the mode shapes matrix of the structure.

15-4-4 Statistical Analysis of Global Modal Parameters

Variability is an inevitable nature of ambient vibration measurement. Different environment conditions, source of vibration excitation, and also noise in instrumentation may affect the response and the extracted modal parameters. To investigate the effect of variability and to estimate the confidence bounds of identified modal parameters, a statistical analysis is essential. By quantifying statistical properties we can interpret the results with confidence. For this purpose, the Bootstrap method [Efron and Tibshirani, 1993] is employed in this study. The Bootstrap method randomly selects and replicates the response from a limited number of records to create an ensemble average of a larger population of response. Statistical properties of the ensemble average are computed to determine the bounds of uncertainty. To implement Bootstrap analysis, a large number of CCF data sets was randomly selected from the available time-normalized CCF data, and the CCF ensembles are formed. On each ensemble, the CCF ensemble average is computed, and then treated as Markov parameter in the Hankel matrix of ERA. This procedure is repeated for a large number of times to form a histogram of the identified modal parameters. The confidence bounds of modal parameters are calculated by the percentile interval method [Bendat and Pierson, 1980] that computes the 95% confidence limit by sorting the mod-

Flowchart of Bootstrap Analysis F.15-6



al parameters in an ordered list and defining the value of upper and lower 2.5% percentile. The complete Bootstrap procedure is illustrated in F.15-6.

15-4-5 Local System Identification

Local system identification allows us to identify damping from single sensor acceleration thus providing a way to observe spatial distribution of damping. It also provides comparison of natural frequencies in addition to global system identification (ERA) and spectrogram analysis. The identification procedure is as follows. At first the auto-spectra of single node acceleration are computed. By applying a bandpass filter for the frequency range of interest and the least-square smoothing technique [Savitzky and Golay, 1964], we obtain the single mode auto-spectra. The result is transferred to time-domain using inverse Fourier transform to obtain the single mode free-vibration response. Using the free-vibration response, the local modal damping ratio is extracted by the logarithmic decrement method as follows.

$$\delta_n = \frac{1}{n}\ln\left(\frac{x_1}{x_{n+1}}\right), \quad \overline{\delta} = \frac{1}{m}\sum_{n=1}^{m}\delta_n \qquad \text{E.15-4}$$

$$\overline{\xi} = \frac{\overline{\delta}}{\sqrt{(2\pi)^2 + \overline{\delta}^2}} \cong \frac{\overline{\delta}}{2\pi} \qquad \text{E.15-5}$$

In the equation above x_n is the j-th peak of single-mode free-vibration response, δ_n is the logarithmic decrement between x_n and x_{n+1}, δ is the averaged logarithmic decrement, and Z is the averaged damping ratio.

15-5 Results of Vibration Analysis for Undamaged and Damaged Stages

Vibration analysis is conducted for the undamaged and damage stage. For damage stages, the analysis consists of three main parts:

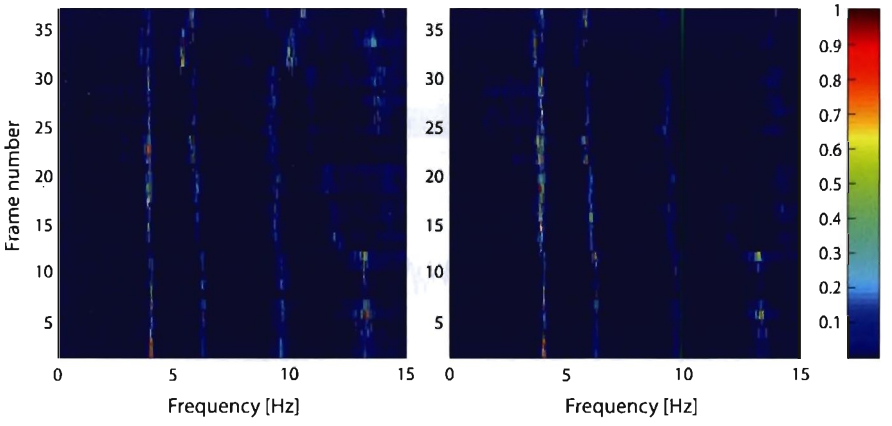
1) during pier cutting (i.e. damage 1–4),
2) when the pier is completely suspended (damage 5), and
3) when a steel-plate was inserted to close the gap between pier and footing (retrofitted).

During all stages the accelerations were recorded, with the main source of vibration coming from traffic. During the first stage of damage, some vibration noise from a cutting machine was noted. However, the effect of machine vibration to the total response can be considered negligible since in both undamaged and damaged stages the level of accelerations remains constant, with the RMS measured at reference channel A and B ranged between 0.3 to 0.9 cm/s^2. In the following section, the results of vibration analysis are presented through spectrogram analysis, global and local system identification.

15-5-1 Spectrogram Analysis

The frequency content of response was observed in the frequency range 1 to 50 Hz. The dominant frequencies at the girder in vertical direction appear in the range of 1 to 15 Hz. F.15-7 shows the spectrogram of reference sensors A and B throughout the measurement. The ordinate consists of two parts: the undamaged part (frame numbers 1 to 10), and damaged part (frame number 11 onward). In the undamaged part, one can see four distinct vertical lines representing four natural frequencies within the range of 3 to

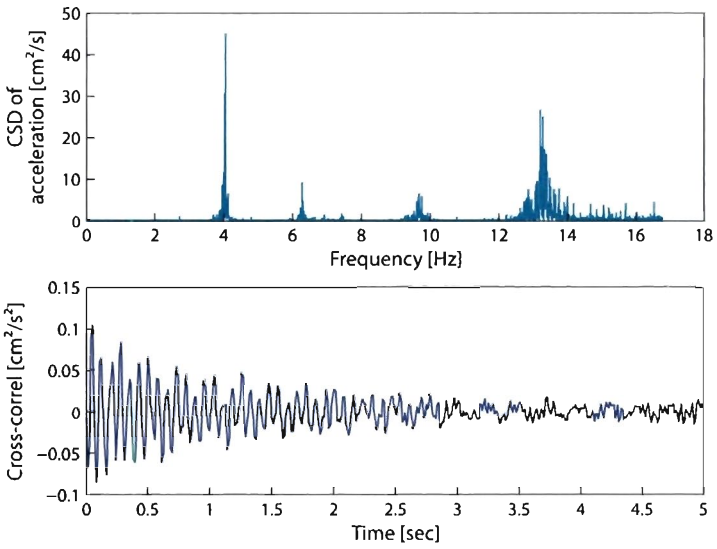
Spectrogram of undamaged and damage stages. Vertical acceleration measured at reference A (left) and reference B (right) F.15-7



14 Hz. The first line is around 4 Hz, the second line is around 6 Hz, the third and the fourth lines are around 9 Hz and 13 Hz respectively. Despite the fact that the amplitude of ambient vibration was small, the frequency spectra show very clear peaks indicating well-separated modes and suggesting that the records have a high signal-to-noise ratio. The four vertical straight lines suggest constant peaks in frequencies plot and small variation of natural frequency estimates.

Unlike the undamaged part, the damaged part shows distinct variation of frequencies. Starting from frame number 11 one can observe the leftward shift of natural frequencies especially the fourth mode (13 Hz). The other modes show an apparent shift starting from frame 20 onward, which corresponds to the time when the bridge experienced 2 cm of vertical settlement. Leftward frequency shifts of the first, second and third modes continue until frame number 34. The largest shifts were observed at the time when the pier was completely suspended indicating the significant reduction of stiffness. Starting from frame number 35 onward, we can observe a rightward shift of the natural frequencies. For the 1st mode, the frequency shifted back almost to its original position, while some residual frequency shifts were observed for the 2nd, 3rd and 4th modes. Note that frame 35 corresponds to the time when the steel-plate was inserted and the structure was in the "retrofitted" state. This result indicates that the steel-plate insertion reduces the vertical flexibility of the structure as evident by the rightward shift of the 1st and 3rd mode (all are bending), but not in the same degree as it reduces the torsional flexibility, as evident by residual frequency shift in 2nd and 4th mode (torsional modes). Results of the spectrogram analysis reveal the evolution of natural frequencies during damage stages.

Typical cross-spectra density and cross-correlation function of acceleration of the undamaged stage F.15-8



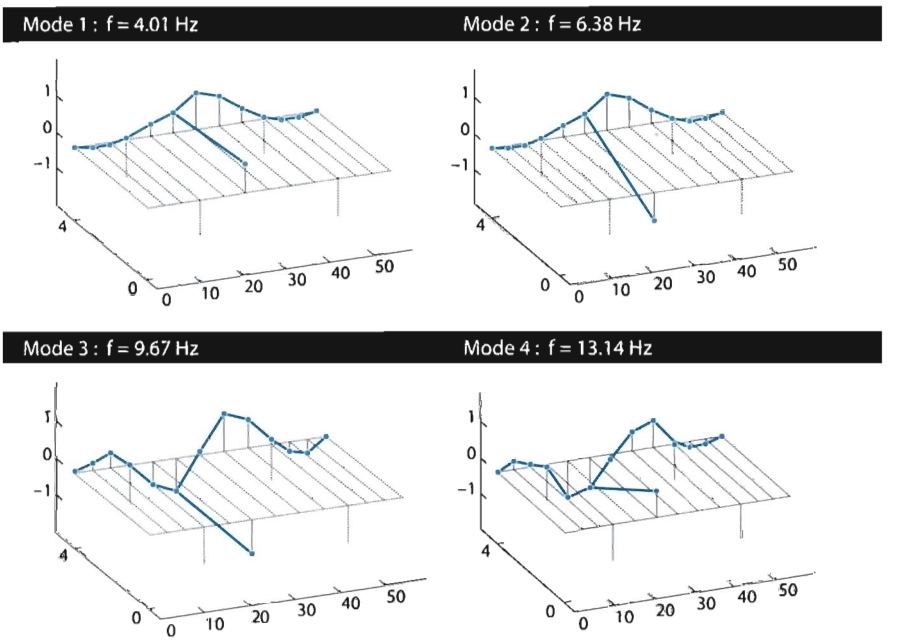
Modal parameters of undamaged bridge identified by ERA T.15-3

Mode	Mean frequency [Hz]	95 % confidence interval [Hz]	Damping [%]	95 % confidence interval [%]
1st bending mode	4.02	0.01	1.37	0.24
1st torsion mode	6.31	0.09	1.19	1.93
2nd bending mode	9.65	0.11	1.30	0.39
2nd torsion mode	13.37	0.22	1.45	1.21

15-5-2 ERA Global System Identification and Statistical Significance of Modal Parameters

For each measurement node the first five seconds of CCF data are utilized as Markov parameter in Hankel matrix. Typical CCF and CSD of vertical acceleration of the undamaged stage are shown in F.15-8. It can be seen that dominant modes clearly present and are well separated within the range of 3 to 18 Hz. T.15-3 lists the identified vertical modes of the undamaged stage along with their statistical properties. The corresponding mode shapes are shown in F.15-9. T.15-3 shows that variations of natural frequencies of the first four modes for undamaged stage are very small, suggesting no significant difference in natural frequencies during a two-day measurement of undamaged stage. For damping, the averaged damping ratios are from 1 to 1.5 %. Larger variances of damping ratios were observed especially for the fourth mode. Therefore it can be concluded that the uncertainty of damping estimates was greater than the natural frequency estimates.

The first four modes of S101 bridge for undamaged condition identified by ERA F.15-9



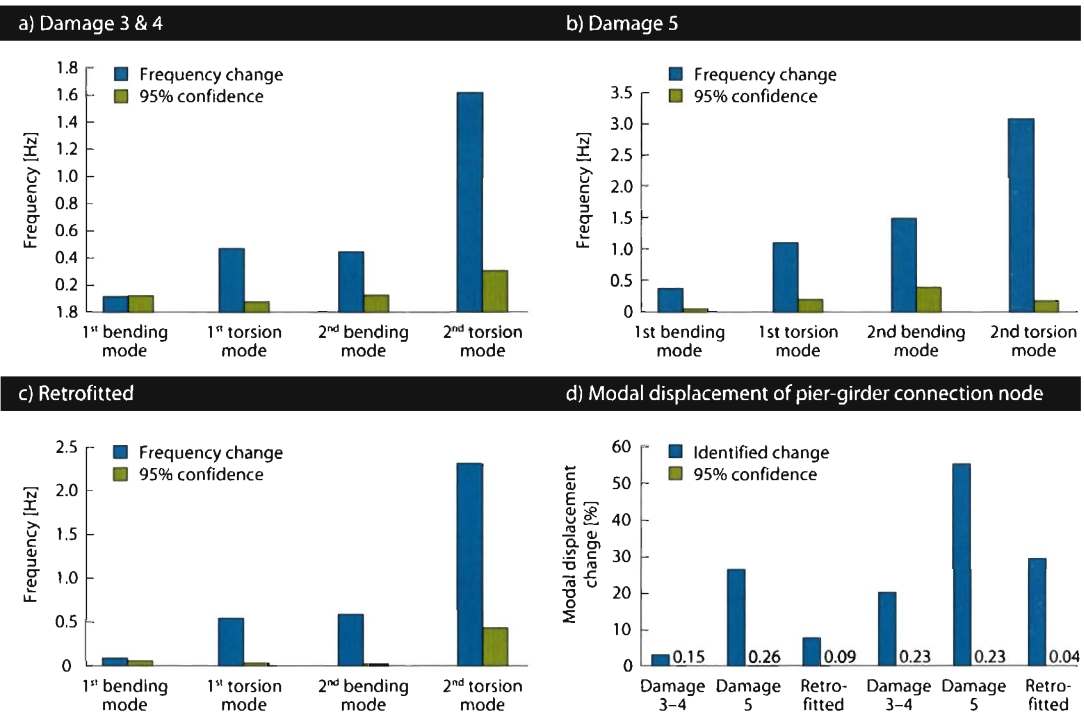
Modal parameters of damaged bridge identified by ERA T.15-4

Mode	Frequency [Hz]			Damping ratio [%]		
	Damage 3 & 4	Damage 5	Retrofitted	Damage 3 & 4	Damage 5	Retrofitted
1st bending mode	3.90 (0.13)	3.65 (0.05)	3.94 (0.07)	1.98 (3.19)	2.10 (1.31)	2.76 (2.62)
1st torsion mode	5.84 (0.08)	5.22 (0.20)	5.76 (0.05)	2.14 (1.23)	2.72 (2.54)	1.93 (1.05)
2nd bending mode	9.21 (0.13)	8.16 (0.39)	9.04 (0.06)	2.12 (1.25)	1.93 (3.91)	2.13 (0.63)
2nd torsion mode	11.76 (0.307)	10.28 (0.16)	11.06 (0.44)	1.49 (3.07)	1.23 (2.29)	1.48 (3.65)

For damage stages, three sensor arrangements are available. However, for the comparison of mode shapes we analyse only data from frame numbers 16 to 37, since the responses from those data frames have equal sensor arrangements (i.e. sensor arrangement no.6). In this arrangement there are six measurement nodes, five nodes aligned on one side of the span near to the damaged pier, while one node (sensor number 4) was located on the other side of the span. For computation of CCF in NExT, sensor number 4 is utilized as the reference. It should be mentioned that since all data were sampled simultaneously, a time synchronization procedure is not required at this time.

Results of identification for damage stages are listed in T.15-4. In this table the results are divided into three groups: damage 3 & 4 (frame numbers 16 to 29), damage 5 (frames

Identified changes of frequencies due to damage F.15-10



ERA-identified changes in frequencies due to damage T.15-5

Mode	Frequency change [%]		
	Damage 3 & 4	Damage 5	Retrofitted
1st bending mode	−3.01	−9.23	−2.01
1st torsion mode	−7.49	−17.31	−8.86
2nd bending mode	−4.51	−15.40	−6.27
2nd torsion mode	−12.02	−23.09	−17.26

30 to 33) and retrofitted stage (frames 34 to 36). F.15-10 shows the comparisons of the 95 % confidence bound estimated by the Bootstrap method and T.15-5 lists the identified change of frequencies as a result of damage. It can be seen in the figure and the table that for damage 3 & 4, natural frequencies of the second, third and fourth modes experience significant changes as denoted by frequency changes that are larger than the 95 % confidence bound. These changes,although small, can be considered statistically significant and be used with confidence as damage indicators. On the contrary, a frequency change of the first mode is statistically insignificant because its value is smaller than the 95 % confidence bound and thus cannot be used as damage indicator. In the damage 5 stage, the changes in natural frequencies of all modes become more significant. All frequency changes are now larger than the 95 % confidence bounds. For damping ratio (T.15-4), there is a slight increase in the mean value as a result of damage. The averaged values of damping for all four modes were between 1.2 to 1.5 % for undamaged structures with small bounds of 95 % confidence. These values increase slightly up to 2 % for damage 3, 4, and 5; and up to 2.7 % for retrofitted condition. Note, however, that in damage condition the 95 % confidence bounds were significantly larger than during the undamaged stage. These large bounds indicate large variation in damping estimates. Therefore, even though damage caused changes in damping, they are statistically insignificant and cannot be used with confidence as damage indicators.

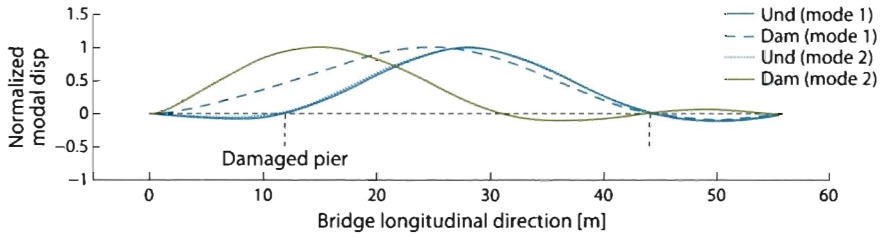
Another important aspect is the effect of damage on the mode shape. Simulation using FEM suggested that when damage altered the support condition, significant changes in mode shapes resulted as shown in F.15-11. Two stationary points that were initially located at the pier-girder connections become only one or shifted next to the undamaged pier. This change is obvious because the pier that restrains vertical movement on the pier-girder-connection node does not function anymore in damage condition. Observation on identified mode shapes reveals a similar outcome. Unfortunately, due to the limited number of sensors, only half-span of mode shapes can be analysed. To compare these half-span mode shapes of a damaged bridge with the complete span mode shape of an undamaged bridge, the first and second modes (i. e. bending and torsion) are normalized to the maximum value that occurred in the midpoint of the span. Mode shape comparisons are shown in F.15-11. In both modes, we can observe large modal displacements at the pier-girder connection during damage stages. The largest modal displacement was observed in damage 5, when the pier was completely suspended. In addition, during damage 5, the highest modal displacement points of the torsion mode shifts toward damaged pier as suggested by FEM.

To quantify the significance of the change in modal displacement, the 95 % confidence bounds of identified mode shapes are computed for all damage stages. For comparison, we compute the modal displacement at the pier-girder connection using FEM for the first and second modes in undamaged and damaged stages. For the undamaged stage, their values are 0.017 and 0.03 for the first and second modes, respectively. And for the damage 5 case, the values become 0.47 and 0.93, respectively. T.15-6 lists the identified values of modal displacement at the pier-girder node for undamaged, damaged and retrofitted cases. One can see that for undamaged stage, modal displacement is very small, 0.02 for modes 1 and 2. For damage 5 the values increase up to 0.28 and 0.57 for the first and the second modes, respectively. Note that the latest values are still below the upper-bounds of 0.47 and 0.93 as predicted by FEM. The values decrease at the retrofitted stage to 0.1 and 0.31 suggesting additional stiffness from the steel plate. Note that the effect of retrofitting is more apparent in vertical bending mode than in torsional mode.

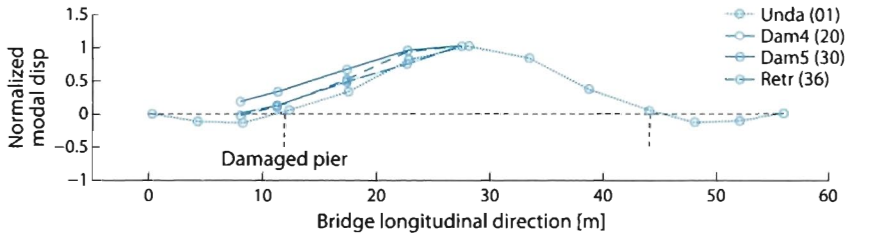
A comparison of the changes of modal displacements due to damage and the 95% confidence bounds is presented in F.15-10d. For mode 1, the changes in mean values are 0.03, 0.26 and 0.07 for damage 3 & 4, damage 5, and retrofitted stage respectively.

Mode shapes of undamaged and damaged stages F.15-11

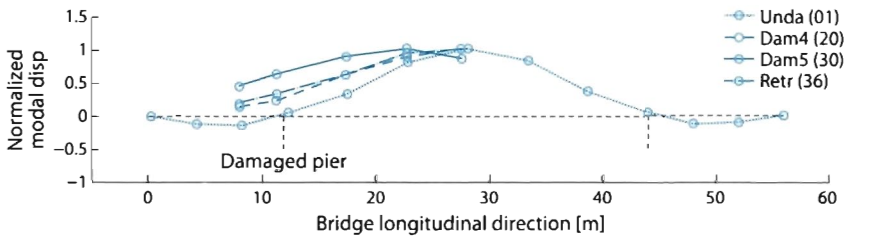
FEM generated mode 1 and mode 2



Experimentally identified mode 1



Experimentally identified mode 2



These changes are significantly larger than the 95 % confidence bounds. For mode 2, the changes in mean values are even larger: 0.2, 0.5 and 0.29 for damage 3 & 4, damage 5 and retrofitted stage respectively. These changes are also significantly larger than the 95 % confidence bounds indicating that for both modes, the changes of modal displacement on the pier-girder connection are statistically significant and can be used as damage indicator.

15-5-3 Comparison of FEM and ERA-Generated Mode Shapes

Three FEM models were built to simulate condition of undamaged, damage 5 and retrofitted stages. To simulate damage 5, one pier in the model is suspended by releasing all of the restraints at the footing level and reducing the pier height by 4 cm. In the retrofitted stage, the model is similar to the undamaged one, but the restraint of one pier is modified from the fixed to partial-hinge condition. In the latter condition, only the vertical and rotational displacement from the x- and y-axis are restrained. This restraint model is selected to represent the condition of plate insertion between the pier and the footing.

Comparisons of the first four modes of the models computed numerically from modal analysis using SAP-2000 software and the ERA identified frequencies are listed in T.15-7. From this table, it can be seen that the results of ERA are within reasonable agreement with the FEM results in all three cases. In the undamaged case the largest frequency discrepancy is 9.9 %, which occurs at the third mode. Note that for undamaged stage the ERA frequencies of modes 1 and 2 are very close to that of FEM. In this study no model updating was performed. The differences between FEM and ERA frequencies are thought to be attributed to the difference between the Young's modulus of concrete used in the model and that of the actual structure considering the age of the bridge. Nevertheless,

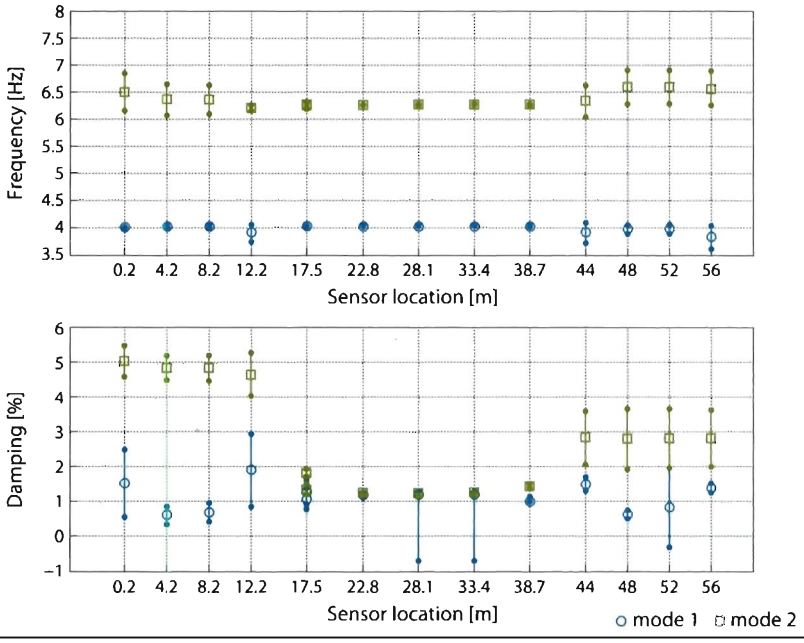
Comparison of modal displacement value at the pier-girder connection with respect to damage stages (values are in %) T.15-6

	Undamaged	Damage 3 &4	Damage 5	Retrofitted
Mode 1 (mean)	2.37	5.37	28.56	10.07
95 % confidence	0.05	0.15	0.26	0.09
Mode 2 (mean)	2.26	22.34	57.29	31.75
95 % confidence	0.11	0.23	0.23	0.04

Comparisons of FEM and ERA frequencies T.15-7

Mode	Undamaged [Hz]			Damage 5 [Hz]			Retrofitted		
	FEM [Hz]	ERA [Hz]	Disc [%]	FEM [Hz]	ERA [Hz]	Disc [%]	FEM [Hz]	ERA [Hz]	Disc [%]
1st bending mode	4.07	4.02	−1.23	3.23	3.65	13.00	3.99	3.94	−1.25
1st torsion mode	6.08	6.31	3.78	5.07	5.22	2.96	6.04	5.76	−4.64
2nd bending mode	10.72	9.65	−9.98	7.60	8.16	7.37	10.58	9.04	−14.56
2nd torsion mode	12.85	13.37	4.05	10.64	10.28	−3.38	12.20	11.06	−13.05

Spatial distribution of frequency and damping for undamaged stage F.15-12



one can see from the results that the decreases of frequencies during damage 5 as suggested by FEM are well verified by ERA results. Likewise, the increase of frequencies during retrofitted stage identified by ERA can be represented in FEM by the change of boundary condition of the damaged pier.

15-5-4 Local System Identification

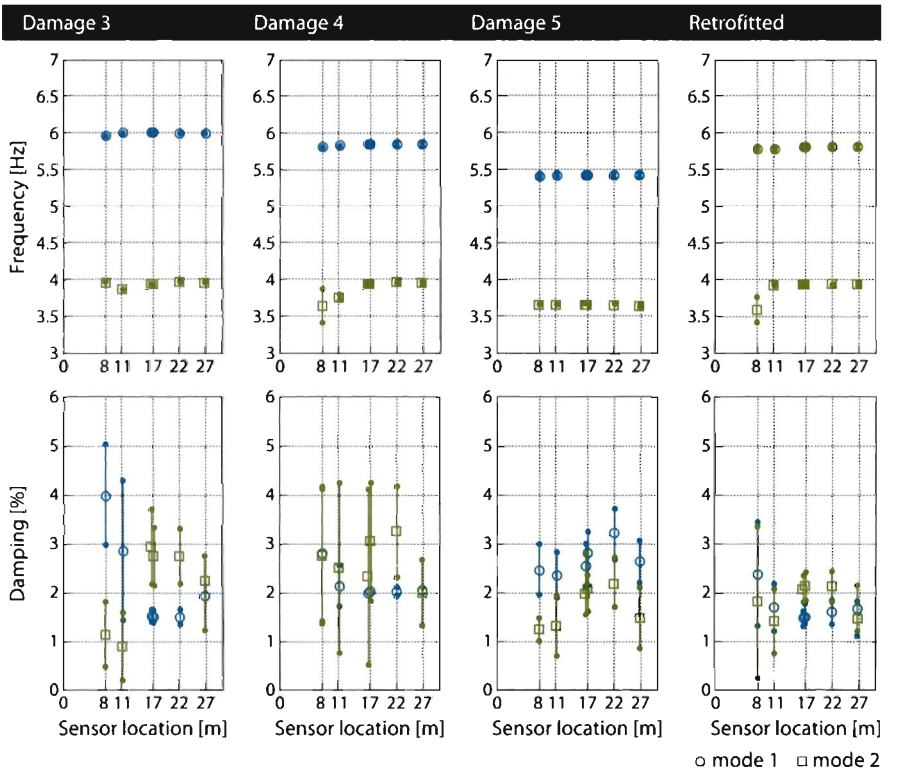
F.15-13 shows the spatial distribution of natural frequency and damping ratio of the undamaged stage identified from single node acceleration response. The figure shows the distribution of frequency and damping ratio of the first and second modes in three spans: side-span 1 (0.2 to 14 m), middle span (14 to 44 m) and side-span 2 (44 to 56 m). For the first mode, the average value of frequency is around 4.0 Hz, in all three spans. Note that the damping ratio does not show large variation spatially, with the average of damping ratio around 1 %. Both estimates are in agreement with the results of the ERA global system identification. It should be mentioned, however, that variation of the damping ratio for the nodes that are close to the pier is larger than that of other nodes.

For the second mode, frequency is identified rather constantly around 6.3 Hz in three spans. Damping estimates, on the other hand, show a distinct pattern. In the middle span, the average damping is 1.3 %, the results that closely match the ERA results. Side-spans' damping are generally higher than that of the middle span. These, however, are followed by larger variation in damping estimates of each node as compared to that of the middle-span nodes. The large variation makes it difficult to consider the result as statistically

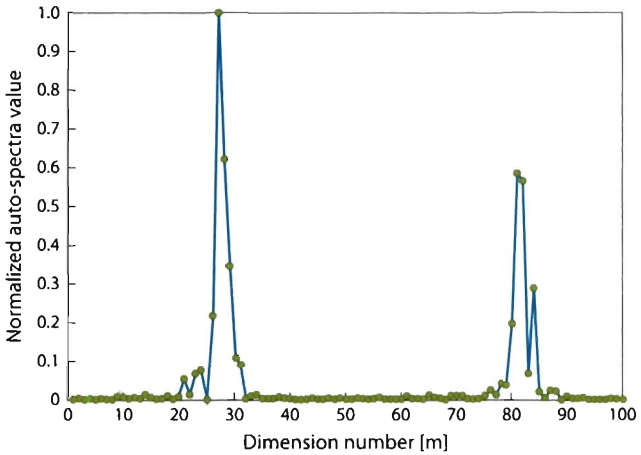
significant. This may be explained as follows. The second mode at the side spans is not well excited by ambient vibration as evident by significantly smaller peaks in frequency compared to that of the first mode. Considering that both ends of the side span firmly rest on the abutments, and that the side-spans are relatively short (i. e. 12 m), the torsional motions may not contribute largely to the total motion of the side span. The frequency peaks of torsional modes identified from single nodes on the side-span are not so sharp and small in amplitude. This generates a wide-band of frequencies under the peak, which yields large local damping estimates.

F.15-14 shows the spatial distribution of frequency and damping of the first and second modes identified from single node acceleration during damage stages. The figure clearly shows that the changes in frequencies due to damage are observable from all sensor nodes. There is no significant variation in spatial distribution of frequency during damage stages. For the first mode, frequency of 4 Hz is estimated from most of the sensor nodes in damage 3, damage 4 and retrofitted condition. The largest change for this mode, 3.6 Hz, occurs during damage 5 and is estimated by all sensor nodes. For the second mode, the change is observable from damage 4 where the frequency shifts to 5.8 Hz. A further decrease is evident in damage 5 (i. e. 5.5 Hz), before increasing to 5.8 Hz in retrofitted condition. Note that spatial variation of the second mode is very small in each damage stage. For damping estimates, relatively large variations were observed in

Spatial distribution of frequency and damping for damaged stages F.15-13



Example of 100 data-points acceleration auto-spectra between 3 and 7 Hz used in calculation of Mahalanobis distance F.15-14



each damage stage. For damage 3, the average values of the damping ratio are 1 to 3% for the first mode, and 1.5 to 4% for the second mode. Note that for the second mode of damage 3 slightly large damping estimates were observed on sensors 3 and 5, which are located on the side span. The reason behind this is as explained in the damping estimate of the side-span of the undamaged stage. Damping estimates slightly increase for damage 4 & 5 with the average values of 2.5 to 3%. Although some spatial variations of damping are present during the two damage stages, no significant local damping changes are observed. During retrofitted stage, damping decreases slightly with the average value of 2%. It should be mentioned that despite some small spatial variations, the values of local damping estimates are within the same range of global damping estimated by the ERA global system identification.

15-6 Damage Detection Using Multivariate Outlier Analysis

Damage detection using statistical pattern recognition has gained increased attention recently. The main idea is to combine the use of damage-sensitive features and statistical novelty detection method to detect the presence of damage. One such method is outlier detection. Outlier is an element of a data set that appears inconsistent with the rest of data and is thus perceived to be governed by other mechanisms. The advantage of this approach over modal-based damage detection is that it only requires data from undamaged structures. Based on these data, the statistical pattern of undamaged structures is formulated and utilized as a baseline for evaluation of future data. When the statistical

property of future data is inconsistent with that of the baseline, they will be considered as possible outliers.

In the case of univariate data, one can detect the outliers by simply employing statistical deviation such as mean and standard deviation. For multivariate data that consist of m variables and n observations, outlier detection is more complicated. A common approach that is based on univariate detection approach is the discordancy test using Mahalanobis squared distance [Worden et al., 2000]:

$$D_M(u) = (u - \mu)^T [\mathbf{S}]^{-1} (u - \mu) \qquad \text{E.15-6}$$

where $D_M(u)$ denotes the squared Mahalanobis distance of multivariate data $u = [u_1 u_2 \ldots u_N]^T$, with mean values $U = [M_1 M_2 \ldots M_N]^T$ and covariance matrix $\mathbf{S}$.

15-6-1 Feature Selection

To implement outlier detection for structural health monitoring, the first and arguably the most important step is to select the damage sensitive feature. The feature should be sensitive to damage and can be preferably extracted directly from measurement without too much preprocessing. The use of outlier detection and several damage sensitive features have been reported in literature. The study by [Worden et al., 2000] utilized the transmissibility function of acceleration response, whereas [Mustapha et al., 2007] used the waveform. Static-strain data in conjunction with auto-regressive integrated moving average (ARIMA) is used by [Omenzetter et al., 2004] to observe different structure changes during construction. [Gul and Catbas, 2009] used the feature vectors of auto-regressive models (AR) of free-vibration response, which was derived from ambient response by Random Decrement technique. In this study we investigate the feasibility of auto-spectra of acceleration as damage sensitive feature. The auto-spectra contain at least two basic pieces of information of structures that are sensitive to damage: natural frequency – indicated by spectra peaks, and damping – indicated by the sharpness of the peaks. It is a simple feature that can be derived directly from ambient measurement and it captures changes in natural frequency and damping simultaneously.

To implement the method, a number of data points (m) within the frequency range of interest are selected from spectra plot and treated as a multivariate feature vector. The procedure is repeated for several data sets under the same undamaged condition. In order to provide a clear distinction between inlier and outlier there needs to be some threshold value. In this study we closely follow the method by [Savitzky and Golay, 1964], in which the threshold value is set by Monte Carlo simulation using the following steps:

1) Creating a data bank for undamaged condition. For this purpose, 100 equally-sampled data points ($m = 100$) are selected as feature vector from auto-spectra of references A and B during undamaged stage. Data in the feature vector are within the frequency range of 3 to 7 Hz. Since there are only 10 data frames for undamaged condition, only 20 numbers of observation (n) are available. This is considered insufficient. To provide an appropriate mean and covariance matrix for undamaged condition a larger number of observation is required. For this purpose, the feature vectors

were randomly copied 500 times, and for each copy Gaussian random vectors with rms of 0.01 of the maximum value were added to simulate noise.

2) Computing the largest Mahalanobis squared distances. The largest values of Mahalanobis distance were calculated exclusively for each observation. This procedure was repeated for a large number of trials (in this study 10000 trials) and all the largest values are ordered. The threshold is then defined as 99.99 percentile value of the largest Mahalanobis squared distance in all trials.

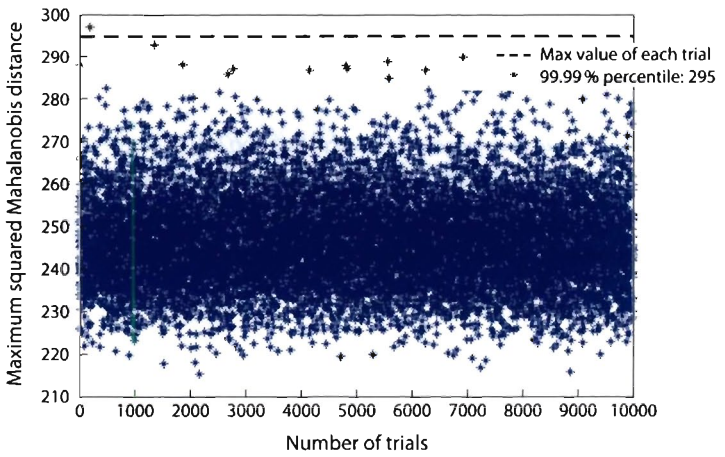
After defining the threshold, Mahalanobis distances for all feature vectors in each damage stage are computed and their status as outliers or inliers are conformed.

15-6-2 Results of Outlier Detection for Damage Stages

The first step in implementing the outlier detection is to select the feature vector of undamaged stage. F.15-14 shows an example of 100-dimensional feature vector data selected from the auto-spectrum of reference sensor B of undamaged stage sampled over the frequency range of 3 to 7 Hz. Within this range, the spectrum is characterized by two peaks that correspond to modes 1 and 2. The next step is to set the threshold value. For this purpose Monte Carlo simulation was performed. In each simulation, 500 feature vectors were generated using the procedure explained in section 15-6-1, and the mean vector μ as well as the covariance matrix [**S**] were calculated. F.15-15 shows the maximum values of Mahalanobis distance after 10000 trials, from which the 99.99 percentile is selected as the threshold value. In this case the Mahalanobis distance set for the threshold value is 295.

After obtaining the threshold value, computation of Mahalanobis distance for damage stages is performed. F.15-16 shows the values of Mahalanobis distance for four damage cases. The figure consists of two parts, one is a training set, which represents undamaged stage, and the other is the testing sets, obtained from auto-spectra of reference

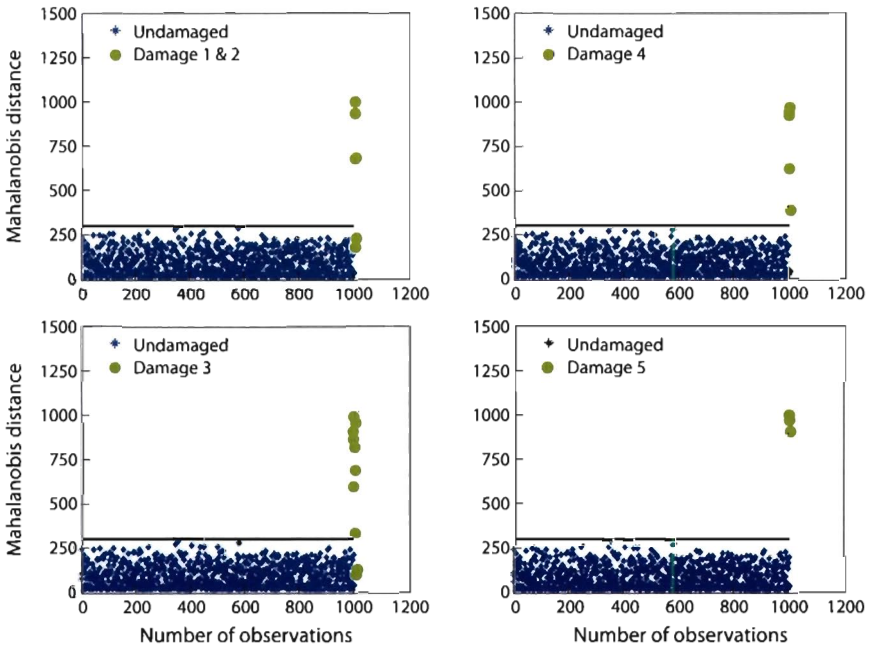
Results of Monte Carlo simulation for outlier threshold setting F.15-15



sensors in damage stages. In the training set, the mean vector and covariance matrix are estimated by following the procedure in section 15-4-6 for 1000 trials. To simulate a realistic condition of the feature vector for undamaged structure, Gaussian random noise is added in the auto-spectra. Simulation yields the horizontal threshold value of 295, which represents 99.99% confidence level of detection. One can see from F.15-16 that all points in the undamaged stage fall well below the threshold line. There are no false negatives observed, indicating that the threshold line clearly separates the condition of damage and undamaged.

For damage 1 & 2, and damage 3 most of the points are detected as outliers. False positives, however, are obtained from two points in each damage stage. These two points are from data sets with the frequencies of 3.8 and 3.9 for mode 1, and frequencies of 6.1 and 5.9 for mode 2, respectively. The two false positive data sets are from frames 11 and 12 that correspond to the time when damage is still in progress. Therefore, it is understandable that the damage has not changed the structure significantly. When damage has significantly changed the characteristics of the structure such as the case of damage 4 and damage 5, all points are unambiguously detected as outliers. Note that the distance between undamaged points and that of damage points of damage 4 and damage 5 are increasing as damage becomes larger. This is a rather expected result since the larger the damage is the more the auto-spectra deviate from the undamaged pattern. In these two cases, the distance between outliers and threshold line can be used as indicator of damage severity.

Mahalanobis distance plots for all damage stages F.15-16



15-7 Summary and Conclusions

Observations and lessons learned from the progressive damage test of an overpass bridge were presented in this paper. The study described the process of vibration measurement and presented the results of vibration analysis. Through systematic data analysis that includes spectrogram analysis, global and local system identification, dynamic characteristics of the bridge before, during and after damage are identified and evaluated. In evaluation of global modal parameters, in particular, statistical analysis by means of Bootstrap method was employed to quantify the confidence level and hence facilitate the statistical interpretation of the results. In addition to data analysis, feasibility of multivariate outlier-detection using auto-spectrum in identifying damage presence and severity were investigated. Important results of the study are summarized as follows:

1) A non-uniform pier settlement simulated as damage in this study, affects global stiffness of structure significantly. This is evident by the significant change in frequency of low-order modes. The effects are more obvious in torsional modes than in bending modes as indicated by larger changes in frequencies of torsional modes than that of bending modes. Accordingly, this finding can be used as an indicator of the presence of a non-uniform pier settlement.
2) Damage in the form of pier settlement also alters the mode shapes locally. Modal displacements at the pier-girder node for damage cases significantly increase suggesting immediate effect of constraint-losing at the boundary condition. The changes are evident from the bending and torsional low-order modes and are well predicted by FEM. It should be mentioned that the effects of damage on mode shapes are more obvious in torsional modes than in bending modes as indicated by larger changes in modal displacements of pier-girder nodes of torsional modes than that of bending modes.
3) In general damping increases as the damage level increases. Estimations from ERA indicate that damping in damage stages increases up to 2.5 to 3 % from previously 1.5 % for undamaged stage. Spatial distribution of damping ratios was also evaluated by extracting individual damping ratios using autocorrelation and logarithmic decrement technique. Spatial distribution of damping reveals that damping of side-spans is generally higher than that of the middle span. During damage stages, some spatial variations of damping were observed. These spatial variations, however, do not reveal any distinct patterns that can be used conclusively as indication of damage location.
4) Feasibility of multivariate outlier detection using auto-spectra as damage features was investigated in this study. The results show that the use of Mahalanobis distance can detect the presence of damage at the earliest stage (i. e. damage 1). When damage has significantly changed the characteristics of the structure such as the case of damage 4 and damage 5, all points are unambiguously detected as outliers indicating the clear presence of damage. The distance between threshold line and damage points in outlier detection is increasing as damage becomes larger. This distance can be used further as indicator of damage severity.

Members of the Bridge and Structure Laboratory measurement team posing with Dr. Helmut Wenzel and colleagues from VCE during the destructive testing. From left to right: Tomonori Nagayama, Helmut Wenzel, Dionysius Siringoringo, Chondro Tandian, Hirotaka Miura, Di Su, Paul Jaornik, Martin Stöger, Monika Widmann F.15-17



Acknowledgement

The authors wish to express their sincere gratitude to Dr. Helmut Wenzel, Robert Veit-Egerer and Monika Widmann from VCE Vienna Consulting Engineers ZT GmbH for this precious test opportunity, and acknowledge their fruitful discussions and assistance during the authors' technical visits. This study was also supported by Japan Society for the Promotion of Science. Full version of this report has been published in the Journal of Engineering Mechanics ASCE [Siringoringo et al., 2013]. The University of Tokyo, Bridge and Structure Laboratory involved in the measurement include F.15-17.

References

Bendat, J.S. and Pierson, A.G., 1980. *Engineering Applications of Correlation and Spectral Analysis*. New York: John Wiley.

Doebling, S.W., Farrar, C.R. and Prime, M.B., 1996. *Damage Identification and Health Monitoring of Structural and Mechanical Systems from Changes in their Vibration Characteristics: a Literature Review*. Los Alamos National Laboratory Report No. LA-13070-MS.

Efron, B. and Tibshirani, R.J., 1993. *An Introduction to the Bootstrap*. New York: Chapmann & Hall, Monographs on Statistics and Applied Probability 57.

Farrar, C.R., Cornwell, P.J., Doebling, S.W. and Prime, M.B., 2000. *Structural Health Monitoring Studies of the Alamosa Canyon and I-40 Bridges*. Los Alamos Laboratory Report No. LA-13635-MS.

Gul, M. and Catbas, N., 2009. *Statistical Pattern Recognition for Structural Health Monitoring Using Time Series Modeling: Theory and Experimental Verifications.* Mechanical Systems and Signal Processing 23(7):2192–2204.

James, G.III, Carne, T.G. and Lauffer, J.P., 1993. *The Natural Excitation Technique (NExT) for Modal Parameter Extraction from Operation Wind Turbines.* Sandia Report SAND92-1666, UC-261.

Juang, J.N. and Pappa, R.S., 1985. *An Eigensystem Realization Algorithm for Modal Parameter Identification and Model Reduction.* Journal of Guidance, Control and Dynamics 8(5):620–627.

Mustapha, F., Worden, K., Manson, G. and Pierce, S.G., 2007. *Damage Detection Using Stress Waves and Multivariate Statistics: an Experimental Case Study of an Aircraft Component.* Strain 43(1):47–53.

Omenzetter, P., Brownjohn, J.M.W. and Moyo, P., 2004. *Identification of Unusual Events in Multi-Channel Bridge Monitoring Data.* Mechanical Systems and Signal Processing 18(2):409–430.

Peeters, B. and DeRoeck, G., 2001. *One-Year Monitoring of the Z24-Bridge: Environmental Effects versus Damage Event.* Earthquake Engineering and Structural Dynamics 30(2): 149–171.

SAP 2000. *Manual Analysis Reference Manual.* Computer and Structures Inc, 1995 Berkeley, California, USA.

Savitzky, A. and Golay, M.J.E., 1964. *Smoothing and Differentiation of Data by Simplified Least Squares Procedures.* Analytical Chemistry 36(8):1627–1639.

Siringoringo, D.M. and Fujino, Y., 2009. *Noncontact Operational Modal Analysis of Structural Members by Laser Doppler Vibrometer.* Computer-Aided Civil and Infrastructure Engineering 24:249–265.

Siringoringo, D.M., Fujino, Y. and Nagayama, T., 2013. *Dynamic Characteristics of an Overpass Bridge in a Full-Scale Destructive Test.* Journal of Engineering Mechanics ASCE 139(6):691–701.

Worden, K., Manson, G. and Fieller, N.R.J., 2000. *Damage Detection Using Outlier Analysis.* Journal Sound and Vibration 229(3):647–667.

16
Worker Safety

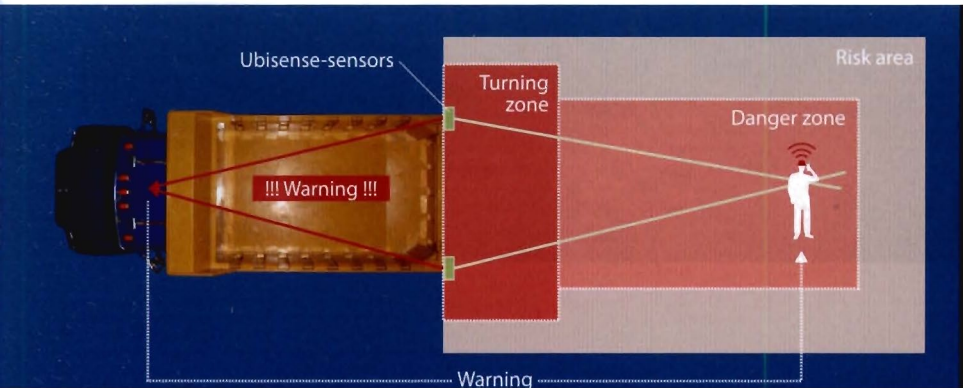
Authors:
Wolfgang Niemeier
Lars Johannes

Motivation

Many industrial accidents are happening on construction sites where moveable equipment provides a threat to the workers. An integrated worker safety concept is desired to decrease the number of fatalities.

Main Results

Measurement based technologies to support worker safety on scaffolding as well as in hazardous outdoor and indoor construction environments have been developed. This online system has been properly tested at the Brenner Base Tunnel construction site.



16-1 Introduction

For the safety of workers in industrial environment it is essential to know the position of these people on the construction site and to have this information available in situ and in a central coordination office. The objective of WP-3 is to develop a robust methodology, covering indoor and outdoor scenarios, how the actual 3D position of workers can be determined and made available for central risk management. A hazardous situation can occur during an external situation (e.g. being in the working range of a crane), lack of knowledge about the real structural behaviour during specific construction phases (temporarily critical phases) or careless behaviour of people with equipment, neglecting valid security rules (F.16-1). Critical situations during construction have to be detected by an installed sensor or by a worker himself. To estimate the risk level and to define the adequate action a decision by the central management is often necessary. Both a single worker or a group of workers can be affected by a critical situation, some of them do not even know about the detected/existing hazard.

16-2 Worker Safety at the Whole Construction Site

16-2-1 Requirements for the Positioning Solution

Site of Installation

It is intended that the system to be developed can be applied in all constructional and industrial environments. The highest demands on the system are at construction sites, as there is a high dynamic of movements and actions over time. Buildings are raised or demolished, walls will be mounted or removed. Signal propagation in such a changing envi-

Building breakdown of the Cologne town archive (left) and two moving workers (right) F.16-1



ronment makes positioning a challenging task. There is a big variety in size and dimension as well if one compares different sites. Those environments can be subdivided into indoor, outdoor and boundary areas, as depicted in F.16-2.

Accuracy

An important part in positioning is the achievable accuracy, defined as geometrical relation between workers, risks and necessary rescue action in the context of a specific local infrastructure, see F.16-3. Summarizing various scenarios for indoor and outdoor tasks, an accuracy level between 0.5 and 3 m is required.

Position Update Rate

The update rate of the position depends on the speed of the imminent danger in combination with the capacity of reaction of the worker. Regarding some risks and individual speed of workers and machines the position update rate of a worker should not be less than 2 Hz, for machines 5 Hz and for risks like fire, gas or smoke 10 Hz. In addition, it will be absolutely necessary to have an up-to-date building documentation or information system, to be able to observe and to react to the construction progress continuously.

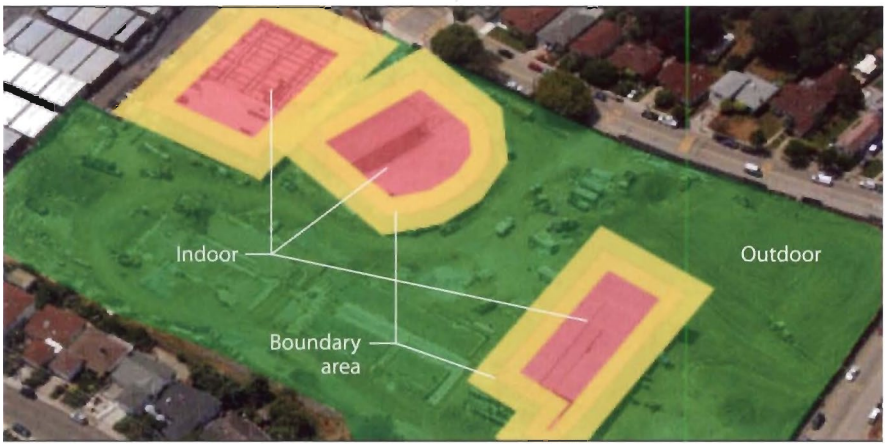
Data Communication

There are multiple interconnections necessary inside the entire system. A linkage between portable sensors and a small data processor carried by the worker has to exist, as well as a multi-directional data communication all over the complete system, realized by fixed sensors to a central office.

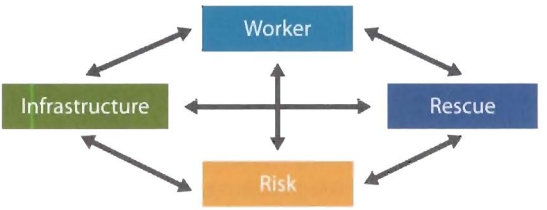
Affordability and Scalability

The system costs, installation and administration effort should be kept low, as the permanent modifications on construction sites makes complex installations problematic. Every positioning system has a defined operable coverage area for a given accuracy and a maximum count of traceable objects for a given time. A continuous expansion of the

Indoor, outdoor and boundary areas on a construction site. F.16-2
Photo by Dave Piper (Common Creative License)



Relations for accuracy considerations of a positioning solution F.16-3



positioning system should be possible and operating costs like the administration and the support should be minimized by the sensor system design. The software solution should be very flexible to account for installation of new sensors or for replacing older ones. Therefore approved and standardized platform-independent software technologies should be used.

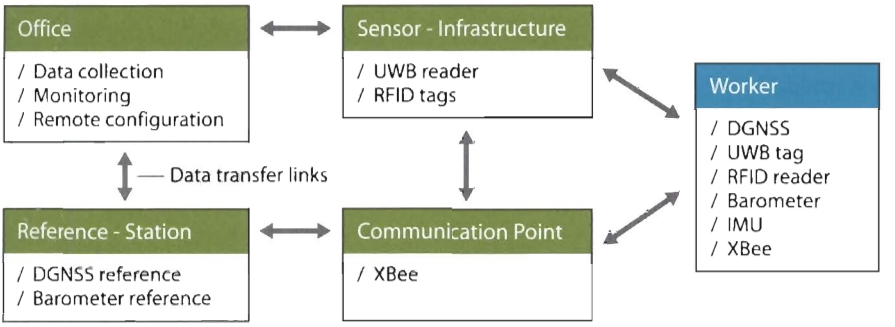
16-2-2 Architecture of the Positioning System

There are many positioning sensors based on different signals, algorithms and operation purposes on the market or in development [Hightower and Borriello, 2001; Mautz, 2009]. T.16-1 shows elements and specifications of the here developed hybrid system, based on Radio-Frequency Identification system (RFID) for indoor and Differential Global Navigation Satellite System (DGNSS) for outdoor environments. The positioning system will be supported by additional hardware like barometric sensors, Inertial Measurement Units (IMU) and an Ultra-Wide Band system (UWB). To realize the required intelligent multi-way communication, XBee communication nodes in mesh configuration will be used for data transfer because they are designed for low power consumption and therefore advantageous for integration. Moreover, the automated self-healing of this communication

Specifications of the used position technology T.16-1

Technology	Signal / technique	Accuracy / rate / weight	Notes and limits
DGNSS	Radio frequency / ToA, lateration	0.6 m horizontal, 0.9 m vertical / 10 Hz / Low to moderate	For outdoor only, needs reference station and communication link
RFID (active)	Radio frequency / Signal strength	<2 m / ~8 Hz / Low	Low-current
Barometer	Air / Air pressure	<0.4 m / 44 Hz / Low	Sensitive towards air pressure variations
UWB	Radio impulse / TDoA, AoA	15 cm (LoS) / 2–9 Hz (4–16 persons) / Low	Power cables (e.g. PoE), synchronization cables
IMU	Translational and rotational acceleration forces, earth's magnetic field / Strapdown, supporting sensor	m / 120 Hz / Low	Measurement accumulation leads to drift

Employed sensors and dataflow of the system F.16-4



solution is advantageous for dynamic surroundings on construction sites. F.16-4 shows the communication framework with the bidirectional data communication links.

Positioning Components

The main concept of our approach is to carry main parts of the positioning system on the worker, see F.16-5 and F.16-6. A normal building-site helmet was modified to carry several sensors; additional equipment is attached to the body-belt.

Building-site helmet with integrated positioning and communication technology F.16-5



Body-belt with integrated positioning technology F.16-6



Differential Global Navigation Satellite System (DGNSS):

A DGNSS system with own reference station makes the positioning task independent of technical troubles of service providers but possible problems of the satellite system itself remain. This concept makes our solution applicable in nearly every location all over the world. For our system the AsteRx1 from [Septentrio, 2010] has been chosen.

The receiver operates with 10 Hz. The typical accuracy is 0.6 m in the horizontal plane and 0.9 m in the vertical plan. F.16-7 illustrates the calculated positions by the DGPS receiver with a reference station on the roof of IGP institute building. For the DGPS-Reference data flow to the receiver the developed communication network based on XBee-Modules is used. The documented test track (F.16-7) is surrounded by buildings with up to three levels which cause high shadowing effects of the satellite signals. To get an impression of the accuracy and variation on the spots 1 and 2 the position was measured over a few seconds on these points. Reasons for wrongly calculated positions or their failure are shadowing effects and unfavourable geometry of the remaining satellites.

Ultra-Wide Band (UWB):

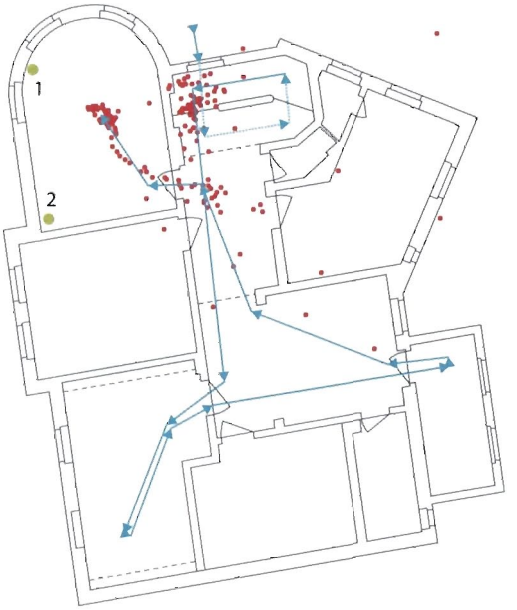
The selected Ubisense 7000 system [Ubisense, 2010] allows accurate positioning indoors, which reaches values of 15 cm (line-of-sight). The set-up of this system needs to build up a costly and complex infrastructure. Therefore, just relatively open areas will be equipped with this system, but see section 16-1-2.

A measurement set-up within a building is shown in F.16-8. It contains two Ubisense-Sensors (green circles) in the same office room. The blue line illustrates the real movement of the used tag. The plotted red dots are the calculated positions. Outside the room the

Positions from the DGPS with own reference station on the roof at the Institute of Geodesy and Photogrammetry (IGP), TU Braunschweig, Germany F.16-7



Positions by using the UWB system within IGP building F.16-8



positions are scattered with a high variation, caused by the non-line of sight to the sensors. The variation from the blue line is getting higher and a valid positioning is rare as the tag is moved away from the sensors. Within the room and a line of sight to both sensors the positioning accuracy is highly accurate, better than 15 cm [Degener, 2010]. Occurring position variations are caused by reflecting equipment.

Radio-Frequency Identification (RFID):

RFID based systems need less installation effort and are much cheaper than the UWB system. The deployed RFID tags and readers are developed by [OpenBeacon, 2010]. The tags operate in the 2.4 GHz ISM band with 5 Hz update rate. The generated impulses are transmitted with four different signal strength levels. With a recursive algorithm, which weights the received signal levels, an accurate positioning between georeferenced RFID tags is possible. F.16-9 illustrates a measured course within a building (red dots). The green dots symbolize the RFID tags and the real track is plotted as the blue line.

Digital Barometer:

To determine an accurate height the BMP085 MEMS pressure sensor from [Bosch, 2010] is used. It can achieve a time resolution of 44 Hz. The calculated height information is seamless during the transition between indoor, boundary areas and outdoor. In static measurements the accuracy is better than 0.4 m. Evoked by the update rate a high number of measured values can be gathered, which allow a smoothing algorithm without falling below the required time resolution for a continuous height determination. The grey

RFID only based positions F.16-9



line in F.16-10 illustrates the derived height information from the recorded pressure data. This 22 second range shows the recordings while going upstairs within the building from the ground floor to the first floor in the IGP building, see F.16-9. The stairs have a height of 19 cm. The distinction between stairs and a podium can be relatively well represented by the use of a moving average with a 30 values window (green line). The attempt to improve the previous representation by using a FIR Low Pass Filter is illustrated by the black line.

Inertial Measurement Unit (IMU):

The combination of RFID and barometer data already achieves good results, see F.16-9 and F.16-10. The additional IMU from [Sparkfun, 2010] improves the accuracy of positioning within all areas. Subsequently, in indoor areas the installation effort is minimized by a reduced number of RFID tags but without loss of accuracy. By using movement models and digital building information it is possible to calculate accurate positions without increasing the number of tags. In combination, IMU, RFID and a barometer can separate typical structures within a building. By recognizing the differences between staircases, a rising floor or an elevator, the structure can be allocated in the digital building data and a rough positioning will be possible.

Communication

For the exchange of data between the different parts of the system a data communication system has to be installed. The main data to be transported between the nodes will be the calculated positions from the worker to the office and reference data for sensors

like DGNSS and the barometer to the worker. Furthermore it shall be possible to use the network for information and remote configuration. F.16-4 has already shown the whole system with employed sensors and therefore the necessary data-flow.

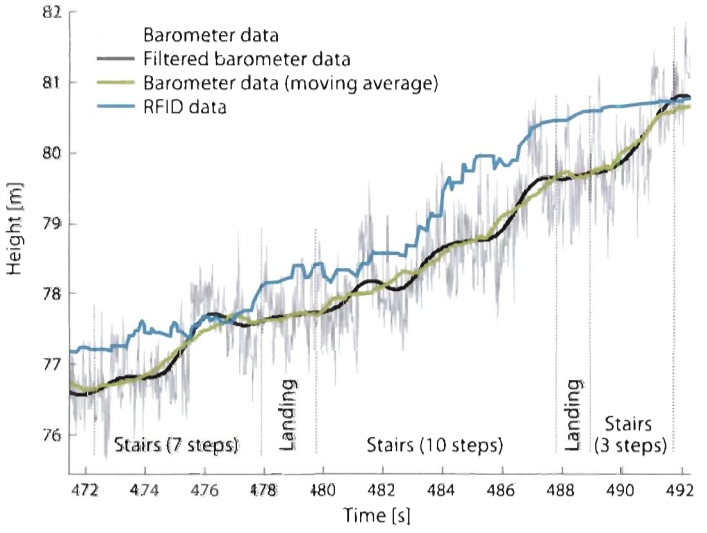
An ad-hoc data network was installed by using XBee-Pro modules (series 1) from Digicom. They fulfil the requirements for light, small and low consumption hardware. In benefit of a flexible mesh network with self-healing data routing over several hops the chosen firmware is Digimesh. Such a network configuration is most flexible as easy build by equal treatment of every node as a router.

The sensors can work in two different modes. The transparent mode allows simple streaming of data to a fixed destination. The whole flexibility and the mesh network advantages are gained in the API mode with source tracking, package acknowledgement and remote configuration of devices. Therefore data have to be wrapped in the Digimesh API structure. This mode comes with a maximum payload per package of 73 bytes, for longer sequences it is necessary to split and reassemble the data. A Java software module is developed to allow a flexible connection between devices for every kind of dataflow. According to the Digimesh documentation [Digi International, 2010] it is possible to reach a throughput between devices up to 27 kbps [Degener, 2010].

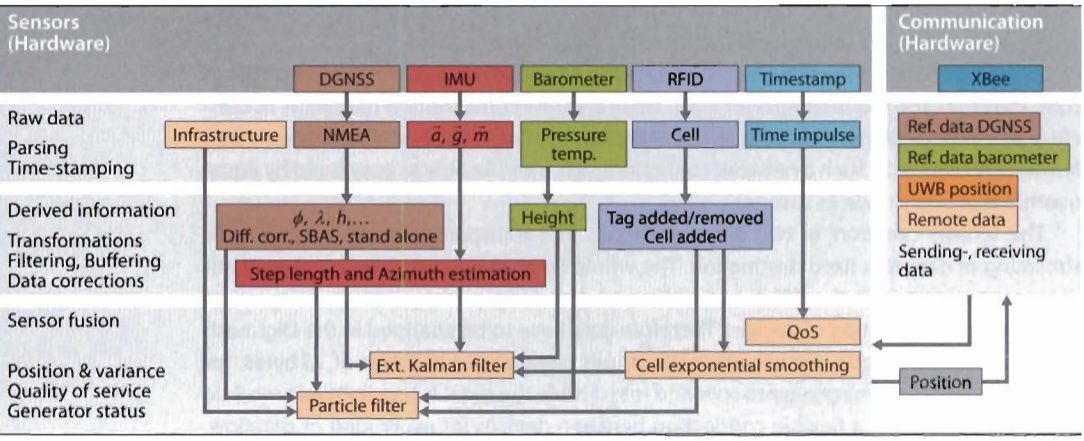
Software Client Site

For processing the data a software framework is developed, where the general interaction of the individual modules is shown in F.16-11. All sensors which are directly connected with the worker are illustrated in box Sensors. They operate with tact frequencies between 1 and 120 Hz and deliver the raw data over serial connections. The data of any measure gets a timestamp, is being parsed and is processed with own software module for the individual sensor (derived information). Further on, all data are available for coupled evaluation, what has to be done as next step within our project.

Stairs and landings by using of a digital barometer F.16-10



Client positioning framework F.16-11



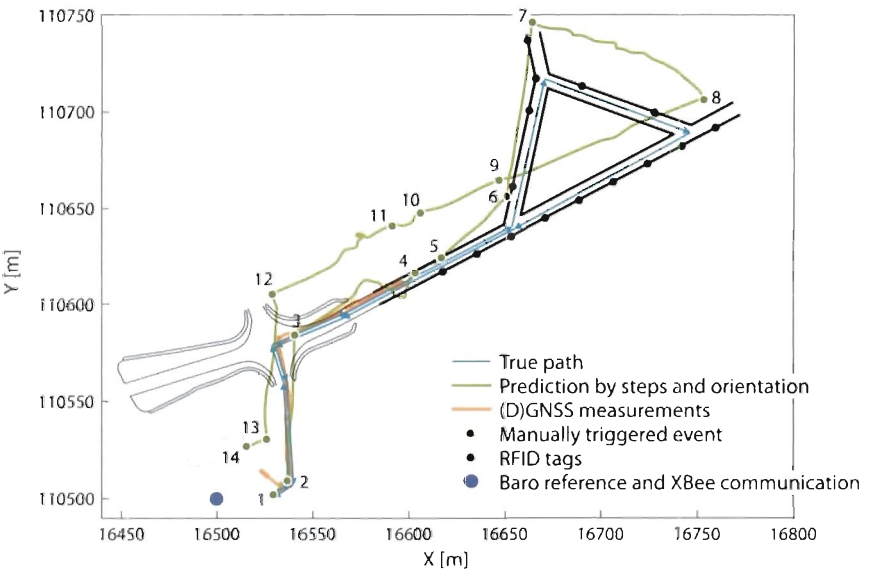
The main part of calculation will be done in an integrated processor directly at the worker. Forwarding all the data to a central server would cause too much traffic for the communication XBee-Network. The traffic has to be kept as low as possible, thus allowing a large network with low latencies. Therefore only the calculated position and additional attributes like health data of the worker are transmitted. The data exchange within the software is designed by an event system to have the most flexibility to couple all kind of collected data. Every retrieval or graphical module has access to these events. The framework is designed and transcribed for real-time applications and simple extensions or changes of sensors.

16-2-3 Installation and Tests of the Prototype at the Tunnel Construction Site

The developed prototype for indoor and outdoor positioning and communication was tested at the Brenner Basis Tunnel. The F.16-12 shows the construction site with the outdoor and indoor area. The test started and ended in the bottom left corner and was performed by a worker equipped with the newly developed device given in section "Positioning Components". The tunnel walls are marked as big black lines and the RFID tags as black points. GNSS measurements outdoors are depicted as orange line. The relative information, derived from IMU only, are given as green lines.

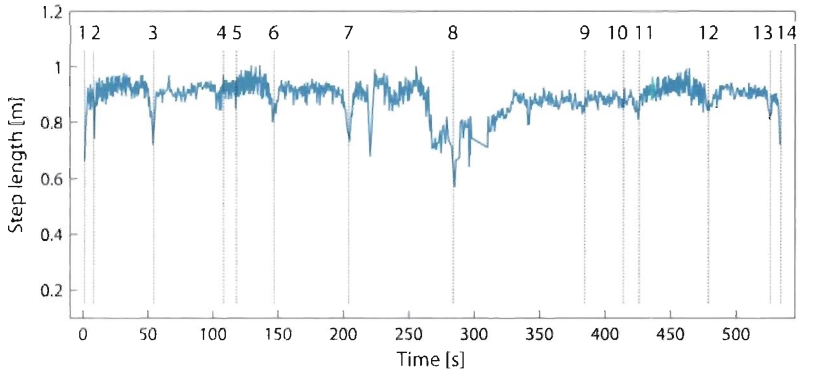
The manually triggered events and their place at the construction site allow to control the quality of the measurements and the filtering. The GNSS measurements fit very well to the given way. The directions of the relative coordinates from the IMU give a good base for the filtering. Important for the success of this project was the derivation of an individual step length out of IMU original readings, here accelerations in the vertical direction. This concept is given in detail in the PhD thesis [Johannes, 2013]. The IMU was carried at the right side, so the acceleration by the left foot is a little bit smaller than at the right foot. The acceleration differences are directly correlated to the step lengths. At event 8 the ground was covered with frozen water, so the steps were shorter. Thereafter the ground heights

The tunnel construction site for practical tests. The numbers are manually triggered events. They are recorded by carrying out the tests. F.16-12

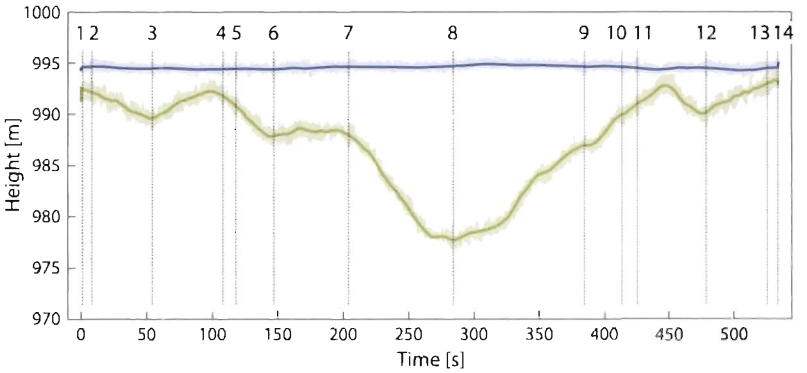


were rising up. That is why the step lengths from event 8 to 11 were shorter than the rest of them. The orientations from the magnetometers of the IMU were corrected by a deviation curve, taking into account influences of magnetometers. The high information inside the tunnel was derived by using a digital barometer, which had to be related to a reference outside, which was located outside the tunnel, see F.16-13. In F.16-14 the mobile heights (green line) represent the variations in height along the way. Due to stable weather conditions, the reference air pressure (blue line) remained constant during the experiment.

Step lengths derived from acceleration differences [Johannes, 2013] F.16-13



Raw data from the reference and the mobile barometer F.16-14

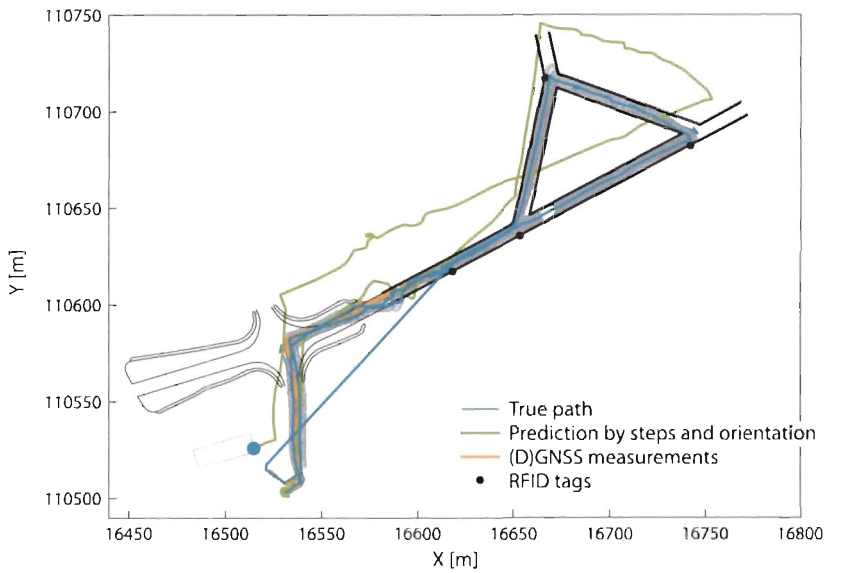


Fusion of the Data by a Particle Filter

The data from the IMU, DGNSS, barometers, RFID and the infrastructure was fused by a particle filter, which is an alternative approach to an Extended Kalman Filter. In [Johannes, 2013] both filtering concepts are described and a detailed comparison is given.

The accuracy for the orientations was set to 30° and for step lengths to 0.2 m. In reality both are more accurate, but for filtering a broader scattering of the particles gives a more stable solution. The positions outside and inside the tunnel fulfil the requirements of accuracy on construction sites. The amount of RFID tags was reduced here, but a positioning within the tags is still possible with this set-up.

Filtered path with a particle filter. For each position a confidence region is given (grey). For comparison the relative positions out of IMU data are depicted (green) F.16-15



16-3 Worker Safety behind Construction Vehicles (Local Positioning System)

One of the main sources of accidents with major injuries or losses of life are vehicles on construction sites. During the work on the high-speed route between Bologna and Florence four out of five fatal accidents were caused by construction machinery driving backwards.

Considering their dimensions it is difficult for the driver to check the area around the vehicle. Accordingly the zone behind it becomes especially dangerous for workers. A warning system to assist the driver while turning around or driving backwards with higher speed could prevent deadly accidents. Therefore a positioning system has been developed, which is installed at the back of the vehicle, to detect people and show the driver if it is safe to turn around or start to drive backwards as well as to give warnings, or stop the machine, if someone is detected in the predefined zones.

A different motivation beside the increasing safety issues is the fact that the residents near construction sites are seriously disturbed by the high-pitched alert from the vehicles while driving backwards. To avoid this tone, which is only interesting for people directly around the vehicle, the warning system could not only warn the driver, but also give a warning to the endangered person if a vehicle came along and especially if the person was in an acute danger zone. This system will be referred to as the "Local Positioning System".

16-3-1 Requirements

There are several requirements for such a system. First of all, it has to be reliable. It has to warn the driver and all workers in the interesting areas of the risk involved, but only if there is a person already in a dangerous zone or the provided way of driving leads to a person being in such a zone, further actions have to be triggered.

The system has to be very robust against dirt, dust, rough handling and the vibration of the vehicle while driving over uneven surface.

To regard different situations like turning, start of driving, slow vehicles in narrow environments or fast driving vehicles it is necessary to define different areas and therefore different warnings and reactions. For a fast moving vehicle the warning system has to cover an adequate distance without long delays. As an example, a truck going with a speed of 40 km/h and a considered reaction time of the driver of about half a second would need around 25 metres for a full stop.

The system has to be able to identify people and send individual messages, otherwise it could warn the driver, but the worker would not be treated as an individual and would not receive individual messages depending on his position to the vehicle. Messages between the system on the vehicle and the detected worker have to be sent without avoidable delays.

16-3-2 Choice of Hardware and Technology

For a turning or starting vehicle the distance of interest around its back is limited to several metres. Therefore an ultrasound-system, which is already used in cars for parking-assistance systems, would be sufficient. It can detect obstacles within narrow distances.

A disadvantage is the limitation of several metres and normally it does not return the position of an object in order to classify it in different areas. A possible solution could be the use of several sensors and to combine these distances to calculate the position by trilateration in the narrow area. With this technique every obstacle will be detected, which can be intended in such a system, but would not be sufficient to identify workers for individual contact messages or to distinguish between workers and construction objects.

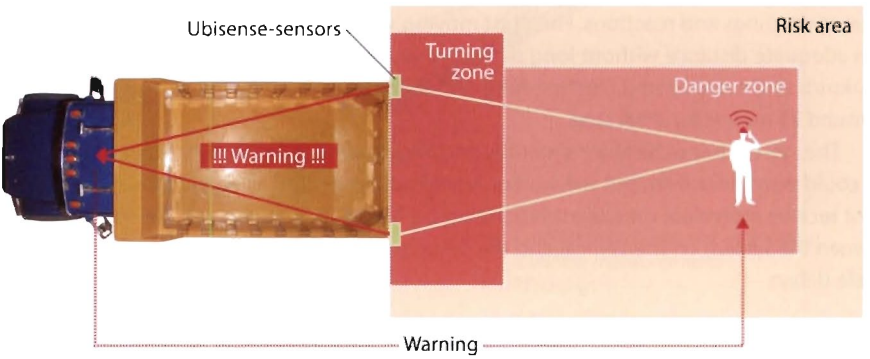
A camera based system including person identification, is not suitable for the adoption directly at vehicles on construction sites as large amounts of dust and dirt would highly affect the ability to provide results. Diffuse light within tunnels might generally pose a problem and total darkness caused by electrical power outage will lead to a failure of the system.

A positioning system which is based on radio waves is able to penetrate dust and dirt and opposed to cameras it is independent of lighting conditions. The maximum distance to receive signals for positioning calculation depends on the used frequencies, transmitted power, the direction of the antennas and the surrounding infrastructure.

Within our project we already worked with the Real-time Location System (RTLS) developed by the Ubisense Corporation [Ubisense, 2010]. This system is based on radio impulses using an ultra-wideband (UWB) frequency spectrum (6–8 GHz). The sensors can measure the angles to a transmitting tag with an implemented antenna array. In combination with the calculation of the time difference of arrival (TDOA) between the used sensors (positions are known) the system can identify the unknown position of the tag.

During our analyses we got very accurate results as long as the tag was in line of sight of at least two sensors [Johannes et al., 2010]. The first results revealed a maximum range of detecting tags of roughly 75 metres [Degener, 2010]. This is suitable for a warning system fulfilling the requirements above.

Intended installation of a warning system behind a vehicle using the Ubisense RTLS F.16-16



The tags have an individual ID so it is possible to separate different people with a maximum update rate of 10 Hz, depending on the amount of detected tags from the sensors. As a stand-alone solution the Ubisense system is not able to send warnings from the server-software back to the detected tag. The global positioning solution enables a communication between vehicles, office and workers.

16-3-3 Intended Installation

The intended installation of a warning system behind vehicles while using the Ubisense RTLS is shown in F.16-16. A minimum of two Ubisense sensors have to be installed at the back of the vehicle with a known distance between each other and their height to the ground. They have to be connected to a processing unit in the driver cabin to calculate the position of tags in range and decide with predefined zones, which are related to the vehicle, if there is an endangered person. The following steps have to be initiated like giving a warning to the driver or a direct intervention in the system of the machine. For sending warnings to the detected person in case of a vehicle coming in his/her direction, or if he/she is already in a dangerous zone, a wireless communication system has to be set up. Such a low-powered system, based on XBee-sensors [Digi International, 2010], has been developed within our work [Johannes et al., 2010].

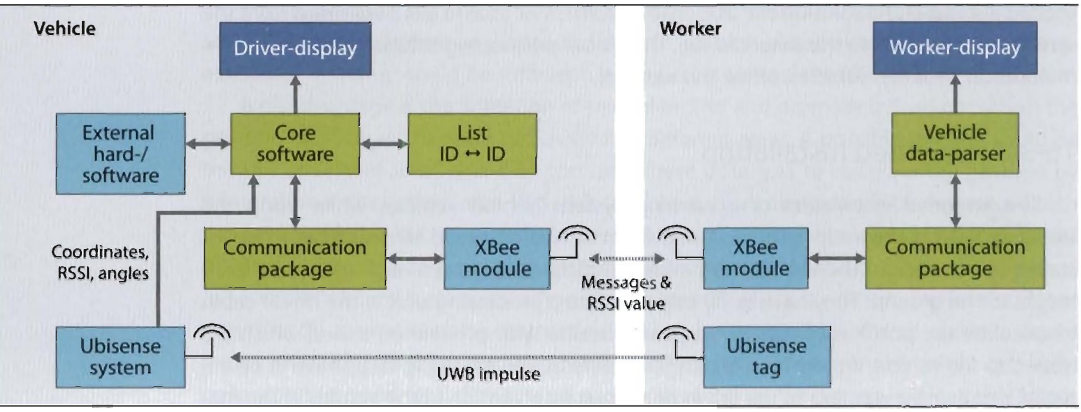
Shown in F.16-16 are two Ubisense sensors which are installed at the back of the vehicle. They can measure the angles to the tag (green lines), worn by a person, and with the calculation of the TDOA of the impulses to the sensors, the system is able to calculate the position of the tag related to the position of the vehicle. The defined zones are always related to the moving vehicle using a local coordinate system. There might be a narrow zone for the area needed by a turning vehicle, a zone with a long distance behind the vehicle which is dangerous while it is driving backwards and a risky area which is wider than the real danger zone. While a person is in these zones, he/she has to be aware of the vehicle by a warning from the system over the communication network.

16-3-4 Structure of the Warning System

Suitable software has to be developed to process the data from the Ubisense-system and other external soft- and hardware. It has to be decided individually in which zone a detected worker is and which warnings and visualizations the workers and the driver will get. There has to be the possibility of an easy connection and processing of additionally external hard- and software to extend the warning system or improve the accuracy. This system has been developed at the IGP. The software is written in Java for the purpose of being independent of the used devices.

In F.16-17 the schematic block diagram of the developed warning system with the hard- and software components is shown. On the left side (vehicle) the installed Ubisense-System is displayed which is receiving impulses from the Ubisense Tag which is worn by the worker. The produced data is sent to the Core-Software via UDP. With the help of an ID-List, containing pairs of XBee-Modul-IDs and Ubisense-Tag-IDs, each worker is known to the system and can be treated individually. The core software is able to give the driver all the necessary information and can send warnings, using the communication package,

Block diagram for the hardware and software components of the warning system F.16-17



to the worker. These messages will depend on the calculated position and the pre-defined zones. The detected worker will receive these messages via the connected XBee-Module. With the communication package and a data parser, both installed on a suitable device (e. g. handhelds); a warning can be displayed or otherwise processed.

16-3-5 Embedding this Warning System in a Construction-Wide Positioning System

The described warning system behind large vehicles is designed to get highly accurate positions related to the machine and create individual warnings. These depend on the actual position of the detected person and the pre-defined zones of the vehicle. The communication between the participants is to directly avoid delays. Each system at a vehicle can take into account the individual parameters like dimension or high speed of the machine. Such a system can work as a stand-alone solution, but beside the mentioned advantages it has its limits and disadvantages. Caused by the strict regulations for the transmission power for UWB-systems the range is limited and despite of the good penetration characteristics of the wide frequency this results in a high shadowing of the signals as analyzed in [Degener, 2010]. The system in this design can identify the workers by their unique XBee-ID and Ubisense-ID and calculate the position related to the mounted sensors. In case of an accident, though, it is not able to either inform a central office or to calculate the position of the whereabouts on the construction site. Finally, the system is only able to detect people in the direction of the adjusted sensors.

Considering these disadvantages, especially the last fact, a combination of the warning system at the vehicle with the developed positioning system for a whole construction site as described in [Johannes et al., 2010] is obvious. Integration in this large solution will take special care of one of the main risks by increasing the accuracy and treating every vehicle and the workers in its area individually.

Over the wider areas on a construction side, especially in indoor areas where the accuracy mainly depends on the amount of RFID-Chips, the calculated position of the workers

can be rougher. In a tunnel it might be adequate enough to have a 1D position along its length. The system is designed to transport all kinds of data to a central office for further proceeding and trigger actions if necessary.

In F.16-18 the integrated warning system at a vehicle as described above in the construction wide positioning system is shown. In the outdoor areas accurate positions can be gathered with the help of global navigation satellite systems (GNSS). In indoor environments the system is mainly based on RFID. Accordingly the accuracy there depends on the amount of used RFID-chips. In both areas additional data from sensors like a barometer or an Inertial Measurement Unit (IMU) is used to improve the accuracy of the calculated positions.

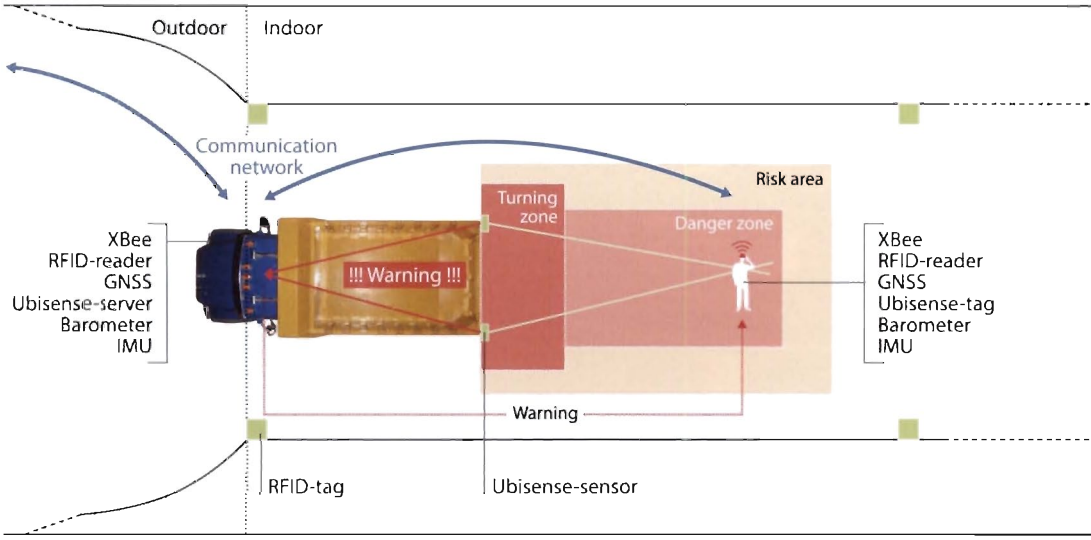
The developed communication solution for the construction wide positioning system is once again the XBee sensor network using the same software as is used for the vehicle warning system as described above. Therefore a fusion of the two systems with the same XBee-IDs for all participants of the systems and the same communication software was done.

16-3-6 Installation and Tests on a Concrete Mixer at the Tunnel Construction Site Brenner Basis Tunnel

Concrete mixers are one type of vehicles beside dumpers which are working close to the workers (F.16-19). When driving backwards the driver looks into his back mirrors so as not to touch the tunnel walls or workers. He stops in front of the injection machine guided by acoustic signals from other workers.

The aim is to assist the driver by recognizing workers behind his vehicle when he is driving backwards. Therefore the concrete mixer was supplied with this new positioning

Embedded warning system at the vehicle in a construction wide positioning system F.16-18



Concrete mixer in the tunnel to supply concrete to stabilize the tunnel walls F.16-19



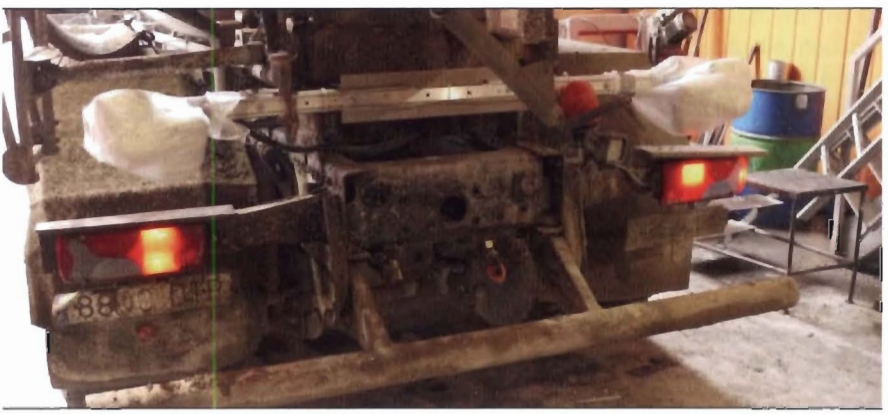
and alert system, developed by the Institute of Geodesy and Photogrammetry of Technische Universität Braunschweig, Germany.

Sensor Installation on a Concrete Mixer

To perform tests in a real environment the Ubisense RTLS positioning system was attached to a concrete mixer (F.16-21). The sensors are covered by plastic bags to protect them against dirt, dust and water.

The opening angles of the Ubisense sensors are 120° in the horizontal and 100° in the vertical direction. Because of the interesting area directly behind the vehicle, the increasing of the covered vertical area has more priority compared to the horizontal area. By that it is possible to detect a worker lying on the ground or a worker staying close to the vehicle. The vehicle is around 7 m long. The sensor installation is one metre inside the vehicle measured from the back to the front. The local coordinate system is a right handed system with its origin at the middle of the basis. The positive x-direction goes backwards and the positive z-direction upwards. The y-direction stays perpendicular to the x and z-directions.

Concrete mixer with the attached Ubisense RTLS positioning system: two sensors on each side to increase the covered area in vertical direction F.16-20

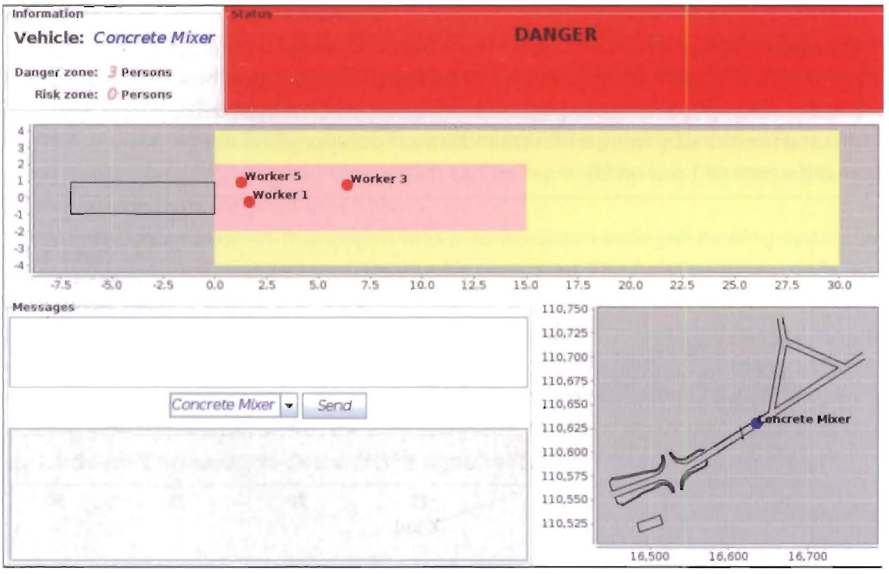


The programme for the visualization of the workers and the alerting of the driver is written in Java and runs on a usual laptop (F.16-21). Further equipment beside the Ubisense RTLS sensors are a 45Ah battery, a PoE-hub (power over ethernet) and a DHCP server. The graphical user interface is shown in F.16-22. The middle shows the vehicle ther as a black rectangle. Behind the vehicle there are two different zones. The danger zone is visualized in red, the risk zone in yellow. At the moment there are three different workers within the danger zone. They are counted and shown in the left top side. The status field to the top right shows the level of risk. The green colour is for no risk, yellow for workers inside the risk zone and red for workers within the danger zone. The bottom right side shows the position of the vehicle on the tunnel construction site. The existing tunnels are

Cabin of the machine: notebook for visualization of workers behind the vehicle F.16-21

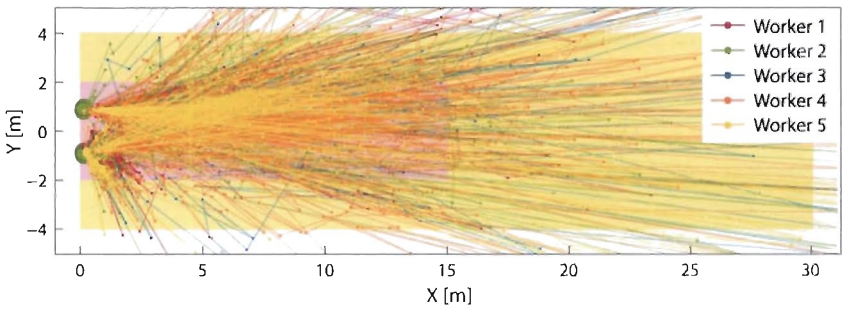


Graphical user interface for the visualization and interaction of the driver. The upper right status field shows red alert right now because some worker is within the danger zone F.16-22

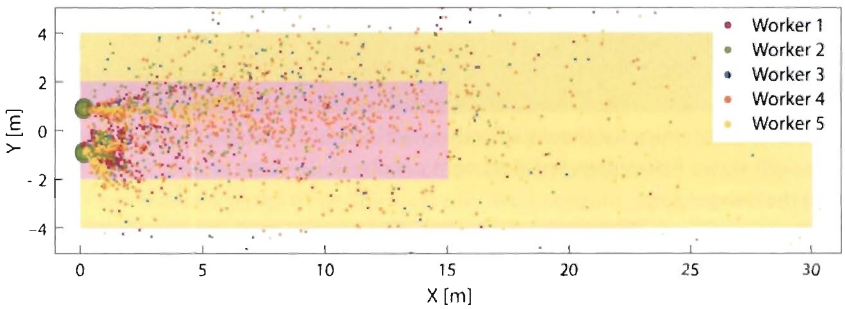


shown by a triangle to the right. Messages to the vehicle are shown in the text area at the bottom left side. Warning messages can be sent by the vehicles to the office, other workers and vehicles.

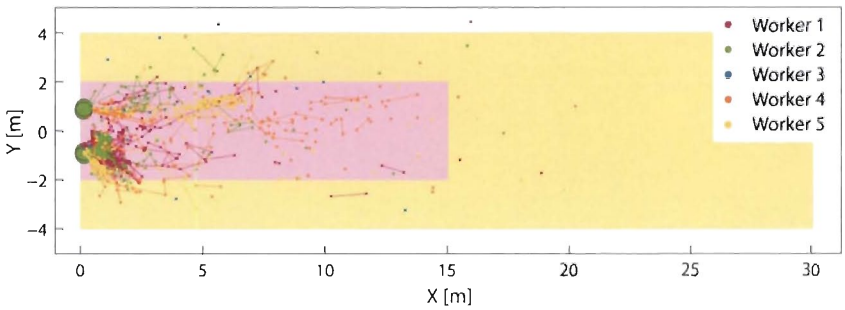
Workers positions behind the concrete mixer. Five workers were tracked over 135.8 minutes. The risk zone is yellow and the danger zone red F.16-23



Tracking points of the five workers over the whole period without connection lines or filters F.16-24



Corrected positions by using a maximum allowed distance of 1.5 metres and time difference of 1.5 seconds F.16-25



Results from the Tests

The F.16-23 shows the tracking of five workers during a time period of 135.8 minutes. The green circles to the left are the four UWB-sensors. The red and the yellow areas are the danger and risk zones. The x-axis is from the back of the vehicle in longitudinal direction and y-axis in transverse direction from the vehicle middle to both sides.

Due to reflection on the tunnel walls some positions were calculated to the wrong place. The differences between the positions in time order are varying very much.

The workers were not constantly behind the vehicle, so the connection lines do not show a continuous tracking. The scatter plot in F.16-24 shows the figure without these lines. As the time difference between different positions is around 0.4 seconds, the positions can be filtered by a maximum time value.

The time limit for this filter was set to 1.5 seconds to forbid bigger time gaps. By that it is possible to cut the lines between positions which are not directly connected to each other. The generalization is caused by shadowing the line of sight from the tags to the sensors. This can happen by rotating of workers together with leaving of the covered receiving area of the sensors. The big differences in distance (F.16-23) can be reduced by a distance limit of 1.5 metres.

The distance limit cut off most of the wrong positions calculated by signal reflections from the tunnel walls.

The time limit of 1.5 seconds additional to the distance limit of 1.5 metres leads to F.16-25.

16-4 Conclusion

One of the main risks on a construction site are large vehicles which caused fatal accidents in the past. The logical step is to develop a warning system to assist the driver and reduce this special risk for the workers.

In this section a system based on the Ubisense RTLS to calculate positions of people related to a vehicle was presented. The mounted system on the vehicle is able to communicate with the detected workers using the described communication network of the construction wide positioning system. The awareness of the vehicle to the workers is currently evoked by a high-pitched tone which can be replaced by warning messages only for the workers in the relevant area now.

With the integration of this system into a construction wide positioning system an improvement of both separate systems can be generated. The functionalities of the systems are developed and tested within the work of the IGP (TUB). First results of set-up of an indoor and outdoor positioning solution as a construction wide positioning system were already presented [Johannes et al., 2010]. Tests with an installed warning system as described above have been realized in laboratory and real conditions. The results lead to positive expectations but also to the conclusion that further research and additional sensor hardware is necessary to deal with the signal reflections from the tunnel walls.

References

Bosch, 2010. *MEMS Pressure Sensors.* www.boschsensortec.com

Degener, J., 2010. *Leistungspotential von UWB in Verbindung mit einem Ad-Hoc Datennetzwerk für Positionierungsaufgaben.* Masterthesis, Technische Universität Braunschweig.

Digi International, 2010. *XBee/XBee-PRO DigiMesh 2.4 RF Modules.*

Hightower, J. and Borriello, G., 2001. *Location Systems for Ubiquitous Computing.* IEEE Computer Society Press, Computer 34(8):57–66.

Johannes, L., Degener, J. and Niemeier, W., 2010. *Set-Up of a Combined Indoor and Outdoor Positioning Solution and Experimental Results.* In: Proceedings of the 2010 International Conference on Indoor Positioning and Indoor Navigation (IPIN), IEEE.

Johannes, L., 2013. *Multisensorsystem und Filterungsansätze zur robusten Ortung von Personen im Innen- und Außenbereich.* Dissertation TU Braunschweig.

Mautz, R., 2009. *Overview of Current Indoor Positioning Systems.* Geodesy and Cartography 35(1):18–22.

OpenBeacon, 2010. *OpenBeacon Active RFID Project.* www.openbeacon.org

Septentrio, 2010. *Septentrio Satellite Navigation nv.* www.septentrio.com

Sparkfun, 2010. *9 Degrees of Freedom – Razor IMU – AHRS compatible.* www.sparkfun.com

Ubisense, 2010. *Real-Time Location Systems (RTLS) and Geospatial Consulting – Ubisense.* www.ubisense.net/en

17

Utilizing Ontologies to Integrate Heterogeneous Decision Support Systems

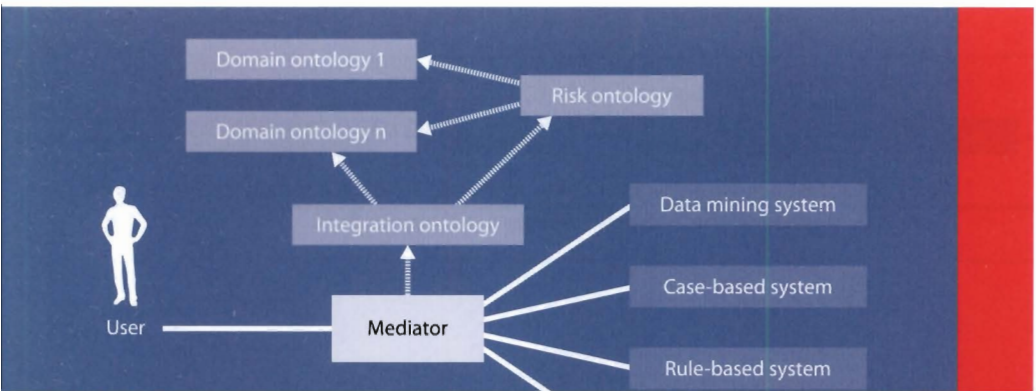
Authors:
Josef Küng
Erik Sonnleitner
Reinhard Stumptner
Andreea Hilda Kosorus
Stefan Anderlik

Motivation

Structural health monitoring (SHM) has been developed in fragmented activities in various regions of the world. The large variety of systems for measurement planning, recording and analysis has disadvantages to be overcome. It is desirable to have a domain ontology enabling communication between the various systems.

Main Results

The IRIS ontology for Decision Support Systems in the field of structural health monitoring has been developed within the project. This enables the implementation of a harmonized Decision Support System.



17-1 Introduction

Structural Health Monitoring (SHM) can be seen as a method for identifying and localizing damages on structures or structural elements. Each structure has its individual dynamic behaviour which can be identified by analyzing the signal response of the monitored structure. Due to the fact that in the area of SHM, individual institutions developed numerous different systems for planning, recording and analyzing measurements, an ontology-based integration of Decision Support Systems (DSS) for SHM is useful or even necessary. The selection of an adequate system for these operations depends, among others, on the kind of measurement data or on the defined monitoring objectives.

Within the scope of the European Union project IRIS, an integration-ontology for DSSs in the field of SHM has been developed and is shortly outlined in this contribution. IRIS was a project of 3.5 years (starting in October 2008) and involved 36 well-known industrial partners and research institutions in different areas of application (mainly SHM) worldwide. One of the main objectives of this research project was the development of an online risk management system to increase the safety degree in industries like oil and mining, as well as in the chemical and energy production sector of industry. To reach this aim, intelligent assessment strategies for structural measurement data have been implemented. As mentioned above, advantages of all conceivable systems within different branches of industry for planning, recording and analyzing measurements can be combined to guarantee industrial safety and to reduce the contamination of environment. For this reason, domain ontologies are useful which shall describe relevant information and knowledge of a certain domain. Matching these ontologies by means of a higher level ontology, shall increase the collaboration levels of different institutions and suggesting the best possible systems for measurement assessment. Therefore, an ontology-based integration approach has been introduced and described by explaining the structure of the ontology, the overall mediator-supported systems and their possible benefits for DSSs in the field of SHM. Moreover, standardization and integration have been two major topics concerning the IRIS project. On these two main objectives, a concept for an integrative usage of different measurement analyzing functions for SHM like Fast Fourier Transformation (FFT) or Wavelet Transformation was required. These operations are partly available within systems like BRIMOS® (Bridge Monitoring System) (see [Wenzel and Pichler, 2005; Anderlik et al., 2010]), but not in an integrative and guided manner. The problem of using such systems is the lack of semantic behaviours and conditions for measurement analysis: Many operations are available, but not everyone knows which function should be executed to what scope (e.g. clustering operations can be useful in addition to certain pre-existence data discovery methods) and how (parameters, semantics, notifications, etc.). Hence, the integration approach of heterogeneous Decision Support Systems (DSS) for SHM in [Anderlik et al., 2010] shall provide a framework for these purposes and provides opportunities for being guided through data analysis, data preparation and assessment tasks.

The integrative usage of DSS in SHM is a major challenge concerning "Black Box" systems like BRIMOS®, where integration is not possible analogous to Open Source APIs like WEKA or RapidMiner. We will subsequently point out, how the integration of various different DSSs has been done, and how it can be used to aid in SHM.

17-2 Decision Support Systems for Structural Health Monitoring

The area of Structural Health Monitoring is an ambitious topic for current Information- and Knowledge-Based Systems like Decision Support Systems. Therefore, BRIMOS® as an ambassador of SHM-Systems will be discussed within this section. The System Description is based on processes and assessment methodologies shown in [Wenzel and Pichler, 2005; Wenzel, 2008].

BRIMOS® can be defined as a method for system identification and damage detection in bridge structures due to its dynamic response to ambient excitation such as wind, traffic and micro seismic activity.

This Bridge Monitoring System has been used for many years in the field of SHM. SHM, in terms of Ambient Vibration Monitoring, comprises recording a structure's dynamic behaviour by using measuring instruments as well as the performing evaluation and analysis tasks of the measured signals. The fundamental tools of health monitoring are system identification, damage determination and localization as well as safety assessment and the maintenance management for infrastructure.

The process itself starts with collecting meta-data of a structure. That meta-data is used for the detailed campaign planning. Campaign planning, in turn, can be divided into several steps like deciding whether detailed, periodic or permanent measurements should be conducted. At this stage, a sensor layout is created and schedules for measurements are written down.

After a detailed campaign planning phase, monitoring takes place. Measurement data is pre-processed depending on the kind of data and usually written into a data base before using it for routine assessment (which, again, depends on the kind of measurement). Routine assessment e.g., provides the determination of the modal parameters, namely the structure's natural frequencies, its mode shapes and its damping coefficients. These parameters, which are gained from the measurements, represent the real condition of a structure. The measurements, often represented by a signal time series provides a degree of precision that they can be used as reference data with a high qualitative value for every future evaluation method.

Routine assessment consists of any combination of assessment parts, which might be rapid frequency analysis, eigenfrequencies, drift calculation, trend cards, modal shapes, vibration intensities, energy levelling, among others. Describing any combination would go beyond the scope of the overall system description. Assessment results are used to

BRIMOS® work-flow F.17-1



update mathematical models of a structure. If previous measurement data and results are available, establishing a simple comparison metric is possible. Otherwise, since a large data pool of previously investigated structures, which may be reasonably similar, is readily available, an integrated Case-based Reasoning (CBR) approach can be applied.

The BRIMOS® process flow is the reference structure for this ontology-based approach. At this point it is important to define a general procedure module, which will be implemented as a mediator system for supporting the whole process during monitoring, computation and assessment as well as interacting with certain end-users who are working with the different DSSs. This general concept is based on BRIMOS® and contains the steps shown in F.17-1. These process steps are modelled within the integration ontology beside much semantic knowledge about the domain SHM and the specific DSS descriptions.

The idea of utilizing an ontology for integration issues is one typical application for technologies within the Semantic Web, but its initial intention differs from the approach discussed in this contribution. Therefore ontologies, in the scope of data and semantic integration, will be explained in the next chapter.

17-3 Ontology-Based Data Integration

The term ontology has its origin in philosophy and metaphysics, within these research areas people think about the being and not being in general and focus on questions concerning the existence of concrete things and their connections [Bunge, 1977]. This point of view is the philosophical perspective, but for computer scientists, an ontology is described as an "explicit and formal specification of a shared conceptualization of a domain of interest [Gruber, 1993]". This initial definition was introduced by [Gruber, 1993] and can be seen as the essential meaning of such a semantic structure. Based on this statement, many authors developed important concepts and technologies for tasks within the area of ontology engineering and development. One major advantage of ontologies can be seen in their aspect of working with peripheral web resources, which are distributed but accessible within the so called Web of Data. If someone wants to develop a system, which has interconnections with other semantically different platforms, frameworks, agents, etc., and their resources, a mechanism is needed which assures a valid syntax and semantic for interoperability. Davenport and Prusak called this explicit, distributed and accessible resource a common vocabulary: "People can't share knowledge, if they don't speak a common language" [Davenport and Prusak, 2000]. This declaration can be extended by substituting the word people with agents. If this is done, ontologies can be seen as knowledge bases, which provide interconnectivity between different agents like human individuals as well as computer agents. This perspective is one of the most important application areas of ontologies. But if we analyze the definition of [Gruber, 1993] an ontology is not a semantically enhanced structure of class assertions, it provides wide and deep knowledge about a domain, which also includes the implicit rules and semantic associations within this area: "... it is an intentional semantic structure that encodes the implicit rules constraining the structure of a piece of reality" [Guarino and Giaretta, 1995].

Today, ontologies are used for more specific areas of application and not only as global vocabularies, knowledge bases, thesaurus, etc. The most important feature is to reason about the domain of interest, to classify certain individuals and to compute new knowledge also dynamically at runtime. Examples for these areas are the search for semantically annotated documents, queries within these information resources, data integration and proper interconnectivity between different and heterogeneous systems, search and composition of (web) services, etc. We will further focus on the application of data integration, but first of all it should be discussed which main concepts are available in this area and what natural idea stands behind using ontologies for combining heterogeneous systems.

Data integration as an important concept in information systems is strongly connected with the architecture of federated databases and with its aspects of combining distributed, autonomous and heterogeneous databases [Buccela er al., 2003]. These concepts characterize the main idea of federation and also include design autonomy, communication autonomy and execution autonomy [Lenzerini, 2002; Oszu and Valduriez, 1999], network characteristics of distributed agents and heterogeneity concerning structure, syntax, system and semantic [Cheng, 2003; Cui and O'Brien, 2000]. These properties of data integration can also be found in areas like application integration and application interoperability [Buccela er al., 2003]. The ontology-based data integration approach for Decision Support Systems is hybrid and combines aspects of distributed stand-alone applications, heterogeneous DSSs, and different syntax and semantics of Structural Health Monitoring. The core of the architecture for interoperability between different DSSs is a central ontology, which contains knowledge about an abstract process flow (see also: chapter 2) and the definitions of every available system, especially its description of input and output parameters (see also: chapters 4 and 5). Beside this single ontology approach someone can use multiple or hybrid ontologies, which are either well known concepts in the area of data integration [Cruz and Xiao, 2005]. Another important factor to clarify is the use of the ontology. The DSS data integration ontology is handled as a global conceptualization, to provide meta information about systems and to support a mediator component to maintain the whole routine by deciding which step should be done next and what are possible applications to work with a certain output (see also: chapter 4). Beside the idea of a global conceptualization, which can be seen as one of the first application areas initially mentioned from [Gruber, 1993], an ontology for (data) integration can also be used for meta-data representation, support for high-level queries, declarative mediation or mapping support [Cruz and Xiao, 2005].

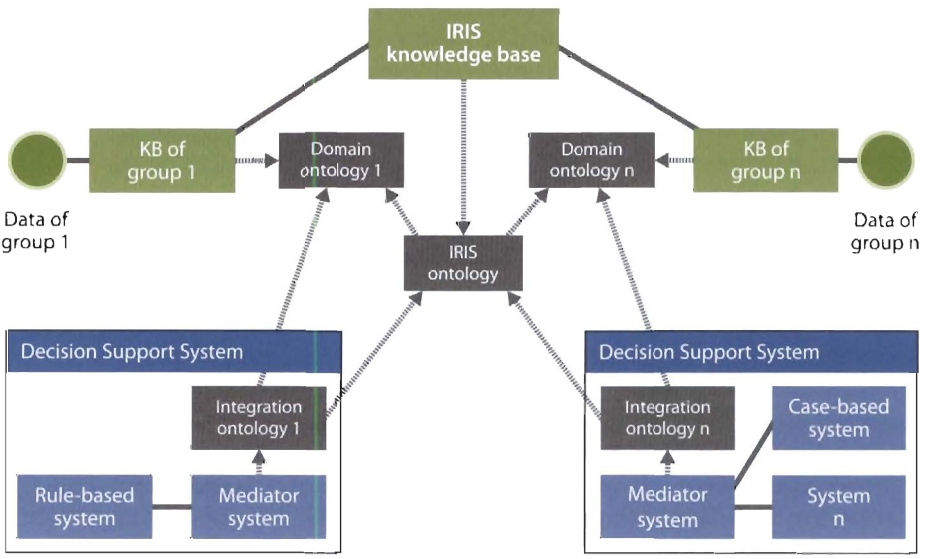
The overall idea of ontology-based data integration is based on the so called semantic data integration. It is not provided that systems within an application area like DSSs for SHM have the same semantic view of a certain input (measure, campaign, damage, etc.) or output (big difference, which ranges from simple results like pure statements to complex results shown in a matrix concerning information about facility state and problems). An appropriate definition of semantic data integration can be found in [Cruz and Xiao, 2005]: "We call semantic data integration the process of using a conceptual representation of the data and of their relationships to eliminate possible heterogeneities". The problems of possible heterogeneities are solved by the ontology, which has to guarantee full semantic support for every available DSS. But [Guarino and Giaretta, 1995] declare the phrase "explicit and formal specification" from [Gruber, 1993] as a very important fact, because

an ontology is only a snapshot of a certain domain and cannot fulfil every issue. But it is possible to constrain the semantic meaning and to provide full semantic support of a certain area of a domain. Therefore the ontology developer has to be aware of the world consumption (open world – OWA; or closed world – CWA) to assure interoperability and well reasoning results. These aspects are very important for the development of the DSS ontology.

Definitions and descriptions, which are discussed in the above paragraphs, deal with the main idea of (semantic) data integration, but it has to be mentioned which concepts are mainly used in this research area and if they are appropriate for the use of DSS data integration. The most referenced and explained approaches are general concepts dealing with different data sources, as well as ontologies, and mappings between them. Depending on the point of view these conceptions are called local-as-view (LAV), global-as-view (GAV) or as a hybrid combination global-local-as-view (GLAV) [Cruz and Xiao, 2005; Lenzerini, 2002]. The LAV approach focuses on the local data sources and formulates these sources as queries over the global schema (vice versa for GAV). The hybrid approach GLAV combines both assertions and formulates conjunctive queries over the global and local schemas, which are mapped together.

The mentioned methodologies are typical for data integration systems, where two or more sources with different schemas have to be merged in a syntactic as well as a semantic manner. The conceptualization of an ontology for heterogeneous DSSs differs from this point of view because this system should work with one single ontology and needs no implementation of concepts like LAV, GAV or GLAV. The introduced architecture will be described and drafted in the next section.

System landscape F.17-2



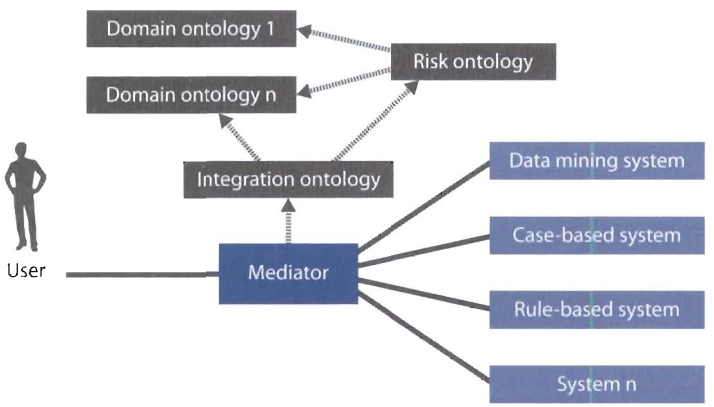
17-4 Integration Ontology for Structural Health Monitoring

In the field of Structural Health Monitoring, different institutions operate a large variety of systems for measurement planning, recording and analysis. As a sophisticated representative BRIMOS® was described in chapter 2. An outlier detection approach [Siringoringo et al., 2009] and a case-based system [Freudenthaler, 2009] can be mentioned in addition. Each of these individual systems has its advantages and disadvantages, mainly depending on certain circumstances of an application, like the type of a regarded structure, the kind of measurement data, defined monitoring objectives, etc. With the intention to increase precision and reliability of SHM processes in general, it is useful to combine the advantages of these individual systems.

Beside further developing sensors, recorders and measurement analysis systems within the EU project IRIS, partners identified collaboration as an important key factor of success. On behalf of that, a concept for computer supported collaboration by means of semantic technologies was worked out. F.17-2 shall illustrate this idea.

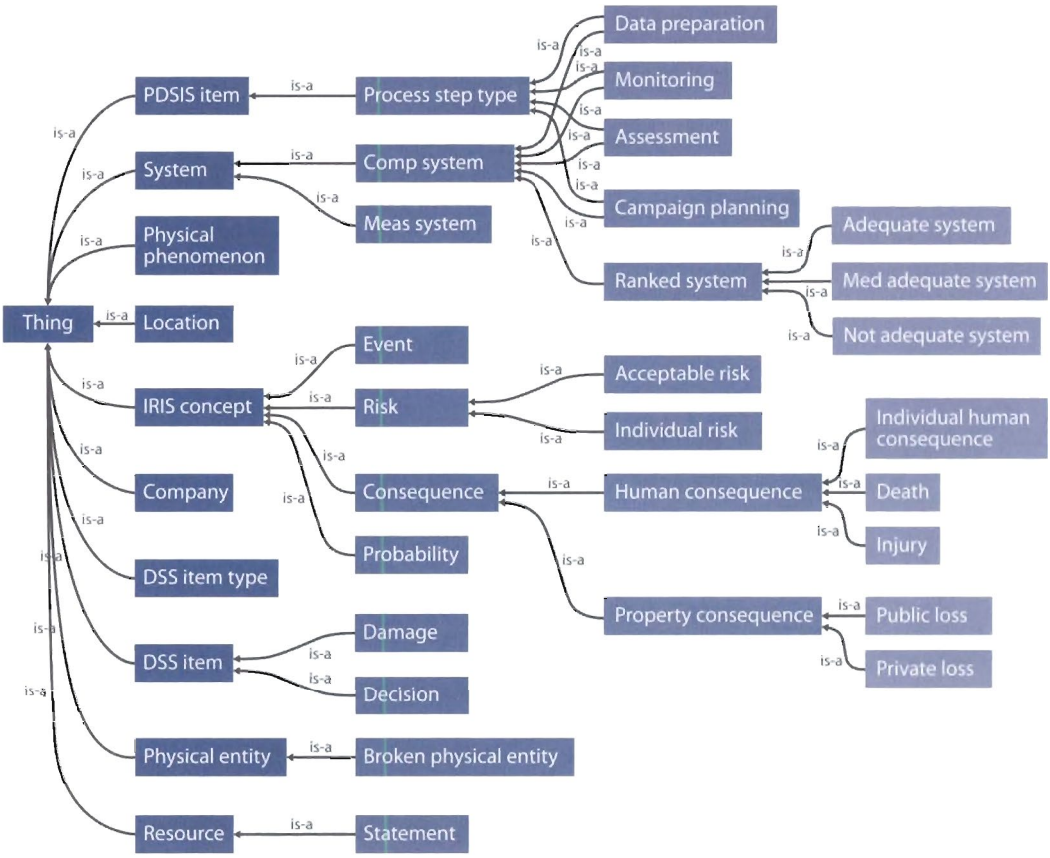
There is a certain number of institutions (civil engineers), called Group in F.17-2, which collected many gigabytes of measuring data and other documents related to SHM over several years. To increase the accessibility of these information sources, each participating institution develops its domain ontology. Furthermore, the participants' knowledge can be integrated by mapping the domain ontologies by means of a higher level ontology (here called IRIS Ontology). A web-based system should make the accumulated information easily accessible to the co-operation partners in the form of a knowledge base. However, this knowledge base is not the main focus of this contribution, but rather another aspect beside sharing knowledge. F.17-3 picks out the relevant parts from the system landscape to clarify the main concern of this contribution.

Integrated Decision Support Systems F.17-3



In addition to supporting knowledge interchange between involved institutions, their systems for planning, running and analyzing measurements should be made available for each other in an automated and integrated manner. On account of this, a concept for an ontology-based integration of DSSs for SHM was developed, as presented in F.17-3. An Integration Ontology, which is based on the certain Domain Ontology and also uses the IRIS Ontology for referring to relevant background information serves as a mediator system: The integration process should be provided by the mediator instance, which classifies certain inputs at runtime by reasoning the ontology and extracting the computed individuals and their class assertions. This retrieved information will be used to decide whether the current process step should be repeated, returned to the previous one or proceeded to the next step. The decisions and operations of the whole system area should not be hard-coded and maintained by an algorithm, the knowledge about the supported and available systems for each process step should be independently available. The mediator system can be seen as a kind of router, which delegates a user through the measuring and analysis process for suggesting the appropriate tooling at the right point of time. To

Integration ontology (excerpt) F.17-4



make this possible, the mediator system has to be aware of the general work-flow shown in F.17-1, which covers a whole measuring campaign on a level of abstraction, which is high enough to make this process suitable to a large variety of applicable DSSs and which enables systems to be handled in a cooperative mode.

At each step, DataPreparation for instance, the mediator should be able to suggest suitable systems to a user and, with the help of an appropriate learning component, the most popular system for a certain process step could be provided. In the course of that, the ability can be gained to generate combined solutions for certain problems, which can rely on the contribution of a certain number of participating systems, making results more reliable and hopefully increasing the overall quality of a measuring campaign. Furthermore, individual DSSs can profit from each other. A case-based system for instance could import input and corresponding output of other systems and generate new cases to extend its case base, which can increase future problem solving capabilities. In recapitulatory terms, the main objective of integrating individual systems is to increase the quality of SHM in general by reaching highly reliable results at each process step of a monitoring campaign.

F.17-4 gives an overview of an Integration Ontology, as represented in F.17-3 and F.17-4. The nodes (classes) System, ProcessStep, CampaignPlanning, Monitoring, DataPreparation and Assessment from F.17-4 are of main interest for the system integration concept. The class System represents available DSSs, a case-based system for instance, while the class ProcessStep realizes a representation of the individual steps of a monitoring campaign, which are campaign planning, monitoring, data preparation and assessment. This concept of an Integration Ontology, also including concrete examples, is presented in the following section.

17-5 The Passive Decision Support System PDSIS

For the purpose of identifying, localizing and assessing damages on structures or structural elements, various different and highly heterogeneous DSS are subject to assist in this process, which includes multiple diverging process steps, each having different syntactic and semantic requirements and communication interfaces to deal with. In order to enforce the integration of multiple heterogeneous DSS, the main concern is the establishment of an integrative system, which aims to implement an additional high-level layer being abstract enough to offer the possibility of covering all conceivable kinds of different DSS in terms of SHM.

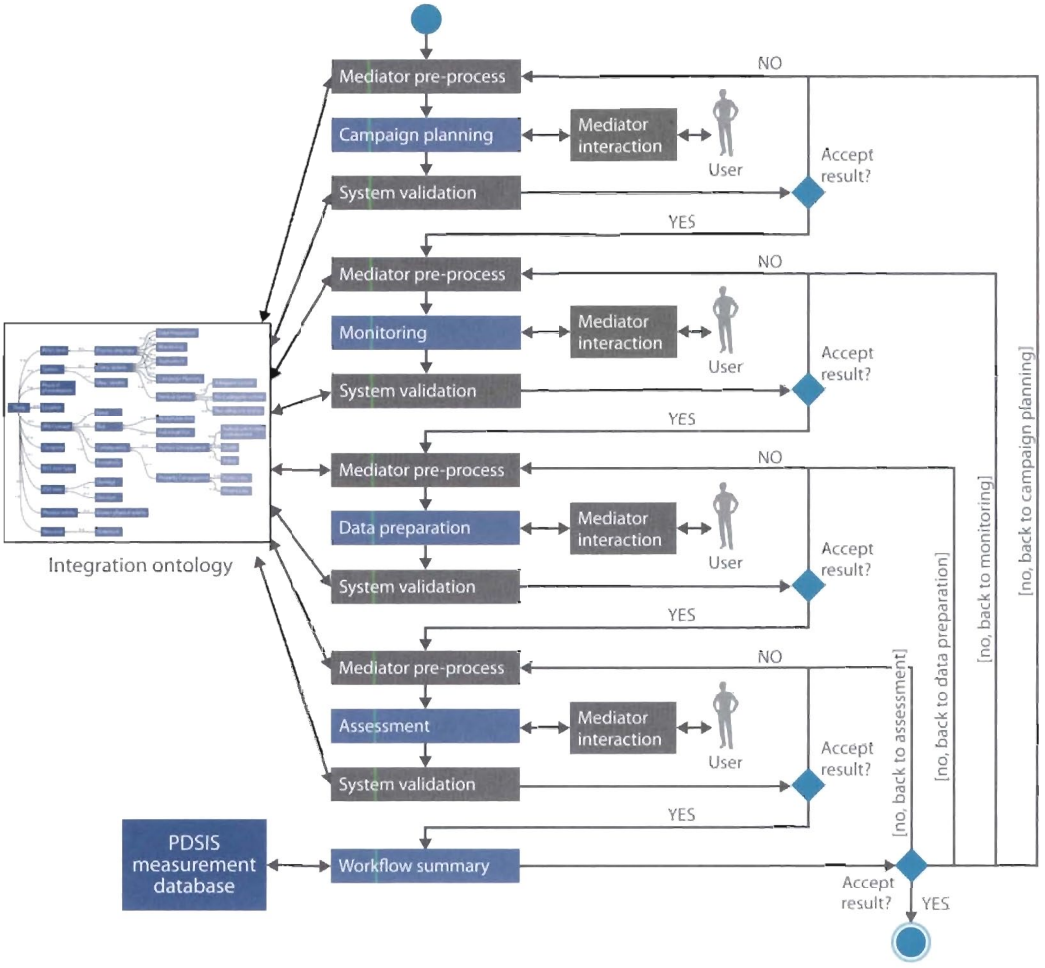
Resulting from intensive research within the frame of the European Union IRIS project as described earlier, an integration system PDSIS (Passive Decision Support Integration System) has been developed which tends to cover all of the previously mentioned requirements by heavily utilizing ontologies.

Since the participating partners of the IRIS project originate from a broad range of industry sectors, the knowledge and expertise of each sector is constituted within a par-

ticular domain ontology. These domain ontologies are very specific and strongly related to the individual industry segments. In order to create an associational and semantic mapping between these, each domain ontology also provides a specific integration ontology which, in turn, uses one central abstract ontology (which we call IRIS ontology) for referring to relevant background information and therefore providing a rather holistic integration approach based on semantic technologies.

The PDSIS architecture consists of a single central user-friendly front end, which interferes with a mediator component which mainly takes care about the integration process through classification at runtime. This is done by reasoning the ontologies and extracting the computed individuals and their class assertions [Cheng, 2003]. Therefore, for each process step in question, the mediator component is able to suggest suitable systems for a specific task

Enhanced general work-flow F.17-5



The following figures show the complete workflow for a monitoring campaign based on BRIMOS®. This process flow is modelled within the integration ontology and also included in the mediator.

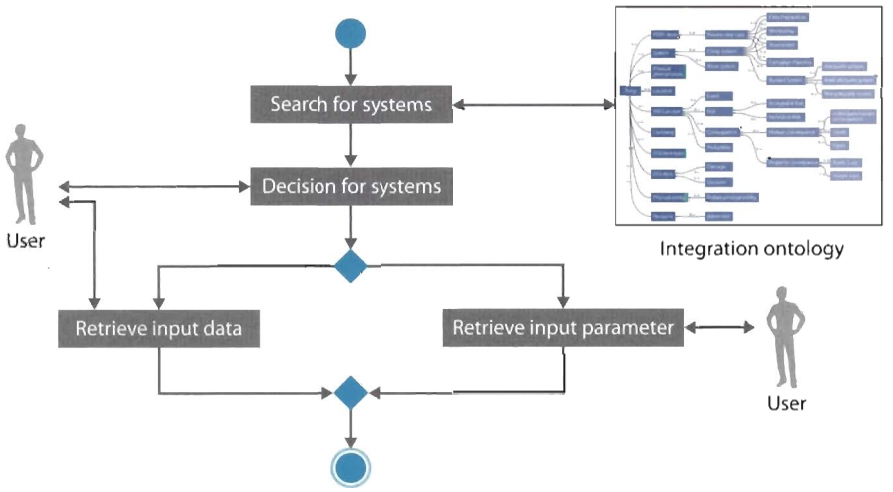
The workflow starts with the first step, campaign planning, by pre-processing of the mediator. This sub-process can be seen in F.17-2. Concerning this application flow, the first activity is to search for an adequate system related to the correspondent process step, e.g. if the current step is "Monitoring" then the mediator searches within the ontology for systems, which are classified as "Monitoring"-systems and the search result is a set of this type of systems. The concept of an integration ontology for SHM and the concrete modelling of such systems matched with the relevant process steps can be found in [Buccela et al., 2003].

The next iteration affects the user because a decision is needed concerning which system should be chosen to be used for the current process step. Furthermore the user passes input parameters, e.g. an activity log-file for BRIMOS®, and input data, e.g. certain measures or modal parameters depending on the type of process step (see [Buccela et al., 2003]). At this point it is really desirable to participate for further improvements of this sub-process and the structure of the input data and parameters. This information is highly heterogeneous and concerning the overall goal of the integration ontology.

After transmission of the required data, the mediator sub process will terminate and the process flow will return to the next step within the enhanced integration workflow (F.17-1).

Back in the enhanced workflow, the next step would be the concrete execution of a certain process and in this context an IRIS DSS. During this computation, the mediator interacts with the chosen DSS and the user. The interoperation with these actors depends on the system itself, so maybe it is important to configure the correspondent DSS manually, e.g. set up the measuring system, configure sensors and recorders, etc.

Mediator pre-processing F.17-6

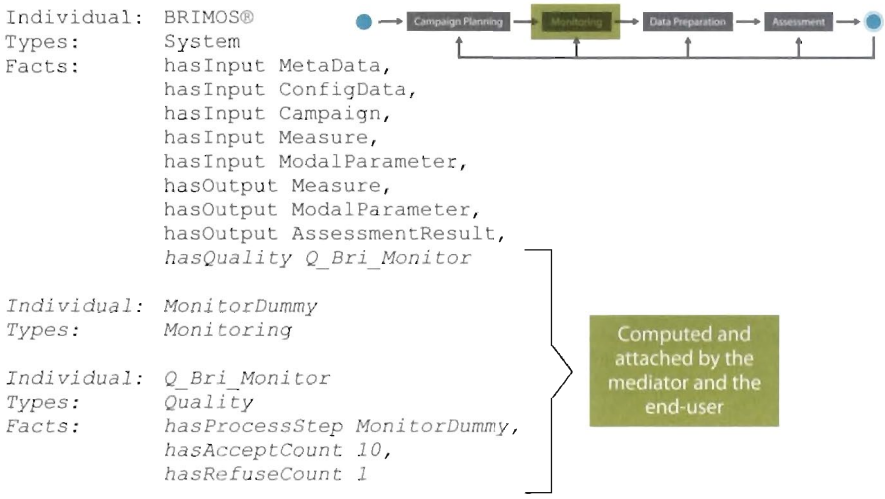


After the main process-step ended, the retrieved process result will be evaluated by the user and therefore also the system itself. Concerning this activity, the validation result will be stored in the ontology by adding additional knowledge about the correspondent system. Referring to the example for quality measurement in [Buccela et al., 2003] such a system description could appear as shown in F.17-3. Therefore, the BRIMOS® system, which was chosen in this example during mediator pre-processing of "Monitoring", will be annotated with a quality mark, which gives information about the acceptance and refused count: a measure for the adequacy of the result. Furthermore, these measures can be used to calculate an acceptance rate, which can help the user by deciding which system is good for what kind of process step.

The topic of how to model a quality measurement within a knowledge grid like an ontology is a rather interesting and huge topic within the current Semantic Web community. Therefore the FAW (Institute for Application-Oriented Knowledge Processing, JKU Linz) will improve the integration ontology by implementing appropriate enhancements. The first step will be the researching of existing quality ontologies, which are mostly based on SOA (Service Oriented Architecture) concepts concerning the so called Quality of Services (QoS). This information is specified by measurements and attributes, which are important for systems (in the field of SOA: services), but it is also important to include deep implicit domain knowledge and experiences from the experts to enhance this first hint. The overall goal is to model QoS measures in a way to construct Quality of Experiences (QoE) [Bunge, 1977].

If we step back to the general integration workflow, the process flow continues with the question whether the user accepted the computed system results during validation or not. Depending on this decision the mediator's internal workflow will start again with the option to step back to another process, if it is adequate. This restart will only be executed, if the current results are refused and the quality mark of the system is modified in the corresponding way as shown in F.17-3. In the case that the user does not accept the

Example quality measurement F.17-7



result, the system has to store already computed figures for further comparison. So PDSIS has to handle this situation and ask the user whether to abandon the results in the current user session or reject it. This issue is only an application-internal feature and therefore not mentioned in the general workflow (see F.17-1).

Beside this refusing back-tracking to a previously executed process, the workflow continues if the user accepts the computed results. In that case, the integration system goes on to the next process "Monitoring", which is different to the other automatically executable steps. Nevertheless it will also start with the mediator internal workflow for searching appropriate systems, decision for a concrete DSS and retrieving input data and several parameters (see also F.17-2). The last steps concerning retrieving of system specific information for computation, the computed results of the previous computation will be taken as input parameters, but it is possible to transmit additional data and parameters if it is important for the next execution.

Furthermore, the execution of the monitoring is not directly covered by the integration system, but it will hold on at this point and only display configuration tasks, which are required for the chosen system to compute measures. These measures will be displayed by the PDSIS online and live via streaming within the workflow, but the user only sees key figures and mash-ups of the computed measures, e. g. how many figures are computed at a certain time stamp, which time range is available, have there been any problems during monitoring and, if yes, which figures are affected, etc. The user can decide at any point of the monitoring process to continue with the workflow and to take the retrieved measurements as input data for the next process. The user can also cancel the monitoring analogical to the "Campaign Planning", but s/he has to do this manually, so the integration system can only get the notification from the system, whether the current monitoring is finished or cancelled.

After finishing or cancelling of the monitoring process, the workflow continues similar to the "Campaign Planning", so computed results will be stored in session if the user wants to compare different results and the application flow continues with the next step "Data Preparation" or delegates the user back to a previous step.

The mediator interaction, computation, execution and validation of "Data Preparation" and "Assessment" are handled similarly to the previous steps (see also F.17-1).

The last step "Workflow Summary" is more specific, but not complex, so the overall integration system and the superordinate PDSIS will show a summary for each process step: chosen system, transmitted input data and parameters, retrieved results or error reports if computation failed and the entire user validation. General information and descriptions of the systems and the specific processes as well as user comments on computed results will also be displayed. At this point the user has the last chance to step back to a specific process and to recover input and output data for re-computation, so if the user proceeds to finish the workflow, the results will be stored within an PDSIS specific database, which has nothing to do with the storage of the data of a certain domain. This database is only for purposes of the PDSIS and the integration system as well for the mediator itself.

17-6 Semantic Integration of Decision Support Systems

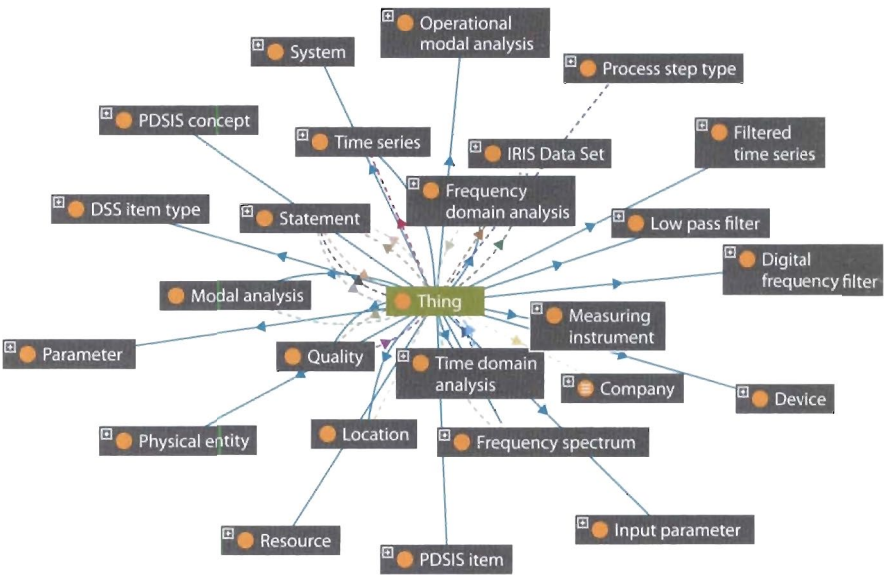
The topic of semantic data integration is a widespread area of different definitions and implementations mainly regarding the alignment, matching, merging or interchange of different schemes and structures not only through their syntactical behaviour, but also by interpreting and analyzing their semantics. Due to this description an overall semantic model with focus on IRIS was developed [Buccela et al., 2003]:

Definition. An integration model for DSS in SHM (I) is defined as a set of systems (S) which contains knowledge about the type of needed parameters and process steps (P), which are mapped (together) by matching their inputs (In) and outputs (Out) such that for each described system there is at least one adequate process step; otherwise the system description is not appropriate (inappropriate systems will be handled as semantically invalid). Therefore the following constraint must be satisfied by the ontology for integrating heterogeneous DSS:

$$\forall_{x:S} \exists_{p:P} \exists_{i:In} \exists_{o:Out} \; (p.i = x.i \wedge p.o = x.o) \qquad \text{(integrity constraint)}$$

Furthermore, o and i are only semantic descriptions of outputs and inputs provided by a certain system and needed by specific process steps. The DSS integration approach classifies systems based on the constraint above by matching their inputs and outputs and therefore classifying a system or not.

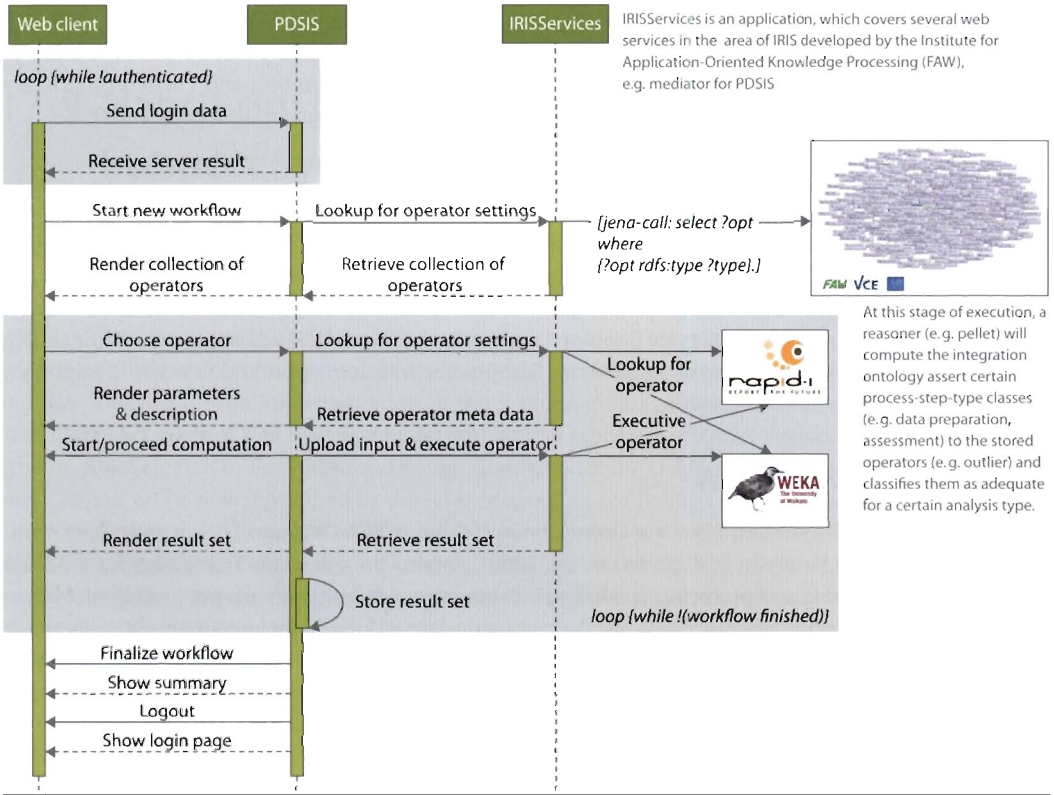
Core integration ontology F.17-8



The ontology was developed by using Protégé (current version 4.1 Beta) and consists of 150 classes, 335 object properties, 32 data properties and currently 240 individuals and their axioms. The TBox and ABox are not finished and will be enhanced in the future. Therefore it is currently not possible to clarify the complexity of the ontology and the performance of the whole proposal, but it is one of the major tasks to be declared in the future work.

The Core Integration Ontology contains all classes, properties and individuals, which are needed for describing several semantic structures of specific operators, which are used within DSSs. Hence, the most important connection between PDSIS and the Integration Ontology, stored in a separate OWL-File (Ontology Web Language; structures and individuals are not stored independently, but this will be part of the future issues concerning the size and performance of the ontology itself), is the property "shortName". This property contains the textual name of the specific operation, which will also be specified in a property file of PDSIS and contains meta-information (not necessary for reasoning and therefore not stored in the ontology) concerning the execution and interaction. Furthermore the interaction model described in the previous section was enhanced and realized through two independent web applications: PDSIS and IRISServices. The first application is the pure web application already discussed. The second application is intended to be

Sequence diagram – interaction of web client, PDSIS and IRISServices F.17-9



used as a service handler for all available services in IRIS. Actually, IRISServices contains the mediator component, which is a web service for handling the communication between the integration ontology (and also the execution of the reasoner), but it is capable of integrating other web services, e.g. the FAW case-based reasoning approach [Bunge, 1977].

The introduced mediator delivers several operations for look up of available operations concerning a given process step type (*lookupOperatorsByType*), the retrieving of parameter information and datatypes (*getParametersByOperatorName*) and the execution (*executeOperator*). Furthermore the mediator is implemented as a Java Web Services, which communicates via SOAP messages with PDSIS. Therefore, the interaction model envisions basic Java classes like collections, or simple object items.

The results of this refinement can be found in F.17-9. Interaction with PDSIS starts by logging in to the web application with a pre-defined user name and password (both stored encrypted in the PDSIS databases, which covers the meta information of all workflows and system executions). Beside the clearly structured page and content, the web-application is designed to be multilingual.

17-7 Integrated Decision Support Systems

Numerous DSSs have been integrated to seamlessly work with PDSIS within the IRIS project. The chosen DSS cover several distinct and important fields within the areas of statistical computing, numerical computing, machine-learning and custom proprietary scripts. The following DSS have been, among others, integrated to work with PDSIS:

17-7-1 RapidMiner

A data mining toolkit, well-suited for processing very large data pools and performing various analytical tasks. Being open source, it offers a programming interface and is primarily intended for data mining [Davenport and Prusak, 2000] operations which makes it a considerable utility for Decision Support. At the time of this writing, the mediator service fully implements the RapidMiner Fast Fourier Transformation and Principal Component Analysis functionalities.

17-7-2 WEKA

Originating from the University of Waikato, WEKA (Waikato Environment for Knowledge Analysis) [Cui and O'Brien, 2000] aims to be a versatile framework for machine learning and predictive modelling including but not limited to pre-processing, text-learning and clustering. Currently, the corresponding IRIS mediator implements Wavelet transformation using the standard WEKA Java API. The specific notification workflow can be interpreted as analogous to RapidMiner.

17-7-3 R (GNU S)

As opposed to the two frameworks outlined above, R [Freudenthaler, 2009] is a non-graphical programming language for statistical computations and became a de facto standard for statistical software development. R implements the S programming language and originates from the University of Auckland. Since R is not developed in Java, it does not offer integrated programming interfaces like RapidMiner and WEKA, although certain third-party expression evaluator interfaces exist [Lenzerini, 2002]. Currently, R has not yet been implemented as mediator service within PDSIS, but approaches towards including R through either web-services or socket communication are in progress. Furthermore, R also supports graphical plotting which, at this time, is not intended to be utilized by PDSIS.

17-7-4 MATLAB (GNU Octave)

MATLAB, and its free open-source equivalent GNU Octave, are programming languages intended for numerical computations. It is interpreter-based yet very fast, offers command-line and API interfaces and may be extended through various dynamically loadable modules. This DSS has been chosen, since many companies utilize MATLAB or GNU Octave for calculations and have already implemented extensive scripts which have proven to offer industrial-strength.

17-8 Hands on: Integrating R as Decision Support System for Time Series Analysis

17-8-1 What is R?

R is a programming language and software environment for statistical computing and graphics. The R language has become a de facto standard among statisticians for the development of statistical software, and is widely used for statistical software development and data analysis. R is an implementation of the S programming language created by John Chambers while at Bell Labs combined with lexical scoping semantics inspired by Scheme. R was created by Ross Ihaka and Robert Gentleman at the University of Auckland, New Zealand, and is now developed by the R Development Core Team. R provides a wide variety of statistical and graphical techniques, including linear and non-linear modelling, classical statistical tests, time-series analysis, classification, clustering, and others. R, like S, is designed to be a true computer language, and it allows users to add additional functionality by defining new functions. R has many features in common with both functional and object oriented programming languages. In particular, functions in R are treated as objects that can be manipulated or used recursively. The capabilities of R are extended through user-submitted packages, which allow specialized statistical techniques, graphical devices, as well as import/export capabilities to many external data formats.

17-8-2 Time Series Analysis

Time series are used in a wide range of domains, especially in econometrics, for example in predicting the opening price of a stock based on its past performance, or computing the interest rates or the monthly rates of unemployment. Beside economics, time series are also used in natural sciences, like meteorology: recording the hourly wind speeds, the daily maximum/minimum temperatures, the annual rainfall or in geophysics: recording the shaking or trembling of the earth in order to predict possible earthquakes. There are also several examples of time series in social sciences: the annual death and birth rates, number of accidents in the home, recording criminal activities, etc. All these examples show us that time series analysis plays an important role in our daily life and they require special analysis methodologies.

What is different about time series, compared to other data, is that they have a natural temporal ordering. This makes time series analysis distinct from other common data analysis problems, in which there is no natural ordering of the observations. A time series model generally reflects the fact that observations close together in time are more closely related than observations further apart. In addition, time series models often make use of the natural one-way ordering of time so that values for a given period are expressed as derived in some way from past values, rather than from future values.

What is the scope of time series analysis? Mainly, when we study time series data we try to gain a better understanding of the data, predict future values, optimally control systems, monitor processes, derive computer simulations, prepare countermeasures in case of unexpected events, improve output/quality/performance of a system, etc. Time series analysis can be, among others, used for:

1) Forecasting

First, and the most common one is forecasting or predicting. The idea is to use observations from a time series available at time t to forecast its value at some future time $t+l$. First, suppose that observations are available at discrete, equispaced intervals of time. As input we have the observations generated until time t: $z_t, z_{t-1}, z_{t-2}, z_{t-3}, \ldots$

The output should be a function $\hat{z}_t(l)$, $l = 1, 2, \ldots$, which is also called the forecast function. It will provide the forecasts at origin t for all future lead times. Our goal is to obtain a forecast function such that the mean square of the deviations $z_{t+1} - \hat{z}_t(l)$ is as small as possible. As an example, if we wanted to predict future values for the next year for the air passengers time series, we would like to obtain a function that describes the behaviour of future data:

2) Determine Relationship between Input and Output

The second problem is the estimation of transfer functions, which will enable us to determine a relationship between, usually, input and output time series. A transfer function can relate an input process X_t to an output process Y_t through a linear relationship, for instance. More precisely, we express Y_t (output) as a linear dependency of the previous input values $X_t, X_{t-1}, X_{t-2}, \ldots$ given by $Y_t = \Sigma_j v_j X_{t-j}, j = 0, \ldots$

The input in this case is the rate of air supply and the output is the concentration of carbon dioxide (CO_2) that is produced in the furnace. The observations were made at

intervals of nine seconds and the linear dependency detected is given by the values of v_t. Another important application of the transfer function models is in forecasting. If, for example, the dynamic relationship between two time series X_t and Y_t can be determined, past values of both series may be used to predict Y_t. In some situations this apporach might lead to a considerable reduction of the estimation error.

3) Analyze Effects of Unusual Events

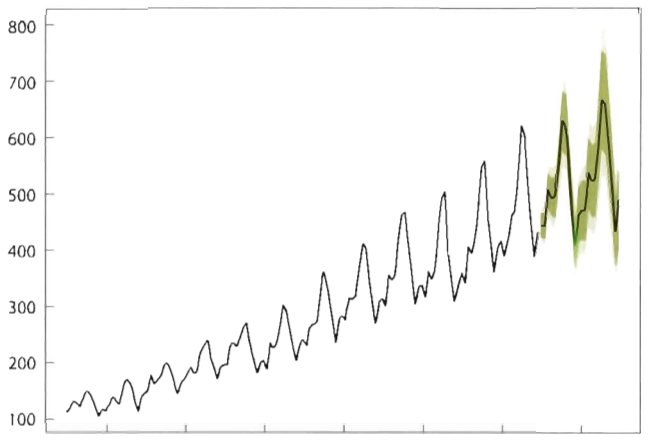
Time series are often affected by special events or circumstances such as policy changes, strikes, advertising promotions, environmental regulations, and similar events, which are usually called intervention events. Examples of such intervention include the incorporation of new environmental regulations, economic policy changes, strikes and promotion events.

In this case intervention analysis is performed in order to obtain a quantitative measure of the impact of the event of the time series or to adjust for any unusual values in the series that might have resulted as a consequence of the intervention event. This will ensure that the results of the time series analysis, like the structure of the model or estimates of the model parameters or forecasts of future values, are not seriously distorted by the influence of these unusual events.

4) Process Control

The fourth application of time series analysis is in discrete control of systems. There are some important scientific notions that need to be explained before. Process control means controlling the output of a specific process usually used in engineering and statistics. A subdomain of process control is statistical process control (SPC), which deals with monitoring a process using statistical tools, like control charts. The main idea here is to detect and correct variations in the process that might affect the quality of the end product or service.

Using time-series analysis for forecasting purposes F.17-10



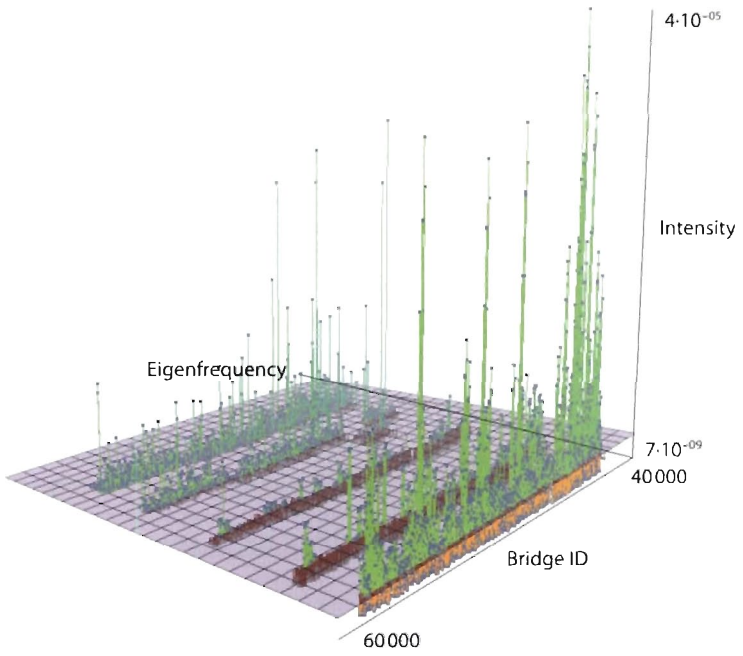
17-8-3 Integration

R has been integrated within PDSIS as generically usable service. R scripts can be run natively within the operator execution process of PDSIS, regardless of what calculations are actually done. This dramatically increases the opportunities instead of only implementing one specific calculation task done with R.

As with almost all other available operators, R has been equipped with a PDSIS-wrapper which basically resembles a number of standardized interface programme calls, like perform-operation and retrieve-results. These interfaces allow seamless and easy integration of multiple DSS which may offer completely different and heterogeneous usages. PDSIS takes care of consistent data alignment in a manner, which enables us to pipeline multiple DSS in both, sequential and parallel manner. This eases comparability of results as well as, if needed, iterating through multiple pre- and post-processing steps which, in turn, may also consist of the execution of operators. This makes PDSIS an utterly versatile tool for Decision Support, and aims to be independent from data formats, implementation details, technical dependencies and service availability.

As a real-life example, F.17-11 shows a graphical representation of a calculation made with a custom-made GNU R script, which can be directly accessed using the PDSIS system. After pre-processing the initial data pool, which has been gathered using the BRIMOS® system in the first place, the data can be pipelined into a *kmeans* time-series computation done via GNU R.

GNU R *kmeans* clustering with PDSIS based on eigenfrequencies of a bridge F.17-11



17-9 Conclusion and Outlook

With PDSIS, we have shown that utilizing multiple different DSSs can significantly improve computation results within the frame of structural health monitoring. GNU R, among multiple other DSS, can be used for data processing in order to analyze and perform qualitative as well as quantitative analysis of measurement data and can dramatically ease and assist in localizing damages and projecting estimated structural lifetimes. The utilization of Passive Decision Support in conjunction with semantic technologies like Ontologies within an integrated environment can effectively simplify the decision making process and all necessary computational steps in order to do so.

Future research and development strategies are supposed to cover an even more in-depth approach towards seamless integration, communication, data forwarding and input/output pipelining from and to distinct DSSs. In order to achieve this, the design of the utilized ontologies in question is still to be refined and broadened for being applicable to as many situations and scenarios as possible, in a more generalized manner.

As the PDSIS system suggests, more experimental calculations and data processing tasks have to be done for the system to enhance its capability of suggesting certain DSSs to a user who wants to find suitable components and processing strategies for a given task. This especially affects the sequential chaining of multiple DSSs for task completion, as well as the hereby strictly necessary normalization and unification of numerical data in order to do so.

Also, the inclusion of new DSS components from a pragmatic and developer-specific point of view is expected to be even easier than now. Given a sufficiently capable ontology for doing so, the higher goal is to be able to add new DSSs almost autonomously without major human intervention, similar to a plug-in based architectural software design, augmented by the utilization of semantic technologies.

Moreover, as more generalized and abstract the high-level design and its corresponding ontologies become, the higher the chances will be for the PDSIS framework to be capable of being a useful toolkit far beyond its initial primary focus within the IRIS project itself. Therefore, the framework is not restricted to being used for SHM only, but also for a broad variety of other conceivable scenarios, especially towards (but not limited to) time series analysis based ones, like climate science, earthquake engineering and disaster scenarios.

We believe that passive Decision Support can dramatically ease the decision making process for both, professionals and non-professionals, and can be applied to virtually every computational task whose outcome relies on analysing number series and performing calculations thereupon. Once the corresponding common infrastructure is established and certain semantic technologies are used and mutually agreed upon, passive Decision Support may seriously assist in choosing the right DSS, speeding up the decision making process, and narrowing down or even eliminating potential sources of errors.

References

Buccella, A., Cechich, A. and Brisaboa, N. R., 2003. *An Ontology Approach to Data Integration. Journal of Computer Science and Technology*. Springer, Berlin/Heidelberg, 3:62–68.

Bunge, M., 1977. *Treatise on Basis Philosophy*. Ontology I: The Furniture of the World. Springer, New York, 1.

Cheng, H. G., 2003. *Representing and Reasoning about Semantic Conflicts in Heterogeneous Information Sources*. Ontology-based Integration of Heterogeneous Decision Support Systems for SHM, MIT Press, Massachusetts.

Cruz, I. F. and Xiao, H.,2005. *The Role of Ontologies in Data Integration*. In: International Journal of Engineering Intelligent Systems for Electrical Engineering and Communications, CRL Publishing, Leicester, 13(4):245–252.

Cui, Z. and O'Brien, P., 2000. *Domain Ontology Management Environment*. In: Hawaii International Conference on System Sciences, IEEE Computer Science, 8:1–9, Washington.

Davenport, T. and Prusak, L., 2009. *Working Knowledge*. Harvard School Press, Boston.

Freudenthaler, B., 2009. *Case-Based Decision Support for Structural Health Monitoring*. PhD thesis, Johannes Kepler University, Linz.

Gruber, T., 1993. *A Translation Approach to Portable Ontology Specifications*. Knowledge Acquisition, 5(2):199–220, Academic Press Ltd., London.

Guarino, N. and Giaretta, P., 1995. *Ontologies and Knowledge Bases: Towards a Terminological Clarification*. In: Mars, N. I. J. (ed.) Towards very large knowledge bases: knowledge building and knowledge sharing, ISO Press, Amsterdam, 24–32.

Lenzerini, M., 2002. *Data Integration: A Theoretical Perspective*. In: 21st Symposium on Principles of Database Systems. Madison, New York, 233–246.

Oszu, M. T. and Valduriez, P., 1999. *Principles of Distributed Database Systems*. 2nd ed., Prentice Hall, New Jersey.

Siringoringo, D. M., Nagayama, T., Fujino, Y., Su, D., Chondro and Tandian, C., 2009. *Dynamic Characteristics of an Overpass Bridge During a Distructive Test*. Bridge and Structure Laboratory Internal Report.

Wenzel, H. and Pichler, D., 2005. *Ambient Vibration Monitoring*. John Wiley & Sons Ltd., UK.

Wenzel, H., 2008. *Health Monitoring of Bridges*. John Wiley & Sons Ltd., UK.

Anderlik, S., Stumptner, R., Freudenthaler, B. and Fritz, M., 2010. *A Proposal for Ontology-based Integration of Heterogeneous Decision Support Systems for Structural Health Monitoring*. In: The 12th International Conference on Information Integration and Web Based Applications & Services (iiWAS2010).

18

Reduction of Risk for Human and Ecosystems in Mine Tailing Properties

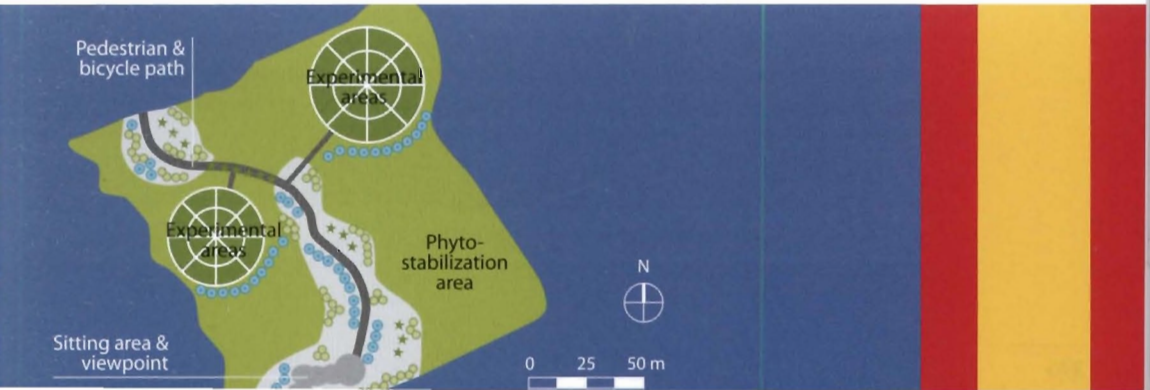
Authors:
Ángel Faz
José A. Acosta
Dora M. Carmona
Sebla Kabas
Silvia Martínez-Martínez
Raúl Zornoza

Motivation

Waste material deposits from mining activities in Spain lasting for more than 2500 years are a threat to environment and society. Methodologies to detect, assess and mitigate these environmental issues are desired.

Main Results

A comprehensive methodology for assessment of affected sites including long term plans for recovery have been developed and demonstrated in Spanish tailing ponds. The vegetation cover has been successfully restored.



18-1 Introduction

Cartagena-La Unión Mining District in southeast of Spain constituted an important mining focus for more than 2500 years until its closure in 1991. Phoenicians, Carthaginians, Romans, Arabians, and Spaniards have been mining silver, lead, zinc, tin, iron, and manganese in this district [Conesa and Faz, 2009; Faz et al., 2001]. Those mineral deposits were likely to be mined for profit, thus, overburden and waste materials (accumulated in tailing ponds) with their consequent environmental risks appear as the fundamental components in the post-mined landscapes [Acosta et al., 2011; Collins, 2001]. Tailing ponds contain materials rich in Fe-oxyhydroxides, sulphides, sulphates, and heavy metals (mainly Cd, Pb, and Zn). As a consequence, these soils remain bare and have low soil organic matter content [Acosta et al., 2011; Conesa et al., 2007]. Consequent environmental risks, especially water and wind erosion and mobility of heavy metals in soil-plant systems stand out with propensity to adversely affect both human health and the functioning of ecosystems. Therefore, it is necessary to take action towards remediation of this contamination [Doumett et al., 2008; Ji et al., 2011].

While surface mining has relatively ancient origins, reclamation is a relatively recent phenomenon with a global concern about the potentially damaging effects which can originate from mining [Burley, 2001]. In this recent phenomenon, phytoremediation takes its place as a newly emerged reclamation technique in the removal or stabilization of soil heavy metals by the usage of plants providing advantages in costing, in in situ applications and in environmental compatibility, among other expensive and often impractical techniques [Pérez-Esteban et al., 2011; Sasmaz and Sasmaz, 2009]. Restoration of a vegetation cover can fulfil the objectives of stabilization, pollution control, visual improvement and removal of threats to human beings (phyto-stabilization) [Wong, 2003]. Vegetation cover is very effective in reducing surface erosion; can return a large proportion of percolating water to the atmosphere through transpiration, thus reducing the concentration of soluble heavy metals entering watercourses; reduces the visual scars in the landscape, so that successful re-vegetation may allow recreational use of the land [Tordoff et al., 2000]. Several studies on the use of metallophytes for re-vegetation of metal toxic mine wastes appear in the literature (e.g. [Peters, 1984; Smith and Bradshaw, 1979; Wong, 2003]). According to these studies, combining metal-tolerant species with proper application of fertilizers and pH adjusters resulted in the successful and rapid re-vegetation of contaminated soils.

The general objective of this chapter is to show an effective methodology for improving soil fertility and environmental risk reduction in mining tailing ponds using organic and inorganic amendments and phyto-stabilization. This general objective can be divided in the following specific objectives:

1) to evaluate the evolution of tailing properties after amendment application,
2) to evaluate the risk reduction for human and ecosystems after amendment application,
3) to study the effect of amendments in the growth of native vegetation (vegetation cover, richness and biodiversity), and finally
4) to design a new landscape for the reclaimed areas.

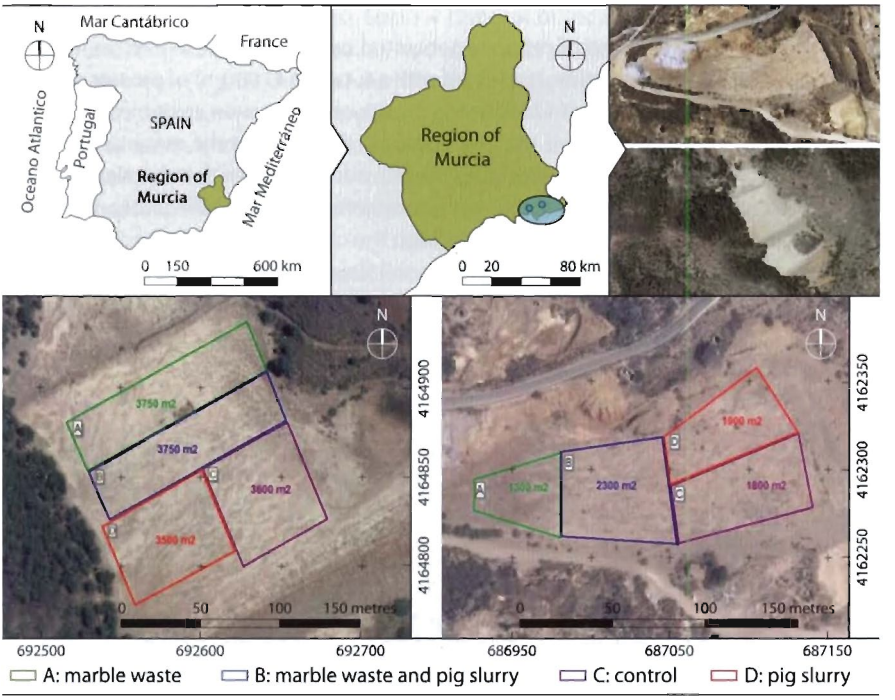
18-2 Study Areas and Experimental Design

Two areas affected by mining activities were selected, El Lirio and El Gorguel tailing ponds. These areas are representative of the rest of existing mining affected areas in the Mining District of Cartagena-La Unión, SE Spain, with similar problems and characteristics (F.18-1). The selection of these two areas was based on their access facilities, physico-chemical characteristics (based on previous studies), hydrological conditions, slope, distance from towns, surrounding landscape, etc. Thus, the conclusions that can be extracted from these zones can be applied to the rest of the areas, at the same mining district, or in other areas from similar metallic mining activities under the same environment. A distribution of the surface areas of the tailing ponds to delimitate the zones with the different treatments was carried out as show in the F.18-1.

Zone A: Application of marble waste is added to increase soil pH for metal immobilization, and to improve soil structure and metal retention. A superficial area of 3750 cm^2 and 1300 cm^2 in El Lirio and El Gorguel, respectively, were amended with marble waste on the top soil and then mixed to the upper first 30 cm, and immediately incorporated into the soil taking care to give several passes to get a good mixture.

Zone B: Marble waste and pig slurry are applied in a superficial area of 3750 cm^2 in El Lirio and 2300 cm^2 in El Gorguel. First, marble waste was applied on the surface soil and then pig slurry allowing the liquid to be absorbed by the soil/marble mixture. After 24

Location and distribution of plots in tailing ponds El Lirio (left) and El Gorguel (right) F.18-1



hours amendments were incorporating into the soil and mixed with the first 15–20 cm of soil by ploughing. This assay allows us to study the influence of amendments in the soil-plant system, and to establish comparisons with zones A and D.

Zone D: Pig slurry is applied to increase soil organic matter and nutrients. Pig slurry was added in a surface area of 3500 cm^2 and 1900 cm^2 in El Lirio and El Gorguel, respectively. We were waiting 24 hours for the water to be adsorbed by the soil and incorporated in 15–20 cm into subsoil. This assay allows us to study the influence of amendments in the soil-plant system, and to establish comparisons with zone B.

Zone C: In this plot none of the amendments studied was applied. It acts as a reference to contrast the effects of the different amendments in the soil-plant system, and to monitor the evolution of physico-chemical and biological soil properties.

18-3 Waste Residues Used as Amendments

Two types of waste materials were used as amendments in this large-scale plot experiment for improving tailing properties and increasing the possibilities of reclamation of the El Lirio and El Gorguel tailing ponds. We chose marble waste and pig slurry as inorganic and organic amendment, respectively, because they are generated in huge quantities, representing a significant disposal problem for pig producer and stone industry in the Region of Murcia.

18-3-1 Marble Waste

In this region the volume of residues generated by non metallic extractive industry, and concretely marble extraction, is relevant with a total of 147 000 m^3 of process product, generating an annual residue of 128 120 tons. Thus, one of the main environmental problems of this extractive industry is the low output in the profit of the material (10–20 %) generating a huge volume of inert residues that are normally taken to industrial disposals. The application of alkaline materials has been considered to prevent the acid conditions to either neutralize the acidification process or stop the oxidation of pyrite, and to promote recovery of plant cover by means of improving soil structure. When limestone dissolves in aqueous media it provides alkalinity and assists in neutralization of acidic solutions and

Generation of marble waste: cutting marble stone, wet and dry conditions of waste F.18-2



immobilization of metals through precipitation and/or adsorption. Marble waste was obtained from marble industries located in Cehegín, Murcia (F.18-2) and had approximately 20% humidity and 94% $CaCO_3$ in dry condition, pH was 8 and salinity 2.2 dSm^{-1}.

The applied amount is based on the equivalent $CaCO_3$ required to neutralize the acidity generated in terms of percentage of oxidizable sulphur present in the mine soil. Eq $CaCO_3$ was calculated according to the method proposed by [Sobek et al., 1978]. Additionally, in management plans which involve liming, a first engineering safety factor, (fs), is considered of at least 1.5 to 2 times the theoretical lime requirements and needs to be used, to allow the slow reactivity of lime and reduce the negative effects of non homogenous mixing in the field. The second is the purity factor, (fp), to reach the equivalent of pure lime.

Analyses of representative soil samples from each tailing pond reported a mean content of 0.25% and 0.57% of sulphur for El Lirio and El Gorguel, respectively; which allows neutralizing the soil potential acidity supplied by sulphur. Thus, we have calculated a mean of quantity requirements for the current conditions of potential acidity in each tailing pond corresponding to 1.4 kg marble/m^2 and 4 kg marble/m^2 for El Lirio and El Gorguel respectively. Marble wastes were applied only once at the beginning of large-scales plot experiments A and B.

18-3-2 Pig Slurry

The Region of Murcia has more than 8% of pig production in Spain, with almost 2 000 000 pigs in 7486 farms. This quantity of pigs generates an annual production of 6.5 Hm^3 of pig slurry (F.18-3). Using pig slurries as soil amendment will address two environmental problems in southeast Spain – disposal of industrial wastes from pig production and reclamation of mine soils. Pig slurry could ameliorate mine soil by providing available nutrients (e.g. nitrogen, phosphorous, potassium etc.), improving physical properties and possibly lowering the availability of toxic metals through complexation with the organic matter. Nitrogen, carbon and nutrients are usually deficient in mine soils and limit vegetation establishment and sustained productivity. Soil organic matter improves nutrient retention by increasing cation exchange capacity (CEC), enhances the availability of nutrients (e.g., NH_4^+, NO_3^-, PO_4^{3-}, SO_4^{2-}) and traces elements by mineralization, improves soil buffering capacity, chelates metallic ions, increases the availability of some nutrients, and decreases the toxicity of others [McBride, 1994; Stevenson, 1994].

Generation of pig slurry: production in farm, pond storage of pig slurry and samples of pig slurry F.18-3



The calculation for application of pig slurry was made according to the agronomic rate established by Spanish legislation RD 61/1996: 170 kg N ha^{-1} yr^{-1} (framed within the Directive 91/676/CEE), to avoid contamination of groundwater by nitrates. Pig slurry was added in plots B (marble and pig slurry) and D (pig slurry) at a rate of application of 3.3 L m^{-2} and 5.9 L m^{-2} in El Lirio and El Gorguel, respectively. Pig slurry was obtained from a pig farm located in Fuente Álamo, Murcia, which was directly pumped from the pond and transported for application by spreading the tank in movement towed by a tractor (F.18-3). The chemical characterization of pig slurry includes a pH of 7.8 and salinity of 39.1 dSm^{-1}, its moisture was 96 %, total nitrogen 5.1 g L^{-1} and total organic carbon 18.7 g L^{-1}. Concentration of metals were 19.3 mg Cu L^{-1} and 28 mg Zn L^{-1}.

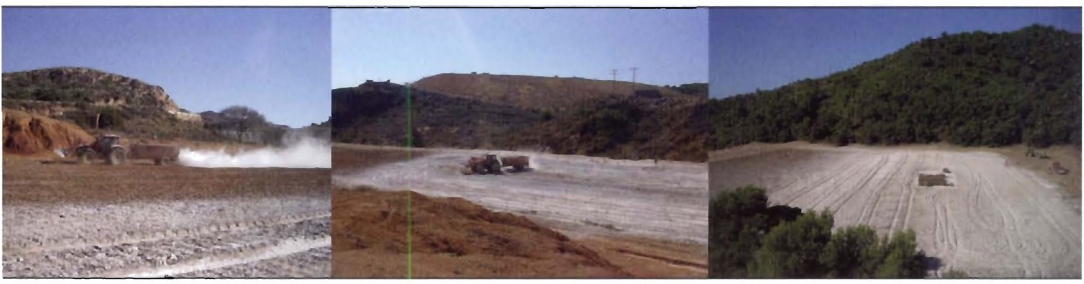
18-4 Initial Site Preparation and Amendment Application

First initial activities including the construction of drainage structures around the plots in order to conduct the runoff water and prevent flooding into the plots in rainy seasons. As the soil surface presents a hard cemented layer it was necessary to use machinery to break-up dense soil through its spiralling action in surface (up to 50 cm depth). Then, soil was redistributed across the surface to produce a relatively uniform reconstructed soil. Finally, after tillage soil surface was levelled, guaranteeing the drainage of waters after rainfalls. Each step can be observed in detail in the F.18-4, F.18-5, F.18-6 and F.18-7 shows the steps taken during the addition of the marble waste and pig slurry amend-

Operational activities for preparing soil surface in the tailing ponds F.18-4



Application of marble waste in the tailing pond F.18-5



Application of pig slurry in the tailing ponds F.18-6



Incorporation of amendments (marble waste and pig slurry) into the soil F.18-7



ments at A and B plots emplaced in El Lirio and El Gorguel tailing ponds. Marble waste was transported to the site by truck and deposited in piles. The piles were then spread and incorporated using an excavator.

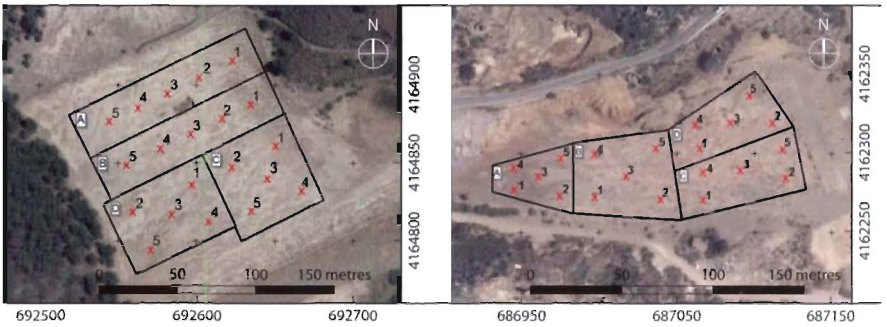
18-5 Monitoring of Soil Properties and Vegetation

18-5-1 Soil Sampling and Analytical Methods

At the beginning of the experiments soil samples were taken in each plot (A, B, C and D) in order to have a reference to compare with results from periodical sampling planning during this long-term experiment. After application of amendments soil samples were again taken in three different periods: one week (to determine the first changes in soil properties), six months and twelve months after application. Soil samples were collected in five replicates distributed into each plot (F.18-8).

In each sampling point, we collected surface soil (0–30 cm) because the roots of the vegetation and the preparatory tillage of the mining lands reached the 30 cm of the soil. The collected samples were transported to the laboratory for analyses. Samples were air-dried for seven days, passed through a 2-mm sieve, homogenized, and stored in plastic bags at room temperature prior to laboratory analyses. In addition, a subset of each sample was grounded for several analytical determinations.

Sampling points in plot experiments for rehabilitation actions in El Lirio and El Gorguel F.18-8



× Sampling point ▭ Study area

A: marble waste B: marble waste and pig slurry C: control D: pig slurry

The analyses for this study were determined as follows: pH and electrical conductivity [Peech, 1965]; total carbon, sulphur and nitrogen in an elemental analyzer, cation exchange capacity [Chapman, 1965], particle size [FAO-ISRIC, 2006], aggregate stability [USDA, 1999], total metals [Risser and Baker, 1990], bioavailable metals [Lindsay and Norwell, 1978; Norvell, 1984] and water soluble metals [Ernst, 1996]. Measurements of metals were carried out using atomic absorption spectrophotometer (AAnalyst 800, Perkin Elmer).

18-5-2 Monitoring of Vegetation

After application of amendments we hope that in time for the chemical stabilization and nutrients added by pig slurry promote the creation of initial structured soil, with immobilization of heavy metals, and increases in organic matter, nutrients, water holding capacity and active microbial communities, in order to initialize the establishment and survival of spontaneous species by the surrounded vegetation. In order to evaluate the evolution of the colonization of spontaneous vegetation, the vegetation cover, richness and biodiversity were quantified every six months.

18-6 Results and Discussion

18-6-1 Tailing Properties Evolution

Soil Acidity (pH)

Soil pH is a measure of active soil acidity. The pH of a given mine soil can change rapidly as the rock fragments weather and oxidize. Pyritic minerals (FeS_2), when present, oxidize to sulphuric acid and drastically lower the pH, while carbonate ($Ca/MgCO_3$) bearing minerals and rocks tend to increase the pH as they weather and dissolve. Unweathered (or unoxidized) mine soils containing an amount of pyritic-S higher than the amount of their neutralizers (e.g. carbonates), will result in a fast drop of the pH to a range of 2.2 to 3.5 after exposure to water and oxygen.

In El Lirio tailing pond, soil pH in plot treatment with marble waste was increased after amendment application (F.18-9). Contrarily, plot amended with pig slurry and control remained with a pH of 4.0 and 5.0 respectively. The change in pH might indicate the "liming effect" of marble waste to modify soil acidity. In El Gorguel, the effect of the amendments on soil pH is not observable, which is due to the fact that initial pH in this pond is already high (~8.0) for all plots. This shows that, after amendment applications, the pH of these ponds is currently adequate for natural plant colonization.

Electrical Conductivity

Electrical conductivity (EC) of a soil solution indicates the concentration of total soluble salts in solution, thus reflecting the degree of soil salinity. Plants are detrimentally affected, both physically and chemically, by excess salts in some soils and by high levels of exchangeable sodium in others.

Initial soil salinity on both ponds and for all plots was high (>2 dSm^{-1}), indicating that salinity is an important limitation for plant colonization; and only resistant plant species will be able to colonize these ponds. Soil EC values for both tailing ponds decreased significantly in plots amended with marble waste, on the contrary that happened when pig slurry was applied (F.18-9). However, for all plots in El Lirio and marble plot in El Gorguel, the general pattern is an increase of EC during the next months after application; this can be explained by the effect of soluble salt movements to the surface due to evaporation and capillary rise and subsequent salt precipitation during the summer period.

Redox Potential

Redox potential (Eh) is a measure of the tendency of a chemical species to acquire electrons and thereby be reduced. Each species has its own intrinsic reduction potential; the more positive the potential, the greater the species' affinity for electrons and tendency to be reduced. Just as the transfer of hydrogen ions between chemical species determines the pH of an aqueous solution, the transfer of electrons between chemical species determines the reduction potential of an aqueous solution.

For both ponds and all plots, including control plots, the observed general pattern was a decrease of the redox potential values during the time, however, some differences

were observed. In El Gorguel, an increase of Eh in the plots treated with pig slurry was observed, however, after six months the values of Eh were even lower than the Eh values before application for these plots (F.18-9). This indicates that the climatic conditions of this area are responsible for the changes in the redox potential.

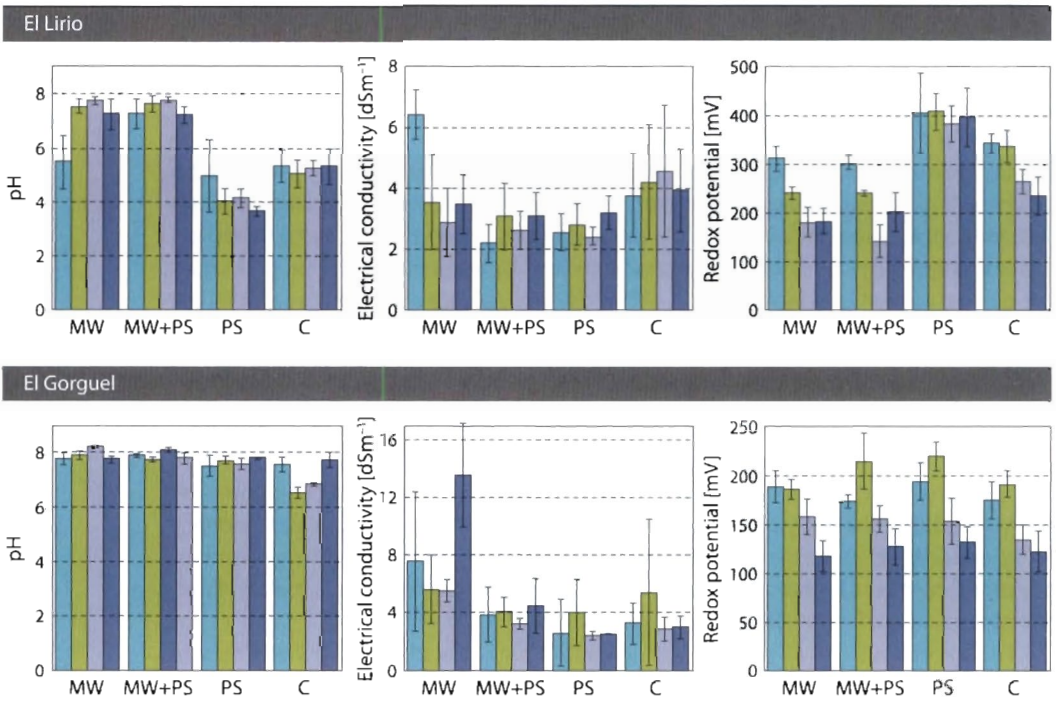
Total Sulphur

Sulphides in the ore deposits and tailing ponds derive from the metalliferous minerals originated by the intense hydrothermal alteration of sub-volcanic rocks from Miocene or Pliocene [Manteca and Ovejero, 1992]. Main sulphides come from pyrite (FeS_2), sphalerite ((Zn, Fe)S) and galena (PbS). The content of sulphides determine the potential acidity of the material, since sulphides oxidize in the presence of O_2, releasing sulphates and protons, as indicated in the following reaction:

$$FeS_2 + 7/2\ O_2 + 3H_2O \rightarrow Fe^{3+} + 2SO_4^{2-} + 2H_3O^+ + e^-.$$

The content of total sulphur in both tailing ponds is very high (25–30 gkg^{-1}), especially in El Gorguel tailing pond, which indicates the potential acidity that can be generated in these ponds, whose data were used for the calculation of the marble waste doses. As can be observed in F.18-10, the variations of total sulphur in the plots do not follow any specific pattern and no effect between treatments was reported. Therefore, the slight differ-

Evolution of pH, EC and Eh in the different plots from El Lirio and El Gorguel tailing ponds F.18-9



ences between plots and periods of time are likely due to the heterogeneity of the tailing material forming the ponds. From the point of view of vegetation, sulphur is an essential element for plant growth, and therefore it must be present in the soil for adequate plant colonization. The amounts of this element in the ponds are more than enough to meet the requirements of potential plants and therefore no deficiencies are expected for this element. However, the generation of acidity and the excessive presence of sulphates could be a limiting factor for plant growth.

Total Nitrogen

Total soil N includes all forms of inorganic soil N. Inorganic N includes soluble forms (e.g., NO_2^- and NO_3^-), exchangeable NH_4^+, and clay-fixed non-exchangeable NH_4^+. Organic N content includes numerous identifiable and non-identifiable forms [Stevenson, 1986] and can be determined by the difference between total soil N and inorganic soil N content. In the abandoned mining areas the loss of soil nutrients due to rapid decomposition of vegetation is an important degradation process. Specifically, losses of nitrogen (N) are often greater than losses of other nutrients [Vitousek et al., 1982].

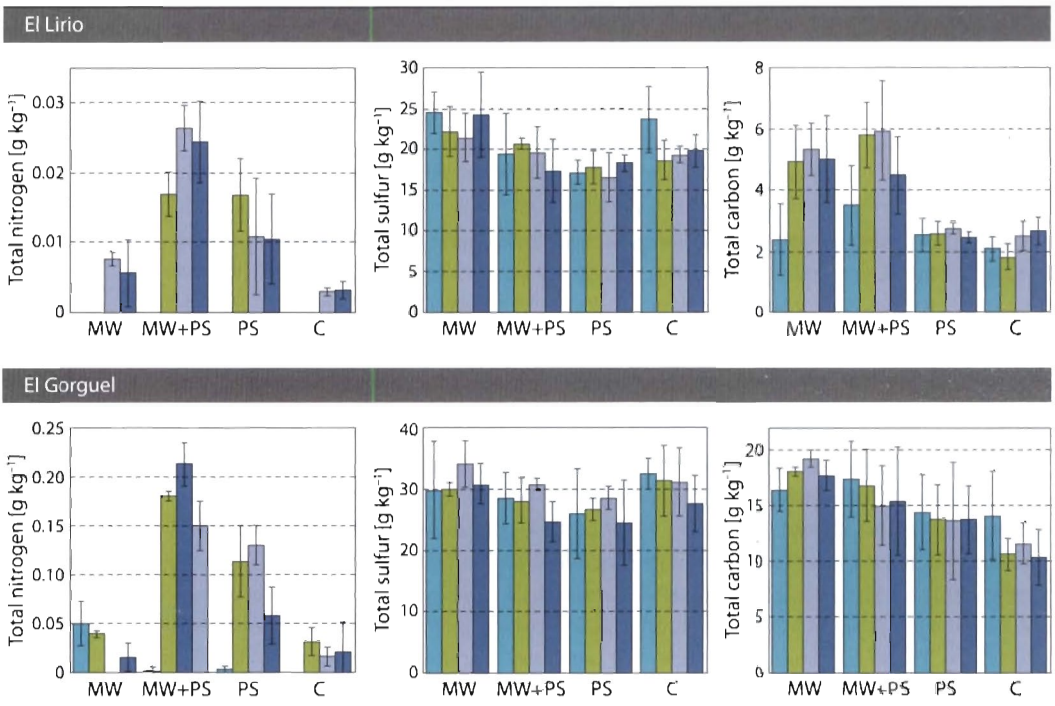
The initial content of nitrogen in both ponds is very scarce, indicating that the presence of nutrients for plant growth is one of the main limiting factors for plant colonization in these ponds. As can be seen in F.18-10, the application of pig slurry results in a significant increase of total nitrogen in the first week and remains six and twelve months after application, however, a decrease after six months is observed, likely due to consumption of nitrogen for plant species and organic matter mineralization and loss for runoff or leaching. Therefore, we can conclude that pig slurry is an important source of this essential element and probably other nutrients, favouring plant colonization; however, a decrease of this element is expected after twelve months.

Total Carbon

Soil carbon is the generic name for carbon held within the soil, primarily in association with its organic content. Soil carbon is the largest terrestrial pool of carbon. Humans have significant impacts on the size of this pool. Soil carbon plays a key role in the carbon cycle and thus is important in global climate models.

The content of total carbon in both studied tailing ponds is very low; however, there are important differences between them. In general, El Gorguel pond has higher content of total carbon than El Lirio (F.18-10), therefore it is expected that the soil conditions in El Gorguel will be more favourable for plant establishment than in El Lirio. However, it must be taken into account that the total carbon in soils is divided in inorganic and organic carbon; and the content of these two pools of carbon in the ponds affects the soil conditions in different ways. A higher presence of inorganic carbon indicates a better buffer capacity against changes of acidity, a better retention of toxic metals and an improvement of the soil structure. On the other hand, a higher presence of organic carbon increases the soil fertility, release of nutrients, better water holding capacity, etc. For these reasons, it is important to study the effect of the used amendments in both organic and inorganic carbon contents.

Evolution of total sulphur, nitrogen and carbon in the different plots from El Lirio and El Gorguel tailing ponds F.18-10



Total Inorganic Carbon

Inorganic carbon occurs in soils generally as carbonate minerals e.g. calcite ($CaCO_3$), dolomite ($CaMg(CO_3)_2$) and siderite ($FeCO_3$). Carbonate in soils can be of primary (inherited from parent material) or secondary (pedogenic) origin. Secondary carbonates are usually aggregates of silt- and clay-sized calcite crystals that are easily identified in grain mounts. Large crystals of calcite or dolomite are of primary origin [Doner and Lynn, 1989]. Soil carbonates affect root and water movement, soil pH [Nelson, 1982], and the nature of the exchange complex [Arnaud and Herbillon, 1973]. The authors showed that soil retention of P, Mn, Zn and Cu was directly related to carbonate content and to the distribution of total and active calcium carbonate between the clay and silt fractions. When total $CaCO_3$ is less than 20%, the retention of those elements is affected mainly by the total amount of carbonates, but, when it is above 20%, nature of the carbonates was more important in governing retention.

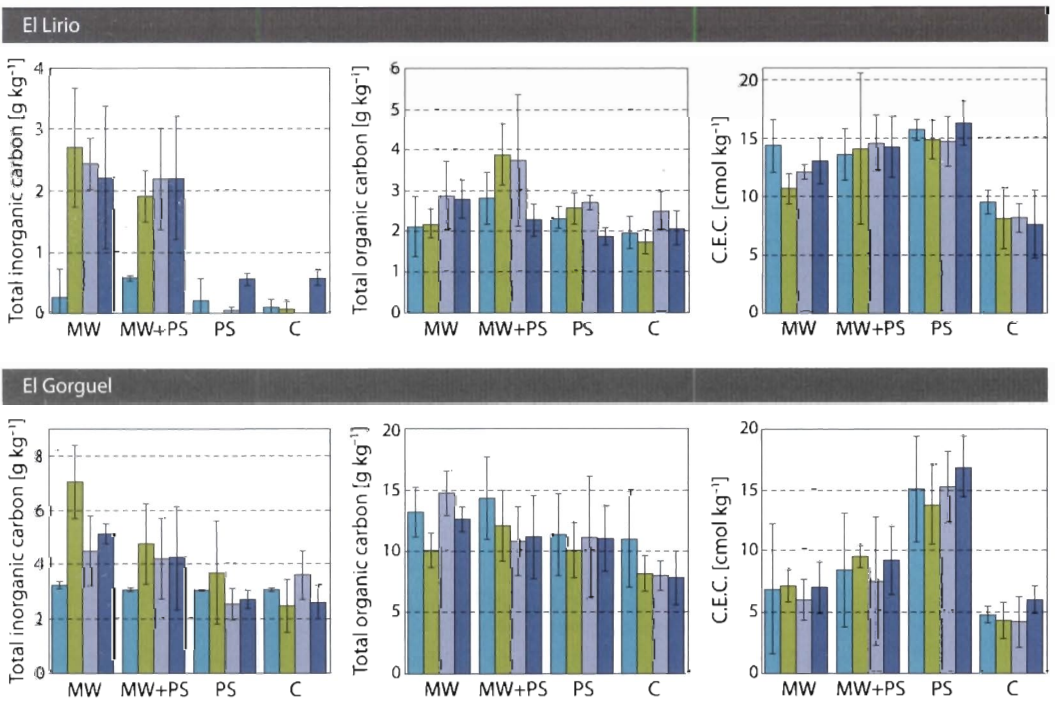
The effect of marble waste application in the inorganic carbon content is immediately observed in both plots where the marble was applied, especially in El Lirio (F.18-11). However, after six months from the application, a slight decrease in the inorganic carbon contents is appreciated, which is likely due to the dissolution of the carbonates in the process of acidity neutralization.

Total Organic Carbon

Soil organic matter is a complex and varied mixture of organic substances. Commonly, soil organic matter is defined as the percentage of humus in the soil. Humus is the unidentifiable residue of plants and animals that becomes fairly resistant to further decay. Soil organic matter, from this point of view, can be divided into two fractions: 1) the recognizable organic material (straw, woodchips, roots, mulches, insects, etc.) with their partially decomposed remains, and 2) humus. Organic matter is very important for the functioning soil system for various reasons. It increases soil porosity, thereby, increasing infiltration and water holding capacity of the soil, providing more water availability for plants and less runoff that may potentially become contaminated. This may be specifically helpful at mine sites where runoff may become acidic and contain high concentrations of heavy metals. The increased porosity also aids in easing tillage of the soil.

In general, El Gorguel tailing pond shows a higher content of organic carbon than El Lirio, indicating that the soil conditions in this pond are better for the spontaneous plant colonization. The effect of pig slurry application in the content of organic carbon in soil is slightly observable after the amendment application (F.18-11). El Lirio tailing pond shows a slight increase in the organic carbon content in plots amended with pig slurry; however, in El Gorguel the effect of pig slurry application in the content of organic carbon is not appreciable, which indicates that the amount of carbon added with the amendment is not enough for increasing significantly the organic carbon content in soil, and therefore future application of organic amendments are recommended.

Evolution of total inorganic carbon, organic carbon and cation exchange capacity in the different plots from El Lirio and El Gorguel tailing ponds F.18-11



Cation Exchange Capacity

Cations are positively charged ions such as calcium (Ca^{2+}), magnesium (Mg^{2+}), potassium (K^{+}), sodium (Na^{+}), hydrogen (H^{+}), aluminum (Al^{3+}), iron (Fe^{2+}), manganese (Mn^{2+}), zinc (Zn^{2+}) and copper (Cu^{2+}). The capacity of soil to hold these cations is called cation exchange capacity (CEC). These cations are held by the negatively charged clay and organic matter particles in the soil through electrostatic forces (negative soil particles attract the positive cations). The cations on the CEC of the soil particles are easily exchangeable with other cations and as a result, they are plant available. Thus, the CEC of a soil represents the total amount of exchangeable cations that the soil can adsorb. F.18-11 shows the effect of amendment application in the cation exchange capacity (CEC) values of the tailing ponds. In general, the cation exchange capacity of El Lirio is higher than in El Gorguel, which is likely due to the different mineralogical composition among both ponds, this indicates that the soils from El Lirio have a higher capacity of retain nutrients. Values of CEC do not significantly change with any of the amendments, and the observable variations are due to heterogeneity of the tailing ponds during the sampling.

Texture

Texture influences plant growth by its direct effect on soil aeration, water infiltration, cation exchange capacity (CEC), and erodibility. Infiltration and permeability are rapid in sandy soils, very slow in clay soils, and intermediate in loam soils. Soils that are granular, with a large diversity in particle size, have many large and small pores, a desirable characteristic for plant growth. Due to the fact that particle soil distribution is very stable during long periods of time, the effect of the amendments has not been evaluated for this soil property. However, the particle size distribution of each plot in both tailing ponds is presented in the F.18-12. The main fraction in both ponds is the sand fraction, with the highest percentages in El Lirio (50 to 80%), followed by silt content, and finally clay percentage, with contents lower than 15%. This particle size distribution indicates that the water holding capacity of these materials is low, and the porosity high.

Stable Aggregates

An aggregate is a group of primary particles that adhere to each other more strongly than to surrounding soil particles [Kemper and Rosenau, 1986]. Aggregate stability can be defined as the resistance to disruption or breakage of the bonds within the aggregates by external forces of impact, shearing, abrasion and internal forces arising from the escape of entrapped compressed air (slaking) and differential swelling. Aggregate stability can serve as an indicator of the resistance of soils to water erosion, surface seal or crust formation, compaction leading to decreased infiltration and subsoil aeration, and as a general soil quality indicator [Doran and Parkin, 1994; Larney et al., 1996; Le Bissonnais and Arrourays, 1996]. Soil aggregates control soil hydrology [Wu et al., 1990], affect soil oxygen diffusion and nutrient availability [Sextone et al., 1985; Wang et al., 2001], influence soil erodibility [Barthes and Roose, 2002] and constitute a pathway of organic carbon stabilization and long term sequestration [Six et al., 2004].

F.18-12 shows the effect of amendment application in the formation of stable aggregates. This parameter was not analysed one week after applications because the aggregate formation needs more time to be observed. After six months the formation of

aggregates was identified in the plots amended with marble and pig slurry alone and in the plots amended with both amendments for both ponds. This indicates that both amendments contribute to the aggregate formation; although, in accord with our results, the marble waste increases the stable aggregates more than pig slurry.

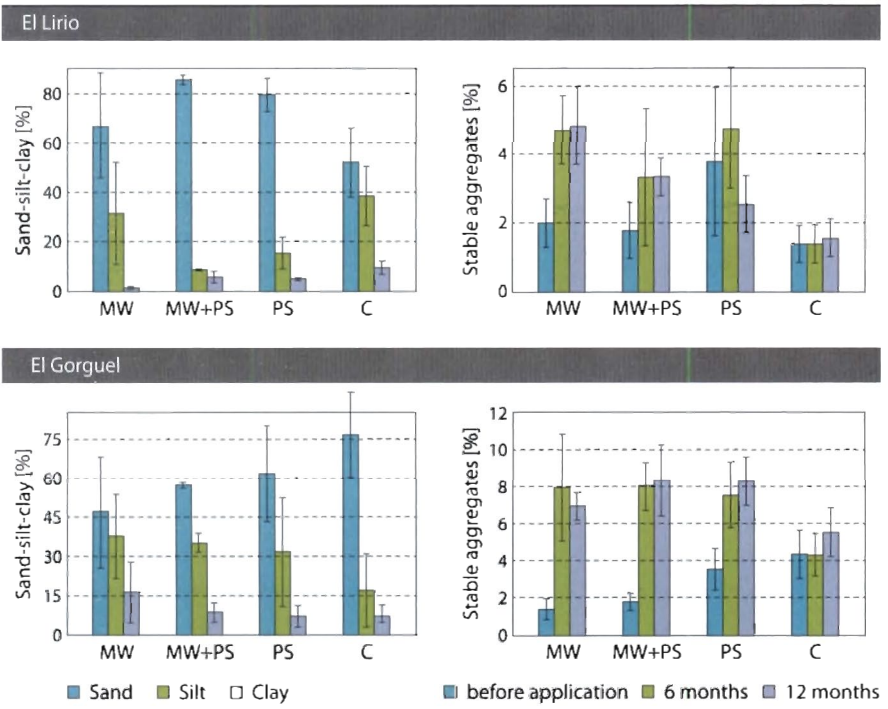
18-6-2 Risk Reduction for Human and Ecosystems

Effect of the Amendments in the Risk of Tailing Pond Erosion

In order to evaluate the effect of the amendment in the risk of tailing pond erosion, land degradation indexes were used. Land degradation, defined as the loss or reduction of the potential utility or productivity of the land [Lal, 1994], is a major environmental problem in arid and semi-arid areas [Chikhaoui et al., 2005], and it can be divided into three classes [Barrow, 1991; Snakin et al., 1996]:

1) physical degradation: including compaction, erosion, loss of water retention, sealing of soil surface etc.,
2) biological degradation: including loss of biodiversity, changes in the rates of microorganisms, contamination by pathogens etc., and
3) chemical degradation: including salinity, alkalinity, heavy metal accumulation, loss of nutrients etc.

Sand, silt and clay distribution in the different plots from El Lirio and El Gorguel tailing ponds F.18-12



Due to the main soil parameters affecting soil erosion are included in the degradation indexes (physical and biological degradation), such as organic matter, aggregate stability and particle size distribution, the evaluation of the amendment effect in these indexes will indicate if the risk of erosion has been reduced by the application of the mentioned amendments. In addition, the evaluation of the total metal content (chemical degradation) in the tailing ponds will be useful to estimate the amount of toxic metals that can be transported by the eroded tailing materials.

Physical Degradation (PDI)

This index was developed by [FAO, PNUMA, UNESCO, 1980] modified by [De Paz et al., 2006]. It is considered the main parameters and properties that play an important role in the evaluation of physical properties of the soil such as porosity, permeability, structure and water retention capacity. They are closely related to water movement, nutrient transport, root penetration, and plant emergence.

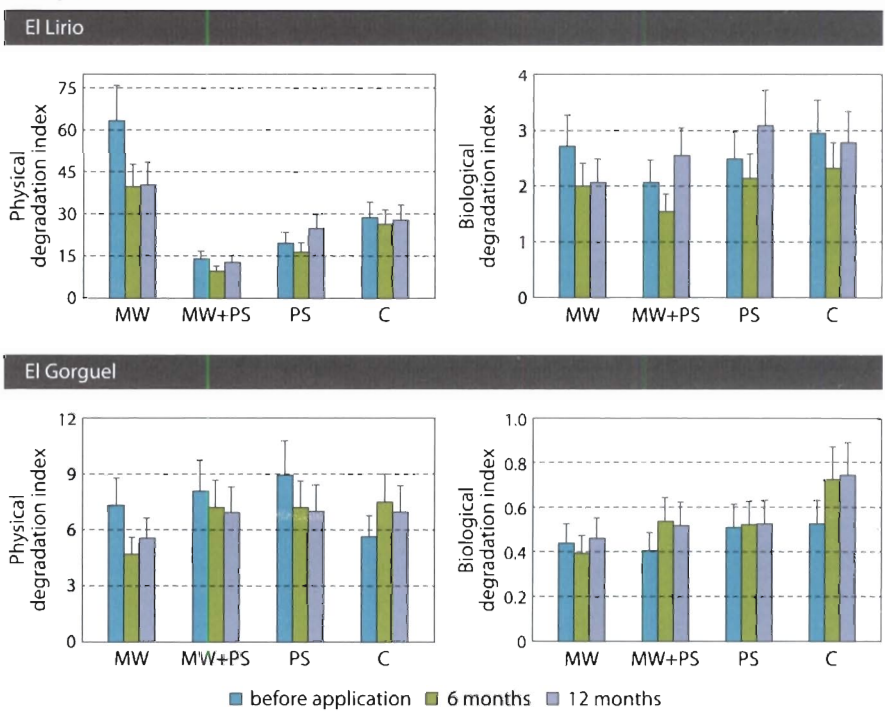
$PDI = (CI / \%SA + (FC - WP) \cdot 100) \cdot 100$

$CI = (1.5 \cdot \%FS + 0.75 \cdot \%CS) / (\%Cy + \%OM \cdot 10)$ [CI: crusting index, FS: fine silt, CS: coarse silt, Cy: clay, OM: organic matter, SA: stable aggregates]

$FC = 0.2391 - 0.0019 \cdot \%Sn + 0.0036 \cdot \%Cy + 0.0299 \cdot \%OM$ [FC: field capacity, Sn: sand]

$WP = 0.0260 + 0.005 \cdot \%Cy + 0.0158 \cdot \%OM$ [WP: wilting point]

Physical and biological degradation indexes for El Lirio and El Gorguel tailing ponds F.18-13



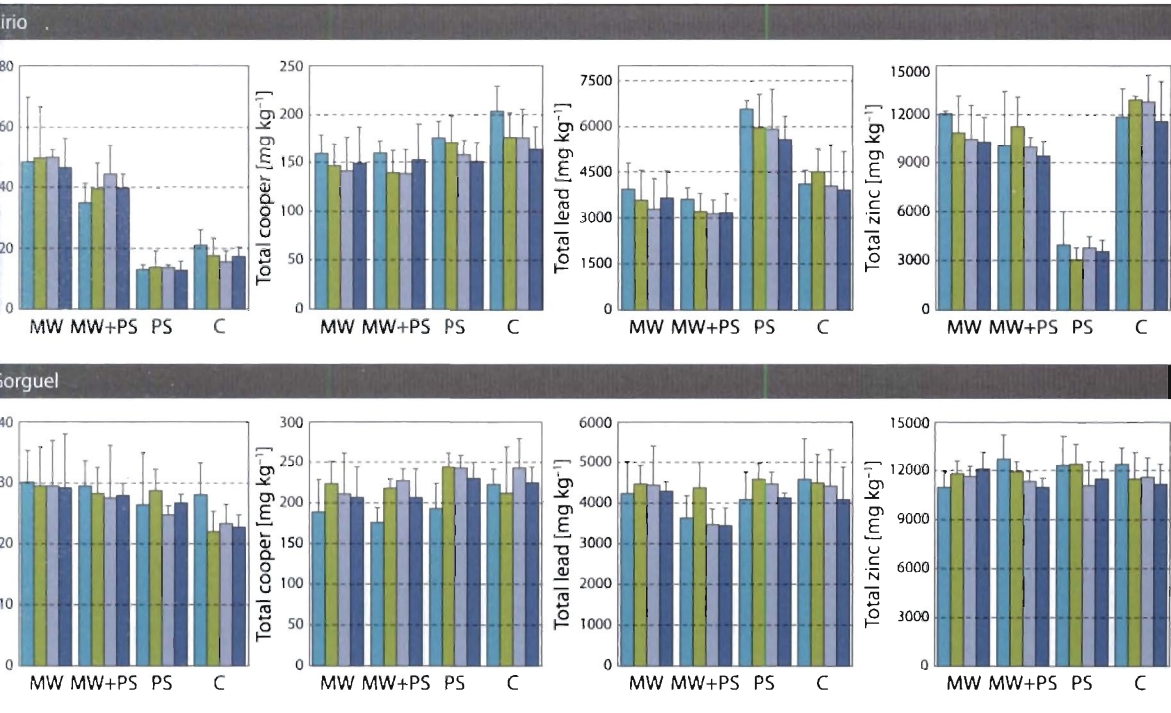
F.18-13 shows the effect of the amendments in the physical degradation index for El Lirio and El Gorguel tailing ponds. Physical degradation in both tailing ponds is generally high, being much higher in El Lirio, which is mainly due to a low content of organic matter and clay, and a high percentage of silt. The relative amounts of these soil constituents result in low water retention capacity, soil crusting etc. causing high physical degradation.

The application of the amendments results in a decrease of the degradation index and therefore less susceptibility to the erosion processes in both ponds, this effect is more intense when marble waste is applied than when pig slurry is used, probably due to formation of stable aggregates using as cemented agent the carbonates (F.18-13). However, after twelve months, the degradation index increased up to the initial values in plot amendments with pig slurry from El Lirio tailing pond; contrarily, the effect of the amendments in the reduction of the physical degradation is maintained over time in El Gorguel.

Biological Degradation (BDI)

This index was proposed by [De Paz et al., 2006], biological degradation is related to the depletion of organic matter content and litter due to a rapid mineralization or soil erosion. This degradation is in part caused by bad soil management practices. Organic matter is the main nutrient source for plants and microorganisms, and also affects the soil aggregation, facilitates the air-entry and water flow and prevents crusting. The biological soil degradation index is: BDI = 1 / OM (OM: organic matter).

Content of total heavy metals in the different plots from El Gorguel and El Lirio tailing ponds F.18-14



As shown in F.18-13, the biological degradation in the tailing ponds is, generally and taking into account the mean of the data, very high for El Lirio and low for El Gorguel, which is, due to the content of organic carbon in El Gorguel, much higher than in El Lirio, therefore it is expected that the erosion processes are more intense in El Lirio.

The application of the amendments, especially pig slurry, results in a decrease of the degradation index in el Lirio, although no effect is appreciable in El Gorguel. However, after twelve months in El Lirio, the degradation index increased up to the initial values, showing that this application is not effective for reducing the biological degradation over time. Therefore, future applications of organic amendments are recommended.

Chemical Degradation

In order to evaluate the chemical degradation of the tailing ponds, total heavy metals were analysed and compared with different legislations. F.18-14 shows the mean values of metals in the plots and in the four sampling periods for both tailing ponds. In addition, the allowed levels of metals for different countries are presented in T.18-1.

The metal with the highest concentrations was zinc, following lead, copper and cadmium in both ponds. In El Lirio tailing ponds some important differences were found between plots, such as the case of cadmium, where the plots amended with pig slurry and

Allowed levels of heavy metals for different countries T.18-1

Country								Reference
European Union	Allowed levels in soils Zn: 150–300 Pb: 50–300 Cu: 50–140 Cd: 1–3							[European Communities Council Directive, 1986]
Italy	Limit A[1] Zn: 150 Pb: 100 Cu: 120 Cd: 2		Limit B[1] Zn: 1500 Pb: 1000 Cu: 600 Cd: 15					[Ministerial Decree, 1999]
The Netherlands	Level A[2] Zn = 50 + 1.5(2C + OM) Pb = 50 + C + OM Cu = 15 + 0.6(C + OM) Cd = 0.4 + 0.007(C + 3OM)		Level B[2] Zn: 500 Pb: 150 Cu: 100 Cd: 5		Level C[2] Zn: 3000 Pb: 600 Cu: 500 Cd: 20			[Ewers, 1991]
The Netherlands	Target value Zn: 140 Pb: 85 Cu: 36 Cd: 0.8		Intervention value Zn: 720 Pb: 630 Cu: 190 Cd: 12					[Ministry of Housing, 1994]
Spain*	pH < 7 Zn: 150 Pb: 50 Cu: 50 Cd: 1		pH > 7 Zn: 450 Pb: 300 Cu: 210 Cd: 3					[B.O.E., 1990]
Canada	Level A[3] Zn: 110 Pb: 50 Cu: 40 Cd: 1.5		Level B[3] Zn: 500 Pb: 500 Cu: 100 Cd: 5		Level C[3] Zn: 1500 Pb: 1000 Cu: 500 Cd: 20			[Ministere de l'Environnement du Québec, 2001]
Turkey	Clean Zn: 300 Pb: 100 Cu: 50 Cd: 1		Polluted Zn: 500 Pb: 150 Cu: 100 Cd: 5		Extr. Polluted Zn: 3000 Pb: 600 Cu: 500 Cd: 20			[T.S.P.C.R., 2000]

[1] Limit A: public and private green areas and residential use; limit B: commercial and industrial use.
[2] Limit A: reference value; level B: maximum allowable limits; level C: decontamination measures.
[3] Limit A: background level; level B: maximum acceptable limit for residential, recreational and institutional sites; level C: maximum acceptable limit for commercial and industrial sites.
* Agricultural soils

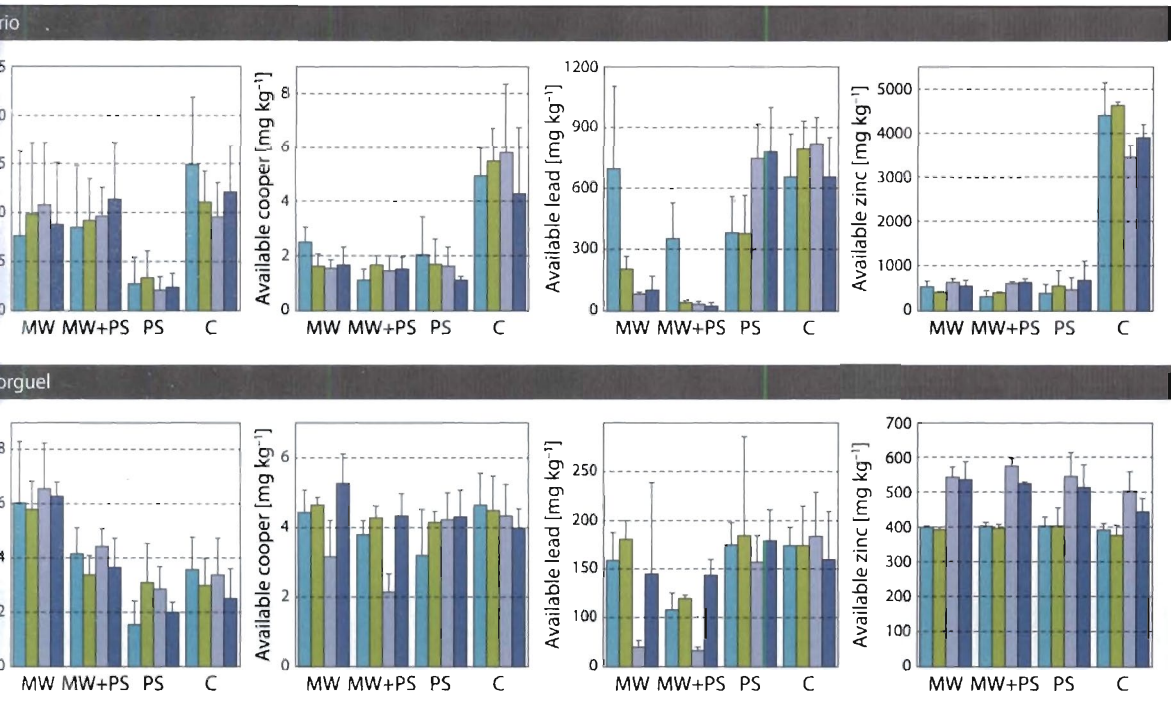
control showed lower concentration than in the other two plots; also the plot amended with pig slurry presented the lowest concentration of zinc compared with the others plots. This behaviour indicates that the waste material forming the ponds is very heterogeneous in the concentration of some metals. Contrarily, in El Gorguel the concentration of each metal in the different plots is more homogeneous, and no important differences between plots were found. Total Cd, Cu, Zn and Pb were above European legislation thresholds [Directive 86/278/ECC, 1986] and most of the compared laws for both ponds and all plots. In accord with the results, no changes with the application of amendments were found, and the variations between concentrations for a specific plot in the different periods of sampling are due to the natural heterogeneity of the tailing materials.

Effect of the Amendments in the Risk of Metals Mobility to the Food Chain

Heavy metals were extracted using DTPA, which is a chelating agent that adsorbs the amount of metals that can be potentially uptaken by plants. Therefore, with the results from this analysis we can determine the potential risk of metal mobility to the food chain, these data are shown in F18-15 for El Lirio and El Gorguel.

In El Lirio, the effect of marble waste was observed in the concentration of available copper, but especially efficient were the levels of available lead (F18-15). The concentrations of these metals decrease immediately with the application of marble. In the case of lead, the available lead decreased from 17% to 5% and was maintained over time,

Effect of the amendments in the content of available heavy metals in the different plots from El Lirio and El Gorguel tailing ponds F.18-15



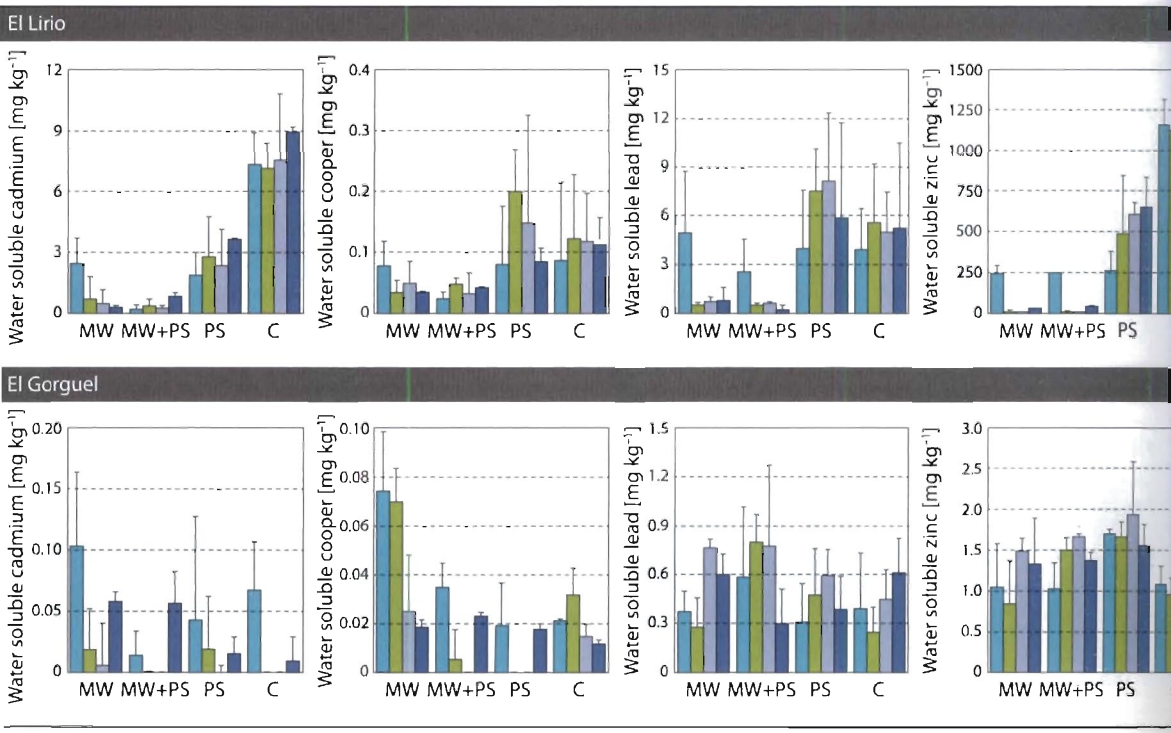
also in the plots amended with marble waste and pig slurry an important decrease was observed, from 10 % to 2 % and also maintained over time. Likely, the formation of stable compounds of carbonates-lead promotes the precipitation of Pb and its reduction in the concentration of available lead. Oppositely, the application of pig slurry alone increased the available Pb after six months from the amendment application, which can be due to formation of organic ligands with lead increasing its mobility. For the rest of the metals no significant differences were observed after amendment application.

In El Gorguel, the effect of marble waste in the reduction of available lead and copper was observed after six months from the amendment application, however, after twelve months the concentrations of these metals went back to the initial concentrations, which indicates that the efficiency of the treatment was not maintained over time. In the case of zinc, a similar pattern was observed for all plots, after six months the concentration of available zinc was increased independent of the treatment, therefore likely an external factor produced this behaviour and cannot be attributed to the applied amendments.

Effect of the Amendments in the Risk of Heavy Metal Leaching

In order to determine the potential concentration of metals that can be mobilized by the effect of rainfall, runoff or leaching, heavy metals were extracted using deionised water. With the results from this analysis we can determine the potential risk of metals leaching, these data are shown in F.18-16 for El Lirio and El Gorguel.

Effect of the amendments in the content of water soluble metals in the different plots from El Lirio and El Gorguel tailing ponds F.18-16



The effect of marble waste reduced the water soluble fraction of cadmium, copper, zinc and lead in El Lirio tailing pond (F.18-16), this decrease can be due to the formation of insoluble carbonates from marble waste [Alvarenga et al., 2008; Liu et al., 2009]. Oppositely, the application of pig slurry increased the concentration of water soluble metals (Cu, Pb, Zn and Cd), which was probably achieved by the effects of complexation by organic matter from pig slurry. In the case of El Gorguel (F.18-16), due to the initial concentrations of soluble metals are very low, the effect of amendments is not easily observed, and probably the variation in the water soluble concentrations are due to other factors more than the effect of the applied amendments.

18-6-3 Evolution of Vegetation after Amendment Application

Soil erosion is increased if the soil has no or very little plant cover. Vegetation cover protects the soil from raindrop impact and splash, tends to slow down the movement of surface runoff and allows excess surface water to infiltrate. The lack of permanent vegetation cover also results in extensive erosion by wind. Loose, dry, bare soil is the most susceptible. The erosion-reducing effectiveness of plant covers depends on the type, extent and quantity of cover. Plant diversity completely covers the soil and intercepts all falling raindrops at and close to the surface, and thus is most efficient in controlling soil erosion. The effectiveness of any vegetation community depends on how much protection is available at various periods during the year, relative to the amount of erosive rainfall that falls during these periods. In this respect, perennial plants, principally grasses, provide a protective cover for a major portion of the year. The absence of vegetation rapidly increases erosion rates and transfer of toxic heavy metals by wind and runoff to the surroundings, including populated areas. Thus, vegetation cover can be used as indicator of erosion risk.

Evolution of vegetation in El Gorguel (top) and El Lirio (bottom) ponds (0, 6 and 12 months) F.18-17



At the beginning of the experiments in El Lirio and El Gorguel tailing ponds, vegetation cover was practically null (F.18-17), with the presence of some sparse stems of *Piptatherum miliaceum, Dittrichia viscosa, Zygophyllum fabago, Diplotaxis lagascana, Phragmites australis* and *Tamarix canariensis*.

Although the vegetation in the tailing ponds was practically absent, the application of amendments conducted to spontaneous colonization of vegetation by the surrounding environment (T.18-2, F.18-17). After six months from the amendment application, in El

Natural colonization of plant species on the different plots from Lirio and Gorguel tailing ponds 6 and 12 months after amendment application T.18-2

	Richness		Vegetation cover [%]		Biodiversity		Plant species	
El Lirio	**6 months**	**12 months**	**6 months**	**12 months**	**6 months**	**12 months**	**6 months**	**12 months**
MW	1	1	0.26	0	0	0	*Zigophyllum fabago*	*Zigophyllum fabago*
MW + PS	5	5	0.52	1.1	0.3	0.3	*Zigophyllum fabago, Phragmites australi, Sonchus tenerrimus, Cakile maritima*	*Piptatherum miliaceum, Zigophyllum fabago, Sonchus tenerrimus, Atriplex halimus, Cakile maritima*
PS	2	5	0.02	2.4	0.1	0.3	*Zigophyllum fabago, Monocotidelónea*	*Zigophyllum fabago, Piptatherum miliaceum, Sonchus tenerrimus, Atriplex halimus, Cakile maritima*
C	0	1	0	0.1	0	0	absence	*Zigophyllum fabago*
El Gorguel								
MW	1	1	0	0	0	0	*Zigophyllum fabago*	*Salsola kali*
MW + PS	5	10	1.1	25.0	0.3	1.3	*Piptatherum miliaceum, Zigophyllum fabago, Sonchus tenerrimus, Atriplex halimus, Cakile maritima*	*Zigophyllum fabago, Piptatherum miliaceum, Beta vilgaris, Dittrichia viscosa, Atriplex halimus, Salsola kali, Chenopodium album, Sonchus tenerrimus, Chenopodium murale, Diplotaxis lagascana*
PS	5	10	2.4	33.3	0.3	1.1	*Zigophyllum fabago, Piptatherum miliaceum, Sonchus tenerrimus*	*Zigophyllum fabago, Dittrichia viscosa, Sonchus tenerrimus, Piptatherum miliaceum, Diplotaxis lagascana, Atriplex halimus, Cakile maritima, Beta vilgaris, Hordeum murinum*
C	1	2	0.1	5.0	0	0.5	*Atriplex halimus, Cakile maritima, Zigophyllum fabago*	*Zigophyllum fabago, Salsola kali*

Lirio tailing ponds, only *Zigophyllum fabago* was present in the marble waste plot, however, in the plots amended with pig slurry the biodiversity was higher with the presence of *Zigophyllum fabago*, *Monocotidelónea*, *Phragmites australis*, *Sonchus tenerrimus*, *Cakile maritime* in the plot amended with marble waste and pig slurry. In the Gorguel, the results were slightly better with the presence of *Piptatherum miliaceum*, *Zigophyllum fabago*, *Sonchus tenerrimus*, *Atriplex halimus*, *Cakile maritime* in the plots amended with pig slurry and a vegetation cover higher than in El Lirio tailing pond.

After twelve months from the amendment application (T.18-2, F.18-17), in El Lirio tailing ponds, only *Zigophyllum fabago* was still present in the marble waste and control plots, however, in the plots amended with pig slurry the biodiversity was higher with the presence of *Piptatherum miliaceum*, *Zigophyllum fabago*, *Sonchus tenerrimus*, *Atriplex halimus*, *Cakile maritime*, also the vegetation cover was slightly higher than six months before but still very low.

In the case of El Gorguel tailing pond the results were different, the marble waste plot remained practically bare, with the presence of some sparse stems of *Salsola kali*. The only species able to grow in the control plot were *Zigophyllum fabago* and *Salsola kali*, while in the plots receiving the organic amendment a richness of 10 was reached, with higher vegetation cover (25–30 %) and biodiversity (H = 1.1–1.3). The understanding of the processes implied in the primary vegetation succession initialized after colonizer establishment is crucial to avoid degradation processes. The fact that two plant species are growing in the control plot may indicate that these concrete species are resistant to highly extractable metal concentrations and, therefore, the previous absence of them may be likely due to adverse physical conditions for vegetation establishment. The initial tillage contributed to reduce compaction and bulk density, increasing porosity, which triggered the germination of seeds and development of seedlings. The application of pig slurry contributed to the improvement of soil fertility facilitating a higher colonization of natural vegetation. In MW plot, the development of plants was inhibited likely due to the presence of higher contents of soluble sulphate salts and clay.

18-6-4 Landscape Design of Tailing Ponds

Mine reclamation has to be formed an integral part of the planning process which includes feasibility studies and environmental impact assessment for new mines. The following objectives have to be provided by the help of reclamation [Mchaina, 2001]:

1) to allow a productive and sustainable post-mining use of the site;
2) to protect public health and safety;
3) to alleviate or eliminate environmental damage;
4) to conserve valuable attributes,
5) to minimize adverse socio-economic impacts.

The aim of design approach is not only recovering the health and biodiversity of ecosystems across the site, but also the spirit and imagination of people who will use the new park by using the ecological process of environmental reclamation.

The problematic features of the area can be transformed to a functional stage by providing their association with landscape components (F.18-18). With a controlled us-

age such as tampon zones, fences etc., the physical character of tailing ponds and colour of acid mine drainage pools can be seen aesthetic and can provide a touristic attraction centre in the region. Solutions for environmental risks can be combined with the main landscape value or specifically with one of the landscape components. For example in our case, phytostabilization can be seen the way of solution for various environmental problems of the area. The phytostabilization process itself has a didactic value which can be utilized in a thematic park in order to improve the knowledge of users. Also mining elements (engine houses, shafts, headframes etc.) can be represented by providing their safeness and restoration; their educative and museum effect can be helpful in the reforming of the area. In this situation the didactic value can be the main value of the area which is prominent in all, or a sub-value which is auxiliary for the main value. Transformation of the ultimate land use decision to a landscape design has to be realized delicately by professions from different disciplines.

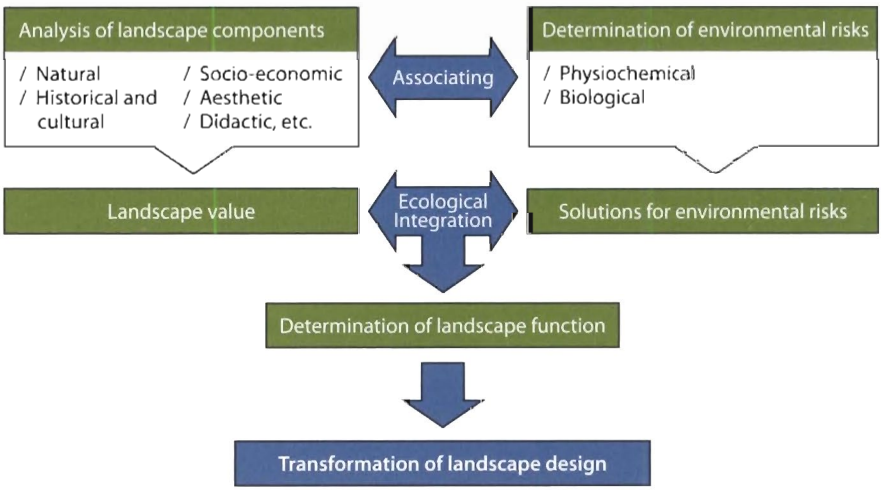
Landscape design approach, which is emerged related to phytostabilization studies in Cartagena-La Union Mining District, required associations between values and solutions. By considering this association, a general approach was tried to explain in order to light the way for similar cases.

Conceptual Landscape Design Application in Tailing Ponds

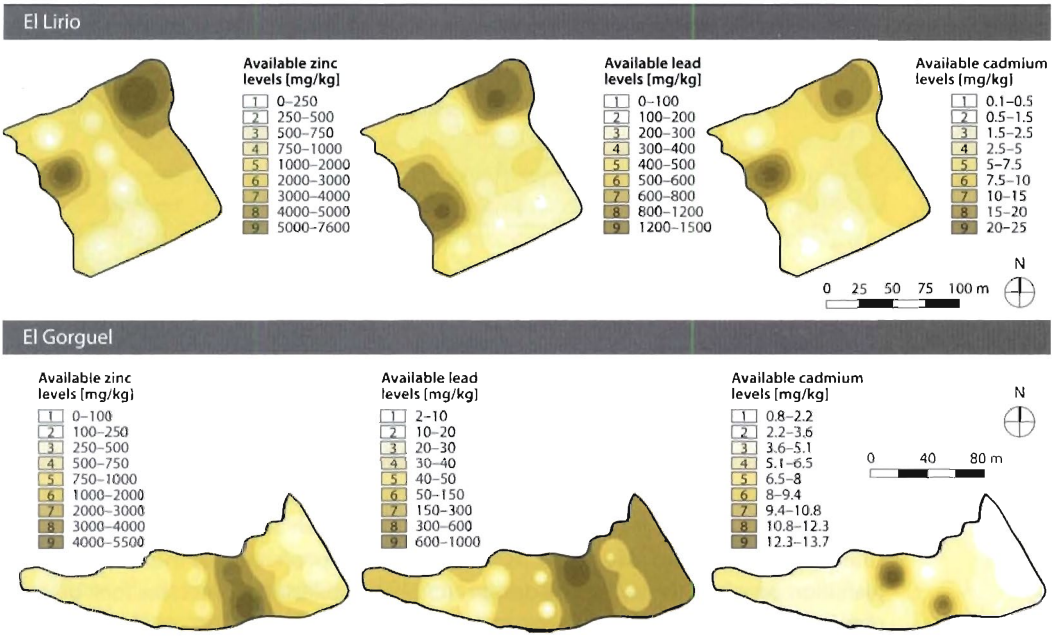
In available heavy metal distribution maps of El Lirio and El Gorguel (F.18-19) mine tailings it is possible to see nine different level polluted areas according to their heavy metal (Zn, Pb, Cd) content.

With respect to the soil plant toxicity levels, 400 mg Zn kg^{-1}, 100–500 mg Pb kg^{-1}, and 3 mg Cd kg^{-1} [Kabata-Pendias, 2001], in El Lirio; Zn is not toxic in level 1 of the area and is partially acceptable in level 2, but in the rest of the mine tailing Zn is approximately from 1.8 to 19 times toxic for plants. Pb is not toxic in the levels 1, 2, 3, 4 and 5 of the area. However, Pb toxicity from levels 6 to 9 of the area reaches until three times more than index.

Scheme of the landscape design approach in problematic areas F.18-18



Spatial distribution of available metals in El Lirio and El Gorguel mine tailing pond F.18-19



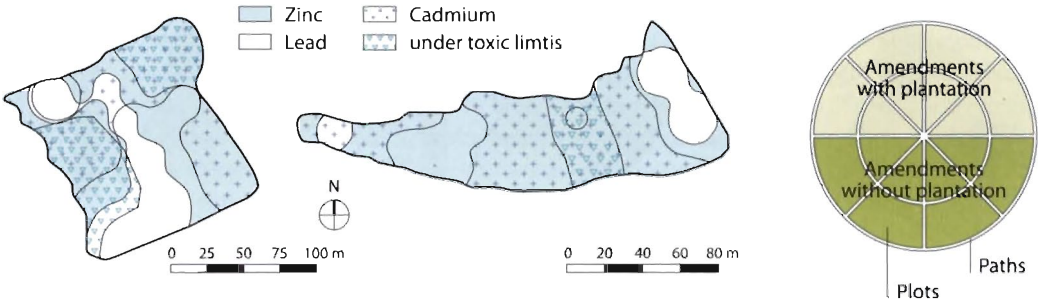
With respect to Cd amount, it is not toxic in levels 1, 2 and 3 of the area, is partially acceptable in level 4, while in the rest Cd toxicity is ranging from 2.5 to 8.3 times for the plants. In El Gorguel; Zn is not toxic in level 1 and 2, partially acceptable in 3, and in the rest almost 14 times toxic for plants. Pb is not toxic until level 7, partially acceptable in 8, and in the last level 2 times toxic. Cadmium is not toxic in 1, partially acceptable in 2, and in the rest until 4 times it seems toxic for plants.

In regard to these gradual changes of available heavy metal density of phytostabilizion measures were separated into graded ranks and the areas which will serve to public use were determined. In F.18-20 toxic amount distribution of metals and the parts under toxic limits is shown. In order to observe the phytostabilization effect of native species triggered by amendments, we suggested establishing experimental trials in the most polluted parts of the tailing ponds. F.18-20 shows the proposed design of the experimental areas which are based on Mel Chin's Revival Field [Collins, 2000; Felson and Pickett, 2005].

The aim is to reduce or eliminate the negative effects on environment and public health of the tailing ponds by creating functional and sustainable landscapes as shown in the F.18-21, which presents the ideal concept designs of tailing ponds.

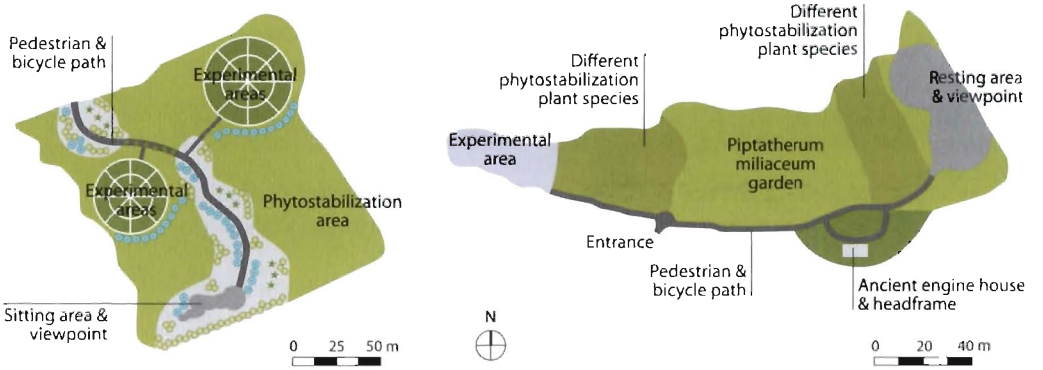
In the conceptual landscape design of the ponds, only the area in which the toxicity level under limits was opened to the visitors as a resting-sitting area and viewpoint. Visitors were not allowed to enter the phytostabilization areas because of the maintenance requirement of phytostabilization processes. Beside phytostabilization plantation, the use

Distribution of toxic metal amounts in El Lirio and El Gorguel Tailing Ponds and Proposed design of the experimental areas F.18-20



of native ornamental plant species was suggested, especially in non contaminated areas for several aims such as increasing attraction, redirecting of visitors. The surroundings of phytostabilization areas were closed by native ornamental plants and fences. In the most contaminated areas of the tailing pond, phytostabilization experimental areas were located in order to make investigations related to the improvement of the technique. Explanation panels of the landscape design and phytostabilization processes took place in required points. The paths were also suitable for the use of bicyclists. At the end of the paths, in the most scenic place of the area, resting and sitting areas were located. In order to provide shadow in this area, pergolas and/or gazebos were proposed. Connection with the cultural heritage was provided with the consideration of the restoration of ancient engine house and headframe.

Proposed design for El Gorguel and El Lirio mine tailings F.18-21



References

Acosta, J. A., Faz, A., Martinez-Martinez, S., Zornoza, R., Carmona, D. M. and Kabas, S., 2011. *Multivariate Statistical and GIS-Based Approach to Evaluate Heavy Metals Behavior in Mine Sites for Future Reclamation*. Journal of Geochemical Exploration 109:8–17.

Alvarenga, P., Gonçalves, A. P., Fernandes, R. M., de Varennes, A., Vallini, G., Duarte, E. and Cunha-Queda, A. C., 2008. *Evaluation of Composts and Liming Materials in the Phytostabilization of a Mine Soil Using Perennial Ryegrass*. Sci. Total Environ. 406:43–56.

Arnaud, R. J. and Herbillon, A. J., 1973. *Occurrence and Genesis of Secondary Magnesium-bearing Calcites in Soils*. Geoderma 9:279–298.

Barrow, C. J., 1991. *Land Degradation: Development and Breakdown of Terrestrial Environments*. Cambridge University Press, 295 pp.

Barthes, B. and Roose, E., 2002. *Aggregate Stability as an Indicator of Soil Susceptibility to Runoff and Erosion: Validation at Several Levels*. Catena 47:133–149.

Burley, J. B., 2001. *Post-Mining Land Use Reclamation: An Introduction from a Planning and Design Perspective*. Burley, J. B., (Ed.), Environmental design for reclaiming surface mines. The Edwin Mellen Press, Lewiston, New York, USA, 1–25.

Chapman, H. D. ,1965. *Cation Exchange Capacity*. In C. A. Black (ed). Methods of Soil Analysis. American Society of Agronomy, Madison, Wisconsin, USA, 2:891–900.

Chikhaoui, M., Bonn, F., Bokoye, A. and Merzouk, A., 2005. *A Spectral Index for Land Degradation Mapping Using ASTER Data: Application to a Semi-Arid Mediterranean Catchments*. International Journal of Applied Earth Observation and Geoinformation 7:140–153.

Collins, G., 2001. *The Principles of Mining*. Burley, J. B., (Ed.), Environmental design for reclaiming surface mines. The Edwin Mellen Press, Lewiston, New York, USA, 27–47.

Collins, T., 2000. *Interventions in the Rust Belt: the Art and Ecology of Post-Industrial Public Space*. Cultural Geographies in Practise. Ecumene 2000, ISSN: 0967-4608, 7(4):461–467.

Conesa, H. M. and Faz, A., 2009. *Metal Uptake by Naturally Occurring Vegetation in a Metal Polluted Salt Marsh in Southeast Spain*. Faz, A., Mermut, A.R., Arocena, J.M., Ortiz, R., (Eds.), Land Degradation and Rehabilitation. Catena Verlag GmbH, Germany, 287–294.

Conesa, H. M., Robinson, B. H., Schulin, R. and Nowack, B., 2007. *Growth of Lygeum Spartum in Acid Mine Tailings: Response of Plants Developed from Seedlings, Rhizomes and at Field Conditions*. Environmental Pollution 145:700–707.

De Paz J. M., Sánchez, J. and Visconti, F., 2006. *Combined Use of GIS and Environmental Indicators for Assessment of Chemical, Physical and Biological Soil Degradation in a Spanish Mediterranean Region*. Journal of Environmental Management 79:150–162.

Directive 86/278/ECC, 1986. *Protection of the Environment, and in Particular of the Soil, when Sewage Sludge is Used in Agriculture*. Official journal L 181.

Directive 91/676/EEC, 1991. *Protection of Waters against Pollution caused by Nitrates from Agricultural Sources*. Official Journal L 375:1–8.

Doner, H. E. and Lynn, W. C., 1989. *Carbonate, Halide, Sulphate and Sulphide Minerals*. In J. B. Dixon and S. B. Weed, Eds., Minerals in Soil Environments, 2nd ed. Soil Science society of America, Madison, WI, 279–330.

Doran, J.W. and Parkin, T.B., 1994. *Defining and Assessing Soil Quality*. In J.W. Doran, D.C. Coleman, D.F. Bezdicek, and B.A. Stewart, Eds. Defining Soil Quality for a Sustainable Environment. SSSA Special Publications No. 35, American Society of Agronomy, Madison, WI, 3–21.

Doumett, S., Lamperi, L., Checchini, L., Azzarello, E., Mugnai, S., Mancuso, S., Petruzzelli, G. and Del Bubba, M., 2008. *Heavy Metal Distribution between Contaminated Soil and Paulownia Tomentosa*. In a pilot-scale assisted phytoremediation study: Influence of different complexing agents. Chemosphere, 72:1481–1490.

Ernst, W.H.O., 1996. *Bioavailability of Heavy Metals and Decontamination of Soils by Plants*. Appl. Geochem. 11:163–167.

FAO, PNUMA, UNESCO, 1980. *Metodología Provisional Para la Evaluación de la Degradación de Los Suelos*. FAO, Rome.

FAO, 2006. *Guidelines for Soil Description*. 4th edition, Rome.

FAO-ISRIC, 2006. *World Reference Base for Soil Resources 2006*. World Soil Resources Reports No. 103. FAO, Rome, Italy.

Faz, A., Lozano R.A., Conesa, H.M. and García, G., 2001. *Soils Affected by Mining and Industrial Activities in Cartagena (SE Spain): Classification Problems*. European Soil Bureau, Research Report 7:165–170.

Felson, A.J. and Pickett, S.T.A., 2005. *Designed Experiments: New Approaches to Studying Urban Ecosystems*. Frontiers in Ecology and the Environment, 3(10):549–556.

Ji, P., Sun, T., Song, Y., Ackland, M.L. and Liu, Y., 2011. *Strategies for Enhancing the Phytoremediation of Cadmium-Contaminated Agricultural Soils by Solanum Nigrum L.* Environmental Pollution 159:762–768.

Kabata-Pendias, A. and Pendias, H., 2001. *Trace Element in Soils and Plants*. 3rd edition, CRC Press, Boca Raton, Florida, USA.

Kemper, W.D. and Rosenau, R.C., 1986. *Aggregate Stability and Size Distribution*. In A. Klute, Ed. Methods of Soil Analysis, Part 1: Physical and Mineraological Methods, 2nd ed., ASA/SSSA, Madison, WI, 425–442.

Lal, R., 1994. *Soil Erosion Research Method*. Soil and Water Conservation Society. St. Lucie Press, Delray Beach, Florida.

Larney, F.J., Janzen, H.H., Olson, B.M., Bullock, M.S. and Selinger, L.J., 1996. *Aggregate Stability: A Soil Quality Indicator for Southern Alberta Soils*. In Proc. 33rd Annual Alberta Soil Science Workshop, February 20–22, 1996, Edmonton, AB, Canada, 262–267.

Le Bissonnais, Y. and Arrourays, D., 1996. *Aggregate Stability and Assessment of Soil Crustability and Erodibility: II. Application to Humic Loamy Soils with Various Organic Carbon Contents*. Journal of Soil Science 48:39–48.

Lindsay, W.L. and Norvell, W.A., 1978. *Development of a DTPA Soil Test for Zn, Fe, Mn, and Cu*. Soil Science Society of America Journal 42:421–428.

Liu, L., Chen, H., Cai, P., Liang, W. and Huang, Q., 2009. *Immobilization and Phytotoxicity of Cd in Contaminated Soil Amended with Chicken Manure Compost*. Journal of Hazardous Materials 163:563–567.

Manteca, J.I. and Ovejero, G., 1992. *Los Yacimientos Zn, Pb, Ag-Fe del Distrito Minero de La Unión-Cartagena, Bética Oriental*. In: García Guinea J., Martínez Frías J. (eds). Recursos Minerales de España. Madrid. CSIC, 1085–1101.

McBride, M.C. 1994. *Environmental Chemistry of Soils*. Oxford University Press, Oxford, UK.

Mchaina, D.M., 2001. *Environmental Planning Considerations for the Decommissioning, Closure and Reclamation of a Mine Site.* International Journal of Surface Mining, Reclamation and Environment 2001, 15(3):163–176.

Nelson, R.E., 1982. *Carbonate and Gypsum.* In A.L. Page et al., Eds., Methods of Soil Analysis, Part 2: Chemical and Microbiological Properties and Crop Yield across and Eroded Prairie Landscape. Journal of Soil and Water Conservation 60:47–54.

Norvell, W.A., 1984. *Comparison of Chelating Agents as Extractants for Metals in Diverse Soil Materials.* Soil Science Society of America Journal 48:1285–1292.

Peech, M., 1965. *Hidrogen-Ion Activity.* C.A. Black (ed.). Methods or Soil Analysis. American Society of Agronomy, Madison, Wisconsin, U.S.A., 2:914–916.

Pérez-Esteban, J., Escolástico, C., Ruiz-Fernández, J., Masaguer, A. and Moliner, A., 2011. *Bioavailability and Extraction of Heavy Metals from Contaminated Soil by Atriplex Halimus.* Environmental and Experimental Botany, doi:10.1016/j.envexpbot.2011.12.003.

Peters, T.H., 1984. *Rehabilitation of Mine Tailings: A Case of Complete Ecosystem Reconstruction and Revegetation of Industrially Stressed Lands in the Sudbury Area, Ontario, Canada.* Sheehan, P.J., Miller, D.R., Butler, G.C., Bourdeau Ph., (eds.), Effects of pollutants at the ecosystem level. Published by John Wiley & Sons Ltd.

Risser, J.A. and Baker, D.E., 1990. *Testing Soils for Toxic Metals.* In R.L. Westerman (Ed.), Soil Testing and plant analysis (275–298). Madison: Soil Science Society of America Special Publication.

Sasmaz, A. and Sasmaz, M., 2009. *The Phytoremediation Potential for Strontium of Indigenous Plants Growing in a Mining Area.* Environmental and Experimental Botany 67:139–144.

Sextone, A.J., Revsbech, N.P., Parkin, T.B. and Tiedje, J.M., 1985. *Direct Measurement of Oxygen Profiles and Denitrification Rates in Soil Aggregates.* Soil Science Society of America Journal 49:645–651.

Six, J., Bossuyt, H., Degryze, S. and Denef, K., 2004. *A History of Research on the Link between Aggregates, Soil Biota, and Soil Organic Matter Dynamics.* Soil and Tillage Research 79:7–31.

Smith, R.A.H. and Bradshaw, A.D., 1979. *The Use of Metal Tolerant Plant Populations for the Reclamation of Metalliferous Wastes.* Journal of Applied Ecology 16:595–612.

Snakin V.V., Krechetov P.P., Kuzovnikova T.A., Alyabina I.O., Gurov A.F. and Stepichev, A.V., 1996. *The System of Assessment of Soil Degradation.* Soil Technology 8:331–343.

Sobek, A.A., Schuller, W.A., Freeman, J.R. and Smith, R.M., 1978. *Field and Laboratory Methods Applicable to Overburdens and Minesoils.* Report EPA-600/2-78-054, U.S. National Technical Information Report PB-280 495.

Stevenson, F.J. 1986. *Carbon Balance of the Soil and Role of Organic Matter in Soil Fertility.* In Cycles of soil. Ed Wiley and Son.

Stevenson, F.J., 1994. *Humus Chemistry: Genesis, Composition, Reactions.* 2nd ed. Wiley, New York.

Tordoff, G.M., Baker, A.J.M. and Willis, A.J., 2000. *Current Approaches to the Revegetation and Reclamation of Metalliferous Mine Wastes.* Chemosphere 41:219–228.

USDA, 1999. *Soil Quality Test Kit Guide.* United Stated Department of Agriculture (ed.) Washington, 82 pp.

Vitousek, P.M., Gosz, J.R., Grier, C.C., Melillo, J.M. and Reiners, W.A., 1982. *A Comparative Analysis of Potential Nitrification and Nitrate Mobility in Forest Ecosystems*. Ecological Monographs 52:155–177.

Wang, X., Yost, R.S. and Linquist, B.A., 2001. *Soil Aggregate Size Affects Phosphorous Desorption from Highly Weathered Soils and Plant Growth*. Soil Science of America Journal 65:139–146.

Wong, M.H., 2003. *Ecological Restoration of Mine Degraded Soils, with Emphasis on Metal Contaminated Soils*. Chemosphere 50:775–780.

Wu, L., Vomocil, J.A. and Childs, S.W. 1990. *Pore Size, Particle Size, Aggregate Size and Water Retention*. Soil Science of America Journal 54:952–956.

19

Assessment of the Soil-Structure-Interaction based on Dynamic Measurements

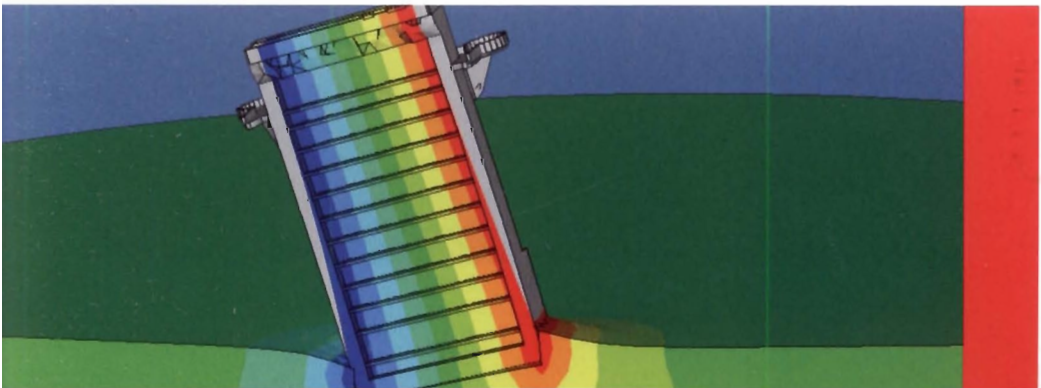
Authors:
Fritz Kopf
Adrian Bekő
David Schäfer
Johannes Pistrol
Michael Pietsch
Ludwig Rossbacher

Motivation

Many monitoring campaigns show large differences between the theoretical model and the practical measurements. A major part of it can be attributed to soil-structure-interaction. It is therefore desirable to have methodologies available that enable quantifying these effects through monitoring campaigns.

Main Results

In an outstanding monitoring campaign a reliable approach has been demonstrated to quantify soil-structure-interaction effects. The power of ambient vibration monitoring on soil has been demonstrated.



19-1 Introduction

The Leitturm in Augarten (Vienna) was built from 1943 till 1944 under the responsibility of Prof. Dr. h.c. Dipl.-Ing. Friedrich Wilhelm August Tamms. It was created as one of three flak-positions, which were designed as a triangle around the centre of the city. At each position there are two towers, one for the radar (Leitturm) and one for the battle (Gefechtsturm). The platforms of the towers were constructed on the same height, so that collimation calculations could be handled more easily. The real purpose of the towers during World War II was as bunkers for the civil population.

The towers are now under monument protection. The Leitturm in the Augarten has been closed since the end of the war and was only inhabited by countless pigeons, which created a huge amount of waste. Nevertheless, historic documents, letters etc. can be still found there. The measurements were also a chance for historians to gain access to the structure, and they found some very interesting documents.

The rigidity of the structure and its tall shape make it the ideal test object. Apart from the special geometry and constitutive features, the location also plays an important part. Since the bunker is located in a quiet park, the data acquisitions were affected by very limited noise.

From the dynamic point of view, the main advantage of this structure is the possibility to distinguish between the vibration of the soil occurring at lower frequencies, and the vibration of the building and its members, which occurs at higher frequencies. Due to the high mass of the structure, the building behaves like a rigid body in the low frequency band, whereas the vibrations of the walls are in a much higher frequency band. Between

The Leitturm in Augarten, Vienna, built during World War II (left) and aperture in the 2.5 m concrete wall of the tower seen from inside (right) F.19-1



high frequencies and low frequencies there is a significant gap. Most of the "normal" buildings do not have such a gap. In that case the frequency bands are mixed and it is very difficult to distinguish between them. In this case, the SSI phenomenon can be determined very conveniently, which is the reason why the Leitturm was instrumented.

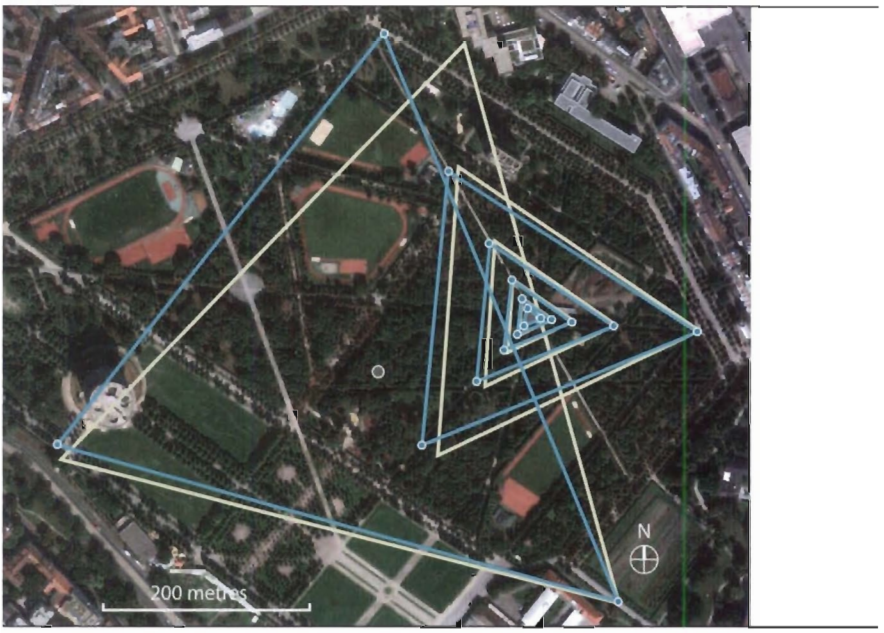
The dynamic properties of the soil can be determined in two different ways. The first one is the common way, using the Rayleigh Waves dispersion on the soil surface, and the back calculation to shear wave profiles. The second approach is the back calculation of the soil stiffness, based on the soil-structure-interaction.

The simultaneous measurement of the dynamic movements of the building allows the determination of the kinematic behaviour of the SSI. The tilting oscillations of the tower occur in both directions with different frequencies. They are transmitted to the soil and they can be measured in the surroundings.

The measurements were carried out separately on the soil surface for the assessment of the soil parameters, and on the tower structure to record the building movements. The next steps were: the measurement of the influence of the tower oscillation on the soil; the determination of the decay of the influence with the distance, and the qualitative estimation of the influence on the H/V-method results.

The results of the dynamic measurements were compared to different numerical simulations. Numerical models present the benefit to be tuned with the real dynamic properties of the measured SSI-system. The methods were compared, highlighting benefits and disadvantages of each one. The calibration of these methods with the measured conditions led to scientific findings and the opportunity to evaluate the different methods.

Triangular setups of sensors for measuring ambient soil vibrations F.19-2



19-2 Measurements on the Soil Surface

The vibrations of the soil surface were measured for the documentation of the surface wave propagation. The phase velocity of Rayleigh waves on the surface is not constant but it depends on the frequency of the wave. Usually the Rayleigh waves with low frequencies are faster than those with higher frequencies. This results in the fact that a vibration signal containing a wide frequency spectrum changes shape with the propagation. This phenomenon is called "dispersion of the waves". Low frequency waves, characterized by longer wave length, reach the measurement point distanced from the impact first. Contrarily, the high frequencies follow later.

To measure this effect, two artificial excitation types were applied: an impulse (for the high frequencies) and a harmonic excitation of the soil (for the low frequencies). The ambient vibrations were recorded in several triangular setups with different dimensions. By analysing the measured vibrations the dispersion curve could be evaluated.

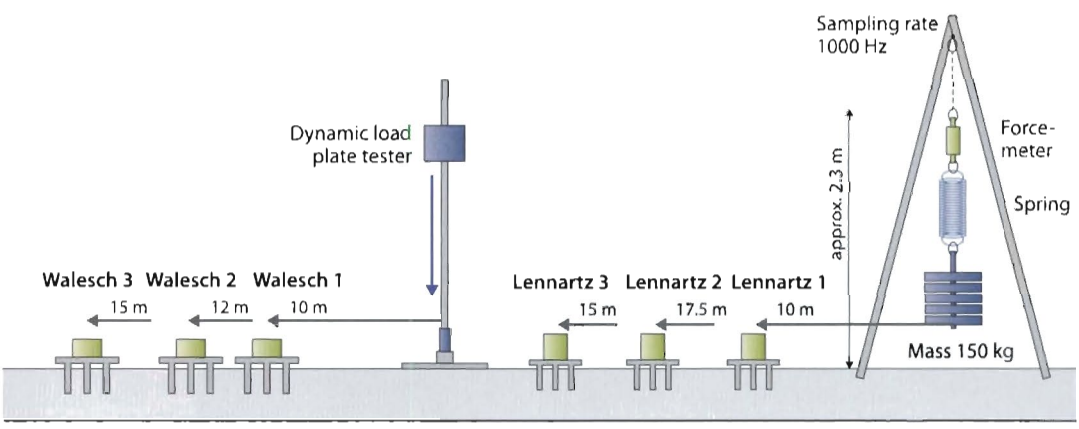
The interpretation of the dispersion curve of the surface waves by means of analytic models was affected by imperfections, arising from working outside of the method assumptions. The natural soil is indeed not a homogeneous infinite half-space but consists of different layers of soil types with diverse soil properties.

The evaluation of the dispersion curve was possible through the numerical simulation of differently layered soil profiles. By modelling each different soil profile it was possible to get an artificial dispersion curve as outcome. A special optimization algorithm was then useful to do the best fitting with the measured one. Even if this inverse analysis method does not yield a unique result, a most likely soil profile can be identified.

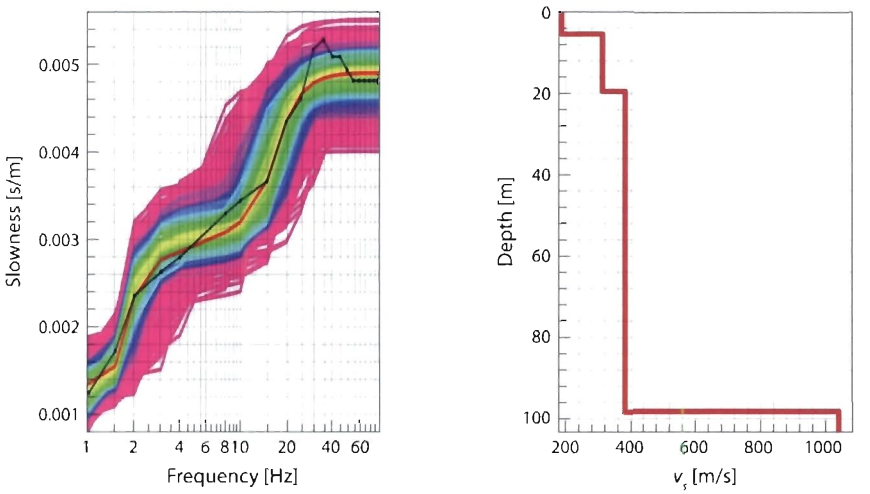
The results of these tests are the shear wave velocity profiles of the soil, the leading parameter for the assessment of the dynamic soil properties. It is a real material parameter because it is constant for all frequencies (shear waves do not disperse).

Surface-wave dispersion test setup with artificial impulse excitation using a light falling weight device F.19-3

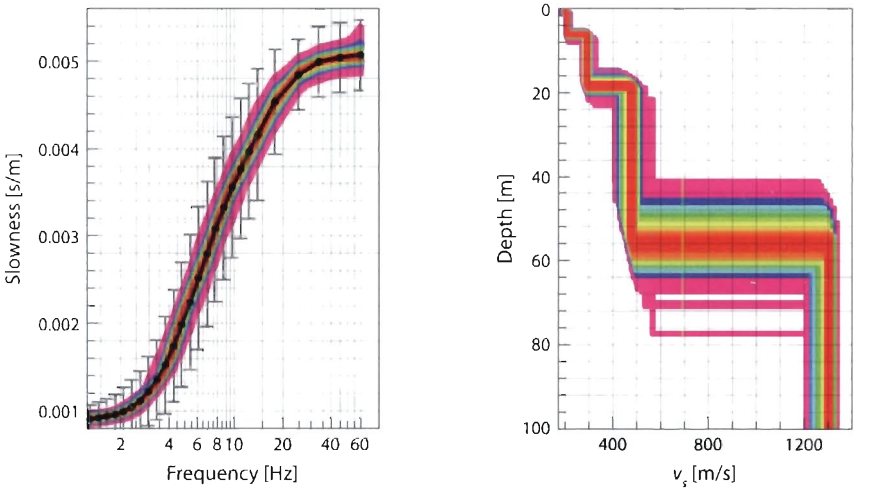
Surface-wave dispersion test setup with artificial harmonic excitation using a "shaker" as a mass-spring-system F.19-4



Dispersion curve with misfit-values and corresponding shear wave velocity profile (Geopsy software) F.19-5



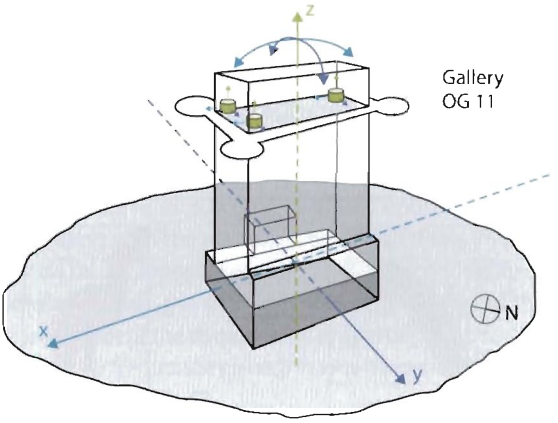
Triangle setup: dispersion of best fitting profiles (left) and shear wave velocities of best fitting profiles (right) F.19-6



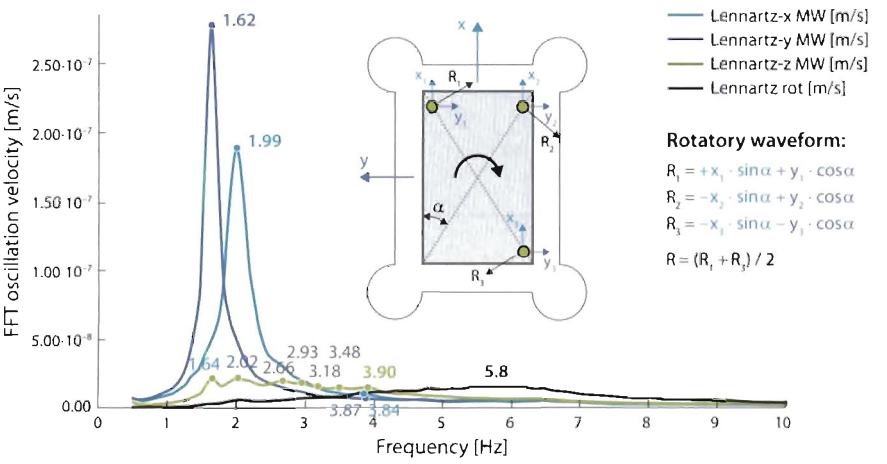
19-3 Measurements on the Tower

The ambient vibrations of the Leitturm-structure were measured with three very sensitive geophones (Lennartz LE-3D-5s) on different levels. The Fast Fourier Transformation (FFT) analysis of the measured data of vibrations on the 11th floor shows the eigenfrequency of 1.6 Hz for the tilting motion in the "weak", y-direction and 2.0 Hz in the "stiffer", x-direction. The peak of the vertical oscillation is not as significant but can be found at 3.9 Hz. Because of the tower's rigid structure, the soil-structure interaction behaviour is governed by the mass of the tower and the stiffness of the soil. By use of the Random Decrement Technique (RDT), the damping ratio of the vibrations can be separately evaluated for each frequency. The algorithm analyses ambient vibrations and looks for "events"

Sensor setup for the measurement on the gallery level inside the tower F.19-7



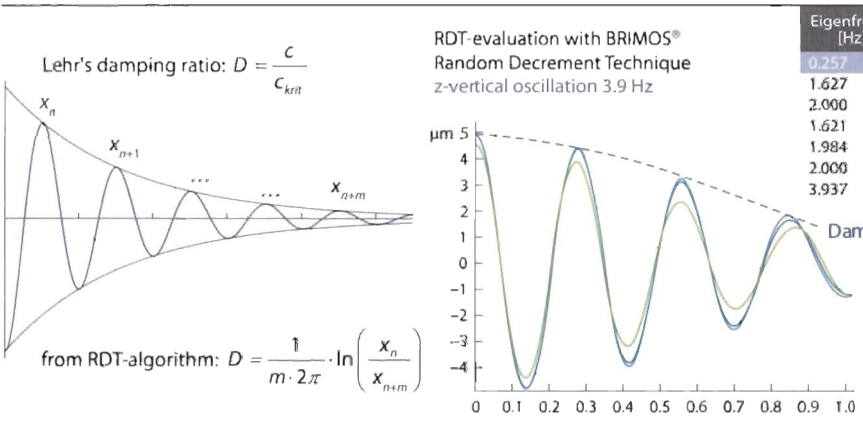
FFT-analysis of combined values from measurements in the corner of the gallery F.19-8



in the signal. All the detected events can be averaged to an artificial event which contains information about the vibrations' decay. The damping ratio of the relating vibration mode can be then determined.

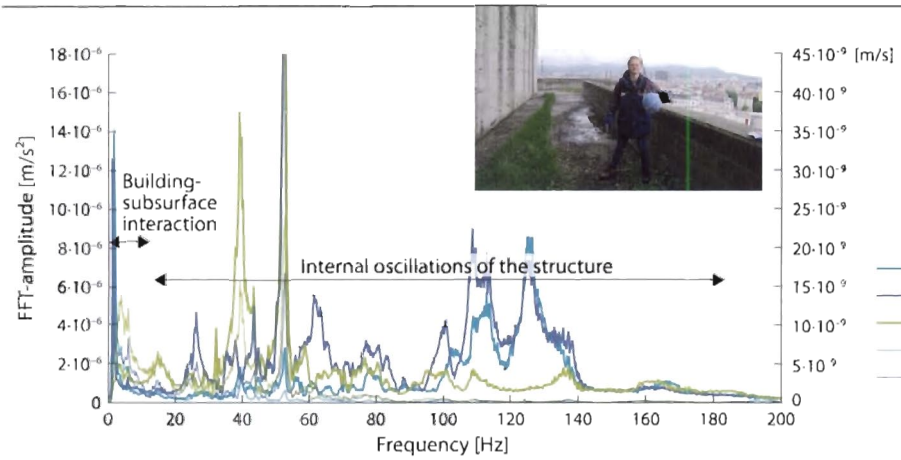
The artificial excitation with impulses of a medicine ball (5 kg) on the gallery of the Leitturm (mass about 40000000 kg) could be detected inside the tower with its 2.5 m thick walls and a ceiling with more than 3.5 m concrete slab. Each individual impact could be clearly detected. From the analysis it was possible to get the natural frequencies caused by the SSI in the low frequency domain, and after a gap without any significant peaks, the internal vibrations of the building in the high frequency domain. In this special case of the Leitturm the metrological evidence of separation between internal vibrations of the building and global movements caused by the soil-structure interaction (F.19-10) subsists. In usual buildings the effects are overlapping and it leads to mixed effects in the measurement signals and difficulties in the interpretation.

RDT-analysis of signals in z-direction, corner points in gallery level F.19-9



Eigenfrequ. [Hz]		Intensity [µm]	Zone	RDT [%]
0.257	1	1033.772	I	
1.627	2	104.011	I	
2.000	3	133.753	I	
1.621	4	0.000		
1.984	5	0.000		
2.000	6	133.753	I	
3.937	7	133.753	I	7.643

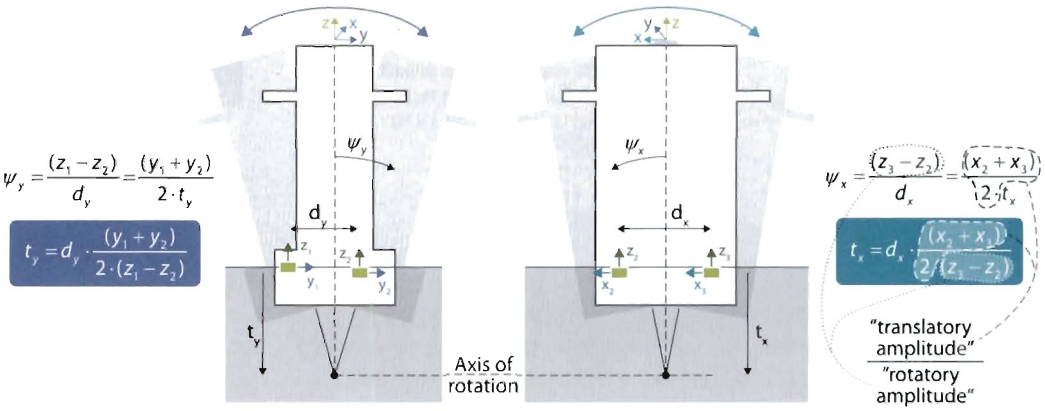
FFT- analysis of signals (acceleration, oscillation velocity) for impulse-excitation of the Leitturm at gallery level F.19-10



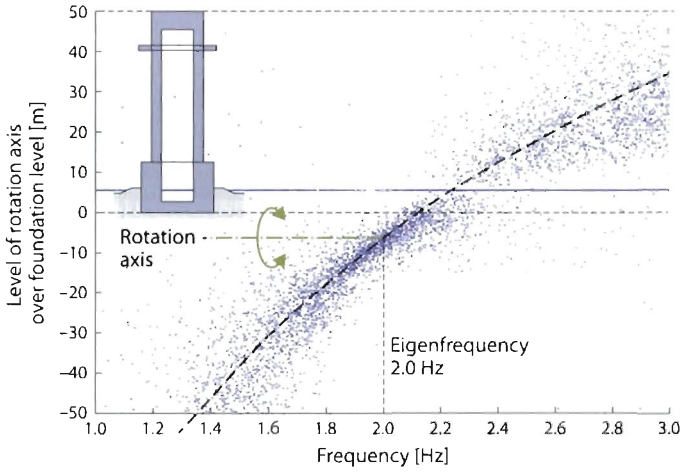
In a first approximation the soil structure interaction of the Leitturm can be understood as a rigid body motion of a concrete block socketing in an elastic half space of soil.

To prove the existence of a centre of rotation for both tilting modes and to find its position, vibration measurements were performed in the cellar of the tower and the signals were processed with the following procedure. In a first approximation, the tilting of the tower can be divided into a rigid translational component and into an independent rigid rotatory one. Combining the signals of two sensors is possible to identify the position of the centre of rotation, in relation to the measurement level. A fixed rotation centre exists only if both the translational and the rotatory oscillation components are oscillating either exactly in phase or exactly out of phase. The outcomes of the evaluation of the level of

Determining the rotatory centre of the rigid body by analysing signals from two sensors on one level F.19-11

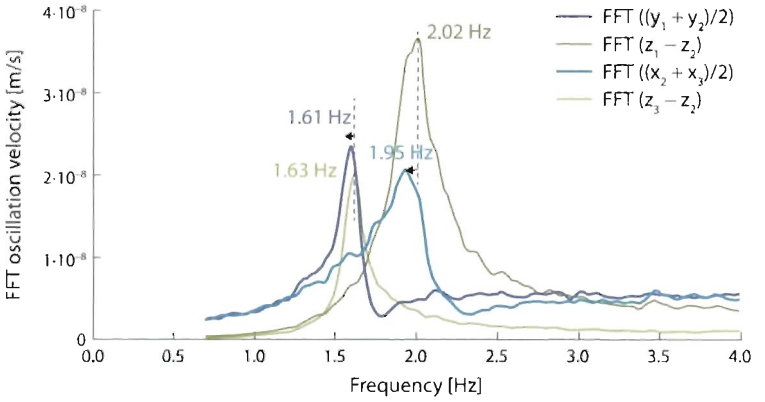


Level of the rotatory centre for tilting oscillations in x-direction depending on the frequency. Only the oscillations in phase or out of phase are considered F.19-12

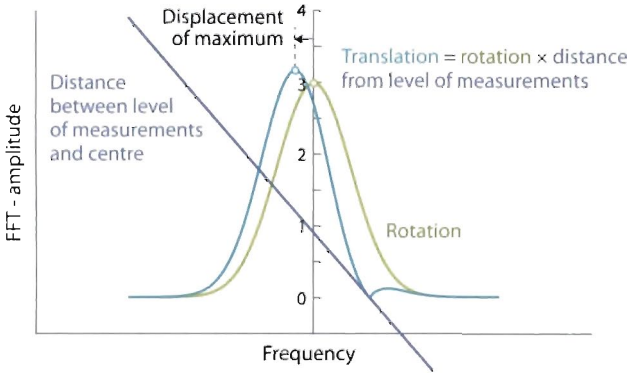


the centre of rotation are represented in F.19-12 as a cloud of blue dots. Every dot corresponds to the centre of rotation for the tilting movement in x-direction for each sample of the FFT analysis in correct phasing. The position of the rotation centre at the eigenfrequency of the tower (2.0 Hz) is well identified. It is the highest density within the red dotted cloud in this domain. It can be seen that a fixed centre of rotation does exist but the position depends on the frequency. This fact that the centre of rotation depends on the frequency is the reason why the frequency at the maximum of the translational component (turquoise, blue) is lower than the related rotatory components (green) in F.19-13. It is not trivial because both of the peaks indicate the frequency of the same oscillation mode and should be exactly the same. But since there are also frequencies besides the eigenfrequency and the translational component is also influenced by the distance to the rotation centre, the peak of this component is shifted according to the sketch in F.19-14.

Translational and rotatory oscillation components of tilting oscillation whose maxima have different positions F.19-13



Sketch of coherence between rotatory oscillation component (green), translational component (turquoise) and distance to rotation centre (blue) F.19-14

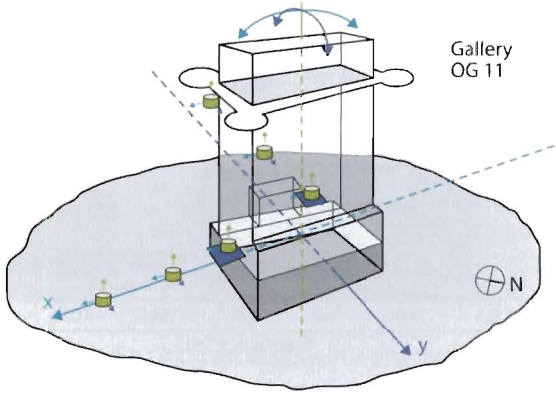


19-4 Measurements of Soil-Structure Interaction

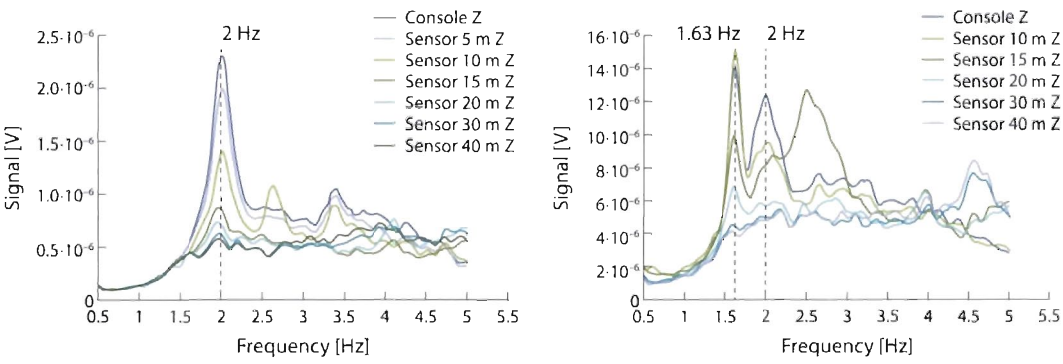
According to the soil-structure interaction mechanism the soil stiffness influences the movements of the building just as the building affects the soil. To measure the effect of the movement in the interaction, the tower oscillation and the vibration on the soil surface were measured simultaneously. One sensor was fixed on the tower and the others were placed in a line on the soil in both axis directions.

The FFT-analysis shows how the tower with its significant eigenfrequencies of 1.6 Hz and 2.0 Hz affects the soil. The movement of the building produces a vibration in the soil, detected with the geophones. This influence (velocity V) decreases with the distance r to the tower (F.19-17). According to the influence depth of the different modes (see F.19-19)

Sketch of the ambient vibration measurement setup on the surface in x- and y-direction F.19-15



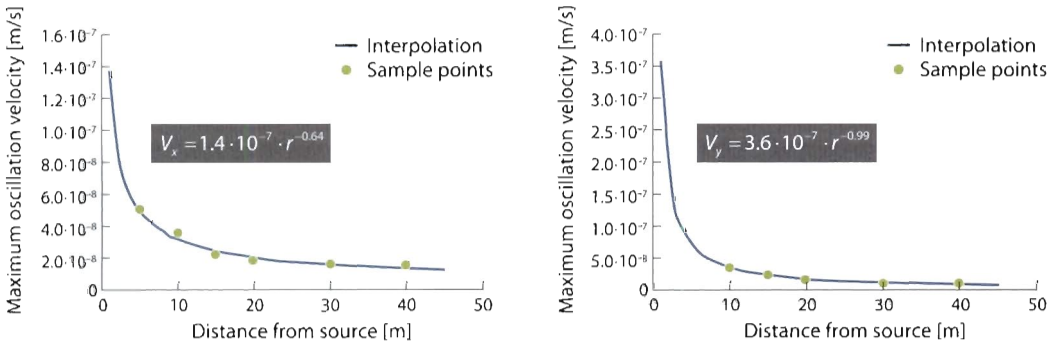
Acceleration measurements for x- (left) and y-direction (right) array: z-component of the sensors F.19-16



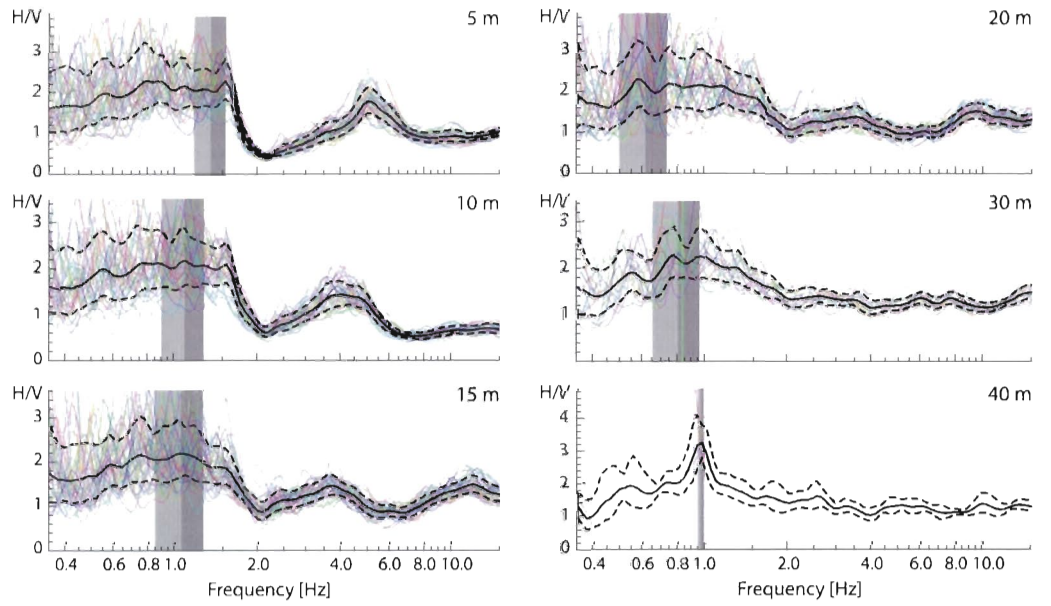
there is more damping in the propagation function in y-direction. The deeper the influence, the less is the decay. This effect can be seen in the value of the damping exponent in this function. Due to the eccentricity of the sensor setup in y-direction, the peak of the x-direction movement (2.0 Hz) can be also detected in F.19-16 (right). Due to the different damping exponents in the formula of propagation, the effect of y-movement becomes dominant with increasing distance from the tower.

The H/V-method evaluates the relationship between the horizontal and the vertical vibrations. This "ellipticity" of the ambient vibrations is an indicator for site effects in case

Propagation of tower vibrations in the soil. Damping function in x-direction F.19-17



H/V – evaluation of measurements in x-direction, distances 5, 10, 15, 20, 30 and 40 m (evaluation with Geopsy) F.19-18

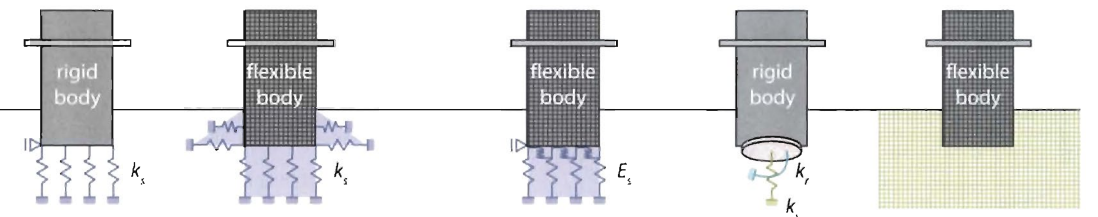


of earthquakes and the eigenfrequency of the soil (peak at 0.9 Hz, 40 m-line) can be evaluated in case of special soil conditions. The soil structure interaction causes a magnification of the vertical vibration component at the eigenfrequency of the tower (2.0 Hz in x-direction) causing a depression of the curves of F.19-18 in the near-field of the tower. Within the first 30 m the vibrations of the tower influence the H/V values.

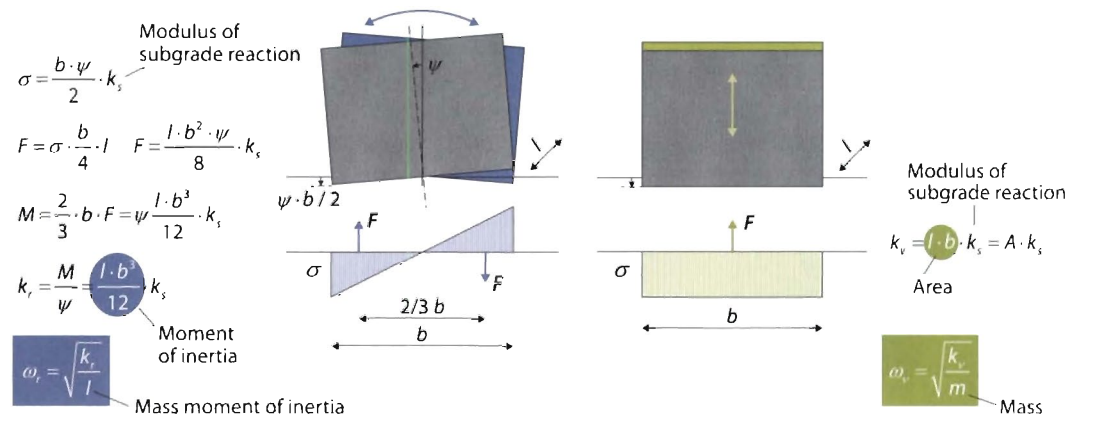
19-5 Numerical Simulation

To show the potential achievement of the different dynamic calculation methods, several numerical analyses have been carried out as shown in F.19-19.

Different methods of numerical modelling F.19-19



Eigenfrequencies with dynamical modulus of subgrade reaction method: tilting motion and vertical motion F.19-20



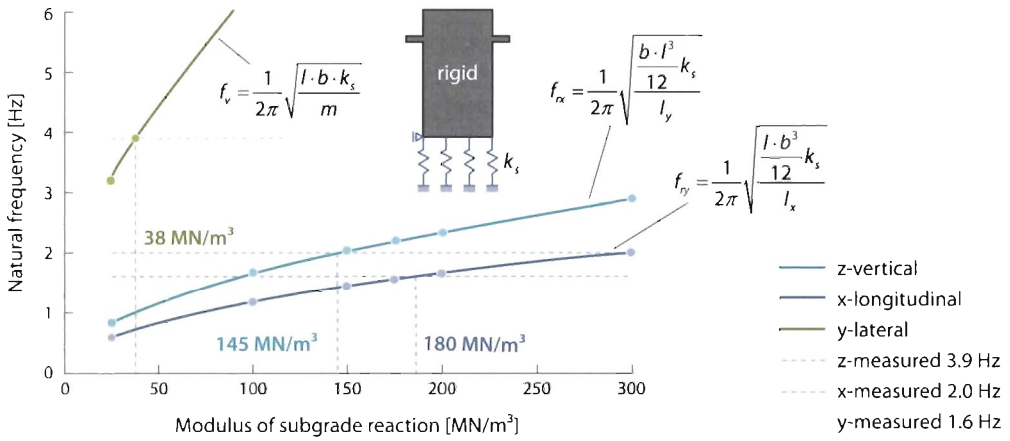
19-5-1 Method of Modulus of Subgrade Reaction

The method of "modulus of subgrade reaction" is the most common method. The effect of the soil is simulated by linear elastic springs distributed on the horizontal projection. The modulus of subgrade reaction k_s is meant as a spring stiffness per square metre. It is not a real soil parameter because it may depend on the geometry, shape, and scale of the building as well as on the influence depth for layered soil profiles.

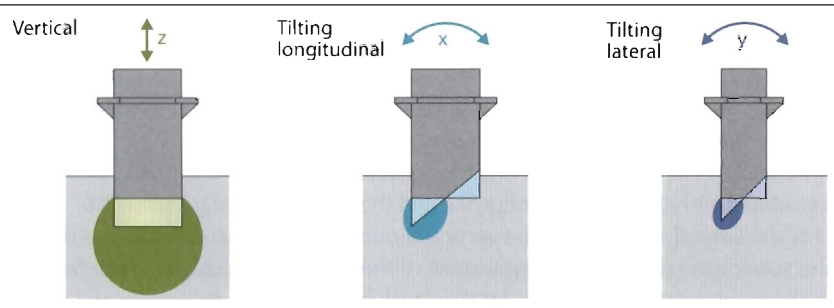
In F.19-21 the results of the calculation with the modulus of subgrade reaction method are reported beside the "reality" case. The results of the measurements are represented with dotted lines. The modulus of subgrade reaction is plotted versus the eigenfrequency of the interaction system.

The problem of the method of modulus of subgrade reaction is evident in F.19-21. There is no value for the modulus of subgrade reaction to fulfil all the oscillation mode frequencies measured in the field on the same soil conditions. This effect can be explained by F.19-22 where the different soil loading and the influence depth of the modes are shown.

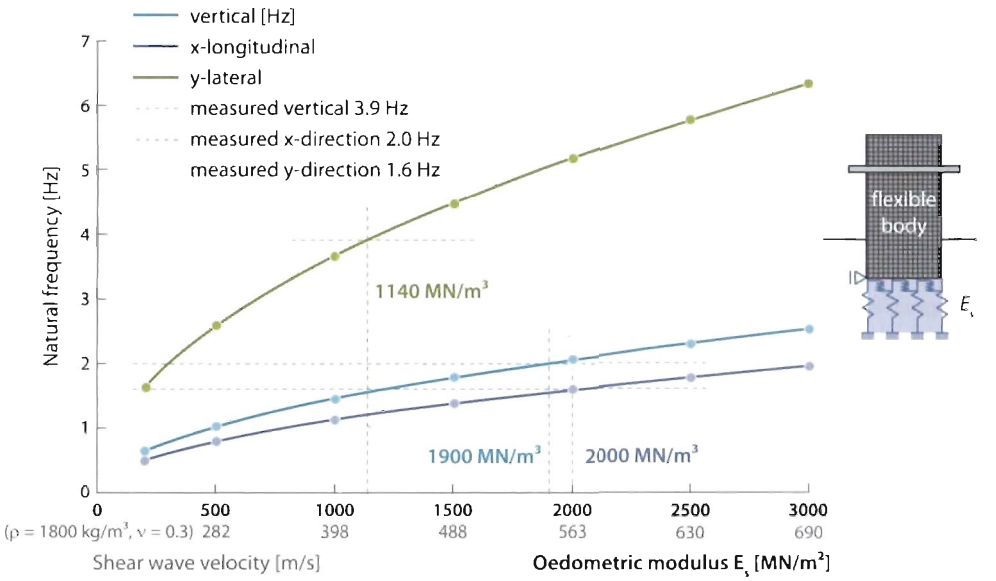
Coherence between modulus of subgrade reaction and eigenfrequency for different oscillation modes, comparison with measured values F.19-21



Effect of missing scale effect on the results of the dynamic modulus of subgrade reaction method F.19-22



Results of back-calculation of eigenfrequencies with the stiffness method F.19-23



The method is theoretically and practically not able to describe the real physical situation. It can only be used for simple estimations within the frame of existing experiences.

19-5-2 Stiffness Method

While the method of modulus of subgrade reaction is limited to normal stresses in the subgrade, the stiffness method allows to take shear stresses into account as well. Therefore the deformation of a single point in the area of contact between soil and tower depends on the loading of the point itself as well as the loading of the surrounding area. Moreover it is possible to take the flexibility of the tower structure into consideration. The method is based on the oedometric modulus, a real physical soil parameter. The oedometric modulus is assumed to be constant for the whole soil domain influenced by the foundation. A stress-dependency of the oedometric modulus and a layered soil structure were not taken into account. For the stiffness method the geometry of the tower is segmented into n single, finite elements. To determine the deformation characteristics of the interacting soil – tower system, a single element i is loaded with the single load $p=1$, which causes a settlement trough with its maximum c_0 under the loaded element i. The settlement under the adjacent elements $(i-1)$ and $(i+1)$ is c_1 et cetera.

The settlement c_0 is evaluated for the characteristic point. The actual settlements can be calculated with these lines of influence and the real loads for each element.

For the natural frequency of the vertical motion the settlements under the dead load of the tower are calculated. An equivalent stiffness per square metre k_s can be derived from the mean settlement w_m. The total equivalent stiffness can be written as

$$k_v = k_s \cdot A$$

where A is the ground area of the building. With the buildings mass m, the natural frequency of the vertical motion is defined as

$$\omega_v = \sqrt{k_v / m} \; .$$

The angle ψ of rotation is calculated for a tilting moment of M=1 to evaluate the natural frequency for the tilting motions, which can be written as

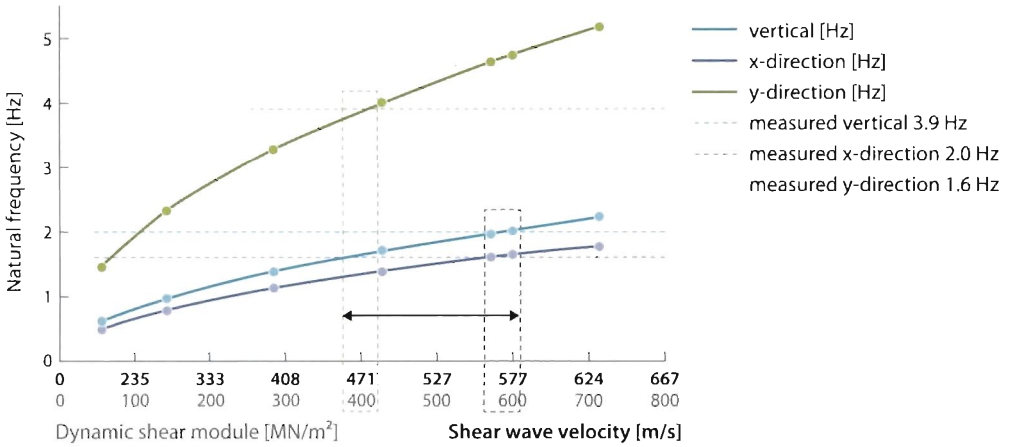
$$\omega_r = \sqrt{k_r / I} \; .$$

with $k_r = m / \psi$ and the mass moment of inertia I of the building.

19-5-3 Analytic Formulas for Circular Rigid Body on Linear Elastic Half-Space

It is possible to use the analytic formulas for circular rigid bodies on linear elastic half-space to get reliable results if the foundation of the building is rigid and can be described by a circular shape. The method is based on real physical soil parameters (shear modulus) [Flesch, 1993; Wolf, 1985]. F.19-24 shows that the results are very well corresponding to the measured tilting modes from the field test. The relationship between the damping ratios fits with the test results, but not in absolute values, because of the small amplitudes.

Results of numerical estimation of eigenfrequencies with dynamic parameters for a rigid circular foundation on elastic isotropic half-space F.19-24



Results with dynamic substitute parameters for a rigid circular foundation on elastic isotropic half-space [Studer, 2007] F.19-25



Circular foundation	Stiffness $\bar{B}$	Mass ratio	Damping ratio D	Additional mass
Vertical	$k_v = \frac{4 \cdot G \cdot r}{1-\nu}$	$\frac{m \cdot (1-\nu)}{4 \cdot \rho \cdot r^3}$	$\frac{0.425}{\sqrt{\bar{B}}}$	$\frac{0.27 \cdot m}{\bar{B}}$
Tilting	$k_\varphi = \frac{8 \cdot G \cdot r^3}{3(1-\nu)}$	$\frac{3 \cdot I \cdot (1-\nu)}{8 \cdot \rho \cdot r^5}$	$\frac{0.15}{(1+\bar{B})\sqrt{\bar{B}}}$	$\frac{0.24 \cdot I}{\bar{B}}$

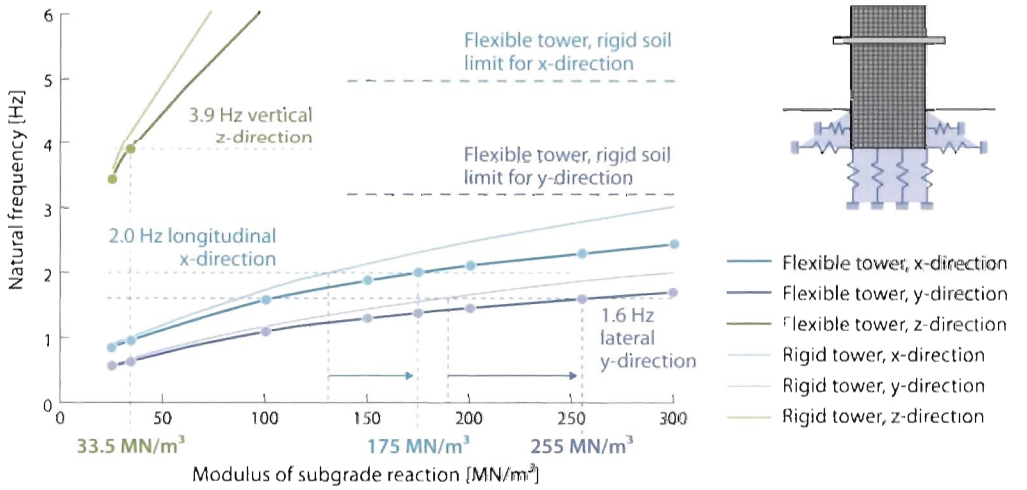
Damping	Measured RDT	Analytical circular foundation	Relationship RDT/analyt.
x-direction: longitudinal	1.915 %	7.686 %	0.25
y-direction: lateral	0.959 %	4.186 %	0.23
z-direction: vertical	7.643 %	36.859 %	0.21

19-5-4 Finite Element Method (FEM)

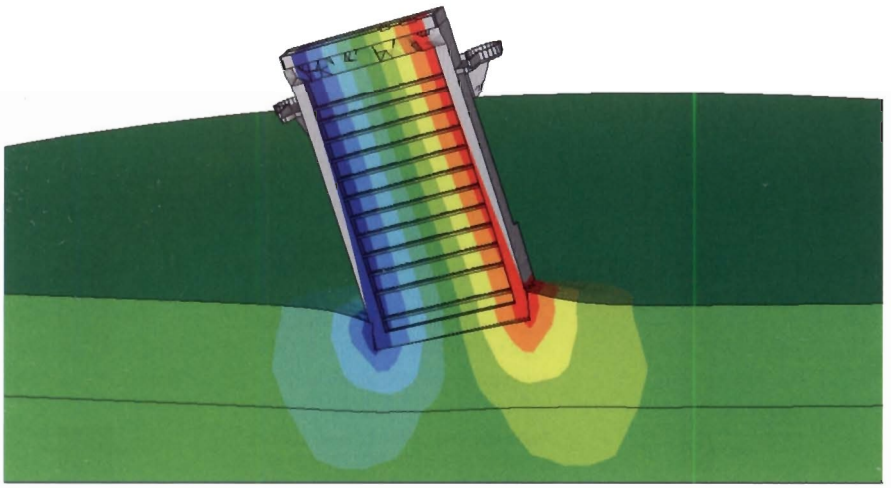
The Finite Element Method (FEM) was used for two separate analyses. First, the method of the modulus of subgrade reaction was applied to investigate the flexibility of the tower structure. The resulting consideration was that as shown in F.19-26, a modulus fulfilling the real dynamic soil conditions for all modes at the same time cannot be found. The reason is described in 19-5-1 and pictured in F.19-22.

In the second analysis with FEM, the soil was modelled with linear elastic elements. This is acceptable because the ambient measurements focus on waves with limited amplitude. By updating the model according to the measured dynamic soil profile and by

Coherency between modulus of subgrade reaction and eigenfrequency for different modes of vibration in case of rigid body movement and elastic building characteristic; comparison of FE computations with measured results F.19-26



FE calculation result: deformation in z-direction, 1st harmonic mode F.19-27



adjusting the soil stiffness, the determination of a solution fulfilling the tilting mode frequencies, the position of the rotation centre and the damping exponent for vibration decay with distance was possible. The fact that the soil of the updated model is stiffer, leads to get higher shear wave velocities than measured, but in this case the fitting relationship between the layers is known.

19-6 Conclusions

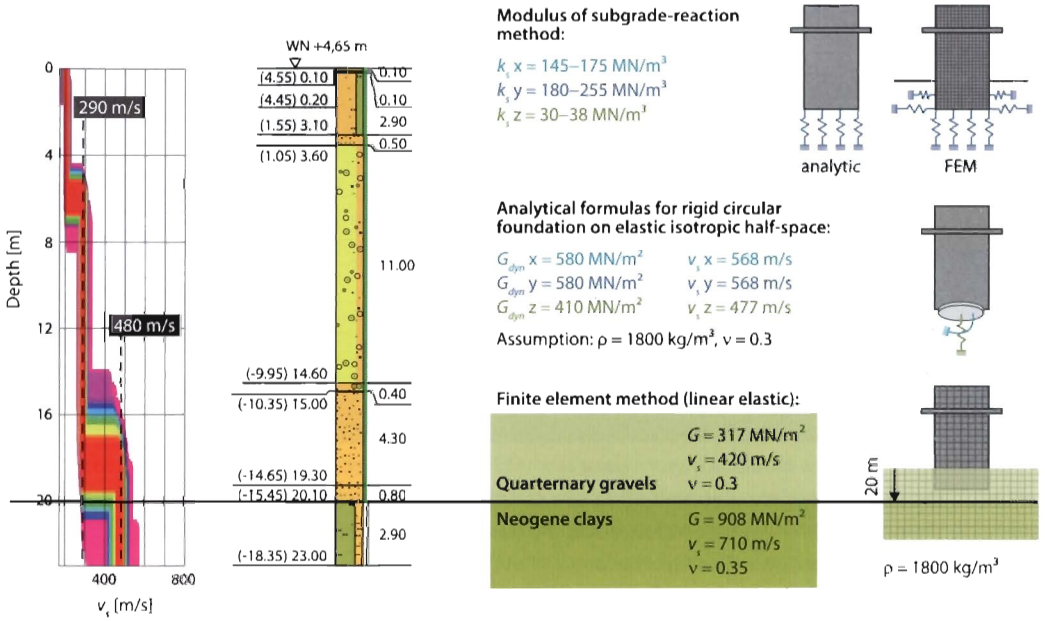
The target of the research work was to find a method to determine dynamic soil parameters using dynamic surface measurements, to find calculation parameters for different numeric simulations and to compare the results with the dynamic measurements of the soil-structure interaction, performed on a simple test object.

It is possible to formulate two main reasons to explain the demonstrated differences between the measured soil properties in the adjacent domain and the stiffer soil behaviour from the back calculation: The water content of the soil has no relevant effect on the shear wave velocity (just the mass difference) but it is important for the dynamic compression stiffness of the soil because of the pore water pressure. The considered modes are dominated by the compression stiffness of the soil.

The second reason for the stiffer soil properties beneath the Leitturm building is the soil consolidation. The average soil pressure of 610 kN/m^2 of the foundation slab of 31 m × 21 m has been loading the soil for the last 66 years. The measurements of the shear wave profiles were carried out on unaffected soil conditions in the adjacent park.

Summarizing the experiments in and around the Leitturm in Augarten in Vienna led to two different metrological approaches for determination of the dynamic soil properties connected with numerical inverse analysis. The benefits and the disadvantages of several

Comparison of the obtained soil-parameters: results from measuring the Rayleigh-waves and from inverse analysis of the soil-structure interaction F.19-28



numerical methods which are used in engineering practice could be pointed out. There is a difference between the dynamic soil structure interaction for the usual load cases (live loads, ambient excitation) and for the extraordinary conditions of earthquakes; the shear wave velocity profile and the H/V-method are developed for these conditions.

References

Seismid. *Boden-Gebäude Interaktion*. Internal report in the project SEISMID. www.seismid.com

Studer, J., Laue, J. and Koller, M., 2007. *Bodendynamik*. 3rd edition, Springer Verlag.

Flesch, R., 1993. *Baudynamik*. Bauverlag, Issue 1.

Achs, G. et al., 2011. *Erdbeben im Wiener Becken*.

Wolf, J. P., 1985. *Dynamic Soil-Structure Interaction*. Prentice-Hall, Inc., Englewood Cliffs, New Jersey.

20
Case Study: S101

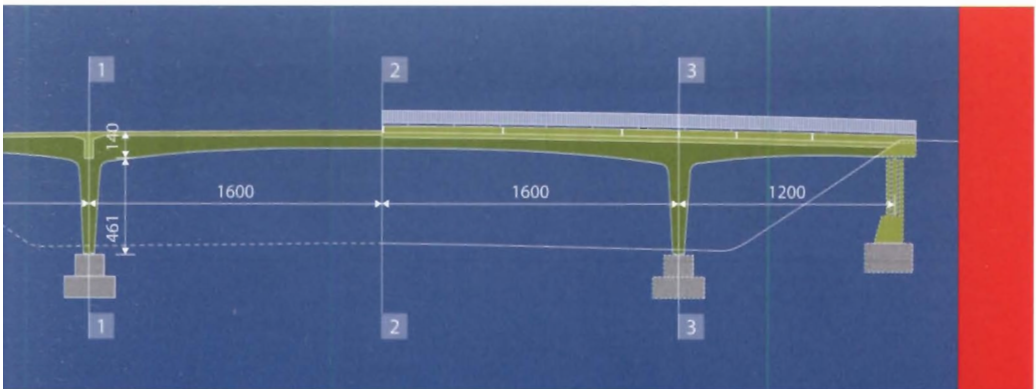
Authors:
Helmut Wenzel
Robert Veit-Egerer
Monika Widmann

Motivation

To prove the concepts of the structural health monitoring community comprehensive data sets of real cases are required. A full scale test enabling the simulation of various damages till collapse is required.

Main Results

A large test campaign featuring pier settlements, loss of post tension forces and other damages has been performed at the beginning of the project enabling many research teams to prove and demonstrate their concepts. The data have been widely disseminated also outside of the consortium and relevant responses have been received.



20-1 Introduction

20-1-1 Scope of Work

The flyover S101 was a typical prestressed concrete bridge built in the early 1960s. Due to its insufficient carrying capacity and its poor maintenance condition – both visual inspection driven ratings – it was decided to replace the bridge. At the same time the bridge did not meet the current requirements, as the structure did not fit into the overall traffic and infrastructure concept anymore. In other words demolition was aspired anyway, because the bridge was too small for the location.

In the course of the IRIS project VCE (together with the Alpine construction company and the University of Tokyo) was given the opportunity by the bridge owner ASFINAG to carry out progressive damage tests before S101 was finally demolished. The major objective of the progressive damage test was to emphasize the value of Structural Health Monitoring by demonstrating refined methods for the analysis of upcoming, slowly progressing damage and its effects on parameters of dynamic response. The benefits of Structural Health Monitoring as an added value to compulsory visual inspections were to be pointed out regarding the decision process of infrastructure owners in the course of maintenance and cost planning.

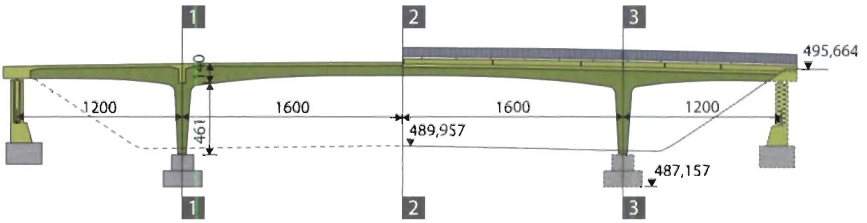
The progressive damage test – performed from 10 December to 13 December 2008 – was divided into two major phases. In the first part the north-western pier was settled stepwise whereas in the second part several tendons were cut through (F.20-1).

To have a reference state of the bridge's condition at that time a reference measurement and a visual inspection following the Austrian RVS 13.03.11 regulations were carried out immediately before the damage tests.

Overview of the damage test at the S101 F.20-1



General plan – Flyover Reibersdorf F.20-2

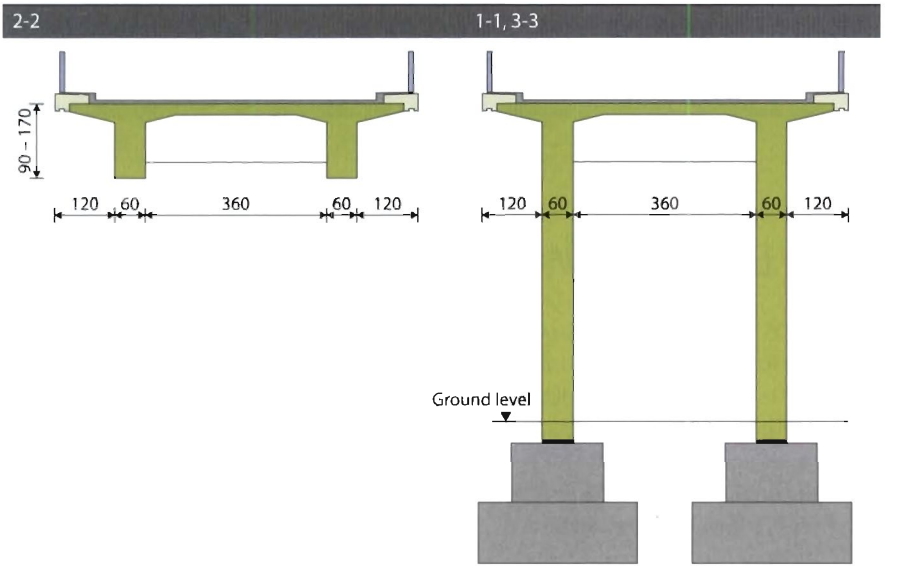


The present chapter summarizes the results of the extensive analyses based on the huge amount of data recorded during the progressive damage test. For detailed information see [Wenzel et al., 2009].

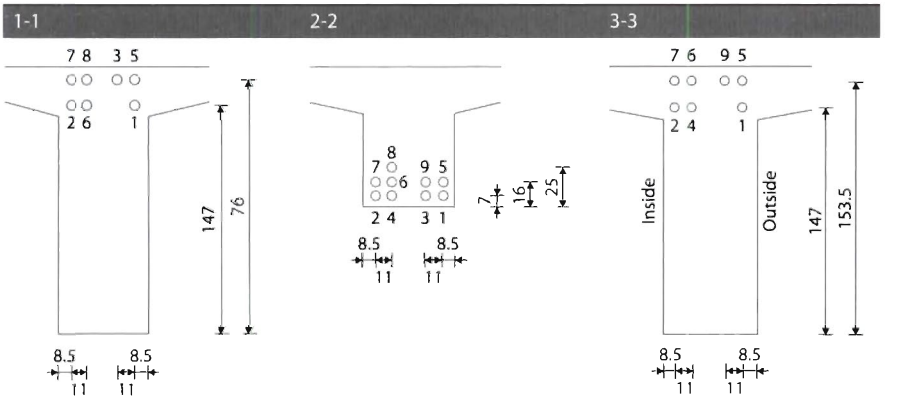
20-1-2 Structural Information

The S101, built in the early 1960s, was a post-tensioned three-span bridge across the A1 Westautobahn in Austria with a 32 m long main span and two 12 m long side spans. The cross-section was 7.2 m wide and was designed as a double-webbed t-beam, whose webs had a width of 0.6 m. The height of the beam varied from 0.9 m in the centre of the main span to 1.7 m above the piers.

Standard cross-section S101 (2-2) and cross-section at the piers (1-1, 3-3) F.20-3



Position of the tendons F.20-4



General photo documentation – Flyover S101 Reibersdorf F.20-5



20-2 BRIMOS® Methodology

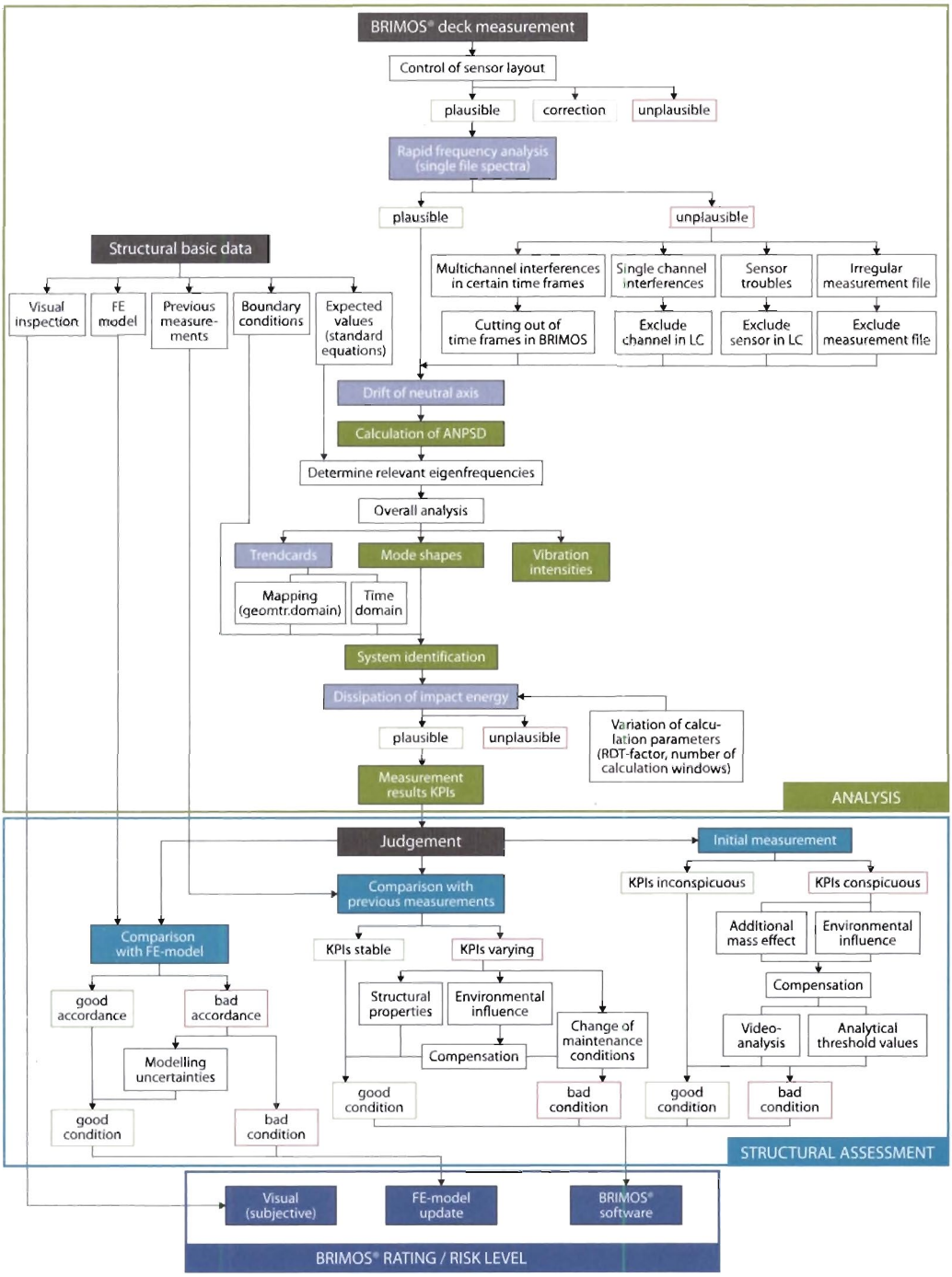
BRIMOS® Structural Health Monitoring is a technology that allows capturing and assessing load bearing behaviour of engineering structures based on the principles of structural mechanics. The monitoring technique was developed in order to be applied with a minimum of traffic impediment or operational disturbance. The measurements are always conducted under ambient (environmentally excited vibrations) conditions on the one hand and under typical operational loading conditions on the other hand. The latter usually represents the most significant impact to be analysed with regard to the structural performance.

BRIMOS® offers a well-defined rating system for investigated structures. Both the maintenance condition and the corresponding risk level are identified based on the following measured dynamic parameters: eigenfrequencies, mode shapes, damping patterns along the structure, vibration intensity and generated trends of structural integrity along the structure and over time.

In addition an accompanying visual inspection focusing on obvious damage is incorporated into the evaluation. Extensive Finite Element analysis provides decisive modal parameters on the one hand and enables a deeper understanding, quantification and interpretation of the field-test based, observed phenomena on the other hand.

Furthermore the results are compared to reference data from the BRIMOS® Database. The experience of about 1000 investigated structures worldwide has been incorporated into the assessment procedure.

BRIMOS® methodology – in detail F.20-6



20-2-1 Objectives of Dynamic Measurements

The objective of a BRIMOS® monitoring campaign is to identify and to evaluate the Key Performance Indicators of an investigated structure with regard to their relevance for civil engineering issues:

// The bridge structure's relevant eigenfrequencies and corresponding mode-shapes provide information about the load bearing capacity and operability, the distribution of the global and local dynamic structural stiffness in the bridge's lengthwise and transversal direction and enable the evaluation of the layout of the bearings.
// Trend analysis of structural integrity (sensitivity analysis and distribution of induced dynamic impact) to investigate the progression, the character, the stability and probable changes in the energy content of the relevant eigenfrequencies to evaluate the load bearing capacity and operability.
// Damping paths in the structure's lengthwise direction (dissipation of the induced vibration energy) to localize problematic sections.
// Vibration intensity at the entire bridge deck to detect weak points with regard to fatigue threat.
// A Finite Element Model representing the undamaged, initial condition provides the decisive modal parameters and enables the quantification of the effective load bearing capacity on the one hand and deeper understanding and interpretation of the field-test based, observed phenomena on the other hand.

BRIMOS® investigations typically comprise the preparation of the measurement, the measurement itself, data analysis, structural assessment and evaluation (rating) as well as the editing of the data for the client on the one hand and in terms of the necessary in-house database administration on the other hand. The flowchart in F.20-6 indicates the complexity of the assessment procedure.

20-3 Visual Inspection

20-3-1 Austrian National Guideline RVS 13.03.11

The Austrian Guideline on bridge inspection RVS 13.03.11 [bmvit, 2011] specifies that every bridge has to be surveyed at least every six years following a given procedure. This inspection consists of a close examination (within touching distance) of all inspectable parts of the structure and focuses on reliability (structural safety, serviceability, durability) and road safety. The detailed findings are combined to a bridge rating which is the basis for decision making during subsequent maintenance planning. Furthermore this periodic condition assessment should enable the bridge owner to retrofit the bridge in a tailored and therefore cost-effective way.

As a result the technical inspection refers to the following relevant aspects:

// Functional capability and load bearing capacity
// Implicitly required measures for safety reasons
// Implicitly required measures for durability reasons
// Recommended measures
// Special instructions concerning the periodic inspection
// Recommended special tests (monitoring)
// Date of the next assessment

In the course of the visual inspection visible imperfections are ascertained on-site and documented with drawings and photo documentations. In the end the bridge object's total rating is composed on the basis of the condition of the individual bridge members (weighted due to their importance for the global condition) with a rating between 1 (very good condition) and 5 (critical condition).

20-3-2 Results of the Visual Inspection

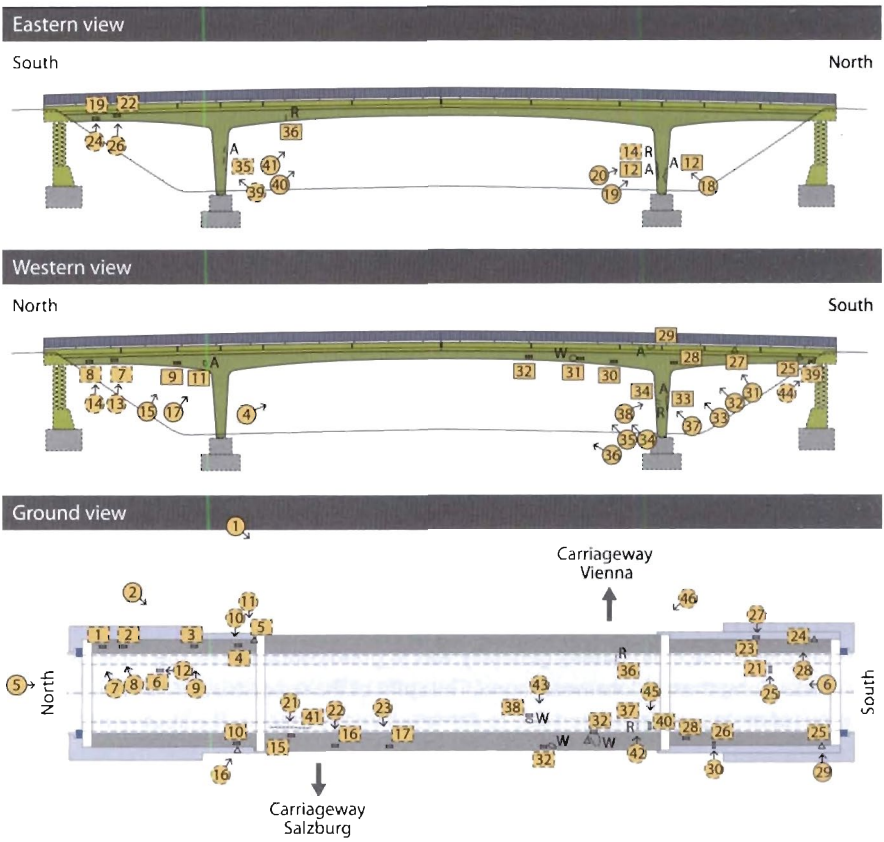
A detailed inspection was undertaken before the progressive damage test was started. In the following an overview about the findings and the resulting conclusions and recommendations is given.

In the case of S101 most of the documented imperfections were spallings and cracks caused by load effects, restraint impacts, minor or lacking concrete cover and corrosion. The concrete of the main girders generally was in good condition. At the same time visible cracks along the tendons were found. The soffit of the superstructure showed several locations of moisture penetration due to damaged waterproofing. The abutments were in good condition but the piers showed spallings and bending cracks caused by load effects. An overview of all the documented imperfections is shown in F.20-8. The numbers placed

Typical findings at S101 F.20-7



Documentation of imperfections – eastern (top) and western view (middle), ground view (bottom) F.20-8



Evaluation schema for structures T.20-1

Periodic Bridge Inspection	December 2008
Substructure	4
Superstructure	4
Bearings	–
Joints	–
Road surface	–
Waterproofing, drainage	–
Edge beam	3
Miscellaneous facilities	–
Entire object	**4**

in boxes signify imperfections, numbers placed in circles indicate the corresponding pictures. F.20-7 illustrates examples of imperfections at the worst rated parts of the bridge. The visual inspection based rating classifies the bridge object S101 to be in category 4 out of 5 – caused by the object's insufficient carrying capacity and its maintenance condition.

T.20-1 shows the ratings for the different structural members as well as the total rating for the entire object.

20-3-3 Conclusions and Recommendations

A strictly visual inspection driven rating would state insufficient load bearing capacity and maintenance condition. The main reason for that is the remarkable correlation between the cracking patterns and the geometric properties of the internal prestressing.

Since 2000 the structural behaviour has also been followed by periodic dynamic measurements. As these investigations always disproved the negative rating, there was no necessity for a change of operational conditions (loading capacity, usability). Despite the poor visual condition of the bridge no implicitly required measures for safety reasons were recommended. Apart from that a sustainable repair of the relevant, grave imperfections (cracking patterns at the main girders and huge spallings at the piers) was recommended in case of further use of the bridge to address the required durability issues.

20-4 Progressive Damage Test

20-4-1 Campaign Description

The progressive damage test was divided into two major phases:

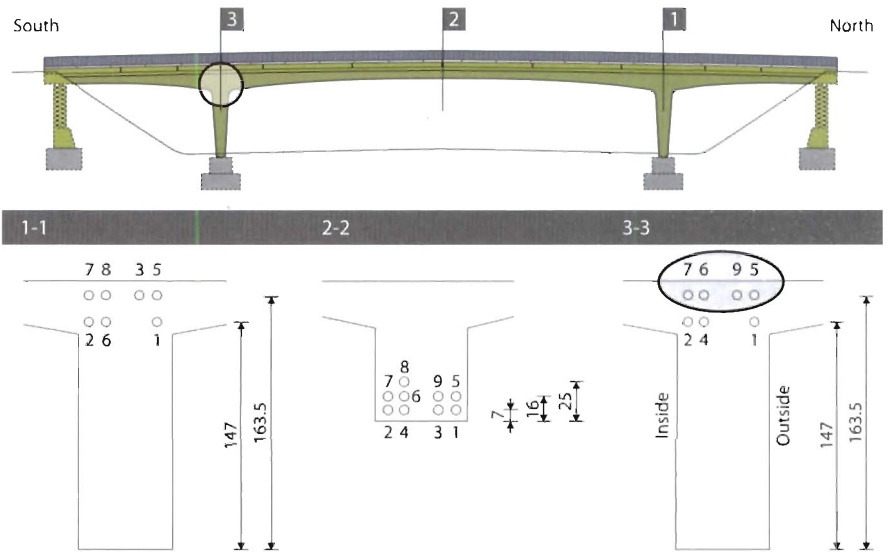
// Cutting and settlement of the north-western pier
// Cutting through of several tendons in the bridge-deck above the north-western pier

Documentation of the pier settlement (column north-west) F.20-9



In the first phase the north-western pier was cut through right above the foundation while the structure was secured by a supporting pier which was combined with a hydraulic jack for a subsequent, artificially induced, stepwise bridge settlement. It was planned to settle the pier up to 5 cm stepwise and to reconstitute the original gradient afterwards (F.20-9). Due to the fact that the elastic limit of the bridge was reached at a vertical deformation of 27 mm this test was quit after the third step of settlement (3 cm).

Position of intersected tendons F.20-10



Documentation of cutting through several bridge deck tendons above the north-western pier F.20-11



The second phase of the damage test – the cutting through of tendons – aimed to demonstrate the effects of a marginal loss of local prestressing reinforcement on the structure's dynamic characteristics. For that purpose four tendons in the area above the north-western pier were intersected (F.20-10 and F.20-11). Three of them were completely cut through while the last one was just partly intersected.

To quantify the loss of local prestressing reinforcement due to the cutting of the listed tendons the intersected cross-sections were related to the total, initially manufactured prestressing steel for each damage stage.

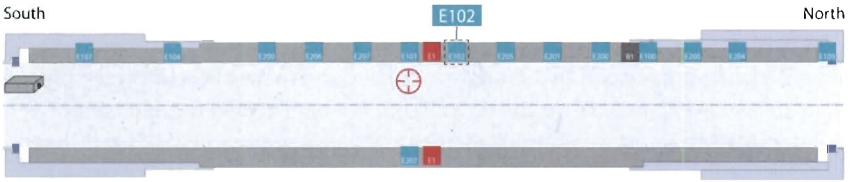
To capture the effects on the dynamic key performance indicators the progressive damage test was accompanied by

// a BRIMOS® measurement using a permanent sensor grid of 15 three-dimensional accelerometers,
// three additional stand-alone systems (one BRIMOS® Recorder and two Etna-Recorders with internal 3D acceleration sensors)
// and a laser-based deformation measurement system (a laser transmitter and an optoelectric receiver unit – see F-20-12).

Reduction of local prestressing reinforcement T.20-2

Number of intact tendons	Number of intersected tendons	Reduction of local prestressing reinforcement [%]
18	0	0
17	1	–5.6
16	2	–11.2
15	3	–16.8
14.75	3.25	–18.1

Sensor layout – BRIMOS® sensor grid during the progressive damage test F.20-12



Documentation of the accompanying measurements F.20-13



Schedule of the progressive damage test and highlighted key stages T.20-3

Start	End	Stages of progressive damage test
10/12/2008 05:16 p.m.	11/12/2008 07:13 a.m.	Undamaged structure
11/12/2008 07:13 a.m.	11/12/2008 10:21 a.m.	North-western pier cut through
11/12/2008 10:21 a.m.	11/12/2008 11:49 a.m.	1st step of lowering the pier (1 cm)
11/12/2008 11:49 a.m.	11/12/2008 01:39 p.m.	2nd step of lowering the pier (2 cm)
11/12/2008 01:39 p.m.	11/12/2008 02:45 p.m.	3rd step of lowering the pier (3 cm)
11/12/2008 02:45 p.m.	12/12/2008 05:52 a.m.	Compensating plates inserted
12/12/2008 08:04 a.m.	12/12/2008 01:12 p.m.	End of damage test lowering the pier
12/12/2008 01:12 p.m.	12/12/2008 03:03 p.m.	1st tendon intersected
12/12/2008 03:03 p.m.	13/12/2008 05:44 a.m.	2nd tendon intersected
13/12/2008 05:44 a.m.	13/12/2008 10:08 a.m.	3rd tendon intersected
13/12/2008 10:08 a.m.	13/12/2008 11:14 a.m.	4th tendon partially intersected

Besides that geodetic levelling was performed after every step of the damage test (F.20-13). Measurements were permanently recorded from 5:16 p.m. on 10 December to 11:14 a.m. on 13 December 2008. T.20-3 shows the time schedule of the progressive damage test and highlights the key stages, which is being referred to during the presentation of the results (see chapter 20-4-2).

20-4-2 Major Lessons

Summary by Means of Structural Frequencies

As an initial dynamic measurement was performed at the object S101 in 2003 (see [Wenzel et al., 2009]), the measurements of 2008 can be referred to that. In T.20-4 the decisive eigenfrequencies of the initial measurement are compared to those of the measurement conducted before the bridge was damaged artificially in 2008. The deviations between the two measurements can be traced back to the mass reduction due to the removed asphalt surfacing (F.20-14) on the one hand and to the effect of the temperature (9 °C in 2003 vs. −2 °C in 2008) on the other hand. The type of load bearing behaviour for the undamaged structure in 2008 remained basically the same as in 2003. Due to the miss-

Decisive eigenfrequencies – undamaged condition 2003 vs. 2008 T.20-4

Vibration mode	Initial measurement 2003 f [Hz]	Undamaged condition 2008 f [Hz]	Deviation 2003–2008 [%]	Specification regard. character of motion & origin of stressing
1st bending mode	3.76	4.05	7.7	1BT main span
1st torsional mode	5.85	6.30	7.7	1TL main span
2nd bending mode	8.99	9.69	7.8	2BT main span
2nd torsional mode	–	13.29	–	2TL main span
3rd bending mode	14.87	15.93	7.1	1BT side span

ing asphalt surfacing the Key Perfomance Indicator Eigenfrequencies clearly reflect a new mechanical reference system with regard to the upcoming results from the damage tests.

Furthermore the undamaged condition – measured in 2008 before the progressive damage tests were started – is used as the relevant reference state for all subsequent damage stages. T.20-5 summarizes the effects of the pier settlement and the cutting of tendons on the eigenfrequencies.

While the reference measurement in 2003 was performed under normal site traffic, the measurements before and during the progressive damage tests in 2008 were basically made under ambient conditions (environmentally excited vibrations) and the vibrations caused by the highway traffic beneath the bridge – which were transmitted through the foundations.

Structural Stiffness

Trend-cards are an essential evaluation instrument for full-scale measurements on bridge structures. The obtained patterns represent the effective structural dynamic stiffness by means of a frequency-time diagram.

To demonstrate the impact of the progressive damage test on the structural stiffness three trend-cards are shown using the signals of Sensor E102 which was located at 0.4 of the main span length (F.20-12). The first trend-card (F.20-15) represents the bridge-structure's relevant vertical stiffness-patterns over the entire time period of the progressive

Bridge deck S101 in 2003 (left) and 2008 (right) already without asphalt surfacing F.20-14



Decisive eigenfrequencies during the different key stages and deviations from the undamaged condition T.20-5

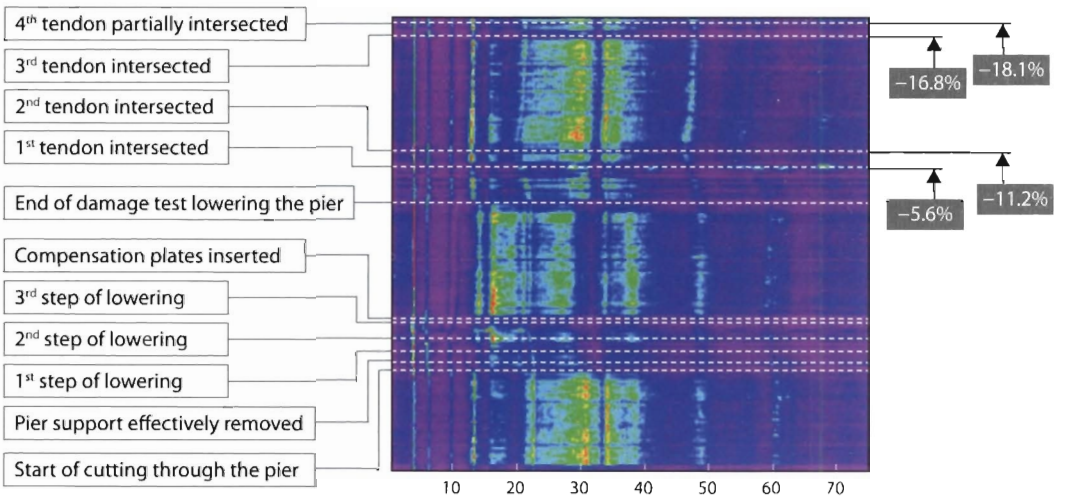
Vibration mode	Undamaged condition f [Hz]	Pier settlement (3 cm) f [Hz]	Pier settlement (3 cm) Deviation [%]	4th tendon cut through f [Hz]	4th tendon cut through Deviation [%]	Specification regard. character of motion & origin of stressing
1st bending mode	4.05	3.62	–10.6	4.04	–0.2	1BT main span
1st torsional mode	6.30	5.39	–14.4	6.18	–1.9	1TL main span
2nd bending mode	9.69	8.22	–15.2	9.67	–0.2	2BT main span
2nd torsional mode	13.29	10.06	–24.3	13.08	–1.6	2TL main span
3rd bending mode	15.93	15.79	–0.9	15.73	–1.3	1BT side span

damage test in the frequency range between 0.2–75 Hz. The second trend-card (F.20-16) shows the frequency range between 0.2 and 8 Hz in detail and the third one (F.20-17) the higher eigenfrequencies between 45 and 75 Hz.

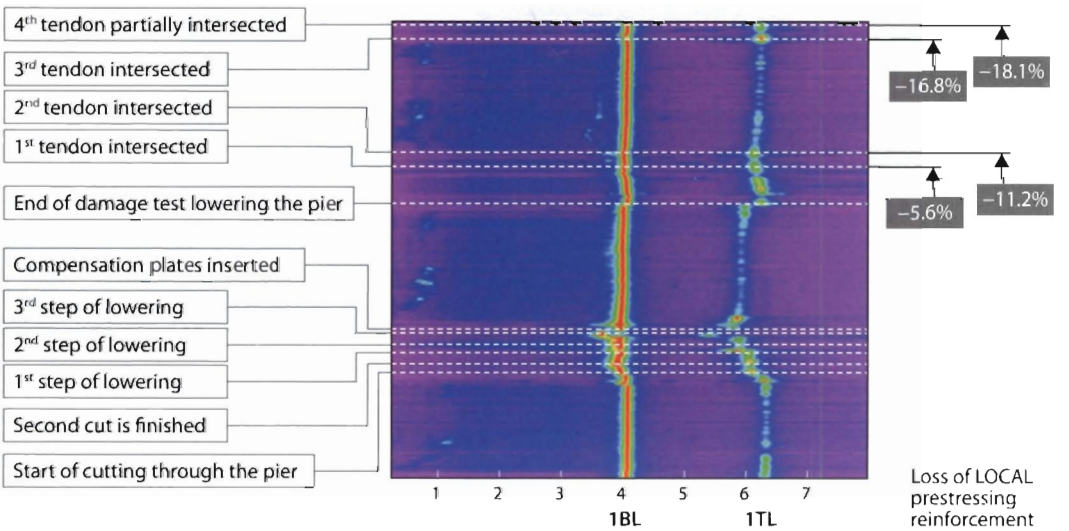
As long as the damage test has not been started the dynamic response follows straight and stable patterns – indicating a good maintenance condition.

In the low frequency range of dynamic response the structure's global resistance is represented reflecting bending and torsion properties – linked with the dynamic stressing of the whole main span of the bridge. During the damage test structural response in

Trend of stiffness in terms of time in the vertical direction, 0.2–75 Hz, sensor E102 F.20-15



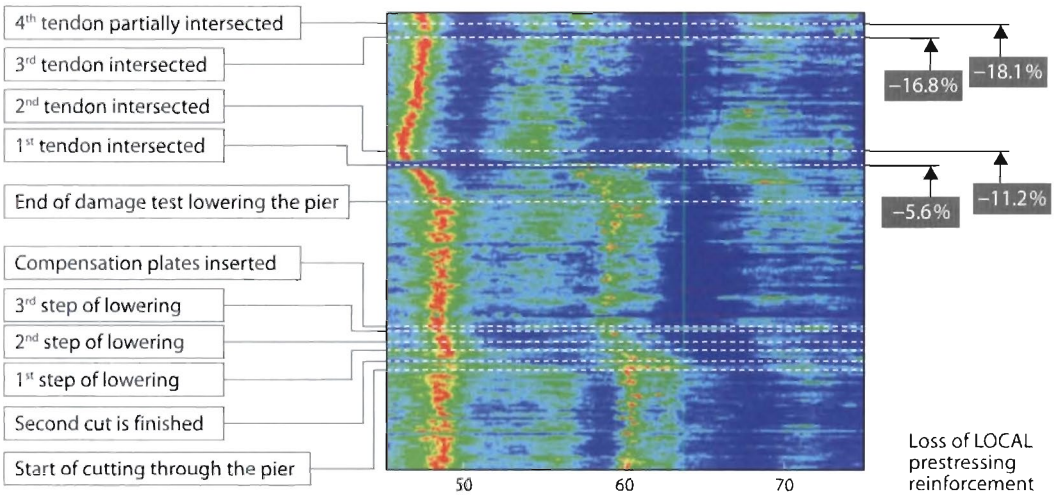
Trend of stiffness in terms of time in the vertical direction, 0.2–8 Hz, sensor E102 F.20-16



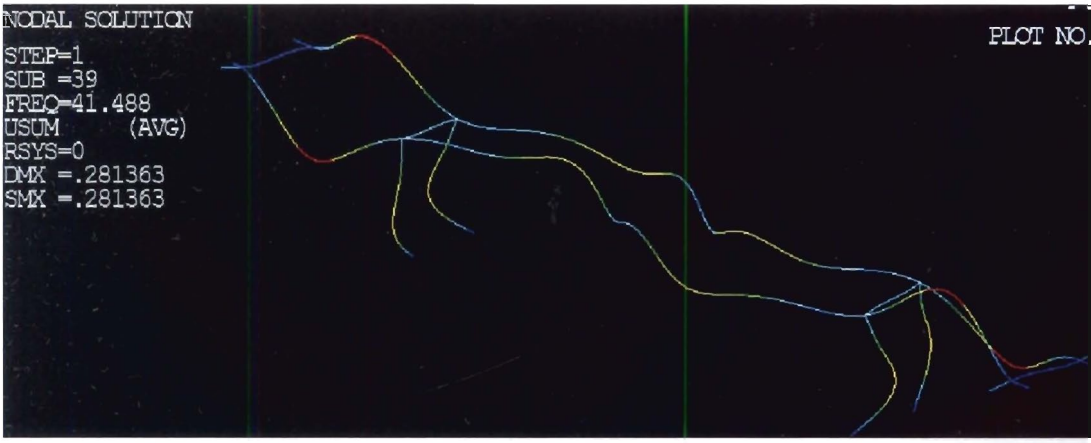
this frequency range clearly responds to the induced pier settlement but remains practically unchanged during the intersection of the tendons. In other words those global eigenfrequencies are mainly affected by the change of structural properties in terms of boundary conditions and vibration length (F.20-16).

In the higher frequency range the local resistance (structural members) is represented. The measured frequencies in this range are mainly affected by the artificial damage (cutting the tendons – F.20-17). Initially the structure responds to the damage with a clear reduction of the load bearing resistance. Then the degradation is stabilized due to the structure's local redundancy, being able to re-establish its load-bearing capacity on a visibly lower level.

Trend of stiffness in terms of time in the vertical direction, 45–75 Hz, sensor E102 F.20-17



Computed modal response – local bending mode of the main girders – in the higher frequency range F.20-18



When generating the change of stiffness from the measured change of the frequencies ($\Delta f \rightarrow \Delta EI$) it can be stated that a continuous local cutting of up to 18 % of the tendons led to 99.3 % remaining global bending resistance (1st bending mode), to 98.4 % remaining global torsional resistance (2nd torsional mode) and to 97.4 % remaining local bending resistance (local structural member's bending mode).

Deformation

In addition to the dynamic measurement the bridge's response to the damage tests was observed by means of vertical deformation measurements. This task was covered by

// monitoring the total vertical displacements in the middle of the bridge's main span during the entire damage test
// and an accompanying geodetic levelling that was conducted after every major step of damaging.

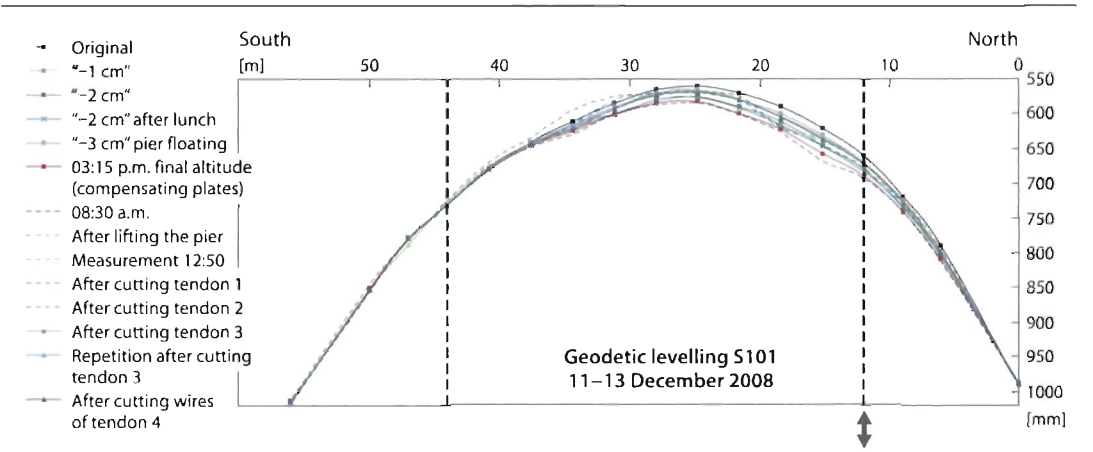
Geodetic Levelling

The data collected by the geodetic levelling confirm the artificial modification of structural properties due to uplifting and lowering the column (F.20-19), the cutting of the tendons was not visible in the measurement results.

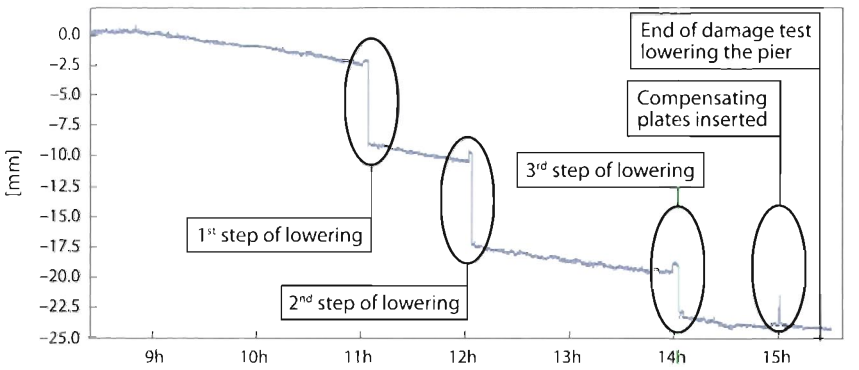
Laser Deformation Measurements

The following visualizations summarize the entire monitored global displacement history – corresponding with the vertical deformation of the bridge's main span (F.20-20 to F.20-22). As the bridge was not loaded with traffic during the progressive damage test significant deformations are only visible when the north-western pier is settled and lifted respectively. Apart from that the influence of changing temperature is visible in a mechanically expected manner.

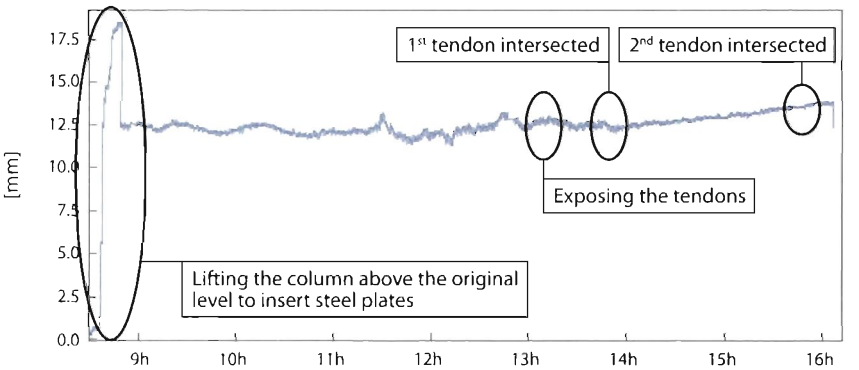
Geodetic levelling conducted after every major step of the progressive damage test at the S101 F.20-19



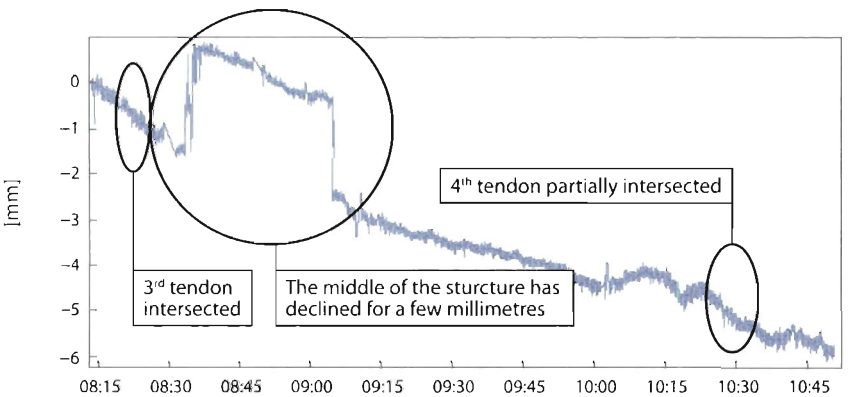
Laser based vertical displacement pattern during 11 December 2008 F.20-20



Laser based vertical displacement pattern during 12 December 2008 F.20-21



Laser based vertical displacement pattern during 13 December 2008 F.20-22



Mode Shapes

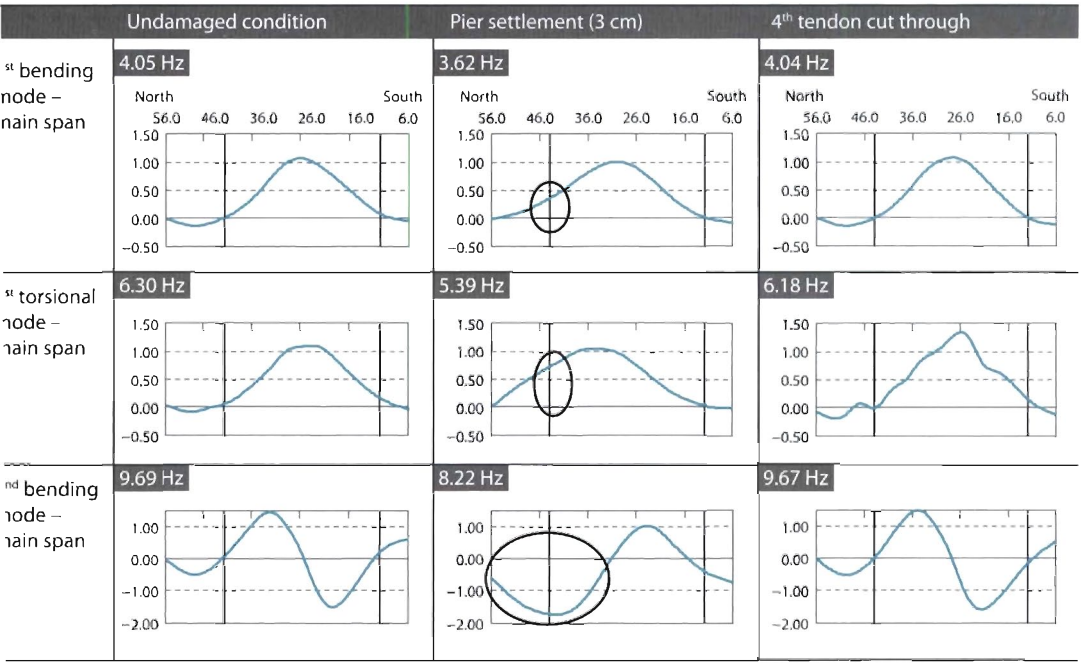
The analysis of the individual mode shapes enables the allocation of the eigenfrequencies to the corresponding motion of the structure. Mode shapes are an important parameter for the assessment of structural integrity and its operational characteristics. Furthermore mode shapes enable the identification of changing boundary conditions of the load-bearing structure, e.g. the operability of the bridge bearing concept.

The effects of both the pier settlement and the cutting of several tendons on this Key Performance Indicator are demonstrated by comparing the mode shapes in the three key stages in F.20-23.

// The mode shapes representing the undamaged condition are characteristic for this kind of structure and correspond to the expected modes of vibration. Distinctively occurring mode shapes indicate a good structural maintenance condition.

// The mode shapes after the pier was settled (F.20-23 – middle) clearly demonstrate the arising change in the boundary conditions. When the north-western pier is cut through and settled the vibration in vertical direction is not restricted anymore at this pier. Thus, the pier is no longer effective and the vibration length is extended to the northern abutment which results in lower values of eigenfrequencies as a consequence, e.g. the first bending mode was found at 4.05 Hz in the undamaged condition but at 3.62 Hz after the third stage of pier settlement. The higher the eigenfrequencies the more this additional degree of freedom gets evident in terms of mode shape amplitudes at the north-western pier.

Mode shapes of the decisive eigenfrequencies in the three key stages F.20-23



// Comparing the bending mode shapes of the very last stage of the damage test (4th tendon partially intersected) and of the undamaged condition hardly any changes can be seen, while the first torsional mode shape now occurs in a less distinctive progression.

Dissipation of Induced Vibration

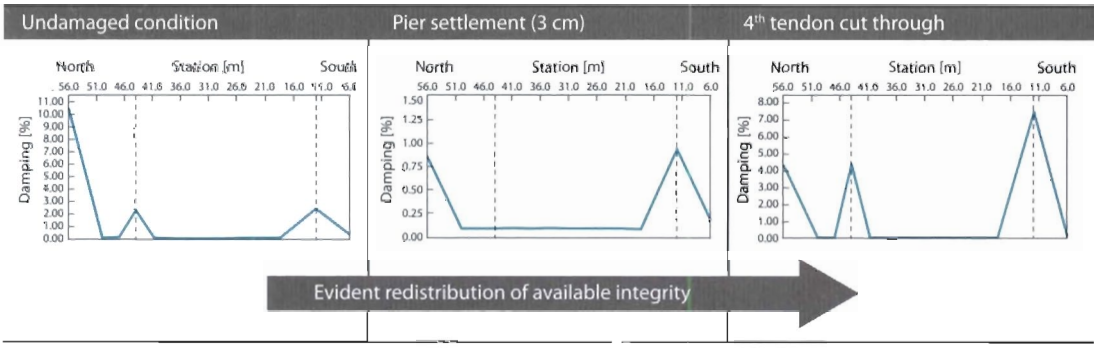
The damping values are a suitable indicator for the condition of a structure and the main girders respectively. "Problematic zones" mostly dissipate energy by means of friction which is reflected in an increase of the local damping values. Higher damping values in the area of abutments or piers are a logical consequence of the static system. Thus, they have no direct influence on the assessment of the structure's condition.

// The pattern of damping values in the lengthwise direction calculated from the undamaged condition's data (F.20-24 – left) is typical for such a structural type. The damping analysis primarily reflects the dominantly occurring system damping due to the mechanical behaviour of the bridge. Increased values from local spots according to material damping, which would point out certain damages (serious cracks, internal prestressing-problems), are not determined.

// The pattern of damping values based on the data when the pier was settled up to 3 cm confirms the conclusions stated after having analysed the mode shapes. Due to the fact that the north-western pier is not effective anymore the initially system-based high value in the area of the pier has decreased and does not differ from the values within the bridge deck anymore (F.20-24 – middle).

// Concerning the cutting through of tendons the pattern of damping differs from that of the undamaged condition when focusing on the relation of the damping values at the north-western pier and the northern abutment (F.20-24 right versus left). In case of the undamaged condition the damping value at the abutment is much higher than at the pier. In the final stage of the progressive damage test energy dissipation is much higher in the pier area itself as it used to be before and much lower at the abutment leading to an equilibrium between the energy dissipation rate at the pier and at the abutment.

Changing patterns of damping values during the progressive damage test (1BT main span; 4.05 Hz) F.20-24



20-5 Concluding Remarks

The demolition of the S101 bridge provided the opportunity to conduct destructive damage tests in order to demonstrate the value of Structural Health Monitoring as a proper method to get a more detailed picture of bridge health and bridge performance.

The visual inspection based rating classifies the bridge object S101 to be in category 4 out of 5 – indicating problematic condition. The dynamic measurement of the undamaged structure – broadening the understanding of the mechanical performance of the bridge reveals the object to be in a satisfactory condition.

Furthermore the destructive damage test was used to emphasize refined methods for the analyses of upcoming, slowly progressing damage and its effects on the parameters of dynamic response. The results demonstrate that Key Performance Indicators are a suitable instrument to identify, to localize and to evaluate damages that affect the bridge performance.

In the low frequency range of dynamic response global resistance is represented. Eigenfrequencies in this range are mainly affected by the change of structural properties in terms of boundary conditions and vibration length.

In the higher frequency range local resistance (structural members) is represented - mainly being affected by the artificial damage change (cutting the tendons) in the present case.

The progressive damage test demonstrated the high redundancy of prestressed bridges with grouted tendons. The loss of local prestressing reinforcement causes slight loss of local bending and torsional resistance only - but did not affect the global load-bearing behaviour in a relevant range.

References

bmvit, 2011. *Forschungsgesellschaft für das Verkehrs- und Straßenwesen: RVS 13.03.11 Überwachung, Kontrolle und Überprüfung von Kunstbauten – Straßenbrücken.* Vienna, 2011.

Wenzel, H., Veit-Egerer, R. and Widmann, M., 2009. *IRIS – Integrated European Industrial Risk Reduction System – IP: SP3 & 7: Workers Safety & Online Monitoring.* European Commission FP7, Project No.: FP7-NMP-2007-LARGE-1,4. Deliverable D11-1: WP3 Demonstration Report, Vienna, October 2009.

21

Life Cycle Analysis Applied to the New Jersey Case Study

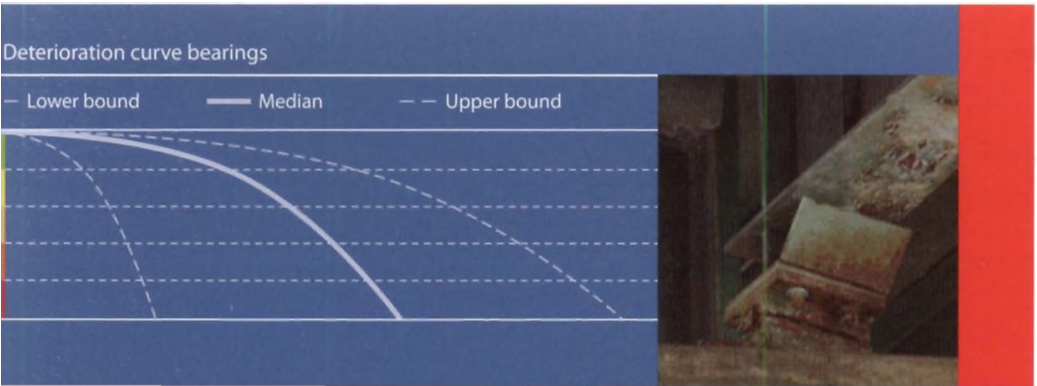
Authors:
Helmut Wenzel
Robert Veit-Egerer
Monika Widmann

Motivation

Considerable effort developing structural assessment and damage detection methodologies has been put in various parts of the world. It is desirable to harmonize the approaches and come up with recommendations on global scale.

Main Results

A comprehensive study using the IRIS technology has been provided on a reference bridge in New Jersey, USA. A comprehensive report on the various national approaches (19 teams from the USA, Europe and Asia), including recommendations became available.



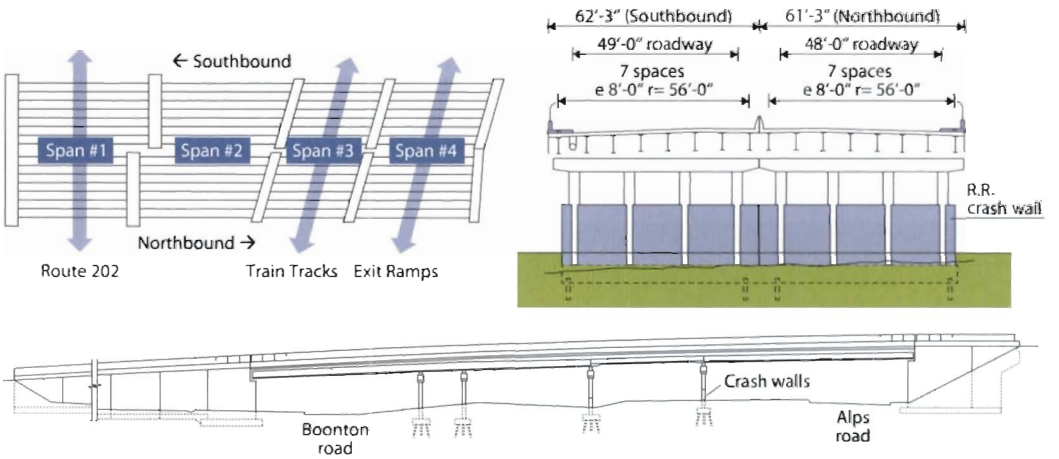
21-1 Introduction

A representative composite bridge has been selected by the Federal Highway Administration (FHWA) for the international collaboration between the Long Term Bridge Performance Project (LTBP) initiated in the U.S. and the FP7 Project IRIS in Europe. Various teams from the U.S., Japan, Korea, UK and EU have performed separate assessment routines including dynamic monitoring and system identification. The various approaches were compared and harmonized in order to achieve a standard model for this type of bridge, representing more than 40 % of the bridge stock in the FHWA network. This comprises a total of about 240000 bridges which could be tested subsequently and assessed following a standard procedure. For reasons of a consistent documentation of the field of investigations of each working group and the corresponding results, the present publication covers only those parts of expertise provided by the authors (VCE).

21-1-1 Structural Information

The bridge object 1618-150 (Reference Bridge New Jersey) is part of the highway US 202 & NJ 23, leading across US 202 (Mountain View Boulevard), the Ramps M & N and the Norfolk Southern Railroad in Wayne, New Jersey. The structure consists of two separate load bearing structures – one for each driving direction. The bridge (F.21-1 and F.21-2) comprises four spans of simply supported composite welded steel plate girders and has a total length of 130.64 m (428.6 ft). The total width is 37.64 m (123.5 ft). Every load bearing structure consists of three lanes and a shoulder. The Southbound Structure was opened to traffic in 1983, the Northbound Structure in 1984. The bridge shows numerous fatigue cracks, bearing problems, joint performance problems, flexibility/vibration problems, extensive deck cracking and movements [Aktan, 2010a]. The overall condition rating (D.O.T. Bridge inspection) was fair – due to the superstructure [Weber, 2006; 2008].

Reference Bridge New Jersey – plan, elevation and section view F.21-1



21-1-2 Critical Questions

The demand on Life Cycle Assessment is driven by the following desire of the bridge owners:

// To receive expertise on the expected remaining lifetime of the structure
// To receive a tool that allows the optimization of mitigation measures
// To perform a financial optimization exercise

The critical questions that need to be answered in the course of dealing with the present structural issues for Life Cycle Analysis are amongst others [Aktan, 2010b]:

// Does this bridge have any strength/capacity issues? If so, what are they?
// How can technology be used to identify, quantify and understand these issues? Structural Health Monitoring?
// What, if any, retrofits or interventions would you recommend?
// Maintenance and repair options for a 75-year Life Cycle?

21-2 Applied Life Cycle Methodology

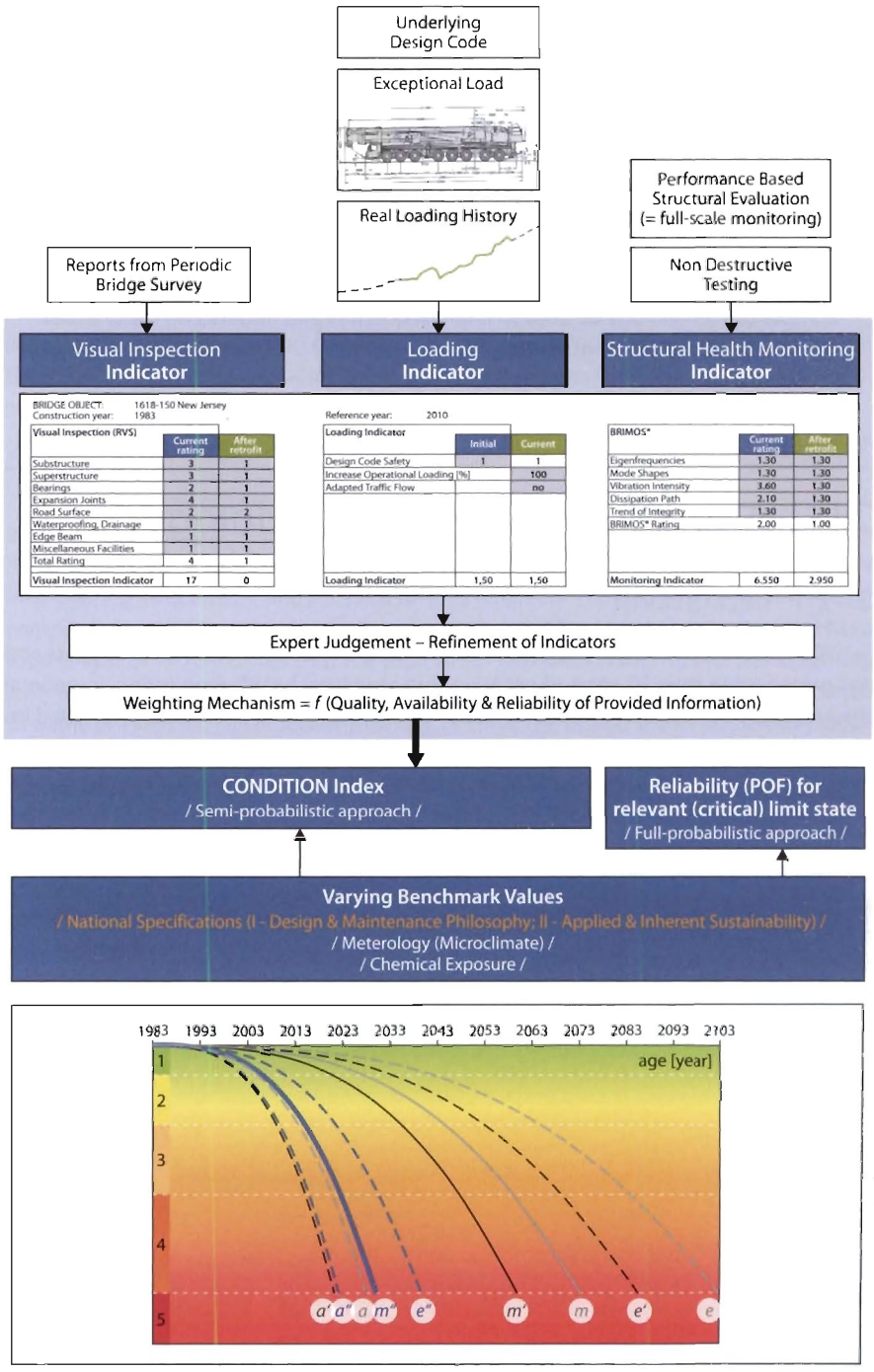
21-2-1 Background

VCE has been working in the field of structural evaluation for more than 50 years and has gained more than 20 years of experience in structural health monitoring. In general the assessment of structures has been done first and foremost by compulsory visual inspections, for critical cases in-depth studies are initiated – mostly in terms of numerical simulations or structural health monitoring. Indeed, up to now these investigations have been done with regard to the further service life of the assessed structures but have not

Reference Bridge New Jersey – bottom view F.21-2



From individual investigations to an integrated Life Cycle Assessment F.21-3



explicitly implied a Life Cycle Analysis. In order to merge the results from all individual investigations and to obtain a more detailed picture of structural health over the entire service life, a theoretical Life Cycle Model (F.21-3) for bridge structures has been developed, which dynamically considers any new information gathered from inspections, the design code, monitoring campaigns or non-destructive testing.

The procedure starts by deriving an accumulated health index from visual inspection of structural elements expressed in terms of structural condition. To represent common practice in bridge engineering the set of ratings according to the national guideline for visual inspections is utilized. Usually these ratings are available for every bridge component (superstructure, substructure, expansion joints, bearings, pavement, edge beam, guard rail and railings, dewatering and miscellaneous facilities). After being put into operation, each member's range of ratings represents the available (total) capacity, which is consumed over time during the entire service life. Due to that idea these ratings are converted into so-called health indices [prCWA, 2012]. The corresponding element performance curves are weighted and incorporated into a semi-probabilistic global lifeline model to cover occurring uncertainties during structural service life.

The applied ageing models are benchmark values on service life in bridge components based on literature, guidelines, bridge owner databases of structures and Vienna Consulting Engineers' (VCE) 50 years of experience in the field of bridge inspections and structural health monitoring and are about to be standardized [prCWA, 2012]. The deterioration curves are adapted for every individual structure and every structural member regarding the structural type, the particular age, the condition and the applied standard (design code) - relevant at the time of construction. Additional to a mean life expectancy upper and lower bounds are derived based on probabilistic methods. The correlation of deterioration curves and their proper threshold limits (end of service life) enable to schedule time frames to be expected for necessary retrofit measures to ensure the functional requirements.

21-2-2 General Description

In order to clearly address the stated problems the approach described below has been developed and standardized by the authors [Veit-Egerer and Widmann, 2010]. The multi-level procedure is based on the entire Life Cycle of the structure and considers certain structural characteristics gained from the following investigations:

- // Visual inspection of the critical elements with detailed assessment following the Austrian RVS 13.03.11 directive that regulates quality assurance for structural maintenance, surveillance, checking and assessment of bridges and tunnels [bmvit, 2011]
- // Design loading and specifications
- // Capturing the dynamic characteristic of the structure using BRIMOS® Structural Health Monitoring. BRIMOS® – standing for BRIdge Monitoring System – is an assessment methodology, which enables accurate observation and evaluation of structural condition and damage detection in relevant infrastructure. The technology was developed by VCE and is constantly modified and optimized in order to

support the decision process of infrastructure owners in the course of maintenance and cost planning. [BRIMOS®]

// Identification of the bridge behaviour on expert level to create the basis for an understanding of the observed damages and physical properties

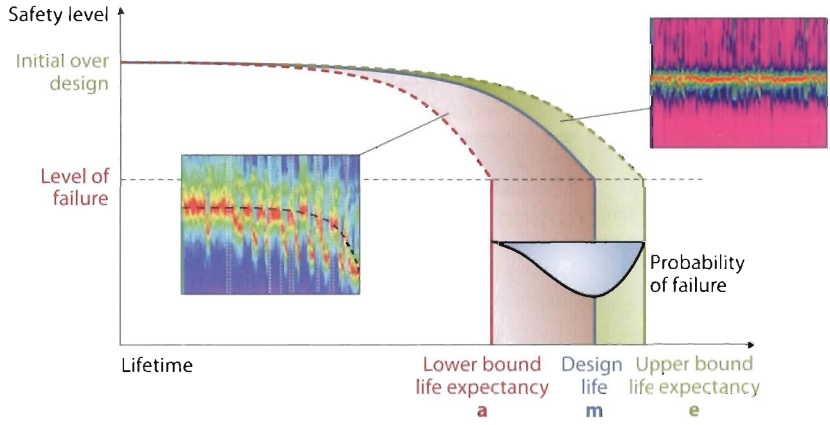
All relevant results of the listed components are incorporated into a probabilistic Life Cycle Model (F.21-4). Furthermore additional parameter studies enable to provide explicit answers to the stated critical questions.

Based on the calculated structural life expectancy tailored maintenance and repair options are recommended to extend service life and to ensure the safety and operability of the structure. Different maintenance strategies, their effects on the structural service life and their costs can be compared to derive the most suitable maintenance concept in order to preserve the structure in the demanded condition (F.21-5).

21-2-3 Assessment Procedure

The BRIMOS® Life Cycle Methodology is based on a multi-level approach (F.21-6). The basic model gives a rough estimation of expected structural service life in general. The adapted model already considers certain structural information and utilizes them for

Conceptual scheme of the probabilistic Life Cycle Model F.21-4



Tailored maintenance schedule and the cost involved F.21-5



proper lifeline progressions. The next step is to provide an update of this Life Cycle Curve based on performance-specific information. The latter refers to three main categories of evaluation:

// Visual inspection
// Design safety according to the applied code
// Other investigations (Structural Health Monitoring, Non Destructive Testing)

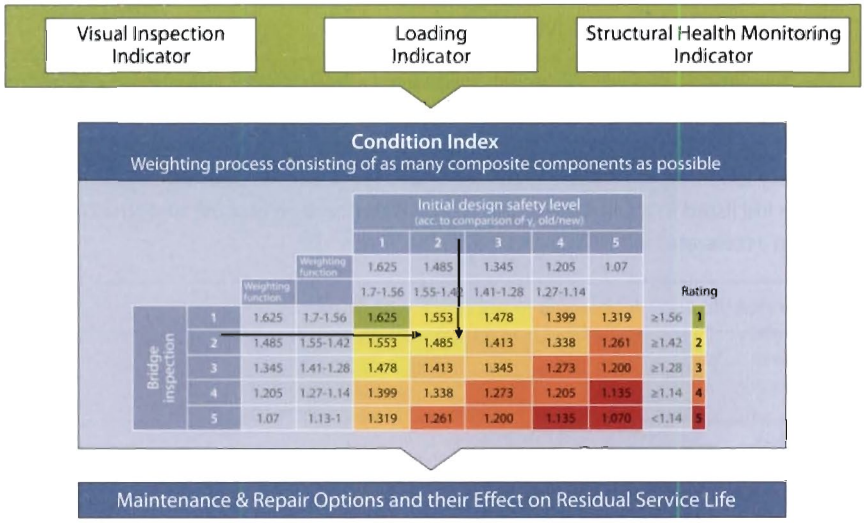
From these key parameters the structure's condition index is calculated which is used as reference point to calculate the life expectancy. The final progression of the Life Cycle Curve is determined by means of multiple, consecutive matrix calculations.

The more complete the information about the structural condition is the better are the results. Thus, for the determination of this methodically refined prediction of the Life Cycle Curve any additional information which is able to contribute to a better understanding of a structure will be used.

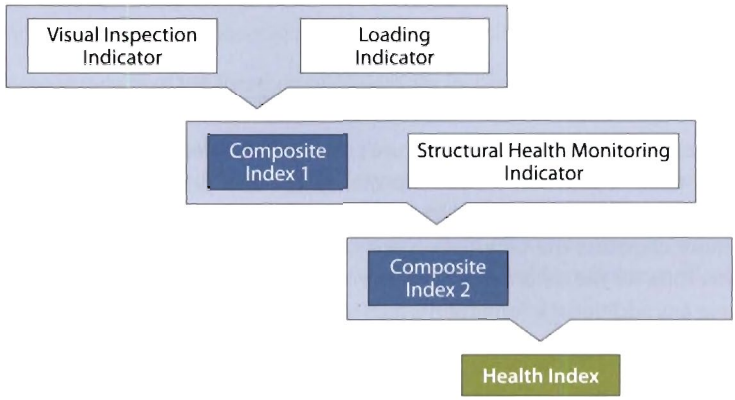
These are:

// Original static calculation (structural design)
// Possible reduction of safety level reflecting a paradigm change from previous binding codes to the current ones
// Judgement/rating from bridge inspections (reports)
// Performed monitoring campaigns
// History of already performed maintenance and rehabilitation measures
// Loading history (historical traffic data)
// Material tests (chloride intrusion/compressive strength, carbonatization etc.)
// Data on the environmental conditions

Calculation of the condition index for Life Cycle Analysis by means of matrix calculations F.21-6



Transformation of individual structural characteristics into a composite health index F.21-7



The more precise this information is the better are the results in terms of remaining service-life prognosis. Depending on the quality of information received a confidence level is introduced to determine the upper and lower bound of the theoretical performance curve. Under normal circumstances a confidence level of 0.95 is applied. This procedure allows a computation of the actual status which might be better or worse than the theoretical value. All those sources of information are incorporated in a weighted composite health index (F.21-7).

21-3 Case Study – Bridge Object 1618-150

21-3-1 Basic Life Cycle Model

The developed Life Cycle Approach starts from a basic model reflecting the expected analytical global service life. This very general, initial assumption states the average life expectancy with 90 years, a lower bound of 45 years and an upper bound of 120 years for the primary load-bearing structure and leads to a residual lifetime and the estimated end of service life listed in table T.21-1. The typical deterioration process of a structure starts slowly but accelerates over time.

End of service life and residual life expectancy – basic model T.21-1

	Residual life expectancy [years]	End of service life [date]
Lower bound	18	2028
Mean	63	2073
Upper bound	93	2103

Reference year: 2010

21-3-2 Adapted Life Cycle Model

Primary Load-Bearing Structure

In the next step a theoretical curve is computed as a mean result derived from benchmark data calibrated from an infrastructure database including a large number of structures [Wicke et al., 2001]. It is composed of the following information:

// Year of construction considering the periodic quality changes
// Character of the cross section considering redundancies
// Character of the structural system considering eventual redundancies
// Type of material used

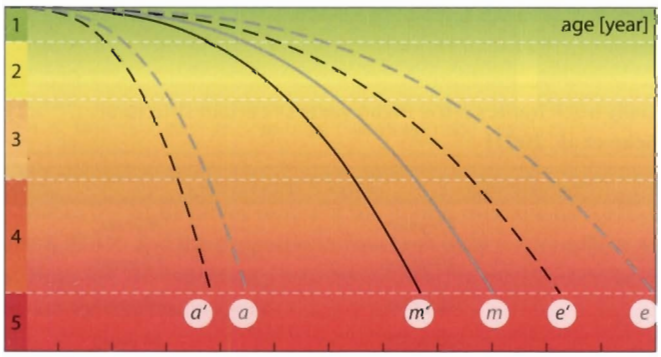
It already sets limits to a realistic range of service life – to be expected. This information is broadened by means of theoretical upper and lower bounds for probabilistic life expectancy. Considering the input parameters stated below (T.21-2) the mean life expectancy of the structure no. 1618-150 is reduced to 77 years with a lower bound of 38 and an

Input parameters for the adapted Life Cycle Model [Wicke et al., 2001] T.21-2

Year of construction	k_1	Static system	k_3
< 1970	0.667	Vault	1.2
1971–1985	0.9	Frames and arches	1.05
> 1986	1	Girder/beam, slab, other	1

Cross section design	k_2	Material	k_4
Solid cross section	1.05	Stone	1.2
Box girder	1	Concrete and reinforced concrete	1.1
T-beam, composite section etc.	0.95	Prestressed concrete, steel-concrete composite	1
Corrugated profile	0.8	Wood	0.8

Theoretical global Life Cycle Curve for the bridge – initial and adapted curve F.21-8



a ... Lower bound life expectancy
m ... Average life expectancy
e ... Upper bound life expectancy
a' ... Adapted lower bound life expectancy
m' ... Adapted average life expectancy
e' ... Adapted upper bound life expectancy

End of service life and residual life expectancy – adapted model T.21-3

	Basic model		Adapted model	
	Residual life expectancy [years]	End of service life [date]	Residual life expectancy [years]	End of service life [date]
Lower bound	18	2028	11	2021
Mean	63	2073	50	2060
Upper bound	93	2103	76	2086

Reference year: 2010

upper bound of 103 years (F.21-8). The corresponding end of service life and the residual life expectancy are listed in T.21-3.

Secondary Load-Bearing Structure

A bridge structure usually consists of a number of components which interact. Thus not only for the primary load-bearing structure but also for each of the components individual performance curves are to be determined (F.21-9). The structural Life Cycle Curve is the superposition of the individual curves of its components and elements. The following categories are considered:

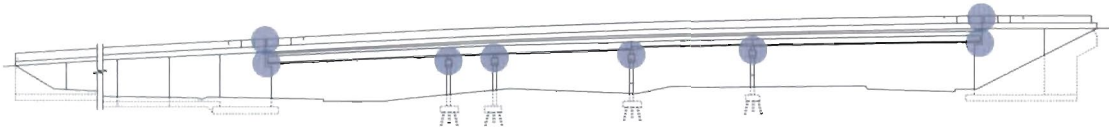
// Superstructure
// Substructure
// Expansion joints
// Bearings
// Pavement
// Edge beam
// Railings and guiderail
// Other bridge equipment
// Drainage and dewatering system

The deterioration curves and their corresponding threshold limits (end of service life) serve as initial assumption for expected time frames concerning necessary retrofit measures to ensure the functional requirements with regard to traffic safety, structural safety and durability. Exemplary target values for the life expectancy (replacement intervals) are provided in subsequent tables T.21-4 and figures F.21-9.

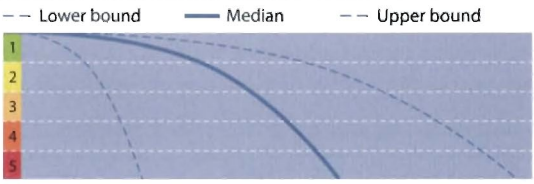
Influence of average daily truck traffic on the mean value of certain structural members' lifetime [Wicke et al., 2001] T.21-4

Average daily truck traffic	Pavement	Expansion joint
> 7000	7.5 years	9 years
≤ 7000 > 4000	10 years	12 years
≤ 4000 > 1000	15 years	18 years
≤ 1000	20 years	24 years

Individual deterioration curves for members of the secondary load bearing structure – a) bearings, b) guiderails, c) sealing and d) expansion joints F.21-9

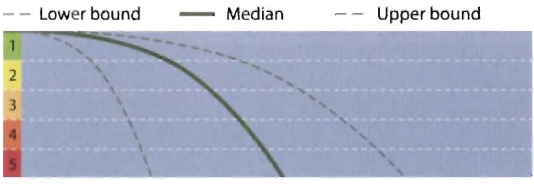


a) Deterioration curve bearings

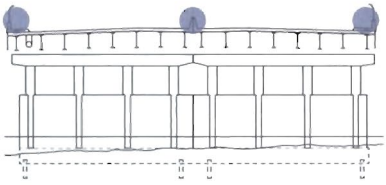




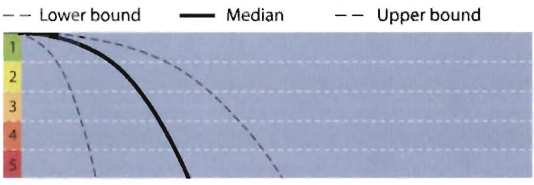
b) Deterioration curve guiderails





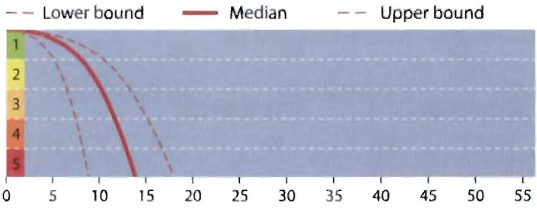


c) Deterioration curve sealing





d) Deterioration curve expansion joints





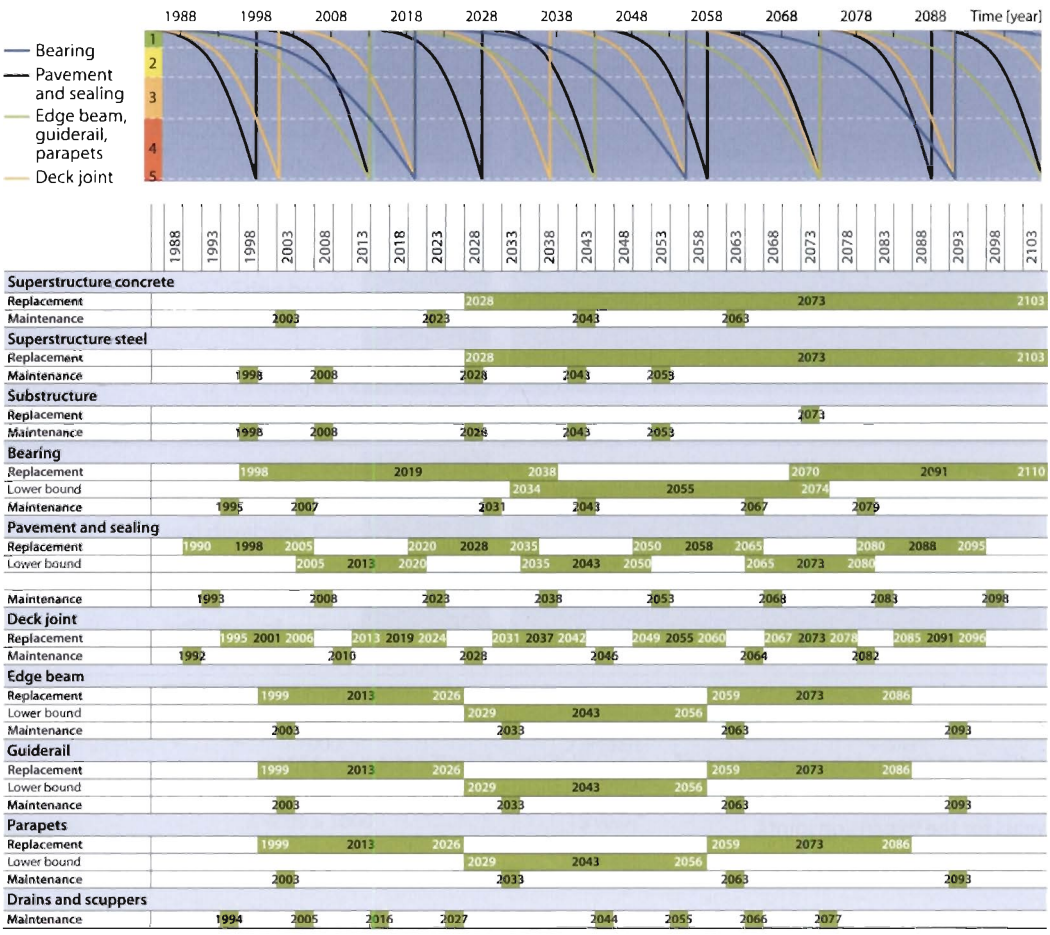
Due to the latest survey report of the bridge structure no. 1618-150 the average daily traffic is 93 400 and the proportion of average daily truck traffic is 4 % or 3736 trucks per day. Thus, the life expectancy is to be assumed to be 15 years for the pavement and 18 years for the expansion joints.

"To-be" Maintenance Schedule

Based on the adapted Life Cycle Model and the given information about global and local structural condition a comprehensive maintenance plan for the bridge object 1618-150 was developed. F.21-10 shows the maintenance concept by means of a time schedule of maintenance interventions proposed for the bridge object 1618-150. The maintenance schedule starts from the year of construction and considers the entire service life. This schedule can be understood as an elaboration stage in terms of an expected (theoretical) maintenance plan according to common practice.

In the next step related costs for replacement and heavy maintenance (T.21-5) – for every single intended retrofit measure are estimated and linked to the calculated points of intervention. Based on the time schedule a cost schedule over the whole service life is provided (F.21-11). The maintenance costs were mainly derived as a percentage of the total replacement costs.

Expected (theoretical) maintenance plan in terms of a time schedule over the whole service life F.21-10



Estimated replacements costs T.21-5

Southbound structure			[%]	[€]	[$]	[%]
Total replacement cost	2400	€/m²	100	6,246,456	8,289,672	
Total top view area	2603	m²				
Superstructure			42	2,623,512	3,481,662	
Bearings			5	312	424	
Expansion Joint			3	187	249	50
Substructure			30	1,873,937	2,486,902	30
Pavement and sealing			6	375	497	
Edge beam			10	625	829	
Guide rail			1	62	83	
Parapets			1	62	83	
Drains and scuppers			2	125	166	20
Sum			100	6,246,456	8,289,672	

Northbound structure			[%]	[€]	[$]	[%]
Total replacement cost	2400	€/m²	100	5,654,544	7,504,145	
Total top view area	2356	m²				
Superstructure			42	2,374,908	3,151,741	
Bearings			5	283	375	
Expansion Joint			3	170	225	50
Substructure			30	1,696,363	2,251,244	30
Pavement and sealing			6	339	450	
Edge beam			10	565	750	
Guide rail			1	57	75	
Parapets			1	57	75	
Drains and scuppers			2	113	150	20
Sum			100	5,654,544	7,504,145	

Relation Replacement/Maintenance: 90/10 %

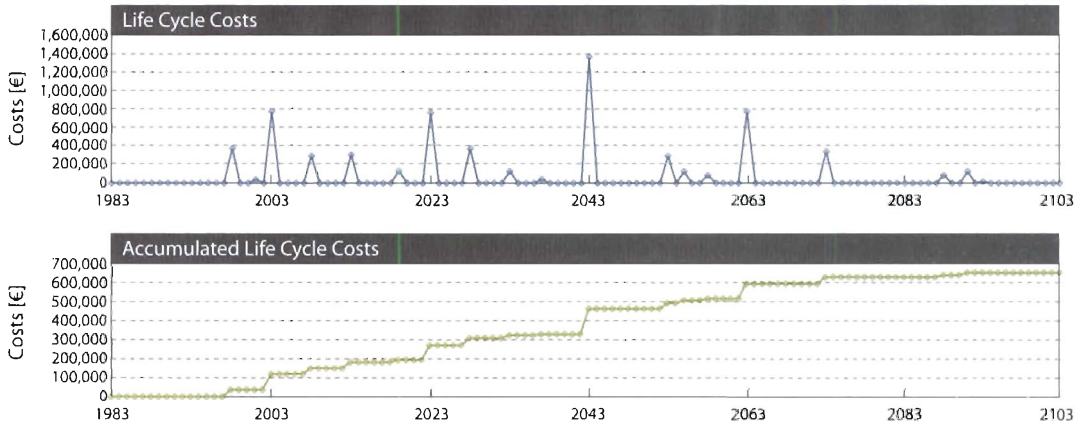
The assumed costs are referred to the reference year 2010 (real value).
The price adjustment over time is not considered (inflation vs. discounting).
Currently translation: yearly average currency rate 2010.

21-3-3 Major Input for Refined Life Cycle Analysis

Visual Inspection Indicator

The Austrian Guideline on bridge inspection RVS 13.03.11 [bmvit, 2011] specifies that every bridge has to be surveyed at least every six years following a given procedure. The detailed results are combined to a bridge rating which is used for decision making. In case of the bridge object 1618-150 a selective inspection has been carried out based on the information provided by the documentation material received in advance. Even if it was decided to concentrate on the critical issues only, the inspection has been complete enough to allow integral assessment and rating of all necessary elements of the structure (T.21-6). For detailed results of the visual inspection see [Wenzel et al., 2010].

Maintenance cost schedule during service life in terms of single (blue) and accumulated costs (green) procedure for refined Life Cycle Analysis F.21-11



The rating from the visual inspection is transferred into the overall assessment procedure by means of the Visual Inspection Indicator of 18 out of 25 (F.21-12).

Loading Indicator

The design of the bridge object 1618-150 followed the regulations stated below:
Design specification: 1977 AASHTO standard specifications for highway bridges including interim 1979 with N.J.D.O.T., modifications dated 1 June 1978; revised 29 February 1980 [Weber, 2006].
Design loading: AASHTO HS 20–44+10% or an alternate military loading of two axles, four feet apart each axle weighing 24,000 LBS., whichever produces greater stress [Weber, 2006].

These design specifications lead to a loading indicator of 1.5 implemented into the overall assessment procedure (F.21-12).

Rating scheme according to RVS 13.03.11 for the surveyed bridge in New Jersey T.21-6

Structure: No. 1618-150, Wayne, New Jersey

Periodic Bridge Inspection, June 2010	
Summary of Ratings according to RVS 13.03.11 (Austrian National Standard)	
Substructure	3
Superstructure	3
Bearings	2
Joints	4
Road Surface	2
Waterproofing, drainage	–
Edge beam	1
Miscellaneous facilities	1
Entire Object	**3**

Monitoring Indicator

A detailed dynamic measurement with BRIMOS® 11.02 was carried out on 21 and 22 June 2010. The objective of the monitoring campaign was to identify the key performance indicators of the structure with regard to their relevance for civil engineering issues [Wenzel, 2009]:

// The bridge structure's relevant eigenfrequencies and corresponding mode-shapes:
  / Load bearing capacity and operability
  / Evaluation of the bearings
  / Distribution of the global and local dynamic structural stiffness in the bridge's lengthwise and transversal direction
// Sensitivity analysis to investigate the progression, the character, the stability and probable changes in the energy content of the relevant eigenfrequencies:
  / Load bearing capacity and operability
// Energy dissipation path in the structure's lengthwise direction:
  / Dissipation of the induced vibration energy, localization of problematic sections

Successively conducted Life Cycle Analysis (supposing "do-nothing maintenance strategy") after evaluation for bridge object 1618-150 F.21-12

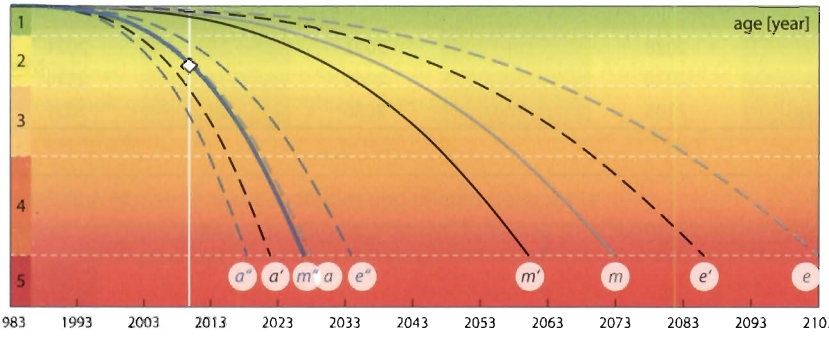
Construction year 1983

Visual Inspection (RVS)	Current rating
Substructure	3
Superstructure	3
Bearings	2
Expansion joints	4
Road surface	2
Waterproofing, drainage	4
Edge beam	1
Miscellaneous facilities	1
Total rating	4
Visual Inspection Indicator	**18**

Reference year 2010

Loading Indicator	Initial
Design code safety	1
Level of operational loads [%]	
Adapted traffic scenario	
Loading Indicator	**1.50**

BRIMOS®	Current rating
Eigenfrequencies	1.30
Mode shapes	1.30
Vibration intensity	3.60
Dissipation path	2.10
Trend of integrity	1.30
BRIMOS® rating	2.00
Monitoring Indicator	**6.550**



Remaining Life
16

Costs	
Retrofit	
476,040 €	
631,753 $	
Replacement	
11,901,000 €	
15,794,000 $	

a ... Lower bound life expectancy
m ... Average life expectancy
e ... Upper bound life expectancy
a' ... Adapted lower bound life expectancy
m' ... Adapted average life expectancy
e' ... Adapted upper bound life expectancy
a'' ... Enhanced prognosis lower bound life expectancy
m'' ... Enhanced prognosis average life expectancy
e'' ... Enhanced prognosis upper bound life expectancy

// Vibration intensity at the entire bridge deck:
/ Localization of weak points with regard to fatigue threat
// Comparison of measured values with the results of the finite element model:
/ Reference to the undamaged initial condition

For detailed results of the dynamic monitoring campaign see [Wenzel et al., 2010]. All the key performance indicators derived for the reference bridge were evaluated by means of ratings from 1 (excellent condition) to 5 (critical condition). The individual ratings were weighted and incorporated into the monitoring indicator.

In case of the bridge object 1618-150 the dynamic monitoring leads to a monitoring indicator of 6.55 implemented into the overall assessment procedure (F.21-12).

21-3-4 Statement on Residual Lifetime

Based on the available findings of the visual inspection, the corresponding rating, the complementary parameters from the project documentation and results of the dynamic measurements an enhanced Life Cycle Curve is generated. The three major sources of evaluation are already implemented at this stage: Visual Inspection Indicator, Design Code Safety Indicator and Structural Health Monitoring Indicator. This final composition for an integral lifetime prognosis is to be updated during the entire life.

By means of F.21-12 and T.21-7 it is shown that according to the current knowledge the remaining lifetime is 16 years. In 2026 the theoretical end of service life for this structure is reached. The calculated, corresponding retrofit costs include a minimum of routine maintenance activities within the stated remaining lifetime. This result meets the expectation that without any retrofit the lifetime of the structure is very limited.

Prognoses on the remaining life time corresponding to F.21-13 T.21-7

	Basic model		Adapted model		Enhanced prediction	
	Residual life expectancy [years]	End of service life [date]	Residual life expectancy [years]	End of service life [date]	Residual life expectancy [years]	End of service life [date]
Lower bound	18	2028	11	2021	11	2021
Mean	63	2073	50	2060	16	2026
Upper bound	93	2103	76	2086	21	2031

Reference year: 2010

21-4 Parameter Study on Relevant Retrofit Measures and their Effect on Residual Lifetime

To extend the remaining lifetime of the Bridge Structure 1618-150 – based on the overall rating composed from visual inspection, the current code requirements and the results of the dynamic monitoring campaign – several retrofit measures are recommended addressing the findings of all the investigations. In the following a parameter study by the variation of single elements was carried out to analyse the effect of the suggested measures on the residual lifetime. The exchange of damaged structural members will improve the overall bridge rating significantly. Furthermore it will also support a more vital progression of the overall ageing function of the structure. In other words these improvements have a positive impact on the damage index and consequently extend service life expectation. The unrestricted deterioration of the structure ("do-nothing"-strategy) and the corresponding remaining life time of 16 years serve as reference for this parameter study (F.21-12).

21-4-1 Recommended Retrofit Measures

Superstructure. Renewal of corrosion protection, repair of the concrete surface and the corroded stringers, repair of fatigue cracks, replacement of the wind bracings.

Substructure. Renewal of corrosion protection, repair of spallings, holes and concrete pockets, removal of contamination of the concrete surface, deep injection of cracks.

Bridge supports. Proper replacement of the bearings.

Dewatering. Establishing of an effective drainage concept.

Expansion joints. Proper detailing and design, full replacement (abutment area) or partial replacement (at least seals above the piers).

21-4-2 Possible Maintenance Strategies

A tailored maintenance concept (T.21-8) was elaborated. A stepwise proposal on the corresponding treatment strategies is given in the following:

Correlation of maintenance strategies and related treatments T.21-8

Strategy	Substructure	Dewatering	Expansion joints	Superstructure	Bearings
1	X	X			
2	X	X	X		
3	X	X	X	X	
4	X	X	X	X	X

Strategy 1

In case that the bridge receives the proposed retrofit the rating of the substructure and the waterproofing would be upgraded in the course of a subsequent visual inspection. Furthermore the proposed measures of heavy maintenance can be assumed to be also already beneficial for the dynamic behaviour (→ reduction of the vibration intensities). With that investment the expected remaining lifetime of the structure can be extended to 19 years (F.21-13).

The corresponding estimated investment costs of €922,000.— ($ 1,224,000) are not based on deep knowledge of the local market prices.

Strategy 2

In case that the bridge receives the proposed retrofit – in addition to the rating of the substructure and the waterproofing – the rating of the expansion joints would be upgraded in the course of a subsequent visual inspection. Furthermore the proposed measures of heavy maintenance can be assumed to be strongly beneficial for the dynamic behaviour (→ considerable reduction of the vibration intensities and proper progressions of the energy dissipation paths). With that investment the expected remaining lifetime of the structure can be extended to 25 years (F.21-14).

The corresponding estimated investment costs of € 1,160,000.— ($ 1,539,000) are not based on deep knowledge of the local market prices.

Strategy 3

In case that the bridge receives the proposed retrofit – in addition to the rating of the substructure, the waterproofing and the expansion joints – the rating of the superstructure would be upgraded in the course of a subsequent visual inspection. Furthermore the proposed measures of heavy maintenance can be assumed to be strongly beneficial for the dynamic behaviour (→ further considerable reduction of the vibration intensities and proper progressions of the energy dissipation paths). With that investment the expected remaining lifetime of the structure can be extended to 32 years (F.21-15).

The corresponding estimated investment costs of € 1,868,000.— ($ 2,479,000) are not based on deep knowledge of the local market prices.

Strategy 4

In case that the bridge receives the proposed retrofit – in addition to the rating of the substructure, the waterproofing, the expansion joints and the superstructure – the rating of the bearings would be upgraded in the course of a subsequent visual inspection. Furthermore the proposed measures of heavy maintenance can be assumed to be strongly beneficial for the dynamic behaviour (→ further considerable reduction of the vibration intensities and proper progressions of the energy dissipation paths of certain bearings). With that investment the expected remaining lifetime of the structure can be extended to 41 years (F.21-16).

The corresponding estimated investment costs of € 2,335,000.— are not based on deep knowledge of the local market prices.

Strategy 1: Life Cycle Analysis F.21-13

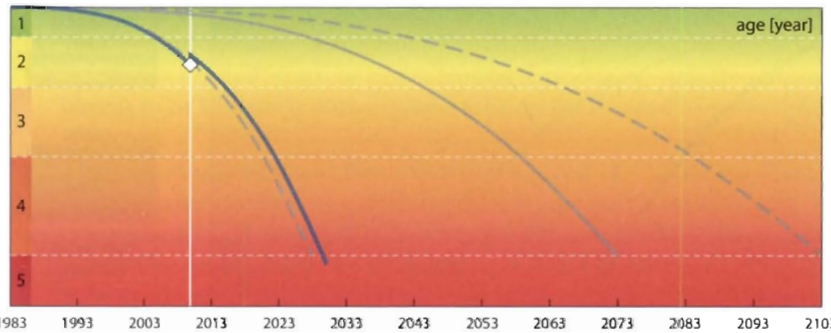
Construction year 1983

Visual Inspection (RVS)	Current rating	After retrofit
Substructure	3	1
Superstructure	3	3
Bearings	2	2
Expansion joints	4	4
Road surface	2	2
Waterproofing, drainage	4	1
Edge beam	1	1
Miscellaneous facilities	1	1
Total rating	4	3
Visual Inspection Indicator	**18**	**14**

Reference year 2010

Loading Indicator	Initial	Current
Design code safety	1	
Level of operational loads [%]		100
Adapted traffic scenario		no
Loading Indicator	**1.50**	**1.50**

BRIMOS®	Current rating	After retrofit
Eigenfrequencies	1.30	1.30
Mode shapes	1.30	1.30
Vibration intensity	3.60	2.95
Dissipation path	2.10	2.10
Trend of integrity	1.30	1.30
BRIMOS® rating	2.00	2.00
Monitoring Indicator	**6.550**	**5.250**



Remaining Life: 19

Costs
Retrofit: 922,000 € / 1,224,000 $
Replacement: 11,901,000 € / 15,794,000 $

Strategy 2: Life Cycle Analysis F.21-14

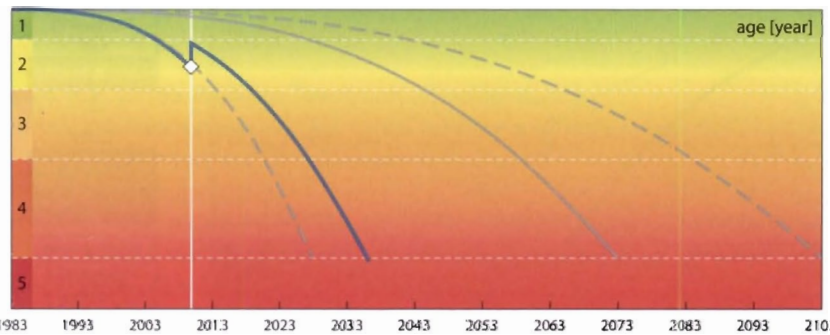
Construction year 1983

Visual Inspection (RVS)	Current rating	After retrofit
Substructure	3	1
Superstructure	3	3
Bearings	2	2
Expansion joints	4	1
Road surface	2	2
Waterproofing, drainage	4	1
Edge beam	1	1
Miscellaneous facilities	1	1
Total rating	4	3
Visual Inspection Indicator	**18**	**9**

Reference year 2010

Loading Indicator	Initial	Current
Design code safety	1	
Level of operational loads [%]		100
Adapted traffic scenario		no
Loading Indicator	**1.50**	**1.50**

BRIMOS®	Current rating	After retrofit
Eigenfrequencies	1.30	1.30
Mode shapes	1.30	1.30
Vibration intensity	3.60	1.70
Dissipation path	2.10	1.80
Trend of integrity	1.30	1.30
BRIMOS® rating	2.00	1.00
Monitoring Indicator	**6,550**	**2,950**



Remaining Life: 25

Costs
Retrofit: 1,160,000 € / 1,540,000 $
Replacement: 11,901,000 € / 15,794,000 $

Strategy 3: Life Cycle Analysis

F.21-15

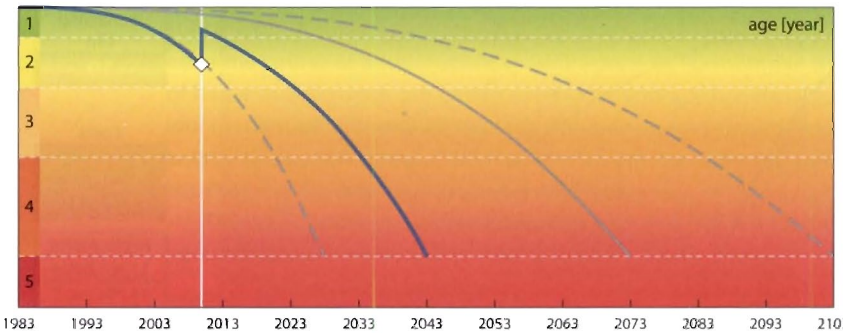
Construction year 1983

Visual Inspection (RVS)	Current rating	After retrofit
Substructure	3	1
Superstructure	3	1
Bearings	2	2
Expansion joints	4	1
Road surface	2	2
Waterproofing, drainage	4	1
Edge beam	1	1
Miscellaneous facilities	1	1
Total rating	4	1
Visual Inspection Indicator	**18**	**2**

Reference year 2010

Loading Indicator	Initial	Current
Design code safety	1	
Level of operational loads [%]		100
Adapted traffic scenario		no
Loading Indicator	**1.50**	**1.50**

BRIMOS®	Current rating	After retrofit
Eigenfrequencies	1.30	1.30
Mode shapes	1.30	1.30
Vibration intensity	3.60	1.40
Dissipation path	2.10	1.80
Trend of integrity	1.30	1.30
BRIMOS® rating	2.00	1.00
Monitoring Indicator	**6.550**	**2.650**



Remaining Life: 32

Costs

Retrofit
1,868,000 €
2,480,000 $

Replacement
11,901,000 €
15,794,000 $

Strategy 4: Life Cycle Analysis

F.21-16

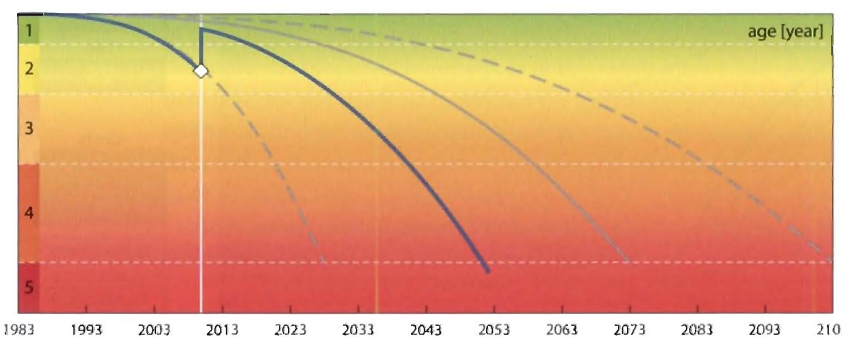
Construction year 1983

Visual Inspection (RVS)	Current rating	After retrofit
Substructure	3	1
Superstructure	3	1
Bearings	2	1
Expansion joints	4	1
Road surface	2	2
Waterproofing, drainage	4	1
Edge beam	1	1
Miscellaneous facilities	1	1
Total rating	4	1
Visual Inspection Indicator	**18**	**0**

Reference year 2010

Loading Indicator	Initial	Current
Design code safety	1	
Level of operational loads [%]		100
Adapted traffic scenario		no
Loading Indicator	**1.50**	**1.50**

BRIMOS®	Current rating	After retrofit
Eigenfrequencies	1.30	1.30
Mode shapes	1.30	1.30
Vibration intensity	3.60	1.30
Dissipation path	2.10	1.30
Trend of integrity	1.30	1.30
BRIMOS® rating	2.00	1.00
Monitoring Indicator	**6.550**	**2.250**



Remaining Life: 41

Costs

Retrofit
2,335,000 €
3,098,000 $

Replacement
11,901,000 €
15,794,000 $

21-5 Concluding Remarks

// The present in-situ assessment indicates that the structure's load-bearing capacity and its operability are available to a satisfactory extent at the time of investigation.
// The current visual inspection and a monitoring-based dynamic analysis with BRIMOS® revealed the main deficiencies of the bridge object 1618-150 leading to an accelerated consumption of the global lifetime.
// Based on the available findings from visual inspection, the corresponding rating, the complementary parameters from the project documentation and results of the dynamic measurements an enhanced Life Cycle Analysis was conducted.
// The three major sources of evaluation (Visual Inspection Indicator, Design Code Safety Indicator and Structural Health Monitoring Indicator) state the remaining lifetime to be 17 years. In 2026 the theoretical end of service life for this structure is reached.
// This result meets the expectation that without any retrofit the lifetime of the structure is very limited → a proper maintenance concept was elaborated.
// In the course of a detailed Life Cycle Parameter Study the effect of recommended maintenance measures on the residual lifetime was analysed. Starting from the most demanding tasks heavy maintenance measures were implemented in the course of certain treatment strategies – stepwise extending the resulting life expectancy.
// The determined Life Cycle Curves represent an estimation based on the structure's current condition and have to be confirmed and – if necessary – adjusted in the course of routine surveys in accordance with the given maintenance concept.
// Prospective changes of the relevant codes and particularly increasing loading (e.g. rising of the permitted total weight of freight traffic) can lead to considerable changes in the deterioration curve.

References

Aktan, A.E., 2010a. *NJ Bridge Preliminary Observations and Recommendations*. Philadelphia, 2010.

Aktan, A.E., 2010b. *IBS Bridge Description*. Philadelphia, 2010.

bmvit, 2011. *Forschungsgesellschaft für das Verkehrs- und Straßenwesen: RVS 13.03.11 Überwachung, Kontrolle und Überprüfung von Kunstbauten – Straßenbrücken*. Vienna, 2011.

BRIMOS®. www.brimos.com

prCWA63, 2012. *prCWA 63:2012 (E): Ageing Behaviour of Structural Components with Regard to Integrated Lifetime Assessment and Subsequent Asset Management of Constructed Facilities*. CEN Enquiry (TC), ON Secretariat, June 2012.

Veit-Egerer, R. and Widmann, M., 2010. *Life Cycle Methodology & Durability Analysis with Regard to Relevant Heavy-Maintenance Instructions*. VCE-WD 220; IRIS (Integrated European Industrial Risk Reduction System – IP: SP3 & 7); European Commission FP7; Project No.: FP7-NMP-2007-LARGE-1, October 2010.

Weber, C. and Associates PC, 2006. *Bridge Re-Evaluation Survey Report, Structure No.1618-150 – Cycle No. 11*. Phillipsburg NJ, 2006.

Weber, C. and Associates PC, 2008. *Bridge Re-Evaluation Survey Report, Structure No.1618-150 – Cycle No. 12*. Phillipsburg NJ, 2008.

Wicke, M., Kirsch, P., Straninger, W. and Scharitzer, B., 2001. *Kostenmodell für den Funktionserhalt von Straßenbrücken*. Bauingenieur Band 76, February 2001.

Wenzel, H., 2009. *Health Monitoring of Bridges*. J. Wiley and Sons Ltd, ISBN0470031735; Chichester England, March 2009.

Wenzel, H., Veit-Egerer, R. and Widmann, M., 2010. *Deliverable D11-2: Demonstration Report*. International Demonstration; US Department of Transportation–Federal Highway Administration; Long Term Bridge Performance Program; Reference Bridge – New Jersey; IRIS (Integrated European Industrial Risk Reduction System – IP: SP3 & 7); European Commission FP7; Project No.: FP7-NMP-2007-LARGE-1, September 2010.

22

Structural Health Monitoring of the Tamar Bridge

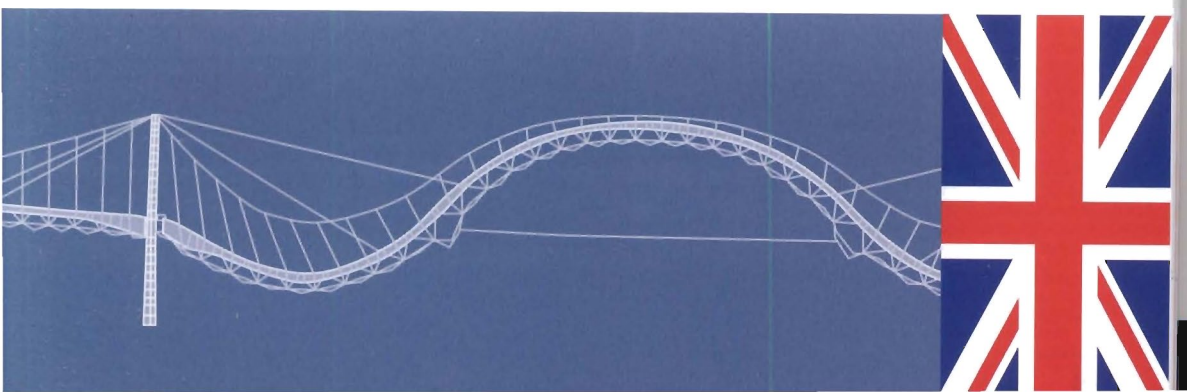
Author:
James Brownjohn

Motivation

Key structures in the transportation infrastructure like the Tamar Bridge in the United Kingdom require effective online monitoring strategies focusing on interpretation and integration into existing operational systems. The methodology for implementation is required.

Main Results

Applying the IRIS Risk paradigm to a monitoring system implemented in the Tamar Bridge, opened in 1961, has demonstrated the feasibility of reducing uncertainties in key structures.



22-1 Introduction

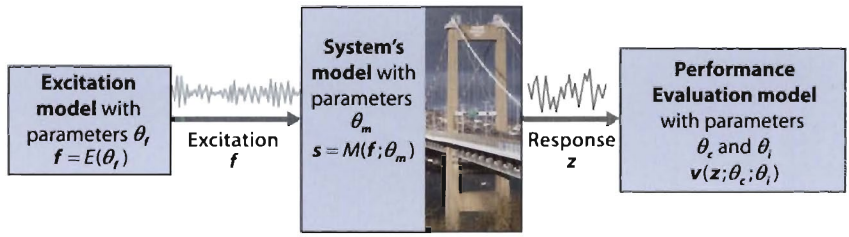
The development of effective on-line monitoring strategies for civil infrastructure, focussing on interpretation and integration into existing operational systems performed by USFD in the framework of IRIS Project are here presented.

The innovation to be provided through IRIS is that rather than emphasising novel instrumentation, developments would be focussed on the software for data management, mining and interpretation. These would be integrated with traditional structural analysis and simulation tools to improve the capability of the structural health monitoring systems to interpret performance, on-line and in real-time and provide operator-friendly information for making decisions relating to safe operation, maintenance and long-term structural management. Software tools available from different disciplines were to be brought together, as follows:

- // Structural system identification procedures able to identify structural attributes and characterise performance mechanisms in real-time.
- // Heuristic data mining tools to track these performance mechanisms and identify anomalies, also in real-time.
- // Structural analysis tools capable of being linked to performance data to create reliable physics-based structural models for interpreting anomalous performance.
- // Interfaces to existing operations systems for presenting and alerting based on the above tools and procedures.

These tools had not before been integrated in any one system. Tamar Bridge (a 335 m main span suspension bridge in the south of England) was chosen as demonstration system. There have been several technology advances brought about by the application at Tamar Bridge. Tamar was used to demonstrate the world's first continuous monitoring of a long span bridge by a total positioning system coupled to a structural health monitoring system and automated real time operational modal analysis (OMA) system on a civil structure. That system was original embedded in the local processor. One of the lessons from the research is that with high speed broadband, a better solution is to store raw data locally, transmit to a remote server (at Sheffield) and do the OMA on the server, which can afford to be more powerful. We realise that embedded processing may be appropriate for wireless sensing with limited data transmission capacity, but it is not necessary, in fact counter-productive (due to slowing the local PC).

System modelling implementation by USFD F.22-1



Tamar was used to build, evaluate and demonstrate the advanced data fusion system enabled through integrated use of SQL data base, internet capabilities and MATLAB processing. The web-viewer capability has been extended and applied to other structures.

Now we have a very good understanding of the load response mechanisms and the nature of the loads themselves. The next step in the research is to apply data-driven meta models developed in parallel research and calibrated/adapted based on the experiences and models described here. These will be used to embed the experiences of the research, filtering out the normal operating conditions so that anomalous performance may be identified and diagnosed, allowing bridge operators to make cost-effective operational management decisions. Achievements of the performed research are here listed:

// Identify typical structure performance anomalies.
Done: for example traffic jams, suddently deformation changes.
// Identify structural/performance events causing the anomalies.
These anomalies have been thoroughly rationalised via supporting information and FEM.
// Develop robust software tools for detecting the anomalies.
These have been done within a separate, EPSRC funded study and are proven successful.
// Develop techniques for embedment in local data gathering systems.
Final decision was to locate the algorithms at the main server.
// Develop user interfaces and effective alerting strategies.
This has been a major success from the project.

22-2 Tamar Bridge

The Tamar Suspension Bridge carries the A38 trunk road over the River Tamar from Saltash (Cornwall) to Plymouth (Devon) and is owned, operated and maintained by the two local authorities. The original bridge (F.22-2), opened in 1961, was designed by Mott Hay and Anderson as a conventional suspension bridge with symmetrical geometry, having a main span of 335 metres and side spans of 114 metres, and with anchorage and approach spans the overall length is 642 metres.

The towers were constructed from reinforced concrete (RCC) and have a height of 73 m with the deck suspended at half this height. The towers sit on caisson foundations founded on rock [Fish and Gill, 1997]; tower walls are 0.6 m in thickness and square in plan but taper from 4.3 m at the base to 2.7 m square at saddle level. The main suspension cables, 350 mm in diameter, each consist of 31 locked coil wire ropes and carry vertical locked coil hangers at 9.1 m intervals. The main cables are splayed at anchorages and anchored some 17 metres into rock.

Trusses are 4.9 m deep with chords of welded hollow box construction, 0.6 m square in section. Other truss bracing consists of mainly rolled sections and utilizes both riveted and bolted connections. Trusses are connected by cross trusses at 9.1 m centres and top and bottom plan bracing resists horizontal wind loads. The original deck, spanning between

cross trusses, was of composite construction with a 150 mm deep reinforced concrete slab supported on five longitudinal universal beams. The deck was surfaced with hand-laid mastic asphalt nominally 40 mm thick. The moment of inertia of whole bridge deck for vertical plane bending is calculated as 2.18 m^4.

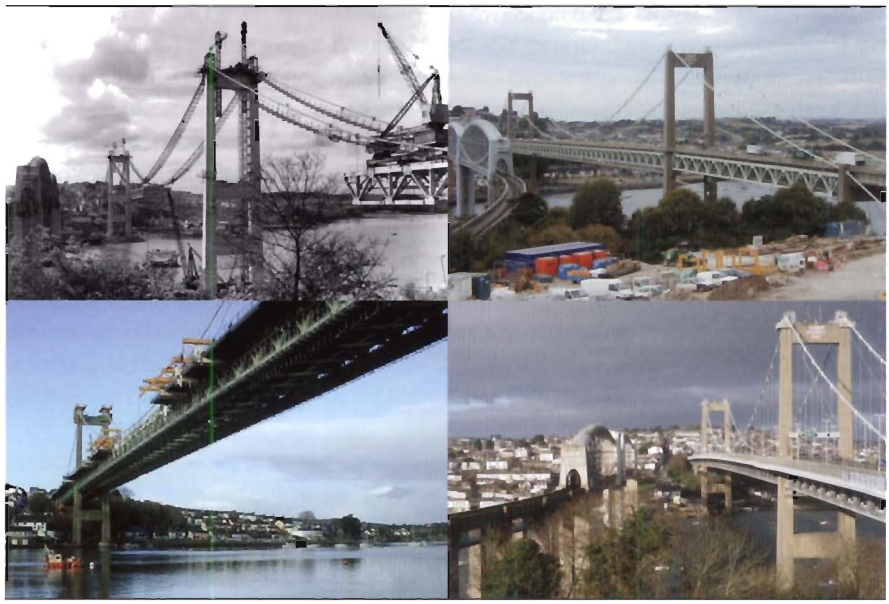
22-2-1 Strengthening and Widening

When opened in 1961, Tamar was the longest suspension bridge in the UK and the first to be built since World War 2. In early life it carried approximately 4000 vehicles a day with a maximum gross weight of 24 tons, but in the late 1990s, it was found that the Tamar Bridge would not be able to meet a new European Union Directive that bridges should be capable of carrying lorries up to 40 tonnes. To accommodate these, the bridge needed to be strengthened or replaced.

The appointed consultant for the strengthing widening, Acer (Now Hyder) proposed replacement of the main deck with a lightweight orthotropic steel deck, and having investigated a range of traffic diversion options, proposed construction of temporary relief lanes cantilevered off the bridge truss, to act as a supplementary diversion route while the main deck was being replaced. As the design developed, it became apparent that the permanent addition of cantilever lanes also offered a cost-effective permanent improvement in terms of both capacity and safety.

At the end of the exercise in December 2001, Tamar Bridge became the world's first suspension bridge to be widened (from three to five lanes) using cantilevers, and the first bridge to undergo strengthening and widening work while remaining open to traffic. The result is shown in F.22-2.

Tamar Bridge under construction, before, during and after strengthening and widening F.22-2



22-2-2 Monitoring during Strengthening and Widening

At this stage environmental and structural monitoring equipment was installed, which supplemented with live loading information obtained from a weigh-in-motion system, allowed the project team to examine the behaviour of the structure under changing environmental and loading conditions. The Structural Monitoring System (SMS) installed by Fugro Structural Monitoring has been used to monitor cable loads, structure and environment temperatures and wind speed and profile. The purpose of SMS has been to provide information on performance and condition of the bridge during and after the widening and strengthening. In particular it was used to track deck profile and cable loads during the strengthening works. The system displays instantaneous values and historical view of acquired data and uses a mimic to illustrate bridge behaviour, with threshold alarms. The sensors used in the SMS include:

// Anemometers to measure wind speed and deflection
// Fluid pressure-based level sensing system measure deck vertical displacement
// Temperature sensors for main cable, deck steelwork and air
// Extensometers and resistance strain gauges to measure loads in additional cables
// Electronic distance measurement between tower tops

Temperature, sampled 1 Hz

Steel and cable temperature monitoring sensors are platinum resistance thermometers stainless steel shim glued in place. Air temperature sensors consist of temperature probe with radiation shield.

Strain Gauges

Type 1, 2, 3 and 4 inclined cables are measured by resistive strain gauges attached to main tensioning bolts at deck anchor points. Fixing is by epoxy (protected by foil-backed putty) or micro-welding (covered by butyl rubber and neoprene). Gauges are arranged in pairs 180 degrees apart, each pair comprising an axial element and an element to measure hoop strain. The four gauges are connected to a full Wheatstone Bridge, with the hoop gauges providing the temperature compensation.

Wind Sensors

Wind speed is measured mechanically at top of Saltash Tower (where direction is also measured), Deck level of Saltash Tower and Saltash Approach.

Level Sensing System

This comprised a fluid manometer system with piles along the main span. Heights are measured at level sensing stations (LSS) 1/8 span centres using pressure measurements on the fluid head. The system is based on a similar system installed on bridges in the Lantau Fixed Crossing. The height measurements were specified to be accurate to ±5 mm and sampled at 1 Hz.

22-2-3 Present Day Performance

The monitoring system continues to provide information about deck temperatures and wind speeds, but the level sensing system no longer functions and some cable load monitoring data are unreliable and discounted. The main concerns for bridge operations are safety, not just in the bridge but in the adjoining Saltash tunnel. CCTV cameras and image tracking software are used to avoid and manage traffic and wind data are used to determine when the bridge should be closed to high sided vehicles.

The additional cables restored 400 mm of the original hogged longitudinal profile of the main deck that had been lost due to main cable creep over the previous 40 years. As part of the ongoing structural assessment programme, deck profile is checked at frequent intervals by surveying.

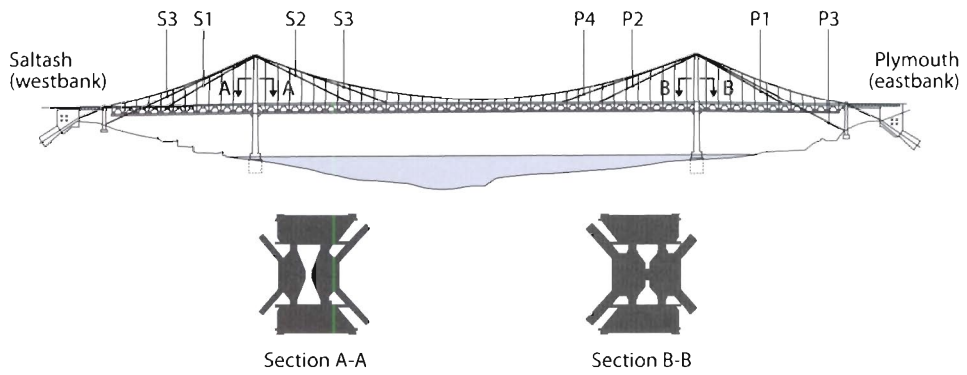
There are two aspects of structural performance resulting from the upgrade that interest bridge management. The first is the behaviour of the bearings and the global deformation of the bridge and the second is the dynamic behaviour of the additional stay cables.

Bridge Deformation and Bearings

In the original configuration, bearings at the Saltash tower comprising vertical swing links and lateral thrust bearings allowed for longitudinal movement and rotation about a vertical axis to allow deck sway, together with an expansion joint in the roadway. At the Plymouth tower the arrangement was the same but with a link connecting the trusses either side of the tower. F.22-3 shows the thrust bearings at each tower together with the truss links at Plymouth.

During the upgrade, the link at the Plymouth tower was severed, and the load path to provide longitudinal restraint on the main span is via the cantilever deck sections. These are continuous either side of the Plymouth tower and incorporate movement joints at the Saltash tower. There is some uncertainty about how these new arrangements are working.

Lateral thrust bearings for truss and span connection arrangements, pre-upgrade and schematic of additional stay cable locations F.22-3



Additional Stay Cables

F.22-3 sketches the layout of the additional stays. P2S, P2N are north and south sides of the main span and supported by the Plymouth tower. Modulus of elasticity for all cables is 155GPa (nominal), and of the total of 18 additional stays, cable numbers 1, 3 and 4 are 102 mm diameter strand while cable number 2 is 112 mm strand.

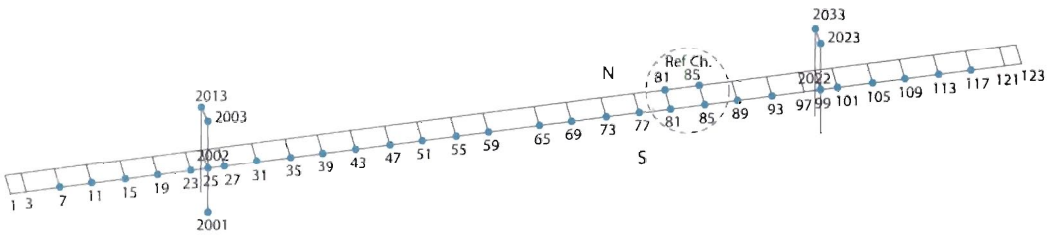
22-2-4 Modal Testing Facilities and Planning

Facilities and staff from the Vibration Engineering Section (vibration.shef.ac.uk) were used for the ambient vibration survey on 28 April 2006, preceding two days of forced vibration testing on floor systems for a new retail development in Plymouth. Testing facilities comprised:

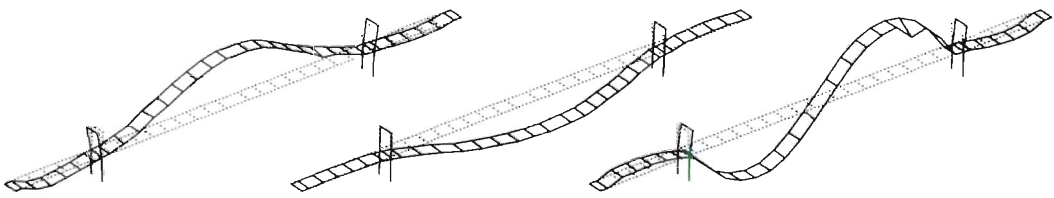
// A set of 16 QA700 and QA750 Quartz-flex servo accelerometers
// Data Physics Mobilyzer multi-channel data acquisition/spectrum analyzer system
// MODAL and Artemis operational modal analysis (OMA) software

F.22-4 shows the test grid; as planned, measurement positions on the deck were located at every 2nd hanger and F.22-5 shows sample modes identified using the eigensystem realization algorithm.

Test measurement grid, showing reference channels F.22-4



Sample of identified modes F.22-5



VS1 0.393 Hz LS1 0.457 Hz VA1 0.595 Hz

22-3 Finite Element Modelling

In order to compare experimental and analytical modal parameters, a high resolution 3D finite element (FE) model was developed in ANSYS, designed to consider varying environmental conditions, such as ambient temperature and wind. Further details of the modelling are found in WD-501. ANSYS replicates the geometric (tension) stiffening by applying internal strains to tension elements then applying vertical acceleration aimed at reaching an equlibirum state. Ideally the resulting state should be the same as the configuration of the prototype with no additional loads, but due to inexact values of initial internal strains there are small differences or deflection errors. The process was applied two ways. Method 1 constructs the bridge as it appeared in 1961; with a concrete deck, and no cantilevered deck and additional cables. Assuming the original initial tensions do not change, the bridge is remodelled into its present state, and the stay cables forces are found by iteration. Method 2 takes the stay cable forces measured from the bridge structure, and determines the required suspension cable forces from the current structure.

In both Method 2 and the first stage of Method 1, the main and side suspension cable forces are iterated to minimise the deflections in the main span and the towers. The second stage of Method 1 requires identifying the forces in the eight pairs of stay cables attached to the truss.

Method 1: Shape Finding the Tamar Bridge's 1961 Configuration

The shape finding process on the 1961 version of the bridge results in deflection errors of only 2 mm over the 335 m main span. The exaggerated displacements in F.22-6 show that the largest errors occur in the cables. Measured vertical mode properties shown in T.22-2 for the 1961 bridge are taken from a paper by [Williams, 1984]. Differences from FE model predictions exceed 10 %.

The next step, the identification of the stay cable forces in 2001, produces some larger deflection error at both mid-span and quarter span of the deck shown in F.22-7, but these are still acceptable. The errors from the dynamic results have also lessened.

Initial configuration of the Tamar Bridge in 1961 F.22-6



Initial configuration of the Tamar Bridge in 2001, identified via the configuration from 1961 F.22-7



Initial configuration, if found via by first identifying the bridge's 1961 configuration T.22-1

Year	Force [kN]						Displacement errors [mm]			
	Suspension cable		Stay cable				Mid-span	Side span	Quarter span	Saltash tower
	Main span	Side span	S3	S1	S2	S4				
1961	21844	22275	N/A	N/A	N/A	N/A	2.14	-2.33	-2.14	2.72
2001	21844	22275	58	747	739	766	86.16	5.96	-38.2	5.46

Dynamic properties of Tamar bridge, with a configuration found using the first shape finding method T.22-2

Year	Dynamic property	Mode 1	Mode 2	Mode 3	Mode 4	Mode 5
1961	Mode shape	LS1	VS1	VA1	VS2	TS!
	Frequency [Hz]	0.295	0.371	0.411	0.795	0.939
	Monitored frequency [Hz]	-	0.32	0.37	0.67	0.83
	Error	-	15.9%	11.1%	18.7%	13.1%
2001	Mode shape	VS1	LS1	VA1	TS1	VS2
	Frequency [Hz]	0.392	0.508	0.540	0.748	0.846
	Monitored frequency [Hz]	0.393	0.457	0.595	0.726	0.975
	Error	0.3%	11.2%	9.2%	3.0%	13.2%

LS1 means first symmetric lateral mode shape, VS1 first symmetric vertical mode shape, and VA1 first asymmetric vertical mode shape.

Method 2: Using Measured Stay Cable Tensions

Method 2 is simpler and uses stay cable forces obtained from the SHM system. The deflected shape in F.22-8 follows a similar W-shape profile to the configuration calculated in Method 1, F.22-7.

T.22-3 shows that the cable forces are significantly different to those in T.22-1, especially the magnitude of the forces in the stay cables. This suggests the suspension cable forces calculated from Method 1 may be too large. If the tensions calculated from Method 2 are used in the 1961 configuration, the largest deflection errors would be at mid-span at 30 cm. The dynamic properties of this configuration shown in T.22-4 are similar to the values in T.22-2 except for the lateral symmetric mode, suggesting this mode is the most dependent on cable tensions.

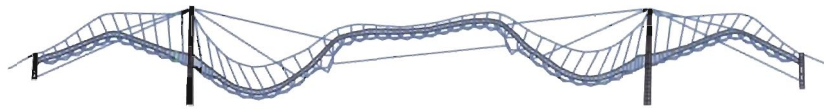
Choice of Configuration

The frequencies for the vertical modes in the FE model using both methods were quite close. The lateral mode in Method 2 is closer to the monitored results compared to Method 1, which suggests the cable tensions in Method 2 are closer to those found in the

Initial configuration, if found via by using measured stay cable forces T.22-3

Year	Force [kN]						Displacement errors [mm]			
	Suspension cable		Stay cable				Mid-span	Side span	Quarter span	Saltash tower
	Main span	Side span	S3	S1	S2	S4				
2001	17368	19518	1907	1984	1670	1988	40.88	43.39	-24.55	5.31

Initial configuration of Tamar suspension bridge; using measured stay cable forces F.22-8



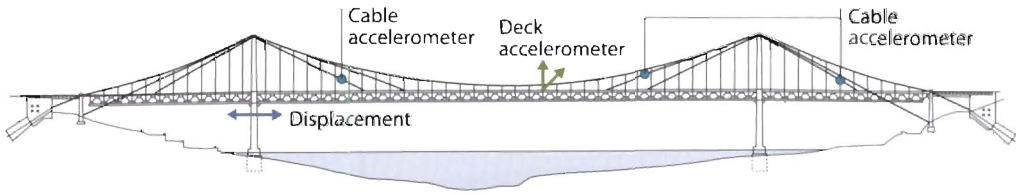
Dynamic properties of Tamar bridge, with a configuration found using the second shape finding method T.22-4

Year	Dynamic property	Mode 1	Mode 2	Mode 3	Mode 4	Mode 5
2001	Mode shape	VS1	LS1	VA1	TS1	VS2
	Frequency [Hz]	0.391	0.472	0.538	0.741	0.841
	Monitored frequency [Hz]	0.393	0.457	0.595	0.726	0.975
	Error	0.5%	3.3%	9.6%	2.1%	13.7%

actual structure. The frequencies from the original version of the bridge (Method 1) also suggests that the FE model of the bridge from 1961 is stiffer than it should be, resulting in incorrect suspension cable force estimates. This is odd, since the deck design from the upgrading scheme was meant to have a similar mass to the bridge deck in 1961.

The problem in the 1961 version of the model might be in the concrete deck, since this is the only part replaced in the upgrading scheme. The deck properties could be adjusted to provide a better match with the dynamic results, however it was simpler to use cable tensions already measured from the structure, alongside modal properties that already bear a similar match. Thus the arrangement calculated from Method 2 was then adopted as the optimised initial configuration.

16 channel data acquisition system added in later 2006 F.22-9



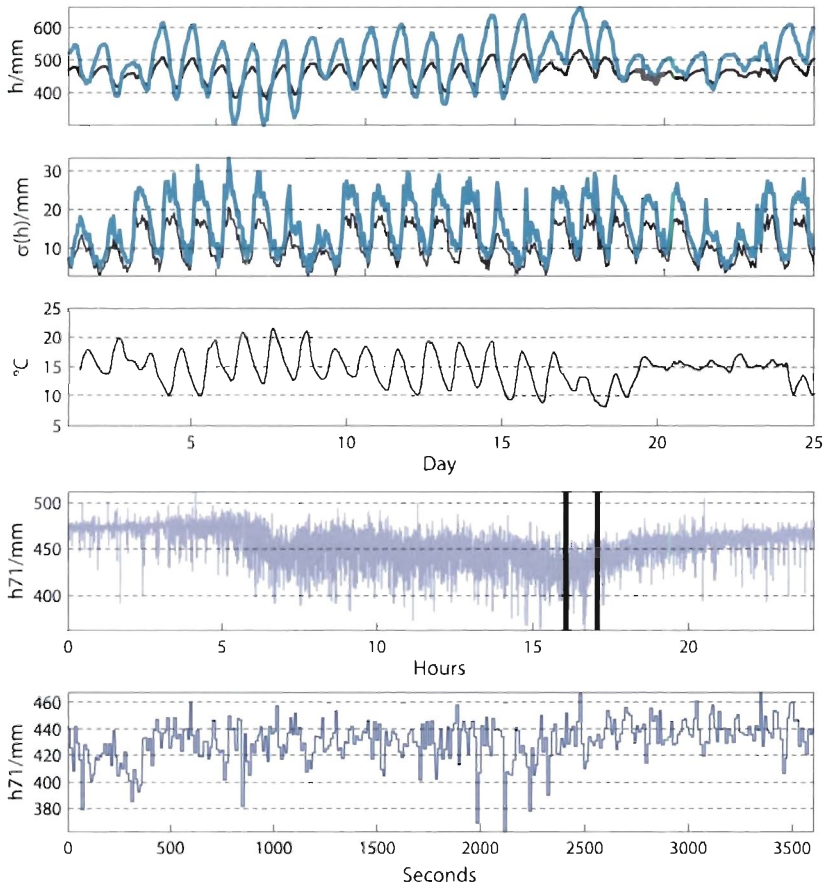


22-4 Real-Time Operational Modal Analysis of Tamar Bridge

22-4-1 16 Channel Data Acquisition System

This section describes the USFD monitoring system and the real-time system identification procedure. The first upgrade to the Fugro system was the 16 channel data acquisition system added in late 2006 and shown in F.22-9. Four pairs of accelerometers were installed on four stay cables: P1N, S2S, P4N and P4S and three extensometers were installed between the main span and Saltash side span. One accelerometer was vertically mounted on each of the north and south sides of the main span near mid span, with one mounted horizontally. The horizontal accelerometer temperature was recorded. Stay cable acceler-

Deck levels from hydrostatic sensors and deck temperature at different zoom levels F.22-10



ometers have since been removed. Also the extensometer signals were found (after a few months operation) to corrupt accelerometer signals (possibly due to an earth loop) and were disconnected. Now the extensometers are managed by a wireless sensor network.

22-4-2 Bridge Performance, 2007

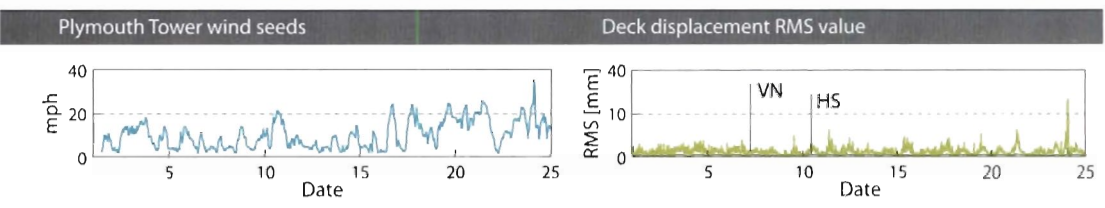
Some of the data from the Fugro system are presented for the same period as the dynamic data.

Deck Level Data

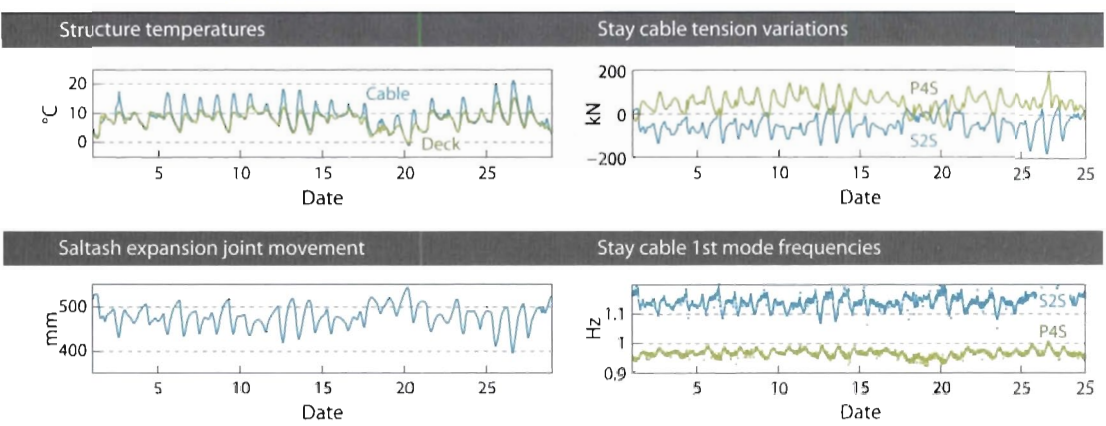
A useful component of the system was the fluid level sensing system, similar to that used in the Lantau Fixed Crossing. F.22-10 shows variation of 1-hour displacements (mean and standard deviation) and mean deck temperature in September 2007. Displacements are shown for mid-span (h62) and 1/8th span towards Plymouth (h71). Standard deviations show a pattern consistent with traffic flow. At this level of resolution the daily variations of the deck level appear to follow the deck temperature cycle. For day 19 the temperature effects on h71 one-hour mean (highlighted) is minimal, consistent with stable temperature, while the standard deviation is similar to other weekday patterns.

F.22-10 zooms in twice on day 19 showing effects at increasing time resolution. The upper plot shows the whole day (zero is midnight) and the lower plot shows fine detail around 04:00 p.m., in the middle of the evening rush hour. The one-day plot variations

Wind speeds and deck dynamic response in September 2007 F.22-11



Temperature, extension, stay cable tension and stay cable frequencies in March 2007 F.22-12



are consistent with traffic patterns and the large excursions may be caused by passage of heavy vehicles. The level sensing instrument samples every 10 seconds, so a heavy vehicle moving at 17.5 m/sec takes only two level sensing samples to cross the main span, hence the lower view of F.22-10 is not conclusive proof.

Temperature, Wind and Traffic Effects

The major loads are wind, temperature and traffic. Dynamic loading by traffic is apparent in standard deviations of deck and cable acceleration and only winds above 25 mph seem to generate significant response (F.22-11). Temperature dominates quasi-static response. F.22-12 shows that as temperature rises, the Saltash expansion joint closes and S2S tensions and frequencies are reduced.

Deck Mode Frequency Variations

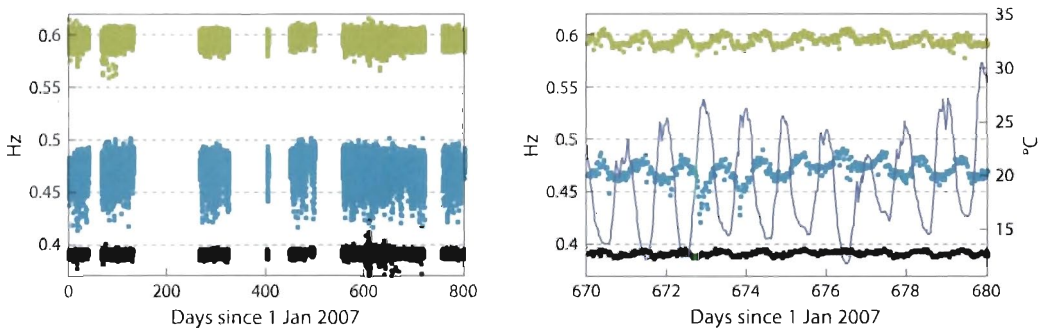
F.22-13 shows variation in the first three modes identified in F.22-4. The wide range of LS1 frequency is remarkable, as it must correspond to changes in mass and/or stiffness totalling 40 %.

22-5 Present Day SHM System and Data Management System

For the period of the IRIS project, the instrumentation used is summarized in F.22-14.

A data management system is a key element of SHM systems to support data mining or knowledge discovery from vast amount of data covering design, construction, maintenance details and measured response of the structure. Conventional ways of storing information in forms of reports, drawings, and photos on shelves and raw measurement files in a PC possibly make the data mining process slower or practically not achievable. An SHM data management system comprising a relational database management system, a web server, and a file server can make all relevant SHM data accessible instantly and easily to all the relevant people of SHM researchers, structure operators, and structural designers.

Variation of first three modes over more than two years and zoom in on ten days F.22-13



In the field of SHM, use of relational database management systems (RDBMS) is now popular for storing sensor measurements and derived quantities, see WD-501 for more literature references. To support knowledge discovery from databases, it is important for SHM researchers to have a platform for convenient database access and signal processing. USFD developed an integrated SHM data management system equipped with an MATLAB interface to MySQL database so that researchers can get access to the database and perform signal processing & analysis in MATLAB. The SHM data management system has also web-interfaces to show time histories of raw measurements and derived quantities showing an overview of the data sets. An overview of the Sheffield SHM data management system is shown in F.22-15. A MATLAB interface to MySQL databases has been built by using an open-source code mYm to produce a MEX function invoked by MATLAB command window. The web interface is available to users though Google Apps. More details about the implementation can be found in WD-501.

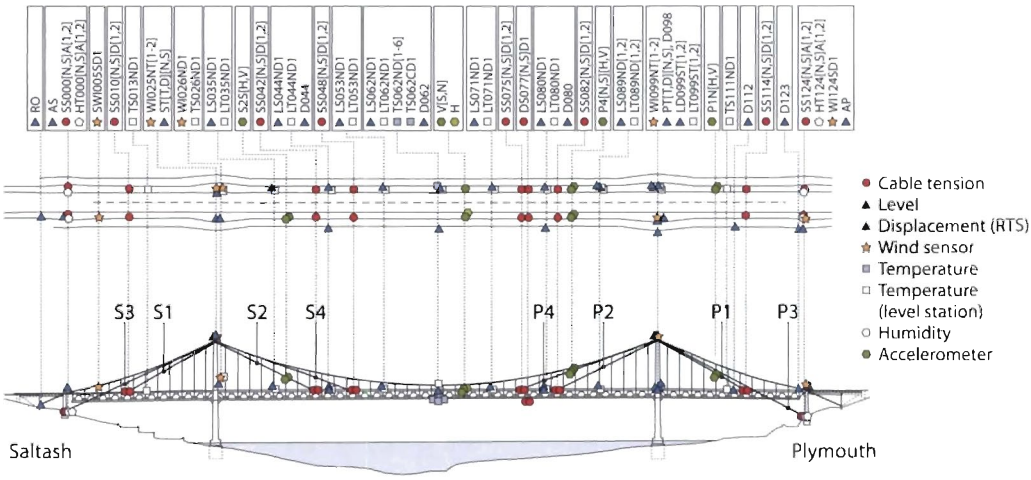
22-5-1 User Interface

The web interface provides two ways of visualizing SHM measurement data: 1) Online panel for displaying time-histories of several pre-selected channels for a user-selectable time-window and 2) Interrogator in which the user browses a list of all channels available and can select channels to show time histories and scatter plots. Access to the Tamar SHM system is via the SHM dashboard which links to the monitored systems.

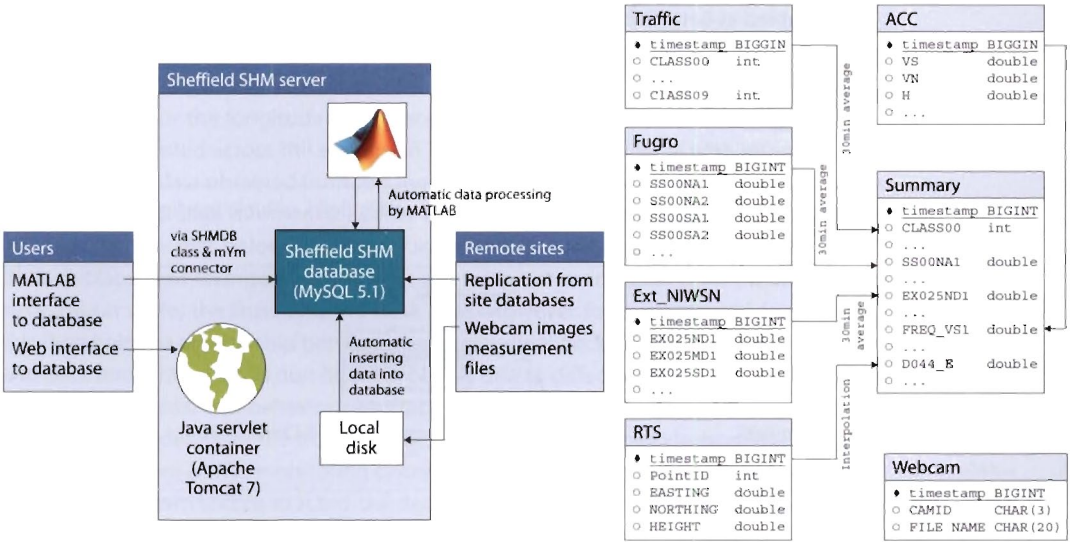
Tamar Online

The first level of viewing is "Tamar online" which presents the most interesting parameters as a view of one day, one week, two weeks or two months. F.22-16 shows 30-minute sampled signals representing wind speeds, temperatures, sample stay cable tensions and mode frequencies.

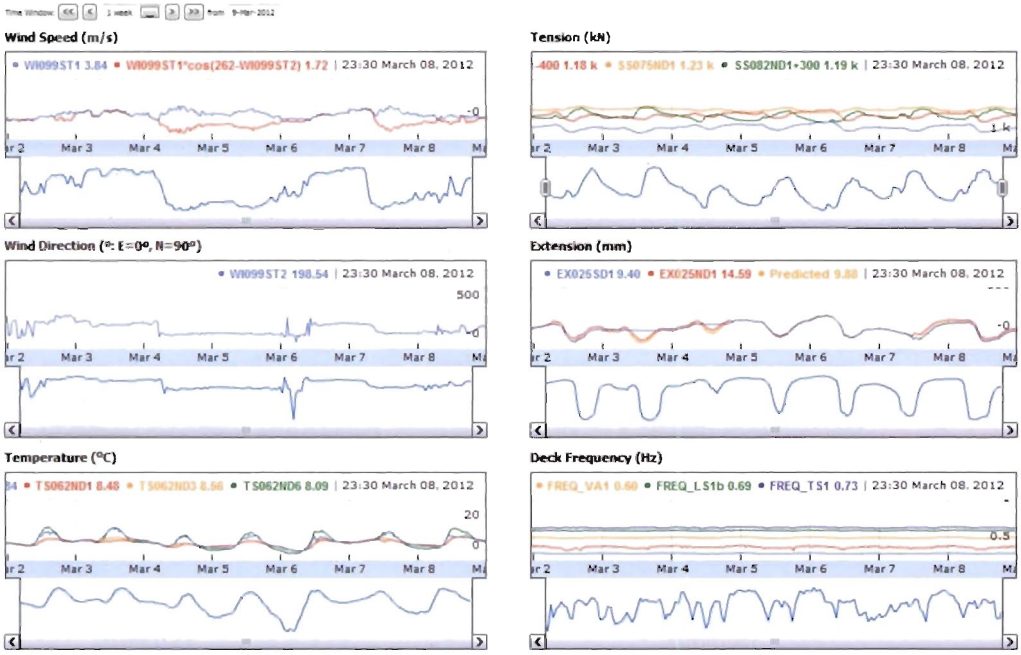
2012 monitoring system F.22-14



Organization of Sheffield SHM data management system (left) and data structure (right) F.22-15



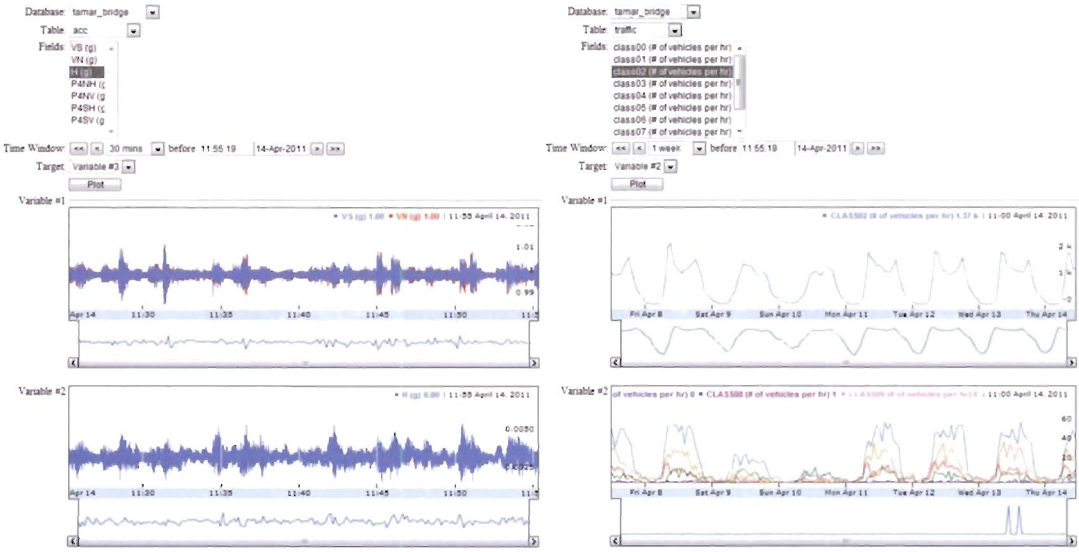
Tamar online – one week snapshot, static and dynamic parameters at 30-minute samples F.22-16



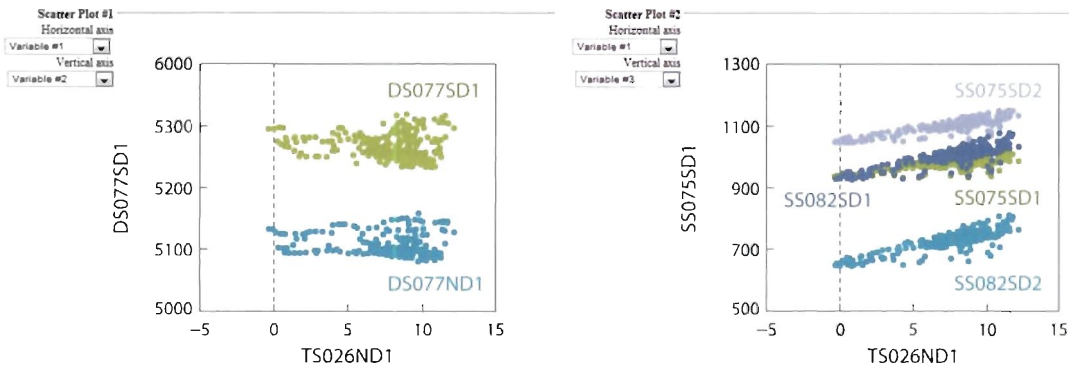
Tamar Interrogator

The more versatile tool is the interrogator. This views any data stream at its own sample rate by access to the appropriate data tables. F.22-17 shows a sample of acceleration data sampled at 8 Hz. This simple view is only appropriate for short periods of time for investigation of large vibrations due to wind or vehicles, or to show deck rotations through shifts in horizontal acceleration mean values. Correlations of displaced variables are also available (F.22-18).

Interrogator sample of: deck acceleration time series (left), vehicle loading data (right) F.22-17



Interrogator sample correlations of cable 5 and other stay cable tensions with deck temperature F.22-18



22-6 Wireless Monitoring of the Longitudinal Displacement

In WD-501 the wireless sensor network which was installed on the Tamar Suspension Bridge to monitor the longitudinal displacement of the main span deck using pull-wire extensometers fitted across the expansion joint is described in detail with interpretation of the data. The data obtained from this monitoring system were fused with environmental and structural data in order to further understand the behaviour of the structure. It has been shown that below a temperature threshold of around 15 °C the longitudinal deck displacement changed linearly with the temperature measured on the main span sus-pension cable, the truss and the deck itself. However for temperatures higher than this threshold the relationship between the longitudinal deck displacement and the truss and deck temperatures was non-linear, probably due to differential heating of the various structural elements. This behaviour was replicated in the FE model by adopting bi-linear temperature gradients for the truss and deck. A comparison of the extensometer readings with the data from an RTS monitoring system has shown that, as the deck and suspension cables cooled down and contracted, the deck rose, with the change in height being greater than the longitudinal displacement. Conversely, when the deck and suspension cables heated up and expanded, the deck sagged. This was also confirmed from the FE model. The third comparison was made between the longitudinal deck displacement and the tension in the stay cables supporting the main deck. As the deck expanded and moved towards the Saltash Tower, the tension in the stay cables connected to the Plymouth Tower increased while the tension in the stay cables connected to the Saltash Tower decreased.

One recurring observation throughout these analyses was that the static configuration and the structural behaviour of the bridge are far from straightforward. The performance of a complex structure like the Tamar Bridge depends on several factors which should be taken into account when designing and monitoring it. Hence the necessity to carry out long-term SHM exercises.

22-7 Total Positioning System

A robotic total station (RTS) comprises a total station with theodolite and servo-electric motors to change vertical and horizontal alignment angles of the electronic distance meter (EDM) for alignment with a target reflector. RTS performs a distance measurement by EDM and horizontal and vertical angle measurements by theodolite to determine three dimensional coordinates of the reflector. The system including reflectors is a total positioning system (TPS). The single measurement procedure can be repeated for multiple reflectors at regular time intervals programmed by the user. The RTS allows unmanned automatic executions of long-term displacement monitoring in many applications such as tunnel deformation during construction. For bridges, RTS is an efficient system of deflection measurement.

WD-501 describes the application of an RTS for 3D displacement monitoring of Tamar Bridge aiming to help understand the displacement behaviour more completely than was possible using the level sensing system. WD-501 presents detailed results, where use of RTS for a single event is described here.

22-8 Environmental Effects on a Suspension Bridge's Dynamic Behaviour

The instrumentation and data management systems described have been used to study the response of a suspension bridge to environmental loads such as temperature in detail. The recorded temperatures on the structure show diurnal variations, with the largest temperatures being on the surface of the deck. The temperature of the cable is generally lower, whilst the truss is the coolest overall since it is shaded from the sun. Temperature differentials were evident on the warmest days of the year, and were thus incorporated into the FE thermal analyses when observed at high temperatures.

Some non-linearities were identified with the stay cable tensions and tower displacements, when compared against the suspension cable temperature. Dividing the data into summer and winter periods has shown that the non-linearities occur when there are also temperature variations across the structure, caused by increased levels of solar radiation in the summer. Separating the data has also indicated that Plymouth stay cables respond differently between each season, which is seemingly due to solar radiation levels and temperature variation across the deck.

22-9 Effect of Vehicle Loading on Suspension Bridge Performance

This section aims to demonstrate that the presence of various levels of traffic has an influence on the structural response of Tamar Bridge. In the first part, sample time-series of modal frequencies are presented, offering a good indication that traffic levels affect the dynamic properties of the structure significantly. The second part studies daily variation of traffic mass and volume.

The remainder of the section considers the relationship of the total mass of the vehicles with the performance of the bridge through a combination of the long-term monitoring data and theoretical results produced from the validated Finite Element (FE) model.

22-9-1 Diurnal Fluctuations of the Frequencies

From several years of monitored data one of the most notable features were the diurnal variations viewed as time series of the bridge's natural frequencies. F.22-19 shows

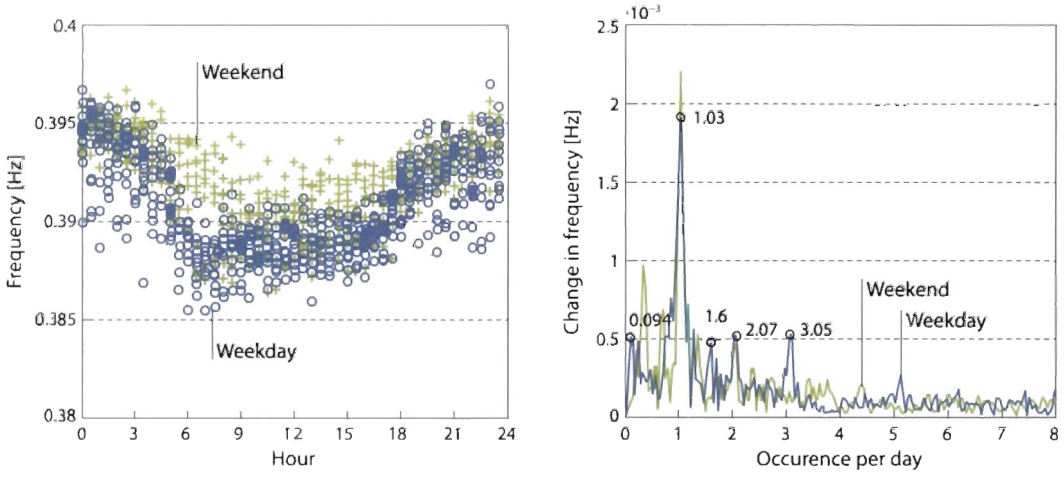
time series results collected from October 2009 rearranged by the hour they occurred for both weekdays and weekends. Profiles in the weekend time series profiles appear more rounded, with less variation.

Fast Fourier transforms were also applied to time series of modal frequencies to check for presence of higher order harmonics in the daily results. The largest peak in all FFT results corresponds to diurnal variations of the natural frequencies. The smaller peaks, especially for mode VS1 may be attributable to the troughs that form between 06:00 and 09:00 and in the afternoons, which may relate to high levels of traffic during rush hour.

22-9-2 Traffic Related Events

The bridge monitoring has the ultimate aim of identifying performance anomalies, and to provide information about 'normal' operational response that can be filtered out to reveal anomalous performance. One such clear performance anomaly occurred on 11 April 2011, when stay cable tensions peaked at 08:00, as shown in F.22-20. Usually variations in P2 and S2 tensions mirror each other over a daily cycle due to the thermal expansion of the deck (as seen in WD-501) so simultaneous increase in both P2 and S2 tensions during a short period is a clear performance anomaly. Webcam images from the Plymouth tower F.22-20 show that the bridge was experiencing a rare 20 minute long traffic jam at the time; three (Plymouth-bound) traffic lanes were filled by closely spaced, slow moving traffic as shown by the right-hand image. It seems that the additional mass of the bridge-long traffic jam increased the stay cable tensions by 200 kN. This event provides an opportunity to study the effect of traffic alone, without any wind or thermal effects.

Diurnal variation frequencies for VS1: 24 hour arrangement (left) and Fast Fourier transform (right) F.22-19



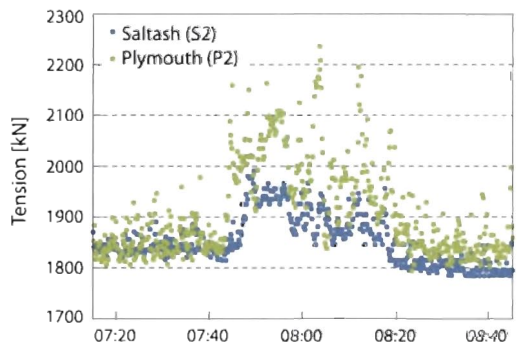
22-9-3 Determination of Gross Traffic Mass

As well as the instrumentation on the bridge, toll records provide hourly-sampled data that categorize and count the vehicles travelling from Saltash to Plymouth. There are ten possible vehicle categories, four of which include trailers and which were lumped together in a higher tier. These categories are presented in T.22-5, of which almost 93 % of the vehicles using the bridge are classed as a car or a van. The average gross weight of the vehicles was determined from a study by the [Department for Transport, 2008]. Whilst cars and vans are in the same classification, vans have nearly double the average gross weight of a car. In order to determine a reasonable weight for CLASS02 vehicles it was assumed that British cars make up 404.1 billion kilometres of road usage, whilst vans use 68.2 billion kilometres. This would mean that nearly 86 % of the vehicles in this category are cars, which is used to factor the vehicle weight accordingly. The only data available on traffic flow is from the toll records and the web-cam images. An approximate value for mass of each vehicle was determined by multiplying traffic counts by average weight of vehicle as given in T.22-5. Cars provide the majority of the traffic mass on the bridge, as shown by F.22-21, with four axle HGVs also providing a significant portion of the remaining total mass.

F.22-21 presents averages for the Plymouth-bound hourly traffic mass arranged in 24 one-hour bins, for samples collected mid-week and on a weekend respectively. The trapezoidal profile is a reflection of the profile previously seen in the frequency results F.22-19; both graphs have a plateau between 07:00 and 17:00 and a distinct peak at 08:00 caused by rush-hour traffic. The similarities in the results suggest that the ideal time to identify bridge modal properties would be between midnight and 04:00, when traffic levels are very low. It is also the time when temperatures are most stable. The weekend traffic mass profile does not have a pronounced peak at 08:00, but instead a shallower rise and fall, with a peak at 11:00. The number of HGVs travelling at the weekend is reduced, so the majority of the additional mass on the bridge consists of cars and vans. Due to the change in commuter behaviour over the weekend, the mass of traffic on the bridge reduces by

Stay cable tensions 11 April 2011, also webcam images of deck at 08:30 a.m. (left) and at 08:50 a.m. (middle) F.22-20





Vehicle classification and bridge traffic T.22-5

Class	Vehicle	Average gross vehicle weight [kg]		% of monitored population
CLASS00	Unknown	N/A		0.01
CLASS01	Motorcycles, etc.	0*		1.75
CLASS02	Cars	(0.856 ×) 1500	1660	92.92
	Vans	(0.144 ×) 2600		
CLASS03, CLASS06	Two axle HGV	6800		3.33
CLASS04, CLASS07	Three axle HGV	17400		0.61
CLASS05, CLASS08, CLASS09	Four (or more) axle HGV	22800		1.39

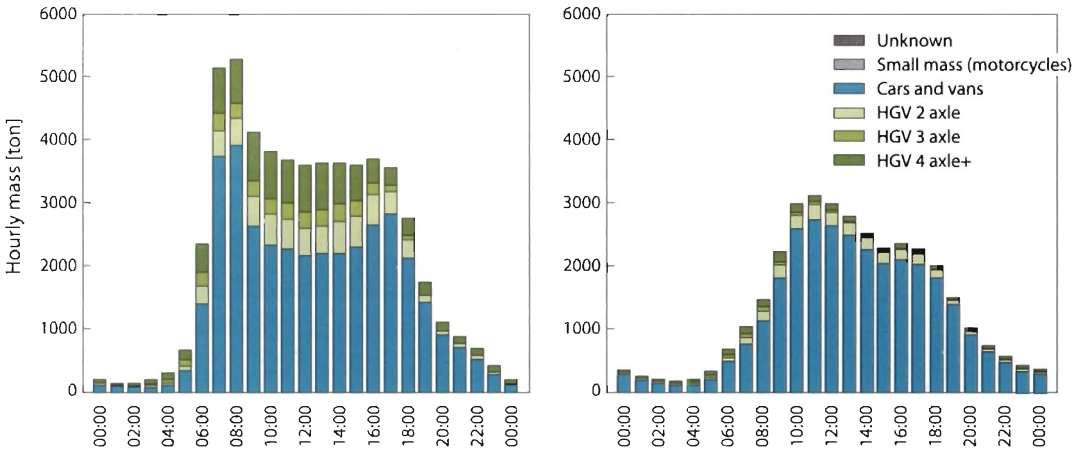
* Unknown average mass; treated as negligible to the overall mass of traffic.

about a third. The mass data were adjusted and scaled to represent vehicle mass on the bridge at instants corresponding to the monitoring system sampling.

22-9-4 Application of Loads to FE Model

Since the frequencies of the monitored modes are low, dynamic interaction would not be an issue, so for this investigation the bridge behaviour was studied by adding frozen vehicle masses to the deck. The masses are applied as a row of three 1660 kg rigid vehicles on the structure, assuming an even distribution, incrementing their number in successive runs of the FE model. To consider the effects of asymmetrical applied masses, the same analyses were done with the vehicles located on the northern lanes with one line of traffic located on the cantilevered deck.

Mean mass of weekend traffic, per hour. Mid-week traffic (left) and weekend traffic (right) F.22-21

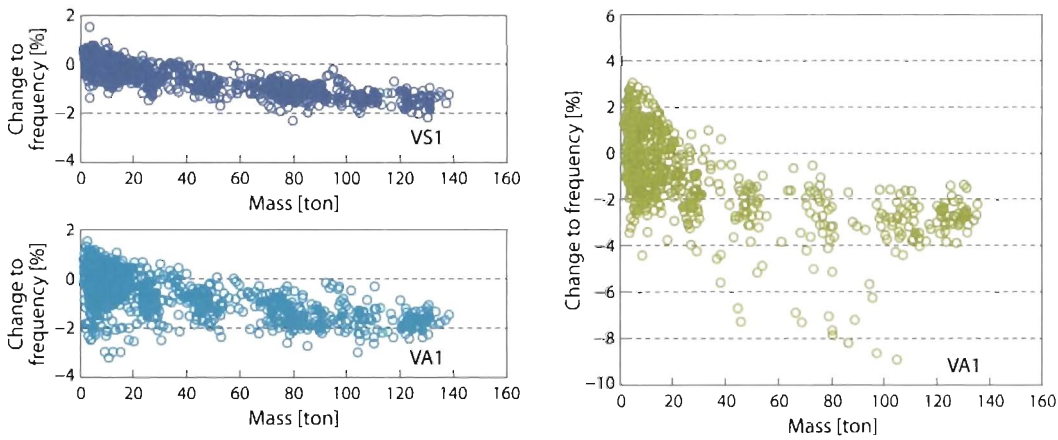


22-9-5 Effect on Modal Properties

The experimentally observed relationships between vehicle mass and modal frequency F.22-22) exhibit considerable scatter but there is a clear inverse correlation. Hence the trapezoidal plots seen in the frequency time series are also linked with the total mass of traffic upon the structure. Of these, LS1a varies by almost 5 % of its base frequency due to the traffic effect identified. The two vertical modes both vary by about 2 % of their base value, although the frequency of mode VA1 is almost twice that VS1, so its variation is much more obvious within the time series results. The frequency of mode VS1 seems to be insensitive to thermal effects, so most of the variation is caused by the traffic loading on the bridge. This feature could be useful for a crude weigh-in-motion system.

The FE model results also show an inverse linear relationship for the first two vertical modes, both decreasing by 1 % when 140 tonnes are applied to the bridge. The difference between measurement and analysis is the behaviour of the first lateral symmetric mode LS1a, for which the FE model predicts an increase in frequency as the traffic mass increases, rather than a decrease. This effect is due to the frequency rise caused by tension stiffening effects, rather than the drop caused by the additional mass on the bridge, as exhibited by the vertical modes. The trend of the FE results for LS1a have a shallower slope than the monitored results as well, only varying by 1 % of its base frequency.

Traffic mass vs. frequency change, from monitored results F.22-22



Relationship of reported frequencies to applied traffic mass T.22-6

Mode	Monitored			FE model		
	[Hz]		[Hz/ton]	[Hz]		[Hz/ton]
VS1	0.394	+	$-5.409 \cdot 10^{-5}$	0.403	+	$-2.967 \cdot 10^{-5}$
LS1a	0.482	+	$-15.405 \cdot 10^{-5}$	0.472	+	$+3.077 \cdot 10^{-5}$
VA1	0.602	+	$-9.802 \cdot 10^{-5}$	0.537	+	$-3.787 \cdot 10^{-5}$
LS1b	0.690	+	$-0.350 \cdot 10^{-5}$	0.751	+	$-2.663 \cdot 10^{-5}$
TS1	0.731	+	$-8.313\ 10^{-5}$	0.772	+	$+0.530 \cdot 10^{-5}$

While linear relationships between the traffic mass and frequencies appear in both monitored and FE model results, the gradient of the trends from the monitored results listed in T.22-6 are generally three times the slope of the FE model results. The table also highlights the different behaviour of mode LS1a between the monitored and FE model results, the slope of the monitored results being almost five times that from the FE model. This shows that while the procedure in the FE model is capable of demonstrating the change in dynamic response, it is unable to provide results that match the monitored data satisfactorily. Apart from variations caused by other ambient conditions, it is suspected that the stochastic distribution of the vehicles in space and time, as well as the location of heavy vehicles, create the deviations in the monitored results.

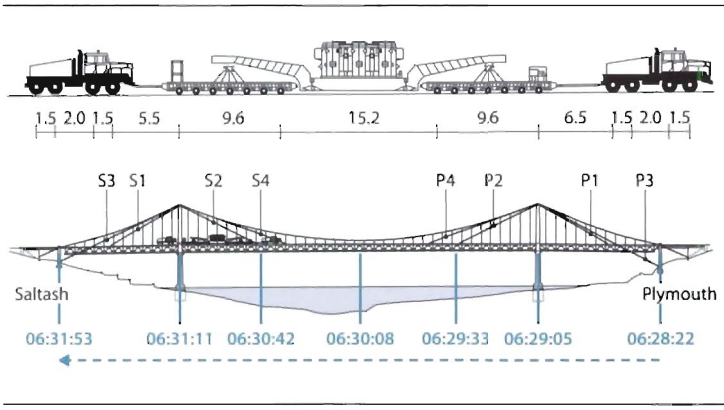
22-10 Suspension Bridge Response due to Extreme Vehicle Load

This section briefly describes a site investigation on the performance of Tamar Bridge during passage of a heavily laden vehicle, which provided an opportunity to observe changes in response to a travelling concentrated mass, with an unusual ratio of vehicle and bridge weights. The objective of this investigation was to record the deflection of the bridge deck and towers, as well as identify the vertical accelerations of the deck. The FE model of the bridge was used to provide a prediction of these which were compared against the results determined from the monitoring system.

22-10-1 Test Details

Measurements were carried out by Full Scale Dynamics Ltd (FSDL), a University of Sheffield spin-off company founded by Vibration Engineering Section (VES) to record the deformation of the bridge while a 151 tonnes electrical transformer for a power station was transferred from Plymouth to Saltash. The trailer carrying the transformer crossed the

Trailer crossing Tamar Bridge (units are in metres) F.22-23





bridge during the early hours of 31 October 2010. The bridge was closed to avoid additional traffic loads while two robotic total stations (RTS) located at the Tamar Bridge office traced the position of two reflectors on the bridge: one monitored the reflector at the top of the northern Saltash tower; the other tracked the reflector at the centre of the main span. Sampling rates were increased for the sensors on the VES system: the RTS measurements were set to approximately 3.0 Hz. Other sensors worked as normal.

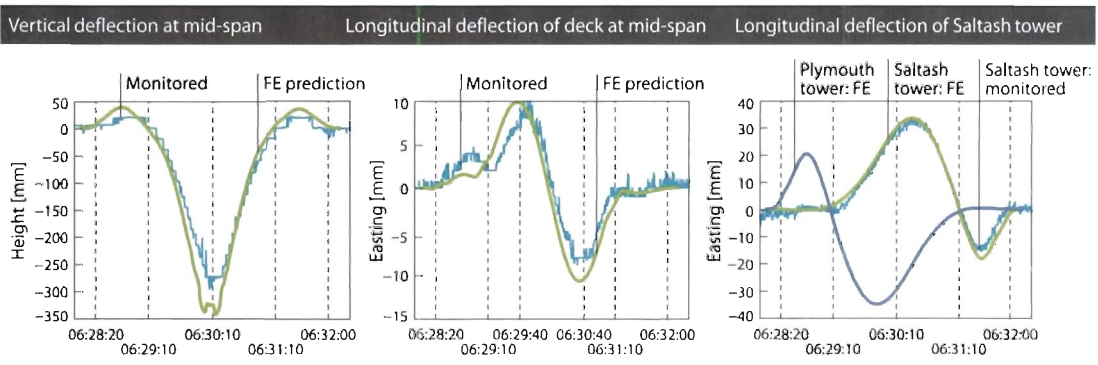
F.22-23 shows arrangement of the trailer, propelled by FAUN trucks either end. Wheelbase and axle weights were approximated from technical drawings and datasheets from similar tractor models [Inter-Commerz, 2008]. The container for the transformer is elevated clearly from the road, providing a 15.2 m unloaded gap along the deck. The total mass, trailer and tractors, is approximately 269 tonnes.

22-10-2 Finite Element Predictions and Quasi-Static Response of Bridge to the Trailer

The vehicle was modelled as a series of travelling masses. Due to the slow speed of the trailer the study was performed as a series of static analyses for each location of the vehicle and the deck was meshed to a higher resolution than previous analyses, with divisions every 0.5 m. F.22-24 compares vertical and longitudinal motion of the main span and tower from the pair of RTS units. The mid-span deflects vertically upwards when the trailer is on the side spans. An interesting feature is the pair of acute troughs in the FE model time series results; the gap created when the 15.2 m of unsupported space between the trailers passes across the mid-span of the bridge.

The longitudinal response of the mid-span shows that as the trailer enters the bridge, the mid-span moves east towards the bridge. This reaches a peak at approximately 06:29:45, when the trailer was close to the quarter span of the structure. This mid-span moves back west and passes back through its original displacement when the trailer arrives at mid-span, then continues in the westerly direction as the vehicle travels on the Plymouth side of the bridge. The easterly deflection of the Saltash towers shown resembles the longitudinal displacements at mid-span; once the trailer moves onto the main span, the deflection of the deck causes both tower tops to move inwards. The towers revert to their original state once the trailer moves beyond the main span. The towers also

Quasi-static tower of bridge F.22-24

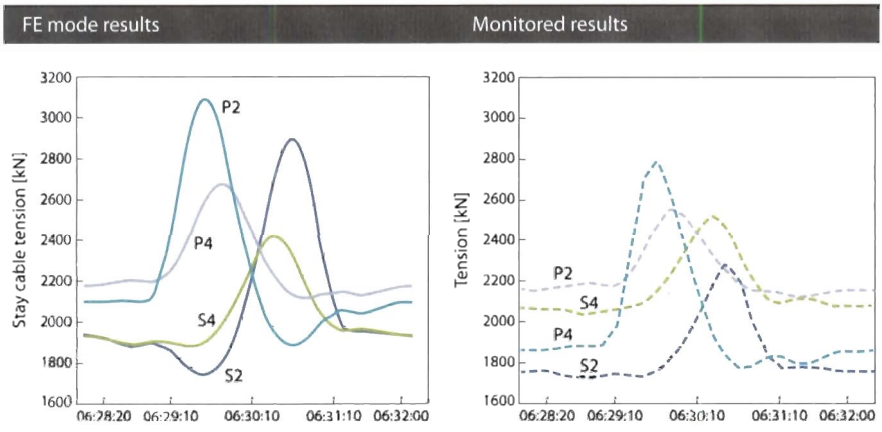


deflect in the opposite direction once the trailer moves onto the Saltash side span. A similar but reversed response is exhibited on the Plymouth towers, which were not monitored. Since the deck deflects vertically and the towers sway as the trailer crosses the bridge, changes in the suspension and stay cables tensions, which links the tower and the deck, was expected. F.22-25 shows that the tensions of the stay cables connected to the main span also peak when the trailer is near the mid-span, as expected. The peaks in the stay cable tensions occur when the trailer passes their connection to the deck.

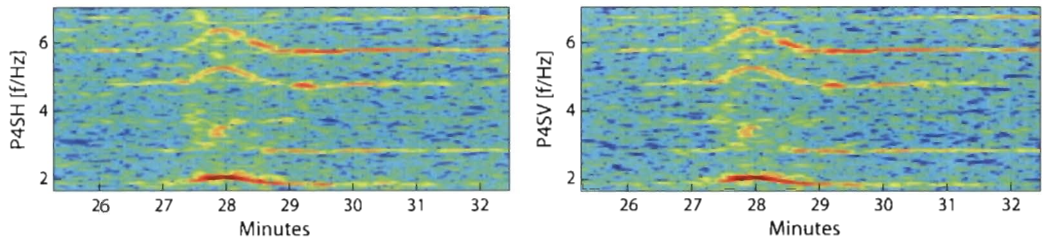
22-10-3 Variation in the Cable Modal Properties

Variation in cable natural frequencies as the vehicle travelled across the bridge are presented in the spectrogram of F.22-26. The average tension in the two stay cables before the bridge was loaded was 2269 kN, which would mean a natural frequency of approximately 0.98 Hz. Consequently the bands in the spectrogram represent the second to sixth harmonics of the cable.

Main span stay cable tensions. F.22-25



Spectrograms of the P4 stay cable frequencies F.22-26



22-11 Conclusion

Tamar Bridge has been studied since 2005, but for the duration of the IRIS project, the research has focussed on performance observations delivered by a structural health monitoring system that includes an efficient data management and viewing system. This records dynamic and static response continuously and has provided a wealth of information about the performance of the bridge. Based on the monitoring and parallel finite element simulations, a comprehensive study has shown a number of important behaviour mechanisms. First, the bridge configuration is strongly dependent on temperature variations in space and time, leading to a combination of sagging and extension of the deck as temperatures rise. This in turn leads to changes in stay cable tensions. Temperature also affects dynamic (modal) properties, but to a smaller degree than the presence of traffic mass. For temperature the effect is a combination of effects on material properties and geometric stiffness, while for traffic there is no obvious effect of interaction. Wind seems only to affect dynamic response levels for strong winds, but all three factors contribute to dynamic behaviour. A traffic jam event and passage of an extreme heavy vehicle have been used to observe how the bridge behaves during unusual loading conditions.

Tamar Bridge turns out to be a very complex structure and from six years of observation anomalous structural events have been detected.

References

Department for Transport, 2008. *Road Statistics 2007: Traffic, Speeds and Congestion*. London, 1–78.

Fish, R. and Gill, J., 1997. *Tamar Suspension Bridge – Strengthening and Capacity Enhancement*. In B. Pritchard (Ed.), Bridge Modification 2: Stronger and safer bridges. Proceedings of the International Conference organized by the Institution of Civil Engineers (London, UK.). London, U.K.: Thomas Telford.

Inter-Commerz, 2008. *Faun "Elephant" SLT 50 8x8 + 8x0 Datasheet*. Retrieved 15 September 2011.

Williams, C., 1984. *Vibration Monitoring of Large Structures*. Experimental Techniques, 8(12):29–32.

23

Bridge Maintenance Management System for Egnatia Motorway

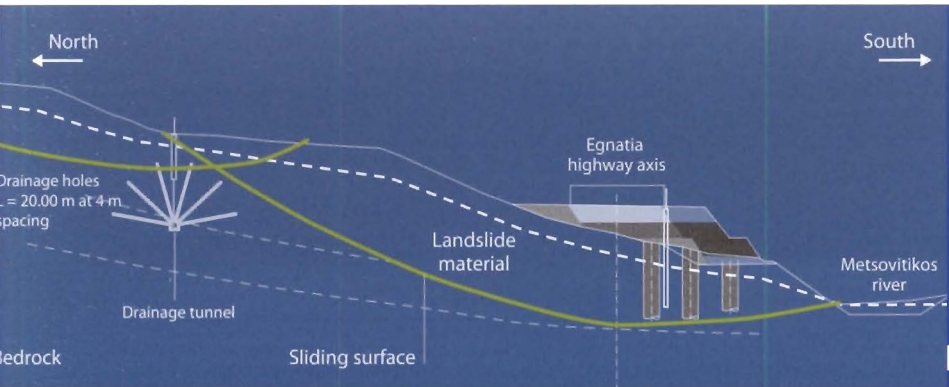
Authors:
Eleni Sakoumpenta
Panagiotis Panetsos
Manolis Haralabakis

Motivation

The feasibility of the application of the IRIS risk paradigm in case of multi-hazards, namely an active landslide in an earthquake prone region, is of interest for assessment. A proof of concept is desired.

Main Results

A monitoring system has been installed at the T11 Bridge within the Egnatia motorway in Northern Greece. The successful application of the new IRIS Risk Paradigm has been demonstrated.



23-1 Introduction

The T9/T11 ravine bridge is located on Egnatia motorway in northern Greece approximately 100 km east of the Adriatic port of Igoumenitsa and 240 km west of Thessaloniki (F.23-1). The motorway in this area runs at a very short distance from the north side of Metsovitikos river. Due to severe geotechnical problems that prevail in this particular area, extensive geological and geotechnical investigations were carried out and several alternative alignments on both sides of the river have been examined. The current alignment was selected as the one that exhibits the least residual geotechnical risk among the other alternatives, however, still not negligible.

The bridge consists of two separate structures, one on each carriageway: T9 on the right carriageway (west-east direction) and T11 on the left. T9 is a 409 m long four-span structure (44 m + 105 m + 155 m + 105 m) monolithically connected on piers M1 and M2 and supported through elastomeric bearings on abutments A1 and A2 and the western pier Ma (F.23-2). T11 is a 365 m long, three-span, continuous structure (105 m + 155 m + 105 m) monolithically connected on piers M1 and M2 and supported through elasto-

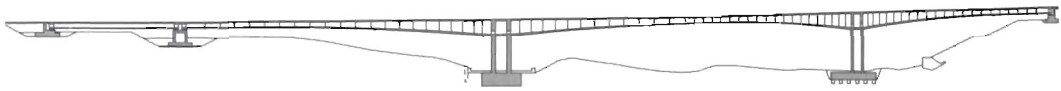
Structure location F.23-1



View of T9/T11 bridge F.23-2



Longitudinal section F.23-3



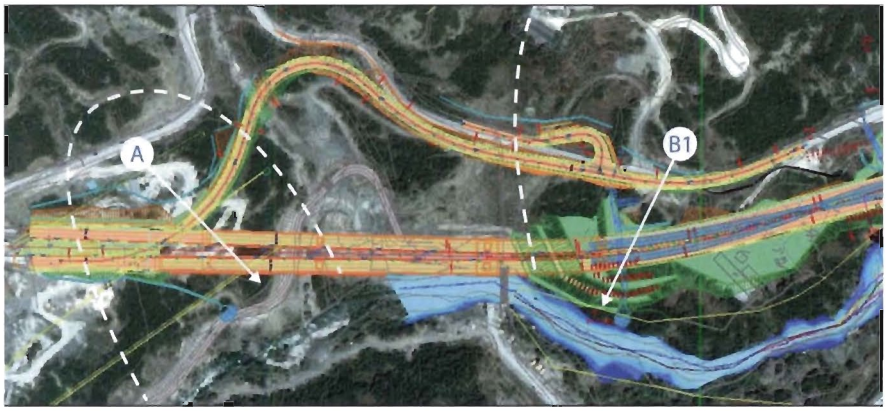
meric bearings on abutments A1 and A2. The bearings are freely sliding in the longitudinal direction and the deck is transversely restrained through hydraulic viscous dampers on abutments and pier Ma. The width of each carriageway is 14.45 m. The deck is a box-girder ranging in height from 4.00 m (midspan) to 10.74 m, (pier supports) longitudinally pre-stressed through internal tendons and constructed with the free balanced-cantilever method.

The pier walls have a hollow rectangular cross-section and a maximum height of approximately 27 m (pier M2). The foundations of piers M1 are rock-sockets whereas of piers M2 there are groups of 1.5 m diameter piles. The foundations of abutments A1 and A2 and pier Ma are spread footings (F.23-3).

The particular feature of bridge T9/T11 is that, unlike piers M1 and M2 which are founded on stable ground, the bridge abutments and pier Ma are founded on active landslide areas (areas A and B1 in F.23-4). According to monitoring data, from inclinometers installed during the design stage, the depth of the sliding surfaces was approximately 25-30 m and the maximum recorded rate of ground movements 30 mm/month. The groundwater level is high and artesian water pressure has been observed in some boreholes. Major stabilization works have been implemented in order to minimize the risk of sliding movements. However, as the risk of sliding movement cannot be completely eliminated, the bridge has been designed to undertake vertical (–10 cm/+3 cm) and horizontal (20 cm) movements at the abutment locations under static conditions induced by slow soil creep or seismic loading. Detailed description of the geotechnical conditions and the stabilization works are included in chapter 23-2-1.

The construction of the bridge has been completed in the beginning of 2010.

Landslide areas at abutment areas (area A at the west abutment, area B1 at the east abutment) and vectors of the ground movements F.23-4



The aim of this report is to describe the application of the Risk Paradigm methodology for the geotechnical risk assessment of the abutment areas and the risk assessment of the bridge and to discuss its results.

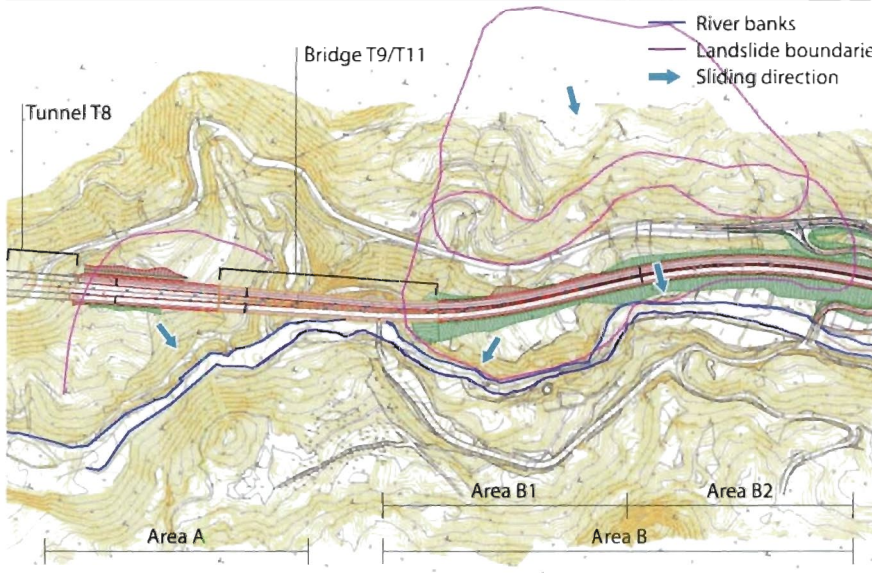
23-2 Geotechnical Risk Assessment of Abutment Areas

23-2-1 Geotechnical Conditions

In the area of the T9/T11 bridge, the motorway runs at a very close distance along the main front of a huge overthrust of the Pindos Unit formation, comprising mainly flysch, over the Ionian Flysch. The tectonic movements associated with it have resulted in stressing of the formations and a consequent degradation of their mechanical properties. Therefore, the geology in the area is very complex and chaotic, containing randomly orientated shear faults with locally weak surfaces, low strength rock masses and landslides of various sizes. The groundwater table is generally high due to the low permeability of the soil and rock formations and the high precipitation received in the area.

The selection of the alignment in this area was an issue of great concern for EOAE. Numerous alternative alignments were investigated during the course of finalizing the highway design. Originally, it passed through the slope south of the river but ground investigation and monitoring with inclinometers indicated that the slope is creeping at a depth in excess of 80 m with a rate of about 18 mm/year. This finding led to the abandon-

Plan with structure location and landslide areas A and B1 F.23-5



ment of the south side of the valley. As the findings of an initial borehole programme revealed, together with the installation of inclinometers and subsequent monitoring, creeping ground also existed north of the river but, in comparison, the ground conditions were overall more favourable: the observed movements were taking place at a much shallower depth, not exceeding 50 m. On average, the depth of movements was less than 20–25 m. A new set of alternative alignments was examined north of the river to establish the safest corridor for the motorway. It was concluded that the alternative that posed the lowest risk was to construct the motorway on embankment at the toe of the valley side and close to the river in order to: a) achieve buttressing of the landslide with the embankment and b) minimize the disturbance of the weak, sliding material.

It should be noted that, during the process of finalizing the highway design, a panel of international experts was employed by EOAE to support the evaluation of the geological-geotechnical investigation results and to endorse the final decision.

The geotechnical conditions for each abutment area and the adopted stabilizing measures are described below.

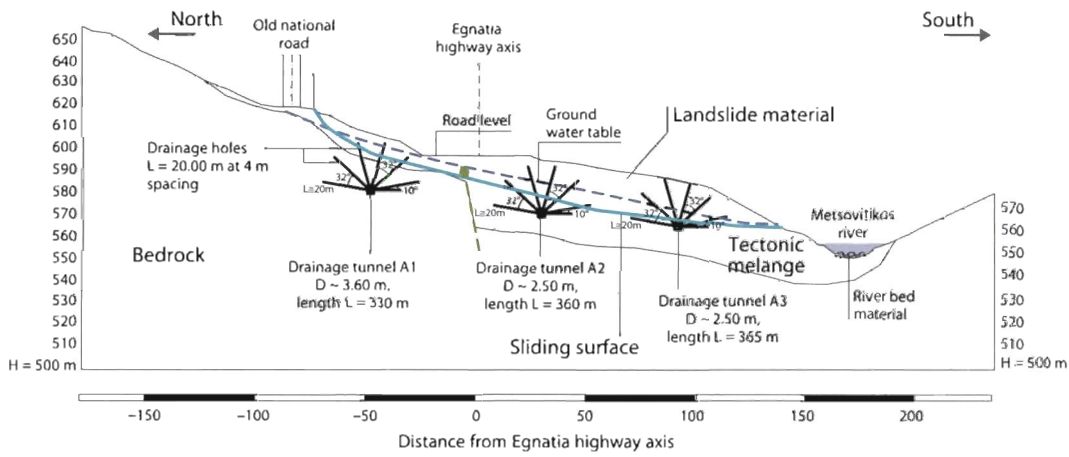
West Abutment (Area A)

Area A measures approximately 200 m by 300 m in plan and lies between the exit portal of tunnel T8 and the beginning of ravine bridge T9/T11 (F.23-5). The western abutment and one pier of the bridge are founded on spread footings within the area of instability. In total, more than 60 boreholes were drilled during different stages of the design. Of these, 20 were equipped with inclinometers and 32 with Casagrande and vibrating wire piezometers. The ground consists of an upper layer of old landslide debris comprising stiff sandy clay and medium to very dense clayey sand with gravel to a depth of 10–15 m in a chaotic and non-layered structure overlaying the tectonic mélange from the Pindos overthrust with a similarly disturbed structure but with stronger soil material. Bedrock is encountered at a depth of 30–35 m and comprises siltstone, sandstone and conglomerate. The groundwater regime is very complex, since water was found at varying levels in all boreholes. It appears that there are numerous perched horizons, while there are indications of seasonal artesian water locally. Overall, water is considered to play a major role in destabilizing the slope.

The depth of the sliding movement along the cross-section at the abutment location is about 12–15 m at the boundary between the landslide debris and the tectonic mélange formation. The maximum depth of movement in the area was measured at 25 m (inclinometer B6) within the tectonic mélange formation. Its rate, before construction, averaged at about 5 mm/year. Back analyses on two representative sections and ring shear tests were carried out to determine the most appropriate residual angle of internal friction, φ_{res}. The results varied between 13° and 17°, values subsequently adopted in the design of the stabilization measures.

Due to geometric restrictions on the alignment posed by the adjoining structures (tunnel T8 and bridge T9/T11) and the river, as well as the steep morphology and limited space at the toe of the landslide, a counterweight which is generally considered preferable as a stabilization measure could not be adopted. Instead, it was decided to construct three drainage tunnels with an array of 20-metre-long drainage holes through them under the entire area as shown in F.23-6. The works were completed in October 2007.

Cross-section showing the sliding surface and the stabilizing measures at the west abutment F.23-6



Although the results of monitoring in this area clearly show that the three drainage tunnels are very effective in reducing the rate of movements to practically zero, there is always a risk that, in the long-term, the drainage holes in the tunnels may fail to function which would lead to an increase of pore pressures in the ground and therefore to the triggering of an instability. This instability would seriously affect the maintenance cost not only of the approach embankment of the bridge but of the structure as well. Moreover, an earthquake loading presents also a great risk of instability in the area. The risk of such instabilities following the risk paradigm methodology is assessed below. Moreover, the horizontal displacements of the west abutment are computed through numerical analyses for various ground water scenarios in order to assess whether and to what degree potential deformations due to ground water rising could affect the bridge superstructure.

East Abutment (Area B1)

To the east of the ravine bridge, there is an extensive area of instability about 450 m long by 700 m divided in areas B1 and B2 (F.23-5). In the framework of this report, the interest is focused in area B1 where the eastern abutment of the bridge is situated. The abutment is founded on a 20-metre-high reinforced earth embankment within the unstable area, followed by motorway embankment with a height varying between 3 and 6 m. A total of 45 boreholes were drilled in this area, 19 of which are equipped with inclinometers and 23 with piezometers (Casagrande and vibrating wire).

The surface is covered by clayey and sandy material with gravel and a maximum thickness of 50 m, generally varying from 10 m to 30 m, identified as old landslide material. This is underlain by the completely weathered zone of bedrock, which is a soil–type material with highly variable percentages of clay, silt, sand and gravel, stiff/very stiff or medium dense/dense, with an average thickness of 15–20 m. Finally, bedrock comprises fractured and slightly weathered siltstone, sandstone and conglomerate. Across most of area B1, a

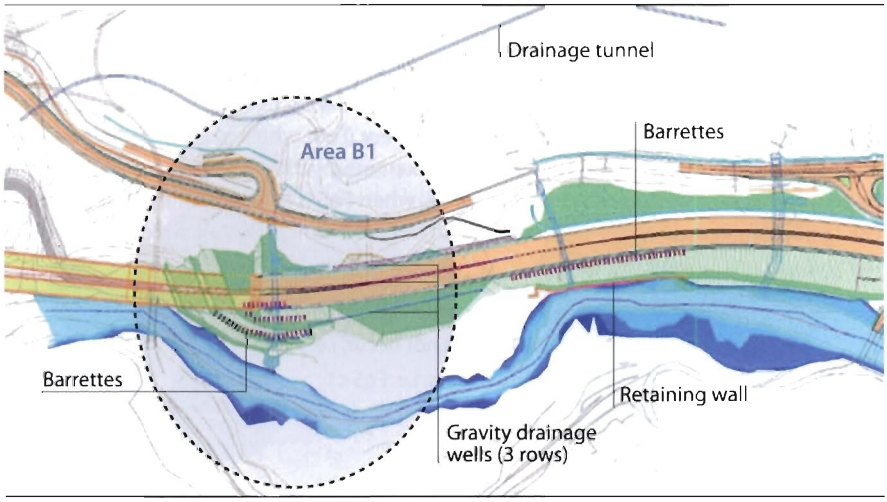
layer of sandy gravel and cobbles was found at approximately river level, having a thickness of about 4 m. This is believed to be part of the river bed before it was buried under the creeping soil mass. Moreover, large limestone boulders originated from the far uphill area of the natural slope slid downhill and piled up at the toe of the natural slope by the river bed. The groundwater table was found at a depth of 5–10 m, contributing significantly to the instability of the area.

Two retrogressive landslides is the prevailing movement mechanism as shown in F.23-5 and F.23-8. The lower one daylights at the river and destabilizes the upper one which, in turn, exerts destabilizing forces to the lower one and extends 450 m above the river. The maximum depth of movement is 45 m, while the average rate of movement was about 10 mm/year. Back analyses and ring shear testing were carried out to derive the shear strength along the slip surface. A representative value of $\varphi_{res} = 20°$ was adopted in the design. The alignment runs parallel to the river at the toe of the landslide. The thickness of the sliding material at the embankment foundation varies from 5 m to 40 m which, in combination with the presence of the river at the toe, makes its removal and replacement with high quality granular material impracticable. The embankment was therefore founded on creeping material at the toe of the lower landslide, acting as a stabilizing berm. However, the embankment alone was not sufficient to achieve the required safety factor of 1.40. In addition, the safety factor in local stability for random surfaces at the toe was inadequate.

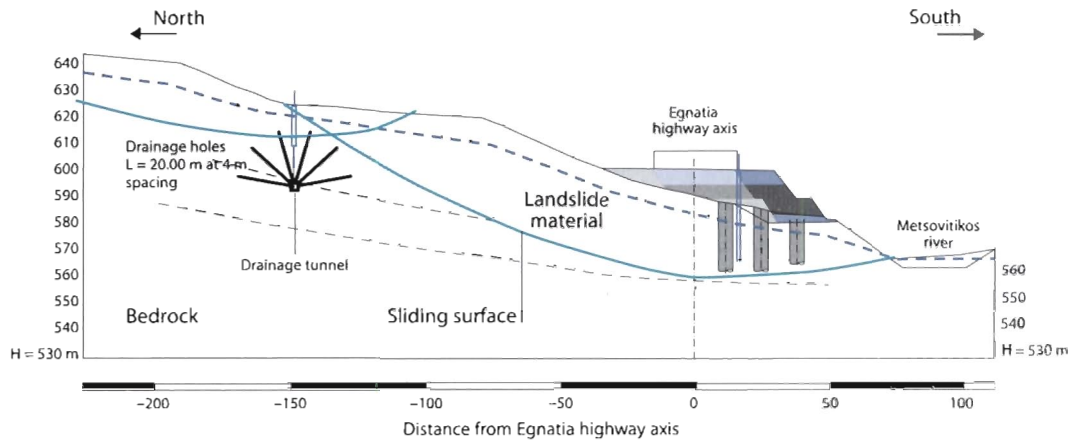
As a result, additional measures to improve stability conditions under all modes of failure were designed. These included a drainage tunnel in the upper landslide, gravity drainage wells in the lower landslide (locally, in area B1, where river gravel was found) and reinforced concrete diaphragm elements in the foundation of the embankment (barrettes) in order to increase the stability of the reinforced embankment to an acceptable level. These are schematically shown in F.23-7 (plan) and F.23-8 (cross-section) and were completed by the end of 2009.

Although the monitoring results in this area clearly show that the stabilizing measures are effective in reducing the rate of movements to practically zero, there is always a risk

Plan with stabilization measures in area B F.23-7



Cross-section showing the sliding surface and the stabilizing measures at the east abutment F.23-8



that, in the long-term, the drainage holes in the tunnel and the drainage wells may fail to function which would lead to an increase of pore pressures in the ground and therefore to the triggering of an instability. This instability would seriously affect the maintenance cost not only of the approach embankment of the structures but of the structure as well. Moreover, an earthquake loading presents also a great risk of instability in the area. The risk of such instabilities following the risk paradigm methodology is assessed below. Moreover, the horizontal displacements of the west abutment are computed through numerical analyses for various ground water scenarios in order to assess whether and to what degree potential deformations due to ground water rising could affect the bridge superstructure.

23-2-2 Geotechnical System Modelling

The risk of this system is a slope failure. The slope stability is checked through Limit Equilibrium Analysis (LEM) on a high number of potential circular slip surfaces. The performance function of the system is the Factor of safety (FoS) which is the sum of the resistance forces over the driving forces along an examined surface. Failure occurs when the driving forces exceed the resistance forces, i. e. when FoS is less than unity. Therefore, the risk consequence measure $h(\theta)$ is equal to an indicator function $I_F(\theta)$ which is defined as follows:

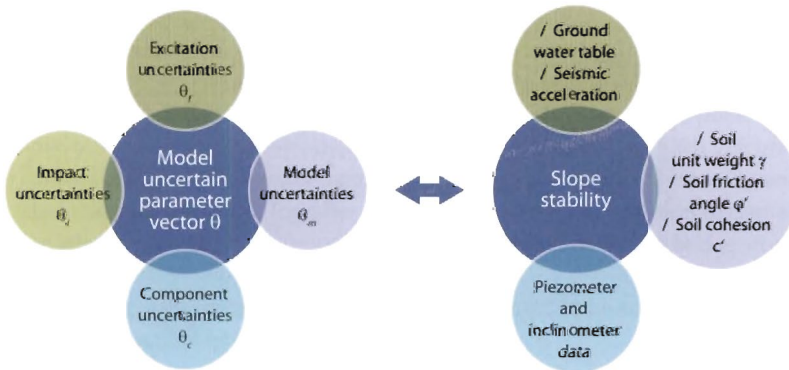
$$I_F(\theta) = \begin{cases} 0 & \text{if failure does not occur, i.e. FoS} \geq 1 \\ 1 & \text{if failure occurs, i.e. FoS} < 1 \end{cases} \quad \text{E.23-1}$$

where θ is the model parameter vector that integrates all the uncertainties involved in the occurrence of the failure. It should be noted that here the risk corresponds to the probability of failure of the system.

The model parameter vector is composed of the parameters of the excitation model (θ_f), the system model (θ_m) and the performance evaluation model distinguished in the component (θ_c) and impact (θ_i) model. In this case, the excitation model comprises the pore pressure and the earthquake loading. These are related to the ground water table and the seismic ground acceleration respectively. The system model consists of the following three parameters: the unit weight γ, the effective friction angle φ' and the effective cohesion c' of each soil layer. A number of geotechnical instruments (piezometer and inclinometers) have been installed in order to monitor the behaviour of the system. The role of these instruments is twofold. In the design stage, the piezometer data served to accurately define the ground water table whereas the inclinometer data served to accurately identify the mechanism (geometry) of failure. Hence, some uncertainties related to excitation and model parameters are eliminated. During the design life of the motorway, the piezometer data contribute to assess the risk in real time by introducing in the model the actual ground water level whereas the inclinometer data to early detect any triggering of shear failure and therefore, the appropriate corrective measures to be timely applied. Finally, the impact vector has no elements since in this case the risk consequence measure $h(\theta)$ is equal to the risk performance measure $I_F(\theta)$ as defined in the E.23-1. The components of the model parameter vector are illustrated in F.23-9.

The geotechnical model in each area was defined from the results of the geological mapping and geotechnical investigation and monitoring. More specifically, the type and thickness of the various layers were defined from the data retrieved from the boreholes. The values of the strength parameters of these layers were determined following a statistical analysis of the laboratory test results. The sliding surface geometry (depth, shape etc.) was determined from the inclinometer readings whereas the ground water surface was established from the piezometer readings. The values of the strength parameters on the sliding surface were defined through back analysis (setting a factor of safety, FoS, equal to unity) and represent residual values since they have been developed after a high level

Model parameter vector F.23-9



of shear deformation. The constructed stabilizing measures achieve to increase the FoS along the sliding surface from a value of 1 to a value of 1.3 and 1.47 for areas A and B respectively so that the motorway is safely accommodated.

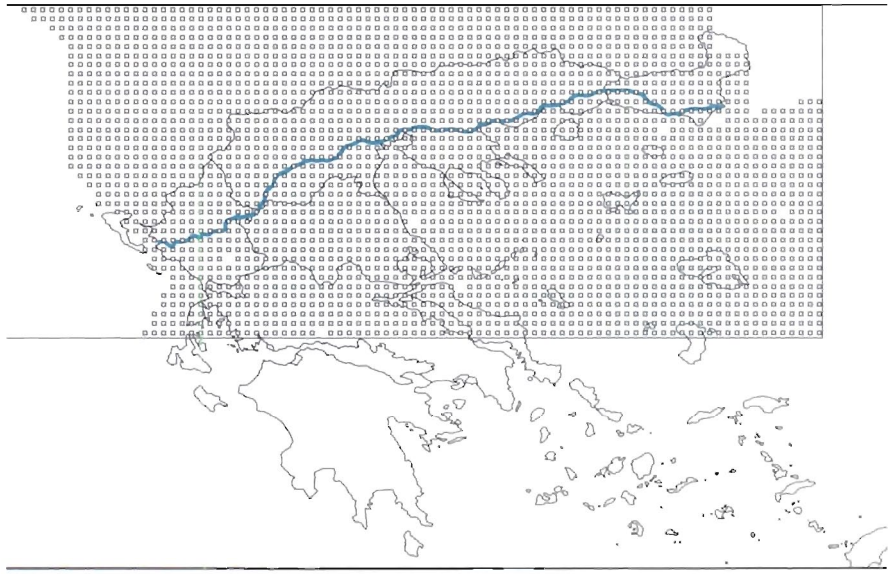
All the LEQ stability analyses of this report were performed with the software SLIDE (Rocscience Inc.) adopting the Bishop simplified method.

23-2-3 Seismic Risk Assessment of Egnatia Bridges

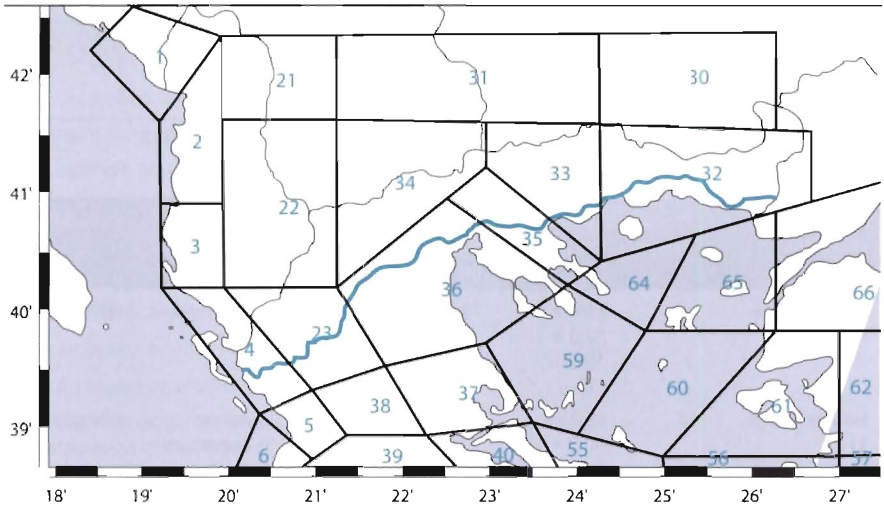
One of the major risks that affect the serviceability and the integrity of the bridges and the structures of the Egnatia motorway is the seismic risk. The most of the bridges of the motorway are built in seismic prone areas. Although the Egnatia bridges are designed and built according to the latest national seismic code and in some cases according to more unfavourable site specific earthquake spectra, a catastrophic seismic event that could lead to major damages on some of the more vulnerable bridges cannot be excluded.

To identify sections of the road most at risk from seismic activity, to assess the damage resulting from various earthquake scenarios and to make emergency plans for the after-shock situation, data from a number of sources and analyses of individual structures or road sections were carried out. As the deterioration rhythm of various bridge components is predicted by the E_BMS model (the bridge management software of Egnatia Odos SA) or other well known curves which consider only the environmentally induced mechanisms, the assessment of the minor or even moderate damage expected from seismic events of smaller return periods, is useful for updating accordingly the life maintenance cycles adopted for the Egnatia bridges, for predicting unexpected seismically induced damages and repairs. Herein the seismic risk assessment was carried out for determining the bridges of Egnatia most at seismic risk for IRIS purposes.

Predefined grid for calculating Egnatia seismic hazard model F.23-10



The Egnatia model. Seismic zones around the motorway, used by the Egnatia software F.23-11



Seismic Hazard Model of Egnatia Motorway

A seismic hazard model, considering historical data for each of 66 zones across the region surrounding the Egnatia road, was prepared by the Greek Institute of Technical Seismology and Earthquake Engineering [Theodoulidis, 2001] and defined: The frequencies of earthquakes of different magnitudes at different points on a pre-defined grid, covered the area shown in WD-471, with grid points spaced at intervals of 0.1°. At each grid point seismic data for magnitudes from 4.5 to 8.5 in 0.25 increments and at varying hypocentral depths were provided. An attenuation relationship for northern Greece was adopted after considering all the historical data of the area.

Seismic Vulnerability Analysis of Bridges

Egnatia bridges were classified to eleven structurally representative categories depending on the structural types of the superstructure, the substructure and their interconnection. For these eleven structural types representing all the major bridges of Egnatia motorway, their seismic fragility curves were analytically derived. The result was a set of vulnerability functions, relating the damage estimate of a bridge (probability of exceeding a damage limit state) with the measure of the seismic intensity at the point-location of this bridge, representative of all the bridges of Egnatia motorway. Each vulnerability curve consists of a mean percentage damage plotted against the hazard intensity, and the associated standard deviation. Together these parameterise a distribution of damage at the given intensity. In T.23-1, the properties of the eleven representative bridge structural types are given.

In F.23-12 the main characteristic of the bridges selected to be analysed as representing the eleven structural types are shown.

Seismic Risk Assessment Software

The Egnatia motorway Authority has developed a software package to assess the vulnerabilities of structures along the motorway to seismic activity of an earthquake [EQE, 2001]. The software brings together data from a number of sources and analyses various

Main characteristics of the bridges for which the fragility curves were determined F.23-12

Structural configuration	Bridge name and class	No. of spans	Span length [m]	Total length [m]	Pier-to-deck connection	Curvature	Foundation
	Pedini Bridge 111	3	19.0 + 32.0 + 19.0	70.0	monolithic	in height	pile groups
	Siatista Bridge 311	3	16.25 + 30.5 + 16.25	63.0	monolithic	minor curvature in plan	pile groups
	T7 (section 14.1.2) Bridge 121	3	27.0 + 45.0 + 27.0	99.0	monolithic	no	footings
	G11 Bridge (right branch) 221	3	64.3 + 118.6 + 64.3	247.2	monolithic	in plan	caissons
	G9 (section 5.1) Bridge 421	2	85.0	170.0	monolithic	in plan	caissons
	Eirini Bridge 122	4	45.0	180.0	through bearings	no	pile groups
	Lissoss River Bridge 422	11	1× 29.56 + 3× 37.05 + 6× 44.35 + 1× 26.50	433.31	through bearings	no	pile groups
	2nd Kavala Ravine Bridge 232	4	42.0 + 2× 43.5 + 42.0	180.0	through bearings	no	caissons
	G2 (section 1.1.6) Bridge 332	3	30.7 + 31.7 + 30.7	93.1	through bearings	no	pile groups
	Kossynthos River Bridge 432	5	35.0 + 3× 36.0 + 35.0	178.0	through bearings	no	pile groups
	Krystallopigi Bridge 223	12	44.17 + 10× 54.98 + 44.17	638.19	monolithic/ through bearings	in plan	pile groups

Structural representative bridge types of Egnatia motorway T.23-1

Type	Code of the bridge	Number of bridges of the same type
Slab on single columns	111	15
Slab on multi columns	311	13
Boxbeam on single circ. columns	121	10
Box beam on single hollow rect. columns	221	30
Box beam on walls	421	12
Box beam on single columns (bearings)	122	10
Box beam on walls (bearings)	422	7
Precast beams on walls (bearings)	432	20
Precast beams on rect. hollow columns (bearings)	232	50
Precast beams on multicolumns (bearings)	223	5
Box beam on single hollow rect. columns (combination of bearings with monolithic)	223	30

bridges or motorway sections for probabilistic damage, or damage caused by real or theoretical seismic scenarios. The various inputs to the software are:

The two parts of the hazard model were combined to generate the shaking intensities for any bridge located in the grid, for any soil type and for a predefined return period.

The vulnerability functions are formulated in terms of the hazard intensity, which is ln(PGA) in the Egnatia software.

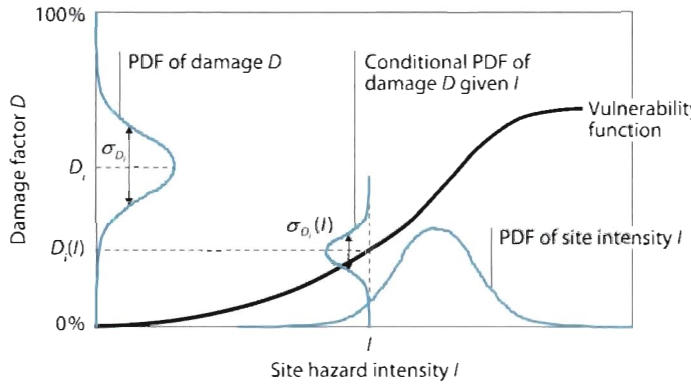
Egnatia software is used herein for the seismic risk assessment of all the bridges of Egnatia motorway, where for each of them a proper vulnerability function was assigned. Both options of the software were used for running probabilistic and user-defined scenario analysis for the selected bridges.

Probabilistic Analysis

A probabilistic analysis incorporates all major sources of shaking hazard, resulting in a probabilistic description of occurrence of the hazard intensity, through hazard curves. For each grid point, the frequency with which a certain intensity of shaking recurs is calculated. The program interpolates between grid points to calculate the shaking intensity at the precise location of the two bridges. The seismic intensity obtained automatically, incorporates the ITSAK soil model, while the model may be further modified by the specification of increments or factors considering new seismological data measured from recent seismic events, or more unfavourable site specific conditions.

Once the shaking intensity is estimated at a site, the induced damage to the structure is quantified using the vulnerability function of the specific bridge, which has been analytically derived for all the structurally representative bridge types of Egnatia motorway. The individual damage estimates for each possible event are probabilistically aggregated to estimate overall expected (annual) damage and associated uncertainty, as well as damage by return period.

Computation of damage for a bridge F.23-13



The hazard module will yield a probability density function of the shaking intensity at the site, as shown in the horizontal axis of F.23-13. For each value of the hazard intensity, I, a mean damage factor, $D_i(I)$ is obtained from the vulnerability function, with its corresponding standard deviation, $\sigma D_i(I)$. The result is a probability density function of the damage factor from which a mean value, D_i, and standard deviation, $\sigma D_i(I)$, for the damage factor of a particular structure, can be obtained. The expected damage is the sum over all events of the product of the mean damage for the event and the event frequency.

The damage distribution may be used to determine the probability of exceeding any particular level of damage. The frequency of exceeding this level of damage is obtained by multiplying the probability by the event frequency. Adding these damage frequencies across all events gives the total frequency of exceeding a given level of damage. If it is assumed that the arrival of earthquakes is a Poisson process, the annual probability of exceeding the level of damage can be calculated. Then the annual probability may be interpreted as a return period by taking its reciprocal. It is important to remember that this is the probability of exceedance smaller levels of damage that will also occur within the return period.

Damage Estimate

The output of the analytical module is a damage estimate for each structure. The damage estimate is provided as a percentage value and is written back into the "analysis_data" column in the Technical GIS. The results may be exported as a text file suitable for import into excel or word, or printed directly from the software. The exact meaning of a given "percentage damage" is discussed below.

Choice of Intensity Parameter

It was preferred to use vulnerability functions in PGA rather than MMI. Although attenuation relationships for intensity in both PGA and MMI were available from ITSAK, the vulnerability analyses carried out by Imperial College [Elnshai and Borzi, 2000] and later by [Moschonas et al., 2009], used PGA as a measure of intensity, and this choice has been

maintained in the software. From an engineering point of view, the damage suffered by an individual structure is directly related to PGA, not to MMI. PGA is a parameter that can be better related to the damage when vulnerability curves are derived analytically, as they have been for the Egnatia software. MMI is derived from the percentage of buildings suffering a given level of damage in an earthquake; it should not, therefore, be used as a measure of intensity in the analysis of a single structure. The analysis of single structures is the main use to which the Egnatia software will be put.

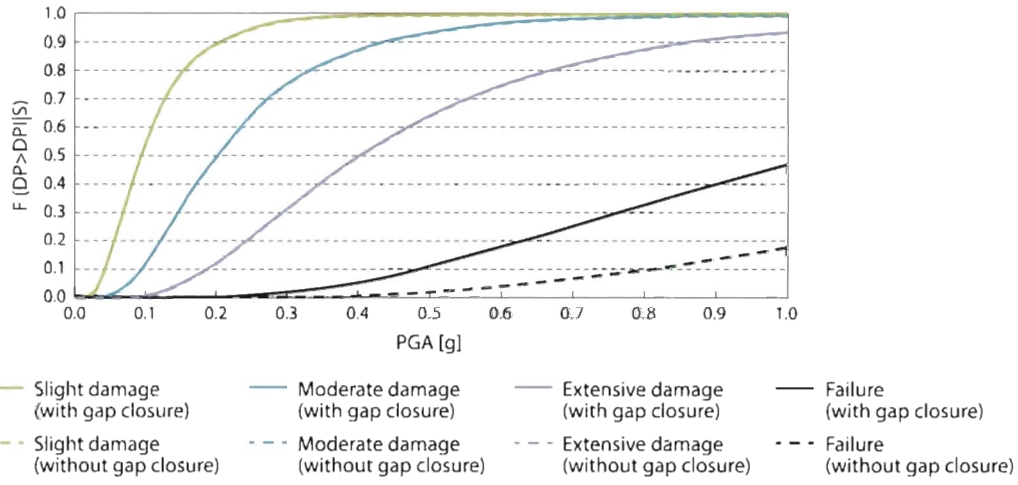
Vulnerability Curves Provided with the Software

Eleven vulnerability curves have been provided with the software for all the bridge structural types of Egnatia motorway by Aristotle University of Thessaloniki [Moschonas et al., 2009], while other five were provided by Imperial College [Elnshai and Borzi, 2000] and [EQE, 2001]. For the purposes of the IRIS project a new vulnerability function was analytically derived for bridge T9/T11, considering the updated characteristics of the bridge as are identified using ambient vibration monitoring and non catastrophic tests. The method used to incorporate these into the software is described below.

Incorporation of Bridge Analytical Vulnerabilities into the Software

The vulnerabilities provided by Imperial College and Aristotle University of Thessaloniki for the Egnatia software comprise curves that show the probability of reaching or exceeding a given limit state. Each limit state represents the boundary of post-earthquake damage conditions, which are related to a percentage of damage. Thus the quantitative description of damage provided by the software may be linked to a qualitative description of the state of the structure following an event. The vulnerability curves cannot be used directly by the software, but must first be translated to the form of curve required to provide an estimate of damage given a shaking intensity from the ITSAK hazard model.

Analytically derived vulnerability functions of Krystallopigi bridge (type 223), for four damage states, in longitudinal direction F.23-14



Quantitative representation of damage limit states T.23-2

Limit state	Level of damage	Repairs required	Damage %
1	No damage	No repairs	10
2	Minor damage	Limited repairs	30
3	Moderate damage	Extended repairs	45
4	Major damage	Partial repairs	60
5	Collapse	Replacement	100

This form of the vulnerability curve, which plots percentage damage against shaking intensity is derived from the Imperial College curves in the following way:

The probability of exceeding a certain damage state, but not exceeding the subsequent damage state are calculated, i.e. of being in a given post-event situation. For the example above, of the vulnerability function of F.23-14, derived by inelastic analyses of Krystallopigi bridge this gives:

Probability of exceeding limit state 1 but not reaching limit state 2 (P(LS1 < damage < LS2)) = 94 % – 62 % = 32 %, P(LS2 < damage < LS3) = 62 % – 22 % = 40 %, P(LS3 < damage < LS4) = 22 % – 2 % = 20 %, P(LS4 < damage < LS5) = 2 % – 0 % = 2 % (where LS5 is taken to be collapse).

Each limit state is associated with a range of percentage damage. The level of damage corresponding to limit states 1, 2, 3 and 4 (no, minor, moderate and major) damage are outlined in T.23-2.

The probabilities of exceeding a damage state but not exceeding the subsequent damage state can therefore be linked to the mean percentage of damage in that limit state. Therefore:

Damage for P(LS1 < damage < LS2) = ½(30 + 10) = 20 %, damage for P(LS2 < damage < LS3) = ½(45 + 30) = 37.5 %, damage for P(LS3 < damage < LS4) = ½(60 + 45) = 52.5 %, damage for P(LS4 < damage < LS5) = ½(100 + 60) = 80 %.

The percentage damage for each hazard intensity is then calculated using:

$$\%\text{damage} = \Sigma\{P(LS_i) \times D(LS_i)\} \qquad \text{E.23-2}$$

where $P(LS_i)$ is the probability of exceeding limit state i but not reaching limit state i+1 and $D(LS_i)$ is the damage associated with limit state i, as defined above. The term "mean damage ratio" is equivalent to the %damage × 100. For the example above, the %damage respecting the peak ground acceleration with return period of 50 years, 0.245 g, is thus computed as follows:

$\%\text{damage} = \Sigma\{P(LS_i) \times D(LS_i)\} = \{((94-62) \times 20) + ((62-22) \times 37.5) + ((22-2) \times 62.5) + ((2-0) \times 80)\} / 100 = 36.1\ \%$.

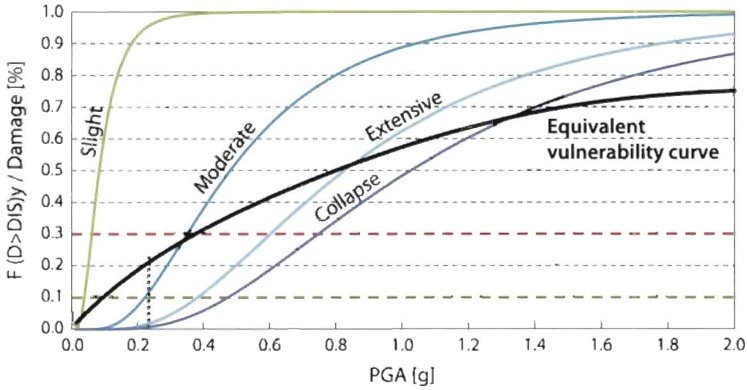
The resulting analytical vulnerability curve for bridge type 332 provided with the software and translated following the previously described methodology is shown in F.23-15:

Using the Egnatia Risk Assessment Software the following probabilistic analysis results were derived in terms of four different seismic return periods: 50-year percentage damage, 100-year percentage damage, 475-year percentage damage, 1000-year percentage damage.

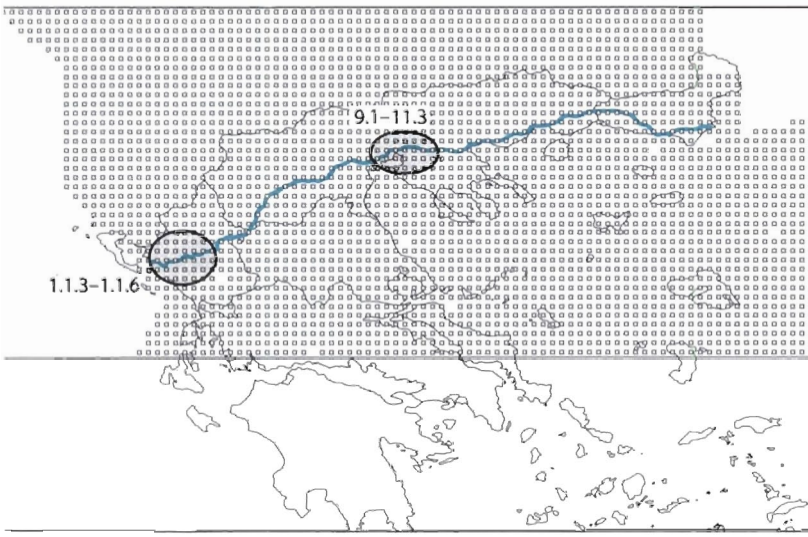
In F.23-17 the results of this probabilistic analysis for all the bridges of Egnatia motorway are given in terms of %damage. In F.23-16 the motorway sections most at seismic risk are projected in the map.

The results verify the high seismicity and therefore the high vulnerability of those bridges built in West Epirus Section as well as in Central Section. It is very important that according to the results, for small return periods (50 and 100 years) moderate damage is predicted for the bridges of these motorway sections. In some cases it is then necessary to consider the damage and repair of critical bridge components earlier than predicted by the typical deterioration curves adopted in Egnatia Life Cycle Maintenance Costs. Specifically for the major bridges of Egnatia motorway the results are given in the following tables.

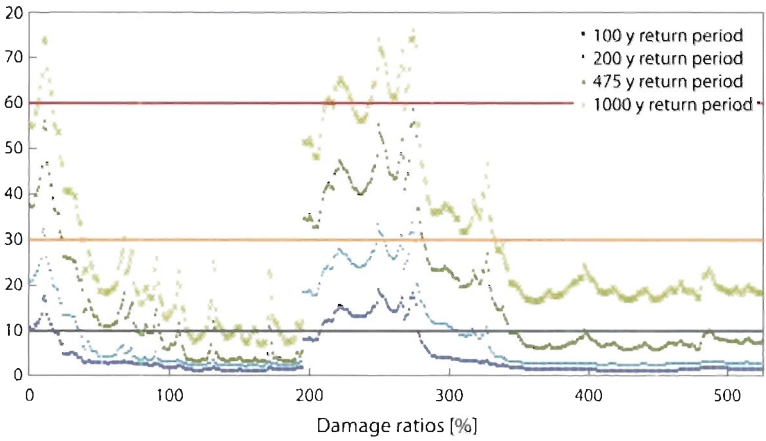
Vulnerability functions for bridge type 332 for 4 limit states and the equivalent vulnerability functions in terms of damage %. Transverse direction F.23-15



Egnatia motorway sections most at seismic risk F.23-16



Distribution of probabilistic damages for Egnatia bridges for four return periods F.23-17



As it is shown in the last table, for some major bridges as Krystallopigi and Messovouni bridges in Epirus, or 5th Kavala bypass and Nestos bridge in the Central/East Sector of Egnatia, although their severe damage or collapse can be excluded as having small probability, their minor or moderate damage due to a seismic event having 100 % probability to happen once in the first 50 years of their life (50 years return period) has to be seriously considered as it will add repair expenses up to these already budgeted for the regular maintenance programme. In the case of Krystallopigi bridge the risk assessment is more unfavourable as it resulted in extended damage (>30 %) within the first 100 years of its total 120 years service life which would probably need extended partial reconstruction/ reinstatement other than this specified.

Seismic Risk Assessment of T9/T11 Ravine Bridge

In line with other similar procedures [FEMA-NIBS, 2004; Mackie and Stojadinovic, 2007], the fragility curve of bridge T9/T11 is analytically determined for IRIS project, following the proposed methodology described in previous paragraphs and expressed by the lognormal probability distribution function:

$$P_f(DP \geq DP_i \mid S) = \Phi\left[\frac{1}{\beta_{tot}} \cdot \ln\frac{S}{S_{mi}}\right] \qquad \text{E.23-3}$$

where $P_f(\cdot)$ is the probability of the damage parameter DP being at, or exceeding, the value DP_i for the i-th damage state for a given seismic intensity level defined by the earthquake parameter S (peak ground acceleration), Φ is the standard cumulative probability function, S_{mi} is the median threshold value of the earthquake parameter S required to cause the i-th damage state, and β_{tot} is the total lognormal standard deviation. The description of the newly determined fragility curve according to E.23-3 involves only two parameters, S_{mi} and β_{tot}.

Expected seismic peak ground acceleration for various return periods T.23-3

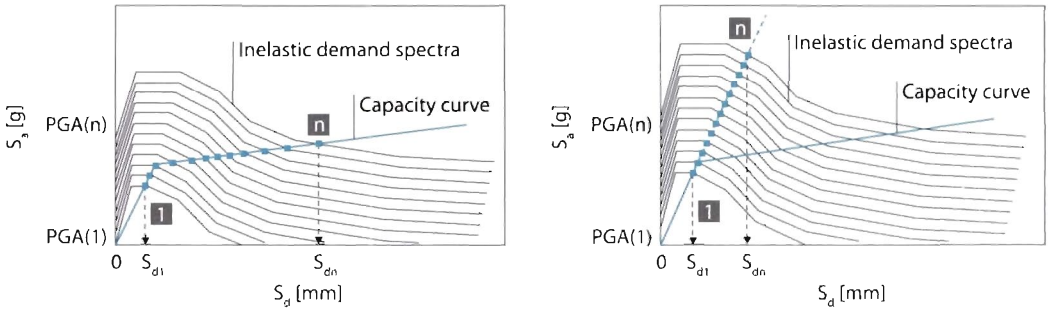
Bridge name	Return periods 50 y	100 y	475 y	1140 y
Metsovo Bridge	0.170	0.217	0.349	0.440
Aracthos Bridge	0.171	0.217	0.348	0.439
Polymylos Bridge	0.117	0.154	0.274	0.361
Krystallopigi Bridge	0.245	0.321	0.523	0.661
Mesovouni Bridge	0.254	0.324	0.524	0.662
5th Kavala Bypass	0.146	0.196	0.362	0.475
Greveniotikos Bridge	0.101	0.131	0.226	0.287
Votonosiou Bridge	0.139	0.176	0.286	0.356
Nestos Bridge	0.091	0.121	0.225	0.311

Expected seismic damage % for various return periods T.23-4

Bridge name	Return periods 50 y	100 y	475 y	1140 y
Metsovo Bridge	7.87	15.33	25.77	34.20
Aracthos Bridge	8.06	15.73	26.02	33.49
Polymylos Bridge	3.55	7.10	18.32	25.95
Krystallopigi Bridge	33.70	38.67	49.75	54.93
Mesovouni Bridge	22.34	26.88	37.89	45.36
5th Kavala Bypass	37.92	44.52	56.17	59.88
Greveniotikos Bridge	3.65	6.30	13.20	20.27
Votonosiou Bridge	7.65	10.27	20.25	25.97
Nestos Bridge	20.60	23.97	32.25	45.40

The first parameter is estimated on the basis of the capacity spectrum method, wherein the demand spectrum is plotted for a range of values of the earthquake parameter S (in spectral acceleration versus spectral displacement format) and it is superimposed on the same plot with the capacity curve of the bridge. The second parameter of E.23-3 is the total lognormal standard deviation β_{tot}, which takes into account the uncertainties in seismic input motion (demand), in the response and resistance of the bridge (capacity) which is governed by the uncertainty of the material stiffness and strengths, and in the definition of damage states. This parameter β_{tot} can be estimated by a statistical combination of the individual uncertainties (in demand, capacity, and damage state definition) assuming these are statistically independent. The value of β_{tot} was calibrated by [Dutta and Mander, 1998] using a theoretical approach and validated on the basis of empirical fragility curves obtained from actual bridge damage data gathered from the Loma Prieta (1989) and Northridge (1994) earthquakes. According to these studies the value of β_{tot} was set to 0.6; due to the lack of a more accurate estimation of uncertainties in capacity, demand and damage states, $\beta_{tot} = 0.6$ was used in the present study. For the purposes of the IRIS research project it was attempted to verify the uncertainty of the resistance of the bridge

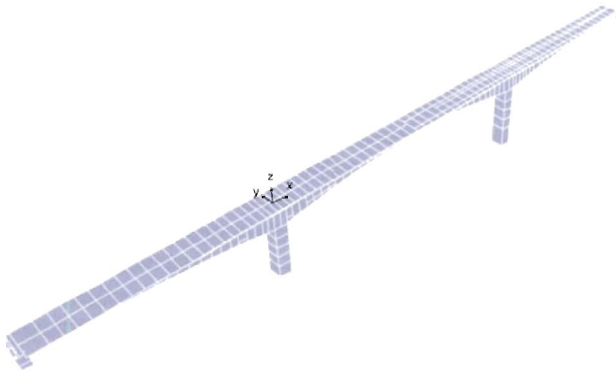
Capacity spectrum method. For T9 (T > 0.5 sec) case 2 elastic demand spectra F.23-18



by statistically analyzing the big number of non catastrophic result Schmidt Hammer and ultrasonic tests. These two material concrete tests represent the basic properties affecting the non-linearities and the t is very important for determining the seismic capacity of the bridge to consider their uncertainty based on experimental data. The statistical analysis resulted to uncertainties well enveloped by the value of β_{tot} considered herein. The log-normal distribution gave a sufficient fit to the distribution of the test results. Therefore the consideration of the uncertainty by Dutta and Mander will be adopted once more for the fragility curve of T9/T11 bridge. The important issue here is that the properties of the nominal inelastic model for the T9/T11 bridge are updated based on the results of the ambient vibration monitoring. The values of the modulus of elasticity for the superstructure and the piers are considered equal to 1.0319 and 1.1177, or 38.75 Gpa and 38.00 Gpa respectively.

The capacity curve of the bridge was analytically determined by calculating the push-over curves using proper static inelastic modelling with the software package SAP2000NL V.14. In F.23-19 and in F.23-20 the analytic inelastic model representing the inelasticity as

3d inelastic model of the T9 Ravine bridge F.23-19



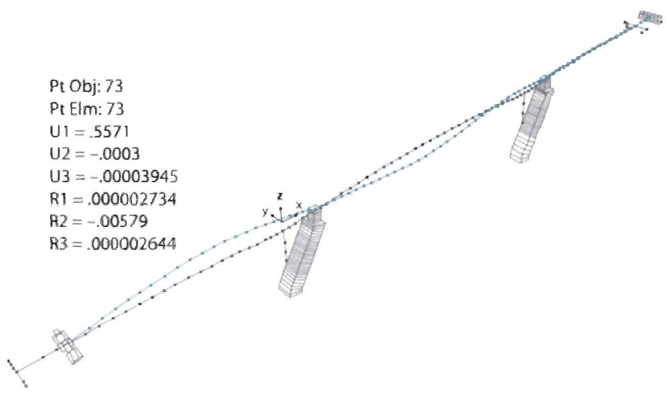
lumped with plastic hinges at both ends of the two piers M1, M2. The mechanism failure due to the formation of plastic hinges in both ends of the two piers is shown in F.23-20, with respect to the ultimate displacement of 0.56 m. The corresponding pushover curve representing the ultimate resistance up to the failure against earthquake is shown in F.23-21.

The final fragility curves representing the cumulative probability of exceeding the predefined damage limits states are shown in F.23-23.

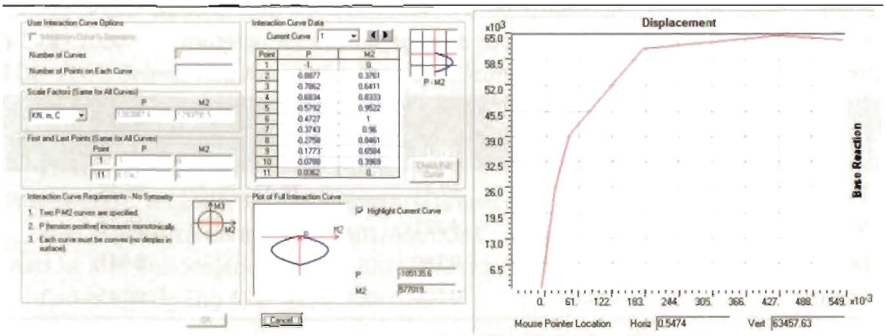
The hazard model of Egnatia incorporated in the seismic assessment tool presented before in this paragraph, estimates the following peak ground accelerations for four different return periods, shown in T.23-5.

Projecting the probabilistic seismic intensities in terms of peak ground acceleration on the new fragility curve of T9 bridge the probabilities of exceeding various damage states can be predicted as shown in T.23-6.

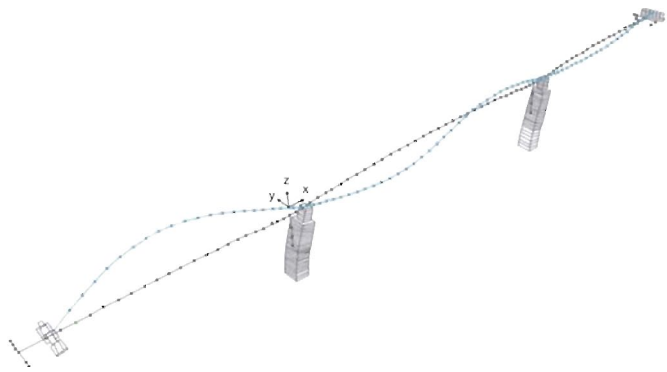
Final failure pushover step (plastic hinges in both piers M1, M2 at the top and base sections) F.23-20



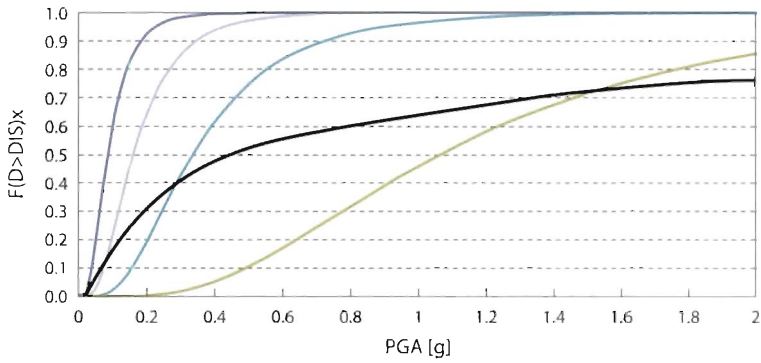
Plastic hinge properties of M2 base (left) and pushover curve (right) F.23-21



Fundamental longitudinal mode shape of T9 bridge (T = 0.94 sec > 0.5 sec) F.23-22



Seismic fragility curve for T9 bridge F.23-23



Expected seismic peak ground acceleration for various return periods on T9 bridge T.23-5

Bridge name	Return periods 50y	100y	475y	1140y
T9/T11 Bridge	0.081	0.165	0.318	0.385

Predicted probability of different various damage states for four return periods, T9 bridge T.23-6

Probability [%]	Return periods 50y	100y	475y	1140y
Minor damage	6.598	37.41	78.02	86.25
Moderate damage	0.213	4.721	28.11	39.71
Extensive damage	0.000	0.260	4.491	8.441
Collapse	0.000	0.000	0.049	0.145

23-3 Progress beyond the Current Practice

A quantitative geotechnical risk assessment was carried out for very critical areas in terms of geotechnical instabilities for which only deterministic analyses were previously carried out. The assessment was carried out applying the IRIS Risk Paradigm methodology. For some failure modes, extremely high risk was calculated. In practice, monitoring data proved that modes of failures with very high calculated risk needed indeed further reviewing and additional stabilizing measures to lower the risk in tolerable margins. The residual risk was finally reassessed taking into account the implementation of the additional measures and the actual piezometer data. The final outcome highlighted specific aspects that need closer attention during the design life of the motorway.

The above actions have established a process to be followed in other areas of the motorway where critical geotechnical conditions may threaten the safety of the motorway. The quantitative estimate of risk supported by continuous monitoring will contribute to focus on areas that exhibit the highest residual risk and allow a proper maintenance plan to be developed and implemented in order to eliminate or mitigate it. The aim of the whole risk management process is to offer a safe motorway to the users with the least maintenance cost escalations.

Furthermore, the seismic risk assessment of major Egnatia motorway bridges and their pre and after shock management is to be upgraded incorporating the methodology developed in the frame of IRIS which combines statistical predictions with bridge models calibrated by experimental monitoring results. This results in a more accurate estimation of the probability to exceed various states of damages during their service life, which will help the maintenance authority to revise their currently adopted Life Cycle Costs, the type and the extent of their preventive measures, and the time of their implementation.

References

Dutta, A. and Mander, J.B., 1998. *Seismic Fragility Analysis of Highway Bridges, INCEDE-MCEER Center-to-Center.* In: Proceedings of the center-to-center workshop on earthquake engineering frontiers in transport systems, Tokyo, Japan, 311–325.

Elnshai, A.S. and Borzi, B., 2000. *Analytically Derived Vulnerability Functions for Egnatia RC Bridges.* Deliverable of Research Contract 330/A01/ΔM/EOAE, box no. S-224, September 2000.

EQE, 2001. *Seismic Risk Assessment Tool, Specification Document.* EQE International Ltd., Deliverable of Contract 330/A01/ΔM/EOAE, box no. S-225A/4/2001.

FEMA-NIBS, 2004. *Multi-Hazard Loss Estimation Methodology – Earthquake Model: HAZUSMH Technical Manual.* Washington, DC.

Theodoulidis, N., 2001. *Seismic Hazard Assessment along Egnatia Motorway.* Final Deliverable of Research Contract 406/A01/ΔM/EOAE., Box. No.S-243, May 2001.

Mackie, K.R. and Stojadinovic, B., 2007. *R-Factor Parameterized Bridge Damage Fragility Curves.* J Bridg Eng ASCE 12(4):500–510.

Moschonas, I. F., Kappos, A. J., Panetsos, P., Papadopoulos, V., Makarios, T. and Thanopoulos, P., 2009. *Seismic Fragility Curves for Greek Bridges: Methodology and Case Studies*. Bulletin of Earthquake Engineering, 7(2):439–468.

24

Application of IRIS Technologies on the Earthquake Damaged Chi Lu Cable-Stayed Bridge

Authors:
Helmut Wenzel
Robert Veit-Egerer
Tzu-Kang Lin
Zheng-Kuan Lee
Monika Widmann
Martin Stöger

Motivation

For proper demonstration of the innovative technologies developed in the IRIS project good demonstration cases are required. The Chi Lu Bridge in Taiwan is situated close to the epicentre of the 1999 Chi Chi Earthquake and was tested by ambient vibration monitoring campaigns in 2001 and 2011. It is a case where real damage has happened after an earthquake and repair works restored the structural function.

Main Results

The main interest within the IRIS project has been put on the demonstration that the repair works restored the structural function. It provided a clear proof of concept that the IRIS methodologies applied for assessment create the required information for the decision makers.



24-1 Introduction

24-1-1 Objectives of the Campaign

Since 2001 VCE has been collaborating with the Taiwanese National Centre of Research on Earthquake-Engineering (NCREE) in the course of several European research projects. There has been exchange of knowledge and reciprocal visits performed within the SAMCO-project. Furthermore IRIS beneficiary VCE has been involved in the design and construction supervision of the Chi Lu Bridge. In combination with the unique earthquake history of this structure this provides a spectacular opportunity for collaboration in the field of structural assessment. While NCREE has been periodically performing monitoring works at this bridge since 2001, VCE conducted an initial dynamic measurement at the cable stays in 1999. In May 2011 a joint monitoring campaign (bridge deck and cables) at this bridge was conducted to compare cable assessment approaches and results. Besides the measurements at the structure a wide spread dissemination was scheduled. There were a number of major points of interest:

// How do the measurements of 1999/2001 compare to the measurements of 2011? Substantial change in structural properties (cable and deck) is to be considered.
// Are there traces of the earthquake-stress-history introduced into the structure?
// Comparison with the NCREE monitoring activities (started in 2001).
// Utilization of available results and findings for Integral Life Cycle Assessment (LCA) based on the Observation Period 2004–2011 [Wenzel, 2011].

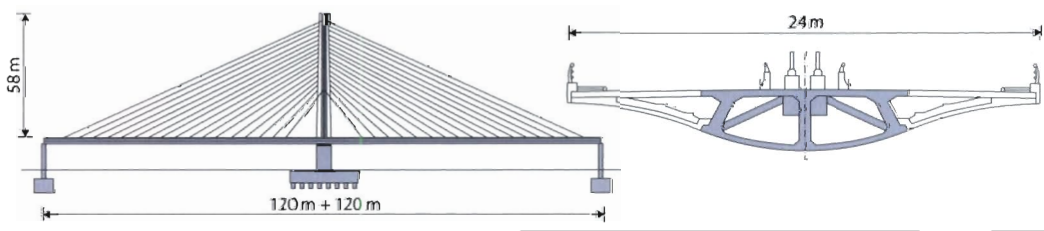
24-1-2 Bridge Description

Chi Lu Bridge, located at Nantou Country, Taiwan, is a modern designed prestressed concrete cable-stayed bridge crossing the longest river, Juosheui River, in Taiwan (F.24-1). The bridge has a single pylon (58 m height), two rows of harped cables (68 cables in total), and a streamline-shape double box girder. With 2.75 m in depth and 24 m in width, the box girder rigidly connects with the pylon and spans 120 m to each side [Lee et al., 2008].

24-1-3 Involved Technology

For their monitoring activities NCREE mainly use optical and wireless sensing and traditional vibration and environmental sensors. VCE made its measurements with the

Elevation and cross-section of the Chi Lu Bridge at Nantou Country F.24-1



in house developed BRIMOS® Wireless system in combination with 3D accelerometers (Kistler, Kinemetrics).

24-2 The Chi-Chi Earthquake

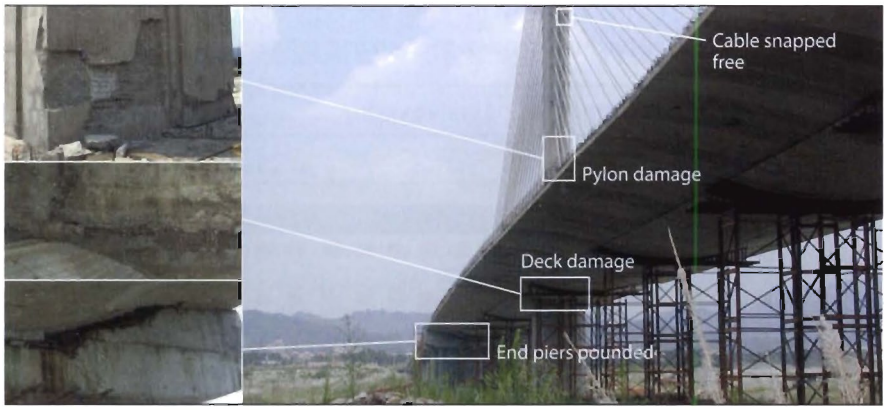
24-2-1 Impact and Damage at Chi Lu Bridge

On 21 September 1999, near the final construction stage of Chi Lu Bridge, a significant earthquake (Chi-Chi Earthquake) with 7.3 ML magnitude seriously struck the central part of Taiwan. For only three kilometres away from the epicentre, Chi Lu Bridge underwent very strong ground motion and several of its structural members were damaged: one cable fell onto the deck, the concrete cover of the pylon peeled off, the cap beams of the two bents were ruined by the pounding force between the deck and the bents, the rebar of the girder near the pylon buckled, and several steel plates between anchors and anchor seats were bent seriously (F.24- 2): it was believed that the cable forces had redistributed [Lee et al., 2008].

24-2-2 Repair History

After the main shock, the emergency repair was implemented immediately to support the bridge for the following aftershocks' striking, and all the mending of the concrete structure was finished by July, 2001. Nevertheless, the repair of the cable system hadn't been finished by 2005 because the status of the bridge was not clear and the ways to repair the cable system were not determined. In order to partly relieve the pressure of local traffic demand for small cars and to prepare the further repair work in the future, the owner, Directorate General of Highways, entrusted National Center for Research on Earthquake Engineering (NCREE) with an in-situ loading test and the investigation of the cable-system and the bridge in July 2002 [Lee et al., 2008].

Damage detected at the Chi Lu Bridge after the Chi-Chi Earthquake on 21 September 1999 [ZEvent] F.24-2



24-3 Methodology – Cable Assessment

24-3-1 NCREE

To calculate real cable force NCREE applies the so-called "inverse-problem" technique to consider the difference between String Theory and a real cable system. The cable force, the moment of inertia and the sag of a cable are derived from a finite element (FE) model which is calibrated and optimized by comparing the measured experimental signal spectrum with the natural frequencies in the FE model. In the analytical model the cable is subjected to gravity and fixed-end boundary conditions [Lee et al., 2008].

24-3-2 VCE

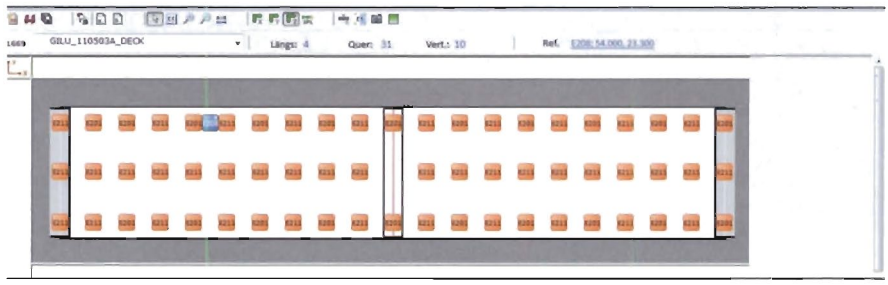
In the course of the European research project IMAC (2001–2004) – coordinated by VCE – the BRIMOS® Method to extract exact cable forces from dynamic measurements was substantially improved after the already existing, simplified approach had been applied in a large number of cable assessment projects worldwide. In the subsequent Austrian research project INNO FORCE (2006–2007) the method was refined and optimized.

With this procedure it is possible to determine the cable force rapidly and in a non-destructive manner. The dynamic characteristics of each individual cable are identified via measurements – which are done under ambient conditions on the one hand and under regular traffic on the other hand.

For the calculation of the exact cable force the determination of the basic and higher vibration frequencies is necessary. A linear relation between the basic and higher order of natural frequencies is only valid for a wire without sag and bending stiffness. For this theoretical (idealized) "string wire" case there would be a harmonic succession of every mode shape starting from the first up to the very high natural frequencies. A real cable brings up a deviation from this idealized case, especially in the higher modes, since the bending stiffness causes an increase of natural frequencies. For an accurate cable force measurement this effect must be considered (IMAC FP5).

From the measurement data the effective cable force can be calculated by the highly specialized BRIMOS® Cable-Software, which is kept on the latest state of the art constantly. The required input for this analysis is the cable geometry and the cable properties. The determination of the natural frequencies, the bending stiffness and the cable forces is

Overview BRIMOS® measurement at the bridge deck F.24-3



done fully automatic in the course of an optimization algorithm, comparing measured and expected cable characteristics (for more details see [Wenzel, 2009]). The identified natural frequency f_1 is a function of the effective cable force, the length, the mass and the stiffness of the cable (E.24-1). For the cable force determination the modes #1 to #10 out of plane were used to minimize the influence of the cable sag.

$$f_k = \frac{k}{2l} \cdot \sqrt{\frac{N}{m}} \cdot \left(1 + \frac{2}{\xi} + \left(4 + \frac{k^2\pi^2}{2}\right)\frac{1}{\xi^2}\right) \qquad \text{E.24-1}$$

f_k Frequency of the order k
N Cable force
m Mass of the cable per metre
l Length of the cable between the nodes of the relevant mode shape
ξ Non-dimensional cable stiffness

24-4 Monitoring Campaign 2011

24-4-1 Deck Measurement with BRIMOS® Wireless

The dynamic measurement of the bridge deck with BRIMOS® 11.05 was carried out on 3 and 4 May 2011. The temperature during the measurements was about 30 °C. The measurements were done under ambient conditions on the one hand (environmentally excited vibrations) and unrestricted traffic including passages of heavy vehicles on the other hand. Due to time constraints and limited available equipment – only two sets of BRIMOS® Wireless equipment had been brought to Taiwan – a sensor layout with 42 different positions in three alignments along the bridge's lengthwise direction had been chosen (F.24-3). This procedure allowed limiting the campaign to two days. In total five hours of monitoring data were available for analysis and assessment. The objective of the deck measurement was to identify the Key Performance Indicators of the structure with regard to their relevance for civil engineering issues [Wenzel, 2009]:

- // The bridge structure's relevant eigenfrequencies and corresponding mode shapes providing information about the load bearing capacity and operability, the distribution of the global and local dynamic structural stiffness in the bridge's lengthwise and transversal direction and enabling the evaluation of the bearings.
- // Sensitivity analysis to investigate the progression, the character, the stability and probable changes in the energy content of the relevant eigenfrequencies to evaluate the load bearing capacity and operability.
- // Energy dissipation path in the structure's lengthwise direction (dissipation of the induced vibration energy) to localize problematic sections.
- // Vibration intensity at the entire bridge deck to detect weak points with regard to fatigue threat.

24-4-2 Cable Force Measurement

The measurements at the cables were performed on 3 May 2011 using a BRIMOS® Wireless sensor unit and two 3D accelerometers (Kistler, Kinemetrics). Starting at the cable pair 34L/34R the cables were measured in pairs – one after the other (F.24-4). In total 68 measurement files were taken on the cables of the Chi Lu Bridge with a sampling rate of 500 Hz (= 2 milliseconds).

24-5 Results of the Measurements

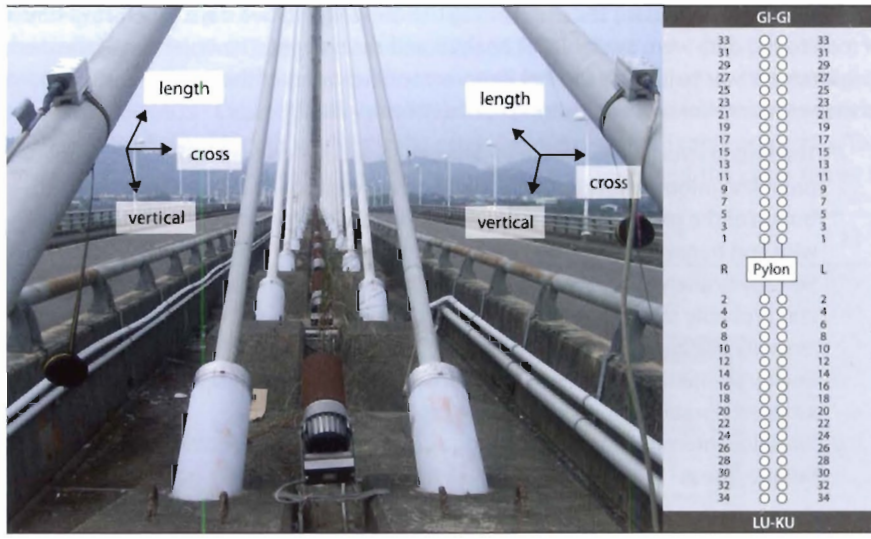
24-5-1 Cable Forces

In May 2011 in total 68 measurement files were taken on the cables of Chi Lu Bridge. From this data the cable forces were analysed considering the natural frequencies #1 to #10 out of plane (transversal). As the BRIMOS analysis takes into account the effects of the cable properties (bending stiffness/vibration length) – it delivers very accurate and reliable results compared to conventional methods.

In principle the frequency spectra of all measured cables show a distinctive characteristic in vertical, cross and lengthwise direction – already in the raw spectra (F.24-5).

The large amount of data enables the extrapolation of different parameters that can be compared to reference values. In the visualizations F.24-6 to F.24-8 the results of the cable force measurement are presented. F.24-6 comprises the design force, the cable force measured in 2011, the deviation between design and measurement (2011) and the utilization ratio – all of them summed up for the given cable harp sections. Even if deviations up to ±32 % between the design force and the measured cable force arise at individual cables

Documentation of the cable force assessment at the Chi Lu Bridge F.24-4

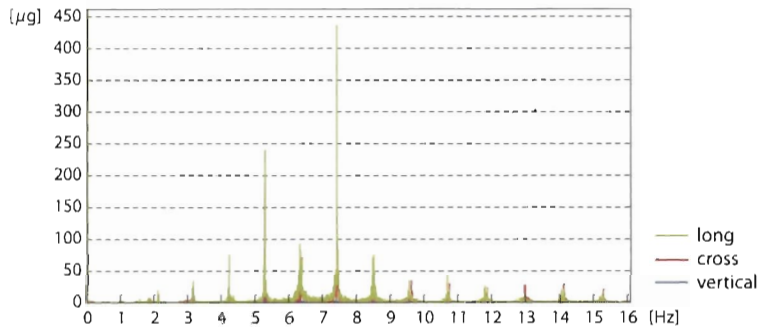


the deviation of the total sum of cable forces within the analysed harps (the mean deviation) is less than 5 %. The derived utilization ratio of the cable towards GI-GI is in the range of 19 % to 30 % and towards LU-KU in the range from 17 % to 31 %. All measured cable forces are by far within the limit states given by the plastic resistance. The figures F.24-7 and F.24-8 present the results of the cable force assessment by VCE in 2011. In F.24-7 the design force is compared to the measured cable force for every cable, in F.24-8 the plastic resistance is added.

24-5-2 Comparison NCREE – VCE

With regard to the reliability and the long-term observation of the extracted cable forces NCREE's and VCE's measurement results were compared. The first eigenfrequencies measured by NCREE in 2004 and by VCE in 2011 (F.24-9) show no significant difference. The mean deviation for every cable harp is 0.3 % (right harp) and 0.4 % (left harp). Singular deviations were found in the range of –5.0 % and +2.7 %.

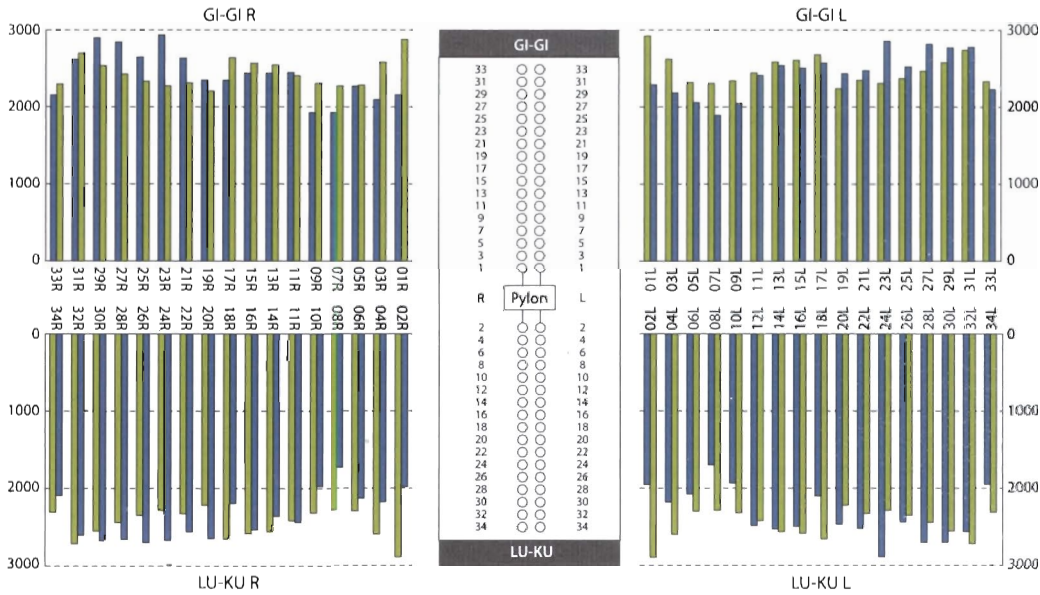
Exemplary raw spectrum in all three measured dimensions – cable 28L, Chi Lu Bridge, May 2011 F.24-5



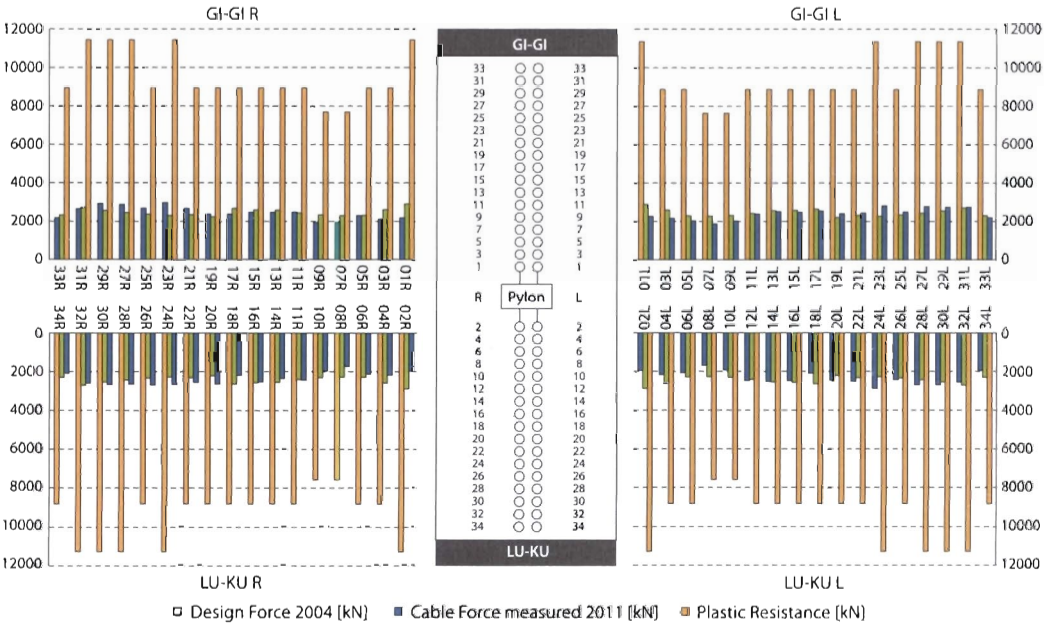
Overall results of the cable force measurements in 2011 F.24-6

GI-GI R						GI-GI L					
	[kN]	[kN]	[%]	[kN]	[%]		[kN]	[kN]	[%]	[kN]	[%]
Sum	41,621	41,179		159,894		Sum	41,621	40,802		159,894	
Mean			–1.1		25.9	Mean			–2.0		25.7
Min			–25.1		19.1	Min			–21.7		20.0
Max			–29.2		30.0	Max			–23.8		28.8
	Design Force 2004	Cable Force Measured 2011	Deviation Design 2004 – Measured 2011	Plastic Resistance	Utilization Ratio		Design Force 2004	Cable Force Measured 2011	Deviation Design 2004 – Measured 2011	Plastic Resistance	Utilization Ratio
Sum	41,621	39,984		159,894		Sum	41,621	39,479		159,894	
Mean			–3.9		25.2	Mean			–5.1		24.8
Min			–31.4		17.5	Min			–32.4		17.2
Max			–19.4		30.5	Max			–26.3		28.5
	[kN]	[kN]	[%]	[kN]	[%]		[kN]	[kN]	[%]	[kN]	[%]
LU-KU R						LU-KU L					

Comparison of design forces (2004) and measured cable forces (2011) for every single cable F.24-7



Comparison design force (2004), measured cable force (2011) and utilization ratio for every single cable F.24-8



The slight and negligible differences with regard to structural judgement can be traced back to varying environmental conditions (temperature, radiation). Altogether, both technologies (NCREE and VCE) turned out to be equivalent.

24-5-3 Results of the Deck Measurement

The results of the dynamic monitoring campaign at the Reference Bridge can be summed up as follows:

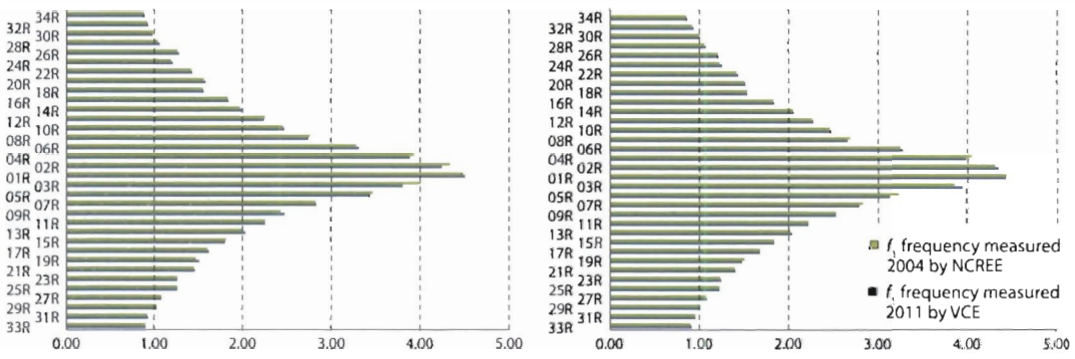
Eigenfrequencies

The frequency spectra of the bridge deck show a clear dynamic characteristic in all three analysed dimensions. The relevant eigenfrequencies for primary loading behaviour were identified in the range of 0.5 to 11.0 Hz.

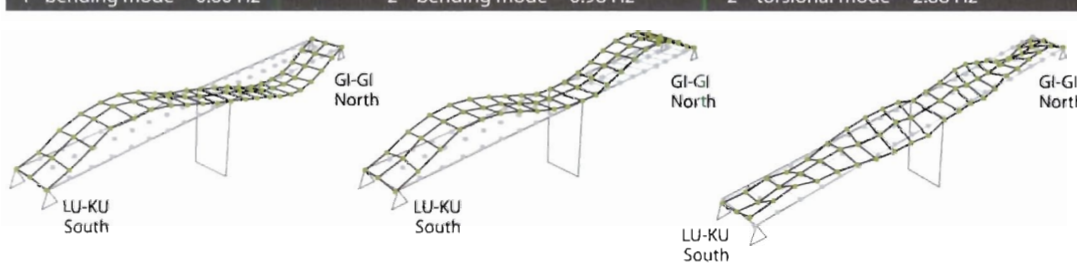
Mode Shapes

The determined mode shapes are characteristic for this kind of structure and correspond to the expected modes of vibration. The distinctively occurring mode shapes indicate a good structural maintenance condition. Some of the derived mode shapes are shown in F.24-10 exemplarily.

Comparison of cable eigenfrequencies measured by NCREE (2004) vs. VCE (2011) F.24-9



Structural response – exemplarily F.24-10



Vibration Intensity

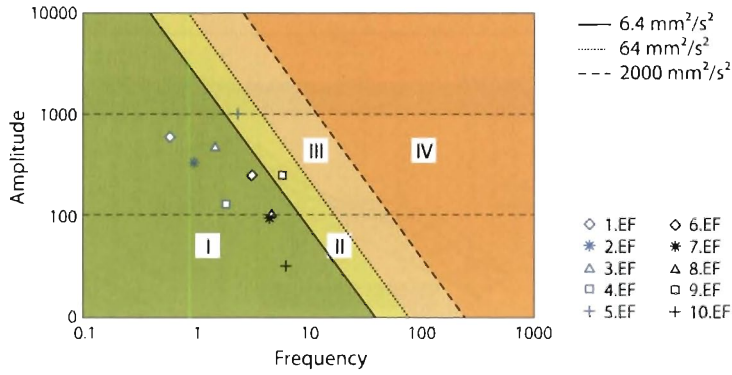
Intensive dynamic loading causes fatigue-failure of structures. The vibration intensity provides a risk level classification according to the induced energy-impact into the structure. The analysis of the vibration intensity shows the relation between the structure's eigenfrequencies and its corresponding oscillation amplitude incorporating all sensor positions. As a basic principle lower amplitudes are permissible for higher eigenfrequencies. If oscillation amplitudes exceed certain limits, damage by overstraining to the structure or to structural elements can be expected. The vibration intensity is subdivided into four zones, ranging from low probability of damage due to dynamic stress (Zone I) up to very high probability of damage (Zone IV) (classification according to [Beards, 1996]).

The Chi Lu Bridge shows values of vibration intensity in the ranges I and II (F.24-11). Range II indicates a zone, where damage might be caused in cases of continuous dynamic stressing on that level of intensity. The local authorities raised concerns about the bridge behaviour under heavy freight traffic coming from the surrounding industrial enterprises. In principle the results of the vibration intensity analysis correspond to these observations. This means there is a tendency of increased energy impact but it is not classified being critical by means of global structural damage. Still a future assessment and observation of the effective loading impact regarding fatigue-relevant damages in periodic time intervals is recommended.

Dissipation of Induced Vibration

The energy dissipation path is a suitable indicator for the condition of a structure and the main girders respectively. "Problematic zones" mostly dissipate energy caused by friction which is reflected in an increase of the local damping values. Higher damping values in the range of abutments or piers are system-based and thus have no direct influence on the assessment of the structure's condition. The pattern of damping values calculated for the Chi Lu Bridge (F.24-12) is typical for such a structural type. The damping analysis primarily reflects the dominantly occurring system damping due to the mechanical behaviour of the bridge (supports, pylon). Increased values from local spots according to material damping which would point out additional certain damage of mechanically grave extent were not determined.

Classification of vibration intensity F.24-11



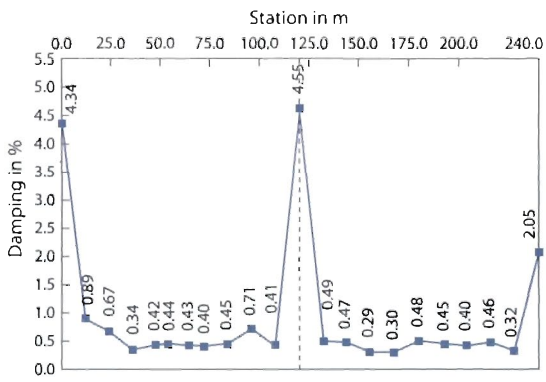
Trend of Stiffness

So-called trend cards are an essential evaluation instrument in the context of full-scale measurements on bridge structures. Trend cards are obtained by evaluating frequency spectra taken from several measurements, telescoping them together and viewing them from above. For reasons of a better descriptiveness a two-dimensional visualization is chosen. Showing the behaviour of the structure during certain timeframes of monitoring observation trend cards enable the identification and assessment of extraordinary behaviour.

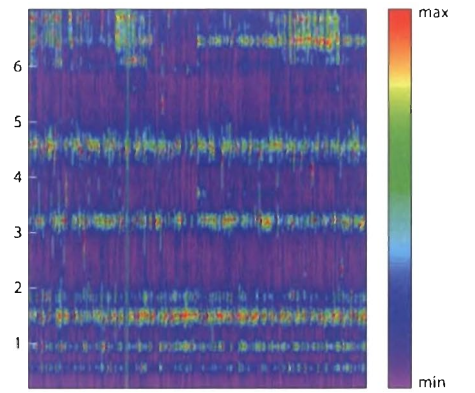
The first trend-card (F.24-13) shows the relevant stiffness-patterns in the vertical direction over the measurement's entire time period in the range from 0.2 to 7 Hz – derived from the data recorded by the reference sensor. This trend card does not show any unusual behaviour in terms of structural resistance and confirms the global structural integrity being satisfactory. The mentioned increased vibration intensity from the industrial based freight traffic impact is evident in terms of some scatter in the stability of dynamic response but is typical for the given structural type and the occurring loading conditions.

The second and third trend-card (F.24-14) present the bridge's relevant stiffness-patterns distributed in the lengthwise direction of the structure. F.24-14 left shows the trend of eigenfrequencies in the range of 0.2 to 10 Hz, F.24-14 right in the range of 2.0 to 4.0 Hz in detail. In the latter a sudden jump in frequency (3.12 Hz – third bending mode) from the southern to the northern span is visible and attracting attention. It is assumed that this is a consequence of the Chi-Chi Earthquake or – more precisely – of the retrofit afterwards. The induced earthquake-damage patterns demanded non uniform, singular maintenance measures affecting the previously symmetrical distribution of stiffness and mass on both bridge spans. Secondly the superstructure was "tuned" in the course of the installation of the new cable stays with regard to an aspired horizontal gradient. Apart from that, the relevant eigenfrequencies follow stable patterns in all trend cards, which confirms the already stated good maintenance condition of the structure. Extraordinary changes indicating arising deficiencies in integrity were not detected in any of the trend cards.

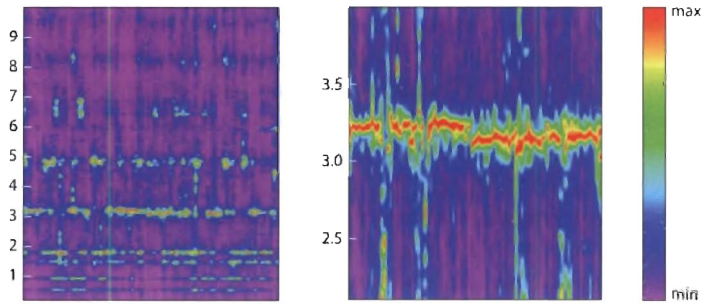
Recorded energy dissipation path F.24-12



Trend of stiffness covering the entire recording period 2011 F.24-13



Trend of stiffness distributed in the lengthwise direction, 0–10 Hz (left) and 2–4 Hz (right) F.24-14



24-6 Conclusion

Being the first earthquake damaged cable-stayed bridge in the world the Chi Lu Bridge is an attractive structure for collaborative bridge testing. Based on the described measurement campaign in May 2011 – consisting of a dynamic deck measurement and a cable force assessment – the structural condition was analysed concerning the entire Life Cycle of the bridge. Compared to investigations of the authors on similar bridges no obvious earthquake-related indication of structural deficiencies was found in the dynamic bridge behaviour. Comparing the cable investigations from different approaches by NCREE and VCE both technologies lead to similar findings. The dense set of results of the investigation performed represents a comprehensive basis for Integral Life Cycle Assessment (LCA) for the observation period 2004–2011.

References

Beards, C. F, 1996. *Structural Vibration-Analysis and Damping*. London: Arnold (A Member of the Hodder Headline Group).

ZEvent. www.zevent.com/Research/Ji_Lu_Bridge/Observable_Damage/Damage.htm

Lee, Z.-K., Chang, K.-C., Loh, C.-H., Chen, C.-C. and Chou, C.-C., 2008. *Gi-Lu Cable Stayed Bridge – From Earthquake Damage to Full Recovery*. In Koh & Frangopol (eds), Bridge Maintenance, Safety, Management, Health Monitoring and Informatics. London: Taylor & Francis Group.

Wenzel, H., 2009. *Health Monitoring of Bridges*. Chichester England: J. Wiley and Sons Ltd, ISBN0470031735.

Wenzel, H., 2011. *International IRIS Demonstration at the Chi Lu Bridge, Taiwan*. VCE-WD 303, IRIS (IP: SP3 & 7: Workers Safety & Online Monitoring), European Commission FP7, Project No.: FP7-NMP-2007-LARGE-1.

25

Stochastic Approach to Slope Stability Analysis with In-Situ Data

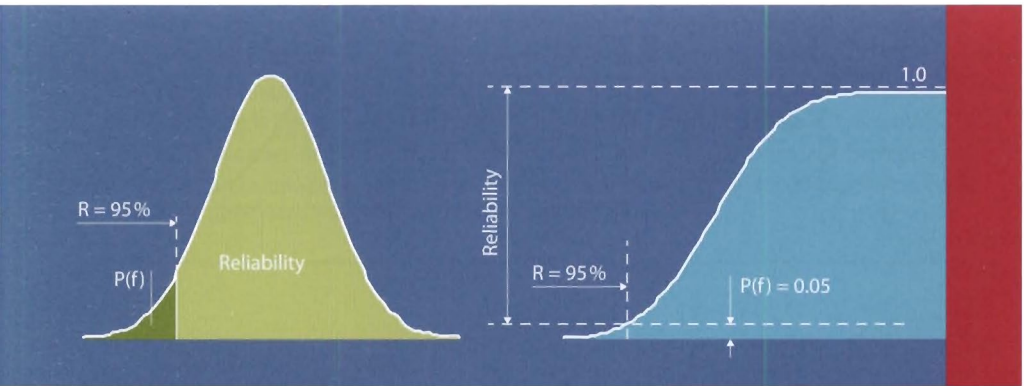
Authors:
Jonathan Nuttall
Michael Hicks
Marti Lloret-Cabot

Motivation

Technologies to properly model the influence of soil heterogeneity on geotechnical performance are desired. Traditional deterministic approaches based on single representative property values are to be replaced by an alternative stochastic approach, combining random field theory with finite elements.

Main Results

A methodology for the stochastic approach has been developed incorporating the spatial variation of material properties, thereby enabling a probabilistic evaluation of the performance of slopes and other geotechnical structures.



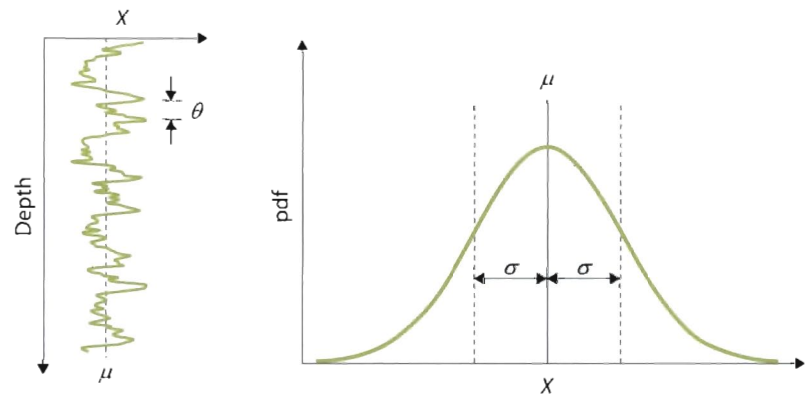
25-1 Introduction

The inherent spatial variability of geo-material properties influences material behaviour and geo-structural response [Hicks and Onisiphorou, 2005]. It also leads to uncertainty in design due to incomplete knowledge regarding in-situ conditions, and thereby leads to the need for statistical definitions of material properties, probabilistic analysis, and global response quantified in terms of reliability and probability of failure [Hicks, 2007]. Spatial variability is particularly important due to structural response typically being governed by the soil profile, with failure mechanisms often following the weaker zones within the soil [Griffiths and Fenton, 2000; 2001; 2004; Hicks and Samy, 2002a; Hicks and Spencer, 2010]. Moreover, the need for adequate representation of soil properties and their variation has been recognized in geotechnical design codes, with the European Union's Eurocode 7 [Eurocode 7, 2004] introducing the concept of characteristic values into the design process [Hicks and Nuttall, 2012].

Probabilistic modelling of slope stability problems has been carried out since the 1970s, albeit mainly through the use of limit equilibrium methods combined with various statistical approaches [El-Ramly et al., 2002]. These statistical approaches have included Monte Carlo methods, as well as so-called "approximate" methods such as the First Order Second Moment (FOSM) and Point Estimation methods. Moreover, the representation of soil variability has generally followed two approaches. [Tang et al., 1976; Harr, 1987; Duncan, 2000] used the point statistics of a material property, implying an infinite spatial correlation of properties; whereas [Vanmarcke, 1977; Mostyn and Soo, 1992; El-Ramly et al., 2002; 2003; 2005] accounted for spatial variation by reducing the variance of material properties along prescribed failure planes as a function of the correlation distance and failure plane length.

However, the Finite Element Method (FEM) has more recently been adopted as a viable alternative to the limit equilibrium method, while random field theory may be used to provide more realistic modelling of the spatial variation of soil properties. For example,

Illustration of the statistics of property X: X as a function of depth (left) and probability density function of X (right) [Hicks and Samy, 2002a; 2002c] F.25-1



[Paice and Griffiths, 1997; Griffiths and Fenton, 2000; 2004; Hicks and Samy, 2002a; 2002b; 2002c; 2004; Hicks and Onisiphorou, 2005] modelled failure mechanism development by combining FEM and random field theory, an approach often referred to as the Random Finite Element Method (RFEM) and which forms the basis of this paper.

This approach gives rise to the need for an adequate spatial representation of the soil, as well as a suitable method of characterization. In particular, in addition to the standard statistical properties typically measured (i.e. mean, μ, and standard deviation, σ), a measure of the spatial variation is required. This is often defined by the scale of fluctuation, θ, which is a measure of the distance between zones of similar property value, or, in other words, the distance over which the property is significantly correlated [Vanmarcke, 1983]. It is important that a site is characterized adequately in terms of θ, in order to represent the spatial variability in both the horizontal and vertical directions, i.e. as given by θ_h and θ_v respectively.

This stochastic approach can be summarized by the following stages [Hicks and Samy, 2002c]:

1) Statistical characterization: The material properties are represented in terms of statistics that may be obtained through site investigation.
2) Prediction of spatial variability and analysis: The soil is modelled according to its statistics, giving rise to an infinite number of possible soil profiles and the need for Monte Carlo analysis, e.g. using the Random Finite Element Method (RFEM).
3) Probabilistic definitions of response: The RFEM results provide the probability of failure and/or reliability; thereby providing the basis for a risk analysis.

This paper discusses these three steps in further detail, from the initial in-situ measurements through to the final risk analysis.

25-2 Site Characterization

An important step in the stochastic approach is to characterize the material properties at a site in terms of their point and spatial statistics. F.25-1 illustrates this process.

F.25-1 (left) shows the variation with depth of a property X in a soil layer. In a typical deterministic analysis X would be represented by a single characteristic value, such as the mean or lower bound. However stochastic analysis uses all the data, by expressing them in the form of a probability density function, or pdf, characterized by the mean and standard deviation of the property value, μ and σ respectively, as shown in F.25-1 (right). A third statistical parameter, the scale of fluctuation, θ, defining the degree of spatial correlation is required as indicated in F.25-1 (left). As θ increases, the degree of spatial correlation increases and the distribution of the property values becomes more uniform.

There are various methods in literature for estimating the vertical scale of fluctuation, θ_v, although there is little research on how to estimate the horizontal scale of fluctuation, θ_h. However a number of studies have demonstrated that θ_h is an important consideration in geotechnical modelling [Hicks and Samy, 2002a; 2002b; 2002c; 2004; Hicks and Onisiphorou, 2005; Hicks and Spencer, 2010; Nuttall, 2011].

Cone Penetration Tests (CPT) may be used to estimate the statistics of the site. Due to the high resolution of the CPT in the vertical direction, θ_v may be easily estimated. However the low resolution of data in the horizontal plane, due to the limited number of CPTs that may be conducted across a site, means that θ_h is more difficult to estimate.

25-2-1 Statistical Evaluation

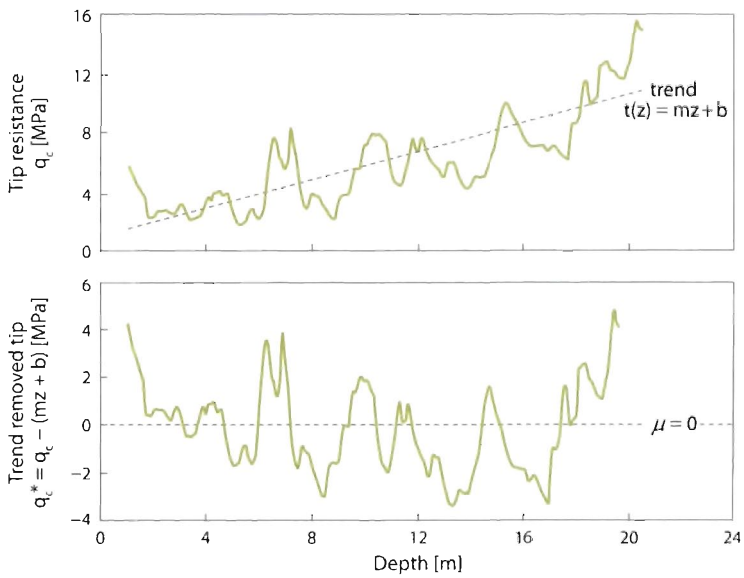
[Wickremesinghe and Campanella, 1993; Wong, 2004; Lloret-Cabot et al., 2013] discuss methods for estimating the scale of fluctuation, θ. The approach outlined in this section was used by [Lloret-Cabot et al., 2013] to study the soil variability of artificial sand islands constructed in the Canadian Beaufort Sea in the 1970s and 1980s; more specifically using data from the Tarsuit P-45 island, which had been the focus of several previous studies [Hicks and Smith, 1988; Wong, 2004; Lloret-Cabot et al., 2012].

In this approach it is assumed that the in-situ data are statistically homogeneous (or stationary), that is:

a) the data have a constant mean and constant standard deviation throughout the profile;
b) the data have an autocorrelation function independent of location and dependent only on the separation, or lag distance, τ, i.e. the correlation between property values at two locations is only a function of the distance that separates them.

Condition a) is achieved by de-trending the data, as illustrated in F.25-2 for CPT tip resistance data. F.25-2 (above) shows the original tip resistance data, q_c, and the underlying

Example of a CPT profile: original data (above) and de-trended data (below) [Lloret-Cabot et al., 2013] F.25-2



depth trend, $t(z)$, whereas F.25-2 (below) shows the same data with the trend removed. This approach has provided a useful approximation in a number of previous studies [Hicks and Onisiphorou, 2005; Uzielli et al., 2005; Lloret et al., 2012]. A constant standard deviation, σ, and condition b) are likely to be present if the data are taken from the same soil layer, as approximately uniform fluctuations are likely to occur in layers of the same soil type [Phoon and Kulhawy, 1999]. However, the data can be de-trended if they exhibit a depth trend in the standard deviation, by using a similiar procedure to that followed for the mean. The next step in this approach is to estimate the scale of fluctuation, θ, by fitting a theoretical correlation function, $\rho(\tau)$ (E.25-1), to the experimental correlation function, $\hat{\rho}(\tau)$ (E.25-2), as illustrated in F.25-3. A number of correlation models exist [Fenton and Griffiths, 2008]; however the exponential correlation model is given by:

$$\rho(\tau) = \exp\left\{\frac{-2|\tau|}{\theta}\right\} \qquad \text{E.25-1}$$

where θ can represent the scale of fluctuation in either the horizontal or vertical directions and τ is the lag distance. The experimental correlation function is given by:

$$\hat{\rho}(j\Delta\tau) = \frac{1}{\hat{\sigma}^2(n-j)}\sum_{i=1}^{n-j+1}(X_i - \hat{\mu})(X_{i+j} - \hat{\mu}) \qquad \text{E.25-2}$$

where $\hat{\mu}$ and $\hat{\sigma}$ are the estimated mean and standard deviation respectively, taken from the in-situ CPT data, and the interval $\Delta\tau$ is the spacing of consecutive data [Fenton and Griffiths, 2008].

F.25-3 illustrates the difficulty of estimating the horizontal scale of fluctuation, θ_h; that is, in the horizontal direction there are often relatively few data points available over the site, as indicated by the circles in F.25-3 (below).

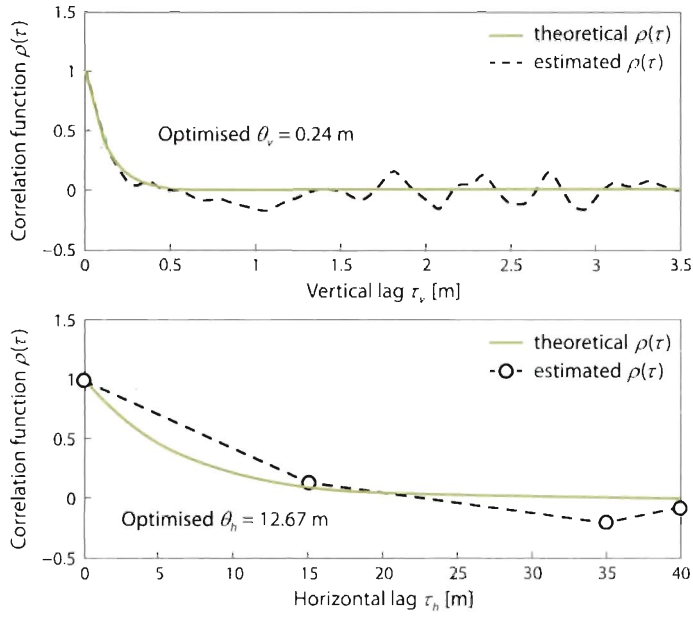
25-3 Modelling Spatial Variability

Having statistically characterized a soil layer based on data obtained at discrete locations, it is possible to generate random field predictions of the spatial variability across the entire site.

25-3-1 Random Field Generation

Random fields are generated using random field theory. The present strategy generates random fields using the Local Average Subdivision (LAS) method [Vanmarcke, 1983; Fenton, 1990; Fenton and Vanmarcke, 1990]; a 2D algorithm was first developed [Hicks and Samy, 2002a; 2004] and subsequently a 3D algorithm [Spencer, 2007; Nuttall, 2011]. The algorithm is broken down into the following basic steps [Hicks and Spencer, 2010]:

Example of estimating the scale of fluctuation θ: vertical direction, θ_v (above) and horizontal direction, θ_h (below) [Lloret-Cabot et al., 2013] F.25-3



1) LAS [Vanmarcke, 1983; Fenton, 1990; Fenton and Vanmarcke, 1990] generates a square (2D) or cubic (3D) isotropic standard normal (Gaussian) random field of size D. The field is generated by uniformly subdividing the domain into square or cubic cells of dimension d, maintaining the mean value of the subdivided cells through upward averaging, with each cell value spatially correlated with its neighbours based upon an exponential Markov covariance function [Fenton and Vanmarcke, 1990]. For 2D this is given by:

$$\beta(\tau_1,\tau_2) = \sigma^2 \exp\left(-\sqrt{\left(\frac{2\tau_1}{\theta_1}\right)^2 + \left(\frac{2\tau_2}{\theta_2}\right)^2}\right) \quad \text{E.25-3}$$

and for 3D:

$$\beta(\tau_1,\tau_2,\tau_3) = \sigma^2 \exp\left(-\frac{2|\tau_1|}{\theta_1} - \sqrt{\left(\frac{2\tau_2}{\theta_2}\right)^2 + \left(\frac{2\tau_3}{\theta_3}\right)^2}\right) \quad \text{E.25-4}$$

where β is the covariance, τ is the lag distance and subscripts 1–3 denote the vertical and the two lateral directions respectively. However, due to the overall statistics being poorly preserved in the anisotropic process, the random field is initially gener-

ated with a constant scale of fluctuation, i.e. $\theta = \theta_1 = \theta_2 = \theta_3$, where θ is taken to be the largest scale of fluctuation over the domain; in geotechnical practice this usually corresponds to the horizontal plane, i.e. $\theta = \theta_h$, due to the method of deposition for most geo-materials.

2) An anisotropic field is generated by squashing the isotropic field; i.e. preserving θ_h in the horizontal plane while compressing θ in the vertical direction to become θ_v. The compressing process averages several layers of cells into a single layer, the number of these cells being equal to the degree of anisotropy of the heterogeneity, $\xi = \theta_h / \theta_v$. F.25-4 illustrates the effect of increasing ξ on a single post-processed random field.
3) The anisotropic field is transformed from a standard normal (Gaussian) distribution to a normal, or other, distribution, by using a suitable transformation, i.e. for the normal conversion:

$$X(\boldsymbol{x}) = \mu(z) + \sigma(z) Z(\boldsymbol{x}) \qquad \text{E.25-5}$$

where $\boldsymbol{x} = (x\ y\ z)^T$ defines the centroid of the random field cell and $Z(\boldsymbol{x})$ is the local average for a random field cell at location $\boldsymbol{x}$. μ and σ are taken from the site statistics and re-incorporate their respective depth trends, removed during the statistical characterization, into the random field.

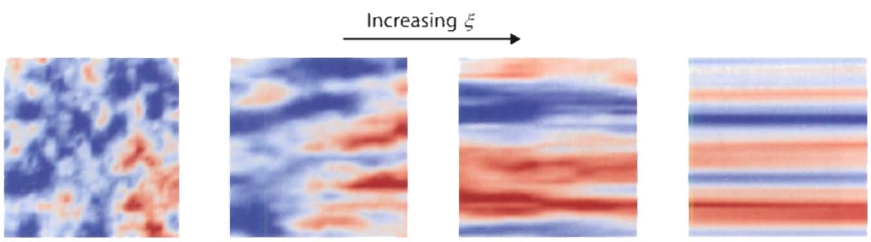
A random field has now been generated that exhibits statistical properties that are consistent to those of the in-situ conditions. An infinite number of possible random fields exist for a given set of statistics. The aim is to analyze the geotechnical problem for a sufficient number of random fields, so as to give a statistically representative solution. One such method is the Random Finite Element Method (RFEM) [Griffiths and Fenton, 2004; Hicks and Onisiphorou, 2005; Nuttall, 2011].

Note that the range of random fields may be reduced by conditioning the random fields to the field measurements (e.g. CPT data) [Lloret-Cabot et al., 2012].

25-3-2 Random Finite Element Method (RFEM)

Although the Random Finite Element Method (RFEM) has been around in various guises since the 1980s, the technique was developed by [Fenton and Griffiths, 1993a; 1993b] in the 1990s. It involves mapping a random field onto a finite element mesh and subsequent analysis of the problem by finite elements. The mapping of the properties in-

Illustration of the effect of increasing anisotropy for a single random field F.25-4



volves assigning each random field cell value to a finite element, or sampling point within the element, thus mapping the spatial variation of the properties to the deterministic FE analysis. Due to the range of possible random fields, the analysis is carried out within a Monte Carlo framework, where, in each realization, the random field is mapped onto the FE domain, a deterministic FE analysis is undertaken, and the required measure of performance is recorded. This repetitive process continues until the performance measure has statistically converged to within an acceptable tolerance.

The results are typically presented in the form of a "performance" pdf or cumulative distribution function (cdf), which expresses the probability of occurrence of a structure response, e.g. in terms of reliability, or probability of failure, P(f), as shown in F.25-5.

25-4 Risk

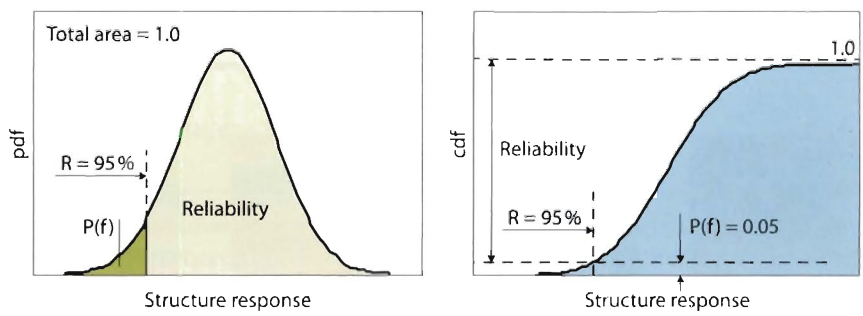
Risk may be defined as (probability of failure) × (consequence of failure). Although RFEM provides the probability of failure of a given structure, until recently little research had been carried out to quantify the consequence. The consequence of a given failure can be far reaching and is often a matter of opinion or conjecture, going beyond the mere financial cost of a failure. Therefore it is difficult to quantify consequence in a simple manner or cost estimation. It could be argued that the ultimate cost, or consequence, of a failure is proportional to the size of the failure; for example, the consequence of a landslide, or liquefaction slide, may be considered to be proportional to the volume of the failure, whereas the consequence of a dike or dam failure may be proportional to the depth of the failure within the structure. Hence:

$$\text{Consequence} \propto \text{Failure (volume, length, etc.)} \qquad \text{E.25-6}$$

and therefore:

$$\text{Risk} \propto P(f) \cdot \text{Failure (volume, length, etc.)} \qquad \text{E.25-7}$$

Illustrations of performance from an RFEM analysis F.25-5



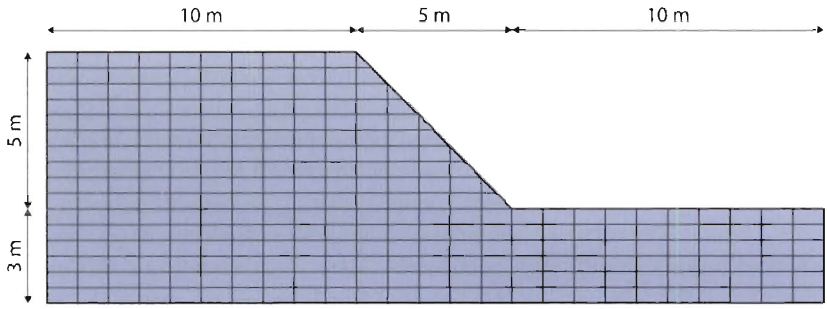
This approach to risk makes it possible to estimate a value for the relative risk associated with a particular structure and failure using RFEM. During each realization, not only is the structure analyzed for global response (or failure), but also the corresponding consequence of the response is measured; i.e. the volume, depth and/or length of the failed zone are determined, which can be used to estimate risk according to E.25-7.

25-5 Case Study

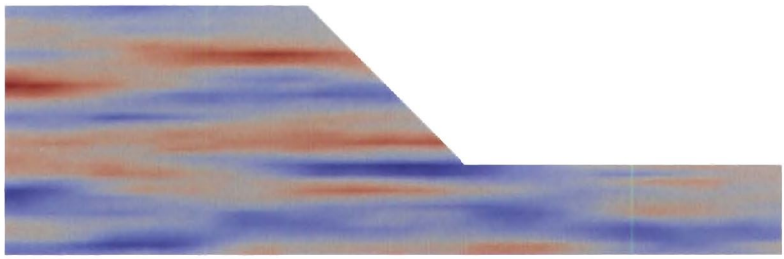
To explore this methodology, a case study is presented using RFEM. F.25-6 shows the geometry and mesh for a 45° slope founded on a 3 m layer of soil. The slope and foundation are considered to be from the same layer. The problem is modelled using eight node quadratic finite elements with 2 × 2 Gaussian integration [Smith and Griffiths, 2004]. The boundary conditions are that the left and right sides of the domain are allowed to move vertically, whereas the base is fixed.

In this analysis the soil is modelled as an elastic, perfectly plastic Von Mises material, characterized by a spatially varying undrained shear strength, c_u, defined at the sampling points. The spatial statistics for the soil layer have been defined to illustrate the application, instead of using actual site data, although in reality they would be taken from in-situ data using the procedure set out in section 25-2. Therefore, random fields of c_u have

Mesh geometry for 2D slope stability analysis F.25-6



A realization of the c_u random field F.25-7



been generated using the LAS method assuming a normal property distribution, with μ = 40 kPa, σ = 8 kPa, θ_v = 1 m and θ_h = 12 m (i.e. ξ = 12).

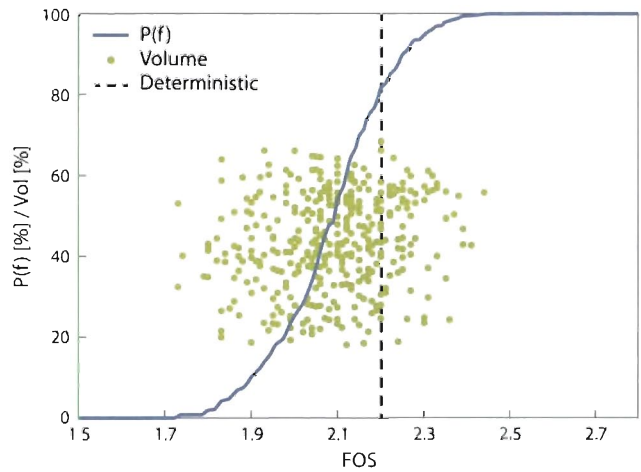
For each realization of the random field (F.25-7), the factor of safety of the slope is calculated, by repeatedly analyzing the slope for increasing gravity loading until failure occurs [Nuttall, 2011]. From these results the probability of failure P(f) of the slope is calculated as a function of the factor of safety (FOS), using a Monte Carlo simulation, in this case with 350 realizations (F.25-8). F.25-8 shows the probability of failure of the slope against FOS. It also indicates the value of FOS computed for a deterministic analysis of the same slope based only on $c_u = \mu$ = 40 kPa (i.e. without the influence of heterogeneity). This graph clearly shows that the spatial variability has a significant impact on the failure of the slope. In comparing the homogeneous and stochastic analyses, it is seen that, for the slope based only on μ, the factor of safety corresponds to a probability of failure of P(f) ≅ 81.5 % when spatial variation is incorporated.

Furthermore, the circles in F.25-8 indicate the failure volumes of the slope, which can be combined with the reliability results to give the associated risk of designing the slope to a specific factor of safety, using E.25-7.

25-6 Conclusions

This paper has demonstrated that traditional deterministic slope stability analyses (i.e. ignoring heterogeneity) provide results that can overestimate the strength of a slope. An alternative stochastic approach has been presented; this starts with the characterization of a soil layer using in-situ data, then representing the soil profile using a random field generated using Local Average Subdivision (LAS), and finally conducting a reliability analysis using the Random Finite Element Method (RFEM). The inclusion of failure volume

Probability of failure and failure volume versus factor of safety (FOS) F.25-8



and consequence, to the analysis, has led to an evaluation of risk that can be incorporated into the design process.

References

Duncan, J.M., 2000. *Factors of Safety and Reliability in Geotechnical Engineering*. J Geotech Eng, 126(4):307–316.

El-Ramly, H., Morgenstern, N.R. and Cruden, D.M., 2002. *Probabilistic Slope Stability Analysis for Practice*. Can Geotech J, 39(3):665–683.

El-Ramly, H., Morgenstern, N.R. and Cruden, D.M., 2003. *Probabilistic Stability Analysis of a Tailings Dyke on Pre-Sheared Clay-Shale*. Can Geotech J, 40(1):192–208.

El-Ramly, H., Morgenstern, N.R. and Cruden, D.M., 2005. *Probabilistic Assessment of Stability of a Cut Slope in Residual Soil*. Géotechnique, 55(1):77–84.

Eurocode 7, 2004. *Eurocode 7: Geotechnical Design. Part 1: General Rules. EN 1997-1*. European Commitee for Standardisation (CEN).

Fenton, G.A., 1990. *Simulation and Analysis of Random Fields*. PhD Thesis, Princeton University, USA.

Fenton, G.A. and Griffiths, D.V., 1993a. *Seepage Beneath Water Retaining Structures Founded on Spatially Random Soil*. Géotechnique, 43(6):577–587.

Fenton, G.A. and Griffiths, D.V., 1993b. *Statistics of Block Conductivity through a Simple Bounded Stochastic Medium*. Water Resources Research, 29(6):1825–1830.

Fenton, G.A. and Griffiths, D.V., 2008. *Risk Assessment in Geotechnical Engineering*. John Wiley & Sons, New Jersey, USA.

Fenton, G.A. and Vanmarcke, E.H., 1990. *Simulation of Random Fields via Local Average Subdivision*. J Eng Mech, 116(8):1733–1749.

Griffiths, D.V. and Fenton, G.A., 2000. *Influence of Soil Strength Spatial Variability on the Stability of an Undrained Clay Slope by Finite Elements*. In Slope Stability 2000, Proceedings of Sessions of Geo-Denver, ASCE, 184–193.

Griffiths, D.V. and Fenton, G.A., 2001. *Bearing Capacity of Spatially Random Soil: the Undrained Clay Prandtl Problem Revisited*. Géotechnique, 51(4):351–359.

Griffiths, D.V. and Fenton, G.A., 2004. *Probabilistic Slope Stability Analysis by Finite Elements*. J Geotech Geoenviron Eng, 130(5):507–518.

Harr, M.E., 1987. *Reliability-Based Design in Civil Engineering*. McGraw-Hill.

Hicks, M.A., 2007. *Risk and Variability in Geotechnical Engineering*. Ed., Thomas Telford.

Hicks, M.A. and Nuttall, J.D., 2012. *Influence of Soil Heterogeneity on Geotechnical Performance and Uncertainty: A Stochastic View on EC7*. Proceedings 10th International Probabilistic Workshop, Universität Stuttgart, Stuttgart, 215–227.

Hicks, M.A. and Onisiphorou, C., 2005. *Stochastic Evaluation of Static Liquefaction in a Predominantly Dilative Sand Fill*. Géotechnique 55(2):123–33.

Hicks, M.A. and Samy, K., 2002a. *Influence of Heterogeneity on Undrained Clay Slope Stability*. Quart J Eng Geol Hydrogeol, 35(1):41–49.

Hicks, M.A. and Samy, K., 2002b. *Influence of Anisotropic Spatial Variability on Slope Reliability*. Proceedings 8th International Symposium on Numerical Models in Geomechanics, Rome, 535–539.

Hicks, M.A. and Samy, K., 2002c. *Reliability-based Characteristic Values: a Stochastic Approach to Eurocode 7*. Ground Engineering, 35(12):30–34.

Hicks, M.A. and Samy, K., 2004. *Stochastic Evaluation of Heterogeneous Slope Stability*. Ital Geotech J, 38(2):54–66.

Hicks, M.A. and Smith, I.M., 1988. *Class A Prediction of Artic Caisson Performance*. Géotechnique, 38(4):589–612.

Hicks, M.A. and Spencer, W.A., 2010. *Influence of Heterogeneity on the Reliability and Failure of a Long 3D Slope*. Computers and Geotechnics, 37(7–8):948–955.

Lloret, M., Hicks, M.A. and Wong, S.Y., 2012. *Soil Characterisation of an Artificial Island Accounting for Soil Heterogeneity*. In GeoCongress 2012, San Francisco, 2816–2825.

Lloret-Cabot, M., Hicks, M.A. and van den Eijnden, A.P., 2012. *Investigation of the Reduction in Uncertainty due to Soil Variability when Conditioning a Random Field using Kriging*. Géotechnique letters, 2(3):123–127.

Lloret-Cabot, M., Hicks, M.A. and Nuttall, J.D., 2013. *Investigating the Scales of Fluctuation of an Artificial Sand Island*. Proceedings International Conference on Installation Effects in Geotechnical Engineering, Rotterdam, the Netherlands, 192–197.

Mostyn, G.R. and Soo, S.W., 1992. *The Effect of Autocorrelation on the Probability of Failure of Slopes*. Proceedings 6th Australia – New Zealand Conference on Geomechanics: Geotechnical Risk, New Zealand, 542–546.

Nuttall, J.D., 2011. *Parallel Implementation and Application of the Random Finite Element Method*. PhD Thesis, University of Manchester, UK.

Paice, G.M. and Griffiths, D.V., 1997. *Reliability of an Undrained Clay Slope Formed from Spatially Random Soil*. Proceedings 9th International Conference on Computer Methods and Advances in Geomechanics, Wuhan, 543–548.

Phoon, K.-K. and Kulhawy, F.H., 1999. *Characterization of Geotechnical Variability*. Can Geotech J, 36(4):612–624.

Smith, I.M. and Griffiths, D.V., 2004. *Programming the Finite Element Method*. 4th ed., Wiley & Sons.

Spencer, W.A., 2007. *Parallel Stochastic and Finite Element Modelling of Clay Slope Stability in 3D*. PhD Thesis, University of Manchester, UK.

Tang, W.H., Yucemen, M.S. and Ang, A.H.S., 1976. *Probability-Based Short-Term Design of Slopes*. Can Geotech J, 13(3):201–215.

Uzielli, M., Vannucchi, G. and Phoon, K.-K., 2005. *Random Field Characterisation of Stress-Normalised Cone Penetration Testing Parameters*. Géotechnique, 55(1):3–20.

Vanmarcke, E.H., 1977. *Reliability of Earth Slopes*. J Geotech Eng Div, 103(11):1247–1265.

Vanmarcke, E.H., 1983. *Random Fields: Analysis and Synthesis*. Cambridge, Massachusetts: The MIT Press.

Wickremesinghe, D.S. and Campanella, R.G., 1993. *Scale of Fluctuation as a Descriptor of Soil Variability*. Proceedings Conference on Probablistic Methods in Geotechnical Engineering, Canberra, 233–239.

Wong, S.Y., 2004. *Stochastic Characterisation and Reliability of Saturated Soils*. PhD Thesis, University of Manchester, UK.

26

Monitoring and Evaluation of an Arch Bridge Affected by the Blasting of the Adjacent Highway Bridge

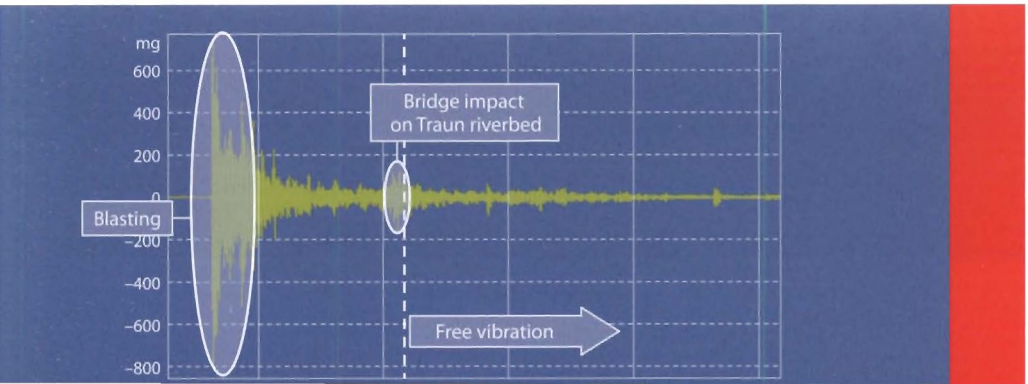
Authors:
Robert Veit-Egerer
Monika Widmann
Helmut Wenzel

Motivation

The assessment of extreme load cases like explosions or the collapses of adjacent structures have an effect on the structural integrity and consequently the remaining life span. Assessment methodologies are desired.

Main Results

The removal of two adjacent arch bridges by blasting allowed calibration of the methodologies developed in the IRIS project in a large field test. The proof of concept has been delivered.



26-1 Introduction

The bridge object W4 Steyrermühl is part of the Austrian highway A1. The original structure from 1959 was composed of two separately built arch bridges. After more than 50 years of service life the bridge did not fit into the overall traffic and infrastructure concept anymore. Due to the increased traffic volume the highway in this section had to be broadened requiring structural adaptation at the bridge also. A broadening of the carriageway slab would have caused an increasing dead load and – due to asymmetric arrangement – inappropriate loading distribution into the bridge's arch. Thus, it was decided to replace the structure stepwise. In August 2010 the traffic in both directions was diverted to the one originally related to the driving direction Vienna. While the structure – related to the driving direction Salzburg – was blown, the remaining one was monitored to evaluate the impact of the blasting with regard to its structural safety and operability. The remaining bridge had to be kept in operation for approximately one more year until the blasted bridge would have been fully replaced. One year later – in September 2011 – the newly built structure was opened to traffic and the old one could also be blasted. This chapter describes the monitoring campaign of the blasting of the first structure.

26-2 Bridge Description

The bridge object W4 Traun Bridge Steyrermühl, constructed in 1959, is part of the Austrian highway A1 and leads across the Traun River. It is composed of 18-spans (reinforced concrete) and has a total length of 240.45 m (F.26-1). The bridge consists of two separate load bearing structures – one for each driving direction – with a width of 13.22 m each. The 11-span main bridge is designed as an arch bridge and is connected to two approach bridges at the western and the eastern side. The arches' cross section is made of a three-cellular 9.0 m wide box girder with a varying height of 3.0 m at the abutments and 1.50 m at the vertex. Due to the fact that the bridge did not fit into the overall traffic and infrastructure concept anymore (the highway is going to be broadened) it was decided to replace it.

26-3 Objectives of the Campaign 2010

While the bridge structure – related to the driving direction Salzburg – was removed (blown) in August 2010, the remaining structure (driving direction Vienna) was monitored in order to evaluate the impact of the blasting with regard to its structural safety and operability. The investigation was focused on the primary load-bearing structure (arch).

The monitoring campaign consisted of two major tasks: The on-site assessment was of crucial importance for the decision to re-open the bridge to traffic after the blasting of

the adjacent structure. In a subsequent stage the effects of the blasting were analysed in further detail – coming up with results which broadened the on-site findings.

26-3-1 Applied Approach

In 2005 referential dynamic BRIMOS® measurements at both load-bearing structures were performed by VCE. Based on these measurements the structural behaviour was analysed in detail. In addition to the dynamic measurement a finite element model of the bridge was developed enabling an extensive system identification of the dynamic behaviour.

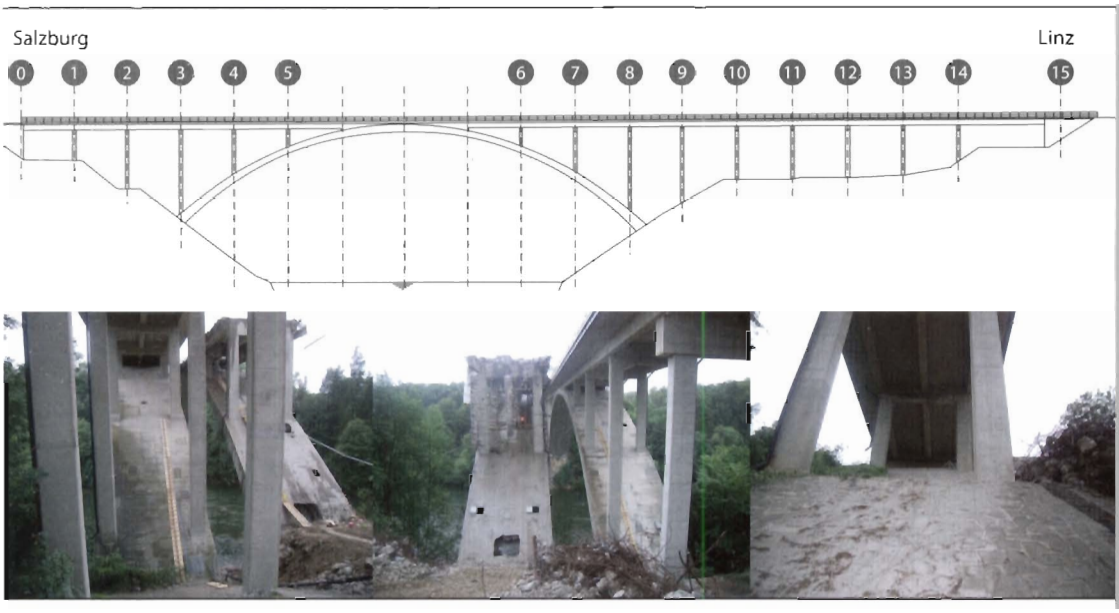
As the measurement from 2005 was used as a reference for the monitoring of the bridge blasting in 2010 the latter one could be performed already more efficiently by means of hot spot measurements. A direct comparison after five years of structural service life (2005–2010) shows the progression of structural behaviour and possible changes respectively under varying loading conditions (bridge deck under the influence of traffic load and the bridge blasting).

In the course of the accompanying monitoring and evaluation process the following tasks had to be covered:

// Preliminary survey and basic model.
Considering the reference measurement in 2005.

// Installation of the follow-up monitoring system.
A permanent online measurement set-up was installed on the day before the blasting and was in operation until the bridge was opened to traffic again.

Elevation for the driving direction Vienna (top) and photo documentation (bottom) – W4 Traun Bridge Steyrermühl F.26-1



// Observation of the current structural behaviour under regular operation.
By means of a measurement lasting several hours the actual dynamic characteristic of the structure under current traffic conditions was captured. The extracted parameters represent reference values for 2010.

// Measurement at the closed bridge and during the blasting.
Capturing of the dynamic characteristics in terms of "unloaded" condition (under ambient – environmentally excited vibrations only), the characteristic during the blasting and afterwards.

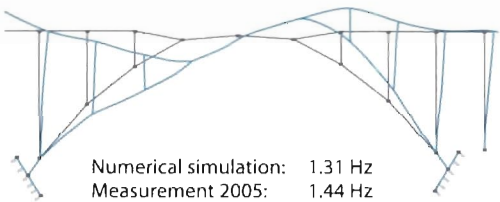
// Comparison of the results.
Based on the measurements before and after the bridge blasting the key performance indicators eigenfrequency, damping and mode shapes were determined and compared. The bridge's load bearing capacity curve was up-dated.

// Re-opening to traffic and confirmation.
In case of unsuspicious behaviour the bridge should be opened to traffic 30 minutes after the blasting at best or within two hours at the latest.

// Subsequent works.
Due to time constraints on-site a detailed analysis of the dynamical behaviour in longitudinal, vertical and transverse direction was carried out afterwards (in the office) to potentially detect phenomena such as displacement of the abutments or deflections. The subsequent analysis focused on temporary changes only. Irreversible changes would have attracted attention already at the on-site analysis.

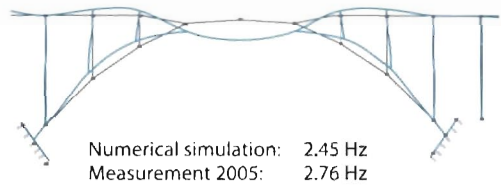
Relevant mode shapes and deviation between the numerical simulation and the measurement 2005 F.26-2

1st mode shape: bending in vertical direction



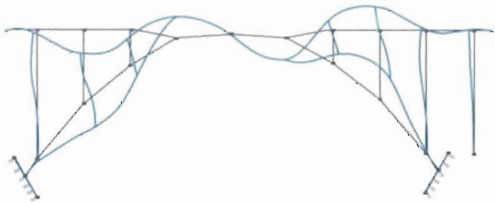
Numerical simulation:	1.31 Hz
Measurement 2005:	1.44 Hz
Deviation:	2.3 %

2nd mode shape: bending in vertical direction



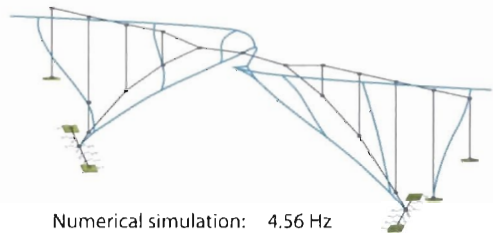
Numerical simulation:	2.45 Hz
Measurement 2005:	2.76 Hz
Deviation:	11.4 %

3rd mode shape: bending in vertical direction



Numerical simulation:	4.55 Hz
Measurement 2005:	4.52 Hz
Deviation:	5.1 %

4th mode shape: bending in vertical direction



Numerical simulation:	4.56 Hz
Measurement 2005:	4.81 Hz
Deviation:	7.0 %

// Determination of the loading level.
Via post-processing of the recorded data a loading factor was calculated reflecting the relation between the level of regular traffic loading and the exceptional loading caused by the blasting.

The assessment was subdivided into several time frames listed below:

// Phase I: regular traffic 2005
// Phase II: regular traffic 2010 (Saturday evening and night)
// Phase III & IV: closed bridge immediately before and after the blasting (Sunday morning)
// Phase V: regular traffic 2010 (Sunday morning)

26-4 Dynamic System Identification – Comparison of Measurement and Numerical Simulation

In addition to the initial dynamic measurement in 2005 a finite element model of the bridge was developed. Since the structure's initial condition immediately after the completion was not stated in terms of a dynamic measurement the undamaged condition was modelled providing expected values from numerical analysis.

The relevant eigenfrequencies are primarily located in the range of 0 to 6 Hz. All of those eigenfrequencies are global eigenfrequencies representing the global stiffness in vertical and transversal direction. F.26-2 shows the relevant eigenfrequencies, their corresponding mode shapes and the deviation between the calculated eigenfrequencies and the results of the measurements in 2005. The comparison of the results from the model with those of the measurements supports the assessment of the structural condition and indicated a satisfying global condition at the time of the measurement.

26-5 Measurement Description 2010

The blasting of the adjacent bridge structure was scheduled for the early morning of 8 August in 2010. To get a reasonable database for the BRIMOS® assessment the measurement – using a mobile acceleration sensor system – was started in the evening of the previous day. The permanent online measurement system was running from 6:30 p.m. on Saturday (7 August) to 12:30 a.m. on Sunday (8 August).

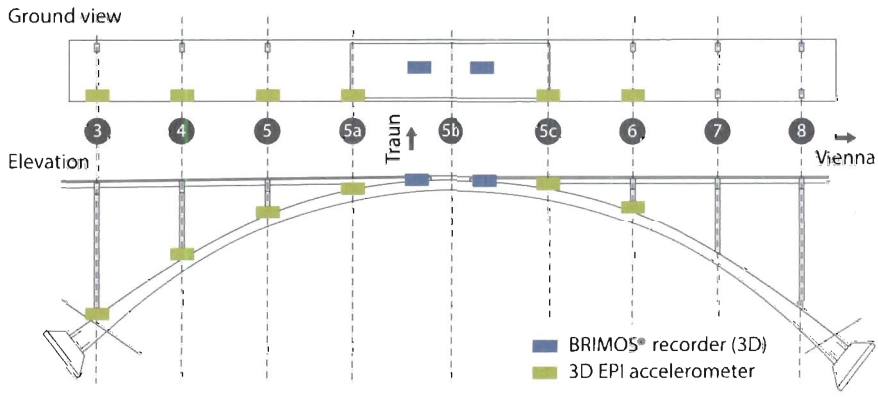
The objective of the monitoring campaign was to document possible changes of the key performance indicators of the structure and to evaluate the condition of the remaining bridge after the blasting of the adjacent one. With regard to their relevance for civil engineering issues the following Key Performance Indicators were used:

// The bridge structure's relevant eigenfrequencies and corresponding mode-shapes
  / Load bearing capacity and operability
  / Evaluation of the bearings
  / Distribution of the global and local dynamic structural stiffness in the bridge's lengthwise and transversal direction
// Sensitivity analysis to investigate the progression, the character, the stability and probable changes in the energy content of the relevant eigenfrequencies:
  / Load bearing capacity and operability
  / Localization of weak points with regard to fatigue threat
// Energy dissipation path in the structure's lengthwise direction:
  / Dissipation of the induced vibration energy, localization of problematic sections
// Comparison of measured values with the results of the finite element model
  / Reference to the undamaged initial condition

The following sketch (F.26-3) shows the measurement layout applied at the measurement in 2010. In total a sensor grid of eight different positions was applied – enabling a comprehensive observation of the primary load bearing structure's characteristics regarding bending and torsional behaviour. Six of the eight sensors were part of the permanent online-measurement system. Those sensors (3D EPI accelerometer) were distributed in an alignment in the southern cell of the 3-cellular arch. Via sensor cables the information was transmitted to the monitoring centre, located at the western abutment, where the measurement data were immediately observed and stored afterwards. The recorded files had a length of 5:30 minutes and a sampling rate of 500 Hz (= 2 milliseconds).

To have a back-up in case of failure of the permanent online measurement system, two redundant sensor units (BRIMOS® Recorder with internal 3D acceleration sensor) were installed on both sides of the arch's vertex (distance from the western abutment x = 77.03 m and 98.33 m).

Sensor layout (elevation and ground view) for the dynamic measurement of the arch – driving direction Vienna F.26-3



26-6 Results of the Measurement 2010

When comparing different measurements possible environmental influences have to be considered to avoid wrong interpretations of the acquired dynamic response [Veit-Egerer, 2007]. In particular the influence of the temperature can be relevant in this context. Due to the fact that – in the present case – the measurement in 2010 was done at a temperature of 15 °C and the measurement in 2005 at 18–19 °C potentially restraints caused by the temperature impact can be excluded.

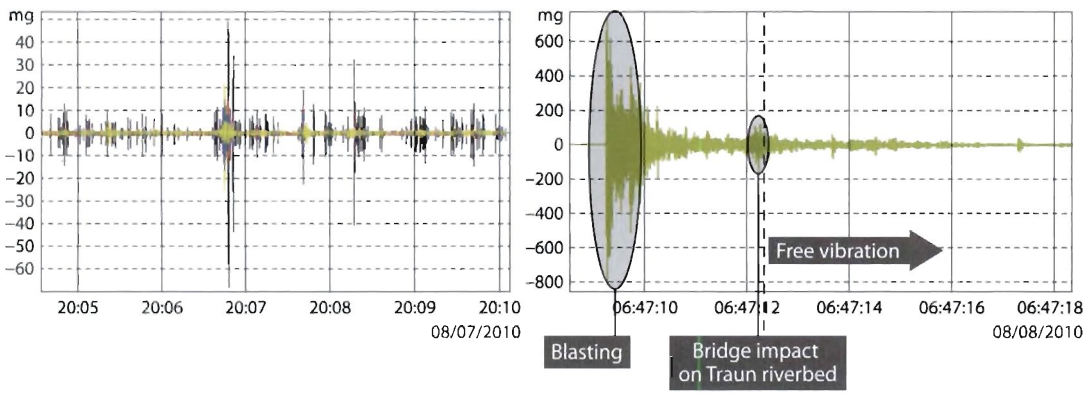
26-6-1 Exceptional Loading Case Bridge Blasting vs. Regular Traffic (Freight Traffic)

F.26-4 demonstrates the significant difference in terms of loading level between regular condition and the exceptional loading case. To quantify this deviation the relation between the effective measured acceleration amplitudes of the given normal load (traffic) and the exceptional load (blasting) was calculated. The data analysis revealed a vertical amplification up to a factor of 21 and a transversal amplification up to a factor of 15.

26-6-2 Eigenfrequencies

The eigenfrequencies extracted from the measurements can be understood as main indicators of the effective dynamic stiffness of the structure. If the blasting had any serious effects on the adjacent bridge changes in the frequency spectra would occur. In fact the comparison of the frequency spectra before and after the blasting shows only deviations of the amplitudes caused by the different excitation intensities. The structural stiffness itself remained stable – showing identical frequencies before and after the blasting. No extraordinary characteristics indicating limited operability or damage of the primary load bearing structure have been identified.

Characteristic acceleration signals under regular loading condition, all measured channels and detailed multi-stage loading history due to the blasting F.26-4



26-6-3 Dissipation of Induced Vibration

The energy dissipation path is a suitable indicator for the condition of a structure and the main girders respectively. "Problematic zones" mostly dissipate energy caused by friction which is reflected in an increase of the local damping values. Higher damping values in the range of abutments or piers are system-based and thus have no direct influence on the assessment of the structure's condition. The BRIMOS® software uses the well-known Random Decrement Technique (RDT) and adapts it over time. For more details see [Wenzel, 2009].

The pattern of damping values along the applied sensor grid (F.26-5) is typical for such a structural type. This applies to the results before the blasting and after the blasting also. The damping analysis primarily reflects the dominantly occurring system damping due to the mechanical behaviour of the bridge. Increased values at local spots according to material damping, which would point out certain damage of mechanically grave extent, were not determined.

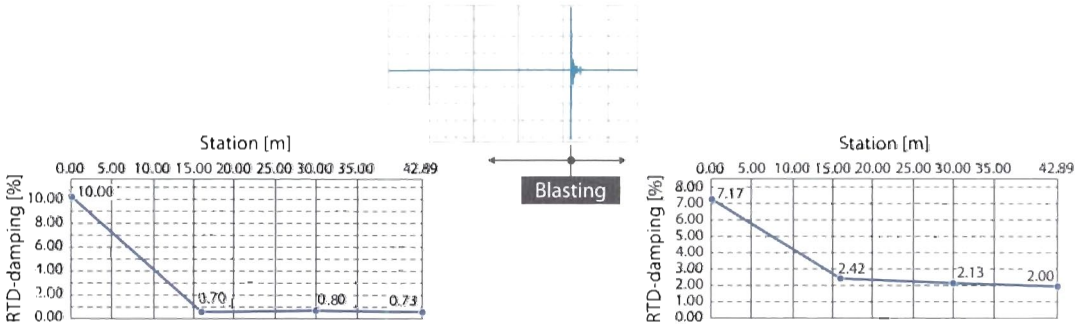
The increased RDT damping values after the blasting are most likely a consequence of the detonation and results in a slightly accelerated consumption of the expected global lifetime. In fact this has not to be classified as critical.

26-6-4 Evaluation of Structural Integrity – Trend of Stiffness over Time

So-called trend cards are an essential evaluation instrument in the context of full-scale measurements on bridge structures. Trend cards are obtained by evaluating frequency spectra taken from several measurements, telescoping them together and viewing them from above. For reasons of a better descriptiveness a two-dimensional visualization is chosen. Showing the behaviour of the structure during certain time frames of monitoring observations trend cards enable the identification and assessment of extraordinary behaviour.

Based on an initial dynamic measurement further periodic measurements provide the possibility to study the structure's maintenance condition in the course of time in order

Pattern of damping values in the lengthwise direction: before the blasting (left) vs. after the blasting (right). F.26-5



to identify remarkable changes of the dynamic structural response. A certain frequency of periodically repeated measurements assures the determination, observation and assessment of slowly progressing processes in the structure, which lead to damage or to deterioration of the structure's operational integrity. The derived patterns represent the effective structural dynamic stiffness related to the observation time. As an initial dynamic measurement at the Steyrermühl Bridge was done in 2005 it is possible to extract the trend of structural stiffness over the last six years in terms of a Life Cycle Curve (lifeline).

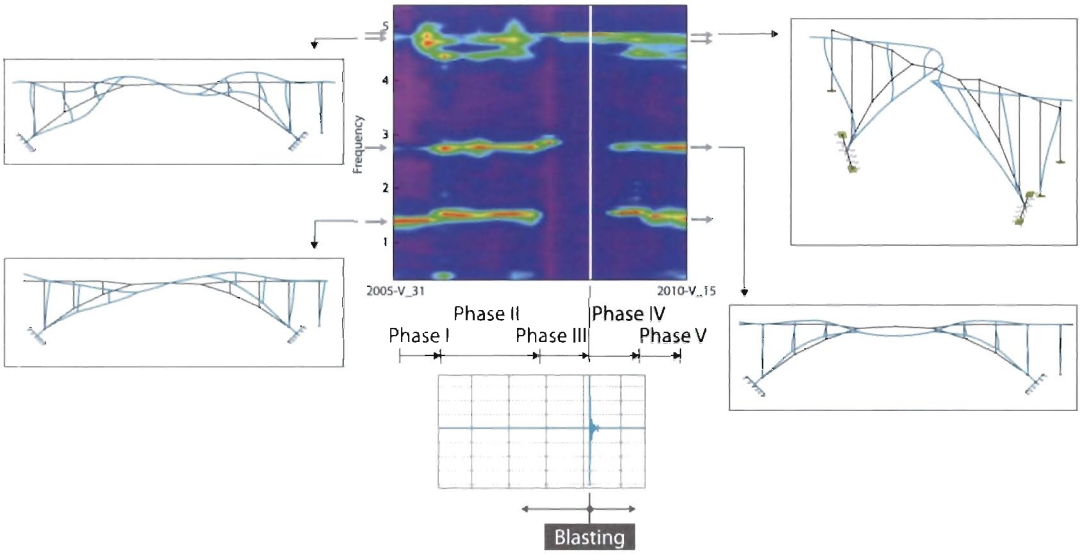
By means of the reference sensor (distance to the western abutment = 75.53 m) several trend cards were derived. The first one (F.26-6) shows the arch's relevant stiffness-patterns in the vertical direction in the range from 0.2 to 5.5 Hz over the entire measurement time period. By way of illustration it is referred to the corresponding mode shapes (global bending stiffness in vertical and transversal direction). F.26-7 represents the trend of eigenfrequencies in detail – in the range of 0.2 to 3.0 Hz and in the range of 4.2 to 5.5 Hz.

The whole investigation was subdivided into five major phases with regard to evaluating the effects of the blasting on the remaining bridge structure.

Relevant eigenfrequencies for structural evaluation T.26-1

Eigenfrequencies	Phase I	Phase II	Phase III	Phase IV	Phase V	Δ Phase V to Phase II [%]
1st bending mode – vertical	1.34	1.49	1.57	1.53	1.44	–3.47
2nd bending mode – vertical	2.73	2.77	2.78	2.79	2.76	–0.29
3rd bending mode – vertical	4.78	4.50	4.60	4.54	4.52	0.35
2nd bending mode – transversal	4.88	4.80	4.90	4.90	4.81	0.31

Trend of stiffness over time 2005–2010 (0.2–5.5 Hz) under the influence of the bridge blasting and after the re-opening to traffic F.26-6



T.26-1 points out those eigenfrequencies which have been considered for further evaluations for every single phase of the multi-level measurement programme – starting with the initial measurement from 2005.

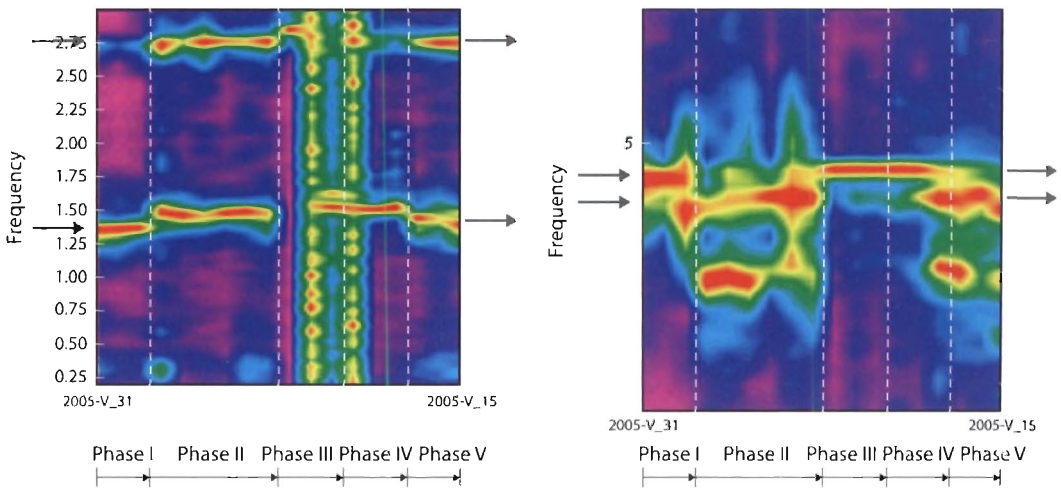
Each of the listed assessment phases is discussed in the following:

// Phase I: regular traffic 2005

// Phase II (to be compared with Phase I): regular traffic 2010 – Saturday evening and night:
The first vertical bending mode measured in 2010 is significantly higher than the one determined in 2005 – due to a change in structural properties. In the course of the traffic assignment three parallel alignments of interlocked Jersey Profiles (concrete guide rails) were distributed lengthwise along the bridge structure – additionally contributing to the cross-sectional stiffness in comparison to the initial measurement in 2005. All the other relevant eigenfrequencies are excited more intensively due to the increased traffic volume (traffic assignment) but are keeping their frequency values.

// Phase III: closed bridge immediately before the blasting – Sunday morning:
In this phase the bridge was already closed – the excitation consists of ambient vibration only. Without the impact of traffic which is normally the most significant loading source the observed frequencies increase. The absence of freight traffic goes hand in hand with a loss of additional effective mass on the structure (less mass – constant structural load bearing resistance).
As the – normally – dominant vertical excitation is missing the vertical modes are less distinctive now, whereas the dynamic mode in transversal direction (influenced by wind and microseismic excitation) is considerably dominant.

Trend of stiffness over time 2005–2010 (0.2–3.0 Hz left and 4.2–5.5 Hz right) under the influence of the bridge blasting and after the re-opening to traffic F.26-7



// Phase IV (to be compared with Phase III): closed bridge immediately after the blasting – Sunday morning:
In comparison to Phase III no frequency changes in terms of their absolute values occurred.

// Phase V (to be compared with Phase II): regular traffic 2010 – Sunday forenoon:
In comparison to Phase II no frequency changes in terms of their absolute values occurred. In comparison to Phase IV a decrease of the relevant eigenfrequencies can be stated. This can be traced back to the fact that in Phase V the bridge was re-opened to traffic, so truck traffic – occasionally moving in queues – is acting as additional effective mass again (more mass – constant structural load bearing resistance).

26-7 Summary on Bridge Assessment

The detailed assessment at the Traun Bridge Steyrermühl leads to the conclusion that the remaining structure withstood the blasting of the adjacent structure in good maintenance condition. At any time of investigation the structure's load-bearing capacity and its operability were available to a satisfactory extent. An imminent threat of collapse was not recognizable. According to the performed measurements no immediate action concerning traffic loading restrictions or rehabilitation measures was required.

The findings are based on the analysis of the dynamic Key Performance Indicators eigenfrequencies, mode shapes, RDT-damping pattern in the lengthwise direction of the bridge, the effective acceleration and the progression of the measured structural dynamic stiffness.

The trend of eigenfrequencies of the primary load bearing structure – comparable with the structural load bearing resistance – shows a stable, straight-lined progression during the entire measurement. This indicates a proper structural resistance and structural behaviour even if the bridge is exposed to changing loading conditions in particular under the influence of the exceptional loading.

Detailed analyses within the dynamic measurement campaign in 2010 and the comparison of the eigenfrequencies over the entire observation period of five years refer to a good global condition of the bridge. Extraordinary changes immediately after the bridge blast affecting the structural integrity were not detected. The only changes observed can be traced back to the varying traffic volume (normal traffic vs. closed bridge vs. queues) and changes in structural properties (Jersey profiles). These phenomena primarily reflect the structural behaviour under changing surrounding conditions but do not affect the evaluation of the structural condition.

The increased structural dissipation behaviour after the blasting is most likely a consequence of the detonation and results in a slightly accelerated consumption of the expected global lifetime.

In summary, it can be stated that the blasting of the adjacent bridge did not affect the analysed structure with regard to its further use.

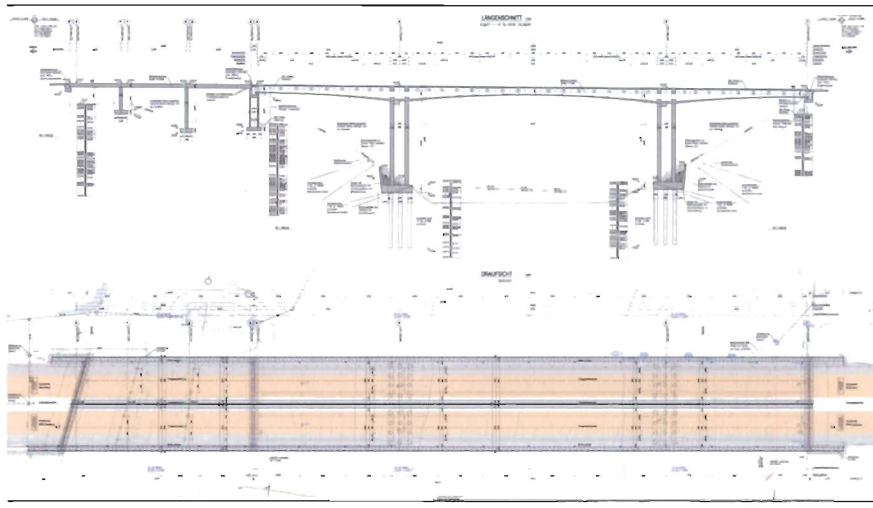
26-8 Subsequent Bridge Assessment 2011

In September 2011 the newly built highway bridge – a three span box girder replacing the former arch bridge and belonging to the driving direction Salzburg – was opened. The whole traffic was diverted to this new bridge object (F.26-8 and F.26-9). In October 2011 the remaining arch bridge – belonging to the driving direction Vienna – was blown. As the adjacent new highway bridge had just entered into its service life it was even more important to ensure that the blasting would not have any impact on structural safety and operability. Again a comprehensive dynamic analysis – by means of BRIMOS® Structural Health Monitoring was conducted. In a first step a detailed reference measurement was

Newly built bridge (driving direction Salzburg) and old arch bridge (driving direction Vienna) before the blasting F.26-8



Overview elevation (top) and plan view (below) of the new Traun Bridge Steyrermühl F.26-9



undertaken at the new structure in September 2011 right after being put into operation. In the course of removing the adjacent arch bridge the new bridge structure was assessed – following a similar monitoring concept to the one described in the current contribution.

Without going into detail it is summarized that the remaining structure withstood the close blasting without any negative impact on its further use.

References

Veit-Egerer, R., 2007. *Condition Compensation in Frequency Analyses – a Basis for Damage Detection in Encyclopedia of Structural Health Monitoring*. Chichester, England: Edited by C. Boller, F-K. Chang, Y. Fujino, J. Wiley and Sons Ltd.

Wenzel, H., 2009. *Health Monitoring of Bridges*. Chichester, England, J. Wiley and Sons Ltd.

27

Ageing Behaviour of Structural Components for Integrated Lifetime Assessment & Asset Management

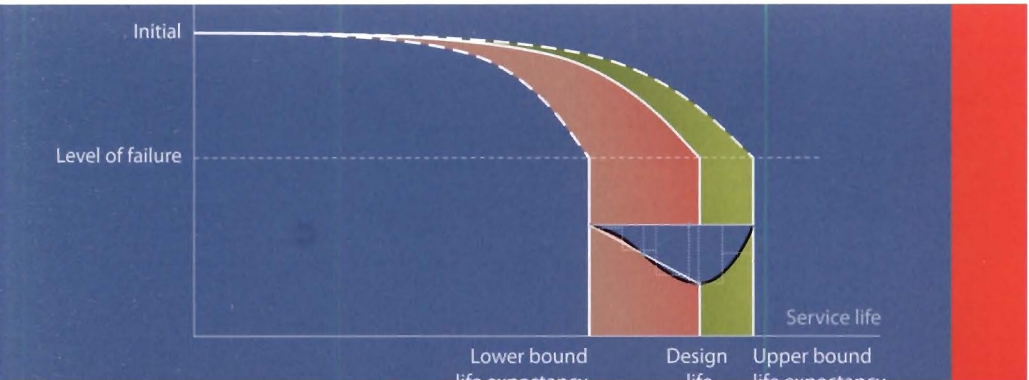
Authors:
Robert Veit-Egerer
Helmut Wenzel
Rui Lima

Motivation

Degradation of structural components is a fact. In order to apply these changes over lifetime in precise cost models a standardized degradation law is desired. Standardization particularly helps in a competitive environment like construction to apply innovative technologies.

Main Results

In CEN-workshop 63 "Condition, Determination for Integrated Lifetime Assessment of Constructed Facilities and Components" a generic degradation law has been developed. It serves to determine the design life or the residual life of existing structures helps to assess the real degradation process and enables the development of optimized maintenance plans.



27-1 Introduction

Managing assets is about making decisions. From this it follows that Life Cycle Cost (LCC) and in some cases Life Cycle Benefit/Cost Analysis is a critical concept for making investment decisions, and therefore should be incorporated in the engineering and management routines of infrastructure systems.

However, several important questions remain before one may conduct a meaningful LCC analysis. These relate to the determination of the Life Cycle of a new, maintained, rehabilitated or retrofitted structure and its expected performance along the Life Cycle regarding the limit states. The impacts of uncertainty in estimating the risk involved in establishing appropriate demand envelopes for various limit events are significant for LCC analysis in design and in maintenance management.

The present chapter was prepared by CEN Workshop 63 "Condition Determination for Integrated Lifetime Assessment of Constructed Facilities and Components" the secretariat of which is held by ASI. It was developed through close collaboration with experts from the IRIS project "Integrated European Industrial Risk Reduction System", supported by the European Union's Seventh Framework Programme. Work in this project was organized in eight work packages.

In the course of the IRIS project methodologies for Life Cycle Management of constructed infrastructure were developed. In order to meet the infrastructure owner's governing requirements regarding safety, operability and durability, the present chapter addresses the following major aspects:

1) The determination/estimation of the design life of new structures
2) The determination/estimation of the residual life of existing structures
3) Assessment criteria whether the real degradation process – determined by proper technologies – corresponds with the assumed and applied Life Cycle Model, in order to take corrective measures in cases of accelerated ageing
4) Maintenance instructions to ensure the intended service life

In IRIS WP 3 and WP 7 and CEN Workshop 63 experts from universities, consultancies, public authorities and standardization bodies contributed to the work. The present chapter has received the support of representatives of these sectors.

27-2 Scope

27-2-1 Ageing Model

The objective of the chapter is to elaborate a standard framework for the results of the IRIS Project, while it is recognized that there cannot be one extensive methodology fit for all specific industries.

There is a simple basic model with considerable uncertainties, which is improved step by step through introduction and evaluation of new knowledge gained about a structure. The ideal result is a precise assessment of the condition with reasonable margins of uncertainty. The model is able to show the successive impact during the long-term deterioration process as well as the effect of sudden changes in condition (retrofit actions of local failure). It is recognized that the individual results from visual inspection and assessment will influence the quality of the prediction. Nevertheless after a number of assessments these uncertainties will be reduced to reasonable levels.

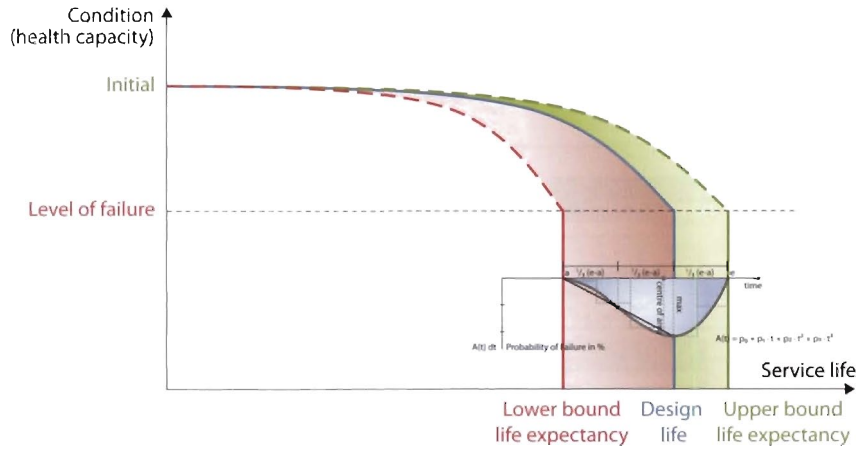
It is acknowledged that the basic model shall be kept simple and transparent for the end-users. In return the background computation is expected to become more and more complex with every new knowledge and methodology developed.

Therefore the concept is to give a common understanding on structural ageing in general, which can be incorporated into different industrial applications and adapted regarding the industry-specific demands.

In further consequence the focus of the chapter is on the area of bridge infrastructure, as there the most mature status within the IRIS Project has been reached.

The aspect of acceptance of structural failure and accidents is always depending on the involved individual society. The current document already reflects the current situation in Austria, Germany, the Netherlands and the USA.

General concept of structural ageing F.27-1



27-2-2 Background – Asset Management

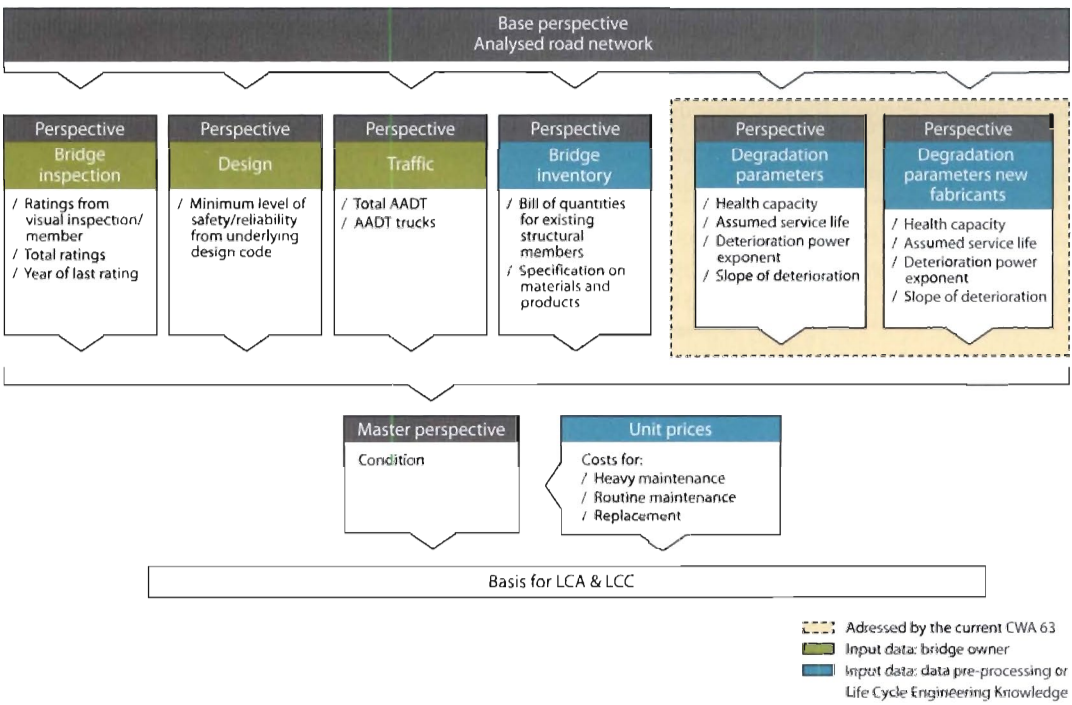
In the following an overall assessment scheme for asset management on the network level is described very briefly. The scheme is divided in two main processes:

// Flowchart 1: Input data with regard to Life Cycle Analysis (LCA) and Life Cycle Cost Analysis (LCCA) (as shown in F.27-2)
// Flowchart 2: LCA and LCCA itself, addressing the determination of maintenance schedules (composed by individual treatments) and linked to budget category-related optimization (as shown in F.27-3).

In both flowcharts those parts, being explicitly covered by the current chapter are highlighted (yellow marking) and are discussed in full detail in the following chapters.

It is to be pointed out, that the shown assessment scheme utilizes conventional ratings (from structural inspection), which are usually available for every structure or can easily be provided. Neither the assessment scheme itself nor the underlying rating process are intended to be standardized – but the curve describing structural ageing (lifeline). Thus the intention of this chapter is to improve the current practice of maintenance budget planning based on ratings. The given ratings are transformed into health indices and

Input data with regard to Life Cycle Analysis (LCA) and Life Cycle Cost Analysis (LCCA) F.27-2

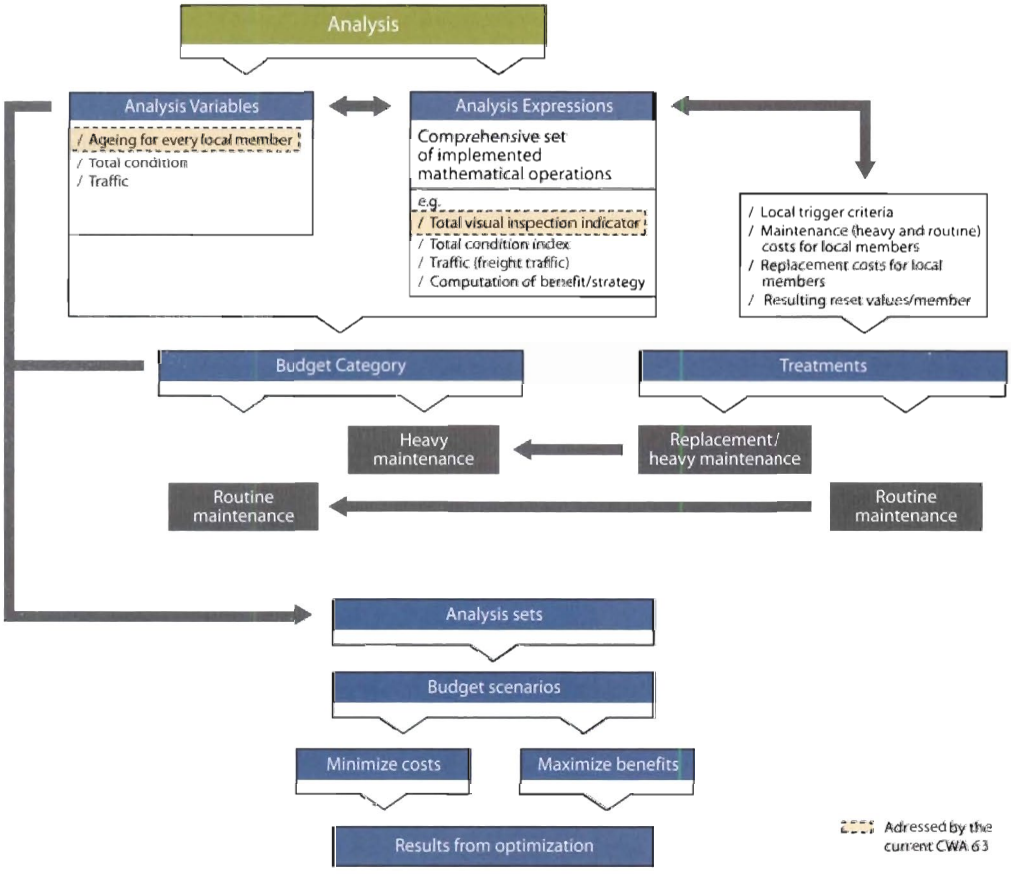


incorporated into comprehensive Life Cycle Calculations. By this means the gap between rating and service life considerations is bridged.

Previous activities and work of other groups worldwide have already produced a basic set of standards. The most sophisticated procedure is established in Germany, where based on existing DIN-standards, specific rules for application in different industries are being developed by VDI (Verein Deutscher Ingenieure). A dense network of certification agencies (managed by TÜV) takes care of sound and safe procedures. Nevertheless the current practice does not take account of the typical end of life situation with assessment of lifetime extension.

In terms of standards, there are no referenced documents being indispensable for the application of this document. Certain relevant literature and a list of standards giving an overview of the related activities have been added to the bibliography.

Life Cycle Analysis (LCA) and Life Cycle Cost Analysis (LCCA) F.27-3



27-3 Terms and Definitions

For the purposes of this document, the following terms and definitions apply, which are taken from selected codes and standards listed in the references.

ageing. Degradation due to long-term influence of operational conditions related to use.

assessment. Set of activities performed to verify the reliability of an existing structure for future use.

asset. Whole building or structure or unit of construction works, or a system or component or part thereof

capacity. Capability to perform

Capacity describes the resistance of a member or component, or a cross-section of a member or component of a structure to actions without mechanical failure e.g. bending resistance, buckling resistance, tension resistance.

condition; health. Characteristic of a structure, system or component which can be observed, measured or trended to infer or directly indicate the current and future ability of the structure, system or component to function within acceptance criteria.

degradation. Process whereby an action on an item causes a deterioration of one or more properties.

Properties affected may be, for example, physical, mechanical or electrical.

demand. Requirement for functionality.

design life. Service life intended by the designer.

Design life is also referred to as intended service life or expected service life.

deterioration. Process which adversely affects the structural performance, including the reliability over time.

durability. Capability of a structure or its parts to perform its required function over a specified period of time under the influence of the agents anticipated in service.

failure. Loss of the ability of a structure or its parts to perform a specified function.

inspection. Regular observation, noting and reporting of structures and components.

Life Cycle. All phases through which a structure passes from its manufacturing to the time it ceases to exist.

It involves all levels of engineering work, including design, construction, inspection, management, repair, improvement and demolition

Life Cycle Cost (LCC). Cost of an asset or its parts throughout its Life Cycle, while fulfilling its performance requirements.

lifeline. Numeric progression of the introduced health index over time.

limit state. Set of performance criteria beyond which the structure no longer fulfils the relevant design criteria.

This reference state must be met by a structure under factored loading.

maintenance. Combination of all technical and associated administrative actions during the service life to retain a structure or its parts in a state in which it can perform its required functions.

operability; functionality. Suitability or usefulness required by users or other stakeholders for a specific purpose or activity.

Operability limit states correspond to conditions beyond which specified service requirements for a structure or structural member are no longer met.

performance. Behaviour in service of a facility for a specified use.

perspective. Database-appropriate tables governing predefined relevant information for asset management on network level.

process. Set of interrelated or interacting activities that transforms inputs into outputs.

rating. Result of a classification process of determining the serviceability of a constructed asset.

rehabilitation. Work required to repair or upgrade an existing structure.

replacement. Changing of parts of an existing item to regain its functionality.

retrofit. Modifying existing structures with additional or new components or members in order to enhance their condition.

risk. Likelihood of the occurrence of an event or failure and the consequences or impact of that event or failure.

safety. Condition of a structure being protected against failure, damage, error, accidents or harm, in both causing and exposure.

service life. Period of time after installation during which a facility, or its component parts, meets or exceeds the performance requirements.

service life prediction. Generic methodology which, for a particular or any appropriate performance requirement, facilitates a prediction of the service life distribution of a structure or its parts for the use in a particular or in any appropriate environment.

structural member. Physically distinguishable part of a structure, e.g. a bearing, a beam, railing.

treatment. Maintenance measure.

uncertainty. Lack of certain, deterministic values for the variable inputs used in an LCC analysis of an asset.

27-4 Performance of Bridge Components

27-4-1 General

All important Key Performance Indicators (KPIs) which influence the performance or durability of a structural member are to be acquired. These datasets are usually implemented into a probabilistic model for service life calculations of the individual items. The reason is to cover occurring uncertainties which have to be considered within the established maintenance plans in terms of lower and upper bound of service life expectancy.

The starting point of the bridge member's service life is mainly based on the applied design code and the underlying safety consideration in the course of the static calculations, while the ageing process in general depends on certain major sources of impact:

// year of construction (generation of the structural manufacturing),
// static system,
// material,
// cross section.

To describe the individual deterioration process properly the following additional aspects are of relevance with regard to structural performance over time:

// direct loading frequency (e.g. freight traffic volume),
// direct loading intensity (level of freight traffic impact),
// quality in manufacturing,
// environment influences (temperature, radiation, frost action),
// chemical exposure.

27-4-2 Service Life Expectancy vs. Prognosis on Remaining Service Life

Service Life Expectancy

The basis for local Life Cycle Considerations is expressed in terms of structural condition. To represent common practice in bridge engineering the set of ratings – according to the national guideline for visual inspections – is utilized. Usually these ratings are available for every bridge component (superstructure, substructure, expansion joints, bearings, pavement, edge beam, guard rail and railings, dewatering and miscellaneous facilities).

After being put into operation, each member's range of ratings represents the available (total) capacity, which is consumed over time during the entire service life. Due to that idea these ratings are converted into so-called health indices, which can be done freely, as long as this single component is analysed individually and independently from its relevance within the whole structure. The proposed ageing law used for Life Cycle Analysis is introduced briefly. It is built on suggestions from [Miyamoto and Ishida, 2008] and was adapted regarding the used terms as well as the further utilization – addressing prognosis on remaining service life. In principle it covers all the major sources of deterioration. It is to be emphasized, that the following equations are intended to describe the lifeline-progression within a stated service life expectancy. The so-called deterioration capacity $C_i(t)$ for an analysed bridge component is determined by the following formula expression:

$$C_i(t) = C_I + a_n \cdot (S_i - S_I)^c \qquad \text{E.27-1}$$

with

$$a_n = (C_F - C_I) / (S_F - S_I)^c \qquad \text{E.27-2}$$

where

C_I initial condition
a_n slope of deterioration
S_i current year of service life
S_I initial year of service life
c deterioration power exponent; empirical, constant value derived from sensitivity analysis; for bridge components $c = 3$ is established
C_F final condition (early-warning level)
S_F final (assumed) year of service life

The ranges for service life expectancy and the total deterioration capacity are of course to be known in advance. An example can be studied in chapter 27-5 (example 1). Certain details on the input data for different types of structural members, materials and product types ca be taken from [prCWA 63:2012 (E)]. They are based on literature, bridge owner databases and long-term expert experience (generic approach). The tables elaborated in [prCWA 63:2012 (E)] address certain infrastructure only (bridges, gantries). As the approach is generic the methodology could be adapted (mainly with regard to c and a_n) and transferred to other infrastructure.

The following visualization, F.27-4, corresponds with the previous formula expressions. The given lifeline can be understood as a reference progression for a continuous observation process during operation with regard to corrective measures in order to ensure the intended service life time frame. In cases that certain bridge components reach the stage of being rated with 4, bridge operators are usually forced to take action with regard to maintenance measures. As the preparation and performance of these measures can still take some time (even years) in practice, the end of rating 4 is defined to be the end of service life. Rating 5 is equivalent to the level of failure and is not accepted in the context of long-term maintenance planning (as this rating reflects a stage, where the structure or component cannot be operated anymore).

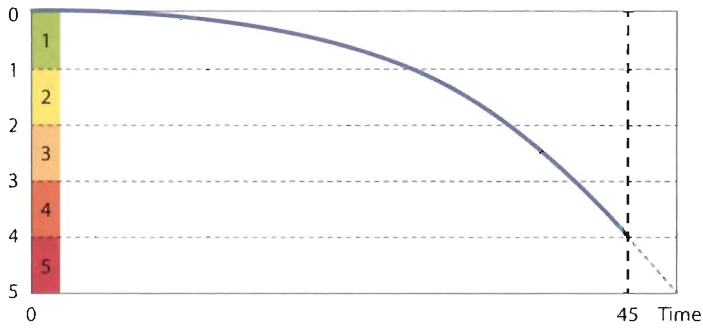
Prognosis on Remaining Service Life

When performing Life Cycle Prognosis, the deterioration capacity $C_i(t)$ which has been used so far, is still the guiding parameter, although the introduced formula expressions are to be adapted:

$$C_i(t) = a_n \cdot \left(\sqrt[c]{\frac{C_{i-1}}{a_n} + 1} \right)^c \qquad \text{E.27-3}$$

E.27-1 and E.27-3 represent the deterioration capacity $C_i(t)$ and are quite similar. However, one is intended to be used to follow the stepwise lifeline progression within a process, which is defined in terms of service life expectancy of a certain structural member

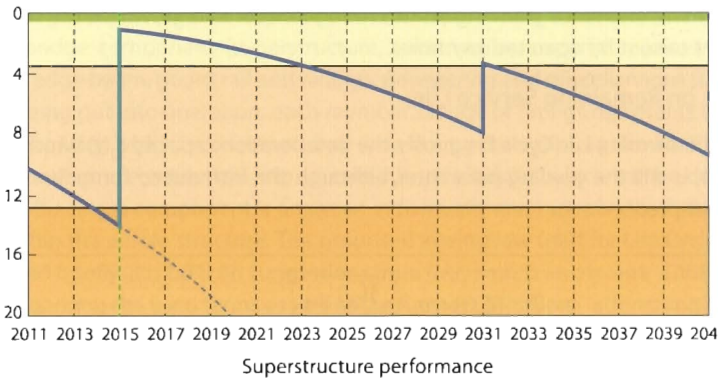
Superstructure life expectancy "do-nothing-strategy" F.27-4



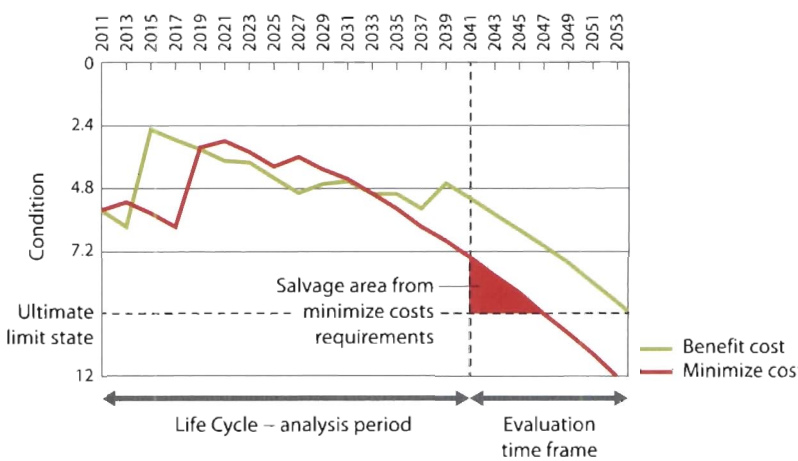
(E.27-1). The other (E.27-3) supports prognosis on remaining service life with regard to threshold analysis and corresponding decision making. The main difference between the two equations is the fact, that the derived prognosis-equation also incorporates the deterioration capacity from the previous year in order to compute the remaining capacity for a current year of service life.

The starting point for local Life Cycle Calculation is linked to the latest rating according to the national guideline for visual inspections. Usually it is available for every bridge component (superstructure, substructure, expansion joints, bearings, pavement, edge beam, guard rail and railings, dewatering and miscellaneous facilities). These ratings are again converted into so-called health indices. Based on the calculated health index for each bridge component and its underlying inspection year a first deterministic lifeline prognosis is performed. This lifeline considers all available information at the time of investigation and assumes the so-called "do-nothing-strategy" (unrestricted deterioration) during the

Prognosis and probable impact of remaining service life F.27-5



Minimize cost strategy F.27-6



entire service life. Consequently the derived lifeline is used as the basis for the elaboration of the maintenance schedules. During the progression of the analysed lifelines (annual analysis variables) routine or heavy maintenance interventions and finally replacement measures of the analysed structural member can be triggered. The introduction of trigger mechanisms is linked with stages, when the structural members are appearing e. g. in the range of rating 3 (maintenance works) or in the range of rating 4 (retrofit, replacement). The trigger mechanisms, deciding about maintenance and replacement, are defined by deterioration analysis on every single structural component, leading to an entry in the maintenance plan to be scheduled. For further details see chapter 27-6.

27-5 Lifeline Calculation

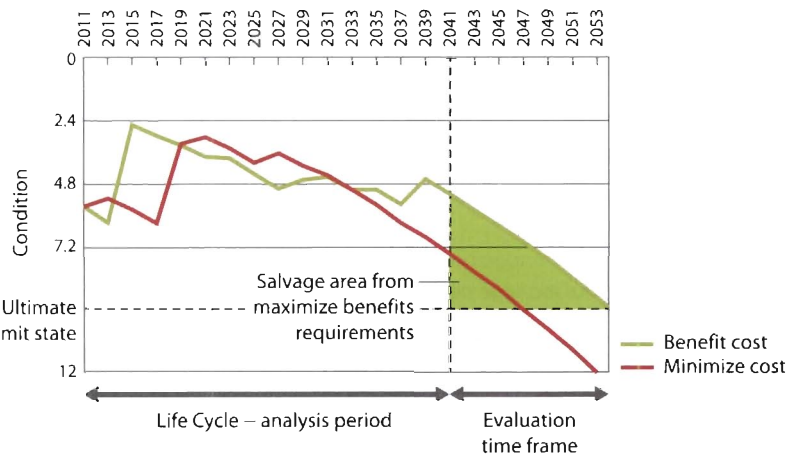
27-5-1 Example 1: Life expectancy

In order to follow the service life expectancy of a certain member it is necessary to define the input data for the equation's progression first. F.27-4 gives an example for a bridge superstructure. The used input data as well as the progression of structural deterioration can be seen (F.27-4).

27-5-2 Example 2: Prognosis and Probable Impact of Remaining Service Life

The starting point for the prognosis on remaining service life is represented by the rating from the latest visual inspection – having been transformed into a health index. As the first year of Life Cycle Calculations will mostly not correspond to the year when the visual inspection was carried out, Visual Inspection Indicator (i. e health index) is to be adapted

Maximize benefit strategy F.27-7



before using it as a starting point for lifetime prognosis. This process differs from the service life expectancy process as it incorporates trigger mechanisms regarding structural retrofit and preventive maintenance. In F.27-5 these effects can be seen.

The lifting in the calculational annual-analysis-variable results from interventions, where certain treatments were applied, and consequently the condition was improved. The extent of the lift depends on the type of intervention and on the incorporated structural member.

Analyses like the one described in the present example are the basis for long-term maintenance planning for highway infrastructure. Depending on the underlying strategy, minimize cost or maximize benefit considerations can be the driving boundary conditions for Life Cycle Analysis of single structures or structural networks (F.27-6).

27-6 Benchmark Values on Service Life in Bridge Components

In [prCWA 63:2012 (E)] input data for lifeline calculations are available. It underlines the consistency between benchmark data available in literature and in an already existing guideline. The unrestricted ageing case (do-nothing strategy) is represented as well as the corresponding service lifetimes including preventive maintenance. The latter leads to ranges of total service life which are achieved in the course of calculational lifetime prognosis presented in chapter 27-5.

References

EN 206-1. *Concrete - Specification, performance and conformity.*
EN 1990 to 1999. *Eurocode.* all parts.
EN 15331. *Criteria for design, management and control of maintenance services for buildings.*
EN 31010. *Risk management – Risk assessment techniques (IEC 56/1268/CDV).*
ISO 13822. *Bases for design of structures – Assessment of existing structures (Revision of ISO 13822:2001).*
ISO 13823. *General principles on the design of structures for durability.*
ISO 13824. *Bases for design of structures – General principles on risk assessment of systems involving structures.*
ISO 14040. *Environmental management – Life Cycle Assessment – Principles and Framework.*
ISO 14044. *Environmental management – Life Cycle Assessment – Requirements and guidelines.*
ISO14963. *Mechanical vibration and shock – Guidelines for dynamic tests and investigations on bridges and viaducts.*

ISO 15686-1. *Buildings and constructed assets – Service life planning – General principles and framework.*

ISO 15686-2. *Buildings and constructed assets – Service life planning – Service life prediction procedures.*

ISO 15686-7. *Buildings and constructed assets Service life planning – Performance evaluation for feedback.*

ISO 15686-8. *Buildings and constructed assets – Service-life planning – Reference service life and service-life estimation.*

ISO 15686-10. *Buildings and constructed assets – Service-life planning – When to assess functional performance.*

ISO 16587. *Mechanical vibration and shock – Performance parameters for condition monitoring of structures.*

ISO 18649. *Mechanical vibration – Evaluation of measurement results from dynamic tests and investigations on bridges.*

ISO 31000. *Risk management – Principles and guidelines.*

Frangopol, D.M., Kong, J.S. and Gharaibeh, E.S., 2001. *Reliability Based Life Cycle Management of Highway Bridges.* Journal of computing in civil engineering.

IAEA. 2007. *Safety Glossary – Terminology Used in Nuclear Safety and Radiation Protection.*

Miyato, A. and Ishida, J., 2008. *Bridge Maintenance Strategy Based on Life Cycle Cost and Rebuild Cost Stabilization.* Bridge Maintenance, Safety, Management, Health Monitoring and Informatics – Koh & Frangopol (eds), Taylor & Francis Group, London, ISBN 978-0-415-46844-2.

prCWA 63:2012 (E). *Ageing Behaviour of Structural Components with regard to Integrated Lifetime Assessment and Subsequent Asset Management of Constructed Facilities.* CEN Enquiry (TC), ON Secretariat, June 2012.

28

An Approach for Reliability Based Control of Post-Tensioned Containment Structure

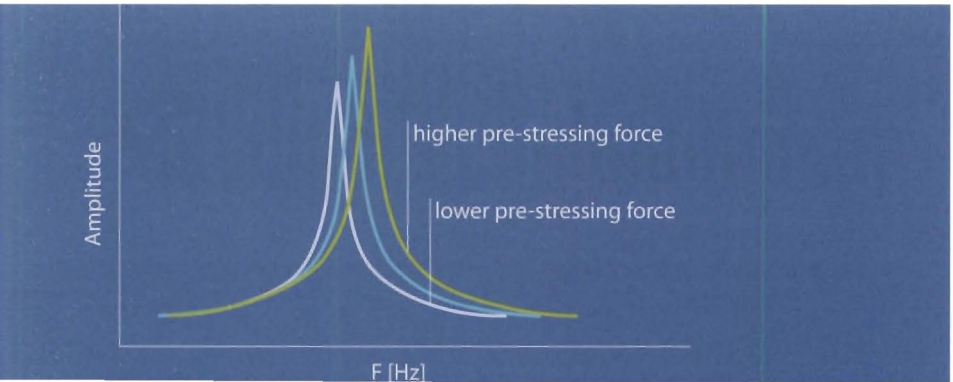
Authors:
Alexander Iliev
Marin Kostov
Anton Andonov

Motivation

Structural elements like the post-tensioning of a containment structure of a nuclear power plant are currently reviewed on 30 year old partly destructive approaches. A reliability based control approach is desired.

Main Results

The feasibility of applying the IRIS Risk Paradigm to establish a consistent approach for reliability based control of post-tensioned containment structures has been demonstrated.



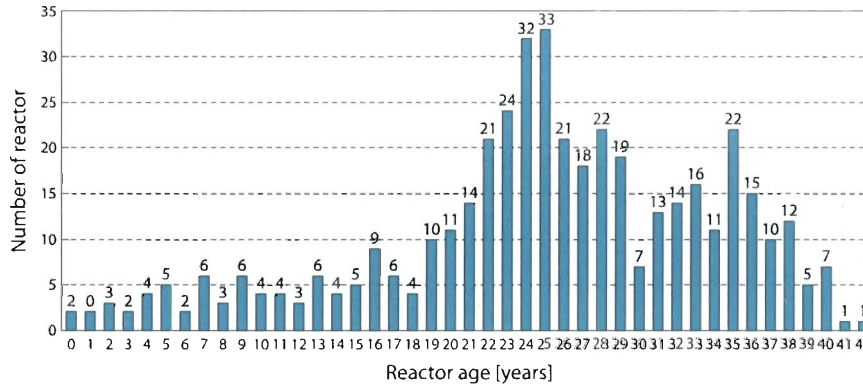
28-1 Introduction

The world's nuclear power plants are, on average, 25 years old [IAEA, 2010] (F.28-1) and most plants are believed to be able to operate for 60 years or more. The design lifetime of a nuclear power plant is typically 30 to 40 years. This may be extended by 10 to 20 years or more provided that the plant operator can demonstrate by analysis, trending, equipment and system upgrades, increased vigilance, testing, ageing management and other means that licence renewal or permission to continue operation based on the original licence poses no threat to public health, safety or the environment.

Special emphasis should be put on the assessment of the aged status and ageing management of those safety-related systems, structures and components that limit the operating lifetime of the plant, i. e. those that cannot be replaced or readily reconstructed, such as the reactor pressure vessel and containment.

An essential component of the nuclear power plant safety is the structural capacity of the containment structure. The containment has to prevent the reactor installation from external impacts, as well as to provide a tight physical barrier against release of radioactive materials in case of severe internal accidents. Therefore, the containment structures are designed to resist to internal pressure and temperature loadings. Common practice is to use post-tensioned concrete for NPP containment structures. The design post-tensioning force is selected in such a way that the produced equivalent external pressure overlaps the expected internal pressure caused by Design Basis Accident (DBA) and thus provides elastic response of the containment structure. The containment ultimate capacity itself is a complex parameter and cannot be considered as a constant value. Generally it depends on a series of variables, e. g. the material properties of the concrete, the liner, the reinforcement and the tendons respectively, as well as the structural composition – the structural system, the arrangement of the post-tensioning tendon system, the presence of penetrations and openings and the measures to mitigate the stress concentrations caused thereof, the arrangement of the liner welding and anchors, etc. In addition, for the case of non-grouted tendons, the actual post-tensioning force can be considered as

Number of reactors in operation by age (as of 31 December 2009) F.28-1



variable rather than constant; it can be influenced by many time-depending processes as corrosion, relaxation, ageing, etc.

Therefore, an essential part of the maintenance of the containment structure is the implementation of regular monitoring on the tendons force and eventual additional post-tensioning if necessary. An important measure from reliability point of view is to set up criteria for minimal allowable post-tensioning force and thus to minimize the interventions on the tendons.

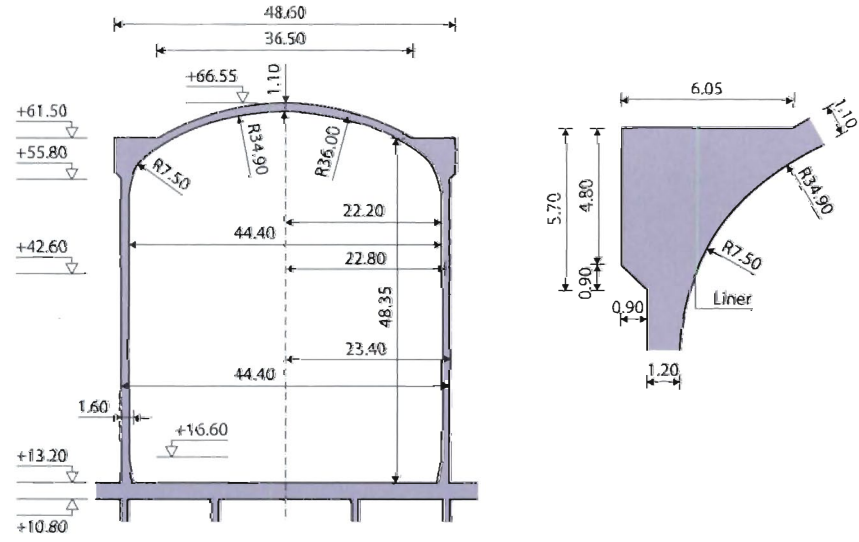
The aim of this paper is to develop an innovative approach for containment structural health monitoring of the stress state of the reactor building structure.

28-2 Description of the Structure of WWER-1000 Reactor Building

The reactor building structure of nuclear power unit type WWER-1000 is a space configuration system which could be considered as composed of four main parts – foundation structure, containment structure, auxiliary structures, and inner structure. These four parts are integrated by a solid 2.40 m thick slab of reinforced concrete, at elevation +13.20 m.

The containment structure is a post-tensioned reinforced concrete structure composed of two parts – cylinder and dome, connected by a thick supporting ring-shaped beam. The containment is entirely separated from the auxiliary structures. The main geometric dimensions of the containment are:

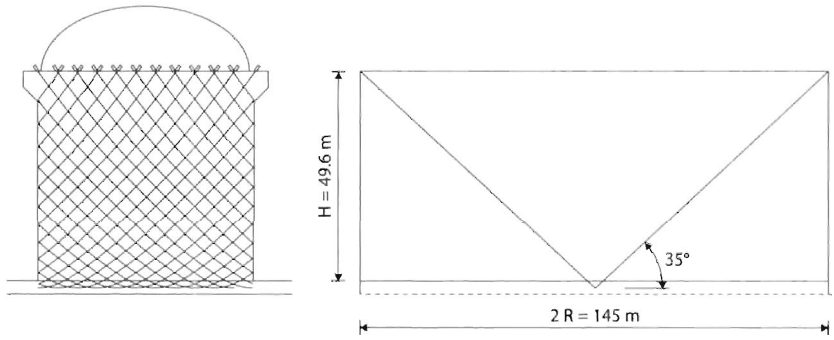
Cross section view of typical WWER-1000 reactor building F.28-2



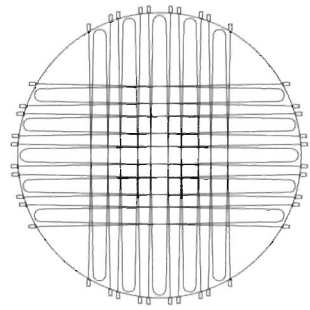
The cylindrical part and the dome are connected by a solid ring-shaped beam which serves also as a base for anchoring the pre-stressing tendons. The post-tensioning is implemented by a total of 132 tendons, whereby 96 of them are arranged helicoidally in the cylinder part, and 36 are arranged orthogonally in the dome part. Every post-tensioning tendon is comprised of 55 cables with cross sections of 140 mm² each. The tendons are post-tensioned on both ends by a design force of 1000 tons (9810 kN). Cross section view of the containment building is shown in F.28-2.

The post-tensioning tendons in the cylindrical part are arranged in three rows of screw line with falling and ascending branch slope to the horizon 35°15'. Both ends of each bundle are anchored in one area – in a single anchor or adjacent niches as in the area of anchoring bundles are placed in four rows. Prestressing tendons in the dome are located in two rows in two perpendicular directions. Both ends of each tendon are anchored in a single block, as the tendon is folded at the opposite end of the dome. The arrangement of the post-tensioning tendons in the cylindrical part is shown in F.28-3 and in the dome part in F.28-4. The manufacture of post-tensioning tendons with lengths from 80 to 180 m is done by the method of continuous winding on custom-built production line. To introduce post-tensioning, anchoring devices are used at both ends of each tendon consisting of ear/koush/anchor screw and nut with pads. The area of the cross section of

Arrangement of the prestressing tendons in the cylindrical part F.28-3



Arrangement of the prestressing tendons in the dome part F.28-4



one cable is 140 mm^2. High strength cables are made from cold drawn wire technology in low temperature under pressure, which achieves high physical and mechanical characteristics. The tendon 55 ∅15.2B7 has an area of 7700 mm^2, ultimate force of 14 300 kN and design post-tensioning force of 9810 kN.

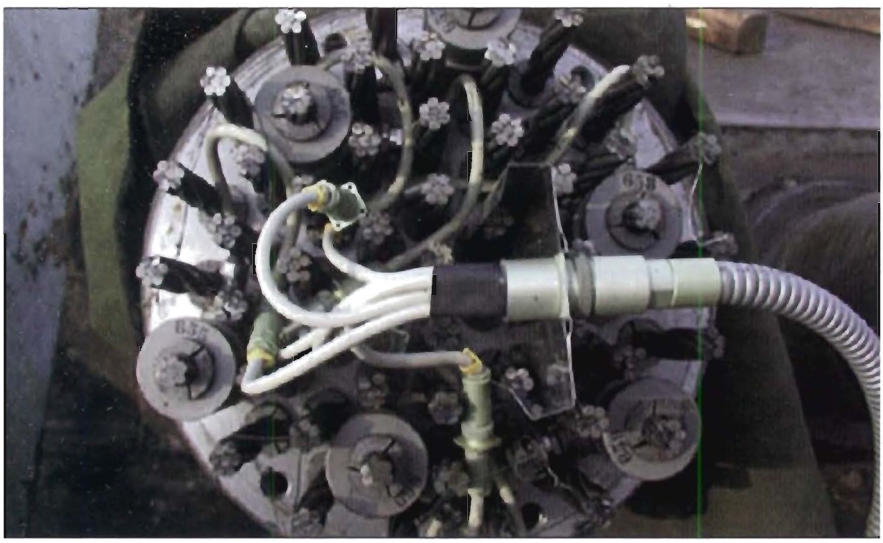
The anchoring device includes an anchor block, 55 pcs three-part wedges, anchor screw and nut with pad. The anchor block is a new element representing a steel plate with thickness of 200 mm with an external threaded bearing S45 °360×16. Each anchor block has 55 pcs concentric holes with a diameter 20 in which the post-tensioning cables are passing. The outer edge of opening is shaped in a manner to accommodate a three-part anchor bolt.

28-3 Motivation for the Current Approach

In case of post-tensioned containments, the control and maintenance of post-tensioning systems is necessary for the safe operation of the nuclear power plant (NPP). Development of non-destructive examination (NDE) and monitoring techniques and methodologies is essential, especially for the control of the ageing process at the non-accessible locations and hidden defects (for example liners in hidden places, reinforcement in massive structures, etc.).

Continuous monitoring is implemented at the start of the nuclear power plant's operation and will end when final shutdown takes place. It gives an accurate picture, throughout the lifetime of the structure, firstly of the phenomena which affect the tension of prestressing cables, and therefore the residual compression prevailing in the structure and, secondly, of the overall and relative settlement of the reactor building.

Monitoring of the tendon force by measurement of the cable forces at selected cables F.28-5



There are basically two current approaches widely used for inspection/monitoring of the tendon post-tensioning force. The first one is based on lift-up tests. During the lift-up process, the pressure in the test press is continuously increased and recorded until the anchor is released, i. e. lifted from the supporting block. The post-tensioning force is derived from the pressure.

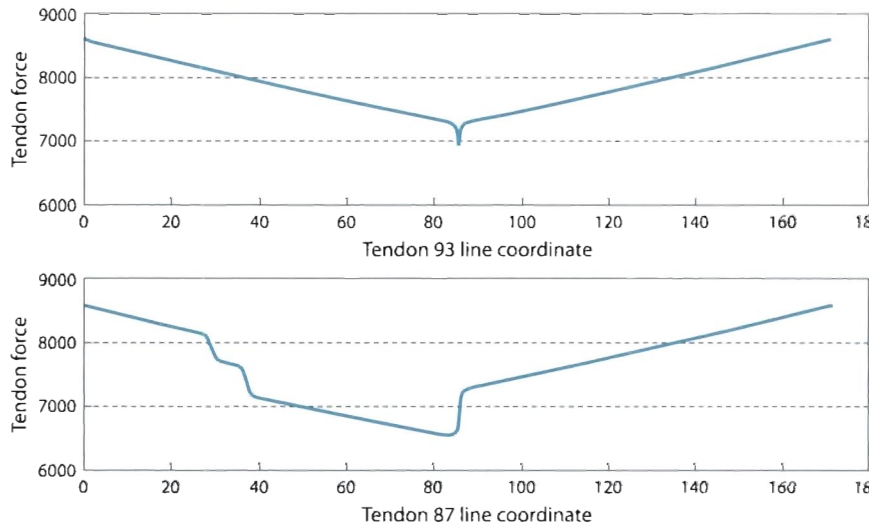
Another widely used monitoring approach is constant measurement of the tendon force on the anchor by strain gauge or pressure cell installed between the anchor and the supporting block. Alternatively, the tendon force can be monitored by measuring the force in few tendon cables and after that estimating the total tendon force, as shown in F.28-5.

Limitations of the Currently Used Methods

The current monitoring approaches mentioned above have a number of limitations. The sensors embedded in the concrete are subjected to ageing processes which affect their reliability and they cannot be replaced. Therefore, it is not expected from such monitoring systems to be operable during the entire reactor building life. One of the main limitations of the lift-up tests is that the test can be performed only during an outage that is usually once a year. Additionally, the lift-up test is considered relatively subjective, due to the uncertainties during detection of the anchor lift. Also, the lift-up tests are demonstrated in the practice to have negative influence on the tendon and anchor durability.

The direct measurement of the post-tensioning force at the anchor is considered the most advanced method from those mentioned above. The disadvantage is that the installation or the replacement of the sensors requires dismounting the tendon where the sensors will be installed. Having in mind that the expected life of such sensors will be significantly shorter than that of the reactor building, such operations should be expected. However they could be performed only in an outage.

Distribution of the prestressing force along the tendon length F.28-6



The described methods for post-tensioning force monitoring have one common disadvantage, that is measurement of the tendon force only at the anchor and that they do not take into account the tendon force distribution along the tendon length. Typical distribution of the tendon force at one regular and one irregular (around an opening) tendon is presented in F.28-6.

The equivalent external pressure as produced by the post-tensioning system and the containment confinement is a function rather of the average tendon force than the tendon force at the anchor. Therefore, the monitoring of the stress state of the containment structure should be based on the global tendon state, as tendon monitoring based only on anchor force readings might produce misleading conclusions.

Currently, there are many NPPs applying for license extension or already licensed to year 2030. Therefore, it is necessary to develop long-term solutions for containment monitoring procedures, which would overcome the above mentioned limitations of the current approaches. One possible solution is monitoring based on ambient vibrations of the structure that is successfully applied to a large number of bridges [Wenzel, 2009].

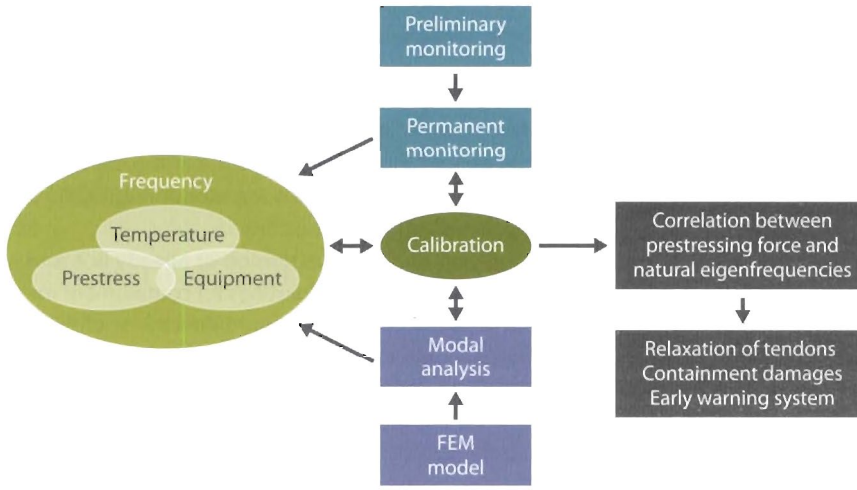
28-4 Methodology of the Current Approach

The proposed approach, applied on NPP reactor building structure can improve the control on the overall stress state of the structure, outline particular areas of the structure with altered stress state and improve the understanding of the structural global and local behaviour. The main idea behind the proposed approach is instead of directly measuring the post-tensioning forces in the tendons, to monitor the effects of the post-tensioning and thus indirectly the containment capacity and the overall NPP safety. The current approach is based on a permanent vibration monitoring system on the NPP reactor building structure, registering the ambient vibrations in different locations on the structure. Eventual changes in the stress state of the containment structure or eventual damage formations will be detected and indicated through alterations in the spectral distribution function.

The method of studying the stress state of a structure, considering alterations in the vibration amplitudes and subsequently in the spectral distribution function, is proposed by VCE [Tanaka et al., 2009]. The basis of this method is that any change in the energy distribution function is related to a particular change in the stress or damaged state of a location of the studied structure. Based on a permanent vibration monitoring it is possible to follow every potential change in the frequency or the amplitudes, which will subsequently affect the energy distribution function. When isolating only the influence of the pre-stressing force on the structural vibrations it will be possible to evaluate the general stressed state of the structure, depending on the ambient vibrations recorded.

The proposed structural health monitoring approach is based on temporary and permanent ambient vibration measurements and finite element analyses. Firstly, numerical simulations should be executed for initial assessment of the structural modal characteristics. Attention should be paid when investigating the higher local modes of the dome and the cylinder, because they are likely to be strongly affected by the stress state of the

Methodology of the current SHM approach F.28-7



structure. Secondly, additional numerical analyses should be performed for studying the influence of the post-tensioning level on the modal behaviour of the main structural parts – dome and cylinder. The analytically obtained modal response is compared with the response obtained experimentally through ambient vibration monitoring and if needed the numerical model will be updated through a consecutive process of finite element model updating. This procedure is based on a mathematical optimization problem: the difference between the numerical and experimental data should be minimized through iterative modal analyses. The entire process should be finalized with specific thresholds and finally implemented into an early warning system. A general methodology scheme is presented in F.28-7.

The influence of the post-tensioning force on the containment dynamic response will be studied numerically. The level of post-tensioning is expected to affect mainly the higher modes of a structure, while the global modes should remain practically unchanged [Wenzel, 2009]. The amplitude changes increase predominantly in the high frequencies with increasing the post-tensioning force of the tendons (F.28-8). These amplitude changes will affect the energy distribution function and a further step in the investigation will be to study the influence of the other factors, influencing the ambient vibrations, in order to isolate the influence of the post-tensioning force itself.

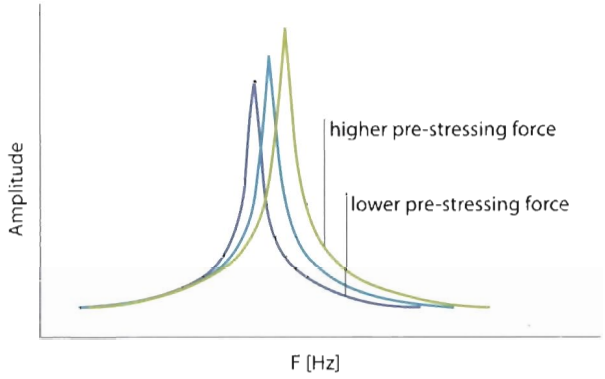
An important step of the analysis is the comparison of the monitoring data and the results of the numerical simulations, where essential conclusions will be obtained regarding the structural mode shapes of the reactor building and the expected frequency and amplitude changes due to the factors indicated above. It is expected that the different temperature zones on the internal and external surface of the structure will affect the structural higher modes characteristics (amplitudes and/or frequencies) and thus the spectral distribution function.

The alteration in the energy distribution function will be independently investigated for each factor affecting it, by numerical analyses. The main tool for studying the influence of the various factors on the structural dynamic response will be the complex-harmonic analyses. They will be performed for different stress states and the resulting frequency spectra in different locations of the structure will be the base for studying of the correlation between the stressed state and the structural vibration behaviour.

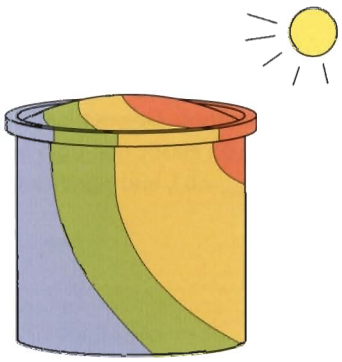
Another main tool used in the current study will be the spectral density function. This function reveals more clearly the fraction of energy transferred to different frequency ranges, resulting in the change of its pattern. The definition of the spectral density function is presented and explained in [Tanaka et al., 2009] and is defined as:

$$E_i(f) = \sum_{k=0}^{f} F_i(k)\Delta k \ , \text{ where}$$

Influence on the pre-stressing force (stressed state) on the modal behaviour of a structure F.28-8



Zones with different temperature at the structure due to sun radiation F.28-9



$F_i(f) = \frac{G_i(f)}{\sigma_i^2}$ is normalized Spectral Density Function and

$\sigma_i^2 = \sum_f G_i(f)\Delta f$ is Spectral Distribution Function.

$G_i(f)$ is the acceleration spectra, calculated by a conventional FFT routine.

The spectral density function $E_i(f)$ varies from 0 to 1 and the observed tendencies in its pattern of the function will be used to indicate the alterations in the stress state [7]. Vibration investigations should be carried out for all disturbances from the external environment acting on the structure and affecting its stressed state.

Expected Advantages of the Proposed Approach

One of the main advantages is that the method offers continuous real-time monitoring of the containment, which in combination with appropriate thresholds and implemented into an intelligent warning system, could provide continuous information about the containment condition capability to serve as ultimate barrier. The estimated stress state could be used for subsequent containment damage detection potential in case of different accidents. Another advantage is that the proposed approach is totally non-destructive and delicate with respect to the containment structure, as far as the accelerometers can be installed and/or replaced at any time, without depending on, or disturbing the NPP operation. Furthermore, the proposed approach is based on measurement of the global effect of the post-tensioning system on the containment, rather than post-tensioning force at the anchor head, thus avoiding misleading conclusions.

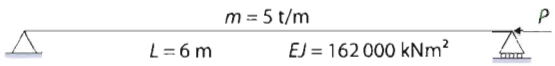
Summarizing the Main Goals of the Current Approach for SHM for the Containment Structure Are:

// Control of the containment stressed state;
// Identification of relaxation in tendons;
// Location of existing damaged or relaxed tendon;
// Better understanding of the structural global and local behaviour.

28-4-1 Change of Dynamic Behaviour because of Compression Stress

Considering the geometric non-linearity of the structure (second order effects) could be noted basically in the following form: $[k] = [k_{ph}] + [k_g]$, total stiffness of a given structure is a sum of its physical and geometric stiffness. Geometric stiffness is in direct relation with internal (axial) forces of the system. In an elastic non-rigid body significant compressive forces decrease the total stiffness ($k_{geom} < 0$), and significant tensile forces increase the total stiffness.

When loss of stability (buckling) is to occur $k_g \rightarrow -k_{ph}$ and the total stiffness is close to 0. This is shown with a simple example:



The equation for calculation of natural frequency of a beam subjected to axial forces (continuous model with neglected shear forces) is:

$$f_i = \frac{\lambda_i^2}{2\pi L^2}\sqrt{\frac{EJ}{m}}\ ;\quad \lambda_i = i^2\pi^2\sqrt{1+\frac{PL^2}{EJi^2\pi^2}}$$ [Belvins, 1979]

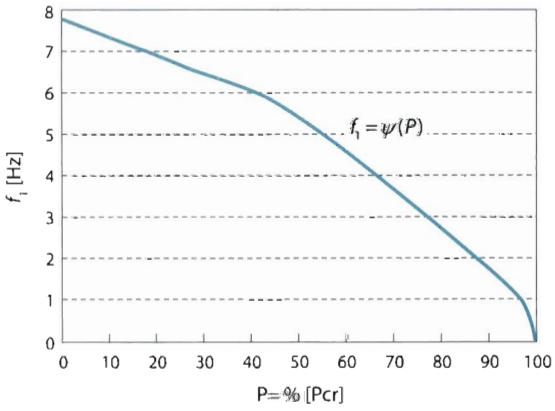
In T.28-1 the first three natural frequencies are given for P=0; P=0.1 Pcr; P=0.25 Pcr; P=0.50 Pcr, and P=0.95 Pcr, where Pcr=41123 kN is the critical force (Euler buckling) of the beam.

The relation $f_1 = \psi(P)$ is shown in F.28-10. There are analogical predictions for tendencies in eigenmodes of the containment for $f < 20$ Hz. Modes with $f > 20$ Hz for spatial vibrations of a relatively stiff structure are of greater interest, because they are difficult to predict with simple models. The concrete stresses due to post-tensioning are less than $0.1\sigma_{CR}$.

Natural frequencies of pre-stressed simply-supported beam T.28-1

	P=0	P=0.1 Pcr	P=0.25 Pcr	P=0.5 Pcr	P=0.95 Pcr
Mode No.	Frequency [Hz]	Frequency [Hz]	Frequency [Hz]	Frequency [Hz]	Frequency [Hz]
1	7.7543	7.3459	6.6869	5.4129	1.2463
2	63.221	62.793	62.145	61.049	59.024
3	152.07	151.59	150.85	149.62	147.38

Relation between compressive force and fundamental frequency F.28-10



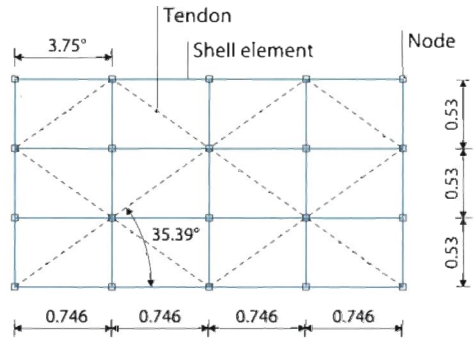
Pcr – critical force for Euler buckling

28-4-2 Development of FE Model with FEMAP and SOLVIA

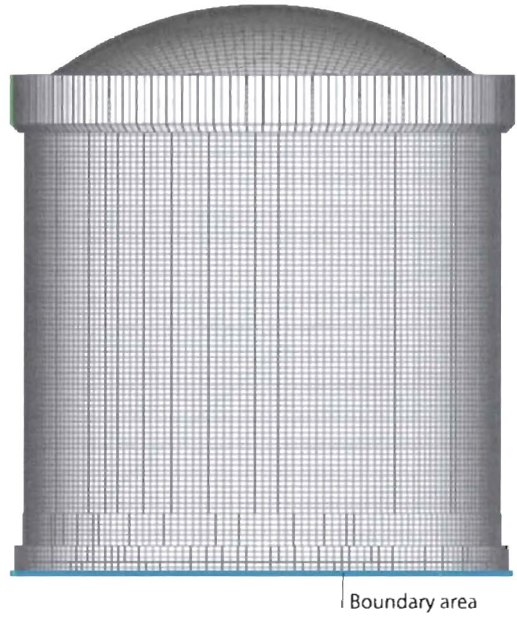
Cylindric Wall

The cylindrical wall is modelled with 4-node rectangular shell elements. The wall is meshed in such way that the tendon's path passes through existing nodes (F.28-11). Openings and penetrations are neglected.

Placement of elements and nodes in the cylinder [m] F.28-11



Boundary condition of the structure F.28-12



28-5 Results and Progress beyond the Current Practice

28-5-1 Dynamic Analyses of the Structure

Complex-Harmonic Analysis

Analysis of frequencies from 0 to 60 Hz, increment step 0.05 Hz. Acceleration load $a = a_0 \cdot \sin \theta t$, where $a_0 = 0.15$ g.

Various types of complex-harmonic analyses are performed, considering different levels of post-tensioning and thus different stress states of the structure:

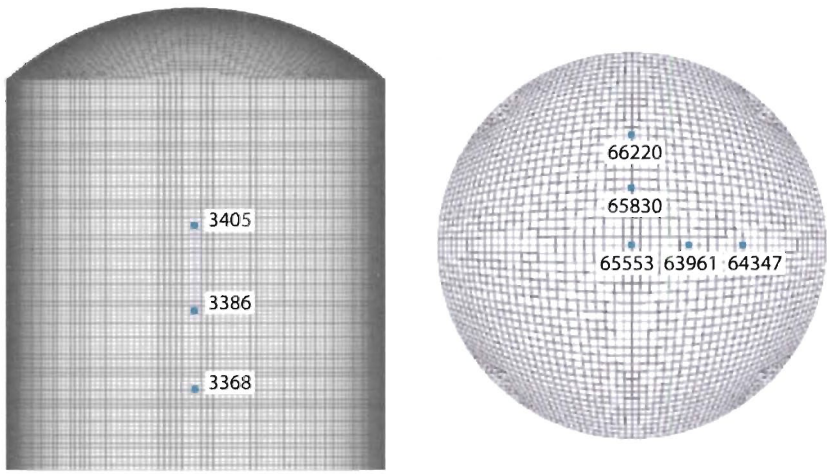
// Analysis of the containment structure without post-tensioning;
// Analysis of the containment with design post-tensioning;
// Analysis of the containment with post-tensioning 80 % from the design (long-term loss of stress during exploitation).

Frequency response spectra are created for displacement [m], velocity [m/s] and accelerations [m/s^2] for some nodes of interest with respect to frequency [Hz]. The controlled nodes are shown in F.28-13.

28-5-2 Analysis of Results

As the permanent vibration monitoring system at the reactor building structure is installed only at the dome part, main attention will be given to this structural part. The significant local modes in the dome part are demonstrated by comparison of the frequency

Placement of controlled nodes F.28-13



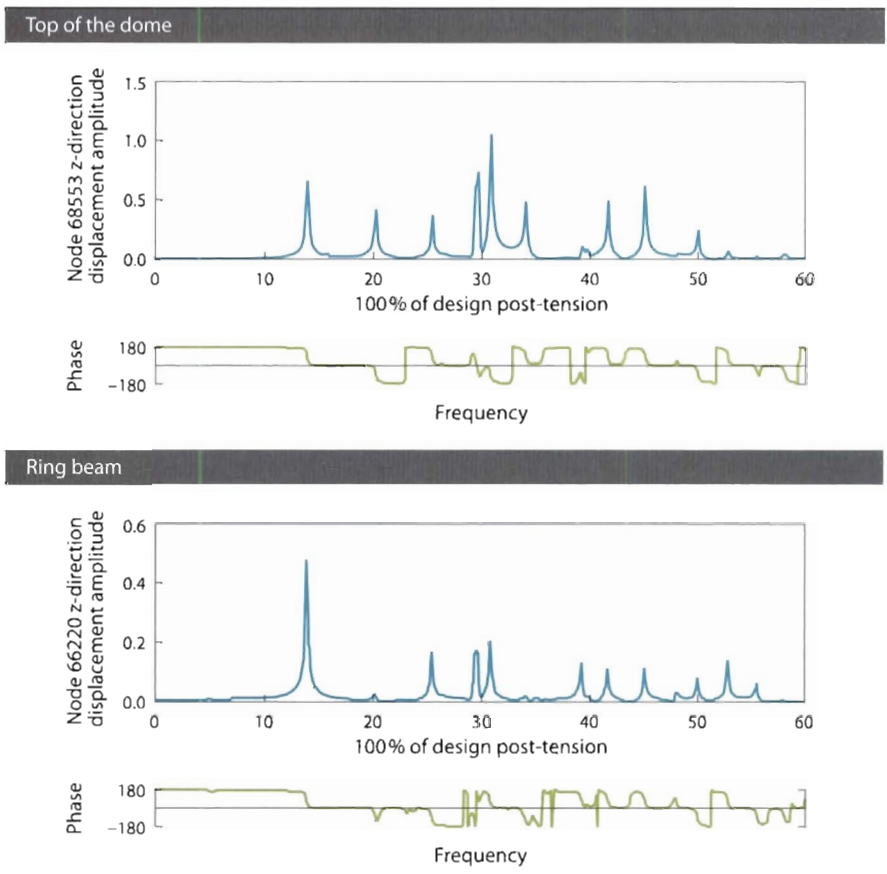
response functions from two dome locations – top of the dome and base of the dome (ring beam). In F.28-14 the frequency response spectra are presented for displacements in vertical direction. The analysis is performed with design values of the post-tensioning force. The peaks in the frequency response spectrum appear exclusively at the top dome location, therefore all of them represent local modes of the dome structure. The range of the local mode frequencies at the dome start at approximately 14 Hz.

The local modes of the dome part of the structure are presented in F.28-15. The modes at 13.9 Hz and 20.25 Hz can be classified as first local modes of the dome. The rest of the observed local modes are of higher orders – 25.5 Hz, 29.7 Hz and 34.1 Hz.

After the series of complex-harmonic analyses with different post-tensioning force, the obtained general results could be summarized as follows:

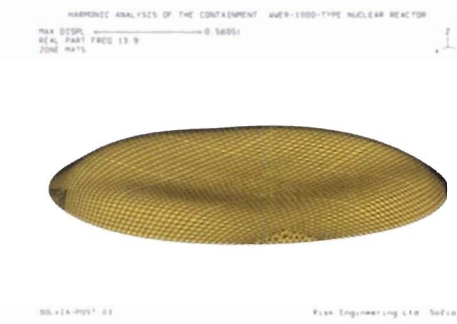
// Change in deformed shapes of vibration of the structure due to post-tensioning
// Shift of natural frequencies of the structure for different states of post-tensioning
// Excitation of additional natural frequencies in post-tensioned state

Displacement spectrum in vertical direction: top of the dome (above) and ring beam (below) F.28-14

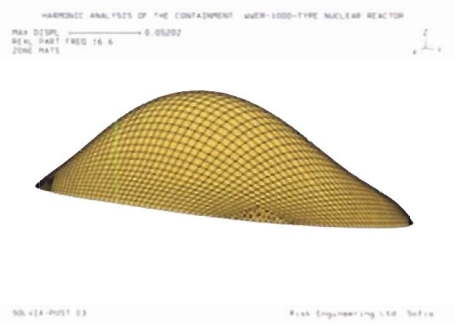


Local mode of dome F.28-15

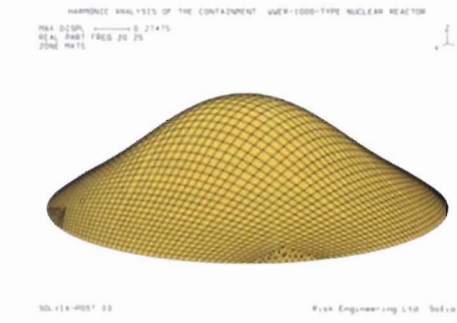
Local mode of dome at 13.9 Hz



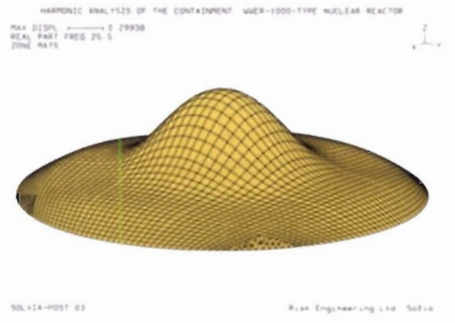
Local mode of dome at 16.6 Hz



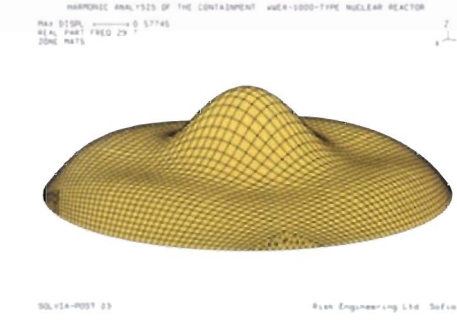
Local mode of dome at 20.2 Hz



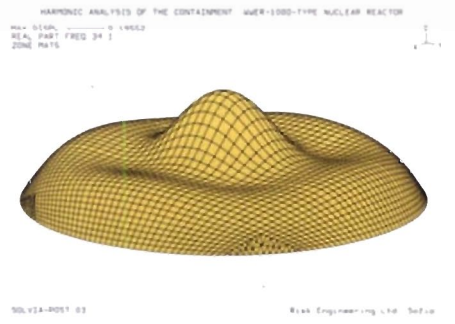
Local mode of dome at 25.5 Hz



Local mode of dome at 29.7 Hz



Local mode of dome at 34.1 Hz



// Amplitude change of the structural response for different states of post-tensioning
// Change of normalized spectral density function $\psi(f)$

The complex-harmonic analyses of the containment structure are performed for design post-tensioning load, 80 % of the design post-tensioning load and for a case without post-tensioning load.

Change in Deformed Shapes of Vibration of the Structure due to Post-Tensioning

Deformed shapes at design post-tensioning and close levels (80 %) differ from low post-tensioning levels. In case of the cylindrical part the reason is the shape of the tensioned containment – the cylindrical wall changes shape to rotational hyperboloid. In case of the dome part – the deformed dome has less curvature. In addition there are local effects from post-tensioning, particularly in the dome. This is clearly observed at frequency 5.25 Hz – in the 0 % level the deformed shape is global translational in horizontal direction. At levels close to design post-tensioning in the dome symmetrical vertical displacements appear. For the rest of the natural frequencies up to 60 Hz clear secondary effects in the dome do not appear, because vertical displacements prevail.

Shift of Natural Frequencies of the Structure for Different States of Post-Tensioning

T.28-2 shows all matching natural modes and their frequencies.

At frequencies up to 20 Hz the deviation is smaller than accuracy of analysis $\varepsilon = 0.05$ Hz (the increment step in the complex-harmonic analyses). At frequencies higher than 25 Hz, an increase of natural frequencies due to post-tensioning is observed, also mentioned in [Wenzel, 2009]. The absolute value of deviations is close to the accuracy of the analysis. The reasons for the small deviations are the significant spatial stiffness of the containment structure and the fact that it is linear elastic. The current results show that frequency shifts due to different post-tensioning forces is insignificant for the containment structure.

Excitation of Additional Natural Frequencies in Post-Tensioned State

In complex-harmonic analyses with post-tensioning additional natural frequencies are excited. They are related to local vibration modes, typical for the changed geometry of the post-tensioning containment and there is also relation to secondary effects from the post-tensioning. The additionally excited natural frequencies are higher than 30 Hz (high-frequency range) and they could be an appropriate base for studying the influence of the post-tensioning force and the overall stress state on the local mode characteristics.

Amplitude Change of the Structural Response for Different States of Post-Tensioning

The increase of post-tensioning force in the tendons changes the shape of the cylindrical and dome part of the structure and as a consequence its geometrical stiffness is increased. This leads to changes in the amplitudes of the natural vibrations at lower and higher frequencies. The following effects are observed:

For frequencies up to 20 Hz in horizontal direction (vibrations in the cylindrical part) the amplitude values are lower for the post-tensioning structure. The reason is the increased geometrical stiffness of the structure mentioned above. The affected vibration modes are global – with significant mass excitations.

For frequencies over 20 Hz in horizontal direction (vibrations in the cylindrical part) and over 10 Hz in vertical direction (vibrations in the dome part) the amplitude values are higher for the post-tensioned structure. The affected vibration modes are mainly local high-frequency modes. The comparison between the amplitude values for 80 % and

100 % post-tensioning shows that an increase of 20 % in the post-tensioning force results in an amplitude increase of 10 to 20 % in the higher order modes. In some cases the amplitude increase is higher for the higher frequency modes than it is for the dome part of the structure.

Change of Normalized Spectral Density Function $E(f)$

The increase of post-tensioning alters the shape of the normalized distribution function $E(f)$. The relative participation of frequencies less than 20 Hz, in the formation of the spectral density function, decreases. For structures without post-tensioning, these frequencies (less than 20 Hz) have the main influence (80 %) of the integral value for $E(f)$. As a conclusion the spectral density function is negligibly affected by the post-tensioning force for frequencies up to 20 Hz, for both structural parts – cylinder and dome.

With increase of post-tensioning forces the participation of the lower modes in $E(f)$ decreases and the main weight comes from frequencies in the range of 20 to 45 Hz, where post-tensioning effects on the higher frequency modes are stronger. The alterations in the spectral density function vary from 2 % to 10 % depending on the location of the observed location. Locations in the cylindrical part of the structure demonstrate higher increase of $E(f)$ than locations in the dome part of the structure. The values of $E(f)$ for full post-tensioning are higher than values of $E(f)$ for 80 % post-tensioning.

For frequencies over 50 Hz, particularly in acceleration spectra, there is a reverse effect – higher amplitudes for the post-tensioning structure at lower frequencies.

28-5-3 Comparison of the Results Obtained by Ambient Vibration Monitoring with the Results from the Finite Element Model

The basic measurements with BRIMOS® on the dome were taken in May 2010 by a team of [VCE, 2010]. For the dynamic assessment of the structure itself five sensors have been placed. The main idea of BRIMOS® is rather simple. The dynamic characteristic of a structure is recorded by acceleration sensors and the signal in time range is changed into a frequency response by use of an FFT (Fast Fourier Transformation). In doing so the

Natural frequencies T.28-2

No. of mode	Natural frequency [Hz]			Deviation [%]
	Complex harmonic 0 %	Complex harmonic 80 %	Complex harmonic 100 %	
1	5.2500	5.2500	5.2500	–
12	13.950	13.950	13.950	–
13	16.600	16.600	16.600	–
26	20.300	20.300	20.300	–
38	25.450	25.500	25.500	0.20
56	29.300	29.450	29.450	0.51
163	58.170	58.185	58.185	0.02

results of this calculation are the natural frequencies of the structure represented in the ANPSD and the raw-spectrum.

Since the methodology of the current approach uses the results from the complex-harmonic analyses in this comparison the obtained eigenmodes and eigenvalues are used. The following conclusions could be done:

// There is general compatibility between the deformed shapes obtained by the ambient vibration monitoring and the finite element analyses.
// The frequencies obtained through the finite element model are generally higher. This could be due to overestimation of the stiffness in the computational model or due to other effects that have not been considered in the numerical simulation.

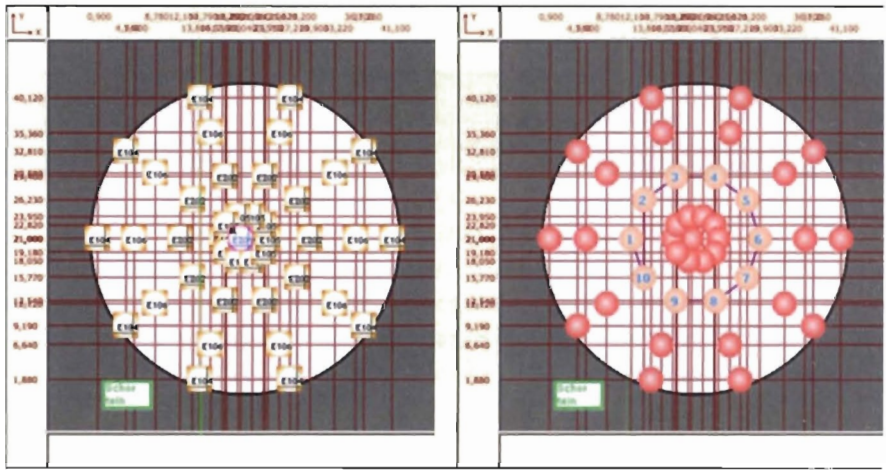
28-5-4 Conclusions and Possibilities for Future Development of the Investigation

The current study puts the basic steps and reveals tendencies in the structural vibration behaviour of the post-tensioned containment of a WWER-1000 type nuclear reactor that should be more deeply investigated. The tendencies of the spectral density function should be further studied and special emphasis should be given to specific structural lo-

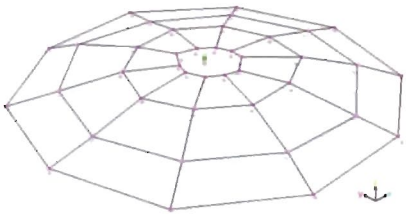
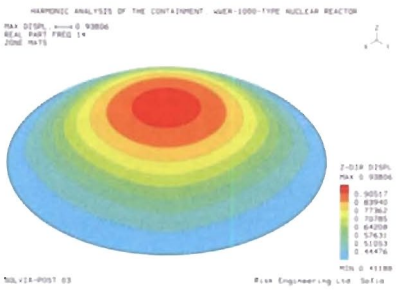
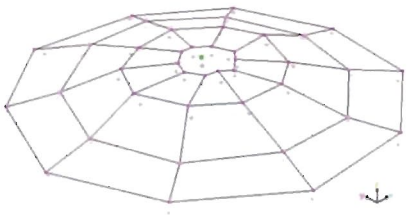
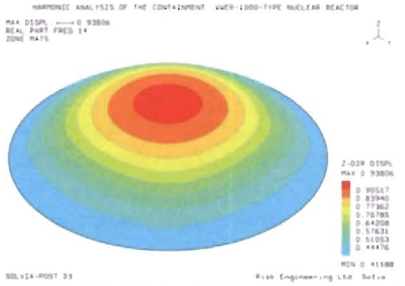
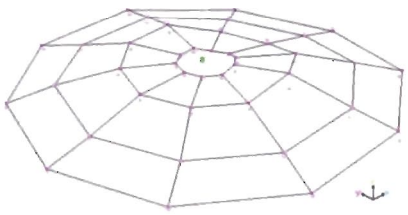
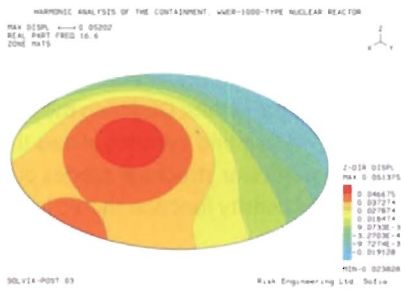
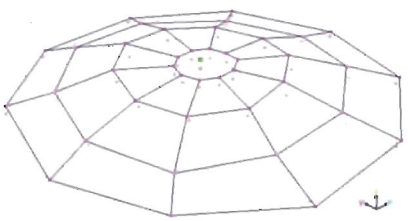
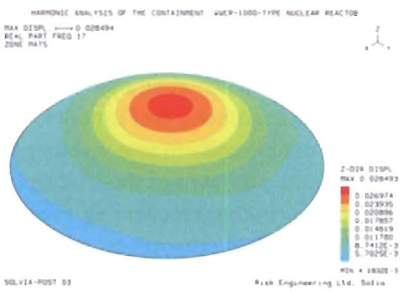
Comparison of natural frequencies T.28-3

Natural frequencies Ambient Vibration Monitoring [Hz]	Natural frequencies Finite Element Model [Hz]
10.01	14.00
12.25	14.00
16.32	16.60
16.57	17.00
18.76	20.25
19.78	21.15

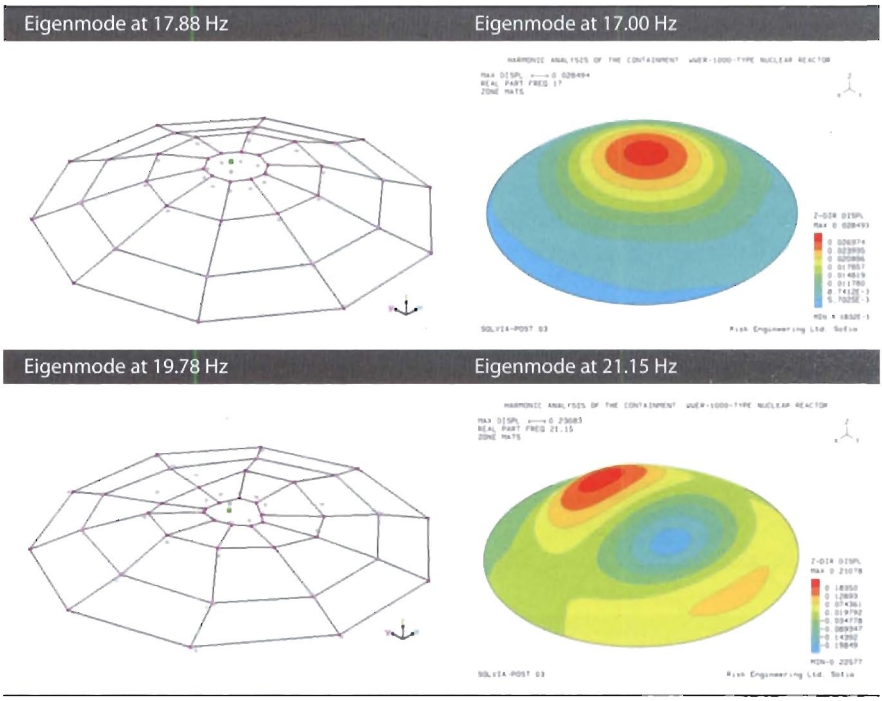
Layout of BRIMOS® data evaluation F.28-16



Eigenmode obtained through ambient vibration monitoring (left) and eigenmode obtained through finite element model (right) F.28-17a

Eigenmode at 10.01 Hz	Eigenmode at 14.00 Hz
	
Eigenmode at 12.25 Hz	**Eigenmode at 14.00 Hz**
	
Eigenmode at 16.32 Hz	**Eigenmode at 16.60 Hz**
	
Eigenmode at 16.57 Hz	**Eigenmode at 17.00 Hz**
	

Eigenmode obtained through ambient vibration monitoring (left) and eigenmode obtained through finite element model (right) F.28-17b



cations, higher variety of post-tensioning force and assumption of specific limited with decreased post-tensioning force.

The comparison of the numerical results and the monitored data showed very close proximity of the results. Outlining the essential structural local modes of both parts of the structure – dome and cylinder, allows the further development of the study by focusing on these particular structural modes of interest. Their behaviour and their influence on the spectral density function should be studied again by both manners – numerically and experimentally.

To obtain statistically stable numerical results further analyses are required – a wider set of output data to summarize, reduce simplifications, include openings and penetrations, where local effects are expected. In a further study these should be included because of the non-regularity of the tendon trajectories and the concrete wall around them.

Another further step should be assessment of the effects of other factors influencing the vibration behaviour: equipment forced vibration, containment temperature and environmental conditions. An FE model with solid elements could be used for analyzing the influence of non-uniform solar heating on the dynamic behaviour.

The limited amount of the study allows rough numerical evaluation of the changes, and focuses on the directions of the spectral density curve shifts. The obtained results are very close to the theoretical, which is an indication for the correct assumptions in the model and the analyses. Improvement of NPPs safety is a main issue for the nuclear in-

dustry. With twenty WWER-1000 type reactors across the world and a number of reactors to be designed and built (of modern technological generation but with similar building structures) spending time and resources for a better understanding of their behaviour is justified.

With rapid improvements of monitoring instrumentation it is possible to apply systems, monitoring permanently the condition of the building structure and based on specific thresholds to evaluate the current state of the structure. In areas with limited access (for example the tendons of the containment) these systems could be used for warnings about internal malfunctions (relaxation or tendons, deterioration of material properties due to ageing etc.) These systems will effectively serve as permanent monitoring tool, presenting the current stress state of the structure and as a warning system, alerting when the structural safety is at risk.

References

IAEA, 2010. *Nuclear Power Reactors in the World.*

Wenzel, H., 2009. *Health Monitoring of Bridges*. John Wiley & Sons Ltd.

Tanaka, H., Höllrigl-Binder, M. and Allmer, H., 2009. *Structural Health Monitoring by Spectral Analysis*. VCE Internal Report.

Blevins, R. D., 1979. *Formulas for Natural Frequency and Mode Shape*. Van Nostrand Reinhold Company.

VCE, 2010. *Monitoring of Kozloduy NPP. Structural Monitoring with BRIMOS®*. Internal report.

29

Assessing Safety of Shear Walls: an Experimental, Analytical and Probabilistic Study

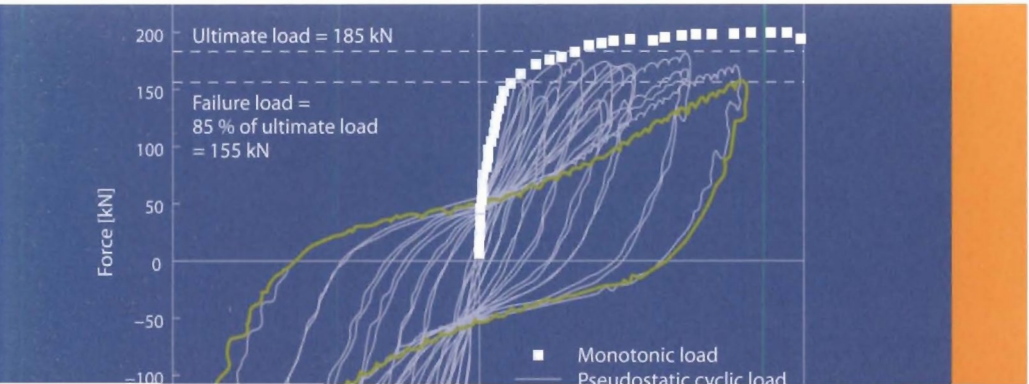
Authors:
Yogita Mahendra Parulekar
Rohit Rastogi
G. Rami Reddy
Vivek Bhasin
Keshav Krishna Vaze

Motivation

The behaviour of shear walls under cyclic loads has not sufficiently been tested in the past. Test results for various shear wall cases are desired.

Main Results

Several large testing campaigns have been performed in India. Results for a specific type of shear wall applied in the nuclear industry became available.



29-1 Introduction

Performance based design approach is gaining importance for assessing structures subjected to earthquake loading. Evaluation of seismic performance of nuclear power plants requires assessment of shear walls which are its main structural elements. In performance based seismic design approach, the failure event occurs when the structure fails to satisfy the requirements of a prescribed performance level e. g. immediate occupancy, life safety or collapse prevention [FEMA-273]. Evaluation can be achieved by performing detailed experiments. It is known that accurate estimates of moment/shear capacity of shear walls under cyclic loading with axial load are extremely difficult to make. This necessitates experimental testing for accurate assessment of shear response and capacity of the shear walls. Experimental studies provide physical insight in the force resisting mechanisms of these walls and help us to validate and improve the numerical models and corresponding constitutive relations.

Damage to structures subjected to earthquakes are observed due to exceeding of design loads, design inadequacy or loss of capacity due to ageing effects. This makes it very important to assess the vulnerability of structures against different levels of earthquake loads. The primary reason of failure of structures due to earthquake is ground shaking. At a very low level of ground shaking, it can be said with confidence that the structure will not fail. However, at a high magnitude of ground shaking the structure may fail. The capacity of the structure is dependent on many parameters. There is always a scatter observed in the values of these parameters. The demand on the structure can also exhibit large scatter especially if the demand is of the postulated accident loads like earthquake. The likelihood that a structure would fail due to different levels of earthquake is estimated using the principles of structural reliability and curve so plotted is termed as the Fragility Curve [EPRI, 1994]. The design of the structure based on the Fragility Curves generated for structures and components provides a quantified safety level against the effect of earthquake loading. This work is aimed at providing a demonstration for estimating the design loading for a typical shear wall used in a nuclear power plant based on the probabilistic theory. The modelling of the shear wall is validated using the experiments.

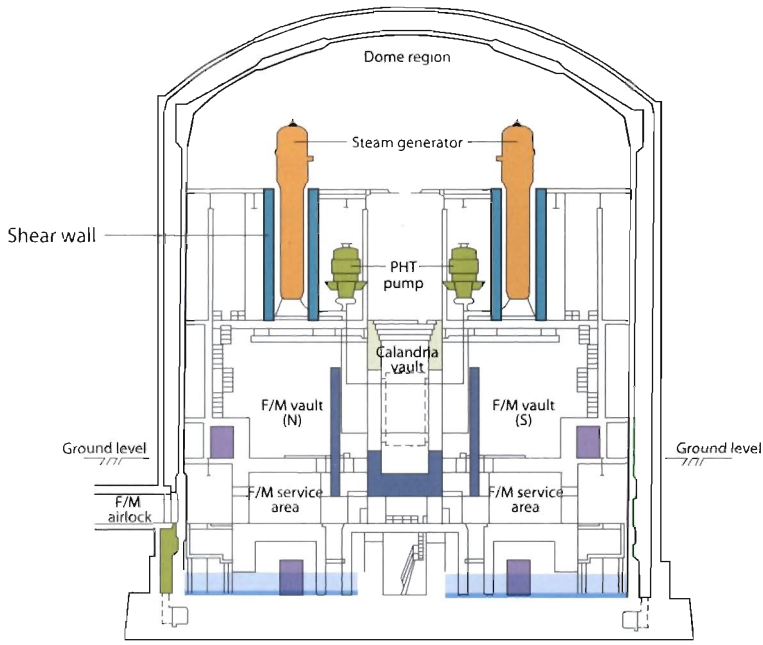
Scaled midrise shear walls of a typical Nuclear Power Plant have been tested under monotonic and cyclic loading. Finite Element Analysis is carried out to evaluate the ultimate load and drift of the shear wall and load displacement relation under cyclic loading is evaluated. The same wall is analyzed based on structural reliability methods and a fragility curve is generated. The IRIS Risk Paradigm model is thus applied to the shear walls used in the nuclear industry. The uncertainty in the design parameters is modelled using the probability distribution function. Thus the design load is arrived using the sound logic of probabilistic analysis rather than a deterministic factor of safety.

Finite Element analysis of short stiff shear wall tested at JRC, Italy in WP1 is also carried out and the comparison between the test and analysis results are presented.

29-2 Performance of Shear Walls

Shear walls used in RCC buildings, nuclear power plants and other structures under sufficient lateral excitation may fail under various mechanisms like flexure, shear or sliding shear thus resulting in significant lateral displacement and strength degradation. The ultimate load on the shear wall as well as the ultimate drift of the shear wall are two important parameters which need to be assessed experimentally. In many investigations, loss of equipment function housed within a nuclear power plant (NPP) structures has been considered to occur when the ultimate drift limits are reached, thus proving that ultimate drift is a failure parameter. Earlier researchers have carried out cyclic tests on squat walls [Lopes, 2001a, 2001b] in which the response was shear dominated. Also predictions of the behaviour of the shear walls for monotonic static and cyclic loading using finite element analysis and simplified approaches have been carried out [Salonikios, 2002; Farrar and Baker, 1990]. The models used were able to predict the maximum load more accurately than the displacements at the peak load. However the ductility of the walls could not be accurately predicted and also accurate prediction of crack pattern from FE analysis was difficult. Tests were also carried out on walls with aspect ratio 1 to 1.5 [Kazaz et al., 2006] wherein sliding shear failure was emphasized. Similarly tests carried out on mid-rise walls [Tasnimi, 2000] and high-rise walls [Ellingwood and Hwang, 1985] showed flexure dominated failure. From the literature available it is found that improvement in the ductility model and hysteretic response is needed. Hence in the present work behaviour of

Schematic of reactor building showing shear wall F.29-1



mid-rise shear walls is investigated through FE analysis and experiments and behaviour of low rise shear walls tested in WP1 tests of IRIS project is simulated by performing non-linear FE analysis.

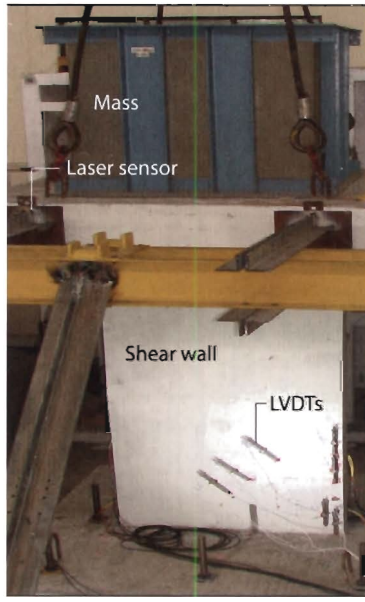
Monotonic and cyclic tests provide the ultimate load and the ultimate drift of the shear walls. Comparison of force displacement data obtained from monotonic tests and cyclic tests with experiments is made for both shear walls. The exact mode of failure of the wall is obtained and parameters like ultimate load, ultimate drift limit and ductility ratio are obtained.

29-3 Details of Mid-Rise Shear Wall

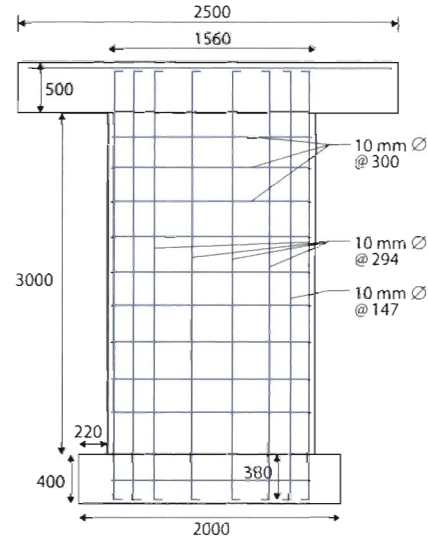
The shear wall considered for the tests is a 1:5 scaled model of the internal structure of a nuclear power plant building. The schematic of the reactor building showing the shear wall is shown in F.29-1. The shear wall (7.8 m wide, 15 m high and 1 m thick) supports the steam generator and floor of Indian type nuclear power plant and its first fundamental frequency is 3.1 Hz. This shear wall shows a cantilever type mode as the mass of steam generators and floor is lumped at the top of the shear wall.

Scaling laws are used and lumped mass on the top of the shear wall is obtained so that the frequency of the shear wall model along with lumped mass is 15.5 Hz. The shear wall is designed as per Indian standard codes [IS13920, 2002] for dead load and 0.4 g earthquake acceleration at the mass level of the wall. The model has 3 m height (h), 1.56 m width and 0.2 m thickness and percentage reinforcement of 0.4 % in vertical direction and 0.3 % in horizontal direction. The foundation is 0.4 m deep and 2 m × 2 m in area and the top slab

Test setup of shear wall F.29-2



Reinforcement details of the shear wall F.29-3



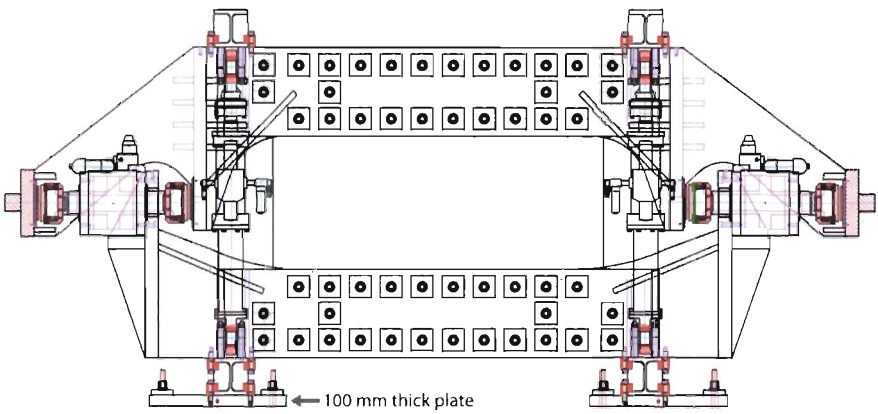
has dimensions of 2.5 m × 2.5 m × 0.5 m. The test setup of the shear wall is shown in F.29-2 and the reinforcement details of the shear wall are given in F.29-3. A mass of 8.5 tons in the form of concrete cube of dimension (1650 m × 1650 m × 1420 m) is added on the top slab and the mass of the top slab is 8 tons. Thus the shear wall will be subjected to a total axial load of 16.5 tons. Three of such shear wall specimens are tested. One wall was tested for monotonic load and two were tested for pseudo-static cyclic displacements till failure.

29-4 Details of Low-Rise Shear Wall

A squat short shear wall with a width of 3 m, a height of 1.2 m and a thickness of 0.4 m was tested at JRC, Italy; the test programme was called TESSH (TEsts on Stiff SHear wall). Vertical reinforcement consisted of 22 bars of 16 mm diameter arranged in two layers and horizontal reinforcement consisted of 6 bars of 16 mm diameter arranged in two layers. Top and bottom beams were 4 m long, 0.8 m deep and 1.25 m thick.

The schematic test setup is shown in F.29-4. Vertically 60 tons of load were applied by vertical actuators. There was control of rotation of the shear wall during testing, however, vertical displacements were allowed. A rigid loading device was designed so that it should transfer the load and be easily mountable. The shear wall is loaded in pure shear with no rotations allowed and the structure was connected to the reaction wall. There were four horizontal actuators, each actuator having a capacity of 300 tons with a total capacity of 1200 tons. Instrumentation was carried out using optical measurements to measure the crack width and crack pattern. Cyclic loading was applied initially starting with three cycles of 50 tons. Then two cycles each of 100, 200, 300, 400, 500, 600, 650, 700 and 750 tons were applied. Finally a monotonic loading test was conducted till failure of the wall.

Test setup of low-rise shear wall F.29-4



29-5 Material Constitutive Law

29-5-1 Concrete Material Constitutive Model

The constitutive model is formulated on the basis of non-linearity of concrete. Concrete model is a damaged-based model in which a smeared approach is used to model both cracks. This model comprises non-linear compressive behaviour that is capable of modelling hardening and softening. The pre-peak relation is based on the [CEB-FIP Model Code 1990]. The post peak compressive behaviour is linear descending (F.29-5), and the strain at zero stress is $4.7\varepsilon_b$. Also, compressive strength in the direction parallel to the cracks is reduced based on work done by [Vecchio and Collins, 1986] and formulated in the Modified Compression Field Theory. Presence of large transverse strains in cracked biaxially stressed concrete serves to decrease the strength and stiffness of the concrete in the direction of principal compression. A reduction of the compressive strength after cracking in the direction parallel to the cracks is done in a similar way as found from experiments of [Vecchio et al., 1994] and formulated in the Compression Field Theory.

In the analysis, a different function in the form of Gauss's function is used for the reduction of concrete strength shown in F.29-6. The parameters for this function were derived from experimental data of [Vecchio et al., 1994].

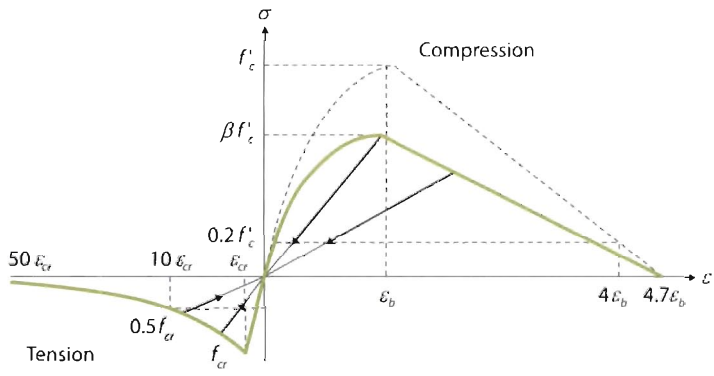
$$f_c'^{ef} = r_c f_c' \qquad \text{E.29-1}$$

$$r_c = c + (1-c)e^{-(128\varepsilon_1)^2} \qquad \text{E.29-2}$$

Thus for zero principal tensile strain there is no strength reduction and for large strain the strength asymptotically approaches value cf_c'. The evaluation of the parameter c is an important factor. F.29-5 shows the uniaxial stress-strain law used for the concrete.

High strength concrete is more brittle with cracks forming through aggregates rather than around them. Thus cracking related damage is more pronounced in high strength concrete. Thus the concrete softening effect is more pronounced in high strength con-

Hysteretic rule for concrete F.29-5



crete. These aspects are taken care in the constitutive model by considering the modification factor to reduce the peak stress of the stress-strain curve of concrete by factor β. The factor suggested by them is given by following relation

$$\beta = \frac{1}{1 + K_c K_f} \qquad \text{E.29-3}$$

Where K_c represents the effect of transverse cracking and K_f represents the dependence on the strength of concrete.

$$K_c = 0.35(-\varepsilon_1 / \varepsilon_2 - 0.28)^{0.8} \qquad \text{E.29-4}$$

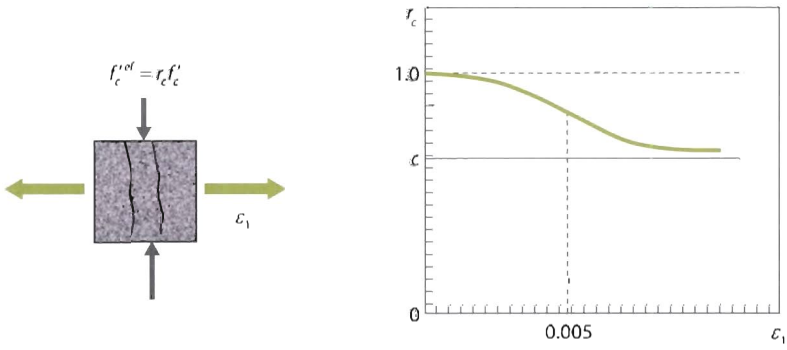
$$K_f = 0.1825\sqrt{f'_c} \qquad \text{E.29-5}$$

Where ε_1 and ε_2 are the principle tensile and compressive strains in the concrete respectively. The maximum value of β will be obtained at peak compressive stress (F.29-5). Thus at peak compressive strain of 0.002 the principal tensile strain will be about 0.0075 as obtained by Vecchio and Collins by testing various shear wall panels having 0.8 % vertical reinforcement [Vecchio et al., 1994]. Thus the value of factor β at the strain value of 0.002 (i.e. strain at peak cylindrical stress) is 0.46. Thus the minimum value of parameter c considered for analysis mentioned in E.29-1 and E.29-2 is 0.46 and its maximum value is 1.

In the analysis, the model also incorporates a biaxial failure criterion as given by [Kupfer et al., 1969]. Under cyclic loading, unloading hysteretic rule is according to origin oriented model. It can be observed from the uniaxial stress-strain diagram (F.29-5) that unloading is a linear function that returns to the origin. Upon reloading, the stress-strain relation follows the unloading path until the last loading point is reached. Also, the tensile response before cracking is considered linear elastic and tension stiffening effects are considered after cracking.

After cracking, the constitutive relation is used in combination with the crack band to model crack propagation based on a crack-opening law and fracture energy. The concrete

Function representing reduction of concrete strength F.29-6



constitutive model considering the FE analysis is based on smeared crack approach. In this analysis smeared fixed crack approach based on non-linear fracture mechanics is used. When equal amounts of reinforcement are provided in the longitudinal and transverse directions, cracks experience minimal rotation, and a fixed crack procedure will provide an accurate simulation. Cracks are formed when the principal tensile stress exceeds the tensile strength of the concrete. In the fixed crack model [Cervanka, 1985; Darwin and Pecknold,1974], once the crack forms, the crack direction is defined by the direction of principal stress. The direction remains the same upon continued loading. Also, the shear modulus is reduced to represent the reduction in shear stiffness due to the crack opening and the crack shear stresses are considered.

29-5-2 Reinforcement Constitutive Relations

Reinforcement is modelled as discrete using truss elements in wall and smeared in top and bottom beams. For smeared reinforcement it is considered as a component of composite material. In either case, the reinforcement stress-strain relationship is defined by the bilinear law in which elastic-plastic behaviour is assumed. The discrete reinforcement elements of the wall are fully bonded to the surrounding concrete with limited prescribed bond strength (cohesion stress). Slippage occurs if the cohesion stress rises above the bond strength. Bond-slip relation is considered using CEB-FIP model code 90 bond model.

29-6 Analysis and Experiments on Mid-Rise Shear Wall

29-6-1 Moment Curvature Relationship

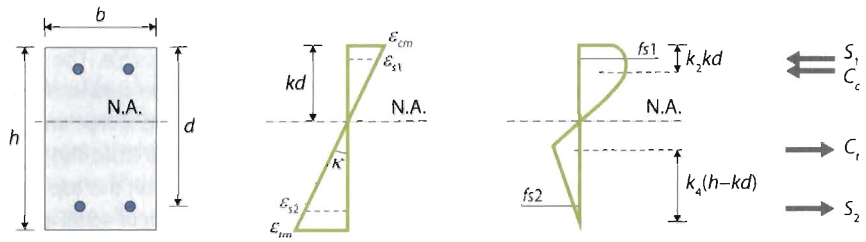
Mid-rise shear wall failure of the shear wall is based on flexural yielding and the evaluation of flexural strength of the shear wall. The shear capacity of the shear wall is quite higher than the flexural strength. For concrete in uniaxial compression the stress-strain relation covering compression softening as shown in F.29-5 is used. The steel is assumed as elastic perfectly plastic.

The normal force, N and moment, M equilibrium conditions for the shear wall using stress-strain distribution across the section shown in F.29-7, are written as follows

$$N = k_1 f_c' bkd + \sum_{j=1}^{8} \sigma_{sj} A_{sj} - k_3 f_t' b(h - kd) \qquad \text{E.29-6}$$

$$M = k_1 f_c' bkd\left(\frac{h}{2} - k_2 kd\right) + \sum_{j=1}^{8} \sigma_{sj} A_{sj}\left(\frac{h}{2} - d_j\right) + k_3 f_t' b(h - kd)\left[\frac{h}{2} - k_4(h - kd)\right] \qquad \text{E.29-7}$$

Stress-strain relation across the cross section of the wall F.29-7



f_c' is the compressive strength of concrete, f_t' is the tensile strength of concrete, σ_{sj} is the stress in steel in the j-th layer and d_j is the distance of the steel layer from top fibre. Where parameter k_1 defines the average compressive stress and the resultant force acts at $k_2 kd$ below the compression face. Similarly k_3 denotes the resultant of tensile stress in concrete and the force acts at distance of $k_4(h-kd)$ from tension face.

The parameters k_1, k_2 and k_3, k_4 are described by expressions given below

$$k_1 = \frac{\int_0^{\varepsilon_{cm}} \sigma_c d\varepsilon_c}{f_c' \varepsilon_{cm}}, \quad k_2 = 1 - \frac{\int_0^{\varepsilon_{cm}} \varepsilon_c \sigma_c d\varepsilon_c}{\varepsilon_{cm} \int_0^{\varepsilon_{cm}} \sigma_c d\varepsilon_c} \qquad \text{E.29-8}$$

$$k_3 = \frac{\int_0^{\varepsilon_{tm}} \sigma_c d\varepsilon_c}{f_t' \varepsilon_{tm}}, \quad k_4 = 1 - \frac{\int_0^{\varepsilon_{tm}} \varepsilon_c \sigma_c d\varepsilon_c}{\varepsilon_{tm} \int_0^{\varepsilon_{tm}} \sigma_c d\varepsilon_c} \qquad \text{E.29-9}$$

The curvature of the shear wall at any moment capacity is given by

$$\kappa = \frac{\varepsilon_{cm}}{kd} \qquad \text{E.29-10}$$

In order to calculate the moment curvature relation, for a given axial load N a succession of values of ε_{cm} increasing in small increments is considered and for each value, kd is obtained using E.29-6. The curvature is then obtained from E.29-10 and finally the moment for the particular value of curvature is obtained from E.29-7. For the shear wall, $b = 200$ mm, $h = 1560$ mm, $A_{sj} = 157$ mm^2 for $j = 1$ to 8, $d = 1520$ mm, $f_c' = 39.1$ MPa, $f_t' = 3.08$ MPa, $E_c = 3.586 \cdot 10^4$ MPa, $f_y = 500$ MPa, $E_s = 2 \cdot 10^5$ MPa. The moment curvature relation is obtained and the maximum displacement of the shear wall is calculated for particular load from moment curvature relationship using the principle of virtual work thus load displacement relation is obtained and the peak load is obtained as 195 kN.

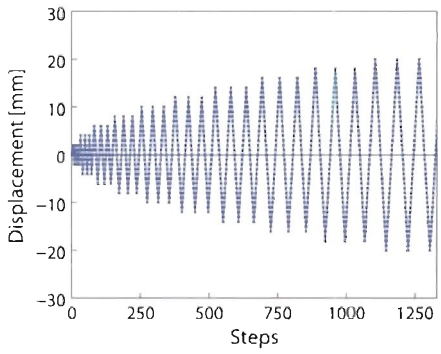
29-6-2 FE Analysis

2D non-linear, FE analyses [ATENA, 2006] are carried out on the RC wall. The testing boundary conditions are simulated in the analyses as accurately as possible. The horizontal and vertical displacement at the base of the wall is assumed to be zero in the FE model. The vertical translational degree of freedom at top slab right end is free and incremental horizontal displacements are applied at that node of top slab from the right towards left direction. The vertical load of 8.5 tons is applied uniformly on the top slab. The concrete is modelled with the non-linear model with a cubic strength of 46 MPa. The steel is modelled as reinforcement bars with a bilinear elastic-plastic model with a yielding strength of 500 MPa. The analysis is carried out for monotonic loading and pseudo-static cyclic loading. Three cycles of each value of maximum lateral displacements will be applied starting with 0.4 mm displacement as cracking occurred at 0.4 mm from analysis for monotonic loading. The loading is applied in incremental displacement with increment of peak displacement of 2 mm displacement after every three cycles till failure. The loading history for pseudo-static cyclic loading is shown in F.29-8. The load deflection relationship obtained for monotonically loading cyclic load is shown in F.29-11. It is observed that the monotonic load deflection characteristics envelopes the cyclic characteristics. It is observed that the ultimate load taken by the wall is 185 KN and the displacement at ultimate load is 16 mm. The drift failure, i.e. at 85 % of ultimate load, is 39 mm (1.3 %) from the analysis for monotonic loading. It is observed from the analysis that the deflections corresponding to the performance states of first cracking, yielding of reinforcement and ultimate state are 0.4 mm, 4 mm and 16 mm respectively. F.29-9 shows the crack pattern in the wall at ultimate load. It is observed from the figure that failure of the shear wall is due to bending loads and flexural cracks are seen in the FE model.

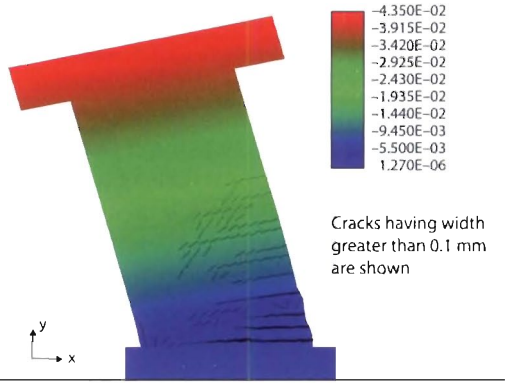
29-6-3 Experimental Programme

Three identical shear wall specimens, considered to represent the critical structural elements with a rectangular cross-section, and the average 28 days strength of concrete

Loading history for pseudo-static cyclic loading F.29-8



Deflected shape of the wall and distribution of cracks at failure F.29-9



obtained was 46 MPa. Tension tests were carried out on six HYSD reinforcement bars with a yield strength of 415 Mpa and average ultimate tensile strength of 555 MPa.

Methodology of Tests

One specimen was subjected to slow monotonic load to obtain the backbone load displacement curve. In order to simulate loading sequence that might be expected to occur during an earthquake, horizontal cyclic loading history was adopted for other two wall specimens. The torsional mode of the wall is prevented by supporting arrangement made for the top slab using rollers as shown in F.29-2. The horizontal load was applied at a quasi-static rate in displacement controlled cycles with a hydraulic actuator having 500 KN capacity through a load cell. Displacements were applied in incremental fashion. Initially one cycle each of 2 mm and 4 mm peak displacement were given till cracking occurred. Then three cycles each of 6 mm, 8 mm, 10 mm, 15 mm, 20 mm, 25 mm, 30 mm, 40 mm peak displacements were given in the loading programmes used for the tests in terms of horizontal load v/s cycles. Strain gauges were used for measuring strains at 16 locations on vertical reinforcement. Extensometers were used at seven locations on the surface of concrete for monitoring crack openings. Laser sensors were used in monitoring the in-plane horizontal displacements at top slab level (height 1560 mm above the foundation) of the wall. In order to ensure that the foundation is fixed to the laboratory's strong floor, vertical displacement of the top of the foundation was measured. The measured values of load, horizontal displacement and strains were recorded by a computer data logger.

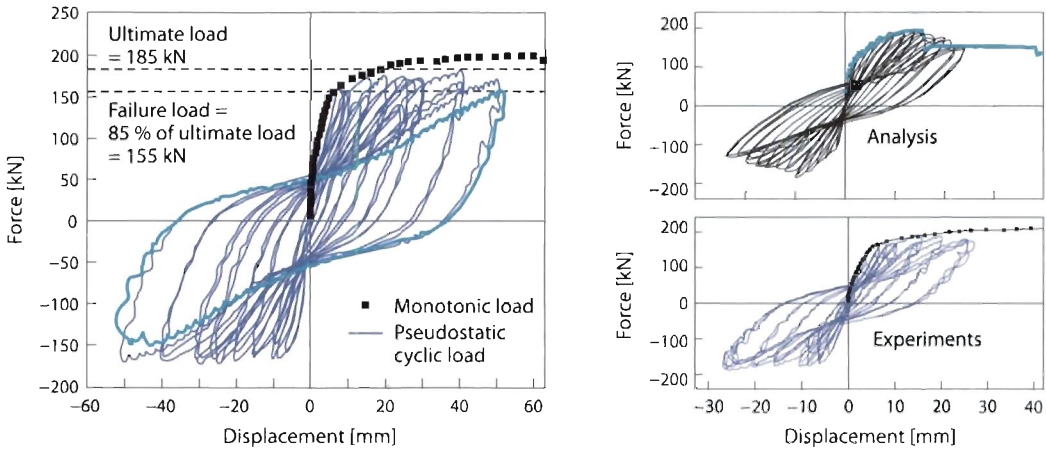
Results of the Tests

For all three wall specimens, flexural cracks initially appeared near the bottom part of the tensile zone of the wall at a load of 80 kN and horizontal displacement of 3 mm. Yielding of the main reinforcement occurred at about 5 mm lateral displacement and strain in longitudinal reinforcement in the walls near bottom reached 2000 micro strain. For specimens subjected to cyclic load at the cyclic lateral displacement of 6 mm flexural cracks progressed and peak load of 155 kN was reached. As the lateral displacement approached 15 mm on ultimate load of 185 kN was reached and significant inclined cracks

Crack pattern in the wall for cyclic load (left) and crushing of concrete in the compression zone of the wall and buckling of main bars (right) F.29-10



Force displacement loop (experiments) (left) and comparison of hysteresis (right) F.29-11



were formed (F.29-10). These cracks continued to penetrate deeply into the centre of the wall towards the compressive zone. These cracks diagonally progressed down and the crack pattern for the two specimens subjected to cyclic load is shown in F.29-10. At a lateral displacement of 40 mm, the width of the major flexural cracks already developed increased. At this displacement which was just prior to failure, few vertical cracks formed in the compressive zone and the concrete cover at the lower compressive edge of the wall spalled off, which finally led to failure of the compressive zone of the wall at 50 mm lateral displacement. The final failure of the wall occurs due to crushing of concrete in the compression zone of the wall and buckling of main reinforcement at the bottom between the two stirrups. This type of failure occurs at both sides at the bottom corners. F.29-10 illustrates the representative mode of failure of the walls which shows the buckling of the main reinforcement in between two stirrups.

F.29-11 illustrates the lateral load versus top displacement curve established from the tests for one of the specimen subjected to cyclic load. It is observed that the average secant stiffness at yield was 30 kN/mm and was reduced at ultimate load. It is clear that the stiffness is gradually decreased for all specimens due to formation of cracks and yield of steel. The ultimate load of the wall is 18.5 tons and the ultimate drift obtained is 50 mm from tests. Displacement at failure load of 85 % of ultimate is 50 mm. The displacement ductility of the wall which is the capacity of the wall to deform beyond its elastic limit is obtained as 10 from the experiment. The force displacement curve obtained from FE analysis is compared with that obtained from experiments in F.29-11. It shows that the experimental and analytical load displacement curve results are in good agreement. However the instabilities, such as rebar buckling, are typically not considered in models. Hence the exact failure displacement of the wall obtained in experiments is not captured in analysis.

29-6-4 Discussions and Inference

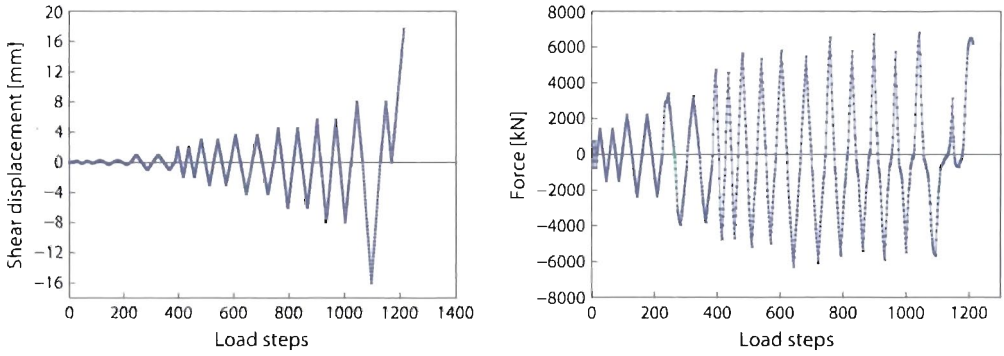
The crack patterns and failure modes of the walls indicate that the wall capacity is affected by the flexural as well as the shear strength of the specimen. This caused considerable reduction in the strength, stiffness and energy dissipation of the specimens. The analysis force displacement relation predicts the test accurately up to a horizontal deflection of 25 mm. From the experiments, the ultimate load is obtained as 185 kN and ultimate drift is obtained as 1.6 % which is more than the drift for collapse prevention performance level of 0.75 % stated in [FEMA-356, 2000]. An analysis of short shear wall tested in WP1 tests is carried out and evaluation force displacement characteristics are presented henceforth.

29-7 Analysis of Stiff Shear Wall (IRIS – WP1 Tests)

29-7-1 Finite Element Model

In complex 3D-RC shear wall slab structures, concrete with material non-linearity is modelled using four noded iso-parametric 2D plane quadrilateral elements for wall, top and bottom beams. Steel is modelled in discrete form of truss element for wall and smeared form in the top and bottom beams. The FE model of a shear wall with a width of 3 m, a height of 1.2 m and a thickness of 0.4 m is made. The RC wall has been investigated through 2D non-linear FE analyses. Concrete strength f_{ck} is considered as 54 Mpa. Steel strength is 500 Mpa. During the experiment, the wall was fixed at the base and the test was conducted for pure shear case, however, vertical deformations were allowed to take place. Also the axial load applied on the wall was 60 tons.

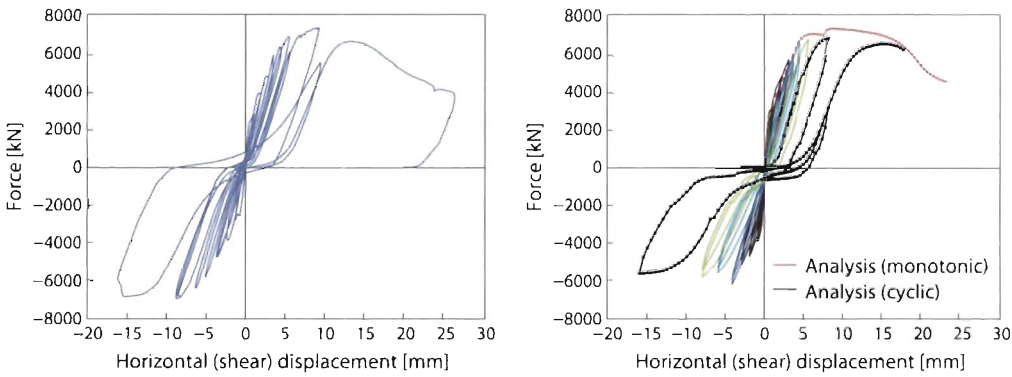
Shear displacement v/s steps (analysis) (left) and shear force v/s steps (analysis) (right) F.29-12



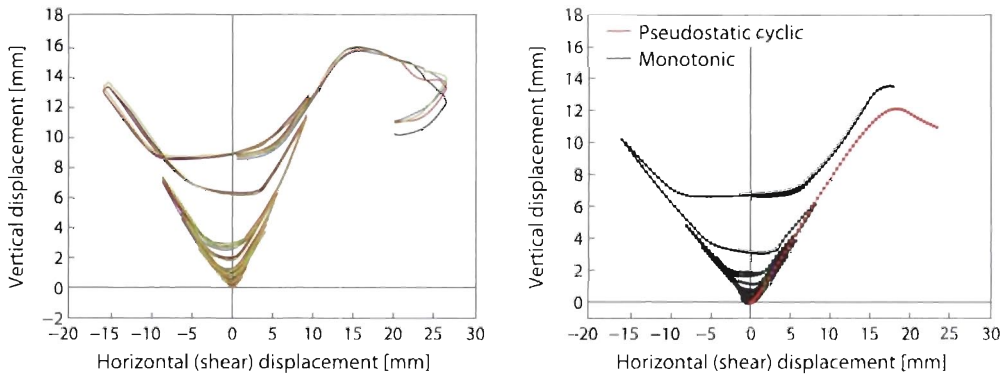
29-7-2 FE Analysis

The exact experimental boundary conditions are simulated in the analysis and the realistic constitutive model described before is used for the concrete. The model is fixed in the horizontal direction and vertical direction at all the nodes of bottom beam. The nodes of the top beam are free. The horizontal displacements are applied at the four nodes of the top beam in incremental fashion (displacement controlled analysis). The vertical load is applied on the wall on junction of the top beam and wall along line so that it creates the same compressive stresses in the wall when the uniformly distributed load (V = 60 tons) is applied on the top beam. Horizontal displacements are applied at the top slab incrementally in cyclic manner. Steel plates with less (fictitious) density are attached to three sides of the top slab so that there is no local failure in the top slab due to point load application. The extension of the steel plates as present in experiments is modelled. Non-linear analysis is carried out for cyclic load on the wall with constant axial load of 60 tons. Analysis is carried out according to the loading cycles given in the experiment till failure of the wall, i.e. the load drops to 85 % of ultimate peak load. The shear displacement v/s steps and shear force taken by wall v/s steps is shown in F.29-12.

Shear force v/s shear displacement of the wall (test and analysis) F.29-13



Vertical displacement v/s shear displacement of the wall (test and analysis) F.29-14



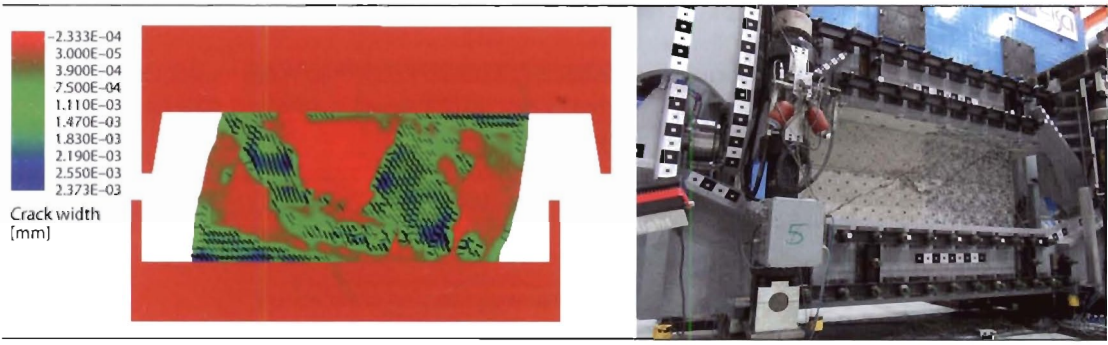
29-7-3 Discussion of Results

The comparison of experimental and analytical load displacement diagram for monotonic load and cyclic load is shown in F.29-13. The comparison of experimental and analytical vertical displacement at the top ends of the top beam v/s the shear displacements of the wall are plotted in F.29-14. The vertical displacement of the wall at failure is obtained from analysis as 14 mm at failure (i.e. at shear displacement of 17.5 mm). The experimentally obtained vertical displacement is 16 mm at failure. Thus there is twelve per cent difference in the analysis and actual experimental vertical displacement. However, the overall nature of the graph showing the relation of horizontal and vertical displacement from analysis is in good agreement with the tests.

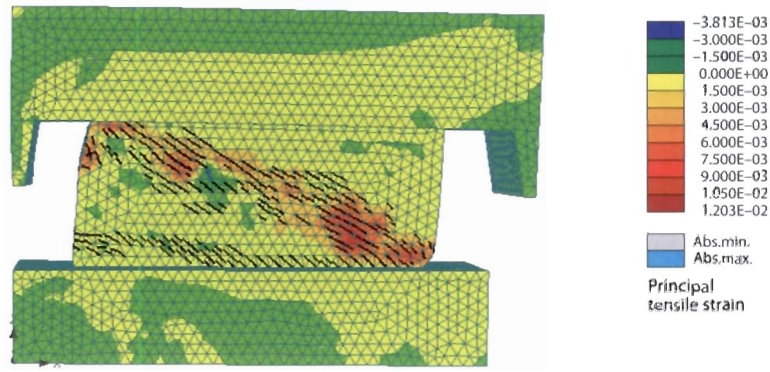
From the analysis it is seen that the first cracks with a crack width of 0.16 mm are observed at 0.8 mm shear displacement and 300 tons horizontal load of the wall. The same is observed in the tests. Analysis showed that at 3.0 mm shear displacement of the wall the longitudinal steel reaches yield strain of 0.002 and maximum principle tensile strain of 0.0065 is reached in the wall. It is observed that at 8 mm shear displacement the wall yields with constant peak load of 7000 kN. Most of the longitudinal reinforcement yields at this load and the maximum principal tensile strain obtained in wall at ultimate load is 0.012 as obtained from analysis. The final failure of the wall is due to concrete crushing after the reinforcement in the wall yields. The maximum strain is observed in the longitudinal steel near the bottom side location. The crack pattern obtained from analysis at the failure of the wall is shown in F.29-15. The maximum crack width at failure is 3.7 mm. The crack pattern observed at the end of the WP1 test is shown in F.29-15. The peak load and displacements from analysis and tests are in good agreement at each step.

However the crack pattern in 2D analysis is not in complete agreement with the test. 3D analysis of the shear wall is then performed for monotonic load using 3D solid wedge elements. The crack pattern obtained in 3D analysis and the principal tensile strain distribution is shown in F.29-16. It is observed that the crack pattern in the wall at failure obtained from 3D analysis is in good agreement with the test results. The force displacement diagram for monotonic loading from 2D analysis, 3D analysis and experiments is compared and is found to be in good agreement. It is observed that 3D analysis monotonic loading gives a fair estimate of crack pattern in the wall and the force displacement diagram.

Crack pattern in the wall at failure: 2D analysis (left) and experiments (right) F.29-15



Crack pattern in the wall at failure: 3D analysis F.29-16



29-8 Fragility Analysis of Mid-Rise Shear Wall

A schematic of the shear wall is shown in F.29-17. The estimation of the maximum load for failure in the shear wall under discussion can be done as follows. Considering the state of stress (horizontal load *Vu*, vertical load *P*) in which the concrete at the bottom is under crushing strain (e_u). The strains in the reinforcement bars is shown in F.29-17. The location of the neutral axis (x_u) is found iteratively by solving E.29-11.

$$P = 0.54 f_{ck} B x_u + \sum A_{st} f_{sc_i} - \sum A_{st} f_{st_j} \qquad \text{E.29-11}$$

P = vertical load
f_{ck} = crushing strength of concrete
B = width of the section
x_u = location of neutral axis
A_{st} = area of the reinforcement cross section
f_{sc_i} = stress in the i-th reinforcement bar under compression
f_{st_j} = stress in the j-th reinforcement bar under tension

Once the location of neutral axis is obtained, the maximum horizontal load (*Vu*) the wall can withstand is estimated by moment balance. Thus the limit state for structural reliability calculation is given by E.29-12.

$$g = Vu(x_i) - V \qquad \text{E.29-12}$$

V = applied shear force
$Vu(x_i)$ = shear capacity of the shear wall, function of variables x_i

$x_1 = f_{ck}$ = crushing strength of concrete
$x_2 = e_u$ = maximum strain in concrete under compression
$x_3 = a_{st}$ = area of the reinforcement bar
$x_4 = P$ = vertical load on the shear wall
x_5 = width of the wall
x_6 = length of the wall
x_7 = height of the wall
x_8 = stress-strain curve of the reinforcement bar

The variables treated as the random variables are f_{ck}, e_u and a_{st} for estimating the fragility of the shear wall. The definition of these variables is given below

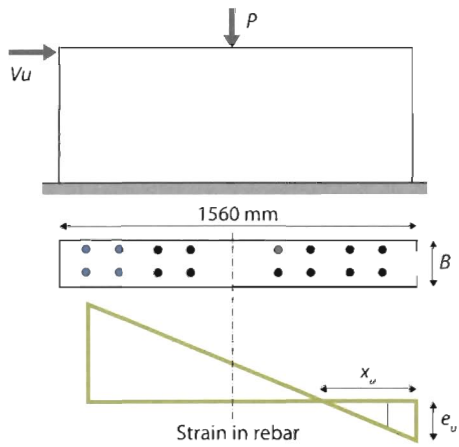
	Distribution	Mean	Standard deviation
f_{ck} [N/mm^2]	Lognormal	47.49	4.96
e_u	Lognormal	0.0035	0.00063
a_{st} [mm^2]	Normal	157.1	7.855

The distribution for the crushing strength is estimated from the actual tests conducted on the concrete specimens. Total data is available for 43 samples. The goodness of fit testing showed that the lognormal distribution is acceptable for these data. A distribution plot of the data is shown in F.29-18.

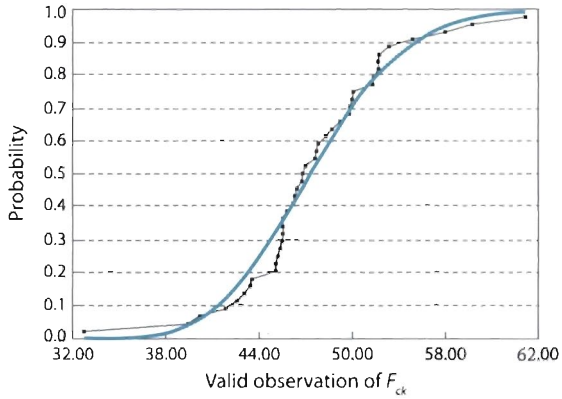
The distribution and the coefficient of variation for e_u is the same as that considered by [Klein and Henkel, 2011]. The distribution of a_{st} is assumed. The scatter in the values of the tensile properties of the steel reinforcement bar is not considered. Full stress-strain curve of the steel is used for estimating the limiting value of the shear load (F.29-19).

The scatter in the stress-strain curve can be modelled if it can be fitted in form of a power law, e.g. [Rahman, 1997]. In this case, a good fit in these terms could not be obtained, hence it is considered as a deterministic design variable.

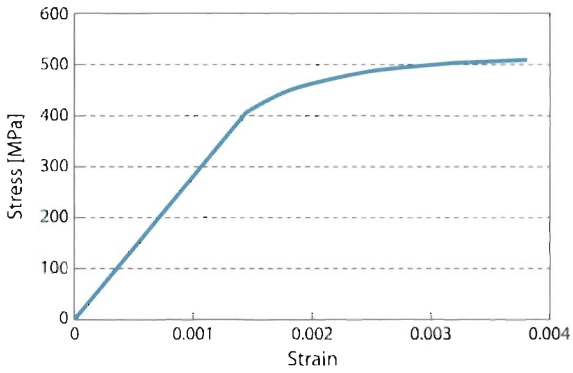
Schematic of the shear wall F.29-17



Distribution plot for F_{ck} data F.29-18



Stress-strain curve for Fe 510 F.29-19



The confidence levels on the fragility curves are obtained by considering the applied shear force to be a lognormal random variable with a coefficient of variation of 20%. Two methods are used to estimate the fragility curves.

Method 1

This method is similar to the method described in [EPRI, 1994]. This method is known as scaling method and assumes lognormal distribution for all random variables. The probability of failure for the given value of shear force V is given by E.29-13.

$$P(V) = \Phi\left\{\frac{\ln\left(\frac{V}{Vu_{med}}\right)}{\beta_{Vu}}\right\} \qquad \text{E.29-13}$$

$\Phi(\bullet)$ = standard normal distribution function
Vu_{med} = median value of the capacity of the wall
β_{Vu} = logarithmic standard deviation of Vu

The median value of Vu is estimated by keeping all variables at their median values. The β_{Vu} is estimated by the following procedure.

For each x_i, if the x_i is a strength variable, β_i is estimated using E.29-14

$$\beta_i = \ln\left(\frac{Vu_{med}}{Vu[\hat{x}_i - \sigma_i]}\right) \qquad \text{E.29-14}$$

$\hat{x}_i$ = median value of x_i
σ_i = standard deviation of x_i

If x_i is a demand variable then β_i is estimated using E.29-15.

$$\beta_i = \ln\left(\frac{Vu[\hat{x}_i + \sigma_i]}{Vu_{med}}\right) \qquad \text{E.29-15}$$

$\hat{x}_i$ = median value of x_i
σ_i = standard deviation of x_i

The β_{Vu} is obtained from E.29-16.

$$\beta_{Vu} = (\sum \beta_i^2)^{1/2} \qquad \text{E.29-16}$$

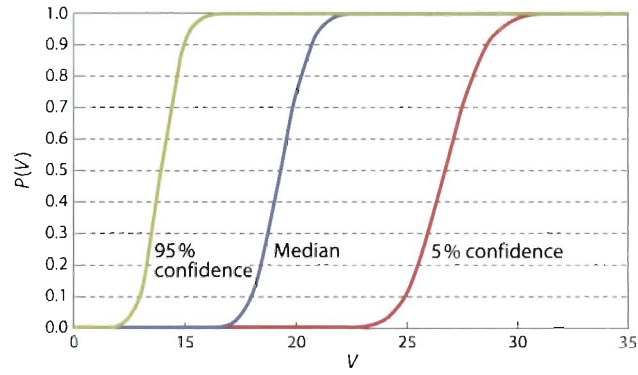
The confidence bounds are obtained using the 20% coefficient of variation on the V which is assumed to be lognormal. F.29-20 shows the fragility curve obtained using the scaling method.

The failure load obtained from tests is 18 tonnes. This corresponds to a probability of failure of 0.1 on the median curve. If the estimation model was perfect i.e. without any modelling uncertainty, then this should correspond to a probability of failure of 0.5 on the median curve. These curves help in arriving at the design value for V for this shear wall. The design value used is High Confidence Low Probability of Failure (HCLPF). This value corresponds to the 95% confidence of a 5% probability of exceedance. Thus, the design value is arrived for a value of V on curve 1, which corresponds to 5% probability of failure. This is shown in F.29-21. The HCLPF value estimated is 12.74 tonnes.

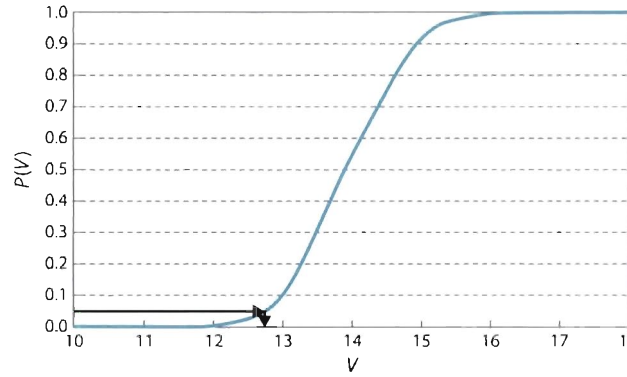
Method 2

The probability of failure is obtained using the Monte Carlo simulation method. The random variables f_{ck}, e_u and a_{st} are simulated and then entered in E.29-7 for the given value of V. A count is maintained of the failure. This simulation is performed a number of times to estimate the probability of failure. The error in probability estimation is kept below 10%. Structural reliability software COMREL [STRUREL, 2003] was used to estimate the probability of failure. The fragility curve for the median value, 95% confidence level and 5% confidence level was estimated. The fragility curve is shown in F.29-22.

Fragility curves using scalability method F.29-20



Estimation of design load using HCLPF value F.29-21



A comparison of the two methods for the median value of V is shown in F.29-23. It is seen that there is no significant difference in the curves obtained from the two methods. The HCLPF value estimated is 12.83 tonnes.

29-9 Conclusions

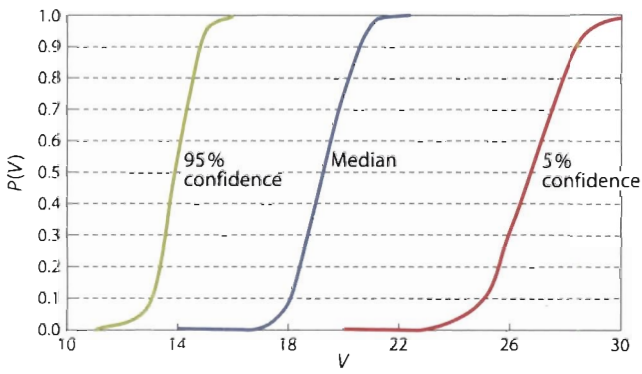
The shear wall is designed for an earthquake load of 0.2 g peak ground acceleration using the IS code. The top mass of 16.5 tons lumped on the shear wall is subjected to 0.4 g horizontal acceleration and the horizontal load at the top of shear wall will be about 7 tons. Thus deterministically the shear wall is designed for a horizontal load of 7 tons. However it is observed analytically and experimentally that the shear wall carries a load up to 18.5 tons. Thus the over-strength factor available for the wall is 2.65.

This reliability based model is applied to the shear walls used in the nuclear industry. The scaled shear wall is modelled analytically as well using the Finite Elements. The uncer-

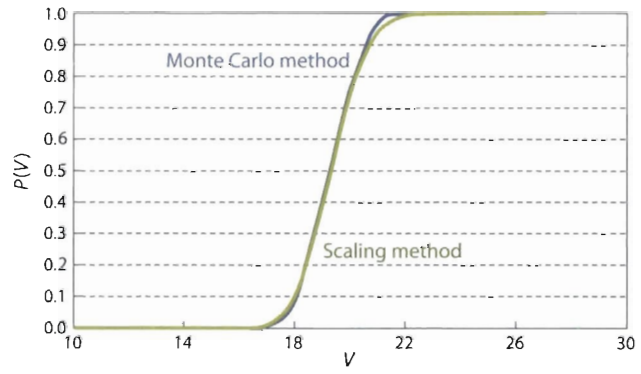
tainty in the design parameters is modelled using the probability distribution function. The model is validated by conducting scaled tests on this wall. The uncertainty propagation across the modelled behaviour is performed using the principles of structural reliability. The outcome of this estimation is the fragility curve. This fragility curve is used to estimate the safe design load for the shear wall. This load for the shear wall studied is 12.8 tons. This the design load is arrived using the sound logic of probabilistic analysis rather than a deterministic factor of safety given in the design code. This study suggests a basis for designing shear walls based on the probabilistic principles.

Non-linear finite element analysis of shear wall tested in WP1, IRIS project is described in detail. The shear wall exhibited ductile load deformation response. Analysis showed that the failure mode involved crushing of concrete occurring after yielding of longitudinal reinforcement. The load deformation characteristics of tests and analysis are also in good agreement with each other. The crack pattern obtained from 3D analysis is in good agreement with test results. In general the analysis considering accurate modelling of compression softening phenomenon of the concrete gives precise representation of the experimental results.

Fragility curves using Monte Carlo simulation F.29-22



Comparing the median fragility curves F.29-23



References

ATENA, 2006. *FE Software for Nonlinear Analysis of Concrete Structures.*

Cervanka, V., 1985. *Constitutive Model for Cracked Reinforced Concrete.* ACI Journal, November–December 1985, 82(6):877–882.

Darwin, D. and Pecknold, D. A. W., 1974. *Inelastic Model for Cyclic Biaxial Loading of Reinforced Concrete.* Civil Engineering Studies, University of Illinois.

Ellingwood, B. and Hwang, H., 1985. *Probabilistic Descriptions of Resistance of Safety-Related Structures in Nuclear Plants.* Nuclear Engineering and Design 88:169–178.

EPRI, 1994. *Methodology for Developing Seismic Fragilities.* Electric Power Research Institute, EPRI TR–103959.

Farrar, C. R. and Baker, W. E., 1990. *Stiffness and Hysteretic Energy Loss of a Reinforced-Concrete Shear Wall.* Experimental Mechanics 30:95–100.

FEMA-273. *IBC Handbook-Structural Provisions.*

FEMA-356, 2000. *Prestandard and Commentary for the Seismic Rehabilitaion of Buildings.*

Kazaz, I., Gulkan, P. and Yakut, A., 2006. *Numerical Simulation of Dynamic Shear Wall Tests: A Bench-Mark Study.* Computers and Structures 84:549–562.

Klein, D. and Henkel, F.-O., 2011. *Calculations of Seismic Fragilities of Concrete Shear Walls by Use of the Methods of Structural Reliability and Safety Analysis.* Proceedings, Post-SMiRT Conference Seminar on: Advances in Seismic Design of Structures, Systems and Components of Nuclear Facilites, 14–15 November, BARC, Mumbai, India, 286–294.

Kupfer, H., Hilsdorf, H. K. and Rusch, H., 1969. *Behavior of Concrete under Biaxial Stress.* ACI Journal, August, 66(8):656–666.

Lopes, M. S., 2001a. *Experimental Shear-Dominated Response of RC Walls Part I: Objectives, Methodology and Results.* Engineering Structures, 23:229–239.

Lopes, M. S., 2001b. *Experimental Shear-Dominated Response of RC Walls Part II: Discussion of Results and Design Implications.* Engineering Structures, 23:564–574.

IS 13920, 2002. *Code of Practice, Ductile Detailing of Reinforce Concrete Structures Subjected to Seismic Forces.*

CEB-FIP Model Code 1990. Comittee Euro-International du Beton, Bulletin d'information 195, 196, Mars.

Rahman, S., 1997. *Probabilistic Fracture Analysis of Cracked Pipes with Circumferential Flaws.* International Journal of Pressure Vessel & Piping 70:223–226.

Salonikios, T. N., 2002. *Shear Strength and Deformation Patterns of R/C Walls with Aspect Ratio 1.0 and 1.5 Designed to Eurocode 8 (EC8).* Engineering Structures 24:39–49.

STRUREL, 2003. *A Structural Reliability Analysis Program System.* RCP Consult GmbH, Munich, Germany.

Tasnimi, A. A., 2000. *Strength and Deformation of Mid-Rise Shear Walls under Load Reversal.* Engineering Structures 22:311–322.

Vecchio, F. J. and Collins, M. P., 1986. *Modified Compression-Field Theory for Reinforced Concrete Beams Subjected to Shear.* ACI Journal, March–April 1986, 83(2):219–231.

Vecchio, F. J., Collins, M. P. and Aspiotis, J., 1994. *High Strength Concrete Elements Subjected to Shear.* ACI Journal, July–August 1994, 91(4):423–433.

30

IRIS Demonstration – Hungary 2011

Authors:
Barbara Theilen-Willige
Helmut Wenzel
Laszlo Weisz
Antal Papp
Gábor Sárossy
Imre Árvai

Motivation

Large projects produce a major number of individual results. It is desirable to try and test the individual approaches in a close-to-reality demonstration. How the interfaces work and which gaps are to be filled in future is to be determined.

Main Results

In a large exercise on earthquake preparedness in central Hungary (IRIS 2011) the application of the IRIS technologies has been tested over a period of three days using live satellite images and employing 500 forces of civil protection. A very successful exercise has been delivered.



30-1 Introduction

The threat of natural hazards impacting chemical facilities and infrastructures with the subsequent release of hazardous substances has been recognized as an emerging risk. Accidents with hazardous-substance releases were often triggered by natural events. There is increasing awareness of the threat that natural hazards and disasters can pose to chemical facilities and critical infrastructures.

Industrial accidents triggered by natural events, such as e.g. earthquakes, floods, lightning etc., are referred to as "Natech" accidents. Natech accidents have occurred in relation to natural hazards and disasters and have resulted in the release of hazardous substances leading to fatalities, injuries, environmental pollution and economic losses [Krausmann et al., 2011]. One of the principal problems of most Natech accidents is the simultaneous occurrence of a natural disaster and a technological accident, both of which require simultaneous response efforts in a situation in which lifelines needed for disaster mitigation are likely to be unavailable. The catastrophic events in March 2011 in Japan have demonstrated this. Natech risk differs from technological or natural risk as its multi-hazard nature requires an integrated approach to risk management.

Industrial facilities and critical infrastructures, as well as individual production or service areas within a facility, are subject to different levels of risk from natural events. Human error, technical failure, terrorism or criminal acts have to be taken into account as well. Areas at particular risk include networks, buildings, production, extracting and processing plants and non-electronic data records [Federal Ministry of the Interior, 2005].

Proper mitigation of damages following disastrous events highly depends on the available information and the quick and proper assessment of the situation. Therefore a standardized, reference data base should be available of industrial facilities with environmental impact in case of accidents and of critical infrastructures, in order to improve the preparedness and mitigation management. The better a pre-existing reference database of an area at risk is prepared and elaborated, the better a crisis-management can react in case of hazards.

GeoInformationSystems (GIS), with the capabilities of data acquisition, storage, retrieval, manipulation, analysis and visualization, have been used for decades for supporting spatial decision-making in the scope of a multiple criteria analysis and GIS integrated spatial analysis. This was the reason to include these methods into the IRIS-project (IRIS-Integrated European Industrial Risk Reduction System). Multi-criteria decision-making methods such as weighted, linear combination of causal factors and information from environmental and economic factors form an essential input into the IRIS-project The EU-funded IRIS- project is led and driven by the industry to consolidate and generate knowledge and technologies which enable the integration of new safety concepts related to technical, human, organizational and cultural aspects. The concept of IRIS is to focus on diverse industrial sector's main safety problems as well as to transform its specific requirements into integrated and knowledge-based safety technologies, standards and services.

In the framework of the IRIS demonstration a large civil protection exercise based on innovative information collection and risk assessment was carried out in Central-Hungary assuming different scenarios of accidents in May 2011. For one of the scenarios - simulating an accident in a gas plant – space technology was implemented.

30-1-1 Assumption of Scenario 1 – Chemical Accident in Pincehely, Tolna

Developing predictions of the trajectories and spreading of contaminants following environmental accidents with cross-border implications is an urgent need. Therefore dispersion models have to be installed and improved continuously. One of the ways to achieve this improvement is to monitor the influence of weather and of topography by the evaluations of satellite imageries.

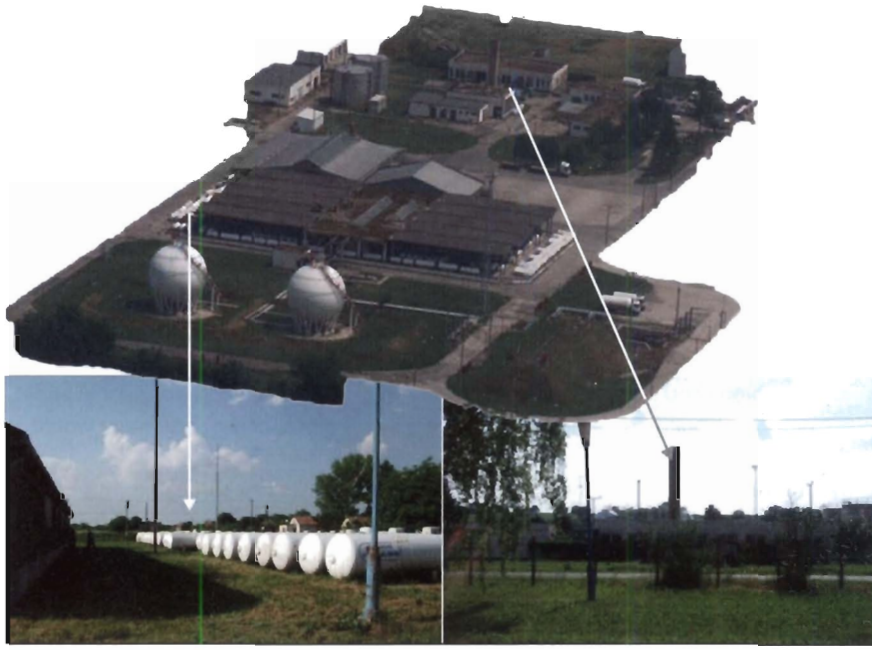
Scenario:

- // Due to an earthquake the pipelines of one of the main containers at the gas filling station of PRIMAGAZ got damaged. Three tons of PB gas got out and spread to the air according to direction of the wind.
- // Assuming wind directions towards the town of Pincehely, explosions could happen. Some buildings (among others the mayor's office) of the settlement would have been damaged.
- // For the chemical accident in Pincehely a total blackout was simulated. This meant that no communications would be possible with normal means. Due to this in the first hour of the exercise teams involved in rescue were able to communicate only with each other. The communication between the county emergency centre and the national HQ of disaster management was established on shortwave by radio-amateurs.

RapidEye satellite scene of Pincehely and topographic map F.30-1



PRIMAGAZ plant in Pincehely, Tolna F.30-2



30-1-2 Objectives

Introduction of actual condition information from various sources and adaptation of the crisis management plan accordingly.

- // Proof that updated information can be usefully managed to improve the civil protection management
- // The main scope of the study is to provide a better understanding, insight and proof that or if the RapidEye space technology works on demand.
- // Integration of the thus provided information into the IRIS Risk Reduction System.

The figures provide an overview of the position of the chemical plant and images taken in the area (F.30-1 and F.30-2).

30-2 Preparation of the Experiment

The toxic cloud was simulated by markers (five markers consisting of 30 × 30 m white sheets, alternate marker: three smoke generators). The smoke generators were placed just near marker number 4 on Monday, just near marker number 5 on Tuesday. The paper sheets were distributed on Monday, 23 May 2011, as well on Tuesday, 24 May 2011, by the VCE- and DTCDM-team, in order to test their visibility on RapidEye data.

The simulation of the cloud in Pinchely lasted about one hour. It was performed on Monday, 23 May from 12:00 to 12:30, and on Tuesday, 24 May 2011.

The intention was to monitor the development and distribution of the toxic cloud based on information from RapidEye satellite imageries and the area reconnaissance team. Information on their position was chequed as well by aerial surveillance. Under consideration of the weather conditions a 24 hour scenario was computed, which was the basis for the simulated decisions on the civil protection teams. Parallel to the RapidEye imageries aerial images were taken at the same time.

The images taken from the airplane by Sebastian Thöns and the VCE team provide an overview of the position of the markers in the landscape.

An important point was the cloud cover during the experiment, as the visibility of the artificial cloud and the markers was depending on the distribution and degree of the cloud cover. Therefore the weather conditions were monitored.

A field excursion was carried out to Pincehely, in order to monitor the weather, land use and vegetation status and to see disaster preparedness measurements of the civil protection institutions.

Artificial cloud and marker (point 4, 23 May 2011) F.30-3



30-3 Meteorological Conditions from 23 to 24 May 2011

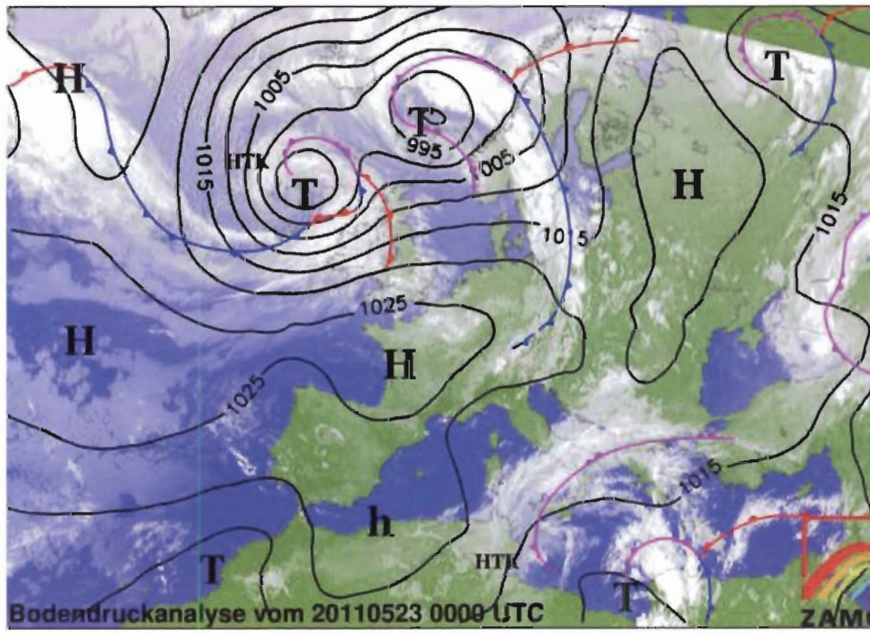
The spread of toxid clouds is not only generated by a source of pollutants, but also by the meteorological conditions under which those pollutants are released. Therefore it is important to know what factors increase the potential for the dispersion of air pollution so that modifications to risk management can be made. For example: calm, cold atmospheric conditions during the cooler months lower the dispersion. In these situations, cold air inversions develop, trapping any pollutants released close to the ground.

Meterologic data were collected and stored as prerequisite for the evaluation of the cloud experiment. High-pressure systems were influencing and dominating the weather during the experiments.

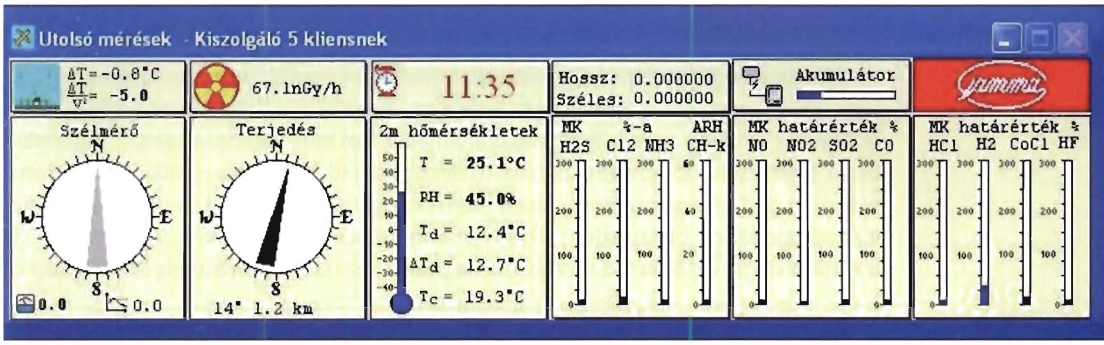
The cloud cover was a limiting factor for the use of the RapidEye satellite imageries in the test site on Monday, 23 May. At 12:00 UTC the weather situation during the experiment was cloudier than visible on the map representing the situation at 9:00 UTC. Tuesday, 24 May, was nearly cloud-free.

During the demonstration exercise northerly winds prevailed in the investigation area, the winds came from northern direction (NNW and N). Air temperatures were ranging between 23–26 °C. The wind speed was relatively higher on Monday, 23 May 2011, ranging between 8 and 9 knots and relatively lower on Thursday, 24 May 2011 ranging between 4 and 5 knots (wind is given in tens of degrees and knots, one knot is 1.15 miles per hour, 1 kn = 1 nm/h = 1.852 km/h).

Weather condition on 23 May 2011 according to ZAMG F.30-4



Measurements from DTCDM-team in Pincehely, Tolna, Hungary F.30-5



More detailed measurements were taken by the DTCDM-team, measuring wind speeds, wind directions, temperature and gas compositions and concentrations, and possible gas spread distance and direction. The measurements were taken from 15:50 local time at the football ground of Pincehely. Although the measurements were collected in the afternoon, they provide an impression of the weather conditions, as the conditions were relatively stable during the day.

The data came in every minute: temperature at 2 m and 0.5 m height, wind speed, directions, average direction and possible gas spread distance and direction.

30-4 Topographic Setting

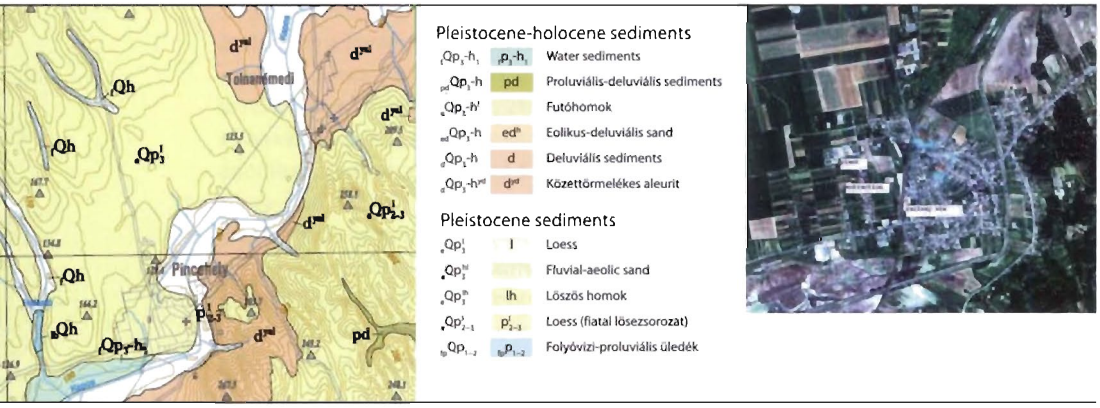
The investigation of the potential influence of the topography on the dispersion of a toxic cloud was one focus of interest during the experiment. Therefore a prerequisite for the planned cloud experiment was the collection, georeferencing and storage of available maps and data in a GIS environment. For getting an overview of the simulated toxic cloud prone areas, information of the geomorphologic settings are required. Height level maps, slope and aspect maps were elaborated based on the available digital elevation data such as SRTM and ASTER DEM-data and topographic maps.

Pincehely is located within a flat, slightly undulated plane on the upper reaches of the Kapos-river which is forming a flat and broader valley, ranging from 80 to 100 m height levels. The valley axis is mostly aligned in a SW-NE orientation, changing its direction east of Pincehely to N-S, and is flanked in the east by hills which reach heights of up to 230 m. The height level map and the RapidEye satellite image in a perspective, 3D-view provide an overview of the topographic setting.

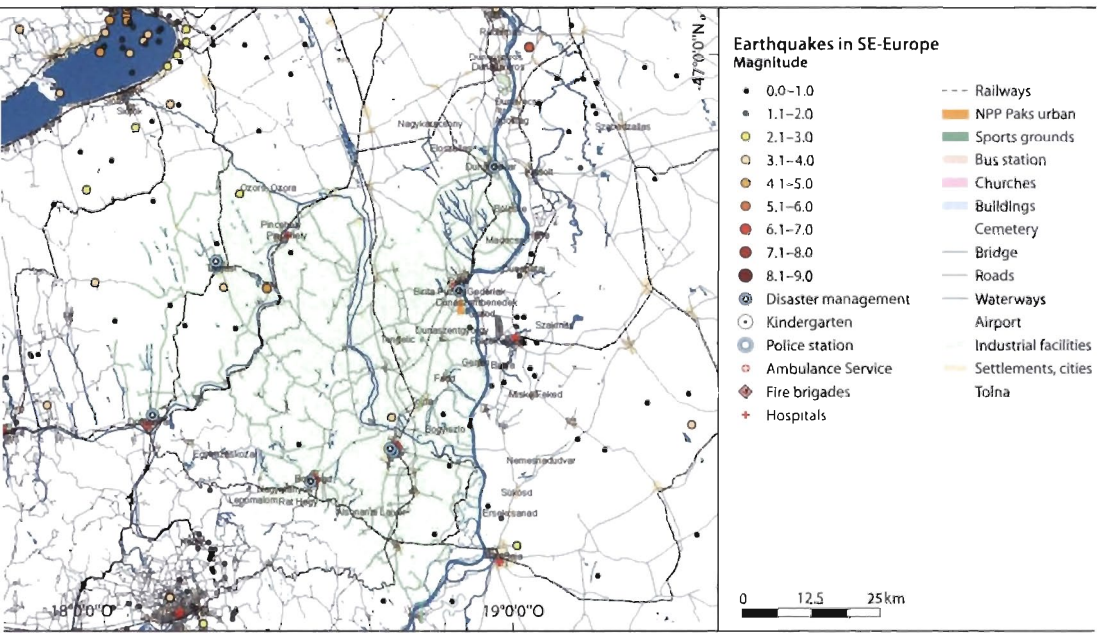
30-5 Geologic and Seismotectonic Setting

Hydrogeologic and geologic-tectonic information provided by the Hungarian Geological Survey and other sources were integrated into the investigations. The spatial distribution of subsiding and uplifting areas and horizontal movements inside the Pannonian basin, often aseismic movements, have to be considered. Inter-plate collision and tectonic extrusion and escape processes since the Tertiary are still active as derived by seismicity and geodetical observations. This is of importance as the railways used for the gas transport might be affected by subsurface processes. F.30-6 shows the geologic map of

Geologic map of the Pincehely area F.30-6



Earthquakes in Central-Hungary F.30-7



the Pincehely area providing an overview of the geologic situation. The area is characterized by outcrops of unconsolidated, Quaternary sediments. The earthquake distribution is visualized in F.30-7. Although this area has been not affected by severe, near-field earthquakes in the past decades, the effect of stronger (> Ml 5) far-field earthquakes has to be taken into account, too that might lead to secondary effects such as liquefaction, and compaction, vertical or horizontal movements, and landslides.

30-6 Evaluations of RapidEye Satellite Data

An important aspect is the delivery of satellite data for both,

// for creating a most actual, high spatial resolution, GIS integrated reference data base visualizing critical points and areas, and
// for providing information of damages in case of emergency due to an accident in an industrial plant or due to natural hazards as fast as possible, as the civil protection units need the information for their management. To deliver information about a disaster in near real time is vital to save lives of people involved and to prepare measurements.

High resolution satellite data are needed for this purpose, however, most of them are only available with a time delay. The five RapidEye satellites simultaneously in orbit have a high spatial and timely resolution. For the first time, there is a constellation of five earth imaging satellites that contain identical sensors, that are in the same orbital plane and are calibrated equally to one another. This means an image from one RapidEye satellite is identical in characteristics to an image from any of the other four satellites, thus allowing access to an unprecedented amount of imagery collected on a frequent basis.

Those data provided for the demonstration/experiment were Level 3A-image products: RapidEye Ortho (Level 3A) are orthorectified products with radiometric, geometric and terrain corrections in a map projection. RapidEye's Ortho Product (Level 3A) offers the highest level of processing available data. Radiometric, sensor and geometric corrections have been applied to the data. These have been rectified using a DTED Level 1 SRTM DEM or better, and with appropriate ground control can meet an accuracy of 6 m 1-sigma (12.7 m CE90), according to RapidEye AG (May 2011).

In the scope of a scientific proposal ("RapidEye Science Archive" – RESA, Proposal No. 438) supported by the German Aerospace Center (DLR), Neustrelitz, and RapidEye AG, Brandenburg, near real-time RapidEye-satellite data with a spatial resolution of 5 m were taken during the cloud experiment. (Real-time means: the whole process takes the time needed for processing and transfer. For satellite application this includes the time constraint arising from the satellites' visibility from a ground station. Only if a satellite is visible from a ground station it can be commanded and data can be downlinked from the satellite.) Previous projects confirmed that RapidEye imageries can be delivered in case of emergency within a time frame from 90 minutes to 13 hours [Hoja et al., 2010]. In this case, – as time and coordinates of the cloud experiment were known in advance (in both cases 12:00 to 12:30) – , the RapidEye satellites were directed at the test site in Pincehely.

// The most important result was the quick response: on Monday, 23 May 2011, the data were available after 7 hours and on Tuesday, 24 May 2011, after **only 3.5 to 5 hours**.
// It has been proved that the RapidEye space technology works on demand with timeliness accuracy for crisis management.

30-6-1 Digital Image Processing

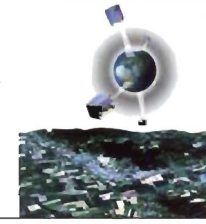
The RapidEye data were processed using various digital image processing methods using ENVI-Software/ITT. Different RGB combinations of the five bands, image classifications and filter techniques were tested for enhancing the visibility of the artificial cloud and the markers. Vegetation index (NDVI) and water index (NDWI) calculations were carried out. The six delivered RapidEye scenes were joined to a mosaic. Then, the images were merged with ASTER DEM data to overlay the information and create perspective 3D-views. An overlay of image products gained by filter techniques with RGB-imageries provides the best suited results for the purpose of this study (F.30-9). When merging the RapidEye-RGB image products with the Filter-Convolutions and Morphology-Directional – image products the visibility of the cloud structure can be enhanced significantly (F.30-9).

The separation between the RapidEye spectral bands leads to some effects that can be seen in the imagery. In the regular RapidEye scene with clouds, the clouds show a red-blue halo around the main cloud. This is due to the fact that the red and blue bands are the furthest apart on the sensor array, and the cloud cannot be fully co-registered due to its movement during the time between the two bands, and also due to the fact that clouds are not reflected within the DEM. If the same scene is viewed as a colour-infrared composite (near-infrared, red and green) the clouds appear with smaller halos of green, because the green band is closer in time to the red and near-infrared than it is to the blue band [RapidEye AG, 2011].

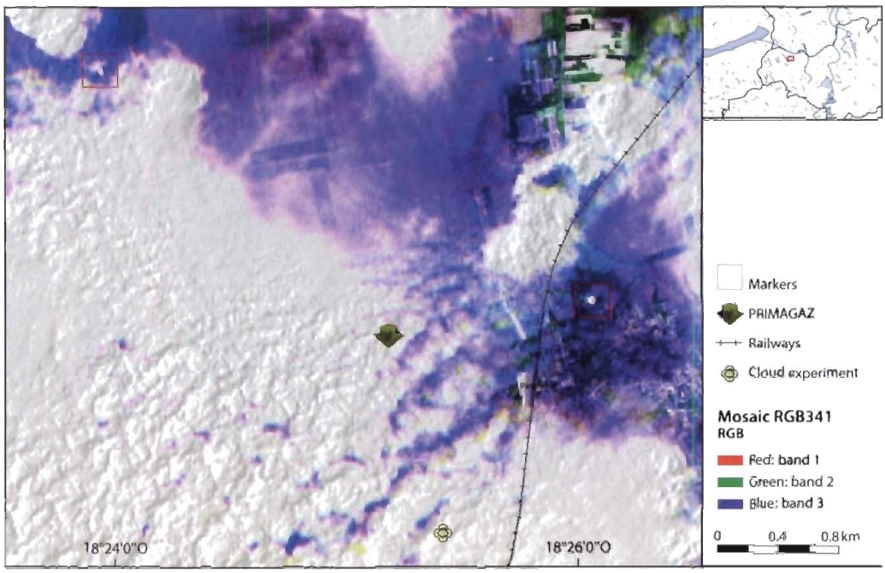
Overview of the delivery times (UTC) as provided by RapidEye AG on 24 May 2011 F.30-8

2011-05-24T103445_RE1_3A-NAC_6341822_110732		Dateiordner	24.05.2011 15:18
2011-05-24T103445_RE1_3A-NAC_6341921_110732		Dateiordner	24.05.2011 17:09
2011-05-24T103446_RE1_3A-NAC_6341824_110732		Dateiordner	24.05.2011 15:18
2011-05-24T103447_RE1_3A-NAC_6341826_110732		Dateiordner	24.05.2011 15:19
2011-05-24T103450_RE1_3A-NAC_6341823_110732		Dateiordner	24.05.2011 15:19
2011-05-24T103450_RE1_3A-NAC_6341825_110732		Dateiordner	24.05.2011 15:19
438_4_RESA-2011-05-24.dbf	2,58 KB	DBF-Datei	24.05.2011 17:09
438_4_RESA-2011-05-24.md5	4,63 KB	MD5-Datei	24.05.2011 17:09
438_4_RESA-2011-05-24.shp	916 Byte	SHP-Datei	24.05.2011 17:09
438_4_RESA-2011-05-24.shx	148 Byte	SHX-Datei	24.05.2011 17:09
438_4_RESA-2011-05-24.txt	4,88 KB	Textdokument	24.05.2011 17:09

Cloud experiment started at: 12:00–12:30 UTC
Availability of RapidEye Data: 15:18–17:09 UTC
Two of the five RapidEye satellites were able to take data from the test site



RapidEye scene of the test site, Monday, 23 May 2011, 12:30 p.m. F.30-9
The red squares indicate the position of the visible markers (white spots)



30-6-2 RapidEye Data of 23 May 2011

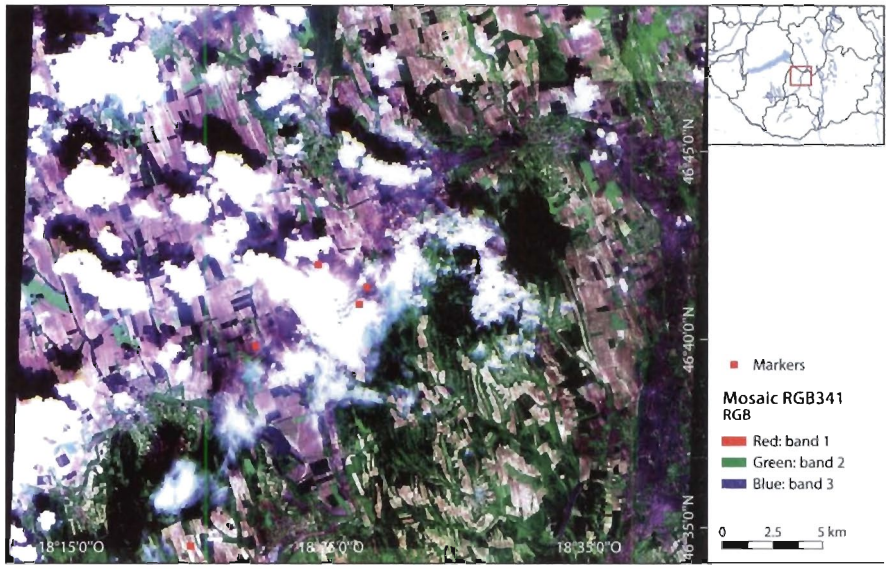
On Monday, 23 May, the cloud cover was relatively dense and hiding almost the artificial cloud of the artifial smokers, but fortunately not all markers. F.30-10 shows the RapidEye satellite image of 23 May 2011. There are two cloud types visible: Lower stratus clouds and stratocumulus clouds, moving to SSE according to the wind direction from north. The supervised classification allows the clear identification of the clouds and their shadows. The lower stratus clouds are influenced in their dynamics by the topography. They appear concentrated in front of the hilly area. The stratus clouds followed the topography in their movements, entering first into valleys oriented towards north and "ascending" the hills. When analyzing the perspective 3D-views the topographic influence on the cloud dynamics becomes visible: **The clouds coming from NNW were obviously trapped in front of the hills and their dispersion lowered.** In case of emergency with comparable weather situations this would mean, that a toxic cloud would remain longer trapped in the valley in front of the hillsides.

The RapidEye images were combined with contour lines for demonstrating the influence of the Kapos valley and the hill chain about 100 m higher on the cloud distribution.

Water index (NDWI) calculations based on the bands 2 and 5 (see F.30-7) help to identify clouds with higher water concentration. The water concentration plays an important role when considering aerosol concentrations.

An overlay of the cloud image of 23 May 2011 with areas above 200 m height level clearly demonstrates the relationship between height level and cloud arrangement. Merging the RapidEye image with the information of an aspect calculation, selecting orientations of hillsides to northern direction, those areas are visualized that are most

RapidEye mosaic of the test site, 23 May 2011 F.30-10



exposed. In case of a real chemical accident with a similar wind situation like the one during the experiment, this topographic influence – trapping and lowering the dispersion in the Kapos valley in front of the hillside – has to be surely considered when planning evacuation measurements. Lower areas below 100 m height level in the valley should be evacuated first.

30-6-3 RapidEye Data of 24 May 2011

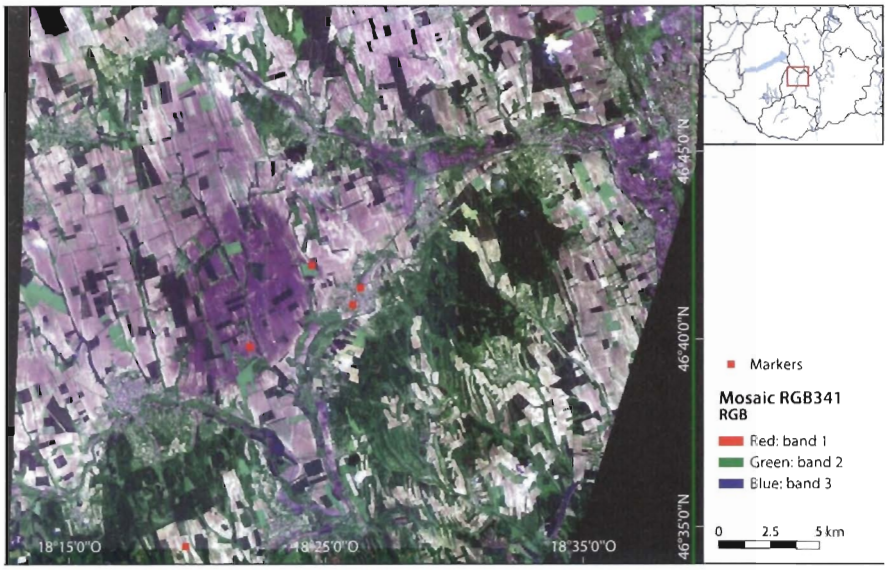
On the nearly cloud-free RapidEye-mosaic of 24 May 2011 an oval-shaped feature becomes visible in darker colours (F.30-11). When comparing the RapidEye image with geologic and structural maps of the area, this feature cannot be correlated with subsurface structures or geologic-lithologic units. Quaternary, sedimentary covers are determining the surface, as visible on the geologic maps provided by the Hungarian Geological Survey. Forests and fields show the same pattern as the environment. The traces of precipitation can be verified and visualized using the water index-calculation based on bands 2 and 5 of the RapidEye data. The areas appearing in white on the corresponding NDWI-scene have the highest NDW-values, that can be correlated with higher soil moistures.

The oval-shaped feature is visible as well on the Principal Component-image of that area. Principal Components Analysis (PCA) is a spectral enhancement which can be used to compress the information content of a multispectral data set. PCA uses mathematical algorithms to transform *n* bands of correlated data into *n* principal components which are uncorrelated, such that the coordinate axes of the components are mutually orthogonal (Corner). The first principal component (PC-1) describes most of the variation of the brightness values for the pixels of the original bands. Subsequent components explain less and less of the data, with the final PC usually corresponding to atmospheric noise in

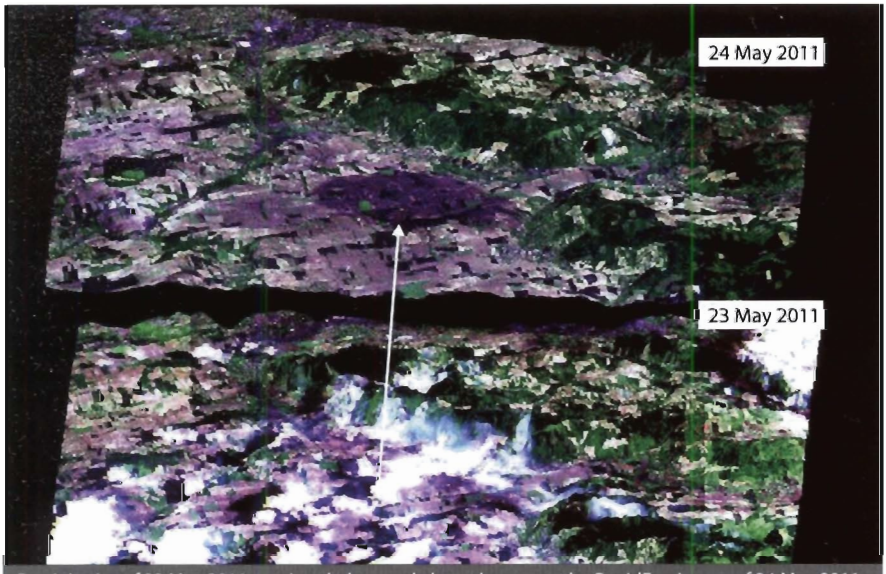
the data rather than any ground features. The main benefit of principal component analysis is that it can reduce the amount of data (bands) without losing much of the information and typically reducing redundancy.)

In case of a real chemical accident, such image processing could be used to detect areas with a probable higher contamination due to rain fall enriched with toxic particles.

RapidEye scene of 24 May 2011, 12:30 p.m. F.30-11



Perspective view comparing both RapidEye-scenes of 23 and 24 May 2011, looking at SE-direction F.30-12



Precipitatios of 23 May 2011 causing darker, oval-shaped areas on the RapidEye-image of 24 May 2011

30-7 Susceptibility to Earthquake Shock and to Earthquake related Secondary Effects

Local geologic conditions are the cause of difference in earthquake shock intensity. But there is little certainty on the particular conditions in a specific area that are most responsible, and the degree to which they affect earthquake shaking. The ground motion during an earthquake predominantly depends on several factors such as the magnitude, properties of fault plane solutions, the distance from the fault and local geologic conditions. The most intense shaking experienced during earthquakes generally occurs near the rupturing fault area, and decreases with distance away from the fault. Within a single earthquake event, however, the shaking at one site can easily be stronger than at another site, even when their distance from the ruptured fault is the same [Gupta, 2003]. The variability in earthquake-induced damage is mainly determined by the local lithologic and hydrogeological conditions. These conditions, internally influence the amplitude, the frequency and duration of ground motion at a site. Groundwater level variations and associated saturation changes in sand layers within near-surface aquifers can influence local response spectra of the ground motion, through modification of shear-wave velocity. Wetlands generally have a higher damage potential during earthquakes due to longer and higher vibrations. Recently formed sediments will slow the velocity of the earthquake waves, trapping the energy and causing large amplitudes of shaking. Older compacted materials that have densified over time or transitioned from sand to sandstone and cemented together are less responsive for example to liquefaction. Changes of the groundwater level can have a considerable influence upon the liquefaction potential of a region due to in-situ pore-water pressure responses in aquifers during earthquakes triggering mechanism of liquefaction [Hannich et al., 2006]. Liquefaction that affects the human-built environments is mostly limited to the upper 15 metres of soil. Liquefaction has occurred and has been documented during historical earthquakes.

30-7-1 Evaluations of Morphometric Maps derived from Digital Elevation Data (DEM)

Morphometric maps such as slope, hillshade, height level, and curvature maps are generated based on SRTM and ASTER Digital Elevation Model (DEM) data using ArcGIS from ESRI and ENVI digital image processing software (CREASO). Step by step factors can be extracted from these data that might be of importance for the detection of local site conditions. For example: The distribution of unconsolidated, youngest sedimentary covers can be often correlated with areas showing less than 10° slope gradient and no curvature. (In the case of the curvature: negative curvatures represent concave, zero curvature represent flat and positive curvatures represent convex landscapes.) Height level maps help to search for topographic depressions covered by almost recently formed sediments, which are usually linked with higher groundwater tables. When extracting the lowest height levels of an area, it becomes visible where the areas with high ground-water tables

can be expected. In case of earthquakes those areas have often shown the highest earthquake damage intensities [Schneider, 2004].

Slope gradient maps help to detect those areas where mass movements are likely to occur. From slope gradient maps those areas with the steepest slopes, and from curvature maps the areas with the highest curvature are extracted as these are susceptible to landslides. Slopes with higher slope gradient (> 20°) are generally more susceptible to mass movements. Special attention is focussed on precise mapping of traces of faults (lineament analysis) on satellite imageries, predominantly on areas with distinctly expressed lineaments, as well as on areas with intersecting/overlapping lineaments. Lineament analysis based on satellite imageries or DEM derived morphometric maps can help to delineate local surface-near fracture systems and faults that might influence seismic wave propagation and influence the intensity of seismic shock or might influence the susceptibility to secondary effects. Areas with intersecting, larger lineaments are probably exposed to relatively higher earthquake shock in case of stronger earthquakes. By combining some of the causal or preparatory factors influencing earthquake shock intensity in a georeferenced GIS environment, those areas can be detected where causal factors occur aggregated and superimpose each other. Causal factors derived from SRTM and ASTER DEM data such as:

- // lowest height levels providing information of areas with relatively higher groundwater tables (here: 80–100 m),
- // lowest slope gradients (< 10°–15°),
- // lowest minimum curvature or no curvature, providing information of flat, broader valleys, basins and depressions with younger sedimentary covers and higher groundwater tables,
- // highest flow-accumulations, providing information of areas with higher surface water-flow input, are combined with lithologic and seisomotectonic information in a GIS data base,
- // Quaternary sediment distributions and faults derived from geologic maps,
- // lineaments derived from LANDSAT ETM imageries,
- // earthquake data downloaded from International Earthquake Centres (GEORISK, International Seismological Centre, ISC, USGS, GFZ, etc.).

Causal or preparatory factors are extracted systematically in ESRI Grid-format. Of course, many further factors and data play an important role, that – if available – should be included into the data base.

The different factors are converted into ESRI-GRID-format and summarized/aggregated and weighted in per cent in the weighted overlay-tool of ArcGIS according to their estimated influence on the local specific conditions or in equal percentages. Those areas are considered to be susceptible more to soil amplification where the following causal factors are summarizing and aggregating their effects: lowest height level of the terrain combined with relative high groundwater tables, flat morphology with low slope gradients and no curvature, loose sedimentary covers within a basin topography or within flat coastal areas. When an area is underlain by larger, active fault zones, especially when intersecting each other, the soil amplification susceptibility will probably rise, depending on given specific earthquake properties and parameters.

The percentage of influence of one factor is changing, for example due to seasonal and climatic reasons, or distance to the earthquake source. As a stronger earthquake during a wet season will probably cause more secondary effects such as landslides or liquefaction than during a dry season, the percentage of its influence has to be adapted. Therefore the percentage of the weight of the different factors has to be adjusted as well to seasonal effects.

The sum over all factors/layers that can be included into GIS provides some information on the susceptibility to amplify seismic signals. After weightening (in per cent) the factors according to their probable influence on ground shaking susceptibility maps can be elaborated, where those areas are considered as being more susceptible to higher earthquake shock intensities, where "negative" factors occur aggregated and interfering with each other. Whenever an earthquake happens in these areas, now it can be derived better where the "islands" of higher ground shaking are most likely to occur by adding the specific information of the earthquake to the susceptibility map using the weighted overlay – approach.

The hereby presented approach is proposed to serve as a first basic data stock for getting a perception of potential sites susceptible to higher earthquake ground motion, including in next steps the integration of further, available data such as movements along active faults, focal planes, uplift/subsidence, 3D structure, lithologic properties and thickness of lithologic units, shear wave velocities, etc.

30-7-2 Evaluations of RapidEye Data

Groundwater table data are an important input when dealing with the seasonal influences on earthquake effects. A promising approach to obtain soil moisture variability is to remotely sense the greenness variations of biomass within an otherwise homogeneous canopy, because variations in soil water directly affect the growth patterns of the overlying vegetation [DeAlwis et al., 2007]. For this purpose vegetation index (NDVI) and water index (NDWI) calculations were carried out. This approach, thus, contributes to the detection and the visualization of areas that might be prone in case of a stronger earthquake to secondary effects such as compaction, liquefaction or soil amplification. As higher values of the NDWI-calculation can be correlated with higher water contents at the surface, higher groundwater tables and surface water, a request was started in ArcMap selecting all values of the NDWI-grey scale image (values: 0–255) above 180. These higher values in this area almost correspond to water surfaces and soils with higher water saturation at the acquisition date of the satellite image, which can be confirmed by the visual evaluation of RGB-imageries.

30-7-3 Shear Wave Velocities

Shear-wave velocity is an important factor when investigating local soil conditions. A standardized approach for mapping seismic site conditions measuring or mapping shear-wave velocity (Vs) was developed by [Wald and Allen, 2007]. As in many seismically active regions of the world, information about surficial geology and Vs either, does not exist, varies dramatically in quality, varies spatially, or is not easily accessible. Wald and Allen

first correlated Vs30 (here Vs30 refers to the average shear-velocity down to 30 m) with topographic slope (m/m) at each Vs30 measurement point for data. The basic premise of the method is that the topographic slope can be used as a reliable proxy for Vs30 in the absence of geologically and geotechnically based site-condition maps through correlations between Vs30 measurements and topographic gradient. By taking the gradient of the topography and choosing ranges of slope that maximize the correlation with shallow shear-velocity observations, it is possible to recover, to first order, many of the spatially varying features of site-condition maps. It is worth to note that the resolution (30 arc sec) of the topography allows relatively detailed maps of site conditions. Many of these details come from small-scale topographic features that are likely to be manifestations of real site differences, such as basin edges and hills protruding into basins and valleys, and are thus easily visible due to their significant slope change signatures. Typically, these edges are important for predicting ground motion variations due to earthquakes [Wald and Allen, 2007]. Thus, the Vs (m/sec) data derived from the Pincehely area were downloaded from the USGS and integrated and interpolated in ArcGIS for getting an overview of the estimated shear velocities in case of larger earthquakes.

Lower shear wave velocities up to 400 m/s as derived by Wald and Allen correspond quite well with the outcrop of unconsolidated, Quaternary sediments in the broader valleys. Merging the weighted-overlay-susceptibility map with the Vs-data derived by [Wald and Allen, 2007] there is partly a coincidence of areas assumed to be more susceptible to soil amplification according to the weighted overlay approach with areas of estimated lower shear wave velocities (Vs < 400 m/sec).

When including the highest NDWI-values, information of areas with probable higher groundwater tables can be derived, where – in case of a stronger earthquake – the earthquake shock intensity can be assumed to be higher.

30-7-4 Shake Maps

Shake maps showing the distribution of recorded peak ground acceleration (PGA) and peak ground velocity (PGV) overlain on regional topography maps allow scientists to gauge the effects of local site amplification because topography is a simple proxy for rock versus deep-basin soil-site conditions. This can lead to more detailed investigations into the nature of the controlling factors in generating localized regions of damaging ground-motions [Wald et al., 2006].

The MAEViz-open-source, seismic loss-assessment software modified by VCE integrates spatial information, data, and visual information into an environment for performing seismic loss assessment and analysis. It can be used to generate damage estimates from scientific and engineering principles, test multiple mitigation strategies, and support modelling efforts to estimate higher level impacts of earthquake hazards, such as impacts on transportation networks, social, or economic systems.

When merging shake maps with the maps based on the weighted overlay of factors influencing the susceptibility to soil amplification in ArcGIS, it can be derived better where "islands" of higher earthquake shock can be expected.

30-8 Conclusions

Satellite images form an important input for preparedness and mitigation of industrial risks. The experiences during the demonstration have shown that the spatial resolution of 5 m is very suited for the purpose of this study. It can be stated that all markers were found on the images. The RapidEye satellite's spatial and radiometric resolution was sufficient for their detection. The size of the data is very good to handle when considering a rapid data transfer and image processing in time. Shortly after having downloaded the data, the processing and the evaluation of the RapidEye data was possible without any problem and time-delay. The objectives of the experiment were fulfilled.

In case of emergency the transfer and image processing of higher resolution data such as of QuickBird or IKONOS-satellite data – if available – would take too long. Another aspect is the fact that not all PCs are suited for the data amount of the very high resolution data.

Acknowledgement

The support of EU, FP7, Large Collaborative Research Project, IRIS – Integrated European Industrial Risk Reduction System, CP-IP 213968-2, is kindly acknowledged.

The authors thank the German Aerospace Center (DLR), RESA Science Team, Neustrelitz and RapidEye AG, Brandenburg an der Havel, Germany, for the support by providing RapidEye satellite imageries from Central Hungary in the scope of the project proposal no. 438. Especially the helpful and reliable support of Mrs. Petra Seiffert , RapidEye AG, has to be mentioned and thanked. We are very grateful for this support.

The excellent organisation of the civil protection exercise carried out by the DTCDM – Disaster Management Directorate of Tolna County, the police, fire brigades and ambulances has supported this demonstration significantly, which is acknowledged as well.

References

Federal Ministry of the Interior, 2005. *Protection of Critical Infrastructures – Baseline Protection Concept, Recommendation for Companies*. www.bmi.bund.de

German Aerospace Center (DLR). *RESA – RapidEye Science Archive*. http://resaweb.dlr.de

Hoja, D., Schwinger, M., Wendleder, A., Löwe, P., Konstanski, H. and Weichelt, H., 2010. *Optimised Near-Real Time Data Acquisition and Preprocessing of Satellite Data for Disaster Related Rapid Mapping*. PFG, 6:429–438.

Hungarian Meteorological Service. www.met.hu/en/

Krausmann, E., Cozzani, V., Salzano, E. and Renni, E., 2011. *Industrial Accidents Triggered by Natural Hazards: an Emerging Risk Issue*. Natural Hazards and Earth System Sciences, 11:921–929. www.nat-hazards-earth-syst-sci.net/11/921/2011/

RapidEye AG, 2011. *Satellite Imagery Product Specifications*. Version 3.2. RapidEye AG, Molkenmarkt 30, D-14776 Brandenburg an der Havel, Germany. www.rapideye.de

Theilen-Willige, B., 2009. *Risikokarten zur Erfassung lokaler Standortbedingungen bei Erdbeben.* iin: DKKV (Ed.), 2010: Katastrophen – Datenhintergrund und Informationen, Dokumentation, 10. Forum Katastrophenvorsorge, 23–24 November 2009, Bonn, DKKV Schriftenreihe 41:14–15.

Theilen-Willige, B. and Wenzel, H., 2010. *Earthquake Emergency Preparedness in Central-Hungary – Preparing Rapid Response Measurements Using Remote Sensing and GIS-Methods.* Proceedings of UN SPIDER Workshop, 12–14 October 2010, Bonn.

Theilen-Willige, B., 2011. *The Use of RapidEye-Satellite Data for Earthquake Emergency Preparedness and Management in Central-Hungary.* 3rd RESA-Workshop – RapidEye Science Archive (RESA), 23–24 March 2011, Neustrelitz.

Theilen-Willige, B. and Wenzel, H., 2011. *Remote Sensing and GIS Contribution to Earthquake Disaster Preparedness in Hungary.* Gi4DM – Geoinformation for Disaster Mangement, 3–8 May 2011, Antalya, Turkey, 7 May 2011, OP62.

Wald, D.J., Worden, B.C., Quitoriano, V. and Pankow, K.L., 2006. *ShakeMap® Manual - Technical Manual, Users Guide, and Software Guide.* Version 1.0 6/19/06, USGS. http://pubs.usgs.gov/tm/2005/12A01/

Windfinder. *Wind and Weather Forecast Map Hungary.* www.windfinder.com/forecasts/wind_hungary_akt.htm

IRIS Project – Working Documents:
www.vce.at/iris/

IRIS Working Document WD-175: *Detection of Local Site Conditions influencing Earthquake Ground Motion in Western Hungary using Remote Sensing and GIS Methods.*

IRIS Working Document WD-206: *IRIS Demonstration 2011 in Hungary.*

IRIS Working Document WD-274: *Mudflow Accident in Hungary.*

IRIS Working Document WD-279: *Earthquake Emergency Preparedness in Central-Hungary – Preparing Rapid Response Measurements.*

IRIS Working Document WD-295: *Geotectonic Investigations as Contribution to the Safety of Infrastructure in Hungary using Remote Sensing and GIS Technologies.*

IRIS Working Document WD-334: *GIS integrated Database for Earthquake Emergency Preparedness in Tolna, Hungary.*

IRIS Working Document WD-354: *Wetland Detection.*

IRIS Working Document WD-431: *Database for the Demonstration in Pincehely.*

Digital Elevation Data:
http://srtm.csi.cgiar.org/SELECTION/inputCoord.asp
http://glcfapp.glcf.umd.edu:8080/esdi/index.jsp
www.gdem.aster.ersdac.or.jp/search.jsp

ShakeMap:
http://earthquake.usgs.gov/earthquakes/shakemap/

31
Authors & Contributors

IRIS Executive Board



Helmut WENZEL (Coordinator), VCE, Austria (born in 1950) is an expert in structural health monitoring, Life Cycle Engineering and project management. He teaches asset management and monitoring of structures at the University of Life Sciences in Vienna. He has successfully coordinated European research projects since 1995. Besides the research activity he is involved in major signature projects on infrastructure on global scale.



Josef KÜNG (Administrative Coordinator) (born in 1962) is associate professor at the Institute of Application-Oriented Knowledge Processing (FAW) at **Johannes Kepler University Linz (JKU), Austria**. His core competencies cover Information Systems, Knowledge Based Systems, Decision Support Systems, Semantic Technologies and Similarity Queries where he has published a fair number of papers. Among other scientific service activities Josef Küng is co-editor-in-chief of the journal on Transactions on Large-Scale Data and Knowledge Centered Systems published by Springer.



Demos ANGELIDES, AUTh, Greece (born in 1947) holds a Civil Engineering degree from AUTh, and an SM in Civil Engineering and a PhD both from M.I.T. He has been Professor of Marine Structures in the Department of Civil Engineering of the Aristotle University of Thessaloniki for the last over 15 years. Prior to that he held engineering and management positions in the USA for about 18 years with McDermott International, Inc., a major design and construction company in the area of Offshore Structures for oil and gas production. He has published extensively in international journals, conference proceedings and edited books.



Christophe DELLIS, CEA, France (born in 1967) is Programme Leader for Specific Facilities Operation and Maintenance from Nuclear Energy Division of the French Alternative Energies and Atomic Energy Commission in Saclay, France. He was previously Head of Thermal and Mechanical Studies Section in Saclay, and involved in the IRIS Project as co-leader with EDF of the nuclear application Work Package, focused on seismic risk management.



Fritz-Otto HENKEL, Woelfel, Germany, PhD TU Darmstadt, is an international expert in structural mechanics and dynamics. He is working in earthquake engineering, in human-induced events on critical infrastructures and in serviceability of structures under dynamic loads worldwide. Extracts of his work are laid down in over 100 papers, a text book about seismic design and dry-walling and contributions to rules and codes. In the company he has been acting as managing director and has also been responsible for research and development for over 20 years.



Klaus KERKHOF, Materials Testing Institute (MPA), University of Stuttgart, Germany (born in 1956) studied Civil Engineering at the University of Stuttgart. He achieved his PhD in the field of vibration behaviour of piping, and he currently specialises in the following research activities: Numerical calculations, structural dynamics, component testing and research for the power generation industry and chemical plant engineering. Since 1987 he has been project manager of industrial projects as well as national and international research projects in the field of numerical calculations, structural dynamics, component testing and lifetime management.



Pierre PEGON, ELSA, JRC, Italy (born in 1957) has worked in the field of numerical modelling and experimental methods in Earthquake Engineering since 1992. He has developed advanced sub-structuring testing methods and implemented them in several relevant projects. He has participated in numerous European projects either at technical and management levels. He is responsible for the Reaction Wall and Hoplab Laboratory activities at ELSA.



Witold PYTEL, KGHM, Poland studied Civil Engineering in Wroclaw. He received his PhD from the Geotechnical Institute of Wroclaw Polytechnic Institute, Poland. For 22 years he worked at Institute of Geotechnics and later at Institute of Mining of the same university. In between 1987–1994 he worked at Southern Illinois University at Carbondale, USA. Since 1995 he has been employed at KGHM Cuprum, presently at a professor's position. In 2003 he received D. Sc. degree from Silesian University of Technology, Gliwice, Poland. His field of interest embraces soil and rock mechanics, geomechanics and all aspects of numerical modelling in civil and mining engineering.



Joachim SCHWENKKROS, working 39 years for Dow, Germany, is one of the initiators of the project. Born in 1945 in Hamburg he facilitated testing the developed systems under real life conditions in the chemical industry and was acting as a coordinator and team leader. He graduated as mechanical and production engineer at FAW Hamburg. He was acting as lecturer at the Technical College in Dar-es-Salaam, Tanzania, until he was taking over responsibility for piping projects and Structural Analysis in the chemical industry.

Authors & Contributors



Günther ACHS, VCE, Austria (born in 1979) has focused above all on the fields of earthquake engineering, structural dynamics as well as vibration and structure-borne sound protection. Since 2010 Dr. Achs has been an accredited expert for acoustics, acoustic measurements and person-related vibration in the field of railway engineering. He is scientific advisor of the Austrian Association for Earthquake Engineering and Structural Dynamics, member of the guideline committee for vibrations and structure-borne sound of FSV (Austrian Association for Research on Road – Rail – Transport) and member of the European Association for Earthquake Engineering.



A. Emin AKTAN, Drexel University, Philadelphia, USA (born in 1946) has contributed to the theory, demonstrations and applications of field measurements, structural identification and performance monitoring of actual operating or decommissioned constructed systems. Following a decade of research on earthquake structural engineering in the laboratory at Urbana, METU and Berkeley, he started conducting research in the field since 1984. His current focus is on the application of asset management to infrastructures. He serves as an editor of ASCE Journal of Structural Eng and Taylor and Francis Journal SIE, and has published a body of articles and reports.



Helga ALLMER, VCE, Austria (born in 1971). After school she studied mechanical engineering. Then she was employed at the Vienna University of Technology for several years. At VCE she started her career in 2007 and is now working both in European and national research projects (IRIS, Mimosa, C2T2) and on commercial projects (Structural Health Monitoring, Life Cycle Assessment).



Stefan ANDERLIK, JKU, Austria (born in 1986) is currently an SAP advisor of the EREMA Ges.m.b.H. He finished his Master Studies and obtained his graduation in 2009 at the Johannes Kepler University in Linz. During the last three years he published six papers at well-established conferences and has been working on several scientific projects in the field of semantic systems and business intelligence. Currently, he is writing his extra-occupational doctoral thesis on SemCockpit – An Ontology-Driven, Interactive Business Intelligence Tool for Comparative Data Analysis.



Anton ANDONOV, Risk Engineering Ltd, Bulgaria (born in 1981) is Chief Expert in Risk Engineering Ltd. His practice is focused on structural analysis and design of various hazardous facilities, mostly in the nuclear and hydro power sectors, for extreme loads as earthquake, blast, elevated/accidental pressure and temperature, aircraft impact, etc. He is member of the WG7 "Earthquake resistant structures" of IABSE, member of the European Association of Earthquake Engineering, the Institution of Structural Engineers (UK), UK Earthquake Engineering Field Investigation Team and the American Institute of Aeronautics and Astronautics.



Stoyan ANDREEV, Risk Engineering Ltd, Bulgaria (born in 1987) is a young engineering professional in the field of structural analysis, design and assessment. After completing his MSc with a thesis on the dynamic properties of the containment of a VVER-1000 (as a part of the IRIS project) he is working in high-profile projects for the nuclear and hydropower industries in Bulgaria. His scope of work is seismic engineering, geotechnical engineering and structural health monitoring.



Kiril APOSTOLOV, Risk Engineering Ltd, Bulgaria is a structural engineer with six years of professional experience in the field of numerical analyses and simulations of critical infrastructure (NPP reactor buildings, dams etc.) or specific equipment, involving non-linearities and a variety of static and dynamic analysis techniques. Application of different approaches for structural assessment including overall structural behaviour, as well as local equipment/components investigations. Experience in seismic risk assessment studies of important facilities.



Stella ARNAOUTI, AUTh, Greece (born in 1979) was awarded her Civil Engineering degree from AUTh in 2003 and her MSc in Soil Mechanics and Engineering Seismology from Imperial College in 2004. Her PhD (AUTh, 2010) dealt with geostatistical analysis of field measurements for ground movement estimation. She worked in the design of various geotechnical projects for Egnatia Motorway and Athens Metro. Having participated in several European research projects, she is currently a research collaborator with AUTh and was recently selected Champion of the European Grid Infrastructure.



Patrick ARNOLD, Delft University of Technology, Netherlands (born 1983 in Germany) is a researcher in the Geo-Engineering Section. He is currently investigating the technical feasibility of a radioactive waste geological disposal facility in Boom Clay in the Netherlands. His research interests include unsaturated soil mechanics, stochastic modelling of geotechnical performance, reliability-based risk assessment and computational geomechanics. Recently he was co-editor of the book "Modern Geotechnical Design Codes of Practice: Implementation, Application and Development" (2012).



Nick BASSILIADES, AUTh, Greece (born in 1969) is an Associate Professor at the Department of Informatics. His research interests include knowledge-based and rule systems, multi-agent systems, ontologies, and the Semantic Web. He has published more than 150 papers and has co-authored two books, with over 800 citations. He has been the Program Chair of RuleML-2008, -2011. He has led nine R&D projects. He is a director of RuleML, Inc. and was the secretary of the Greek Artificial Intelligence Society.



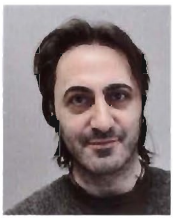
Adrian BEKŐ, VCE, Austria was born in Dunajská Streda, Slovakia in 1978. He majored in structural engineering and acquired a PhD in applied mechanics. Since 2007 he has been with VCE as technical mathematician. His main research focus is on developing identification routines and signal processing. He is also engaged in engineering tasks which are centred on problems of dynamics and special mechanics. In the field of structures his fascination lies with spatial beam and truss structures.



Alexey BERKOVSKY, CVS, Russia (born in 1962). His professional career includes over 25 years in analysis and design of nuclear and industrial structures, systems and components under operational, seismic and accidental loads. His recent activities are mostly in the field of piping flexibility and stress analysis with focus on piping dynamic response, as well as piping behaviour during elevated temperature service where the effects of creep are significant. Mr. Berkovsky is author of more than 20 papers and involved as consultant for Developing of International Atomic Energy Agency Technical Documentation.



Vivek BHASIN, BARC, India is an expert in the area of Reactor Safety, Structural Integrity Assessment, Experimental and Analytical Fracture Mechanics and Structural Reliability. He has an experience of 25 years in this area. At present he holds the post of Head, Reactor Structures Section in BARC. He has more than 200 journal and conference papers to his credit.



Giuseppe BOF, ELSA, JRC, Italy (born in 1972) is a specialized welding technician working at ELSA for more than ten years in the execution of experimental setups and management and maintenance of welding systems in the laboratory. He is also responsible for some safety aspects.



James MW BROWNJOHN, University of Exeter, UK started off as a mechanical engineer working in defence and oil industries, before doing a PhD in full-scale performance of large civil structures. Over an academic career of twelve years in Singapore, then eight years in the UK, he developed interests in structural health monitoring (SHM) with several applications to long and tall structures. In 2008 he co-founded the University of Sheffield spinout company Full Scale Dynamics Ltd. He is Vice President of the International Society for SHM of intelligent Infrastructure.



Martin BRUNNHUBER, VRVis, Austria (born in 1982) has worked in research in the field of visualization and rendering for five years. He wrote his diploma thesis already at VRVis in the area of Computational Fluid Dynamics (CFD) and started his work in information visualization and rendering afterwards. His current main areas are rendering of large point clouds made by laser scanners and visualization of human behaviour in public buildings. He presented his work in five research papers on international conferences.



Philippe CAPÉRAN, ELSA, JRC, Italy (born in 1953) has a previous experience in fluid mechanics. He has worked at the ELSA laboratory for more than fifteen years on the development of advanced optical methods for measurements of displacements and strain fields on large structures.



Pierluigi CIVERA, Politecnico di Torino, Italy joined the Electronics Department as a graduate researcher. Since 1991 he is Associated Professor at the same department. His major interests include microsystems, computer architecture, MEMS and VLSI design for research and industry applications, ASIC design, technology transfer activities toward small and medium enterprises. Recent design activities are mainly devoted to microsystems (MEMS + ASIC) supporting nanotechnology research, processes and applications. Industrial developments and technology transfer activities are mainly addressed toward medical and biochemical applications.



Andrea E. DEL GROSSO, University of Genoa, Italy (born in 1945), Fellow of the Institute of Physics, is full professor of structural engineering; he authored more than 170 papers published in national and international conference proceedings and journals. In the last 20 years he dedicated his research activity to adaptive structures and structural health monitoring. He is associate editor of the journal Smart Materials and Structures and member of the board of the journal Structural Control and Health Monitoring.



Alessandro DE STEFANO, Politecnico di Torino, Italy (born in 1945) is full professor of Earthquake Engineering and Structural Dynamics and active in the research fields: earthquake engineering, structural identification, experimental modal analysis of structures under ambient excitation, analysis of dynamical and seismic signals, neural networks in structural diagnostics. Local and national coordinator of three R&D projects of national interest; key partner of the EU FP7 Project IRIS. Member of the scientific committee and key-note speaker in several international conferences. Editor in chief of the IJLCPE journal published by INDERSCIENCE, Geneve.



Michael DÖHLER, Inria, France has completed his PhD at Inria in 2011 on the topic of subspace-based system identification and fault detection for large mechanical systems. Since, he has had postdoc positions at Northeastern University, Boston, USA, and at BAM, Berlin, Germany. His research focuses on fast and robust methods for Structural Health Monitoring. So far he has published six journal papers and more than 30 conference papers. He was awarded the IRIS Prize of Excellence 2011 for his contribution together with Falk Hille (BAM) to the IRIS project.



Jürgen ENGELHARDT, Woelfel, Germany, PhD TU Darmstadt, is an expert in structural dynamics and mechatronics. He is working in the field of active and passive vibration control solving vibration problems ranging from automotive engineering, wind energy, paper machinery to applications in chemical plants. In the company he acts as manager in the area of mechanical dynamics and mechatronics, working as a consultant as well as developer of systems for vibration control.



Jose ESTEVES, ELSA, JRC, Italy (born in 1953) is a specialized construction technician working at ELSA for more than twenty years in the execution of experimental setups and maintenance of laboratory.



Ángel FAZ is the director of the research Group "Sustainable Use, Management and Reclamation of Soil and Water", and full professor belonging to the Agrarian Sciences and Technology Department of the Technical University of Cartagena, Spain, which has an ample experience in the fields of waste treatment and management, implementation of innovative and cost-effective technologies for waste treatment, waste minimization, waste reuse and valorization, soil recovery and protection, and risk reduction. He has participated as main investigator in more than 25 European, international and national projects. He has published more than 50 peer-reviewed articles.



Bernd FRANKENSTEIN, Fraunhofer IZFP Dresden, Germany leads the working group for Structural Health Monitoring. He has a special interest in the development of monitoring systems in respect of efficiency and low power solutions. He has been working in this field for more than 30 years.



Herbert FRIEDMANN, Wölfel Beratende Ingenieure GmbH + Co. KG, Germany was born in 1951, PhD at University of Würzburg. He is head of R&D with Wölfel and has been working in the field of condition monitoring and structural health monitoring for nearly ten years. Herbert Friedmann coordinates national and international R&D-projects and has published more than 30 papers.



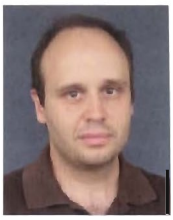
Yozo FUJINO is Professor for Bridge and Structure, University of Tokyo, Japan. His area of expertise comprises dynamics, control and monitoring of bridges and structures, earthquake- and wind-effects on structures. He has been involved in many international projects including Akashi Kaikyo Bridge, Japan, Millennium Bridge, UK and Stonecutter Bridge, Hong Kong. He received many awards; recent ones are Medal with Purple Ribbon from the Emperor of Japan, the Raymond C. Reese Research Prize and Robert H. Scanlan Medal, both from ASCE. He is presently the president of Int. Assoc. of Structural Control and Monitoring and the vice president of IABSE.



Peter FURTNER, VCE, Austria (born in 1975) is responsible for the business field "Structural Health Monitoring" and the related research activities at VCE. He is member of IABSE, IALCCE, ISHMII and the IRF working group "Road Finance and Economics". The focus of his research work is on Life Cycle Assessment and management of the built infrastructure.



Luca GIOANOLA, graduated in Electronic and Communication Engineering, Master and PhD degrees, at Politecnico di Torino, Italy. He obtained a Master certificate at Microchip Technology Inc, AZ, USA. He works at Polytechnic of Turin as researcher and he has been involved in several national and European projects such as OASIS (On ASymmetry In Sphincters), SAFESPOT (CN IST-4-026963-IP), IRIS (CP-IP 213968-2) coordinating activities and realizing patented devices and prototypes for automotive, structural and biomedical applications.



Manolis HARALABAKIS, Egnatia Odos S. A., Greece (born in 1972) Civil Engineer (Aristotle University of Thessaloniki, 1997). He is head of Geotechnical Instrument Monitoring Team of EGNATIA ODOS S. A., with over ten years of experience in monitoring and team management and published more than ten papers on monitoring case studies. He has work experience in road construction (ERGAS S. A.) and supervision. He has taken part in three European Research projects (OASYS 2003–2006, ΑΣΠΡΟΓΕ 2006–2008, IRIS 2008–2012).



Karl HARNISCH, RWE Power AG, Germany (born in 1951) is an expert in power plant pipe construction. He has successfully participated in the work on rules and regulations in the committees of VGB (European technical association for power and heat generation) and VDI (Association of German Engineers). His vision is to find a health monitoring system that shows the material condition in a pipe system during operation and online for increased plant safety and conservation of natural resources. As an Owner's Engineer he has taken an active part in the design of pipe systems, vessels and equipment in conventional and nuclear power plants for more than 30 years.



Gerd HESINA, VRVis, Austria (born in 1974) has experience in software development in various programming languages for 23 years, experience in 3D visualization projects for 13 years and has been senior researcher and project manager at the VRVis research centre since 2002. He is author and co-author of several internationally refereed scientific papers. In addition to his work at VRVis he is also lecturing at University of Applied Sciences Technikum Wien. He received both his Master degree and his PhD in computer science from Vienna University of Technology.



Michael HICKS is Professor of Soil Mechanics and Head of Geo-Engineering at Delft University of Technology, the Netherlands. His research interests include the statistical characterisation and numerical modelling of soil heterogeneity and assessing its influence on geotechnical performance using finite elements. Focus areas include slope stability and soil liquefaction. He was awarded the Institution of Civil Engineers' Geotechnical Research Medal in 1999 and is Chairman of the Organising Committee for the 8th European Conference on Numerical Methods in Geotechnical Engineering, Delft, 2014.



Falk HILLE, BAM, Germany (born in 1967) has been research associate at BAM, Division 7.2 Buildings and Structures since 2002. He graduated from Technical University Berlin in 1997 and is currently working on his doctoral thesis. His research interests include the development of monitoring strategies and systems for measurement based damage diagnostics and condition assessment of civil engineering structures.



Michaela HÖLLRIGL-BINDER, VCE, Austria (born in 1984) studied Technical Mathematics at Vienna University of Technology from 2002 to 2009. She concentrated on the field of Mathematics in Science and graduated in spring 2009 with the diploma thesis "Mathematical Models Describing Physiological Processes". Michaela Höllrigl-Binder has been working as a research engineer at VCE since June 2009, where she was involved in research and monitoring activities concerning Structural Health Monitoring. In recent times, she is primarily working on sound and vibration protection in infrastructure.



Stanislav HRISTAKIEV, Kozloduy Nuclear Power Plant plc, Bulgaria (born in 1959), head of civil structures section. In his projects public and residential buildings are built. He has participated in the construction of the building sites. As a head of section of building structures in Kozloduy NPP he took part in the development, designing and modernization of nuclear plants in Bulgarian and international projects.



Olivier HUBERT, ELSA, JRC, Italy (born in 1962) is a specialized instrument technician working at ELSA for more than fifteen years in the execution of instrumentation and video setups.



Alexander ILIEV, Risk Engineering Ltd., Bulgaria (born in 1985) is a young expert, specialized in numerical simulation and assessment of structures for external hazards. He has taken part in more than ten commercial projects related to nuclear and hydro power safety and several research projects funded by the European Commission. Since 2012 he has been part-time assistant at the department of "Steel, Timber and Plastic Structures" in UACG Sofia on "Earthquake Resistant Design of Structures". He has ten publications in international conferences.



P. A. JADHAV, BARC, India has been working in the domain of probabilistic fracture mechanics, residual life estimation of flawed components and software development for the past ten years. He has co-authored several technical publications. Currently he works on qualification of components used in nuclear power plants using codes of practices and experiments.



Lars JOHANNES, TUB, Germany (born in 1977) obtained his engineering diploma in surveying and mapping at the Technical University Berlin, Germany, in 2004. From September 2005 to May 2012, he was a research associate at the Institute of Geodesy and Photogrammetry, University of Braunschweig – Institute of Technology, Germany. His research focuses are multi-sensor systems and filtering methods for the robust positioning of objects in indoor and outdoor environments. In 2012 he defended his doctoral thesis entitled "Multisensorsystem und Filterungsansätze zur robusten Ortung von Personen im Innen- und Außenbereich".



Daniel KIESER, ERF Production Würzburg GmbH, Germany (born in 1979; chemist) is responsible for the production and development of electro-rheological (ER) fluids. ERF GmbH is part of Fludicon GmbH, a global leader in the technology of electro-rheological devices for industrial and automotive applications. These applications in mechanical, hydraulic and pneumatic systems range from regulation and control of movements to attenuation, positioning and vibration reduction. Especially vibration reduction can therefore ensure that hazardous states of system resonances can be mitigated.



Dietrich KLEIN, Woelfel, Germany (born in 1947) is an international expert for structural mechanics in civil and mechanical engineering. He is working in static, dynamic and non-linear analysis, especially under earthquake and impact loads. His professional experiences for 30 years are the realistic, non-linear analysis of reinforced concrete structures and probabilistic investigations. He participated at the German Risk Study of Nuclear Power Plants and at different seismic probabilistic safety analyses. Extracts of his work are laid down in numerous publications.



Margit KLOCKER, VCE, Austria (born in 1982) studied Comparative Literature at the University of Vienna. She joined VCE in 2011 as Assistant to Dr. Wenzel with the main focus on the administration of several projects, including Integrated European Industrial Risk Reduction System (IRIS), Network of European Research Infrastructures for Earthquake Risk Assessment and Mitigation (NERA) and SEISMID®. Furthermore she is responsible for translations and revisions of publications, reports and reference material.



Fritz KOPF, VCE, Austria (born in 1967) studied structural engineering at the Vienna University of Technology where he worked as assistant at the Institute for Foundation Engineering and Soil Mechanics and received his PhD in 1999. The academic teaching licence (venia docendi) for soil mechanics was awarded to him in 2011 (TU Vienna, Institute for Geotechnical Engineering). Since 2005 he has worked for VCE and is head of the department Geotechnical Engineering and Natural Hazards. He is member of the European Association for Earthquake Engineering.



Andrea Hilda KOSORUS, JKU, Austria (born in 1986) is a senior researcher at the Institute of Applied Knowledge Processing. She finished her Master Studies and obtained her Master of Science degree in 2010 at the Johannes Kepler University in Linz. During the past two years she published nine papers at well-established conferences and has been working on several scientific projects in the field of recommender systems and fault detection and prediction. Currently, she is writing her doctoral thesis on Temporal Semantic Query Recommendation.



Marin KOSTOV, Risk Engineering Ltd., Bulgaria (born in 1953), expert of IAAE for earthquake engineering and seismic hazard assessment. Head of Earthquake Engineering department at Bulgarian Academy of Sciences. Head of projects for research in wave propagation, structure dynamics, risk analysis, impact analyses, severe accidents, risk mitigation, risk monitoring, risk assessment, elements of risk studies, normative documents, standards and regulations. Participation in more than 20 international site safety review missions. More than 150 scientific reports and papers on seismic risk, structural dynamics and safety evaluation of nuclear installations.



Zdeněk KOUBA, Czech Technical University, Czech Republic is an Associate Professor with the Czech Technical University in Prague. His research interests include design of information and knowledge based systems, data modelling and knowledge representation. He is head of the knowledge-based and software systems group in the department of Cybernetics at the faculty of electrical engineering, Czech Technical University. His team has participated in six international research projects of the European Commission in the last 15 years.



Petr KŘEMEN, Czech Technical University, Czech Republic is a researcher at the knowledge-based and software systems group in the department of Cybernetics, faculty of electrical engineering, Czech Technical University, Prague. His research interests include applications of semantic web technologies in information systems, in particular ontology development, design of information systems based on ontologies, and high-level ontological reasoning services, including ontology comparison (OWLDiff), error explanation and query answering (OWL2Query).



Nicole KRIMS-STEINER, VCE, Austria (born in 1970) studied English and Italian at the Institute for Translation and Interpretation of the University of Vienna. Since 2001 her activities within VCE have mainly focused on the support, administration and accounting of several research projects sponsored by the European Commission, e. g. Integrated European Industrial Risk Reduction System (IRIS), Network of European Research Infrastructures for Earthquake Risk Assessment and Mitigation (NERA) and SYNER-G as well as the translation and revision of publications, reports and reference material.



Pierre LABBÉ, EDF, France (born in 1951) is the EDF most senior expert in seismic risk management, covering fields of seismic hazard as well as of structures, systems and components. His position is at the headquarters of the EDF Nuclear Engineering Division. He is Professor of Structural Dynamics, Soil Dynamics and Earthquake Engineering in Master Degrees of Lyon University and ParisTech (Paris Institute of Technology). His fields of research are relating to stochastic processes and non-linearity effects in earthquake engineering. He is Honorary President of the French Association for Earthquake Engineering.



Rui LIMA, VCE, Austria (born in 1987 in Portugal) studied at the University of Minho where he got his MSc degree in Structural and Geotechnical Engineering. He also did an exchange semester at the Czech Technical University in Prague. In 2011 he joined VCE after finishing his education and has been working both in research and commercial projects. He has been mainly focused on the Life Cycle Analysis of civil infrastructures.



Eva LOUKOGEORGAKI, AUTh, Greece (born in 1979) is a lecturer at the Department of Civil Engineering of AUTh. She has shown successful and continuous research activities in the subject of marine structures. Her research interests include fluid-structure interaction, analysis of offshore structures (floating and fixed bottom) and of novel coastal structures, offshore wind turbines, risk assessment and structural health monitoring of marine structures. She has published more than 20 papers in journals and conferences, while she holds international distinctions.



Tzvetomir MARINOV (born in 1964), head of Department of Hydraulic Installation and Construction Works Kozloduy Nuclear Power Plant plc, Bulgaria, has more than 25 years of experience in the field of hydraulic engineering and water supply, the past 14 of which were spent working for Kozloduy NPP. He has taken part in projects involving engineering and construction of hydraulic and water supply installations. His main task is to monitor and maintain the structural health of such installations. He is also in charge of geodesic and seismic-related activities.



Kamil MATOUŠEK, ČVUT, Czech Republic (born in 1973) is a researcher in artificial intelligence, he published papers on knowledge-based systems, ontology engineering, temporal reasoning, social network portals, healthcare information systems, and data warehousing. He reads lectures on systems with artificial intelligence and information and knowledge-based systems. He is a programme committee member and reviewer at international scientific conferences. He participated at several European as well as local projects. He is a member of the Gerstner laboratory at Czech Technical University in Prague.



Georgios MEDITSKOS, CERTH, Greece received the PhD degree in computer science in 2009 from the Department of Informatics, Aristotle University of Thessaloniki, Greece. He also holds an MSc and a BSc degree from the same department. His research interests include Knowledge Representation and Reasoning in the Semantic Web (RDF/OWL, rule-based ontology reasoning, combination of rules and ontologies) and Semantic Web Services (discovery, composition). Since January 2012 he has been working as a postdoctoral research fellow at the Informatics and Telematics Institute (ITI) of the Center for Research and Technology, Hellas (CERTH).



Laurent MEVEL, INRIA, France is an expert in system identification and change detection for signals and systems. He has published on structural health monitoring and worked and developed algorithms for structural identification for ten years. His interests include: structural health monitoring, monitoring and detection for vibration mechanics, modelling and rejection of environmental effects, model validation and uncertainty estimations and model reduction of large systems. He has published over 30 journal papers and around one hundred conference papers. He is organizer of the EWSHM conference in 2014. He was part of FP7 IRIS and ISMS projects.



Bianca Mick, VCE, Austria (born in 1976) has been working as graphic designer for VCE since 1995 and is responsible for the corporate identity of VCE. Her main tasks are logo design for a coherent and harmonious company presentation as well as the development and design of print media like image brochures, folders, posters and books, above all the design and realization of the book "Erdbeben im Wiener Becken". Since 2001 Ms. Mick has been also responsible for VCE's web design. She implemented the web site of the company as well as of several research projects and company cooperations.



Francisco Javier MOLINA, ELSA, JRC, Italy (born in 1961) has worked in the field of Structural Mechanics in the University in Spain. Since 1995 his work has been dedicated to the execution of experiments in the ELSA Reaction Wall. He has developed advanced testing methods as well as data treatments for identifying the properties of the experimental models or assessing the reliability of the performed tests.



Wolfgang NIEMEIER, TU Braunschweig, Germany (born in 1949) is an internationally well-established expert in engineering geodesy, known for his developments on new sensors and methodologies. He is chairing a series of international symposia on deformation monitoring and wrote a successful textbook on adjustment theory and computations (2008). His research projects cover topics like determination of tectonic movements, modelling the behaviour of bridges with neural networks, concepts for continuous monitoring systems, terrestrial laser-scanning and radar interferometry for construction sites.



Plamen NIKOLOV, VCE, Austria was born in Veliko Tarnovo, Bulgaria in 1981. He studied civil engineering in Sofia. Since 2007 he has been working for VCE. In these years he has been working especially with FEM software for static and dynamic problems of transportation infrastructure (bridges) and buildings.



Jonathan NUTTALL, TU Delft, the Netherlands (born in 1981) is a Research Assistant in Geo-Engineering and Soil Mechanics. He completed his PhD entitled "Parallel Implementation and Application of the Random Finite Element Method" in 2011 and has over ten years of experience in numerical modelling and geotechnical analysis. His research interests include stochastic, probabilistic and risk analysis for geotechnical applications, inverse modelling, the statistical characterisation and numerical modelling of soil heterogeneity, large scale slope stability analysis, and numerical modelling using High Performance Computing and advanced technologies.



Panagiotis PANETSOS, Egnatia Odos S.A., Greece (born in 1965). He received the PhD degree in Structural Dynamics in 1998 from Aristotle University of Thessaloniki, Greece. Head of Structural Health Monitoring and Maintenance Discipline (Egnatia Odos S.A.). 10 years of experience in development and application of ambient vibration monitoring on motorway and railway bridges in Greece and in Balkans. 22 years of experience in design and supervision of buildings, bridges as well as of monuments' restoration. 11 years of teaching Reinforced/Prestressed Concrete and Statics courses in universities of Thessaly and West Macedonia, Greece (visitor ass. professor).



Antal PAPP, DTCDM, Hungary fire fighter colonel (born in 1957), is the director of the Disaster Management Training Centre, Ministry of the Interior, Budapest. As a practical and theoretical specialist for 30 years he has been working in the field of industrial and natural disaster prevention, release and reconstruction. Among others he participated in the mitigation of the flood (2001) and the cyanide poisoning (2002) of the Tisza River and the red sludge disaster in Hungary (2010). He is the author, co-author and specialist of several books and notes.



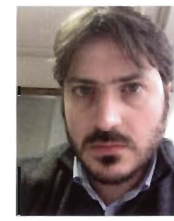
Yogita Mahendra PARULEKAR, PhD in Civil Engineering, has been working as Scientific Officer in BARC, India (since 1997). She has been involved in design and analysis of nuclear facility structures. She has done significant contributions in seismic response control of structures and seismic qualification of equipments using analyses and experiments. She has published about 70 technical papers



Patrick PETIT, ELSA, JRC, Italy (born in 1962) is a specialized software engineer working at JRC for more than twenty years. He joined ELSA in 2006 where he is in charge of the hardware and software development and maintenance of controllers and electronics used for the experiments.



Robert PRETHALER, Aplica, Austria (born in 1965) is an experienced developer of data acquisition systems and monitoring software. With GreenEye he designed and developed a popular visualization tool for all kinds of measurement and monitoring data. He is the co-founder of Aplica Advanced Solutions where he is responsible for the research and development team. In several national and international research projects on structural health monitoring he could help to substantially improve the data acquisition and data processing issues.



Antonino QUATTRONE, Politecnico di Torino, Italy (born in 1978) is currently post-doc research fellow at the Department of Structural, Geotechnical and Building Engineering at Politecnico di Torino, where he got the PhD in Structural Engineering in 2012. His present research topics are in the fields of structural dynamics, structural health monitoring and seismic engineering. He is author of about 20 publications on international journals and conference proceedings.



Rohit RASTOGI, BARC, India has been contributing in the domain of Structural Reliability, Fitness for Service Assessment of flawed components and Software Development for the past 18 years. He has co-authored more than 50 technical publications including book chapters. Currently his research interests are in the areas of Development of Partial Safety Factors for Fitness for Purpose Codes, Modelling of Flow Accelerated Corrosion and System Identification using Markov Chain Monte Carlo Methods.



G. Rami REDDY is Head of the Structural and Seismic Engineering Section in BARC, India and Professor, HBNI. Since 1984 he has been working in the area of earthquake engineering. He has made significant contributions in design of reactor buildings and executed large number of requalification and life extension projects related to nuclear facilities. For the purpose of life extension of the existing facilities of the Department of Atomic Energy he evolved methods for performing seismic retrofitting of structures, systems and components. He has more than 285 publications to his credit.



Anton RIEDER, BBT SE, Austria, gained substantial experience in experimental research and development in his capacity as head of a mechanical testing laboratory. Within the EOTA Working Group "Anchors" he was technical advisor regarding the development of new seismic testing procedures to be implemented in the ETAG 001. He was corresponding member of the fib Special Activity Group 4 responsible for the preparation of bulletin 58 (published 2011). Since 2010 he has been coordinator for research at BBT SE in the field of tunnel engineering with special emphasis on sustainable planning of transportation infrastructure.



Werner RÜCKER, BAM, Germany (born in 1949), holds a PhD in Civil Engineering. He defended his thesis about propagation of ground vibrations in 1979. His research topics include prediction and reduction of traffic induced ground vibrations, SHM of civil engineering structures including offshore wind turbines, dynamic analysis and vibration based assessment of structural conditions, load carrying behaviour of steel pile foundations for offshore wind turbines and pile-ground interaction. Since 1996 he has been head of BAM, Division 7.2: Buildings and Structures.



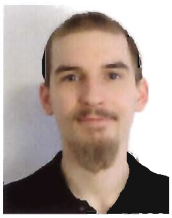
Eleni SAKOUMPENTA, Egnatia Odos S.A., Greece, holds a Civil Engineering degree from Aristotle University of Thessaloniki and an MSc degree from University of California at Davis. She has worked as a Geotechnical Engineer for over 15 years in the Egnatia Motorway project in Greece. She served as Geotechnical Discipline Head dealing with geotechnical challenges in engineering solutions for the crossing of the motorway through mountainous, geologically complex and unstable terrain. She has been involved in the evaluation of geotechnical monitoring data in landslide areas and contributed in the landslide risk assessment and management of the company.



David SCHÄFER, VCE, Austria (born in 1984) started to study Technical Physics at the Vienna University of Technology in 2003. After receiving his diploma in 2009 he started to work at VCE as project engineer in the field of natural hazards and geotechnical engineering. His activities include earthquake simulations, damage predictions and system identification as well as soil dynamics. The focus of his work now is on earthquake engineering.



Dionysius SIRINGORINGO, University of Tokyo, Japan (born in 1976) is a research assistant professor in the Bridge and Structure Division, University of Tokyo. He obtained his doctoral degree from University of Tokyo in 2005 and fellowship from Japan Society of Promotion of Science in 2007. His research interests are in bridge engineering, structural health monitoring, earthquake and wind engineering. He has been involved in many long-span bridge monitoring projects in Japan including ambient and strong wind-induced vibration of Hakucho Suspension Bridge, and a series of long-span bridge seismic monitoring in Tokyo metropolitan expressway.



Erik SONNLEITNER, JKU, Austria (born in 1984) is Senior Scientist at the Institute for Application-Oriented Knowledge Processing. He studied Networks & Security and is currently focusing on digital distortive watermarking strategies in information systems, wherein he published various articles on and writes his doctoral thesis about. His interests and research topics cover system, network and application-security in general, and steganographic approaches on volatile data carriers in particular.



Angela STANCA (born in 1955), Senior Researcher, Head of Environment Department from Energy Research and Development Institute, ICEMENERG, Romania is a reputed researcher recognized in the university environment, in the field of research, as well as in the industrial environment of the energy system. She has expertise in environmental risk, water chemistry, soil and air. She is member of EURACHEM Association, Balkan Environmental Association, Romanian National Committee of World Energy Council and Water Romanian Association. She published 10 papers in ISI journals and 50 articles in other scientific publications. She is the author of five patents.



Martin STÖGER, VCE, Austria (born in 1971) has been working for VCE since 2000. He has worked in the field of ambient vibration monitoring from the very beginning and started the development of a wireless, highly portable dynamic monitoring equipment. In the last few years the branch of permanent monitoring solutions became more and more important. Based on the power of the internet a web-based platform was developed allowing online access to monitoring data and monitoring results of structures spread all over the world.



Reinhard STUMPTNER, JKU Linz, Austria (born in 1977) is senior researcher in data management and machine learning at the Institute for Application-Oriented Knowledge Processing. Since 2007 one of his focuses has been the application of these techniques in the area of structural health monitoring. Moreover, he has experience in interpreting spatial-temporal data and in data warehousing. Reinhard Stumptner published various articles on the application of machine learning in the area of structural health monitoring.



Alexandros TAFLANIDIS, University of Notre Dame, USA (born 1979) holds a Civil Engineering degree and an MSc degree from the Aristotle University of Thessaloniki, Greece and a PhD from Caltech, USA. He is an Associate Professor at the University of Notre Dame, and the Director of the High Performance System Analysis and Design Laboratory. His work focuses on risk assessment/mitigation, with emphasis on the impact of natural hazards in communities in developed and developing countries. His work has been recognized internationally with several awards.



Hiroshi TANAKA is an expert in Structural Dynamics and Wind Engineering. After receiving his PhD from the University of Tokyo, he joined the Boundary Layer Wind Tunnel Laboratory of the University of Western Ontario. After this experience, he joined the Faculty of Engineering at the **University of Ottawa, Canada** in 1979, where he carried out teaching, research and administrative duties including Chair of Civil Engineering and Director of Ottawa-Carleton Institute for Civil Engineering. He is a well-recognized expert in the field of Wind Engineering, particularly in Bridge Aerodynamics, and has published over 200 scientific papers, engineering reports and articles.



Barbara THEILEN-WILLIGE (born in 1952) is working in the **Bureau of Applied Geoscientific Remote Sensing (BAGF), Germany**, and is lecturing "Geoscientific Remote Sensing and GIS-Applications" at the TU Berlin, Institute of Applied Geosciences. She is consulting in the fields of remote sensing and Geo Information Systems (GIS) and has about 40 years of experience in the fields of geomorphologic and geologic evaluation of satellite and aerial imageries for the detection of areas exposed to natural hazards. Prof. Dr. Theilen-Willige is author and co-author of about 115 articles and book publications.



Sebastian THÖNS (born in 1975) is a research associate at **BAM**, Division 7.2., **Germany**. He received his PhD in 2011 from ETH Zurich. At BAM, Sebastian Thöns has been responsible for the new founded research field SAFEINFRA: Risk and Reliability of Infrastructures and Wind Turbines since 2011. His major research interests comprise risk analysis, reliability analysis and structural integrity management in the whole Life Cycle of infrastructures aiming at the explication of technological knowledge relevant for decision making in business economics and macroeconomics.



Keshav Krishna VAZE, BARC, India obtained his B.Tech. degree in Mechanical Engineering and joined 17th batch of BARC Training School. After graduation he joined the Nuclear Systems Division of Indira Gandhi Centre for Atomic Research and the Reactor Safety Division of BARC, Mumbai. His current fields of work include design and detailed engineering of advanced heavy water reactor, reactor safety, earthquake engineering, fatigue and fracture analysis, experimental stress analysis, fitness-for-purpose evaluation, residual life estimation and life extension. At present he holds the post of Director, Reactor Design & Development Group in BARC.



Robert VEIT-EGERER, VCE, Austria (born in 1978). After achieving his MSc in Civil Engineering at the Vienna University of Technology he joined the R&D group of VCE in 2003. Today he is Head of the "Asset Management & BRIMOS" Department which is constantly involved in international consulting and research projects. His list of publications comprises more than 100 records, including book and journal publications, conference papers etc. – representing ten years of worldwide experience in the fields of Structural Assessment, Structural Health Monitoring and Life Cycle Management of infrastructure.



Bernard VIACCOZ, ELSA, JRC, Italy (born in 1950) is a mechanical engineer with long experience in instrumentation. Since his arrival in ELSA in 1999 he has been in charge of the mechanical designs in the laboratory. He also coordinates the preparation and execution of the experimental setups. He is responsible for the hydraulic devices used in the experiments.



Dimitris VRAKAS, AUTh, Greece (born in 1977) is a lecturer at the Department of Informatics at the Aristotle University of Thessaloniki, Greece. He has taught undergraduate and postgraduate courses on Programming, Artificial Intelligence and Robotics at the Aristotle University, the University of Macedonia and the University of Thessaly. His research interests include Artificial Intelligence, Web Services and Automated Planning. He has published more than 40 papers in journals and conferences and co-edited two international books.



Bianca WEIHNACHT, Fraunhofer IZFP Dresden, Germany works in the field of Structural Health Monitoring and is responsible for the development of monitoring techniques for steel structures like pipes and containers. Her main research interests are guided waves techniques like acoustic emission or acousto ultrasonics.



Felix WENZEL, VCE, Austria (born in 1988) has successfully passed an engineering college (HTL) in mechatronics. He is currently master student of civil engineering at the University of Applied Sciences in Vienna. He has been involved in VCE's monitoring activities for several years and actively participates in various campaigns.



Monika WIDMANN, VCE, Austria achieved her MSc in Environmental Engineering at the University of Natural Resources and Life Sciences in Vienna and joined the R&D group of VCE in 2007. Today she is Senior Consultant in the Department "Asset Management & BRIMOS© Structural Health Monitoring". Her field of experience covers professional consulting applications worldwide and participation in national and European research projects.



Mengxi WU, IMECH CAS, China (born in 1967) is one of the Chinese top experts in numerical analysis of hydraulic and geotechnical engineering. He has been working for the numerical simulations of the seepage, stress and deformation of soils and slope stability for over 20 years. He has published research papers on underground flows, constitutive model of soils and slope stability, and developed corresponding software.



Yiannis XENIDIS, AUTh, Greece (born in 1974) is a Faculty member at the Department of Civil Engineering at the Aristotle University of Thessaloniki (AUTh). He has published more than 30 peer-reviewed papers in international journals and conferences, while he has contributed with invited chapters to six books and has edited two special issues in international journals as a guest editor. He has also acted as a member of scientific committees in several international conferences. His current research interests and activities focus on resilient infrastructure systems, Life Cycle Risk Management and decision-making theory



Antonio ZORZAN, ELSA, JRC, Italy (born in 1963) is a specialized mechanical technician working at ELSA for more than twenty years in the execution of experimental setups and management and maintenance of laboratory tool machines.

32 Index

3D finite element model *472*

A

ABAQUS *189*
abutment *494*
acceleration measurement *113*
accelerometer *115, 172*
acoustic measurement system *297*
acousto ultrasonics *295*
active vibration absorber *280*
actuator *284*
adaptivity *148*
ADINA Finite Element package *111*
ageing *558*
aggregate *388*
agronomic rate *380*
alignment *494*
ambient vibration *113*
ambient vibration monitoring *505, 583*
ambient vibration test *307*
anisotropic field *533*
ANSYS *472*
arch bridge *540*
assessment *543, 558*
ASTER *243*
ASTER Global Digital Elevation Model *242*
auto-spectra *325*

B

back analysis *499*
biological degradation *391*
blasting *541*
Bootstrap method *313*
borehole *495*
boxplot *68*
BRIMOS® *355, 583*
BRIMOS® measurement system *102*
building structural damage *269*

C

cable force *517*
cable-stayed bridge *516*
carbon *385*
Casagrande *495*
cash flow *81*
cation *388*
cation exchange capacity *388*
causal factor *244*
centre of rotation *413*
centroid *62*
chemical degradation *392*
communication system *338*
competitiveness *7*
complete failure *215*

concrete cracking *226*
condition *558*
Cone Penetration Tests (CPT) *530*
Consequence-based Risk Management (CRM) *258*
consequence model *86*
containment structure *568*
control system *128*
cost model *86*
counterweight *495*
create scenario earthquake *267*
cyclic loading *590*
cyclic quasi-static load *217*

D

damage detection *306, 324*
damage detection algorithms *128*
damage distribution *504*
damage estimate *504*
damping *227*
damping ratio *91, 174, 182*
Darcy equation *197*
data management system *477*
Decision Support System *354*
deck measurement *519*
degradation *558*
degradation index *390*
degrees of freedom *153*
descent difference scheme *206*
design data *79*
design life *7, 558*
design solution *127*
design study *177*
destructive test *109, 307*
deterministic method *202*
de-trending data *530*
Differential Global Navigation Satellite System (DGNSS) *336*
digital barometer *337*
Digital Elevation Data (DEM) *624*
digital image processing *620*
dilatation coefficient *135*
disaster management *257*
dispersion curve *408*
drainage tunnel *495*
ductility ratio *231*
durability *558*
dynamic measurement *457, 516, 543*
dynamic response *424*
dynamic risk analysis *26*
dynamic testing *113*
dynamic vibration absorber *168*

E

earthquake-damage *525*
eigenfrequency *177*
eigenmode *177*
electrical conductivity *383*
electro-dynamic shaker *119*
electro-mechanical shaker *113*
electronic distance meter *481*
energy dissipation *170*
equation of motion *59*
EQvis *251, 257*
ESRI-geodata *243*
event tree *83*
excitation model *28, 499*
exponential correlation model *531*
exponential Markov covariance function *532*

F

factor of safety of a slip surface *203*
FEM tool *189*
fibre optic *116*
fibre optic deformation sensor *131*
finite element *169*
finite element algorithm *197*
Finite Element Method *31, 420*
Finite Element Model (FEM) *309, 583*
Finite State Control Strategy *154*
fluctuation *529*
flume test *109, 111*
flux boundary *198*
forecasting *370*

Fourier-transformation *300*
fragility curve *269*
framework *151*
frequency *174*
frequency shift *188*

G

Gaussian numerical method *203*
Geographic Information Systems (GIS) *237, 612*
GIS *242*
GNU Octave *369*
Google Earth *243*
gross traffic mass *484*
groundwater table *494, 497*

H

Hankel matrix H *94*
health index *447*
heavy metal *393*
heuristic approach *202*
Hilbert-transformation *300*
horizontal displacements *598*
H/V-method *407*

I

identification algorithm *93*
impact hammer *113, 169*
inclinometer *495, 499*
Inertial Measurement Unit (IMU) *338*
inner seepage face *199*
inorganic carbon *386*
inspection tool *139*
integration model *366*
intervention analysis *371*
IRIS *7*
IRIS Risk Paradigm *12*

J

joint displacement *33*

K

Key Performance Indicator *519, 543*
knowledge base *359*

L

land degradation *389*
LANDSAT *243*
landslide *493*
lateral displacement *598*
level sensing station *469*
Life Cycle *558*
Life Cycle Assessment *445*
Life Cycle Cost-Benefit Analysis *81*
Life Cycle Risk *34*
limit equilibrium analysis *498*
limit equilibrium method *202*
limit state *505*
linear-time-invariant system *92*
load-bearing structure *540*
load-displacement curve *226*
loading system *218*
Local Average Subdivision (LAS) method *531*
local wall thinning *176*
lognormal probability distribution function *508*
lognormal standard deviation *509*
low-rise shear wall *593*
low-rise wall *214*

M

MAEviz *258*
Mahalanobis squared distance *325*
maintenance strategy *448*
MATLAB *369, 478*

meandering river *254*
mediator system *360*
meta-heuristic *154*
mid-rise shear wall *592*
modal parameter *186*
modulus of subgrade reaction *417*
monitoring benefit *83*
monitoring data *77*
monitoring technology *41*
monotonic loading *598*
Monte Carlo framework *534*
Morison equation *32*
morphometric maps *624*
Mualem's unsaturated relative permeability function *197*
MySQL database *478*

N

Navier-Stokes equation *60*
Neumann boundary *198*
new knowledge *11*
nitrogen *385*
noise effect *120*
non-linear characteristic *58*
nuclear power plant safety *568*
numerical model *27, 109*

O

offshore wind park *76*
online monitoring *12*
online monitoring system *294*
ontology *356*
open-street-map *243*
operability *540*
organic carbon *387*
outlier analysis *120*
outlier detection *305, 324*
ovalization *180*

P

pattern recognition *12*
performance anomalies *483*
performance evaluation model *28*
permanent vibration monitoring system *573*
pH *383*
phase correction *300*
physical degradation *390*
phytostabilization *398*
piezometer *499*
pore pressure *496*
positioning sensors *334*
post-tensioning tendon system *568*
power-spectra-density *312*
prestressed concrete *424*
probabilistic analysis *503*
probabilistic method *447*
probability density function *529*
probability model *28*
probability of detection *139*
probability of false alarm *139*
process control *371*
progressive damage test *424*
pseudo-static cyclic loading *598*
purity factor *379*

Q

quantification *23*

R

Radio-Frequency Identification (RFID) *337*
radio waves *344*
random field theory *531*
Random Finite Element Method (RFEM) *533*
RapidEye *614*
RapidEye satellite data *619*
Real-time Location System (RTLS) *344*
Receiver Operating Characteristic *141*
redox potential *383*

redundancy *149, 437*
reference state *132*
rehabilitation *559*
reliability-risk *34*
remote sensing *237*
renewable energies *88*
reservoir *196*
residual lifetime *450, 459*
resonance test *119*
response spectrum *184*
return period *504*
Reynolds and Keulegan-Carpenter number *32*
Richards' equation *197*
risk *7, 534*
risk assessment *11, 12, 23, 494*
Risk Assessment Tool (RAT) *26, 27*
risk-based decision making *42*
risk identification *12*
Risk Identification Methodology (RIM) *25*
Risk Inventory (RI) *25*
risk management *257*
Risk Monitoring and Control System (RIMOCOS) *26*
Risk Ontology *46*
Risk Paradigm methodology *494*
Risk Prevention and Mitigation Strategy (RIPREMIS) *27*
risk quantification *23*
risk reduction strategy *257*
robotic total station *481*
root mean square *311*
routine assessment *355*
R programming language *369*

S

safety factor *379, 497*
safety of workers *332*
safety policy *7*
sampling rate *71*
scour *107*
seepage face *199*
seepage simulation *196*
seismic fragility curve *501*
seismic hazard model *501*
seismic risk *500*
semantic data *357*
sensitivity analysis *30*
sensor *469*
service life *83*
service life prediction *559*
shake map *627*
shaking intensity *503*
shear capacity *229*
shear strength *203, 497*
shear wall *214, 591*
shear wave velocity *626*
shear wave velocity profile *408*
shift function *300*
SHM system *477*
singular value decomposition *313*
site condition *239*
slope failure *498*
slope stability analysis *196*
soil erosion *395*
soil-structure-interaction *405*
spectral density function *61, 575*
spectral distribution function *62*
spectrogram *315*
spread footing *495*
stabilization diagram *95*
standard deviation *504*
standardization *12*
state space model *281*
stick-slip effect *191*
stiffness method *418*
stochastic simulation *29*
Stochastic Subspace Identification method *93*
Stokes wave theory *32*
strain deformation *113*
strain gauge *115, 469*
stress ratio *33*
stress state *154*
stress-strain relation *597*
structural assessment *516*
structural behaviour *541*

Structural Health Monitoring *120, 124, 354, 424, 445*
structural integrity *426, 525*
structural monitoring system *469*
structural reliability *79*
structural reliability analysis *84*
structural response *58*
structural safety *540*
subsurface erosion *196*
sulphur *384*
support structure *84*
surrogate model *34*
suspension bridge *467*
system identification *444, 541*

T

tailing pond *376*
temperature *469*
terrain feature *242*
texture *388*
theodolite *481*
thermo-elastic strain *137*
thick shear wall *214*
time series *370*
topology *154*
total positioning system *481*
total safety *11*
toxic cloud *615*
transducer *172*
transfer function *370*
treatment *559*
triggering mechanism *244*
tuned mass damper *167*
turbulent fluid flow *59*

U

ultrasound-system *344*
Ultra-Wide Band (UWB) *336*
uncertainty propagation *96*

V

Vandermonde-matrix *299*
Van Genuchten's equation *197*
variable geometry structure *151*
vegetation cover *395*
vertical displacement *598*
vertical load *222*
vibrating wire piezometer *495*
vibration measurement *187*
vibration monitoring *306*
Virtual Force Density Method *154*
visual inspection *424, 445*
von Mises stress *178*
vulnerability function *504*

W

warning system *345*
web-interface *478*
Weighted-Overlay for Soil Amplification Detection (WOSAD) *247*
wind sensor *469*
wireless sensor network *481*
WWER-1000 Reactor Building *569*

Imprint

Publisher:
VCE Vienna Consulting Engineers ZT GmbH, Hadikgasse 60, 1140 Vienna, Austria
www.vce.at

Overall direction: Prof. Dr. Helmut Wenzel
Design: Ing. Bianca Mick
Organization: Mag. Margit Klocker
Editor: Mag. Nicole Krims-Steiner
Printed by: GRASL Druck & Neue Medien GmbH, www.grasl.eu

The texts and figures were very carefully composed, however, errors cannot be completely excluded. The authors are responsible for the contents of their respective chapters. VCE has tried to find all holders of copyrights. Should any further rights verifiably exist please contact VCE.

© 2013 by VCE Vienna Consulting Engineers ZT GmbH, Vienna
ISBN 978-3-200-03179-1

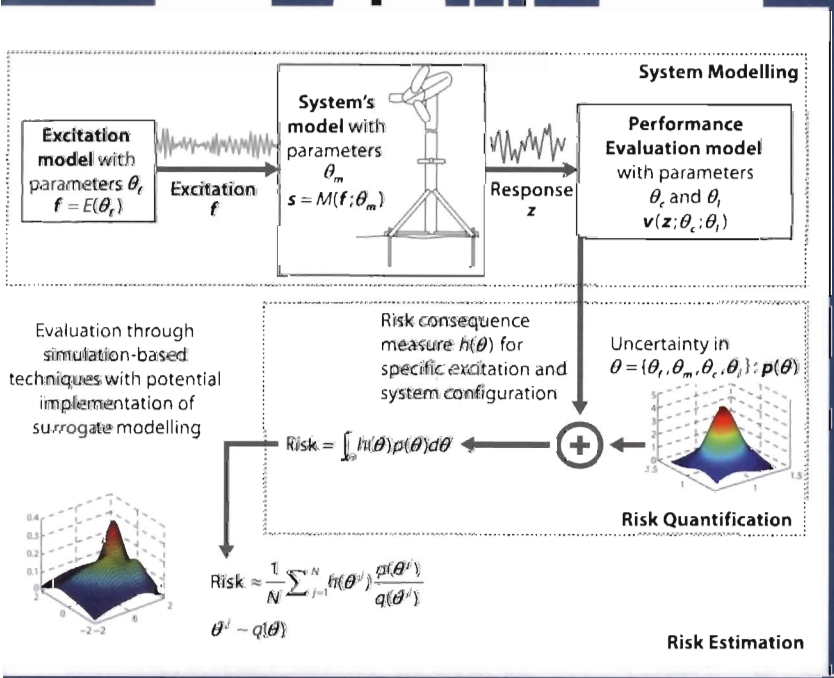
For European Industry, Consultants and Scientists in Industrial Safety and Life Cycle Engineering

Technologies have been developed for a competitive and sustainable European industry. This book reports about the state of science and technology in **Industrial Safety** and **Life Cycle Engineering**. It covers the following content:

- / The new IRIS risk paradigm for industrial risk management
- / Life Cycle Engineering for condition assessment and extension of lifetime
- / Methodologies for risk identification, assessment and control
- / Knowledge and technologies for the quantification of risk and its respective reduction
- / Online monitoring and decision support systems to reduce uncertainties in the process
- / Pattern recognition in signal processing for monitoring of key performance indicators
- / A standardized degradation law and application to various case studies

Innovations that will allow operating Europe's industry in a safer but as well more economic process are presented.





9 783200 031791